frontiers | Research Topics

Oceanographic processes linking nearshore, continental shelf, and shelf break

Edited by
Kuoping Chiang, Wei-Jen Chen, Hiroaki Saito, Chin-Chang Hung, Toru Kobari and William Savidge

Published in
Frontiers in Marine Science



FRONTIERS EBOOK COPYRIGHT STATEMENT

The copyright in the text of individual articles in this ebook is the property of their respective authors or their respective institutions or funders. The copyright in graphics and images within each article may be subject to copyright of other parties. In both cases this is subject to a license granted to Frontiers.

The compilation of articles constituting this ebook is the property of Frontiers.

Each article within this ebook, and the ebook itself, are published under the most recent version of the Creative Commons CC-BY licence. The version current at the date of publication of this ebook is CC-BY 4.0. If the CC-BY licence is updated, the licence granted by Frontiers is automatically updated to the new version.

When exercising any right under the CC-BY licence, Frontiers must be attributed as the original publisher of the article or ebook, as applicable.

Authors have the responsibility of ensuring that any graphics or other materials which are the property of others may be included in the CC-BY licence, but this should be checked before relying on the CC-BY licence to reproduce those materials. Any copyright notices relating to those materials must be complied with.

Copyright and source acknowledgement notices may not be removed and must be displayed in any copy, derivative work or partial copy which includes the elements in question.

All copyright, and all rights therein, are protected by national and international copyright laws. The above represents a summary only. For further information please read Frontiers' Conditions for Website Use and Copyright Statement, and the applicable CC-BY licence.

ISSN 1664-8714
ISBN 978-2-83251-540-2
DOI 10.3389/978-2-83251-540-2

About Frontiers

Frontiers is more than just an open access publisher of scholarly articles: it is a pioneering approach to the world of academia, radically improving the way scholarly research is managed. The grand vision of Frontiers is a world where all people have an equal opportunity to seek, share and generate knowledge. Frontiers provides immediate and permanent online open access to all its publications, but this alone is not enough to realize our grand goals.

Frontiers journal series

The Frontiers journal series is a multi-tier and interdisciplinary set of open-access, online journals, promising a paradigm shift from the current review, selection and dissemination processes in academic publishing. All Frontiers journals are driven by researchers for researchers; therefore, they constitute a service to the scholarly community. At the same time, the *Frontiers journal series* operates on a revolutionary invention, the tiered publishing system, initially addressing specific communities of scholars, and gradually climbing up to broader public understanding, thus serving the interests of the lay society, too.

Dedication to quality

Each Frontiers article is a landmark of the highest quality, thanks to genuinely collaborative interactions between authors and review editors, who include some of the world's best academicians. Research must be certified by peers before entering a stream of knowledge that may eventually reach the public - and shape society; therefore, Frontiers only applies the most rigorous and unbiased reviews. Frontiers revolutionizes research publishing by freely delivering the most outstanding research, evaluated with no bias from both the academic and social point of view. By applying the most advanced information technologies, Frontiers is catapulting scholarly publishing into a new generation.

What are Frontiers Research Topics?

Frontiers Research Topics are very popular trademarks of the *Frontiers journals series*: they are collections of at least ten articles, all centered on a particular subject. With their unique mix of varied contributions from Original Research to Review Articles, Frontiers Research Topics unify the most influential researchers, the latest key findings and historical advances in a hot research area.

Find out more on how to host your own Frontiers Research Topic or contribute to one as an author by contacting the Frontiers editorial office: frontiersin.org/about/contact

Oceanographic processes linking nearshore, continental shelf, and shelf break

Topic editors

Kuoping Chiang — National Taiwan Ocean University, Taiwan
Wei-Jen Chen — National Taiwan University, Taiwan
Hiroaki Saito — The University of Tokyo, Japan
Chin-Chang Hung — National Sun Yat-sen University, Taiwan
Toru Kobari — Kagoshima University, Japan
William Savidge — University of Georgia, United States

Citation

Chiang, K., Chen, W.-J., Saito, H., Hung, C.-C., Kobari, T., Savidge, W., eds. (2023). *Oceanographic processes linking nearshore, continental shelf, and shelf break*. Lausanne: Frontiers Media SA. doi: 10.3389/978-2-83251-540-2

Table of contents

07 Editorial: Oceanographic processes linking nearshore, continental shelf, and shelf break
Feng-Hsun Chang, Yun-Chi Lin, Kuo-Ping Chiang, Ya-Han Nien, Chih-hao Hsieh, Wei-Jen Chen, Chin-Chang Hung, Toru Kobari, Hiroaki Saito and William Savidge

13 Community Assembly Processes as a Mechanistic Explanation of the Predator-Prey Diversity Relationship in Marine Microbes
Feng-Hsun Chang, Jinny Wu Yang, Ariana Chih-Hsien Liu, Hsiao-Pei Lu, Gwo-Ching Gong, Fuh-Kwo Shiah and Chih-hao Hsieh

25 Phytoplankton Increase Along the Kuroshio Due to the Large Meander
Daniel Andres Lizarbe Barreto, Ricardo Chevarria Saravia, Takeyoshi Nagai and Takafumi Hirata

40 Impact of Ship Traffic on the Characteristics of Shelf Sediments: An Anthropocene Prospective
Chengfeng Xue, Yang Yang, Peipei Zhao, Dongyun Wei, Jianhua Gao, Peng Sun, Zhiyang Huang and Jianjun Jia

56 Surface-Layer Circulations in Suruga Bay Induced by Intrusions of Kuroshio Branch Water
Takahiro Toyoda, Kei Sakamoto, Norihisa Usui, Nariaki Hirose, Kiyoshi Tanaka, Takaaki Katsumata, Daisuke Takahashi, Masato Niki, Kunio Kutsuwada, Toru Miyama, Hideyuki Nakano, L. Shogo Urakawa, Kensuke K. Komatsu, Yuma Kawakami and Goro Yamanaka

76 Dynamics of Nutrients and Colored Dissolved Organic Matter Absorption in a Wetland-Influenced Subarctic Coastal Region of Northeastern Japan: Contributions From Mariculture and Eelgrass Meadows
Tomonori Isada, Hiroya Abe, Hiromi Kasai and Masahiro Nakaoka

95 On the Advection of Upwelled Water on the Western Yucatan Shelf
Jorge. A. Kurczyn, Rodrigo Duran, Emilio Beier and Alejandro J. Souza

109 Land-Ocean Interaction Affected by the Monsoon Regime Change in Western Taiwan Strait
Rick J. Yang, James T. Liu, Chih-Chieh Su, Yi Chang, Jimmy J. Xu and Hon-Kit Lui

125 Shelf Transport Pathways Adjacent to the East Australian Current Reveal Sources of Productivity for Coastal Reefs
Moninya Roughan, Paulina Cetina-Heredia, Nina Ribbat and Iain M. Suthers

139 Reoxygenation of the Hypoxia in the East China Sea: A Ventilation Opening for Marine Life
Chung-Chi Chen, Dong S. Ko, Gwo-Ching Gong, Chun-Chi Lien, Wen-Chen Chou, Hung-Jen Lee, Fuh-Kwo Shiah and Yu-Sin Wita Huang

154 Primary Productivity in the Mid-Atlantic Bight: Is the Shelf Break a Location of Enhanced Productivity?
Jiejie Ma and Walker O. Smith Jr.

168 Effects of the Coastal Uplift on the Kuroshio Ecosystem, Eastern Taiwan, the Western Boundary Current of the North Pacific Ocean
Chung-Chi Chen, Chun-Yi Lu, Sen Jan, Chih-hao Hsieh and Chih-Ching Chung

181 Impact of Mesoscale Circulation on the Structure of River Plumes During Large Rainfall Events Inshore of the East Australian Current
Junde Li, Moninya Roughan, Colette Kerry and Shivanesh Rao

198 Cross-Shelf Exchange in the Southwestern Atlantic Shelf: Climatology and Extreme Events
Giuliana Berden, Alberto R. Piola and Elbio D. Palma

217 Wind-Controlled Transport of Saltwater in the Southeastern Baltic Sea: A Model Study
Victor Zhurbas and Germo Väli

227 Offshore Freshwater Pathways in the Northern Gulf of Mexico: Impacts of Modeling Choices
Guangpeng Liu, Annalisa Bracco and Daoxun Sun

242 Shelf Water Export at the Brazil-Malvinas Confluence Evidenced From Combined *in situ* and Satellite Observations
Gaston Manta, Sabrina Speich, Marcelo Barreiro, Romina Trinchin, Camila de Mello, Rémi Laxenaire and Alberto R. Piola

261 Distribution of Harmful Algae (*Karenia* spp.) in October 2021 Off Southeast Hokkaido, Japan
Hiroshi Kuroda, Yukiko Taniuchi, Tsuyoshi Watanabe, Tomonori Azumaya and Natsuki Hasegawa

278 Variability and Intensity of the Sea Surface Temperature Front Associated With the Kuroshio Extension
Jingyuan Xi, Yuntao Wang, Zhixuan Feng, Yang Liu and Xinyu Guo

293 Prediction of Long-Term Beach Profile Evolution Due to Episodic Wave Incidence Under Tidal Environment
Sahong Lee, Changbin Lim and Jung-Lyul Lee

307 Seasonal Distributions of Methane in a Populous Urban Coastal Sea Area
Hsiao-Chun Tseng, Chia-Chia Lin, Hui-Juan Pan, Yokie Tai Yuh Han and Gwo-Ching Gong

318 Elevated Nutrient Supply Caused by the Approaching Kuroshio to the Southern Coast of Japan
Gloria Silvana Durán Gómez and Takeyoshi Nagai

333 Enhanced Cross-Shelf Exchange Between the Pacific Ocean and the Bungo Channel, Japan Related to a Heavy Rain Event
Akihiko Morimoto, Menghong Dong, Mahiro Kameda, Taiga Shibakawa, Makiko Hirai, Kouhei Takejiri, Xinyu Guo and Hidetaka Takeoka

345 Differences in the Composition of Abundant Marine Picoeukaryotes in the Marginal Sea Derived from Flooding
Chih-Ching Chung, Gwo-Ching Gong, Yun-Chi Lin and Ching-Wei Hsu

362 Shear Instability and Turbulent Mixing in the Stratified Shear Flow Behind a Topographic Ridge at High Reynolds Number
Jia-Lin Chen, Xiao Yu, Ming-Huei Chang, Sen Jan, Yiing Jang Yang and Ren-Chieh Lien

381 Kuroshio Intrusion and Its Impact on Swordtip Squid (*Uroteuthis edulis*) Abundance in the Southern East China Sea
Yi-Chen Cheng, Sen Jan and Chung-Chi Chen

394 A Cycle of Wind-Driven Canyon Upwelling and Downwelling at Wilmington Canyon and the Evolution of Canyon-Upwelled Dense Water on the MAB Shelf
Haixing Wang, Donglai Gong, Marjorie A. M. Friedrichs, Courtney K. Harris, Travis Miles, Hao-Cheng Yu and Yinglong Zhang

410 Local And Deep-Ocean Forcing Effects on the West Florida Continental Shelf Circulation and Ecology
Robert H. Weisberg and Yonggang Liu

433 An Observation-Based Study of Gulf Stream Meander Kinematics Offshore of Cape Hatteras
Mike Muglia, Harvey Seim, John Bane and Patterson Taylor

449 Delineation of Eastern Beaufort Sea Sub-regions Using Self-Organizing Maps Applied to 17 Years of MODIS-Aqua Data
Andrea Hilborn and Emmanuel Devred

468 The Spatial Variation in Chlorophyte Community Composition From Coastal to Offshore Waters in a Subtropical Continental Shelf System
Yun-Chi Lin, Chien-Pang Chin, Wei-Ting Chen, Ching-Ting Huang, Gwo-Ching Gong, Kuo-Ping Chiang and Xin-Bei Chen

481 Fluorescent signatures of autochthonous dissolved organic matter production in Siberian shelf seas
Anastasia N. Drozdova, Ivan N. Krylov, Andrey A. Nedospasov, Elena G. Arashkevich and Timur A. Labutin

499 Temporal and regional variabilities in the attenuation of sinking particulate organic carbon in the Kuroshio region
Hideki Fukuda, Kiyotaka Hidaka, Takashi Setou, Akira Kusaka, Daisuke Ambe and Hiroaki Saito

516 Coastal seascape variability in the intensifying East Australian Current Southern Extension
Lachlan R. Phillips, Neil Malan, Moninya Roughan, Robert Harcourt, Ian Jonsen, Martin Cox, Andrew S. Brierley, David Slip, Adam Wilkins and Gemma Carroll

frontiers | Frontiers in Marine Science

TYPE Editorial
PUBLISHED 18 January 2023
DOI 10.3389/fmars.2023.1137312

Check for updates

OPEN ACCESS

EDITED AND REVIEWED BY
Marta Marcos,
University of the Balearic Islands, Spain

*CORRESPONDENCE
Feng-Hsun Chang
fhchang422@ntu.edu.tw
Yun-Chi Lin
yunchi@mail.ntou.edu.tw
Kuo-Ping Chiang
kpchiang@mail.ntou.edu.tw

SPECIALTY SECTION
This article was submitted to Coastal Ocean Processes, a section of the journal Frontiers in Marine Science

RECEIVED 04 January 2023
ACCEPTED 09 January 2023
PUBLISHED 18 January 2023

CITATION
Chang F-H, Lin Y-C, Chiang K-P, Nien Y-H, Hsieh C-h, Chen W-J, Hung C-C, Kobari T, Saito H and Savidge W (2023) Editorial: Oceanographic processes linking nearshore, continental shelf, and shelf break.
Front. Mar. Sci. 10:1137312.
doi: 10.3389/fmars.2023.1137312

COPYRIGHT
© 2023 Chang, Lin, Chiang, Nien, Hsieh, Chen, Hung, Kobari, Saito and Savidge. This is an open-access article distributed under the terms of the Creative Commons Attribution License (CC BY). The use, distribution or reproduction in other forums is permitted, provided the original author(s) and the copyright owner(s) are credited and that the original publication in this journal is cited, in accordance with accepted academic practice. No use, distribution or reproduction is permitted which does not comply with these terms.

Editorial: Oceanographic processes linking nearshore, continental shelf, and shelf break

Feng-Hsun Chang[1*], Yun-Chi Lin[2*], Kuo-Ping Chiang[2,3*], Ya-Han Nien[2], Chih-hao Hsieh[1,4,5,6,7], Wei-Jen Chen[1], Chin-Chang Hung[8], Toru Kobari[9], Hiroaki Saito[10] and William Savidge[11,12]

[1]Institute of Oceanography, National Taiwan University, Taipei, Taiwan, [2]Institute of Marine Environment and Ecology, National Taiwan Ocean University, Keelung, Taiwan, [3]Center of Excellence for the Oceans, National Taiwan Ocean University, Keelung, Taiwan, [4]Research Center for Environmental Changes, Academia Sinica, Taipei, Taiwan, [5]Institute of Ecology and Evolutionary Biology, National Taiwan University, Taipei, Taiwan, [6]Department of Life Science, National Taiwan University, Taipei, Taiwan, [7]National Center for Theoretical Science, National Taiwan University, Taipei, Taiwan, [8]Department of Oceanography, National Sun Yat-sen University, Kaohsiung, Taiwan, [9]Aquatic Sciences, Faculty of Fisheries, Kagoshima University, Kagoshima, Japan, [10]Atmosphere and Ocean Research Institute, The University of Tokyo, Kashiwa, Japan, [11]Skidaway Institute of Oceanography, University of Georgia, Savannah, GA, United States, [12]Department of Marine Sciences, University of Georgia, Athens, GA, United States

KEYWORDS

biogeochemical cycling, coastal ocean, human activities, physical processes, western boundary current

Editorial on the Research Topic
Oceanographic processes linking nearshore, continental shelf, and shelf break

The coastal ocean is a body of water that connects the coast to the shelf break. As a highly dynamic region lying on the outer edge of a continent, the coastal ocean's various processes interactively influence its physical, chemical, and biological dynamics. To promote a holistic understanding of the coastal ocean and its influences, we collected studies investigating physical, chemical, and biological dynamics and their interactions in coastal oceans. Through the collected studies we aim to determine the impacts of physical processes, like the interactions between currents and topography, on the distribution and dynamics of chemical substances, such as nutrients and gases. Moreover, to delineate how the influences of chemical dynamics will propagate to organisms and food-web dynamics, like plankton biogeography or fishery production. Under this premise, we organize this editorial by first introducing the studies that investigate marine physical processes, and then the studies that describe the consequent chemical dynamics and biological interactions. We compile the studies in the same region in the editorial for the sake of coherence (Table 1).

Northwestern Pacific

The western boundary current in the northwest Pacific Ocean, Kuroshio, and its interactions with local weather and topographical features influence the hydrological and

TABLE 1 Summary of research contributions within this research topic.

Authors	Topic	Oceans	Currents	Methods	Scientific fields
Berden et al. (2022)	Cross-shelf exchange	Atlantic	Southwestern Atlantic shelf	Model	Physics
Chang et al. (2021)	Predatory-prey diversity	Pacific	Southern East China Sea	Sequencing	Biology
Chen et al. (2022)	Reoxygenation of the hypoxia	Pacific	East China sea	Measurement	Chemistry
Chen et al. (2022)	Effects of the coastal uplift (picoplankton)	Pacific	Kuroshio	Cruise	Biology
Chen et al. (2022)	Shear flow	Pacific	Kuroshio	Model	Physics
Cheng et al. (2022)	*Uroteuthis edulis*	Pacific	Kuroshio	Cruise	Biology
Chung et al. (2022)	Picoeukaryotes	Pacific	East China Sea	Sequencing	Biology
Drozdova et al. (2022)	DOM production	Siberian shelf sea	East Siberian and Laptev seas	Cruise	Chemistry
Durán Gómez and Nagai (2022)	Nutrients	Pacific	Kuroshio	Model	Chemistry
Fukuda et al. (2022)	Sinking POC	Pacific	Kuroshio	Cruise	Chemistry
Hilborn and Devred (2022)	MODIS-Aqua data	Arctic	Eastern Beaufort Sea	Satellite	Biology/ Chemistry
Isada et al. (2021)	Nutrients and organic matters	Pacific	Oyashio current	Coastal region	Chemistry
Kurczyn et al. (2021)	Advection of upwell water	Gulf of Mexico	Yucatan Current.	Measurement/ Satellite/ Model	Physics
Kuroda et al., 2022	Harmful algae (*Karenia* spp.)	Pacific	Oyashio	Cruise	Biology
Lee et al. (2022)	Wave and tidal	Pacific	Tairua Beach, New Zealand	Model	Physics
Li et al. (2022)	Impact of mesoscale circulation	Pacific	East Australian Current	Satellite	Physics
Lin et al. (2022)	Chlorophyte	Pacific	East China Sea	Sequencing	Biology
Liu et al. (2022)	Freshwater pathway	Atlantic	Gulf of Mexico	Model	Physics
Lizarbe Barreto et al. (2021)	Phytoplankton increase	Pacific	Kuroshio	Satellite	Biology
Ma and Smith (2022)	Primary productive	Atlantic	Gulf stream	Measurement	Biology/ Chemistry
Manta et al. (2022)	Shelf water exchange	Atlantic	Western boundary currents	Model	Physics
Morimoto et al. (2022)	Heavy rain	Pacific	Kyucho current	Model	Physics
Muglia et al. (2022)	Gulf stream	Atlantic	Gulf stream	Model	Physics
Phillips et al. (2022)	Coastal seascape	Pacific	East Australian Current	Cruise	Biology/ Physics
Roughan et al. (2022)	Shelf transport pathway adjacent	Pacific	East Australian Current	Model	Physics
Toyoda et al. (2021)	Surface-layer circulation	Pacific	Kuroshio	Satellite	Physics
Tseng et al. (2022)	Methane	Pacific	Tamsui River in Taiwan	Measurement	Chemistry
Wang et al. (2022)	Wind-driven upwelling and downwelling	Atlantic	Wilmington Canyon, Mid-Atlantic Bight	Measurement	Physics
Weisberg and Liu (2022)	Shelf circulation and ecology	Atlantic	Gulf of Mexico Loop Current	Review	Physics
Xi et al. (2022)	Temperature	Pacific	Kuroshio	Satellite	Physics
Xue et al. (2021)	Shelf-sediment	Pacific	Coastal region	Measurement	Chemistry
Yang et al. (2021)	Land-ccean interaction	Pacific	South China Sea & East China Sea	Measurement	Physics/ Chemistry
Zhurbas and Väli (2022)	Wind control	Atlantic	Southeastern Baltic sea	Model	Physics

biogeochemical dynamics along its pathway. In the subtropical region where Kuroshio travels northward and passes the steep east coast off Taiwan, the isotherms and isopycnals typically exhibit onshore lifting and offshore deepening (Jan et al., 2017). As a result of the tilting isotherms, cold and nutrient-rich subsurface water is upwelled to the euphotic zone (Chen et al.), while the magnitude of the coastal uplifting is proportional to Kuroshio's current speed. Subsequently, the higher nutrient level raises the chlorophyll-*a* concentration and the biomass of autotrophic picoplankton, which in turn raises the heterotrophic bacterial biomass. The upwelling along the Kuroshio also reduces the abundance of *Prochlorococcus* while increasing the abundance of *Synechococcus* and picoeukaryotes, both of which are favorable at high nutrient concentrations. Further north, the Kuroshio encounters submarine canyons northeast of Taiwan and impinges onto the East China Sea's (ECS) continental shelf. The Kuroshio impingement interacts with the winter monsoon, forming a nutrient-rich cold dome off the coast of northeastern Taiwan (Jan et al., 2011), sustaining high productivity in the area (Wong et al., 2000; Liu et al., 2003). Cheng et al. in this issue provides another line of evidence showing the positive impacts of Kuroshio impingement on the catch rate of swordtip squid (*Uroteuthis edulis*), a primary target species of the commercial fishery in this region.

At the continental shelf of ECS, the hydrographical and biogeochemical dynamics are further complicated by the interaction of multiple water masses, including the Kuroshio, China Coastal Current, Taiwan Warm Current, and Changjiang River runoff. Among these water masses, the nutrient and CO_2-laden freshwater discharge from Changjiang River typically causes hypoxia and low pH level on the inner shelf of the ECS, particularly outside the estuary. According to Chen et al. (2022) in this issue, coastal upwelling events associated with the intrusion of the Kuroshio can alleviate the hypoxia. Upwelling allows the accumulated CO_2 in the hypoxic layer to be ventilated while allowing the regenerated nutrients reaching the surface to be utilized. Vertical mixing during upwelling events also replenishes oxygen to the deeper water column, relieving oxygen stress on the resident fauna. Meanwhile, the freshwater discharge from Changjiang River influences the community composition of picoeukaryotes in addition to the influences directed to biogeochemical cycling. According to Chung et al. in this issue, such a phenomenon happens as the picoeukaryotic community composition shifts from photosynthetic picoeukaryote dominance in the non-flooding season to mixotroph and heterotroph dominance during the flooding season. Furthermore, chlorophytes are an important component among eukaryotic picophytoplankton in the ocean (Not et al., 2004). Lin et al. in this issue suggest that chlorophyte composition is closely related to water masses, as its salinity, temperature, and silicate concentration significantly influence the distribution of chlorophytes. This study discovered that Chloropicophyceae in oligotrophic Kuroshio water and Mamiellophyceae in more eutrophic waters dominate chlorophyte communities. Chang et al. in this issue investigates the diversity and community relationships between planktonic bacteria and their main predator, heterotrophic nanoflagellates (HNF) within the biologically diverse and hydrographically complex ECS environment. They find that bacterial and HNF diversity are positively associated, and this relationship is possibly governed by the trophic interaction between bacteria and HNF. The ECS shelf's complex hydrography promotes highly dynamic biological interactions. However, the consequences for the pelagic ecosystem and biogeochemical cycles still worth further investigation.

The Kuroshio has long been known to either take a relatively straight path or take a large meander path along the south coast of Japan after leaving the ECS shelf (Kawabe, 1985). To depict the Kuroshio path, Barreto et al. analyzed the altimetry data and revealed that the Kuroshio takes a large meander path from 2004-2005 and from 2017 to the present. When taking the large meander path, the Kuroshio flows closer to the southeast coast of Kyushu after passing the Tokara Strait south of Kyushu. The path that is closer to the coast induces stronger trapped near-inertial internal waves as well as more turbulent mixing in the coastal regions of southeastern Japan (Nagai et al., 2019). Chen et al. in this issue provides additional theoretical support explaining the increased shear instability and turbulent kinetic energy that appears as the Kuroshio flows through topographical ridges. Meanwhile, Durán Gómez and Nagai in this issue developes an ecosystem model showing how strong vertical turbulent mixing, associated with the passage of the Kuroshio over abrupt topography, propagates eastward along the coast and increases the chlorophyll-*a* concentration in the coastal region. Following that, the Kuroshio path bends further seaward (southward) as it approaches the Izu Ridge and flows nearly northward before meeting the south-flowing subarctic western boundary current called Oyashio. On the Kuroshio's landside, the large meander path creates cyclonic eddies. These cyclonic eddies, combined with turbulence, supply ample nutrients to the euphotic zone, elevating the chlorophyll-*a* concentration (Lizarbe Barreto et al.).

On the other hand, the large meander regime creates anti-cyclonic circulations in some regions located on the south side of Japan's main island, such as Suruga Bay. Combining mathematical simulations with *in situ* observations, Toyoda et al. in this issue discovers that Kuroshio's northward intrusion into the western Suruga Bay creates an anti-cyclonic circulation in the bay, which contrasts the cyclonic circulation during a non-large meander regime. In addition, regional circulation is also affected by local weather. Combining observational data and numerical modeling, Morimoto et al. in this issue shows that heavy rain around the Bungo Channel between Kyushu and Shikoku decreases water density, intensifies the gravitational circulation, and thus induces the intrusion of large amounts of cold and nutrient-rich bottom water to the Bungo Channel. The bimodal characteristic of Kuroshio's path, the local topographical features, and weather interactively influence the circulation patterns, hydrography, and biological dynamics of the coastal regions south of Japan.

Further north, the Kuroshio converges with the Oyashio, a colder and fresher subarctic ocean current, and turns eastward to form the so-called Kuroshio Extension. The convergence zone – the Kuroshio-Oyashio Inter-Frontal Zone (KOIZ) – and the Kuroshio Extension are characterized by dynamic hydrography and active frontal features due to the contrasting properties of the two currents (Yasuda, 2003). The temporal and spatial variability, as well as the intensity of those fronts, are critical for the subsequent biogeochemical dynamics in the KOIZ and the Kuroshio Extension region. Analyzing 17 years of satellite observations of sea surface temperature (SST), Xi et al. in this issue investigates the spatial and temporal variations of the KOIZ fronts. Xi et al. report that fronts are more common on the north side of KOIZ in winter but become more common on the south side in spring. In addition to frequency, the cross-frontal gradients are steeper north of

the KOIZ due to stronger mesoscale eddies. Meanwhile, the basin-scale ocean-atmosphere climate variability, including the Pacific Decadal Oscillation and North Pacific Gyre Oscillation, significantly influences the interannual variability of fronts in the KOIZ and the Kuroshio Extension region. Aside from influencing the hydrography in offshore regions, Oyashio can also interplay with marine heatwaves and warmer coastal currents, such as Modified Soya Warm Current and Tsugaru Warm Current, to trigger the onset of a harmful algal bloom on the southeast coast of Hokkaido, Japan (Kuroda et al.).

Along the coastal regions from Taiwan to Japan, physical processes can increase phytoplankton biomass, which in turn influences the cycling of particulate and dissolved organic matters (POM and DOM). Yang et al. in this issue measures the elemental (N/P) ratio, ^{7}Be and $^{210}Pb_{ex}$ isotopes of suspended sediments to specifically pinpoint the time when the monsoon regime shifts from southwestern to northeastern in October in the Taiwan strait, and depict the dynamics of circulation and frontogenesis as a result of the interactions between river runoffs, coastal currents, and the seasonal monsoon. In the Kuroshio region south of Japan, Fukuda et al. in this issue measures the flux and attenuation of POM. They argue that particle size affects the POC flux and attenuation, while chemical properties (e.g., the C/N ratio of sinking particles) do not cause any effect. In the semi-enclosed coastal sea of northeastern Japan, Isada et al. in this issue characterizes seasonal and spatial changes in the optical absorption properties of CDOM, phytoplankton, and non-algal particles (NAP) as a function of temperature, salinity, nutrients, and water transparency along the river–salt marsh–eelgrass meadows–coastal waters continuum. They discover that in addition to the river input, mariculture and eelgrass meadows influence nutrient cycling and CDOM absorptive characteristic, which in turn influence the water transparency of the system. Moreover, further north in Siberian Sea Shelf in the Arctic Ocean. Drozdova et al. in this issue examines the spectral signatures of fluorescent dissolved organic matter (FDOM) and its spatial distribution. They argue that microbial activity is enhanced on the east part of the shelf as the autochthonous-derived chromophoric DOM components, which are suggestive of heterotrophic reworking of marine organic matter, dominate the shelf waters. These studies demonstrate how biological interactions affect the production, transportation, and fates of organic matters, which subsequently affect biogeochemical cycling.

Southwestern Pacific

The East Australian Current (EAC) is the western boundary current of the west Pacific Ocean in the southern hemisphere. The EAC flows poleward along southeastern Australia, often intruding onto the continental shelf on Australia's central east coast. The physical processes and subsequent biogeochemical dynamics accompanied with the EAC to some degree resemble those in the Kuroshio region. Roughan and Middleton (2002), for example, have identified four mechanisms bringing nutrients onto the continental shelf: wind-driven upwelling, encroachment of the EAC onto the continental shelf, topography-induced current acceleration, and the separation of the EAC from the coast. In this issue, Roughan et al. further demonstrates the circulation variability of EAC, influences of such circulation on shelf-ocean water transportation, and the upwelling processes around the productive Hawkesbury Shelf. In addition, Li et al. in this issue investigates the largest river plume (Hawkesbury River plume) in the Hawkesbury Shelf region. The authors find that the circulation of EAC and rainfall interactively influence the north and south extensions of the plume, but the river plume is largely trapped in the shelf region. These findings clarify the fate of river-borne material on the adjacent continental shelf under various forcing scenarios. To better understand and manage the ecosystem, Phillips et al. in this issue uses satellite and *in situ* measurements of temperature, salinity, and current velocity, together with acoustic measurements of pelagic biomass (zooplankton and fish), to characterize the seascape variability in southeast Australia. The southeast Australia is known for being a hotspot of ocean warming and ecosystem tropicalization. According to Phillips et al., two seascape categories are identified: one characterized by warm and less saline water and the other characterized by cool and more saline water. The seascape category made up of less warm saline water indicates a greater influence of the EAC on the coastal region. These findings emphasize the critical role of offshore oceanographic processes in driving coastal seascape variability and biological activity in a region experiencing rapid ocean warming and ecosystem changes.

Northwest Atlantic

The western boundary current in the western North Atlantic Ocean, the Gulf Stream, interacts with some topographical features (e.g., shelf break and seabed rises) and local processes (e.g., wind and river discharge) to influence the hydrography and biogeochemical cycles. When the Gulf Stream travels northward, it meanders and encounters the Charleston Bump, a rocky seabed that rises around 31-32°N. The meander and subsequent propagation of the Gulf Stream is depicted by Muglia et al. in this issue, who analyzes data from a bottom-moored Acoustic Doppler Current Profiler (ADCP) with high-frequency radar (HFR) offshore of Cape Hatteras. They reveal that when the Gulf Stream deflects seaward, the induced vertical circulation and vertical shear create a cold dome that pumps nutrients from the deep. In addition to the Gulf Stream, local wind also generates upwelling events in coastal regions. Wang et al. in this issue combines measurements from underwater gliders and numerical modeling to show that upwelling favorable winds induced a cross-slope pressure gradient that injected deep cold canyon water onto the Mid-Atlantic Bight (MAB) shelf. The cold, nutrient-rich upwelling plume spread northeastward along the shelf and broadened in the cross-shelf direction until a wind reversal produced downwelling favorable conditions, causing some upwelled waters to return to depth in the canyon. The significant amount of nutrients entrained by upwelling events have the potential to nourish this region and make it a productive and important fishing ground. Ma and Smith in this issue demonstrates that the complex physical processes and ensuing nutrient dynamics propagate to affect the primary production at the MAB shelf. Surprisingly, the shelf break frontal features might not significantly contribute to the increased productivity at the MAB. Ma and Smith (2022) also claim that combining satellite chlorophyll, sea surface temperature, photosynthetically active radiation (PAR), and a photosynthesis model promotes a more robust resolution of primary

productivity at smaller vertical and horizontal scales than by using traditional ^{14}C incubations.

Aside from the Gulf Stream, the Yucatán Current and Loop Current in the Gulf of Mexico also causes an upwelling and interact with freshwater discharge and local winds. The Yucatán Current commonly induces upwelling on the eastern side of the Yucatan shelf, but upwelling events at the west side of the Yucatán Peninsula received relatively little attention. Combining *in situ* and remote observations as well as numerical modeling, Kurczyn et al. in this issue describe the westward advection of upwelled Caribbean Subtropical Underwater from the eastern Yucatan Shelf across the Campeche Banks. Kurczyn et al. note that the colder, denser water was confined to a thin near-bottom later as it propagated westward. However, further investigation is needed to understand the chemical and biological consequences of such upwelling at the shelf west of the Yucatán Peninsula. On the other hand, the Loop Current and its accompanying mesoscale eddies influence both the vertical and horizontal transport of freshwater discharged from the Mississippi River and the neighboring Atchafalaya River (MARS) into the Gulf of Mexico. In their study, Liu et al. in this issue finds that, the MARS discharge is largely transported westward in winter but can be transported either westward to the continental shelf or eastward out of the Gulf in summer. Reviewing decades of studies on the Loop Current, local wind, and their collective influences on the hydrography, nutrient dynamics, and the ecological consequences at the west Florida continental shelf, Weisberg and Liu argue that the variation of the Loop Current path on an inter-annual basis, as well as the variation of wind direction and stress at the intra-annual basis, collectively determine the vertical movement of water on the shelf.

Northeast Atlantic

Zhurbas and Väli examines the effects of regional wind forcing on deep water transport within the Baltic Sea. They discovered that winds blowing perpendicular to the channel orientation enhance deep-layer water transport through channels due to the Ekman transport. Thus, the surface wind field has a stronger influence on the flushing and renewal of bottom water in the Baltic Sea basins.

Southwest Atlantic

In the south Atlantic Ocean, a major western boundary current, the Brazil Current, and a branch of the Antarctic Circumpolar Current, the Malvinas Current, converge around 30-40°S off the coast of Argentina and Uruguay. Because the warm and salty Brazil Current meets the cold, fresh and nutrient-rich Malvinas Current, the Brazil-Malvinas convergence (BMC) zone has highly dynamic hydrology. Cross-shelf exchange between the Southwestern Atlantic shelf and the open ocean is also highly variable in the BMC zone. To depict the variability and drivers of the cross-shelf exchanges, Berden et al. in this issue implements a high-resolution ocean model (Copernicus Marine Environment Monitoring Service (CMEMS) global ocean reanalysis (GLORYS12V1) during 1993–2018). They verify the model results with satellite altimetry data and *in situ* on-board observation. Berden et al. reports that the annual mean cross-shore transport is 2.09 ± 1.60 Sv toward the open ocean, with a maximum in January and a minimum in June due to local alongshore wind stress that affects the sea level anomaly. Inshore transportation can occur and reaches 6.53 Sv. during certain extreme conditions. Complementing Berden et al.'s research findings, Manta et al. combined *in situ* observation, Argo temperature and salinity profiles, and satellite data to depict a 3-D circulation structure in the BMC zone. They discovered that the Rio de la Plata waters plume near the surface, as well as the Subantarctic Shelf Waters under the subtropical thermocline, also transport comparable amounts of water offshore.

Anthropogenic influences on coastal processes

Aside from the physical processes mentioned above, human activities and global changes profoundly impact marine environments. To address this issue, Lee et al. in this issue proposes a new model framework for predicting the long-term evolution of beach profiles under rising sea levels or severe weather caused by climate changes. Meanwhile, Hilborn and Devred in this issue partition 17 years of satellite-measured sea-surface temperature, suspended particulate matter, and chlorophyll-*a* concentration of the Eastern Beaufort Sea into six regions using the self-organizing maps technique. Their regional classification corresponds to the physical characteristics of the EBS, as observed in other studies. With the inter-annual and monthly variation of sea-ice concentration in these regions, Hilborn and Devred shows that the Eastern Beaufort Sea experiences more non-uniform impacts from climate changes than previously thought. Furthermore, Xue et al. in this issue indicates that increasing ship traffic significantly decreases the seabed sediment's particle size and changes the biogenic element ratio of the sediments. Tseng et al., on the other hand, in this issue describes the seasonal distributions of methane in a populous urban coastal sea area in the Tamsui River, the third longest river in Taiwan. Their study emphasized the anthropogenic impacts of climate change and the biogeochemical dynamics in coastal regions across the globe.

Summarily, the diversity of the contributions of this Special Issue highlights the complexity of biogeochemical responses to physical forcing in the sea. These results demonstrate the interactive impacts of physical processes occurring at multiple spatial and temporal scales on biogeochemical cycles, food-web dynamics, and biodiversity. This Special Issue emphasizes the need for holistic approaches and/or interdisciplinary studies to investigate the physical oceanography, biogeochemical cycles and ecosystem structure, and dynamics of the coastal ocean.

Author contributions

F-HC and Y-CL wrote the draft of the manuscript; K-PC and Y-HN organized the articles; C-HH, W-JC, C-CH, TK, HS, WS contributed substantially to revisions. All authors contributed to the article and approved the submitted version.

Conflict of interest

The authors declare that the research was conducted in the absence of any commercial or financial relationships that could be construed as a potential conflict of interest.

Publisher's note

All claims expressed in this article are solely those of the authors and do not necessarily represent those of their affiliated organizations, or those of the publisher, the editors and the reviewers. Any product that may be evaluated in this article, or claim that may be made by its manufacturer, is not guaranteed or endorsed by the publisher.

References

Jan, S., Chen, C.-C., Tsai, Y.-L., Yang, Y. J., Wang, J., Chern, C.-S., et al. (2011). Mean structure and variability of the cold dome northeast of Taiwan. *Oceanography* 24, 100–109. doi: 10.5670/oceanog.2011.98

Jan, S., Mensah, V., Andres, M., Chang, M. H., and Yang, Y. J. (2017). Eddy-Kuroshio interactions: Local and remote effects. *J. Geophysical Research: Oceans* 122, 9744–9764. doi: 10.1002/2017JC013476

Kawabe, M. (1985). Sea Level variations at the izu islands and typical stable paths of the Kuroshio. *J. Oceanographical Soc. Japan* 41, 307–326. doi: 10.1007/BF02109238

Liu, K.-K., Peng, T.-H., Shaw, P.-T., and Shiah, F.-K. (2003). Circulation and biogeochemical processes in the East China Sea and the vicinity of Taiwan: An overview and a brief synthesis. *Deep Sea Res. Part II: Top. Stud. Oceanogr.* 20 (6,7), 1055–1064. doi: 10.1016/S0967-0645(03)00009-2

Nagai, T., Durán, G. S., Otero, D. A., Mori, Y., Yoshie, N., Ohgi, K., et al. (2019). How the Kuroshio current delivers nutrients to sunlit layers on the continental shelves with aid of near-inertial waves and turbulence. *Geophysical Res. Lett.* 46, 6726–6735. doi: 10.1029/2019GL082680

Not, F., Latasa, M., Marie, D., Cariou, T., Vaulot, D., and Simon, N. (2004). A single species, *Micromonas pusilla* (Prasinophyceae), dominates the eukaryotic picoplankton in the western English channel. *Appl. Environ. Microbiol.* 70, 4064–4072. doi: 10.1128/AEM.70.7.4064-4072.2004

Roughan, M., and Middleton, J. H. (2002). A comparison of observed upwelling mechanisms off the east coast of Australia. *Continental Shelf Res.* 22, 2551–2572. doi: 10.1016/S0278-4343(02)00101-2

Yasuda, I. (2003). Hydrographic structure and variability in the Kuroshio-Oyashio transition area. *J. Oceanography* 59, 389–402. doi: 10.1023/A:1025580313836

Wong, G. T. F., Chao, S.-Y., Li, Y.-H., and Shiah, F.-K. (2000). The Kuroshio edge exchange processes (KEEP) study — an introduction to hypotheses and highlights. *Cont. Shelf Res.* 20, 335–347. doi: 10.1016/S0278-4343(99)00075-8

frontiers in Marine Science

ORIGINAL RESEARCH
published: 31 May 2021
doi: 10.3389/fmars.2021.651565

Community Assembly Processes as a Mechanistic Explanation of the Predator-Prey Diversity Relationship in Marine Microbes

*Feng-Hsun Chang[1], Jinny Wu Yang[2], Ariana Chih-Hsien Liu[1], Hsiao-Pei Lu[3], Gwo-Ching Gong[4,5], Fuh-Kwo Shiah[1,4,6] and Chih-hao Hsieh[1,6,7,8]**

[1]Institute of Oceanography, National Taiwan University, Taipei, Taiwan, [2]Ecology and Evolutionary Biology, University of Michigan, Ann Arbor, MI, United States, [3]Department of Biotechnology and Bioindustry Sciences, National Cheng Kung University, Tainan, Taiwan, [4]Institute of Marine Environment and Ecology, National Taiwan Ocean University, Keelung, Taiwan, [5]Center of Excellence for the Oceans, National Taiwan Ocean University, Keelung, Taiwan, [6]Research Center for Environmental Changes, Academia Sinica, Taipei, Taiwan, [7]Institute of Ecology and Evolutionary Biology and Department of Life Science, National Taiwan University, Taipei, Taiwan, [8]National Center for Theoretical Sciences, Taipei, Taiwan

OPEN ACCESS

Edited by:
Chin-Chang Hung, National Sun Yat-sen University, Taiwan

Reviewed by:
Antonio Bode, Spanish Institute of Oceanography, Spain
Bangqin Huang, Xiamen University, China

***Correspondence:**
Chih-hao Hsieh
chsieh@ntu.edu.tw

Specialty section:
This article was submitted to Marine Ecosystem Ecology, a section of the journal Frontiers in Marine Science

Received: *10 January 2021*
Accepted: *29 April 2021*
Published: *31 May 2021*

Citation:
Chang F-H, Yang JW, Liu AC-H, Lu H-P, Gong G-C, Shiah F-K and Hsieh C-h (2021) Community Assembly Processes as a Mechanistic Explanation of the Predator-Prey Diversity Relationship in Marine Microbes. Front. Mar. Sci. 8:651565. doi: 10.3389/fmars.2021.651565

Predator and prey α-diversities are often positively associated; yet, understandings of the underlying mechanisms require manipulative experiments and thus remain unclear. We attempt to address this issue by deciphering how α-diversity of predator and prey influences each other's community assembly processes, which subsequently determine their α-diversity. The occurrence of assembly processes was indicated by the mean pairwise taxonomic index within a community (α*MPTI*), assuming assembly processes left traceable imprints on species' phylogeny. Specifically, α*MPTI* quantifies deviations of observed phylogenetic distances from that of random, so that it can be used to hint at the occurrence of non-random/deterministic assembly processes. Larger α*MPTI* of a community implies the occurrence of weaker homogenizing deterministic assembly processes, which suggests that this community might be comprised of less similar species and thus has higher α-diversity. We hypothesize that higher predator and prey α-diversity would be positively associated with each other's α*MPTI*, which would then be positively associated with their α-diversity. To test the hypothesis, we calculated Shannon diversity and α*MPTI* for heterotrophic nanoflagellates (HNF; predator) and bacteria (prey) communities in the East China Sea (ECS). The HNF Shannon diversity was found to be positively associated with α*MPTI* of bacteria, which was then positively associated with bacterial Shannon diversity. In contrast, bacterial Shannon diversity did not correlate with HNF's α*MPTI*. We argue that top-down control is one of the explanations to the positive α-diversity association among trophic levels in microbes of the ECS.

Keywords: biodiversity, community assembly processes, homogeneous versus heterogeneous selection, predator-prey diversity relationship, phylogeny

INTRODUCTION

The α-diversities of predator and prey communities are often found to be positively associated in natural systems (Haddad et al., 2009). To explain this positive association, studies have been conducted, including observational (Yang et al., 2018) and experimental (Haddad et al., 2009) studies as well as meta-analyses (Castagneyrol et al., 2012). The mechanisms proposed by these studies can be classified into three categories. The first one is that predator and prey α-diversities respond to the same external forces in the same direction so that they are positively correlated (e.g., Hawkins and Porter, 2003; Axmacher et al., 2009). The other two are related to trophic interactions between the predators and prey (Hunter and Price, 1992; Power, 1992) and can be further categorized into top-down or bottom-up control mechanisms. The top-down control mechanisms occur when predators either directly suppress the dominant prey and prevent competitive exclusion (Leibold, 1996; Proulx and Mazumder, 1998) or indirectly create an environment that fosters the diversity of prey (Borer et al., 2014). In contrast, bottom-up control mechanisms take place, while more diverse prey community provides greater diversity (Hutchinson, 1959; Southwood et al., 1979) or greater amount (Siemann, 1998; Srivastava and Lawton, 1998) of resources to promote predator diversity. These three mechanisms are not easy to disentangle because they can act jointly to determine diversity associations between predator and prey in nature.

To unveil the causes underlying the positive association between predator and prey α-diversities, manipulative experiments that include multiple trophic levels are often required (e.g., Scherber et al., 2010; Hertzog et al., 2016). Conducting this kind of complex and long-term experiments often costs large amount of labor and resources. Consequently, despite many efforts, identifying and disentangling the mechanisms remains challenging.

To address this issue, we propose an analytical framework that quantifies community assembly processes of predators and prey to decipher the bi-trophic diversity association. The community assembly processes are inferred from the degree of relatedness among species, i.e., phylogenetic similarity, within a community (Webb et al., 2002; Cavender-Bares et al., 2009) because phylogenetic similarity is considered as an imprint left by evolutionary and ecological processes (Mouquet et al., 2012; Gerhold et al., 2015). These community assembly processes have been synthesized in Vellend's conceptual synthesis of community ecology (Vellend, 2010; Götzenberger et al., 2012), including four fundamental processes – ecological drift, selection, speciation, and dispersal. We propose to use phylogenetic similarity within a community as a hint of the occurrence of these processes that collectively determine the species composition and thus the diversity of a community (Logares et al., 2018).

Specifically, the analytical framework, we proposed here consists of two steps (**Figure 1**) to investigate mechanisms underlying the α-diversity association between predator and prey. First, we investigate how predator's (or prey's) α-diversity affects assembly processes of the other community. Then, we examine how the assembly processes of prey (or predator) community are associated with their own α-diversity. When we find significant effect of predator's α-diversity on prey's assembly processes, which are then significantly associated with the α-diversity of prey, we infer that top-down control mechanisms are likely to be responsible for the bi-trophic diversity association. On the other hand, significant association of prey's α-diversity and predator's assembly processes along with significant association between predator's assembly processes and α-diversity would evidence bottom-up control mechanisms. When none of the above is found, the predator-prey diversity association may be a result of their congruent responses to the same external forces.

The first step of the analytical framework is to investigate the roles of predator and prey α-diversities in each other's assembly processes. Here, we mainly focus on the two unambiguously deterministic processes, i.e., selection and speciation. We chose to make inferences based on deterministic processes because they result from species' different responses given a set of biotic and/or abiotic environment, including predator-prey interactions (Vellend et al., 2014). The deterministic processes could thus be used to represent how those biotic and/or abiotic environments affect each other's community diversity. In contrast, ecological drift is not our focus because it represents the random/stochastic events governing the presence of species in a community rather than predator-prey interactions (Hubbell, 2001). We also restrict ourselves from making inferences based on dispersal because dispersal could be deterministic or stochastic depending on whether species differ in dispersal ability or respond idiosyncratically to dispersal force (Nemergut et al., 2013; Lowe and McPeek, 2014). Consequently, in this study, we only investigate how the deterministic assembly processes of predator and prey community are affected by each other's α-diversity.

After clarifying the effects of predator and prey α-diversity on each other's deterministic assembly processes, we proceed to examine how the deterministic processes are associated with their own community diversity. Deterministic processes are positively or negatively associated with community diversity because those processes can weakly or strongly homogenize the community, respectively (MacArthur and Wilson, 1967; Zhou and Ning, 2017). When the deterministic processes weakly homogenize the community *via* selecting for different species and/or promoting speciation, species that are less similar to each other comprise a community. Such weak homogenizing deterministic processes should be positively associated with community diversity. On the other hand, when the deterministic processes impose consistent selection pressure to select for similar species or prevent speciation in a community (e.g., Dini-Andreote et al., 2015), species that are more similar to each other comprise a community. Such strong homogenizing processes should be negatively associated with community diversity. This second step in our analytical framework examines how the deterministic assembly processes (i.e., weak or strong homogenizing the community) is associated with community diversity. This framework can be used to deconstruct the positive α-diversity association in order to discern whether the positive association stems from the top-down control mechanisms or the bottom-up control mechanisms (**Figure 1**).

We apply this two-step analytical framework to deconstruct the α-diversity association between heterotrophic nanoflagellates

(HNF) as the predators and bacteria as prey in the marine planktonic system of southern East China Sea (ECS). A previous study in the ECS has found a positive association between the α-diversity of HNF and bacteria, even after accounting for confounding environmental factors (Yang et al., 2018). According to our analytical framework, the positive α-diversity can result from the occurrence of either top-down control or bottom-up control, or both, mechanisms. When either mechanism occurs, the diversity of one trophic level is expected to make the deterministic processes weakly homogenizing the other community and thus lead to higher diversity of the other community. We thus hypothesize that the positive α-diversity association between bacteria and HNF results from the occurrence of either top-down control or bottom-up control, or both mechanisms.

MATERIALS AND METHODS

Microbial Samples and Environmental Variables

Heterotrophic nanoflagellate and bacterial communities were revealed by using sequence data collected in the southern ECS from 14 cruises in the period of April 2014 to July 2017. In each sampling cruise, we visited the same six stations along a transect in the southern ECS (**Supplementary Figure 1**). Thus, a total of 84 samples each for HNF and bacteria were included in analysis. At each sampling, GoFlo bottles (General Oceanics) mounted on a conductivity, temperature, and depth profiler (CTD profiler, Sea-Bird Electronics, Bellevue, WA, United States) were used to collect 20 L of seawater from 5 m beneath surface. The seawater was first pre-filtered through a screen mesh with 20 μm openings to remove large organisms like zooplankton. The pre-filtered seawater was sequentially filtered onto 1.2 μm-pore-size filters (Millipore Isopore™ hydrophilic polycarbonate membrane) to collect nanoflagellates and then onto 0.2 μm-pore-size filters (Millipore Isopore™ hydrophilic polycarbonate membrane) to collect bacteria (Yang et al., 2018). After filtration, both the 0.2 and 1.2 μm-pore size filters were stored in liquid nitrogen and then at −20°C until molecular analysis (Yang et al., 2018).

Environmental variables, including temperature, salinity, and photosynthetic active radiation, were recorded by the CTD profiler. In addition, seawater samples for chlorophyll-a concentration as well as nutrient variables, including nitrite,

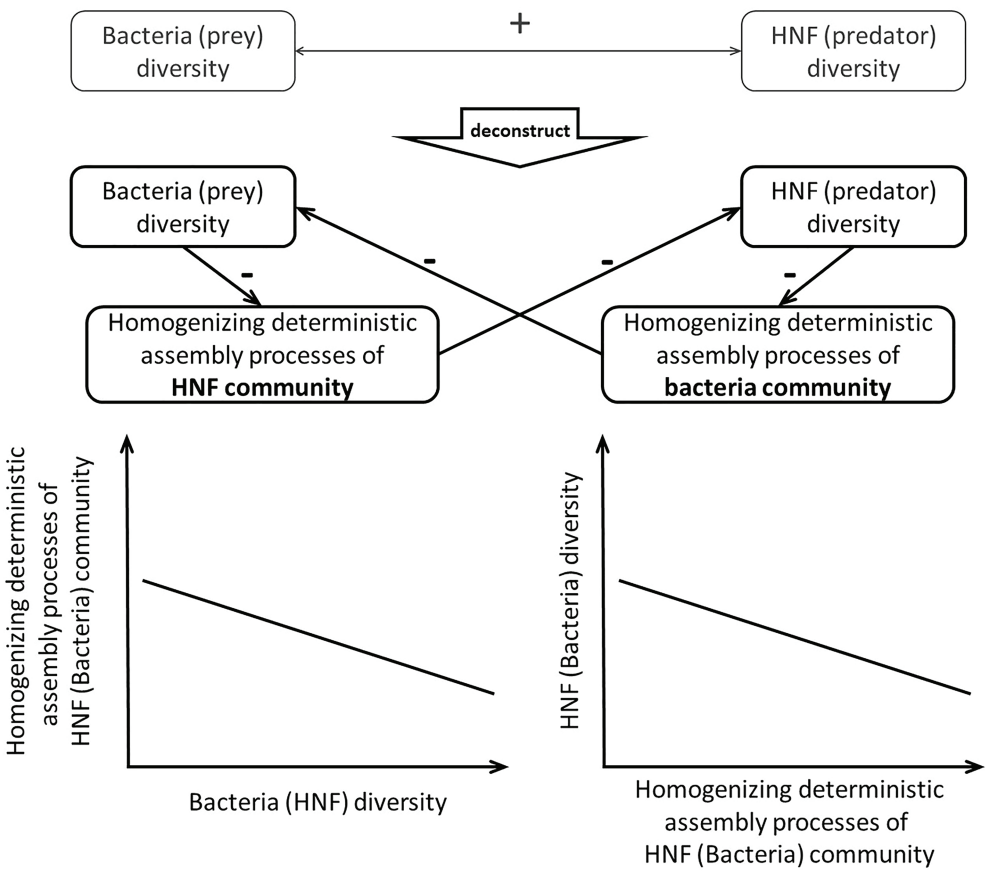

FIGURE 1 | Schematic plots visualizing the two-step analytical framework and the ensuing expectations. We argue that the positive HNF (predator)-bacteria (prey) diversity association can be caused by top-down and/or bottom-up control mechanisms. The top-down control mechanisms should cause the HNF α-diversity to weaken the homogenizing deterministic assembly processes of bacteria community and thus lead to higher bacteria α-diversity. On the other hand, the bottom-up control mechanisms should cause the bacteria α-diversity to weaken the homogenizing deterministic assembly processes of bacteria community and thus lead to higher HNF α-diversity.

nitrate, and phosphate concentrations, were collected and measured according to the standard methods developed by Gong et al. (2003).

DNA Extraction, Sequencing and Sequence Processing

We briefly introduced how we extracted DNA and analyzed sequences in this section (detailed methods are explained in **Supplementary Material 1**). Total DNA was extracted separately from the 0.2 and 1.2 μm-pore size filters with the PowerWater DNA Extraction Kit (PowerWater, Qiagen) according to the manufacturer's instructions. DNA extracts from the 0.2 to 1.2-μm-pore size filters were used as templates of PCR to amplify the 16S rRNA gene for prey and 18S rRNA gene for predators, respectively. PCR was performed in two steps to gain better reproducibility and consistent results (Berry et al., 2011); see **Supplementary Material 1** for details of the two-step PCR procedures. After obtaining 16S and 18S rRNA gene sequences, the DADA2 pipeline was used for quality filtering and assembling sequences into amplicon sequence variant (ASV; Callahan et al., 2016a; see **Supplementary Material 1.2** for sequence merging procedures). Taxonomy assignment was performed on ASVs to recognize and select for predators from 18S rRNA gene and prey from 16S rRNA gene. From 18S rRNA gene, the Protist Ribosomal Reference database (PR2) database (Guillou et al., 2012; Vaulot and Guillou, 2019) was used to recognize taxonomy. Those belonging to the HNF taxonomy were further selected as the predators (see **Supplementary Table 1** from Yang et al. (2018) for the list of HNF taxonomy). From 16S rRNA gene, the Silva 132 database (Quast et al., 2013) was used and only those classified under the bacteria kingdom were selected as prey. Finally, in order to obtain the phylogeny, we used maximum likelihood method (with negative edges length = 0; Callahan et al., 2016a) to build phylogenetic trees for bacteria and HNF from 16S rRNA gene and 18S rRNA gene of all cruises, respectively.

Quantifying Diversity of Predator (HNF) and Prey (Bacteria)

Before calculating the Shannon diversity index of HNF (predators) and bacteria (prey), each community was resampled once to achieve the same number of reads among stations, which were 331 for HNF and 13,129 for bacterial communities. The rarefaction yielded 93.76 ± 3.81 and 97.91 ± 0.69% sample coverage for HNF and bacterial communities, respectively (**Supplementary Figure 2**). Although this procedure addresses the disparity issue, i.e., unequal reads among stations, it is not appropriate when comparing the relative abundance of AVSs across stations (McMurdie and Holmes, 2014). Therefore, in order to have a fair among-station comparison, we applied method of Chao et al. (2014) to rarefy and estimate the expected Shannon diversity index of both HNF and bacteria communities for the following analyses (Chao and Chiu, 2016; Hsieh et al., 2016).

Inferring Community Assembly Processes

To hint the community assembly processes experienced by each HNF and bacteria community, we calculated the α mean pairwise taxonomic index ($\alpha MPTI$). The $\alpha MPTI$ is akin to Webb's net relatedness index (NRI; Webb, 2000; Webb et al., 2002), which quantifies the deviation of the observed mean pairwise phylogenetic distance (MPD_{obs}) from a null distribution of mean pairwise phylogenetic distance (MPD). The MPD_{obs} was the mean branch length among all pairs of species within each community. The null distribution of MPD was generated by random processes so that the distribution represented the values of MPD if a community is assembled by completely random processes, e.g., ecological drift. The deviation of MPD_{obs} from the null thus represents the non-random/deterministic processes by which a community is assembled. To generate a null distribution of MPD by random processes, we first randomly shuffled the phylogeny (i.e., shuffled the tips of the phylogenetic tree) of all species within a community (i.e., each cruise-station). With the randomized phylogeny, we calculated MPD of each community. Repeating this randomization technique 999 times, we generated the null distribution of MPD. Finally, $\alpha MPTI = (MPD_{obs} - meanMPD_{null})/sdMPD_{null}$, where $meanMPD_{null}$ represents the mean of the null distribution of MPD, and $sdMPD_{null}$ represents the SD of the null distribution of MPD.

When calculating $\alpha MPTI$, we did not multiply −1 as in the NRI calculation (Webb, 2000; Webb et al., 2002). Therefore, the sign of $\alpha MPTI$ should more intuitively represent whether the observed phylogenetic distance is more different or less different from random. A positive value of $\alpha MPTI$ of a community means that species are phylogenetically more different than expected by random. Accordingly, positive $\alpha MPTI$ hints the occurrence of weak homogenizing assembly processes following the same logic, negative $\alpha MPTI$ hints the occurrence of strong homogenizing assembly processes.

α-Diversity Association and Impacts of Community Assembly Processes

Before testing our hypotheses, we first conducted univariate regression modeling to show that HNF and bacteria α-diversity were positively associated. To do so, we performed generalized linear mixed effect model (GLMM) to regress the HNF Shannon diversity on bacteria Shannon diversity, with cruise as the random effect. Here, making cruise as a random effect should account for the temporal autocorrelations among cruises. After confirming the positive association, we proceed to test the hypothesis that HNF and bacteria α-diversity negatively affects each other's deterministic assembly processes and in turn increases each other's α-diversity (**Figure 1**). To do so, we performed two sets of univariate GLMMs to separately test for top-down control mechanisms and bottom-up control mechanisms. Each set of univariate GLMM consisted of two steps corresponding to the two steps of our analytical framework. First, we regressed the $\alpha MPTI$ of bacteria (or HNF) community on the Shannon diversity of HNF (or bacteria) to test how the Shannon diversity of predator (or prey) influenced prey's (or predator's) $\alpha MPTI$, i.e., community assembly processes. We then regressed the Shannon diversity of bacteria (or HNF) on its own $\alpha MPTI$ to test how the community assembly processes of bacteria (or HNF) determined its Shannon diversity.

The objective of this study is to detect the effects of ecological interactions by statistically accounting for other potential

confounding environmental factors. Therefore, when conducting the two sets of GLMMs, we used backward selections to identify the variables that also have significant effects but did not attempt to make inference from those variables. To conduct backward selection, we first included all available environmental variables in the GLMMs and then step-wisely removed variables that are not significant based on *p*-values. The environmental variables include temperature, salinity, total dissolved inorganic nitrogen (TN), total dissolved inorganic phosphorous (TP), chlorophyll a (Chla), and photosynthetically active radiation (PAR). In addition, we built Moran's Eigenvector Maps (MEM; Dray et al., 2006, 2012) that are orthogonal vectors to account for the spatial autocorrelations among stations. These spatial eigen-vectors were always included in the backward selection processes in order to account for the effects of dispersal because bacteria and HNF are passive dispersers (Declerck et al., 2013). In all above GLMM analyses, cruise was set as a random effect to avoid spurious correlations simply due to seasonal variation among cruises.

Computation

We used the "phyloseq" package to perform sequence subsampling to achieve parity in total number of reads (McMurdie and Holmes, 2013), the "iNEXT" package to perform rarefaction and calculate the Shannon diversity index (Hsieh et al., 2016), the "phangorn" package to build phylogenetic trees (Callahan et al., 2016b), the "picante" package to calculate phylogenetic distances to derive *αMPTI* (Kembel et al., 2010) and the "nlme" package to perform GLMMs (Pinheiro et al., 2019). All packages were built and computation was carried out in R version 4.0.4 (R Core Team, 2020).

RESULTS

Hydrology, HNF (Predator) and Bacteria (Prey) α-Diversities in Southern East China Sea

In the southern Each China Sea, temperature and salinity were significantly lower at the most nearshore station than other stations, especially in the spring time ($p < 0.01$; **Supplementary Figure 3**). This reflects the influences of river runoff from the Min River. The river runoff caused the concentrations of total dissolved inorganic nitrogen and phosphorous as well as chlorophyll a to be significantly higher at the most nearshore station than others ($p < 0.01$; **Supplementary Figure 3**), except for the station northeast of Taiwan (station 9; **Supplementary Figure 3**). The region northeast of Taiwan has long been reported to be influenced by the upwelling of subsurface Kuroshio waters that provide a large amount of nutrients to the East China Sea (Wong et al., 2000). Although the hydrology varied in the southern East China Sea,

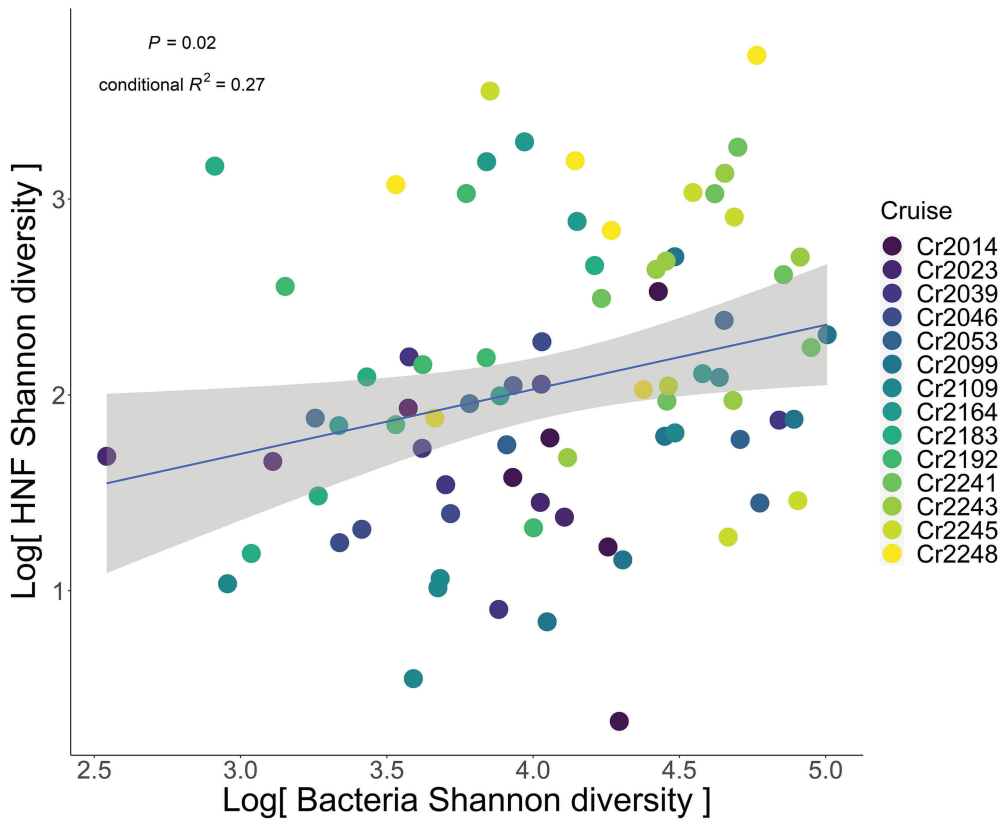

FIGURE 2 | Relationship between heterotrophic nanoflagellate (predator) and bacteria (prey) Shannon diversity. Blue solid line indicates the significant regression line fitted by the GLMM, with cruise as the random effect. Gray shaded area represents the 95% confidence interval of the regression line. The colors of dots represent different sampling cruises.

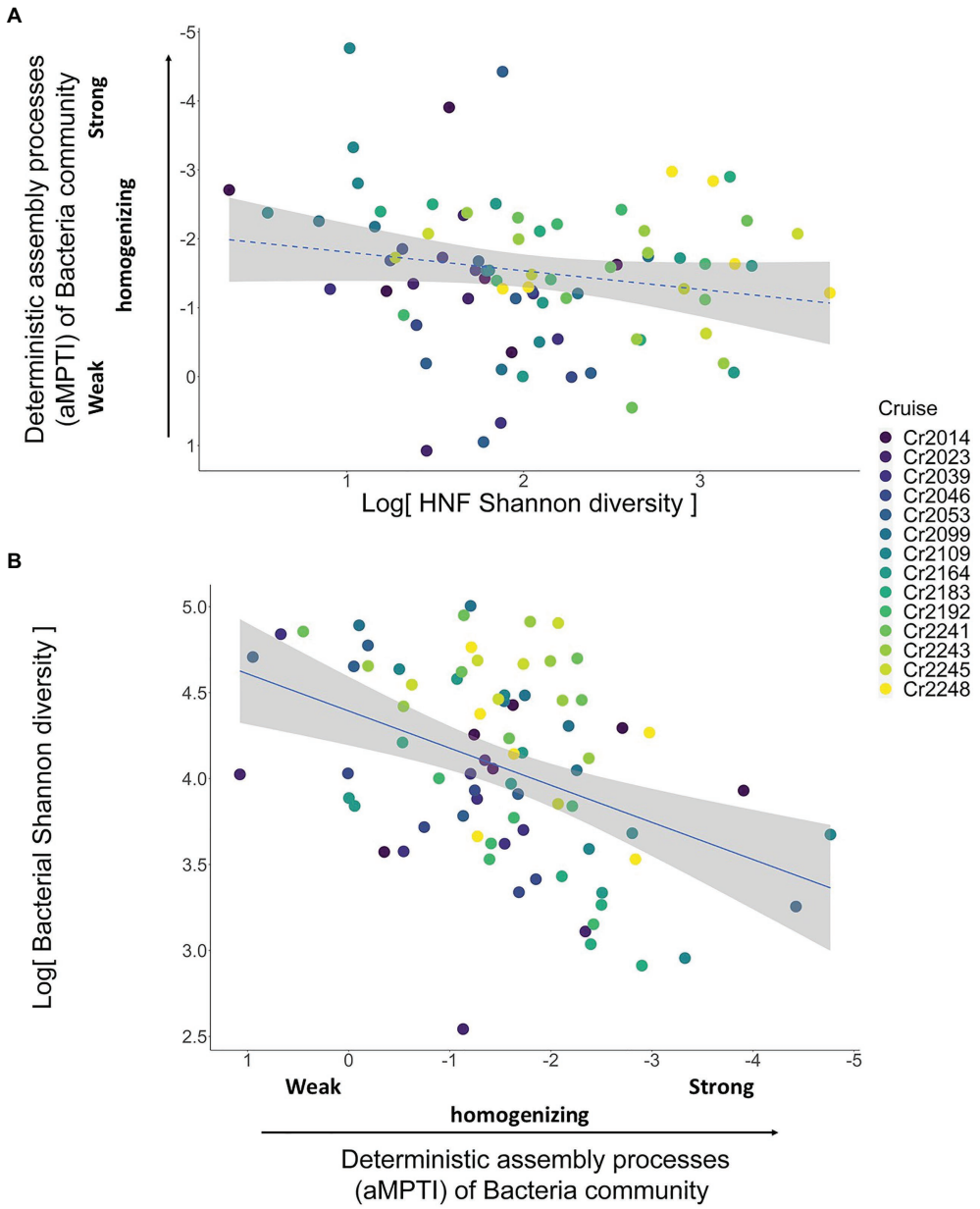

FIGURE 3 | Scatterplots showing the test for top-down control mechanisms. Panel **(A)** shows the non-significant relationship with $p = 0.1$ (dashed blue line) between HNF Shannon diversity and the deterministic assembly processes (α*MPTI*) of bacteria community. This relationship becomes significant after including other environmental variables (**Table 1**). Panel **(B)** shows the significant relationship (solid blue line) between the α*MPTI* of bacteria community and the Shannon diversity of bacteria. Including other environmental variables does not qualitatively alter this result (**Table 1**). The *p*-value and R^2 are derived from univariate GLMM. Note that the α*MPTI* of bacteria are mostly negative, so that, we reversed the *y* axis of panel **(A)** and *x* axis in panel **(B)** for visual intuition. The gray shaded area around the blue line indicates the 95% confidence interval of the regression line (GLMM). The colors of dots represent different sampling cruises.

the HNF ($p = 0.8$) and bacteria ($p = 0.08$) α-diversity did not exhibit such clear spatial variation (**Supplementary Figure 3**). Rather, we found a negative, but weak ($R^2 = 0.08$), association between HNF Shannon diversity and chlorophyll a concentration (**Supplementary Figure 4**). This finding suggests that HNF communities might not be strongly affected by abiotic environmental factors (Yang et al., 2018). On the other hand, bacteria Shannon diversity was positively associated with salinity (**Supplementary Figure 4**), which is consistent with a previous study (Fuhrman et al., 2008).

α-Diversity Association Between HNF (Predator) and Bacteria (Prey) Community

After accounting for the aforementioned hydrological processes, we found a positive association between the Shannon diversity of HNF and bacteria in the southern ECS (**Figure 2**). The positive

TABLE 1 | Results of generalized linear mixed effect model (GLMM) after backward selection to test for top-down control mechanisms.

Independent variable	Regression coefficient	Standard error	*p*-value
Step 1: Bacteria *αMPTI* as dependent variable			
HNF Shannon	0.34	0.16	0.04
Log (PAR)	0.04	0.02	0.02
Step 2: Bacteria Shannon as dependent variable			
Bacteria α*MPTI*	0.23	0.04	<0.01

These results indicate that heterotrophic nanoflagellate (HNF) Shannon diversity positively affects the α mean pairwise taxonomic index (αMPTI) of bacteria community after accounting for other confounding environmental factors. αMPTI of bacteria community in turn increases the bacteria Shannon diversity.

TABLE 2 | Results of generalized linear mixed effect model (GLMM) after backward selection to test for top-down control mechanisms.

Independent variable	Regression coefficient	Standard error	*p*-value
Step 1: HNF *αMPTI* as dependent variable			
Bacteria Shannon	−0.11	0.29	0.71
Spatial autocorrelation	0.3	0.14	0.03
Step 2: HNF Shannon as dependent variable			
HNF α*MPTI*	−0.09	0.06	0.13

These results indicate that bacteria Shannon diversity does not influence the αMPTI of HNF community, which also does not determine its Shannon diversity. This conclusion is qualitatively the same as that drawn from the univariate GLMM.

association was still significant after either setting station as a random effect (p = 0.02), or setting station as a random effect nested within cruise to account for spatial autocorrelation (p = 0.02).

In order to reveal whether the underlying mechanisms are top-down control and/or bottom-up control, we then applied the two-step analytical framework to deconstruct this positive association. From the top-down control perspective, we found that the *αMPTI* of bacteria community was not significantly associated with the Shannon diversity of HNF community with p = 0.1 (univariate regression coefficient = 0.27; **Figure 3A**). However, after accounting for other environmental variables *via* backward selections (**Supplementary Tables 1** and **2**), the *αMPTI* of bacteria community became significantly less negative with the increase of HNF Shannon diversity (**Table 1**). Less negative *αMPTI* of bacteria community was in turn associated with higher bacterial Shannon diversity (univariate regression coefficient = 0.23; p < 0.01; **Figure 3B**). These findings suggest that, after statistically accounting for the environmental factors, the α-diversity of HNF community possibly made the deterministic processes weakly homogenizing the bacteria community, which then led to higher diversity of bacteria community.

From the bottom-up control perspective, we first found that of HNF community was independent of the bacteria Shannon diversity (univariate regression p = 0.29; **Figure 4A**). Subsequently, we found that the HNF community did not significantly affect its Shannon diversity (p = 0.09; **Figure 4B**). Including other environmental variables did not alter these findings (**Table 2**). These results suggest that the bacteria α-diversity did not influence the assembly processes of HNF community, and these assembly processes did not determine the α-diversity of HNF community.

DISCUSSION

In the southern ECS, the diversity of HNF (predator) and bacteria (prey) community are positively associated (**Figure 2**), which is consistent with a previous study that included data from the whole ECS (Yang et al., 2018). Positive association between predator and prey diversity is also observed in other aquatic systems (Aranguren-Riaño et al., 2011). More importantly, our novel analytical framework allows us to decipher how this positive association likely results from the associations between predator α-diversity and weak homogenizing deterministic assembly processes of prey community, which are then associated with higher prey α-diversity (**Figure 3**). Our findings echo the argument that top-down control mechanisms determine the α-diversity of prey community (Lovejoy et al., 2000; Vázquez-Domínguez et al., 2005a; Longnecker et al., 2010) and may propagate to affect energy flows in marine ecosystem (Vázquez-Domínguez et al., 2005b; Pradeep Ram et al., 2015).

The importance of top-down control mechanisms revealed in this study contradicts with many studies that emphasize the impacts of bottom-up control mechanisms (e.g., Scherber et al., 2010; Hertzog et al., 2016; Otero et al., 2020). One possible explanation to this disagreement is the fact that our data come from an aquatic system, whereas the majority studies demonstrating bottom-up control mechanisms is conducted in terrestrial systems (as reviewed in Haddad et al., 2009). In aquatic systems, predators have been demonstrated to impose larger impacts on prey than in terrestrial systems (Shurin and Borer, 2002; Shurin et al., 2006). Stronger predation pressures may act as a weak homogenizing deterministic processes for prey community, i.e., make the *αMPTI* of prey community less negative, and thus increase prey α-diversity. However, more detailed analyses are required to test this conjecture.

The prevalence of top-down control in aquatic systems implies that HNF community might also be controlled by their predators (Gasol, 1994; Segovia et al., 2014). Top-down control on HNF community is reportedly more prominent in productive regions because productive regions can sustain more diverse top predators, such as ciliates or other microzooplankton (Gasol et al., 2002; Pernthaler, 2005). Since the productivity in the southern East China Sea is not particularly low (Gong et al., 2000; Chen et al., 2004), it is possible that HNF diversity could be controlled by their predators instead of bacteria. Besides, lack of evidence for bottom-up control on HNF diversity could result from the fact that HNF have alternative food resources other than bacteria. It has been shown that HNF feed on picoeukaryotes with similar rate as that on prokaryotes (Parslow et al., 1986; Christaki et al., 2005). The α-diversity of HNF community could be affected not only by the diversity of bacteria but also picoeukaryotes. These speculations require empirical feeding experiments to be verified; these create some possibilities for future work.

The other possible explanation why the bottom-up control mechanisms are non-significant in our study is that the

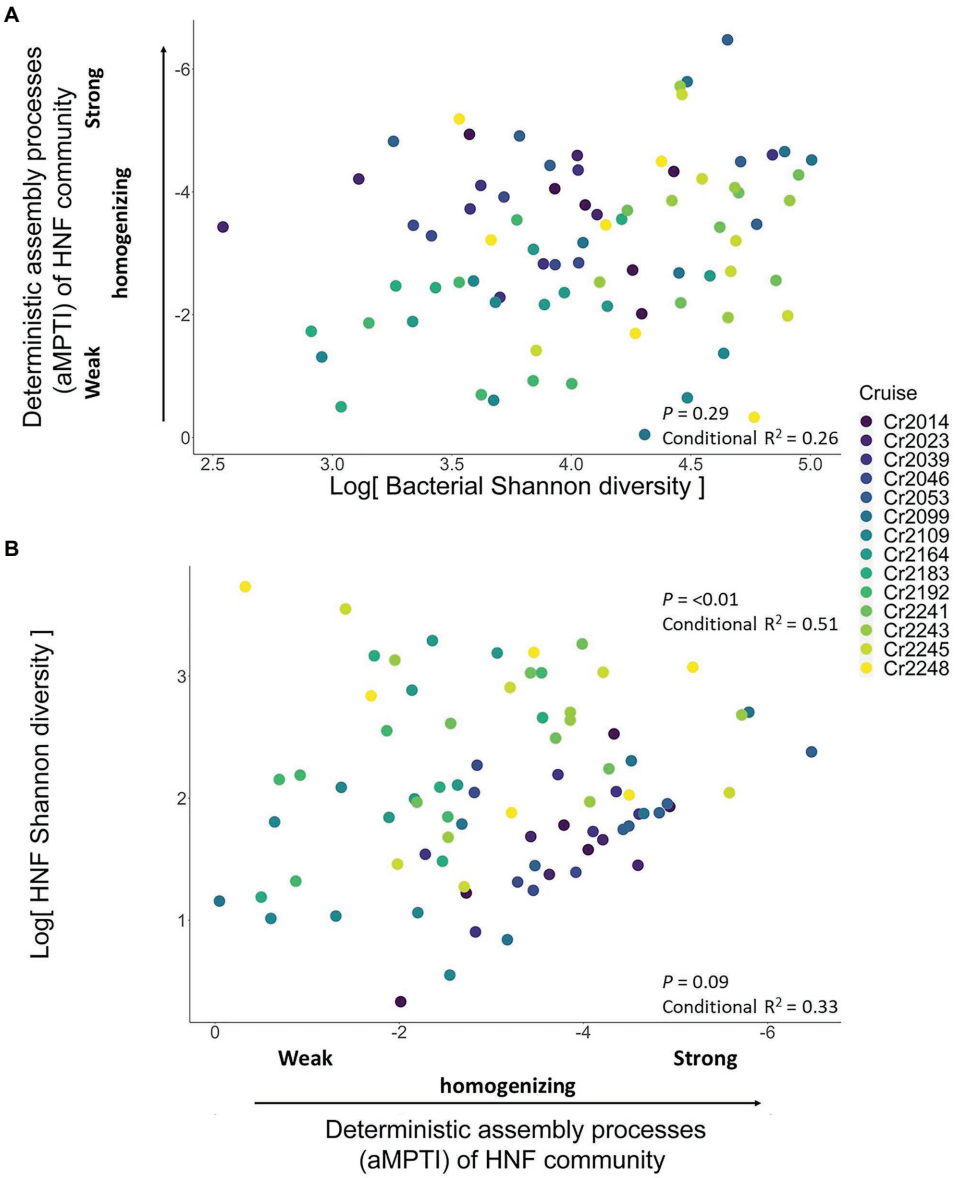

FIGURE 4 | Scatterplots showing the test for bottom-up controlled mechanisms. Panel **(A)** shows the non-significant relationship (dashed blue line) between bacteria Shannon diversity and the deterministic assembly processes (α*MPTI*) of HNF community. Panel **(B)** shows the non-significant relationship (dashed blue line) between the α*MPTI* of HNF community and the Shannon diversity of HNF. The *p*-value and R^2 are derived from univariate GLMM, whereas including other environmental variables does not qualitatively alter the conclusions (**Table 1**). Note that the α*MPTI* of bacteria are mostly negative, so that, we reversed the *y* axis of panel **(A)** and *x* axis in panel **(B)** for visual intuition. The gray shaded area around the blue line indicates the 95% confidence interval of the regression line (GLMM). The colors of dots represent different sampling cruises.

phylogeny of HNF in the southern ECS might not faithfully represents their ecological niche. Faithfully approximating species' ecological niche using their phylogeny is a critical assumption that underpins the inferences based on species' phylogeny (Losos, 2008). We did find significant phylogenetic signals, i.e., significant correlations phylogeny and habitat preferences, for both the HNF and bacteria community (**Supplementary Figure 5**). However, the phylogenetic signals of the HNF community were much weaker than that of bacteria (**Supplementary Figure 5**). For the HNF, the phylogenetic signal was only significant in a narrow range of phylogenetic distance (panel B of **Supplementary Figure 5**), meaning that the index based on phylogenetic distance (here, the *αMPTI*) might not completely represent the ecological processes experienced by the HNF community. Consequently, we do not completely rule out possible the occurrence of bottom-up control mechanisms in mediating bi-trophic diversity associations in the southern ECS.

We demonstrated that the top-down control mechanisms likely explain the positive association of predator and prey diversities; nevertheless, top-down control processes encompass

a variety of detailed mechanisms (Hillebrand and Shurin, 2005). HNF have been shown to exhibit selective feeding behavior that can promote the diversity of their prey, including bacteria (Montagnes et al., 2008; Gerea et al., 2013). HNF have also been demonstrated to suppress dominant prey species and promote prey diversity, i.e., the kill the winner hypothesis (Winter et al., 2010). In addition, HNF, as predators, can indirectly increase prey diversity through regenerating resources (Attayde and Hansson, 1999), maintaining the diversity of resources for prey (Abrams, 2001), and/or trait-mediated indirect interactions (Werner and Peacor, 2003). For example, in a tri-trophic food web consisted of a basal resource (an isopod *Jaera nordmanni*), an intermediate consumer (an amphipod *Echinogammarus marinus*), and a top-predator fish (*Lipophrys pholis*), the presence of top-predator can reduce the feeding rate of an intermediate consumer (Alexander et al., 2013). Furthermore, both bacteria and HNF communities interact with other trophic groups, including marine viruses, phytoplankton, and zooplankton (Needham et al., 2017; Zeldis and Décima, 2020; Zimmerman et al., 2020). We cannot rule out the impacts from those organisms in this analysis. By including those trophic groups in the analysis could potentially resolve the puzzles. Clarifying the above mechanisms is a venue beyond the scope of this study but will render fruitful results.

One major concern of our analytical framework is that interpretations of *αMPTI*, or phylogenetic similarity in general, are controversial. Using phylogenetic similarity to approximate species' ecological difference is an assumption commonly made in the field of microbial ecology (Webb, 2000; Webb et al., 2002). Ever since Webb developed the net related index (NTI) and nearest taxon index (NRI), species' phylogenetic similarity has been used to indicate whether a community is subject to environmental filtering (e.g., Horner-Devine and Bohannan, 2006) or competition (e.g., Cooper et al., 2008). More recently, species' phylogeny has been used to decipher the structure or underlying processes of a meta-community (Stegen et al., 2013, 2015; Dini-Andreote et al., 2015; Wu et al., 2018). Based on this assumption of using phylogenetic similarity to approximate species' ecological difference, we developed the analytical framework with the attempt to decipher the positive association between predator and prey diversity. However, as suggested in several studies, phylogenetic similarity is an imperfect proxy of species' ecological difference because ecological interactions, e.g., trophic interactions, might not leave traceable footprints on species' evolutionary history. Species' phylogenetic similarity thus may not be used to faithfully represent community assembly processes (Mayfield and Levine, 2010; Pavoine and Bonsall, 2011). We are fully aware of this controversy and believe that quantifying ecological interactions, e.g., feeding rates, is the most direct way to decipher predator and prey diversity associations. However, without resorting to manipulative experiments, here, we assume that phylogeny could approximate species' ecological niche. Verifying this assumption requires further investigations so that we mindfully regard the *αMPTI* as an implication of the occurrence of certain community assembly processes. Through our analyses, we offer a possible explanation to the diversity association but our findings critically hinge on the fidelity of phylogeny to ecological niche.

In spite of some caveats, we still provide a useful analytical framework to better decipher why the diversity of predator and prey are associated. This analytical framework can be an alternative to manipulative experiments that are often required to understand the mechanisms underpinning the association between the diversity of predator and prey (e.g., Scherber et al., 2010; Hertzog et al., 2016). Besides being costly and labor intensive, manipulative experiments could suffer from unsatisfying spatial or temporal scale (Briggs and Borer, 2005). Our analytical framework can potentially provide an alternative approach that can be applied in any predator-prey system.

In summary, our analyses support top-down control as the underlying mechanisms of positive α-diversity association between HNF and bacteria in the southern ECS. We showed a positive association between predator α-diversity and weak homogenizing deterministic assembly processes of prey community, which then are positively associated with the α-diversity of prey community. These results suggest that predators are likely the driver of the positive association between predator and prey α-diversity in the southern ECS microbes.

DATA AVAILABILITY STATEMENT

The datasets generated and analyzed for this study can be found in the NCBI Sequence Read Archive (SRA) under the accession numbers: PRJNA662424 (https://www.ncbi.nlm.nih.gov/sra/?term=PRJNA662424).

AUTHOR CONTRIBUTIONS

F-HC and C-hH developed the hypothesis, conducted the analyses, and composed the manuscript. All other authors contributed equally to collect data and help polish the manuscript.

FUNDING

This work was supported by the National Center for Theoretical Sciences, National Taiwan University, Foundation for the Advancement of Outstanding Scholarship, and the Ministry of Science and Technology, Taiwan.

ACKNOWLEDGMENTS

We thank Hon-Tsen Yu for providing facilities and advice on laboratory work.

SUPPLEMENTARY MATERIAL

The Supplementary Material for this article can be found online at: https://www.frontiersin.org/articles/10.3389/fmars.2021.651565/full#supplementary-material

REFERENCES

Abrams, P. A. (2001). The effect of density-independent mortality on the coexistence of exploitative competitors for renewing resources. *Am. Nat.* 158, 459–470. doi: 10.1086/323113

Alexander, M. E., Dick, J. T. A., and O'Connor, N. E. (2013). Trait-mediated indirect interactions in a marine intertidal system as quantified by functional responses. *Oikos* 122, 1521–1531. doi: 10.1111/j.1600-0706.2013.00472.x

Aranguren-Riaño, N., Guisande, C., and Ospina, R. (2011). Factors controlling crustacean zooplankton species richness in neotropical lakes. *J. Plankton Res.* 33, 1295–1303. doi: 10.1093/plankt/fbr028

Attayde, J. L., and Hansson, L.-A. (1999). Effects of nutrient recycling by zooplankton and fish on phytoplankton communities. *Oecologia* 121, 47–54. doi: 10.1007/s004420050906

Axmacher, J. C., Brehm, G., Hemp, A., Tünte, H., Lyaruu, H. V. M., Müller-Hohenstein, K., et al. (2009). Determinants of diversity in afrotropical herbivorous insects (Lepidoptera: Geometridae): plant diversity, vegetation structure or abiotic factors? *J. Biogeogr.* 36, 337–349. doi: 10.1111/j.1365-2699.2008.01997.x

Berry, D., Mahfoudh, B. K., Wagner, M., and Loy, A. (2011). Barcoded primers used in multiplex amplicon pyrosequencing bias amplification. *Appl. Environ. Microbiol.* 77, 7846–7849. doi: 10.1128/AEM.05220-11

Borer, E. T., Seabloom, E. W., Gruner, D. S., Harpole, W. S., Hillebrand, H., Lind, E. M., et al. (2014). Herbivores and nutrients control grassland plant diversity via light limitation. *Nature* 508, 517–520. doi: 10.1038/nature13144

Briggs, C. J., and Borer, E. T. (2005). Why short-term experiments may not allow long-term predictions about intraguild predation. *Ecol. Appl.* 15, 1111–1117. doi: 10.1890/04-1776

Callahan, B. J., McMurdie, P. J., Rosen, M. J., Han, A. W., Johnson, A. J. A., and Holmes, S. P. (2016a). DADA2: high-resolution sample inference from Illumina amplicon data. *Nat. Methods* 13, 581–583. doi: 10.1038/nmeth.3869

Callahan, B. J., Sankaran, K., Fukuyama, J. A., McMurdie, P. J., and Holmes, S. P. (2016b). Bioconductor workflow for microbiome data analysis: from raw reads to community analyses. *F1000Research* 5:1492. doi: 10.12688/f1000research.8986.2

Castagneyrol, B., Jactel, H., and Cardinale, B. J. (2012). Unraveling plant-animal diversity relationships: a meta-regression analysis. *Ecology* 93, 2115–2124. doi: 10.1890/11-1300.1

Cavender-Bares, J., Kozak, K. H., Fine, P. V. A., and Kembel, S. W. (2009). The merging of community ecology and phylogenetic biology. *Ecol. Lett.* 12, 693–715. doi: 10.1111/j.1461-0248.2009.01314.x

Chao, A., and Chiu, C.-H. (2016). Species richness: estimation and comparison. Wiley Stats Ref Stat. Ref. Online, 1–26.

Chao, A., Gotelli, N. J., Hsieh, T. C., Sander, E. L., Ma, K. H., Colwell, R. K., et al. (2014). Rarefaction and extrapolation with Hill numbers: a framework for sampling and estimation in species diversity studies. *Ecol. Monogr.* 84, 45–67. doi: 10.1890/13-0133.1

Chen, Y.-L. L., Chen, H.-Y., Gong, G.-C., Lin, Y.-H., Jan, S., and Takahashi, M. (2004). Phytoplankton production during a summer coastal upwelling in the East China Sea. *Cont. Shelf Res.* 24, 1321–1338. doi: 10.1016/j.csr.2004.04.002

Christaki, U., Vázquez-Domínguez, E., Courties, C., and Lebaron, P. (2005). Grazing impact of different heterotrophic nanoflagellates on eukaryotic (*Ostreococcus tauri*) and prokaryotic picoautotrophs (*Prochlorococcus* and *Synechococcus*). *Environ. Microbiol.* 7, 1200–1210. doi: 10.1111/j.1462-2920.2005.00800.x

Cooper, N., Rodríguez, J., and Purvis, A. (2008). A common tendency for phylogenetic overdispersion in mammalian assemblages. *Proc. R. Soc. B Biol. Sci.* 275, 2031–2037. doi: 10.1098/rspb.2008.0420

Declerck, S. A. J., Winter, C., Shurin, J. B., Suttle, C. A., and Matthews, B. (2013). Effects of patch connectivity and heterogeneity on metacommunity structure of planktonic bacteria and viruses. *ISME J.* 7, 533–542. doi: 10.1038/ismej.2012.138

Dini-Andreote, F., Stegen, J. C., van Elsas, J. D., and Salles, J. F. (2015). Disentangling mechanisms that mediate the balance between stochastic and deterministic processes in microbial succession. *Proc. Natl. Acad. Sci. U. S. A.* 112, E1326–E1332. doi: 10.1073/pnas.1414261112

Dray, S., Legendre, P., and Peres-Neto, P. R. (2006). Spatial modeling: a comprehensive framework for principal coordinate analysis of neighbour matrices (PCNM). *Ecol. Model.* 196, 483–493. doi: 10.1016/j.ecolmodel.2006.02.015

Dray, S., Pélissier, R., Couteron, P., Fortin, M.-J., Legendre, P., Peres-Neto, P. R., et al. (2012). Community ecology in the age of multivariate multiscale spatial analysis. *Ecol. Monogr.* 82, 257–275. doi: 10.1890/11-1183.1

Fuhrman, J. A., Steele, J. A., Hewson, I., Schwalbach, M. S., Brown, M. V., Green, J. L., et al. (2008). A latitudinal diversity gradient in planktonic marine bacteria. *Proc. Natl. Acad. Sci. U. S. A.* 105, 7774–7778. doi: 10.1073/pnas.0803070105

Gasol, J. M. (1994). A framework for the assessment of top-down vs bottom-up control of heterotrophic nanoflagellate abundance. *Mar. Ecol. Prog. Ser.* 113, 291–300. doi: 10.3354/meps113291

Gasol, J. M., Pedros-Alio, C., and Vaque, D. (2002). Regulation of bacterial assemblages in oligotrophic plankton systems results from experimental and emperi. *Antonie Van Leeuwenhoek* 81, 435–452. doi: 10.1023/A:1020578418898

Gerea, M., Queimaliños, C., Schiaffino, M. R., Izaguirre, I., Forn, I., Massana, R., et al. (2013). In situ prey selection of mixotrophic and heterotrophic flagellates in Antarctic oligotrophic lakes: an analysis of the digestive vacuole content. *J. Plankton Res.* 35, 201–212. doi: 10.1093/plankt/fbs085

Gerhold, P., Cahill, J. F., Winter, M., Bartish, I. V., and Prinzing, A. (2015). Phylogenetic patterns are not proxies of community assembly mechanisms (they are far better). *Funct. Ecol.* 29, 600–614. doi: 10.1111/1365-2435.12425

Gong, G. C., Shiah, F. K., Liu, K. K., Wen, Y. H., and Liang, M.-H. (2000). Spatial and temporal variation of chlorophyll a, primary productivity and chemical hydrography in the southern East China Sea. *Cont. Shelf Res.* 20, 411–436. doi: 10.1016/S0278-4343(99)00079-5

Gong, G., Wen, Y., Wang, B., and Liu, G. (2003). Seasonal variation of chlorophyll a concentration, primary production and environmental conditions in the subtropical East China Sea. *Deep Sea Res. Part II Top. Stud. Oceanogr.* 50, 1219–1236. doi: 10.1016/S0967-0645(03)00019-5

Götzenberger, L., de Bello, F., Bråthen, K. A., Davison, J., Dubuis, A., Guisan, A., et al. (2012). Ecological assembly rules in plant communities-approaches, patterns and prospects. *Biol. Rev. Camb. Philos. Soc.* 87, 111–127. doi: 10.1111/j.1469-185X.2011.00187.x

Guillou, L., Bachar, D., Audic, S., Bass, D., Berney, C., Bittner, L., et al. (2012). The Protist ribosomal reference database (PR2): a catalog of unicellular eukaryote small sub-unit rRNA sequences with curated taxonomy. *Nucleic Acids Res.* 41, D597–D604. doi: 10.1093/nar/gks1160

Haddad, N. M., Crutsinger, G. M., Gross, K., Haarstad, J., Knops, J. M. H., and Tilman, D. (2009). Plant species loss decreases arthropod diversity and shifts trophic structure. *Ecol. Lett.* 12, 1029–1039. doi: 10.1111/j.1461-0248.2009.01356.x

Hawkins, B. A., and Porter, E. E. (2003). Does herbivore diversity depend on plant diversity? The case of California butterflies. *Am. Nat.* 161, 40–49. doi: 10.1086/345479

Hertzog, L. R., Meyer, S. T., Weisser, W. W., and Ebeling, A. (2016). Experimental manipulation of grassland plant diversity induces complex shifts in aboveground arthropod diversity. *PLoS One* 11:e148768. doi: 10.1371/journal.pone.0148768

Hillebrand, H., and Shurin, J. B. (2005). "Biodiversity and aquatic food webs," in *Aquatic Food Webs – An Ecosystem Approach*. eds. A. Belgrano, U. Scharler, J. Dunne and R. Ulanowicz (Oxford, United Kingdom: Oxford University Press), 184–197.

Horner-Devine, M. C., and Bohannan, B. J. M. (2006). Phylogenetic clustering and Overdispersion in bacterial communities. *Ecology* 87, S100–S108. doi: 10.1890/0012-9658(2006)87[100:PCAOIB]2.0.CO;2

Hsieh, T. C., Ma, K. H., and Chao, A. (2016). iNEXT: an R package for rarefaction and extrapolation of species diversity (Hill numbers). *Methods Ecol. Evol.* 7, 1451–1456. doi: 10.1111/2041-210X.12613

Hubbell, S. P. (2001). *The Unified Neutral Theory of Biodiversity and Biogeography (MPB-32)*. Princeton, New Jersey, United States: Princeton University Press.

Hunter, M. D., and Price, P. W. (1992). Playing chutes and ladders: heterogeneity and the relative roles of bottom-up and top-down forces in natural communities. *Ecology* 73, 724–732.

Hutchinson, G. E. (1959). Homage to Santa Rosalia or why are there so many kinds of animals? *Am. Nat.* 93, 145–159. doi: 10.1086/282070

Kembel, S. W., Cowan, P. D., Helmus, M. R., Cornwell, W. K., Morlon, H., Ackerly, D. D., et al. (2010). Picante: R tools for integrating phylogenies and ecology. *Bioinformatics* 26, 1463–1464. doi: 10.1093/bioinformatics/btq166

Leibold, M. A. (1996). A graphical model of keystone predators in food webs: trophic regulation of abundance, incidence, and diversity patterns in communities. *Am. Nat.* 147, 784–812. doi: 10.1086/285879

Logares, R., Tesson, S. V. M., Canbäck, B., Pontarp, M., Hedlund, K., and Rengefors, K. (2018). Contrasting prevalence of selection and drift in the community structuring of bacteria and microbial eukaryotes. *Environ. Microbiol.* 20, 2231–2240. doi: 10.1111/1462-2920.14265

Longnecker, K., Wilson, M. J., Sherr, E. B., and Sherr, B. F. (2010). Effect of top-down control on cell-specific activity and diversity of active marine bacterioplankton. *Aquat. Microb. Ecol.* 58, 153–165. doi: 10.3354/ame01366

Losos, J. B. (2008). Phylogenetic niche conservatism, phylogenetic signal and the relationship between phylogenetic relatedness and ecological similarity among species. *Ecol. Lett.* 11, 995–1003. doi: 10.1111/j.1461-0248.2008.01229.x

Lovejoy, C., Legendre, L., Therriault, J.-C., Tremblay, J.-E., Klein, B., and Grant Ingram, R. (2000). Growth and distribution of marine bacteria in relation to nanoplankton community structure. *Deep Sea Res. Part II Top. Stud. Oceanogr.* 47, 461–487. doi: 10.1016/S0967-0645(99)00115-0

Lowe, W. H., and McPeek, M. A. (2014). Is dispersal neutral? *Trends Ecol. Evol.* 29, 444–450. doi: 10.1016/j.tree.2014.05.009

MacArthur, R. H., and Wilson, E. O. (1967). *The Theory of Island Biogeography*. Princeton, New Jersey, United States: Princeton University Press.

Mayfield, M. M., and Levine, J. M. (2010). Opposing effects of competitive exclusion on the phylogenetic structure of communities. *Ecol. Lett.* 13, 1085–1093. doi: 10.1111/j.1461-0248.2010.01509.x

McMurdie, P. J., and Holmes, S. (2013). Phyloseq: An R package for reproducible interactive analysis and graphics of microbiome census data. *PLoS One* 8:e61217. doi: 10.1371/journal.pone.0061217

McMurdie, P. J., and Holmes, S. (2014). Waste not, want not: why rarefying microbiome data is inadmissible. *PLoS Comput. Biol.* 10:e1003531. doi: 10.1371/journal.pcbi.1003531

Montagnes, D. J. S., Barbosa, A. B., Boenigk, J., Davidson, K., Jürgens, K., Macek, M., et al. (2008). Selective feeding behaviour of key free-living protists: avenues for continued study. *Aquat. Microb. Ecol.* 53, 83–98. doi: 10.3354/ame01229

Mouquet, N., Devictor, V., Meynard, C. N., Munoz, F., Bersier, L. F., Chave, J., et al. (2012). Ecophylogenetics: advances and perspectives. *Biol. Rev.* 87, 769–785. doi: 10.1111/j.1469-185X.2012.00224.x

Needham, D. M., Sachdeva, R., and Fuhrman, J. A. (2017). Ecological dynamics and co-occurrence among marine phytoplankton, bacteria and myoviruses shows microdiversity matters. *ISME J.* 11, 1614–1629. doi: 10.1038/ismej.2017.29

Nemergut, D. R., Schmidt, S. K., Fukami, T., O'Neill, S. P., Bilinski, T. M., Stanish, L. F., et al. (2013). Patterns and processes of microbial community assembly. *Microbiol. Mol. Biol. Rev.* 77, 342–356. doi: 10.1128/MMBR.00051-12

Otero, J., Álvarez-Salgado, X. A., and Bode, A. (2020). Phytoplankton diversity effect on ecosystem functioning in a coastal upwelling system. *Front. Mar. Sci.* 7:592255. doi: 10.3389/fmars.2020.592255

Parslow, J. S., Doucette, G. J., Taylor, F. J. R., and Harrison, P. J. (1986). Feeding by the zooflagellate Pseudobodo sp. on the picoplanktonic prasinomonad *Micromonas pusilla*. *Mar. Ecol. Prog. Ser.* 29, 237–246. doi: 10.3354/meps029237

Pavoine, S., and Bonsall, M. B. (2011). Measuring biodiversity to explain community assembly: a unified approach. *Biol. Rev.* 86, 792–812. doi: 10.1111/j.1469-185X.2010.00171.x

Pernthaler, J. (2005). Predation on prokaryotes in the water column and its ecological implications. *Nat. Rev. Microbiol.* 3, 537–546. doi: 10.1038/nrmicro1180

Pinheiro, J., Bates, D., DebRoy, S., and Sarkar, D., R Core Team (2019). nlme: Linear and nonlinear mixed effects models. R-project. Available at: https://cran.r-project.org/package=nlme (Accessed January 10, 2021).

Power, M. E. (1992). Top-down and bottom-up forces in food webs: do plants have primacy. *Ecology* 73, 733–746. doi: 10.2307/1940153

Pradeep Ram, A. S., Colombet, J., Perriere, F., Thouvenot, A., and Sime-Ngando, T. (2015). Viral and grazer regulation of prokaryotic growth efficiency in temperate freshwater pelagic environments. *FEMS Microbiol. Ecol.* 91, 1–12. doi: 10.1093/femsec/fiv002

Proulx, M., and Mazumder, A. (1998). Reversal of grazing impact on plant species richness in nutrient-poor vs. nutrient-rich ecosystems. *Ecology* 79, 2581–2592. doi: 10.1890/0012-9658(1998)079[2581:ROGIOP]2.0.CO;2

Quast, C., Pruesse, E., Yilmaz, P., Gerken, J., Schweer, T., Yarza, P., et al. (2013). The SILVA ribosomal RNA gene database project: improved data processing and web-based tools. *Nucleic Acids Res.* 41, D590–D596. doi: 10.1093/nar/gks1219

R Core Team (2020). R: a language and environment for statistical computing. Available at: https://www.r-project.org/ (Accessed January 10, 2021).

Scherber, C., Eisenhauer, N., Weisser, W. W., Schmid, B., Voigt, W., Fischer, M., et al. (2010). Bottom-up effects of plant diversity on multitrophic interactions in a biodiversity experiment. *Nature* 468, 553–556. doi: 10.1038/nature09492

Segovia, B. T., Pereira, D. G., Bini, L. M., and Velho, L. F. M. (2014). Effects of bottom-up and top-down controls on the temporal distribution of planktonic heterotrophic nanoflagellates are dependent on water depth. *Hydrobiologia* 736, 155–164. doi: 10.1007/s10750-014-1904-7

Shurin, J., and Borer, E. (2002). A cross ecosystem comparison of the strength of trophic cascades. *Ecol. Lett.* 5, 785–791. doi: 10.1046/j.1461-0248.2002.00381.x

Shurin, J. B., Gruner, D. S., and Hillebrand, H. (2006). All wet or dried up? Real differences between aquatic and terrestrial food webs. *Proc. R. Soc. B Biol. Sci.* 273, 1–9. doi: 10.1098/rspb.2005.3377

Siemann, E. (1998). Experimental tests of effects of plant productivity and diversity on grassland arthropod diversity. *Ecology* 79, 2057–2070. doi: 10.1890/0012-9658(1998)079[2057:ETOEOP]2.0.CO;2

Southwood, T. R. E., Brown, V. K., and Reader, P. M. (1979). The relationships of plant and insect diversities in succession. *Biol. J. Linn. Soc.* 12, 327–348. doi: 10.1111/j.1095-8312.1979.tb00063.x

Srivastava, D. S., and Lawton, J. H. (1998). Why more productive sites have more species: an experimental test of theory using tree-hole communities. *Am. Nat.* 152, 510–529. doi: 10.1086/286187

Stegen, J. C., Lin, X., Fredrickson, J. K., Chen, X., Kennedy, D. W., Murray, C. J., et al. (2013). Quantifying community assembly processes and identifying features that impose them. *ISME J.* 7, 2069–2079. doi: 10.1038/ismej.2013.93

Stegen, J. C., Lin, X., Fredrickson, J. K., and Konopka, A. E. (2015). Estimating and mapping ecological processes influencing microbial community assembly. *Front. Microbiol.* 6, 1–15. doi: 10.3389/fmicb.2015.00370

Vaulot, D., and Guillou, L. (2019). Protist ribosomal reference database (PR2) - SSU rRNA gene database.

Vázquez-Domínguez, E., Casamayor, E. O., Català, P., and Lebaron, P. (2005a). Different marine heterotrophic nanoflagellates affect differentially the composition of enriched bacterial communities. *Microb. Ecol.* 49, 474–485. doi: 10.1007/s00248-004-0035-5

Vázquez-Domínguez, E., Gasol, J. M., Agustí, S., Duarte, C. M., and Vaqué, D. (2005b). Growth and grazing losses of prokaryotes in the Central Atlantic Ocean. *J. Plankton Res.* 27, 1055–1066. doi: 10.1093/plankt/fbi074

Vellend, M. (2010). Conceptual systhesis in community ecology. *Q. Rev. Biol.* 85, 183–206. doi: 10.1086/652373

Vellend, M., Srivastava, D. S., Anderson, K. M., Brown, C. D., Jankowski, J. E., Kleynhans, E. J., et al. (2014). Assessing the relative importance of neutral stochasticity in ecological communities. *Oikos* 123, 1420–1430. doi: 10.1111/oik.01493

Webb, C. O. (2000). Exploring the phylogenetic structure of ecological communities: an example for rain forest trees. *Am. Nat.* 156, 145–155. doi: 10.1086/303378

Webb, C. O., Ackerly, D. D., McPeek, M. A., and Donoghue, M. J. (2002). Phylogenies and community ecology. *Annu. Rev. Ecol. Syst.* 33, 475–505. doi: 10.1146/annurev.ecolsys.33.010802.150448

Werner, E. E., and Peacor, S. D. (2003). A review of trait-mediated indirect interactions in ecological communities. *Ecology* 84, 1083–1100. doi: 10.1890/0012-9658(2003)084[1083:AROTII]2.0.CO;2

Winter, C., Bouvier, T., Weinbauer, M. G., and Thingstad, T. F. (2010). Trade-offs between competition and defense specialists among unicellular planktonic organisms: the "killing the winner" hypothesis revisited. *Microbiol. Mol. Biol. Rev.* 74, 42–57. doi: 10.1128/MMBR.00034-09

Wong, G. T. F., Chao, S.-Y., Li, Y.-H., and Shiah, F.-K. (2000). The Kuroshio edge exchange processes (KEEP) study — an introduction to hypotheses and highlights. *Cont. Shelf Res.* 20, 335–347. doi: 10.1016/S0278-4343(99)00075-8

Wu, W., Lu, H.-P., Sastri, A., Yeh, Y.-C., Gong, G.-C., Chou, W.-C., et al. (2018). Contrasting the relative importance of species sorting and dispersal limitation in shaping marine bacterial versus protist communities. *ISME J.* 12, 485–494. doi: 10.1038/ismej.2017.183

Yang, J. W., Wu, W., Chung, C. C., Chiang, K. P., Gong, G. C., and Hsieh, C. H. (2018). Predator and prey biodiversity relationship and its consequences on marine ecosystem functioning - interplay between nanoflagellates and bacterioplankton. *ISME J.* 12, 1532–1542. doi: 10.1038/s41396-018-0111-3

Zeldis, J. R., and Décima, M. (2020). Mesozooplankton connect the microbial food web to higher trophic levels and vertical export in the New Zealand subtropical convergence zone. *Deep Sea Res. Part I Oceanogr. Res. Pap.* 155:103146. doi: 10.1016/j.dsr.2019.103146

Zhou, J., and Ning, D. (2017). Stochastic community assembly: does it matter in microbial ecology? *Microbiol. Mol. Biol. Rev.* 81, e00002–e00017. doi: 10.1128/MMBR.00002-17

Zimmerman, A. E., Howard-Varona, C., Needham, D. M., John, S. G., Worden, A. Z., Sullivan, M. B., et al. (2020). Metabolic and biogeochemical consequences of viral infection in aquatic ecosystems. *Nat. Rev. Microbiol.* 18, 21–34. doi: 10.1038/s41579-019-0270-x

Conflict of Interest: The authors declare that the research was conducted in the absence of any commercial or financial relationships that could be construed as a potential conflict of interest.

Copyright © 2021 Chang, Yang, Liu, Lu, Gong, Shiah and Hsieh. This is an open-access article distributed under the terms of the Creative Commons Attribution License (CC BY). The use, distribution or reproduction in other forums is permitted, provided the original author(s) and the copyright owner(s) are credited and that the original publication in this journal is cited, in accordance with accepted academic practice. No use, distribution or reproduction is permitted which does not comply with these terms.

frontiers in Marine Science

ORIGINAL RESEARCH
published: 10 August 2021
doi: 10.3389/fmars.2021.677632

Phytoplankton Increase Along the Kuroshio Due to the Large Meander

Daniel Andres Lizarbe Barreto[1]*, *Ricardo Chevarria Saravia*[1], *Takeyoshi Nagai*[2] and *Takafumi Hirata*[3]

[1] Facultad de Pesquería, Universidad Nacional Agraria La Molina, Lima, Peru, [2] Department of Ocean Sciences, Tokyo University of Marine Science and Technology, Tokyo, Japan, [3] Arctic Research Center, Hokkaido University, Sapporo, Japan

The Kuroshio Large Meander (LM) is known to be highly aperiodic and can last from 1 to 10 years. Since a stationary cold core formed between the Kuroshio and the southern coast of Japan off Enshu-Nada and approaching warm saltier water on the eastern side of the LM changes the local environment drastically, many commercially valuable fish species distribute differently from the non-LM period, impacting local fisheries. Despite this importance of the LM, the influences of the LM on the low trophic levels such as phytoplankton and zooplankton have still been unclear. In this study, satellite daily sea surface chlorophyll data are analyzed in relation to the LM. The results show positive anomalies of the chlorophyll-a concentration along the Kuroshio path during the LM periods, 2004–2005 and 2017–2019, from the upstream off Shikoku to the downstream (140°E). These positive anomalies are started by the triggering meander generated off south of Kyushu, which then slowly propagates to the downstream LM region in both the LM periods. Even though the detailed patterns along the Kuroshio region in the two LM periods were different, similar formations of the positive anomalies on the western side of the LM with shallower mixed layer depth are observed. Furthermore, we found clear relationships between the minimum distance from several stations along the coast to the Kuroshio axis and the mean chlorophyll-a anomaly, with significant correlations with the distance from different stations.

Keywords: phytoplankton, eddy re-stratification, remote sensing, submesoscale eddies, Kuroshio large meander

OPEN ACCESS

Edited by:
Hiroaki Saito,
The University of Tokyo, Japan

Reviewed by:
Sachihiko Itoh,
The University of Tokyo, Japan
Antonio Bode,
Spanish Institute of Oceanography, Spain

***Correspondence:**
Daniel Andres Lizarbe Barreto
20141316@lamolina.edu.pe

Specialty section:
This article was submitted to Coastal Ocean Processes, a section of the journal Frontiers in Marine Science

Received: *08 March 2021*
Accepted: *05 July 2021*
Published: *10 August 2021*

Citation:
Lizarbe Barreto DA, Chevarria Saravia R, Nagai T and Hirata T (2021) Phytoplankton Increase Along the Kuroshio Due to the Large Meander. Front. Mar. Sci. 8:677632. doi: 10.3389/fmars.2021.677632

1. INTRODUCTION

The Kuroshio south of Japan is known to exhibit a characteristic path bimodality, switching between relatively straight paths and a meandering one (Masuda, 1982; Kawabe, 1985). This different types of path (bimodal feature) cannot be found in other western boundary currents. Uda (1937) was the first to report the abnormally cold water temperature in the stationary cold core formed off Enshu-Nada (137–139°E, see **Figure 1A**) by the Kuroshio Large Meander (LM). The LM is considered to have important effects on storm tracks, extratropical cyclone activities, and local precipitations (e.g., Xu et al., 2010; Nakamura et al., 2012; Hayasaki et al., 2013), as well as an influence on local fishery activities (Uda, 1937), marine resources and ship navigation (Kawabe, 1995; Liu et al., 2018). Therefore, extensive studies have been carried out to understand the mechanisms of the formation and the decay of the LM. Earlier studies using limited *in-situ* observation data provided several hypotheses on the formation of the LM, such as the Oyashio intrusion, El Niño variability, and solar activities (see Stommel and Yoshida, 1972). Later,

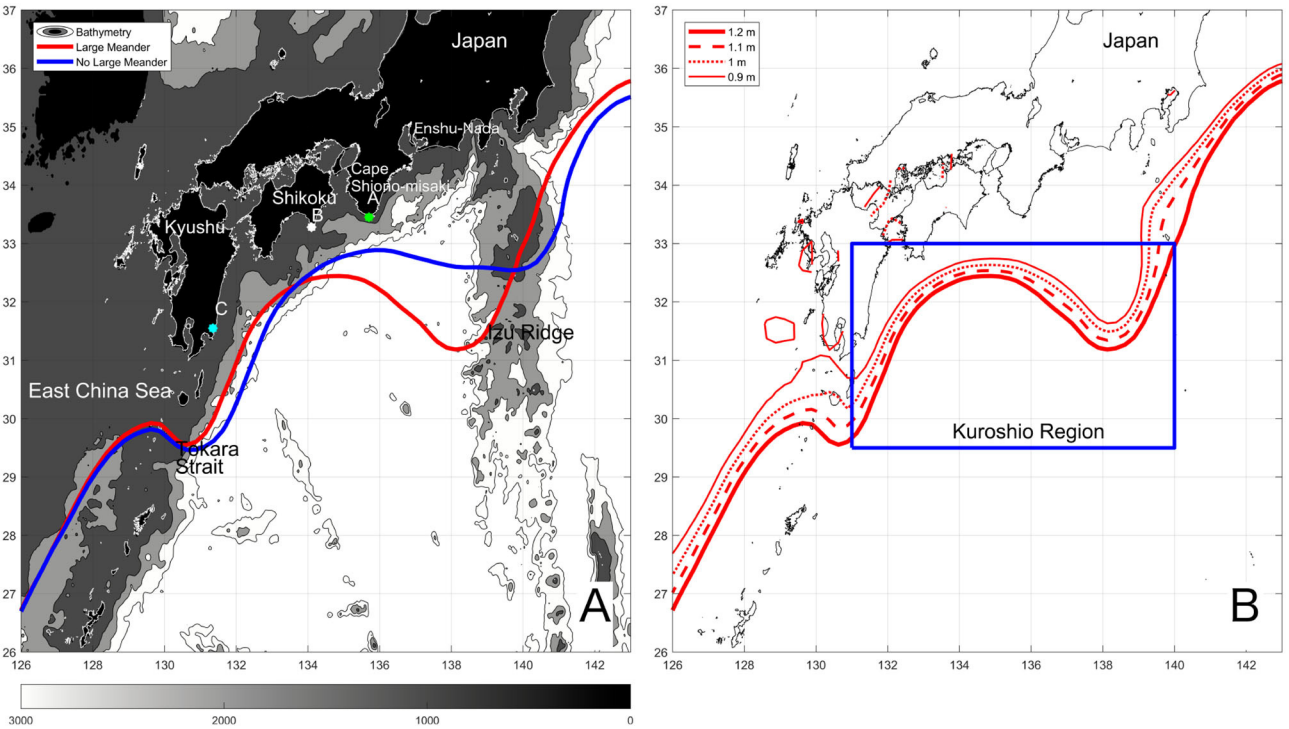

FIGURE 1 | (A) Bimodal paths of the Kuroshio for the No Large Meander (blue line) and the Large Meander (red line) paths. Contours are drawn for the bathymetry with an interval of 1,000 m. **(B)** The Kuroshio axes during the LM defined with the different definitions with SSH values at 1.2, 1.1, 1, and 0.9 m. The blue box represents the Kuroshio region, in which the path length, chlorophyll-a, mixed layer depth, and wind stress are extracted along the Kuroshio axes.

Kawabe (1985, 1986, 1987, 1995) found that the Kuroshio path modulations can be detected by tidal height data along the Kii Peninsula (136°E in **Figure 1A**), and Hachijojima Island (∼33°N, ∼140°E), and that slight north-south shifts of the Kuroshio paths in the upstream Tokara regions (**Figure 1A**) could lead to the formations of the LM or the non-Large Meander (NLM). In addition to the *in-situ* observations, idealized regional numerical models have been utilized to investigate the formation mechanisms of the LM (e.g., White and McCreary, 1976; Chao, 1984; Yasuda et al., 1985; Akitomo et al., 1991). These regional scale numerical studies have reproduced bimodal paths and demonstrated the importance of mesoscale variabilities near the jet. However, to resolve mesoscale eddies with the limited computer power, these simulations needed to be conducted with small size domains. This made impossible to consider the variations in the mesoscale eddy activities caused by the decadal changes in basin scale atmospheric disturbances, that was recently revealed by the satellite altimetry data. These altimetry data have enabled us to identify the mesoscale eddies in a wide area and analyze their roles in forming the LM (Ambe et al., 2004, 2009). The mesoscale eddies are ubiquitous in the ocean. They propagate westward as the first baroclinic mode Rossby waves with swirling water and large thermocline displacements (e.g., Waseda et al., 2002).

The Kuroshio and its downstream, the Kuroshio Extension are known to be rich in these mesoscale eddies (Xu et al., 2010). Previous satellite observations have suggested that the short-term Kuroshio meander and the LM formations are involved with these mesoscale eddies (Waseda et al., 2002; Miyazawa et al., 2004).

The state-of-the-art ocean assimilation and reanalysis studies on the Kuroshio became feasible with these satellite observations. These assimilated data are very useful to capture the processes involved in the Kuroshio path variations (Miyazawa et al., 2005; Kagimoto et al., 2008; Usui et al., 2008) and resolve interactions between mesoscale eddies and the Kuroshio (Ebuchi and Hanawa, 2000, 2003; Ichikawa, 2001; Ambe et al., 2004, 2009). Using one of such ocean assimilation experiments, Usui et al. (2013) and Usui (2019) proposed three necessary conditions to form the LM. First, the Kuroshio Extension has to be in the stable state to maintain the end point of the LM near the coast through the gap north of the Izu Ridge. Second, the low sea surface height anomaly needs to propagate from west to the region off south of Kyushu. Lastly, the positive sea surface height anomaly needs to be formed east of Taiwan. The latter two negative and positive sea surface height anomalies form dipole structures off south of Kyushu to reinforce each other, leading to a formation of a trigger meander that could result in the LM formation.

In addition to the altimetry data, the ocean color satellite remote sensing has enabled us to have a wide view of the chlorophyll-a distributions (e.g., Yamada et al., 2004). Despite

of this, little has been known about the influence of the LM on the surface chlorophyll-a distribution patterns during the LM periods. A previous study by Nakata (1994) has pointed out that the stationary state of the Kuroshio LM may suppress the production of prey for sardine larvae, while the LM in the initial stages may induce upwelling events which may increase the abundance of the prey. These upwelling events can also be expected when cyclonic eddies are generated behind islands in subinertial currents. For example, cyclonic eddies generated by the Kuroshio branch current encountering the Izu Oshima Island have been reported to increase the chlorophyll-a (Kimura et al., 1997). Although the trigger meander of the LM formed south of Kyushu and propagates to the downstream also has cyclonic circulations, it is still unclear whether and how the nutrients are supplied to the surface and what the influences of the cyclonic trigger meander on the lower trophic levels are. In this study, relatively long-term satellite sea surface chlorophyll-a data that include recent two LM events are analyzed. The objective of this research is to clarify the effects of the LM events from its formation and decay including the trigger meanders on the phytoplankton abundance and distribution patterns.

2. DATA AND METHODS

2.1. Kuroshio Data

The Kuroshio Current exhibits a remarkable bimodal feature (also referred to as the Kuroshio path variations) (Taft, 1972): The Non-Large Meander (NLM) path along which the Kuroshio flows along the southern coast of Japan and the Large Meander (LM) path along which the Kuroshio flows far away from the coast off Enshu-Nada (Kawabe, 1987, 1995). In order to differentiate the LM periods, average paths of the LM and the NLM are computed using reprocessed (Jason-3, Sentinel-3A) satellite altimetry data obtained from Copernicus Climate Change Service (C3S) (**Figure 1A**). The average LM path of the Kuroshio defined at sea surface height of 1.2 m is obtained for the last two LM periods (2004–2005 and 2017–2019).

The LM occurrence is highly aperiodic and the LM state can last from 1 to 10 years. During the study period, the Kuroshio south of Japan took the LM path twice. The first LM occurred during the period from August 2004 through August 2005 after a NLM period of 13 years (Miyazawa et al., 2008). Prior to the LM, a trigger meander was generated off southeastern coast of Kyushu in February 2004, which then propagated eastward from south of Shikoku up to Cape Shiono-Misaki in about 4 months (**Figure 1A**, Endoh and Hibiya, 2009). The second LM during the study period is still currently (June 2021) underway since August 2017 (Usui, 2019). After 12 years since the LM 2004–2005 (Nagano et al., 2018), a small meander developed in late March, 2017 southeast of Kyushu Island, propagated eastward to the region off the Enshu-Nada in August, 2017, which was considered to have induced the Kuroshio LM.

2.2. Ocean Satellite Reprocessed Data

Similar to the previous studies (e.g., Qiu and Chen, 2005), the Kuroshio paths were determined by the longest contours at several values of sea surface height. Along these contours, the longitude and latitude are interpolated at a regular distance interval, at which other variables such as chlorophyll-a concentrations, wind stress, and mixed layer depths (MLDs) are interpolated. The range considered for the interpolation is 115–165°E, 22–48°N. Within this region, the data of 4 × 4 km daily chlorophyll-a satellite data obtained from Ocean Color reprocessed L4 (Cloud Free) observations-CMEMS, 0.25 × 0.25 degree resolution monthly mixed layer depth obtained from MERCATOR GLORYS12V1 REANALYSIS-CMEMS, and 0.25 × 0.25 degree 6 hourly wind stress from CERSAT reprocessed observations-CMEMS within 131–140°E (Kuroshio region) were extracted.

2.3. Data Analysis

First, monthly climatologies (September 1997–January 2019) for chlorophyll-a concentration and mixed layer depth were prepared from the daily data, which were then used to obtain anomalies of these variables. The anomalies were then moving averaged with a 13-month window when they are shown as the time-series. To investigate the differences in spatial patterns between the LM and the NLM periods, the mean chlorophyll-a anomaly and the sea surface height as the plan view were computed for the LM and NLM periods (**Figure 2**). Although the subtraction of the monthly climatology of the chlorophyll-a to compute its anomaly may suppress seasonality, obtained spatial patterns in the chlorophyll-a anomaly could reflect the difference in the number of spring and autumn months during the blooming periods. For this reason, the number of spring and autumn months during the LM and NLM periods were counted and divided by the total number of months (**Supplementary Table 1**). The percentage of the spring months (March–May), which are thought to be the largest bloom in a year, during the LM is found to be <20% of the total, whereas it is more than 25% for the NLM period. On the other hand, it is 29 and 26% for the secondary blooming months in autumn (September–November) for the LM and the NLM periods, respectively. In total, the percentages of spring and autumn months are 48 and 53% for the LM and the NLM periods, respectively, suggesting that overestimation of the chlorophyll-a, if exists, is more expected in the NLM rather than the LM period because the NLM period includes more spring and autumn months.

In this study, the Kuroshio axis was determined by the longest contours of the sea surface height at several different values, 1.2, 1.1, 1.0, and 0.9 m. With the higher sea surface height values, the defined Kuroshio axis tends to appear on the offshore side, and vice versa with the lower values (**Figure 1B**). The path length was measured within the Kuroshio region (131–140°E) and was used to illustrate the LM and NLM periods after performing a 13-month moving average (**Figure 3**).

To investigate the relation between the surface chlorophyll-a concentrations and the MLD, the MLD anomaly was computed using the MERCATOR GLORYS12V1 REANALYSIS-CMEMS. For this, the monthly climatology of MLD was first calculated using the data during 1997–2019, which was then subtracted from the MLD. After performing the 13-month running average,

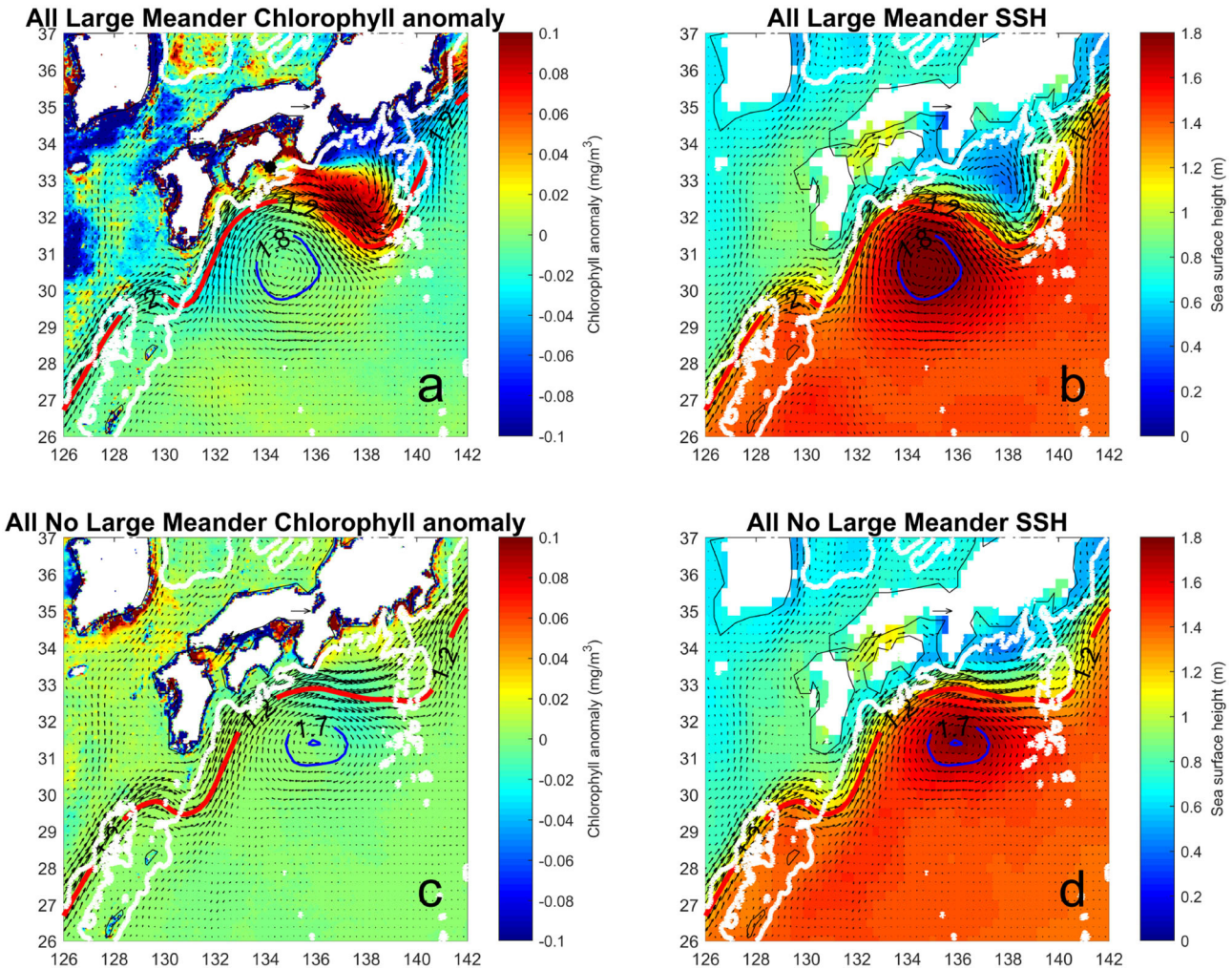

FIGURE 2 | Chlorophyll anomaly and sea surface height (SSH) or absolute dynamic topography during the Large Meander **(a,b)** and No Large Meander **(c,d)**. Geostrophic flow is represented with arrows and a recirculation gyre is illustrated with the blue SSH contours. The red curves represents the Kuroshio axis defined by the SSH contour at 1.2 m.

the MLD anomaly was obtained and compared with the sea surface chlorophyll-a concentrations.

The Pearson correlation coefficient (R) and *P*-value were computed between the physical parameters, such as the mixed layer depth (MLD) or wind stress and the chlorophyll-a anomaly along the Kuroshio axis for the entire period of this study as well as for each LM period (**Supplementary Table 2**). The chlorophyll-a anomaly and the MLD anomaly during the LM periods were extracted during the course of each LM occurrence from its trigger meander through the end, to calculate the Pearson correlation coefficient and the *P*-value. In addition, the Pearson correlation coefficient (R) was computed also between the MLD and the wind stress and shown in **Supplementary Table 3** for the entire period of the study.

When the Kuroshio takes the LM path, the quasi stationary large cyclonic eddy like meander with the doming isopycnal structure is formed off Enshu-Nada, which may lift up the nutrient rich deep water. The influence of the doming nutricline on the phytoplankton, is therefore, likely to appear within the region between the Kuroshio with this cyclonic meander and the coast. Thus, an area off Enshu-Nada within the cyclonic meander (**Supplementary Table 4**) was chosen to identify the effect of the LM on the chlorophyll-a anomaly. Note that the area close to the shore was excluded from the analysis to avoid including the overestimated chlorophyll-a concentrations due to CDOM (colored dissolved organic matter).

To compare the average chlorophyll-a anomaly within the area with the distances between the Kuroshio axis and the coast, several stations such as at Cape Shiono-Misaki (A), Shikoku (B), and south of Kyushu (C) were selected (**Figure 1A**, **Supplementary Table 4**), similar to Kawabe (1995). The minimum distance between the Kuroshio axis defined with the SSH at 1.2 m and each station was computed. In addition to the minimum distance, the maximum value of the SSH was

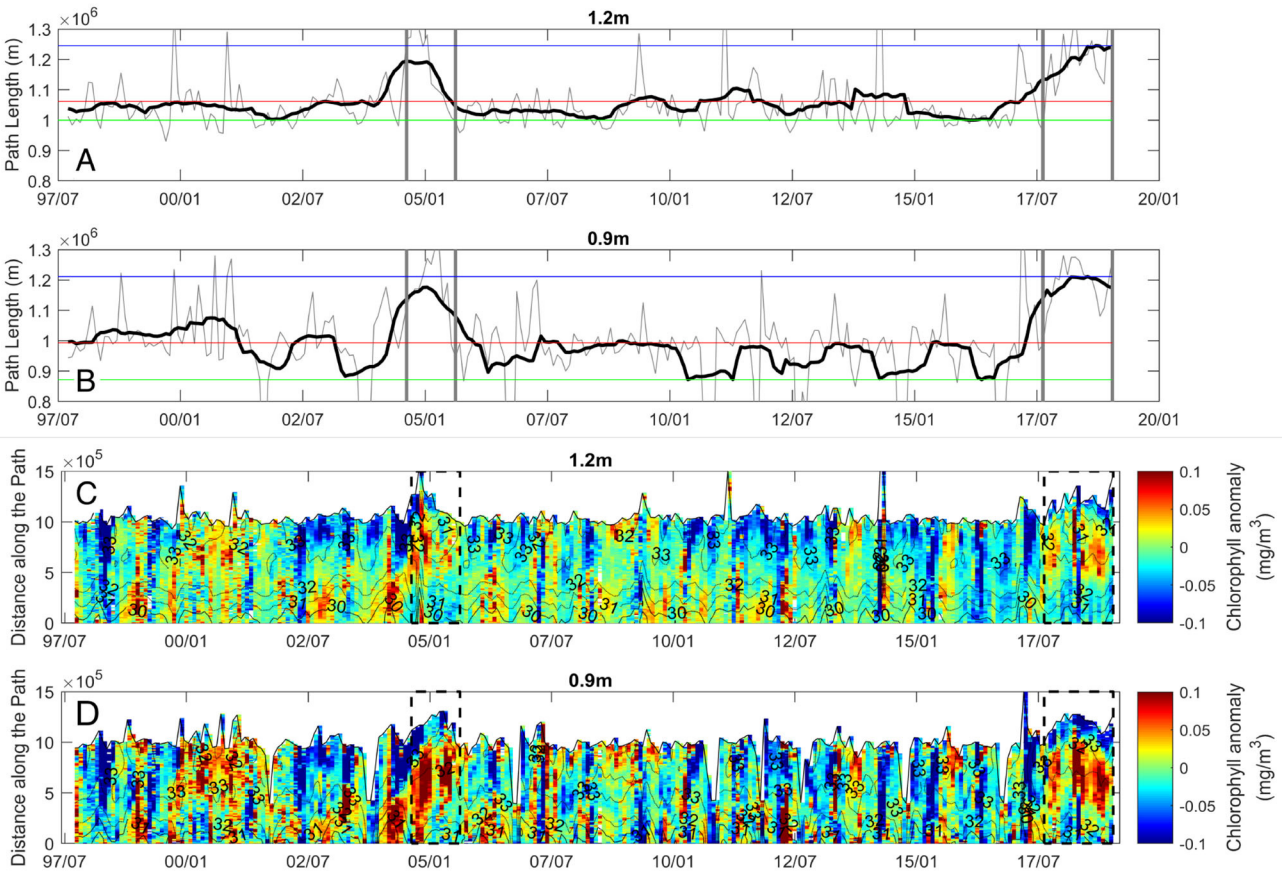

FIGURE 3 | The Kuroshio path lengths within the Kuroshio region (131–140°E) defined in the **Figure 1A** as a blue box with different SSH values for the Kuroshio definition, for **(A)** 1.2, and **(B)** 0.9 m of SSH values. Black lines show the path lengths after 13-month running average of the monthly data, which are shown as the gray lines. The periods indicated with the gray lines represent the large meander periods. Red line indicates the average path length, and blue line the maximum and green line the minimum path length. Chlorophyll anomaly in color as a function of time and path length (distance along the Kuroshio path) with different definitions of the Kuroshio axis with the SSH values for **(C)** 1.2 and **(D)** 0.9 m. Black dashed line indicates the large meander periods. Gray shaded thin line indicates the Path length. The contours are avergae latitude.

computed within the region 130–140°E, 28–35°N, where the center of the anticyclonic recirculation gyre off Shikoku appears. These variables, such as average chlorophyll-a concentrations within the cyclonic meander off Enshu-Nada, the minimum distances, and the maximum SSH values were 13-month running averaged before computing the Pearson correlation coefficients (R) and *P*-values (**Supplementary Table 5**).

3. RESULTS

3.1. The Kuroshio Large Meander and Sea Surface Chlorophyll-a

The average LM path is found to be closer to the continental shelf in Kyushu (Station C in **Figure 1A**) than that during the NLM period, which is contradict to what suggested by Kawabe (1985, 1995) showing based on the tidal gauge data that the NLM Kuroshio flows closer to the coast. During the last two large meander periods, latitudes of the Kuroshio path may not fall below 31°N within the Kuroshio region and over the Izu Ridge.

To illustrate the difference in phytoplankton distribution between the LM and the NLM periods, the chlorophyll-a anomaly and the SSH are averaged during the entire LM (**Figures 2a,b**) and NLM (**Figures 2c,d**) periods. The positive chlorophyll-a anomaly extending southeastward from off Shikoku is seen during the LM period, which is absent in the NLM period indicating that the chlorophyll-a concentrations are higher during the LM than the NLM period along the Kuroshio south of Enshu-Nada (**Figures 2a,c**). The enhanced chlorophyll-a concentrations seem to be advected from southeast of Shikoku and Cape Shiono-Misaki to the downstream region, which corresponds to the region near the cyclonically meandering LM path from the meander crest to the trough. The values of this positive chlorophyll-a anomaly are found to be much greater than the standard errors (**Supplementary Figure 1**). On the other hand, in the near shore regions off Enshu-Nada, negative chlorophyll-a anomalies are observed during the same LM period. Blue contours of SSH at 1.8 m (**Figures 2a,b**) and 1.7 m (**Figures 2c,d**) represent the anticyclonic recirculation

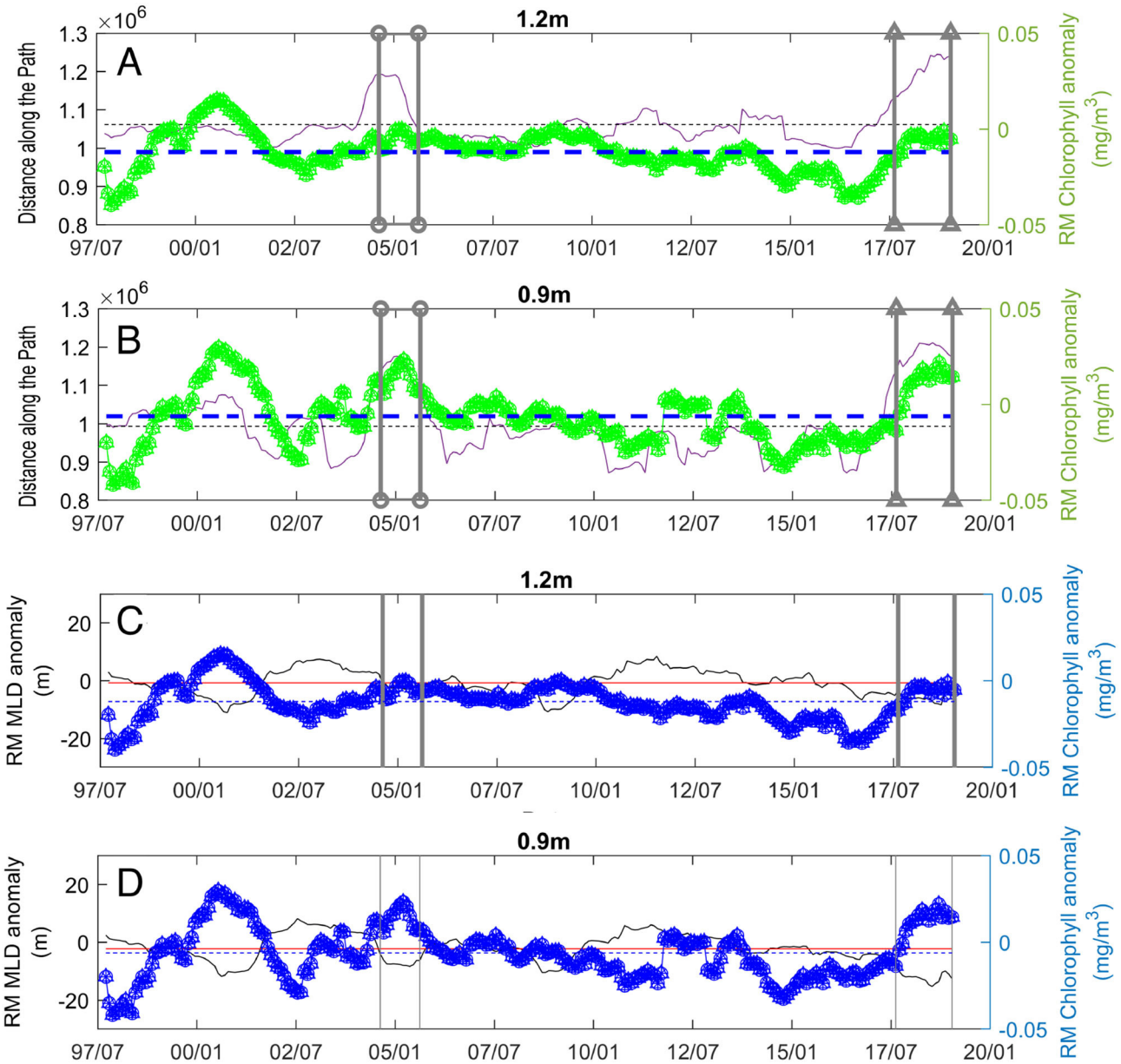

FIGURE 4 | Time series of the 13-month running-mean path length (magenta line) and the chlorophyll anomaly (green line) with different definitions of the Kuroshio axis with the SSH values for **(A)** 1.2 and **(B)** 0.9 m. Each monthly value is averaged along the path before the running average. Large meander years are enclosed in gray boxes. Blue dashed line indicates the mean chlorophyll anomaly and black dashed line indicates the mean path length. Time series of the 13-month running-mean mixed layer depth in black and chlorophyll-a anomaly in blue along the Kuroshio path with different definitions of the Kuroshio axis with the SSH values for **(C)** 1.2 and **(D)** 0.9 m. Each monthly value is averaged along the path before the running average. Large meander years are enclosed in gray boxes. Red line indicates the average mixed layer depth anomaly. Blue dashed line indicates the average chlorophyll-a anomaly.

gyre off Shikoku, which strengthens and intensifies during the LM periods and plays an essential role in reinforcing baroclinic instability (Usui, 2019). Although a cyclonic circulation is also formed during NLM between the Kuroshio and Enshu-Nada (**Figures 2c,d**), the strength of the circulation is much weaker than that during the LM. To evaluate the effects of the Kuroshio LM on the sea surface chlorophyll-a quantitatively, the LM formation and decay are tracked by measuring the Kuroshio path length within the Kuroshio region (131–140°E, **Figure 1B**) similar to (Usui, 2019). For these analyses along the Kuroshio path, the Kuroshio axis is defined with the longest contour of SSH at four different values. The 13-month running averaged path lengths are found to show larger values than their average path length since the occurrence of the LM triggering meander south of Kyushu (**Figures 3A,B**). After several months, the path lengths increased until they reach $\sim 1.2 \times 10^6$ m. The increase of

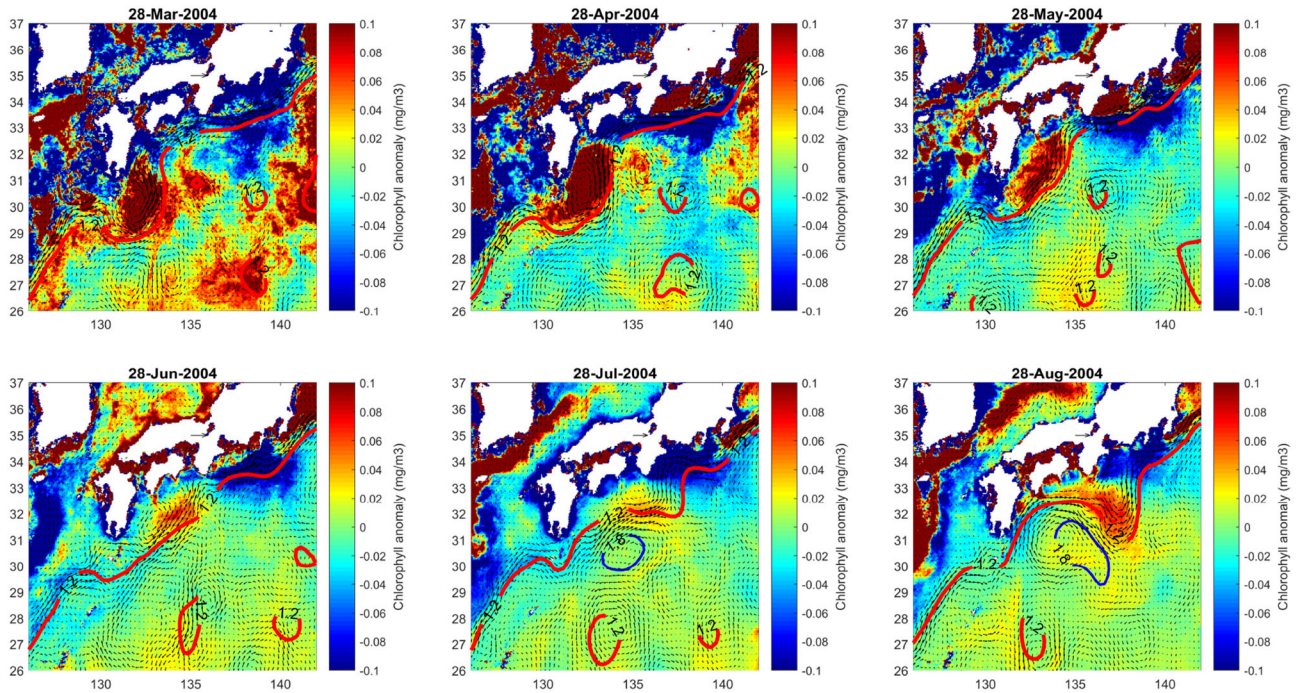

FIGURE 5 | The positive chlorophyll anomaly propagation from the south of Kyushu to the LM trough during the LM formation during the LM 2004–2005.

the path length for the LM since August 2017 seems to be more gradual taking several years to reach $\sim 1.2 \times 10^6$ m than that during August 2004 and 2005. Besides the path length increase during these two LM periods, there seems to be interseasonal and interannual modulations in the path lengths. The former can be seen for the entire time series that can be attributed to the mesoscale variability, and the latter is observed during the NLM periods.

The chlorophyll-a anomaly along two Kuroshio axes (**Figures 3C,D**) is extracted and shown as a function of time and distance along the path from the westernmost longitude of the Kuroshio region, 131°E. Although the patterns of the chlorophyll-a distributions along the axes are similar regardless of the definitions of the axis, the chlorophyll-a anomalies during the LM show somewhat smaller positive anomaly with the axis defined at higher SSH values, for example, at 1.2 m, which corresponds to the offshore most path (**Figure 3C**). On the other hand, the higher positive anomaly during the LM period is found with the axes closer to the coast with the lower SSH values (**Figure 3D**). The results with all the SSH values to define the Kuroshio axis are shown in **Supplementary Figure 2**. These positive anomaly values during the LM seem to propagate from the upstream toward the downstream along the path. The propagation during 2004–2005 is clearer than that of the LM 2017-present. Average chlorophyll anomalies along the Kuroshio axis within the Kuroshio region show that as the meander grows, the positive chlorophyll anomaly increases (**Figures 4A,B**) with values above their means (blue dashed line). This positive anomaly increase is particularly clearer when the average is computed along the Kuroshio with the definition of SSH at 0.9 m. Although the period during 2001–2002 is not defined as the LM period, the large positive anomaly is accompanied by the relatively longer path length in the same period. The correlation coefficient computed between the chlorophyll-a anomaly for the entire time series during 1997–2019 and the path length with the Kuroshio axis defined by the SSH at 0.9 m is as high as $R = 0.57$. The relatively high correlation coefficient suggests that the LM development leads to the phytoplankton increase. It should be noted that the correlation coefficient decreases when computed for the same variables along the Kuroshio axis but defined with the higher SSH values, suggesting that the chlorophyll-a increase on the shore side of the front is more tightly linked with the LM.

3.2. Propagation of Positive Chlorophyll-a Anomaly in Large Meander Periods

During the LM 2004–2005, chlorophyll-a anomaly off south of Kyushu started to increase in February 2004. After a month, on March 28, 2004, the positive chlorophyll anomaly slightly moved northeastward to the region off southeast of Kyushu (**Figure 5**). The initial increase of the positive anomaly coincides with a trigger meander formation south of Kyushu, which is accompanied by a cyclonic circulation between the Kuroshio and the coast with increasing chlorophyll-a. The positive anomaly then propagates toward the downstream. Finally, in August–October 2004, the positive chlorophyll-a anomaly reached the farthest part of the LM from the shore, and remained appearing around the distance of 5–10 $\times 10^5$ m as long as the LM continues. The highest positive chlorophyll anomaly is found at 32°N (contours in **Figure 6B**). The speed of the anomaly propagation from south of Kyushu to the Izu-Ogasawara Ridge is estimated

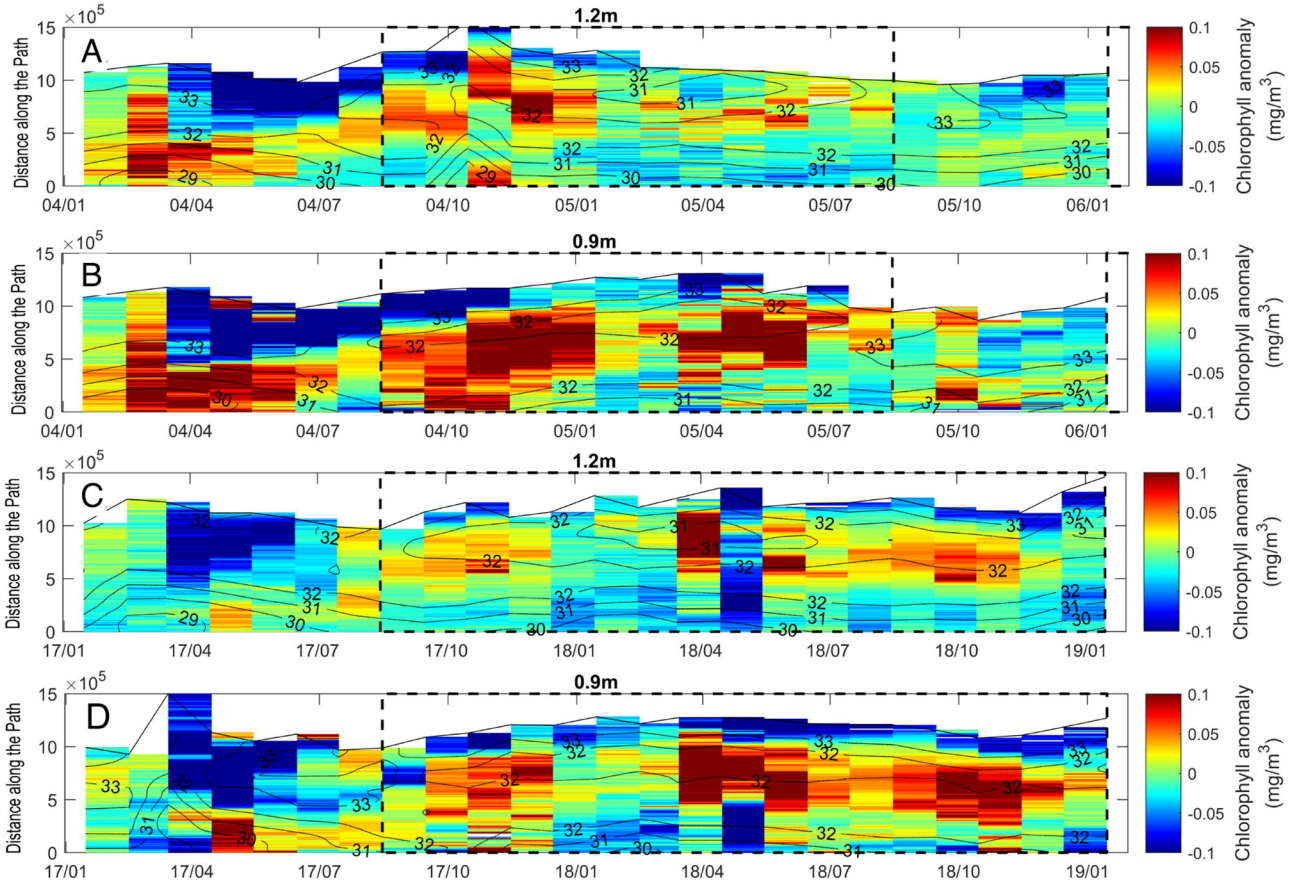

FIGURE 6 | Monthly chlorophyll anomaly extracted during the two large meander periods shown in color as a function of time and distance along the Kuroshio path with different definitions of the Kuroshio axis with the SSH values for **(A,C)** 1.2 and **(B,D)** 0.9 m. **(A,B)** shows LM 2004–2005 and **(C,D)** LM 2017–2019. Black dashed line indicates the large meander periods. Black dotted contour indicates the latitude.

to be 3.0 km day^{-1}, which corresponds to 3.5 cm s^{-1}. This propagation speed is much less than the current speed of the Kuroshio ∼1 ms^{-1}.

The Pearson correlation coefficient (**Supplementary Table 2**) computed between the path length and the chlorophyll-a anomaly only for the LM 2004-2005 including the trigger meander formation shows much higher value, 0.91 than that computed for the entire period, 0.57. The higher correlation coefficient during the LM period suggests that the chlorophyll-a increase along the Kuroshio is strongly affected by the processes associated with the LM.

A similar propagation pattern is found during the LM 2017-present with a trigger meander generated in the end of March 2017, which then propagated toward the downstream region with a similar propagation speed. However, the value of the positive anomaly is slightly less than that during the LM 2004–2005. The positive anomaly is enhanced later when the relatively higher values reaches 5–10 × 10^5 m and the large anomaly persists until the latest time analyzed in this study (**Figure 6B**). Similar to the previous LM 2004–2005, the highest concentration of chlorophyll-a anomaly along the path is found at 32°N (**Figure 6**) on the southwest side of the cyclonic circulation of the LM (**Figure 2a**). The LM grows bigger on average reaching 1.25 × 10^6 m of the running averaged path length during the LM 2017-present compared to the LM 2004–2005 with the path length <1.2 × 10^6 m. The correlation coefficient computed between the path length and the chlorophyll-a anomaly for the LM 2017-present shows also high values with both the definitions for the Kuroshio axis of SSH = 1 m (0.95) and 0.9 m (0.84).

3.3. Mixed Layer Depth and Chlorophyll-a Anomalies Along the Kuroshio

The persistent positive chlorophyll-a anomaly during the LM periods along the Kuroshio could be induced by deeper mixed layer depths (MLDs) that can entrain nutrient rich lower layer water into the surface layers. Interestingly, the 13-month running average MLD shows opposite trend with the chlorophyll-a along the path for the entire period of the analysis (**Figures 4C,D**), suggesting that the positive chlorophyll-a anomaly is associated with the shallower mixed layer depth. The correlation coefficient between the MLD anomaly and chlorophyll-a anomaly shows a negative value of −0.53 with the Kuroshio axis definition of SSH = 0.9 m (**Supplementary Table 2**). When the data are

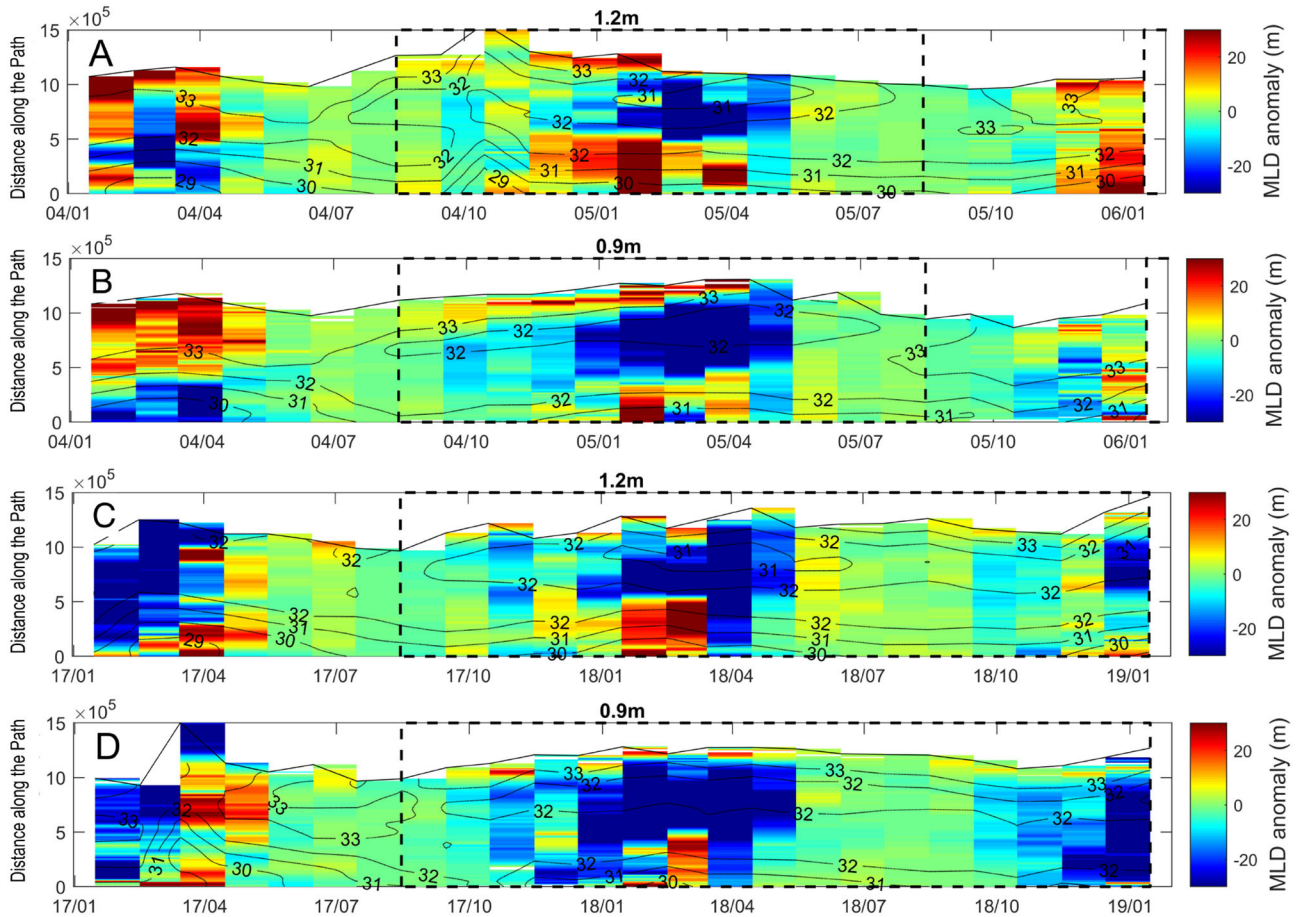

FIGURE 7 | Monthly mixed layer depth anomaly extracted during the two large meander periods shown in color as a function of time and distance along the Kuroshio path with different definitions of the Kuroshio axis with the SSH values for **(A,C)** 1.2 and **(B,D)** 0.9 m. **(A,B)** shows LM 2004–2005 and **(C,D)** LM 2017–2019. Black dashed line indicates the large meander periods. Black dotted contour indicates the latitude.

extracted only for the LM 2004–2005, the MLD and chlorophyll-a anomaly show an even stronger negative correlation with $R = -0.79$. Also for the LM 2017-present, the correlation coefficient is −0.86 with the Kuroshio axis definition at SSH = 1 m (**Supplementary Figure 3C**).

The MLD anomaly as a function of time and distance along the path during the LM 2004–2005 shows that the MLD is shallow along the path where the LM occurs. The clearer negative MLD anomaly during the LM 2004–2005 is seen with the smaller SSH values for the definition of the Kuroshio axis, suggesting that shoaling of the MLD occurs more on the cold side of the front. The latitude range of the MLD shoaling is between 31 and 32°N (contour in **Figure 7**) which coincides with that of the positive chlorophyll-a anomaly during the LM (**Figure 2a**). However, unlike the chlorophyll-a anomaly, the negative anomaly of the MLD does not show clear propagation patterns toward the downstream (**Figure 7**).

Similar mixed layer variations along its path are found also during the LM 2017-present (**Figures 7C,D**). The negative MLD anomaly during the LM 2017-present is also clearer with the smaller SSH values along the Kuroshio axis, i.e., on the dense or cold side of the front. In the 2 year period shown in **Figures 7C,D**, there appears to be a seasonal shoaling of the MLD from autumn to spring. This seasonal MLD variation is, however, less clear during the LM 2004–2005 (**Figures 7A,B**). It should be noted that even after removing seasonality with 13-month running mean, the tendency to have shallow MLD during both the LM periods still remains (**Figures 4A–D**, lower). Wind stress on the surface of the ocean is one of the major forcing mechanisms to cause changes in the MLD. As oppose to the clearer negative MLD anomaly found on the dense side of the front, the higher correlation coefficients between wind stress and MLD are found with higher SSH values for the Kuroshio axis definition. The highest correlation coefficient is 0.51 on the less dense side of the front, which becomes as low as 0.18 on the dense side, where the MLD shoals. These results suggest that the shoaling of the MLD on the dense side of the front is not caused by the weak wind (**Supplementary Table 3**).

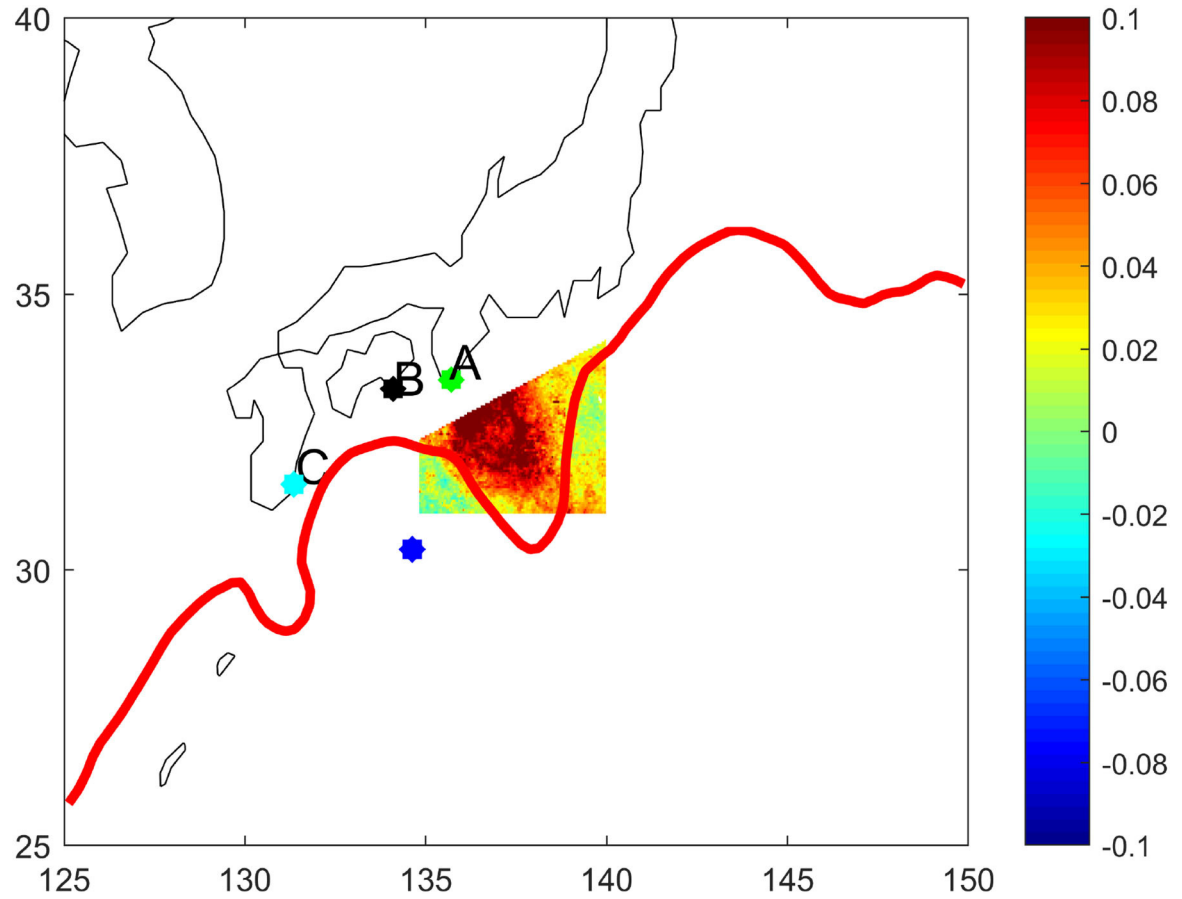

FIGURE 8 | Selected area for representing the LM chlorophyll-a anomaly in color shading and three coastal stations in Cape Shiono-Misaki (A), Shikoku (B), and south of Kyushu (C). Red contour indicates the Kuroshio axis defined with the SSH value at 1.2 m. Blue dot shows an example of the SSH maximum within the recirculation gyre.

3.4. Minimum Distance Between the Kuroshio and the Coastal Stations

It is well-known that an anticyclonic recirculation gyre off Shikoku plays an important role in the LM formation process, as the baroclinic instability near the recirculation gyre south of the small trigger meander slowly propagating eastward grows to the LM (Miyazawa et al., 2008; Usui et al., 2008; Usui, 2019). Also, Mitsudera et al. (2001) reported that the Kuroshio meander grows as the anticyclonic eddy strengthens off the Kii Peninsula (Shiono-Misaki) and decays when the eddy detaches. To investigate the relation among chlorophyll-a anomaly within the LM, the minimum distances between the Kuroshio and the coastal stations, and the strength of the anticyclonic re-circulation, an area within 134.8–140°E, 31–35.5°N is selected (**Figure 8**) to average the surface chlorophyll-a within the LM. The minimum distances between three stations, (A) Cape Shiono-Misaki, (B) Shikoku, and (C) south of Kyushu and the Kuroshio defined as the SSH value of 1.2 m are measured (**Figure 8**, **Supplementary Table 4**). Also, the maximum value of SSH within the recirculation gyre south of Shikoku is examined.

Figure 9B shows that the minimum distance from the station C to the Kuroshio decreases during both the LM periods, indicating that during the LM, the Kuroshio flows closer to the continental shelf southeast of Kyushu near the station C. On the other hand, the minimum distances increase during LM periods for the station A and B. The maximum value of SSH seems to be inversely proportional to the minimum distance from the station C over the long term (**Supplementary Table 5**) with a correlation coefficient, R of −0.73. The correlation coefficient between the minimum distance from the station A and chlorophyll-a anomaly within the selected area calculated during 1997–2019 (January) is found to be high, 0.7145 (**Supplementary Table 5**), reflecting a fact that large distance from the station A to the large meandering Kuroshio coincides with the positive anomaly of the chlorophyll-a. On the other hand, the correlation coefficient between the minimum distance from the station C and chlorophyll-a anomaly shows a negative value, −0.53, suggesting that the more closely flowing Kuroshio to the coast of southeast of Kyushu near the station C during the LM coincides with the positive chlorophyll-a anomaly.

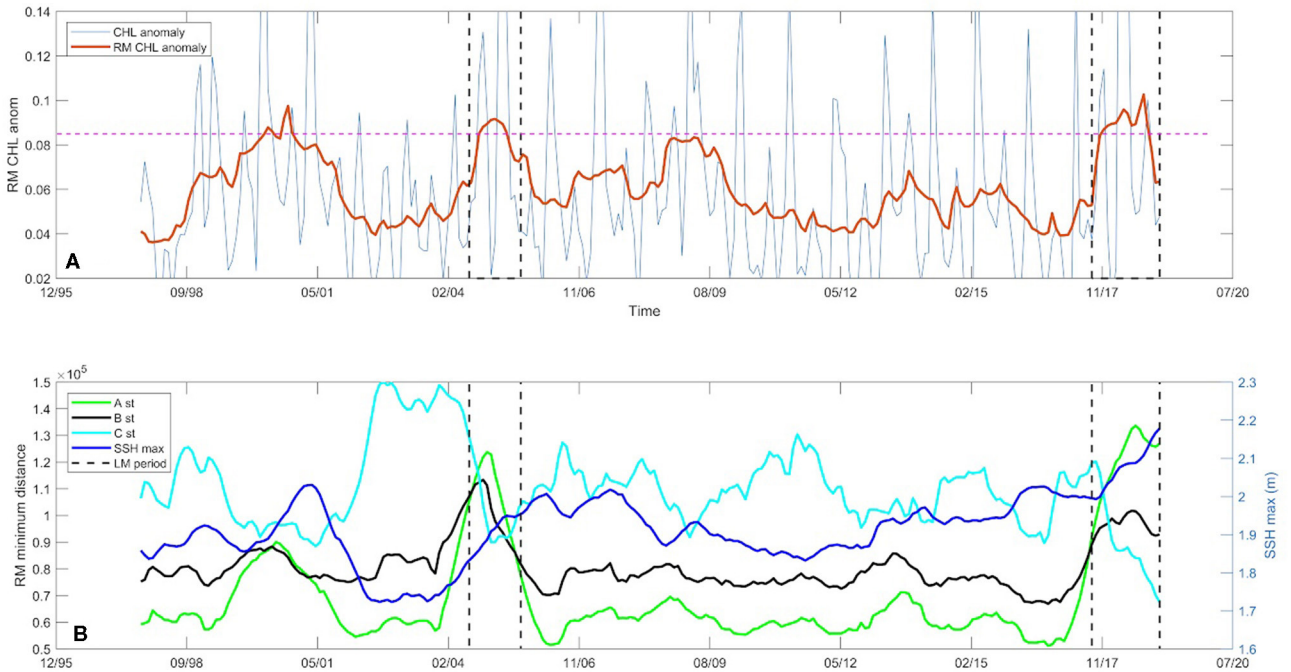

FIGURE 9 | Time series of the 13 month running-mean chlorophyll-a anomaly within the selected area in the LM is shown as red with monthly values in blue line. Black dashed lines indicate the LM periods **(A)**. Time series of the minimum distance from the stations A (green), B (black), and C (cyan) to the Kuroshio axis defined with the SSH value at 1.2 m with a 13-month running average. Blue line indicates the 13 month running mean maximum SSH value in the recirculation gyre **(B)**.

4. DISCUSSION

The mean LM path of the Kuroshio obtained by averaging them during the two LM events, the LM 2004–2005 and the LM 2017-present, shows differences compared to the NLM path not only in the region south of Enshu-Nada, but also southeast of Kyushu (**Figure 1A**). The previous study by Kawabe (1987) has defined the LM and NLM paths, which show that the NLM Kuroshio flows closer to the coast from the upstream Kyushu toward the downstream. In contrast, the mean LM path in this study is closer to the coast than the NLM path in the region southeast of Kyushu (**Figure 1A**). One possible explanation for this discrepancy is that our analyzed period is relatively longer over 20 years than that in Kawabe (1987). Also, as SSH satellite data is only available since 1993, prior LM periods than this could only be studied by SST satellite data and tide gauge data (Kawabe, 1985, 1986, 1987, 1995), which might induce inaccurate estimate on the path position. On the other hand, the recent LM periods analyzed in this study are not as enduring as the LMs studied by Kawabe, which could have also influenced the variability of the path. Nevertheless, the more closely flowing Kuroshio to the continental slope off southeast of Kyushu may induce strong turbulence. A previous observational study using a tow-yo microstructure profiler by Nagai et al. (2019a) showed that near-inertial internal waves trapped within the Kuroshio flowing closely to the continental slope generate large turbulent kinetic energy dissipation rates and associated large nitrate diffusive fluxes in the Hyuga Nada Sea, southeast of Kyushu. The nutrients injected through this mechanism can be advected by the strong Kuroshio flow and provided to phytoplankton in a few hundred kilometers downstream, which would correspond to the region where the positive chlorophyll-a anomaly within the LM. The elevated diapycnal mixing caused by the closely flowing Kuroshio may keep supplying nutrients to primary producers along the Kuroshio. However, the previous observations using an autonomous microstructure profiling float and a BGC float by Nagai et al. (2021) showed that the downstream increase in the chlorophyll-a in response to the nutrient diffusive flux occurred at the subsurface chlorophyll maximum, which can not be observed by the satellite.

On the other hand, the most notable surface chlorophyll-a anomaly during the course of the LM events is always associated with the small cyclonic meander slowly propagating eastward from south of Kyushu to the LM (**Figures 4A,B**, **6**). One of the important elements for the LM formation is this small cyclonic meander appearing south of Kuyshu (Solomon, 1978; Usui, 2019). The Kuroshio axis defined with the SSH value of 0.9 and 1 m are better to track chlorophyll-a propagation during LM periods, suggesting that the propagation occurs on the coastal side of the front, rather than along the main stream of the Kuroshio. The propagation speed of this cyclonic meander is estimated as 3.5 cm s^{-1}. The corresponding time required to travel from south of Kyushu to the region off Enshu-Nada is ∼10 months. This propagation time scale is much longer than the phytoplankton doubling time of ∼1 day, suggesting that observed positive anomaly needs to be sustained by the

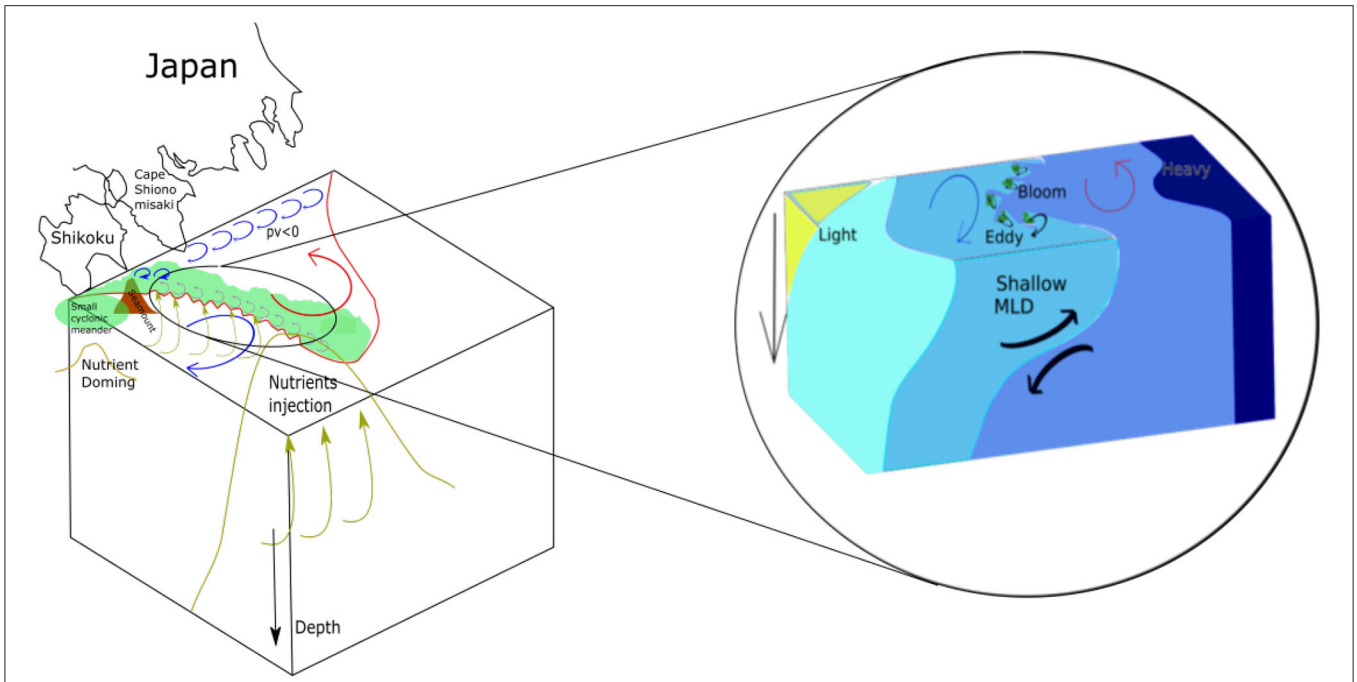

FIGURE 10 | Hypothesis to arise positive chlorophyll-a anomaly in the LM. The small cyclonic trigger meander slowly propagates eastward from the region south of Kyushu, and emerges as the LM off Enshu-Nada. The small cyclonic meander is expected to retain the nutrient doming structure accompanied by the surface chlorophyll-a positive anomaly. As the LM occurs, the Kuroshio flows closer to the coast in the region south of Kyushu, which could induce strong turbulent mixing and nutrient supply (Nagai et al., 2019a). Also, the small seamounts along the Kuroshio, and/or the strong westward counter current along the south coast of Enshu-Nada could produce negative potential vorticity, that can induce turbulence and inject domed subsurface nutrient to the upper layers. The mixed layer restratification seems to increase the phytoplankton on the western part of the LM.

continuous nutrient supply. Also, as the Kuroshio entrains waters from the nearshore regions, the phytoplankton communities within the positive chlorophyll-a anomaly is most likely advected laterally across the front.

During 2000–2001, the chlorophyll-a anomaly rises (**Figures 4A–D**, upper) along the Kuroshio path due to a similar process triggered by a small meander southeast of Kyushu, which did not develop as a LM. It is well-known that mesoscale eddies propagating westward in the Kuroshio recirculation region sometimes impinge on the Kuroshio off the southeast of Kyushu and subsequently a small meander is generated (Ebuchi and Hanawa, 2003; Usui, 2019). The generation of the trigger meander is associated with the supply of cyclonic vorticity at the southern coast of Kyushu (Endoh and Hibiya, 2000, 2001).

One of the turbulence generation mechanisms involved with the Kuroshio besides the near-inertial wave trapping, is the centrifugal instability within the streak of the negative potential vorticity (PV) (Gula et al., 2016). However, when the Kuroshio approaches to the south coast of Japan, the frictional generation of the cyclonic vorticity over the sloping bottom boundary layer does not lead to the negative PV generation. The negative PV generation caused by the Kuroshio south of Honshu is possible when there are seamounts and shills. On the northern slope of these seamounts, the Kuroshio can generate the negative PV leading to the centrifugal instability, which has recently pointed out by Durán Gómez and Nagai (2020) in the Hyuga Nada Sea. Furthermore, when the LM develops, the large cyclonic meandering at the LM may provide a westward counter current near the coast. When this counter current becomes strong, the negative PV can be generated on the continental slope of the south coast of Honshu. Within the cyclonic meander of the LM, nutricline is expected to have a doming structure similar to the isopycnal doming in a cyclonic eddy. These turbulence generation mechanisms near the Kuroshio could, therefore, inject the domed nutrients in the LM to the sunlit surface layers (**Figure 10**).

The doming of the nutricline seen near the center of a cyclonic eddy can be more susceptible to the upper layer mixing and entrainment, that may supply domed nutrients to the euphotic zone. If this is the dominant cause of the phytoplankton increase during the LM, then the enhanced chlorophyll-a concentrations should occur at the center of the cyclonic circulation of the LM. However, the clear positive chlorophyll-a anomaly signal appears on the western side of the LM. In addition to the mesoscale doming of the nutrients in the cyclonic meander of the LM, submesoscale vertical motions can drive the localized injection of nutrients into the euphotic layer. The vertical motion associated with submesoscale dynamics is much stronger than that associated with mesoscale dynamics (Mahadevan and Tandon, 2006; Capet et al., 2008a,b; Lévy et al., 2012; McWilliams, 2016; Brannigan et al., 2017; Guo

et al., 2019) and could induce changes in phytoplankton growth or biomass (Martin and Richards, 2001; Klein and Lapeyre, 2009). As the small trigger meander is also a cyclonic eddy with the scale in the range of submesoscale, the nutrient could be supplied also through these submesoscale processes to the euphotic zone.

Recent studies have shown that the growth of instabilities within the mixed layer can tap potential energy of the mixed layer front to develop energetic submesoscale eddies, initially 1–10 km in horizontal extent and as deep as the ML. These eddies drive net horizontal transfer of lighter water above heavier water that can stratify the ML on a time scale of days to weeks. In addition, the eddy-driven restratification is important for light-limited phytoplankton to bloom at high latitude ocean fronts (Boccaletti et al., 2007; Fox-Kemper and Ferrari, 2008; Taylor and Ferrari, 2011; Mahadevan et al., 2012). This causes the surface sunlit layer to retain phytoplankton for longer periods, promoting a phytoplankton bloom. The Critical Depth Hypothesis (Sverdrup, 1953) posits out that vernal phytoplankton blooms occur when surface mixed layer depth shoals to a depth shallower than a critical depth at which integrated phytoplankton growth exceeds losses when nutrients are sufficient, and phytoplankton distribute homogeneously in the mixed layer. A deep MLD transports more phytoplankton to the dark subsurface layers, which does not allow them to grow with no light. On the other hand, when nutrients are not sufficient, the deeper mixed layer may increase the nutrients in sunlit layers, which would increase the phytoplankton; this is the case in autumn bloom. Therefore, the coincidence of chlorophyll-a positive anomaly with the shallower mixed layer during the Large Meander implies that the former phytoplankton increase mechanism caused by the re-stratification could be effective.

Our analysis on the MLD anomaly shows that the negative MLD anomaly is found in the LM with the positive chlorophyll-a anomaly during both the LM periods. However, for the occurrence of the phytoplankton increase caused by mixed layer restratification, nutrients need to be sufficient and the light has to be a major limiting factor for their growth. Because there is the mesoscale nutrient doming in the LM with several smaller scale nutrient injection mechanisms, such as the submesoscale vertical motions, and enhanced turbulence near the Kuroshio, the shallower MLD accompanied by the higher chlorophyll-a supports the hypothesis that the mixed layer re-stratification is also important for the formation of positive chlorophyll-a anomaly along the front in the LM (**Figure 10**). The satellite images during the current LM show that the higher concentration of chlorophyll-a on the western side of the LM with submesoscale chlorophyll filaments (**Supplementary Figure 4B**) and wiggles (**Supplementary Figure 4A**), consistent with the above notion.

The MLD anomalies for both the positive and negative signs seem to be intensified during autumn to spring (**Figure 7**). Although this is caused just by a fact that the deeper MLD during these seasons could have induced larger anomalies, these seasons are consistent with the submesoscale favorable seasons (Sasaki et al., 2014). Therefore, the coincidence of chlorophyll-a positive anomaly with the shallower mixed layer during the Large Meander implies that the former phytoplankton increase mechanism caused by the restratification could be effective.

The variations of phytoplankton community structures between LM and NLM have yet to be known. A study by Hidaka and Nakata (2010) reported that the interannual variations in the plankton ecosystem regarding sea surface chlorophyll and copepod biomass is attributed to local temperature and/or variation in surface irradiance. Besides, the phytoplankton distribution and biological production in coastal waters depend primarily on the nutrient availability in the euphotic zone. Near the Izu Peninsula the dominant phytoplankters are the diatoms in particular *Chaetoceros* spp. in September 1980 (Takahashi and Kishi, 1984).

5. SUMMARY AND CONCLUSIONS

In this study, the influence of the Kuroshio Large Meander (LM) on the surface chlorophyll-a concentration is investigated using the satellite chlorophyll-a data from 1997 to January 2019. We found for the first time that during large meander periods the positive chlorophyll-a anomaly appears along the Kuroshio from the regions south of Kyushu and Cape Shiono-Misaki to the southernmost part of the LM off Enshu-Nada. The positive chlorophyll-a anomaly during the LM periods coincides with the shallower mixed layer depth (MLD), implying that mixed layer re-stratification caused by submesoscale flows along the Kuroshio could be effective to support phytoplankton growth. During the course of the LM events, the positive chlorophyll-a anomaly appears first in the region south of Kyushu within the small cyclonic meander on the coast side of the Kuroshio front. This cyclonic meander, known as the trigger meander of the LM, slowly propagates toward the downstream retaining the positive chlorophyll-a anomaly, which then reaches the LM region. As this small meander has the cyclonic circulation characters, nutrients doming structures are expected. The domed nutricline can be more susceptible to the stirring and mixing processes in the upper layers, such as the submesoscale upwelling, and microscale turbulent mixing, both of which are known to be enhanced at ocean fronts (Mahadevan and Tandon, 2006; Nagai et al., 2009, 2012, 2017, 2019a,b, 2021; D'Asaro et al., 2011). Although it is contradict to the previous results (Kawabe, 1987), our results show that the distance between the Kuroshio and the southeastern coast of Kyushu decreases during the LM periods. The closely flowing Kuroshio to the continental slope in the upstream region may induce the strong turbulence, which keeps supplying nutrients to the downstream regions (Nagai et al., 2019a; Durán Gómez and Nagai, 2020).

The enhanced chlorophyll-a concentration during the LM periods on the western part of the LM along the Kuroshio could play an important role for the higher trophic levels. However, it still remains unclear how the positive chlorophyll-a anomaly is formed right at the LM region. Intensive multidisciplinary observations to measure turbulence,

high-resolution three-dimensional density structures, nutrient concentrations, and abundance and community structures of primary and secondary producers are required to understand the cause and influences of the enhanced chlorophyll-a in the LM.

DATA AVAILABILITY STATEMENT

Publicly available datasets were analyzed in this study. This data can be found at: https://marine.copernicus.eu/.

AUTHOR CONTRIBUTIONS

DALB analyzed the satellite data and provided the figures of the paper. RCS, TN, and TH assisted the analyses. DALB provided the first draft of the manuscript. DALB, RCS, TN, and TH edited the manuscripts. All authors contributed to the article and approved the submitted version.

ACKNOWLEDGMENTS

TN and DALB thank SKED (JPMXD0511102330). TN and RCS thank OMIX (KAKENHI16H01590 and 18H04914) and KAKENHI (19H01965). TN, DALB, and RCS thank continuous support from the pAnTS project.

SUPPLEMENTARY MATERIAL

The Supplementary Material for this article can be found online at: https://www.frontiersin.org/articles/10.3389/fmars.2021.677632/full#supplementary-material

REFERENCES

Akitomo, K., Awaji, T., and Imasato, N. (1991). Kuroshio path variation south of Japan. Part 1: barotropic inflow-outflow model. *J. Geophys. Res.* 96, 2549–2560. doi: 10.1029/90JC02030

Ambe, D., Endoh, T., Hibiya, T., and Imawaki, S. (2009). Transition to the large meander path of the Kuroshio as observed by satellite altimetry. *Mer* 47, 19–27.

Ambe, D., Imawaki, S., Uchida, H., and Ichikawa, K. (2004). Estimating the Kuroshio axis south of Japan using combination of satellite altimetry and drifting buoys. *J. Phys. Oceanogr.* 60, 375–382. doi: 10.1023/B:JOCE.0000038343.31468.fe

Bocaletti, G., Ferrari, R., and Fox-Kemper, B. (2007). Mixed layer instabilities and restratification. *J. Phys. Oceanogr.* 37, 2228–2250. doi: 10.1175/JPO3101.1

Brannigan, L., Marshall, D. P., Naveira Garabato, A., Nurser, G., and Kaiser, J. (2017). Submesoscale instabilities in mesoscale eddies. *J. Phys. Oceanogr.* 47, 3061–3085. doi: 10.1175/JPO-D-16-0178.1

Capet, X., McWilliams, J. C., Molemaker, M. J., and Shchepetkin, A. F. (2008a). Mesoscale to submesoscale transition in the California Current System. Part II: Frontal processes. *J. Phys. Oceanogr.* 38, 44–64. doi: 10.1175/2007JPO3672.1

Capet, X., McWilliams, J. C., Molemaker, M. J., and Shchepetkin, A. F. (2008b). Submesoscale transition in the California Current system. Part I: Flow structure, eddy flux, and observational tests. *J. Phys. Oceanogr.* 38, 29–43. doi: 10.1175/2007JPO3671.1

Chao, S. Y. (1984). Bimodality of the Kuroshio. *J. Phys. Oceanogr.* 14, 92–103. doi: 10.1175/1520-0485(1984)014<0092:BOTK>2.0.CO;2

D'Asaro, E., Lee, C., Rainville, L., Harcourt, L., and Thomas, L. (2011). Enhanced turbulence and energy dissipation at ocean fronts. *Science* 332, 318–322. doi: 10.1126/science.1201515

Durán Gómez, G. S., and Nagai, T. (2020). "Elevated nutrient supply caused by the kuroshio approaching to the continental shelf associated with submesoscale flows and near-inertial waves," in *Fall Meeting, AGU Presented at 2020* (San Francisco, CA).

Ebuchi, N., and Hanawa, K. (2000). Mesoscale eddies observed by TOLEX-ADCP and TOPEX/POSEIDON altimeter in the Kuroshio recirculation region south of Japan. *J. Oceanogr.* 56, 43–57.

Ebuchi, N., and Hanawa, K. (2003). Influence of mesoscale eddies on variations of the Kuroshio path south of Japan. *J. Oceanogr.* 59, 25–36. doi: 10.1023/A:1022856122033

Endoh, T., and Hibiya, T. (2000). Numerical study of the generation and propagation of trigger meanders of the Kuroshio south of Japan. *J. Oceanogr.* 56, 409–418. doi: 10.1023/A:1011176322166

Endoh, T., and Hibiya, T. (2001). Numerical simulation of the transient response of the kuroshio leading to the large meander formation south of Japan. *J. Geophys. Res.* 106, 26833–26850. doi: 10.1029/2000JC000776

Endoh, T., and Hibiya, T. (2009). Interaction between the trigger meander of the Kuroshio and the abyssal anticyclone over Koshu Seamount as seen in the reanalysis data. *Geophys. Res. Lett.* 36:L18604. doi: 10.1029/2009GL039389

Fox-Kemper, B., and Ferrari, R. (2008). Parameterization of mixed layer eddies. Part II: prognosis and impact. *J. Phys. Oceanogr.* 38, 1166–1179. doi: 10.1175/2007JPO3788.1

Gula, J., Molemaker, M. J., and McWilliams, J. (2016). Submesoscale dynamics of a Gulf Stream frontal eddy in the South Atlantic Bight. *J. Phys. Oceanogr.* 46, 305–325. doi: 10.1175/JPO-D-14-0258.1

Guo, M., Xiu, P., Chai, F., and Xue, H. (2019). Mesoscale and submesoscale contributions to high sea surface chlorophyll in subtropical gyres. *Geophys. Res. Lett.* 46, 13217–13226. doi: 10.1029/2019GL085278

Hayasaki, M., Kawamura, R., Mori, M., and Watanabe, M. (2013). Response of extratropical cyclone activity to the Kuroshio large meander in northern winter. *Geophys. Res. Lett.* 40, 2851–2855. doi: 10.1002/grl.50546

Hidaka, K., and Nakata, K. (2010). Interannual variations of the planktonic ecosystem in the slope water and Kuroshio south of Japan in February in the years 1990–2002. *J. Oceanogr.* 66, 741–753. doi: 10.1007/s10872-010-0061-5

Ichikawa, K. (2001). Variation of the Kuroshio in the Tokara Strait induced by meso-scale eddies. *J. Oceanogr.* 57, 55–68. doi: 10.1023/A:1011174720390

Kagimoto, T., Miyazawa, Y., Guo, X., and Kawajiri, H. (2008). "High resolution Kuroshio forecast system: description and its applications," in *High Resolution Numerical Modelling of the Atmosphere and Ocean,* eds K. Hamilton and W. Ohfuchi (New York, NY: Springer).

Kawabe, M. (1985). Sea level variations at the Izu Islands and typical stable paths of the Kuroshio. *J. Oceanogr. Soc. Jpn.* 41, 307–326. doi: 10.1007/BF02109238

Kawabe, M. (1986). Transition processes between the three typical paths of the Kuroshio. *J. Oceanogr. Soc. Jpn.* 42, 174–191. doi: 10.1007/BF02109352

Kawabe, M. (1987). Spectral properties of sea level and time scales of Kuroshio path variations. *J. Oceanogr. Soc. Jpn.* 43, 111–123. doi: 10.1007/BF02111887

Kawabe, M. (1995). Variations of current path, velocity, and volume transport of the Kuroshio in relation with the large meander. *J. Phys. Oceanogr.* 25, 3103–3117. doi: 10.1175/1520-0485(1995)025<3103:VOCPVA>2.0.CO;2

Kimura, S., Kasai, A., Nakata, H., Sugimoto, T., Simpson, J. H., and Cheok, J. V. S. (1997). Biological productivity of meso-scale eddies caused by frontal disturbances in the Kuroshio. *ICES J. Mar. Sci.* 54, 179–192.

Klein, P., and Lapeyre, G. (2009). The oceanic vertical pump induced by mesoscale and submesoscale turbulence. *Annu. Rev. Mar. Sci.* 1, 351–375. doi: 10.1146/annurev.marine.010908.163704

Lévy, M., Iovino, D., Resplandy, L., Klein, P., Madec, G., Tréguier, A.-M., et al. (2012). Large-scale impacts of submesoscale dynamics on phytoplankton: local and remote effects. *Ocean Model.* 43, 77–93. doi: 10.1016/j.ocemod.2011.12.003

Liu, X., Mu, M., and Wang, Q. (2018). The nonlinear optimal triggering perturbation of the Kuroshio large meander and its evolution in a regional ocean model. *J. Phys. Oceanogr.* 48, 1771–1786. doi: 10.1175/JPO-D-17-0246.1

Mahadevan, A., D'Asaro, E., Lee, C., and Perry, M. J. (2012). Eddy-driven stratification initiates North Atlantic spring phytoplankton blooms. *Science* 337, 54–58. doi: 10.1126/science.1218740

Mahadevan, A., and Tandon, A. (2006). An analysis of mechanisms for submesoscale vertical motion at ocean fronts. *Ocean Model.* 14, 241–256. doi: 10.1016/j.ocemod.2006.05.006

Martin, A. P., and Richards, K. J. (2001). Mechanisms for vertical nutrient transport within a North Atlantic mesoscale eddy. *Deep Sea Res. Part II Top. Stud. Oceanogr.* 48, 757–773. doi: 10.1016/S0967-0645(00)00096-5

Masuda, A. (1982). An interpretation of the bimodal character of the stable Kuroshio path. *Deep Sea Res. Part A Oceanogr. Res. Pap.* 29, 471–484. doi: 10.1016/0198-0149(82)90071-1

McWilliams, J. C. (2016). Submesoscale currents in the ocean. *Proc. R. Soc. A Math. Phys. Eng. Sci.* 472:20160117. doi: 10.1098/rspa.2016.0117

Mitsudera, H., Waseda, T., Yoshikawa, Y., and Taguchi, B. (2001). Anticyclonic eddies and Kuroshio meander formation. *Geophys. Res. Lett.* 28, 2025–2028. doi: 10.1029/2000GL012668

Miyazawa, Y., Guo, X., and Yamagata, T. (2004). Roles of mesoscale eddies in the Kuroshio paths. *J. Phys. Oceanogr.* 34, 2203–2222. doi: 10.1175/1520-0485(2004)034<2203:ROMEIT>2.0.CO;2

Miyazawa, Y., Kagimoto, T., Guo, X., and Sakuma, H. (2008). The Kuroshio large meander formation in 2004 analyzed by an eddy-resolving ocean forecast system. *J. Geophys. Res.* 113:C10015. doi: 10.1029/2007JC004226

Miyazawa, Y., Yamane, S., Guo, X., and Yamagata, T. (2005). Ensemble forecast of the Kuroshio meandering. *J. Geophys. Res.* 110:C10026. doi: 10.1029/2004JC002426

Nagai, T., Clayton, S., and Uchiyama, Y. (2019b). "Multiscale routes to supply nutrients through the kuroshio nutrient stream," in *Kuroshio Current,* eds T. Nagai, H. Saito, K. Suzuki, and M. Takahashi.

Nagai, T., Durán Gómez, G. S., Otero, D. A., Mori, Y., Yoshie, N., Ohgi, K., et al. (2019a). How the Kuroshio Current delivers nutrients to sunlit layers on the continental shelves with aid of near-inertial waves and turbulence. *Geophys. Res. Lett.* 46, 6726–6735. doi: 10.1029/2019GL082680

Nagai, T., Hasegawa, D., Tanaka, T., Nakamura, H., Tsutsumi, E., Inoue, R., et al. (2017). First evidence of coherent bands of strong turbulent layers associated with high-wavenumber internal- wave shear in the upstream Kuroshio. *Sci. Rep.* 7:14555. doi: 10.1038/s41598-017-15167-1

Nagai, T., Rosales Quintana, G. M., Durán Gómez, G. S., Hashihama, F., and Komatsu, K. (2021). Elevated turbulent and double-diffusive nutrient flux in the kuroshio over the Izu Ridge and in the Kuroshio Extension. *J. Oceanogr.* 77, 55–74. doi: 10.1007/s10872-020-00582-2

Nagai, T., Tandon, A., Yamazaki, H., and Doubell, M. J. (2009). Evidence of enhanced turbulent dissipation in the frontogenetic Kuroshio Front thermocline. *Geophys. Res. Lett.* 36:L12609. doi: 10.1029/2009GL038832

Nagai, T., Tandon, A., Yamazaki, H., Doubell, M. J., and Gallager, S. (2012). Direct observations of microscale turbulence and thermohaline structure in the Kuroshio Front. *J. Geophys. Res.* 117:C08013. doi: 10.1029/2011JC007228

Nagano, A., Yamashita, Y., Hasegawa, T., Ariyoshi, K., Matsumoto, H., and Shinohara, M. (2018). Characteristics of an atypical large-meander path of the Kuroshio Current south of Japan formed in september 2017. *Mar. Geophys. Res.* 40, 525–539. doi: 10.1007/s11001-018-9372-5

Nakamura, H., Nishina, A., and Minobe, S. (2012). Response of storm tracks to bimodal Kuroshio path states south of Japan. *J. Clim.* 25, 7772–7779. doi: 10.1175/JCLI-D-12-00326.1

Nakata, K. (1994). Variations in food abundance for Japanese sardine larvae related to the Kuroshio meander. *Fish. Oceanogr.* 3, 39–49. doi: 10.1111/j.1365-2419.1994.tb00046.x

Qiu, B., and Chen, S. (2005). Variability of the Kuroshio Extension jet, recirculation gyre, and mesoscale eddies on decadal time scales. *J. Phys. Oceanogr.* 35, 2090–2103. doi: 10.1175/JPO2807.1

Sasaki, H., Klein, P., Qiu, B., and Sasai, Y. (2014). Impact of oceanic-scale interactions on the seasonal modulation of ocean dynamics by the atmosphere. *Nat. Commun.* 5:6636. doi: 10.1038/ncomms6636

Solomon, H. (1978). Occurrence of small "trigger meanders" in the Kuroshio off southern kyushu. *J. Oceanogr. Soci. Jpn.* 34, 81–84.

Stommel, H., and Yoshida, K. (1972). *Kuroshio: Its Physical Aspects.* Tokyo: University of Tokyo Press.

Sverdrup, H. (1953). On conditions for the vernal blooming of phytoplankton. *J. Conseil Permanent Int. l'Explor.* 18, 287–295.

Taft, B. A. (1972). "Characteristics of the flow of the Kuroshio south of Japan," in *Kuroshio-Its Physical Aspects,* eds H. Stommel and K. Yoshida (University of Tokyo Press), 165–216.

Takahashi, M., and Kishi, M. J. (1984). Phytoplankton growth response to wind induced regional upwelling occurring around the Izu islands off Japan. *J. Oceanogr. Soc. Jpn.* 40, 221–229. doi: 10.1007/BF02302556

Taylor, J. R., and Ferrari, R. (2011). Ocean fronts trigger high latitude phytoplankton blooms. Geophys. Res. Lett. 38:L23601. doi: 10.1029/2011GL049312

Uda, M. (1937). On the recent abnormal condition of the Kuroshio to the south of Kii Peninsula, (in Japanese). *Kagaku* 7, 360–361.

Usui, N. (2019). "Progress of studies on Kuroshio path variations south of Japan in the past decade," in *Kuroshio Current,* eds T. Nagai, H. Saito, K. Suzuki, and M. Takahashi.

Usui, N., Tsujino, H., Fujii, Y., and Kamachi, M. (2008). Generation of a trigger meander for the 2004 Kuroshio large meander. *J. Geophys. Res.* 113:C01012. doi: 10.1029/2007JC004266

Usui, N., Tsujino, H., Nakano, S., and Matsumoto, S. (2013). Long-term variability of the Kuroshio path south of Japan. *J. Oceanogr.* 69, 647–670. doi: 10.1007/s10872-013-0197-1

Waseda, T., Mitsudera, H., Taguchi, B., and Yoshikawa, Y. (2002). On the eddy-Kuroshio interaction: evolution of the mesoscale eddy. *J. Geophys. Res.* 107, 3–1–3–19. doi: 10.1029/2000JC000756

White, W. B., and McCreary, J. P. (1976). On the formation of the Kuroshio meander and its relationship to the large-scale ocean circulation. *Deep-Sea Res.* 23, 33–47. doi: 10.1016/0011-7471(76)90806-8

Xu, H., Tokinaga, H., and Xie, S.-P. (2010). Atmospheric effects of the Kuroshio large meander during 2004–05. *J. Clim.* 23, 4704–4715. doi: 10.1175/2010JCLI3267.1

Yamada, K., Ishizaka, J., Yoo, S., cheol Kim, H., and Chiba, S. (2004). Seasonal and interannual variability of sea surface chlorophyll a concentration in the Japan/East sea (JES). *Prog. Oceanogr.* 61, 193–211. doi: 10.1016/j.pocean.2004.06.001

Yasuda, I., Yoon, J. H., and Suginohara, N. (1985). Dynamics of the Kuroshio large meander-barotropic model. *J. Oceanogr. Soc. Jpn.* 48, 259–273. doi: 10.1007/BF02109275

Conflict of Interest: The authors declare that the research was conducted in the absence of any commercial or financial relationships that could be construed as a potential conflict of interest.

The handling editor declared a past collaboration with one of the authors, TN.

Publisher's Note: All claims expressed in this article are solely those of the authors and do not necessarily represent those of their affiliated organizations, or those of the publisher, the editors and the reviewers. Any product that may be evaluated in this article, or claim that may be made by its manufacturer, is not guaranteed or endorsed by the publisher.

Copyright © 2021 Lizarbe Barreto, Chevarria Saravia, Nagai and Hirata. This is an open-access article distributed under the terms of the Creative Commons Attribution License (CC BY). The use, distribution or reproduction in other forums is permitted, provided the original author(s) and the copyright owner(s) are credited and that the original publication in this journal is cited, in accordance with accepted academic practice. No use, distribution or reproduction is permitted which does not comply with these terms.

frontiers in Marine Science

ORIGINAL RESEARCH
published: 24 August 2021
doi: 10.3389/fmars.2021.678845

Impact of Ship Traffic on the Characteristics of Shelf Sediments: An Anthropocene Prospective

*Chengfeng Xue[1], Yang Yang[2], Peipei Zhao[1], Dongyun Wei[1], Jianhua Gao[3], Peng Sun[4], Zhiyang Huang[4] and Jianjun Jia[1]**

[1] State Key Laboratory of Estuarine and Coastal Research, School of Marine Sciences, East China Normal University, Shanghai, China, [2] School of Marine Science and Engineering, Nanjing Normal University, Nanjing, China, [3] Ministry of Education Key Laboratory of Coast and Island Development, School of Geography and Ocean Science, Nanjing University, Nanjing, China, [4] Shanghai Waterway Engineering Design and Consulting Co., Ltd., Shanghai, China

Humans have been sailing across seas and oceans for thousands of years. However, the story of large ships capable of affecting coastal ecology and shelf sedimentary processes is only about 100 years old. Modern large seagoing vessels with a draft of 10–20 m can cause resuspension of seabed sediment, erosion of the channel slope and shoal, enhancement of seafloor sediment activity and thickening of the active layer, thereby having a significant impact on seabed topography and sedimentation processes. However, little is known about the effects of this anthropogenic agent on shelf sedimentation due to limited observational data. Here, two sediment cores were collected from a shipping lane used by vessels of 5,000- to 50,000-ton off the coast of China to analyze their sedimentary properties, with focus on both the grain size and elements. It was found that ship disturbance selectively modified the sedimentary record, with the fine-grained sediment becoming increasingly unstable. In addition, there was a reduction in grain size of sediment finer than 6.25 Φ, which decreased by 11% after the disturbance by ship. Biogenic elements that were closely related to the ecological environment were significantly altered, with Br/Cl, Si/Ti, and Ca/Ti ratios all becoming significantly smaller. This indicated that frequent disturbance caused by ships had reduced the productivity in the waters near the shipping lane. In terms of sensitivity to the effects of ship navigation, the sedimentation response was relatively rapid and began to emerge from the commencement of ship navigation, whereas the ecological response became evident later than the sedimentation response and only appeared after a significant growth in the maritime transportation of China. Following the comparison of the two sediment cores, we propose that the constant rate of supply (CRS- with ship disturbance)–constant initial concentration (CIC- without ship disturbance) dual dating model be used to establish a dating framework in waters frequently disturbed by ship. This type of anthropogenic sedimentary dynamic process and its sedimentary–ecological effects deserve attention on this era where there is a surge in shipping globally. Shipping lanes present an excellent area for quantitative studies on the impacts of human activity and defining the Anthropocene in the context of shipping.

Keywords: human activity, ship disturbance, sedimentary record, ecosystem, environment

OPEN ACCESS

Edited by:
Kuoping Chiang, National Taiwan Ocean University, Taiwan

Reviewed by:
Helena Granja, University of Minho, Portugal
Xiaolei Liu, Ocean University of China, China

****Correspondence:***
Jianjun Jia
jjjia@sklec.ecnu.edu.cn

Specialty section:
This article was submitted to Coastal Ocean Processes, a section of the journal Frontiers in Marine Science

Received: *10 March 2021*
Accepted: *26 July 2021*
Published: *24 August 2021*

Citation:
Xue CF, Yang Y, Zhao PP, Wei DY, Gao JH, Sun P, Huang ZY and Jia JJ (2021) Impact of Ship Traffic on the Characteristics of Shelf Sediments: An Anthropocene Prospective. Front. Mar. Sci. 8:678845. doi: 10.3389/fmars.2021.678845

INTRODUCTION

Humans and the natural environment interact with each other (Ye et al., 2009; Syvitski and Kettner, 2011), and humans have been influencing the natural environment significantly for thousands of years (Ren, 1989; Debret et al., 2009; Jenny et al., 2019). Since the Industrial Revolution, humans have become the main agents of environmental change, and the concept of the Anthropocene was born in 2000 (Crutzen and Stoermer, 2000). The fact that humans act as an important force in nature brings a new scientific challenge to earth scientists, that is, the impacts of various human activities should be quantified and integrated into the existing earth science system (Ye et al., 2009).

Estuaries and offshore waters are places where the imprints of human activity are particularly prominent. For example, coastal and ocean engineering can alter the original dynamic field, leading to changes in the morphological structure and ecological function of the modern delta and decreased sustainability of the modern delta (Powell et al., 2006; De Vriend et al., 2011; Day et al., 2016; Luan et al., 2016). The impact of shelf trawling on the resuspension of fine sediment on the seabed is comparable with that of large storms (Ferré et al., 2008).

Marine vessels are undoubtedly one of the most prominent symbols of human activities in the ocean. Large ships cause significant disturbances in sediment dynamic processes mainly in three ways: (i) the jet flow generated by ships' propellers causes resuspension of sediment on the bed of shipping lanes (Soon and Lam, 2014; Hong et al., 2016); (ii) the propagation of ship-induced waves may cause erosion of the channel slope and shoal (Rapaglia et al., 2011); and (iii) prolonged and frequent ship shuttle services enhance seabed sediment activity and increase the thickness of the active layer (Hong et al., 2013). Consequently, suspended sediment concentration increases significantly during ship navigation, and can be 30 times higher than the average background concentration (Rapaglia et al., 2011). More than that, turbid water affects the growth of phytoplankton, which in turn affects marine productivity (Huang et al., 1986; Pan and Shen, 2009).

Compared to known ship-related hydrodynamics (e.g., propeller-jet, ship wave, ship wakes, etc.), little is known about the impact of ship traffic on marine sedimentation records (e.g., the characteristics of shelf sediments), largely due to the scarcity of studies dedicated to this field. Considering that maritime transport is responsible for 80% of the total volume of international trade (Notteboom et al., 2021), this rising anthropogenic-force induced sedimentary process deserves more attention, and research related to this will be important for marine biogeochemistry, sedimentary dynamics, and geomorphology.

Over the past 70 years, China's maritime transport has experienced explosive growth. Shanghai Port and Ningbo-Zhoushan Port have become the world's leading ports in terms of container and cargo throughput. Due to these two ports, the coastal shipping lanes along Zhejiang Province are particularly busy. This area represents an ideal place to analyze the effects of seagoing traffic on the shelf sedimentary record. In this study, a shipping lane suitable for 5,000 ∼ 50,000 tons ships along the Zhejiang coast of the East China Sea was selected as the study site, and two short sediment cores were collected from the centerline and the periphery of the lane to analyze their ages and sediment characteristics. We use an improved ^{210}Pb dating model to establish a more accurate depth-age framework in regions with frequent ship disturbance. In combination with development of China's offshore shipping lanes, we explore the possible linkage between ship traffic and the changes in sedimentation.

STUDY AREA

The booming development of China's coastal and ocean-going shipping began in the late 20th century, with coastal transport accounting for 60% of the total domestic transport [China Port Yearbook (1999–2019)]. After decades of development, Shanghai Port and Ningbo-Zhoushan Port have become the world's leading ports in terms of container and cargo throughput. The coastal shipping lanes along Zhejiang Province are particularly busy due to these two ports and the coastal shipping lanes intersect. The north–south lanes throughout the East China Sea include four main lanes: the Outer Shipping Lane, the Eastern Shipping Lane, the Middle Shipping Lane, and the Western Shipping Lane (**Figure 1**). The eastern and western shipping lanes intersect outside Aiwan Bay, where shipping is well-developed and traffic is frequent in the north–south direction. The lanes can allow ships of 5,000- to 50,000-ton to pass through, even up to 100,000 tons on some sections. This area is close to the Wenzhou Port, where many passenger ship lanes lead to the surrounding islands (He, 2008). Therefore, it is an ideal area to study about the disturbance caused by ships. The tides are regular semidiurnal tides with an average tidal range of 4 m, and the maximum can be 7 m. The wave height is approximately 1 m. During typhoons, the wave height is up to 5 m, and the maximum can reach 10 m (China Gulf Annals, 1993). The bottom sediment is clayey silt and silt (Jia et al., 2018).

MATERIALS AND METHODS

We obtained two cores off the coast of Aiwan Bay, Zhejiang Province, China, to analyze grain size and geochemical elements. Combined with the dating framework, we analyzed the changes in sediment characteristics over time. A literature review was conducted to understand the history of the marine transport industry and the shipping lanes where the cores have been located over the past decades, with a view to quantify the sedimentation effects of ship disturbance.

Coring

Two cores were collected in May 2018 using a gravity coring tube. Core Z7 (28°3′0″N, 121°33′36″E), 1.5 m long with a water depth of 13.2 m, was collected at the intersection of two main shipping lanes used by vessels of 5,000- to 50,000-ton. Core Z8 (28°5′21″N, 121°32′36″E), 1.5 m long

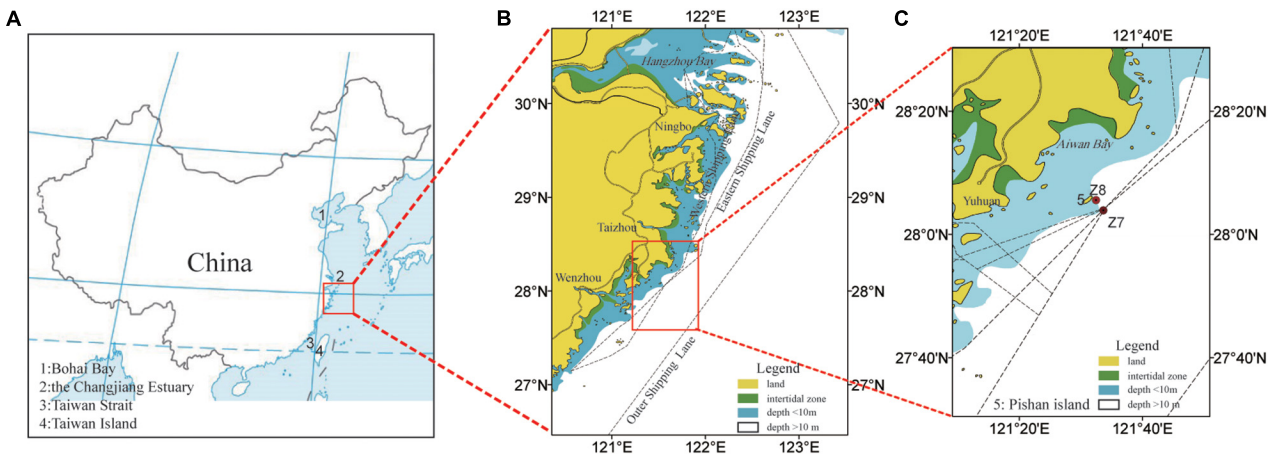

FIGURE 1 | Maps of the shipping lane indicate **(A,B)** the study area (according to He, 2008) and **(C)** the sampling site. Core Z7 was located at the intersection of the eastern and western shipping lane, and a control core (core Z8) was collected outside the shipping lane at a distance of 4.7 km northwest to core Z7.

with a water depth of 12 m, was collected outside the shipping lane at a distance of 4.7 km from core Z7 in the northwestern direction. The natural sedimentary environments in the region of two cores are nearly identical because of the short distance between the two cores, which will better ensure an accurate representation of the effects of disturbance on the sediment due to maritime traffic through contrast analysis.

XRF Core Scan

The cores were each split into two parts using a GeoTek Core Splitter. One half of the core was covered with a 4 μm thick Ultralene film to avoid the contamination of the X-ray fluorescence (XRF) core scanner (Avaatech 3RD, Netherlands) measurement unit and the desiccation of the sediment (Richter et al., 2006). Instrument settings were optimized to minimize the mean square error (MSE) values, and the step size was 0.5 cm. Count times for XRF analysis ranged from 10 to 30 s (**Table 1**). Reliable data were obtained for 29 elements. Four powdered standards were analyzed every day before and after the analysis of the sediment cores to monitor signal drift and indicated that the signal remained stable during the analytical runs. The experiment was completed at the State Key Laboratory of Marine Environmental Science, Xiamen University, Xiamen.

Grain Size Analysis

Grain size analysis of 1 cm sub-samples was conducted using a laser particle analyzer (Mastersizer-2000, United Kingdom), which has a measurement range of 0.02–2000 μm with a relative error of <3% for repeated measurements. The experiment was completed at the Key Laboratory of Coastal and Island Development, Nanjing University, Nanjing. The matrix formula of McManus (1988) was used to calculate the sample statistics of the grain size distribution, that is, mean grain size (*Mz*), sorting (*S*), skewness (*Sk*), and kurtosis (*K*). The above four parameters refer to: the average size, the spread of the sizes around the average, the symmetry or preferential spread to one side of the average, and the degree of concentration of the grains relative to the average, respectively (Blott and Pye, 2001). The grain size standard deviation at 10 cm intervals was calculated to extract the sensitive grain size fraction (Sun et al., 2003). The changes in the sensitive grain size fraction over time can reflect the evolution of sedimentary dynamic processes and depositional environments.

Age Models

Age models are of critical importance in interpreting sedimentary records. One of the most important means for dating recent sediments (0–150 years) is by ^{210}Pb (half-life 22.3 years), a natural radioactive isotope of lead (Appleby, 2001). The dried sample was homogeneously pulverized, weighed, and then sealed in a plastic box (70 × 70 mm) for 3 weeks. The activities of ^{210}Pbex and ^{137}Cs in the sediment samples were measured following the method described by Du et al. (2010). The radioactivities of the above nuclides were measured using an HPGe γ-ray detector (Canberra Be3830, United States) with a relative counting efficiency of 35% and an energy resolution of 1.8 keV (at 1332 keV). The detector has multilayer shielding (ultralow cryostat and no peak background in the isotopes of interest). The activity of ^{210}Pbex was calculated from the activity of total ^{210}Pb (46.5 keV, 4.25%)

TABLE 1 | Range of options to optimize scanning conditions for the sample.

Element classification	Voltage (kV)	Current (mA)	Count time (s)	Step size (cm)
Light elements (Al, Si, P, S, Cl, K, Ca, Ti, Cr, Mn, Fe, Rh)	10	0.5	10	0.5
Medium elements (Cu, Zn, Ga, Br, Rb, Sr, Y, Zr, Nb, Mo, Pb, Bi)	30	0.5	20	0.5
Heavy elements (Ag, Cd, Sn, Te, Ba)	50	0.75	30	0.5

minus the activity of ^{226}Ra, determined using the γ lines at 351.9 keV (37.6%) for ^{214}Pb and 609.3 keV (46.1%) for ^{214}Bi. The efficiency calibration of the detector systems was conducted using LabSOCS (Baronson, 2003). The experiments were performed at the State Key Laboratory of Estuarine and Coastal Research, East China Normal University, Shanghai. The commonly used ^{210}Pb data processing and computation mainly include the CIC dating mode and the CRS dating model (Appleby, 2001). Given the strengths and weaknesses of the two computational models, the ^{210}Pb chronology of this study was determined using both models.

Historical Documents

To study the response of sediment characteristics to the disturbance effects of ships, it is necessary to be familiar with the shipping lanes near the study area and the frequency of ship navigation. Compared to bulk cargo ships, container ships have the characteristics of large loading capacity, fast speed, and fixed throughput, which are more representative indicators to better reflect the impacts of ship disturbance on sedimentation. The China Port Yearbook comprehensively and accurately recorded the development of China's port navigation and shipping industry, and recorded the container throughput of China's coastal ports from 1979 to date, which could reflect the intensity of disturbance by ship movement on the shipping lanes. Therefore, the container throughput of the whole country and three ports, namely Qingdao Port, Shanghai Port, and Guangzhou Port, were calculated for the period 1979–2018. These three ports are important coastal ports in the Yellow Sea, East China Sea, and South China Sea, respectively.

RESULTS

Depth-Age Framework

The excess^{210}Pb of Z7 and Z8 remained in the law of radioactive decay. The linear fitting result of the excess ^{210}Pb of Z7 was good, with a correlation coefficient of 0.66 by the CIC model and a sedimentation rate of 1.09 cm/yr. The Z8 was better, with a correlation coefficient of 0.91 and a sedimentation rate of 1.54 cm/yr (**Figure 2**). Considering that the locations of the two cores were not far from each other, approximately 4 km—expecting a great difference in sedimentation rate would be unreasonable. According to sedimentation rate data of the mud area along the coast of Zhejiang and Fujian (Jia et al., 2018), the average sedimentation rate here is approximately 1.5 cm/yr. The entire 150 cm long sedimentation sequence was recorded from approximately 100 years ago, which was before the emergence of container ships navigation along the coast of China in the late 1970s. Thus, it would be inaccurate to use uniform sedimentation rates to infer the age of sediment before and after the emergence of shipping lanes.

In theory, the CIC model of ^{210}Pb dating is suitable for a stable sedimentary environment, but for a less stable sedimentary environment, the CRS model may provide more accurate dating results (Zhang et al., 2008). It was found that above 70 cm depth both models gave similar curves for Z8 (**Figure 3D**), whereas for Z7, the difference was extremely large, with some layers up to 24 years (**Figure 3A**).

The CRS dating results of the two cores above a depth of 70 cm were almost identical, and the sedimentation records were from 1977 to 2018; below a depth of 70 cm, the CRS model algorithm led to older dating results, and increasing depth (Zhang et al., 2008), with a small sedimentation rate. Therefore, in this study, the CRS dating model was used at depths above 70 cm and the CIC dating model at depths below 70 cm. The sedimentation rate was assumed to be uniform below 70 cm, and the sedimentation rate at 70 cm was used as the sedimentation rate for the 70–150 cm section. On this basis, the dating framework was established for the two cores, and the age of sediment for each layer at the same depth were almost identical, with a mean time difference of 0.4 year. The two cores showed the sedimentation records of 1873–2018 (**Figures 3B,E**). The sedimentation rates of Z7 and Z8 were in the ranges of 0.77–2.76 cm/yr and 0.77–2.53 cm/yr (**Figures 3C,F**), respectively.

Grain Characteristics of Sediments

The grain size components of Z7 and Z8 were dominated by silt, followed by clay, with the least amount of sand (**Figure 4**). Overall, the content of the grain size component did not fluctuate significantly with time. The sediment type was mainly clayey silt, with an occasional silt layer. Through comparative analysis of the two cores, it was found that the grain size parameters were quite different below and above 70 cm.

Segment I (150–70 cm) of Z7 fluctuated less in the grain size parameters, with mean grain size in the range of 6.5–7.25 Φ, sorting coefficient fluctuating approximately 1.6, skewness value approximately 1.2, and kurtosis value between 1.9 and 2.2.

Segment II (70–0 cm) of Z7 fluctuated considerably in the grain size parameters, with mean grain size in the range of 6–7.5 Φ, sorting coefficient in the range of 1.4–1.75, skewness value of approximately 1.2, and kurtosis value between 1.8 and 2.3.

Segment I (150–70 cm) of Z8 had a large fluctuation in the grain size parameters, with mean grain size in the range of 5–7.5 Φ, sorting coefficient in the range of 1.3–1.9, skewness value in the range of 0.75–1.75, and kurtosis value in the range of 1.85–2. 35.

Segment II (70–0 cm) of Z8 had a small fluctuation in the grain size parameters, with a mean grain size of approximately 7 Φ, sorting coefficient in the range of 1.4–1.7, skewness value approximately 1, and kurtosis value in the range of 1.95–2.15.

The sensitive grain size fraction was calculated at 10 cm intervals. Both Z7 and Z8 had two sensitive grain size fractions—the first between 4 and 6 Φ, and the second between 6 and 9 Φ. The peak heights (standard deviation values) of the two sensitive grain size fractions below and above 70–60 cm were very different for the two cores, with the 70 cm value corresponding to the year 1977 (**Figure 3**). Generally, before 1977, the standard deviation of Z7 was smaller than that of Z8, whereas after 1977, the standard deviation of Z7 was larger than that of Z8. To better illustrate the variation in the sensitive grain size fraction over time, the layer at 70–60 cm was selected and two layers below and above 70–60 cm were shown, such as 150–140 cm, 120–110 cm, 30–20 cm, and 10–0 cm (**Figure 5**).

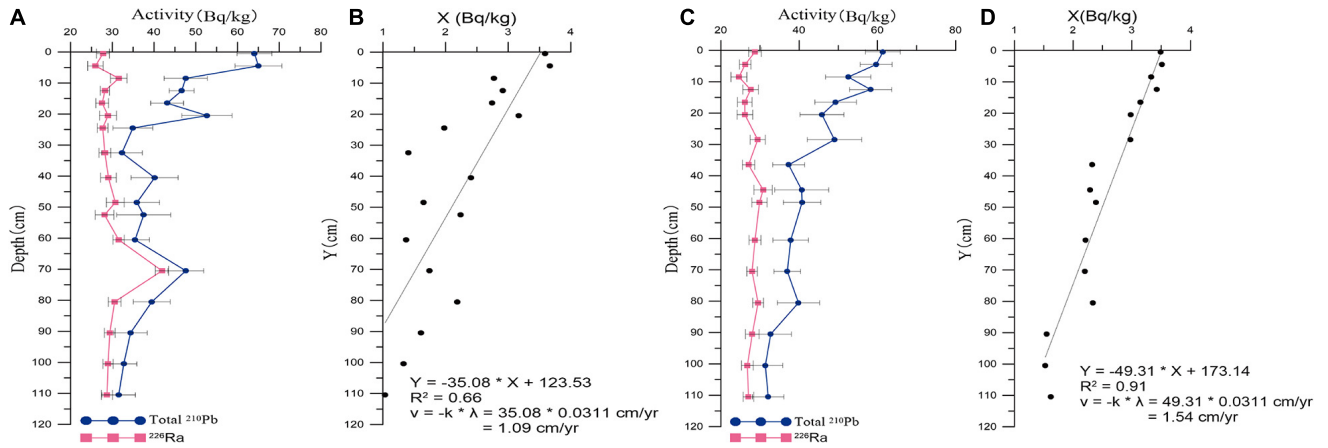

FIGURE 2 | Vertical distribution of ^{210}Pb, ^{226}Ra in core Z7 **(A)**, and Z8 **(C)**. The linear fitting between depth (*Y* axis: cm) and ln(^{210}pb$_{ex}$) (*X* axis: Bq/kg) of core Z7 **(B)** and Z8 **(D)**. v=− k· λ., where v is the sedimentation rate, k is the slope of the linear fitting equation, and λ is the decay constant of ^{210}Pb (i.e., 0.0311/yr).

Here we can see the difference below and above 70–60 cm for the two cores (**Table 2**), which indicated that the sedimentary dynamics of the environment had changed considerably since 1977. Before 1977, the standard deviation of Z7 was smaller than that of Z8, which meant that the sedimentary dynamics of Z7 were more stable than those of Z8. However, after 1977, the standard deviation of Z7 was larger than that of Z8, which meant that the sedimentary dynamics of Z7 were more turbulent than those of Z8. Moreover, after 1977, both the first and second sensitive grain sizes of Z7 were finer than those of Z8, which assumed that the finer particles were more affected by ship disturbance (**Table 2**).

The first sensitive grain size fraction of Z7 (4.50–5.75 Φ) did not change significantly in the 150–110 cm section, with a moderate increase in the 110–70 cm section, a sudden increase in the 70–60 cm section, and a moderate increase above 60 cm (**Figure 6**). The second sensitive grain size fraction of Z7 (6.75–8.25 Φ) did not change significantly in the 150–110 cm section, with a moderate decrease in the 110–70 cm section, a sudden decrease in the 70–60 cm section, and a moderate decrease above 60 cm. The first grain size fraction of Z8 (4.25–5.50 Φ) showed a significant change in the 150–70 cm section, a moderate increase and then a decrease, and it changed very little above 70 cm, with a moderate decrease. The second grain size fraction of Z8 (6.50–8.00 Φ) varied significantly in the 150–70 cm section, with a moderate decrease and then an increase, and it changed very little above 70 cm, with a moderate increase.

The measured grain size distribution curve (in the range of 2–12 Φ) was divided into 40 small cells in units of 0.25 Φ. The difference between two cores at the same time in these small cells was calculated separately. The content of Z8's grain size component was subtracted from that of Z7 on the same layer, with the difference shown on a two-dimensional contour plot (**Figure 7**). Here we can see the quantity of coarser or finer particles difference between two cores at the same time.

The results showed that the sediment can be divided into two groups—coarse and fine—using 6.25 Φ as the boundary, and the sediment varied considerably over time. In the section of 150–140 cm, the difference in relative content between the two cores was approximately zero. In the section of 140–80 cm, the coarser particles (<6.25 Φ) of Z7 were significantly less than those of Z8, whereas the finer particles (>6.25 Φ) were significantly more than those of Z8. In the section of 80–0 cm, the opposite occurred, especially above 70 cm, where the coarser particles of Z7 were significantly more than those of Z8. This indicates that the sediment on the shipping lane showed an increase in the coarse particulate fraction and a decrease in the fine particulate fraction from 1977.

Elemental Characteristics of Sediment

Elements with specific indicators, including S, Cl, Br, Si, Ti, and Ca, were selected for comparative analysis. These elements have steady repeat scanning results and reliable detection, and have often been used by previous researchers (Thomson et al., 2006; Marsh et al., 2007; Agnihotri et al., 2008; Croudace and Rothwell, 2015; Grygar and Popelka, 2016). The content of elements is a relative value, and the data quality is influenced by several factors, such as grain size and water content variations, core surface imperfections, and the presence of organic matter (Croudace and Rothwell, 2015). In order to attenuate above effects, element-to-element ratios were used, which can allow comparison between the cores. Ti is a typical reference element used for normalization (Grygar and Popelka, 2016). The element ratios Br/Cl, S/Ti, Si/Ti, and Ca/Ti, were selected for the study (**Figure 8**).

The Br/Cl ratio for Z7 ranged from 0.06 to 0.17, with a mean value of 0.12, and the element ratio decreased slightly in the 0–40 cm section, with a mean value of 0.11. The S/Ti ratio ranged from 0.12 to 0.38, with a mean value of 0.20, and the element ratio increased significantly in the 0–40 cm section, with a mean value of 0.24. The Si/Ti ratio ranged from 2.77 to 6.79, with a mean value of 5.01, and the element ratio decreased significantly in the 0–40 cm section, with a mean value of 4.87. The Ca/Ti ratio ranged from 2.86 to 4.32, with a mean value of 3.54, and

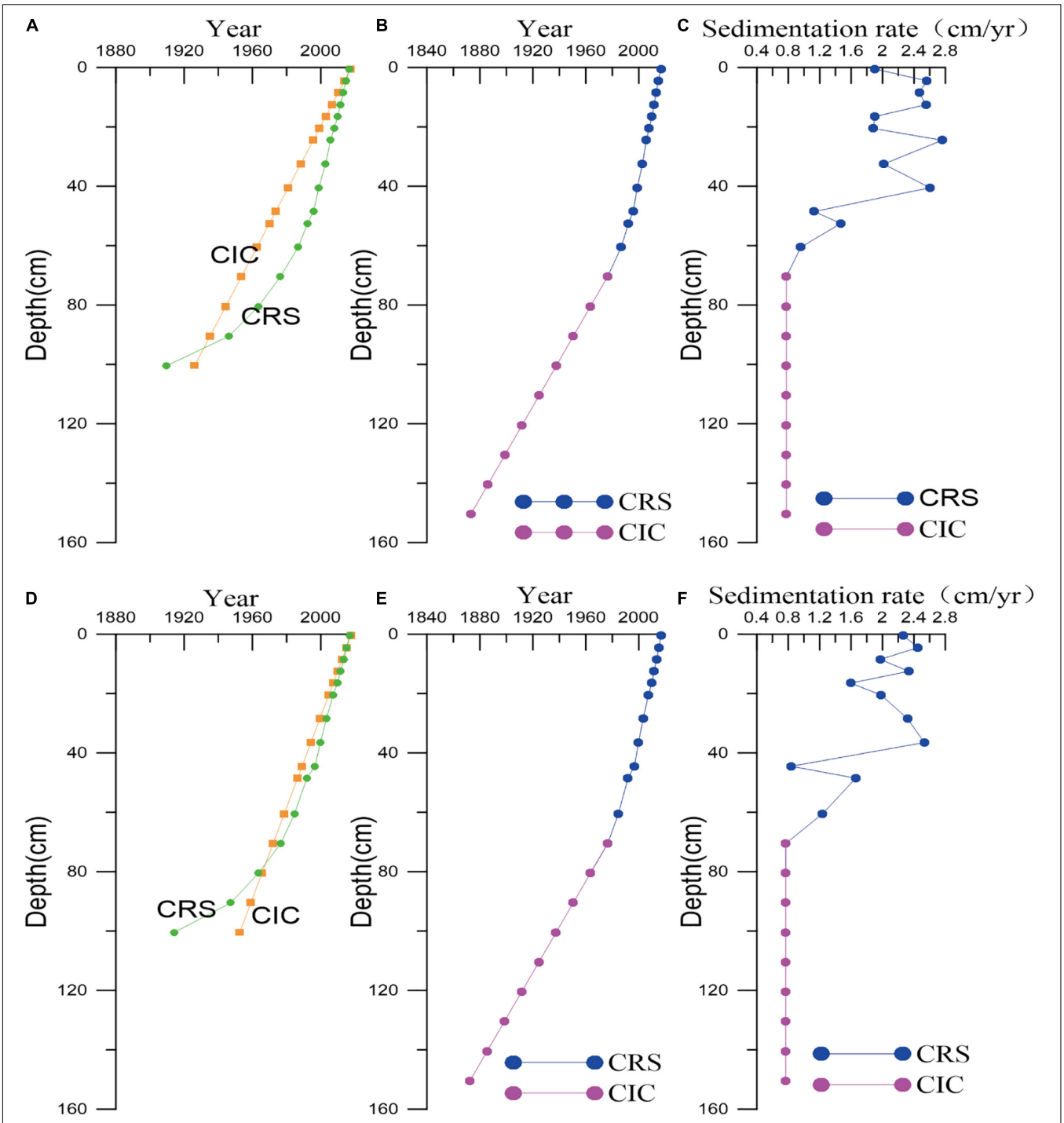

FIGURE 3 | Dating result and sedimentation rate for core Z7 **(A–C)** and Z8 **(D–F)**. The CRS and CIC dating models were combined to establish a dating framework for core Z7 **(B)** and Z8 **(E)**, with the CRS model being used for depths of 0–70 cm and the CIC model for depths of 70–150 cm, to get a more accurate dating framework. **(A**,**D)** Show the difference between CIC and CRS single dating model results for depths of 0–100 cm. The sedimentation rate for core Z7 **(C)** and Z8 **(F)**.

the element ratio decreased slightly in the 0–40 cm section, with a mean value of 3.48.

The element ratios shifted at approximately 40 cm. According to the established dating framework (**Figure 3B**), the year was estimated to be approximately 1999.

For Z8, the most significant shift was Si/Ti, which transformed at 77 cm, with a decrease in the 0–77 cm section. The Br/Cl ratio for Z8 ranged from 0.08 to 0.21, with a mean value of 0.14. The S/Ti ratio ranged from 0.14 to 0.34, with a mean value of 0.21. The Si/Ti ratio ranged from 3.92 to 7.20, with a mean value of

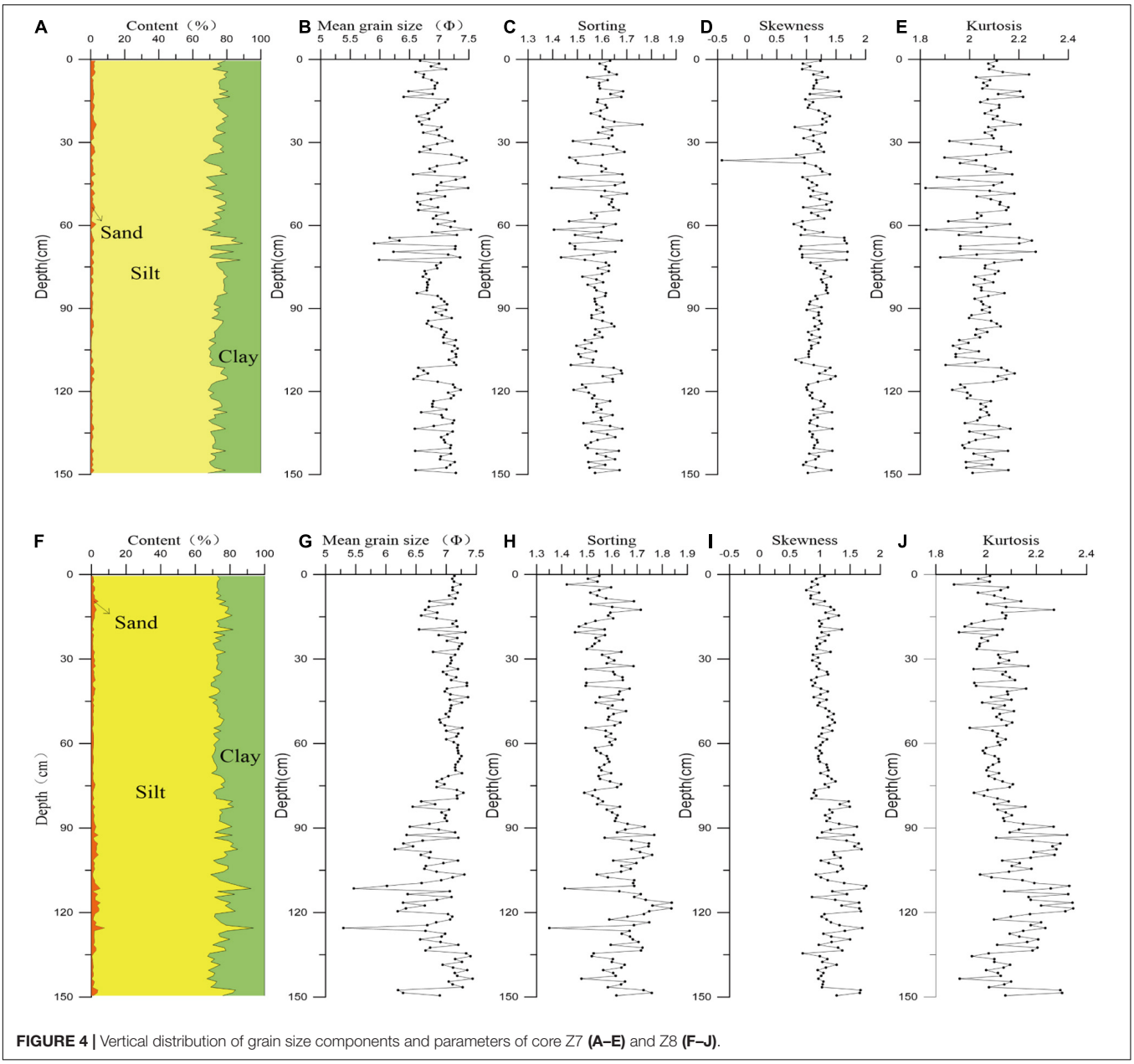

FIGURE 4 | Vertical distribution of grain size components and parameters of core Z7 **(A–E)** and Z8 **(F–J)**.

5.50, and the element ratio decreased significantly in the 0–70 cm section, with a mean value of 5.17. The Ca/Ti ratio ranged from 3.05 to 4.73, with a mean value of 3.63.

DISCUSSION

Development of China's Offshore Shipping Lanes

Containerized maritime transport plays an important role in global trade, accounting for 80% of international cargo trade and growing at an average annual rate of 4% (Ducruet and Notteboom, 2012). A country's container transshipment capability and accessibility directly reflect its maritime transport capacity, as well as its level of maritime transport development. China's container industry began in 1979, with a container throughput of 32,900 twenty-foot equivalent unit (TEU). The late 20th century was in a period of rapid growth (**Figure 9**). According to statistics, the average annual container throughput in 1979–1999 was 2.95 million TEU, and in 1999–2018 it was 127.18 million TEU, a staggering 42-fold increase. The Port of Shanghai has held the top position for container throughput of the world's largest ports since 2010. The external and internal feeders of foreign trade from the Port of Shanghai pass through the outside of Wenzhou Port, where our cores were collected.

Combining the model with global economic development scenarios, it is suggested that global maritime traffic will increase

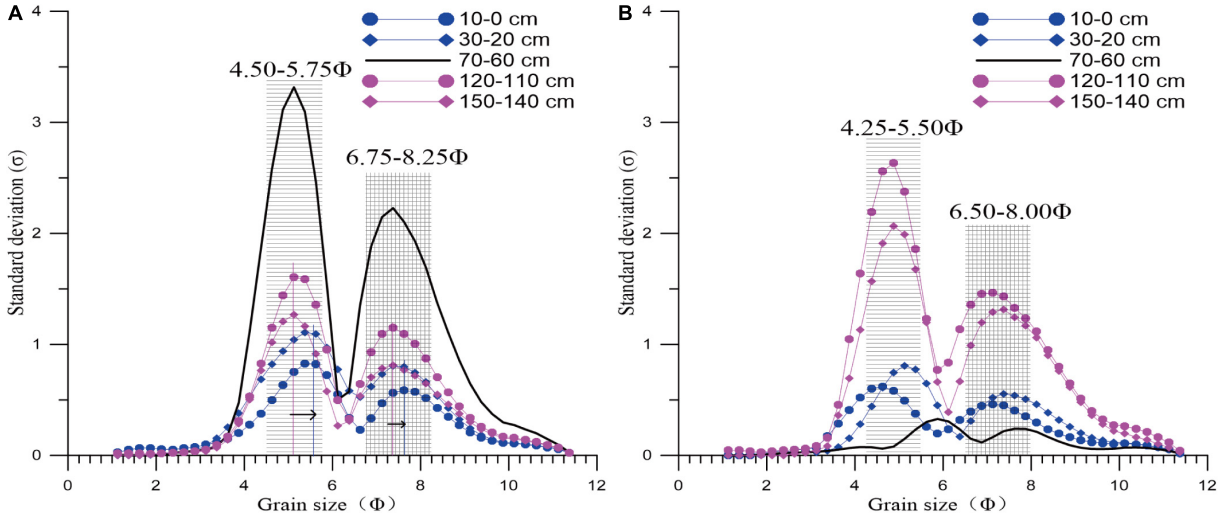

FIGURE 5 | Sensitive grain size fractions of core Z7 **(A)** and Z8 **(B)** of the selected layer were as follows: the sensitive grain size of Z7 was relatively finer than that of Z8; the sensitive grain size fraction of Z7 tended to be finer after 1977, and Z8 had no obvious tendency. The black horizontal arrows indicate that the sensitive grain size has become finer after 1977.

by 240–1,209% by 2050 (Sardain et al., 2019). In addition, the shipping industry entered the so-called megaship era in 2007 when a leading container shipping company deployed a fleet of mega-containerships with a carrying capacity of more than 10,000 TEUs (Imai et al., 2013). The development of megaships requires deeper draft depths and the sea areas affected by ship disturbance is expanding into deeper water accordingly, thus the disturbance effect of megaships will have an increasing impact on relatively deep waters.

China's coastal shipping lanes are traversed in dense networks, with frequent passenger and cargo lanes. Vessels with a container load of more than 5,000 TEU, bulk cargo of more than 100,000 tons, and tankers of more than 100,000 tons meet our definition of a megaship. The southeast coast of China, the Bohai Bay, the Changjiang Estuary, the Taiwan Strait, and the eastern side of Taiwan Island are all areas affected by the disturbance of megaships (**Figure 10**). The study of modern sedimentary dynamics and its products in these areas should consider the influence of megaships on shipping lanes.

TABLE 2 | Grain size and peak heights of the sensitive grain size fraction of the selected layer.

Layer	Grain size (Φ)				Standard deviation (σ)			
	First		Second		First		Second	
	Z7	Z8	Z7	Z8	Z7	Z8	Z7	Z8
10–0 cm	5.38	4.63	7.63	7.13	0.83	0.62	0.59	0.46
30–20 cm	5.38	5.13	7.38	7.38	1.11	0.81	0.81	0.56
70–60 cm	5.13	5.88	7.38	7.63	3.32	0.33	2.23	0.24
120–110 cm	5.13	4.88	7.38	7.13	1.61	2.63	1.15	1.46
150–140 cm	5.13	4.88	7.38	7.38	1.27	2.07	0.81	1.31

After 1977, there was a tendency toward finer sensitive grain size fractions in Z7, whereas there was no clear trend in Z8. The sensitive grain size fraction of Z7 has always been finer than that of Z8, with a more pronounced refinement after 1977.

Differential Performance of Grain Size and Elements

The element content in the sediment is mainly controlled by its mineral composition. In addition, hydrodynamic conditions, adsorption and flocculation of fine particles, redox conditions, and human activities all have an influence on the variation of element content (Dong et al., 2009; Singh, 2009; Ye et al., 2013; Grygar and Popelka, 2016). The grain size of marine sediment is closely related to geochemical elements, both of which are in accordance with the "law of elements controlled by grain size" (Zhao and Yan, 1994). Fine-grained sediment can be readily enriched in some chemical elements, either because they are present in the clay minerals or because of the adsorption effect of the fine-grained particles. This is due to the correlation between particle size and elements, which are often used as a proxy for particle size (Zhou et al., 2019). However, as mentioned above, the particle size changed significantly approximately 1977, whereas the elemental ratios of S/Ti, Ba/Ca, Si/Ti, and Br/Cl did not change significantly until approximately 1999. The behavior of particle size and elements was not identical, and it was therefore worthwhile to investigate the underlying mechanism.

Correlation analysis was conducted between the element ratios selected in this study and the sand, silt, and clay contents. Both were found to be poorly correlated, with the correlation coefficient almost always less than 0.3 (**Table 3**). There was therefore no significant correlation between the grain size and the elements.

The factors influencing the change in the grain size of marine sediments can be summarized into two categories: the first is the change in sediment sources (sources or sediment flux), and the second is the change of sedimentary dynamics environment,

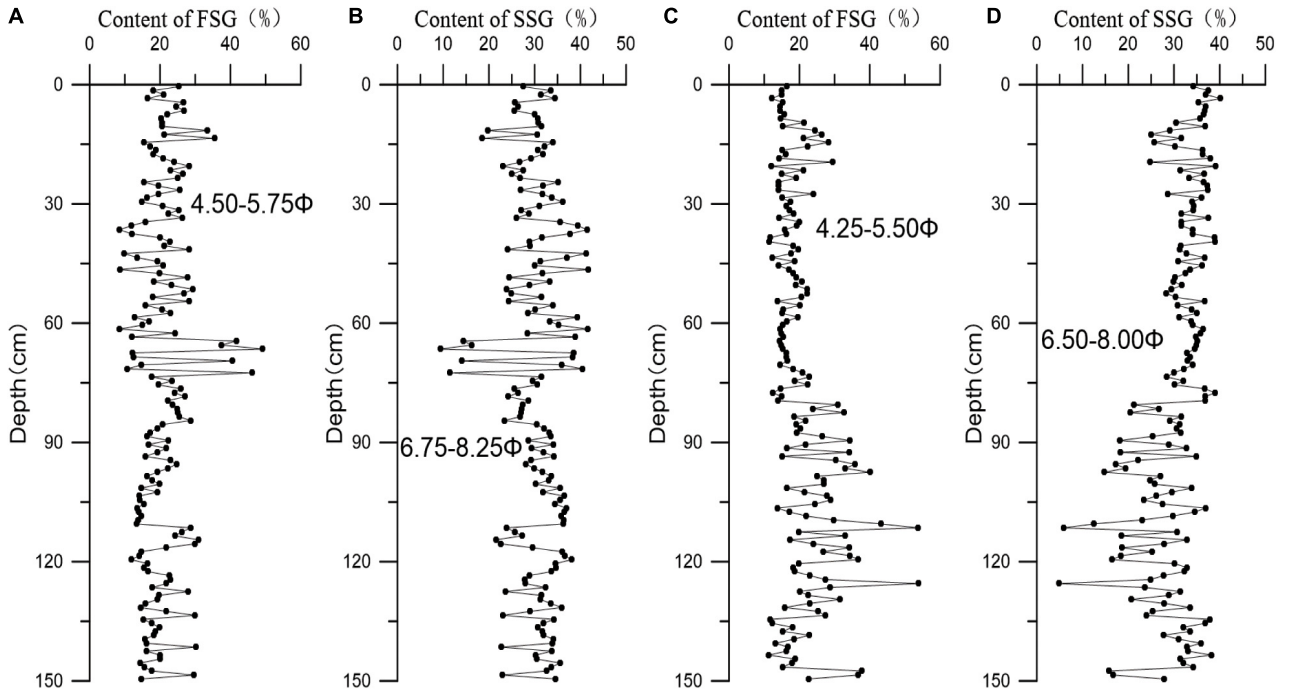

FIGURE 6 | Variations in content of two sensitive grain size fractions of cores Z7 **(A,B)** and Z8 **(C,D)**. FSG, first sensitive grain size; SSG, second sensitive grain size.

which is closely related to the coastal circulation system and extreme climate events (Liu et al., 2010). The study area is located in the distal mud of the subaqueous Changjiang River delta, and the sediment mainly comes from the Changjiang River. Thus, the annual sediment flux of the Changjiang River Datong Station was counted during the period 1953–2018 (**Figure 11**). Before 2000, the annual sediment load was more than 300 Mt. After 2003, due to the influence of the Three Gorges Reservoir, the annual sediment load was less than 200 Mt. In this study, the grain size transition occurred early before the drastic change in sediment flux, so the grain size transition was not influenced by the change of sediment source. Some studies suggest that the load, grain size and sediment composition deposited over the coastal and shelf water adjacent to the estuary have changed in response to the Three Gorges Dam. However, this phenomenon occurs mostly downstream of the reservoirs and estuaries, and after long-distance transport, the signal of changing grain size in the study area has been difficult to detect (Gao et al., 2019). Even in the downstream of the reservoir, the median grain size variation is only about 5 μm (Gao et al., 2015), which is smaller than the variation caused by the navigation channel. Therefore, the transition of grain size was caused by changes in the sedimentary dynamics environment, mainly due to disturbance by ships.

Marine sediments are mainly composed of terrestrial debris, biogenic materials, and marine authigenic substances, whose relative content determines the distribution of elements in the sediment. The elements, especially the biogenic elements related to the ecological environment, can reflect the evolution of the sedimentary environment.

The time of element ratios shift lags behind the time of grain size shift, which was most likely a response of the ecological environment to the effects of ship disturbance. This occurred approximately 1999, when the frequency of navigation began to increase rapidly (**Figure 9**). At the beginning of ship navigation, the effects of ship disturbance did not cause significant changes in elements, until the rapid growth in the maritime transportation of China in 1999. There are complex mechanisms behind this response, involving processes such as the migration and transformation of marine biological production, biogeochemical cycling of marine substances and elements, especially redox-driven processes (Schubert et al., 1998; Duan et al., 2010). All of these processes were influenced by the environmental characteristics include suspended sediment concentration, salinity, total dissolved organic carbon, temperature, depth, pH, Eh, phytoplankton, and water circulation (Marcussen et al., 2008). Only after the disturbance frequency reached a certain level, would the elemental variation manifest. Therefore, grain size variations were expressed soon after the start of navigation, whereas the biogenic elements did not change significantly until 1999.

Sedimentary–Ecological Response to Ship Disturbance

Quantitative studies on the impact of human activities on ecology are of vital importance. In recent years, global reductions in riverine sediment fluxes have become widespread (Syvitski et al., 2005; Milliman and Farnsworth, 2011). Studies to investigate the impact of human activities, mainly in terms of changes

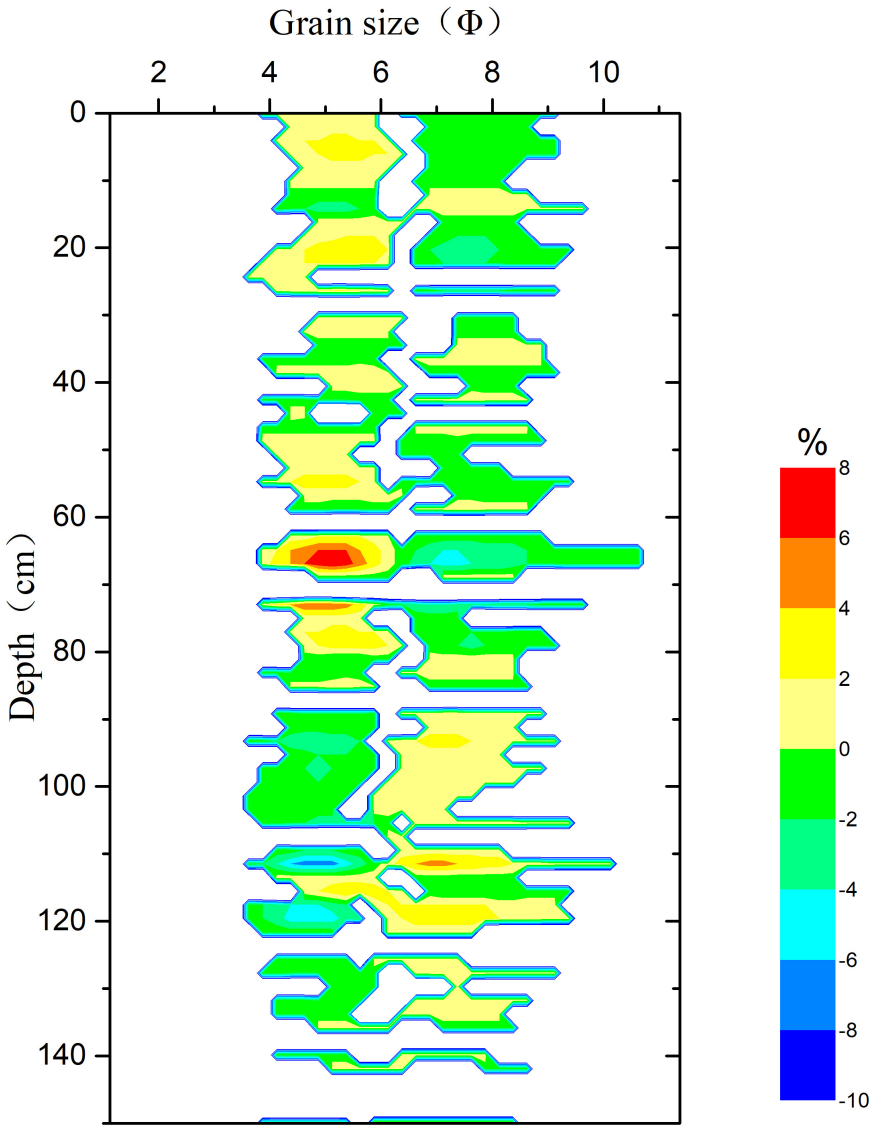

FIGURE 7 | Difference in grain size components between two cores at 1-cm-intervals. It was obtained by subtracting the content of the grain size components of Z8 from that of Z7. % is represented the content of special grain size components. So a positive value (+) meant the content of the grain size components of Z7 was more than that of Z8 in that layer, and a negative value (–) meant the content of the grain size components of Z7 was less than that of Z8. The results showed that there was a tendency for grains in Z7 to coarsen relative to those in Z8 from 1977 (the depth of 70 cm).

in the fluxes and sediment properties of the sea (Dai et al., 2008; Gao et al., 2014; Yang et al., 2019), have made good progress in quantifying these impacts. For example, Dai et al. (2008) argued that, for the Changjiang River, the contribution of climate change to the reduction of sediment flux into the sea was only approximately 3%, with anthropogenic contributions accounting for 97%.

Ship navigation is an important anthropogenic agent. During navigation, ships alter the local hydraulic regime, i.e., the generation of currents and ship-induced waves (Rapaglia et al., 2011; Fleit et al., 2016). The highest near-bed velocities resulting from ship generated waves range between 0.1 and 0.4 m/s in Danube River of Hungary, which was obtained by computational fluid dynamics (CFD) modeling (Fleit et al., 2016). The average flow velocity with no ship is 0.02 m/s, which means an increase of an order of magnitude due to ship (Fleit et al., 2016). *In situ* measurement shows that the water velocity increases to 2.1 m/s when the ship passes by, which is more than an order of magnitude higher than the typical tide and wind driven current speed in the channels of Venice (Coraci et al., 2007). The increased current speed can increase bottom shear stress, which will cause the resuspension of sediment in shallow water areas and the erosion of the channel slope and seabed (Rapaglia et al., 2011; Ji et al., 2014; Fleit et al., 2016). It is found that the ship-generated waves (including drawdown and surge waves) have much more effects on sediment resuspension than wind

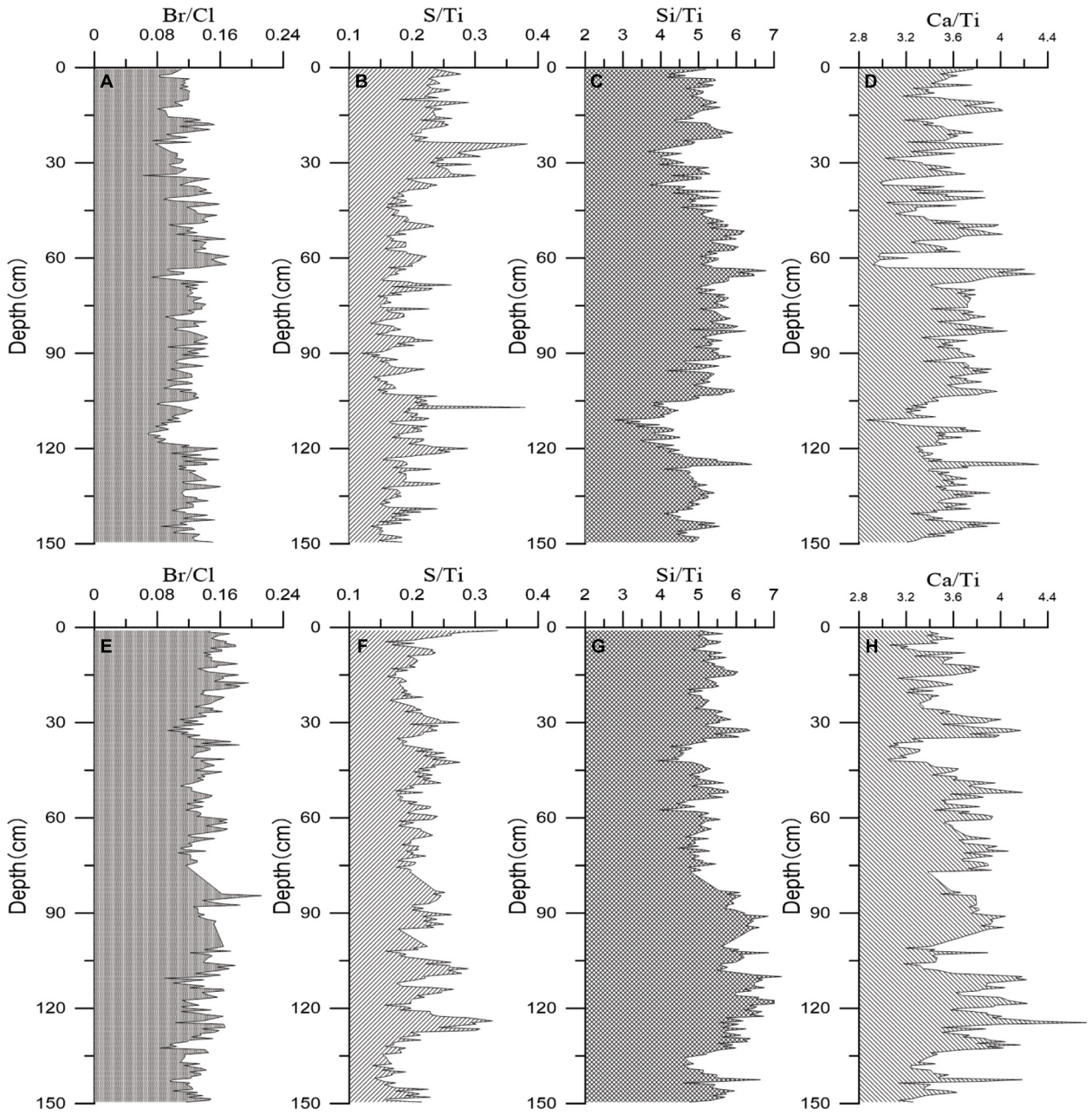

FIGURE 8 | Variation of the element ratios over time in core Z7 **(A–D)** and Z8 **(E–H)**. Element ratios of Z7 shifted significantly after 1999 (the depth of 40 cm), and element ratios of Z8 did not show a clear shift.

waves (Houser, 2014). Once the shear stress generated by the ship is larger than the critical shear stress which is further determined by sedimentary characteristics, the seabed sediment would move in suspension, saltation, and creep (Liou and Herbich, 1976; Liao et al., 2015). The bottom shear stress caused by propeller scour is an important mechanism contributing to sediment resuspension and subsequent erosion (Liao et al., 2015). In the same situation, the resuspension of coarser particles requires a greater incipient velocity (Liou and Herbich, 1976). Finer particles are easier to resuspend. Ship-generated waves are capable of resuspending significant quantities of bottom sediment and suspended sediment concentration increases with increment of turbulent kinetic energy of the ship wakes (Houser, 2014; Ji et al., 2014). *In situ* observation showed that suspended sediment concentration rose from 12 mg/L to 400 mg/L in Venice Lagoon, Italy, after the ship had sailed (Rapaglia et al., 2011). The intensity of sediment disturbance by a ship is related to the speed, propeller rotation speed, water depth, and draft of the ship (Liou and Herbich, 1976; Hong et al., 2013). Generally, the faster the speed of ships, the shallower the water depth, and the deeper the

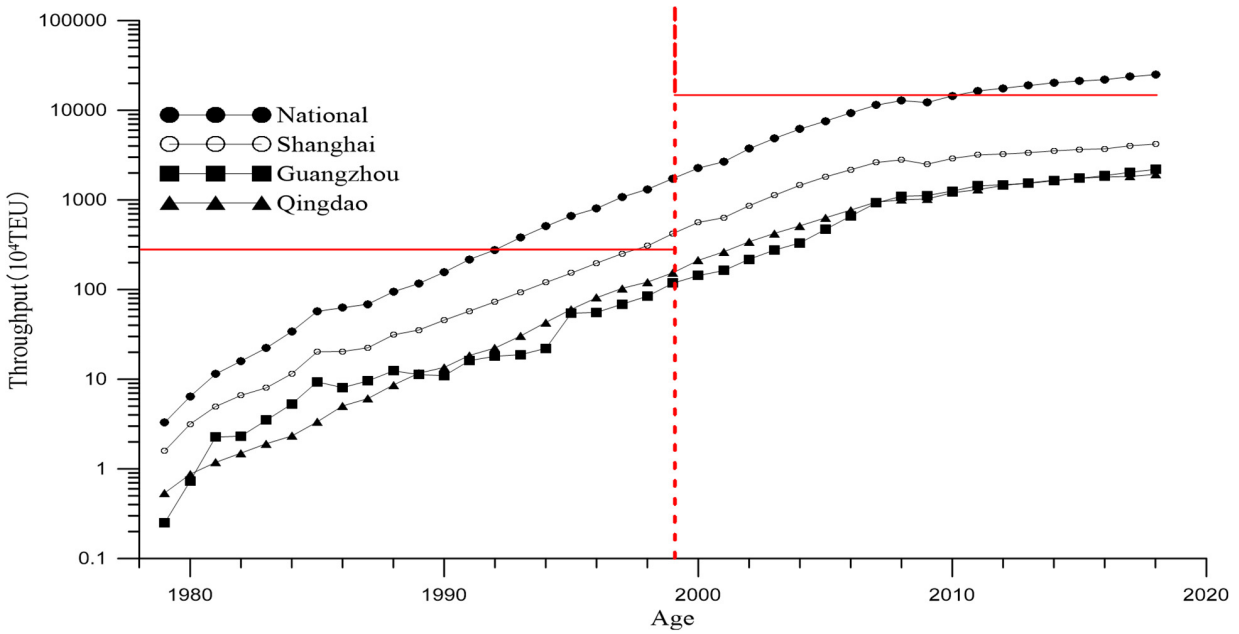

FIGURE 9 | Throughput evolution of Chinese containers, 1979–2018. The 21st century began with rapid growth, and in 2008 the volume of seaborne trade declined as a result of the global financial crisis. The vertical dashed red line indicates the year 1999 and the two horizontal red lines indicate the average annual container throughput for the periods 1979–1999 and 1999–2018, respectively. *Source:* China Ports Yearbook (1999–2019).

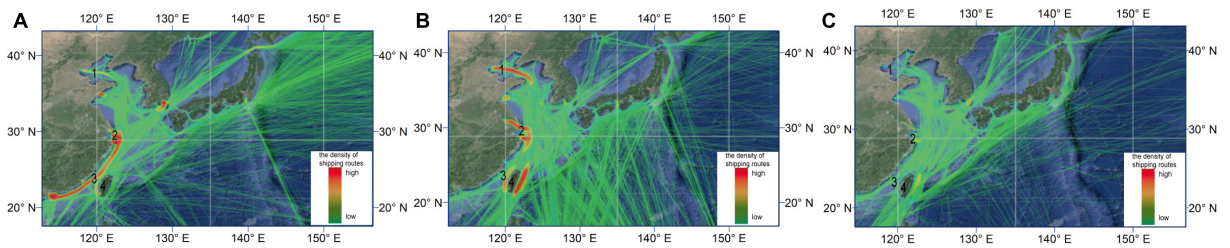

FIGURE 10 | Thermal map of megaship tracks around China based on more than 5,000 TEU of containers **(A)**, more than 100,000 tons of bulk cargo **(B)**, and more than 100,000 tons of tankers **(C)** 1, the Bohai Bay; 2, the Changjiang Estuary; 3, the Taiwan Strait; 4, the Taiwan Island (*Source: Shipping News, 2020* http://www.shipxy.com).

draft, the stronger the intensity of the disturbance. Sediment resuspension caused by ship disturbance has led to a series of changes in both the sedimentary environment and ecology.

In this study, when establishing the dating framework, it was found that in a relatively stable sediment environment (such as the location of core Z8), the dating results obtained by the CIC and CRS dating models were consistent. However, in an unstable sediment environment (such as the location of core Z7), the results of the two dating models differed greatly, and the age difference of the same layer could be up to 24 years. Because of the inherent shortcomings of the CRS model, the bottom age is biased toward aging, whereas the CIC model homogenizes the sedimentation rate, which is obviously not applicable in an unstable sediment environment. A single dating model cannot establish a convincing and comparable dating framework. The best approach is to combine the two models, using the CRS model in the layer affected by ships and the CIC model in the lower part, to establish a CRS–CIC dual dating model. **Figure 3** shows that the CRS–CIC dual dating model can be used with reliable results to address sedimentation rates in an overall sedimentary environment, but locally influenced by frequent ship motion.

Since the development of coastal shipping in China in 1977, the fluctuations of grain size has changed largely. Before 1977, the fluctuation of grain size of Z8 is wider than that of Z7, which shows an opposite trend after 1977. Core Z8 is located near a small bedrock island called "Pishan," which will cause more complicated hydrodynamics (tidal and wave) compared to core Z7 before 1977. In this case, the fluctuation of grain size at Z8 is wider than that of core Z7. However, the hydrodynamic condition is more complicated at core Z7 than that of core Z8 after 1977 due to the disturbance of ships, causing the fluctuation of grain size of Z7 is wider than that of Z8.

In addition, the sensitive grain size at Z7 has been finer (**Figure 5A**). With 6.25 Φ as the boundary, the grain fraction

TABLE 3 | Correlation matrix between grain size component and element ratio.

Correlation coefficient	Sand	Silt	Clay	Br/Cl	S/Ti	Si/Ti	Ca/Ti
Sand	1.00	0.29	−0.44	−0.08	0.18	0.08	0.02
Silt	0.29	1.00	−0.99	−0.15	−0.05	0.26	0.33
Clay	−0.44	−0.99	1.00	0.15	0.02	−0.25	−0.31
Br/Cl	−0.08	−0.15	0.15	1.00	−0.17	0.31	−0.26
S/Ti	0.18	−0.05	0.02	−0.17	1.00	−0.28	−0.25
Si/Ti	0.08	0.26	−0.25	0.31	−0.28	1.00	0.60
Ca/Ti	0.02	0.33	−0.31	−0.26	−0.25	0.60	1.00

finer than 6.25 Φ decreased (**Figure 7**). It was calculated that before 1977, core Z7 had a significantly higher fine grain fraction (>6.25 Φ) than core Z8, with a mean value of approximately 6%, but after 1977, core Z7 had a significantly lower fine grain fraction (>6.25 Φ), with a mean value of approximately 5%. This indicated an 11% reduction in the grain fraction finer than 6.25 Φ at the shipping lane and a significant coarsening of the sediment. Ship motion affected the local sedimentary dynamic environment. Although the total sedimentary flux was the same as the flux outside the shipping lane, it has a selective modifying effect on the sedimentary record: in the sediment on the shipping lane, which was dominated by silt, all grain fractions became more active under frequent ship disturbance. Due to differences in sedimentation mechanisms, it was relatively slow for fine grain to settle, and a significant proportion of the fine grain fraction may leave the shipping lane, causing a reduction in the fine grain fraction entering the seabed sediment. It has been shown that vessel-induced wakes can increase the concentration of suspended sediment by a factor of 30 above background values, but this surge only lasts for a few minutes, and then the high concentration persists for almost an hour before returning to background values (Rapaglia et al., 2011). The sustained high concentration is due to the slow settling velocity of fine particles.

Ship disturbance also caused ecological changes. After 1999, the value of Br/Cl in the Z7 core decreased from 0.12 to approximately 0.11, the value of S/Ti increased significantly from 0.20 to 0.24, the value of Si/Ti decreased from 5.01 to 4.87, and the value of Ca/Ti decreased from 3.54 to 3.48. The decrease in Br/Cl could indicate, to some extent, the decline of primary productivity in the region (Thomson et al., 2006). High S-levels tend to indicate a low oxygen zone (Croudace and Rothwell, 2015). Si/Ti is an important indicator of siliceous phytoplankton productivity. The principle of reduced Ca/Ti is the same as that of Si/Ti, both of which belong to the response of biogenic elements to the marine environment (Marsh et al., 2007; Agnihotri et al., 2008). Specific to the above individual indicator, small changes in value may not be evidence of significant changes in the ecological environment. However, the changes in the four indicators pointed to consistency, which may be related to the disturbance of ships in the waterway. For example, frequent disturbance by ships made the shipping lane waters turbid, and light became the most important factor limiting marine productivity. The turbidity and high concentration of suspended solids was not conducive to the growth and reproduction of phytoplankton, and this reduced primary productivity (Jiang, 1993; Pan et al., 2011). In addition, the amount of phytoplankton directly affected the dissolved oxygen content in seawater. The reduction of phytoplankton decreased the dissolved oxygen content in seawater, leading to the dissolution of iron oxides and the formation of pyrite (FeS_2), which increased the amount of elemental S in the sediment (Jiang, 1993; Croudace and Rothwell, 2015). Frequent

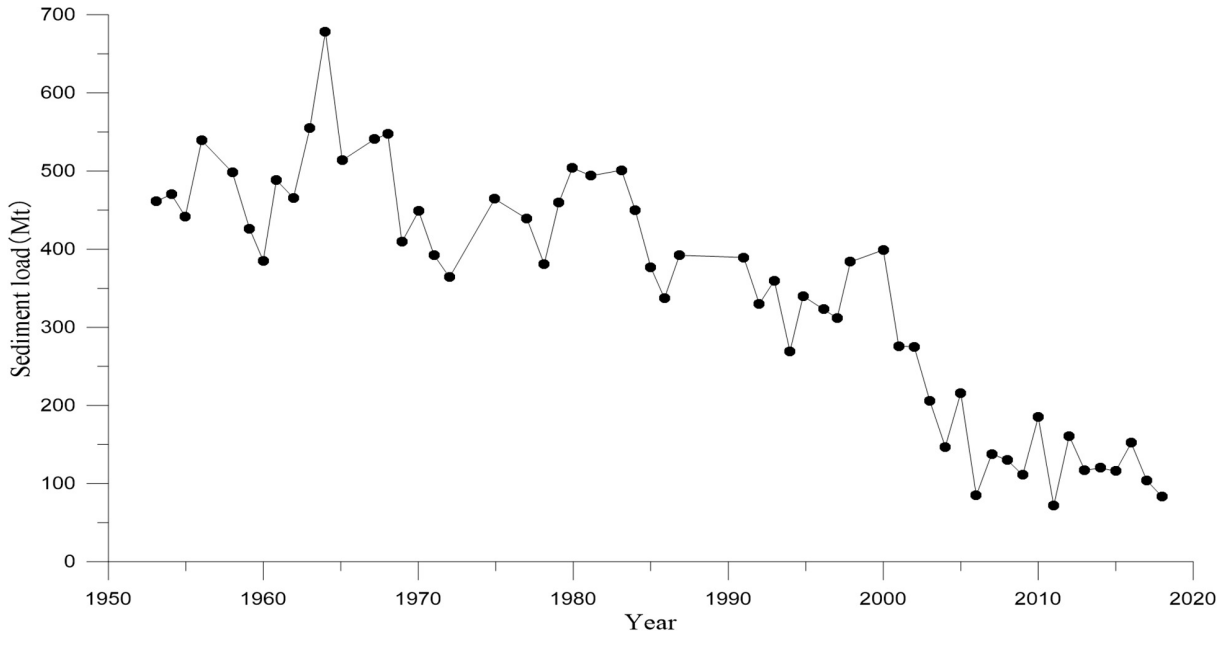

FIGURE 11 | Suspended sediment load changes over a 66-year period (1953–2018) at Datong Station.

disturbance was detrimental to diatom growth and reproduction, and decreased the biotransformation rate of silicates in seawater and the "silicon fixation" effect, thus decreasing the Si/Ti value in sediment (Huang et al., 1986; Pan and Shen, 2009). Calcareous phytoplankton such as coccolithophores are widely distributed and abundant in the ocean, are well preserved in the sediment and are important sources of biogenic Ca in the sediment (Poulton et al., 2007, 2013). Frequent disturbance was also detrimental to the growth of coccolithophores, and made it difficult for biogenic Ca to adhere to the particulate matter, which can reduce the Ca/Ti ratio in the sediment. Overall, the quality of habitat conditions along the shipping lane was significantly different from those outside the shipping lane. The content of each element in the sediment of the shipping lane was controlled by a combination of physical, chemical, and biological interactions. Suspension of fine particles caused by physical disturbance affected the marine ecosystem and ultimately changed the elements in the sediment.

Human activity has left a universal and lasting imprint on Earth. The debate continues over whether the Anthropocene deserves recognition as a new unit of geological time (Waters et al., 2016). The Anthropocene Working Group (AWG) has recommended the recognition of the beginning of the Anthropocene as the mid–late 20th century. However, some researchers questioned the time starting point, arguing that significant human-induced changes to the Earth's environment occurred long before the 20th century (Ruddiman, 2018). The Anthropocene is currently defined from a variety of perspectives, including paleontology, micropaleontology, stratigraphy, and archeology (Barnosky, 2013; Wilkinson et al., 2014; Zhuang and Kidder, 2014), as a time when humans have played an important role in changing the global environment at an unprecedented rate. The study of the Anthropocene can bring into focus the transformation of the natural environment by humans. By studying the development of the global shipping industry and its sedimentary–ecological effects since the 20th century, one can attempt to define the Anthropocene from the new perspective of ship navigation.

CONCLUSION

China's container shipping industry originated in 1979 and has been growing rapidly since 1999. By studying characteristics of shelf sediments from shipping lane, our study found that over the past few decades, with the development of China's maritime transport industry, significant changes in shelf mud deposition have occurred. Our conclusions are as follows:

(1) There were significant changes in the sediment grain size composition after ship disturbance, with the sedimentation response at the beginning of navigation. Ship disturbance selectively modified the sedimentary record. The fine-particle fraction of the sediment became more active and the particles finer than 6.25 Φ were significantly reduced (by approximately 11%) after being disturbed by the ship.

(2) Ship disturbance caused changes in the ecology of waterways, which was observed in biogenic elements. As the frequency of navigation increased, the elemental ratios of Br/Cl, Si/Ti, and Ca/Ti decreased from 0.12, 5.01, and 3.54 to 0.11, 4.87, and 3.48, respectively, but the S/Ti ratio increased from 0.20 to 0.24. The ecological response appeared later than the sedimentation response, when the growth of Chinese maritime transportation is significant. Element indicators revealed that the productivity of the shipping lane waters was reduced due to frequent ship disturbance.

(3) During their voyage, the ship disturbed the seabed sediment, thereby affecting the centennial-scale dating of the sediment record. In regions with frequent ship disturbance, we propose to use the CRS (with ship disturbance)–CIC (without ship disturbance) dual dating model approach to establish a more accurate chronological framework.

DATA AVAILABILITY STATEMENT

The original contributions presented in the study are included in the article/**Supplementary Material**, further inquiries can be directed to the corresponding author/s.

AUTHOR CONTRIBUTIONS

CX, JJ, and YY developed the idea and elaborated the concept. CX and JG designed and conducted the field survey. CX, PZ, and DW provided experimental data and organized and conducted the data analyses. PS and ZH collected some data on the shipping along China's coastal ship lanes. CX, JJ, and YY wrote the manuscript. All authors contributed to the revision of the manuscript.

FUNDING

This study was financially supported by the National Natural Science Foundation of China (Grant numbers: 41876092, 41706095, and 41776048).

ACKNOWLEDGMENTS

Sheng Xu, Zhaoxiang Yang, Yaping Mei, and Zhenqiao Liu are thanked for their assistance in the core acquisition and laboratory analyses. Li Tian is thanked for the guidance to the XRF experiment. Yifei Sun is thanked for providing information about the propeller.

SUPPLEMENTARY MATERIAL

The Supplementary Material for this article can be found online at: https://www.frontiersin.org/articles/10.3389/fmars.2021.678845/full#supplementary-material

REFERENCES

Agnihotri, R., Altabet, M. A., Herbert, T. D., and Tierney, J. E. (2008). Subdecadally resolved paleoceanography of the peru margin during the last two millennia. *Geochem. Geophys. Geosyst.* 9:Q05013.

Appleby, P. G. (2001). "Chronostratigraphic techniques in recent sediments," in *Tracking Environmental Change Using Lake Sediments: Basin Analysis, Coring, and Chronological Techniques*, Vol. volume 1, eds W. M. Last and J. P. Smol (Dordrecht: Kluwer Academic), 171–203. doi: 10.1007/0-306-47669-x_9

Barnosky, A. D. (2013). Palaeontological evidence for defining the Anthropocene. *Geol. Soc. Spec. Publ.* 395, 149–165. doi: 10.1144/sp395.6

Baronson, F. L. (2003). Validation of the accuracy of the LabSOCS software for mathematical efficiency calibration of Ge detectors for typical laboratory samples. *J. Radioanal. Nucl. Chem.* 255, 137–141.

Blott, S. J., and Pye, K. (2001). GRADISTAT: a grain size distribution and statistics package for the analysis of unconsolidated sediments. *Earth Surf. Process. Landf.* 26, 1237–1248. doi: 10.1002/esp.261

China Gulf Annals. (1993). *China Gulf Annals*, Vol. 6. North Melbourne: Ocean Press.

China Port Yearbook. (1999–2019). China Ports Year Book Editorial Department. Shanghai: China Port Magazine Press.

Coraci, E., Umgiesser, G., and Zonta, R. (2007). Hydrodynamic and sediment transport modeling in the channels of Venice (Italy). *Estuar. Coast. Shelf Sci.* 75, 250–260. doi: 10.1016/j.ecss.2007.02.028

Croudace, I. W., and Rothwell, R. G. (2015). *Micro-XRF Studies of Sediment Cores: Applications of a Non-Destructive Tool for the Environmental Sciences*. Dordrecht: Springer.

Crutzen, P. J., and Stoermer, E. F. (2000). The "Anthropocene". *Glob. Change Newslett.* 41, 17–18.

Dai, S. B., Lu, X. X., Yang, S. L., and Cai, A. M. (2008). A preliminary estimate of human and natural contributions to the decline in sediment flux from the Yangtze River to the East China Sea. *Quat. Int.* 186, 43–54. doi: 10.1016/j.quaint.2007.11.018

Day, J. W., Agboola, J. I, Chen, Z., Delia, C. F., Forbes, D. L., Giosan, L., et al. (2016). Approaches to defining deltaic sustainability in the 21st century. *Estuar. Coast. Shelf Sci.* 183, 275–291. doi: 10.1016/j.ecss.2016.06.018

De Vriend, H. J., Wang, Z. B., Ysebaert, T., Herman, P. M., and Ding, P. (2011). Eco-morphological problems in the Yangtze Estuary and the Western Scheldt. *Wetlands* 31, 1033–1042. doi: 10.1007/s13157-011-0239-7

Debret, M., Sebag, D., Crosta, X., Massei, N., Petit, J. R., Chapron, E., et al. (2009). Evidence from wavelet analysis for a mid-Holocene transition in global climate forcing. *Quat. Sci. Rev.* 28, 2675–2688. doi: 10.1016/j.quascirev.2009.06.005

Dong, A. G., Zhai, S. K., Zabel, M., and Yu, Z. H. (2009). The distribution of heavy metal contents in surface sediments of the Changjiang Estuary in China and surrounding coastal areas. *Acta Oceanol. Sin.* 31, 54–68.

Du, J., Wu, Y., Huang, D., and Zhang, J. (2010). Use of 7Be, 210Pb and 137Cs tracers to the transport of surface sediments of the Changjiang Estuary China. *J. Mar. Syst.* 82, 286–294. doi: 10.1016/j.jmarsys.2010.06.003

Duan, L. Q., Song, J. M., Xu, Y. Y., Li, X. G., and Zhang, Y. (2010). The distribution, enrichment and source of potential harmful elements in surface sediments of bohai bay, north china. *J. Hazard. Mater.* 183, 155–164. doi: 10.1016/j.jhazmat.2010.07.005

Ducruet, C., and Notteboom, T. (2012). The worldwide maritime network of container shipping: spatial structure and regional dynamics. *Glob. Netw.* 12, 395–423. doi: 10.1111/j.1471-0374.2011.00355.x

Ferré, B., Durrieu de Madron, X., Estournel, C., Ulses, C., and Corre, G. L. (2008). Impact of natural (waves and currents) and anthropogenic (trawl) resuspension on the export of particulate matter to the open ocean: application to the Gulf of Lion (NW Mediterranean). *Cont. Shelf Res.* 28, 2071–2091. doi: 10.1016/j.csr.2008.02.002

Fleit, G., Baranya, S., Rüther, R., Bihs, H., Krámer, T., and Józsa, J. (2016). Investigation of the effects of ship induced waves on the littoral zone with field measurements and cfd modeling. *Water* 8, 300–300. doi: 10.3390/w8070300

Gao, J. H., Jia, J. J., Kettner, A. J., Xing, F., Wang, Y. P., Xu, X. N., et al. (2014). Changes in water and sediment exchange between the Changjiang River and Poyang Lake under natural and anthropogenic conditions China. *Sci. Total Environ.* 481, 542–553. doi: 10.1016/j.scitotenv.2014.02.087

Gao, J. H., Jia, J. J., Wang, Y. P., Yang, Y., Zou, X. Q., Li, J., et al. (2015). Variations in quantity, composition and grain size of Changjiang sediment discharging into the sea in response to human activities. *Hydrol. Earth Syst. Sci.* 19, 645–655. doi: 10.5194/hess-19-645-2015

Gao, J. H., Shi, Y., Sheng, H., Kettner, A. J., Yang, Y., Jia, J. J., et al. (2019). Rapid response of the Changjiang (Yangtze) river and East China Sea source-to-sink conveying system to human induced catchment perturbations. *Mar. Geol.* 414, 1–17. doi: 10.1016/j.margeo.2019.05.003

Grygar, T. M., and Popelka, J. (2016). Revisiting geochemical methods of distinguishing natural concentrations and pollution by risk elements in fluvial sediments. *J. Geochem. Explor.* 170, 39–57.

He, Y. P. (2008). Navigation Diagram of Zhejiang Coastal and Main Ports. Zhejiang Maritime Safety Administration. Dalian: Dalian Maritime University Press. doi: 10.1016/j.gexplo.2016.08.003

Hong, J. H., Chiew, Y. M., and Cheng, N. S. (2013). Scour caused by a propeller jet. *J. Hydraul. Eng.* 139, 1003–1012. doi: 10.1061/(asce)hy.1943-7900.0000746

Hong, J. H., Chiew, Y. M., Hsieh, H. C., Cheng, N. S., and Yeh, P. H. (2016). Propeller jet–induced suspended-sediment concentration. *J. Hydraul. Eng.* 142:04015064. doi: 10.1061/(asce)hy.1943-7900.0001103

Houser, C. (2014). Sediment resuspension by vessel-generated waves along the Savannah River, Georgia. *J. Waterw. Port Coast. Ocean Eng.* 137, 246–257. doi: 10.1061/(asce)ww.1943-5460.0000088

Huang, S. G., Yang, J. D., Ji, W. D., Yang, X. L., and Chen, G. X. (1986). Spatial and temporal variation of reactive Si, N, P and their relationship in the Changjiang estuary water. *Tawan Strait* 5, 115–123. (In Chinese with English abstract).

Imai, A., Nishimura, E., and Papadimitriou, S. (2013). Marine container terminal configurations for efficient handling of mega-containerships. *Transport. Res. Part E Log. Transport. Rev.* 49, 141–158. doi: 10.1016/j.tre.2012.07.006

Jenny, J. P., Koirala, S., Gregory-Eaves, I., Francus, P., Niemann, C., Ahrens, B., et al. (2019). Human and climate global-scale imprint on sediment transfer during the Holocene. *Proc. Natl. Acad. Sci. U. S. A.* 116, 22972–22976. doi: 10.1073/pnas.1908179116

Ji, S. C., Ouahsine, A., Smaoui, H., Sergent, P., and Jing, G. Q. (2014). Impacts of ship movement on the sediment transport in shipping channel. *J. Hydrodyn.* 26, 706–714. doi: 10.1016/s1001-6058(14)60079-2

Jia, J., Gao, J., Cai, T., Li, Y., Yang, Y., Wang, Y. P., et al. (2018). Sediment accumulation and retention of the Changjiang (Yangtze River) subaqueous delta and its distal muds over the last century. *Mar. Geol.* 401, 2–16. doi: 10.1016/j.margeo.2018.04.005

Jiang, G. C. (1993). The preliminary study on the eutrophication and the red tide in the south coastal area of Zhejiang. *Donghai Mar. Sci.* 11, 55–61. (In Chinese with English abstract)

Liao, Q., Wang, B., and Wang, P. F. (2015). In situ measurement of sediment resuspension caused by propeller wash with an underwater particle image velocimetry and an acoustic doppler velocimeter. *Flow Meas. Instrum.* 41, 1–9. doi: 10.1016/j.flowmeasinst.2014.10.008

Liou, Y. C., and Herbich, J. B. (1976). *Sediment Movement Induced by Ships in Restricted Waterways*. COE Report No. 188. College Station, TX: Texas A & M University.

Liu, Y., Zhai, S. K., and Li, J. (2010). Depositional records in the mud areas of Changjiang estuary and off Min-Zhe coast and their influence factors. *Mar. Geol. Quat. Geol.* 2010, 1–10. (In Chinese with English abstract)

Luan, H. L., Ding, P., Wang, Z. B., Ge, J. Z., and Yang, S. L. (2016). Decadal morphological evolution of the Yangtze Estuary in response to river input changes and estuarine engineering projects. *Geomorphology* 265, 12–23. doi: 10.1016/j.geomorph.2016.04.022

Marcussen, H., Dalsgaard, A., and Holm, P. E. (2008). Content, distribution and fate of 33 elements in sediments of rivers receiving wastewater in Hanoi, Vietnam. *Environ. Pollut.* 155, 41–51. doi: 10.1016/j.envpol.2007.11.001

Marsh, R., Mills, R. A., Green, D. R., Salter, I., and Taylor, S. (2007). Controls on sediment geochemistry in the Crozet region. *Deep Sea Res. Part II Top. Stud. Oceanogr.* 54, 2260–2274. doi: 10.1016/j.dsr2.2007.06.004

McManus, J. (1988). "Grain size determination and interpretation," in *Techniques in Sedimentology*, ed. M. E. Tucker (Oxford: Blackwell), 63–85.

Milliman, J. D., and Farnsworth, K. L. (2011). *River Discharge to the Coastal Ocean: A Global Synthesis*. Cambridge: Cambridge Univ. Press.

Notteboom, T., Pallis, A., and Rodrigue, J. P. (2021). *Port Economics, Management and Policy*. New York, NY: Routledge.

Pan, B. Z., Wang, Z. Y., and He, X. B. (2011). Studies on assemblage characteristics of macrozoobenthos in the West River. *Acta Hydrobiol. Sin.* 035, 851–856. (In Chinese with English abstract).

Pan, S. J., and Shen, Z. L. (2009). Distribution and variation of silicate in the Changjiang estuary and its adjacent waters. *Stud. Mar. Sin.* 49, 10–18. (In Chinese with English abstract)

Poulton, A. J., Adey, T. R., Balch, W. M., and Holligan, P. M. (2007). Relating coccolithophore calcification rates to phytoplankton community dynamics: regional differences and implications for carbon export. *Deep Sea Res. Part II Top. Stud. Oceanogr.* 54, 538–557. doi: 10.1016/j.dsr2.2006.12.003

Poulton, A. J., Painter, S. C., Young, J. R., Bates, N. R., Bowler, B., Drapeau, D., et al. (2013). The 2008 *Emiliania huxleyi* bloom along the Patagonian shelf: ecology, biogeochemistry and cellular calcification. *Glob. Biogeochem. Cycles* 27, 1–11. doi: 10.3354/meps09445

Powell, M. A., Thieke, R. J., and Mehta, A. J. (2006). Morphodynamic relationships for ebb and flood delta volumes at florida's tidal entrances. *Ocean Dyn.* 56, 295–307. doi: 10.1007/s10236-006-0064-3

Rapaglia, J., Zaggia, L., Ricklefs, K., Gelinas, M., and Bokuniewicz, H. J. (2011). Characteristics of ships' depression waves and associated sediment resuspension in Venice Lagoon. Italy. *J. Mar. Syst.* 85, 45–56. doi: 10.1016/j.jmarsys.2010.11.005

Ren, M. E. (1989). Human impact on the coastal morphology and sedimentation of north China. *Sci. Geogr. Sin.* 9, 1–8. (In Chinese with English abstract). doi: 10.1016/s0070-4571(08)70138-9

Richter, T. O., Van der Gaast, S., Koster, B., Vaars, A., Gieles, R., de Stigter, H. C., et al. (2006). The Avaatech XRF core scanner: technical description and applications to NE Atlantic sediments. *Geol. Soc. Lond. Spec. Publ.* 267, 39–50. doi: 10.1144/gsl.sp.2006.267.01.03

Ruddiman, W. F. (2018). Three flaws in defining a formal 'Anthropocene. *Prog. Phys. Geogr.* 42, 451–461. doi: 10.1177/0309133318783142

Sardain, A., Sardain, E., and Leung, B. (2019). Global forecasts of shipping traffic and biological invasions to 2050. *Nat. Sustain.* 2, 274–282. doi: 10.1038/s41893-019-0245-y

Schubert, C. J., Villanueva, J., Calvert, S. E., Cowie, G. L., Rad, U. V., Schulz, H., et al. (1998). Stable phytoplankton community structure in the arabian sea over the past 200,000 years. *Nature* 394, 563–566.

Singh, P. (2009). Major, trace and REE geochemistry of the Ganga River sediments: influence of provenance and sedimentary processes. *Chem. Geol.* 266, 242–255. doi: 10.1016/j.chemgeo.2009.06.013

Soon, C., and Lam, W. H. (2014). Ship's propeller jet-induced scour in westports Malaysia. *Paper Presented at the 24th International Society of Offshore and Polar Engineers*, Busan.

Sun, Y. B., Gao, S., and Li, J. (2003). Preliminary analysis of grain-size populations with environmentally sensitive terrigenous components in marginal sea setting. *Chin. Sci. Bull.* 48, 83–86. (In Chinese)

Syvitski, J. P., and Kettner, A. J. (2011). Sediment flux and the Anthropocene. *Philos. Trans. R. Soc. A* 369, 957–975. doi: 10.1098/rsta.2010.0329

Syvitski, J. P. M., Vorosmarty, C. J., Kettner, A. J., and Green, P. (2005). Impact of humans on the flux of terrestrial sediment to the global coastal ocean. *Science* 308, 376–380. doi: 10.1126/science.1109454

Thomson, J., Croudace, I. W., and Rothwell, R. G. (2006). "A geochemical application of the ITRAX scanner to a sediment core containing eastern Mediterranean sapropel units," in *New Techniques in Sediment Core Analysis*, Vol. 267, ed. R. G. Rothwell (London: Geological Society Special Publication), 65–77. doi: 10.1144/ GSL.SP.2006.267.01.05

Waters, C. N., Zalasiewicz, J., Summerhayes, C., Barnosky, A. D., Poirier, C., Galuszka, A., et al. (2016). The Anthropocene is functionally and stratigraphically distinct from the Holocene. *Science* 351:2622.

Wilkinson, I. P., Poirier, C., Head, M. J., Sayer, C. D., and Tibby, J. (2014). Microbiotic signatures of the Anthropocene in marginal marine and freshwater palaeoenvironments. *Geol. Soc. Lond. Spec. Publ.* 395, 185–219. doi: 10.1144/sp395.14

Yang, Y., Jia, J., Zhou, L., Gao, W., Shi, B., Li, Z., et al. (2019). Human-induced changes in sediment properties and amplified endmember differences: possible geological time markers in the future. *Sci. Total Environ.* 661, 63–74. doi: 10.1016/j.scitotenv.2019.01.115

Ye, D. Z., Ji, J. Y., Yan, Z. W., Wang, Y., and Yan, X. D. (2009). Anthroposphere—an interactive component in the earth system. *Chin. J. Atmos. Sci.* 33, 409–415. (In Chinese with English abstract).

Ye, S., Laws, E. A., and Gambrell, R. (2013). Trace element remobilization following the resuspension of sediments under controlled redox conditions: City Park Lake, Baton Rouge, LA. *Appl. Geochem.* 28, 91–99. doi: 10.1016/j.apgeochem.2012.09.008

Zhang, J., Mou, D. H., Du, J. Z., and Zhang, J. (2008). Study on comparison of excess 210Pb chronology of several models. *Mar. Environ. Sci.* 27, 370–374. (In Chinese with English abstract).

Zhao, Y. Y., and Yan, M. C. (1994). *Sediment Geochemistry in China's Shallow Seas*. Beijing: Science Press.

Zhou, L., Yang, Y., Wang, Z., Jia, J., Mao, L., Li, Z., et al. (2019). Investigating ENSO and WPWP modulated typhoon variability in the South China Sea during the mid–late Holocene using sedimentological evidence from southeastern Hainan Island China. *Mar. Geol.* 2019:105987. doi: 10.1016/j.margeo.2019.105987

Zhuang, Y. J., and Kidder, T. R. (2014). Archaeology of the anthropocene in the yellow river region, china, 8000–2000 cal. bp. *Holocene* 24, 1602–1623. doi: 10.1177/0959683614544058

Conflict of Interest: The authors declare that the research was conducted in the absence of any commercial or financial relationships that could be construed as a potential conflict of interest.

Publisher's Note: All claims expressed in this article are solely those of the authors and do not necessarily represent those of their affiliated organizations, or those of the publisher, the editors and the reviewers. Any product that may be evaluated in this article, or claim that may be made by its manufacturer, is not guaranteed or endorsed by the publisher.

Copyright © 2021 Xue, Yang, Zhao, Wei, Gao, Sun, Huang and Jia. This is an open-access article distributed under the terms of the Creative Commons Attribution License (CC BY). The use, distribution or reproduction in other forums is permitted, provided the original author(s) and the copyright owner(s) are credited and that the original publication in this journal is cited, in accordance with accepted academic practice. No use, distribution or reproduction is permitted which does not comply with these terms.

frontiers in Marine Science

ORIGINAL RESEARCH
published: 08 September 2021
doi: 10.3389/fmars.2021.721500

Surface-Layer Circulations in Suruga Bay Induced by Intrusions of Kuroshio Branch Water

Takahiro Toyoda[1], Kei Sakamoto[1], Norihisa Usui[1], Nariaki Hirose[1], Kiyoshi Tanaka[2], Takaaki Katsumata[3,4], Daisuke Takahashi[5], Masato Niki[5], Kunio Kutsuwada[5], Toru Miyama[6], Hideyuki Nakano[1], L. Shogo Urakawa[1], Kensuke K. Komatsu[1], Yuma Kawakami[1] and Goro Yamanaka[1]*

[1] Department of Atmosphere, Ocean, and Earth System Modeling Research, Meteorological Research Institute, Japan Meteorological Agency, Tsukuba, Japan, [2] International Coastal Research Center, Atmosphere and Ocean Research Institute, The University of Tokyo, Otsuchi, Japan, [3] Liberal Arts Education Center Shimizu Campus, Tokai University, Shizuoka, Japan, [4] National Institute of Technology, Numazu College, Numazu, Japan, [5] School of Marine Science and Technology, Tokai University, Shizuoka, Japan, [6] Application Laboratory, Japan Agency for Marine-Earth Science and Technology, Yokohama, Japan

OPEN ACCESS

Edited by:
Magdalena Andres,
Woods Hole Oceanographic Institution, United States

Reviewed by:
Dujuan Kang,
Rutgers, The State University of New Jersey, United States
Zhaoqing Yang,
Pacific Northwest National Laboratory (DOE), United States

***Correspondence:**
Takahiro Toyoda
ttoyoda@mri-jma.go.jp
orcid.org/0000-0001-7926-5754

Specialty section:
This article was submitted to Coastal Ocean Processes, a section of the journal Frontiers in Marine Science

Received: 07 June 2021
Accepted: 11 August 2021
Published: 08 September 2021

Citation:
Toyoda T, Sakamoto K, Usui N, Hirose N, Tanaka K, Katsumata T, Takahashi D, Niki M, Kutsuwada K, Miyama T, Nakano H, Urakawa LS, Komatsu KK, Kawakami Y and Yamanaka G (2021) Surface-Layer Circulations in Suruga Bay Induced by Intrusions of Kuroshio Branch Water. Front. Mar. Sci. 8:721500. doi: 10.3389/fmars.2021.721500

The water mass structure in Suruga Bay is strongly influenced by open-ocean water. In particular, it is suggested that intermittent intrusions of the Kuroshio water generate characteristic circulations in the surface layer of the bay. In this study, we investigated the processes of the intrusions of open-ocean water into the bay and related generation of bay-scale cyclonic and anti-cyclonic circulation patterns. In doing so, we used an ocean simulation product with observational data constraint on meso and larger scales and with a resolution fine enough to resolve the smaller-scale intrusion structure. Cyclonic and anti-cyclonic circulation patterns as suggested by previous observational studies were detected as positive and negative first leading empirical orthogonal function (EOF) modes of the velocity field in Suruga Bay. The time scale of occurrences of these patterns was estimated as about 1 month, which was consistent with short-term Kuroshio fluctuations as reported in previous studies. Conditions favorable for generating these patterns were analyzed for three typical Kuroshio path periods individually. As suggested by previous studies, relatively strong northward flow to the west of Zeni-su generally promoted the open-ocean water intrusions into the eastern bay mouth, leading the cyclonic circulation in Suruga Bay. Our results showed that the correlation of this relation was significant for each Kuroshio path period. The open-ocean water intrusion increased the surface-layer temperature in Suruga Bay by about 0.7°C on average. On the other hand, the anti-cyclonic circulation pattern in Suruga Bay tended to be generated with relatively weak northward flow to the west of Zeni-su during the large meander Kuroshio path period, whereas this relation was rather weak during other periods. These results were mostly supported by available observations and would be useful for integrating our understanding of the influences of the western boundary current fluctuations on the circulation and temperature variations in proximal bays.

Keywords: Suruga Bay, Kuroshio, OGCM, data assimilation, coastal circulation, western boundary current

INTRODUCTION

Suruga Bay, located on the south side of the main island of Japan, is characterized by a widely open bay mouth (about 56 km width) and a deep bottom canal, the Suruga Trough (reaching >1,000 m depth near the bay head), leading from the Nankai Trough (**Figure 1**). Variability in the circulation and water mass distribution in Suruga Bay is important for communities in the region (e.g., fishery) and has been investigated. Freshwater discharge mainly from the Fuji, Kano, Abe, and Oi Rivers influences the surface layer in particular near the western coast, where salinity is about 33.0–34.0 (e.g., Nakamura, 1972). The spreading of this low-salinity water varies with the discharge amount (seasonal maximum in summer) and surface wind stress pattern (e.g., Tanaka et al., 2009, 2010; Niki et al., 2011). Beneath the low-salinity water near the surface, warm and salty water originating in the Kuroshio occupies the main thermocline layer (e.g., Iwata et al., 2005). Under the Kuroshio water, there is a salinity minimum layer (<34.3) centered at 400–500 m depth, which originates in the North Pacific Intermediate Water, while the North Pacific Deep Water occupies the deeper layer below approximately 1,000 m (Nakamura, 1982).

The processes by which the Kuroshio water intrudes into the bay are rather complicated. Kimura (1950) showed the existence of a cyclonic circulation over Suruga Bay by means of drifting bottles, which was also implied from bay-wide hydrographic observations (Sato, 1967). Later, an accumulation of hydrographic data enabled the circulation variability to be estimated, with a predominant cyclonic circulation (76%) and an anticyclonic circulation (18%) appearing sporadically (Nakamura and Muranaka, 1979). In addition to hydrographic surveys, current measurements have also been conducted (e.g., Inaba, 1982, 1984; Katsumata, 2004, 2016). Besides the predominant semi-diurnal and diurnal tidal currents (e.g., Inaba, 1981; Takeuchi and Hibiya, 1997), both northward and southward surface-layer currents were observed on a longer time scale (more than a day) at stations on the western and eastern sides of the bay mouth. These observations further indicated that the northward (southward) current in the eastern bay mouth and the southward (northward) current in the western bay mouth tend to appear simultaneously when the location of the Kuroshio axis fluctuates to the north (south) (Inaba, 1984). Based on these observations, a schematic picture was drawn for the surface-layer current in the southern part of Suruga Bay that cyclonic and anti-cyclonic circulations appear intermittently, affected by Kuroshio water intrusions (Inaba et al., 2001). These variations can extend vertically downward to at least 200–300 m depth (Inaba et al., 2001; Katsumata, 2016).

Awaji et al. (1991) found that, besides a long-term variation associated with transitions of the Kuroshio path south of Japan (Kawabe, 1986), notable short-term variations in the Kuroshio axis with a period of about 1 month and an amplitude exceeding a few tens of kilometers occur regardless of the Kuroshio path. In addition, their numerical experiments revealed that, in the shelf and coastal region south of Japan, the formation and disappearance of eddies repeatedly take place in response to the short-term transitions in the Kuroshio axis, leading to drastic changes in the coastal currents and water exchange between the coastal region and the Kuroshio. A time scale of 30 days for the Kuroshio fluctuations was also indicated by using HF radar observations to the south of Sagami Bay (Ramp et al., 2008). Miyama and Miyazawa (2014), by using a high-resolution ocean model, detected predominant frontal-wave fluctuations on a time scale of 18–36 days along the Kuroshio and zonally from Shiono-misaki to the Izu Ridge. They further indicated that the amplitude of the fluctuations is relatively large when the Kuroshio takes a nearshore path. In Suruga Bay, typical time scales for the surface-layer current variations were estimated from spectrum analyses of the above-described current observations as 37 and 18 days by Inaba et al. (2001) and as 20–25 days by Katsumata (2016). Katsumata (2016) also estimated the period of the Kuroshio axis fluctuations, which generated the warm-water intrusion events to Suruga Bay, as 25.6 days by using high-frequency tide-gauge data. These previous studies suggested that the Kuroshio fluctuations on a time scale of about 1 month play an important role in generating the coastal current variations in and around Suruga Bay.

Recently, Sugimoto et al. (2020) showed that, when the Kuroshio takes a large meander (LM) path (**Figure 2A**), marked coastal warming from the surface down to as much as 300 m appears off the Tokai distinct despite the existence of a cool water pool within the large meandering between the Kuroshio and the southern coast of Japan. They clarified that the coastal warming is attributed to the westward Kuroshio bifurcation at around 138°E, 34°N. Note that Suruga Bay was included in this warming region of their analysis. Thus, the long-term Kuroshio path variations also affect the coastal region around Suruga Bay. Katsumata (2016) discussed that the Kuroshio path being close to Suruga Bay (within 120 km) is a necessary condition for the short-term Kuroshio fluctuations to affect the bay. However, the above-described current observations in Suruga Bay investigated the Kuroshio water intrusions during the periods 1977–1980 (Inaba, 1984) and 1990 (Katsumata, 2016), when the Kuroshio took the LM path; during the period 1997–1999, which was investigated by Inaba et al. (2001), the Kuroshio took a relatively small but obvious meander path (offshore non-LM (oNLM) path; e.g., Kawabe, 2005). Thus, the varying influence of the Kuroshio water depending on the Kuroshio path types has not been clarified sufficiently. In addition, the time evolution of the generation of circulation patterns should be further examined.

In this study, we investigated the spatial structure and driving process of the surface-layer circulation variability associated with the Kuroshio water intrusions, which have not been fully clarified because of the limitations of observational data. For this purpose, we used a high-resolution ocean data-assimilative simulation product (Hirose et al., 2019). This product was derived by using a sophisticated system, with an explicit representation of the main tidal constituents and a four-dimensional variational data assimilation technique, for example. Taking into consideration the difference between the typical horizontal scale of the Kuroshio meandering and the bifurcation flow (a few hundreds of km) and the width of Suruga Bay (about 50 km), frontal waves (Miyama and Miyazawa, 2014) around the large-scale Kuroshio structures would be the direct contributors to the inflow to the

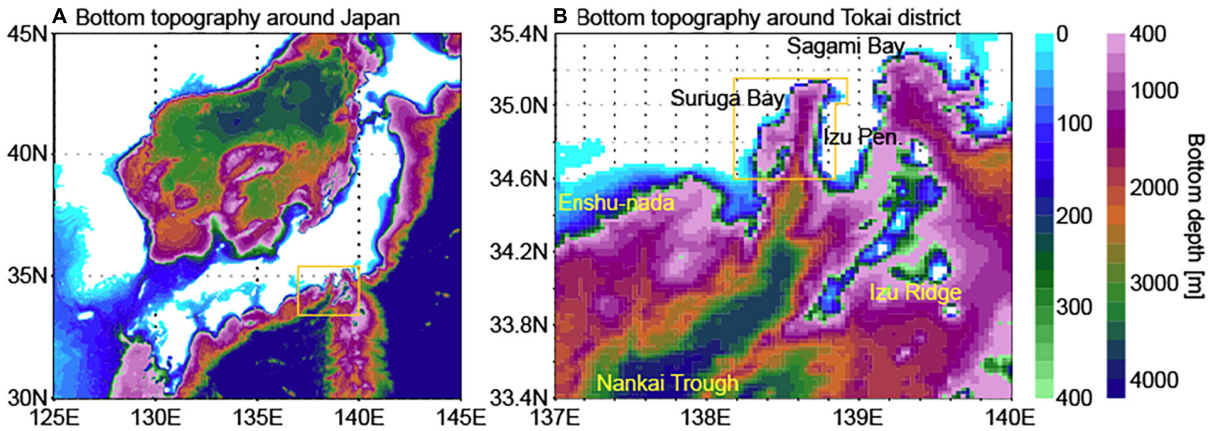

FIGURE 1 | Bottom topography of the ocean reanalysis product around Japan **(A)** and around the Tokai district **(B)**. Yellow line in **(A)** indicates the boundary of **(B)**. Yellow line in **(B)** indicates Suruga Bay as defined in this study.

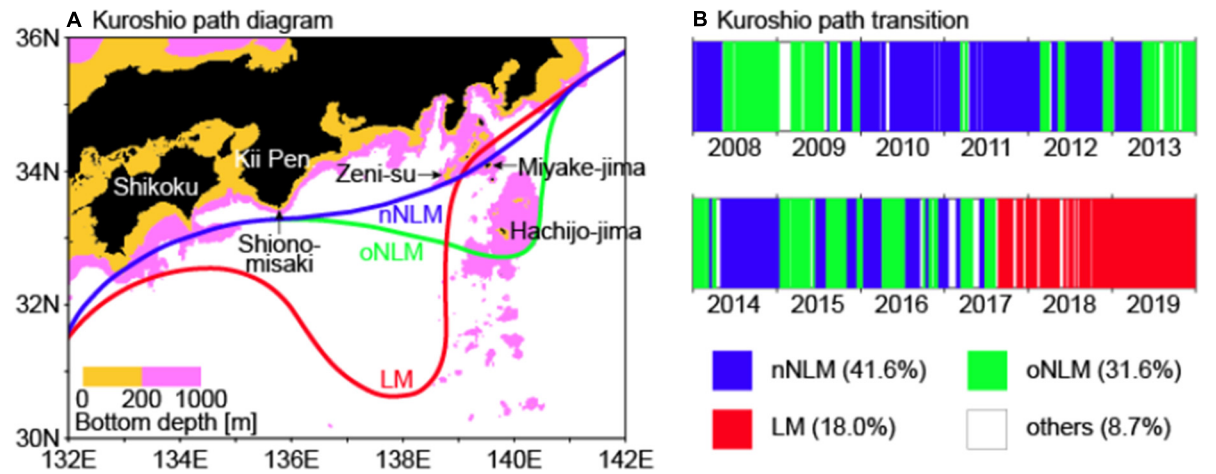

FIGURE 2 | (A) Three typical paths of the Kuroshio: nearshore non-large meander (nNLM), offshore non-large meander (oNLM), and large meander (LM). These path lines were traced from Kawabe (1995). **(B)** Transition of the Kuroshio path during the period 2008–2019 as defined by using the simulation product.

bay. Hence, processes on a scale that is smaller than meso-scale eddies (e.g., 15 km for the width of the intrusions; Katsumata, 2004) would be necessary to represent the intrusion events. A nesting approach adopted in the simulation system enabled the product to represent the Kuroshio and coastal regions around Japan with a horizontal resolution of about 2 km. Thus, a detailed analysis including the variability within the bay is possible under a realistic reproduction of the larger-scale background conditions (e.g., locations of the Kuroshio axis and meso-scale eddies) by data assimilation. Relationship between the flow to the south of Suruga Bay and the generation of circulation patterns in the bay (as depicted from limited observations in previous studies) is quantitatively investigated for individual three typical Kuroshio path periods which are covered by the simulation product (2008–2019). By using this product, we examined the dynamic structure of the surface circulation of Suruga Bay. The results were validated by available observations. These analyses of the processes for generating surface-layer circulation variability provide useful information for understanding the regional climate and ecosystem in Suruga Bay.

The simulation product and other data used for validating its reproduction are described in section "Materials and Methods." The variability in the surface-layer circulation in Suruga Bay is investigated by using the simulation product and the processes that generate the circulation patterns are discussed in section "Results." A summary and further discussion are provided in section "Summary and Discussion."

MATERIALS AND METHODS

We use an ocean data-assimilative simulation product for the period 2008–2019 derived from the MOVE/MRI.COM-JPN system (Hirose et al., 2019). This system was based on an ocean general circulation model developed by the Meteorological Research Institute (MRI), MRI.COM version

4 (Tsujino et al., 2017). The surface boundary conditions were given by the 3-hourly JRA55-do dataset (Tsujino et al., 2018). Three domains (global, North Pacific, and around Japan) were connected through a nesting technique; the innermost domain around Japan (117–160°E, 20–52°N) has a resolution of 1/33° zonally and 1/50° meridionally (about 2 km). Various satellite and *in situ* observations were assimilated in the outer two domains and the assimilation increments obtained there were also used in the inner domain (around Japan) to constrain the meso-scale variations. Note that sea surface temperature (SST) data were not assimilated in several coastal areas including Suruga Bay based on the data resolution of 1/4° (MGDSST; Kurihara et al., 2006). Details of this sophisticated system were described by Hirose et al. (2019). See also Usui et al. (2017) for details of the data assimilation method and the assimilated data.

Validation of the simulation product (for their study period 2008–2017) was provided by Hirose et al. (2019). In addition to the constraint to observation data of large-scale SST and sea surface height (SSH) fields, power spectra of *in situ* SSTs (buoy observations) at station Mera and Uchiura (in southeastern and northeastern Suruga Bay) were realistically reproduced by the simulation product, in contrast to the MGDSST particularly in the high-frequency domain (shorter period than a few month); comparison of SSHs with tide-gauge data showed correlation coefficients (capture ratios) of 0.91–0.93 (0.83–0.88) at 6 stations around Suruga Bay, 0.95 (0.90) and 0.98 (0.96) at Miyake-jima and Hachijo-jima, respectively.

In this study, daily climatologies were calculated on each grid by averaging over the product period 2008–2019 and were used to remove the mean seasonal variation. In addition, the types of Kuroshio path were defined by using daily horizontal velocities at 100 m depth of the simulation product. Conditions for the LM path were set as follows (e.g., Miyama et al., 2018): (1) the Kuroshio axis (horizontal velocity maximum at 135.5–136°E) separates from Shiono-misaki (south of 33°N); (2) the southernmost location of the Kuroshio axis (averaged over 0.5° bins between 136 and 138°E) is situated south of 32°N; and (3) the Kuroshio axis is located north of Hachijo-jima (north of 33.1°N at 139.5–140°E) or west of Hachijo-jima (west of 139.8°E at 32.7–33.2°N). When conditions (1) or (2) were not satisfied, the path type was classified as NLM paths: the nearshore NLM (nNLM) path satisfies condition (3) and the offshore NLM (oNLM) path does not. The remaining paths were classified as "others," which represents the transitioning paths between the above typical paths. In addition, when a path type did not appear stably (no longer than 10 days), it was also classified as "others." The durations of these paths (**Figure 2B**) were mostly consistent with previous studies (e.g., Sugimoto et al., 2020).

A gridded SSH and surface velocity product with 0.25° resolution (Mertz et al., 2018) was provided by the Copernicus Marine and Environment Monitoring Service (CMEMS). SST estimates with 2 km resolution based on measurements from the Himawari-8 geostationary satellite (Kurihara et al., 2016) were provided by the Japan Aerospace Exploration Agency. Sea level observations at tide gauge stations around Japan were provided by the Japan Oceanographic Data Center. We use time series of the observation data at tide-gauge stations, Tago and Yaizu. The data at these stations were collected by the Geospatial Information Authority of Japan.

Current data based on acoustic Doppler current profiler (ADCP; Teledyne RD Instruments Workhorse Sentinel 300 kHz) observations from the sightseeing ferry *Fuji*, round-tripping between Shimizu Harbor and Toi Harbor four times a day (Niki et al., 2014), were used. The original data include predominant diurnal and semi-diurnal tidal current variations (e.g., Inaba, 1981), which are not targets of this study. In order to eliminate tidal components from these snapshot data (during the daytime operations only), we carried out the following process. (1) The ADCP data were sorted onto the model grid bins horizontally. Vertically, grids with intervals of 4 m were set as the ADCP observations. Hourly averages were calculated on each grid. (2) Hourly climatology time series were calculated for these gridded hourly data by averaging interannually (2008–2018; overlapped period between the ferry data and the simulation product), which include from seasonal to intra-daily variabilities. (Climatology was not defined for hours when the ferry did not operate, such as at night). (3) Hourly anomaly time series were calculated from these differences. (4) Daily mean anomaly time series were derived from available hourly anomaly data.

RESULTS

EOF Mode Decomposition

First, we examined the horizontal velocity field at a surface-layer depth in the simulation product. We used values at the sixth level grid whose vertical spacing, 18–26 m, includes 20 m depth as investigated from direct measurements by using current meters in previous studies (e.g., Inaba, 1984; Inaba et al., 2001; Katsumata, 2016). In this study, Suruga Bay was defined as the region to the north of the 34.6°N zonal line (within the region bounded by the yellow line in **Figure 1B**; e.g., Tanaka et al., 2008).

As a long-term mean for the simulation product field (2008–2019), an anti-cyclonic circulation over the central and southern parts of Suruga Bay was obtained (**Figure 3A**). Maximum speed, smaller than 10 cm s^{-1}, was seen near the eastern bay mouth. For the variational components of zonal and meridional velocities, we performed a combined empirical orthogonal function (EOF) analysis. The daily mean time series of the horizontal velocities (zonal and meridional components) at 20 m depth in Suruga Bay during our study period of 2008–2019 were decomposed into the EOF modes. Note that mean seasonal cycle was not removed for this analysis, the validity of which is discussed later in association with comparison of monthly occurrences of the EOF modes (**Figure 4C**). Obtained first to third leading EOF modes (hereafter, EOF1, EOF2, and EOF3, respectively) explained 41, 16, and 9% of the total variance. Higher modes exhibited variations on much smaller scales and explained less than 5% of the total variance (not discussed in this study). The EOF1 pattern showed a circulation similar to the previous schematic picture (Inaba, 1988; Inaba et al., 2001), e.g., when the EOF1 time coefficient is positive, northward inflow in the eastern side of the bay mouth and southward outflow in the western side are connected by a half-round cyclonic circulation in the central–southern part of

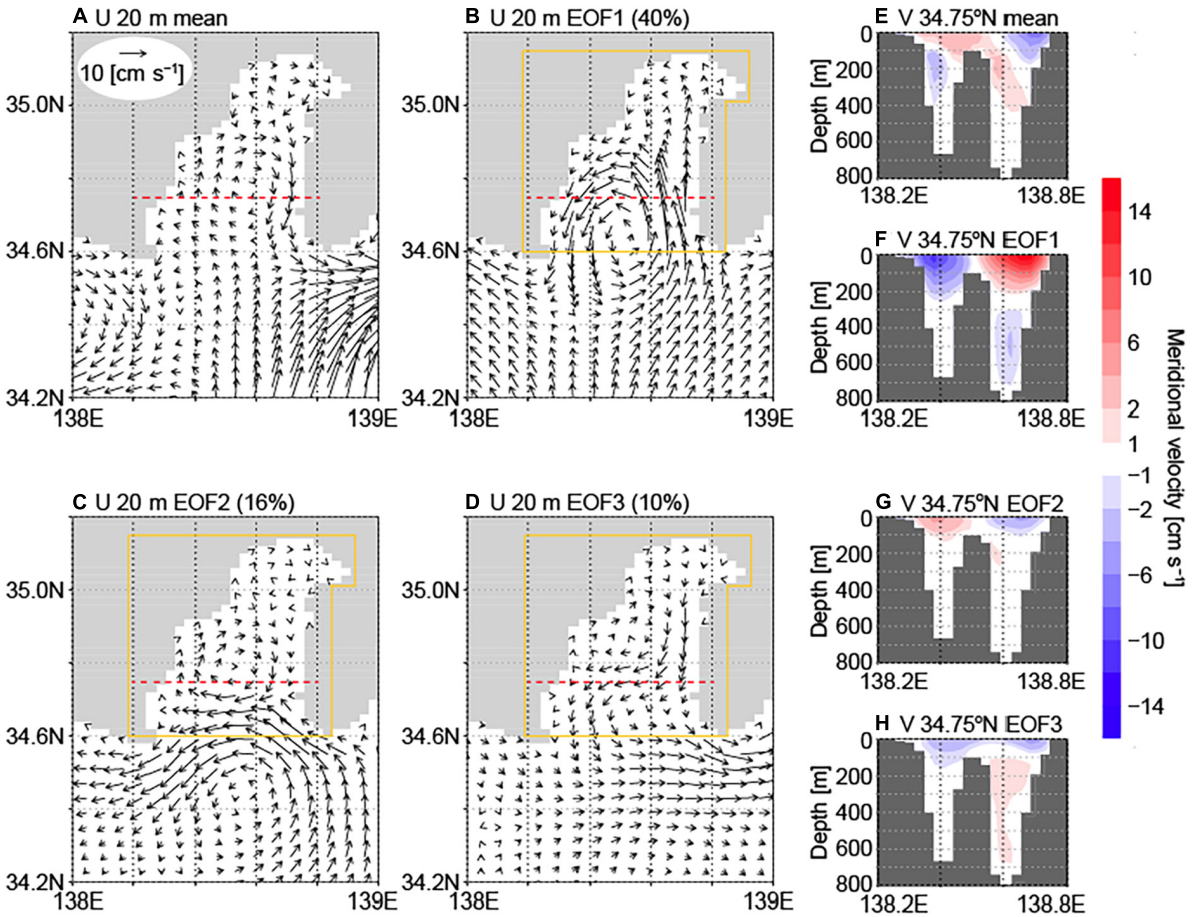

FIGURE 3 | (A–D) Distributions of horizontal velocities at 20 m depth. **(E–H)** Distributions of the meridional velocities on the vertical cross section along the 34.75°N line as indicated by red dashed lines in **(A–D)**. **(A,E)** Long-term mean field averaged over the product period 2008–2019. **(B,F)** EOF1. **(C,G)** EOF2. **(D,H)** EOF3. EOF analysis was conducted for the 20 m velocities in Suruga Bay (inside yellow lines) and projections to the EOF time series were plotted in the other region for **(B–D,F–H)**.

the bay (**Figure 3B**). Note that circulation patterns in the bay head region as drawn in the previous schematic picture were not captured in our analysis. The distribution of the meridional velocities on a vertical cross section in the middle of the cyclonic circulation (along the 34.75°N line; red dashed line in **Figure 3B**) indicated that the circulation pattern at 20 m depth extends to 200–300 m depth (**Figure 3F**). Here, projections to the EOF time series were plotted for the values outside Suruga Bay and other than at 20 m depth. The EOF2 pattern showed a rather closed circulation in the central part and inflow and outflow at the bay mouth connected in the southernmost part of the bay (**Figure 3C**). The positive (negative) EOF3 pattern showed basically southward (northward) surface-layer flow in the bay (**Figure 3D**). Magnitudes of these velocity variations for EOF2 and EOF3 were smaller than that for EOF1 (**Figures 3G,H**).

A spectrum analysis of the time series of the EOF time coefficients (**Figure 4A**) indicated that the EOF1 mode (red line) takes a peak power spectrum density on a time scale of about 25–40 days [frequencies of 0.04 to 0.025 $(\text{day})^{-1}$]; the EOF2 mode takes power spectrum density peaks of around 100 days and 1 year (blue line) and the EOF3 mode takes a peak of around 1 year (green line). Actually, repeated variations on a time scale of about 1 month can be seen in the EOF1 time series for 2017, for example (**Figure 4B**; see **Supplementary Figure 1** for the whole product period 2008–2019). In addition, we counted the number of days when the time coefficient takes a large value (**Figures 4C,D**; thresholds of 0.5 and 1 (light and thick color bars, respectively) were used for these figures, but the conclusions are not changed by summing the positive/negative EOF values). Mean monthly values for this number during the whole period 2008–2019 did not exhibit a notable seasonal signal for EOF1 (**Figure 4C**). These features of the EOF1 pattern and time series representing bay-scale and surface-layer (about 0–200 m depth) circulation pattern variation on a time scale of about 1 month were consistent with the cyclonic and anti-cyclonic pattern variation as described in previous observational studies (e.g., Inaba, 1984; Katsumata, 2016). Therefore, we considered that the observed short-term variations in the surface-layer current in Suruga Bay were generally captured by the EOF1 mode. The EOF2 mode with another horizontal circulation pattern and the

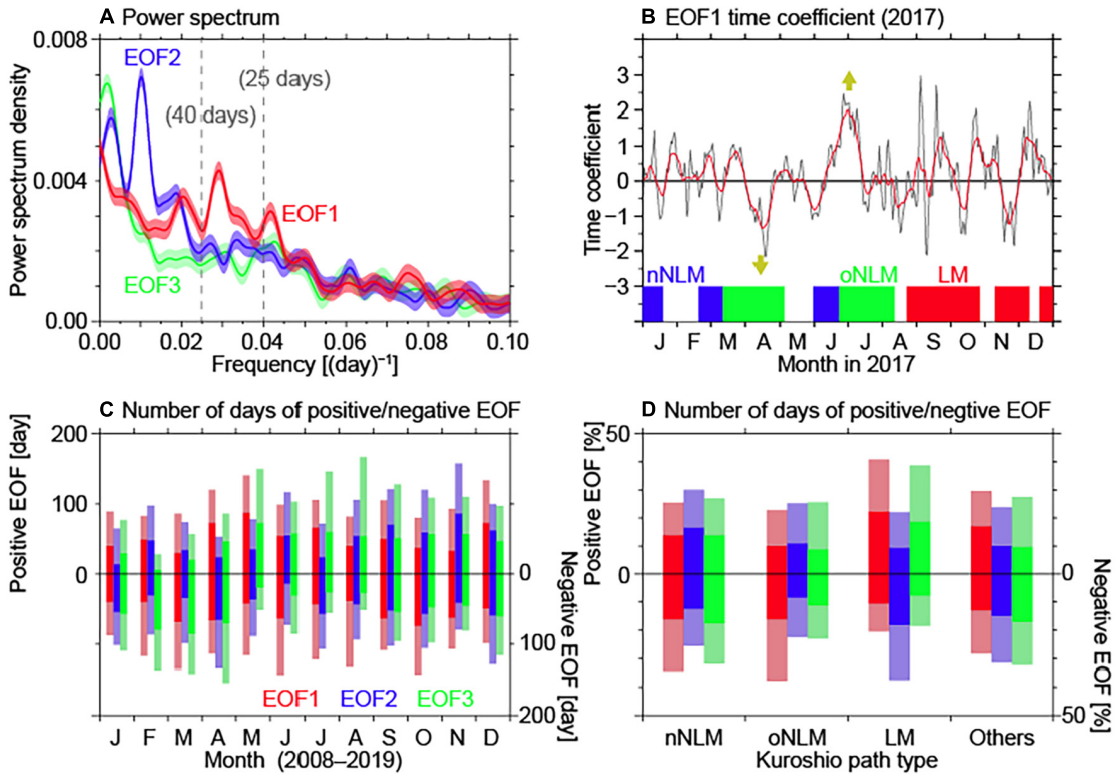

FIGURE 4 | (A) Power spectra for daily time coefficients of the EOF modes (red, blue, and green for EOF1, EOF2, and EOF3, respectively) based on the fast Fourier transform method. A Tukey filter with the effective width of 0.005 [frequency in $(day)^{-1}$] was applied. Shading denotes the 1% significance level. **(B)** Daily and smoothed (11-day running mean) time series of the time coefficients of EOF1 for 2017 (black and red line, respectively). The Kuroshio path types are indicated by color bars as in **Figure 2B**. **(C)** Total number of days when the EOF time coefficient (red, blue, and green for EOF1, EOF2, and EOF3, respectively) is greater than +1 (left axis; upper half) and smaller than −1 (right axis; lower half) for each month during the period 2008–2019 (thick colors). Thin colors indicate the same but using a threshold of ±0.5. **(D)** Same as **(C)** but for each type of the Kuroshio path and units are in % of the total days for each type.

EOF3 mode with an overturning pattern (**Figure 3**) might have an additional effect on the circulation variability. Note that, for EOF2 (blue bars in **Figure 4C**), the number of days with large positive values was notably larger (smaller) than the number with large negative values in August–November (January–May); the number of positive-value days was relatively large in May–August and relatively small in February–March for EOF3 (green bars in **Figure 4C**). Thus, the mean seasonal variation was reflected in these modes, although the intensities of these modes also varied interannually. For a measure of the interannual variability, numbers of days with large (negative/positive) EOF time coefficients were counted for the individual Kuroshio path periods (**Figure 4D**). Similar numbers of days were counted for the negative and positive EOF1 days during the nNLM and oNLM periods, although slightly larger numbers of negative EOF1 days than positive EOF1 days were seen with the threshold of 0.5. During the LM path period, the number of days was much larger for positive EOF1 than for negative EOF1 based on both thresholds of 0.5 and 1. This suggested that environmental conditions, such as the type of Kuroshio path, influence the occurrence of the intrusions into Suruga Bay and related generation of the bay-wide circulation patterns. In addition, during the LM path period, the number of days was larger for negative EOF2 than for positive EOF2 and also larger for positive EOF3 than for negative EOF3, as discussed later (see section "Summary and Discussion").

Large-Scale Environments for Generating Intrusion Circulations

Hereafter, we mainly focus on the processes for generation of the EOF1 circulation pattern (**Figure 3B**), which would be associated with the open-ocean water intrusions. We investigated the conditions associated with the EOF mode outside Suruga Bay. Since the types of Kuroshio path greatly influence the large-scale temperature and velocity distributions, averages/composites of the EOF1 mode over the period including several Kuroshio path types would be mainly determined by fractions of the periods for the path types, and hence inadequate for our purpose. Instead, we took composites of daily potential temperature anomaly and horizontal velocity fields of large EOF1 time coefficient (EOF1 < -1 and EOF1 $> +1$) for the three typical Kuroshio path periods (**Figure 2B**) separately. The 100-m depth fields were used for reducing the near-surface variability due to surface forcing. As assumed for this classification, both negative and positive EOF1 composites represented the large-scale characteristics of

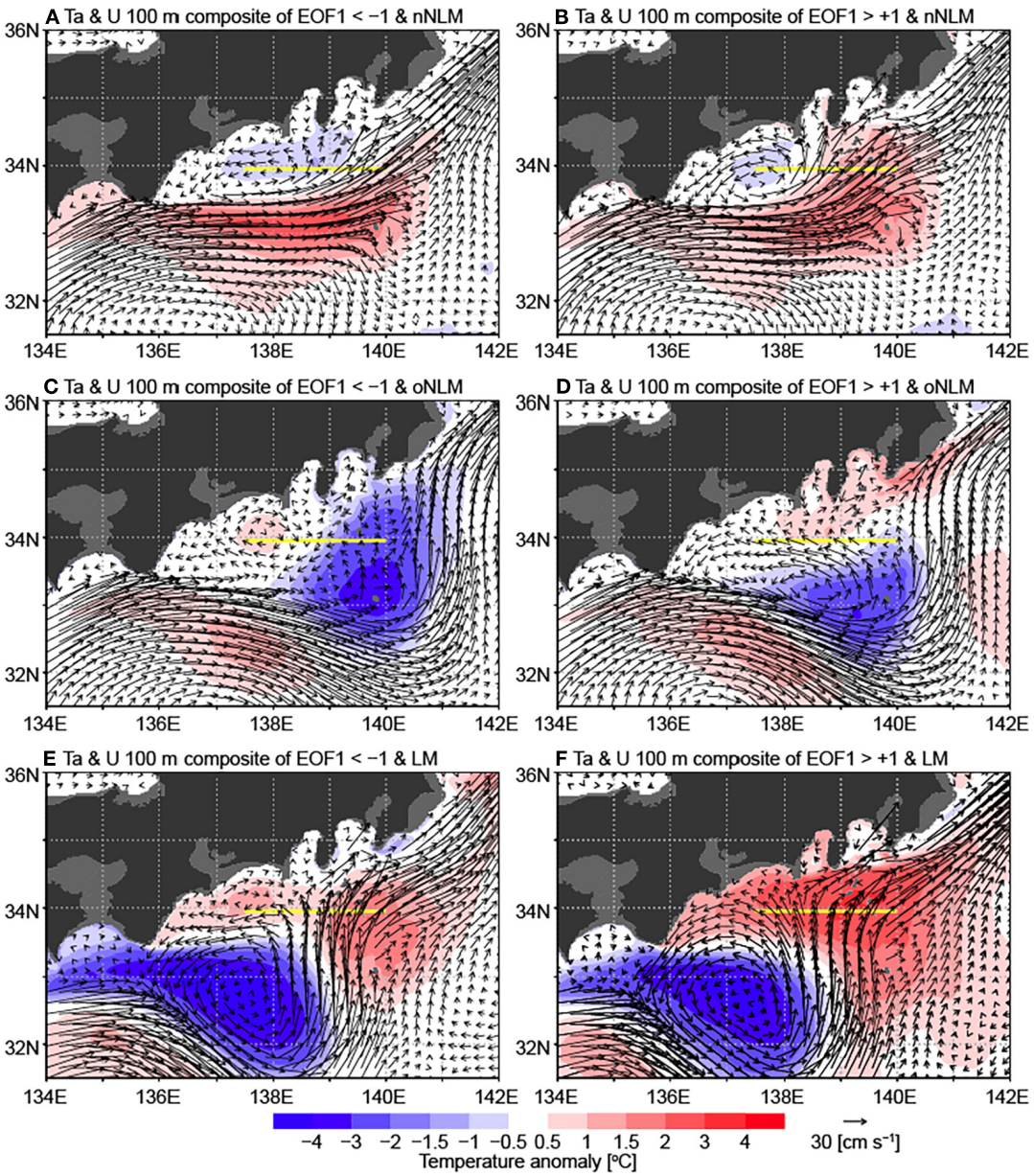

FIGURE 5 | Horizontal distributions of potential temperature anomalies (from daily climatologies; shading) and velocities (arrows) at 100 m depth. Composites of the daily values when the EOF1 time coefficient is smaller than −1 **(A,C,E)** and greater than +1 **(B,D,F)** for the nNLM **(A,B)**, oNLM **(C,D)**, and LM **(E,F)** periods. Yellow lines denote the 33.95°N zonal section as examined in **Figure 6**.

the Kuroshio path types: the Kuroshio passes relatively near the coast with warm anomalies along the path between 135 and 141°E during the nNLM period (**Figures 5A,B**); the Kuroshio passes south of Hachijo-jima with cold anomalies between 137 and 141°E to the coastal side during the oNLM period (**Figures 5C,D**); the Kuroshio separates from the Kii Peninsula (about 136°E), meanders to the south of 32°N around 137–138°E and then northward, and flows along the coast of the Kanto district (about 139–140°E) during the LM period (**Figures 5E,F**). These gross features were consistent with previous studies (e.g., Kawabe, 2005). Differences between the negative and positive composites were examined for each Kuroshio path period as described below.

From a comparison between the negative and positive EOF1 composites during the nNLM period (**Figures 5A,B**), the negative EOF1 composite exhibited more zonally spread cold anomalies between the Kuroshio and the whole Tokai district, whereas the cold anomalies were relatively confined around Enshu-nada for the positive composite. Northward flow was seen to the east of these cold anomalies and this partly directed to Suruga Bay for the positive composite case. From a comparison during the oNLM period (**Figures 5C,D**), cold anomalies inside the

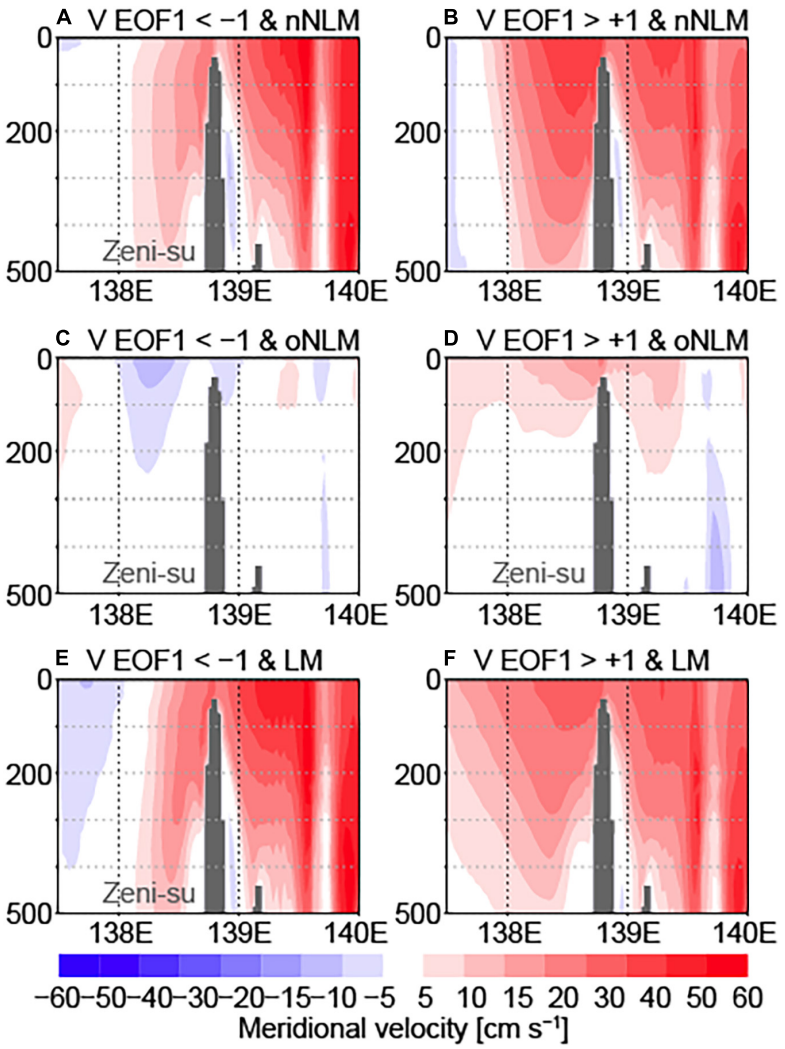

FIGURE 6 | Same as **Figure 5** but for meridional velocities on the vertical cross section along 33.95°N (yellow lines in **Figure 5**).

Kuroshio meandering extended between the Kuroshio and the Kanto district, and the Kuroshio mostly flowed to the east of Hachijo-jima for the negative EOF1 composite; for the positive composite, a branch flow bifurcated around 139°E, 33°N, and partly turned in direction northeastward along the coast from Suruga Bay to the Kanto district, forming warm anomalies. From a comparison during the LM period (**Figures 5E,F**), the northward Kuroshio flow around 138–140°E extended more widely for the positive composite than for the negative composite, resulting in stronger flow toward Suruga Bay for the former case with warmer anomalies along the Tokai and Kanto districts.

Inaba et al. (2001) indicated that the position of the Kuroshio axis relative to a shallow group reef, Zeni-su, (about 75 km south of the southern cape of Izu Peninsula, Irozaki) can be a useful measure of the influence of the Kuroshio water on Suruga Bay. We examined the composite velocities on the zonal section crossing Zeni-su (33.95°N; yellow lines in **Figure 5**). During the nNLM path period, the Kuroshio passed mainly to the east of Zeni-su for the negative EOF1 composite (**Figure 6A**), whereas large northward velocities (40 cm s^{-1}) in the surface layer were seen for the positive EOF1 composite (**Figure 6B**). Note that relatively large velocities were also seen around 139.5 and 139.9°E, to the west of shallow regions related to Mikura-jima and Izu Ridge, respectively. During the oNLM path period, although the Kuroshio mainly flowed to the east of this cross section (**Figures 5C,D**), relatively large northward velocities (>15 cm s^{-1}) associated with the above-described branch flow were also seen to the west of Zeni-su for the positive EOF1 composite (**Figure 6D**) in contrast to the negative EOF1 composite (**Figure 6C**). During the LM path period, large northward velocities (>50 cm s^{-1}) were centered to the east of Zeni-su for the negative EOF1 composite (**Figure 6E**); large northward velocities (>30 cm s^{-1}) were seen on both sides of Zeni-su for the positive EOF1 composite (**Figure 6F**), although these were small in magnitude relative to the peak value for the negative composite and to the subsurface northward

velocities associated with the above-described eastern shallow regions. These results (**Figures 5**, **6**) generally supported the relationship deduced from limited observations in previous studies. In addition, our results suggested that the Kuroshio branch flow to the west of Zeni-su, instead of the main axis, is important in cases where the Kuroshio main flow passes far from the region around Zeni-su (i.e., to the east of Izu Ridge) during the oNLM period.

Examples of Cyclonic and Anti-cyclonic Circulation Events

In order to advance our understanding of the process involved in the Kuroshio water intrusions and generation of the circulation pattern (EOF1), we examine time evolutions of event examples in this section. We selected a negative event in April 2017 (EOF1 time coefficient $<$-0.5 from 3 to 20 April 2017; downward arrow in **Figure 4B**) and a positive event in June–July 2017 (EOF1 time coefficient $>+0.5$ from 11 June to 10 July 2017; upward arrow in **Figure 4B**). We discuss other events during the whole experimental period later.

Current distributions before the events are shown in **Figure 7**. On 2 April 2017 (**Figures 7A,C,E**), the Kuroshio took the oNLM path. The Kuroshio flowed northeastward to the east of Hachijo-jima (141–142°E) and then turned to the west around 34°N and again turned to the east along the coast. On 10 June 2017 (**Figures 7B,D,F**), the Kuroshio took the nNLM path, flowing to the north of Hachijo-jima. These large-scale current distributions as represented in the simulation product (**Figures 7C,D**) were consistent with the satellite altimeter product (CMEMS; **Figures 7A,B**). On the other hand, small-scale structures that form around the Kuroshio main flow were not represented in the satellite product (**Figures 7A,B**) but only visible in the simulation product (**Figures 7C–F**). As discussed below, generation of the EOF1 pattern flows in Suruga Bay was affected by the latter small-scale structures that were resolved in the simulation product.

We first investigated the development of the positive EOF1 event in detail. On the initial date (10 June 2017), the northward flow to the west of Zeni-su merged with the eastward flow from Enshu-nada, forming a strong eastward flow to the south of the mouth of Suruga Bay (**Figure 7F**). **Figure 8** shows the time evolution of SSH and relative vorticity distributions at 100 m depth during the positive EOF1 event. Note that SSH isolines roughly indicate the directions of horizontal velocities. On 10 June 2017 (top left; corresponding to **Figure 7F**), the SSH isolines that passed to the south of the shallow ($<$100 m) coastal shelf region near the western bay mouth (about 138.2°E, 34.4°N) extended eastward without touching the eastern bay mouth region. Hence, no intrusion occurred from the eastward flow outside the bay. The EOF1 time coefficient was small (0.03) at that time. On day 3 (from the initial day 10 June, i.e., 13 June; "Day+3" in **Figure 8**), the eastward flow partly went into the eastern part of the bay. Positive vorticities were seen in the intrusion region, which stemmed from the south of the western shallow region. This suggested that the northward intruding fluctuation of the flow can be attributed to the shear-induced positive vorticity inputs in this region (e.g., vorticity supply from the southern tip of Kyushu; Akitomo et al., 1991). The intrusion once ceased on day 6, then took place again on days 9–12, and eventually generated a cyclonic circulation in the central and southern parts of the bay on days 15–18, when the EOF1 time coefficient was greater than 2. On day 18, the strong circulation shifted southward, suppressing the northward fluctuation of the eastward flow to the south. Without additional intrusion, the circulation in the bay weakened on day 21 and then merged into the eastward flow outside the bay on day 24. Although the EOF1 time coefficient was still large on day 27, the cyclonic circulation was migrating out of the bay. The event terminated when the circulation was fully discharged.

The time evolution of potential temperature anomalies (from daily climatologies) at 100 m depth during the event is also shown in **Figure 8**. In the beginning (10 June), there existed cold anomalies both inside the bay and in the region extending southward from the bay mouth bounded by shallows on both the western and eastern sides (light gray for regions $<$100 m depth in **Figure 8**) and warm anomalies to the south. The eastward flow (**Figure 7F**) prevailed in the transition region between the cold and warm anomalies. When the intrusion event began (day 3), the circulation pattern was reflected in the potential temperature field; cold anomalies were concentrated near the center of the circulation. On day 9, the positive vorticities associated with the intrusion extended to almost the northern bay head, where the intrusion flow turned anti-clockwise to the south; at that time, cold anomalies weakened in the east of the bay (**Figure 8**). Afterward, the region to the south of the bay gradually became warmer. As a result, the region outside the bay was mostly occupied by relatively warm water on days 15–18, leading to further increases of the warm anomalies in Suruga Bay through the intrusions, while the contrast in the potential temperatures between the center and rim of the circulation remained. Thus, a large-scale environmental change took place during this intrusion event. This was attributable to an approach of the Kuroshio branch and was also consistent with both warm anomalies to the south of Suruga Bay and relatively strong northward flow to the west of Zeni-su in the composite distributions (**Figures 5**, **6**).

A similar time evolution (on both the large scale and the scale within the bay) was generally seen for the potential temperature anomalies near the surface (e.g., **Figure 9C**), which suggests that these changes occurred consistently within the surface layer, although surface forcing also has an effect near the surface. Hence, satellite-derived SST data can be used for evaluating our results. **Figure 9** compares the SST distributions between the observational estimate and the simulation product on 29 June 2017. Note that the day with less cloud cover and near the EOF1 peak was selected. Relatively warm SSTs in the rim of the central–southern part of Suruga Bay and relatively cold SSTs inside were represented in the simulation product (**Figure 9B**), which corresponded to northward flow in the eastern part and southward flow in the western part and the doming structure of potential temperature between these flows (e.g., 15 and 20°C (green) isolines in **Figure 9C**). The above SST distribution was basically captured by the satellite observational estimates

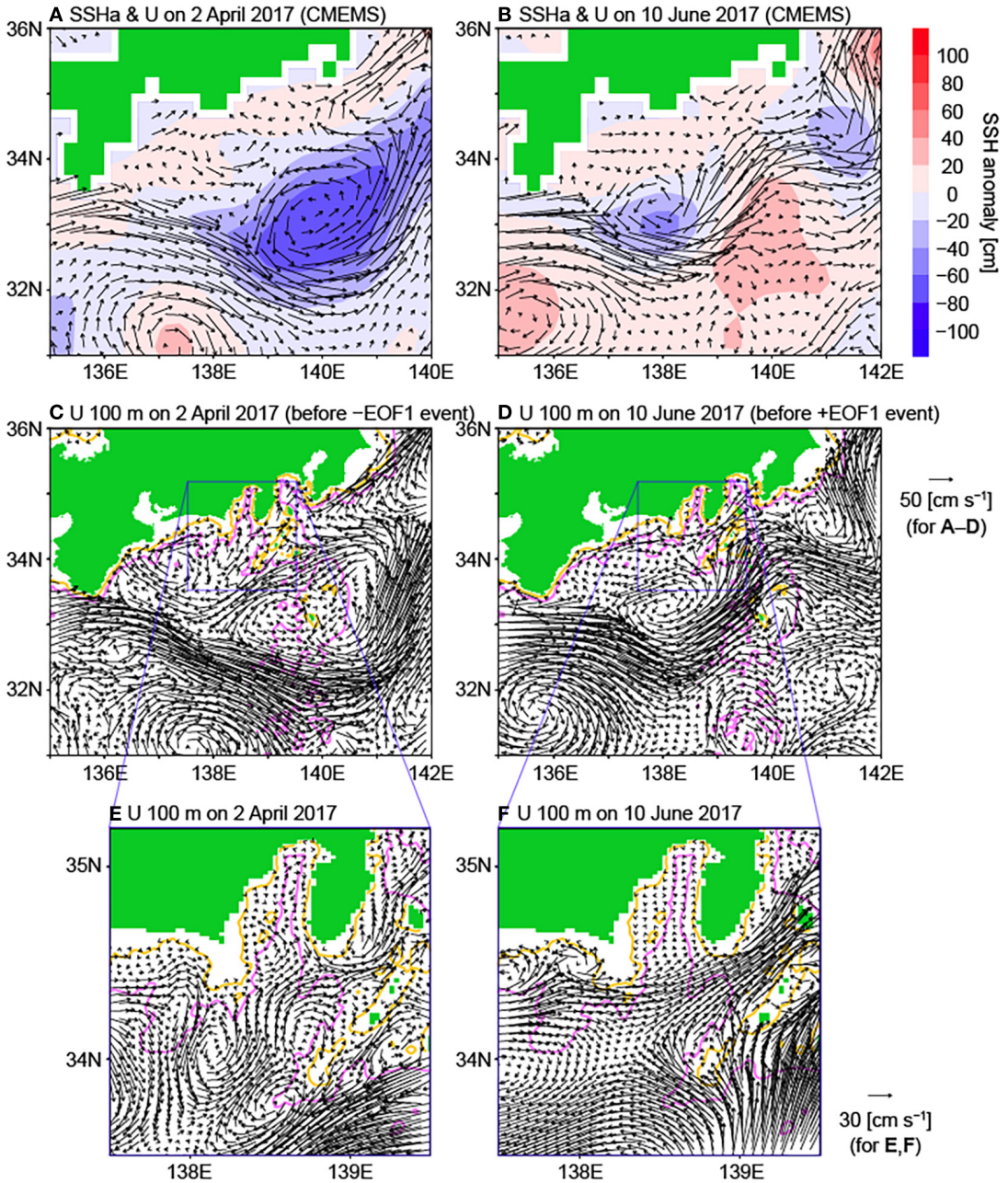

FIGURE 7 | (A,B) Distributions of SSH anomalies and surface velocities from the satellite altimeter product (CMEMS) before the negative **(A)** and positive **(B)** EOF1 events (2 April 2017 and 10 June 2017, respectively). **(C,D)** Distributions of horizontal velocities at 100 m depth on the same days as **(A,B)** from the simulation product, respectively. Yellow and pink lines indicate 200 and 1,000 m depth isolines (see **Figure 2A**). **(E,F)** Same as **(C,D)** but expanded near Suruga Bay.

(**Figure 9A**), although the frontal area with large SST gradients was represented relatively in the north in the simulation product.

In addition, we used the tide-gauge data for another validation of our results, since the above changes in the surface layer were reflected in the SSH field (e.g., **Figure 9C**). We compared the SSH time series in the simulation product with the sea-level observations at Tago and Yaizu tide-gauge stations (**Figure 9D**). At both stations, the sea-level increases of about 20 cm from the middle of June to the beginning of July and the decreases afterward were consistently represented in the observational and simulation data; on the other hand, relatively strong and delayed peak was seen on 9 July in the simulation product. Note that comparisons at the other stations in Suruga Bay indicated similar results (not shown). The latter discrepancy can be attributed to the fact that the simulated bay-scale eddy related to the cyclonic circulation pattern in this event extended to the north (about 34.9°N; **Figure 9B**) compared with the satellite observational estimates (around 34.85°N; **Figure 9A**), as described for the SST

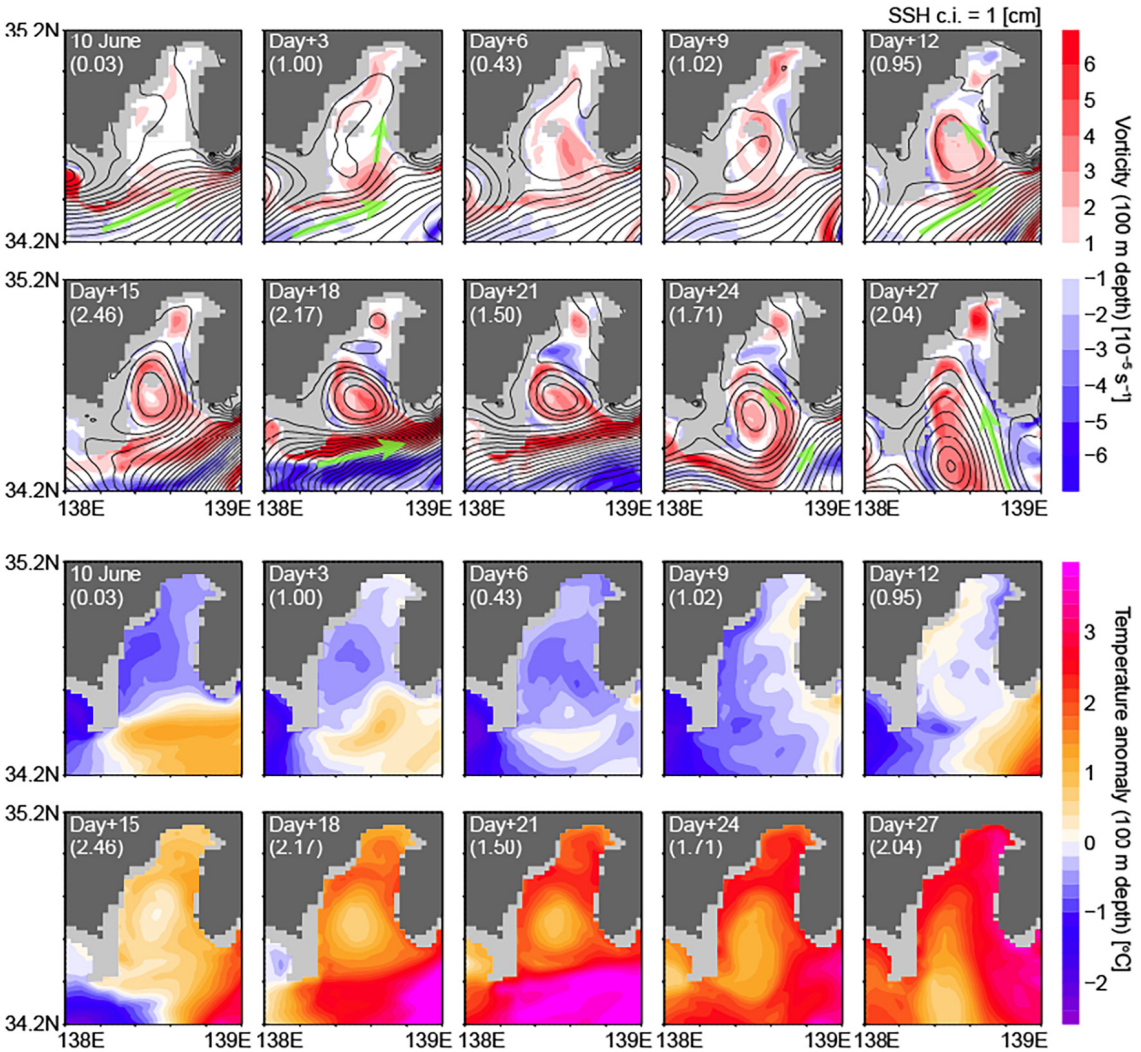

FIGURE 8 | Distributions of SSHs (contours with 1 cm intervals) and relative vorticities at 100 m depth (shading) (upper 2 rows) and potential temperature anomalies at 100 m depth (lower 2 rows) during a positive EOF1 event starting from 10 June 2017 (**top left**). Time series for every 3 days are plotted (**top left** to **top right** and then **bottom left** to **bottom right** for each series). Days from 10 June and the EOF1 time coefficient are indicated in each figure. Relative vorticity was defined in this study as $\zeta = v_x - u_y$, where u and v are zonal (x-ward) and meridional (y-ward) components of horizontal velocity, respectively. Broad flow directions are indicated by green arrows.

comparison on 29 June. This would affect the following evolution of this eddy, leading to the delayed southward migration in the simulation product. Note that small-scale variations as described for this event were not constraint by the data assimilation (Hirose et al., 2019). Although validation of our results on this scale was not sufficient due to the limitation of observation data, the above validations with the available data supported that this event was basically represented in the simulation product.

As described above, our results showed an increase of the potential temperature anomalies in Suruga Bay during the positive EOF1 event example in June 2017 (**Figure 8**). It was also considered that the warming through the intrusions can be more effective when the region to the south of Suruga Bay becomes warmer due to the approach of the Kuroshio branch. We next examined whether or not warming similar to this case occurs in the other positive EOF1 events. **Figure 10B** shows the changes in the potential temperature anomaly during the individual positive EOF1 events as sorted on the basis of the EOF1 peak days. Although the individual time series (thin black lines) fluctuated greatly, an increase of about 0.7°C was seen on average (red line) around the EOF1 peak. After the increase, the temperature gradually decreased to the value before the event on average (about −0.4°C) as the impact of the intrusion events was gradually damped. As shown in **Figure 10B** (green line), the potential temperature increase was relatively large during the event in June 2017. The magnitude of the temperature change varied greatly among the events: for example, the mean and standard deviation of the temperature change from 2 days before the peak to 1 day after the peak were 0.58 and 0.59°C, respectively. Note that generation of the intrusion flow would

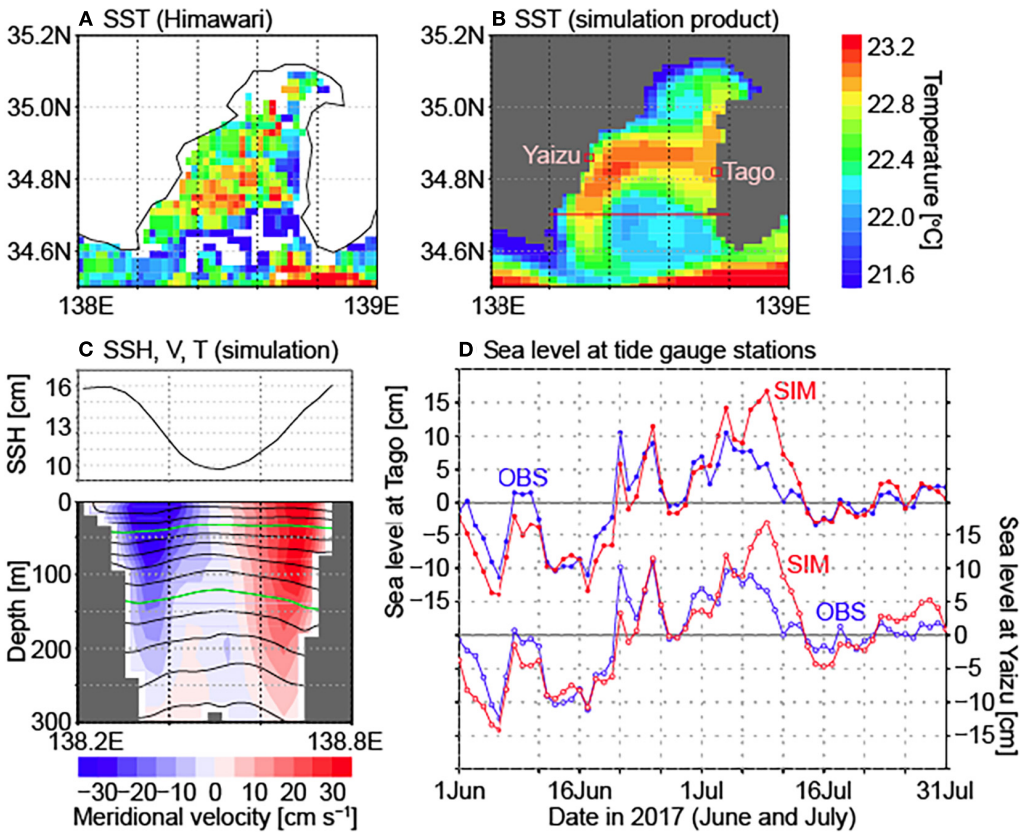

FIGURE 9 | (A) Distribution of SSTs derived from satellite (Himawari-8) observations on 29 June 2017. Missing values are due to cloud cover flags. **(B)** Same as **(A)** but from the simulation product. **(C)** Distributions of SSHs (upper panel), meridional velocities (shading in lower panel), and potential temperature (contours in lower panel with 1°C intervals; green contours indicate 15 and 20°C) along the 34.7°N zonal line [red line in **(B)**]. **(D)** Daily time series of sea levels at the tide-gauge stations [red rectangles in **(B)**], Tago (138.76°E, 34.81°N; closed circles; left axis) and Yaizu (138.33°E, 34.87°N; open circles; right axis), in June and July 2017. Blue and red lines indicate tide-gauge observation data and the simulation product, respectively. Note that these time series include the effect of surface pressure.

depend on large-scale environmental conditions. It was thus suggested that, in the positive EOF1 events, the current variability outside the bay induces the warm water intrusions into Suruga Bay which have a warming effect of about 0.7°C on average, but the thermal conditions outside the bay also vary during the events, resulting in the additional warming/cooling in Suruga Bay with a similar magnitude.

We next examined the negative EOF1 mode. At the beginning of the negative EOF1 event in April 2017, a Kuroshio branch flowed southwestward between Zeni-su and Hachijo-jima (**Figures 7C,E**). Part of this flow circulated clockwise around Enshu-nada, changed direction toward the north to the south of Omaezaki (around 138°E, 33.5°N–34°N) and then passed near Irozaki (eastern cape of the mouth of Suruga Bay) toward Sagami Bay (**Figure 7E**).

As shown in the time evolution of the SSH and vorticity distributions (**Figure 11**), a fluctuation upon the above-described large-scale flow to the south of the bay mouth (on 2 April) grew into an anti-cyclonic circulation in the central–southern part of Suruga Bay as seen on days 10–13. In the initial days, this fluctuation took place outside of the meandering of the large-scale flow and was attributable to the inertia effect of this flow (e.g., Usui et al., 2013). A pair of separated cyclonic and anti-cyclonic circulations developed from the fluctuation on day 7. As the large-scale flow migrated southward, the anti-cyclonic (negative vorticity) circulation remained and occupied the central to southern mouth regions of Suruga Bay (days 13 and 16). The EOF1 time coefficient took the largest negative value for this event of −2.17 on day 14 (16 April 2017). As the large-scale flow separated from Irozaki, the anti-cyclonic circulation gradually dissipated without additional inertial vorticity input.

As described above, the large-scale Kuroshio branch flow migrated southward, away from the bay mouth region, during this event. This generated the temperature decreases around the coastal region, and also in Suruga Bay through the intrusions. **Figure 10A** shows the potential temperature changes for all negative EOF1 events (including the above example; green line). For the negative EOF1 events, the mean and standard deviation of the temperature changes from 2 days before the peak to 1 day after the peak were estimated as −0.62 and 0.57°C, respectively. The standard deviation value was similar to that for the positive EOF1 events. We discuss below (see section "Relationship Between Flows Over Surrounding Regions") why the intrusion water is relatively warm in the

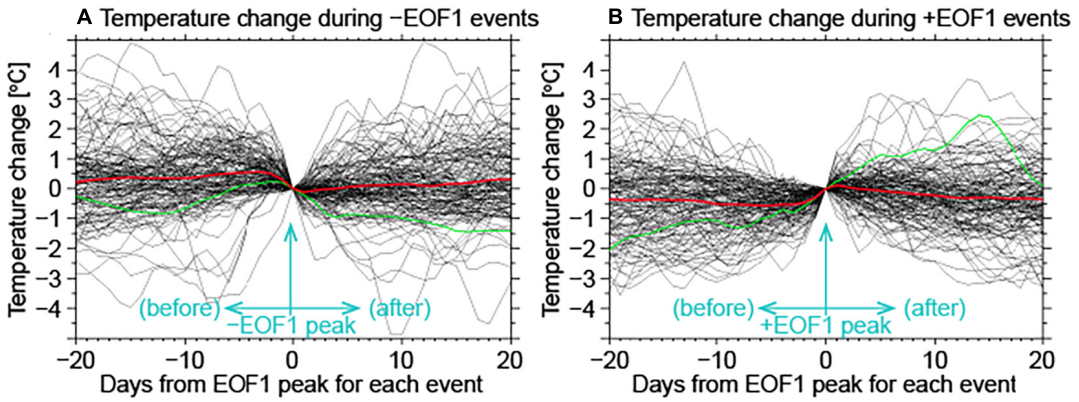

FIGURE 10 | Time series of changes in the potential temperature at 100 m depth in Suruga Bay during the negative **(A)** and positive **(B)** EOF1 events. *x*-axis denotes days from the EOF1 peak; *y*-axis denotes potential temperature changes from the value on the EOF1 peak day. Thin black lines indicate the individual events. Red line indicates the averaged time series. Green lines in **(A,B)** indicate the negative EOF1 event in April 2017 and the positive EOF1 event in June 2017, respectively.

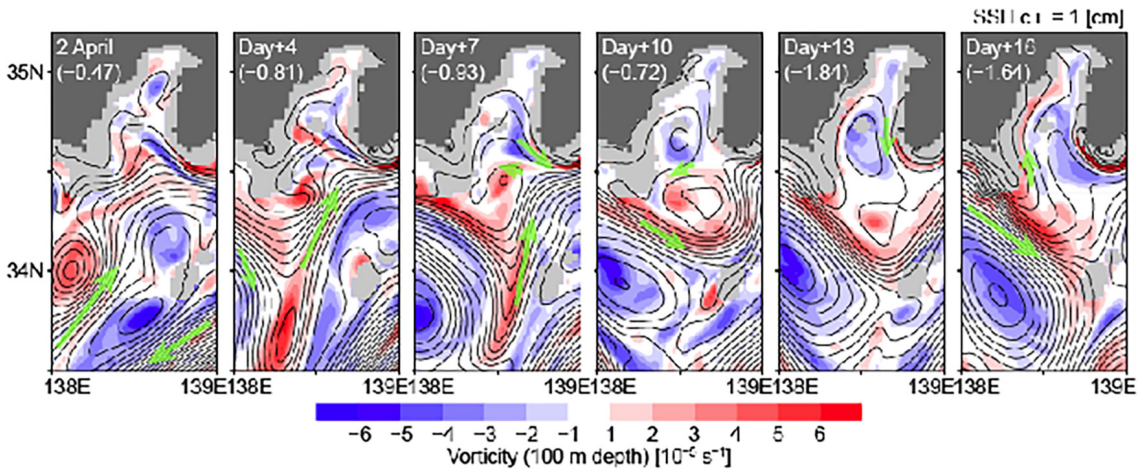

FIGURE 11 | Distributions of SSHs (contours with 1 cm intervals) and relative vorticities at 100 m depth (shading) during a negative EOF1 event starting from 2 April 2017 (**left** to **right**). Days from 2 April and the EOF1 time coefficient are indicated in each figure. Broad flow directions are indicated by green arrows.

positive EOF1 events and relatively cold in the negative EOF1 events on average.

The examples of the EOF1 events as presented in this section suggests strong influences of bay-size eddies on the circulation patterns for both negative and positive EOF1 modes. Here, general importance of the bay-size eddies is discussed by examining the composites fields of the negative and positive EOF1 events. As shown in **Figure 12**, SSH, relative vorticity, and potential temperature anomaly fields of the negative EOF1 composite indicated consistent structures of a bay-scale anti-cyclonic eddy centered near the bay mouth; those of the positive EOF1 composite indicated a bay-scale cyclonic eddy, as seen in the event examples (**Figures 8**, **11**). The circulation pattern of the EOF1 mode (**Figures 3B,F**) was consistent with the influences of these eddies, including its vertical structure (not shown for the composite fields). These features also corresponded to the co-occurrence of currents with the opposite (northward/southward) directions in the eastern and western bay mouths as indicated by the direct observations (Inaba, 1984). Thus, we concluded that bay-scale anti-cyclonic and cyclonic eddies generally characterize the circulation patterns of the negative and positive EOF1 events, respectively.

Relationship Between Flows Over Surrounding Regions

As described above, the composites and event examples for the positive and negative EOF1 modes represented relatively stronger northward velocities to the west of Zeni-su during the positive EOF1 mode (**Figures 5–7**), which was basically consistent with the suggestions in previous studies that used the position of the Kuroshio axis. Here, we examine this relationship by using a long-term simulation product. As a measure of the northward flow strength to the west of Zeni-su, we took averages of the meridional velocities at 100 m depth over a section where differences between the negative–positive composite meridional

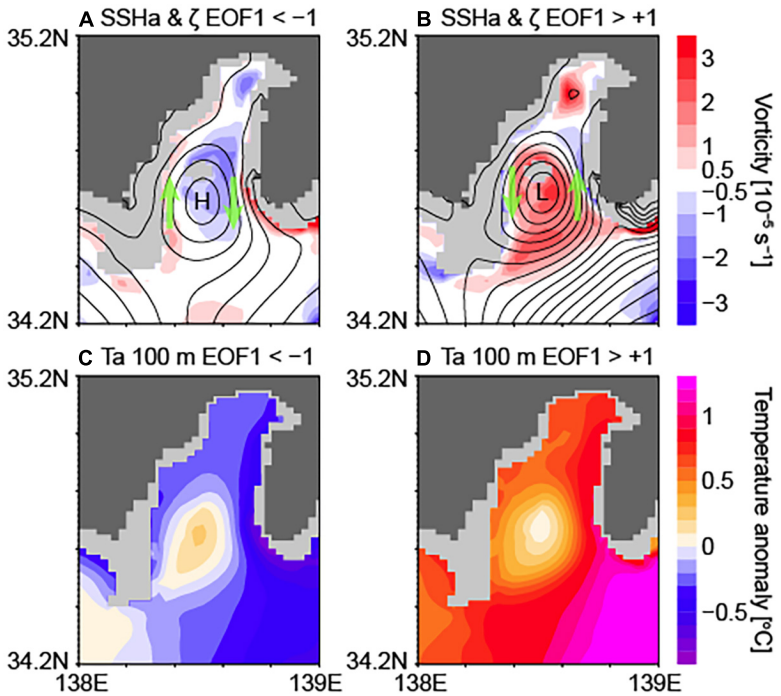

FIGURE 12 | (A,B) Distributions of SSH anomalies (contours with 1 cm intervals) and relative vorticities at 100 m depth (shading). **(C,D)** Distributions of potential temperature anomalies at 100 m depth. Composites of the daily values when the EOF1 time coefficient is smaller than −1 **(A,C)** and greater than +1 **(B,D)**. Maximum and minimum locations of the SSH anomaly fields are indicated by "H" and "L," respectively. Broad flow directions are indicated by green arrows.

velocities (**Figure 6**) were relatively large. Note that different sections were assumed for the individual Kuroshio path periods (see caption of **Figure 13**).

Figure 13 shows the relationship between the northward flow strength (Vz) and the EOF1 time coefficient (PC). For the individual Kuroshio path periods, positive correlations were detected between Vz and PC. These correlations were significant at 90, 90, and 99% confidence levels for the nNLM, oNLM, and LM periods, respectively (here, the event peak number was used as the least sample number for each period, taking into consideration the autocorrelations of the daily values). As seen in **Figure 13**, the mean Vz values (indicated by vertical thin gray lines) largely differed between the Kuroshio path periods, which supported the necessity of conducting this analysis separately for the individual periods.

For all three periods, Vz averages over the days with $PC > +1$ ($PC < -1$) (vertical red segments) were larger (smaller) than the whole Vz averages (i.e., $\overline{Vz|_{PC<-1}} < \overline{Vz} < \overline{Vz|_{PC>+1}}$); PC averages over the days with Vz larger (smaller) than $\overline{Vz}$ by one standard deviation (horizontal green segments) were positive (negative). Hence, the suggested relationship basically held for all these periods. However, the relationship was rather weak in several quadrants: Vz averages for $PC < -1$ (red segments in the third quadrant) were close to $\overline{Vz}$ within a half of the standard deviation during the nNLM and oNLM periods; PC averages for $Vz < \overline{Vz} - std(Vz)$ (green segments in the third quadrant) were rather small (close to zero) during the same periods. Thus, it was suggested that these distributions were skewed during the nNLM and oNLM periods. In contrast, the linear relationship was relatively robust during the LM path period.

As discussed above, the warming of about 0.7°C occurred in Suruga Bay during the positive EOF1 events on average. The relatively strong flow to the west of Zeni-su is consistent with warm anomalies according to the approach of the Kuroshio axis to the Tokai district coast during the nNLM and LM periods (**Figures 5B,F**) and that of the Kuroshio branch during the oNLM period (**Figure 5D**). Thus, the warming can generally occur around the coastal region of the Tokai district when the positive EOF1 events are generated. The intrusion flow brings the warm anomalies particularly in the rim of the circulation as generated in Suruga Bay. On the contrary, the cooling of about 0.6°C during the negative EOF1 events on average can be attributed to the separation of the Kuroshio path from the coastal region of the Tokai district. Again, the meridional flow at the latitude of Zeni-su is consistent with the temperature anomalies.

In addition, the time evolution of the positive EOF1 event example (in June 2017) suggested that eastward flow to the south of the western bay mouth plays an important role in generating the intrusions into the eastern bay mouth in that event (**Figure 8**). We examined the existence of this flow for all positive EOF1 events during the whole product period. In many of the large positive EOF1 events, strong eastward flow to the south of the western bay mouth (Omaezaki) was found during the initial days before the EOF1 time coefficient became large (**Supplementary Figure 1**). In other events, which did not

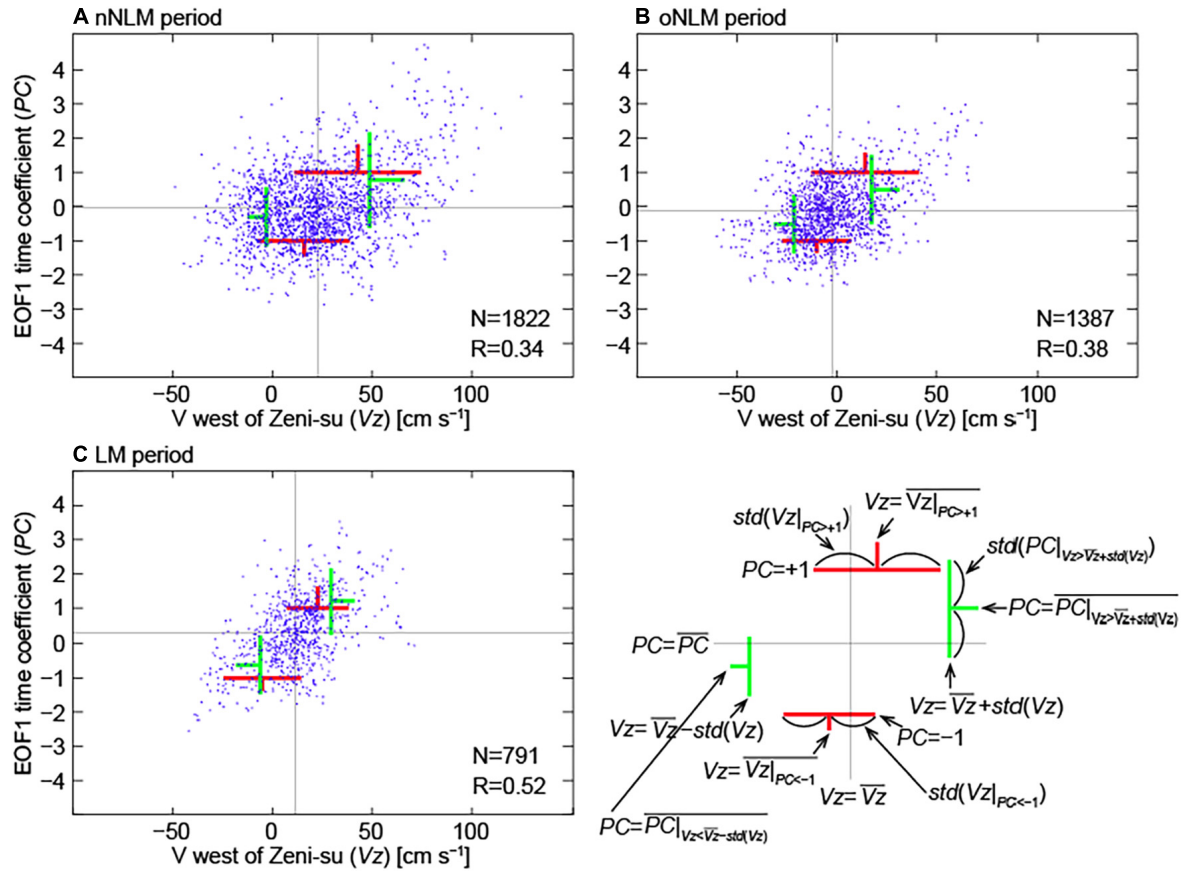

FIGURE 13 | Scatter diagrams between meridional velocity to the west of Zeni-su (*Vz*) and EOF1 time coefficient (*PC*) during the individual Kuroshio path period. **(A)** nNLM. **(B)** oNLM. **(C)** LM. Meridional velocities to the west of Zeni-su at 100 m depth were averaged along the 33.95°N line over 138.3°E–138.6°E **(A)**, 138.15°E–138.45°E **(B)**, 137.75°E–138.15°E **(C)** based on the differences of the positive and negative composites during the individual periods (**Figure 6**). Lags of *PC* from *Vz* by 1, 4, and 3 days for **(A–C)**, respectively, were considered to represent maximum correlations (R). Averages (denoted by overbar) and standard deviations ("*std*") of *Vz* values when $PC < -1$ and $PC > +1$ are indicated by red segments. Similarly, averages and standard deviations of *PC* values when $Vz < \overline{Vz} - std\,(Vz)$ and when $Vz > \overline{Vz} + std\,(Vz)$ are indicated by green segments.

accompany such flow, cyclonic eddies were generated outside the bay and migrated into the bay. Thus, shear-induced positive vorticity input into the eastward flow to the south of the western bay mouth, as in the event example, would be one of the mechanisms for generating the eastern bay mouth intrusion and cyclonic circulation in Suruga Bay.

SUMMARY AND DISCUSSION

In this study, we analyzed the circulation patterns in the surface layer of Suruga Bay by using an ocean data assimilative simulation product. Cyclonic and anti-cyclonic circulation patterns, as suggested by observational studies, were detected as the positive and negative first leading EOF modes of the velocity field in Suruga Bay. The former (latter) accompanied the intrusion into the eastern (western) bay mouth and outflow from the western (eastern) bay mouth. SSH, relative vorticity, and temperature anomaly fields consistently suggested that bay-scale cyclonic and anti-cyclonic eddies centered near the bay mouth contribute to the positive and negative EOF1 circulation patterns, respectively. The time scales of occurrences of these patterns were estimated as about 1 month, which was consistent with the time scale of fluctuations of the Kuroshio axis as reported in previous studies (e.g., Awaji et al., 1991; Miyama and Miyazawa, 2014; Katsumata, 2016). Temperature changes during the cyclonic circulation events differed among the events depending on the large-scale (open-ocean) thermal conditions but were estimated as about 0.7°C on average. Reproduced SST and coastal sea level distributions during the events were consistent with available satellite and tide-gauge observation data.

The location of the Kuroshio axis relative to Zeni-su has been suggested as an indicator of the generation of the intrusion circulations in Suruga Bay in previous observational studies (e.g., Inaba, 1984). The use of the simulation product during the period 2008–2019 enabled us to investigate this relationship corresponding to the individual Kuroshio path types, which is necessary since mean velocity field greatly differs between the different Kuroshio path periods. In addition, our results suggested that the strength of the northward velocity to the west

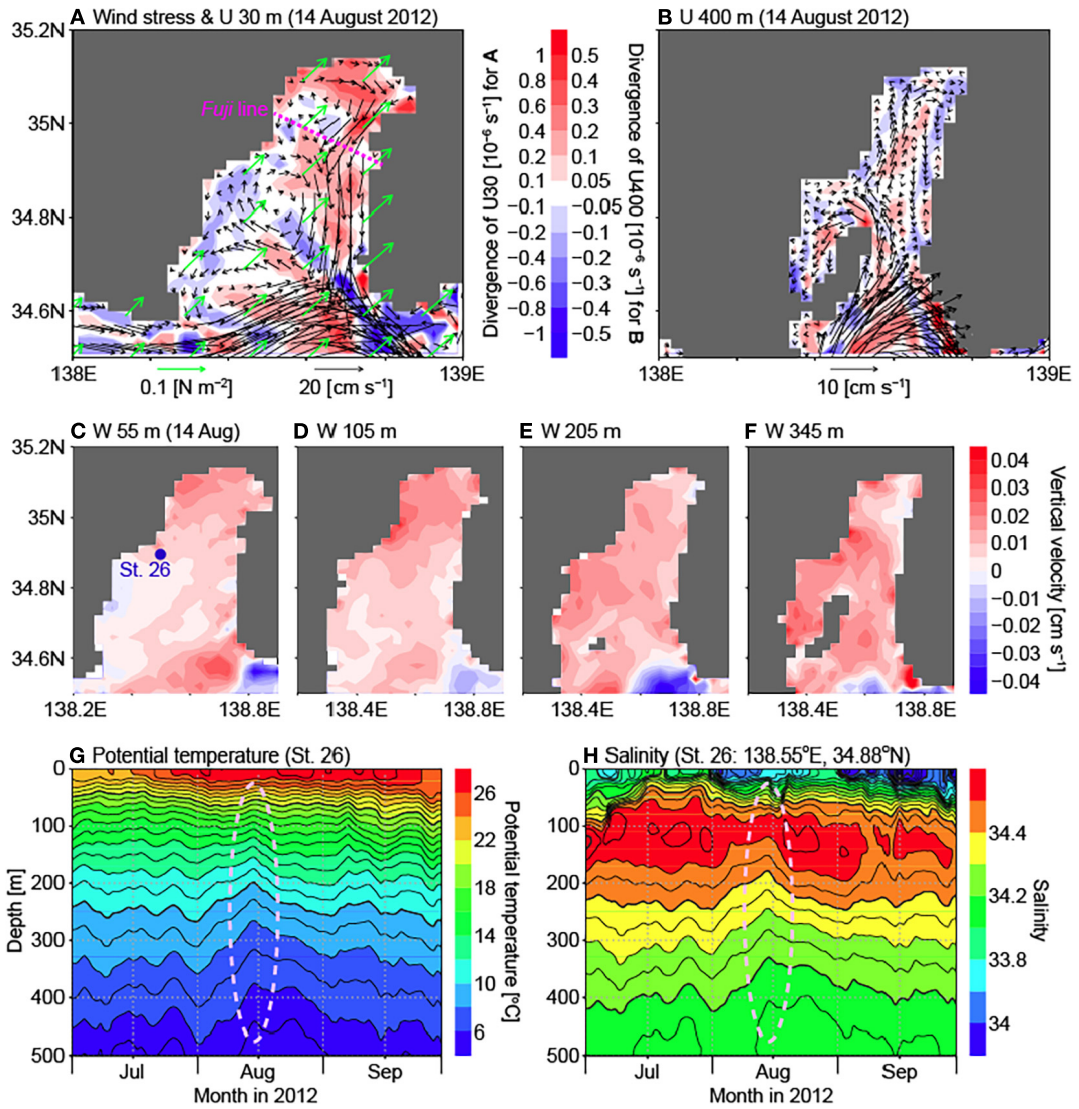

FIGURE 14 | (A) Distributions of surface wind stresses (green arrows), horizontal velocities (black arrows) and horizontal velocity divergences (shading) at 30 m depth. **(B)** Distributions of horizontal velocities (black arrows) and horizontal velocity divergences (shading) at 400 m depth. **(C–F)** Distributions of vertical velocities (positive upward) at 55, 105, 205, and 345 m depths, respectively. These distributions **(A–F)** are for the peak day of the positive EOF3 event, 14 August 2012. **(G,H)** Time evolutions of potential temperature and salinity profiles at Station 26 of Nakamura (1982) [138.55°E, 34.88°N; blue closed circle in **(C)**]. Potential temperature and salinity changes during the EOF3 event are indicated by dashed ellipses. Purple dashed line in **(A)** denotes the ordinary track of the sightseeing ferry *Fuji*.

of Zeni-su would be a measure for the EOF1 event generation, instead of the Kuroshio axis position. The relationship between the flow strength to the west of Zeni-su and the EOF1 time coefficient was robust during the LM period. During the nNLM and oNLM periods, the relationship for generating the negative EOF1 circulation in Suruga Bay was rather weak in contrast to the robust relationship for generating the positive EOF1 circulation. Although the skewed relationship suggested the limitation of our analysis with the EOF decomposition, our results were basically consistent with previous observational studies and useful for discussing the generation of the surface-layer circulation patterns from several aspects by using the high-resolution simulation product.

Here, we briefly discuss the second and third leading EOF modes. As shown in **Figure 3C**, the EOF2 mode represented the pattern that a circulation centered outside the bay passes by the southernmost part of the bay. A candidate for this circulation was the one that was discharged from Suruga Bay at the end of an EOF1 event. For example, the EOF2 time coefficient was 1.12 on day 24 (4 July) of the positive EOF1 event example when the cyclonic circulation that characterized the EOF1 pattern migrated out of Suruga Bay (**Figure 8**; the distribution with a peak EOF2 of 1.42 on day 26 is not shown). In fact, the EOF2 time coefficient of the same sign as the EOF1 time coefficient was often seen at the end of the EOF1 events. However, the increases in magnitude of the EOF2 time coefficient in these cases were rather transient

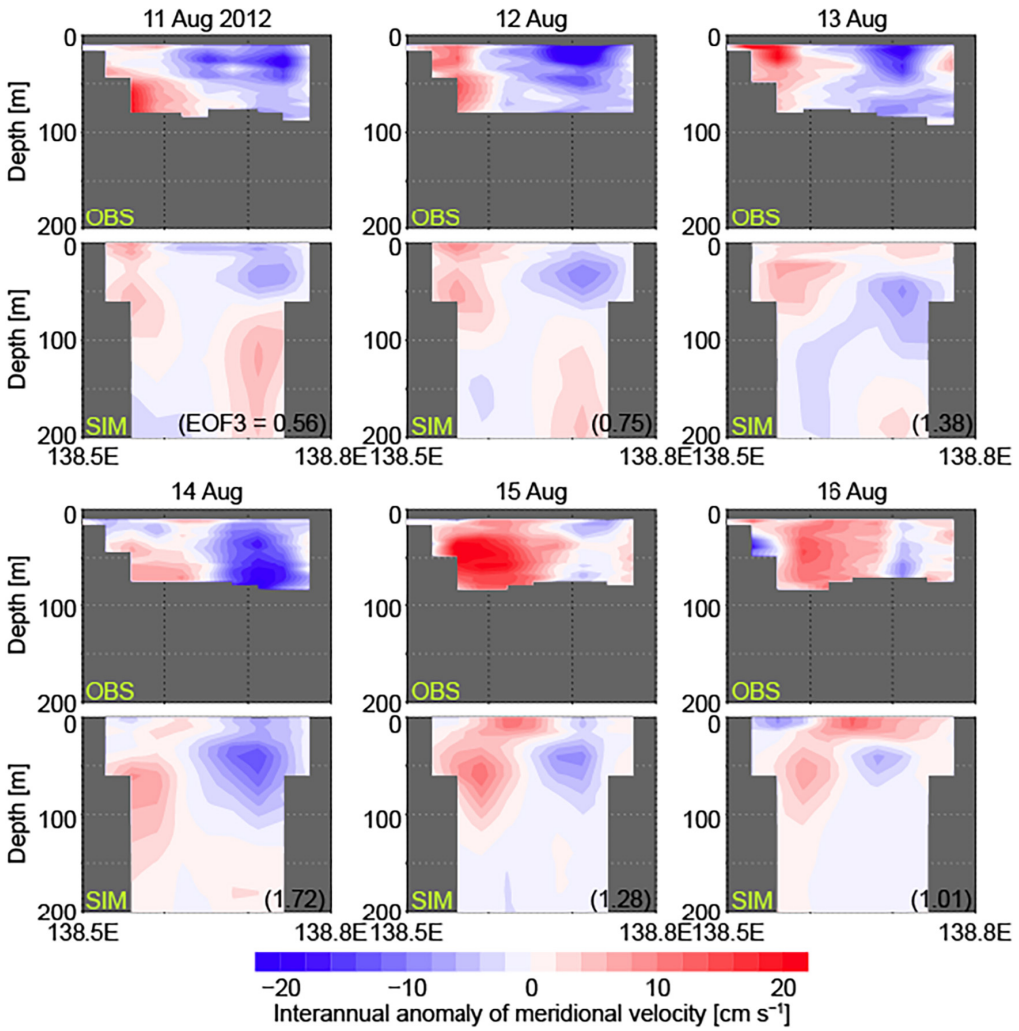

FIGURE 15 | Distributions of daily-mean interannual anomalies of meridional velocities on a cross section along the regular operation line of the sightseeing ferry *Fuji* (purple dashed line in **Figure 14A**) between Shimizu Harbor (138.50°E, 35.01°N) and Toi Harbor (138.79°E, 34.91°N) during 11–16 August 2012. ADCP observation data (OBS; upper) and the simulation product (SIM; lower; with EOF3 time coefficient) are compared for each day. Missing values (due to observation limit and land cover) are indicated by gray shading.

(e.g., 0.07 on day 28 in the above case). On the other hand, EOF2 events lasting longer with larger time coefficient sometimes occurred, although less frequently. In these latter cases, the flow that passed by the southernmost bay was attributed to eddies that were larger than the above bay-scale ones, i.e., on a horizontal scale similar to the Kuroshio meandering and cold pool. This was consistent with the relatively long time period for the EOF2 mode (about 100 days; **Figure 4A**).

As described in section "EOF Mode Decomposition," southward surface-layer flow was represented by the positive EOF3 pattern (**Figures 3D,H**). **Figure 14** shows an example of the positive EOF3 event in the summer of 2012 with a peak EOF3 time coefficient of 1.72 on 14 August. During the event (about 13–18 August 2012), the surface wind stresses in Suruga Bay were approximately northeastward (green arrows in **Figure 14A**). Since the regressed surface wind stress field for the EOF3 time coefficients (not shown) was dominated by westerlies around Suruga Bay, the strong eastward components in the example event played an important role in generating the flow that characterizes the positive EOF3 mode. The southward surface flow from the bay head region to the outer region (i.e., divergent flow for the bay; **Figures 3D**, **14A**) was consistent with the southward Ekman flow generated by the westerly surface wind stresses. This surface divergent flow required the northward convergent flow and upwelling in the subsurface layer. A consistent structure with broad upwelling within the bay was actually presented (down to 500 m depth approximately) in the example event, although the region with strong upwelling varied with depth (**Figures 14C–F**).

Nakamura (1982) reported that temperatures lower than the previous month ("secondary temperature minimum" after the primary temperature minimum in winter) appeared at about

50–200 m depths in the summer of several years during 1964–1974, despite the net surface heating in summer. Nakamura and Uehara (2020) also found that large subsurface cooling consistent with the secondary temperature minimum phenomenon took place in the bay head region based on recent observations during the period 2008–2017; relatively large subsurface cooling was seen in the summer of 2012 in their figures. In the simulation product, time evolutions of potential temperature and salinity profiles (**Figures 14G,H**) exhibited decreases of potential temperatures and changes of salinities (increases above the salinity maximum at about 100 m depth; decreases below it) in the subsurface layer during the event in the summer of 2012 (dashed ellipses), which were basically consistent with the upwelling as described above. The similarities of our results to the figures as presented in Nakamura (1982) suggested the possibility that the upwelling for compensating the southward divergent flow in the surface layer generated by westerly wind stresses can influence the phenomenon as in the above example. We should note that, since the resolution of the surface forcing field of the simulation product (Tsujino et al., 2018) was about 55 km based on the JRA-55 reanalysis (Kobayashi et al., 2015), surface wind variability on a regional scale (e.g., Kawamura, 1966) was not resolved. Thus, further investigation with forcing fields that resolve the regional variability (e.g., Tanaka et al., 2007, 2008) is necessary for improving the reproduction of the wind-induced circulation in Suruga Bay, which remains for future work. In addition, summertime atmospheric responses to the local SST increases around the Kanto–Tokai district related to the Kuroshio large meander have recently been indicated with an atmospheric model (Sugimoto et al., 2021). Atmospheric feedback should be important for understanding the larger number of positive EOF3 days than negative EOF3 days during the LM period (**Figure 4D**). Therefore, high-resolution boundary conditions or interacting processes are necessary for both ocean and atmosphere simulations for clarifying and predicting the comprehensive variability in this region. Accumulated hydrographic observation data (e.g., Kutsuwada et al., 2007) would be important data sources for initialization and validation in these modeling studies.

Reproduction of the EOF3 event was validated by using the ADCP data along the regular operation line of the sightseeing ferry *Fuji* in the bay head region. **Figure 15** compares the meridional velocity anomalies along the ferry track line during the EOF3 event. Note that hourly climatology that includes predominant diurnal and semi-diurnal tidal variations as well as seasonal variations (see section "Materials and Methods") was subtracted for calculating these daily anomalies but qualitatively similar results were obtained (not shown) when we used simple daily averages of available data as in previous studies (e.g., Katsumata et al., 2020). On 11 and 12 August 2012, the observation data indicated southward flow in the central–eastern part and northward flow to the west of 138.6°E approximately in 20–80 m depths. The simulation results basically reproduced this flow structure, although the magnitudes of both southward and northward flows were rather smaller. The EOF3 time coefficient for the simulation result became greater than +1 on 13 August and took a maximum on 14 August; the bay-scale EOF3 flow pattern (**Figure 3D**) was clear on these days (**Figure 15A**). At the peak time, southward flow in the surface layer (<100 m depth) with relatively large magnitude (about 14 cm s^{-1}) was formed at about 138.7°E for both data. On 15 and 16 August, the southward flow weakened and the northward flow in the western part became stronger (in magnitude) than the southward flow. Within the observational limit, the time evolution of the simulation results was basically consistent with the ADCP observations, which lends support to our use of the simulation product. Nevertheless, the differences in details, which can be attributed to errors in calculating interannual anomalies (for both data) and in the parameterizations and forcing of the simulation, should be reexamined in the future for understanding more local-scale variability necessary for fishery use, for example.

The surface-layer flow patterns and related environmental fields as obtained in this study provided useful information for understanding the circulation variability and hence the variabilities in temperature and other properties (e.g., salinity and nutrient) in Suruga Bay. Water exchange between the western boundary current and coastal ocean is one of the key processes in representing these variabilities, which requires reproduction on the horizontal scale ranging from eddies within the bays to the Kuroshio meandering. In this regard, the simulation product used in this study (Hirose et al., 2019) would be an effective tool, resolving bay-scale eddies under the data assimilative constraints on larger scales. Nevertheless, further collaborative feedback between the observational and modeling studies and between the regional and large-scale climate studies is necessary in order to understand the sophisticated interaction processes between scales, which would improve our ability to provide adequate information to society.

DATA AVAILABILITY STATEMENT

Publicly available datasets were analyzed in this study. This data can be found here: https://mri-ocean.github.io/mricom/mri.com-user_jpn_start.html, https://resources.marine.copernicus.eu/?option=com_csw&view=details&product_id=SEALEVEL_GLO_PHY_L4_REP_OBSERVATIONS_008_047, https://www.eorc.jaxa.jp/ptree/userguide.html, https://jdoss1.jodc.go.jp/vpage/tide.html.

AUTHOR CONTRIBUTIONS

TT performed the analysis and wrote the first draft of the manuscript. TT, KT, TK, KK, and TM contributed to the conception and design of this study. KS, NU, and NH contributed to the processing and analysis of the simulation product. KS, HN, LSU, KKK, YK, and GY contributed to the model description, analysis methodology, and interpretation of the model results. TK, DT, MN, and KK contributed to the processing and publication of the shipboard ADCP data. All authors authored the manuscript, contributed to the revision, and approved the final draft.

FUNDING

This research was supported by the Japan Society for the Promotion of Science (KAKENHI Grants 20H01968 and 19K03978).

ACKNOWLEDGMENTS

We are indebted to Hiroyuki Tsujino (Department of Climate and Geochemistry Research, MRI/JMA) who has long been involved in the development of MRI.COM. We are grateful to the reviewers, DK and ZY, for their constructive comments.

SUPPLEMENTARY MATERIAL

The Supplementary Material for this article can be found online at: https://www.frontiersin.org/articles/10.3389/fmars.2021.721500/full#supplementary-material

REFERENCES

Akitomo, K., Awaji, T., and Imasato, N. (1991). Kuroshio path variation south of Japan: 1. Barotropic inflow-outflow model. *J. Geophys. Res.* 96, 2549–2560. doi: 10.1029/90JC02030

Awaji, T., Akitomo, K., and Imasato, N. (1991). Numerical study of shelf water motion driven by the Kuroshio: barotropic model. *J. Phys. Oceanogr.* 21, 11–27. doi: 10.1175/1520-0485(1991)021<0011:nsoswm>2.0.co;2

Hirose, N., Usui, N., Sakamoto, K., Tsujino, H., Yamanaka, G., Nakano, H., et al. (2019). Development of a new operational system for monitoring and forecasting coastal and open-ocean states around Japan. *Ocean Dyn.* 69, 1333–1357. doi: 10.1007/s10236-019-01306-x

Inaba, H. (1981). Circulation pattern and current variations with respect to tidal frequency in the sea near the head of Suruga Bay. *J. Oceanogr. Soc. Jpn.* 37, 149–159. doi: 10.1007/bf02309052

Inaba, H. (1982). Relationship between the oceanographic conditions of Suruga Bay and locations of the Kuroshio path. *Bull. Coast. Oceanogr.* 19, 94–102.

Inaba, H. (1984). Current variation in the sea near the mouth of Suruga Bay. *J. Oceanogr. Soc. Jpn.* 40, 193–198. doi: 10.1007/bf02302552

Inaba, H. (1988). Oceanographic environment of Suruga Bay. *Bull. Jpn. Soc. Fish. Oceanogr.* 52, 236–240.

Inaba, H., Katsumata, T., and Yasuda, K. (2001). Temporal variations of current and temperature at 300 m in Suruga Bay. *Deep Ocean Water Res.* 2, 1–8.

Iwata, T., Shinomura, Y., Natori, Y., Igarashi, Y., Sohrin, R., and Suzuki, Y. (2005). Relationship between salinity and nutrients in the subsurface layer in the Suruga Bay. *J. Oceanogr.* 61, 721–732. doi: 10.1007/s10872-005-0079-2

Katsumata, T. (2004). *Intrusion Process of Oceanic Water to Suruga Bay*. Ph.D. thesis. (Shizuoka: Tokai University), 110.

Katsumata, T. (2016). Generation of periodic intrusions at Suruga Bay when the Kuroshio follows a large meandering path. *Cont. Shelf Res.* 123, 9–17. doi: 10.1016/j.csr.2016.04.005

Katsumata, T., Niki, M., Tanaka, A., Tan, H., Takashima, K., Takahashi, D., et al. (2020). The current of the inner part of Suruga Bay in 2008 – The current observation by using acoustic Doppler current profiler (ADCP) mounted on the Suruga-wan ferry. *Bull. Inst. Oceanic Res. Dev.* 42, 15–24.

Kawabe, M. (1986). Transition processes between the three typical paths of the Kuroshio. *J. Oceanogr. Soc. Jpn.* 42, 174–191. doi: 10.1007/BF02109352

Kawabe, M. (1995). Variations of current path, velocity and volume transport of the Kuroshio in relation with the large meander. *J. Phys. Oceanogr.* 25, 3103–3117. doi: 10.1175/1520-0485(1995)025<3103:vocpva>2.0.co;2

Kawabe, M. (2005). Variations of the Kuroshio in the southern region of Japan: conditions for large meander of the Kuroshio. *J. Oceanogr.* 61, 529–537. doi: 10.1007/s10872-005-0060-0

Kawamura, T. (1966). Surface wind systems over central Japan in the winter season. *Geogr. Rev. Jpn.* 39, 538–554. doi: 10.4157/grj.39.538

Kimura, K. (1950). Investigation of ocean current by drift-bottle experiments (No. 1)—Current in Suruga Bay with special reference to its anti-clockwise circulation within the bay. *J. Oceanogr. Soc. Jpn.* 5, 70–83.

Kobayashi, S., Ota, Y., Harada, Y., Ebita, A., Moriya, M., Onoda, H., et al. (2015). The JRA-55 Reanalysis: general specifications and basic characteristics. *J. Meteorol. Soc. Jpn.* 93, 5–48. doi: 10.2151/jmsj.2015-001

Kurihara, Y., Murakami, H., and Kachi, M. (2016). Sea surface temperature from the new Japanese geostationary meteorological Himawari-8 satellite. *Geophys. Res. Lett.* 43, 1234–1240. doi: 10.1002/2015GL067159

Kurihara, Y., Sakurai, T., and Kuragano, T. (2006). Global daily sea surface temperature analysis using data from satellite microwave radiometer, satellite infrared radiometer and in-situ observations. *Weather Bull.* 73, 1–18.

Kutsuwada, K., Tanikawa, M., Hagiwara, Y., and Katsumata, T. (2007). Long-term variability of upper oceanic condition in Suruga Bay and its surrounding area. *Oceanogr. Jpn.* 16, 277–290.

Mertz, F., Pujol, M. I., and Faugère, Y. (2018). Product User Manual for Sea Level SLA Products. CMEMS-SL-PUM-008-032-051, COPERNICUS Marine and Environment Monitoring Service. Available online at: https://resources.marine.copernicus.eu/documents/PUM/CMEMS-SL-PUM-008-032-051.pdf (accessed August 13, 2019).

Miyama, T., and Miyazawa, Y. (2014). Short-term fluctuations south of Japan and their relationship with the Kuroshio path: 8- to 36-day fluctuations. *Ocean Dyn.* 64, 537–555. doi: 10.1007/s10236-014-0701-1

Miyama, T., Miyazawa, Y., Varlamov, S., and Hihara, T. (2018). Development of the Kuroshio large meander in 2017. *Kaiyo Monthly* 50, 107–113.

Nakamura, M., and Uehara, K. (2020). *Multi-Layer Temperature Variability at Kurasawa on the Back of Suruga Bay. JpGU–AGU Joint Meeting 2020, AOS18-AOS17*. Available online at: https://confit.atlas.jp/guide/event/jpgu2020/subject/AOS18-P07/detail

Nakamura, Y. (1972). Hydrographic studies in Suruga Bay, II—The flowing at the surface in the inner part. *Bull. Coast. Oceanogr.* 9, 44–53.

Nakamura, Y. (1982). Oceanographic feature of Suruga Bay from view point of fisheries oceanography. *Bull. Shizuoka Pref. Fish. Exp. Stn.* 17, 1–153.

Nakamura, Y., and Muranaka, H. (1979). Temporal fluctuation of oceanographic structure in Suruga Bay and Enshu-Nada. *Bull. Jpn. Soc. Fish. Oceanogr.* 34, 128–133.

Niki, M., Katsumata, T., and Sugimoto, T. (2014). Study on the estimation of harmonic analysis method using ADCP data measured by regular ferry. *J. Jpn. Soc. Civil Eng.* 70, I_486–I_490. doi: 10.2208/kaigan.70.I_486

Niki, M., Sugimoto, T., Katsumata, T., and Sakaguchi, A. (2011). Field observation for spreading of Fuji River water in the inner part of Suruga Bay. *J. Jpn. Soc. Civil Eng.* 67, I_346–I_350. doi: 10.2208/kaigan.67.I_346

Ramp, S. R., Barrick, D. E., Ito, T., and Cook, M. S. (2008). Variability of the Kuroshio Current south of Sagami Bay as observed using long-range coastal HF radars. *J. Geophys. Res.* 113:C06024. doi: 10.1029/2007JC004132

Sato, K. (1967). *On the sea conditions in Suruga Bay*. (Tokyo: Maritime Safety Agency), 124.

Sugimoto, S., Qiu, B., and Kojima, A. (2020). Marked coastal warming off Tokai attributable to Kuroshio large meander. *J. Oceanogr.* 76, 141–154. doi: 10.1007/s10872-019-00531-8

Sugimoto, S., Qiu, B., and Schneider, S. (2021). Local atmospheric response to the Kuroshio large meander path in summer and its remote influence on the climate of Japan. *J. Clim.* 34, 3571–3589. doi: 10.1175/JCLI-D-20-0387.1

Takeuchi, K., and Hibiya, T. (1997). Numerical simulation of baroclinic tidal currents in Suruga Bay and Uchiura Bay using a high resolution level model. *J. Oceanogr.* 53, 539–552.

Tanaka, K., Michida, Y., and Komatsu, T. (2007). A numerical experiment on ocean circulations forced by seasonal winds in Suruga Bay. *Coast. Mar. Sci.* 31, 30–39.

Tanaka, K., Michida, Y., and Komatsu, T. (2008). Numerical experiments on wind-driven circulations and associated transport processes in Suruga Bay. *J. Oceanogr.* 64, 93–102. doi: 10.1007/s10872-008-0007-3

Tanaka, K., Michida, Y., and Komatsu, T. (2010). Impact of sporadically enhanced river discharge on the climatological distribution of river water in Suruga Bay. *Coast. Mar. Sci.* 34, 1–6.

Tanaka, K., Michida, Y., Komatsu, T., and Ishigami, K. (2009). Spreading of river water in Suruga Bay. *J. Oceanogr.* 65, 165–177. doi: 10.1007/s10872-009-0016-x

Tsujino, H., Nakano, H., Sakamoto, K., Urakawa, S., Hirabara, M., Ishizaki, H., et al. (2017). *Reference manual for the Meteorological Research Institute Community Ocean Model version 4 (MRI.COMv4). Tech. Rep. 80*. Tsukuba: Meteorological Research Institute. doi: 10.11483/mritechrepo./80

Tsujino, H., Urakawa, S., Nakano, H., Small, R. J., Kim, W. M., Yeager, S. G., et al. (2018). JRA-55 based surface dataset for driving ocean-sea-ice models (JRA55-do). *Ocean Modell.* 130, 79–139. doi: 10.1016/j.ocemod.2018.07.002

Usui, N., Tsujino, H., Nakano, H., and Matsumoto, S. (2013). Long-term variability of the Kuroshio path south of Japan. *J. Oceanogr.* 69, 647–670. doi: 10.1007/s10872-013-0197-1

Usui, N., Wakamatsu, T., Tanaka, Y., Hirose, N., Toyoda, T., Nishikawa, S., et al. (2017). Four-dimensional variational ocean reanalysis: a 30-year high-resolution dataset in the western North Pacific (FORA-WNP30). *J. Oceanogr.* 73, 205–233. doi: 10.1007/s10872-016-0398-5

Conflict of Interest: The authors declare that the research was conducted in the absence of any commercial or financial relationships that could be construed as a potential conflict of interest.

Publisher's Note: All claims expressed in this article are solely those of the authors and do not necessarily represent those of their affiliated organizations, or those of the publisher, the editors and the reviewers. Any product that may be evaluated in this article, or claim that may be made by its manufacturer, is not guaranteed or endorsed by the publisher.

Copyright © 2021 Toyoda, Sakamoto, Usui, Hirose, Tanaka, Katsumata, Takahashi, Niki, Kutsuwada, Miyama, Nakano, Urakawa, Komatsu, Kawakami and Yamanaka. This is an open-access article distributed under the terms of the Creative Commons Attribution License (CC BY). The use, distribution or reproduction in other forums is permitted, provided the original author(s) and the copyright owner(s) are credited and that the original publication in this journal is cited, in accordance with accepted academic practice. No use, distribution or reproduction is permitted which does not comply with these terms.

frontiers in Marine Science

ORIGINAL RESEARCH
published: 11 October 2021
doi: 10.3389/fmars.2021.711832

Dynamics of Nutrients and Colored Dissolved Organic Matter Absorption in a Wetland-Influenced Subarctic Coastal Region of Northeastern Japan: Contributions From Mariculture and Eelgrass Meadows

Tomonori Isada[1], Hiroya Abe[2,3], Hiromi Kasai[4] and Masahiro Nakaoka[1]*

[1] Akkeshi Marine Station, Field Science Center for Northern Biosphere, Hokkaido University, Akkeshi, Japan, [2] Graduate School of Environmental Science, Hokkaido University, Sapporo, Japan, [3] Biodiversity Division, National Institute for Environmental Studies, Tsukuba, Japan, [4] Fisheries Resources Institute, Japan Fisheries Research and Education Agency, Kushiro, Japan

OPEN ACCESS

Edited by:
Hiroaki Saito, The University of Tokyo, Japan

Reviewed by:
Dimosthenis Traganos, German Aerospace Center, Helmholtz Association of German Research Centres (HZ), Germany
Joji Ishizaka, Nagoya University, Japan
Jeonghyun Kim, Jeju National University, South Korea

***Correspondence:**
Tomonori Isada
t-isada@fsc.hokudai.ac.jp

Specialty section:
This article was submitted to Coastal Ocean Processes, a section of the journal Frontiers in Marine Science

Received: *19 May 2021*
Accepted: *16 September 2021*
Published: *11 October 2021*

Citation:
Isada T, Abe H, Kasai H and Nakaoka M (2021) Dynamics of Nutrients and Colored Dissolved Organic Matter Absorption in a Wetland-Influenced Subarctic Coastal Region of Northeastern Japan: Contributions From Mariculture and Eelgrass Meadows. Front. Mar. Sci. 8:711832. doi: 10.3389/fmars.2021.711832

Coastal oceans interacting with terrestrial ecosystems play an important role in biogeochemical cycles. It is therefore essential to research land–ocean interactions for further understanding of the processes influencing nutrients dynamics in coastal areas. We investigated the seasonal and spatial distribution of nutrient concentrations and light absorption coefficients of colored dissolved organic matter (CDOM), non-algal particles (NAP), and phytoplankton in a wetland-influenced river–eelgrass meadows–coastal waters continuum in the protected and semi-enclosed coastal sea of Akkeshi-ko estuary (AKE) and Akkeshi Bay (AB), Japan from April 2014 to February 2015. The mixing dilution lines of the CDOM absorption coefficient at 355 nm [$a_{CDOM}(355)$] relative to salinity predicted by two end-members between freshwater and coastal water showed conservative mixing in AB. Silicate concentrations were significantly correlated with salinity and $a_{CDOM}(355)$ in AB in each month except for December 2014. These results suggest that silicate and CDOM in AB primarily originates from wetland-influenced river discharge. However, samples collected from the eelgrass meadows of AKE, where mariculture is developed, showed non-conservative mixing of silicate concentrations and $a_{CDOM}(355)$ with salinity except for June 2014. Elevated phosphate concentrations, probably released from sediments, were also found in the eelgrass meadows of AKE, especially during summer. These results suggest that the metabolic activities of mariculture and seagrass ecosystem significantly contribute to the nutrient cycles and CDOM absorption in AKE and to the distinct water-mass systems inside and outside AKE. The relative absorption properties of NAP [$a_{NAP}(443)$], phytoplankton [$a_{ph}(443)$], and $a_{CDOM}(443)$ showed that CDOM is the main factor affecting the light distribution in AKE. However, the relative absorption properties varied seasonally in AB because of spring and autumn phytoplankton blooms and ice cover during winter. Significant relationships were observed between the Secchi disk depth (Z_{SD}), $a_{NAP}(443)$, and

$a_{CDOM}(443)$. Chl *a* concentration and $a_{ph}(443)$ were not good indicators for predicting Z_{SD} in our study region. These results suggest that incorporating inherent optical properties and CDOM from mariculture and seagrass ecosystem into ecosystem models could improve predictions of light distribution along the freshwater–eelgrass–coastal waters continuum in optically complex coastal waters.

Keywords: colored dissolved organic matter (CDOM), inherent optical properties (IOPs), Secchi disk, wetland, seagrass, mariculture, blue carbon, optically complex coastal waters

INTRODUCTION

Coastal oceans account for approximately 7–10% of the ocean's surface, but contribute significantly to biogeochemical cycles (Walsh, 1991; Borges, 2005; Muller-Karger et al., 2005). The coastal ocean also provides important ecosystem services, including carbon burial in salt marshes (Duarte et al., 2005; Zedler and Kercher, 2005) and nursery habitats for many commercially valuable fish and carbon stocks (i.e., blue carbon) in seagrass beds (Fourqurean et al., 2012; Bertelli and Unsworth, 2014; Macreadie et al., 2019). However, the extent of coastal wetlands (Hu et al., 2017a,b) and seagrass beds (Waycott et al., 2009) is declining due to various anthropogenic activities. Coastal oceans are formed by the interconnection among several distinct ecosystems, such as rivers, coastal wetlands, including saltmarshes and seagrass meadows, estuaries, and the continental shelf (Hedges et al., 1997; Duarte et al., 2005; Bauer et al., 2013). It is therefore essential to research land–ocean interactions and the processes influencing the sources, sinks, exchange, and fate of nutrients in coastal areas.

In coastal areas, nutrients and particulate and dissolved organic matter (DOM) are transported from the land to the ocean through rivers (Blough et al., 1993; Hedges et al., 1997; Canuel and Hardison, 2016). Silicate chemical weathering is one of the most importance process for transporting dissolved silicate from land to coastal areas via rivers (Tréguer et al., 1995; Tréguer and De La Rocha, 2013). Especially, wetland ecosystems are large reservoirs of silicate and important places for silicate transport to the adjacent estuary (Struyf and Conley, 2009). Therefore, the relationship between salinity and silicate concentration is used to interpret conservative mixing between freshwater and seawater in coastal areas (e.g., Zhang et al., 2020). DOM is one of the largest carbon pools in most aquatic ecosystems (Ogawa and Tanoue, 2003; Hansell and Carlson, 2014). The portion of DOM that exhibits strong absorption in the ultraviolet (UV) and blue visible wavebands in water is defined as colored dissolved organic matter (CDOM) (Bricaud et al., 1981; Nelson and Seigel, 2013). CDOM mainly consists of fulvic and humic acids originating from soils, terrestrial land plants, and wetlands (Coble, 2007). In particular, wetlands provide an important source of DOM and CDOM from terrestrial to coastal environments (Yamashita et al., 2010; Tzortziou et al., 2011, 2015; Wagner et al., 2015; Najjar et al., 2018). The optical absorption properties of CDOM [$a_{CDOM}(\lambda)$] can be used to identify different sources of DOM and dissolved organic carbon (DOC) along estuarine salinity gradients and are a valuable tool for tracing the influence of river discharge on coastal ecosystems (Coble, 2007; Stedmon and Nelson, 2014). The slope parameters of $a_{CDOM}(\lambda)$ at 275–295 nm ($S_{275-295}$) and 350–400 nm ($S_{350-400}$), as well as the ratio of the two spectral slope parameters ($S_R = S_{275-295}/S_{350-400}$), are used as indicators of CDOM history in response to biological and photochemical changes (Helms et al., 2008; Fichot and Benner, 2012). CDOM also plays an important role in many biological and photochemical processes of the carbon cycle in aquatic environments. For example, the characteristics of UV-absorbing CDOM can protect UV-sensitive aquatic organisms (Tedetti and Sempéré, 2006), but can also alter and reduce the water transparency and intensity and spectral distribution of light in the water column (IOCCG, 2000). Thus, variability in nutrients, CDOM, and suspended sediments from rivers to coastal waters could affect the photosynthesis and photoacclimation strategies of primary producers, including seagrass (Waycott et al., 2005; Tanaka and Nakaoka, 2007; Park et al., 2021) and phytoplankton (Isada et al., 2013; Urtizberea et al., 2013).

The Bekanbeushi wetlands and Akkeshi-ko estuary (AKE), designated as wetland sites of international importance under the Ramsar Convention (Ramsar Information Sheet [RIS], 2005), are located in the eastern part of Hokkaido, Japan (**Figure 1**). The northern part of AKE is connected to the mouth of the Bekanbeushi River, which is a cold-temperate wetland-influenced river. In contrast, the southwestern part of AKE is connected to Akkeshi Bay (AB), which is affected by the Oyashio Current, a cold western boundary current in the western subarctic Pacific (Yasuda, 2003; Isada et al., 2019). The shallow areas of AKE are covered with eelgrass (*Zostera marina*) meadows. Additionally, mariculture of Manila clams and Pacific oysters is currently prospering in both AKE and AB (Hasegawa et al., 2014, 2015). Thus, the Akkeshi watershed is characterized by several distinct ecosystems: the Bekanbeushi wetland/river, salt marshes, eelgrass meadows, oyster and Manila clam mariculture, and the coastal waters of the Oyashio Current, as well as ice cover in AKE during winter (**Figure 1**). Maie et al. (2014) conducted snapshot observations of the DOC concentration and optical properties of CDOM at the mouth of AKE along the lower salinity range (salinity < 10) during summer, and suggested plankton and/or submerged aquatic vegetation as additional sources besides terrestrial inputs. Moreover, recent studies have shown the contribution of aquaculture as a source of CDOM in the water column (Zhang et al., 2018; Tanaka et al., 2019). Therefore, eelgrass meadows and mariculture in AKE may provide key CDOM cycles in the Akkeshi watershed. However, the seasonal and spatial distribution of nutrients and CDOM from the river through the brackish AKE to AB and the relationships between

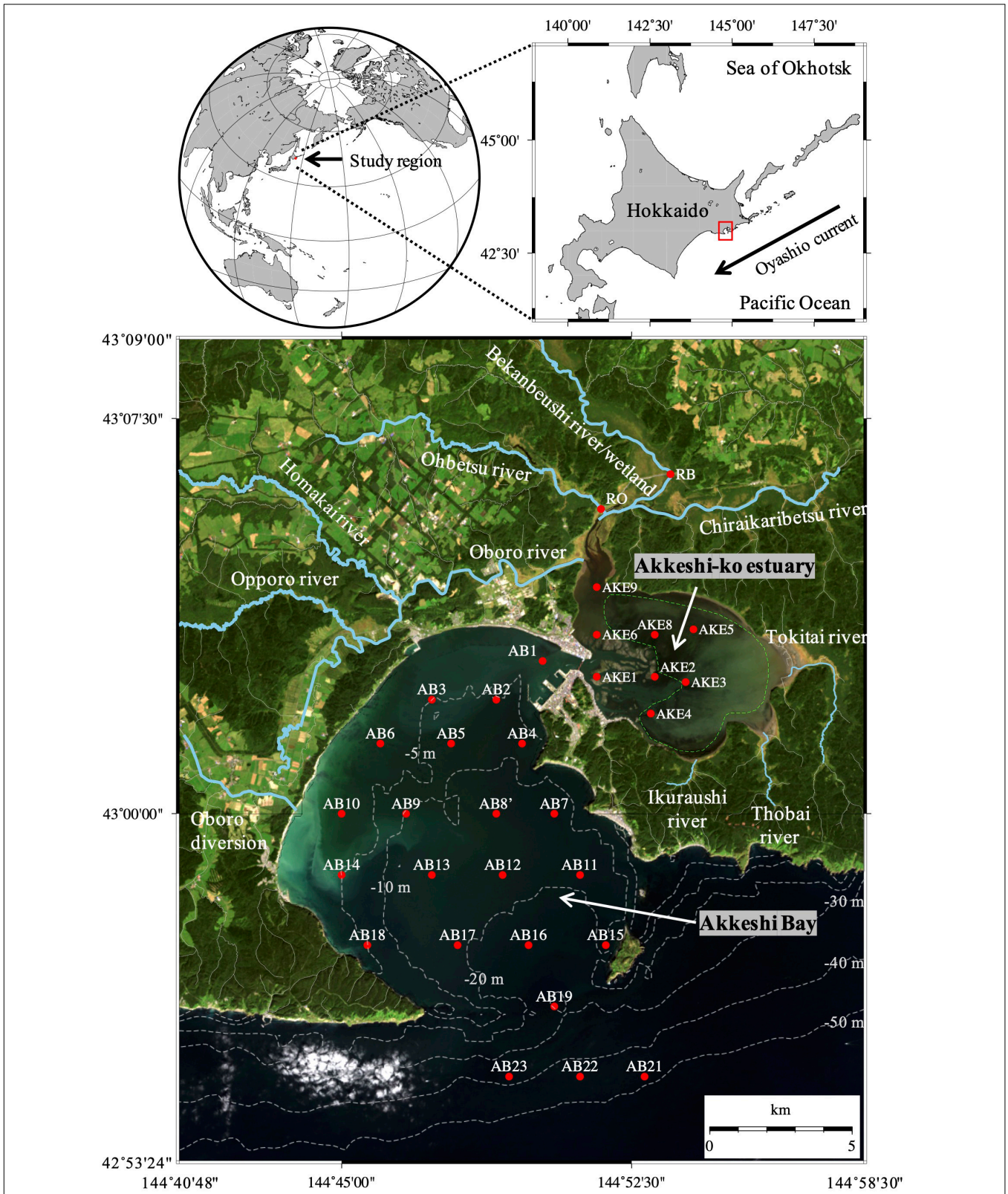

FIGURE 1 | Sampling stations in the rivers (RO and RB), Akkeshi-ko estuary (AKE), and Akkeshi Bay (AB) superimposed on a quasi-true color image derived from Landsat 8 (USGS/NASA) on September 22, 2014. Area enclosed by the green dashed line in AKE represents the eelgrass (*Zostera marina*) meadow after Hasegawa et al. (2008).

nutrients and light absorption properties have not yet been fully evaluated.

Therefore, the objectives of this study are to: (1) characterize seasonal and spatial changes in the optical absorption properties of CDOM, phytoplankton, and non-algal particles (NAP) as a function of temperature, salinity, nutrients, and water transparency along the river–salt marsh–eelgrass meadows–coastal waters continuum in the semi-enclosed coastal sea of AKE and AB, Japan; and (2) identify the factors controlling water transparency in the water column of the Akkeshi watershed. The importance of integrating light absorption properties and CDOM from mariculture and eelgrass ecosystem into ecosystem models for predicting the intensity and spectral distribution of light in optically complex coastal waters is also discussed.

MATERIALS AND METHODS

Site Description

The Bekanbeushi wetland is the second largest wetland in Japan and includes the 43-km-long Bekanbeushi River, which is a cool-temperate river. The Bekanbeushi River runs through low moorland and is connected with the brackish water of AKE in the semi-enclosed coastal area (**Figure 1**). These regions (total area of 527.7 km^2) were designated as a Ramsar wetland site in June 1993 (Ramsar Information Sheet [RIS], 2005) and a Quasi-National Park of Japan in March 2021. Although the upper stream of the catchment has experienced periods of deforestation (Inukai and Nishio, 1937), the Akkeshi watershed has largely preserved the natural characteristics of forests and wetlands because of its protected status, which is attributed to strong leadership from Akkeshi Town Government and the engagement of citizens and interest groups (Fletcher et al., 2011). The surface area of AKE is approximately 35 km^2, and the water depth in most parts is typically less than 2 m. Most of AKE is covered with eelgrass, i.e., *Zostera marina* (**Figure 1**). From December to March, AKE and the rives are covered with ice. The Akkeshi watershed has a microtidal regime, and the tidal ranges during the spring and neap tides are approximately 1.2 and 0.7 m, respectively. AKE is connected to AB by a narrow channel 500 m wide and 10 m deep. The south of Akkeshi Bay is open to the western subarctic Pacific, and influenced by the cold Oyashio Current (Yasuda, 2003).

Sampling

Water sampling was conducted at eight stations in AKE and 22 stations in AB from April 2014 to February 2015 on the research boats *Etopirika*, *Umiaisa,* and TR/V *Misago Maru* (**Figure 1**). Before water sampling, vertical profiles of temperature and salinity were measured with a conductivity, temperature, and depth (CTD) instrument (RINKO-Profiler, ASTD 102, JEF Advantech Inc.), with recording at 0.1-m intervals. In AB, water transparency in the water column was measured using a Secchi disk. The Secchi disk depth (Z_{SD}, m) was defined as the depth of the disk when it was no longer viewable by an observer at the surface. In this study, Z_{SD} was measured at 0.5-m intervals. Samples for subsequent analysis of nutrients, chlorophyll *a* (Chl *a*) concentrations, and light absorption coefficients of non-algal particles [$a_{NAP}(\lambda)$], phytoplankton [$a_{ph}(\lambda)$], and CDOM [$a_{CDOM}(\lambda)$] at the surface were collected using an acid-clean bucket. Sampling for the analysis of nutrients and $a_{CDOM}(\lambda)$ in the Bekanbeushi (RB) River was also conducted from April to November 2014, excluding August, when samples of $a_{CDOM}(\lambda)$ were taken only from Ohbetsu (RO) River. The salinity at both stations was assumed to be zero (Nagao et al., 2016).

Nutrient Concentration

Samples for nutrient analysis (50 mL) were filtered through a 0.45-μm syringe filter (ADVANTEC MFS, Inc.) and stored at −80°C in a deep freezer prior to analysis. Nitrates and nitrites (hereafter denoted as nitrates), phosphate, and silicate concentrations were measured with a BL-Tec autoanalyzer (QuAAtro) and a BRAN + LUEBBE autoanalyzer (TRACCS 800). Nutrient concentrations measured in this study were quality controlled against reference material for nutrients in seawater (RMNS) (KANSO TECHNOS CO., Ltd.) (Aoyama et al., 2012).

Chlorophyll *a* Concentration

Samples (120–200 mL) were filtered through glass-fiber filters (Whatman GF/F, 25 mm diameter) under a gentle vacuum (<0.013 MPa). The filters were folded in half, blotted with filter paper, and soaked in 6 mL of *N,N*-dimethylformamide (FUJIFILM Wako Pure Chemical Corporation, Ltd.) in a Fisherbrand™ Disposable borosilicate glass tubes (Fisher Scientific) at –20°C for more than 24 h (Suzuki and Ishimaru, 1990). The Chl *a* concentration was determined using a Turner Designs fluorometer (Model 10-AU) according to the non-acidification method of Welschmeyer (1994).

Particle and Colored Dissolved Organic Matter Absorption

Water samples (200–1,000 mL) for the measurement of particle absorption were filtered through glass-fiber filters (Whatman GF/F, 25 mm diameter) under gentle vacuum pressure (<0.013 MPa). The filters were immediately analyzed on land. The optical density of all particles (OD_p) was measured from 350 to 750 nm at 1-nm intervals using a double beam spectrophotometer (UV-2600, Shimadzu) equipped with an integrated sphere (ISR-2600, Shimadzu) following the glass-fiber filter technique of Kishino et al. (1985). A blank filter wetted with filtered seawater was used as a baseline correction. Next, the filters containing particles were soaked in a methanol solution to extract phytoplankton pigments. The extracted filters were then sufficiently rinsed with filtered seawater and measured to obtain the optical densities of non-algal particles (OD_{NAP}). Correction for the path length amplification effect for the measured OD_p and OD_{NAP} values was performed using the equation of Stramski et al. (2015), which converted these values to absorption coefficients for particles [$a_p(\lambda)$] and non-algal particles [$a_{NAP}(\lambda)$]. The absorption coefficients of phytoplankton [$a_{ph}(\lambda)$] were obtained by subtracting $a_{NAP}(\lambda)$ from $a_p(\lambda)$.

For the measurement of $a_{CDOM}(\lambda)$, water samples were filtered into acid-cleaned amber glass bottles using 0.2-μm

Nuclepore Trach-Etch membranes (Whatman, 47 mm diameter) under low vacuum pressure (<0.013 MPa). The optical density of CDOM [$OD_{CDOM}(\lambda)$] was measured in a 10-cm quartz cylinder cell (Shimadzu) from 250 to 750 nm at 1-nm intervals using a double beam spectrophotometer (UV-2600, Shimadzu) with reference to Milli-Q water. A baseline correction for the $OD_{CDOM}(\lambda)$ spectrum was made following the method described in Babin et al. (2003). Finally, the measured $OD_{CDOM}(\lambda)$ values were converted into absorption coefficients for CDOM [$a_{CDOM}(\lambda)$] using the following equation:

$$a_{CDOM}(\lambda) = 2.303 OD_{CDOM}(\lambda)/0.1 \quad (1)$$

where 2.303 is a factor for converting between $\log_{10}$ and $\log_e$, and 0.1 is the optical path length (m). We also estimated the spectral slope parameter (S) of CDOM for wavelengths of 275–295 nm ($S_{275-295}$) and 350–400 nm ($S_{350-400}$), as well as their ratio (slope ratio, $S_R = S_{275-295}/S_{350-400}$) following the methods of Helms et al. (2008) and Fichot and Benner (2012).

In this study, $a_{CDOM}(355)$ was used as a tracer of river discharge and CDOM abundance. To characterize the dominant absorption component, $a_{CDOM}(443)$, $a_{NAP}(443)$, and $a_{ph}(443)$ were selected because of an absorption peak of chlorophyll pigments at 443 nm and ocean color remote sensing application. The values of $a_{CDOM}(443)$ were linearly correlated with $a_{CDOM}(355)$ in this study ($y = 0.2258x + 0.0062$, $R^2 = 0.995$, $n = 265$).

Statistical Analyses

The differences in temperature, salinity, Chl *a* concentration, and nutrient concentrations between AKE and AB in each month were evaluated using the Wilcoxon rank sum test. The relationships between nutrients, environmental variables (temperature, salinity, and Chl *a* concentration), and light absorption properties [$a_{CDOM}(355)$, $a_{CDOM}(443)$, $a_{ph}(443)$, $a_{NAP}(443)$] in AKE and AB were evaluated using the non-parametric Kendall rank correlation coefficient (τ). In this study, a p-value less than 0.01 is defined as statistically significant. The data with small sample size ($n < 5$) were eliminated for the Kendall rank correlation analysis. The linear regression analysis was performed to examine conservative mixing between salinity and $a_{CDOM}(355)$ in AKE and AB samples and to calculate the mixing lines by two end-members between freshwater and coastal water. The relationships among water transparency (Z_{SD}), Chl *a* concentrations, and optical absorption properties in AB were evaluated using linear regression of the log-transformed power law function. All statistical analyses were conducted with the R software v. 4.1.1 (R Core Team, 2021) with exactRankTests (Hothorn and Hornik, 2021) and psych (Revelle, 2021) packages.

RESULTS

Hydrographic Conditions of the Akkeshi Watershed

The hydrographic conditions in AKE and AB during this study period showed remarkable seasonal and spatial changes in temperature and salinity (**Table 1** and **Figure 2**). A high to low spatial gradient of sea surface temperature (SST) was found from AKE to AB during April to September 2014 (Wilcoxon rank sum test; each month: $p < 0.001$) (**Figures 2A–F**). In contrast, low to high SST gradients were found from AKE to AB in October and December 2014 and January 2015 (Wilcoxon rank sum test; each month: $p < 0.01$) (**Figures 2G,I,J**). No significant difference in SST between AKE and AB was found in November 2014 (Wilcoxon rank sum test; $p = 0.07$) (**Figure 2H**). The SST of AB in February 2015 was less than 0°C. Salinity at the surface (SSS) showed low to high spatial gradients from AKE to AB throughout the study period due to the influence of river discharge (Wilcoxon rank sum test; each month: $p < 0.01$).

Nitrates remained from April to June 2014 in AKE due to fresh water from snowmelt, but were almost depleted from April to August of 2014 in AB (**Table 1** and **Figures 3A,B**). After August 2014, the nitrate concentrations in both AKE and AB gradually increased. Higher nitrate concentrations were found in AKE and AB in January and February 2015. Phosphate concentrations in AKE showed seasonal changes, with the highest concentrations in September 2014 (**Figure 3C**). The phosphate concentrations in AB relatively remained stable from April to August 2014 then increased slightly after August 2014 (**Figure 3D**). The phosphate concentrations in AB were significantly higher than those in AKE in April 2014 and January 2015 (Wilcoxon rank sum test; each month: $p < 0.01$). In contrast, the phosphate concentrations in AKE were significantly higher than those in AB in July, September, and October 2014 (Wilcoxon rank sum test; each month: $p < 0.01$). Silicates were not depleted at either station throughout the study period (**Figures 3E,F**). The silicate concentrations in AKE were higher than those in AB throughout the study period (Wilcoxon rank sum test; each month: $p < 0.01$) except for June 2014. To better understand the potentially limiting nutrients for primary production of phytoplankton, nutrient ratios were compared to the Redfield ratio (N:P:Si = 16:1:16; Redfield, 1958) (**Figures 3G,H**). Higher Si:N ratios (>1) relative to the Redfield ratio were found in almost all samples throughout the study period. Nutrient concentrations in rivers exhibited higher N:P ratios (>16). Although the N:P ratios of some samples taken from AKE and AB in April ($n = 9$), May 2014 ($n = 1$), and January 2015 ($n = 1$) were higher than the Redfield ratio of 16:1, the N:P ratios of all other samples taken in AKE and AB ($n = 228$) fell within the stoichiometric N-limited range.

The Chl *a* concentration in AKE and AB showed more than a 40-fold variation across all seasons. Spring phytoplankton blooms with higher Chl *a* concentrations were found in AB in April 2014 (**Table 1** and **Figure 4A**). Subsequently, Chl *a* concentrations at the surface were low in AB. Spatially heterogeneous Chl *a* concentrations were found in AKE from April to July 2014 and in AB in August 2014 (**Figures 4A–E**). Although Chl *a* concentrations in AKE were significantly higher than those in AB in May 2014 (Wilcoxon rank sum test; $p < 0.001$), the opposite trend was observed from September to October 2014 (Wilcoxon rank sum test; September: $p < 0.001$; October: $p < 0.01$) (**Figures 4F,G**). In other seasons, no significant difference in Chl *a* concentration between AKE and AB was found (**Figures 4A,C,D,H–K**). Secchi disk depths (Z_{SD}) in AB

TABLE 1 | Summary of temperature, salinity, and Chl *a* concentration at the surface and Secchi disk depth (Z_{SD}) during sampling cruises.

Sampling date	Tide status	Temperature (°C)		Salinity		Z_{SD} (m)		Chl *a* (mg m^{-3})	
AKE		**Average ± SD**	**Range**	**Average ± SD**	**Range**	**Average ± SD**	**Range**	**Average ± SD**	**Range**
April 15th, 2014	S, LL	6.6 ± 1.3	4.79–8.06	17.58 ± 3.20	12.48–22.46	–	–	6.02 ± 3.40	1.01–11.21
May 13th, 2014	S-2, LL	13.4 ± 1.7	11.20–15.90	23.06 ± 3.83	14.88–25.48	–	–	4.72 ± 2.75	1.72–9.15
June 17th, 2014	N-2, E	16.1 ± 1.8	14.07–18.40	20.91 ± 1.76	18.89–23.41	–	–	5.62 ± 4.55	0.87–10.80
July 29th, 2014	S+2, E	19.2 ± 2.8	14.76–21.88	24.69 ± 2.70	21.63–28.34	–	–	4.68 ± 3.72	1.01–11.10
August 25th, 2014	–	–	–	–	–	–	–	–	–
September 18th, 2014	N + 2, F	18.5 ± 0.3	18.10–19.08	28.32 ± 1.52	26.22–30.56	–	–	2.79 ± 1.01	1.28–4.31
October 20th, 2014	M, E	12.7 ± 0.4	11.91–13.15	26.42 ± 1.76	23.11–28.82	–	–	2.40 ± 0.73	1.28–3.40
November 19th, 2014	M, F	6.6 ± 1.0	4.92–7.66	29.28 ± 2.50	25.26–31.96	–	–	1.84 ± 0.53	1.07–2.58
December 12th, 2014	N-2, HL	2.5 ± 0.7	1.65–3.65	27.87 ± 2.02	24.28–30.46	–	–	2.82 ± 1.54	1.32–5.88
January 14th, 2015	N + 1, F	0.0 ± 0.6	–0.70 to 0.41	28.16 ± 1.12	24.28–30.46	–	–	1.37 ± 1.04	0.27–2.34
February 12th, 2015	–	–	–	–	–	–	–	–	–
Sampling date		**Temperature (°C)**		**Salinity**		**Z_{SD} (m)**		**Chl *a* (mg m^{-3})**	
AB		**Average ± SD**	**Range**	**Average ± SD**	**Range**	**Average ± SD**	**Range**	**Average ± SD**	**Range**
April 15–16th, 2014	S, F; S + 1, E	2.6 ± 1.0	0.95–5.09	30.11 ± 2.49	20.80–31.51	4.87 ± 0.91	2.5–6.0	8.06 ± 2.15	5.34–12.85
May 13–14th, 2014	S-2, F; S-1, E	8.1 ± 1.5	5.44–11.31	29.98 ± 1.29	25.04–31.37	5.98 ± 2.32	3.0–10.0	1.00 ± 0.72	0.29–3.35
June 17–18th, 2014	N-2, E; N-1, E	11.4 ± 1.9	7.27–13.83	27.97 ± 2.48	22.18–32.15	2.60 ± 1.35	1.5–6.0	2.06 ± 1.15	0.89–6.21
July 29th, 2014	S + 2, F	14.6 ± 1.8	11.94–17.50	31.01 ± 1.15	27.16–32.05	3.09 ± 1.23	1.0–5.0	3.25 ± 1.36	1.57–5.88
August 25th, 2014	S, LL	17.4 ± 1.1	16.31–19.98	30.43 ± 2.19	24.13–32.32	3.69 ± 1.59	1.5–6.0	6.40 ± 3.27	2.77–13.33
September 18–19th, 2014	N + 2, F; M, F	17.3 ± 0.4	16.58–18.09	32.22 ± 0.67	30.10–33.01	5.32 ± 1.75	2.5–8.5	5.76 ± 0.09	4.03–6.99
October 20th, 2014	M, E	13.2 ± 0.1	12.98–13.35	31.28 ± 1.27	28.88–32.80	2.56 ± 1.18	1.0–3.5	4.89 ± 1.25	2.56–6.63
November 19–20th, 2014	M, E; S-2; E	7.5 ± 1.0	5.91–9.13	32.30 ± 0.82	30.96–33.15	4.22 ± 3.62	3.0–13.5	2.20 ± 1.42	0.46–5.72
December 10th, 2014	M, E	5.9 ± 1.0	4.10–6.47	32.47 ± 0.66	31.43–32.94	8.38 ± 1.75	6.5–10.5	1.57 ± 0.59	1.02–2.30
January 14th, 2015	N + 1, HH	0.9 ± 0.4	0.31–1.56	31.89 ± 0.55	31.43–32.94	3.89 ± 1.04	2.0–6.0	0.72 ± 0.27	0.49–1.09
February 12th, 2015	N, F	–0.6 ± 0.2	–0.97 to –0.30	31.63 ± 0.81	28.87–32.20	1.42 ± 0.31	1.0–2.0	1.14 ± 0.26	0.72–1.52

AKE, Akkeshi-ko estuary; AB, Akkeshi Bay; S, spring tide; N, neap tide; M, tide between spring and neap tides; LL, lower low tide; HL, higher low tide; HH, higher high tide; E, ebb tide; F, flood tide; SD, standard deviation. S and N with –1, –2, +1, or +2 represent one or 2 days before and after spring or neap tide.

showed a 10-fold variation across all seasons. Higher values of Z_{SD} were observed in November and December 2014, whereas lower values of Z_{SD} were observed in February 2015 (**Table 1**).

Characteristics of Colored Dissolved Organic Matter Absorption Coefficient and Spectral Slope

The absorption coefficient of CDOM at 355 nm [$a_{CDOM}(355)$] in surface waters showed large spatial gradients from freshwater to coastal waters (**Figure 5**). The values of $a_{CDOM}(355)$ were highest in RB and RO, ranging from 4.454 to 19.210 m^{-1}. These values decreased to 0.510–8.249 m^{-1} in AKE and to 0.258–7.350 m^{-1} in AB. Comparisons of the regression lines between salinity and $a_{CDOM}(355)$ in AKE and AB samples with the mixing lines predicted by two end-members between freshwater and coastal water indicated conservative mixing in $a_{CDOM}(355)$ with salinity from CDOM-rich wetland water to the coastal waters in AB during each month (**Table 2** and **Figure 5**). In contrast, the regression lines in AKE indicated non-conservative mixing in CDOM with salinity. Although the slope and y-intercept of the regression line for AKE samples in April 2014 was about the same values calculated by the mixing line predicted by two end-members, the coefficient of determination (R^2) was low in comparison to the regression line for AB samples (**Table 2**). The spectral slope coefficient ($S_{275-295}$) in the river was lower than that at the AKE and AB sampling stations. The values of $S_{275-295}$ ranged from 0.0114 to 0.0282 nm^{-1} and showed an exponential dependence on salinity (**Figure 6A**). In contrast, $S_{350-400}$, which ranged from 0.0105 to 0.0182 nm^{-1}, showed a lack of dependence on salinity (**Figure 6B**). As a result, S_R increased with increasing salinity along the freshwater–estuary–coastal ocean continuum (**Figure 6C**). However, samples collected from AKE lay outside of the exponential mixing line from river to marine samples.

Relationships Between Nutrients, Environmental Variables, and Light Absorption Properties

The relationships between nutrients, environmental variables, and light absorption properties in AKE were distinct from those in AB (**Tables 3**, **4**). The significant relationships between silicate concentrations and both salinity and $a_{CDOM}(355)$ were found in June 2014 only. No significant relationships between nitrates and phosphate concentrations and any valuables in AKE

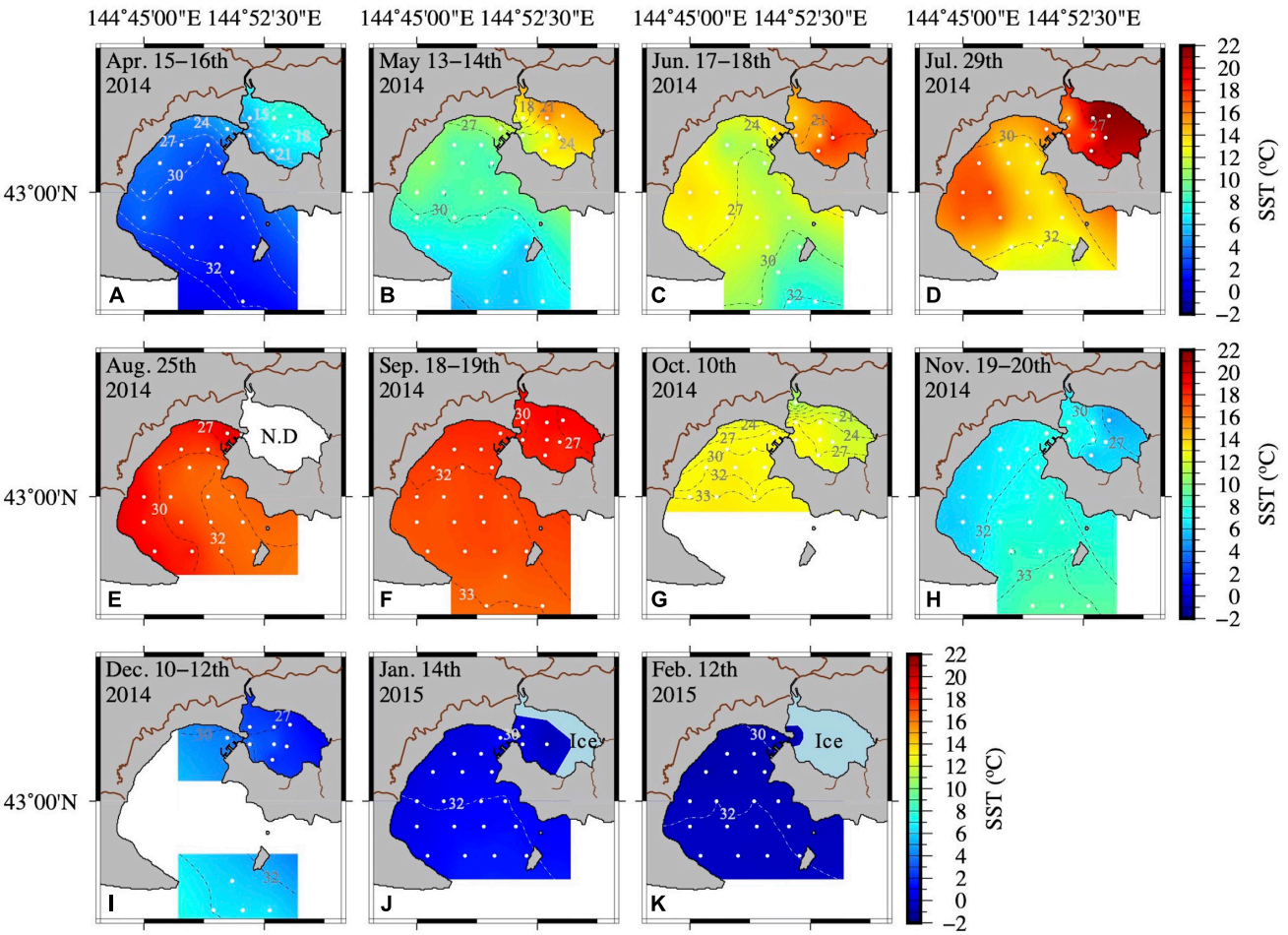

FIGURE 2 | Spatial distribution of seawater temperature and salinity at the surface **(A–K)** from April 2014 to February 2015. Inter- and extrapolation of temperature and salinity were implemented by the General Mapping Tools. White symbols and dashed lines in each figure represent the sampling sites and salinity, respectively.

except for April and November 2014 (**Table 3**). In contrast, silicate concentrations were negatively correlated with salinity and positively correlated with $a_{CDOM}(355)$ and $a_{CDOM}(443)$ in AB during each month except for December 2014 when the sample size was small (**Table 4**). Significant relationships between silicate concentration and temperature in AB were found in April, May, June, August, September, November 2014 and February 2015. Therefore, in addition to the regression analysis between salinity and $a_{CDOM}(355)$ as described above (See section "Characteristics of CDOM Absorption Coefficient and Spectral Slope"), these results indicated conservative mixing between salinity and silicate concentration from the river to the coastal waters at the surface in AB and non-conservative mixing between them in AKE.

Absorption Budget and Correlation to Z_{SD}

To characterize the dominant absorption component, the relative contributions of each absorption parameter to total non-water absorption at 443 nm [$a_{t-w}(443) = a_{NAP}(443) + a_{ph}(443) + a_{CDOM}(443)$] were examined (**Figure 7**). Although $a_{CDOM}(443)$ was the dominant light-absorbing component in AKE, except in December 2014, the relative proportion of each absorption component in AB was highly complex. Phytoplankton [$a_{ph}(443)$] was the main factor affecting light absorption during spring blooms in April 2014. Subsequently, $a_{CDOM}(443)$ dominated the absorption components in May and June 2014. Then, the relative proportion of each absorption component mainly lay within the mixed range of the ternary plot from July 2014 to January 2015; however, [$a_{ph}(443)$] was dominant again at some stations during the autumn blooms in September 2014 (**Figure 7F**). In February 2015, the majority of $a_{NAP}(443)$ values in AB were greater than 50% due to ice cover.

The relationships among water transparency (Z_{SD}), Chl *a* concentrations, and optical absorption properties in AB throughout the study period are shown in **Figure 8**. Although the values of Z_{SD} were not correlated with Chl *a* levels or $a_{ph}(443)$ (**Figures 8A,B**), Z_{SD} was correlated with $a_{NAP}(443)$, $a_{CDOM}(443)$, and a_{Total} (443) (**Figures 8D–F**). No significant relationships were observed between $a_{CDOM}(355)$ and Chl *a* concentration

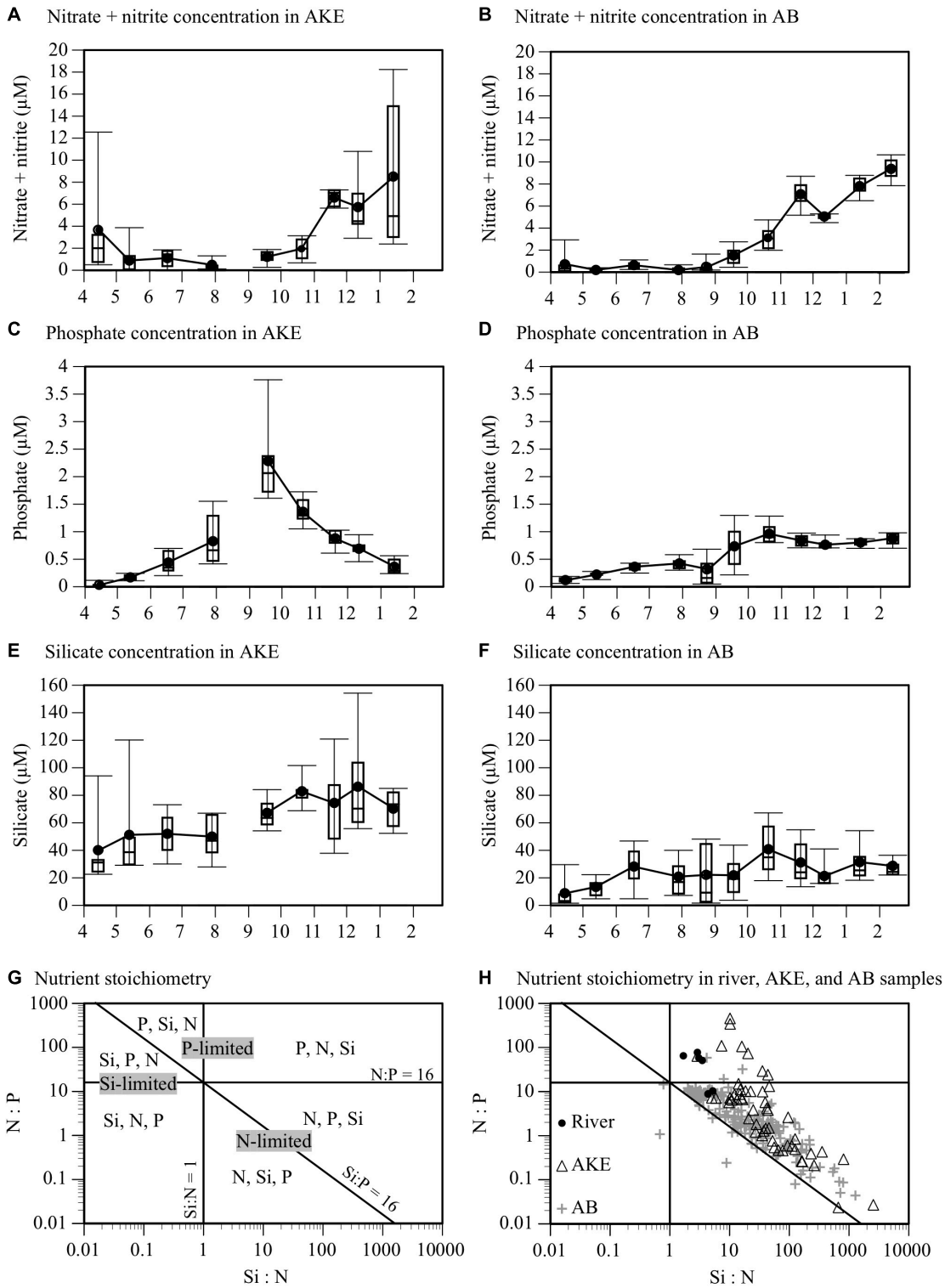

FIGURE 3 | Time-series box plots of **(A,B)** nitrate plus nitrite, **(C,D)** phosphate, and **(E,F)** silicate concentrations in AKE and AB from April 2014 to February 2015. Rectangles, horizontal lines in boxes, black closed circles, and I-bars represent inter-quartile ranges, medians, means, and minimum and maximum values, respectively, except for outliers exceeding 1.5 times the interquartile range. **(G)** Synthetic graph of the N:P:Si nutrient stoichiometric ratio. The vertical (Si:N), horizontal (N:P), and diagonal (Si:P) lines and each area delimited by the lines represent the Redfield ratio (N:P:Si = 16:1:16) and the potential limiting nutrients. Nutrients are given in the order of their limitations for each area determined by the Redfield ratio. **(H)** Scatter plot of N:P:Si ratio at the surface in rivers, AKE, and AB from April 2014 to February 2015.

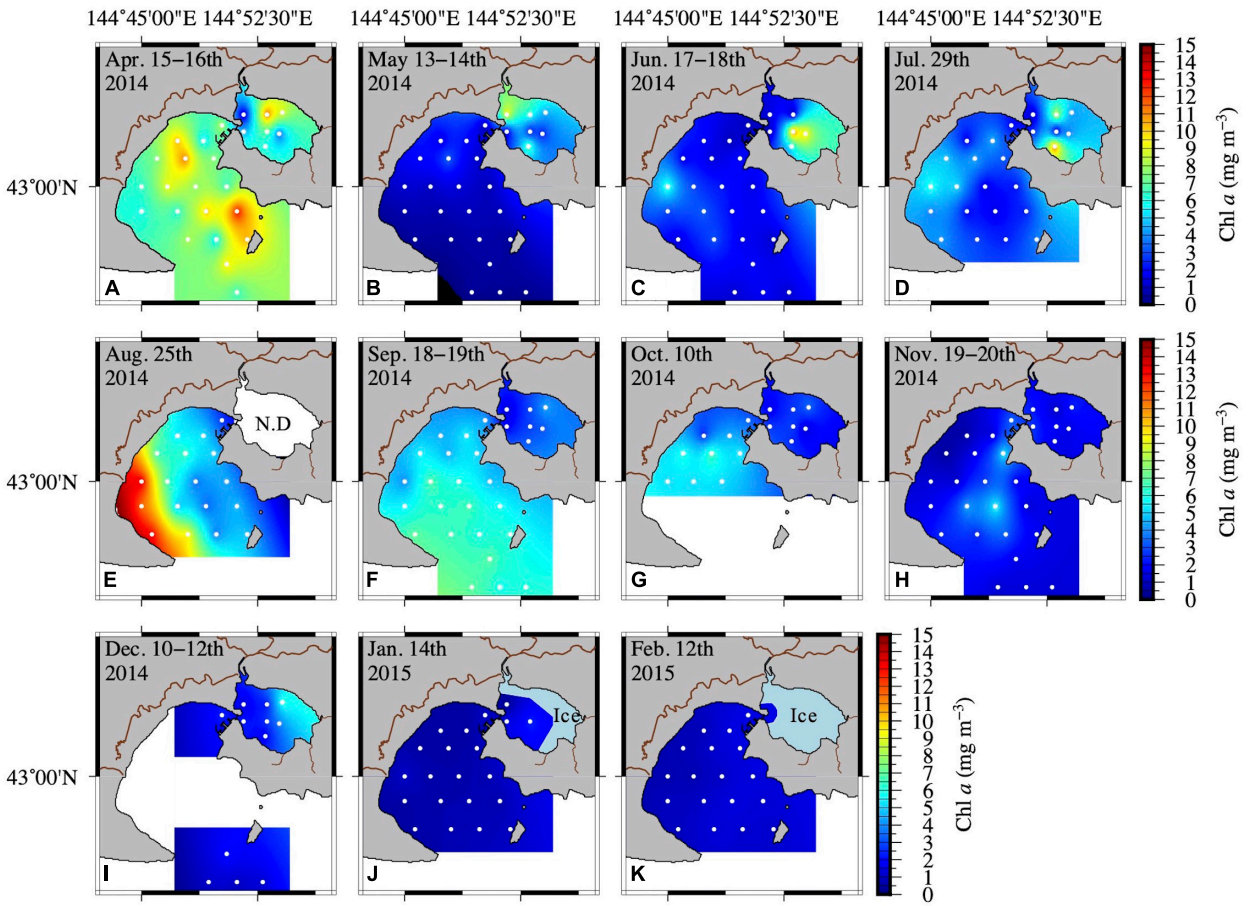

FIGURE 4 | Spatial distribution of Chl *a* concentration at the surface **(A–K)** from April 2014 to February 2015. Inter- and extrapolation of the data were implemented by the General Mapping Tools. White symbols in each figure represent the sampling sites.

(Pearson's product-moment correlation; $r = 0.05$, $p = 0.47$, $n = 192$) or between $a_{CDOM}(443)$ and $a_{ph}(443)$ (Pearson's product-moment correlation; $r = 0.12$, $p = 0.11$, $n = 189$) in AB.

DISCUSSION

Nutrient Cycles

We conducted monthly observations with high spatial resolution in AKE (a Ramsar protected site) and AB in Japan, both of which are affected by river discharge influenced by the second largest wetland (the Bekanbeushi wetland) in Japan. The SST in AKE was higher than that in AB from April to September 2014 because river temperatures increase before sea temperatures in the study region (Nagao et al., 2016). The SST in AB was below 20°C, even in summer, which is consistent with the findings of previous studies (Hasegawa et al., 2015; Momota and Nakaoka, 2018). Nutrient concentrations in most of the rivers samples showed higher N:P and Si:N ratios than the Redfield ratio due to excess nitrate originating from river inputs and the adsorption of phosphate by the soil (Howard-Williams, 1985; Reddy et al., 1999). As a result, the river samples in our study fell into the P-limited region (**Figure 3H**). However, lower N:P ratios than the Redfield ratio were widespread in both AKE and AB, indicating that nitrate is the main factor limiting the growth and photosynthesis of primary producers. Moreover, the phosphate concentrations in AKE were significantly higher than those in AB in July, September, and October 2014 (**Figures 3C,D** and see section "Hydrographic Conditions of the Akkeshi Watershed"). The elevated phosphate concentrations from late spring to summer in AKE (**Figure 3C**) suggested other sources of phosphate, such as phosphate release from the sediment, excretions from mariculture, and different flows of river discharge. Iizumi et al. (1995) also reported a higher phosphate concentration in AKE during the summer. The release of nutrients from sediments to the water column has also been reported in estuaries and seagrass-dominated regions (Iizumi et al., 1982; Cowan et al., 1996; Ziegler and Benner, 1999b). In AKE, eelgrass beds are most abundant from June to August (Hasegawa et al., 2007; Momota and Nakaoka, 2018). Subsequently, the ammonium flux from the sediments to the water column increases during this time (Hasegawa et al., 2008). Nakagawa et al. (2019) used quantitative PCR to investigate the abundance of nitrous oxide

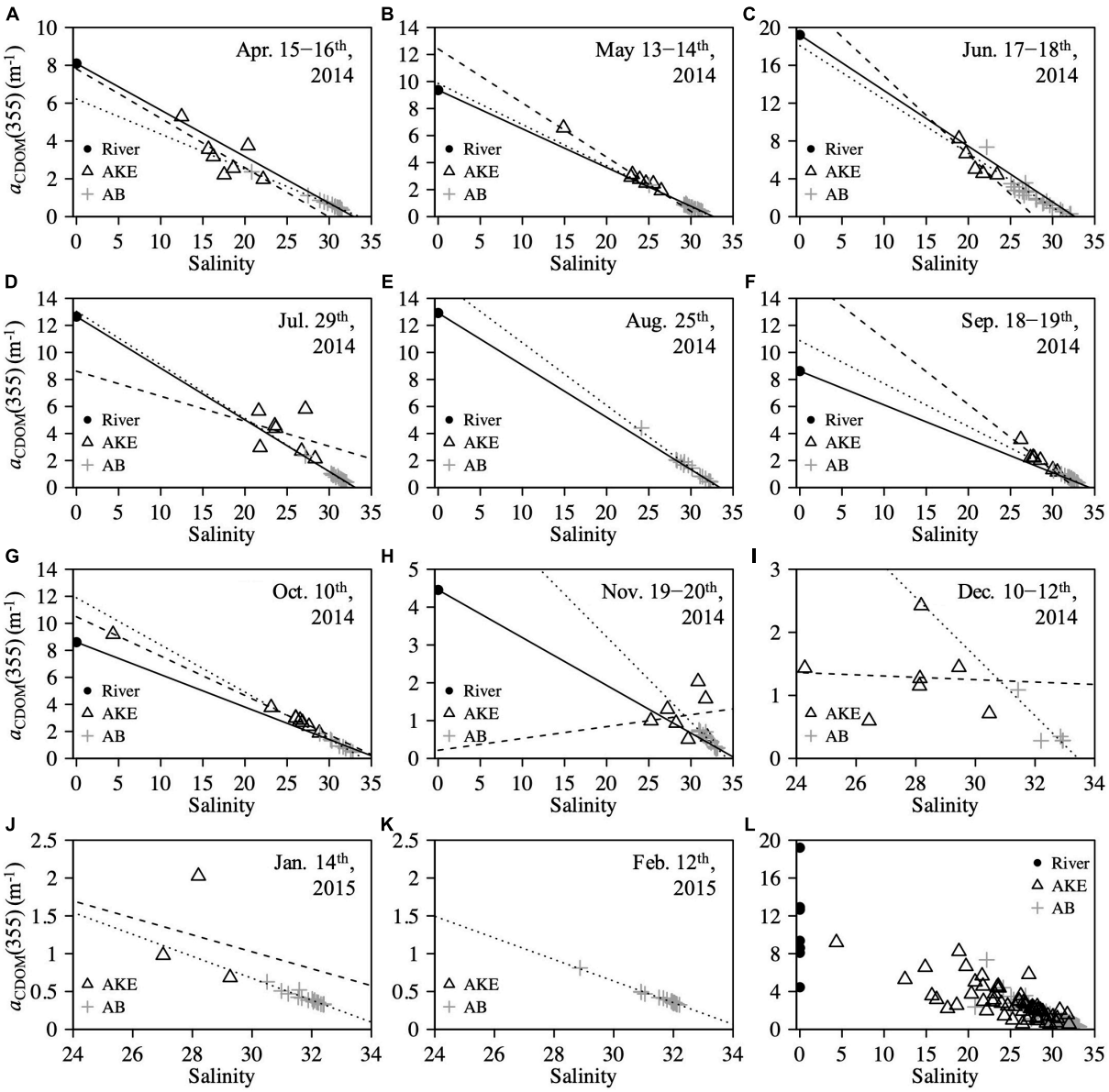

FIGURE 5 | Relationships between salinity and $a_{CDOM}(355)$ at the surface **(A–K)** from April 2014 to February 2015 and **(L)** throughout the study period. Solid line in each figure represents the conservative mixing line of two-end-members between freshwater (RB) and coastal water based on salinity. Sample taken in RO was used as the freshwater end-member in **(E)** August 2014. Dashed and dotted lines represent the regression lines estimated from AKE and AB samples, respectively.

(N_2O)-reducing microorganisms in both *in situ* and cultivated sediments in the non-eelgrass and eelgrass zones of AKE, and showed that the microbiomes in eelgrass meadow sediments contributed to the N_2O sink. Additionally, mariculture of Manila clams and Pacific oysters is well developed in AKE (Hasegawa et al., 2014, 2015). Previous studies on the metabolic activities of clams and oysters have shown that they increase ammonium and phosphorous concentrations in the sediment and water column of mariculture regions (Dame et al., 1989; Bartoli et al., 2001; Nelson et al., 2004; Nizzoli et al., 2006; Welsch et al., 2015). Because the development of the eelgrass canopy contributes to a reduction in current velocity in the shallow areas of AKE (Hasegawa et al., 2008), which in turn led to the decreases in water masses exchange between AKE and AB as well as freshwater, sediments in eelgrass meadows and mariculture could contribute to the increase in phosphate concentration of the water column in the semi-enclosed coastal area of AKE during summer. This could produce the lower N:P ratios in AKE.

Nitrate in AB was almost depleted from spring to summer. Diatom blooms occur every spring in the coastal Oyashio water, leading to decreased nutrient concentrations (Kasai et al., 1997; Saito et al., 2002; Isada et al., 2019). Therefore, water masses with high Chl *a* concentrations and low nutrient concentrations observed in AB in April 2014 (**Figure 4A**)

TABLE 2 | Results of linear regression analysis between salinity and $a_{CDOM}(355)$ in AKE and AB and for two-end-members between freshwater (RB) and coastal water based on salinity.

Month	Area	Slope	y-Intercept	R^2	n
April 2014	AKE	–0.261	7.809	0.544	7
	AB	–0.185	6.217	0.998	19
	Two-endmember	–0.246	8.095	1.000	2
May 2014	AKE	–0.401	12.417	0.986	7
	AB	–0.304	9.861	0.978	22
	Two-endmember	–0.286	9.364	1.000	2
June 2014	AKE	–0.832	23.188	0.803	5
	AB	–0.570	18.078	0.858	22
	Two-endmember	–0.589	19.210	1.000	2
July 2014	AKE	–0.185	8.612	0.118	7
	AB	–0.396	13.042	0.991	18
	Two-endmember	–0.382	12.654	1.000	2
August 2014	AKE	–	–	–	–
	AB	–0.464	15.354	0.987	18
	Two-endmember	–0.386	12.920	1.000	2
September 2014	AKE	–0.486	15.875	0.895	7
	AB	–0.318	10.870	0.977	22
	Two-endmember	–0.251	8.621	1.000	2
October 2014	AKE	–0.291	10.489	0.998	8
	AB	–0.349	11.891	0.993	9
	Two-endmember	–0.240	8.605	1.000	2
November 2014	AKE	0.031	0.216	0.020	7
	AB	–0.225	7.712	0.963	22
	Two-endmember	–0.126	4.454	1.000	2
December 2014	AKE	–0.019	1.822	0.004	7
	AB	–0.469	15.683	0.758	5
	Two-endmember	–	–	–	–
January 2015	AKE	–0.112	4.383	0.032	3
	AB	–0.145	5.023	0.914	18
	Two-endmember	–	–	–	–
February 2014	AKE	–	–	–	–
	AB	–0.143	4.921	0.993	17
	Two-endmember	–	–	–	–

Sample taken in RO was used as the freshwater end-member in August 2014. R^2 and n represent the coefficients of determination and sample size.

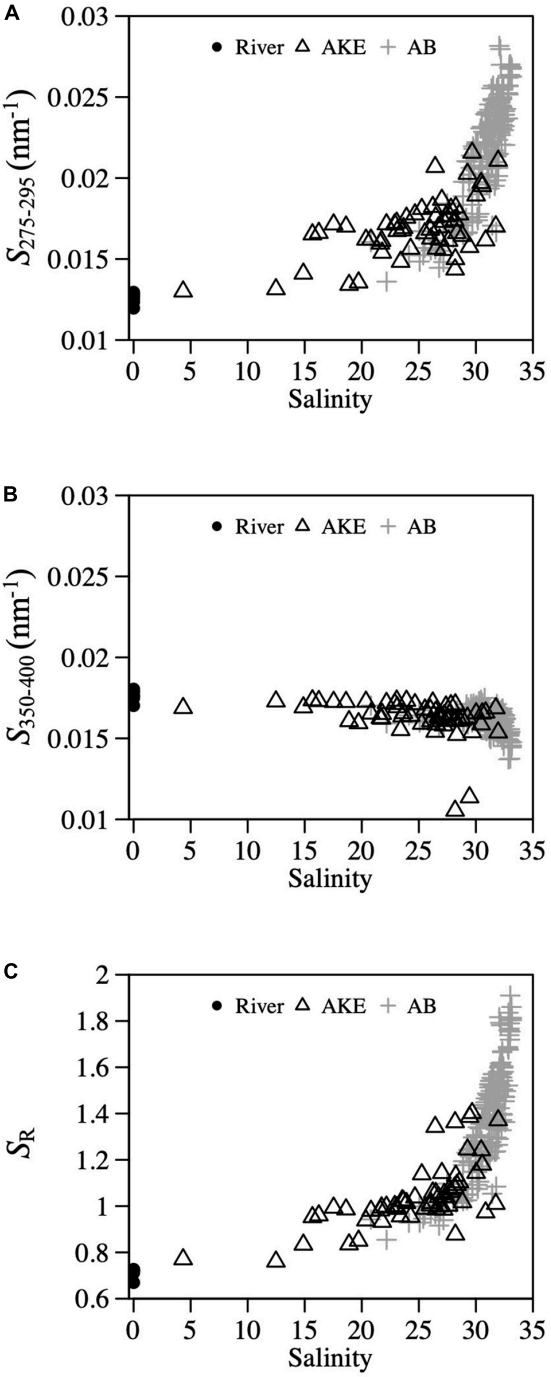

FIGURE 6 | Relationships between salinity and **(A)** $S_{275-295}$, **(B)** $S_{350-400}$, and **(C)** S_R.

indicate nitrate depletion by spring diatom blooms in the bay. Nutrient concentrations in AB from August 2014 to February 2015 gradually increase through strong vertical mixing and remineralization of organic matter (Kasai et al., 1997; Taguchi et al., 1977; Saito et al., 2002), which is consistent with the results obtained in our study.

Influence of River Discharge, Mariculture, and Eelgrass Meadows on the Colored Dissolved Organic Matter Cycle

Conservative mixing between $a_{CDOM}(355)$ and salinity (**Figure 5**) and the strong salinity – silicate concentration – $a_{CDOM}(\lambda)$ relationships in AB (**Table 4**) indicated that silicate and CDOM in AB are primarily terrestrial in origin from wetland-influenced river discharge. Salt marsh and wetlands are the largest source of silicate to coastal area through rivers (Struyf et al., 2006; Struyf and Conley, 2009; Carey and Fulweiler, 2014). Previous studies have shown the significant relationship between salinity and silicate concentration in river estuaries (e.g., Carbonnel et al., 2013; Tedetti et al., 2020; Zhang et al., 2020). In addition, many

TABLE 3 | Kendall rank correlations coefficient (τ) between nutrient concentrations, environmental variables (temperature, salinity, Chl *a* concentration), and light absorption properties at the surface in AKE during sampling cruises.

Month	Nutrients	Temp	Sal	Chl *a*	$a_{CDOM}(355)$	$a_{CDOM}(443)$	$a_{ph}(443)$	$a_{NAP}(443)$
April 2014	Nitrates	0.524	**–0.905**	0.238	0.429	0.429	–0.333	0.810
n = 7	Phosphate	**–0.905**	0.333	–0.810	0.143	0.143	–0.238	–0.238
	Silicate	0.333	**–0.905**	0.048	0.429	0.429	–0.143	0.619
May 2014	Nitrates	–0.400	–0.200	0.200	0.200	0.400	0.200	0.800
n = 5∼7	Phosphate	0.238	–0.143	–0.048	0.238	0.143	–0.048	–0.143
	Silicate	0.238	–0.714	0.333	0.619	0.714	0.143	0.810
June 2014	Nitrates	NA	NA	NA	NA	NA	NA	NA
n = 5	Phosphate	0.600	0.000	0.200	0.000	–0.200	0.200	–0.800
	Silicate	0.000	**–1.000**	–0.800	**1.000**	0.800	–0.800	–0.200
July 2014	Nitrates	–0.048	–0.143	–0.143	0.810	0.810	NA	0.333
n = 7	Phosphate	0.429	–0.429	0.524	0.143	0.143	NA	0.238
	Silicate	–0.048	–0.143	0.048	0.810	0.810	NA	0.524
September 2014	Nitrates	–0.714	0.524	–0.619	–0.619	–0.619	–0.524	–0.524
n = 7	Phosphate	0.238	–0.810	0.905	0.714	0.714	0.810	0.429
	Silicate	–0.143	–0.619	0.524	0.524	0.524	0.429	0.238
October 2014	Nitrates	0.714	0.714	–0.098	–0.714	–0.714	–0.429	0.048
n = 7	Phosphate	0.524	0.524	–0.098	–0.524	–0.333	–0.810	–0.333
	Silicate	–0.333	–0.333	0.098	0.333	0.333	0.238	0.143
November 2014	Nitrates	0.524	0.524	0.048	–0.333	–0.333	–0.143	0.429
n = 7	Phosphate	0.714	0.714	0.048	–0.143	–0.143	0.048	0.429
	Silicate	**–1.000**	**–1.000**	–0.143	0.048	0.048	–0.333	–0.143
December 2014	Nitrates	0.524	–0.238	–0.429	–0.333	–0.333	–0.429	–0.048
n = 7	Phosphate	0.714	0.333	–0.619	0.048	0.048	–0.810	–0.619
	Silicate	–0.238	**–1.000**	–0.048	–0.143	–0.143	0.143	0.333

The values which are significant at the $p < 0.01$ level are in bold.

previous studies have shown strong high to low spatial gradients of CDOM with the increases in salinity in coastal waters (e.g., Ferrari and Dowell, 1998; Rochello-Newall and Fisher, 2002; Del Vecchio and Blough, 2004; Guo et al., 2007) and wetland-influenced estuaries (e.g., Helms et al., 2008; Tzortziou et al., 2011). No significant relationships between $a_{CDOM}(355)$ and Chl *a* concentration or between $a_{CDOM}(443)$ and $a_{ph}(443)$ in AB suggested that (1) the release of CDOM from phytoplankton is small even during spring and autumn phytoplankton blooms in AB and (2) there are no large *in situ* sources or sinks of CDOM within the bay. The exponential dependence of $S_{275-295}$ and S_R on salinity and the constant values of $S_{350-400}$ (**Figure 6**) showed that photobleaching also plays a major role in the regulation of $S_{275-295}$ during transport and mixing from the river to the coastal waters in AB. $S_{275-295}$ is sensitive to photobleaching in comparison to $S_{350-400}$ and thus, the values of $S_{275-295}$ with increase with photobleaching (Helms et al., 2008; Fichot and Benner, 2012; Danhiez et al., 2017). Fichot and Benner (2012) also showed that the values of $S_{275-295}$ is closely related to the average molecular weight of CDOM and lignin. Accordingly, terrestrial CDOM-rich river waters have higher $a_{CDOM}(\lambda)$ and lower values of $S_{275-295}$, which is consistent with our results (**Figure 6A**).

In contrast, non-conservative mixing in $a_{CDOM}(355)$ with salinity was observed in AKE (**Table 2** and **Figure 5**). No significant relationships between silicate concentration and $a_{CDOM}(355)$ were found except for June 2014 (**Table 3**). Changes in the slope parameters of CDOM in AKE were also distinct from those in AB (**Figure 6**), suggesting different mixing processes inside and outside AKE, as well as other potential inputs from mariculture and eelgrass meadows within AKE. Some studies have shown the importance of seagrass meadows as a DOM and CDOM source in water columns (Ziegler and Benner, 1999a; Stabenau et al., 2004; Tanaka et al., 2019). Based on the analysis of DOC-specific UV absorbance at 254 nm ($SUVA_{254}$) and the fluorescence excitation-emission matrix spectroscopy coupled with parallel factor analysis (EEM-PARAFAC) of DOM, Maie et al. (2014) showed the conservative behavior of $SUVA_{254}$ in a salinity range of less than 10 in the mouth of the Bekanbeushi River. They also showed seven EEM-PARAFAC components and suggested diverse DOC sources, including terrestrial origin, seagrass, and epiphytic algae. More recently, Zhang et al. (2018) revealed that aquaculture organisms have a significant impact on CDOM production in the mariculture area of the Northern Yellow Sea. Therefore, our results suggest that the contribution of mariculture followed by the eelgrass ecosystem significantly to the nutrients cycles and CDOM absorption in AKE and to the distinct water-mass systems inside and outside AKE. However, the role of mariculture and eelgrass meadows as a source of DOM and CDOM (i.e., the Blue Carbon aspect of seagrass) has yet to be fully investigated in AKE. Additionally, little is known about the role of the microbial carbon pump (Azam et al., 1983; Jiao et al., 2011) in the transfer of DOM and CDOM to higher trophic levels through bacteria, flagellates, and ciliates in the Akkeshi watershed as a whole. Further studies using $SUVA_{254}$ and EEM-PARAFAC

TABLE 4 | Kendall rank correlations coefficient (τ) between nutrient concentrations, environmental variables (temperature, salinity, Chl *a* concentration), and light absorption properties at the surface in AB during sampling cruises.

Month	Nutrients	Temp	Sal	Chl *a*	$a_{CDOM}(355)$	$a_{CDOM}(443)$	$a_{ph}(443)$	$a_{NAP}(443)$
April 2014	Nitrates	0.367	−0.400	0.167	0.467	0.500	0.100	0.233
n = 16∼19	Phosphate	−0.474	0.439	0.193	−0.450	−0.427	−0.041	−0.029
	Silicate	**0.661**	**−0.743**	−0.099	**0.708**	**0.637**	−0.287	0.029
May 2014	Nitrates	0.082	−0.030	−0.013	0.117	0.091	0.056	0.030
n = 22	Phosphate	−0.359	0.411	−0.212	−0.307	−0.281	−0.177	−0.169
	Silicate	**0.697**	**−0.628**	0.481	**0.714**	**0.688**	**0.602**	0.420
June 2014	Nitrates	0.415	−0.524	0.200	0.543	0.533	0.352	**0.686**
n = 21∼22	Phosphate	−0.191	0.238	0.065	−0.229	−0.221	−0.022	−0.126
	Silicate	**0.633**	**−0.723**	0.143	**0.714**	**0.706**	0.385	0.506
July 2014	Nitrates	0.029	−0.309	0.096	0.382	0.397	0.150	0.353
n = 17∼18	Phosphate	0.033	−0.216	0.144	0.255	0.268	0.176	0.242
	Silicate	0.412	**−0.647**	0.210	**0.686**	**0.725**	0.397	**0.647**
August 2014	Nitrates	0.190	−0.255	0.150	0.268	0.346	0.020	0.438
n = 18	Phosphate	0.349	−0.414	0.283	0.467	0.520	0.151	**0.625**
	Silicate	**0.712**	**−0.778**	0.516	**0.869**	**0.869**	0.438	**0.752**
September 2014	Nitrates	0.381	−0.467	**−0.619**	0.505	0.524	−0.019	0.438
n = 21∼22	Phosphate	**0.673**	**−0.740**	**−0.578**	**0.778**	**0.797**	0.100	**0.616**
	Silicate	**0.762**	**−0.829**	−0.505	**0.867**	**0.886**	0.152	**0.629**
October 2014	Nitrates	−0.056	−0.444	−0.222	0.444	0.444	0.167	−0.111
n = 9	Phosphate	0.167	−0.444	−0.222	0.444	0.444	0.056	0.111
	Silicate	0.111	**−0.833**	−0.389	**0.833**	**0.833**	0.111	−0.167
November 2014	Nitrates	−0.229	−0.299	−0.022	0.160	0.186	−0.022	0.255
n = 22	Phosphate	−0.255	−0.342	−0.134	0.238	0.281	−0.100	0.351
	Silicate	**−0.758**	**−0.844**	−0.186	**0.758**	**0.784**	0.056	**0.714**
December 2014	Nitrates	−0.600	−0.800	0.000	0.200	0.600	−0.200	0.200
n = 5	Phosphate	**−1.000**	−0.800	0.400	0.600	**1.000**	0.200	0.600
	Silicate	−0.400	−0.200	**1.000**	0.800	0.400	0.800	0.800
January 2015	Nitrates	0.373	0.203	0.373	−0.307	−0.268	0.242	−0.386
n = 18	Phosphate	0.399	0.255	0.320	−0.359	−0.320	0.242	−0.516
	Silicate	−0.490	**−0.765**	−0.359	**0.739**	**0.647**	−0.490	0.556
February 2015	Nitrates	**0.595**	0.529	0.033	−0.559	−0.603	0.137	−0.569
n = 17∼18	Phosphate	**0.765**	**0.909**	0.020	**−0.912**	**−0.809**	0.176	−0.529
	Silicate	**−0.699**	**−0.869**	0.150	**0.853**	**0.838**	−0.007	**0.621**

The values which are significant at the $p < 0.01$ level are in bold.

analyses are required to clarify the contribution of wetlands, salt marshes, eelgrass meadows, and mariculture to DOM and CDOM in AKE and AB.

Implications for Ecosystem Models in Optically Complex Coastal Waters

Ternary plots of absorption components showed that CDOM absorption was the main factor affecting light distribution at the surface of AKE across all seasons (**Figure 7**). These results suggest that the water mass in AKE was affected by CDOM-rich wetland river discharge and the release of CDOM from eelgrass meadows and mariculture. $a_{NAP}(443)$, which reflects the presence of suspended particles, had a small impact on the light absorption budget in AKE, except in December 2014 because development of the eelgrass canopy contributed to a reduction in current velocity and a corresponding decrease in sediment resuspension in eelgrass meadows (Hasegawa et al., 2008). On the other hand, our monthly observations with high spatial resolution revealed that the main light-absorbing component in AB varied widely among seasons. Absorption by phytoplankton assemblages accounted for more than half of the total absorption budget at some stations during the spring and autumn blooms in April and September 2014 (**Figures 7A,F**). The contribution of NAP to the total absorption budget increased in February because particles resuspension is enhanced by strong vertical mixing and the river waters and water mass in AKE are frozen solid during the winter (**Figure 7K**). Therefore, our results suggest that the dominant absorption property varies seasonally, even in the wetland-influenced coastal region.

Moreover, we found significant relationships between Z_{SD} and $a_{NAP}(443)$ and $a_{CDOM}(443)$ in AB for all samples across all seasons (**Figures 8D–F**). Chl *a* concentrations and $a_{ph}(443)$ were not correlated with Z_{SD} in the study area (**Figures 8A,B**). Accordingly, our results highlighted that the inherent optical properties (IOPs), including NAP and CDOM, are crucial

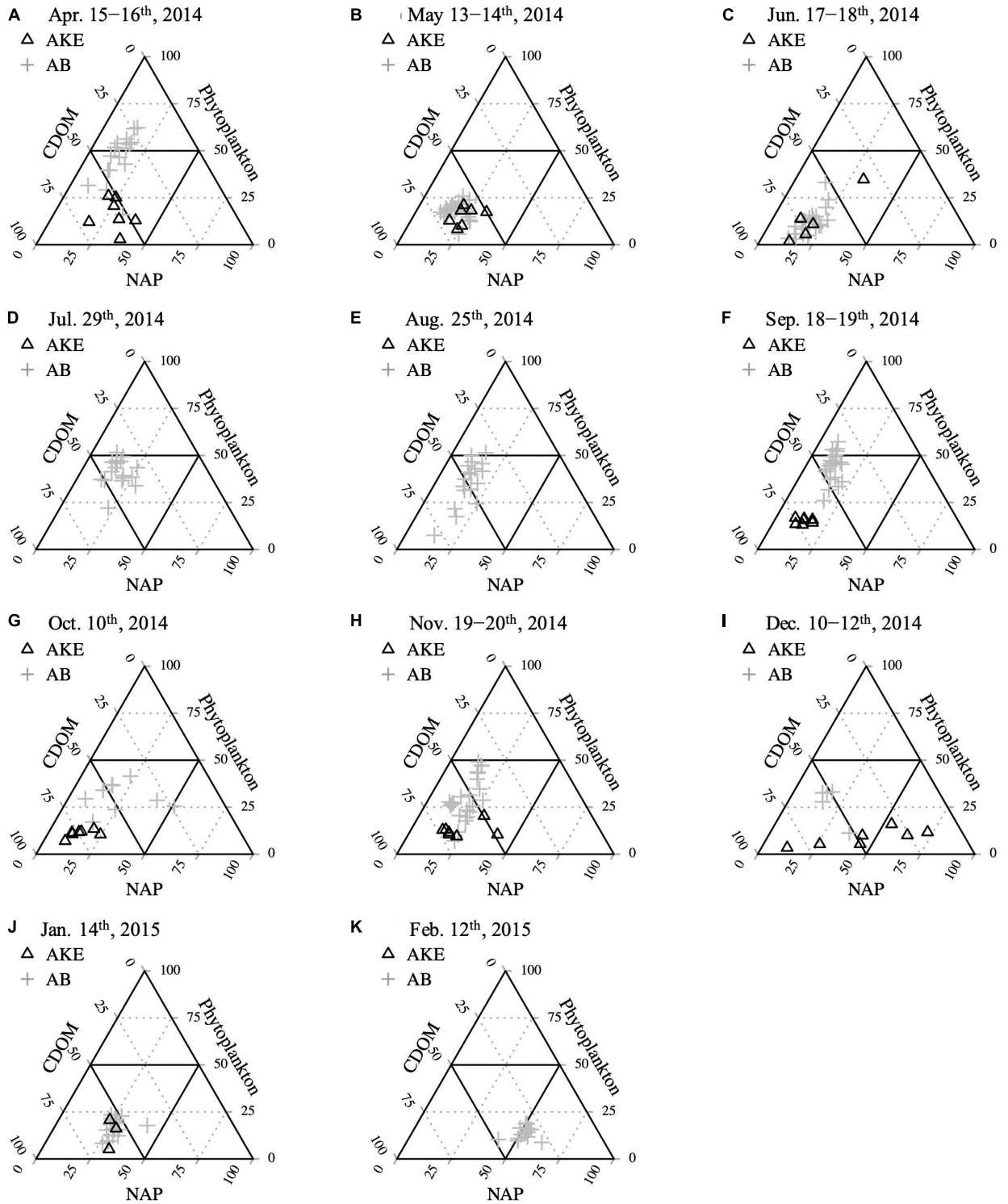

FIGURE 7 | Relative contributions of CDOM, NAP, and the phytoplankton absorption component to total non-water absorption at 443 nm **(A–K)** from April 2014 to February 2015.

for estimating water transparency in optically complex coastal waters. Because the parameters of Chl *a* concentration and Z_{SD} are often used as indicators of eutrophication and turbidity in inland, coastal, and oceanic waters, many previous studies (e.g., Lewis et al., 1988; Falkowski and Wilson, 1992; Morel et al., 2007; Boyce et al., 2010, 2012; Doron et al., 2011) have used the

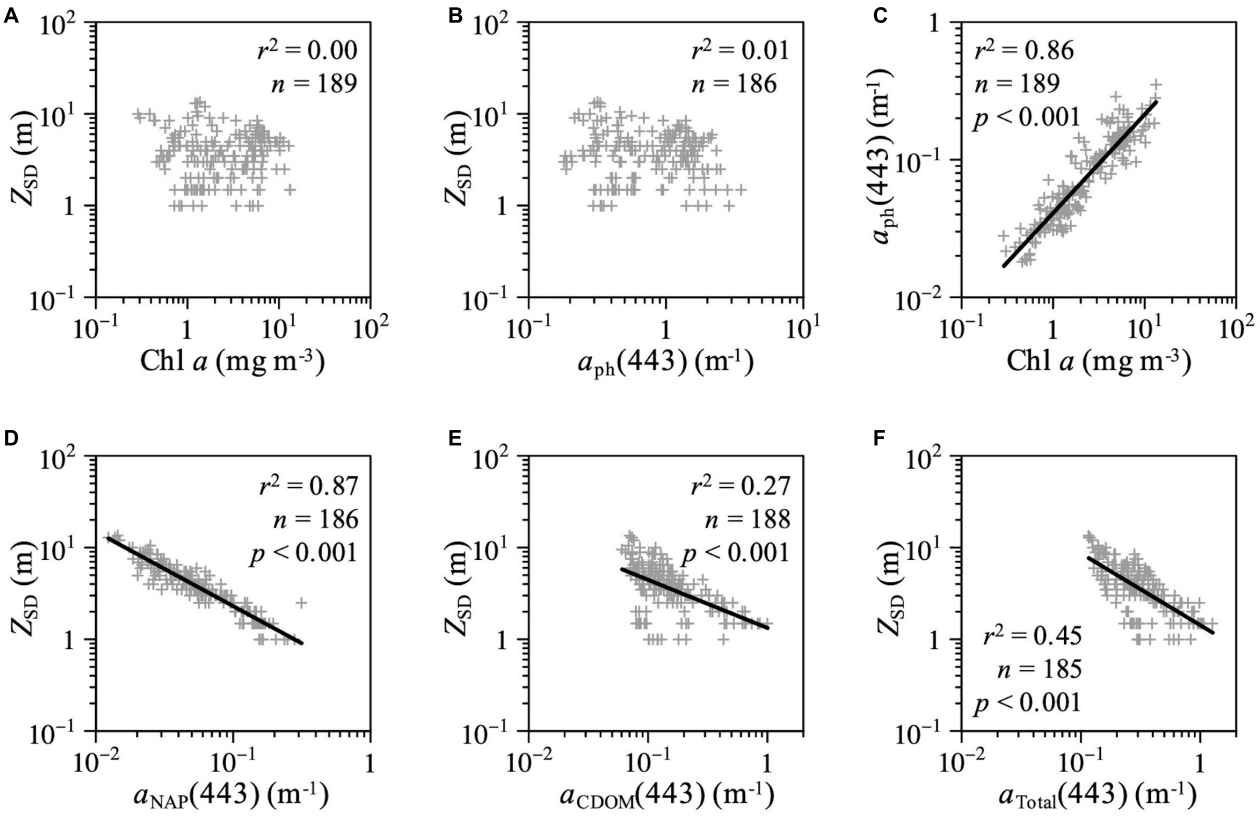

FIGURE 8 | Scatterplots of Z_{SD} as a function of **(A)** Chl *a* concentration, **(B)** $a_{ph}(443)$, **(D)** $a_{NAP}(443)$, **(E)** $a_{CDOM}(443)$, and **(F)** total absorption coefficient at 443 nm in AB. **(C)** Scatterplots of Chl *a* concentration versus $a_{ph}(443)$ in AB.

empirical relationship between Z_{SD} and Chl *a* concentrations to investigate phytoplankton productivity and develop algorithms for satellite ocean color remote sensing, especially in open oceans with optically simple Case I water, where phytoplankton is the primary factor affecting the IOPs of a water body (Morel and Prieur, 1977; Prieur and Sathyendranath, 1981; IOCCG, 2000). However, the variations of IOPs in optically complex coastal waters (Case II water) interacting with terrestrial waters are determined by phytoplankton, NAP, and CDOM (IOCCG, 2000; Hooker et al., 2020, 2021). Although many empirical conversion factors have been reported for predicting the diffuse attenuation coefficient of the photosynthetically available radiation (PAR) (K_{PAR}, m^{-1}), which is an apparent optical property (AOP) that varies with the sun angle (Preisendorfer, 1986), there is no universal conversion factor because Z_{SD} is affected by the bulk optical properties, especially in Case II waters (Lee et al., 2018 and references therein).

Colored dissolved organic matter also exhibits strong absorption in the UV range (Bricaud et al., 1981; Coble, 2007; Nelson and Seigel, 2013) and plays an important role in shading aquatic organisms from harmful UV radiation (Walsh et al., 2003; Tedetti and Sempéré, 2006). In fact, Taguchi et al. (1994) investigated the influence of UV radiation on the natural assemblage of phytoplankton during spring and autumn diatom blooms in AB and showed an enhanced photosynthetic rate in the absence of UV-B radiation. CDOM could protect primary producers in AKE and AB and contribute to the enhanced growth and photosynthesis of primary producers. Additionally, in AKE, the changes in the intensity and spectral distribution of light associated with the changes in CDOM and NAP absorption could influence below-ground organic carbon storage in seagrass soils, which constitute the majority of the total carbon stocks of seagrasses (Fourqurean et al., 2012).

In the Akkeshi watershed, some three-dimensional physical–biological coupled models including eelgrass and aquaculture components have been developed for the environmental conservation and sustainable management of aquaculture and fisheries (Oshima et al., 1999, 2006; Akabane et al., 2003; Yoon et al., 2013; Abe et al., 2015). These ecosystem models employ a simple formulation to describe light distribution in the water column. However, previous studies have emphasized the importance of considering the spectral light field using the bio-optical and/or radiative transfer model in ecosystem models (Fujii et al., 2007; Kettle and Merchant, 2008; Dutkiewicz et al., 2015; Bengil et al., 2016). For example, Urtizberea et al. (2013) conducted a sensitivity analysis of the influence of CDOM on the euphotic zone using marine ecosystem models, and showed that the simulated euphotic zone properties are strongly influenced by variations in CDOM attenuation. They therefore suggested that CDOM variations are useful for constraining uncertainties

in water column predictions in marine ecosystem models. Adams et al. (2016) proposed the seagrass-sediment-light (SSL) feedback for ecosystem models to help with the spatial prioritization of conservation and restoration efforts in the seagrass meadows of coastal environments. Furthermore, Clark et al. (2019) proposed a mechanistic photochemical model of CDOM for the carbon cycle model, especially in regions with strong gradients of CDOM along salinity. The results presented herein indicate that IOPs, including CDOM released from the mariculture and eelgrass meadows, could improve ecosystem model predictions of light distribution and spectral quality in the water column, as well as evaluations of the carbon budget in coastal waters, which are highly productive and important for sustainable management and the livelihood of coastal communities.

CONCLUSION

This study is the first to investigate the seasonal and spatial distribution of the absorption properties of CDOM, NAP, and phytoplankton as a function of temperature, salinity, nutrients, and water transparency along the river–eelgrass meadows–coastal waters continuum in the semi-enclosed coastal sea of Akkeshi-ko estuary and Akkeshi Bay, Japan, which includes the second largest Ramsar protected wetland (the Bekanbeushi wetland) in Japan. Although silicate concentrations and CDOM absorption in the Akkeshi watershed is primarily influenced by wetland-influenced river discharge from the Bekanbeushi River, our study suggests that mariculture and eelgrass meadows contribute to nutrient cycle and CDOM absorption, even in wetland-influenced coastal waters. Our study also shows that the absorption spectra of NAP and CDOM, rather than Chl *a* concentration, have a significant impact on water transparency in the coastal waters of Akkeshi Bay. The results of this research indicate that IOP components as well as CDOM derived from the metabolic activities of mariculture and eelgrass meadows could improve the prediction of light intensity and quality in the water column in ecosystem models of the freshwater–eelgrass–coastal waters continuum with optically complex coastal waters. However, further studies on the contribution of multiple sources to nutrients and CDOM are required to better understand Blue Carbon in coastal regions.

DATA AVAILABILITY STATEMENT

The original contributions presented in the study are included in the article/supplementary material, further inquiries can be directed to the corresponding author/s.

AUTHOR CONTRIBUTIONS

TI conceived and designed this research. TI and HA conducted the fieldwork. TI, HA, and HK did the experiment and analyses. TI drafted the manuscript. TI, HA, HK, and MN contributed to improving the final manuscript. All the authors contributed to the article and approved the submitted version.

FUNDING

This work was partially supported by the JSPS KAKENHI (Grant Number 19K06181) and the Joint Research Program of the Institute of Low Temperature Science, Hokkaido University (17K004 and 20S013).

ACKNOWLEDGMENTS

We thank S. Hamano and H. Katsuragawa for their helpful assistance and sampling during field expedition. We are grateful to T. Yoshioka for helpful discussions.

REFERENCES

Abe, H., Hasegawa, N., Yoon, S., and Kishi, M. J. (2015). Evaluation of Manila clam (*Ruditapes philippinarum*) growth and microphytobenthos resuspension in a subarctic lagoon in Japan. *Hydrobiologia* 758, 87–98. doi: 10.1007/s10750-015-2275-4

Adams, M. P., Hovey, R. K., Hipsey, M. R., Bruce, L. C., Ghisalberti, M., and Lowe, R. J. (2016). Feedback between sediment and light for seagrass: where is it important? *Limnol. Oceanogr.* 61, 1937–1955. doi: 10.1002/lno.10319

Akabane, H., Kishi, M. J., Mukai, H., and Iizumi, H. (2003). The response of the ecosystem of Akkeshi Lake, an estuary in northern Japan, to nutrients input from terrestrial area. *Bull. Coast. Oceanogr.* 40, 171–179.

Aoyama, M., Ota, H., Kimura, M., Kitao, T., Mitsuda, H., Murata, A., et al. (2012). Current status of homogeneity and stability of the reference materials for nutrients in seawater. *Anal. Sci.* 28, 911–916.

Azam, F., Fenchel, T., Field, J. G., Gray, J. S., Meyer-Reil, L. A., and Thingstad, F. (1983). The ecological role of water-column microbes in the sea. *Mar. Ecol. Prog. Ser.* 10, 257–263.

Babin, M., Stramski, D., Ferrari, G. M., Claustre, H., Bricaud, A., Obolensky, G., et al. (2003). Variations in the light absorption coefficient of phytoplankton, nonalgal particles, and dissolved organic matter in coastal waters around Europe. *J. Geophys. Res.* 108:3211. doi: 10.1029/2001JC000882

Bartoli, M., Nizzoli, D., Viaroli, P., Turolla, E., Castaldelli, G., Fano, E. A., et al. (2001). Impact of Tapes philippinarum farming on nutrient dynamics and benthic respiration in the Sacca di Goro. *Hydrobiologia* 455, 203–212.

Bauer, J. E., Cai, W. J., Raymond, P. A., Bianchi, T. S., Hopkinson, C. S., and Regnier, P. A. G. (2013). The changing carbon cycle of the coastal ocean. *Nature* 504, 61–70. doi: 10.1038/nature12857

Bengil, F., McKee, D., Beşiktepe, S. T., Calzado, V. S., and Tree, C. (2016). A bio-optical model for integration into ecosystem models for the Ligurian Sea. *Prog. Oceanogr.* 149, 1–15. doi: 10.1016/j.pocean.2016.10.007

Bertelli, C. M., and Unsworth, R. K. F. (2014). Protecting the hand that feeds us: seagrass (*Zostera marina*) serves as commercial juvenile fish habitat. *Mar. Pollut. Bull.* 83, 425–429. doi: 10.1016/j.marpolbul.2013.08.011

Blough, N. V., Zafiriou, O. C., and Bonilla, J. (1993). Optical absorption spectra of waters from the Orinoco River outflow: terrestrial input of colored organic matter to the Caribbean. *J. Geophys. Res.* 98, 2271–2278. doi: 10.1029/92JC02763

Borges, A. V. (2005). Do we have enough pieces of the jigsaw to integrate CO_2 fluxes in the coastal ocean? *Estuaries* 28, 3–27.

Boyce, D. G., Lewis, M., and Worm, B. (2012). Integrating global chlorophyll data from 1890 to 2010. *Limnol. Oceanogr. Methods* 10, 840–852. doi: 10.4319/lom.2012.10.840

Boyce, D. G., Lewis, M. R., and Worm, B. (2010). Global phytoplankton decline over the past century. *Nature* 466, 591–596. doi: 10.1038/nature09268

Bricaud, A., Morel, A., and Prieur, L. (1981). Absorption by dissolved organic matter of the sea (yellow substance) in the UV and visible domains. *Limnol. Oceanogr.* 26, 43–53.

Canuel, E. A., and Hardison, A. K. (2016). Sources, ages, and alteration of organic matter in estuaries. *Annu. Rev. Mar. Sci.* 8, 409–434. doi: 10.1146/annurev-marine-122414-034058

Carbonnel, V., Vanderborght, J. P., Lionard, M., and Chou, L. (2013). Diatoms, silicic acid and biogenic silica dynamics along the salinity gradient of the Scheldt estuary (Belgium/The Netherlands). *Biogeochemistry* 113, 657–682. doi: 10.1007/s10533-012-9796-y

Carey, J. C., and Fulweiler, R. W. (2014). Salt marsh tidal exchange increases residence time of silica in estuaries. *Limnol. Oceanogr.* 59, 1203–1212. doi: 10.4319/lo.2014.59.4.1203

Clark, J. B., Neale, P., Tzortziou, M., Cao, F., and Hood, R. R. (2019). A mechanistic model of photochemical transformation and degradation of colored dissolved organic matter. *Mar. Chem.* 214:103666. doi: 10.1016/j.marchem.2019.103666

Coble, P. G. (2007). Marine optical biogeochemistry: the chemistry of ocean color. *Chem. Rev.* 107, 402–418.

Cowan, J. L. W., Pennock, J. R., and Boynton, W. R. (1996). Seasonal and interannual patterns of sediment-water nutrient and oxygen fluxes in Mobile Bay, Alabama (USA):regulating factors and ecological significance. *Mar. Ecol. Prog. Ser.* 141, 229–245.

Dame, R. F., Spurrier, J. D., and Wolaver, T. G. (1989). Carbon, nitrogen and phosphorus processing by an oyster reef. *Mar. Ecol. Prog. Ser.* 54, 249–256.

Danhiez, F. P., Vantrepotte, V., Cauvin, A., Lebourg, E., and Loisel, H. (2017). Optical properties of chromophoric dissolved organic matter during a phytoplankton bloom. Implication for DOC estimates from CDOM absorption. *Limnol. Oceanogr.* 62, 1409–1425. doi: 10.1002/lno.10507

Del Vecchio, R., and Blough, N. V. (2004). Spatial and seasonal distribution of chromophoric dissolved organic matter and dissolved organic carbon in the Middle Atlantic Bight. *Mar. Chem.* 89, 169–187. doi: 10.1016/j.marchem.2004.02.027

Doron, M., Babin, M., Hembise, O., Mangin, A., and Garnesson, P. (2011). Ocean transparency from space: validation of algorithms estimating Secchi depth using MERIS, MODIS and SeaWiFS data. *Remote Sens. Environ.* 115, 2986–3001. doi: 10.1016/j.rse.2011.05.019

Duarte, C. M., Middelburg, J. J., and Caraco, N. (2005). Major role of marine vegetation on the oceanic carbon cycle. *Biogeosciences* 2, 1–8. doi: 10.5194/bg-2-1-2005

Dutkiewicz, S., Hickman, A. E., Jahn, O., Gregg, W. W., Mouw, C. B., and Follows, M. J. (2015). Capturing optically important constituents and properties in a marine biogeochemical and ecosystem model. *Biogeosciences* 12, 4447–4481. doi: 10.5194/bg-12-4447-2015

Falkowski, P. G., and Wilson, C. (1992). Phytoplankton productivity in the North Pacific Ocean since 1900 and implications for absorption of anthropogenic CO_2. *Nature* 358, 741–743. doi: 10.1038/358741a0

Ferrari, G. M., and Dowell, M. D. (1998). CDOM absorption characteristics with relation to fluorescence and salinity in coastal areas of the Southern Baltic Sea. *Estuar. Coast. Shelf Sci.* 47, 91–105. doi: 10.1006/ecss.1997.0309

Fichot, C. G., and Benner, R. (2012). The spectral slope coefficient of chromophoric dissolved organic matter ($S_{275-295}$) as a tracer of terrigenous dissolved organic carbon in river-influenced ocean margins. *Limnol. Oceanogr.* 57, 1453–1466. doi: 10.4319/lo.2012.57.5.1453

Fletcher, S., Kawabe, M., and Rewhorn, S. (2011). Wetland conservation and sustainable coastal governance in Japan and England. *Mar. Pollut. Bull.* 62, 956–962. doi: 10.1016/j.marpolbul.2011.02.048

Fourqurean, J. W., Duarte, C. M., Kennedy, H., Marbà, N., Holmer, M., Mateo, M. A., et al. (2012). Seagrass ecosystems as a globally significant carbon stock. *Nat. Geosci.* 5, 505–509. doi: 10.1038/NGEO1477

Fujii, M., Boss, E., and Chai, F. (2007). The value of adding optics to ecosystem models: a case study. *Biogeosciences* 4, 817–835. doi: 10.5194/bg-4-817-2007

Guo, W., Stedmon, C. A., Han, Y., Wu, F., Yu, X., and Hu, M. (2007). The conservative and non-conservative behavior of chromophoric dissolved organic matter in Chinese estuarine waters. *Mar. Chem.* 107, 357–366. doi: 10.1016/j.marchem.2007.03.006

Hansell, D. A., and Carlson, C. (2014). *Biogeochemistry of Marine Dissolved Organic matter (2nd)*. Cambrdige: Academic press.

Hasegawa, N., Hori, M., and Mukai, H. (2007). Seasonal shifts in seagrass bed primary producers in a cold-temperate estuary: dynamics of eelgrass *Zostera marina* and associated epiphytic algae. *Aquat. Bot.* 86, 337–345. doi: 10.1016/j.aquabot.2006.12.002

Hasegawa, N., Hori, M., and Mukai, H. (2008). Seasonal changes in eelgrass functions: current velocity reduction, prevention of sediment resuspension, and control of sediment–water column nutrient flux in relation to eelgrass dynamics. *Hydrobiologia* 596, 387–399. doi: 10.1007/s10750-007-9111-4

Hasegawa, N., Onitsuka, T., Takeyama, S., and Maekawa, K. (2015). Oyster Culture in Hokkaido, Japan. *Bull. Fish. Res. Agen.* 40, 173–177.

Hasegawa, N., Sawaguchi, S., Unuma, T., Onitsuka, T., and Hamaguchi, M. (2014). Variation in Manila clam (*Ruditapes philippinarum*) fecundity in eastern Hokkaido. *Japan. J. Shellfish Res.* 33, 739–746. doi: 10.2983/035.033.0308

Hedges, J. I., Keil, R. G., and Benner, R. (1997). What happens to terrestrial organic matter in the ocean? *Org. Geochem.* 27, 195–212. doi: 10.1016/S0146-6380(97)00066-1

Helms, J. R., Stubbins, A., Ritchie, J. D., Minor, E. C., Kieber, D. J., and Mopper, K. (2008). Absorption spectral slopes and slope ratios as indicators of molecular weight, source, and photobleaching of chromophoric dissolved organic matter. *Limnol. Oceanogr.* 53, 955–969. doi: 10.4319/lo.2008.53.3.0955

Hooker, S. B., Houskeeper, H. F., Kudela, R. M., Matsuoka, A., Suzuki, K., and Isada, T. (2021). Spectral modes of radiometric measurements in optically complex waters. *Cont. Shelf Res.* 219:104357. doi: 10.1016/j.csr.2021.104357

Hooker, S. B., Matsuoka, A., Kudela, R. M., Yamashita, Y., Suzuki, K., and Houskeeper, H. F. (2020). A global end-member approach to derive $a_{CDOM}(440)$ from near-surface optical measurements. *Biogeosciences* 17, 475–497. doi: 10.5194/bg-17-475-2020

Hothorn, T., and Hornik, K. (2021). *exactRankTests: Exact Distributions for Rank and Permutation Tests. R Package Version 0.8-32.*

Howard-Williams, C. (1985). Cycling and retention of nitrogen and phosphorus in wetlands: a theoretical and applied perspective. *Freshw. Biol.* 15, 391–431. doi: 10.1111/j.1365-2427.1985.tb00212.x

Hu, S., Niu, Z., and Chen, Y. (2017a). Global Wetland Datasets: a Review. *Wetland* 37, 807–817. doi: 10.1007/s13157-017-0927-z

Hu, S., Niu, Z., Chen, Y., Li, L., and Zhang, H. (2017b). Global wetlands: potential distribution, wetland loss, and status. *Sci. Total Environ.* 586, 319–327. doi: 10.1016/j.scitotenv.2017.02.001

Iizumi, H., Hattori, A., and McRoy, C. P. (1982). Ammonium regeneration and assimilation in eelgrass (*Zostera marina*) beds. *Mar. Biol.* 66, 59–65. doi: 10.1017/BF00397255

Iizumi, H., Taguchi, S., Minami, T., and Maekawa, S. (1995). Distribution and variability of nutrients, chlorophyll a, particulate organic matters, and their carbon and nitrogen contents, in Akkeshi-ko, an estuary in northern Japan. *Bull. Hokkaido Natl. Fish. Res. Inst.* 59, 43–67.

Inukai, T., and Nishio, S. (1937). A limnological study of Akkeshi Lake with special reference to the propagation of the oyster. *J. Fac. Agric. Hokkaido Imp. Univ.* 40, 1–33.

IOCCG (2000). "Remote sensing of ocean colour in coastal, and other optically-Complex, Waters," in *Reports of the International Ocean-Colour Coordinating Group, No. 3*, ed. S. Sathyendranath (Dartmouth: IOCCG).

Isada, T., Hattori-Saito, A., Saito, H., Kondo, Y., Nishioka, J., Kuma, K., et al. (2019). Responses of phytoplankton assemblages to iron availability and mixing water masses during the spring bloom in the Oyashio region, NW Pacific. *Limnol. Oceanogr.* 64, 197–216. doi: 10.1002/lno.11031

Isada, T., Iida, T., Liu, H., Saitoh, S.-I., Nishioka, J., Nakatsuka, T., et al. (2013). Influence of Amur River discharge on phytoplankton photophysiology in the Sea of Okhotsk during late summer. *J. Geophys. Res.* 118, 1995–2013. doi: 10.1002/jgrc.20159

Jiao, N., Herndl, G. J., Hansell, D. A., Benner, R., Kattner, G., Wilhelm, S. W., et al. (2011). The microbial carbon pump and the oceanic recalcitrant dissolved organic matter pool. *Nat. Rev. Microbiol.* 9:555. doi: 10.1038/nrmicro2386-c5

Kasai, H., Saito, H., Yoshimori, A., and Taguchi, S. (1997). Variability in timing and magnitude of spring bloom in the Oyashio region, the western subarctic Pacific off Hokkaido, Japan. *Fish. Oceanogr.* 6, 118–129.

Kettle, H., and Merchant, C. J. (2008). Modeling ocean primary production: sensitivity to spectral resolution of attenuation and absorption of light. *Prog. Oceanogr.* 78, 135–146. doi: 10.1016/j.pocean.2008.04.002

Kishino, M., Takahashi, M., Okami, N., and Ichimura, S. (1985). Estimation of the spectral absorption coefficients of phytoplankton in the sea. *Bull. Mar. Sci.* 37, 634–642.

Lee, Z., Shang, D., Du, K., and Wei, J. (2018). Resolving the long-standing puzzles about the observed Secchi depth relationships. *Limnol. Oceangr.* 63, 2321–2336. doi: 10.1002/lno.10940

Lewis, M. R., Kuring, N., and Yentsch, C. (1988). Global patterns of ocean transparency: implications for the new production of the open ocean. *J. Geophys. Res.* 93, 6847–6856. doi: 10.1029/JC093iC06p06847

Macreadie, P. I., Anton, A., Raven, J. A., Beaumont, N., Connolly, R. M., Friess, D. A., et al. (2019). The future of Blue Carbon science. *Nat. Commun.* 10:3998. doi: 10.1038/s41467-019-11693-w

Maie, N., Sekiguchi, S., Watanabe, A., Tsutsuki, K., Yamashita, Y., Melling, L., et al. (2014). Dissolved organic matter dynamics in the oligo/meso-haline zone of wetland-influenced coastal rivers. *J. Sea Res.* 91, 58–69. doi: 10.1016/j.seares.2014.02.016

Momota, K., and Nakaoka, M. (2018). Seasonal change in spatial variability of eelgrass epifaunal community in relation to gradients of abiotic and biotic factors. *Mar. Ecol.* 39:e12522. doi: 10.1111/maec.12522

Morel, A., Huot, Y., Gentili, B., Werdell, P. J., Hooker, S. B., and Franz, B. A. (2007). Examining the consistency of products derived from various ocean color sensors in open ocean (Case 1) waters in the perspective of a multi-sensor approach. *Remote Sens. Environ.* 111, 69–88. doi: 10.1016/j.rse.2007.03.012

Morel, A., and Prieur, L. (1977). Analysis of variations in ocean color. *Limnol. Oceanogr.* 22, 709–722. doi: 10.4319/lo.1977.22.4.0709

Muller-Karger, F. E., Varela, R., Thunell, R., Luerssen, R., Hu, C., and Walsh, J. J. (2005). The importance of continental margins in the global carbon cycle. *Geophys. Res. Lett.* 32:L01602. doi: 10.1029/2004GL021346

Nagao, S., Kumegawa, M., Kodama, H., and Terashima, M. (2016). Transport behavior of dissolved organic matter and iron in river waters from the Bekanbeushi River System in eastern Hokkaido, Japan. *Low Temperature Sci.* 74, 1–12.

Najjar, R. G., Herrmann, M., Alexander, R., Boyer, E. W., Burdige, D. J., Butman, D., et al. (2018). Carbon budget of tidal wetlands, estuaries, and shelf waters of eastern North America. *Global Biogeochem. Cyc.* 32, 389–416. doi: 10.1002/2017GB005790

Nakagawa, T., Tsuchiya, Y., Ueda, S., Fukui, M., and Takahashi, R. (2019). Eelgrass Sediment microbiome as a Nitrous Oxide Sink in Brackish Lake Akkeshi, Japan. *Microbes Environ.* 34, 13–22. doi: 10.1264/jsme2.ME18103

Nelson, K. A., Leonard, L. A., Posey, M. H., Alphin, T. D., and Mallin, M. A. (2004). Using transplanted oyster (*Crassostrea virginica*) beds to improve water quality in small tidal creeks: a pilot study. *J. Exp. Mar. Biol. Ecol.* 298, 347–368. doi: 10.1016/S0022-0981(03)00367-8

Nelson, N. B., and Seigel, D. (2013). The global distribution and dynamics of chromophoric dissolved organic matter. *Annu. Rev. Mar. Sci.* 5, 447–476. doi: 10.1146/annurev-marine-120710-100751

Nizzoli, D., Bartoli, M., and Viaroli, P. (2006). Nitrogen and phosphorous budgets during a farming cycle of the Manila clam *Ruditapes philippinarum*: an in situ experiment. *Aquaculture* 261, 98–108. doi: 10.1016/j.aquaculture.2006.06.042

Ogawa, H., and Tanoue, E. (2003). Dissolved organic matter in oceanic waters. *J. Oceanogr.* 59, 129–147. doi: 10.1023/A:1025528919771

Oshima, Y., Kishi, M. J., and Mukai, H. (2006). Numerical study on nutrient cycle in Akkeshi estuary focused on the influence of bivalve. *Japan. J. Benthol.* 61, 66–76. doi: 10.5179/benthos.61.66

Oshima, Y., Kishi, M. J., and Sugimoto, T. (1999). Evaluation of the nutrient budget in a seagrass bed. *Ecol. Model.* 115, 19–33. doi: 10.1016/S0304-3800(98)00155-0

Park, S. R., Moon, K., Kim, S. H., and Lee, K.-S. (2021). Growth and photoacclimation strategies of three *Zostera* species along a vertical gradient: implications for seagrass zonation patterns. *Front. Mar. Sci.* 8:594779. doi: 10.3389/fmars.2021.594779

Preisendorfer, R. W. (1986). Secchi disk science: visual optics of natural waters. *Limnol. Oceangr.* 31, 909–926. doi: 10.4319/lo.1986.31.5.0909

Prieur, L., and Sathyendranath, S. (1981). An optical classification of coastal and oceanic waters based on the specific spectral absorption curves of phytoplankton pigments, dissolved organic matter, and other particulate materials. *Limnol. Oceanogr.* 16, 671–689. doi: 10.4319/lo.1981.26.4.0671

R Core Team (2021). *R: A Language and Environment for Statistical Computing*. Vienna: R Foundation for Statistical Computing.

Ramsar Information Sheet [RIS] (2005). *Information Sheet on Ramsar Wetlands: Akkeshi-ko and Bekambeushi-shitsugen. Rmasar Bureau*. Available Online at: https://rsis.ramsar.org/ris/614 (accessed September 28, 2021).

Reddy, K. R., Kadlec, R. H., Flaig, E., and Gale, P. M. (1999). Phosphorus retention in streams and wetlands: a review. *Crit Rev. Env. Sci. Technol.* 29, 83–146. doi: 10.1080/10643389991259182

Redfield, A. C. (1958). The biological control of chemical factors in the environment. *Am. Sci.* 46, 205–221.

Revelle, W. (2021). *Psych: Procedures for Personality and Psychological Research*. Evanston: Northwestern University.

Rochello-Newall, E. J., and Fisher, T. R. (2002). Chromophoric dissolved organic matter and dissolved organic carbon in Chesapeake Bay. *Mar. Chem.* 77, 23–41. doi: 10.1016/S0304-4203(01)00073-1

Saito, H., Tsuda, A., and Kasai, H. (2002). Nutrient and plankton dynamics in the Oyashio region of the western subarctic Pacific Ocean. *Deep-Sea Res. II* 49, 5463–5486. doi: 10.1016/S0967-0645(02)00204-7

Stabenau, E. R., Zepp, R. G., Bartels, E., and Zika, R. G. (2004). Role of the seagrass *Thalassia testudinum* as a source of chromophoric dissolved organic matter in coastal south Florida. *Mar. Ecol. Prog. Ser.* 282, 59–72. doi: 10.3354/meps282059

Stedmon, C. A., and Nelson, N. B. (2014). "The optical properties of DOM in the Ocean," in *Biogeochemistry of Marine Dissolved Organic Matter (2nd)*, eds D. A. Hansell and C. A. Carlson (San Diego: Academic press), 481–508.

Stramski, D., Reynolds, R. A., Kaczmarek, S., Uitz, J., and Zheng, G. (2015). Correction of pathlength amplification in the filter-pad technique for measurements of particulate absorption coefficient in the visible spectral region. *Appl. Opt.* 54, 6763–6782. doi: 10.1364/AO.54.006763

Struyf, E., and Conley, D. J. (2009). Silica: an essential nutrient in wetland biogeochemistry. *Front. Ecol. Environ.* 7, 88–94. doi: 10.1890/070126

Struyf, E., Dausse, A., Van Damme, S., Bal, K., Gribsholt, B., Boschker, H. T. S., et al. (2006). Tidal marshes and biogenic silica recycling at the land–sea interface. *Limnol. Oceanogr.* 51, 838–846. doi: 10.4319/lo.2006.51.2.0838

Suzuki, R., and Ishimaru, T. (1990). An improved method for the determination of phytoplankton chlorophyll using N, N-dimethylformamide. *J. Oceanogr.* 46, 190–194. doi: 10.1007/BF02125580

Taguchi, S., Iseki, K., and Kawamura, T. (1977). The estimation of annual production by phytoplankton in Akkeshi Bay, Japan. *J. Oceanogr. Soc. Japan* 33, 97–102. doi: 10.1007/BF02110015

Taguchi, S., Saito, H., and Kasai, H. (1994). Enhanced photosynthetic rate of natural phytoplankton assemblages in the absence of ultraviolet radiation in Akkeshi Bay, Japan. *Bull. Plankton Soc. Japan* 41, 143–159.

Tanaka, Y., Bahrin, A., and Lamit, N. (2019). Production of chromophoric dissolved organic matter by seagrasses in brackish aquaculture water. *Aquac. Res.* 50, 1731–1734. doi: 10.1111/are.14033

Tanaka, Y., and Nakaoka, M. (2007). Interspecific variation in photosynthesis and respiration balance of three seagrasses in relation to light availability. *Mar. Ecol. Prog. Ser.* 350, 63–70. doi: 10.3354/meps07103

Tedetti, M., Bigot, L., Turquet, J., Guigue, C., Ferretto, N., Goutx, M., et al. (2020). Influence of Freshwater Discharges on Biogeochemistry and Benthic Communities of a Coral Reef Ecosystem (La Réunion Island, Indian Ocean). *Front. Mar. Sci.* 7:596165. doi: 10.3389/fmars.2020.596165

Tedetti, M., and Sempéré, R. (2006). Penetration of ultraviolet radiation in the marine environment. A Review. *Photochem. Photobiol.* 82, 389–397. doi: 10.1562/2005-11-09-IR-733

Tréguer, P., and De La Rocha, C. L. (2013). The world ocean silica cycle. *Annu. Rev. Mar. Sci.* 5, 477–501. doi: 10.1146/annurev-marine-121211-172346

Tréguer, P., Nelson, D. M., van Bennekom, A. J., DeMaster, D. J., Leynaert, A., and Quéguiner, B. (1995). The balance of silica in the world ocean: a re-estimate. *Science* 268, 375–379. doi: 10.1126/science.268.5209.375

Tzortziou, M., Neale, P. J., Megonigal, J. P., Pow, C. L., and Butterworth, M. (2011). Spatial gradients in dissolved carbon due to tidal marsh outwelling into a Chesapeake Bay estuary. *Mar. Ecol. Prog. Ser.* 426, 41–56. doi: 10.3354/meps09017

Tzortziou, M., Zeri, C., Dimitriou, E., Ding, Y., Jaffé, R., Anagnostou, E., et al. (2015). Colored dissolved organic matter dynamics and anthropogenic influences in a major transboundary river and its coastal wetland. *Limnol. Oceanogr.* 60, 1222–1240. doi: 10.1002/lno.10092

Urtizberea, A., Dupont, N., Rosland, R., and Aksnes, D. L. (2013). Sensitivity of euphotic zone properties to CDOM variations in marine ecosystem models. *Ecol. Model.* 256, 16–22. doi: 10.1016/j.ecolmodel.2013.02.010

Wagner, S., Jaffé, R., Cawley, K., Dittmar, T., and Stubbins, A. (2015). Associations between the molecular and optical properties of dissolved organic matter in the Florida Everglades, a model coastal wetland system. *Front. Chem.* 3:66. doi: 10.3389/fchem.2015.00066

Walsh, J. J. (1991). Importance of continental margins in the marine biogeochemical cycling of carbon and nitrogen. *Nature* 350, 53–55. doi: 10.1038/350053a0

Walsh, J. J., Weisberg, R. H., Dieterle, D. A., He, R., Darrow, B. P., Jolliff, J. P., et al. (2003). Phytoplankton response to intrusions of slope water on the West Florida Shelf: models and observations. *J. Geophys. Res.* 108:3190. doi: 10.1029/2002JC001406

Waycott, M., Duarte, C. M., Carruthers, T. J. B., Orth, R. J., Dennison, W. C., Olyarnik, S., et al. (2009). Accelerating loss of seagrasses across the globe threatens coastal ecosystems. *Proc. Natl. Acad. Sci. U. S. A.* 106, 12377–12381. doi: 10.1073/pnas.0905620106

Waycott, M., Longstaff, B. J., and Mellors, J. (2005). Seagrass population dynamics and water quality in the Great Barrier Reef region: a review and future research directions. *Mar. Pollut. Bull.* 51, 343–350. doi: 10.1016/j.marpolbul.2005.01.017

Welsch, D. T., Nizzoli, D., Fano, E. A., and Viaroli, P. (2015). Direct contribution of clams (*Ruditapes philippinarum*) to benthic fluxes, nitrification, denitrification and nitrous oxide emission in a farmed sediment. *Estuar. Coast. Shelf Sci.* 154, 84–93. doi: 10.1016/j.ecss.2014.12.021

Welschmeyer, N. A. (1994). Fluorometric analysis of chlorophyll-a in the presence of chlorophyll-b and phaeopigments. *Limnol. Oceanogr.* 39, 1985–1992.

Yamashita, Y., Scinto, L. J., Maie, N., and Jaffé, R. (2010). Dissolved organic matter characteristics across a Subtropical Wetland's landscape: application of optical properties in the assessment of environmental dynamics. *Ecosystems* 13, 1006–1019. doi: 10.1007/s10021-010-9370-1

Yasuda, I. (2003). Hydrographic structure and variability in the Kuroshio-Oyashio transition area. *J. Oceanogr.* 59, 389–402. doi: 10.1023/A:1025580313836

Yoon, S., Abe, H., and Kishi, M. J. (2013). Responses of Manila clam growth and its food sources to global warming in a subarctic lagoon in Japan. *Prog. Oceanogr.* 119, 48–58. doi: 10.1016/j.pocean.2013.06.005

Zedler, J. B., and Kercher, S. (2005). WETLAND RESOURCES: status, trends, ecosystem services, and restorability. *Annu. Rev. Environ. Res.* 30, 39–74. doi: 10.1146/annurev.energy.30.050504.144248

Zhang, Y., Gao, X., Guo, W., Zhao, J., and Li, Y. (2018). Origin and dynamics of dissolved organic matter in a mariculture area suffering from summertime hypoxia and acidification. *Front. Mar. Sci.* 5:325. doi: 10.3389/fmars.2018.00325

Zhang, Z., Cao, Z., Grasse, P., Dai, M., Gao, L., Kuhnert, H., et al. (2020). Dissolved silicon isotope dynamics in large river estuaries. *Geochim. Cosmochim. Acta* 273, 367–382. doi: 10.1016/j.gca.2020.01.028

Ziegler, S., and Benner, R. (1999b). Nutrient cycling in the water column of a subtropical seagrass meadow. *Mar. Ecol. Prog. Ser.* 188, 51–62. doi: 10.3354/meps188051

Ziegler, S., and Benner, R. (1999a). Dissolved organic carbon cycling in a subtropical seagrass-dominated lagoon. *Mar. Ecol. Prog. Ser.* 180, 149–160. doi: 10.3354/meps180149

Conflict of Interest: The authors declare that the research was conducted in the absence of any commercial or financial relationships that could be construed as a potential conflict of interest.

The handling editor declared a past co-authorship with one of the authors TI.

Publisher's Note: All claims expressed in this article are solely those of the authors and do not necessarily represent those of their affiliated organizations, or those of the publisher, the editors and the reviewers. Any product that may be evaluated in this article, or claim that may be made by its manufacturer, is not guaranteed or endorsed by the publisher.

Copyright © 2021 Isada, Abe, Kasai and Nakaoka. This is an open-access article distributed under the terms of the Creative Commons Attribution License (CC BY). The use, distribution or reproduction in other forums is permitted, provided the original author(s) and the copyright owner(s) are credited and that the original publication in this journal is cited, in accordance with accepted academic practice. No use, distribution or reproduction is permitted which does not comply with these terms.

frontiers in Marine Science

ORIGINAL RESEARCH
published: 26 October 2021
doi: 10.3389/fmars.2021.723452

On the Advection of Upwelled Water on the Western Yucatan Shelf

Jorge. A. Kurczyn[1*†], *Rodrigo Duran*[2,3], *Emilio Beier*[4] *and Alejandro J. Souza*[5]

[1] *Instituto Epomex, Universidad Autónoma de Campeche, Campeche, Mexico,* [2] *National Energy Technology Laboratory, Albany, OR, United States,* [3] *Theiss Research, La Jolla, CA, United States,* [4] *Centro de Investigación Científica y de Educación Superior de Ensenada (CICESE), Unidad La Paz, Laboratorio de Macroecología Marina, La Paz, Mexico,* [5] *Recursos del Mar, Centro de Investigación y Estudios Avanzados del Instituto Politécnico Nacional (CINVESTAV), Mérida, Mexico*

Upwelling events over the Yucatan Shelf are an important physical phenomenon to the region. They typically happen during spring and summer and had been studied for some time with a primary focus on the development on the eastern side of the shelf and later transport to the central part of the Peninsula. There has been very little effort looking at the impact of upwelling on the western shelf, on the Campeche side. Using a combination of observations and modeling from 2018, we show evidence for the first time, of the presence of upwelled water on the western side. Particle tracking, integrated back-in-time, was used to identify the origin of the upwelled water. Our results show that Caribbean Subtropical Underwater was brought from the northeast shelf, over 500 km away from the study area, by advection. This water took over a month (40 days) to arrive at the study region, traveling along-shelf with an average velocity of 14.5 cm/s. In the nearshore waters off the Campeche Coast, Caribbean Tropical Water was underlain by upwelling Caribbean Subtropical Underwater. Monthly averaged sea surface temperature (SST) anomalies from a 39-year time series suggest that upwelled water off Campeche is a regular phenomenon during summer, while the recurrence of westward advection is supported by climatological Lagrangian Coherent Structures. More studies are needed to explore the frequency of occurrence and impact of these events on the western shelf.

Keywords: upwelling events, shelf processes, transport of upwelled waters, climatological Lagrangian Coherent Structures, Yucatan Peninsula

OPEN ACCESS

Edited by:
William Savidge, University of Georgia, United States

Reviewed by:
Atsushi Kaneda, Fukui Prefectural University, Japan
Emilio Hernandez-Garcia, Institute of Interdisciplinary Physics and Complex Systems (IFISC), Spain

****Correspondence:***
Jorge. A. Kurczyn
jkurczynr@iingen.unam.mx

†Present address:
Jorge A. Kurczyn, Laboratorio de Ingeniería y Procesos Costeros, Instituto de Ingeniería, Universidad Nacional Autónoma de México, Sisal, Mexico

Specialty section:
This article was submitted to Coastal Ocean Processes, a section of the journal Frontiers in Marine Science

Received: *10 June 2021*
Accepted: *16 September 2021*
Published: *26 October 2021*

Citation:
Kurczyn JA, Duran R, Beier E and Souza AJ (2021) On the Advection of Upwelled Water on the Western Yucatan Shelf. Front. Mar. Sci. 8:723452. doi: 10.3389/fmars.2021.723452

INTRODUCTION

The Yucatan Continental Shelf is located on the southeast Gulf of Mexico (GoM) (hereafter Yucatan Shelf), and it is an important economic area rich in fishing resources, gas, oil, and tourism (**Figure 1**). It is a wide shallow marine region distinguished by mean westward current speeds of 5–7 cm/s (Martínez-López and Pares-Sierra, 1998; Ruíz-Castillo et al., 2016), low significant wave heights (0.63 m on average) with periods of <5 s, and microtidal tides, mainly diurnal. Winds blow preferentially toward the west all year-round (also known as easterlies or trade winds), forcing the ocean to produce a persistent westward circulation (Martínez-López and Pares-Sierra, 1998; Zavala-Hidalgo et al., 2003). From September to June, atmospheric cold fronts, coming from continental North America (Kurczyn et al., 2020), dramatically shift the regional wind flow and interrupt the upwelling processes of the northeast (Merino, 1997).

Oceanographic surveys (black dots) and location of the acoustic Doppler current profilers (ADCPs) (blue dots). Red dots show stations used to depict cross-shore (L1) and along-shore (L2) views of the hydrographic properties. Mean surface current vectors and variance ellipses (in blue) during July 2018 are also shown. Orange dots depict the spatial location chosen to display the vertical distribution of the HYCOM model observations (LHycom). The background color is the bathymetry. GoM, Gulf of Mexico; YS, Yucatan Shelf; YC, Yucatan Current.

The Yucatan Shelf, also known as the Campeche Bank, is situated in a tropical region with an abundant amount of precipitation, where its karst nature absorbs all the rainwater and leaves no surface runoff. The freshwater inputs to the sea are through coastal lagoons and underground water holes scattered along the seabed on the northern coast (Herrera-Silveira et al., 2002; Valle-Levinson et al., 2011; Enríquez et al., 2013). High temperatures in the summer produce high levels of evaporation in the shallow lagoons, which become hyperhaline. The Yucatan Shelf has a strong oceanic influence from the Yucatan Current, a branch of the large North Atlantic Anticyclonic Ocean Gyre; although the exchange of properties is limited due to the shallowness of the region, some important processes occur on the northeastern flank of the shelf, such as the upwelling events (Ruiz-Renteria, 1979; Furnas and Smayda, 1987; Reyes-Mendoza et al., 2019), and some on the western side, where coastally trapped waves along the shelf break had been found to play an important role in the interchanging of nutrients between the shelf and the ocean (Estrada-Allis et al., 2020).

Upwelling onto the Yucatan shelf has been investigated by many authors (Belousov et al., 1966; Cochrane, 1966, 1968, 1969; Bogdanov et al., 1968; Bessonov et al., 1971; Bulanienkov and Garcia, 1973; Ruiz-Renteria, 1979). Multiple mechanisms driving upwelling have been proposed (Cochrane, 1966; Ruiz-Renteria, 1979; Furnas and Smayda, 1987; Merino, 1997; Reyes-Mendoza et al., 2016; Ruíz-Castillo et al., 2016; Jouanno et al., 2018); nevertheless, the subject is still a matter of investigation. Although the dominant winds are parallel to the coast, it appears that their strength is not enough to drive the typical upwelling. The most convincing hypothesis suggests that the Yucatan upwelling is driven by the interaction of the Yucatan Current and the Yucatan Shelf, driving bottom Ekman pumping in the shelf break (Furnas and Smayda, 1987; Merino, 1997; Jouanno et al., 2018), which at the east of the Peninsula presents a notch (Cabo Catoche) that manages to introduce subsurface waters from the Caribbean from ∼250 m deep to the surface, which is then carried westwards on the shelf and redistributed it along the coast (Reyes-Mendoza et al., 2016; Ruíz-Castillo et al., 2016; Estrada-Allis et al., 2020).

The Yucatan upwelling has been studied for some time with a primary focus on its development on the eastern side and its later transport to the central part of the Peninsula. There has been very little effort looking at the impact of this upwelling on

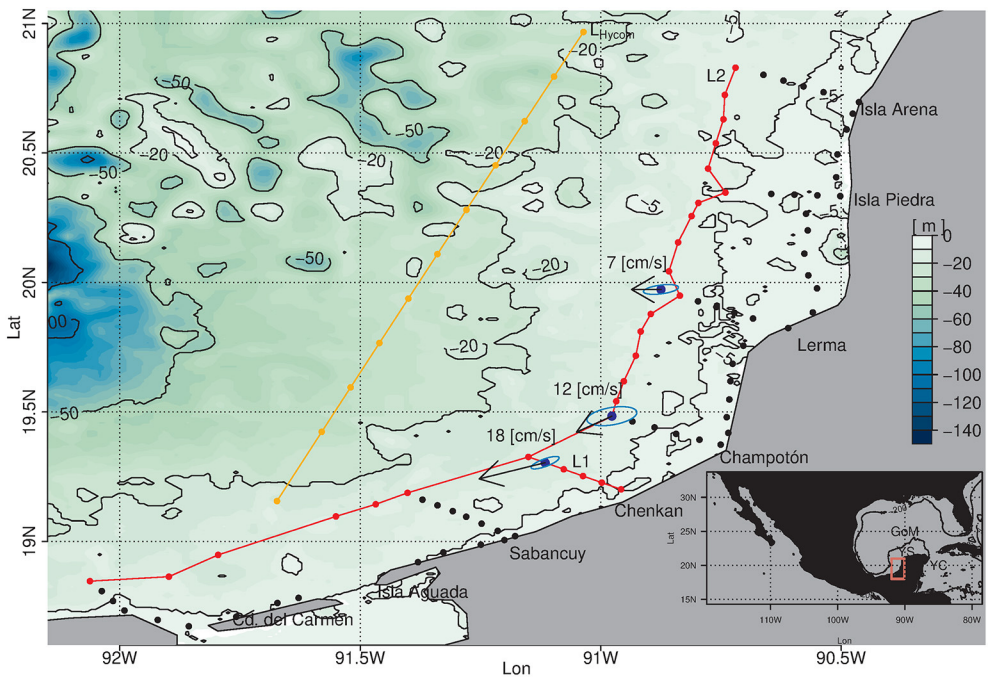

FIGURE 1 | Oceanographic surveys (black dots) and location of the acoustic Doppler current profilers (ADCPs) (blue dots). Red dots show stations used to depict cross-shore (L1) and along-shore (L2) views of the hydrographic properties. Mean surface current vectors and variance ellipses (in blue) during July 2018 are also shown. Orange dots depict the spatial location chosen to display the vertical distribution of the HYCOM model observations (LHycom). The background color is the bathymetry. GoM, Gulf of Mexico; YS, Yucatan Shelf; YC, Yucatan Current.

the western shelf, on the Campeche side. With evidence from hydrographic data, this study shows for the first time the presence of upwelling waters on the western shelf. These observations are supplemented with climatological Lagrangian integrations based on a 12-year HyCOM Gulf of Mexico simulation, which helped discern the origin of the observed phenomenon and how it was transported more than 500 km to the west of its source. Also, the climatological simulations suggested the recurrence of the westward advection toward the study region, which was corroborated using sea surface temperature (SST) images remotely sensed. This study aids to understand how primary productivity in the central and western Yucatan Shelf is driven.

MATERIALS AND METHODS

In situ Data

Oceanographic Survey

Five oceanographic surveys from July 2017 to July 2018 were conducted on small boats covering the first ∼30 km offshore of the western Yucatan Peninsula to observe the seasonal variation of the hydrography of the shelf. Each survey took about 1 week to be completed and was planned 3 months apart from each other. This study shows the result of the 5th campaign that occurred during summer 2018 (July 23–28). The vessels were equipped with a handheld, factory-calibrated Valeport miniCTD, to collect temperature, conductivity, and depth data, at all sampling stations (see **Supplementary Table 1**). These data were later transformed to observations of conservative temperature (CT) and absolute salinity (SA) using the thermodynamic equation of seawater TEOS-10 toolbox (McDougall and Barker, 2011). To show the surface distribution of SA and CT in the study region, surface samplings of these variables were optimum-interpolated using the Data-Interpolating Variational Analysis software (Troupin et al., 2012). All *in situ* data were processed using R software (R Core Team, 2014). The raw CTD data from this survey are publicly available at https://doi.org/10.6084/m9.figshare.15125214.v1

Acoustic Doppler Current Profiler Observations

Two acoustic Doppler current profilers (ADCPs) were moored on the western continental shelf of the Yucatan Peninsula. These were 1 MHz Nortek-acoustic wave and current profilers (AWACs) measuring bins starting at 1.4 m above the bottom until ∼3 m below the surface, recording 6 s averages every 20 min. The ADCPs were used to measure three sites, two of these simultaneously (**Table 1**). Tides were removed from the ADCP observations using a Lanczos filter with a cutoff frequency of 24 h, leaving only the currents driven by wind stress and geostrophy, modified by the bottom friction. The raw ADCP data for June and July 2018 are publicly available at:

(1) Lerma: https://doi.org/10.6084/m9.figshare.15127434.v1

(2) Champoton: https://doi.org/10.6084/m9.figshare.15127470.v1

(3) Chenkan: https://doi.org/10.6084/m9.figshare.15127464.v1

Satellite Data

For illustrative purposes, the regional distribution of the SST and winds was depicted during July 2018, where the following data sets were employed:

Optimum Interpolation Sea Surface Temperature

The National Oceanic and Atmospheric Administration (NOAA) 1/4° daily Optimum Interpolation Sea Surface Temperature (or daily OISST) is an analysis constructed by combining observations from different platforms (satellites, ships, and buoys) on a regular global grid. A spatially complete SST map is produced by interpolating to fill in gaps. The methodology includes bias adjustment of satellite and ship observations (referenced to buoys) to compensate for platform differences and sensor biases (Reynolds et al., 2002). These data were provided by the NOAA/OAR/ESRL PSD, Boulder, Colorado, USA, from their website at https://www.esrl.noaa.gov/psd/.

ASCAT

Daily wind and wind stress fields are estimated over global oceans from Metop/Advanced Scatterometer (ASCAT) retrievals using an objective method. The resulting fields have spatial resolutions of 0.25° in longitude and latitude. The calculation of daily estimates uses ascending and descending available and valid retrievals. Data and documentation are freely distributed on Cersat/Ifremer FTP site (ftp://ftp.ifremer.fr/ifremer/cersat/products/gridded/MWF/L3/ASCAT/Daily/).

Ocean Model

Model simulations come from the Hybrid Coordinate Ocean Model (HyCOM), and its coordinates are isopycnal in the open stratified ocean, terrain-following in shallow coastal regions (σ), and z-level near the surface mixed layer. It has a 1/25° spatial resolution and 27 layers in the vertical. Forcing for the ocean model comes from the National Centers for Environmental Prediction (NCEP) Climate Forecast System Reanalysis (CFSR). The open boundary conditions are provided by the global HYCOM reanalysis. The K-Profile Parameterization (KPP) turbulence closure scheme is employed. Model bathymetry is derived from the Naval Research Laboratory Digital Bathymetry Data Base 2-minute. It includes eight tidal constituents from topex inversion: M2, S2, K1, O1, N2, P1, K2, and Q1, and data assimilation from the Navy Coupled Ocean Data Assimilation (NCODA). These incorporate satellite altimeter observations (along-track data), satellite and *in situ* SST, and *in situ* vertical temperature and salinity profiles from XBTs, ARGO floats, and moorings. The version used was the HyCOM GOM10.04 expt. 32.5.

Trajectory Simulations

Trajectories were integrated back in time for 40 days, from July 19 to June 10, in one experiment using the 2018 velocities, and in another experiment using the 2003–2014 HyCOM climatological velocity described in Duran et al. (2018). The almost 7,000 trajectories in each experiment were computed using a fourth-order Runge-Kutta with cubic interpolation, a combination that is efficient and accurate when integrating

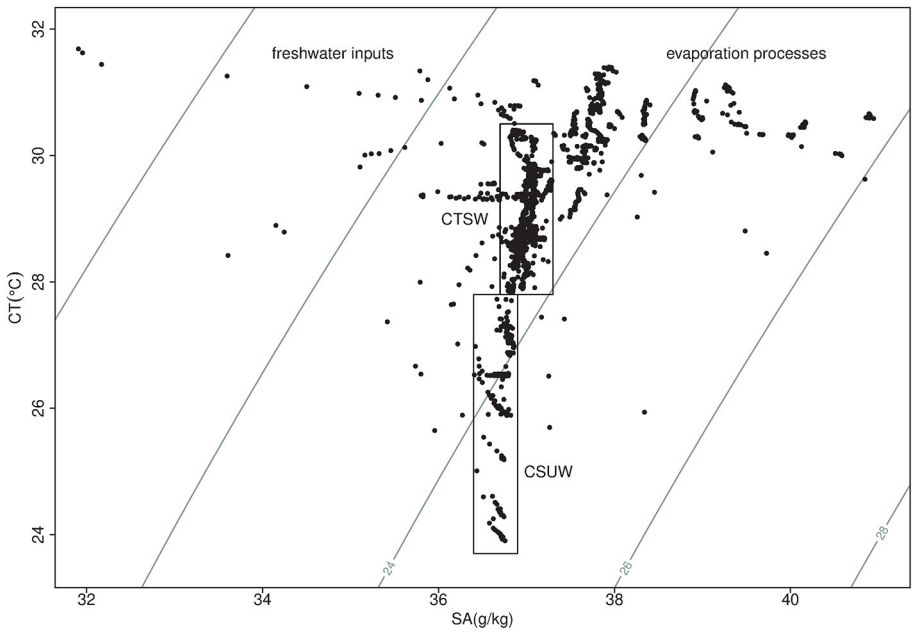

FIGURE 2 | Temperature (conservative temperature) and salinity (absolute Salinity) diagram for July 2018. Water type signatures found during this survey are as follows: (1) The CTSW—Caribbean Tropical Surface Water, and (2) the CSUW—Caribbean Subtropical Under Water. Contours represent σ_θ values.

TABLE 1 | Position, time span, and water depth of the deployed acoustic Doppler current profilers (ADCPs).

	Fixed ADCP	ADCP 2.a	ADCP 2.b
Location	Lerma	Champoton	Chenkan
Position	19°58'22.80"N, 90° 52'29.03"W	19°29'1.86"N, 90°58'36.12"W	19°18'15.48"N, 91°6'56.34"W
Time span	24/Agu/2016 to 13/Feb/2019 (∼ 2.5 years)	06/Apr/2017 to 13/Jul/2018 (∼ 1.25 years)	26/Jul/2018 to 02/May/2019 (∼ 9 months)
Water depth	11 m	12 m	15 m

discrete data (Nordam and Duran, 2020). The 2018 velocity was a two-dimensional field at 5 m depth, while the climatological velocity was a surface field.

Comparative Analysis Between Modeled Currents and ADCP Observations

To evaluate the agreement between HyCOM and ADCP data, we estimated the daily mean for the ADCP data and compared the 5 m depth observations of both data sets. Three comparative analyses were carried: complex correlation (corrcoef), Normalized Root Mean Square Error (N_{RMSE}), and Skill Score (SS) (Willmott et al., 1985; Lorente et al., 2021). To estimate the N_{RMSE}, we divided the RSME by the SD of the observations, whereas the SS is defined as a dimensionless number from 0 to 1 where the highest value (SS = 1) means a perfect agreement between the two data sets:

$$SS = 1 - \frac{\sum |X_{model} - X_{observation}|^2}{\sum \left(|X_{model} - mean\,(X_{observation})| + |X_{observation} - mean\,(X_{observation})|\right)^2}$$

Climatological Lagrangian Coherent Structures

Climatological Lagrangian Coherent Structures (cLCSs) were developed in Duran et al. (2018) to identify persistent or recurrent Lagrangian transport patterns from large time series of Eulerian velocity. The instantaneous trajectories in this study are compared with the Gulf of Mexico cLCS computed in Duran et al. (2018). The code for cLCS is described and freely available (Duran et al., 2019); the climatological velocity (with which the results of Duran et al., 2018 can be replicated) is also available at that repository.

Climatological Lagrangian Coherent Structure differs from typical Lagrangian Coherent Structures (LCSs), and in that the Cauchy-Green tensor is averaged over different initial times, and that the time-dependent velocity is climatological. Regarding the climatological averaging, it is shown in the first section of the results in Duran et al. (2018) that the Eulerian climatological velocity preserves the main Lagrangian circulation in an ensemble-mean sense, where ensemble averaging of the instantaneous trajectories is over different initial times spanning several years. However, the averaging of the Cauchy-Green tensor formally destroys the transport-barrier property of LCS Haller (2015)). Thus, the interpretation of cLCS requires careful comparison with additional Eulerian and Lagrangian information, for example, described in Gouveia et al. (2021) where it is shown that cLCS may deform as chevrons. When cLCS deform as chevrons, they do not represent transport barriers, but instead, they identify a jet-like structure, as is the case in this study where cLCS identifies a coastal jet-like

current. However, depending on the local circulation, cLCS may also indicate persistent and efficient transport barriers (Duran et al., 2018; Gough et al., 2019) or recurrent attractive pathways (Duran et al., 2018; Aljaz et al., 2020). The different interpretations for cLCS follow the fact that cLCS can be thought of as a superposition of 7-day LCS from the climatological velocity, with the integration initiating at different times (see, e.g., Appendix C of Duran et al., 2018). In the Supporting Information (Appendix A) of Duran et al. (2018), it is shown that the deformation due to along-path horizontal divergence is negligible, and therefore, the patterns identified by cLCS are due to large-scale two-dimensional flow (see also Supporting Information in Gouveia et al., 2021). This does not exclude the possibility of a vertical circulation due to superimposed upwelling, as an example.

RESULTS

In situ and Remote Observations

The Yucatan Shelf is a shallow environment defined by a very smooth slope, 1 m/3,000 m off Campeche and 1 m/1,000 m off Yucatan, where the accessibility of the vessels is limited by draft restrictions. In this study, the sampling stations of the surveys fell on depths ranging between 2- and 20 m depth, capturing the thermohaline variations of the first ∼30 km of the coast. **Figure 2** depicts the T/S diagram of the campaign, where two water types were found: (1) Caribbean Tropical Surface Water (CTSW), also called Yucatan Seawater (off Yucatan, Enríquez et al., 2013), and (2) Caribbean Subtropical Under Water (CSUW), also called Gulf Common Water (off the west coast of the GoM, Vidal et al., 1994). The former occupied most of the study region, showing a modification of the CTSW having saltier values than those presented in previous reports (**Table 2**). Waters located in the first 5 m showed very warm temperatures (29.6 ± 1°C) with large salinity and density ranges, influenced mainly by evaporation processes and to a lesser extent by nearshore freshwater inputs from the Champoton river, coastal lagoons, and submarine groundwater discharges, and the latter particularly located near the coast in the northern part of the study area, between Lerma and Isla Arena (20–21°N, 91°W).

On the other hand, water temperatures below 26°C were seen between 7 and 16 m depth on the furthest sampling stations to the shore (particularly from Champton to Carmen), which correspond to the Caribbean Subtropical Under Water, modified with saltier values. Thermohaline distributions of the deepest parts of the study region illustrated the existence of two water types: CTSW above CSUW, locally modified by evaporation/freshwater inputs processes. During this survey, evaporation processes greatly exceeded precipitation (or freshwater inputs) as both water types showed saltier values, even though the survey was carried in the middle of the rainy season, defined from May to November. CSUW is commonly located in the Yucatan Channel at 250 m depth, and its presence over the Yucatan Shelf is attributed to upwelling processes occurring at the northeastern side of the Peninsula, triggered by the interaction of the Yucatan current with the continental shelf (Merino, 1997; Jouanno et al., 2018). On the west side of the shelf, ∼500 km away, the existence of this water type can only be attributed to advection; in general, currents over the Yucatan Shelf present a smooth-westward flow forced mainly by the trade winds (Zavala-Hidalgo et al., 2003; Ruíz-Castillo et al., 2016). Off Campeche, ADCP observations depicted a markedly southwestward flow (**Figure 3; Supplementary Figure 1**), exhibiting the continuation of the shelf circulation on the western side, responsible for bringing Caribbean subsurface waters (CSUW) into the study area. Estrada-Allis et al. (2020) proposed a schematic diagram of the cross-shelf transport of nutrients all along the Yucatan Shelf. On the west shelf, their sketch is very similar to what we found with our ADCP observations corroborating this hypothesis (see the mean current vectors in **Figure 1**).

Figure 4 shows the surface salinity and temperature distribution during the days of the survey, which can be thought of as a 6-day composite of observations. At the northwestern edge of the sampling region (off Isla Arena), upwelled waters coming from the Yucatan coast entered the study area bringing colder temperatures and mild salinities (27°C and 37.2 g/Kg, respectively). From Isla Piedra to Lerma, salty and warm CTSW values were found, located over a very shallow depth (notice the

TABLE 2 | Reported T and S intervals for CTSW and CSUW, for different seasons and regions within the GoM.

References	Region	CTSW	CSUW
Nowlin and Mclellan (1967)	Yucatan area and the eastern Gulf Loop (during winter)	35.9 ≤ S ≤ 36.2 psu	Salinity maxima 36.75 psu
		–	22.5°C
Vidal et al. (1994)	Given names	–	Gulf common water
	GoM west coast (during winter)	–	36.3 ≤ S ≤ 36.4
		–	∼ 22.5°C
Merino (1997)	Given names	Caribbean surface water	Yucatan upwelling water
	Eastern Yucatan Shelf (different seasons)	36.3 ≤ S ≤ 36.4 psu	36.1 ≤ S ≤ 36.5 psu
		26 ≤ T ≤ 27.5°C	16 ≤ T ≤ 20°C
Aldeco et al. (2009)	Given names	Modified CTSW	Modified CSUW
	Bay of Campeche (during summer)	36.4 ≤ S ≤ 36.8 psu	36.4 ≤ S ≤ 36.6 psu
		28 ≤ T ≤ 30 °C	22 ≤ T ≤ 26 °C
Enríquez et al. (2013)	Given names	Yucatan sea water	Modified CSUW
	Yucatecan coast (during summer)	36.4 ≤ S ≤ 36.8 psu	36.4 ≤ S ≤ 36.7 psu
		26 ≤ T ≤ 31 °C	22 ≤ S ≤ 26 °C
This work	Given names	Modified CTSW	Modified CSUW
	Campeche coast (during summer)	36.7 ≤ S ≤ 37.3 g/kg	36.4 ≤ S ≤ 36.9 g/kg
		27.8 ≤ T ≤ 30.5 °C	23.7 ≤ T ≤ 27.8 °C

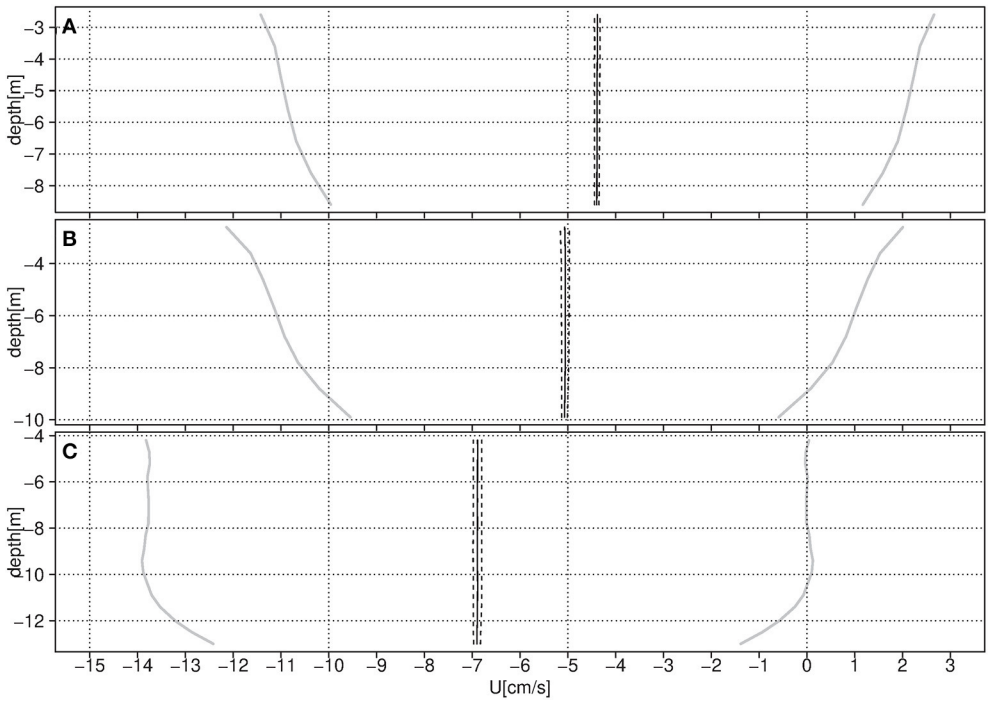

FIGURE 3 | Mean zonal current profile (*U* in cm/s) for **(A)** Lerma, **(B)** Champoton, and **(C)** Chenkan. Solid line—mean profile, dash line-–95% CI, and gray solid line—one SD.

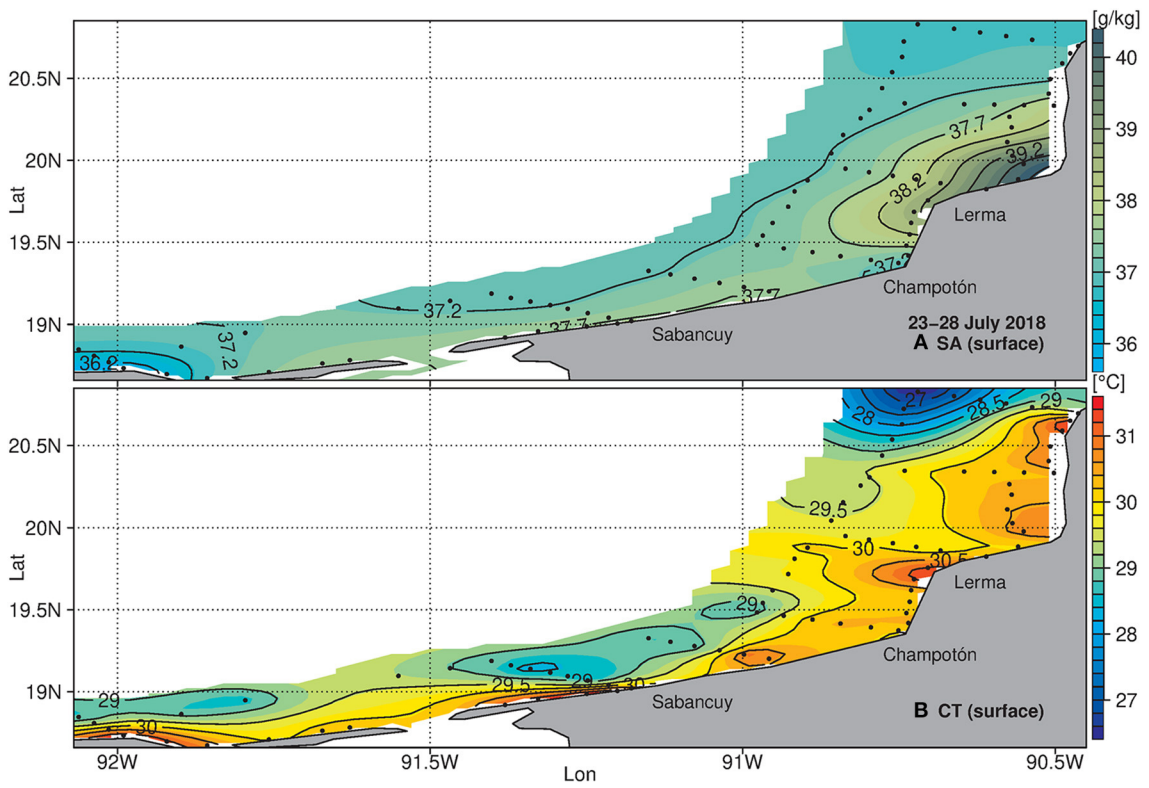

FIGURE 4 | Surface distribution of **(A)** absolute salinity (g/Kg) and **(B)** conservative temperature (°C), optimum-interpolated. This figure synthesizes 6 days of observations, from July 23 to July 28, 2018.

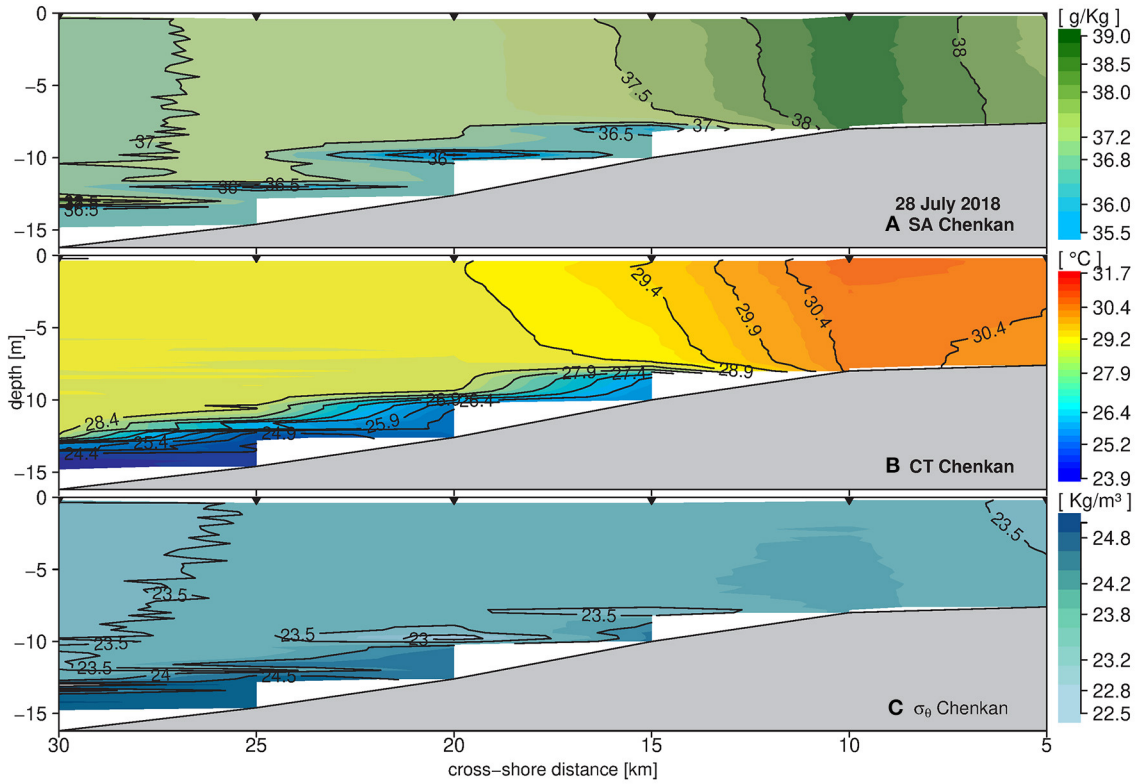

FIGURE 5 | Cross-shore view of the vertical distribution of **(A)** absolute salinity (g/Kg), **(B)** conservative temperature (°C), and **(C)** density (σ_θ in kg/m3), off Chenkan locality (L1 on **Figure 1**). Black triangles on top depict sampling stations. This figure represents the observations taken during July 28, 2018.

−5 m contour in **Figure 1**), that prevented the upwelled waters from approaching the coast. From Champoton to the rest of the study area, upwelled waters were seen furthest to the coast. Off Terminos lagoon (at 92°W, 18.5°N), the flushing waters from this body of water expelled warm and less salty water (30°C, 36.2 g/Kg, respectively) through its southern mouth, Boca del Carmen, to the adjacent ocean.

During summer 2018, we decided to move the Champoton ADCP further south, off Chenkan (**Table 1**); while positioning it on its new location, during the diving maneuver we noticed that the water column was divided into what it seemed two different water types, a wide layer of warm and clear water above a narrow layer of greenish low-visibility cold water, located very next to the floor. We felt curious about this phenomenon, which was unnoticeable during the recovery of this ADCP some days before off Champoton. **Figure 5** illustrates the cross-shore thermohaline distribution along the Chenkan section, where the saltier and warmer values of the CTSW were located above the fresher and colder values of the CSUW, found between 7 and 15 m depth in a narrow band extended on more than 15 km long, away from the coast. As mentioned before, CTSW salinity and temperature contours span from the surface until 7 m depth. Next to the shore, they occupied the whole water column exhibiting thermohaline contours vertically distributed, but in the region where both water types met, a small gradient was built and now the thermohaline contours were horizontally distributed.

Figure 6 shows the along-shore distribution of the thermohaline properties on the furthest stations to the shore. As with **Figure 4**, this is a 6-day combination of the CTD observations but of the depth allocation of both water types along the study area, it is a snapshot of thermohaline distribution along the western coast. As shown by the previous results, CSUW is seen entering the study region off Isla Arena, occupying the whole water column in the northern region, but when passing by Champoton it was restricted to a thin layer close to the bottom extended until Sabancuy. Off Terminos Lagoon, the upwelled water type signature is absent, at least inside the domain of the sampling region. To examine the hydrographic data further offshore, we used the hydrographic data for the Yucatan Peninsula provided by Hycom (**Figure 7**). We inspected this information along a transect located at the middle of the west shelf for the same dates as the survey. The upwelled water (CSUW) can be seen below the local CTSW, extended from Isla Arena (at the north) until Sabancuy (near Laguna de Terminos in the south), like what is seen in the survey (**Figure 6**) but further offshore.

Remotely sensed observations were used to supplement the spatial and temporal extent of the study and illustrate the behavior of SST and winds, during the dates of the upwelling event. SST anomalies exhibited a cold tongue of seawater extending from the north-eastern coast of the Yucatan Peninsula to Isla Aguada, in southern Campeche, reaching a

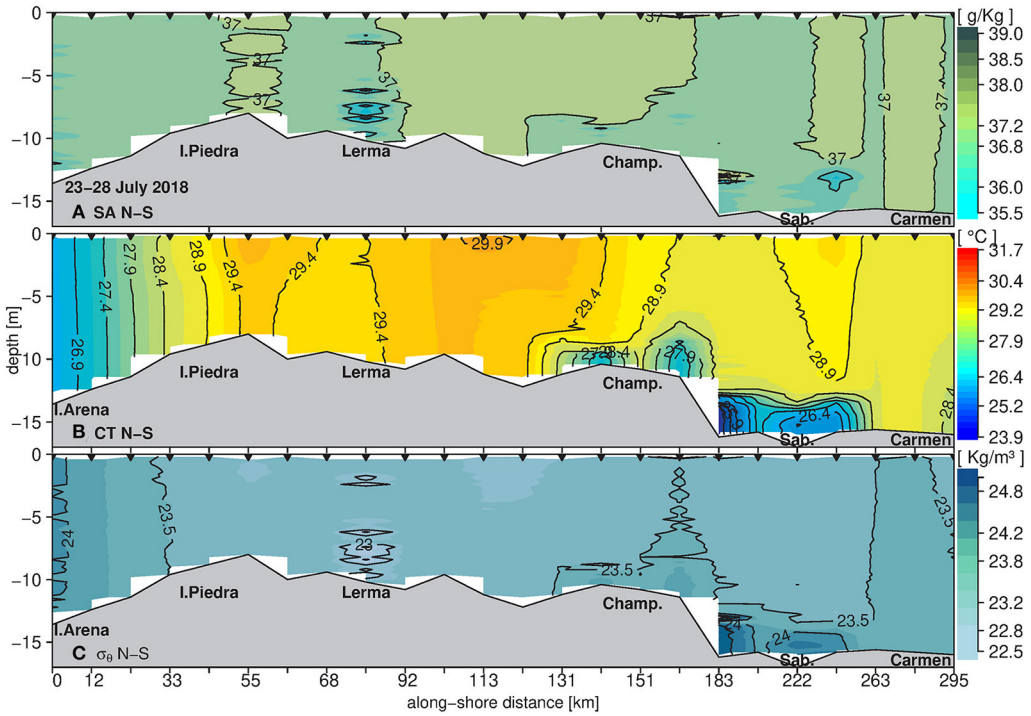

FIGURE 6 | Along-shore view of the vertical distribution of **(A)** absolute salinity (g/kg), **(B)** conservative temperature (°C), and **(C)** density (σ_θ in kg/m3), for the sampling stations aligned from north to south (L2 on **Figure 1**). Black triangles on top depict sampling stations. This figure synthesizes 6 days of observations, from July 23 to July 28, 2018.

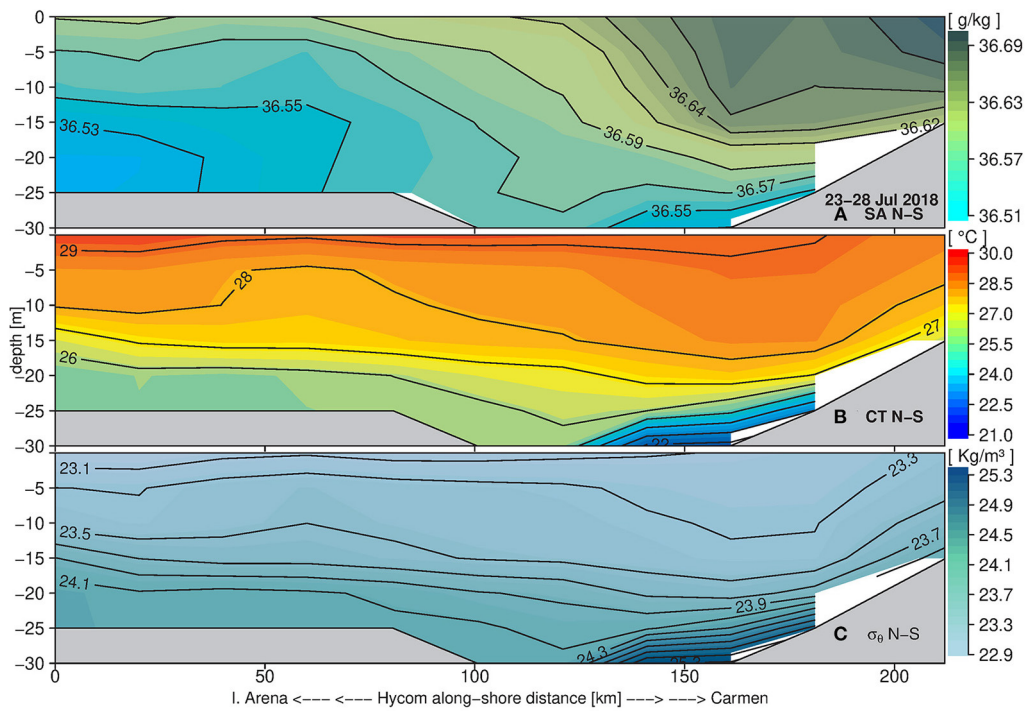

FIGURE 7 | Along-shore view of the vertical distribution of **(A)** absolute salinity (g/kg), **(B)** conservative temperature (°C), and **(C)** density (σ_θ in kg/m^3), from north to south, extracted from the Hycom modeled observations (L_{Hycom} on **Figure 1**).

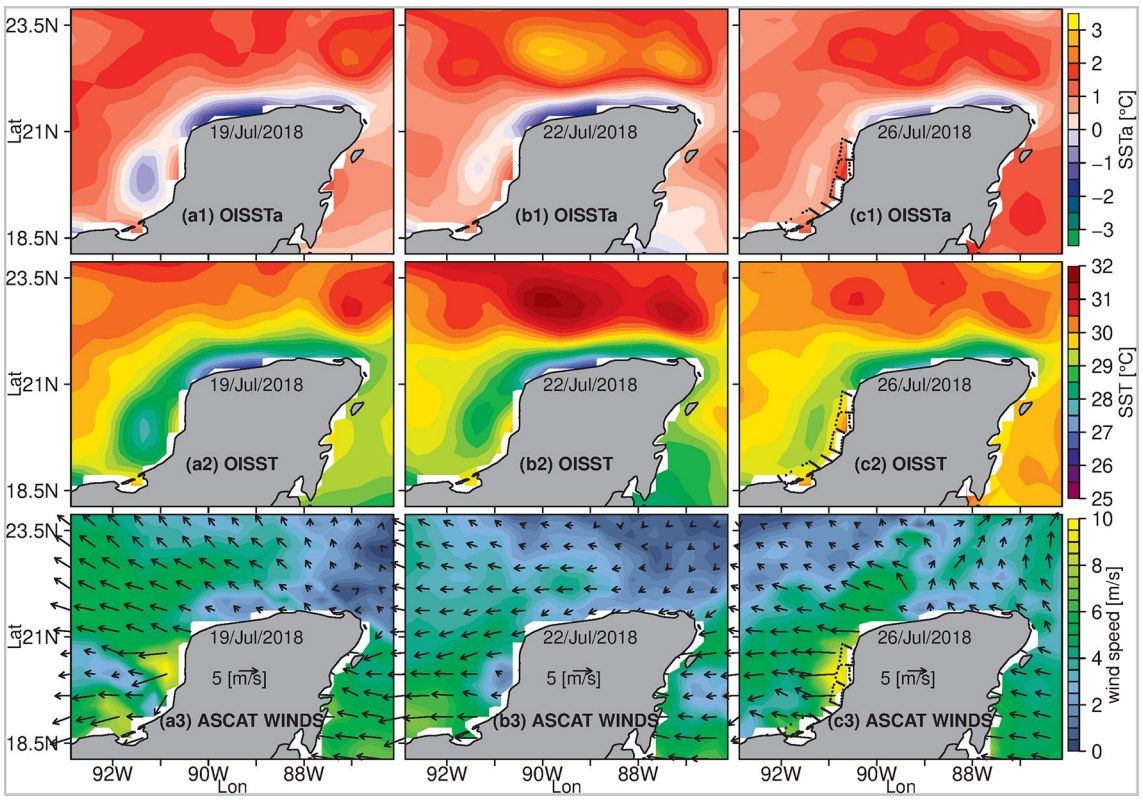

FIGURE 8 | Satellite images of the end of July 2018, of the regional distribution of Sea Surface Temperature anomalies **(a1,b1,c1)**, SST **(a2,b2,c2)**, and surface winds **(a3,b3,c3)**.

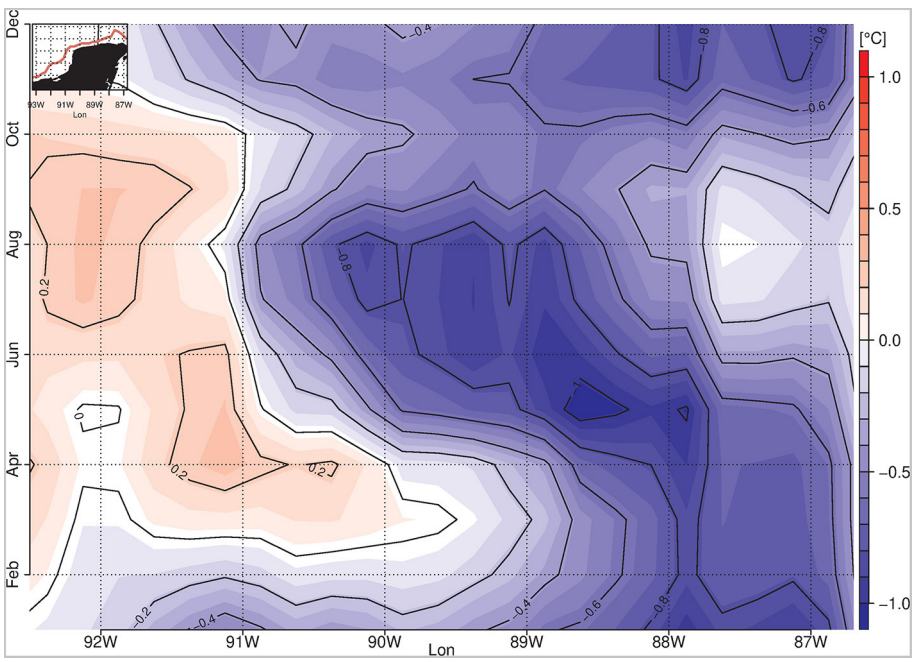

FIGURE 9 | Hovmöller diagram of the monthly averaged remotely sensed SST anomalies. Red (blue) color shows warmer (colder) temperatures than the 39 years spatial-temporal mean (1981–2020). The transect used for the calculations is in the top left (in red).

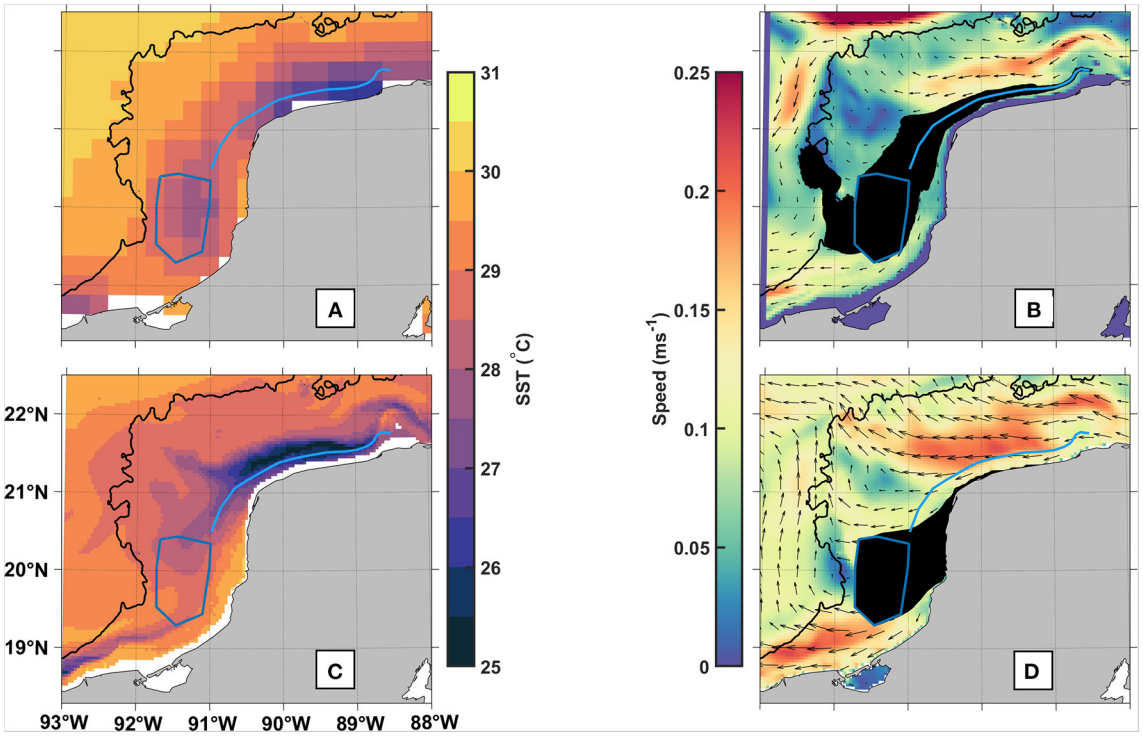

FIGURE 10 | Sea surface temperature (°C) from satellite **(A)** and HyCOM GoM **(C)** on July 19, 2018. The blue polygon is used as initial conditions for back-in-time trajectories to investigate the cool water pool origin in the satellite data **(A)**. Black dots in the right column are points from trajectories initiated within the blue polygon (July 19, 2018) and integrated back-in-time for 40 days (June 10, 2018) using HyCOM GoM velocity at 5 m depth **(B)**, and a 1994–2014 climatological velocity at the surface **(D)**. Color contours in the right column are the velocity magnitude (ms^{-1}) used for the trajectories after time averaging, HyCOM GoM at 5 m depth is shown in **(B)**, and the velocity climatology at the surface is shown in **(D).** The blue line is used as a path representative of most of the trajectories shown in **(B)** and is plotted as a reference in the other panels. The 50-m isobath is shown in black (**Figure 10**).

minimum SSTa during July 19 (**Figure 8a1**). Near the coast, the bathymetric restriction off northern Campeche (20–21°N, 91°W) presented warmer anomalies in the period of the event, as shown in the CTD observations. During the time of the survey (**Figure 8c1**), this phenomenon was weakening and retracting, showing smoother SSTa with positive values off Campeche and low-negative values off Yucatan. This explains why in **Figure 6** off Terminos Lagoon the influence of the upwelled water is absent, and it is not because the water does not reach up to there but rather than the event was already weakening, since in previous dates (**Figure 8a1**) the SSTa contours showed negative anomalies in this region. Winds were always easterlies during the time of the event (**Figure 8**, lower panels).

Using a Hövmuller diagram (**Figure 9**) of the along-shore SST anomaly distribution from the Caribbean Sea (87°W) until the Tabasco coast (>92°W), we explored the regularity of the advected upwelled waters over the western coast, where cooling events are related to negative anomalies (blue color values). From the eastern side of the shelf until the Campeche coast, cooling events are seen along-shore all year-round. Although SST is related to different surface heat budget processes and could be noisy to be attributed solely to the upwelling events, it showed an interesting resemblance to the findings of Merino (1997) and Ruíz-Castillo et al. (2016), exhibiting colder SST anomalies between July and August (in summer) off Campeche, and between April and August (spring and summer) off the Yucatecan coast. During winter (from January to March), surface cooling events encompassed all the region, from the Caribbean until Tabasco, although SST anomalies were low and are rather related to the synoptical effect of the northerly cold wind burst events that affect the GoM.

Lagrangian Simulations

Trajectories were initiated from a regular grid of initial positions with a constant spacing of 0.01 degrees within a polygon encompassing the Campeche pool of cool water as determined from satellite SST on July 19, 2018 (**Figure 10**). Back-in-time trajectories indicate that the water within the polygon of initial positions mainly came from the northeast in the 2018 experiment and only from the northeast in the climatological experiment. Comparative analyses between the ADCP currents and HyCOM observations were carried at the three recording sites, and in general, the results showed a reasonable agreement between *in situ* and modeled observations (**Table 3**), with the best comparisons found at Chenkan.

Using the 2018 velocity, about 18% of all trajectories had at least one point to the west of the westernmost point of the initial-position polygon, and 80% of all trajectories had at least

TABLE 3 | Results of the comparative analyses between ADCP currents and modeled observations.

Location	Lerma			Champoton			Chenkan		
Comparison period	24/Agu/2016 to 31/Dec/2018 (∼ 2.3 years)			06/Apr/2017 to 13/Jul/2018 (∼ 1.25 years)			26/Jul/2018 to 31/Dec/2018 (∼ 5 months)		
Analyses results	**Corrcoef**	**N_{RMSE}**	**SS**	**Corrcoef**	**N_{RMSE}**	**SS**	**Corrcoef**	**N_{RMSE}**	**SS**
	R:0.44	U:1.2	U:0.52	R:0.48	U:1.1	U:0.62	R:0.39	U:1.2	U:0.58
	θ:64°	V:4.0	V:0.29	θ:42°	V:2.2	V:0.52	θ:3.9°	V:1.3	V:0.61

one point to the east of the easternmost point of the initial-position polygon (**Figure 10B**). In the climatological experiment, in contrast, trajectories originate only from the Yucatan Shelf to the northeast (**Figure 10**). At the surface, advection of the ocean model SST also shows cool water moving along the same path as the trajectories (**Figure 10C**). Satellite and model SST are in good agreement, although the model has additional variability as should be expected from a higher resolution (**Figures 10A,C**).

Water parcels ending within the cool water polygon (initial-position for the back-in-time trajectories) traverse most of their path along a region of relatively intense upwelling of about 1–4 m per day that is present through the water column from the bottom to 5 m deep, in the 40 days leading to the observation of the cool satellite SST pool (**Figure 11**). The maxima in upward velocity along the representative horizontal trajectory coincide with the SST minima from satellite and HyCOM data (cf. **Figures 10A,C, 11**).

There is good agreement between trajectories from the 2018 experiment computed here and cLCS from Duran et al. (2018). Trajectories from the east move across weak cLCS that are deformed as chevrons within the Yucatan Shelf, while trajectories from the northwest move along strong cLCS until they meet within the initial position polygon (**Figure 12**). The advection of cool SST coincides with most trajectories (**Figure 10C**), in crossing weak cLCS that deformed as chevrons and indicate the direction of weak transport, like in Gouveia et al. (2021), where along-slope SST advection happens through weak cLCS deformed as chevrons. cLCSs with relatively strong climatological attraction indicate transport barriers along which transport is often directed (see also Climatological Lagrangian Coherent Structures section for more details on interpreting cLCS).

DISCUSSION

The hydrographic features and the numerical simulations described here confirm the existence of northeastern upwelled waters along the western Yucatan Shelf. They were brought from the northeast by advection. In their works of upwelling events over the northeastern Yucatecan coast, Ruiz-Renteria (1979), Merino (1997), and Jouanno et al. (2018) proposed that local wind acts indirectly in the upwelling intensity and variability by inducing high-frequency variations in the current magnitude over the platform. Once the upwelled water intrudes the shelf at the Cabo Catoche, the wind-forced currents spread this water along the north coast, particularly during spring and summer (Martínez-López and Pares-Sierra, 1998; Zavala-Hidalgo et al., 2003). The long time series average, of the water column velocities measured with the ADCPs (**Figure 3**), exhibited a southwestward flow of ∼5 cm/s in Lerma and Champoton, and 7 cm/s in Chenkan. While in July 2018, mean surface velocities span from 7 to 18 cm/s (vectors in **Figure 1**), responsible for bringing Caribbean subsurface waters (CSUW) into the study area. If we consider the 500 km traveled by the upwelled waters in 40 days, as shown by the simulated trajectories, we found an average velocity of 14.5 cm/s, which agrees with the ADCP observations. At the northern shelf, off the Yucatecan coast, other studies have reported average westward velocities of 5–20 cm/s (Martínez-López and Pares-Sierra, 1998; Ruíz-Castillo et al., 2016).

An interesting feature promoted by the upwelling events is the suggestion of a two-layer water column distribution in such an open and shallow environment. Merino (1997) reported that during spring and summer the interaction between the upwelled and shelf waters (CSUW and CTSW, respectively) creates a two-layered water column with strong stratification that inhibits mixing between them. In some areas of our study, hints of a two-layer system are apparent, as reported by Merino (1997), and the bottom layer is water that rises to the platform (the CSUW), while the top layer is the water that was already on the Yucatan platform (modified CTSW). As the CSUW is advected westward, it mixes with the local waters and upwells in a more traditional wind-induced type of upwelling along its path. Thus, the cooler water can be seen as a bottom layer and a surface layer, although additional observations are needed to better define the stratification and mixing mechanisms of these two water types within the shelf.

Other authors had shown evidence of the large spatial coverage of these upwelling events in the northern Yucatan Shelf (Ruíz-Castillo et al., 2016) and its duration from spring to autumn (Merino, 1997), demonstrating its importance on the productivity of the region, as nitrate distributions of the upwelled water layer fertilize the shelf (Furnas and Smayda, 1987; Merino, 1997; Estrada-Allis et al., 2020). Although we did not present any nitrate, we believe that the upwelling events we report should enhance productivity off the coast of Campeche. Additional interdisciplinary data are needed to improve our understanding of the role that upwelling may play in the seasonal and interannual variability of nutrients and primary productivity, and their impact on regional fishing resources.

Studies on the seasonality of the upwelling events over the Yucatan Shelf (Molinari, 1980; Merino, 1997) attributed it to the Yucatan Current flow intensity, which strengthens during spring and summer and weakens in autumn-winter, implies bottom friction mechanisms. On the other hand, Ruíz-Castillo et al. (2016) explored the relationship between the along-shore wind stress over the shelf and the seasonality of the upwelling events, using a longitude-time (Hövmuller) diagram of the mean monthly upwelling index. They found upwelling events

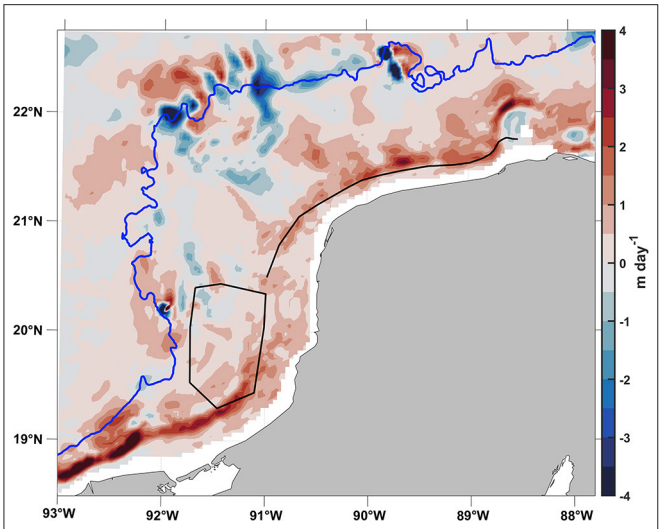

FIGURE 11 | Vertical velocity (mday^{-1}) from HyCOM GoM, time-averaged June 10, 2018, through July 19, 2018, and depth-averaged between 5 and 50 m, or bottom when <50 m. The 50 m isobath is shown in blue; the polygon used for initial trajectory positions, and a representative trajectory (see **Figure 10**) are shown in black.

throughout the year with two strong periods: March–July and October–December, the former being stronger. As mentioned above, the monthly averaged SST anomalies (**Figure 9**) showed a resemblance to the findings of Merino (1997) and Ruíz-Castillo et al. (2016), exhibiting colder SST anomalies between July and August (in summer) off Campeche, and between April and August (spring and summer) off the Yucatecan coast. Also, the climatological Lagrangian Coherent Structures (**Figure 12**) support the recurrence of westward advection toward the study area, suggesting that the 2018 upwelling and advection event were not an isolatedone.

The climatological Lagrangian results presented here agree with the ensemble-mean Lagrangian circulation sustained by the instantaneous HyCOM-GOM10.04 velocity from 1994 through 2014, depicted, for example, in Figure 1 of Duran et al. (2018). In that figure, the ensemble-mean distribution of a passive tracer moves westward over the Yucatan Shelf. To obtain the ensemble-mean distribution of tracer in Duran et al. (2018), the ensemble averaging is taken over a series of different initial conditions spanning from 1994 to 2014, thus linking climatological Lagrangian transport and ensemble-averaged instantaneous Lagrangian transport. Blue tracer reaches the furthest toward the west at the location where cLCSs deform as chevrons toward the west and where the climatological attraction is weakest. This is in excellent agreement with the 2018 model SST advection and trajectory simulation presented here (**Figure 10**), where trajectories originating in the Yucatan Shelf move across cLCS where the climatological strength of attraction is weakest and deform as chevrons toward the west (**Figure 12**). Thus, the existence of a predominant pathway connecting the eastern Yucatan Shelf and the Bay of Campeche becomes clear. The different experiments supporting a persistent along-slope Lagrangian link from the Yucatan Shelf to the Campeche shelf include the 2018 trajectory simulation presented here (**Figure 10**), the ensemble-mean tracer distribution from an instantaneous velocity spanning from 1994 through 2014, and cLCS computed from 1994 to 2014 climatological velocity (Duran et al., 2018). Trajectories computed directly from the climatological velocity are also in good agreement with this pattern, although when initiated in the Campeche pool of cool water and integrated backward in time, trajectories move westward closer to the coast, where strongly attracting cLCSs align with the coastline, thus confirming the cLCS' strong attraction (**Figures 10**, **12**). These simulated results are supported by observations of water masses as described above.

CONCLUSIONS

Upwelling events over the Yucatan Shelf are an important physical phenomenon to the region. There has been very little effort looking at the impact of upwellings on the western shelf, on the Campeche side. This study used a combination of observations and numerical modeling to show evidence for the first time, of the presence of upwelled waters on the western side. The 2018 velocity from HyCOM, along with the climatological Lagrangian Coherent Structures (cLCS) methodology, identifies recurrent pathways from Yucatan to Campeche. Lagrangian simulations, integrated back-in-time, identified the time and place of origin of the upwelled water. In agreement, our observational results show that Subtropical Caribbean Underwater (CSUW) was brought from the northeast shelf, over 500 km away from the study area, by ocean current advection. Numerical outputs demonstrated that these flows took over a month (40 days) to arrive at the study region, traveling along-shelf with an average velocity of 14.5 cm/s, comparable to the magnitude and direction of the ADCP observations off Campeche. Near the bottom, in the regions where the bathymetry allowed the upwelled water to approach the shore, the water column exhibited two different water types, evidencing Tropical Caribbean Waters (CTSW) on the surface, and CSUW extending near the ocean floor. A Hovmüller diagram of the monthly averaged SST anomalies from a 39-year time series suggested that upwelled waters off Campeche are a regular phenomenon during summer. The recurrence of westward advection toward the study area is also supported by climatological Lagrangian Coherent Structures and by the ensemble-mean Lagrangian simulations of Duran et al. (2018) spanning from 1994 to 2014.

More information is needed to address this interesting phenomenon and improve our understanding of their frequency of occurrence and the important implications that they must have on the marine biota over the west shelf, by bringing upwelled colder and nutrient-rich subsurface waters. The following are some questions that remain open and would be interesting to address in future work: (1) the role that upwelled waters play in the heat budget of the Yucatan Shelf that in spring and summer exhibits high atmospheric temperatures (>35°C). (2) Northerly cold wind burst phenomena are known to diminish upwelling events on the eastern Yucatan Shelf, but can they bring subsurface waters from the northwestern shelf? (3) To the west

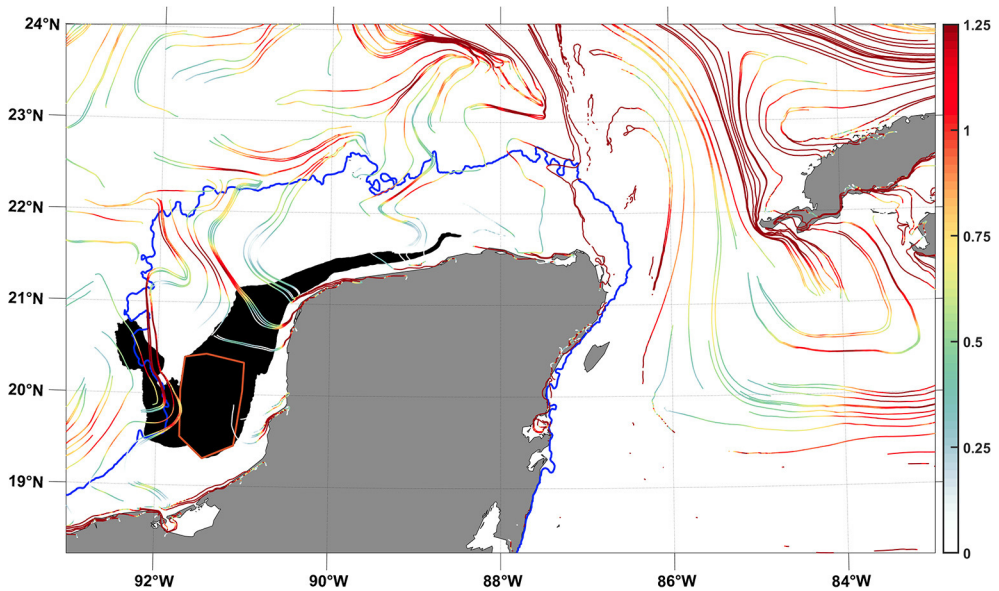

FIGURE 12 | Climatological Lagrangian Coherent Structures (lines) colored according to their climatological strength of attraction (cρ, logarithmic scale) for July. The trajectories from **Figure 10B** are plotted in black, with the polygon used for their initial positions is plotted for reference in dark orange. The 50 m isobath is shown in blue.

of the study region, off the Tabasco coast, trade winds produce upwelling events, is there any connection between them and the Campeche coast?

DATA AVAILABILITY STATEMENT

The datasets presented in this study can be found in online repositories. The names of the repository/repositories and accession number(s) can be found below: https://doi.org/10.6084/m9.figshare.15125214.v1; https://doi.org/10.6084/m9.figshare.15127434.v1; https://doi.org/10.6084/m9.figshare.15127470.v1; https://doi.org/10.6084/m9.figshare.15127464.v1.

AUTHOR CONTRIBUTIONS

JK: conceptualization, methodology, software, writing—original draft preparation, and funding acquisition. RD: conceptualization, methodology, software, and writing—original draft preparation. EB and AS: writing—reviewing and editing. All authors contributed to the article and approved the submitted version.

FUNDING

JK would like to thank the financial aid of CONACyT grants: Cátedras CONACyT (1912), Ciencia Básica (257075), and Apoyo al Fortalecimiento y Desarrollo de la Infraestructura Científica y Tecnológica (270455). AS was partially funded by the CONACYT Sabbatical visit (265894) and by the NOC core funding. RD wants to express that the funding for the development of HyCOM has been provided by the National Ocean Partnership Program and the Office of Naval Research. Data assimilative products using HyCOM are funded by the U.S. Navy. Computer time was made available by the DoD High-Performance Computing Modernization Program. The output is publicly available at https://hycom.org.

ACKNOWLEDGMENTS

Special thanks to Gabriel May Uc, Julio Uc Medina, and Heber Uc González for their fieldwork support in the oceanic surveys and to the Instituto EPOMEX for all the facilities provided to carry out this work. We would like to thank the fruitful contributions of three reviewers.

SUPPLEMENTARY MATERIAL

The Supplementary Material for this article can be found online at: https://www.frontiersin.org/articles/10.3389/fmars.2021.723452/full#supplementary-material

Supplementary Table 1 | Spatial location and dates of the CTD stations during the 2018 summer sampling.

Supplementary Figure 1 | ADCP zonal currents (*U* in cm/s) for **(A)** Lerma, **(B)** Champoton, and **(C)** Chenkan. Blue (red) colors represent westward (eastward) velocities.

REFERENCES

Aldeco, J., Monreal, M. A., Signoret, M., Salas de León, D. A., and Hernández, D. U. (2009). Occurrence of a subsurface anticyclonic eddy fronts, and *Trichodesmium* spp. *Cienc. Mar.* 35, 333–344. doi: 10.7773/cm.v35i4.1551

Aljaz M., Azevedo Correia de Souza J. M., Andrade-Canto F., and Rodríguez Outerelo J. (2020). Connectivity of deep waters in the

Gulf of *Mexico. J. Mar. Syst.* 203:103267. doi: 10.1016/j.jmarsys.2019.103267

Belousov, I. M., Ivanov, Y. A., Pasternak, S. A., Rass, T. S., and Rossov, V. V. (1966). Oceanographic research by the Soviet-Cuban Marine Expedition. *Oceanology* 6, 312–320.

Bessonov, N., Gonzalez, O., and Elizarov, A. (1971). "Resultados de las investigaciones Cubano-Sovieticas en el Banco de *Campeche,*" in *Coloquio Sobre Investigaciones y Recursos Del Mar Caribe y Regiones Adyacentes*. UNESCO.

Bogdanov, D. V., Sokolov, V. A., and Khromov, N. S. (1968). Regions of high biological and commercial productivity in the Gulf of Mexico and Caribbean Sea. *Oceanology* 8, 371–381.

Bulanienkov, S. K., and Garcia, C. (1973). "Influencia de los procesos atmosfericos en el afloramiento del Banco de Campeche," in *Cuarta Reunión De Balance De Trabajo, Centro De Investigaciones Pesqueras/Instituto NacionaI De La Pesca, Cuba, Informe De Investigación*, *vol 2.*

Cochrane, J. D. (1966). *The Yucatan Current, upwelling off North-eastern Yucatan, and currents and waters of Western Equatorial Atlantic.* Oceanography of the Gulf of Mexico. Progress Rep., TAMU, Ref No. 66-23T, 14–32.

Cochrane, J. D. (1968). *Currents and Waters of the Eastern Gulf of Mexico and Western Caribbean, of the Western Tropical Atlantic Ocean, and of the Eastern tropical pacific ocean. Dep. Oceanogr. Meteorol.* Texas: A&M Univ. 19–28. (Unpubl. Rep.)

Cochrane, J. D. (1969). *Water and Circulation on Campeche Bank in May*. Bull. Jpn. Soc. Fish. Oceanogr. Spec. No. (Prof. Uda's Commemorative Papers), 123–128.

Duran, R., Beron-Vera, F. J., and Olascoaga, M. J. (2018). Extracting quasi-steady Lagrangian transport patterns from the ocean circulation: an application to the Gulf of Mexico. *Sci. Rep.* 8, 1–10. doi: 10.1038/s41598-018-23121-y

Duran, R., Beron-Vera, F. J., and Olascoaga, M. J. (2019). *CIAM Climatological Isolation and Attraction Model–Climatological Lagrangian Coherent Structures*. Albany: National Energy Technology Laboratory-Energy Data eXchange; NETL. doi: 10.18141/1558781

Enríquez, C., Mariño-Tapia, I., Gilberto, J., and Capurro-Filograsso, L. (2013). Thermohaline processes in a tropical coastal zone. *Continent. Shelf Res.* 69, 101–109. doi: 10.1016/j.csr.2013.08.018

Estrada-Allis, S., Sheinbaum, J., Azevedo, J., Enriquez, C., Mariño-Tapia, I., and Herrera-Silveira, J. (2020). Dissolved inorganic nitrogen and particulate organic nitrogen budget in the Yucatán shelf: driving mechanisms through a physical–biogeochemical coupled model. *Biogeosciences* 17, 1087–1111. doi: 10.5194/bg-17-1087-2020

Furnas, M. J., and Smayda, T. J. (1987). Inputs of subthermocline waters and nitrate onto the Campeche Bank. *Cont. Shelf Res.* 7, 161–175. doi: 10.1016/0278-4343(87)90077-X

Gough, M. K., Beron-Vera, F. J., Olascoaga, M. J., Sheinbaum, J., Jouanno, J., and Duran, R. (2019) Persistent Lagrangian transport patterns in the northwestern *Gulf of Mexico. J. Phys. Oceanogr*. doi: 10.1175/JPO-D-17-0207.1

Gouveia, M. B., Duran, R., Lorenzzetti, J. A., Assireu, A. T., Toste, R., de, F., et al. (2021). Persistent meanders and eddies lead to quasi-steady Lagrangian transport patterns in a weak western boundary current. *Sci. Rep.* 11, 1–18. doi: 10.1038/s41598-020-79386-9

Haller, G. (2015) Langrangian coherent structures. *Annu. Rev. Fluid Mech.* 47:140906185740003. doi: 10.1146/annurev-fluid-010313-141322

Herrera-Silveira, J. A., Medina-Gomez, I., and Colli, R. (2002). Trophic status based on nutrient concentration scales and primary producers community of tropical coastal lagoons influenced by groundwater discharges. *Hydrobiologia* 475, 91–98. doi: 10.1023/A:1020344721021

Jouanno, J., Pallàs-Sanz, E., and Sheinbaum, J. (2018). Variability and dynamics of the Yucatan upwelling: high-resolution simulations. *J. Geophys. Res. Oceans* 123, 1251–1262. doi: 10.1002/2017jc013535

Kurczyn, J. A., Appendini, C. M., Beier, E., Sosa-López, A., López-González, J., and Posada-Vanegas, G. (2020). Oceanic and atmospheric impact of central American cold surges (Nortes) in the Gulf of Mexico. *Int. J. Climatol.* 41, E1450–E1468. doi: 10.1002/joc.6779

Lorente, P., Lin-Ye, J., García-León, M., Reyes, E., Fernandes, M., Sotillo, M. G., et al. (2021). On the performance of high frequency radar in the western mediterranean during the record-breaking storm Gloria. *Front. Mar. Sci.* 8:645762. doi: 10.3389/fmars.2021.645762

Martínez-López, B., and Pares-Sierra, A. (1998). Circulation in the gulf of mexico induced by tides wind and the yucatan current. *Cienc. Mar.* 24, 65–93. doi: 10.7773/cm.v24i1.740

McDougall, T. J., and Barker, P. M. (2011). "Getting started with TEOS-10 and the Gibbs Seawater (GSW) oceanographic toolbox," in *SCOR/IAPSO WG127*, 28.

Merino, M. (1997). Upwelling on the Yucatan Shelf: hydrographic evidence. *J. Mar. Syst.* 13, 101–121. doi: 10.1016/s0924-7963(96)00123-6

Molinari, R. L. (1980). Current variability and its relation to sea-surface topography in the Caribbean Sea and Gulf of Mexico. *Mar. Geodesy* 3, 409–436.

Nordam, T., and Duran, R. (2020). Numerical integrators for Lagrangian oceanography. *Geosci. Model Dev.* 13, 5935–5957. doi: 10.5194/gmd-13-5935-2020

Nowlin, W. D., and Mclellan, H. J. (1967). A Characterization of the Gulf of Mexico waters in winter. *J. Mar. Res.* 25, 29–59.

R Core Team (2014). *R: A Language and Environment for Statistical Computing*. Vienna: R Foundation for Statistical Computing.

Reyes-Mendoza, O., Herrera-Silveira, J., Mariño-Tapia, I., Enriquez, C., and Largier, J. L. (2019). Phytoplankton blooms associated with upwelling at Cabo Catoche. *Continent. Shelf Res.* 174, 118–131. doi: 10.1016/j.csr.2018.12.015

Reyes-Mendoza, O., Mariño-Tapia, I., Herrera-Silveira, J., Ruiz-Martínez, G., Enriquez, C., and Largier, J. L. (2016). The effects of wind on upwelling off Cabo Catoche. *J. Coast. Res.* 32, 638–650. 10.2112/JCOASTRES-D-15-00043.1

Reynolds, R. W., Rayner, N. A., Smith, T. M., Stokes, D. C., and Wang, W. (2002). An improved in situ and satellite SST analysis for climate. *J. Clim.* 15, 1609–1625. doi: 10.1175/1520-0442(2002)015<1609:AIISAS>2.0.CO;2

Ruíz-Castillo, E., Gomez-Valdés, J., Sheinbaum, J., and Rioja-Nieto, R. (2016). Wind-driven coastal upwelling and westward circulation in the Yucatan shelf. *Continent. Shelf Res.* 118, 63–76. doi: 10.1016/j.csr.2016.02.010

Ruiz-Renteria, F. (1979). *Upwelling North of the Yucatan Peninsula (Master's thesis)*. Texas: Texas A&M University.

Troupin, C., Barth, A., Sirjacobs, D., Ouberdous, M., Brankart, J.M., Brasseur, P., et al. (2012). Generation of analysis and consistent error fields using the Data Interpolating Variational Analysis (DIVA). *Ocean Model.* 52–53, 90–101. doi: 10.1016/j.ocemod.2012.05.002

Valle-Levinson, A., Mariño-Tapia, I., Enriquez, C., and Waterhouse, A. M. (2011). Tidal variability of salinity and velocity fields related to intense point-source submarine groundwater discharges into the coastal ocean. *Limnol. Oceanogr.* 56, 1213–1224. doi: 10.4319/lo.2011.56.4.1213

Vidal, V. M. V., Vidal, F. V., Hernández, A. F., Meza, E., and Zambrano, L. (1994). Winter water mass distributions in the western Gulf of Mexico affected by a colliding anticyclonic ring. *J. Oceanogr.* 50, 559–588. doi: 10.1007/bf02235424

Willmott, C. J., Ackleson, S. G., Davis, R. E., Feddema, J. J., Klink, K. M., Legates, D. R., et al. (1985). Statistics for the evaluation and comparison of models. *J. Geophys. Res.* 90, 8995–9005.

Zavala-Hidalgo, J., Morey, S. L., and O'Brien, J. J. (2003). Seasonal circulation on the western shelf of the Gulf of Mexico using a high-resolution numerical model. *J. Geophys. Res.* 108:C12. doi: 10.1029/2003jc001879

Conflict of Interest: The authors declare that the research was conducted in the absence of any commercial or financial relationships that could be construed as a potential conflict of interest.

Publisher's Note: All claims expressed in this article are solely those of the authors and do not necessarily represent those of their affiliated organizations, or those of the publisher, the editors and the reviewers. Any product that may be evaluated in this article, or claim that may be made by its manufacturer, is not guaranteed or endorsed by the publisher.

Copyright © 2021 Kurczyn, Duran, Beier and Souza. This is an open-access article distributed under the terms of the Creative Commons Attribution License (CC BY). The use, distribution or reproduction in other forums is permitted, provided the original author(s) and the copyright owner(s) are credited and that the original publication in this journal is cited, in accordance with accepted academic practice. No use, distribution or reproduction is permitted which does not comply with these terms.

frontiers in Marine Science

ORIGINAL RESEARCH
published: 28 October 2021
doi: 10.3389/fmars.2021.735242

Land-Ocean Interaction Affected by the Monsoon Regime Change in Western Taiwan Strait

Rick J. Yang[1], James T. Liu[1], Chih-Chieh Su[2], Yi Chang[3], Jimmy J. Xu[1] and Hon-Kit Lui[1]*

[1] Department of Oceanography, National Sun Yat-sen University, Kaohsiung, Taiwan, [2] Institute of Oceanography, National Taiwan University, Taipei, Taiwan, [3] Graduate Institute of Marine Affairs, National Sun Yat-sen University, Kaohsiung, Taiwan

The Taiwan Strait is a conduit between East China Sea (ECS) and South China Sea (SCS). Seasonal monsoon winds drive the southbound Zhejiang-Fujian Coastal Current and northbound SCS Warm Current through the strait. Water masses carried by these major current systems also carry fluvial signals from two major rivers, the Changjiang (Yangtze) River in ECS and the Zhujiang (Pearl) River in SCS through the strait. Here we show a switch occurred to signify the monsoon regime change on the western side of this conduit around 10:00 on May 8, 2015. Our data came from water mass properties and environmental proxies of N/P ratio in the surface water and ^{7}Be and $^{210}Pb_{ex}$ isotopes in surface sediments. The timings of the demarcation were identical in the water column and on the water-sediment interface. Our findings put a specific time point in the monsoon regime change in 2015.

Keywords: water mass, fluvial source proxies, Changjiang River, Zhujiang River, East China Sea, South China Sea

OPEN ACCESS

Edited by:
William Savidge, University of Georgia, United States

Reviewed by:
Milena Menna, Istituto Nazionale di Oceanografia e di Geofisica Sperimentale, Italy
Yunhai Li, Third Institute of Oceanography, China

***Correspondence:**
James T. Liu
james@mail.nsysu.edu.tw

Specialty section:
This article was submitted to Coastal Ocean Processes, a section of the journal Frontiers in Marine Science

Received: *02 July 2021*
Accepted: *11 October 2021*
Published: *28 October 2021*

Citation:
Yang RJ, Liu JT, Su C-C, Chang Y, Xu JJ and Lui H-K (2021) Land-Ocean Interaction Affected by the Monsoon Regime Change in Western Taiwan Strait. Front. Mar. Sci. 8:735242. doi: 10.3389/fmars.2021.735242

INTRODUCTION

Major rivers in the world contribute approximately 40% of fresh water and particulate material to the global ocean (Milliman and Meade, 1983; Corbett et al., 2004; Dagg et al., 2004). The impact of fluvial discharge by major rivers can extend hundreds of kilometers beyond the river mouth such as the Amazon River, Columbia River, Changjiang (Yangtze) River, and Zhujiang (Pearl) River (Berdeal et al., 2002; Bai et al., 2014, 2015; Lee et al., 2021; Liu et al., 2021; Nittrouer et al., 2021). The fate of river exported material in the distal marine environments is dominated by marine processes such as wind, tide, and coastal currents (Berdeal et al., 2002; Liu et al., 2002, 2009, 2021; Nittrouer et al., 2021). Different physical processes have different contributions to terrestrial material dispersal with corresponding timescales. On inner shelves, wind-driven currents with seasonality affect the properties of the associated water masses (Hopkins et al., 2013; Zavala-Hidalgo et al., 2014; Chen et al., 2019).

The scene of this study is in the Taiwan Strait (TS), which connects two major Asian marginal seas, the ESC and the SCS (Jan et al., 2010; Hu et al., 2019), where two world large rivers the Changjiang River (CJR) and the Zhujiang River (ZJR), function as distal sources to the TS (**Figure 1A**). The TS system is also influenced by the world's most active Asian monsoon system, having strong seasonality in wind and rainfall patterns, and close coupling between atmospheric and the oceanic circulations (Wang et al., 2019). In the TS, the net transport in summer is from the SCS to ECS which is relatively reduced in winter (Wang et al., 2003; Jan et al., 2010; Hu et al., 2019). In summer, large river discharges and strong southwesterly winds allow the ZJR effluent to enter the

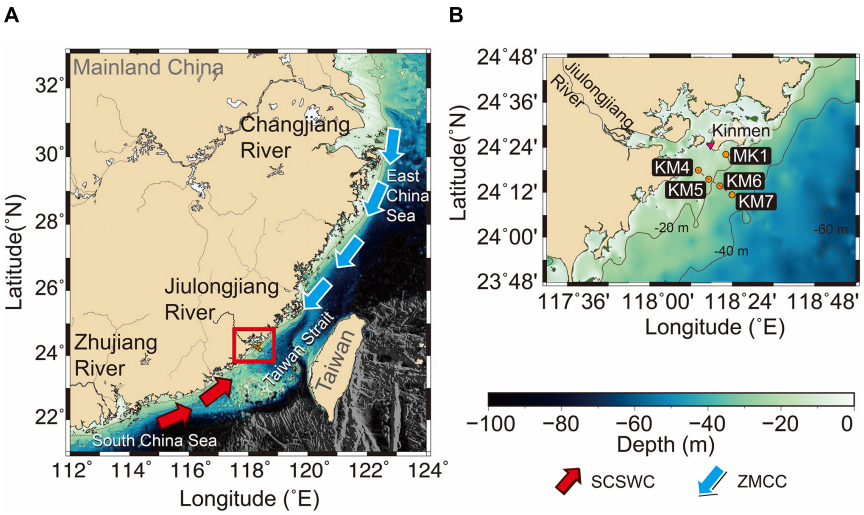

FIGURE 1 | (A) The map showing the Taiwan Strait that links the South China Sea and East China Sea. The red box indicates the location of the study area (Xiamen Bay). Red arrows represent the direction of SCSWC, blue arrows roughly represent the direction of the ZMCC. **(B)** Enlarged map of the red box showing the fixed sampling station at MK1 and transect stations KM4∼KM7 by orange circles. The bright purple triangle showing the Kinmen Weather Station.

TS (Bai et al., 2015). In addition, river effluents along the TS also deliver large amount of terrestrial material into the strait (Liu et al., 2019). Liu et al. (2019) described TS as a monsoon-driven artery that intermittently pump nutrient-rich water that carries terrestrial-sourced material to the ECS in summer. Previous studies also pointed out a major conduit to transport the CJR-derived terrestrial material from ECS into SCS along the coast of Mainland China (Xu et al., 2009; Liu et al., 2010, 2014, 2018; Hu et al., 2012). Furthermore, the influence of the monsoon on the hydrological setting also controls the primary productivity and the biota structures in the TS (Tseng et al., 2008; Hong et al., 2011b; Hsieh et al., 2013). In addition to the seasonal influence of monsoon on the flow field, the monsoon's control on the interannual timescale is also modulated by the El Niño and La Nina events. During the El Niño, the weakened northeast monsoon reduces the cold water from the north and enhances intrusion of the warm water from the south, resulting in warming in the TS (Wu et al., 2007; Huang et al., 2015). Conversely, during the La Niña, the strengthening of northeast monsoon increases the southward reach of cold water (Zhang et al., 2020).

Studies show that the coast-hugging China Coastal Current or Zhejiang (Zhe)-Fujian (Min) Coastal Current (ZMCC) flows southwestward in the western part of the TS in winter, and the northern SCS Warm Current (SCSWC) and Kuroshio Branch Current flow northward to the western and eastern parts of the TS, respectively, in summer (Jan et al., 2002, 2010; Chen, 2003; Hu et al., 2010; Hong et al., 2011b). These surface currents are controlled by seasonal monsoons, which strengthen the northward flow in summer and the southward flow in other seasons (Jan et al., 2002; Zhu et al., 2013). When two water masses of different origins meet, a front is formed due to the contrast in water properties across the boundary (Chen, 2009). Mapped fronts in satellite images of sea surface temperature (SST) and chlorophyll-a have been used to show boundaries of different water masses in the region (Chang et al., 2006; Chen and Wang, 2006; Liu et al., 2019). These fronts also indicate coupling between physics and waterborne properties such as fluorescence and turbidity (Chen, 2009; Liu et al., 2019).

Many shipboard observations of hydrographic surveys, surface drifters for spatial variability, and fixed-point time-series records from moorings, and high-frequency ground wave radar scanning exist (Qiu et al., 2011; Zhu et al., 2013; Du and Liu, 2017; Liu et al., 2019). They reveal that the monsoon or the wind field condition plays an important role in the changes of the currents in the TS. In the nearshore area, apart from different sources of water mass, the contribution of river plume water is significant (Du and Liu, 2017; Liu et al., 2019). The presence and absence of the river plume determines the coastal water-column density structure, which in turn, affects the nepheloid layers. These layers are major pathway of terrigenous and biogenic particles (Du and Liu, 2017).

In central TS, the effluent of the Jiulongjiang River (JLJR) debouches into the western part of the TS in the form of a hypopycnal plume (Wang et al., 2013; Liu et al., 2019). During the southwesterly monsoon, the JLJR effluent has four spatial expansion modes: flowing northward along the coastline, a bidirectional plume spreading concurrently northeastward and southwestward at the same time, extending just out of the Xiamen Bay, and flowing offshore in the northeastward direction (Wang et al., 2013). It is highly likely that the effluent disperses to the northeast into the interior of the TS. Thus, the effluent of JLJR, the ZMCC water, and the SCSWC water forms the basic constituency of water masses on the west side of the TS.

The encounter of ZMCC water and SCSWC water in the TS also induces the exchanges between the two distal fluvial sources of the CJR and the ZJR. The ZMCC and SCSWC in the TS under different monsoon conditions have been well documented in many studies. However, it is not clear how the regime change of

the monsoons affects the interaction of two distal fluvial sources in the TS conduit.

The interactions among the different water masses can be delineated by mapping sea-surface temperature fronts from satellite images (Liu et al., 2019). The near-surface current reversals between different seasons can be monitored by High-Frequency Ground Wave Radar system (Zhu et al., 2008). To resolve the entire water column structures, ship-based observations are essential. However, the short window of the monsoon transition has been rarely captured by ship-based surveys.

The goal of this study was to capture the rare occasion of expected monsoon regime change at the key point offshore of JLJR mouth (**Figure 1**) between May 7 and 10, 2015. It was fortuitus as the spring-summer monsoon transition occurred in the short window in 2015 was captured in this study. In this paper we present detailed background information of water-mass properties at a critical region in central TS to accentuate our observations from the water column and surface sediment to pinpoint the timing of monsoon regime change.

MATERIALS AND METHODS

Shipboard Monitoring and Sampling

In the short window of monsoon regime change in 2015, a research cruise was conducted on R/V Ocean Researcher III (OR3)-1850 (04:00 May 7–15:00 May 9) near the mouth of JLJR. The observations consisted of shipboard profiling at hourly intervals (10:00 May 7–10:00 May 9) at MK1 and a transect survey (12:00 May 9–15:00 May 9) from KM4 to KM7 (**Figure 1**).

A CTD rosette (SBE 911plus) was used in hydrographic profiling (salinity, temperature, fluorescence, and DO) at each station. A LISST-100x (Laser *in-situ* Scatting and Transmissometer, type C) was added to the rosette to record the volume concentration (VC, in μl/l) of 32 size-classes from 0.25 to 500 μm (on a logarithmic scale) of suspended particles. The rosette was lowered at approximately 1 m/s and the LISST-100x sampled at 1-s intervals (taking an average of 10 measurements), resulting in VC profiles of suspended sediment with 1-m resolution in the vertical. Accordingly, other CTD data were synchronized and averaged into 1-m vertical segments. In addition, water samples were collected at the surface, and near-bottom using 10 l Niskin bottles and seafloor surface sediment samples were taken by a SHIPEK Grab (Wildco 860-A10) at 2-h intervals. To obtain the suspended sediment concentrations (SSC, in mg/l) in different size-classes simultaneously, a nested filtration system Catnet was used to filter water samples onboard, having sieves of three mesh sizes of 153, 63, and 10 μm (Hsu and Liu, 2010; Lee et al., 2016). The Catnet and rosette were directly connected through the water pipe, and 10 l of water sample was introduced into the Catnet for filtration. The suspended particles were collected in a 100 ml bottle at the bottom of the three sieves. Other particles that attached to the sieve were washed into the bottle by hand after the Niskin bottles were drained. At this time, the PC case of the Catnet still contains suspended particles smaller than 10 μm, which were emptied into a jug. Those water in the bottles and the jug were further filtered with a GF filter (0.7 μm). Deionized distilled water (DDW) was used to wash the filter paper to remove salt. During the filtration process, DDW was used to rinse carefully to ensure that no particles remained in each step. Afterward, the filters were freeze-dried and weighed to render the SSC of the following size-classes: >153, 63–153, 10–63, and <10 μm. A portion of each surface water sample (100 ml) was placed in liquid nitrogen for rapid freezing and stored at −4°C for nutrient measurements. Realizing that the radioisotopes in the surface sediments were susceptible to disturbance, the SHIPEK Grab was recovered at a rate of less than 0.5 m/s to avoid disturbance. In addition, the surface sediment in the SHIPEK Grab was confirmed with the naked eye that the uppermost part of the sediments was not disturbed due to overturning, slumping, or serious mixing. After confirmation, the sample was taken within a range of 20*20 cm^2 in the center of bucket of the SHIPEK Grab and freezed for radioisotope analysis. The wind field was measured every minute by shipboard anemometer.

After the fixed-point observations, a hydrographic survey was carried out along a transect from seaward of the river mouth to offshore (Stas. KM 4∼7) during the flood tide. In addition, to verify our observations, other measurements for May from 2000 to the present near our stations were obtained from the World Ocean Database (WOD) for comparison (marked by a to j in **Figure 2**; Boyer et al., 2018).

The Observations of Suspended Sediments

The volume concentration (VC) of suspended sediments, measured by LISST-100x, were divided into four particle size groups (<10, 10–63, 63–153, >153 ·m) corresponding to the partition by the onboard nested filtration system Canet (Lee et al., 2016; Du and Liu, 2017). The SSC obtained by the Catnet was combined with the VC observed by the LISST to calculate the bulk density of suspended sediments follows (Hsu and Liu, 2010). Here ρ_p is the density of primary particles that is assumed 2.65 g/cm^3 and $\rho_{IW}$is the density of seawater.

$$\rho_f = \rho_{IW} + \left(1 - \frac{\rho_{IW}}{\rho_p}\right)\frac{SSC}{VC}$$

Analyses of Water and Surface Sediment Samples

After the cruise, all samples were analyzed immediately in the laboratory to obtain inorganic nitrogen (NO_3^-, NO_2^-), phosphate (PO_4^{3-}), and silicate (SiO_2), as well as to measure $^{210}Pb_{ex}$ and ^7Be of surface sediments.

The azo dye colorimetric method combining cadmium reduction on flow injection analyzer was used to measure the concentration of nitrate and then calculated nitrate (NO_3^-) by reducing nitrate to nitrite (NO_2^-) (Pai et al., 1990b; Pai and Riley, 1994; Chen et al., 2004). The ascorbic acid/oxalate reduction-colorimetric method on flow injection analyzer was used to measure the concentration of phosphate (PO_4^{3-}) and silicate (SiO_2) (Pai et al., 1990a; Chen et al., 2004).

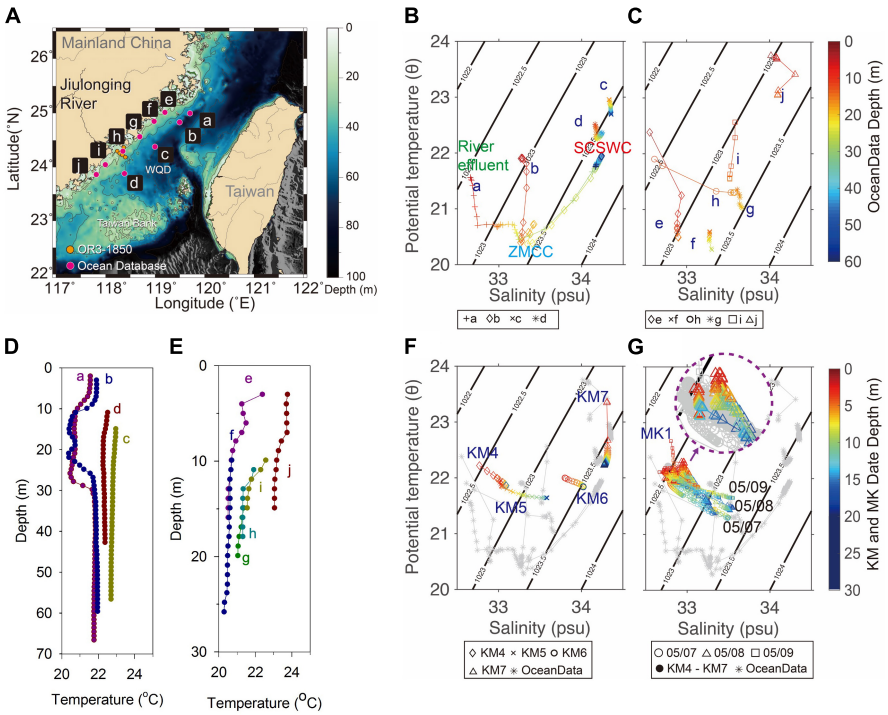

FIGURE 2 | (A) A map showing the WOD data points a∼j. **(B)** Depth-referenced θ-S diagram at offshore stations a∼d. The surface layer of Sta. a corresponds to coastal water. The middle layer of Sta. a and b corresponds to ZMCC water. Stas. c and d correspond to SCSWC water. **(C)** Depth-referenced θ-S diagram of near shore stations e∼j. **(D)** The temperature profiles at a∼d. **(E)** The temperature profiles at e∼j. **(F)** Depth-referenced θ-S diagram observed at KM4∼KM7. **(G)** θ-S diagram observed at KM1 on 5/7∼9 showing circles (5/7), triangles (5/8), and squares (5/9). The temporal changes on 5/8 when the regime change occurred are enlarged in the dashed circle. The θ-S plots in **(B,C)** are plotted in the background in gray **(F,G)** to provide perspective to the present data.

After the surface sediment samples were freeze-dried, the water content of the wet sediments was determined. Dried samples were then transferred to plastic jars (inside diameter, 8.5 cm; height, 7.5 cm) for non-destructive gamma-ray spectrometric assay of radionuclides. The data reported in this study were calculated based on salt-free dry weight. Three radionuclides (^{210}Pb, ^{7}Be, and ^{214}Pb) were counted by HPGe detectors connected with the digital gamma-ray spectrometer and analyzed by Gamma Vision 32s software. The detectors can be used to determine ^{210}Pb, ^{214}Pb and, ^{7}Be simultaneously based on photon peaks centered at 46.52, 351.99, and 477.56 keV, respectively (Huh et al., 2009, 2011). The ^{214}Pb is the precursor of ^{210}Pb and was used as an index of supported ^{210}Pb whose activity concentration was subtracted from that of the measured, total ^{210}Pb to obtain excess ^{210}Pb (^{210}Pb$_{ex}$) (Su and Huh, 2002; Huh et al., 2009).

The Eigen Function Analysis

A multivariate technique Empirical Orthogonal/Eigen Function (EOF) analysis was used to characterize the correlations (standardized covariability) of variables in the upper water column and near-bottom water column and radioisotopes in seafloor sediment. This technique is based on internal correlations (Resio and Hayden, 1975), which present the statistical characteristics of a group of data through the spatial or temporal correlation of the data (Du and Liu, 2017; Liu et al., 2019; Lee et al., 2021). Each eigenmode in the EOF result was ranked according to the quotient between the eigenvalue of the eigenmode and the sum of all the eigenvalues. The highest mode (mode 1) explains most of the covariability (correlation) in the data set, followed by mode 2, mode 3…etc. In this study, variables in water column at 0∼2 m depth and 0∼2 mab were analyzed separately. Variables from the upper water column included water-mass properties (temperature, salinity, fluorescence, DO, and nutrients), suspended sediment attributes (SSC, VC of four size-groups), tidal height (tidal forcing), and N-S and E-W wind velocity components. In the water-sediment interface, analyzed variables included water-mass properties (temperature, salinity, fluorescence, DO, and nutrients), suspended sediment attributes (SSC, VC of four size-groups), surface sediment proxies (^{210}Pb$_{ex}$ and ^{7}Be), tidal height (tidal forcing), and N-S and E-W wind velocity components (Lee et al., 2016, 2021; Liu et al., 2019).

Identifying Fronts in Satellite Sea Surface Temperature Image

Daily images of SST for the TS obtained by NOAA's AVHRR satellites throughout the year were collected. The entropy-based edge detection method was used to computed front gradient magnitude (GM) using the equation (Chang et al., 2006, 2010): $GM = \sqrt{(dT/dx)^2 + (dT/dy)^2}$ where T is SST, and x and y axes

are directed toward east and north, respectively. After computing the GM from all daily image, the monthly mean GM can be obtained. The monthly mean GM map was used to show the frontal patterns and scale the intensity of frontal systems in different month. In this study, to compare the difference of front in each month more clearly, the fronts of different months were digitized and plotted through GMT software.

RESULTS

Time Series Observations

The transition of the seasonal wind field in the TS in 2015 occurred in May as in previous years. At the beginning of April, the wind field was mainly northeast wind, from late April to May were the transition period, and the southwest wind dominated in June (**Supplementary Figure 1A**). During the transition period, the northeasterly wind alternated with the southwesterly wind. The time series observation was carried out at Sta. MK1 station during this period. One month before the observation period, the wind mainly blew from the northeast between 40 and 70° (**Supplementary Figure 1B**). One and a half months after the observation period, the wind was mainly from the southwest between 210 and 240° (**Supplementary Figure 1C**). In this article, the 0° wind direction is defined as the wind blowing from the north, and the wind direction from the east is at 90°. During the time series observation period, the first half was dominated by northeasterly winds and the second half was dominated by southerly winds. The average speed of the northeasterly winds was 4.94 m/s, and the average speed of the southerly wind was 2.69 m/s (**Figure 3A**). To corroborate with our short shipboard measurement, a longer record (4/9∼6/24) of hourly wind data from the Weather Station on the nearby Kimen Island (**Figure 1**) and rose diagrams of the wind speed and direction for the NE and SW monsoon periods are shown in **Supplementary Figure 1**. The data has been averaged for 24-h running mean to reduce the variation due to daily sea and land breezes.

According to the observed water level, the interval between high tide and low tide was about 12 h, which is a semi-diurnal tidal cycle (two high waters and two low waters each day), and the tidal range was about 5 meters (**Figure 3** blue curve). The flood-half tidal cycles referred to the period when the sea level rose from low water to high water, and conversely, the period when sea level dropped from high water to low water level was the ebb-half tidal cycle. A total of 4 full tidal cycles were observed during the time series observation period.

The temperature and salinity structures at Sta. MK1 showed the water column consisted of distinctive surface and bottom layers (**Figures 3B,C**). Temperature, salinity, fluorescence, and dissolved oxygen (DO) showed strong tidal signals. During flood, the water column was better mixed with warmer, less saline water (**Figures 3B,C**). During ebb, the water column was stratified due to the presence of colder, more salinity water. However, for two flood-half tidal cycles, the water column was well mixed with high temperature and low salinity water (marked by red dashed boxes in **Figures 3B,C**), suggesting the influence of river effluent. The fluorescence (**Figure 3D**) showed different patterns. In general, its values were higher in the surface and lower near the bottom. In one full tidal cycle and one ebb-half tidal cycle (marked by black dashed boxes in **Figure 3D**), low values existed throughout the water column and remained high in the surface throughout the following tidal cycle. DO values in general were higher in the surface and lower at depth (**Figure 3E**). There was one episode that high DO coincided with high fluorescence (marked by blue dashed boxes in **Figures 3D,E**). The temporal changes of the vertical structures of these parameters suggest coupling among physical and biogeochemical processes.

At the surface, the salinity fluctuations were less than 1 PSU (**Figure 3C**). During the two episodes of river effluent presence (<32.8 PSU, **Figure 3C**) the nutrient concentrations of NO_3^-, NO_2^-, PO_4^{3-}, SiO_2, and the volume concentration of suspended sediments increased (**Figures 4A,B** and **Supplementary Figure 2**). This indicates JLJR as the source. During flood tide, the effluent was pushed northeastward from the JLJR mouth to reach the MK1 station. The two episodes of river effluent occurred in periods of northeasterly winds and southwesterly winds, respectively. Based on the salinity and the nutrient concentrations, the effluent during the southwesterly winds was stronger than in northeasterly wind period. In addition, the N/P ratio showed gradual decreasing trend during the observation period (**Figure 4C**).

Near the bottom, four tidally modulated intrusion events of low temperature and high salinity water occurred. Each event commenced at the low water through the rising tide, reaching the peak at the high water, and abated during the following falling tide (**Figures 3B,C**). The intruded water could almost reach the surface, which contained lower fluorescence and lower DO (**Figures 3D,E**). These associations suggest upwelling (Hu and Wang, 2016). The intrusion of cold and saline water was still present after the wind directions shifted from northeasterly to southerly (**Figure 3**), suggesting wind was not a major forcing on the local cold-water events. In addition, the temperature, fluorescence of the bottom water and ^{7}Be in the surface sediments tended to increase after the wind field change (**Figures 4D–F**).

Observations of suspended sediment are presented in **Supplementary Figures 2**, **3**. The volume concentration (VC) measurements suggest that the suspended particles larger than 153 μm mainly appeared in the upper water column (**Supplementary Figure 2**), and the suspended particles smaller than 153 ·m appeared near the bottom during river effluent events at Sta. Mk1 (**Figure 3C** and **Supplementary Figure 2**). Similarly, river effluent events during the southerly wind have higher SSC than northeasterly wind. SSC of four particle size groups showed that the sediment finer than <10 μm contributed the most to the total SSC both at the surface and near bottom. The peaks in the SSC coincided with the flood tide (**Supplementary Figures 3A,B**). The bulk density of most suspended particles in the upper water column was higher than that in the lower water column (**Supplementary Figures 3C,D** and **Supplementary Table 1**), which may be due to the presence of terrigenous particles delivered by the JLJR effluent. In addition, the bulk density of suspended sediment particle size 63–153 μm in the upper water column increased during the period of cold-water intrusion (**Figure 3B** and **Supplementary Figure 3C**). The

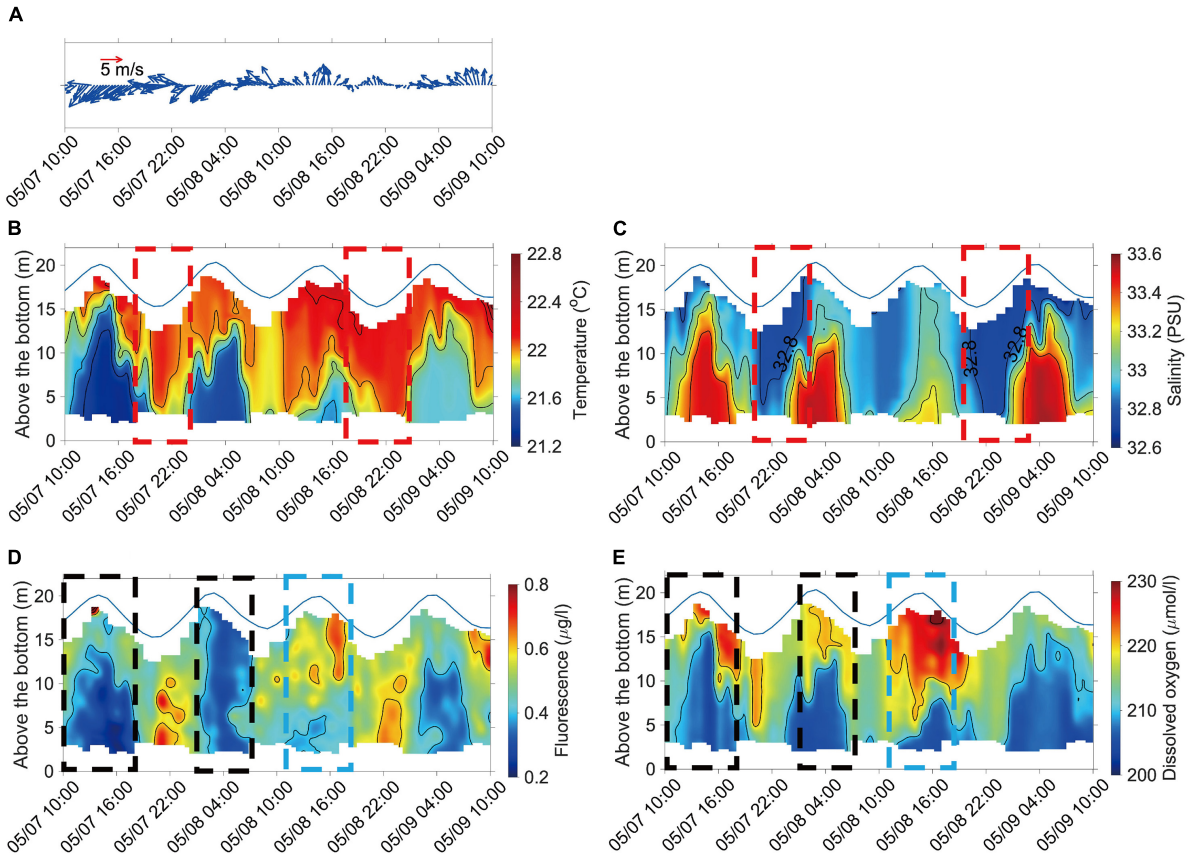

FIGURE 3 | Fixed-point shipboard observations of **(A)** wind speed and direction (plotted according to the oceanographic convention, north direction is upward, and the scale of the sticks is also shown in the upper left corner; vertical structures of **(B)** temperature; **(C)** salinity; **(D)** fluorescence; **(E)** dissolved oxygen (DO). The blue curve shows the fluctuations of the water depth. The red dashed rectangles indicate the time of strong river effluent events. The black dashed rectangles indicate vertically well mixed events of fluorescence values. The blue dashed rectangles indicate the corresponding event of fluorescence and DO values.

higher bulk density values suggest that the sediment may be terrigenous material.

Spatial Transect Observations

During the flood tide, a hydrographic transect survey was conducted along Sta. KM4∼KM7 (**Figure 1B**). In general, the 2-D temperature structure showed relative homogeneous distribution in the vertical at each station. There was a distinct land-to-sea gradient along the transect (**Figure 5A**). An ascending "cold dome" existed at KM5, indicating the presence of upwelling (**Figure 5A**). The dominant feature in the salinity structure also showed land-to-sea pattern as the effluent of JLJR encountered the ambient coastal water, forming a frontal zone in the upper water column between KM5 and KM6 where the hypopycnal plume pinched out (**Figure 5B**). The lower water column was vertically homogeneous between KM4 and KM5 suggesting mixing by currents from below (Liu et al., 2002; Du and Liu, 2017). Coinciding with the "cold dome," was a "low DO dome" (**Figure 5C**). Seaward and landward from the low DO dome, high DO areas existed in the surface. High fluorescence layer coexisted with high DO, suggesting the link through primary production (**Figures 5C,D**). The structural patterns that distinguish salinity from those of temperature and DO indicate different forcing. The salinity pattern was caused by the seaward dispersal of the river effluent as a hypopycnal plume, whereas temperature and DO were mainly affected by the alongshore current transport.

According to the characteristics of temperature and salinity along the transect, three different water masses were identified. Firstly, near the river mouth at KM4 was the JLJR plume with the lowest salinity. The second type was the upwelling water with the lowest temperature and DO that occupied the bottom of Sta. KM5. The third type was the ambient water with the highest temperature and salinity in the offshore area at KM7.

Observations of suspended sediments are presented in **Supplementary Figure 4**. According to the characteristics of VC along the transect (Sta. KM4 to KM7), the 2-D structures of the VC of suspended sediments show size-fractionated spatial patters (**Supplementary Figures 4A–D**). All four grain sizes show concentrated distributions near the seafloor in the form of a benthic nepheloid layer (BNL). BNLs are a common phenomenon along the coast of Zhejiang and Fujian, mainly formed by the resuspension of seabed sediments (Du and Liu, 2017). The thickness of observed BNL increased with

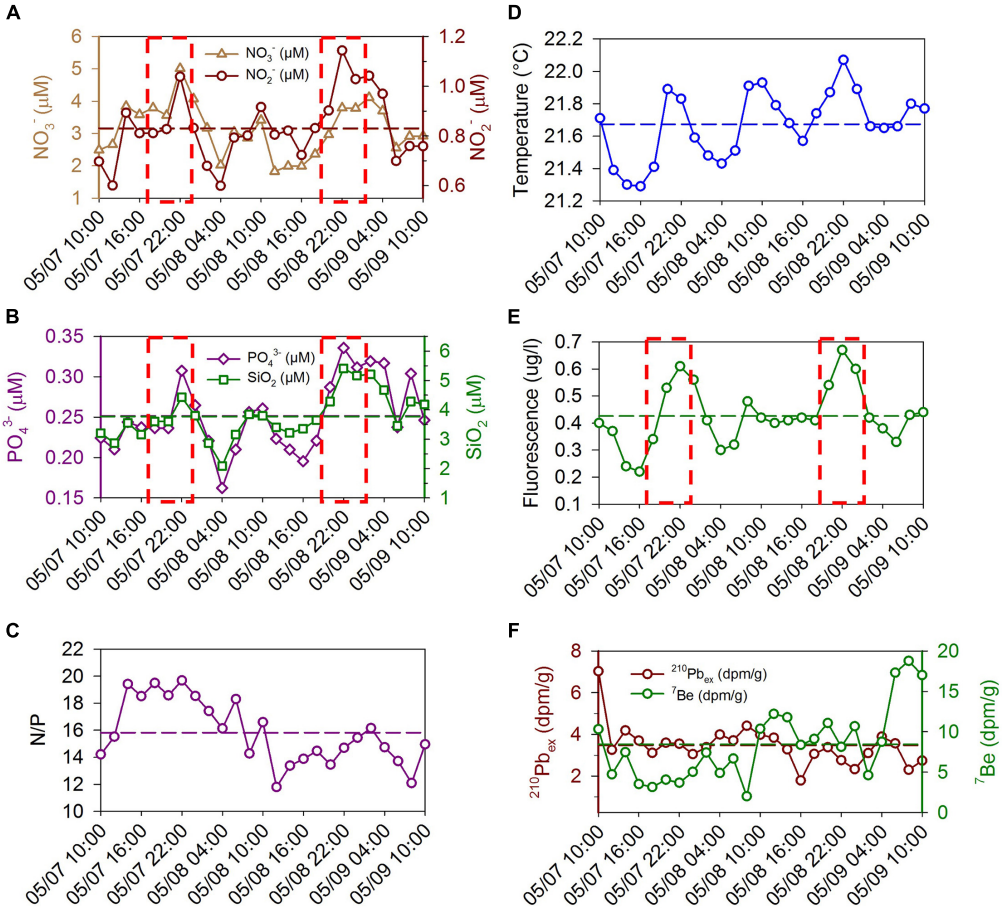

FIGURE 4 | Temporal changes of **(A)** nitrate and nitrite (NO_3^-, NO_2^-); **(B)** phosphate (PO_4^{3-}) and silicate (SiO_2); **(C)** N/P ratio in the upper water column (dashed line indicates the mean value); and changes of **(D)** temperature; **(E)** fluorescence in the lower water column; and **(F)** $^{210}Pb_{ex}$ and ^{7}Be in the surface sediment. The red rectangles correspond to the dashed red rectangles in **Figures 3B,C**.

decreasing particle size. The finest size of <10 μm had the thickness of 5∼10 m (**Supplementary Figure 4A**). Intermediate nepheloid layer (INL) also appeared as extensions of the BNL in deeper depths forming finger-like structures following isopycnals surfaces especially for the two coarser particles (**Supplementary Figures 4C,D**). All the structures in deeper than 5-m depth seem to display a common land-sea boundary around KM6 that separates the estuarine and coastal influences. However, the finest < 10 and the coarsest > 153 μm sizes also form surface nepheloid layer (SNL) (**Supplementary Figures 4A,D**). Both SNLs were related to the hypopycnal plume of the JLJR. But the former consisted of fine-grained terrigenous sediment and the latter consisted of biogenic particles (Du and Liu, 2017).

Source of Water Masses

Previous studies show the coastal area near the JLJR mouth is affected by the ZMCC along the coast in winter and the SCSWC in summer (Hu et al., 2010). Different water masses that may be present in the study area were delivered by the effluent of the JLJR, the SCSWC, and the ZMCC. The SCSWC water is warmer and more saline, the ZMCC water is colder and less saline, while the effluent from the JLJR is the least saline (Wang et al., 2013). The latest (2002) May temperature and salinity data from the western part of the TS in the WOD confirm this scenario (Boyer et al., 2018). The temperature is converted to potential temperature (θ) at reference pressure 0 dbar by polynomial fit for adiabatic lapse rate and Runge-Kutta fourth order integration algorithm (Bryden, 1973). The depth-referenced θ-S diagrams of measurements at offshore locations (a, b, c, d) and inshore locations (e, f, g, h, i, j) differentiate the water masses of the two current systems (**Figures 2A–C**).

Historical data show that along the offshore transect, the surface water is warmer and more saline at stations c and d than that at a and b (**Figures 2B,D**). Stations c, d are in the shallower part of the TS whereas a, b are in deeper water of the Wuqiu Depression (WQD) (**Figure 2A**). At c and d, the temperature and salinity are vertically homogenous (**Figure 2D**). At a and b, the vertical structure shows three segments of mixed layers between surface and 10 m (a and b); 10∼28 m (a), 10∼22 m (b); and 30∼bottom (a), 25∼bottom (b). Thermoclines exist between adjacent segments. On the θ-S diagram the segments are also separated by the salinity. The surface layer is less saline.

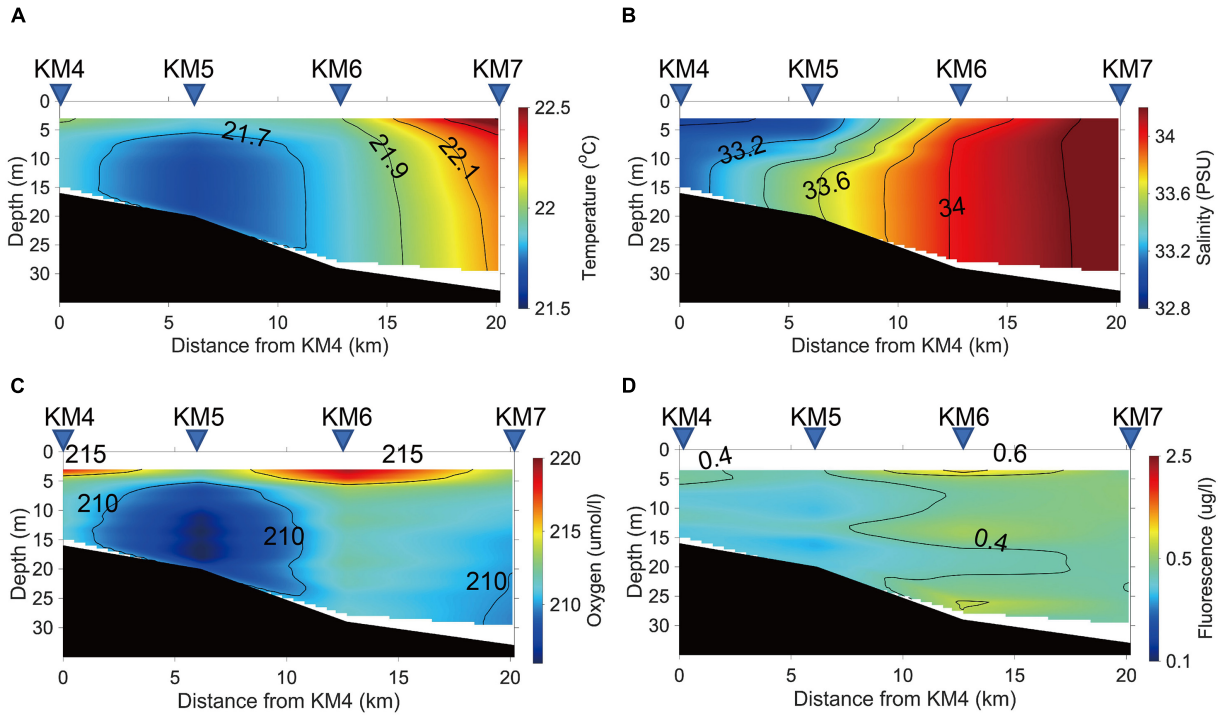

FIGURE 5 | 2-D structures along the transect between KM4 and KM7 of **(A)** temperature; **(B)** salinity; **(C)** DO; **(D)** fluorescence. The black area represents the sea floor.

The middle layer becomes gradually colder and more saline. The bottom layer is the warmest and most saline. The thermohaline coincides with the halocline (**Figure 2B**).

Along the inshore transect, there is a general southward warming trend from e to j (**Figures 2C,E**). On the other hand, the water is fresher at e than at j (**Figure 2C**). In general, at each station, the temperature is more vertically homogeneous. The θ-S characteristics of these selected stations in WOD reveal the signatures and pathways of the water-masses of the warmer and more saline SCSWC and colder, less saline ZMCC.

Boundary of Water Masses

For a broader regional view of the water masse boundary driven by ZMCC and SCSWC, NOAA's Advanced-Very-High-Resolution-Radiometer (AVHRR) sea-surface temperature (SST) images in the TS were obtained from the regional HRPT Data Library at Tohoku University and National Taiwan Ocean University. Monthly mean values of frontal gradient magnitude were computed (**Supplementary Figure 5**; Chang et al., 2006). The entropy-based edge detection method was used to describe the SST fronts. Such fronts can represent where different water masses meet. The monthly synthesized fronts were digitized and plotted over the bathymetry to show shifting boundaries between the two systems (**Figure 6**). From spring to summer, the fronts gradually recede northward in response to the monsoon change. Beginning in winter, the fronts extend southward. The front not only represents the interface of warm and cold-water masses, but also the density gradient between different water masses that prevented the mixing of water and sediment (Qiao et al., 2020). The position of the JLJR mouth seems to be at the southward limit of the retreating front. This phenomenon could be due to the constraint of bathymetry. The WQD accommodated the descending dense warm SCSWC water under the ZMCC water so the front could not progress northward in the surface (**Figure 2B**).

Eigen Function Analysis of Upper Water Column

Finally, EOF analysis was used to examine the covariability among the 19 measured variables at the upper water column (0∼2 m) (**Supplementary Figure 6**). Results show the first mode explains 37.8% of the standardized covariability (correlation) in the data. The signs of the eigenvectors of this mode show that the tidal height, salinity, temperature and DO are in the negative group whereas the rest of the variables are in the positive group (**Figure 7A**). The eigenweighting curve of this mode represents the temporal characteristics of this mode showing diurnal inequality in the tidal signals (**Figure 7B**). This curve mimics the temporal patterns of the variables that have strong tidal signals, including water mass properties, particle attributes, and biogeochemical feedbacks. For illustration, PO_4^{3-} from the positive group mimics the eigenweighting curve, and salinity from the negative group shows the mirror image of the curve (**Figure 7B**). Basically, the grouping of this mode indicates that when the values of tidal height and salinity decreased, the values of all other variables (except for the winds) increased. Therefore,

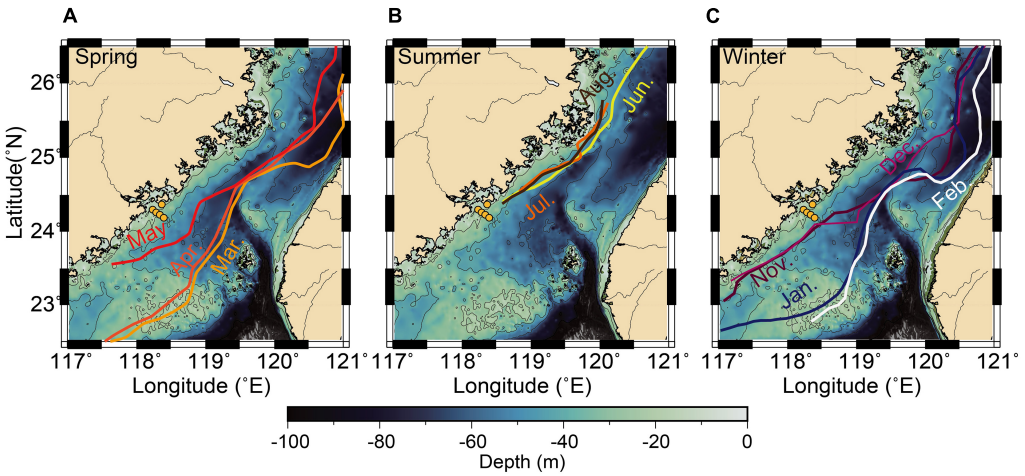

FIGURE 6 | Maps showing the frontal zones digitized from satellite images of monthly SST (**Supplementary Figure 4**) in **(A)** spring including March, April, May; **(B)** summer including Jun, July, Aug.; and **(C)** winter including Nov., Dec., Jan., Feb. Fronts in September, and October are not clear and thus are not included.

this mode is interpreted as the tidally driven coastal water mode, which describes the effluent from the JLJR that transported particles and waterborne substances to the study site during ebb. The mode indicates that tide is the primary physical process to influence the covariability of the measured variables.

The second mode explains 16.3% covariability in the data. The prominent variables in the positive group are the temperature, salinity, and other variables including all nutrients except for NO_3^-, and the two wind components. The positive grouping indicates that the temperature and salinity increased with the strength of the SW-monsoon (**Figure 7C**). Comparisons among the eigenweighting curve with the time series of the measured variables show the curve closely mimics the gradually rising temperature (**Figure 7D**). The zero-crossing time (10:00 on 5/8) of this eigenweighting curve is a demarcation between regimes dominated by the NE-monsoon and SW-monsoon (**Figure 7D**). Therefore, this mode reflects the monsoon influence. The groupings of this mode indicate that as the surface temperature rose due to the increasing of the SW-monsoon, the SSC and NO_3^- decreased. The SW monsoon drove the SCSWC bringing warmer and low NO_3^- water to the sampling site. When plotting the N/P ratio against the eigenweighting curve of this mode (**Figure 7D**), one can see the N/P mimics the eigenweighting curve in the NE-monsoon regime but is a mirror image in the SW-monsoon regime. The low N/P values are the characteristics of oligotrophic and nitrogen-limited water from the SCS (Huang et al., 2020). In addition, the upwelling on the southwest side of Taiwan Bank during the SW-monsoon regime also provides some nutrients and are transported northward, especially phosphates, which may also be responsible for the decrease in N/P ratio (Gan et al., 2009; Hong et al., 2011a). Therefore, this mode clearly describes a regime change between the winter and summer monsoons. During this transition, water temperature increased, and N/P and terrestrial SSCs from the ZMCC both decreased.

The third mode explains 14.2% of the covariability. In this mode, the wind components and temperature are the dominant variables in the positive group. Other variables in the possible group include fluorescence and the 4 SSC sizes (**Figure 7E**). Among variables in the negative group, the two nutrients NO_3^-, NO_2^- are the important ones, of which NO_3^- is the dominant variable. Fluorescence and the two nitrogenous nutrients are in opposite groups indicating the uptake of NO_3^- and NO_2^- by primary producers whose sizes correspond to the 4 SSC sizes. This mode describes the similar scenario as the second mode that the transition in monsoon winds caused the temperature to rise. In this physical setting nitrogenous nutrients were utilized in the production of biogenic particles of the four particle-size classes and increased the fluorescence (**Figure 7F**). Previous studies show that the uptake of nutrients in phytoplankton production is controlled by the concentration of nitrogen and phosphorus in water masses. The uptake varies depending on the phytoplankton species (Lui and Chen, 2011). Another study also pointed out that low nutrient concentration with high chlorophyll-a concentration is common southwest of Taiwan Bank during summer (Hu et al., 2015). The upwelled water was transported northward. In this water mass, phytoplankton grew rapidly at the favorable temperature, N/P ratio, and sunlight, consuming most of the nutrients (Gan et al., 2009; Hu et al., 2015). Therefore, this model is interpreted as the primary production mode.

Eigen Function Analysis of Bottom Water Column and Surface Sediment

The EOF analysis was also used to examine the covariability among the 17 variables in the bottom water (at 2 m above the bed) and on the seabed (**Supplementary Figure 7**). Results show the first mode explains 35.2% covariability of the data. The negative group includes salinity, DO, and $^{210}Pb_{ex}$. The other variables are all in the positive group including temperature, fluorescence, all particle attributes, ^{7}Be, and wind velocities (**Figure 8A**). Since temperature and salinity are in opposite groups, this mode describes the influence of JLJR effluent driven by the NE-directed monsoon winds. Also, fluorescence and all particle

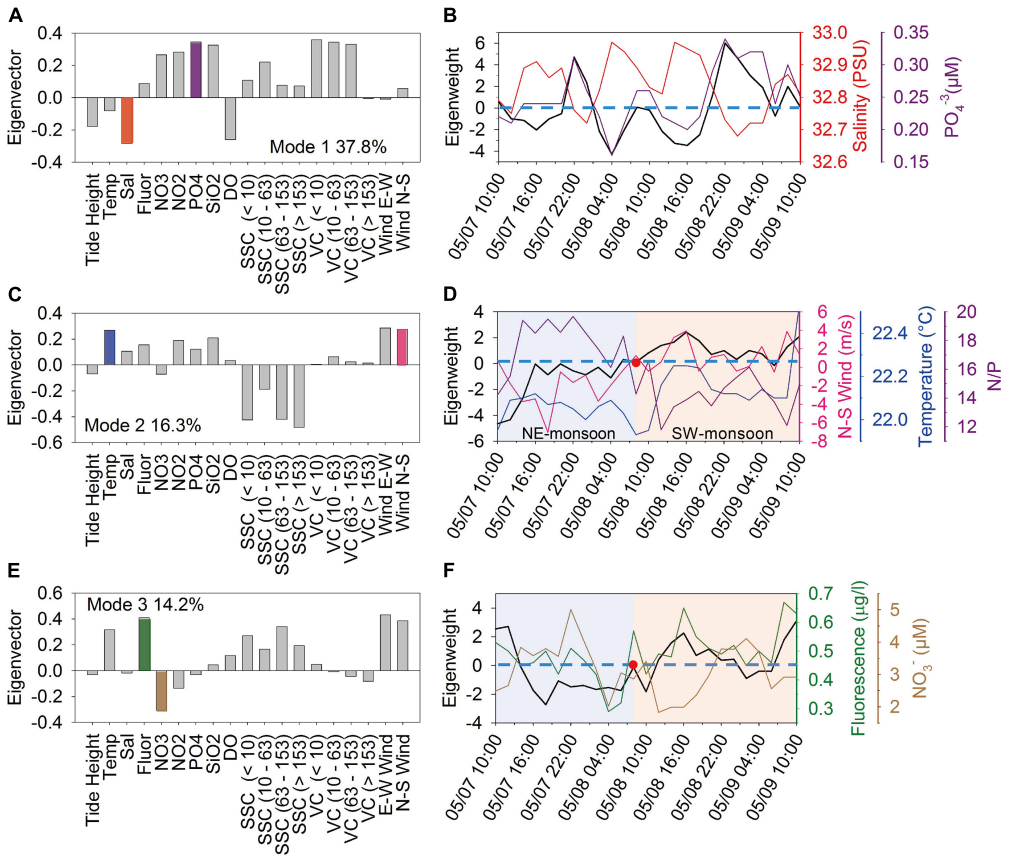

FIGURE 7 | Plots of EOF analysis result on the 19 variables in the upper water column showing **(A)** Mode 1 eigenvectors; **(B)** Mode 1 eigenweighting curve with salinity and PO_4^{3-} as comparison; **(C)** Mode 2 eigenvectors; **(D)** Mode 2 eigenweighting curve with N-S wind, temperature, and N/P as comparison; **(E)** Mode 3 eigenvectors; **(F)** Mode 3 eigenweighting curve with fluorescence and NO_3^- as comparison (the dotted blue line shows the zero value of the eigenweightings). The red dots show the position of zero-crossing on Mode 2 and 3 eigenweighting curves.

attributes are opposite to salinity, implying primary producers of all sizes are associated with the effluent. The eigenweighting curve of this mode shows an increasing secular trend along tidal oscillations (**Figure 8B**), indicating increases in value of variables in the positive group (illustrated by temperature and fluorescence plotted in **Figures 4D,E**).

The second model explains 20.1% covariability. The temperature and salinity are also in opposite groups. This mode describes the effect of cold-water intrusion (**Figure 8C**). The negative portions of the eigenweighting curve of this mode (**Figure 8D**) correspond to episodes of low temperature, high salinity, and low DO near the seabed (**Figures 3B,C,E**). As a result, the eigenweighting curve of this mode mimics the temporal changes of temperature and DO very well (**Figure 8D**). However, fluorescence and surface sediment proxies of $^{210}Pb_{ex}$, ^{7}Be co-varied inversely with the salinity, suggesting their riverine association.

The third model explains 15.9% of the covariability which is dominated by ^{7}Be and the two wind-velocity components in the positive group (**Figure 8E**). DO and $^{210}Pb_{ex}$ covaried inversely in the negative group. The eigenweighting curve of this mode shows a pronounced increasing secular trend that mimics the temporal changes of ^{7}Be and the N-S wind velocity well (**Figure 8F**). The grouping of this mode points out when the southwesterly monsoon wind strengthened, in the surface sediment the ^{7}Be concentration increased and $^{210}Pb_{ex}$ activities decreased, and the DO in the bottom water decreased (**Figures 8E,F**).

DISCUSSION

Based on previous studies and the θ-S characteristics of water masses from WOD in this study (Hu et al., 2010; Zhu et al., 2013), the ZMCC is coastal hugging, flowing southward along the inshore area near the coastline. The SCSWC, flows over the Taiwan Bank and follows along the WQD (**Figure 2A**). At Station a and b, the two current systems encounter each other. At the surface the upper 10 m is occupied by the coastal water. Since the ZMCC water mass is the coldest, it formed the colder and less saline middle mixed layer between 10 and 30 m. The warmer SCSWC water mass occupied the lower part of the water column below 30 m. Similar water mass structures have been described in previous studies in the northern TS and the ECS (Du and Liu, 2017; Wu et al., 2021). Within this overall setting, along the

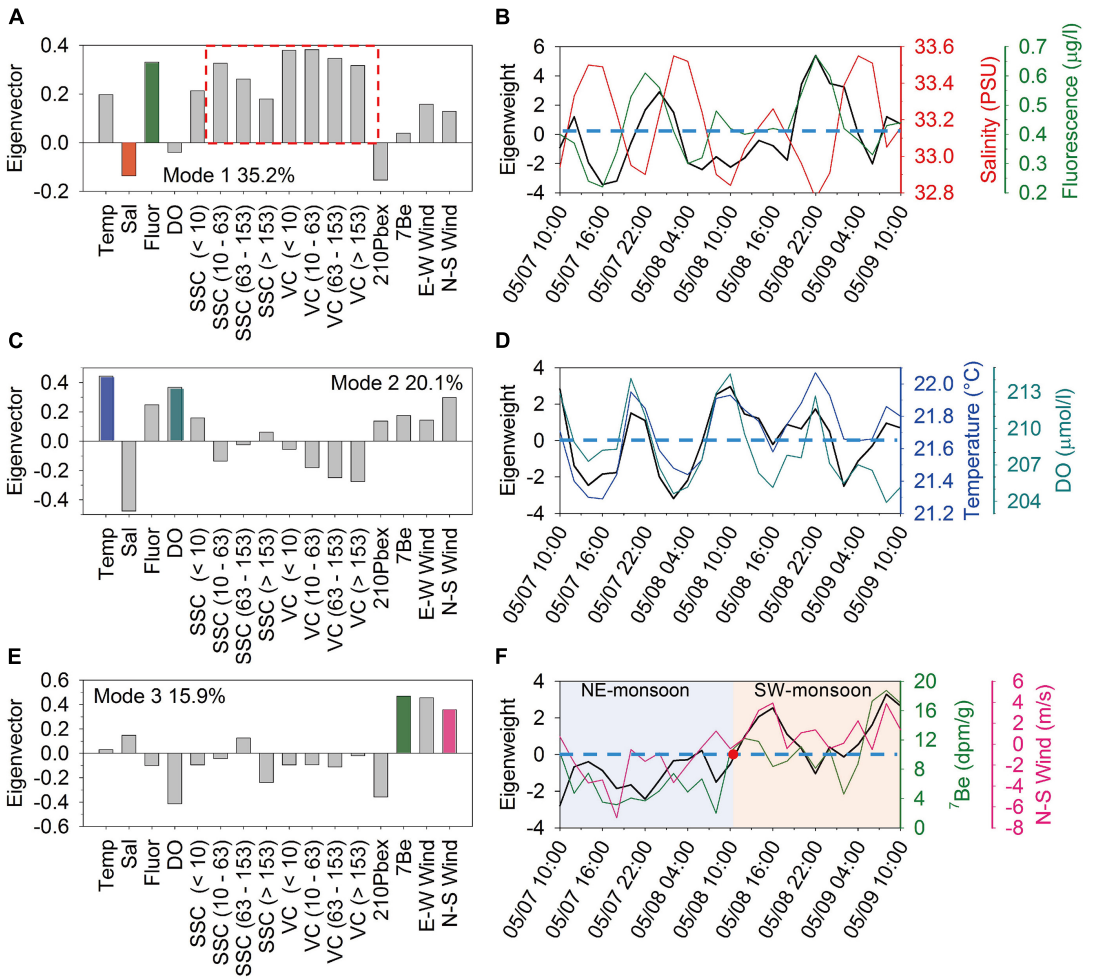

FIGURE 8 | Plots of EOF analysis result on the 16 variables in the lower water column and in the surface sediment showing **(A)** Mode 1 eigenvectors (the red dashed box show the suspended sediment attributes); **(B)** Mode 1 eigenweighting curve with salinity and fluorescence as comparison; **(C)** Mode 2 eigenvectors; **(D)** Mode 2 eigenweighting curve with temperature and DO as comparison; **(E)** Mode 3 eigenvectors; **(F)** Mode 3 eigenweighting curve with ^{7}Be and N-S wind as comparison (the dotted blue line shows the zero value of the eigenweightings). The red dot shows the position of zero-crossing on Mode 3 eigenweighting curve.

transport route of the ZMCC, the colder and more saline water at f and g than at e and h (**Figures 2C,E**) might be caused by coastal upwelling as described by Liu et al. (2019). Additionally, the fresher and warmer water in the upper water column creating stratification might be caused by the river effluent from the JLJR (at h) and Mulanxi River (at e) (**Figure 2C**).

Having established the spatial patterns of properties of the coastal water masses and current systems on the western side of the TS, we now put our observations in perspective. The surface layer at KM4 and KM5 closer to the mouth of the JLJR was the river effluent water, and the values of salinity and temperature in the bottom layers were in between those of SCSWC and ZMCC following isopycnals (**Figure 2F**), indicating the mixing of the SCSWC and ZMCC. At KM6, the θ-S signals of surface water were between the SCSWC water and the ZMCC water, while the bottom layer were almost the values of the SCSWC water (**Figure 2F**). At KM7, the θ-S signals of the surface and bottom layers were identical to those of the SCSWC water, indicating that the influence of the SCSWC became stronger farther away from the river/land.

The observed shipboard time series are also plotted on the θ-S diagram to show the same perspective (**Figure 2G**). The θ-S signal characteristics at the MK1 station are like those at the KM4 and KM5 stations, showing influence of the JLJR effluent in the upper water column and the mixed water of the SCSWC and the ZMCC in the lower water column. Comparing with KM4 and KM5, the bottom water at MK1 was closer to that of the ZMCC, due to the stronger influence of ZMCC. The fixed-point θ-S profile observations at MK1 are marked according to the date. The data show that the bottom θ-S signals gradually deviated from that of ZMCC as the wind field changed to southerly on May 8. Specifically, from 10:00 to 18:00 on May 8, with the strengthening of the southwesterly wind, the θ-S signals of the entire water column turned closer to that of the SCSWC (**Figure 2G**).

Through EOF results, the measured variables near the JLJR mouth were mainly controlled by the tidally driven river effluent.

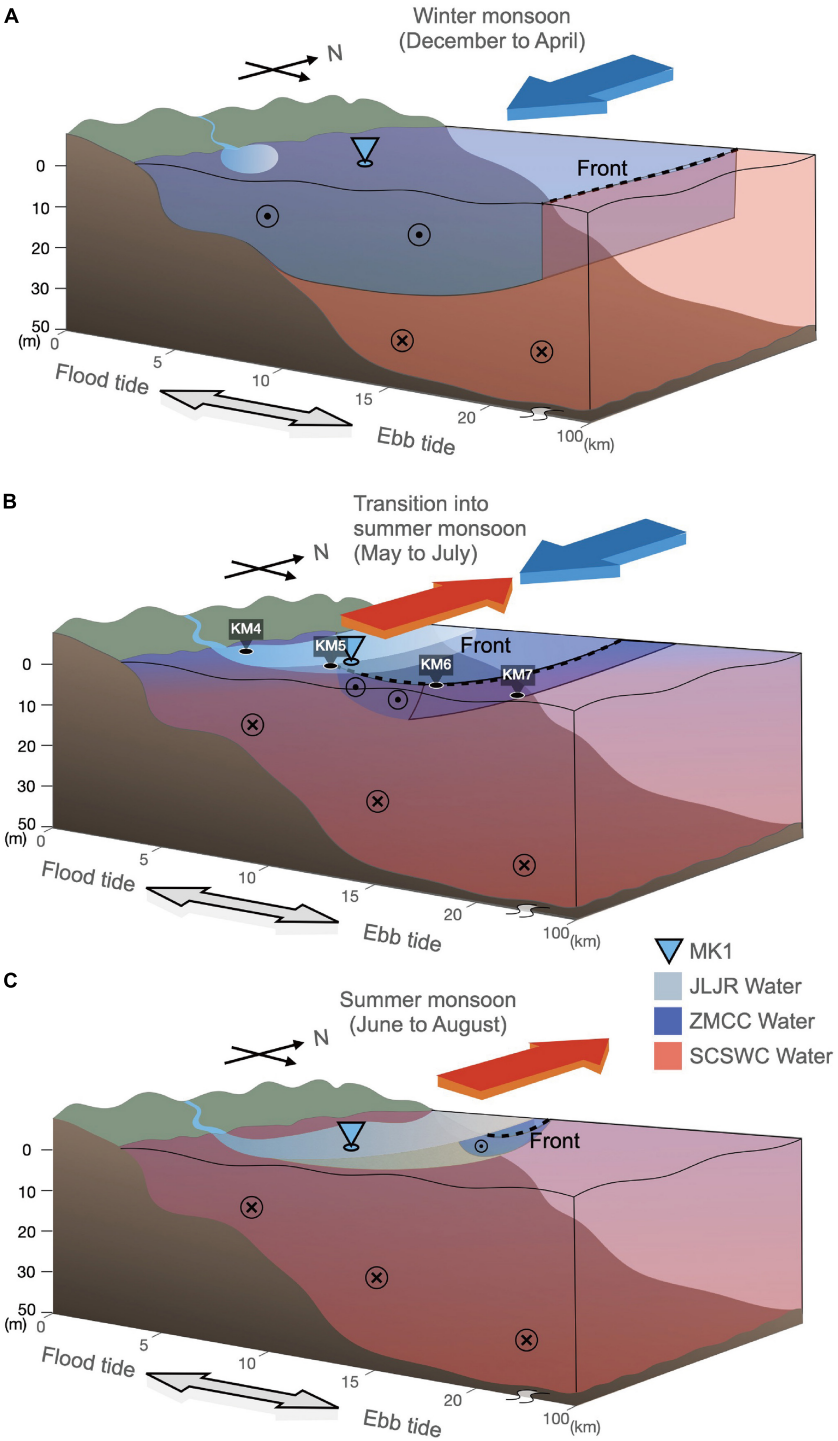

FIGURE 9 | Schematic presentations of how the monsoon regime change affected land-ocean interactions in the western side of the TS. Bold blue and red arrows represent the NE and SW monsoon winds. Flow symbols on the side of each block facing the page show ZMCC coming out of the page (southbound) and SCSWC going into the page (northbound). Translucent red and blue color blocks represent SCSWC and ZMCC water masses and the solid light blue represents JLJR water, respectively. The inverse triangle shows the location of MK1 station. The black dotted line marks the approximate location of the SST front between ZMCC and SCSWC. **(A)** Under NE monsoon dominance in winter, ZMCC water occupies the upper water column, the SCSWC water is in deeper layer and is seaward of the ZMCC water. **(B)** In the transitional period of the regime change in spring, the ZMCC water recedes northward and shoreward and begin to mix with the encroaching SCSWC water from the south and from below. The dispersal of the effluent of JLJR parallels the front between the ZMCC and SCSWC. **(C)** Under SW monsoon dominance in summer, SCSWC water almost occupies the entire nearshore water column. River plume water replaces the ZMCC water at the surface near the coast. Traces of ZMCC water can still be seen.

Secondly, EOF results reflects the duel between the ZMCC and SCSWC under the dominance of monsoon. Previous studies have classified the diffusion patterns of JLJR plume water within two meters of the surface (Wang et al., 2013). High-frequency ground wave radar scanning results also explain the reversal of the flow field dominated by the monsoon (Zhu et al., 2008). However, the influencing factors such as tides and monsoon winds on the variations of water properties is still unclear.

In fact, from the percentage of explained eigenmodes, the tide played an important role in the variability of water properties. During a tidal cycle, the effluent of JLJR spreads northeastward in the flood tide. During ebb, the southwestward flow caused the mixed water of the ZMCC and the SCSWC to intrude into the lower water column at MK1 station. However, in the offshore area (beyond 25 m isobath), the influence of tides and river effluent was weakened, the θ-S signature was determined by the duel between the ZMCC and SCSWC. Due to the offshore topography, the ZMC and the SCSWC water masses did not fully mix, and the dense SCSWC water sank under the ZMCC water. If the transect of KM4-KM7 was used as the boundary, south of this boundary the SCSWC dominated the θ-S characteristics. North of this boundary a three-layered structure existed. The lower part (deeper than 25 m) of the water column was mainly affected by the SCSWC. The middle part (10–25 m) was affected by the ZMCC and the upper part by the river effluent. River effluent is also affected by rainfall and other factors, so it does not necessarily continue to exist on the surface. Therefore, the monthly average temperature front is a result of the duel between ZMCC and SCSWC.

The changes of monsoons determined the outcome of the duel between ZMCC and SCSWC, and affected the changes of the water properties offshore JLJR mouth on a longer time scale. The zero-crossing of the eigenweighting curves in the EOF analysis results can clearly illustrate such a change. The zero-crossing of the second mode in the surface water data set occurred on 10:00 May 8, which was the same time as that of that of the third mode in the bottom water data set. This coincidence points out a significant phenomenon and yet has not been discovered before.

In the surface water, the southwesterly monsoon winds enhanced the strength of the SCSWC, which had lower N/P ratio, causing a secular decreasing trend in the surface water (**Figure 4C**). On the other hand, the weakening of the northeasterly monsoon winds weakened the ZMCC, which carried colder water having higher N/P ratio (Chen, 2003). The covarying changes in the temporal waterborne properties caused by the monsoon regime change were captured by the second eigenmode and the exact timing of the regime change occurred on 10:00 May 8 (**Figures 7C,D**). At the MK1 station, although the tide was the dominant forcing affecting the water column stratification and waterborne properties, there was a warming trend by the SCSWC water in the upper water column (dashed circle in **Figure 2G**) toward the end of the shipboard monitoring.

On the sediment-water interface, the effect of the regime change was described by the third eigenmode (**Figures 8E,F**). This mode is dominated by two fine-grained sediment tracers of $^{210}Pb_{ex}$ and ^{7}Be in opposite groups. $^{210}Pb_{ex}$ in coastal waters is supplied by ocean water, riverine export, *in situ* decay of ^{226}Ra, and atmospheric fallout (Dukat and Kuehl, 1995; Sommerfield et al., 2007). $^{210}Pb_{ex}$ is due to the scavenging effect of fine-grained particles to remove ^{210}Pb in the water column (Huh and Su, 1999; Baskaran and Santschi, 2002). The values of $^{210}Pb_{ex}$ are largely determined by the supply and duration of the scavenging process (Huh and Su, 1999; Su and Huh, 2002). ^{7}Be on the other hand, often indicates fresh terrestrial sediment related to storm rainfall and river flood events (Allison et al., 2005; Sommerfield et al., 2007; Liu et al., 2013). Because of its short half-life (53 days), in marine environments, ^{7}Be can be detected only in freshly deposited terrestrial sediment less than about 200 days old (Huh et al., 2011; Du et al., 2012). Spatially, the longer the fluvial sediment gets transported away from the riverine source, the weaker the ^{7}Be signals become (Liu et al., 2018).

In this study, the two distal fluvial sources, the ZJR and the CJR, are 600 and 900 km away from the JLJR, respectively, and the effluent of JLJR was weak during the observation period. Therefore, the change of ^{7}Be concentration in surface sediment can exclude the effect of proximal terrestrial source, mainly due to the sorption of ^{7}Be by the particles in surface water. With the monsoon regime change, the fluorescence and the VC of large particle increased simultaneously, indicating that these large particles may belong to biological particles (**Supplementary Figure 6**). Compared with ^{210}Pb, which can always be removed from seawater by particles, ^{7}Be scavenging in surface seawater requires more particles (^{210}Pb has a higher sorption distribution coefficient than that of ^{7}Be for suspended matter) (Allison and Allison, 2005). Previous studies have also shown that the sorption of all radionuclides was significantly enhanced in the presence of organic particles, and the sorption of ^{7}Be by organic particles is the most significant (Chuang et al., 2014).

The demarcation between monsoon regimes illustrated by the zero-crossing eigenweighting curves (**Figure 8F**) is further illustrated by the plot of the temporal changes in $^{7}Be/^{210}Pb_{ex}$ (**Supplementary Figure 8**). The time-averaged value is indicated by the dashed line which intercepts with the $^{7}Be/^{210}Pb_{ex}$ curve at the same demarcation time of 10:00 on May 8. Before and after this time point, the $^{7}Be/^{210}Pb_{ex}$ values are below and above the average, respectively. This transition indicates the switch of water masses increases the biological particles (fluorescence increased in the upper water, **Supplementary Figure 9**). These particles adsorbed more ^{7}Be to the bottom, which in turn led to a transition in the bottom sediments (**Supplementary Figure 9**). The monsoon regime change not only directly affects the properties of the water masses, but also indirectly affects the properties of the surface sediments.

The effects of river effluent, tides and monsoon winds on water borne properties on the diurnal to 3-day time scales have been quantified by the EOF analysis. Findings of this study are further illustrated in three schematic diagrams (**Figure 9**). Monsoon winds were the primary drivers of all the changes described in this study. The Southbound ZMCC was enhanced by northwesterly monsoon winds to have stronger magnitude and wider spread into the TS, forming a strong vertical front at the seaward boundary (**Figure 9A**). Cold and less saline water masses were driven southward carrying terrestrial sourced and suspended biogenic and clastic particles. In the upper water column, the

water masses carried terrestrial sourced nutrients with higher N/P ratio from ECS and higher DO (**Figure 4C** and **Supplementary Figure 6**). Cold and saline water was also transported landward in the lower water column modulated by the tide.

During the short window of 3 days, the monsoon regimes changed from NE dominance to SW dominance on May 8 at 10:00. The wind field changed abruptly. Temperature in the lower water column quickly warmed up (**Figures 3B**, **9B**). As the SW-monsoon assumed dominance, the frontal zone between the water masses of ZMCC and SCSWC began to retreat northward and landward (**Figures 6A,B**). A front was also formed between the ZMCC and the encroaching SCSWC at the location of Sta. MK6. In addition, the JLJR effluent became weakened as it was dispersed farther seaward (**Figures 5B**, **9B**). Near the mouth of JLJR, water masses of the river effluent, ZMCC, and SCSWC occupied different depths in the water column and interacted with one another in a complex manner. In the on-offshore direction, the brackish effluent pinched out on the saline SCSWC water at the surface. However, the brackish effluent and the less saline ZMCC were indistinguishable. They could be distinguished from the warmer SCSWC water only by temperature (**Figure 5**).

During the SW-monsoon regime, warm water masses occupied the entire water column except for the narrow nearshore zone (**Figure 9C**). Nutrients in upper water column had lower N/P ratio but higher primary production (**Figures 4C**, **7E**). The frontal zone between the water masses of ZMCC and SCSWC retreated farther northward (**Figure 9C**).

CONCLUSION

In conclusion, water masses off the mouth of JLJR can be roughly distinguished into coastal water containing river effluent, the ZMCC water, and the SCSWC water during the study period. In the nearshore area, coastal water dominated the surface, and the bottom is dominated by the mixture of ZMCC and SCSWC water masses. The influence of coastal water is weakened in the offshore (beyond 25-m isobath) where the ZMCC and SCSWC meet. The seaward extension from the JLJR mouth to offshore is roughly a physical boundary during the period of monsoon regime change. South of the boundary the SCSWC water dominates the water column, and north of this boundary ZMCC water dominates. When the two water masses meet, the denser SCSWC flows northward, sinks under the ZMCC. Spatially, the frontal boundary of the two water masses changes with the seasons. Overall, physical processes that affect the area in the western part of the TS near the JLJR mouth are the river effluent dispersal and tidal motions on smaller spatial scales. On larger spatial scales the monsoon winds dominate the ZMCC and SCSWC and the water masses they carry. In this setting, our study reveals the critical period when the regime change occurred, which not only affected land-sea interaction in the physics and biology coupling in the proximal area of the site, but also the alternating dominance of terrestrial signals of the two major distal fluvial sources.

DATA AVAILABILITY STATEMENT

The raw data supporting the conclusions of this article will be made available by the authors, without undue reservation.

AUTHOR CONTRIBUTIONS

JL conceived and designed the study, supervised the work, and co-wrote the manuscript. RY participated in the cruise design, onboard sampling, and sample analyses, plotted and interpreted the data, and co-wrote the manuscript. C-CS contributed to the analysis of the radio isotopes and data interpretation. YC did temperature gradient magnitude computation and plotting from composite satellite sea-surface data and interpretation. JX digitized front from gradient magnitude plots and frontal interpretation. H-KL contributed to the nutrient data interpretation. All authors contributed to the article and approved the submitted version.

FUNDING

This study was funded by the ROC Ministry of Science and Technology (MOST) under grant nos. MOST 104–2611-M-110–011, MOST 108-2611-M-110-011–, and MOST 109-2611-M-110-014- to JL.

ACKNOWLEDGMENTS

We appreciate the help of Chen-Tung Arthur Chen's Laboratory in the Department of Oceanography for nutrient analysis, National Sun Yat-sen University. We thank the two reviewers for their helpful comments and suggestions to improve the manuscript.

SUPPLEMENTARY MATERIAL

The Supplementary Material for this article can be found online at: https://www.frontiersin.org/articles/10.3389/fmars.2021.735242/full#supplementary-material

REFERENCES

Allison, J. D., and Allison, T. L. (2005). *Partition Coefficients for Metals in Surface Water, Soil, and Waste*. Washington, DC: U.S. Environmental Protection Agency, 74.

Allison, M. A., Sheremet, A., Goni, M. A., and Stone, G. W. (2005). Storm layer deposition on the Mississippi-Atchafalaya subaqueous delta generated by Hurricane Lili in 2002. *Cont. Shelf Res.* 25, 2213–2232. doi: 10.1016/j.csr.2005.08.023

Bai, Y., He, X. Q., Pan, D. L., Chen, C. T. A., Kang, Y., Chen, X. Y., et al. (2014). Summertime Changjiang River plume variation during 1998-2010. *J. Geophys. Res. Oceans* 119, 6238–6257. doi: 10.1002/2014jc009866

Bai, Y., Huang, T. H., He, X. Q., Wang, S. L., Hsin, Y. C., Wu, C. R., et al. (2015). Intrusion of the Pearl River plume into the main channel of the

Taiwan Strait in summer. *J. Sea Res.* 95, 1–15. doi: 10.1016/j.seares.2014.10.003

Baskaran, M., and Santschi, P. H. (2002). Particulate and dissolved Pb-210 activities in the shelf and slope regions of the Gulf of Mexico waters. *Cont. Shelf Res.* 22, 1493–1510. doi: 10.1016/s0278-4343(02)00017-1

Berdeal, I. G., Hickey, B. M., and Kawase, M. (2002). Influence of wind stress and ambient flow on a high discharge river plume. *J. Geophys. Res. Oceans* 107:24. doi: 10.1029/2001jc000932

Boyer, T. P., Baranova, O. K., Coleman, C., Garcia, H. E., Grodsky, A., Locarnini, R. A., et al. (2018). *"World Ocean Database 2018". A.V. Mishonov, Technical Ed*. Silver Spring, MD: NOAA.

Bryden, H. L. (1973). New polynomials for thermal expansion, adiabatic temperature gradient and potential temperature of sea water. *Deep Sea Res. Oceanogr. Abstr.* 20, 401–408. doi: 10.1016/0011-7471(73)90063-6

Chang, Y., Shieh, W. J., Lee, M. A., Chan, J. W., Lan, K. W., and Weng, J. S. (2010). Fine-scale sea surface temperature fronts in wintertime in the northern South China Sea. *Int. J. Remote Sens.* 31, 4807–4818. doi: 10.1080/01431161.2010.485146

Chang, Y., Shimada, T., Lee, M. A., Lu, H. J., Sakaida, F., and Kawamura, H. (2006). Wintertime sea surface temperature fronts in the Taiwan Strait. *Geophys. Res. Lett.* 33:4. doi: 10.1029/2006gl027415

Chen, C. T. A. (2003). Rare northward flow in the Taiwan Strait in winter: a note. *Cont. Shelf Res.* 23, 387–391. doi: 10.1016/s0278-4343(02)00209-1

Chen, C. T. A. (2009). Chemical and physical fronts in the Bohai, Yellow and East China Seas. *J. Mar. Syst.* 78, 394–410. doi: 10.1016/j.jmarsys.2008.11.016

Chen, C. T. A., Hsing, L. Y., Liu, C. L., and Wang, S. L. (2004). Degree of nutrient consumption of upwelled water in the Taiwan Strait based on dissolved organic phosphorus or nitrogen. *Mar. Chem.* 87, 73–86. doi: 10.1016/j.marchem.2004.01.006

Chen, M. J., Pattiaratchi, C. B., Ghadouani, A., and Hanson, C. (2019). Seasonal and inter-annual variability of water column properties along the Rottnest continental shelf, south-west Australia. *Ocean Sci.* 15, 333–348. doi: 10.5194/os-15-333-2019

Chen, T. A., and Wang, S. L. (2006). A salinity front in the southern East China Sea separating the Chinese coastal and Taiwan Strait waters from Kuroshio waters. *Cont. Shelf Res.* 26, 1636–1653. doi: 10.1016/j.csr.2006.05.003

Chuang, C. Y., Santschi, P. H., Jiang, Y. L., Ho, Y. F., Quigg, A., Guo, L. D., et al. (2014). Important role of biomolecules from diatoms in the scavenging of particle-reactive radionuclides of thorium, protactinium, lead, polonium, and beryllium in the ocean: a case study with *Phaeodactylum tricornutum*. *Limnol. Oceanogr.* 59, 1256–1266. doi: 10.4319/lo.2014.59.4.1256

Corbett, D. R., Mckee, B., and Duncan, D. (2004). An evaluation of mobile mud dynamics in the Mississippi River deltaic region. *Mar. Geol.* 209, 91–112. doi: 10.1016/j.margeo.2004.05.028

Dagg, M., Benner, R., Lohrenz, S., and Lawrence, D. (2004). Transformation of dissolved and particulate materials on continental shelves influenced by large rivers: plume processes. *Cont. Shelf Res.* 24, 833–858. doi: 10.1016/j.csr.2004.02.003

Du, J. Z., Zhang, J., and Baskaran, M. (2012). "Applications of short-lived radionuclides (7Be, 210Pb, 210Po, 137Cs and 234Th) to trace the sources, transport pathways and deposition of particles/sediments in rivers, estuaries and coasts," in *Handbook of Environmental Isotope Geochemistry*, Vol. I, ed. M. Baskaran (Berlin: Springer Berlin Heidelberg), 305–329.

Du, X. Q., and Liu, J. T. (2017). Particle dynamics of the surface, intermediate, and benthic nepheloid layers under contrasting conditions of summer monsoon and typhoon winds on the boundary between the Taiwan Strait and East China Sea. *Prog. Oceanogr.* 156, 130–144. doi: 10.1016/j.pocean.2017.06.009

Dukat, D. A., and Kuehl, S. A. (1995). Non-steady-state 210Pb flux and the use of 228Ra/226Ra as a geochronometer on the Amazon continental shelf. *Mar. Geol.* 125, 329–350. doi: 10.1016/0025-3227(95)00018-t

Gan, J. P., Cheung, A., Guo, X. G., and Li, L. (2009). Intensified upwelling over a widened shelf in the northeastern South China Sea. *J. Geophys. Res. Oceans* 114:15. doi: 10.1029/2007jc004660

Hong, H. S., Chai, F., Zhang, C. Y., Huang, B. Q., Jiang, Y. W., and Hu, J. Y. (2011a). An overview of physical and biogeochemical processes and ecosystem dynamics in the Taiwan Strait. *Cont. Shelf Res.* 31, S3–S12. doi: 10.1016/j.csr.2011.02.002

Hong, H. S., Liu, X., Chiang, K. P., Huang, B. Q., Zhang, C. Y., Hu, J., et al. (2011b). The coupling of temporal and spatial variations of chlorophyll a concentration and the East Asian monsoons in the southern Taiwan Strait. *Cont. Shelf Res.* 31, S37–S47. doi: 10.1016/j.csr.2011.02.004

Hopkins, J., Lucas, M., Dufau, C., Sutton, M., Stum, J., Lauret, O., et al. (2013). Detection and variability of the Congo River plume from satellite derived sea surface temperature, salinity, ocean colour and sea level. *Remote Sens. Environ.* 139, 365–385. doi: 10.1016/j.rse.2013.08.015

Hsieh, H. Y., Yu, S. F., and Lo, W. T. (2013). Influence of monsoon-driven hydrographic features on siphonophore assemblages in the Taiwan Strait, western North Pacific Ocean. *Mar. Freshw. Res.* 64, 348–358. doi: 10.1071/mf12151

Hsu, R. T., and Liu, J. T. (2010). *In-situ* estimations of the density and porosity of flocs of varying sizes in a submarine canyon. *Mar. Geol.* 276, 105–109. doi: 10.1016/j.margeo.2010.07.003

Hu, J., Lan, W. L., Huang, B. Q., Chiang, K. P., and Hong, H. S. (2015). Low nutrient and high chlorophyll a coastal upwelling system–a case study in the southern Taiwan Strait. *Estuar. Coast. Shelf Sci.* 166, 170–177. doi: 10.1016/j.ecss.2015.05.020

Hu, J. Y., Kawamura, H., Li, C. Y., Hong, H. S., and Jiang, Y. W. (2010). Review on current and seawater volume transport through the Taiwan Strait. *J. Oceanogr.* 66, 591–610. doi: 10.1007/s10872-010-0049-1

Hu, J. Y., and Wang, X. H. (2016). Progress on upwelling studies in the China seas. *Rev. Geophys.* 54, 653–673. doi: 10.1002/2015rg000505

Hu, L. M., Shi, X. F., Yu, Z. G., Lin, T., Wang, H. J., Ma, D. Y., et al. (2012). Distribution of sedimentary organic matter in estuarine-inner shelf regions of the East China Sea: implications for hydrodynamic forces and anthropogenic impact. *Mar. Chem.* 142, 29–40. doi: 10.1016/j.marchem.2012.08.004

Hu, Z. F., Qi, Y. Q., He, X. Q., Wang, Y. H., Wang, D. P., Cheng, X. H., et al. (2019). Characterizing surface circulation in the Taiwan Strait during NE monsoon from Geostationary Ocean Color Imager. *Remote Sens. Environ.* 221, 687–694. doi: 10.1016/j.rse.2018.12.003

Huang, T. H., Chen, C. T. A., Bai, Y., and He, X. Q. (2020). Elevated primary productivity triggered by mixing in the quasi-cul-de-sac Taiwan Strait during the NE monsoon. *Sci. Rep.* 10:9. doi: 10.1038/s41598-020-64580-6

Huang, T. H., Chen, C. T. A., Zhang, W. Z., and Zhuang, X. F. (2015). Varying intensity of Kuroshio intrusion into Southeast Taiwan Strait during ENSO events. *Cont. Shelf Res.* 103, 79–87. doi: 10.1016/j.csr.2015.04.021

Huh, C. A., Chen, W. F., Hsu, F. H., Su, C. C., Chiu, J. K., Lin, S., et al. (2011). Modern (<100 years) sedimentation in the Taiwan Strait: rates and source-to-sink pathways elucidated from radionuclides and particle size disttibution. *Cont. Shelf Res.* 31, 47–63. doi: 10.1016/j.csr.2010.11.002

Huh, C. A., Lin, H. L., Lin, S., and Huang, Y. W. (2009). Modern accumulation rates and a budget of sediment off the Gaoping (Kaoping) River, SW Taiwan: a tidal and flood dominated depositional environment around a submarine canyon. *J. Mar. Syst.* 76, 405–416. doi: 10.1016/j.jmarsys.2007.07.009

Huh, C. A., and Su, C. C. (1999). Sedimentation dynamics in the East China Sea elucidated from Pb-210, Cs-137 and Pu-239,Pu-240. *Mar. Geol.* 160, 183–196. doi: 10.1016/s0025-3227(99)00020-1

Jan, S., Tseng, Y. H., and Dietrich, D. E. (2010). Sources of water in the Taiwan Strait. *J. Oceanogr.* 66, 211–221. doi: 10.1007/s10872-010-0019-7

Jan, S., Wang, J., Chern, C. S., and Chao, S. Y. (2002). Seasonal variation of the circulation in the Taiwan Strait. *J. Mar. Syst.* 35, 249–268. doi: 10.1016/s0924-7963(02)00130-6

Lee, J., Liu, J. T., Hung, C. C., Lin, S., and Du, X. Q. (2016). River plume induced variability of suspended particle characteristics. *Mar. Geol.* 380, 219–230. doi: 10.1016/j.margeo.2016.04.014

Lee, J., Liu, J. T., Lee, I. H., Fu, K.-H., Yang, R. J., Gong, W., et al. (2021). Encountering shoaling internal waves on the dispersal pathway of the pearl river plume in summer. *Sci. Rep.* 11:999. doi: 10.1038/s41598-020-80215-2

Liu, J. T., Chao, S. Y., and Hsu, R. T. (2002). Numerical modeling study of sediment dispersal by a river plume. *Cont. Shelf Res.* 22, 1745–1773. doi: 10.1016/s0278-4343(02)00036-5

Liu, J. T., Hsu, R. T., Yang, R. J., Wang, Y. P., Wu, H., Du, X. Q., et al. (2018). A comprehensive sediment dynamics study of a major mud belt system on the inner shelf along an energetic coast. *Sci. Rep.* 8:14. doi: 10.1038/s41598-018-22696-w

Liu, J. T., Huang, B. Q., Chang, Y., Du, X. Q., Liu, X., Yang, R. J., et al. (2019). Three-dimensional coupling between size-fractionated chlorophyll-a, POC and physical processes in the Taiwan Strait in summer. *Prog. Oceanogr.* 176:102129. doi: 10.1016/j.pocean.2019.102129

Liu, J. T., Hung, J. J., Lin, H. L., Huh, C. A., Lee, C. L., Hsu, R. T., et al. (2009). From suspended particles to strata: the fate of terrestrial substances in the Gaoping (Kaoping) submarine canyon. *J. Mar. Syst.* 76, 417–432. doi: 10.1016/j.jmarsys.2008.01.010

Liu, J. T., Kao, S. J., Huh, C. A., and Hung, C. C. (2013). "Gravity flows associated with flood events and carbon burial: Taiwan as instructional source area," in *Annual Review of Marine Science*, Vol. 5, eds C. A. Carlson and S. J. Giovannoni (Palo Alto, CA: Annual Reviews), 47–68.

Liu, J. T., Lee, J., Yang, R. J., Du, X., Li, A., Lin, Y.-S., et al. (2021). Coupling between physical processes and biogeochemistry of suspended particles over the inner shelf mud in the East China Sea. *Mar. Geol.* 442:106657. doi: 10.1016/j.margeo.2021.106657

Liu, S. F., Shi, X. F., Fang, X. S., Dou, Y. G., Liu, Y. G., and Wang, X. C. (2014). Spatial and temporal distributions of clay minerals in mud deposits on the inner shelf of the East China Sea: implications for paleoenvironmental changes in the Holocene. *Quat. Int.* 349, 270–279. doi: 10.1016/j.quaint.2014.07.016

Liu, S. F., Shi, X. F., Liu, Y. G., Qia, S. Q., Yang, G., Fang, X. S., et al. (2010). Records of the East Asian winter monsoon from the mud area on the inner shelf of the East China Sea since the mid-Holocene. *Chin. Sci. Bull.* 55, 2306–2314. doi: 10.1007/s11434-010-3215-3

Lui, H. K., and Chen, C. T. A. (2011). Shifts in limiting nutrients in an estuary caused by mixing and biological activity. *Limnol. Oceanogr.* 56, 989–998. doi: 10.4319/lo.2011.56.3.0989

Milliman, J. D., and Meade, R. H. (1983). World-wide delivery of river sediment to the oceans. *J. Geol.* 91, 1–21. doi: 10.1086/628741

Nittrouer, C. A., Demaster, D. J., Kuehl, S. A. Jr., Sternberg, A. G. F., Faria, R. W., Silveira, L. E. C., et al. (2021). Amazon Sediment transport and accumulation along the continuum of mixed fluvial and marine processes. *Ann. Rev. Mar. Sci.* 13, 501–536. doi: 10.1146/annurev-marine-010816-060457

Pai, S. C., and Riley, J. P. (1994). Determination of nitrate in the presence of nitrite in natural-waters by flow-injection analysis with a non-quantitative online cadmium reductor. *Int. J. Environ. Anal. Chem.* 57, 263–277. doi: 10.1080/03067319408027460

Pai, S. C., Yang, C. C., and Riley, J. P. (1990a). Effects of acidity and molybdate concentration on the kinetics of the formation of the phosphoantimonyl molybdenum blue complex. *Anal. Chim. Acta* 229, 115–120.

Pai, S. C., Yang, C. C., and Riley, J. P. (1990b). Formation kinetics of the pink azo dye in the determination of nitrite in natural-waters. *Anal. Chim. Acta* 232, 345–349. doi: 10.1016/s0003-2670(00)81252-0

Qiao, L. L., Liu, S. D., Xue, W. J., Liu, P., Hu, R. J., Sun, H. F., et al. (2020). Spatiotemporal variations in suspended sediments over the inner shelf of the East China Sea with the effect of oceanic fronts. *Estuar. Coast. Shelf Sci.* 234:10. doi: 10.1016/j.ecss.2020.106600

Qiu, Y., Li, L., Chen, C. T. A., Guo, X. G., and Jing, C. S. (2011). Currents in the Taiwan Strait as observed by surface drifters. *J. Oceanogr.* 67, 395–404. doi: 10.1007/s10872-011-0033-4

Resio, D. T., and Hayden, B. P. (1975). Recent secular variations in mid-Atlantic winter extratropical storm climate. *J. Appl. Meteorol.* 14, 1223–1234. doi: 10.1175/1520-04501975014<1223:Rsvima<2.0.Co;2

Sommerfield, C. K., Ogston, A. S., Mullenbach, B. L., Drake, D. E., Alexander, C. R., Nittrouer, C. A., et al. (2007). "Oceanic dispersal and accumulation of river sediment," in *Continental Margin Sedimentation*, eds C. A. Nittrouer, J. A. Austin, M. E. Field, J. H. Kravitz, J. P. M. Syvitski, and P. L. Wiberg (Blackwell Publishing Ltd), 157–212. doi: 10.1002/9781444304398.ch4

Su, C. C., and Huh, C. A. (2002). Pb-210 Cs-137 and Pu-231,Pu-240 in East China sea sediments: sources, pathways and budgets of sediments and radionuclides. *Mar. Geol.* 183, 163–178. doi: 10.1016/s0025-3227(02)00165-2

Tseng, L. C., Kumar, R., Dahms, H. U., Chen, Q. C., and Hwang, J. S. (2008). Monsoon-driven succession of copepod assemblages in coastal waters of the northeastern Taiwan strait. *Zool. Stud.* 47, 46–60.

Wang, D. F., Zheng, Q. A., and Hu, J. Y. (2013). Jet-like features of Jiulongjiang River plume discharging into the west Taiwan Strait. *Front. Earth Sci.* 7:282–294. doi: 10.1007/s11707-013-0372-0

Wang, P. X., Clemens, S. C., Tada, R., and Murray, R. W. (2019). Blowing in the monsoon wind. *Oceanography* 32, 48–59. doi: 10.5670/oceanog.2019.119

Wang, Y. H., Jan, S., and Wang, D. P. (2003). Transports and tidal current estimates in the Taiwan Strait from shipboard ADCP observations (1999-2001). *Estuar. Coast. Shelf Sci.* 57, 193–199. doi: 10.1016/s0272-7714(02)00344-x

Wu, C. R., Chao, S. Y., and Hsu, C. (2007). Transient, seasonal and interannual variability of the Taiwan Strait current. *J. Oceanogr.* 63, 821–833. doi: 10.1007/s10872-007-0070-1

Wu, R., Wu, H., and Wang, Y. (2021). Modulation of shelf circulations under multiple river discharges in the East China Sea. *J. Geophys. Res. Oceans* 126:e2020JC016990. doi: 10.1029/2020JC016990

Xu, K. H., Milliman, J. D., Li, A. C., Liu, J. P., Kao, S. J., and Wan, S. M. (2009). Yangtze- and Taiwan-derived sediments on the inner shelf of East China Sea. *Cont. Shelf Res.* 29, 2240–2256. doi: 10.1016/j.csr.2009.08.017

Zavala-Hidalgo, J., Romero-Centeno, R., Mateos-Jasso, A., Morey, S. L., and Martinez-Lopez, B. (2014). The response of the Gulf of Mexico to wind and heat flux forcing: what has been learned in recent years? *Atmosfera* 27, 317–334. doi: 10.1016/s0187-6236(14)71119-1

Zhang, C. Y., Huang, Y., and Ding, W. X. (2020). Enhancement of Zhe-Min coastal water in the Taiwan Strait in winter. *J. Oceanogr.* 76, 197–209. doi: 10.1007/s10872-020-00539-5

Zhu, D. Y., Li, L., and Guo, X. G. (2013). Seasonal and interannual variations of surface current in the southern Taiwan Strait to the west of Taiwan Shoals. *Chin. Sci. Bull.* 58, 4171–4178. doi: 10.1007/s11434-013-5907-y

Zhu, D. Y., Li, L., Li, Y., and Guo, X. G. (2008). Seasonal variation of surface currents in the southwestern Taiwan Strait observed with HF radar. *Chin. Sci. Bull.* 53, 2385–2391. doi: 10.1007/s11434-008-0207-7

Conflict of Interest: The authors declare that the research was conducted in the absence of any commercial or financial relationships that could be construed as a potential conflict of interest.

Publisher's Note: All claims expressed in this article are solely those of the authors and do not necessarily represent those of their affiliated organizations, or those of the publisher, the editors and the reviewers. Any product that may be evaluated in this article, or claim that may be made by its manufacturer, is not guaranteed or endorsed by the publisher.

Copyright © 2021 Yang, Liu, Su, Chang, Xu and Lui. This is an open-access article distributed under the terms of the Creative Commons Attribution License (CC BY). The use, distribution or reproduction in other forums is permitted, provided the original author(s) and the copyright owner(s) are credited and that the original publication in this journal is cited, in accordance with accepted academic practice. No use, distribution or reproduction is permitted which does not comply with these terms.

frontiers in Marine Science

ORIGINAL RESEARCH
published: 07 January 2022
doi: 10.3389/fmars.2021.789687

Shelf Transport Pathways Adjacent to the East Australian Current Reveal Sources of Productivity for Coastal Reefs

Moninya Roughan[1]*, *Paulina Cetina-Heredia*[1], *Nina Ribbat*[1] and *Iain M. Suthers*[2]

[1] Coastal and Regional Oceanography Lab, School of Mathematics and Statistics, University of New South Wales, Sydney, NSW, Australia, [2] School of Biological Earth and Environmental Sciences, University of New South Wales, Sydney, NSW, Australia

The region where the East Australian Current (EAC) separates from the coast is dynamic and the shelf circulation is impacted by the interplay of the western boundary current and its eddy field with the coastal ocean. This interaction can drive upwelling, retention or export. Hence understanding the connection between offshore waters and the inner shelf is needed as it influences the productivity potential of valuable coastal rocky reefs. Near urban centres, artificial reefs enhance fishing opportunities in coastal waters, however these reefs are located without consideration of the productivity potential of adjacent waters. Here we identify three dominant modes of mesoscale circulation in the EAC separation region ($\sim$ 31.5 – 34.5°S); the 'EAC mode' which dominates the flow in the poleward direction, and two eddy modes, the 'EAC eddy mode' and the 'Eddy dipole mode', which are determined by the configuration of a cyclonic and anticyclonic eddy and the relationship with the separated EAC jet. We use a Lagrangian approach to reveal the transport pathways across the shelf to understand the impact of the mesoscale circulation modes and to explore the productivity potential of the coastal waters. We investigate the origin (position and depth) of the water that arrives at the inner-mid shelf over a 21-day period (the plankton productivity timescale). We show that the proportion of water that is upwelled from below the euphotic zone varies spatially, and with each mesoscale circulation mode. Additionally, shelf transport timescales and pathways are also impacted by the mesoscale circulation. The highest proportion of upwelling (70%) occurs upstream of 32.5°S, associated with the EAC jet separation, with vertical displacements of 70–120 m. From 33 to 33.5°S, water comes from offshore above the euphotic layer, and shelf transport timescales are longest. The region of highest retention over the inner shelf is immediately downstream of the EAC separation region. The position of the EAC jet and the location of the cyclonic eddy determines the variability in shelf-ocean interactions and the productivity of shelf waters. These results are useful for understanding productivity of temperate rocky reefs in general and specifically for fisheries enhancements along an increasingly urbanised coast.

Keywords: East Australian Current System, water transport pathways, Hawkesbury Shelf, Lagrangian particle tracking, Great Southern Reef, coastal productivity, cross-shelf exchange, eddies

OPEN ACCESS

Edited by:
William Savidge,
University of Georgia, United States

Reviewed by:
Pierrick Penven,
Institut de Recherche pour le Développement (IRD), France
Andrea Cucco,
National Research Council (CNR), Italy

***Correspondence:**
Moninya Roughan
mroughan@unsw.edu.au

Specialty section:
This article was submitted to Coastal Ocean Processes, a section of the journal Frontiers in Marine Science

Received: *05 October 2021*
Accepted: *06 December 2021*
Published: *07 January 2022*

Citation:
Roughan M, Cetina-Heredia P, Ribbat N and Suthers IM (2022) Shelf Transport Pathways Adjacent to the East Australian Current Reveal Sources of Productivity for Coastal Reefs. Front. Mar. Sci. 8:789687. doi: 10.3389/fmars.2021.789687

1. INTRODUCTION

Production on the continental shelf—and the proximity to ports and markets—is why more than 90% of the global fisheries catch is harvested from continental shelves (Pauly et al., 2002). Further inshore, the valuable coastal rocky reefs support a productive habitat which relies on the delivery of plankton to the reef (Holland et al., 2020). In particular, the delivery of zooplankton, is essential for fisheries production as zooplankton link primary production with higher trophic levels and fisheries (Marshak and Link, 2021).

Phytoplankton and zooplankton growth responds when deep nutrient rich water is uplifted (Brink, 2016) over timescales of 7–21 days (Mongin et al., 2011; Rocha et al., 2019). Zooplankton production advected from upstream of a coastal reef provides a food source for vast schools of small forage fish (Truong et al., 2017; Morais and Bellwood, 2019). The coastal reefs of southeastern Australia have great socio-economic value, but are experiencing environmental stress due to urbanisation and climate change (Bennett et al., 2015). Additionally, demands of growing coastal populations for fresh seafood have impacted the productivity of many coastal ecosystems Chou (1997). Therefore, understanding the physical oceanographic setting, including the source of water reaching the inner shelf and coastal reefs, the shelf transport pathways, residence times and their temporal variability is necessary for understanding the productivity and sustainability of temperate rocky reefs.

To enhance natural reef habitats and local fish stocks, artificial reefs are increasingly being deployed to promote ocean productivity, and increase recreational fishing opportunities for the adjacent urban populations (Champion et al., 2015; Keller et al., 2017). In 2011, Australia's first purpose designed coastal artificial reef was deployed off the coast of Sydney, Australia (33.9°S 151.3°E, **Figure 1**). By 2020, nine new clusters of designed reefs had been deployed along southeastern Australia. However, little consideration has been given to the oceanographic setting and the pathway of water to the reefs when choosing deployment locations.

The circulation along southeastern Australia is generally poleward (Godfrey et al., 1980) influenced by the East Australian Current (EAC) and its eddy field (**Figure 1**) downstream of its separation from the coast (31 − 32.5°S). It is thought that the narrowing of the shelf at Smoky Cape (31°S) and acceleration of the jet prior to separation drives upwelling (Oke and Middleton, 2001; Roughan and Middleton, 2002) that may contribute to productivity over the Hawkesbury Shelf. South of the EAC separation the Hawkesbury Shelf broadens, and the inner shelf circulation (from the coast to the 50 m isobath) is fairly coherent in the along shore (Ribbat et al., 2020b). Nevertheless, the influence of EAC jet drives a dominant along-shore (poleward) transport and the eddy field drives an intermittent cross-shelf transport and even northward flow facilitated by eddy dipoles (Archer et al., 2020; Malan et al., 2020; Ribbat et al., 2020b). Eddying in the region has been shown to be increasing (Li et al., 2021a,b). Thus, the origin of waters flowing across the shelf (e.g., inshore vs. offshore, shallow vs. deep) may be dictated by the mesoscale circulation.

The EAC and its eddies have been shown to influence plankton abundance and cross-shelf phytoplankton composition and distribution, (Armbrecht et al., 2014, 2015). Both modelling (Roughan et al., 2011; Cetina-Heredia et al., 2019a,b) and observational studies (Everett et al., 2015; Roughan et al., 2017)

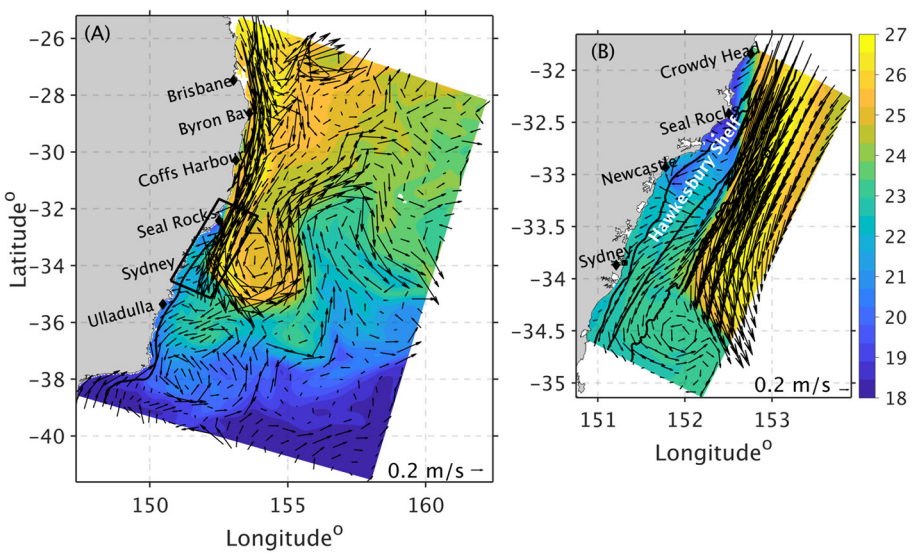

FIGURE 1 | Maps of sea surface temperature (°C) and surface velocity vectors along the east coast of Australia for 9th Jan 2013 shown in **(A)** the EAC-ROMS parent model domain described by Kerry et al. (2016), where the black rectangle shows the domain of the HSM model and the black solid line indicates the 2,000 m isobaths. **(B)** the HSM model domain described by Ribbat et al. (2020a,b) and the location of the Hawkesbury Shelf, black solid lines indicate the 100, 200, and 2,000 m isobaths. The black dot by the coast of Sydney indicates the position of the first coastal artificial reef (OAR).

have revealed the influence of the EAC and its eddies in the supply and/or export of plankton and larvae to or from the shelf. Hence understanding the shelf circulation and its variability is important for understanding delivery of nutrients and plankton to inner shelf waters and the distribution of zooplankton.

Lagrangian particle tracking driven by velocity outputs from a hydrodynamic ocean circulation model is a useful tool with which to investigate the transport pathways of water and particulates in space and time (e.g., Roughan et al., 2003, 2011; Cowen et al., 2006; Cetina-Heredia et al., 2019). Passive particles can be used to represent zooplankton (Roughan et al., 2005a; Cetina-Heredia et al., 2019b; Norrie et al., 2020), nutrients (e.g., Cetina-Heredia et al., 2018), kelp (e.g Coleman et al., 2011, 2013), watermasses (Roughan et al., 2003; Cetina-Heredia et al., 2014), oil (Paris et al., 2012) or other tracers in order to identify typical dispersal pathways (van Sebille et al., 2018) under present and future scenarios (e.g., Cetina-Heredia et al., 2015).

In this study we identify the dominant modes of circulation over the Hawkesbury Shelf offshore of the large Australian cities of Newcastle and Sydney and the Hawkesbury River (**Figure 1B**). We use Lagrangian particle tracking to identify the transport pathways of water flowing across the shelf. We quantify the water sources (position and depth) over a representative 2 year period (2012-2013) and explore the connection to mesoscale circulation of the EAC and its eddy field (section 3) during different circulation scenarios.

By revealing the oceanographic processes that determine the source of water 7–21 days prior to arrival at the inner shelf we aid understanding of the shelf productivity potential. In section 4 these results are placed in the context of coastal productivity, for both natural and artificial reefs. Our technique may be of benefit when selecting locations for placement of additional artificial reefs in the future for maximising biological productivity and efficiency.

2. METHODS

2.1. The Study Site

The study region is located on the continental shelf, between 31.5 and 34.5°S (**Figures 1A,B**) off southeastern Australia. The region is downstream of the typical EAC separation point (Cetina-Heredia et al., 2014; Ribbat et al., 2020b), it encompasses the productive Hawkesbury Bioregion and is offshore of Australia's largest city Sydney. A purpose built coastal artificial reef (named the OAR) is located 1.2 km off the coast of Sydney (33°50'S, 151°17.9'E; **Figure 1B**) in a water depth of 38 m. It is a 40 tonne steel structure that extends to within approximately 26 m of the surface (Champion et al., 2015), designed to increase fishing opportunities.

2.2. The Hawkesbury Shelf Hydrodynamic Model (HSM)

We use velocity outputs from a high-resolution configuration of the Regional Ocean Modelling System (ROMS, V3.4, www.myroms.org) for the Hawkesbury Shelf region. The model domain extends from 31.5 to 34.5°S off SE Australia (**Figure 1B**) and is referred to as the Hawkesbury Shelf Model (HSM) which is described fully in Ribbat et al. (2020a,b). The HSM has a spatial resolution of 750 m, a total of 197 x 477 grid cells, 30 vertical s-layers and 2 h velocity outputs. The HSM is nested inside a 2.5-6 km data assimilating reanalysis of the EAC System (Kerry et al., 2016, 2020), the parent model (EAC-ROMS, **Figure 1A**), and represents the circulation on the shelf for a 2 year period between January 1, 2012 and December 30, 2013. The use of data assimilation in the parent model ensures a realistic depiction of the mesoscale flow for the time period (Kerry et al., 2016, 2018), which makes it ideal for use as boundary conditions.

The nested HSM includes tidal forcing at the boundaries, which is important in coastal regions such as this. The high spatial resolution is needed to ensure that we can resolve the circulation variability over both the inner and outer shelf and to ensure that the bathymetry over the shelf is realistic. Freshwater inflow is generally negligible in this region (Kerry et al., 2016; Ribbat et al., 2020b) and hence has not been included. The full model configuration and validation is described in Ribbat et al. (2020b) who showed that it represents the circulation and temperatures over the shelf region when validated against moored and satellite observations of velocity and temperature.

2.3. Lagrangian Trajectories to Simulate Transport Pathways

We simulate the Lagrangian transport pathways across the shelf through Lagrangian particle trajectory modelling. Particles are seeded throughout the model domain, and are advected offline using the Connectivity Modelling System (CMS) (Paris et al., 2013). CMS uses a fourth order Runge-Kutta advection scheme based on the 3D velocity outputs obtained from the hydrodynamic model. CMS has been used successfully for a wide range of applications in the EAC region including to diagnose watermass transport (Cetina-Heredia et al., 2014, 2019), transport of lobster larvae (Cetina-Heredia et al., 2015, 2019b), and to investigate marine park connectivity (Coleman et al., 2017).

Velocity outputs from the HSM were converted from the ROMS s-grid to a regular z-level grid for compatibility with CMS using 62 vertical layers. A variable vertical resolution was used for the conversion to z-levels, with 2 m resolution in the upper 40 m, 10 m between 40 and 400 m and 100 m from 400 m to the bottom. This conversion is reasonable as the vertical de-correlation length scale has been shown to be 8 m in the region (Roughan et al., 2013, 2015) and our analysis is focused on shelf scales to depths of 200 m. In order to parameterize flow at scales finer than the HSM model (750 m) we use a horizontal diffusivity coefficient of 0.416 m^2 s^{-1} following Okubo (1971). Diffusion coefficients derived from Okubo (1971) have previously been used within CMS to parameterize the impact of flow at spatial scales smaller than modelled outputs along southeast Australia (Cetina-Heredia et al., 2014, 2015, 2019,b).

In order to explore the pathway and origin of the waters that flow across the shelf, particles were advected backwards in time from their release site and tracked for up to 21 days. By releasing particles along the coast over the shelf and tracking them backward in time, we are able to identify the origin (position

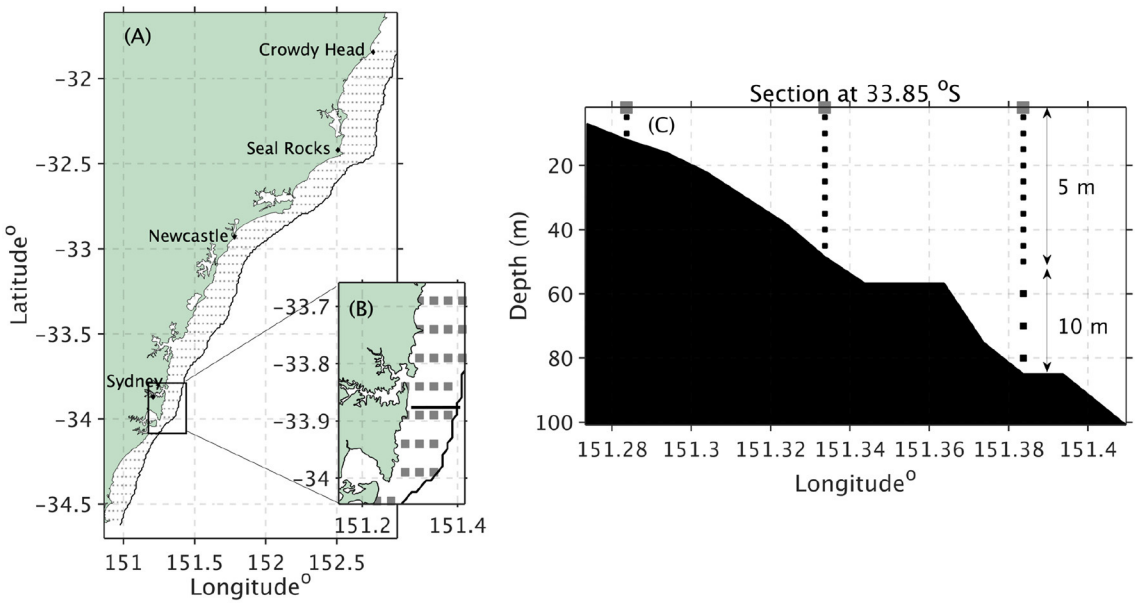

FIGURE 2 | Schematic diagram showing map of particle release locations. **(A)** Surface map of particle release sites along the HSM model domain. The grey squares show the release sites from the coast to the 100 m isobath. **(B)** Zoom in on the Sydney region to show the particle release positions and the location of the transect shown in **(C)**. **(C)** The depth structure of the releases across the inner shelf (black dots), particles are seeded every 5 m from the surface to 50 m, and 10 m from 50 to 100 m.

and depth) of water reaching the inner-mid shelf (0–100 m) and the water transport pathways across the shelf. Using these data we explore a) shelf regions that receive water from below the euphotic zone, b) shelf regions that receive upwelled water and the depth from which it was upwelled, and c) the amount of time that water spent travelling across the shelf where it can be depleted of plankton by feeding of fish and invertebrates. We also explore the impact of different circulation scenarios.

Particles were released throughout the model domain (31.5°S to 34.5°S), from the coastline to the 100 m isobath. The particles are released every 5th along-shore grid cell (3.75 km) and every 3rd across-shelf (2.25 km) grid cell, with a depth interval of every 5 m through the water column from the surface to 50 m and then every 10 m (50 m and deeper) as shown in **Figures 2A,B**. Particles were released at 2-h intervals over the 2 year period and tracked backwards for 21 days. To understand the pathway the particles took across the shelf and to quantify the uplift, the positions of all particles (i.e., latitude, longitude and depth) were recorded every 6 h for 21 days. We use particle tracking results from the full 2 year period, as well as results from three circulation case studies to explore the particle trajectories over the shelf. In each of the case studies we use the particle trajectories over a 21 day period, centred on the specific dates in **Figures 3G–I** (explained further in section 3.1).

3. RESULTS

3.1. Oceanographic Context

The results of the hydrodynamic model simulations show the currents and temperatures over the Hawkesbury Shelf (**Figure 3**). We compare the dominant modes of circulation variability in the HSM domain with satellite derived observations of geostrophic velocity from AVISO (over ∼ 25 years from 1994 – 2019). Three dominant circulation modes (calculated as empirical orthogonal functions) are shown in **Figures 3A–F**. We identify the first mode as the 'EAC mode' where the system is dominated by the poleward flowing EAC, representing 47.3% of the variance over the AVISO record and 53.8% of the variance over the 2012 – 2013 HSM period. The second is the 'EAC eddy mode' where the EAC separates in the north of our domain, and a cyclonic eddy is over the shelf (representing 20.1 and 12.4% of the variance in AVISO and HSM, respectively). The third mode is the 'Eddy dipole mode' where an anticyclone/cyclone eddy dipole lies downstream of the EAC separation (representing 13.4 and 10.5% of the variance, respectively). It is expected that there is some difference in the percentage variability explained by the long term AVISO observations and the 2 year HSM run. However, the first three modes identified in our 2 year period are representative of the typical circulation modes as shown. Hence we have confidence using the outputs of this model configuration to investigate cross shelf transport.

3.2. Circulation Case Studies

We use the circulation modes identified above to guide 3 case studies where we explore the impact of mesoscale circulation on the shelf water origin, depth and shelf transport pathways and timescales. A snapshot of the circulation representing each of the case studies is shown in **Figures 3G–I**. For the particle tracking case studies we use the particle trajectories over a 21 day period, centred on the snapshots shown.

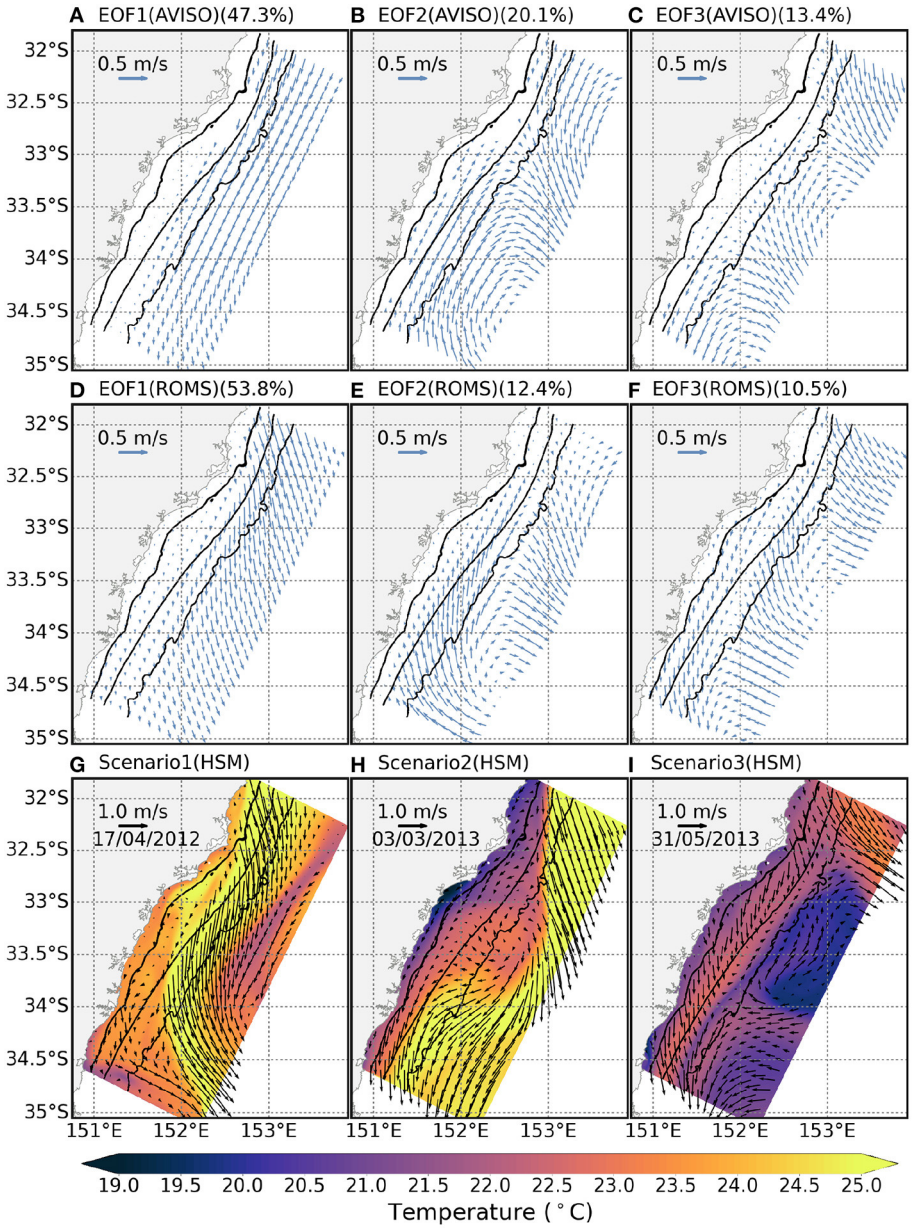

FIGURE 3 | (A–C) Empirical Orthogonal Functions (EOFs) of geostrophic velocity from AVISO, **(D–F)** EOFs from surface velocity from the HSM, percentage of variance explained by each mode is shown in the title. **(G–I)** Snapshots of surface currents and sea surface temperature for three dates as shown in the panels. Solid black lines show the 100, 200, and 2,000 m isobaths.

Figures 3G–I shows that velocities can reach a maximum of 1.5 m s^{-1} in the north of the domain in all three modes driven by the EAC jet. Flows are weaker in the southern half of the domain, and northward flow occurs associated with the position of a cyclonic eddy as seen in circulation mode 2 and mode 3 (**Figures 3D–F**). It is the position of the cyclonic eddy and its positioning with respect to the jet and the anticyclone that determine mode 2 (jet and cyclone) and mode three (jet, cyclone anticyclone) and therefore the direction of the coastal currents.

Snapshots of sea surface temperature (SST) during each of the case studies representing each of the three circulation modes are shown in **Figures 3G–I**. SST is warmest in the northern part of the model domain, under the influence of the poleward flowing EAC and along the inner shelf temperatures are lower. SST is a minimum when shelf waters are influenced by the cyclonic eddies in mode 2 and mode 3. The Eddy dipole case study is centred on a cyclonic eddy during late Autumn showing minimum temperatures of 19 — 20°C (**Figure 3I**).

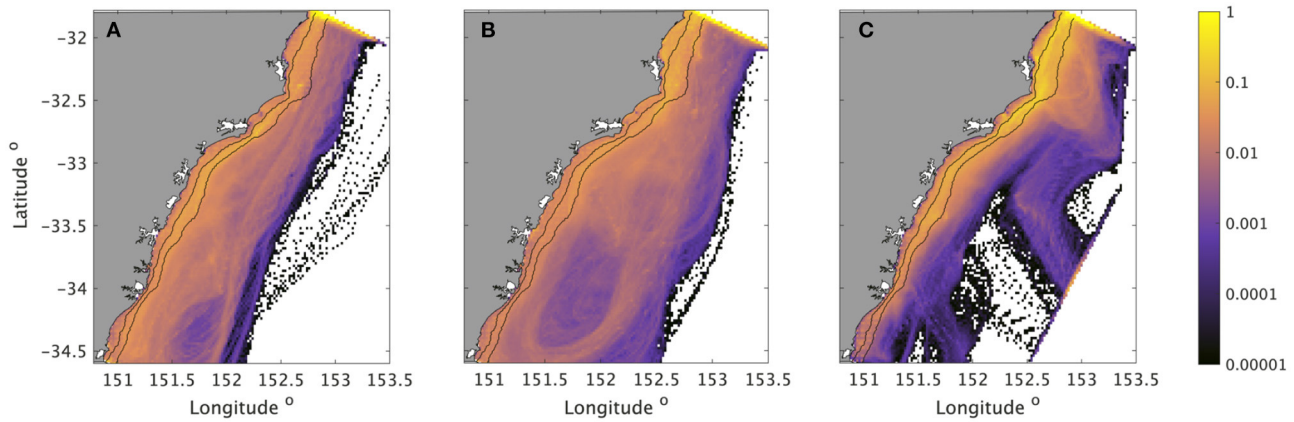

FIGURE 4 | Example shelf transport pathways from particles released by the coast and backtracked in time for up to 21 days illustrated through probability density maps (logarithmic scale as a percentage of particles released). Trajectories are shown for each of the three case studies representing the 3 circulation modes **(A)** EAC mode, **(B)** EAC eddy mode and **(C)** Eddy dipole mode. The black solid lines indicate the 50 and 100 m isobath, respectively.

3.3. Shelf Transport Pathways

Probability density maps were constructed using the backward trajectories from the Lagrangian simulations. These maps represent the probability that a particle will pass through a location over the given time period, and it is expressed as a percentage of the total number of particles released (Mitarai et al., 2009; Roughan et al., 2011). It follows that a high value indicates a greater percentage of particles crossing the grid cell over the specified time frame (Mitarai et al., 2009) and shows the likelihood that water has come from this region (Roughan et al., 2011). The variability in the shelf transport pathways is demonstrated in the probability density maps in **Figure 4** for each of our three case studies that represent the circulation modes: EAC (mode 1), EAC eddy (mode 2) and Eddy dipole (mode 3) as shown in **Figures 3G–I**.

3.4. Across-Shelf Distribution and Source of Inner Shelf Waters

Knowing the source of inner shelf waters gives an indication of productivity potential. The horizontal position (latitude, longitude, depth) of each particle is recorded along their backward trajectory across the shelf and is classified as inshore (coast-50 m), mid-shelf (50–100 m) or offshore (100 m or deeper) based on the water depth along the trajectory. Using all the release data, the percentage of particles found in each of the shelf regions is then determined at 7, 14, and 21 days prior to reaching the coast to give an indication of which section of the shelf particles were sourced. We show the position at origin (by percentage) of particles that arrive between the coast and the 100 m isobath in **Figure 5** using release data for the entire 2 years.

Results reveal that the vast majority of particles that arrive at the coast (60 − 80%) were sourced from the inner shelf over the 3 timescales (7, 14, and 21 days, shown in **Figures 5A–C**, respectively as yellow) from 31.8 − 33.8°S. For waters arriving offshore of the 50 m isobath (**Figure 5D**) ∼ 50% were sourced from the mid-shelf in the 7 day time frame, with offshore sources (60 − 70%) for waters that arrive between 33 and 33.5°S over 14–21 days (**Figures 5H,I**).

3.5. Time Spent Across the Shelf

We explore the time that particles spent over different parts of the shelf (inner shelf, mid-shelf, offshore) which helps us understand the productivity potential as predation is more likely to occur in shallow waters, i.e., over inner shelf rocky reef environments than in offshore waters or at depth and over longer timescales. We assess the impact of the different mesoscale circulation modes on the time particles spent in the 3 across-shelf regions in each of our 3 circulation scenarios (**Figures 3G–I**). The number of days a particle spent within each across-shelf region (inshore, mid-shelf and offshore) over the preceding 21 days was counted and is shown in **Figure 6** for each of the circulation case studies that represent the EAC (mode 1), EAC Eddy (mode 2) and Eddy dipole (mode 3).

For the EAC and EAC eddy modes, water reaching the shelf north of 33 and 32°S, respectively, spent most time mid-shelf; polewards of these latitudes, water spent most of the time offshore before being brought onshore. In contrast, for the Eddy dipole mode, water spent most time in the mid-shelf throughout the domain indicating the influence of the dipole on retention. For all 3 modes, the water spent a short time over the inner shelf (3 − 6 days), with the longest timescales in the dipole mode.

Using all particles released over the 21 days of each case study, we calculated the time taken for the particles to reach the boundary along its backwards trajectory. This gives an estimate of time spent in the domain. For the three circulation mode case studies we get mean residence times of 10 ± 7.5, 12 ± 8.8 and 13±7.5 days, with 69, 63, and 76% of particles leaving the domain, respectively. This means that in the Eddy dipole mode (3), water is retained for up to 3 days longer on the shelf, and that in the EAC eddy mode (2) the most number of particles are retained.

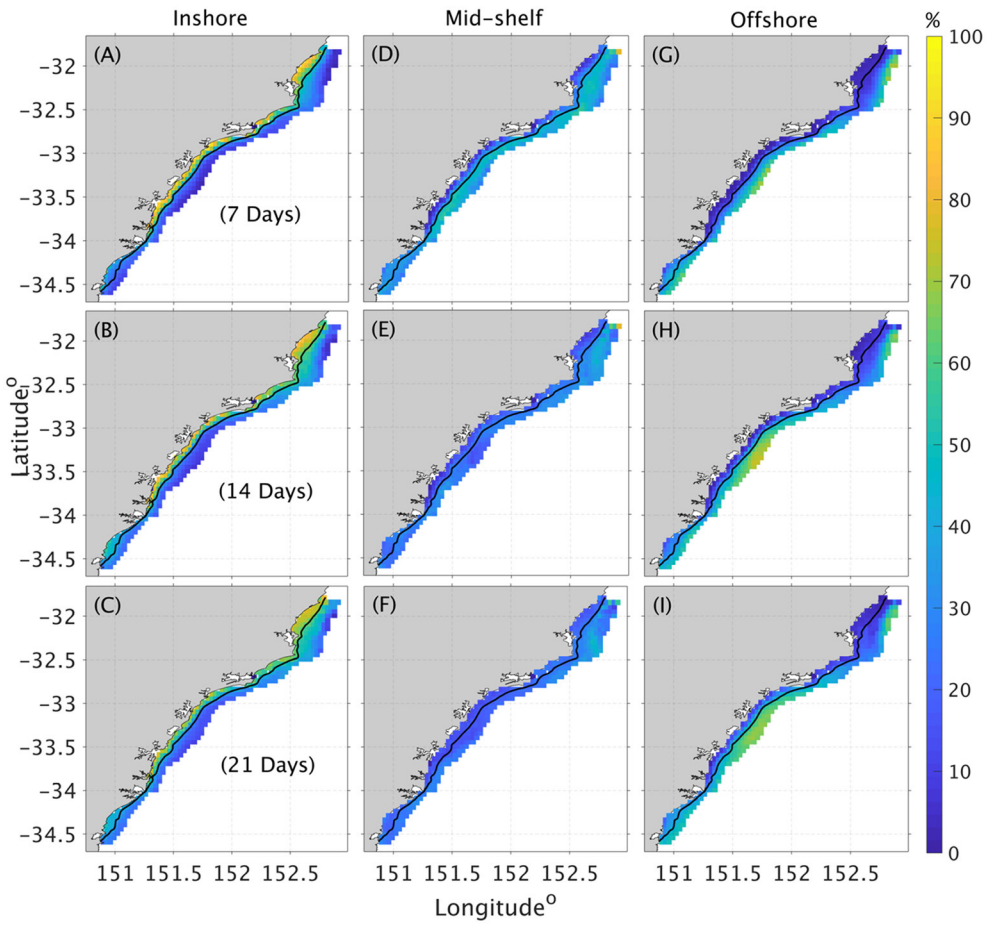

FIGURE 5 | Percentage of simulated particles arriving at each grid cell along the coastal (for particles released between the coast and the 100 m isobath) that come from: **(A–C)**, inner shelf region (0–50 m); **(D–F)** mid-shelf region (50–100 m) and **(G–I)** offshore region (>100 m) from 7, 14, and 21 days prior (top to bottom). The black solid line shows the 50 m isobath.

3.6. Vertical Distribution of Source Waters That Reach the Inner Shelf

Investigating the depth of the source waters that reach the inner shelf region allows us to further understand the potential productivity of the water flowing across the shelf and to identify regions more likely to receive upwelled water (with potential for higher nutrient concentration). Using trajectories of all releases adjacent to the coastline, depths recorded 21 days prior to the release date were used to identify the depth range (in intervals of 10 m) where waters that arrived at the inner shelf originated (**Figure 7**).

The histograms for all particle trajectories over the 2 year period show the proportion of upwelled waters (**Figure 7**). Overwhelmingly, the majority of the water that arrives at the coast originates at depths of 0–20 m over 7, 14, and 21 days. Some upwelled waters arrive at the coast from depths greater than 60 m in the northern and southern extents of the model domain, more so on the 7 day timescale. In the middle of the domain, from 32 to 34°S upwelling is less prevalent.

3.7. Impact of Mesoscale Circulation on Vertical Distribution of Source Waters

For each of our 3 circulation case studies we quantify the proportion of water that comes from depths below the euphotic layer 21 days prior (**Figures 8A–C**), considered to be ∼ 50 m in this region (Rocha et al., 2019). Using trajectories of releases adjacent to the seafloor, we compare the coastal release depth (final position) and the depth 21 days before (source depth), to discern if water was upwelled or downwelled (**Figures 8D–F**). We then explore the vertical displacement averaged across all particles that were upwelled (**Figures 8G–I**).

During the EAC scenario (mode 1), when the poleward alongshore flow is strong, waters are sourced from below the euphotic depth (**Figures 8A,D,G**), upwelling is persistent the length of the study area and across the mid and outer shelf. Vertical displacements are a maximum (80 – 120 m) in the southern part of the domain (from 33.5 to 34.5°S).

During the EAC eddy scenario (mode 2, **Figures 8B,E,H**) only 20–30% of the waters are from below the euphotic depth,

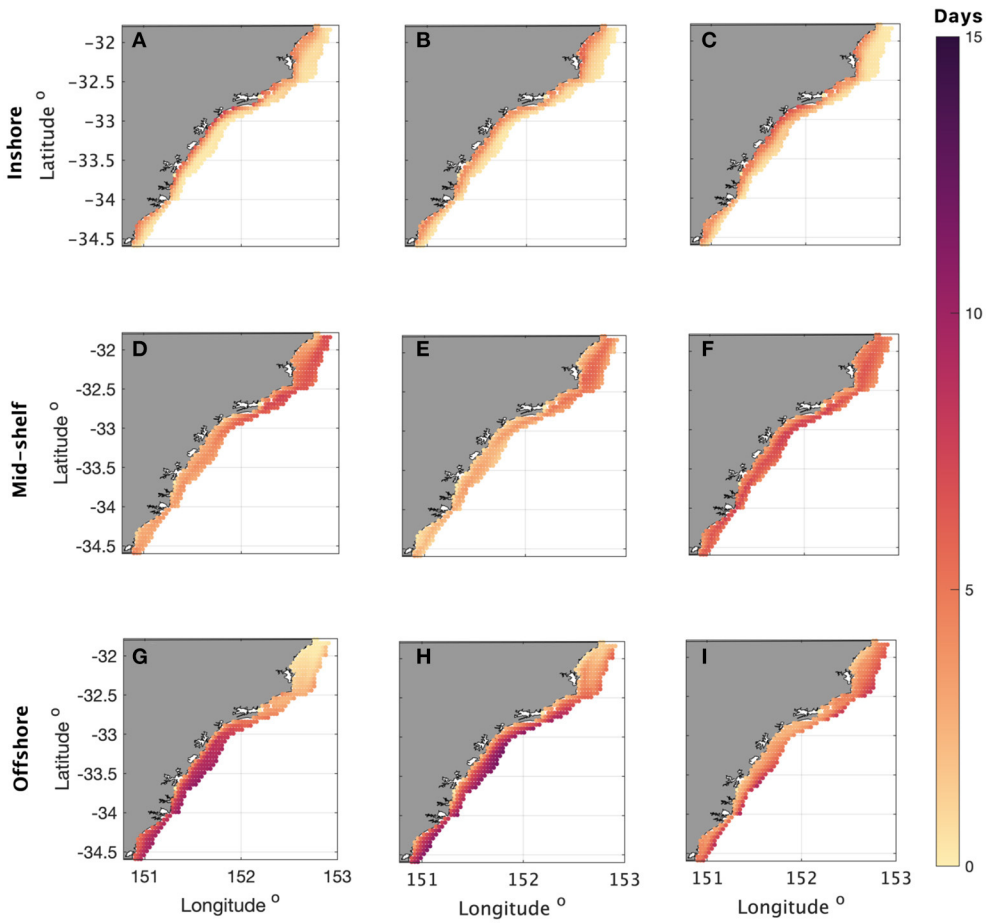

FIGURE 6 | Quantification of the number of days the water spent in each region across the shelf before arriving at the coast. i.e., the time spent inshore—between the coast and the 50 m isobath **(A–C)**, over the mid-shelf, between the 50 and 100 m isobaths **(D–F)**, and offshore, between the 100 m isobath and deeper **(G–I)**, shown for each of the three case studies representing the 3 circulation modes ('EAC mode', 'EAC eddy mode', and 'Eddy dipole mode', respectively left to right). The number of days shown for each grid cell was computed as an average across all the particles released at each coastal grid cell.

although across the mid-outer shelf, much of the bottom waters are sourced from below, with vertical displacements of 40–60 m. In the EAC dipole scenario, waters come from below the euphotic depth least often, but waters that are upwelled involve displacements of over 80 m and maximum displacements occur in the northern region of our study area, between 32° and 32.5°S (**Figures 8C,F,J**).

3.8. Distance Travelled

We explore the linear distance (L) travelled by the water parcels i.e., the distance between the release location and the particle's position 7, 14, and 21 days before. Similarly, we measured the distance along the backward water trajectory (T) of each water parcel (particle). The distances were grouped in 30 km bins to show how far a watermass has travelled in the preceding days. Additionally, the ratio between the linear and along-trajectory distance (L/T) was computed to compare how direct the trajectories were; a value of one implies the trajectory was straight, whereas a lower value shows the parcel trajectory was more convoluted or eddying (**Figure 9**). For this analysis we use particles released at the location of Sydney's coastal artificial reef (OAR) as shown in **Figure 7** in the southern end of our domain.

Over 7 days prior to reaching the OAR, the linear distance to the source ranges 30–60 km, and over 21 days the distance ranges 90–120 km (**Figure 9A**). By following the watermass along its trajectory, we observe that the distances actually travelled are more than 50% higher with the majority of particles covering a distance between 180 and 240 km over the 21 days prior to reaching the OAR, with the longest particle paths exceeding 450 km (**Figure 9B**). Interestingly a small percentage of particles that arrived at the inner shelf OAR site travelled up to 600 km. Over the 21 days only 11% of the particles have a linear to along-trajectory distance (L/T) ratio between 0.75 and 1, (vs. 40% over 7 days, **Figure 9C**). This ratio indicates that the longer a parcel is tracked, the more convoluted the path travelled to arrive at the coast, and can indicate increased retention over the shelf.

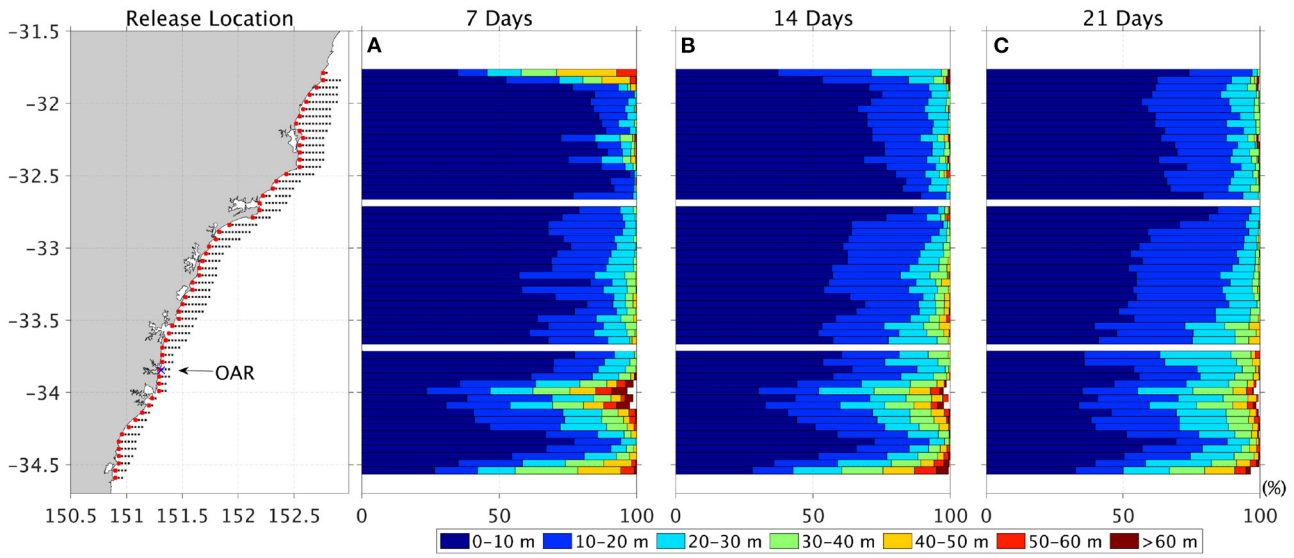

FIGURE 7 | Histograms (by latitude) showing the depth that the waters came from as a percentage of the total. The colors indicate the depth ranges from which the water particles came **(A)** 7, **(B)** 14, and **(C)** 21 days prior to the release date, arriving at the red dots at the coast.

4. DISCUSSION

The origin and transport pathways of water flowing across the inner-mid shelf of the Hawkesbury Bioregion off SE Australia was examined from Lagrangian backtracking simulations to reveal the connection between mesoscale circulation and shelf transport. These trajectories showed dispersal patterns and sources of water parcels reaching the inner-mid shelf, which differed under three different mesoscale circulation patterns. We explore the shelf transport pathways the depth of origin and relationship to upwelling in order to understand the likely productivity of waters flowing across the inner-mid shelf. Here we place the results in the context of water arriving at coastal rocky reefs and Sydney's first coastal artificial reef and discuss possibilities for future positioning of purpose built coastal reefs.

4.1. Impact of Mesoscale Circulation on Shelf Transport Pathways

The EAC varies on 90 – 110 day timescales, associated with mesoscale eddy shedding and a retraction in the EAC separation latitude (Cetina-Heredia et al., 2014). In this region, the mesoscale circulation is characterised by 3 modes, the 'EAC mode', 'EAC eddy mode', and 'Eddy dipole mode', as exemplified in **Figure 3**. These modes were depicted in the schematic diagram of Ribbat et al. (2020b) based on just 2 years of data. However, the similarity between the 3 modes calculated from long term AVISO observations and those from our HSM model **Figure 3**) give confidence in the robustness of the modes, and the use of the model snapshots to explore each of the three scenarios.

These mesoscale dynamics dominate the circulation over the mid-outer shelf, and in the north of the domain which is mostly upstream of the EAC separation. This is consistent with the results of Wood et al. (2016) who showed that the EAC and its eddies drive the outer shelf circulation (**Figure 3**). Our results show that this has an impact on the cross shelf trajectories and water transport pathways (**Figure 4**). When the circulation is Mode 1 (EAC mode), the EAC is strong poleward along the outer shelf, flow is from the north, and eddy impacts are a minimum. Across the inner shelf the water is sourced from the inshore and upstream (**Figures 3**, **4**) particularly on short time scales.

When the EAC separates in the north of the domain (Eddy mode or Eddy dipole mode) water transport pathways are more variable across the shelf and water was sourced from offshore as well as along shore (**Figure 4**). Consistent with the sourcing of waters from offshore in this region, Ribbat et al. (2020b) showed that onshore transport was maximum at about 34°S, during this period. Vertical displacement is also a maximum during EAC transport (mode 1) (**Figure 8C**). These results show that the position of the EAC jet and the location of the cyclonic eddy determines the variability in shelf-ocean interactions in each of these scenarios which has potential to drive the productivity of shelf waters.

4.2. Upwelling and Shelf Transit Timescales

The region that extends from 32 – 32.5°S is a known region of upwelling, driven by the acceleration of the EAC jet and its separation from the coast (Roughan and Middleton, 2002, 2004). An example of this is observed in the snapshot of sea surface temperature and velocity as shown in **Figure 1** and our mode 1 case study (**Figures 3D,G**). From 32 – 32.5°S is the only region in our model domain that consistently receives water from below the euphotic depth over the 2 year period. Ribbat et al. (2020b) showed that during this period, the EAC separated from the coast between 32.5 and 33.5°S up to 70% of the time. This means that

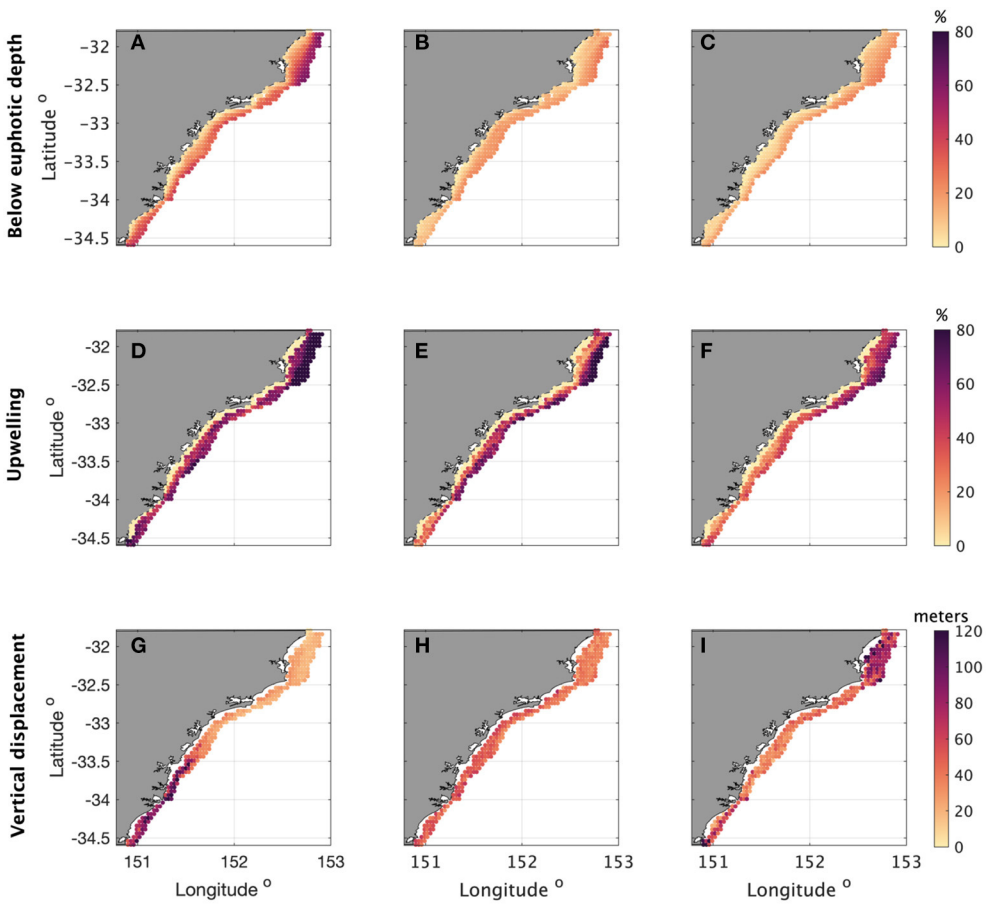

FIGURE 8 | Proportion of water that comes from (below the euphotic depth) **(A–C)**; the proportion of water that was upwelled **(D–F)**; and the mean vertical displacement (meters) of water parcels that were upwelled **(G–I)** for the three case studies, 'EAC mode' (left), 'EAC eddy mode' (middle), and 'Eddy dipole mode' (right) columns. The proportion of water below the euphotic depth was computed across particles released throughout the water column. The proportion of water that was upwelled was computed only considering the trajectories of particles that were released close to the sea floor.

for much of the simulation, the shelf region from 32 to 32.5°S was considered inshore and upstream of separation. Upwelling in this region is consistent with the results of Schaeffer et al. (2014) who showed that onshore transport in the bottom boundary layer was more intense and frequent upstream of separation than downstream.

From 33 – 33.5°S we show that water comes from offshore (e.g., **Figures 5G–I**), but from above the euphotic layer (**Figures 8A,D,G**) with vertical displacements ranging 10 – 30 m. In this region onshore transport is associated with EAC eddy dipoles (Malan et al., 2020, 2021), which occur regularly in the region. Our results suggest that while onshore transport occurs, waters are not upwelled from depths greater than 50 m. Interestingly however in this region, retention and shelf transit times are longer (**Figures 6B,E,H**) with the mid-shelf having the longest transport pathways of the entire domain. This could help increase the productivity of the region by retaining plankton over the shelf. The transport pathway ratios L/T show the convoluted path that a water parcel could to reach the inner shelf, indicative of increased residence time over the shelf (**Figure 9**). This is important, as in an advection dominated regime some degree of shelf retention is needed for phytoplankton blooms to occur (Roughan et al., 2005b).

The Stockton Bight region immediately downstream of the EAC separation (32.25 – 33.25°S) has been shown to be more productive than other sections of the shelf, at times containing more than 20% of the total shelf chlorophyll (Everett et al., 2014). However, the relationship between EAC circulation modes, water mass variability and chlorophyll concentrations on the shelf is not yet clear. Repeat glider missions collecting hydrographic data through the domain (supported by Australia's Integrated Marine Observing System Roughan et al., 2015; Schaeffer et al., 2016a,b) provide the ideal dataset with which to explore drivers of chlorophyll variability in the EAC separation zone in the future.

4.3. Productivity of Coastal Reefs

The transport and upwelling processes described in our study are a key contributor to the persistent coastal fringe of phytoplankton, referred to on other coasts as the 'green ribbon' (Lucas et al., 2011). This is especially evident inshore of the EAC

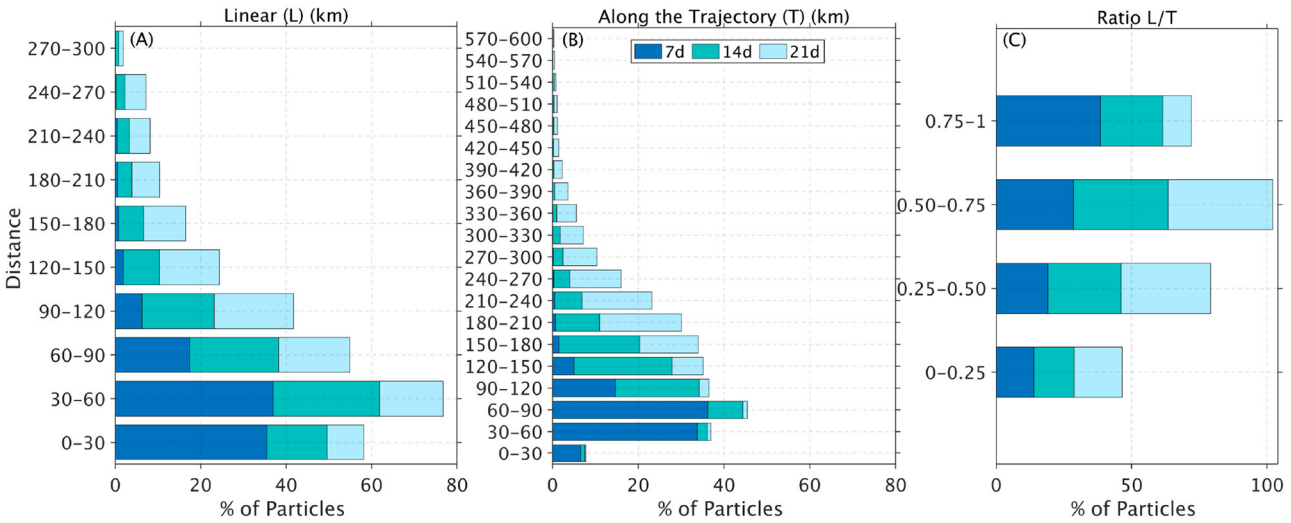

FIGURE 9 | Distance travelled by particles that arrive at the coastal artificial reef (OAR), where particles were back-tracked over 7, 14, and 21 days, presented as a percentage (stacked histogram), showing **(A)** the linear distance (L) from the start to the end point at each time period, **(B)** the total along-trajectory distance (T) travelled by the particle, and **(C)** the ratio between Linear and Trajectory distance L/T for each time period, where a ratio of 1 shows the particle travelled in a straight line. The location of the OAR is shown in **Figure 7**.

separation zone at the northern sector of our domain, which sustains the economically important Hawkesbury Bioregion. This region is exceptionally productive in phytoplankton (Everett et al., 2014) and is the predominant region for eddy formation (Cetina-Heredia et al., 2014; Ribbat et al., 2020b) as well as onshore transport Cetina-Heredia et al. (2019b), Malan et al. (2020). The region therefore benefits from the major EAC / eddy separation processes (Oke and Middleton, 2001; Roughan and Middleton, 2002), delivering nutrients to where the shelf widens to its furthest extent for southeastern Australia. Together, these processes not only underpin the coastal fisheries for this highly urbanised coastline (Holland et al., 2020), but it is known to be a white shark nursery area (Lee et al., 2021). The coastal reefs in this region are part of the Great Southern Reef which refers to Australia's 8000 km coastline of temperate rocky reef, from southern Queensland to Western Australia (Bennett et al., 2015). The associated kelp forest and other macroalgae are highly productive and sustain these valuable ecosystems for a quarter of Australia's population.

The kelp forests and macroalgae are however, only part of the reason for region's productivity. The majority of fish biomass on the valuable temperate reefs in the region is not only based on macroalgae, but on the supply of zooplankton (Truong et al., 2017; Holland et al., 2020). A similarly important process is recognised on tropical coral reefs, referred to as a pelagic subsidy (Morais and Bellwood, 2019). In the case of coastal reefs along southeastern Australia, the phytoplankton which sustains benthic filter feeders (such as sponges, oysters and ascidians) is produced over the previous 7–14 days over the water transport pathway. We determined that the production of zooplankton over the previous 21 days is mostly sourced from 30 to 100 km north. The majority of this production is maintained along the inner shelf, such that schools of small forage fish along the inner shelf may have the potential to reduce zooplankton densities if cross-shelf flows are infrequent.

4.4. Placement of Artificial Reefs

Artificial reefs are often placed within close proximity to the coast to enhance accessibility for both construction logistics, and recreational fishing opportunities (Chou, 1997; Champion et al., 2015). For example, proximity to a population centre with an easy transit to a safe harbour will enhance use by the recreational fishing community. Additionally, local morphological and habitat features may also enhance productivity. Hence, artificial reefs are also often placed in the vicinity of natural reefs (Champion et al., 2015) to aid recruitment and improve connectivity between reefs.

An important factor influencing the productivity of an artificial reef however is the supply of zooplankton for small forage fish, which attract larger fish of interest to the recreational fishing industry (Champion et al., 2015). The likelihood for water to contain zooplankton and nutrients when flowing over an artificial reef can vary depending on its source region and trajectory. Our results show that the Sydney OAR (see **Figure 1B** for location) broadly receives waters from the inner shelf, directly upstream, and that upwelling across this reef is limited, especially when compared to other sites along the shelf. If the reef was located over the mid-shelf region, or further to the south, the productivity potential would likely be increased.

If reefs were to be deployed in upwelling regions, our results suggest reefs should be located in the north of the domain, e.g., from 32 to 32.5°S, although this would not allow sufficient time for zooplankton production. Furthermore, the longer retention times between 33 and 33.5°S mid-shelf are more

suited for retention of zooplankton production, while between 34 and 34.5°S regions close to the coast receive upwelled waters from offshore.

This work is a first step towards understanding Lagrangian transport pathways and timescales across the Hawkesbury Shelf and shows the influence of the mesoscale circulation, which in turn can impact coastal reef productivity. Understanding the spatial and temporal patterns of primary and secondary productivity (phytoplankton and smaller zooplankton) as well as the quantification of the flux of zooplankton in shelf waters will aid future reef placements. Ultimately, a better understanding of zooplankton abundance and delivery to natural and artificial reefs would be beneficial in order to estimate the sustainability of the on-going deployments of artificial reefs.

While socio-economic arguments and proximity to natural reefs and habitat are important when considering the placement of coastal artificial reefs, our results show that knowledge of the predominant shelf transport pathways and upwelling characteristics are also important considerations due to their impact on the productivity potential of the reef. Our findings have implications for the ecosystem basis for other socio-economically valuable temperate reefs adjacent to other western boundary currents, such as off eastern Japan, eastern Florida, and the Natal coast.

DATA AVAILABILITY STATEMENT

The datasets presented in this study can be found in online repositories. The names of the repository/repositories and accession number(s) can be found below: The Hawkesbury Shelf model output used in this study can be found at the Research Data Australia repository at https://doi.org/10.26190/5ec35ca34752e and should be cited as Ribbat et al. (2020a). Satellite data used in **Figure 3** was obtained from https://resources.marine.copernicus.eu/?option=com_csw&view=details&product_id=SEALEVEL_GLO_PHY_L4_REP_OBSERVATIONS_403008_047.

AUTHOR CONTRIBUTIONS

MR and IS conceived the study and developed the conceptual framework, and obtained the funding. NR and PC-H conducted the model runs and generated the figures. PC-H and MR led the analysis. All authors contributed to interpreting the results, writing and editing the manuscript.

FUNDING

NR was partially supported by an Australian Research Council Industry Linkage Project LP120100592 to IS and MR. The EAC-ROMS model development was supported by an Australian Research Council Discovery Project DP140102337 to MR. NR received a tuition fee scholarship from UNSW Sydney.

ACKNOWLEDGMENTS

This research was undertaken with the assistance of resources and services from the National Computational Infrastructure (NCI), which is supported by the Australian Government. This research also includes computations using the computational cluster Katana supported by Research Technology Services at UNSW Sydney. We acknowledge C. Kerry, B. Powell, and S. Rao for assistance with earlier model development, J. Smith for discussions on the OAR and J. Li for AVISO data in **Figure 3**.

REFERENCES

Archer, M., Schaeffer, A., Keating, S., Roughan, M., Holmes, R., and Siegelman, L. (2020). Observations of submesoscale variability and frontal subduction within the mesoscale eddy field of the Tasman Sea. *J. Phys. Oceanogr.* 50, 1509–1529. doi: 10.1175/JPO-D-19-0131.1

Armbrecht, L. H., Roughan, M., Rossi, V., Schaeffer, A., Davies, P. L., Waite, A. M., et al. (2014). Phytoplankton composition under contrasting oceanographic conditions: upwelling and downwelling (Eastern Australia). *Cont. Shelf Res.* 75, 54–67. doi: 10.1016/j.csr.2013.11.024

Armbrecht, L. H., Schaeffeer, A., Roughan, M., and Armand, L. K. (2015). Interactions between seasonality and oceanic forcing drive the phytoplankton variability in the tropical-temperate transition zone (30° S) of Eastern Australia. *J. Mar. Syst.* 144, 92–106. doi: 10.1016/j.jmarsys.2014.11.008

Bennett, S., Wernberg, T., Connell, S. D., Hobday, A. J., Johnson, C. R., and Poloczanska, E. S. (2015). The "Great Southern Reef": social, ecological and economic value of Australia's neglected kelp forests. *Mar. Freshwater Res.* 67, 47–56. doi: 10.1071/MF15232

Brink, K. (2016). Cross-shelf exchange. *Ann. Rev. Mar. Sci.* 8, 59–78. doi: 10.1146/annurev-marine-010814-015717

Cetina-Heredia, P., Roughan, M., Liggins, G., Coleman, M. A., and Jeffs, A. (2019a). Correction: Mesoscale circulation determines broad spatio-temporal settlement patterns of lobster *PLoS ONE.* 14:2 (e02214996). doi: 10.1371/journal.pone.0214996

Cetina-Heredia, P., Roughan, M., Liggins, G., Coleman, M. A., and Jeffs, A. (2019b). Mesoscale circulation determines broad spatio-temporal settlement patterns of lobster. P*LoS ONE.* 14:e0211722. doi: 10.1371/journal.pone.0211722

Cetina-Heredia, P., Roughan, M., Sebille, E., Keating, S., and Brassington, G. B. (2019). Retention and leakage of water by mesoscale eddies in the East Australian Current System. *J. Geophys. Res. Oceans* 124, 2485–2500. doi: 10.1029/2018JC014482

Cetina-Heredia, P., Roughan, M., van Sebille, E., and Coleman, M. A. (2014). Long-term trends in the East Australian Current separation latitude and eddy driven transport. *J. Geophys. Res. Oceans* 119, 4351–4366. doi: 10.1002/2014JC010071

Cetina-Heredia, P., Roughan, M., Van Sebille, E., Feng, M., and Coleman, M. A. (2015). Strengthened currents override the effect of warming on lobster larval dispersal and survival. *Glob. Chang Biol.* 21, 4377–4386. doi: 10.1111/gcb.13063

Cetina-Heredia, P., van Sebille, E., Matear, R. J., and Roughan, M. (2018). Nitrate sources, supply, and phytoplankton growth in the Great Australian Bight: an eulerian-lagrangian modeling approach. *J. Geophys. Res. Oceans* 123, 759–772. doi: 10.1002/2017JC013542

Champion, C., Suthers, I. M., and Smith, J. A. (2015). Zooplanktivory is a key process for fish production on a coastal artificial reef. *Mar. Ecol. Prog. Ser.* 541, 1–14. doi: 10.3354/meps11529

Chou, L. M. (1997). Artificial reefs of Southeast Asia-do they enhance or degrade the marine environment? *Environ. Monit. Assess* 44, 45–52. doi: 10.1023/A:1005759818050

Coleman, M. A., Cetina-Heredia, P., Roughan, M., Feng, M., van Sebille, E., and Kelaher, B. P. (2017). Anticipating changes to future connectivity within a network of marine protected areas. *Glob. Chang Biol*. 23, 3533–3542. doi: 10.1111/gcb.13634

Coleman, M. A., Feng, M., Roughan, M., Cetina-Heredia, P., and Connell, S. D. (2013). Temperate shelf water dispersal by Australian boundary currents: implications for population connectivity. *Limnol. Oceanogr. Fluids Environ*. 3, 295–309. doi: 10.1215/21573689-2409306

Coleman, M. A., Roughan, M., Macdonald, H. S., Connell, S. D., Gillanders, B. M., Kelaher, B. P., et al. (2011). Variation in the strength of continental boundary currents determines continent-wide connectivity in kelp. *J. Ecol*. 99, 1026–1032. doi: 10.1111/j.1365-2745.2011.01822.x

Cowen, R. K., Paris, C. B., and Srinivasan, A. (2006). Scaling of connectivity in marine populations. *Science* 311, 522–527. doi: 10.1126/science.1122039

Everett, J. D., Baird, M. E., Roughan, M., Suthers, I. M., and Doblin, M. A. (2014). Relative impact of seasonal and oceanographic drivers on surface chlorophyll a along a Western Boundary Current. *Prog. Oceanogr*. 120, 340–351. doi: 10.1016/j.pocean.2013.10.016

Everett, J. D., Macdonald, H., Baird, M. E., Humphries, J., Roughan, M., and Suthers, I. M. (2015). Cyclonic entrainment of preconditioned shelf waters into a frontal eddy. *J. Geophys. Res. Oceans* 120, 677–691. doi: 10.1002/2014JC010301

Godfrey, J., Cresswell, G., Golding, T., Pearce, A., and Boyd, R. (1980). The separation of the East Australian Current. *J. Phys. Oceanogr*. 10, 430–440. doi: 10.1175/1520-0485(1980)010andlt;0430:TSOTEAandgt;2.0.CO;2

Holland, M. M., Smith, J. A., Everett, J. D., Vergés, A., and Suthers, I. M. (2020). Latitudinal patterns in trophic structure of temperate reef-associated fishes and predicted consequences of climate change. *Fish Fish*. 21, 1092–1108. doi: 10.1111/faf.12488

Keller, K., Steffe, A. S., Lowry, M. B., Murphy, J. J., Smith, J. A., and Suthers, I. M. (2017). Estimating the recreational harvest of fish from a nearshore designed artificial reef using a pragmatic approach. *Fish Res*. 187, 158–167. doi: 10.1016/j.fishres.2016.11.022

Kerry, C., Powell, B., Roughan, M., and Oke, P. (2016). Development and evaluation of a high-resolution reanalysis of the East Australian Current region using the regional ocean modelling system (ROMS 3.4) and incremental strong-constraint 4-dimensional variational (IS4D-Var) data assimilation. *Geosci. Model Dev*. 9, 3779–3801. doi: 10.5194/gmd-9-3779-2016

Kerry, C., Roughan, M., and Powell, B. (2018). Observation impact in a regional reanalysis of the East Australian Current System. *J. Geophys. Res. Oceans* 123, 7511–7528. doi: 10.1029/2017JC013685

Kerry, C., Roughan, M., Powell, B., and Oke, P. (2020). A high-resolution reanalysis of the East Australian Current System assimilating an unprecedented observational data set using 4D-Var data assimilation over a two-year period (2012-2013). Version 2017. UNSW.dataset, Sydney doi: 10.26190/5ebe1f389dd87

Lee, K. A., Butcher, P. A., Harcourt, R. G., Patterson, T., Peddemors, V. M., Roughan, M., et al. (2021). Oceanographic conditions associated with white shark (*Carcharodon carcharias*) habitat use along eastern Australia. *Mar. Ecol. Prog. Ser*. 659, 143–159. doi: 10.3354/meps13572

Li, J., Roughan, M., and Kerry, C. (2021a). Dynamics of interannual eddy kinetic energy modulations in a Western Boundary Current. *Geophys. Res. Lett*. 48:e2021GL094115. doi: 10.1029/2021GL094115

Li, J., Roughan, M., and Kerry, C. (2021b). Variability and drivers of ocean temperature extremes in a warming western boundary current. *J. Clim*. 1–10. doi: 10.1175/JCLI-D-21-0622.1

Lucas, A. J., Dupont, C. L., Tai, V., Largier, J. L., Palenik, B., and Franks, P. J. S. (2011). The green ribbon: Multiscale physical control of phytoplankton productivity and community structure over a narrow continental shelf. *Limnol. Oceanogr*. 56, 611–626. doi: 10.4319/lo.2011.56.2.0611

Malan, N., Archer, M., Roughan, M., Cetina-Heredia, P., Hemming, M., Rocha, C., et al. (2020). Eddy-driven cross-shelf transport in the East Australian Current separation zone. *J. Geophys. Res. Oceans* 125:e2019JC015613. doi: 10.1029/2019JC015613

Malan, N., Roughan, M., Stanley, G. J., Holmes, R. M., and Li, J. (2021). Quantifying cross-shelf transport in the East Australian Current system: a budget- based approach. *J. Phys. Oceanogr*. [Epub ahead of print].

Marshak, A. R., and Link, J. S. (2021). Primary production ultimately limits fisheries economic performance. *Sci. Rep*. 11, 12154. doi: 10.1038/s41598-021-91599-0

Mitarai, S., Siegel, D. A., Watson, J. R., Dong, C., and McWilliams, J. C. (2009). Quantifying connectivity in the coastal ocean with application to the southern Californian Bight. *J. Geophys. Res*. 114:C10026. doi: 10.1029/2008JC005166

Mongin, M., Matear, R., and Chamberlain, M. (2011). Seasonal and spatial variability of remotely sensed chlorophyll and physical fields in the saz-sense region. *Deep Sea Res. Part II Top. Stud. Oceanogr*. 58, 2082–2093. doi: 10.1016/j.dsr2.2011.06.002

Morais, R. A., and Bellwood, D. R. (2019). Pelagic subsidies underpin fish productivity on a degraded coral reef. *Curr. Biol*. 29, 1521.e6–1527.e6. doi: 10.1016/j.cub.2019.03.044

Norrie, C., Dunphy, B., Roughan, M., Weppe, S., and Lundquist, C. (2020). Spill-over from aquaculture may provide a larval subsidy for the restoration of mussel reefs. *Aquacult. Environ. Interact*. 12, 231–249. doi: 10.3354/aei00363

Oke, P. R., and Middleton, J. H. (2001). Nutrient enrichment off Port Stephens: the role of the East Australian Current. *Cont. Shelf Res*. 21, 587–606. doi: 10.1016/S0278-4343(00)00127-8

Okubo, A. (1971). Oceanic diffusion diagrams. *Deep Sea Res. Oceanogr. Abstracts* 18, 789–802. doi: 10.1016/0011-7471(71)90046-5

Paris, C. B., Helgers, J., van Sebille, E., and Srinivasan, A. (2013). Connectivity modeling system: a probabilistic modeling tool for the multi-scale tracking of biotic and abiotic variability in the ocean. *Environ. Model. Softw*. 42, 47–54. doi: 10.1016/j.envsoft.2012.12.006

Paris, C. B., Hénaff, M. L., Aman, Z. M., Subramaniam, A., Helgers, J., Wang, D.-P., et al. (2012). Evolution of the macondo well blowout: simulating the effects of the circulation and synthetic dispersants on the subsea oil transport. *Environ. Sci. Technol*. 46, 13293–13302. doi: 10.1021/es303197h

Pauly, D., Christensen, V., Guénette, S., Pitcher, T. J., Sumaila, U. R., Walters, C. J., et al. (2002). Towards sustainability in world fisheries. *Nature* 418, 689–695. doi: 10.1038/nature01017

Ribbat, N., Roughan, M., Powell, B., Kerry, C., and Rao, S. (2020a). *A High-Resolution (750m) Free-Running Hydrodynamic Simulation of the Hawkesbury Shelf Region Off Southeastern Australia (2012-2013) using the Regional Ocean Modeling System*. Sydney, SY: UNSW.dataset.

Ribbat, N., Roughan, M., Powell, B., Rao, S., and Kerry, C. (2020b). Transport variability over the Hawkesbury Shelf (31.5–34.5°S) driven by the East Australian Current. *PLoS ONE* 15:e0241622. doi: 10.1371/journal.pone.0241622

Rocha, C., Edwards, C. A., Roughan, M., Cetina-Heredia, P., and Kerry, C. (2019). A high-resolution biogeochemical model (roms 3.4 + bio_fennel) of the East Australian Current system. *Geosci. Model Dev*. 12, 441–456. doi: 10.5194/gmd-12-441-2019

Roughan, M., Keating, S., Schaeffer, A., Cetina-Heredia, P., Rocha, C., Griffin, D., et al. (2017). A tale of two eddies: the bio-physical characteristics of two contrasting cyclonic eddies in the Tasman Sea. *J. Geophys. Res. Oceans*. 2494–2518. doi: 10.1002/2016JC012241

Roughan, M., Macdonald, H. S., Baird, M. E., and Glasby, T. M. (2011). Modelling coastal connectivity in a Western Boundary current: Seasonal and inter-annual variability. *Deep Sea Res. II Top. Stud. Oceanogr*. 58, 628–644. doi: 10.1016/j.dsr2.2010.06.004

Roughan, M., Mace, A. J., Largier, J. L., Morgan, S. G., and Fisher, J. L. (2005a). Sub-surface recirculation and larval retention in the lee of a small headland: a variation on the upwelling shadow theme. *J. Geophys. Res*. 110:C10027. doi: 10.1029/2005JC002898

Roughan, M., and Middleton, J. H. (2002). A comparison of observed upwelling mechanisms off the east coast of Australia. *Cont. Shelf Res*. 22, 2551–2572. doi: 10.1016/S0278-4343(02)00101-2

Roughan, M., and Middleton, J. H. (2004). On the East Australian Current: variability, encroachment, and upwelling. *J. Geophys. Res*. 109, 1–16. doi: 10.1029/2003JC001833

Roughan, M., Oke, P. R., and Middleton, J. H. (2003). A modelling study of the climatological current field and the trajectories of upwelled particles in the East Australian Current. *J. Phys. Oceanogr*. 33, 2551–2564. doi: 10.1175/1520-0485(2003)033andlt;2551:AMSOTCandgt;2.0.CO;2

Roughan, M., Schaeffer, A., and Kioroglou, S. (2013). "Assessing the design of the NSW-IMOS moored observation array from 2008-2013: recommendations for the future," in *Oceans* (San Diego, CA), 1–7.

Roughan, M., Schaeffer, A., and Suthers, I. M. (2015). "Chapter 6-Sustained Ocean observing along the coast of southeastern Australia: NSW-IMOS 2007-2014," in *Coastal Ocean Observing Systems*, eds Y. Liu, H. Kerkering, and R. H. Weisberg (Boston, MA: Academic Press), 76–98.

Roughan, M., Terrill, E. J., Largier, J. L., and Otero, M. P. (2005b). Observations of divergence and upwelling around Point Loma, California. *J. Geophys. Res. Oceans* 110:C4. doi: 10.1029/2004JC002662

Schaeffer, A., Roughan, M., Austin, T., Everett, J. D., Griffin, D., Hollings, B., et al. (2016a). Mean hydrography on the continental shelf from 26 repeat glider deployments along Southeastern Australia. *Sci. Data* 3:160070. doi: 10.1038/sdata.2016.70

Schaeffer, A., Roughan, M., Jones, E., and White, D. (2016b). Physical and biogeochemical spatial scales of variability in the East Australian Current separation from shelf glider measurements. *Biogeosciences* 13, 1967–1975. doi: 10.5194/bgd-12-20101-2015

Schaeffer, A., Roughan, M., and Wood, J. E. (2014). Observed bottom boundary layer transport and uplift on the continental shelf adjacent to a Western Boundary Current. *J. Geophys. Res. Oceans* 119, 4922–4939. doi: 10.1002/2013JC009735

Truong, L., Suthers, I. M., Cruz, D. O., and Smith, J. A. (2017). Plankton supports the majority of fish biomass on temperate rocky reefs. *Mar. Biol.* 164, 73. doi: 10.1007/s00227-017-3101-5

van Sebille, E., Griffies, S. M., Abernathey, R., Adams, T. P., Berloff, P., Biastoch, A., et al. (2018). Lagrangian ocean analysis: fundamentals and practices. *Ocean Model.* 121, 49–75. doi: 10.1016/j.ocemod.2017.11.008

Wood, J. E., Schaeffer, A., Roughan, M., and Tate, P. M. (2016). Seasonal variability in the continental shelf waters off southeastern Australia: fact or fiction? *Cont. Shelf Res.* 112, 92–103. doi: 10.1016/j.csr.2015.11.006

Conflict of Interest: The authors declare that the research was conducted in the absence of any commercial or financial relationships that could be construed as a potential conflict of interest.

Publisher's Note: All claims expressed in this article are solely those of the authors and do not necessarily represent those of their affiliated organizations, or those of the publisher, the editors and the reviewers. Any product that may be evaluated in this article, or claim that may be made by its manufacturer, is not guaranteed or endorsed by the publisher.

Copyright © 2022 Roughan, Cetina-Heredia, Ribbat and Suthers. This is an open-access article distributed under the terms of the Creative Commons Attribution License (CC BY). The use, distribution or reproduction in other forums is permitted, provided the original author(s) and the copyright owner(s) are credited and that the original publication in this journal is cited, in accordance with accepted academic practice. No use, distribution or reproduction is permitted which does not comply with these terms.

frontiers in Marine Science

ORIGINAL RESEARCH
published: 27 January 2022
doi: 10.3389/fmars.2021.787808

Reoxygenation of the Hypoxia in the East China Sea: A Ventilation Opening for Marine Life

Chung-Chi Chen[1,2], Dong S. Ko[3], Gwo-Ching Gong[4,5], Chun-Chi Lien[6], Wen-Chen Chou[4,5], Hung-Jen Lee[7], Fuh-Kwo Shiah[4,8] and Yu-Sin Wita Huang[1,9]*

[1] Department of Life Science, National Taiwan Normal University, Taipei, Taiwan, [2] College of Marine Sciences, National Dong Hwa University, Hualien, Taiwan, [3] Oceanography Division, Naval Research Laboratory, Stennis Space Center, Washington, DC, United States, [4] Institute of Marine Environment and Ecology, National Taiwan Ocean University, Keelung, Taiwan, [5] Center of Excellence for the Oceans, National Taiwan Ocean University, Keelung, Taiwan, [6] Department of Atmospheric Sciences, National Taiwan University, Taipei, Taiwan, [7] Department of Marine Environmental Informatics, National Taiwan Ocean University, Keelung, Taiwan, [8] Research Center for Environment Changes, Academia Sinica, Taipei, Taiwan, [9] Biodiversity Program, Taiwan International Graduate Program, Academia Sinica, Taipei, Taiwan

Hypoxia and upwelling co-occur in the summer, and well-mixed water typically reaches the subsurface in the East China Sea (ECS), especially off the Changjiang River estuary. The impact of upwelling on hypoxia and, therefore, on the ecosystem in the ECS is not known. This study demonstrates both positive and negative effects of upwelling on hypoxia and its impact on the ecosystem. With upwelling, the spatial extent of hypoxic water increases with a lower pH but waters with high regenerated nutrients and fugacity of CO_2 (fCO_2), which are normally confined to the near-bottom, are found just up to 5–10 m below the surface. This upwelled high nutrient water can enhance phytoplankton growth in this region. On one occasion in August 2014, upwelling reached to the surface and lasted for 3 weeks, with the area of coverage ranging from 326.8 to 24,368.0 km^2. During this event, the water was mixed thoroughly throughout the water column, with high concentrations of nutrients, chlorophyll *a*, and slightly undersaturated dissolved oxygen but saturated fCO_2, alongside a normal pH. This event may have served as an important pathway from the ocean to the atmosphere for the regenerated CO_2. It also provided a productive and suitable environment for marine life and ventilation to alleviate low-oxygen stress in this hypoxic but upwelling region in the ECS.

Keywords: acidification, fugacity of CO_2, hypoxia, nutrient regeneration, upwelling, Yangtze River

OPEN ACCESS

Edited by:
Magdalena Andres, Woods Hole Oceanographic Institution, United States

Reviewed by:
Dewang Li, Second Institute of Oceanography, China
Wei-Dong Zhai, Shandong University (Qingdao), China

****Correspondence:***
Chung-Chi Chen
ccchen@ntnu.edu.tw

Specialty section:
This article was submitted to Coastal Ocean Processes, a section of the journal Frontiers in Marine Science

Received: *01 October 2021*
Accepted: *22 December 2021*
Published: *27 January 2022*

Citation:
Chen C-C, Ko DS, Gong G-C, Lien C-C, Chou W-C, Lee H-J, Shiah F-K and Huang Y-SW (2022) Reoxygenation of the Hypoxia in the East China Sea: A Ventilation Opening for Marine Life. Front. Mar. Sci. 8:787808. doi: 10.3389/fmars.2021.787808

INTRODUCTION

In coastal oceans, the hypoxic zone (commonly known as a "dead zone") has been expanding globally over the last half-century (Diaz and Rosenberg, 2008; Breitburg et al., 2018). The frequency, duration, and severity of hypoxic events are increasing mainly because of human activities such as nutrient pollution from agricultural runoff, fossil fuel burning, and wastewater treatment effluents (Rabalais et al., 2002; Diaz and Rosenberg, 2008; Vaquer-Sunyer and Duarte, 2008). In the inner shelf of the East China Sea (ECS), especially outside the Changjiang River estuary (CRE, or Yangtze River; **Figure 1**), hypoxia has been frequently observed since the 1950s using evidence from sediment microfossils (Li et al., 2002, 2011). This and the nearby area also form an important fishing ground (Zhang et al., 2016). The

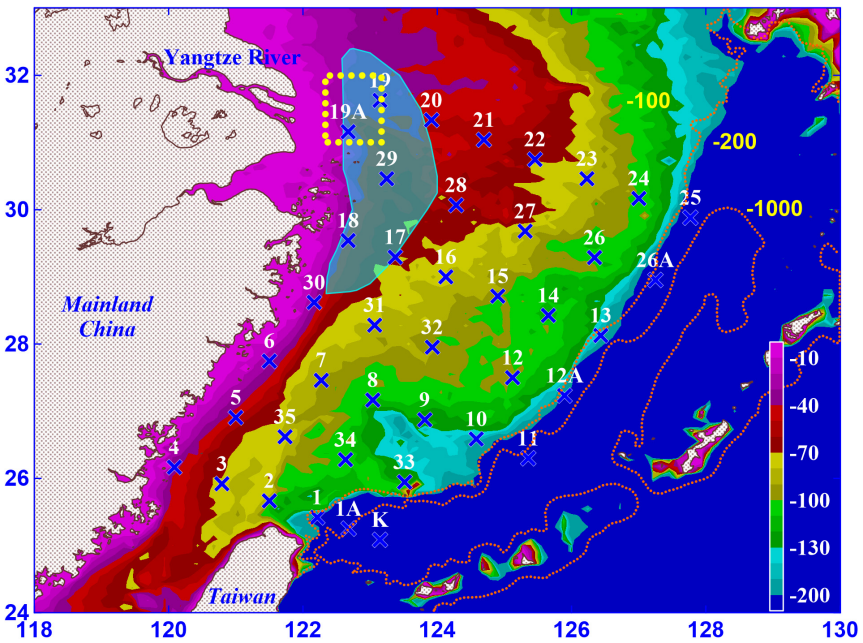

FIGURE 1 | Designed sampling stations in East China Sea are marked by an "x" with station number above the mark. The frequently observed hypoxic region off the Changjiang River estuary is shaded with light blue, modified after Li et al. (2002). The rectangle with a yellow a broken yellow line indicates the observed upwelling region proposed by Zhao et al. (2001). Bottom depth is indicated by color coding, and depth contours of 100, 200, and 1,000 m are also played as dashed lines.

extent of the hypoxic region can reach 15,400 km^2 in the summer (Chen et al., 2007; Zhu et al., 2017), comparable to that observed in the northern Gulf of Mexico or the northwest shelf of the Black Sea (Rabalais et al., 2002; Obenour et al., 2013; Scavia et al., 2017; Fennel and Testa, 2019). Hypoxia has a severe impact on coastal waters, causing the death of marine life, changing benthic communities with a catastrophic effect on the marine ecosystem, and altering sedimentary structures and biogeochemical cycles (Rabalais et al., 2002; Vaquer-Sunyer and Duarte, 2008; Conley et al., 2009; Breitburg et al., 2018). Acidification and high nutrient regeneration have also been observed in the hypoxic regions in the ECS (Cai et al., 2011; Wang et al., 2016; Zhu et al., 2017; Chen et al., 2020).

Interestingly, upwelling often has been observed within or near the region of frequent hypoxia of 122° 20′–123° 10′ E and 31° 00′–32° 00′ N, with an upwelling rate estimated to be 1.0–5.0 × 10^{-3} cm s^{-1} (**Figure 1**; Zhao et al., 2001; Lü et al., 2006; Hu and Wang, 2016). This upwelling may be induced result from multiple forcing mechanisms, including the tide, intrusion of Kuroshio subsurface water (KSW), and discharge of Changjiang River water over a deep trough located outside the CRE where upwelling is forced by the pressure gradient because of vertical squeezing of the vortex tube and bottom frictional effect (Zhao et al., 2001; Lü et al., 2006; Liu and Gan, 2015). Even though this upwelling has been observed over the past two decades, it is located away from the coast and has received relatively little attention (Zhao et al., 2001). Some studies have focused on the impact of this upwelling on this hypoxic region and how the combined effect of upwelling and hypoxia impact the ecosystem (Hu and Wang, 2016; Xu et al., 2017; Chen et al., 2021b).

In summer, the bottom water off the CRE is generally upwelled to 5–10 m below the surface but does not reach the surface (Zhao et al., 2001; Lü et al., 2006; Liu and Gan, 2015; Hu and Wang, 2016). In contrast, in this study, the upwelling did reach to the surface during August 2014. Here we examine the underlying mechanisms that caused the bottom water to upwell to the surface. Further we examine whether this intensified upwelling event had a different effect on hypoxia compared to the typical upwelling in this region. This study explores the hypothesis that upwelling to the surface opens a ventilation pathway for dissolved gases, especially for O_2 and CO_2, from the bottom water to the water surface. To explore this, shipboard observations, an ocean model, and remote sensing data are examined to evaluate the physical, chemical, and biological ocean variables in the area during the summer of 2014. This time period during which the bottom water reached the surface is contrasted with another year (2003) when bottom water was isolated below a warm and saline surface layer.

MATERIALS AND METHODS

Study Area and Sampling

Water samples were collected from the ECS during four cruises in the summer of 2003 (June 18–26 and August 13–23) and 2014 (July 16–29 and August 20–31) on the R/V Ocean Researcher I and V. The planned sampling stations were distributed throughout the ECS (**Figure 1**), but the actual sampling stations in different sampling periods varied as displayed in **Figure 2**. The samples were collected in Teflon-coated Go-Flo bottles (20 L;

General Oceanics Inc., Miami, GL, United States) mounted on a Rosette assembly (Model 1015; General Oceanics Inc.). At each station, 5–10 samples were taken at depths ranging from 2 to 50 m, depending on the total water depth. Subsamples were taken for immediate analyses (DO, dissolved inorganic nutrients, and Chl *a*). The methods used to collect the hydrographic data and analyze the response variables followed those described by Chen et al. (2006, 2009, 2013, 2017, 2021a). The descriptions of the methods used are presented briefly in the following sections. Note that portions of these data were published by Chen et al. (2007) and Chou et al. (2016).

Physical, Chemical, and Biological Hydrographics

Conductivity, temperature, and depth (CTD) were recorded throughout the water column with a CTD instrument (SBE9/11 Plus; Sea-Bird Electronics Inc., Bellevue, WA, United States). The mixed layer depth (M_D) was based on the potential density criterion of 0.125 kg m^{-3} (Levitus, 1982).

Water subsamples for dissolved inorganic nutrient analysis (NO_3^- and PO_4^{3-}) were collected from every sampling depth with 100-ml polypropylene bottles and frozen immediately with liquid nitrogen. A custom-made flow injection analyzer was used for nitrate and phosphate analyses, for which the detection limits were 0.3 and 0.01 μM, respectively (Gong et al., 2003).

The water subsamples for DO from every sampling depth were siphoned into 60-ml BOD bottles and fixed immediately by adding 0.5 ml manganese chloride and 0.5 ml alkaline iodide reagent (Pai et al., 1993). The concentration of O_2 was measured using a direct spectrophotometry method, with a precision of 0.02 mg L^{-1}. If applicable (e.g., August of 2003 and 2014), for a continuous profile, the concentration of O_2 was measured using a DO sensor (SBE 43; Sea-Bird Electronics Inc.) attached to the Sea-Bird CTD and calibrated by the directly measured concentration of O_2 (all $p < 0.001$).

Water subsamples for pH, dissolved inorganic carbon (DIC), and total alkalinity (TA) measurements were collected following standard operating procedures (Dickson et al., 2007). pH was determined spectrophotometrically at 25°C on the total hydrogen ion concentration scale (pH_T at 25°C) (Clayton and Byrne, 1993). DIC was measured by coulometry using a single-operator, multiparameter metabolic analyzer, with a precision of 0.1% (Johnson et al., 1993). TA was measured by Gran titration using the open-cell method with a semiautomatic titration system (AS-ALK2; Apollo SciTech, Newark, DE, United States; Gran, 1952). This TA titration system has a precision better than 0.2% (Cai et al., 2010). For details on pH, DIC, and TA measurements,

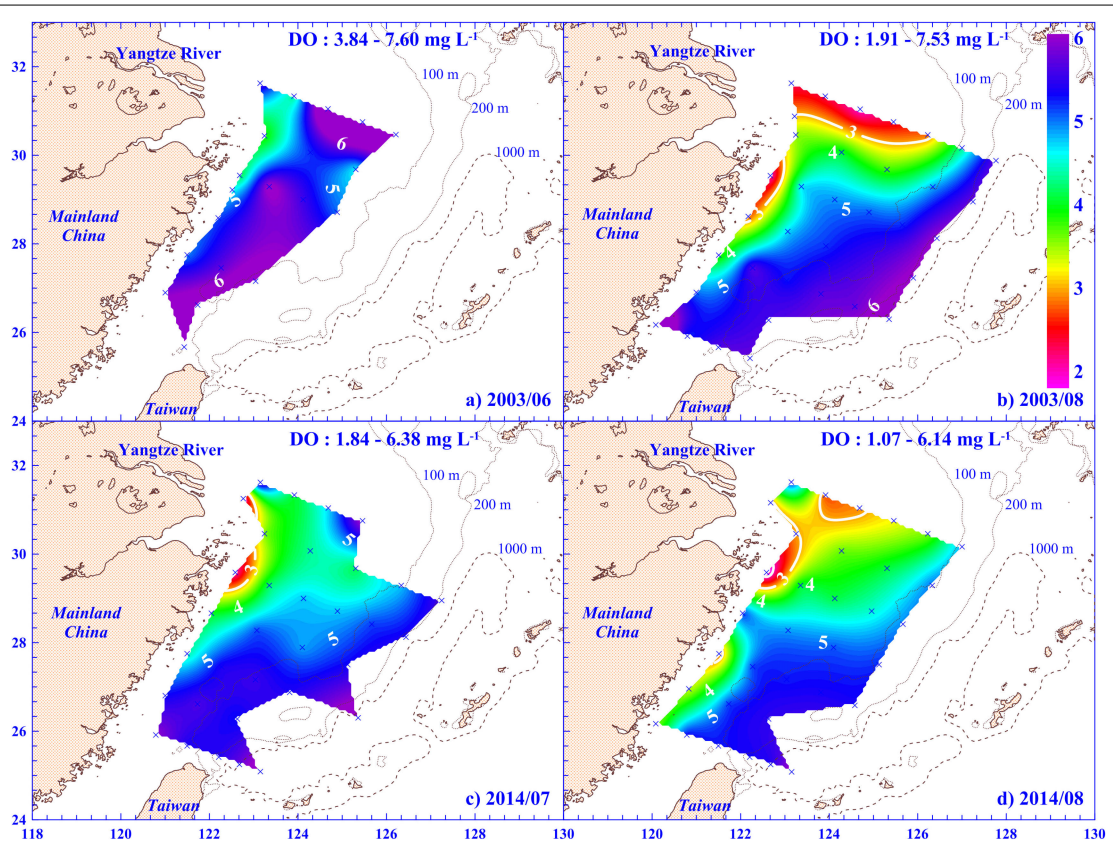

FIGURE 2 | Contours of concentration of dissolved oxygen (DO) in bottom water column or at 100 m if water column depth was >100 m in East China Sea in **(a)** June and **(b)** August 2003 and **(c)** July and **(d)** August 2014. Contour lines of DO = 3 mg L^{-1} are provided in white bold for reference. Please note that panels **(a,b)** were modified from Chen et al. (2007).

please refer to Chou et al. (2016). The fugacity of CO_2 (fCO_2) was estimated from DIC and TA data using the designed CO2SYS program (Lewis and Wallace, 1998; Pierrot et al., 2006).

The concentration of Chl *a* was measured with a fluorometer (AquaTracka III; Chelsea Instruments Ltd., England) attached to the Sea-Bird CTD for a continuous profile of *in vivo* fluorescence and calibrated by *in vitro* fluorometry (all $p < 0.001$). Water samples (2 L) for *in vitro* Chl *a* measurement were immediately filtered through a GF/F filter paper (Whatman, 47 mm), and the GF/F filter was stored in liquid nitrogen. The Chl *a* retained on the GF/F filter was determined fluorometrically (10-AU-005; Turner Designs, CA, United States; Parsons et al., 1984).

Model Description

To explore the potential mechanisms that drove upwelling in the ECS off the CRE, the East Asian Seas Ocean Nowcast/Forcast System (EASNFS) was used (Ko et al., 2008). This data assimilative ocean model combines data assimilation, a dynamic ocean model (the Navy Coastal Ocean Model), a statistical data analysis model (the Modular Ocean Data Assimilation System), and various data sources for ocean bathymetry, climatological data, surface forcing, open boundary forcing, and observations for data assimilation (Martin, 2000; Ko et al., 2008). This model domain covers the entire East Asian marginal seas and part of the West Pacific Ocean from 17.3° S to 52.2° N and from 99.2° E to 158.2° E. The horizontal resolution (∼1/12°) ranges from approximately 9.8 km at the equator to approximately 6.5 km at the model's northern boundary. There are 41 sigma-z levels with more closely spaced levels in the upper ocean to increase resolution. EASNFS also implemented river forcing and astronomical tides. Inside the model domain 142 rivers derived from the World Meteorological Organization Global Runoff Data Center archives were included with monthly climatologic mass flux, temperature and zero salinity from their respective river mouths. The preliminary numerical experiments noted the importance of tides in driving enhanced upwelling in the seas around Taiwan and ECS so eight tidal constituents (K1, O1, P1, Q1, K2, M2, N2, and S2) were included (Ko et al., 2016). These were obtained from the Oregon State University Tidal Prediction Software (Egbert and Erofeeva, 2002). To simulate a typhoon event, the atmospheric forcing input was included from high-resolution Weather Research and Forecasting model outputs, supplemented with Navy Operational Global Atmospheric Prediction System products (Rosmond, 1992). For more details on the model, refer to Ko et al. (2008, 2016).

Satellite Sea Surface Temperature and Surface Wind Data

To help evaluate the temporal duration and spatial distribution of upwelling off the CRE, daily SST with 9 km spatial resolution was examined using optimally interpolated satellite microwave and infrared (MW_IR OI) data product. For details of the data processing, refer to the Remote Sensing Systems website.[1] The daily surface wind was obtained from the National Centers for Environmental Prediction–National Center for Atmospheric Research. The daily wind speed field was calculated for the CRE from July 15 to September 16, 2014.

[1]http://www.remss.com/measurements/sea-surface-temperature/oisst-description/

RESULTS

Hypoxia Off the Changjiang River Estuary

Hypoxia was observed in July 2014, and it covered a wider area in the ECS in August of 2003 and 2014, especially off the CRE and along the Zhejiang coast (**Figures 2b–d**). The lowest DO was 1.07 mg L^{-1} (ca. 14.5% of DO saturation) at St. 18 in August 2014 (**Figure 2d**). In the hypoxic regions, high concentrations of nutrients (e.g., nitrate and phosphate) were observed in the bottom water (**Figures 2**, **3a,b,e,f**, **4c–f,i,k**, **5c–f,i,k**). For example, both nitrate and phosphate concentrations of bottom water reached 17.9 and 1.82 μM in the hypoxic region at St. 18 in August 2014, respectively (**Figures 3b,e**). Additionally, significant negative linear relationships were between DO saturation and concentrations of nitrate or phosphate were evident (both with $p < 0.001$; **Figure 6**). Interestingly, compared to nitrate, a relatively high phosphate concentration (e.g., 2.07 μM) was observed in the low-DO (≤3 mg L^{-1}) water, with a lower N to P molar ratio of 5.62. Low pH was also measured in low-DO and hypoxic regions in 2014, with values as low as 7.64 (**Figures 3c,g**, **7a,b**). However, the fugacity of carbon dioxide (fCO_2) value was high, reaching 906 μatm in the bottom water in the hypoxic region (**Figures 3d,h**, **7c,d**).

High concentrations of nutrients, such as nitrate and phosphate, were also observed in the surface water of the hypoxic region and the entire ECS, particularly before hypoxia occurred (**Figures 5a,b,f,g** and **Table 1**). For example, before the onset of hypoxia in July 2014, the nitrate concentration reached 47.7 μM in the surface water at St. 19A (**Figure 5f**). Notably, linear relationships were significant between concentrations of nitrate (all $p < 0.001$) or phosphate (all $p < 0.05$) vs. salinity in the surface water for almost the entire sampling period, except phosphate in August, 2003. Fueled by high concentrations of nutrients, phytoplankton generally flourished in periods prior to hypoxic events in our observations (**Figures 5a,b,f,h** and **Table 1**). This pattern was especially pronounced in the hypoxic region; for example, phytoplankton biomass here reached 66.7 and 10.5 mg Chl m^{-3} in June 2003 and July 2014, respectively (**Figures 5b,h**). During the bloom period, high primary production resulted in a supersaturated level of DO, reaching as high as 139% in June 2003 (St. 19; **Figure 4a**).

Physically, hypoxic formation is strongly related to water column stratification. Strong stratification was observed during the summers in this study (**Table 2**); it was associated with the higher temperature (21.0°C) and lower salinity (27.2) water near the surface relative to the colder (17.8°C) and saltier (31.0) bottom water using St. 19 in June, 2003 as an example (**Figure 4**). Both the halocline and thermocline contributed to water column stratification, but their relative contribution varied

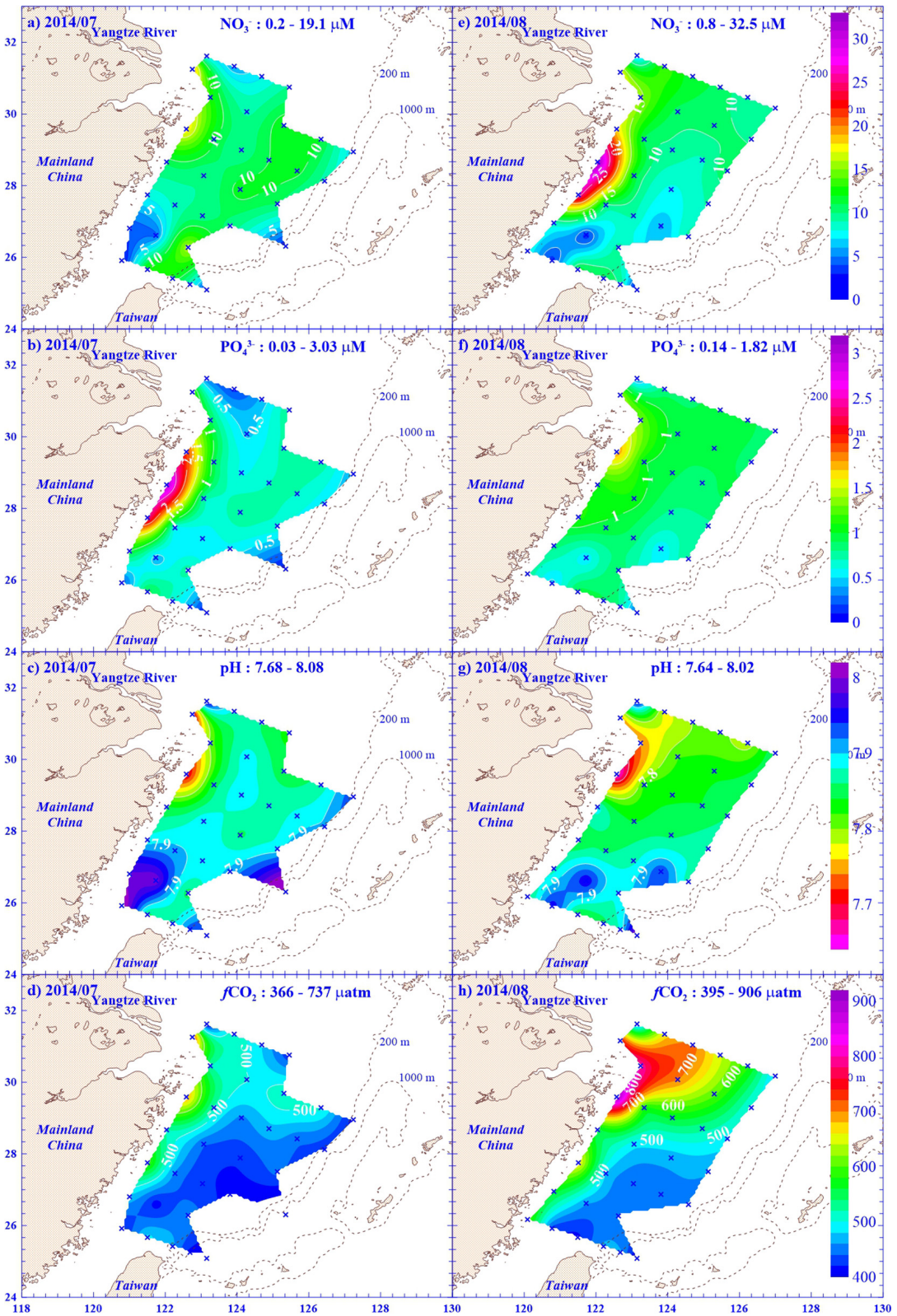

FIGURE 3 | Contours of different variables, including nitrate (NO_3^-), phosphate (PO_4^{3-}), pH, and fugacity of CO_2 (fCO_2), in bottom water column or at 100 m if water column depth was >100 m in East China Sea in **(a–d)** July and **(e–h)** August 2014. The range of variables are also displayed at the top of each panel. Color codes for the values of each variable are given in the left panels.

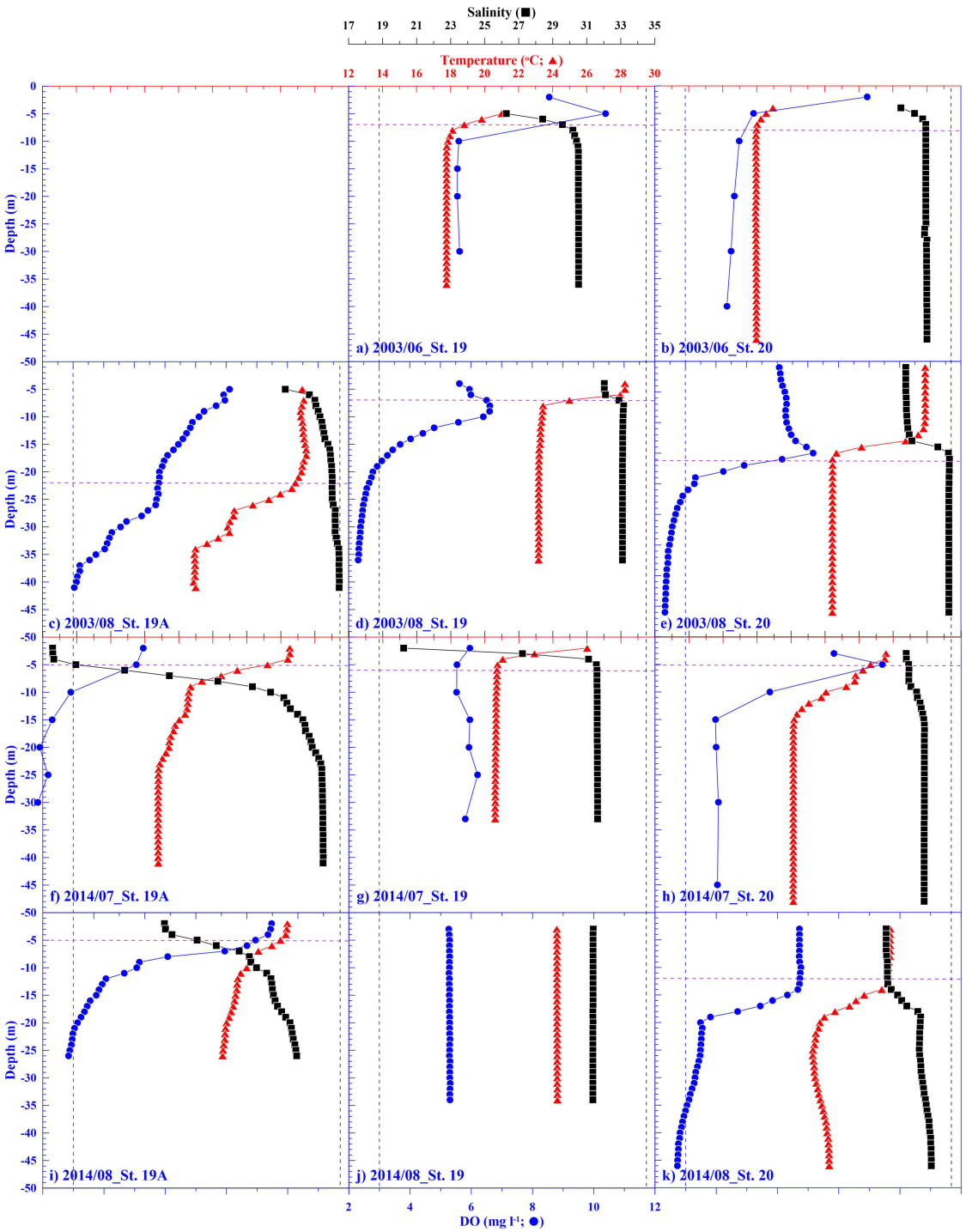

FIGURE 4 | Depth profiles of temperature (▲), salinity (■), and dissolved oxygen (DO; ●) at St. 19A, 19, and 20 in different sampling periods in the East China Sea. Please refer to **Figure 1** for stations. For reference, the horizontal dashed lines indicate the mixed layer depth at stations, and the vertical dashed lines indicate where DO = 3 mg L^{-1} (blue) and Salinity = 34.26 (black). Please note that panels **(a–e)** were modified from Chen et al. (2007).

temporally (**Table 2**). For example, the thermocline contributed more to water column stratification in August, 2003 (**Table 2**), even though the bottom water temperature was generally higher in August than in June or July (**Figure 4**, **Supplementary Figure 1**, and **Table 2**). Even so, the sharper density gradient was observed in this study (**Table 2**). For example, the average density difference between surface and bottom water was greater than -2.5 kg m^{-3} for the four northwestern-most stations (**Table 2**).

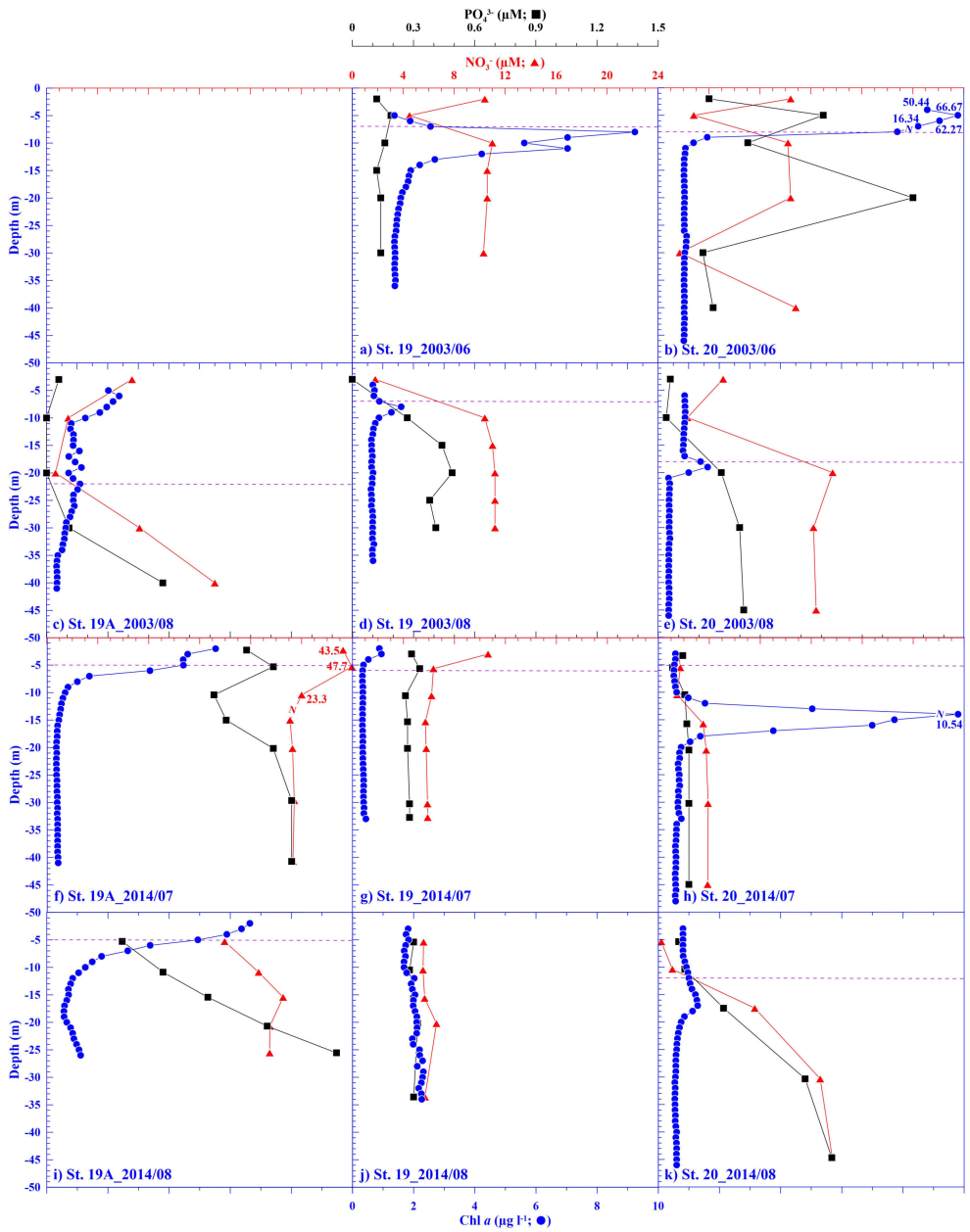

FIGURE 5 | Depth profiles of nitrate (▲), phosphate (■), and chlorophyll *a* (Chl *a*; ●) at St. 19A, 19, and 20 in different sampling periods in East China Sea. Please refer to **Figure 1** for stations. For reference, the horizontal dashed lines indicate the mixed layer depth at stations. Please note that panels **(a–e)** were modified from Chen et al. (2007).

Additionally, the mixed layer depths were generally shallower in June and July than in August in the hypoxic regions (**Table 2**).

Upwelling Off the Changjiang River Estuary

Upwelling in to a Sub-Surface Layer (5–15 m Below the Surface)

Upwelling events occurred during the hypoxia in this region off the CRE. The bottom water upwelled to within 5–15 m below the surface, especially at Sts. 19A, 19, and 20 (**Figures 1**, **4a,b,d–h**). Using St. 19 in June and August of 2003, and July 2014, respectively (**Figures 4a,d,g**) as an example, bottom water advected vertically to 10, 10, and 5 m below the surface with average salinity values (± SD for this and all parameters discussed henceforth) over the upwelling water of 31.02 (± 0.02), 33.11 (± 0.01), and 31.60 (± 0.01). Hypoxia was associated with decreased DO saturation and pH, but increased nutrients and fCO_2 in the bottom water in the ECS (**Figures 2–7**). However, the affected water was shoaled to the subsurface when hypoxia

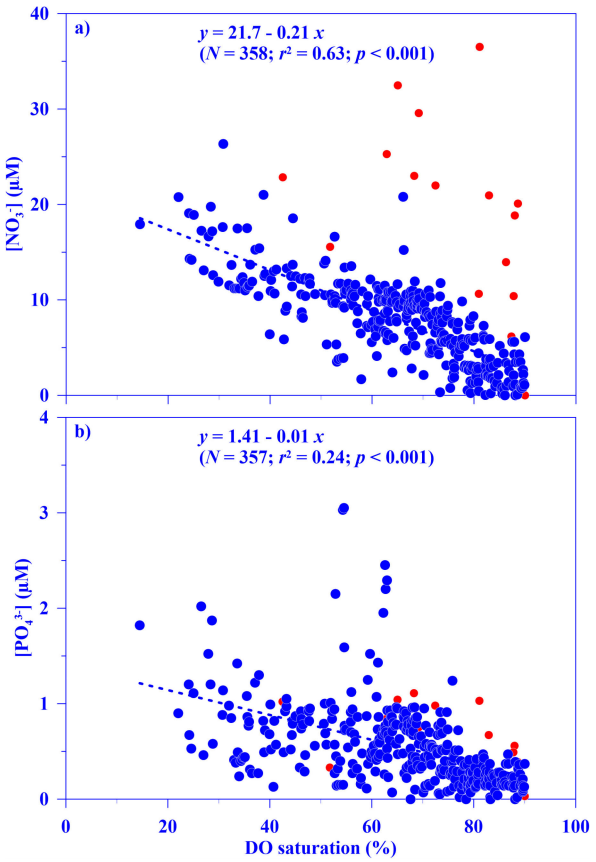

FIGURE 6 | Relationships between dissolved oxygen (DO) saturated rate (%) vs. concentrations (μM) of **(a)** nitrate (NO_3^-) and **(b)** phosphate (PO_4^{3-}) for all pooled data in this study, except for DO rate >90%. Data marked with red represent salinity <30. Linear regression is displayed and applies only to the data marked with blue (or salinity ≥30).

was located within the upwelling region, namely, off the CRE in the ECS (**Figures 4d–f,k**, **7**). For example, the low-DO bottom water could shoal to 10 m below the surface water at St. 19A in July of 2014, where pH and fCO_2 values were 7.77 and 581 μatm, respectively (**Figures 4f**, **7a**). Accompanied by the upwelled hypoxic water, high-nutrient water was also uplifted to the mixed layer, and the highest NO_3^- and PO_4^{3-} concentrations reached 23.3 and 1.11 μM, respectively (**Figures 4d–f,k**, **5d–f,k**).

Upwelling to Surface Water Event

Instead of upwelling to 5–15 m below the surface, the bottom water upwelled to the surface at St. 19 in August 2014, referred to as "upwelling to the surface event" hereafter (**Figures 4j**, **5j**). The water was well mixed throughout the water column during this upwelling to the surface event. This phenomenon is apparent in the small vertical variation of water properties and concentrations over the water column at St. 19 that include the following: temperature [24.24 (± 0.01)°C], salinity [31.35 (± 0.01)], DO [5.29 (± 0.01) mg L^{-1} or 75.6 (± 0.2)% of saturation], nitrate [5.81 (± 0.44) μM], phosphate [0.30 (± 0.01) μM], and chlorophyll *a* [Chl *a*; 2.01 (± 0.20) mg Chl m^{-3}; **Figures 4j**, **5j**]. Similar to other variables at St. 19, the fCO_2 was also well mixed throughout the water column with an average value of 463.3 (± 12.0) μatm; it also suggests that a huge quantity of fCO_2 contained in the bottom water was fluxed into the atmosphere during this event (**Figure 7d**). This is indirectly supported by the large difference of fCO_2 between bottom water and surface water, namely, 292 μatm observed at St. 19A, the nearby hypoxic station close to this upwelling to the surface event (**Figure 7d**). During this event, there was acidification relief at St. 19 with a mean pH value of 7.97 (± 0.01) over the water column compared to the adjacent stations (St. 19A and 20; **Figure 7b**), where pH values were as low as 7.64 (**Figure 3g**).

The MW_IR OI SST data was used to explore the temporal and spatial coverage of this upwelling to the surface event. On the sampling date in August 2014, the SST around St. 19 was lower than that of the surrounding water and close to the observation (**Figures 4j**, **8d**). However, this phenomenon was not observed during other summer study periods (**Figures 8a–c**). This upwelling to the surface event lasted for longer than 3 weeks, starting on August 13 and ending on September 6, 2014 (**Supplementary Figure 2**). Assuming the SST where the bottom water upwelled to the surface was below 24.5°C, similar to the observed temperature in the upwelling to surface water, the coverage area of this event was estimated to be around 6,000 km^2 on the sampling date (August 26, 2014) and it ranged from 326.8 to 24,368.0 km^2 during this event period (**Figure 8d** and **Supplementary Figure 2**). A similar upwelling to the surface event was also observed prior to this event, occurring from July 31 to August 4, 2014 (**Supplementary Figures 2b,c**). During that event, Typhoon "Nakri" passed by the ECS shelf with a wind speed reaching 10.43 m s^{-1} in the upwelling region (**Supplementary Figure 3**).

DISCUSSION

Impact of Hypoxia on the Ecosystem Off Changjiang River Estuary

Hypoxia was found in the ECS, with its coverage area varying for the different sampling periods (**Figure 2**). For example, low-DO (≤3 mg L^{-1}) water covered an area greater than 12,000 km^2 (or 432 km^3 in volume) in August 2003 (**Figure 2b**; Chen et al., 2007). The lowest DO level was 1.07 mg L^{-1} in this study, and it has been reported to be as low as 0.71 mg L^{-1} in the ECS according to other studies (**Figure 2d**; Zhu et al., 2017). In the hypoxic region, high concentrations of nutrients were observed in the bottom water of this study (**Figure 3**). The high nutrient concentrations may be partially regenerated during hypoxic events such that the concentrations increased with increasing oxygen consumption (**Figure 6**; Zhu et al., 2017; Chen et al., 2020). Additionally, this low-DO water also had a low N to P molar ratio (5.62) or relatively high phosphate concentration (2.07 μM). This may have provided an important source of phosphate for this phosphate-limited coastal ecosystem in the ECS (Tseng et al., 2014; Chen et al., 2021b). Furthermore, some recent studies have shown that the metabolic decomposition process may not only induce high O_2 consumption but also DIC

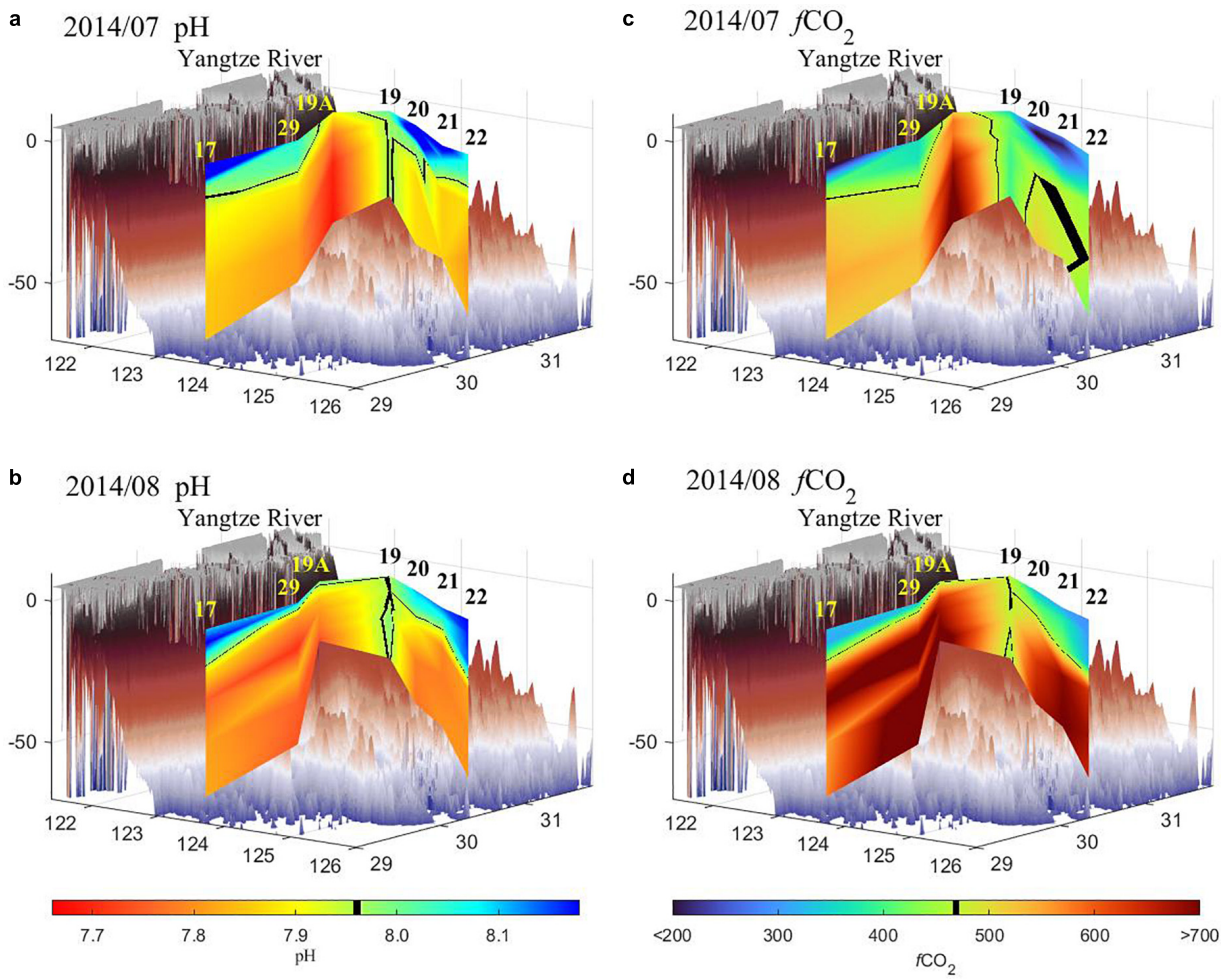

FIGURE 7 | Depth profiles of pH and fugacity of CO_2 (fCO_2) at sampling stations off the Changjiang River estuary along northern-most transect line (e.g., St. 19, 20, 21, and 22) and near-coast transect line (e.g., Sts. 19, 19A, 29, and 17) in July **(a,c)** and August **(b,d)** 2014. For reference, the values of fCO_2 = 468–471 μatm and pH = 4.96 were marked in black. The bathymetry/elevation data retrieved from GEBCO (https://www.gebco.net/data_and_products/gridded_bathymetry_data/). Please refer to **Figure 1** for stations.

regeneration, and thereby forming high fCO_2 and low pH in the bottom water in the hypoxia area off the CRE (Chou et al., 2013; Xiong et al., 2020). This phenomenon was also observed in the hypoxic bottom water in this study where the fCO_2 value reached 906 μatm and pH was as low as 7.64 (**Figures 3g,h**, **7c,d**). This implies that a significant quantity of CO_2 can be released into the atmosphere once the surface mixed layer disappears during winter or under strong physical disturbance (e.g., typhoons) when high-CO_2 water reaches the surface (Chen et al., 2006; Li et al., 2019).

The formation of hypoxia in the ECS has been attributed to water column stratification and decomposition of marine-derived organic matter enhanced by the enrichment of nutrients from river runoff (Chen et al., 2007; Wang et al., 2016; Chi et al., 2020). Strong water column stratification was apparent in this study (**Table 2**; Chen et al., 2007; Wei et al., 2015; Chi et al., 2020). The halocline and/or thermocline may contribute to water column stratification, and their relative contribution varied temporally; for example, thermocline contributed more in August and it may be more attributed to halocline in June or July (**Table 2**). Temporally, these episodic hypoxic events occurred seasonally and are especially common during the highly productive summer period as in this study (**Figures 2b,d**; Wei et al., 2015; Chen et al., 2020; Chi et al., 2020). High phytoplankton production here is normally fueled by nutrient enrichment through riverine discharge, especially from the Changjiang River (Gong et al., 2011). High nutrient concentrations were also measured in the surface water off the CRE in this study; for example, nitrate concentration here reached 47.7 μM (**Figure 5f**). This evidence suggests that, in addition to being a terrigenous source, the high phytoplankton biomass enhanced by riverine input of inorganic nutrients might be an important source providing marine-derived organic matter for the following O_2 consumption during the formation of hypoxia (Li et al., 2011; Wang et al., 2016).

TABLE 1 | Mean (± SD) concentrations of nitrate (NO_3^-; μM), phosphate (PO_4^{3-}; μM), and chlorophyll *a* (Chl *a*; mg Chl m^{-3}) of surface water over entire East China Sea in different sampling periods.

Date variables	June 2003	August 2003	July 2014	August 2014
NO_3^-	5.22 (± 6.23)	1.02 (± 2.14)	3.89 (± 9.01)	3.31 (± 7.40)
PO_4^{3-}	0.19 (± 0.17)	0.07 (± 0.07)	0.18 (± 0.37)	0.12 (± 0.13)
Chl *a*	3.6 (± 1.1)	0.4 (± 0.1)	1.3 (± 2.3)	1.6 (± 1.9)

TABLE 2 | Mean (± SD) values of mixed layer depth (M_D; m) and bottom temperature ($Temp_{Bot}$; °C), and difference between surface and bottom water of temperature ($Temp_{Diff}$), salinity (Sal_{Diff}), and density ($\delta_{\theta Diff}$; kg m^{-3}) in different sampling periods of East China Sea.

Date variables	June 2003	August 2003	July 2014	August 2014
M_D	11.0 (± 4.2)	15.3 (± 6.4)	5.5 (± 0.6)	7.7 (± 3.8)
$Temp_{Bot}$	18.7 (± 1.1)	22.5 (± 2.0)	20.4 (± 1.1)	22.1 (± 1.7)
$Temp_{Diff}$	2.1 (± 1.1)	5.7 (± 2.2)	5.5 (± 2.1)	4.1 (± 3.0)
Sal_{Diff}	–3.7 (± 2.7)	–1.1 (± 1.0)	–4.1 (± 2.1)	–2.0 (± 1.3)
$\delta_{\theta Diff}$	–3.3 (± 2.3)	–2.5 (± 0.9)	–4.7 (± 1.7)	–2.7 (± 1.9)

*For a systematic comparison, only four northwestern-most stations (i.e., St. 19, 20, 28, and 29) were used for the calculation (**Figure 1**).*

Alongside previous factors, the inflow of KSW and the bottom topography associated with the deep trough just off the CRE (the similar regions as the hypoxic area of this study), may also play key roles in the development of hypoxia (Wang, 2009; Zhang et al., 2019). In this study, the intrusion of lower temperature and high salinity (>34.26) of the KSW was observed to reach the northwestern-most stations (over 31° N), especially within the bottom water; this is apparent in the salinity and stands out in a temperature vs. salinity diagram (**Figures 4c,e**, **Supplementary Figures 1d, 4**, and **Supplementary Table 1**). The low-O_2 of the KSW was observed in the bottom water at stations, including Sts. 34, 8, 31, 17, 29, along the track of this KSW intrusion, with average DO values over the stations ranging from 4.37 (± 1.03) to 5.46 (± 1.41) mg L^{-1}. Additionally, it could also be supported by the average DO saturation with values ranging from 57.1 (± 12.5) to 75.7% (± 21.8) in different sampling periods (**Figure 1** and **Supplementary Table 1**). The results suggest that the inflow of the KSW may serve as an important water source for the hypoxic formation off the CRE since it not only has waters with low-O_2 level but also with high salinity and lower temperature (during summer), providing an essential prerequisite for water column stratification (Wang, 2009; Zhang et al., 2019).

Potential Formation Mechanisms of Upwelling (to Surface Event) Off Changjiang River Estuary

In the hypoxic region off the CRE, a typical upwelling was also observed; namely, the upwelled bottom water was capped around 5–10 m below the sea surface by a layer of low-salinity and high-temperature surface water, especially at Sts. 19A, 19, and 20, consistent with other studies (**Figures 1**, **4a,b,d,h**; Lü et al., 2006; Hu and Wang, 2016). To explore potential formation mechanisms for the typical upwelling vs. for the upwelling to the surface event off the CRE, output from a data assimilative ocean model, EASNFS, was examined (Ko et al., 2016). The model demonstrates that an upwelling event appeared around

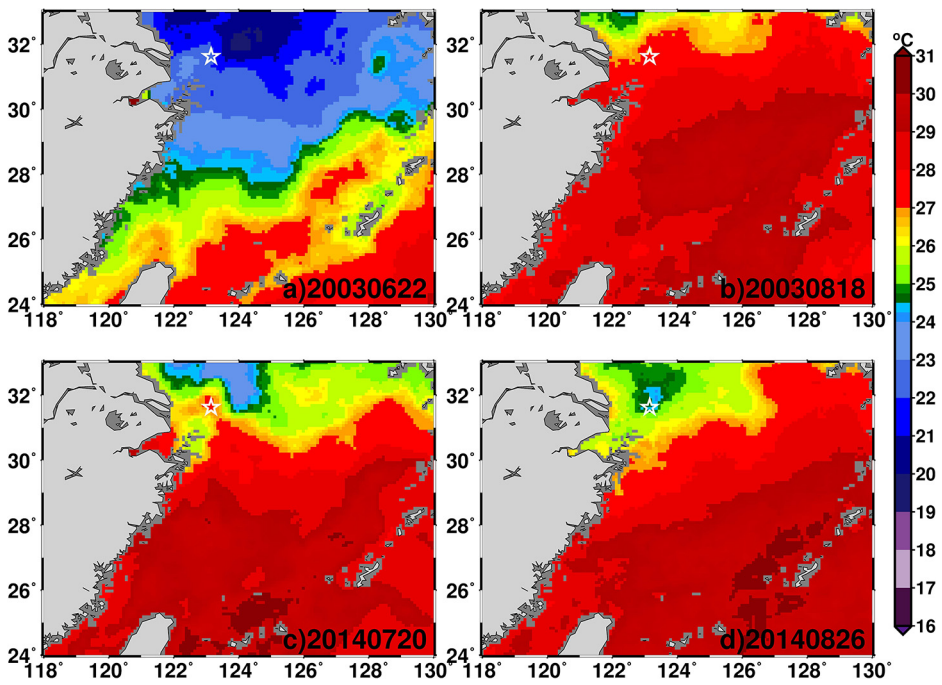

FIGURE 8 | Images of sea surface temperature (SST) of optimally interpolated satellite microwave and infrared (MW_IR OI SST) data on sampling date, displayed in labels, of St. 19 marked with ☆ in different sampling periods. Color code for SST is given for reference.

the submarine valley off the CRE (**Figure 1**). The tide has been suggested and demonstrated as one of the major drivers of the upwelling in this model (Ko et al., 2016). For comparison of results with and without the tidal effect on upwelling, please refer to Figure 5 of Ko et al. (2016) for details. Additionally, the effect of the KSW on upwelling can be revealed by examining whether KSW reaches the northwestern-most stations (over 31° N) in the model output, as stated described above (**Figure 4**, **Supplementary Figure 4**, and **Supplementary Table 1**). As for the Changjiang River discharge water, its contribution to upwelling may be inferred by examining (in the model output) the baroclinic effects associated with the density gradient plume (**Figure 4** and **Supplementary Figure 4**; Lü et al., 2006). It is found here that overall, this upwelling was induced by combined physical forcing, including the tide, KSW, and Changjiang River discharge water over the canyon (Lü et al., 2006). The wind played only a limited role in inducing upwelling since the summer monsoon was generally weak, for example, 4.9 m s^{-1} in July 2014 in the ECS (**Supplementary Figure 3b**). This phenomenon was reproduced and revealed in the model results (**Figure 9**). For example, at the end of July 2014 (before Typhoon Nakri), the bottom water upwelled to 5–10 m below the surface in the upwelling region (along 31.625° N transect; **Figure 9a**).

This upwelling reached to the surface in August 2014, which has rarely been observed in the summer in the ECS (**Figures 4j**, **5j** and **Supplementary Figure 2**; Zhao et al., 2001; Lü et al., 2006). During this upwelling to the surface event, the water was well mixed throughout the water column for all measured variables, e.g., temperature, salinity, DO, nitrate, phosphate, Chl *a*, pH, and fCO_2 (**Figures 4j**, **5j**, **7b,d**). In this study, the upwelling to the surface event was found during two periods: (1) the Typhoon Nakri period and (2) a few days after the passing of this typhoon (including the one on August 26, 2014) using MW_IR OI SST data and the EASNFS model results (**Figures 8d**, **9b,d** and **Supplementary Figure 2**). The previous upwelling mechanisms also serve as the fundamental forcing for this upwelling to the surface event. At the onset of Typhoon Nakri, the water became well-mixed throughout the water column; this upwelling outpoured to the surface water and it may be mostly induced by strong vertical wind mixing with a wind speed of 10.6 ($\pm$ 0.6) m s^{-1} (**Figure 9b** and **Supplementary Figures 2d, 3b**). A significant drop in surface temperature was observed during this event, especially off the CRE (**Supplementary Figures 2b,c, 3**). This upwelling to surface event ended 2 days after the passing of the typhoon, the water was weakly restratified, and the surface heating over warmer water was not as effective as that over colder water (**Figure 9c**).

As for the upwelling to the surface event that occurred a few days after the passing of the typhoon (including the one on August 26, 2014; **Figures 8d**, **9d** and **Supplementary Figure 2**), this event may have been associated with the lasting impact induced by Typhoon Nakri (**Figure 9d**). Prior to the typhoon, a strong density gradient was observed in July 2014 since the bottom water was relatively cold and covered by warm and fresher surface water, especially in the vicinity off the CRE (**Figures 4f,g**, **9a**). After the strong wind mixing induced by the typhoon, the bottom water became well mixed and warm along the track and in the vicinity of Typhoon Nakri, and it continued to flow north- or northwestward in the ECS (**Supplementary Figures 1e,g, 4c,d**). This warm water made the heating of the surface water less effective. The heating from solar radiation on warm water is roughly the same as that on cold water; the radiation of heat out of the ocean as long waves is greater over warm water than cold water. The heating from the sensible heat flux, which depends on the air–sea temperature difference, is less over warm water, and the heating due to the latent heat flux, which depends on the sea temperature and air moisture, is mostly negative over warm water; namely, it may evaporate and lose heat. Conversely, the moisture in the air may condense, and the ocean may gain heat over cold water. Together, the temperature would increase less in warm water than in cold water, assuming the atmospheric condition is the same. These all resulted in the small density gradient (or weak stratification) near the surface, and it allowed the tidal mixing to upwell the bottom water to the surface and completely mix the water column (**Figures 9c,d**).

Potential Impact and Implication of Upwelling on Hypoxic Region Off Changjiang River Estuary

How upwelling impacts on the hypoxic ecosystem has been rarely evaluated, especially in the ECS (Chen et al., 2021b). In the hypoxic bottom water, it was normally associated with a decrease in DO and pH, but an increase in concentrations of nutrients and fCO_2, and the phenomena were also observed in this study (**Figures 2–7**; Chen et al., 2020, 2021b). In the upwelling region, the hypoxic water shoaled to the subsurface water (e.g., 10 m below the surface water), especially near Sts. 19 and 20 in August 2003 and St. 19A in July 2014 off the CRE (**Figures 1**, **4d–f,k**, **7**). This may have caused more severe negative effects on marine life when low-DO and low-pH water were uplifted near the surface, filling the subsurface water column and increasing the total hypoxic water volume. Additionally, the negative effect of combined hypoxia and acidification may even more severely threaten marine life (Gobler and Baumann, 2016). Accompanied by this upwelled hypoxic water, high-nutrient water was also uplifted to the mixed layer (**Figures 4d–f,k**, **5d–f,k**). These uplifted nutrients might significantly increase phytoplankton growth. The organic matter, derived from phytoplankton production, is the primary source of organic matter that fuels microbial oxygen consumption and causes more severe hypoxia in this region (Wang et al., 2017).

However, the impact of upwelling on hypoxia and its effect on the ecosystem may be quite different when upwelling outpoured to the surface, for example, St. 19 in this study (**Figures 4j**, **5j**, **7b,d**). The water column was well mixed from the bottom to the surface during the event, with a DO value of 5.29 $\pm$ 0.01 mg L^{-1} (75.6 $\pm$ 0.2% of DO saturation; **Figure 4j**). The higher DO suggests that this event may have provided a ventilation opening for marine life in this hypoxic region. Additionally, high concentrations of nitrate, phosphate, and Chl *a* were also well mixed throughout the entire water column (**Figure 5h**). This provided a productive environment for marine organisms near the surface, inducing blooms. Similar events have

occasionally been observed, mainly caused by the passage of typhoons (Ni et al., 2016; Wang et al., 2017; Li et al., 2019). However, more severe hypoxia was observed immediately after the sinking of bloom-derived organic matter and restratification of the water column.

During the upwelling to the surface event, the fCO_2 was also well mixed throughout the water column (**Figure 7d**). This suggests that this upwelling to the surface event could release the regenerated CO_2 sealed under the mixed layer and diffuse it into the atmosphere, serving as an important pathway for CO_2 in this generally well-stratified coastal ecosystem in the summer (Chen et al., 2006; Chou et al., 2009). To estimate the CO_2 efflux during this event, the deficit of averaged CO_2 values over the water column between St. 19 and nearby stations (e.g., Sts 19A and 20) during the event period (i.e., 13–26 August, 2014) were estimated. As expected, the estimated CO_2 efflux was high, with a value of + 247.7 mmol m^{-2} day^{-1}. This estimated value is higher than that typhoon-induced CO_2 efflux which reached + 111.6 mmol m^{-2} day^{-1} in hypoxic water off the CRE (Li et al., 2019). On average (1997–2018), it has been estimated that typhoon-induced CO_2 efflux is approximately + 0.2 Tg C $year^{-1}$, which accounts for 18% of summer CO_2 influx in the ECS shelf (Li et al., 2019). Overall, a tremendous quantity of fCO_2 diffused into the atmosphere during this episodic upwelling to the surface event. However, it provided a more productive and suitable environment, such as normal pH, and a ventilation opening for marine life to alleviate low-O_2 stress in this frequently hypoxic, but upwelling, region in the ECS.

CONCLUSION

Hypoxia and upwelling occurred simultaneously during the summers of 2003 (June and August) and 2014 (July and August) in a region off the CRE in the ECS. Typically, well-mixed water often reaches 5–10 m below the surface in this upwelling during summer. With upwelling, hypoxic water expands up to the subsurface with a lower pH but high regenerated nutrients and fCO_2, which are normally confined to the near-bottom water. In regions with low DO or hypoxia, the pH value could be as low as 7.64, and fCO_2 could reach 906 μatm. The results demonstrated that this upwelling could shoal its hypoxic and acidified bottom water to the subsurface water, and it also increased the stress environment for marine life. The over-saturated fCO_2 was capped by surface water, but it was more easily released to the atmosphere once the shallower mixed layer disappeared. A high concentration of nutrients (e.g., nitrate and phosphate) in the bottom water may be partially regenerated during hypoxic events or under low-redox conditions. This upwelled high nutrient water could enhance phytoplankton growth in this region. Afterward, the sinking of

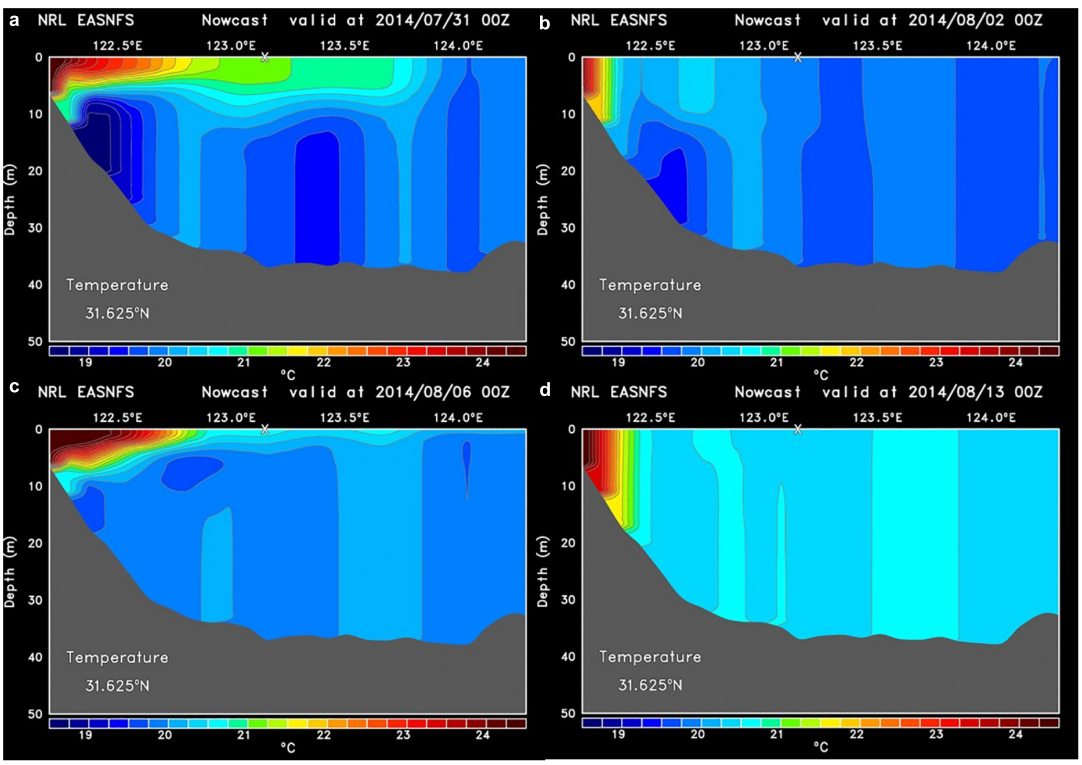

FIGURE 9 | Temperature profiles along 31.625° N transect predicted by East Asian Seas Nowcast/Forecast System (EASNFS): **(a)** At the end of July 2014, the water was well stratified with a 5–10-m warm layer on the top. **(b)** At the onset of Typhoon Nakri, the water column became well mixed. **(c)** After the passing of the typhoon, the water was weakly restratified. **(d)** Tidal mixing was able to fully mix the water column under weak stratification.

newly formed labile organic matter may enhance microbial O_2 consumption and cause more severe hypoxia in this region.

On one occasion in August 2014, this upwelling, normally upwelled to 5–10 m below the surface, outpoured to the surface. This phenomenon has rarely been observed previously. Based on a data assimilation ocean model, the East Asian Seas Nowcast/Forecast System, this upwelling to the surface event occurred during Typhoon Nakri, which passed by the ECS shelf at the beginning of August 2014. This event reoccurred 1 week after the typhoon and lasted for over 3 weeks, which may have been associated with the lasting impact induced by Typhoon Nakri. The coverage area of this event ranged from 326.8 to 24,368.0 km^2. Notably, such an event induced by the lasting impact of a typhoon has never been observed previously. Moreover, the impact of this event was quite different from when the upwelling reached the subsurface, as described previously. The water column was well mixed throughout the event and had a DO value of 5.29 ($\pm$ 0.01) mg L^{-1} in this region. This was also evidenced from variables with mean $\pm$ standard deviation values over the water column in this region, including temperature (24.24 $\pm$ 0.01°C), salinity (31.35 $\pm$ 0.01), nitrate (5.81 $\pm$ 0.44 μM), phosphate (0.30 $\pm$ 0.01 μM), pH (7.97 $\pm$ 0.01), fCO_2 (463.3 $\pm$ 12.0 μatm), and chlorophyll *a* (2.01 $\pm$ 0.20 mg Chl m^{-3}). The results suggest that this event may have served as an important conveyor from the ocean to the atmosphere for the regenerated CO_2. It also provided a productive and suitable environment for marine life and ventilation to alleviate low oxygen stress in this frequently hypoxic but upwelling region in the ECS. Its importance may be even greater than expected in the ECS, where typhoons frequently occur in the summer months.

DATA AVAILABILITY STATEMENT

The datasets presented in this study can be found in online repositories. The names of the repository/repositories and accession number(s) can be found below: doi.org/10.5061/dryad.nvx0k6dt6.

AUTHOR CONTRIBUTIONS

C-CC contributed to designing of the research, performed the research (dissolved oxygen), analyzed the data, and wrote the manuscript. DK performed the model simulation and wrote part of manuscript. G-CG analyzed and provided chemical hydrographic data. C-CL analyzed and provided satellite images. W-CC analyzed and provided data of pH, DIC, and TA. H-JL analyzed and provided surface wind data. F-KS organized and analyzed the data. Y-SH created part of the art works. All authors contributed to manuscript revision and approved the submitted version.

FUNDING

This study was part of the multidisciplinary "Effects of Global Change on Ocean Biogeochemistry and Ecosystem in the Sea surrounding Taiwan in the Northwest Pacific" (ECOBEST) and "Plankton Ecological Processes in Subtropical-shelf Ecosystems II" (PEPSE II) programs, which were supported by the Ministry of Science and Technology, Taiwan (MOST; 102-2611-M-003-001, 105-2611-M-003-002, 107-2611-M-003-001-MY3, and 110-2611-M-003-002 to C-CC).

ACKNOWLEDGMENTS

We are indebted to the officers and crew of the Ocean Researcher I and V for their assistance during the research cruise. We also appreciate I.-I. Lin, National Taiwan University, for providing the MW_IR OI SST data. This article was subsidized by the National Taiwan Normal University (NTNU).

SUPPLEMENTARY MATERIAL

The Supplementary Material for this article can be found online at: https://www.frontiersin.org/articles/10.3389/fmars.2021.787808/full#supplementary-material

REFERENCES

Breitburg, D., Levin, L. A., Oschlies, A., Gregoire, M., Chavez, F. P., Conley, D. J., et al. (2018). Declining oxygen in the global ocean and coastal waters. *Science* 359:eaam7240. doi: 10.1126/science.aam7240

Cai, W.-J., Hu, X., Huang, W.-J., Jiang, L.-Q., Wang, Y., Peng, T.-H., et al. (2010). Alkalinity distribution in the western North Atlantic Ocean margins. *J. Geophy. Res.* 115:C08014. doi: 10.1029/2009JC005482

Cai, W.-J., Hu, X., Huang, W.-J., Murrell, M. C., Lehrter, J. C., Lohrenz, S. E., et al. (2011). Acidification of subsurface coastal waters enhanced by eutrophication. *Nat. Geosci.* 4, 766–770. doi: 10.1038/ngeo1297

Chen, C.-C., Chiang, K. P., Gong, G. C., Shiah, F. K., Tseng, C. M., and Liu, K. K. (2006). Importance of planktonic community respiration on the carbon balance of the East China Sea in summer. *Glob. Biogeochem. Cycles* 20:Gb4001. doi: 10.1029/2005gb002647

Chen, C.-C., Gong, G. C., and Shiah, F. K. (2007). Hypoxia in the East China Sea: one of the largest coastal low-oxygen areas in the world. *Mar. Environ. Res.* 64, 399–408. doi: 10.1016/j.marenvres.2007.01.007

Chen, C.-C., Gong, G. C., Chou, W. C., Chung, C. C., Hsieh, C. H., Shiah, F. K., et al. (2017). The influence of episodic flooding on a pelagic ecosystem in the East China Sea. *Biogeosciences* 14, 2597–2609. doi: 10.5194/bg-14-2597-2017

Chen, C.-C., Gong, G. C., Shiah, F. K., Chou, W. C., and Hung, C. C. (2013). The large variation in organic carbon consumption in spring in the East China Sea. *Biogeosciences* 10, 2931–2943. doi: 10.5194/bg-10-2931-2013

Chen, C.-C., Shiah, F.-K., Gong, G.-C., and Chen, T.-Y. (2021b). Impact of upwelling on phytoplankton blooms and hypoxia along the Chinese coast in the East China Sea. *Mar. Pollut. Bull.* 167:112288. doi: 10.1016/j.marpolbul.2021.112288

Chen, C.-C., Gong, G.-C., Chiang, K.-P., Shiah, F.-K., Chung, C.-C., and Hung, C.-C. (2021a). Scaling effects of a eutrophic river plume on organic carbon consumption. *Limnol. Oceanogr.* 66, 1867–1881. doi: 10.1002/lno.11729

Chen, C.-C., Gong, G.-C., Chou, W.-C., and Shiah, F.-K. (2020). Hypoxia in autumn of the East China Sea. *Mar. Pollut. Bull.* 152:110875. doi: 10.1016/j.marpolbul.2019.110875

Chen, C.-C., Shiah, F. K., Chiang, K. P., Gong, G. C., and Kemp, W. M. (2009). Effects of the Changjiang (Yangtze) River discharge on planktonic community respiration in the East China Sea. *J. Geophys. Res. Oceans* 114:C03005. doi: 10.1029/2008jc004891

Chi, L., Song, X., Yuan, Y., Wang, W., Cao, X., Wu, Z., et al. (2020). Main factors dominating the development, formation and dissipation of hypoxia off the Changjiang Estuary (CE) and its adjacent waters, China. *Environ. Pollut.* 265:115066. doi: 10.1016/j.envpol.2020.115066

Chou, W.-C., Gong, G.-C., Cai, W.-J., and Tseng, C.-M. (2013). Seasonality of CO2 in coastal oceans altered by increasing anthropogenic nutrient delivery from alrge rivers: evidence from the Changjiang-East China Sea system. *Biogeosciences* 10, 3889–3899. doi: 10.5194/bg-10-3889-2013

Chou, W.-C., Gong, G.-C., Sheu, D.-D., Jan, S., Hung, C.-C., and Chen, C.-C. (2009). Reconciling the paradox that the heterotrophic waters of the East China Sea shelf act as a significant CO2 sink during the summertime: evidence and implications. *Geophys. Res. Lett.* 36:L15607. doi: 10.1029/2009gl038475

Chou, W.-C., Gong, G.-C., Yang, C.-Y., and Chuang, K.-Y. (2016). A comparison between field and laboratory pH measurements for seawater on the East China Sea shelf. *Limnol. Oceanogr. Methods* 14, 315–322. doi: 10.1002/lom3.10091

Clayton, T. D., and Byrne, R. H. (1993). Spectrophotometric seawater pH measurements: total hydrogen ion concentration scale calibration of m-cresol purple and at-sea results. *Deep Sea Res. Part I Oceanogr. Res. Pap.* 40, 2115–2129. doi: 10.1016/0967-0637(93)90048-8

Conley, D. J., Carstensen, J., Vaquer-Sunyer, R., and Duarte, C. M. (2009). Ecosystem thresholds with hypoxia. *Hydrobiologia* 629, 21–29. doi: 10.1007/s10750-009-9764-2

Diaz, R. J., and Rosenberg, R. (2008). Spreading dead zones and consequences for marine ecosystems. *Science* 321, 926–929. doi: 10.1126/science.1156401

Dickson, A. G., Sabine, C. L., and Christian, J. R. (eds.) (2007). *Guide to Best Practices for Ocean CO2 Measurements. PICES Special Publication 3*. Sidney, BC: North Pacific Marine Science Organization, 1–191.

Egbert, G. D., and Erofeeva, S. Y. (2002). Efficient inverse modeling of barotropic ocean tides. *J. Atmos. Ocean. Technol.* 19, 183–204.

Fennel, K., and Testa, J. M. (2019). Biogeochemical controls on coastal hypoxia. *Ann. Rev. Mar. Sci.* 11, 105–130. doi: 10.1146/annurev-marine-010318-095138

Gobler, C. J., and Baumann, H. (2016). Hypoxia and acidification in ocean ecosystems: coupled dynamics and effects on marine life. *Biol. Lett.* 12:20150976. doi: 10.1098/rsbl.2015.0976

Gong, G.-C., Liu, K. K., Chiang, K. P., Hsiung, T. M., Chang, J., Chen, C. C., et al. (2011). Yangtze River floods enhance coastal ocean phytoplankton biomass and potential fish production. *Geophys. Res. Lett.* 38:L13603. doi: 10.1029/2011gl047519

Gong, G.-C., Wen, Y.-H., Wang, B.-W., and Liu, G.-J. (2003). Seasonal variation of chlorophyll a concentration, primary production and environmental conditions in the subtropical East China Sea. *Deep Sea Res. II Top. Stud. Oceanogr.* 50, 1219–1236. doi: 10.1016/S0967-0645(03)00019-5

Gran, G. (1952). Determination of the equivalence point in potentiometric titrations. *Part II Analyst* 77, 661–671. doi: 10.1039/an9527700661

Hu, J. Y., and Wang, X. H. (2016). Progress on upwelling studies in the China seas. *Rev. Geophys.* 54, 653–673. doi: 10.1002/2015RG000505

Johnson, K. M., Wills, K. D., Butler, D. B., Johnson, W. K., and Wong, C. S. (1993). Coulometric total carbon dioxide analysis for marine studies: maximizing the performance of an automated gas extraction system and coulometric detector. *Mar. Chem.* 44, 167–187. doi: 10.1016/0304-4203(93)90201-x

Ko, D. S., Chao, S.-Y., Wu, C.-C., Lin, I. I., and Jan, S. (2016). Impacts of tides and Typhoon Fanapi (2010) on seas around Taiwan. *Terr. Atmos. Ocean. Sci.* 27, 261–280.

Ko, D. S., Martin, P. J., Rowley, C. D., and Preller, R. H. (2008). A real-time coastal ocean prediction experiment for MREA04. *J. Mar. Syst.* 69, 17–28. doi: 10.1016/j.jmarsys.2007.02.022

Levitus, S. (1982). *Climatological Atlas of the Word Ocean, NOAA Professional Paper No. 13*. Silver Spring, MD: US Government Printing Office.

Lewis, E., and Wallace, D. W. R. (1998). *Program Developed for CO2 System Calculations*. Oak Ridege, TN: Oak Ridge National Laboratory Environmental Sciences Division, Carbon Dioxide Information Analysis Center.

Li, D. J., Zhang, J., Huang, D. J., Wu, Y., and Liang, J. (2002). Oxygen depletion off the Changjiang (Yangtze River) Estuary. *Sci. China Ser. D Earth Sci.* 45, 1137–1146. doi: 10.1360/02yd9110

Li, D., Chen, J., Ni, X., Wang, K., Zeng, D., Wang, B., et al. (2019). Hypoxic bottom waters as a carbon source to atmosphere during a typhoon passage over the East China Sea. *Geophys. Res. Lett.* 46, 11329–11337. doi: 10.1029/2019GL083933

Li, X. X., Bianchi, T. S., Yang, Z. S., Osterman, L. E., Allison, M. A., Dimarco, S. F., et al. (2011). Historical trends of hypoxia in Changjiang River estuary: applications of chemical biomarkers and microfossils. *J. Mar. Syst.* 86, 57–68. doi: 10.1016/j.jmarsys.2011.02.003

Liu, Z., and Gan, J. (2015). Upwelling induced by the frictional stress curl and vertical squeezing of the vortex tube over a submerged valley in the East China Sea. *J. Geophys. Res. Oceans* 120, 2571–2587. doi: 10.1002/2015JC010715

Lü, X. G., Qiao, F. L., Xia, C. S., Zhu, J. R., and Yuan, Y. L. (2006). Upwelling off Yangtze River estuary in summer. *J. Geophys. Res.* 111:C11S08. doi: 10.1029/2005JC003250

Martin, P. J. (2000). *Description of the Navy Coastal Ocean Model Version 1.0*. Stennis Space Center, MS: Naval Research Laboratory.

Ni, X., Huang, D., Zeng, D., Zhang, T., Li, H., and Chen, J. (2016). The impact of wind mixing on the variation of bottom dissolved oxygen off the Changjiang Estuary during summer. *J. Mar. Syst.* 154, 122–130. doi: 10.1016/j.jmarsys.2014.11.010

Obenour, D. R., Scavia, D., Rabalais, N. N., Turner, R. E., and Michalak, A. M. (2013). Retrospective analysis of midsummer hypoxic area and volume in the northern Gulf of Mexico, 1985-2011. *Environ. Sci. Technol.* 47, 9808–9815. doi: 10.1021/es400983g

Pai, S.-C., Gong, G.-C., and Liu, K.-K. (1993). Determination of dissolved oxygen in seawater by direct spectrophotometry of total iodine. *Mar. Chem.* 41, 343–351. doi: 10.1016/0304-4203(93)90266-Q

Parsons, T. R., Maita, Y., and Lalli, C. M. (1984). *A Manual of Chemical and Biological Methods for Seawater Analysis*. New York, NY: Pergamon Press.

Pierrot, D. E., Levis, E., and Wallace, D. W. R. (2006). *MS Excel Program Developed for CO2 System Calculations*. Oak Ridge, TN: U.S. Department of Energy: Carbon Dioxide Information Analysis Center, Oak Ridge National Laboratory.

Rabalais, N. N., Turner, R. E., and Wiseman, W. J. Jr. (2002). Gulf of Mexico hypoxia, a.k.a. "The dead zone". *Annu. Rev. Ecol. Syst.* 33, 235–263. doi: 10.1146/annurev.ecolsys.33.010802.150513

Rosmond, T. E. (1992). The design and testing of the navy operational global atmospheric prediction system. *Weather Forecast.* 7, 262–272.

Scavia, D., Bertani, I., Obenour, D. R., Turner, R. E., Forrest, D. R., and Katin, A. (2017). Ensemble modeling informs hypoxia management in the northern Gulf of Mexico. *Proc. Natl. Acad. Sci. U.S.A.* 114, 8823–8828. doi: 10.1073/pnas.1705293114

Tseng, Y.-F., Lin, J., Dai, M., and Kao, S.-J. (2014). Joint effect of freshwater plume and coastal upwelling on phytoplankton growth off the Changjiang River. *Biogeosciences* 11, 409–423. doi: 10.5194/bg-11-409-2014

Vaquer-Sunyer, R., and Duarte, C. M. (2008). Thresholds of hypoxia for marine biodiversity. *Proc. Natl. Acad. Sci. U.S.A.* 105, 15452–15457. doi: 10.1073/pnas.0803833105

Wang, B. (2009). Hydromorphological mechanisms leading to hypoxia off the Changjiang estuary. *Mar. Environ. Res.* 67, 53–58. doi: 10.1016/j.marenvres.2008.11.001

Wang, B., Chen, J. F., Jin, H. Y., Li, H. L., Huang, D. J., and Cai, W. J. (2017). Diatom bloom-derived bottom water hypoxia off the Changjiang estuary, with and without typhoon influence. *Limnol. Oceanogr.* 62, 1552–1569. doi: 10.1002/lno.10517

Wang, H., Dai, M., Liu, J., Kao, S.-J., Zhang, C., Cai, W.-J., et al. (2016). Eutrophication-driven hypoxia in the East China Sea off the Changjiang estuary. *Environ. Sci. Technol.* 50, 2255–2263. doi: 10.1021/acs.est.5b06211

Wei, Q. S., Wang, B. D., Chen, J. F., Xia, C. S., Qu, D. P., and Xie, L. P. (2015). Recognition on the forming-vanishing process and underlying mechanisms of the hypoxia off the Yangtze River estuary. *Sci. China Ser. D Earth Sci.* 58, 628–648. doi: 10.1007/s11430-014-5007-0

Xiong, T., Wei, Q., Zhai, W., Li, C., Wang, S., Zhang, Y., et al. (2020). Comparing subsurface seasonal deoxygenation and acidification in the Yellow Sea and northern East China Sea along the north-to-south latitude gradient. *Front. Mar. Sci.* 7:686. doi: 10.3389/fmars.2020.00686

Xu, Q., Zhang, S., Cheng, Y., and Zuo, J. (2017). Interannual feature of summer upwelling around the Zhoushan Islands in the East China Sea. *J. Coast. Res.* 33, 125–134. doi: 10.2112/JCOASTRES-D-15-00197.1

Zhang, S., Jin, S., Zhang, H., Fan, W., Tang, F., and Yang, S. (2016). Distribution of bottom trawling effort in the Yellow Sea and East China Sea. *PLoS One* 11:e0166640. doi: 10.1371/journal.pone.016664

Zhang, W., Wu, H., Hetland, R., and Zhu, Z. (2019). On Mechanisms Controlling the Seasonal Hypoxia Hot Spots off the Changjiang River Estuary. *J. Geophys. Res. Oceans* 124, 8683–8700. doi: 10.1029/2019JC015322

Zhao, B. R., Ren, G. F., Cao, D. M., and Yang, Y. L. (2001). Characteristics of the ecological environment in upwelling area adjacent to the Changjiang River estuary. *Oceanol. Limnol. Sin.* 32, 327–333. (in Chinese with English abstract),

Zhu, Z.-Y., Wu, H., Liu, S.-M., Wu, Y., Huang, D.-J., Zhang, J., et al. (2017). Hypoxia off the Changjiang (Yangtze River) estuary and in the adjacent East China Sea: quantitative approaches to estimating the tidal impact and nutrient regeneration. *Mar. Pollut. Bull.* 125, 103–114. doi: 10.1016/j.marpolbul.2017.07.029

Conflict of Interest: The authors declare that the research was conducted in the absence of any commercial or financial relationships that could be construed as a potential conflict of interest.

Publisher's Note: All claims expressed in this article are solely those of the authors and do not necessarily represent those of their affiliated organizations, or those of the publisher, the editors and the reviewers. Any product that may be evaluated in this article, or claim that may be made by its manufacturer, is not guaranteed or endorsed by the publisher.

Copyright © 2022 Chen, Ko, Gong, Lien, Chou, Lee, Shiah and Huang. This is an open-access article distributed under the terms of the Creative Commons Attribution License (CC BY). The use, distribution or reproduction in other forums is permitted, provided the original author(s) and the copyright owner(s) are credited and that the original publication in this journal is cited, in accordance with accepted academic practice. No use, distribution or reproduction is permitted which does not comply with these terms.

frontiers in Marine Science

ORIGINAL RESEARCH
published: 07 February 2022
doi: 10.3389/fmars.2022.824303

Primary Productivity in the Mid-Atlantic Bight: Is the Shelf Break a Location of Enhanced Productivity?

Jiejie Ma[1] *and Walker O. Smith Jr.*[1,2]*

[1] School of Oceanography, Shanghai Jiao Tong University, Shanghai, China, [2] Virginia Institute of Marine Science, William & Mary, Gloucester Point, VA, United States

Estimates of primary production represent the input of carbon into food webs, as well as the initial step in the biological pump. For the past 60 years, much of the productivity information has been obtained using measurements of ^{14}C-bicarbonate removal during simulated in situ incubations. However, such measurements often do not reflect the complexity of the environment, and also suffer from uncertainties, biases and limitations. A vertically resolved bio-optical model has been used to estimate productivity based on profiles commonly assessed in oceanographic investigations, but comparisons with simultaneous measurements of ^{14}C-uptake are limited. We conducted three cruises off the coast of New England that included sampling continental shelf waters, the shelf-break region, and deeper waters at scales of 7 km, all of which had productivity estimated by a vertically resolved productivity model as well as by traditional ^{14}C-uptake measurements using simulated in situ techniques. We found that the vertically resolved bio-optical model gave results that appear to be more robust and resolved productivity at smaller vertical and horizontal scales, and seem less biased by some of the uncertainties in ^{14}C-uptake measurements. Both estimates suggest that the New England waters are highly productive due to a variety of biological and physical processes occurring at different times of the year, but there was no consistent stimulation at the shelf break over the time scales of these estimates.

Keywords: primary productivity, Mid-Atlantic Bight, vertically resolved model, temperature, chlorophyll, ^{14}C-uptake, continental shelf

OPEN ACCESS

Edited by:
Kuoping Chiang, National Taiwan Ocean University, Taiwan

Reviewed by:
Frank Dehairs, Vrije University Brussel, Belgium
Terry Whitledge, Retired, Fairbanks, AK, United States

***Correspondence:**
Walker O. Smith Jr.
wos@vims.edu

Specialty section:
This article was submitted to Coastal Ocean Processes, a section of the journal Frontiers in Marine Science

Received: *29 November 2021*
Accepted: *13 January 2022*
Published: *07 February 2022*

Citation:
Ma J and Smith WO Jr (2022) Primary Productivity in the Mid-Atlantic Bight: Is the Shelf Break a Location of Enhanced Productivity? Front. Mar. Sci. 9:824303. doi: 10.3389/fmars.2022.824303

INTRODUCTION

The Mid-Atlantic Bight (MAB) continental shelf supports extensive and productive fisheries (O'Reilly and Busch, 1984; Townsend et al., 2006). The diverse and productive ecosystem results from a number of processes, such as the fluxes onto the shelf of nutrient-rich deep waters, convective mixing, and land-based nutrient inputs, all of which stimulate primary productivity. The region is characterized by relatively high chlorophyll concentrations, which vary substantially over broad spatial and temporal scales. A winter phytoplankton bloom occurs on the middle and outer shelf, while a spring bloom occurs on the outer shelf-break and slope region (Yoder et al., 1993, 2001, 2002; Xu et al., 2011; Zhang et al., 2013). Summer conditions tend to be oligotrophic throughout the shelf and slope regions.

Frontal systems play a significant role in many continental shelf regions, as they separate cool and fresh shelf water from the more saline slope waters, resulting in biological and physical differences between these two regions (Linder and Gawarkiewicz, 1998; Xu et al., 2011; Zhang et al., 2013). The shelf-slope front in the Mid-Atlantic Bight persists over the entire annual cycle, albeit with a different structure, extending from the bottom to the surface in winter, and in summer between the bottom to the seasonal thermocline (Marra et al., 1982; Houghton et al., 1988; Linder and Gawarkiewicz, 1998; Lozier and Gawarkiewicz, 2001). Fontal systems have also been implicated as an important potential site of upwelling (Linder and Gawarkiewicz, 1998), and hence may be loci for enhanced biological activity.

A number of mechanisms have been suggested to drive upwelling at the shelf break (Linder et al., 2004; Zhang et al., 2011; Zhang and Gawarkiewicz, 2015). Despite the potential for upwelling, monthly satellite composites do not show enhanced mean chlorophyll concentrations at the shelf break (Zhang et al., 2013; Oliver et al., 2022), and only a few images show a clear shelf-break enhancement (Ryan et al., 1999a,b). This may result from either the short duration of upwelling and its biological effects (Oliver et al., 2022), enhanced phytoplankton growth and accumulation below the depth of satellite detection, or the rapid removal of phytoplankton by zooplankton grazing (Zhang et al., 2013). Deep waters (near the 1% isolume) have been shown to be dominant features in summer offshore waters influenced by warm core ring intrusions (Oliver et al., 2021), but the importance of deep production as a general feature has not been established.

We focus on the estimation of primary production and analyze whether the chlorophyll and productivity are enhanced at the shelf break. Primary productivity has traditionally been assessed by short (24 h or less) measurements of ^{14}C-uptake. The method is simple, and has been applied by numerous investigators over broad areas of the ocean and has provided a valuable data set to assess photosynthesis in the ocean (Marra et al., 2021). However, questions remain on the interpretation of these incubations (Marra et al., 1990, 2021; Marra and Barber, 2004). For example, the quantitative impact of phytoplankton respiration remains unclear, and variations among studies with regard to the starting time of incubations, length of incubations, size of bottles, measurement of dissolved organic carbon release during incubations, and temperature control during incubations remain. As a result, comparison among different studies is problematic. Regardless, previous estimates of productivity of the mid-Atlantic Bight region suggested that the annual rate of production is about 12 mol C m^{-2} ($\pm$20%) (Marra et al., 1992). Daily estimates can exceed 2 g C m^{-2} d^{-1}.

Satellite estimates of chlorophyll have driven the development of new means of estimating productivity. Behrenfeld and Falkowski (1997a,b) described a method to estimate integrated productivity based solely on euphotic zone chlorophyll (estimated from chlorophyll concentrations in the upper water column), sea surface temperature, and photosynthetically active radiation (PAR), all of which are coupled to an established photosynthesis model. This method allows for far greater spatial and temporal resolution of primary productivity than can be obtained from discrete sampling, and is a powerful indication of how much carbon is being fixed into particulate matter over broad regions of the ocean. A second, related method is the vertically resolved method of estimating productivity, which again uses temperature, chlorophyll concentrations, and PAR in combination with a photosynthesis model. This allows for the primary productivity to be estimated throughout the water column at discrete depths and then integrated to give daily productivity estimates, and can be applied to different locations where highly resolved chlorophyll and temperature data are available (e.g., from closely spaced CTD measurements; Oliver et al., 2021; Smith et al., 2021). Such a method allows for the incorporation of small-scale features (e.g., narrow chlorophyll maxima) to be included in estimates of integrated productivity (Oliver et al., 2021), as well as to more reliably account for vertical temperature changes. Various algorithms to estimate primary productivity have been developed and compared (Campbell et al., 2002). They found that the algorithms tested generally were within a factor of two when compared to ^{14}C-uptake measurements, and that the performance of algorithms was independent of the algorithm's complexity.

We investigated the primary productivity on the continental shelf and the slope in the Mid-Atlantic Bight (**Figure 1**) and hypothesized that the continental shelf break would be a site of enhanced primary productivity, despite its lack of appearance in satellite chlorophyll images or composites. Oliver et al. (2022) showed that wind-driven events of short (a few days) durations could enhance productivity at the shelf break by enhancing frontal stratification, but a complete assessment of the importance of these events on longer time scales was not conducted. To test the importance of the shelf-break productivity relative to that on the shelf and slope, we analyzed productivity by three methods: simulated in situ incubations using a vertically resolved bio-optical model,^{14}C-uptake measurements, and surface variable estimates.

MATERIALS AND METHODS

We conducted three cruises as part of the SPIROPA project (Shelf-break Productivity Interdisciplinary Research Operation at the Pioneer Array). The cruises were conducted in early spring (April 16–29, 2018 on the *R.V. Armstrong*), one in late spring (May 12–25, 2019 on the *R.V. Brown*) and one in summer (July 06–18, 2019 on the *R.V. Thompson*; **Figure 1**). A total of 161, 109, and 125 CTD casts were completed in the three cruises, with 11, 9, and 11 transects generally sampling from location A5 to A18, respectively (**Figure 1**). A majority of stations were occupied along a 125 km north-south transect perpendicular to the shelf break at 70.8°W (**Figure 1**). Station spacing was ca. 7 km, allowing the observation of mesoscale and sub-mesoscale processes. Twenty-four, 24 and 23 stations were sampled for ^{14}C-incubations during the early spring (AR29), late spring (RB1904) and summer (TN368; **Supplementary Table 1**).

At each station, water was collected using a CTD-rosette system that had 24 10-L Niskin bottles, a PAR sensor, fluorometer, and transmissometer. Surface PAR data were

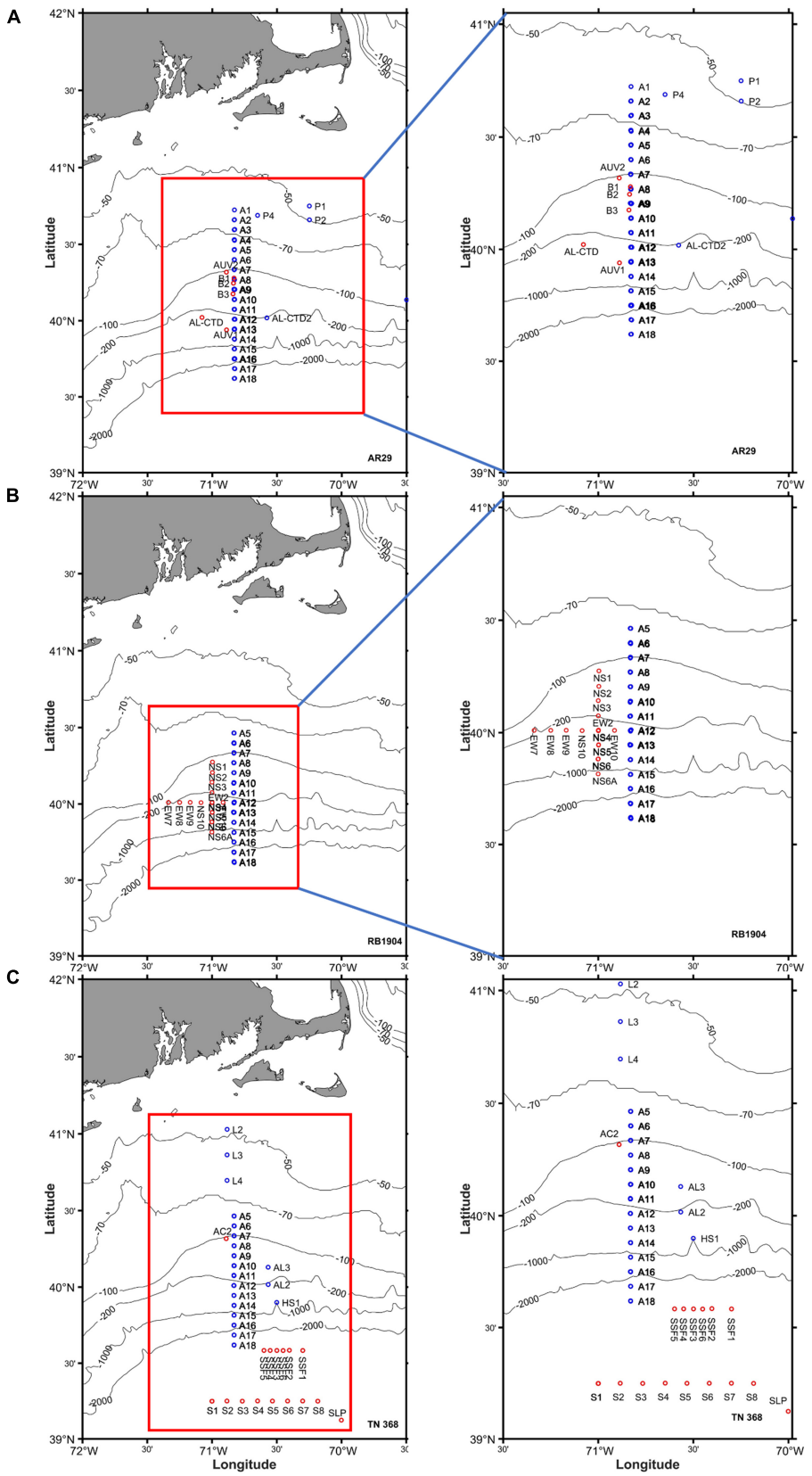

FIGURE 1 | The locations of CTD stations occupied during **(A)** AR29, **(B)** RB1904, and **(C)** TN368 on the continental shelf and the slope waters off New England.

collected continuously using a BioSpherical Model 240 quantum sensor. Water sampling depths were either standard depths (0, 10, 20, 30, 40, 50, 70, 100, 125, 150, 200, 250, and 500 m) or depths chosen by irradiance levels (selected during the down cast) for isotopic productivity determinations. Euphotic depths were the depths to which 1% irradiance of surface irradiance penetrated. Mixed layer depths were determined from the depth which increased by 0.03 σ_T units from the 5 m value. The σ_T values were irregular at some stations in the Armstrong cruise; therefore, a mean σ_T value in the upper 10 m was used to determine surface layer density. The location of the front was determined as the 34.5 isohaline (Zhang et al., 2013). The main transects were divided into inshore, frontal and offshore zones based on the 34.5 isohaline location (shelf-break stations were defined as those within 15 km on each side of 34.5 isohaline and generally included 2 stations on each side of the front). Isolumes chosen for productivity measurements were 100, 50, 25, 15, 5, 1, and 0.1% of surface irradiance. Water samples were collected for nutrients, chlorophyll, particulate organic carbon and nitrogen, biogenic silica, and phytoplankton taxonomy. Nutrients were filtered through polycarbonate filters, placed in acid-washed 50 mL polycarbonate bottles, frozen and analyzed using automated procedures at the Woods Hole Nutrient Facility. Chlorophyll samples were filtered through 25 mm Whatman GF/F filters under low pressure and frozen in liquid nitrogen for later analyses. Samples were extracted in 90% acetone and analyzed by fluorometry, and the fluorometer calibrated using commercially purified chlorophyll *a* (Knap et al., 1996). Particulate organic carbon and nitrogen samples were filtered through combusted (450°C for 4 h) 25 mm GF/F filters, rinsed with ca. 5 mL 0.01N HCl in filtered seawater, placed in combusted glass vials, and covered with combusted aluminum foil. Samples were dried at 60°C and analyzed on a Costech ECS Model 4010 elemental analyzer (Gardner et al., 2000).

Productivity was also measured using ^{14}C-uptake (Smith et al., 2000, 2021). Briefly, samples were collected from known isolumes and placed into sterile 280 mL Qorpak bottles to which ca. 100 μCi $NaH^{14}CO_3$ were added (pH = 9.6). Bottles were then placed in an incubator through which surface seawater flowed and which had tubes wrapped with neutral density screening to reduce irradiance to that of the sampling depth. Incubations lasted 24 h. Most incubations were started prior to local noon. After incubation, samples were filtered through 25 mm GFF filters, which were rinsed with 0.01N HCL in seawater to remove inorganic carbon from the filter. Filters were placed in 7 mL scintillation vials and had 5 mL Ecolume® added. All samples were kept in the dark for at least 24 h to reduce chemiluminescence. The total amount of added isotope was quantified from a sample of 0.1 mL unfiltered sample placed into a scintillation vial. All samples were counted on a scintillation counter and the counts converted into carbon units.

Productivity was also modeled using two methods. The first was a model that originally used satellite estimates of surface temperature, chlorophyll concentrations and daily PAR information combined with a photosynthesis model to predict productivity (Behrenfeld and Falkowski, 1997a; Campbell et al., 2002). We used our surface CTD observations of surface temperatures and chlorophyll along with the measured PAR to estimate productivity in this manner. We also generated vertically resolved estimates of productivity using the CTD data from our casts and the measured PAR. Fluorescence values were converted to chlorophyll concentrations by regressing the extracted chlorophyll concentrations with the fluorescence values at the same depth. At each depth the available PAR was either measured or calculated from attenuation coefficients, and P^B_{opt} values derived from temperature (Behrenfeld and Falkowski, 1997b). PAR and P^B_{opt} values were used to calculate the photosynthetic rates using a hyperbolic tangent photosynthesis model (Platt and Jassby, 1976) at 1-m intervals and converted to carbon units using the vertical chlorophyll distributions. Photoinhibition effects were included using the relationship determined by Behrenfeld and Falkowski (1997b). Daily productivity was derived by integrating the rates through the 1% isolume depth (Oliver et al., 2021; Smith et al., 2021). All variables of both models are listed in **Table 1**.

RESULTS

Vertical Distributions of Temperature, σ_t, Chlorophyll, and Nitrate

The temperature ranges encountered during AR29, RB1904 and TN368 cruises were 5.9– 18.3, 5.6 – 20.9, and 7.0 – 25.8°C, respectively (**Figures 2**, **3**, **4**; additional sections provided in **Supplementary Figures 1–3**). A salinity front generally separated coastal waters from the more saline, Gulf Stream waters and at times restricted water movement off the shelf, but the strength and location of the front varied temporally (**Figures 2–4**; transects near the beginnings and ends of the three cruises). During the summer the 34.5 isohaline did not penetrate to the surface, so the location of the front was chosen as the shallowest penetration of that isohaline. These sections were chosen to help us to understand how temperature, the position of front and chlorophyll affect primary productivity (**Figures 2–4**).

TABLE 1 | The variables used in the two bio-optical models and their units, and the types of primary productivity estimates.

Variable	Abbreviation	Units
Photosynthetically active radiation	PAR	mol photons m^{-2} d^{-1}
Depth of euphotic zone	Z_{eu}	m
Maximum photosynthetic rate	P^B_{opt}	mg C (mg Chl) $^{-1}$ h^{-1}
Sea surface irradiance	E_0	mol photons m^{-2} d^{-1}
Percentage of photoinhibition	*Inh*	%
Chlorophyll concentration	C_z	μg L^{-1}
Photoperiod	DL	h
Euphotic zone primary productivity estimated by vertically resolved productivity model	PP_1	mg C m^{-2} d^{-1}
Euphotic zone primary productivity estimated by ^{14}C-uptake measurements	PP_2	mg C m^{-2} d^{-1}
Euphotic zone primary productivity by surface variable productivity model	PP_3	mg C m^{-2} d^{-1}

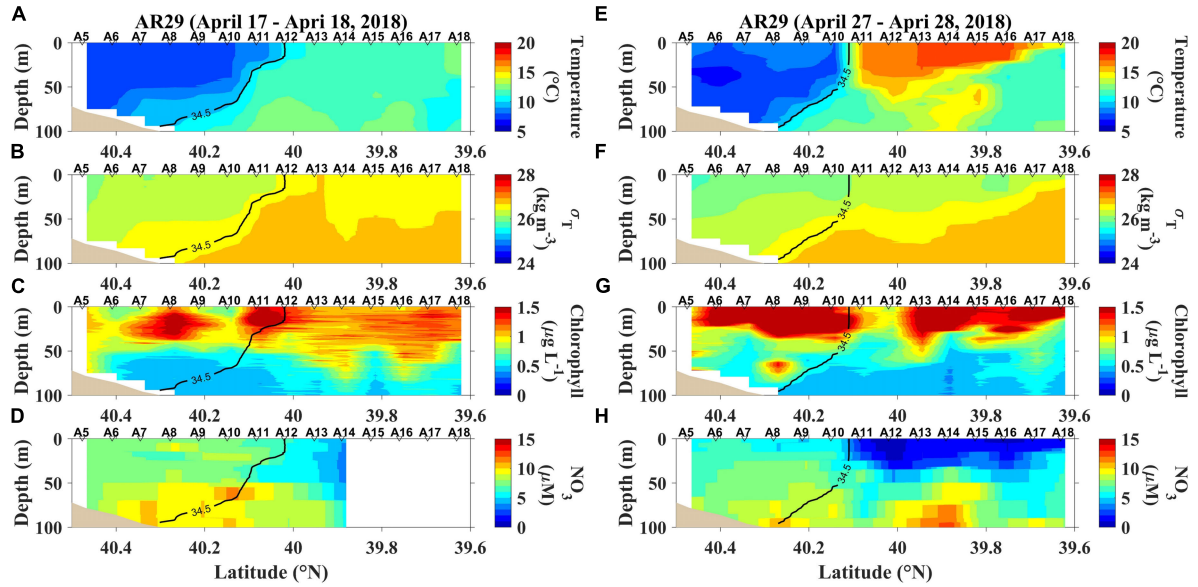

FIGURE 2 | The first and last section occupied during AR29. **(A)** temperature, **(B)** density (expressed as σ_T), **(C)** chlorophyll and **(D)** nitrate concentrations (NO_3) sampled from April 17–18, 2018, and **(E)** temperature, **(F)** density (expressed as σ_T), **(G)** chlorophyll and **(H)** nitrate concentrations (NO_3) sampled from April 27–28, 2018.

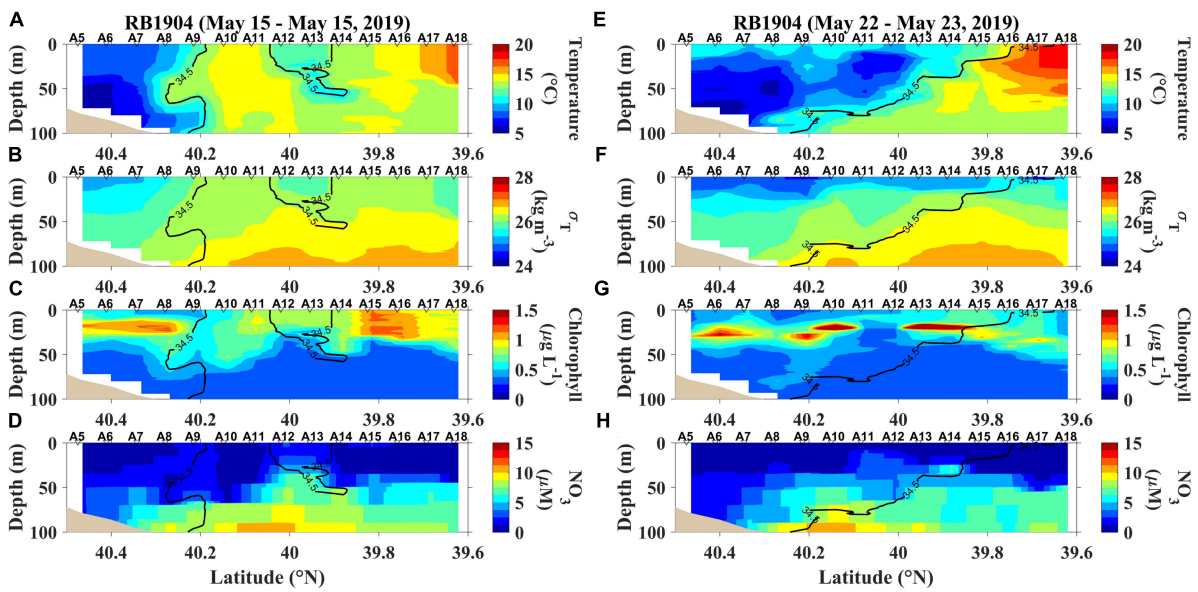

FIGURE 3 | The first and last section occupied during RB1904; **(A)** temperature, **(B)** density (expressed as σ_T), **(C)** chlorophyll and **(D)** nitrate concentrations (NO_3) sampled on May 15, 2019, and **(E)** temperature, **(F)** density (expressed as σ_T), **(G)** chlorophyll and **(H)** nitrate concentrations (NO_3) sampled from May 22–23, 2019.

Temperature increased markedly from inshore to offshore during AR29 (**Figures 2A,E**), and on April 25, 2018, the offshore area was substantially warmer (> 15°C; **Supplementary Figure 1**) than that inshore. The inner shelf's chlorophyll was initially relatively low, but increased through time. Chlorophyll in offshore waters was elevated during the entire cruise. From April 17 to April 24, offshore movement of the front (the position of the 34.5 isohaline) was consistent with a westward motion of the front oriented in a WNW-ESE direction. The spring inshore bloom was at times dominated by *Phaeocystis pouchetii,* but the chlorophyll offshore was dominated by diatoms (Smith et al., 2021). Nitrate concentrations exceeded 5 μM inshore but less in offshore waters. By the end of the cruise offshore water nitrate concentrations were less than 1 μM (**Figures 2D,H**).

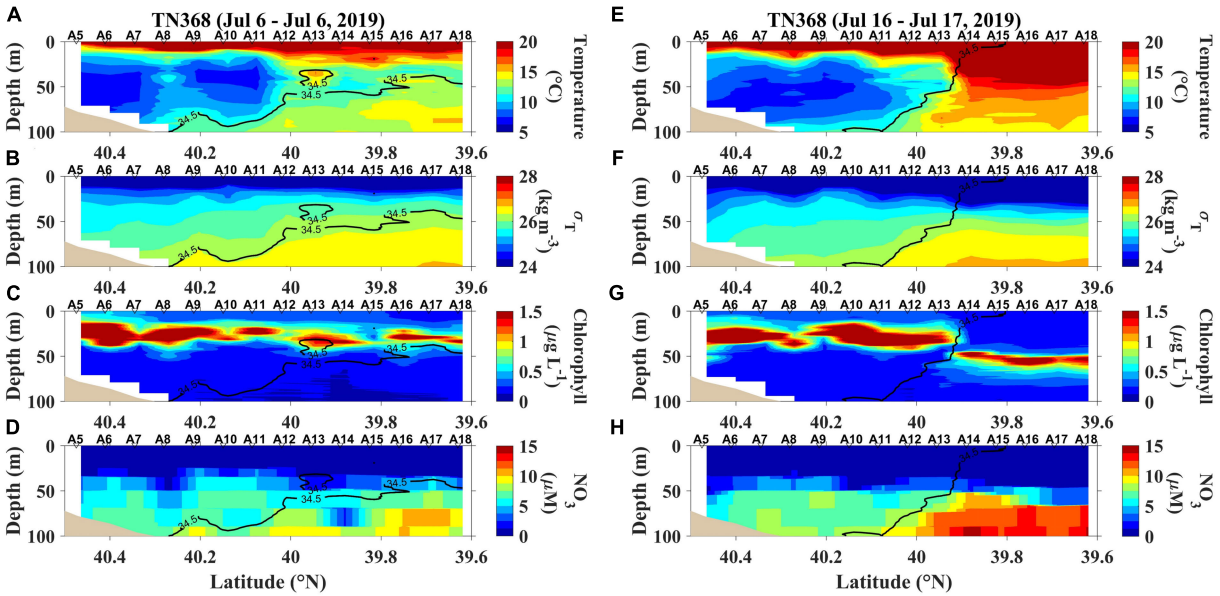

FIGURE 4 | The first and last section occupied during TN368; **(A)** temperature, **(B)** density (expressed as σ_T), **(C)** chlorophyll and **(D)** nitrate concentrations (NO_3) sampled on July 6, 2019, and **(E)** temperature, **(F)** density (expressed as σ_T), **(G)** chlorophyll and **(H)** nitrate concentrations (NO_3) sampled from July 16–17, 2019.

During RB1904, we observed two shelf-break eddies (**Figure 3**). From May 22-May 23 the subsurface shelf water was indicative of upwelling at the front, resulting in high nitrate water from the deeper part of the shelf being brought into the euphotic zone. A warm-core ring to the southeast of our sampling propagated north and west during sampling, which caused upwelling and may have led to substantial chlorophyll enhancement. The chlorophyll is enhanced by May 17 due to the effect of the ring streamer (**Supplementary Figure 2**). High abundance of diatoms also was observed at the offshore edge of the front during RB1904 (Oliver et al., 2022). Nitrate concentrations were low (2 μM or less) in the surface layer, but during the first transect a clear increase was noted in the frontal region (**Figure 3D**).

During TN368, surface temperatures were increased by solar radiation absorption and in turn generated strong stratification in the upper 30 m throughout the entire transect (**Figure 4**). Low-salinity shelf water was pulled southward by the ring streamer, and the 34.5 isohaline didn't reach the surface (**Figure 4**). The stratification flattened isopycnals in the upper ocean (**Figure 4**), facilitating exchange of water masses across the front. As a result, the shelf water characteristics in the surface layer extended to station A18 (**Figure 4** and **Supplementary Figure 3**). The strong stratification reduced the transport of nutrients into the surface layer, leading to low surface chlorophyll levels and elevated subsurface chlorophyll accumulations (**Figure 4**). Nitrate concentrations were very low (<0.5 μM in the upper 25 m) over the entire transect (**Figure 4D,H**).

Chlorophyll concentrations in the frontal area averaged ~1.2 μg L^{-1} in early spring, 0.8 μg L^{-1} in late spring, and 0.7 μg L^{-1} in summer, although they were not statistically different (**Figure 5**). In AR29 chlorophyll concentrations averaged 1.2, 1.1, and 1.1 μg L^{-1} in the three regions. Mean chlorophyll concentrations in offshore waters decreased through time (from 1.2 to 0.4 μg L^{-1}). In summer, chlorophyll generally decreased with distance from the coast: 0.9 μg L^{-1} in inshore areas, 0.6 μg L^{-1} at the front and 0.4 μg L^{-1} in offshore areas (**Figure 5**), whereas there was no marked trend in early and late spring. There was no obvious chlorophyll enhancement at the front in any season based on mean chlorophyll levels.

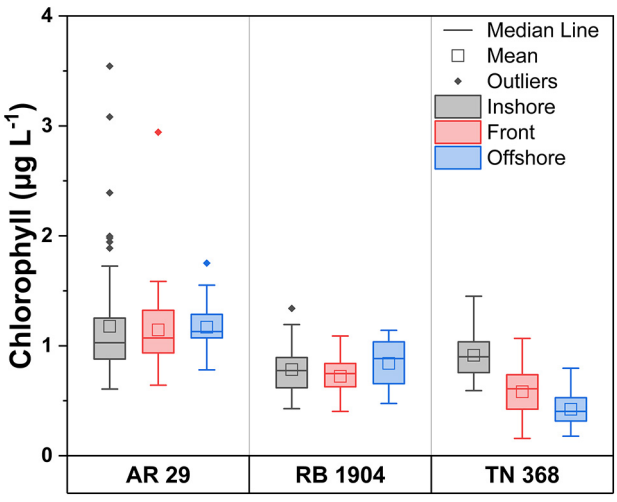

FIGURE 5 | The distribution of chlorophyll at stations inshore of the front, near the front, and offshore of the front within the three cruises. The dots outside of the boxes are extreme values that were not included in the means. Error bars represent the standard deviations.

Productivity Estimates

Primary productivity was measured using a vertically resolved bio-optical model (PP_1), ^{14}C-uptake incubations (PP_2), and surface variable estimates (PP_3; **Tables 2–4**). The euphotic zone depths (and standard deviations) were 40.7 ± 12.2, 35.2 ± 6.6, and 39.2 ± 9.3 m during the AR29, RB1904, and TN368 cruises, suggesting that light reached similar depths in each cruise to support water column photosynthesis. Mixed layer depths decreased from early spring to summer due to the temperature effects on stratification. At most stations, the primary productivity measured via ^{14}C-incubations was greater than the estimates of either the vertically resolved model or the surface variable estimates (**Tables 2–4**), but certainly within the range based on the Campbell et al. (2002) comparison. The average primary productivity was measured by ^{14}C-incubations in early spring was ca. 1,560 mg C m^{-2} d^{-1}, and decreased to 1,090 mg C m^{-2} d^{-1} in late spring and 456 mg C m^{-2} d^{-1} in summer. The vertically resolved model productivity averaged 575, 444, and 292 mg C m^{-2} d^{-1} in AR29, RB1904, and TN368. Primary productivity estimated from surface parameters was larger than those of the vertically resolved model and similar to those measured isotopically: 1,510, 1,000 and 524 mg C m^{-2} d^{-1} during the three cruises.

As assimilation numbers (productivity per unit chlorophyll) are influenced by nutrients, we investigated the relationship of the maximum assimilation number within those stations where ^{14}C-incubations were completed and nitrate concentrations at that isolume (data not shown). We found no significant correlation in any cruise, suggesting nutrients did not have a major impact on regulating maximum photosynthetic rates.

The Distribution of Primary Productivity

The distribution of primary productivity in early spring increased from inshore to offshore when estimated by the bio-optical model and surface variables estimates, but the ^{14}C-estimates suggested a slight productivity enhancement near the front (**Figure 6**). Individual transects derived from the vertically resolved model suggested a temporary enhancement as well (**Figures 6**, **7**). In late spring the same spatial trend with chlorophyll occurred: an increase with distance from the coast.

TABLE 2 | Primary productivity during AR29.

Cast	Date	Location	SSS	SST (°C)	PAR_s (mol photons m^{-2} d^{-1})	Z_{eu} (m)	Z_{mix} (m)	Chl *a* (μg L^{-1})	PP_1 (mg C m^{-2} d^{-1})	PP_2 (mg C m^{-2} d^{-1})	PP_3 (mg C m^{-2} d^{-1})
Inshore											
5	2018/4/17	A7	33.47	7.58	51.2	30	36	1.08	365	602	722
15	2018/4/18	A5	33.33	7.10	50.8	36	58	1.08	471	1,273	1,002
41	2018/4/20	A5	33.24	6.71	66.5	35	66	1.01	374	1,138	910
60	2018/4/21	A9	33.39	7.30	65.5	36	38	0.91	328	178	914
70	2018/4/22	A6	33.23	6.75	67.3	37	56	0.92	347	109	825
129	2018/4/26	A2	32.99	6.95	54.0	26	9	2.90	197	646	466
Front											
9	2018/4/17	A10	33.62	7.95	47.9	40	37	0.73	411	179	814
16	2018/4/18	A14	34.90	11.14	42.8	53	75	1.01	910	2,793	1,562
29	2018/4/19	A13	34.12	9.17	21.0	47	14	1.23	1411	1,065	2,142
33	2018/4/19	A12	33.73	8.17	38.1	44	28	0.97	629	1,359	1,062
42	2018/4/20	A14	35.47	13.54	67.1	36	74	1.54	909	1,340	2,102
65	2018/4/21	A13	34.18	9.35	65.5	35	15	1.07	439	483	916
77	2018/4/22	A13	34.03	9.39	65.8	32	9	1.38	460	2,470	732
83	2018/4/23	A13	33.91	8.98	64.1	31	5	1.54	741	2,398	1,336
87	2018/4/23	A12	33.84	9.08	64.5	40	11	1.13	451	2,957	914
112	2018/4/25	A11	33.58	8.65	12.8	48	21	1.04	529	1,293	1,145
152	2018/4/27	A10	33.32	7.98	52.4	39	19	1.54	453	3,570	1,499
Offshore											
19	2018/4/18	A16	35.00	11.67	28.5	55	63	1.13	1,282	2,113	1,880
114	2018/4/25	A16	35.81	16.79	22.5	49	24	1.21	1,181	1,259	3,213
131	2018/4/26	A16	34.69	11.79	44.1	33	13	1.90	566	4,010	1,585
143	2018/4/27	A18	35.24	13.90	29.2	59	5	0.78	706	1,773	3,791
148	2018/4/27	A14	35.95	17.43	41.2	53	26	1.07	1,111	383	4,314
Others											
100	2018/4/24	AUV2	33.37	8.75	35.2	56	8	0.69	461	1,263	786
102	2018/4/24	AL-CTD	33.44	8.76	13.3	35	6	1.44	511	2,704	927

SSS = sea surface salinity; SST = sea surface temperature; PAR_s = surface photosynthetically active radiation; Z_{eu} = euphotic zone depth; Z_{mix} = mixed layer depth; Chl a = mean euphotic zone depth chlorophyll a; PP_1 = primary productivity estimated from the vertically resolved productivity model; PP_2 = primary productivity estimated from ^{14}C-incubations; PP_3 = primary productivity estimated from surface variables.

TABLE 3 | Primary productivity during RB1904.

Cast	Date	Station Location	SSS	SST (°C)	PAR_s (mol photons m^{-2} d^{-1})	Z_{eu} (m)	Z_{mix} (m)	Chl *a* (μg L^{-1})	PP_1 (mg C m^{-2} d^{-1})	PP_2 (mg C m^{-2} d^{-1})	PP_3 (mg C m^{-2} d^{-1})
Inshore											
13	2019/5/14	A5	32.56	8.10	35.5	31	26	0.72	327	913	634
14	2019/5/14	A6	33.26	9.85	36.0	34	13	0.56	295	921	525
16	2019/5/14	A7	32.87	8.57	36.8	34	25	0.59	277	931	452
43	2019/5/17	A10	32.89	7.37	53.7	52	6	0.56	416	1,310	831
44	2019/5/17	A9	33.47	10.3	53.7	33	12	0.60	283	1,337	572
69	2019/5/19	A12	33.37	11.4	70.6	38	10	0.69	350	913	945
76	2019/5/20	A10	32.39	8.87	69.0	38	12	0.63	344	3,401	1,034
78	2019/5/20	A12	33.24	10.8	69.0	26	12	1.34	377	2,186	864
94	2019/5/22	A12	32.51	9.58	64.7	31	7	0.46	194	498	517
95	2019/5/22	A11	32.95	10.6	61.4	34	5	0.43	205	363	598
98	2019/5/22	A8	32.29	10.4	52.5	45	10	0.52	279	473	548
102	2019/5/23	A5	32.46	11.1	28.1	44	13	0.52	343	279	580
Front											
24	2019/5/15	A11	34.93	14.1	61.0	33	27	0.86	546	1,674	1,381
25	2019/5/15	A10	35.08	14.6	59.8	34	60	0.65	409	626	967
27	2019/5/15	A9	34.32	12.0	60.0	36	10	0.54	312	500	716
34	2019/5/16	A12	34.10	11.5	65.6	45	15	0.64	515	664	1,130
41	2019/5/17	A12	34.19	12.2	50.5	32	15	0.88	580	2,063	1,320
79	2019/5/20	A13	33.95	12.7	68.8	27	16	0.83	236	794	519
Offshore											
9	2019/5/13	A13	33.70	10.2	33.3	39	6	0.59	438	1,032	816
32	2019/5/16	A18	35.87	17.8	59.2	29	31	1.12	735	823	1,854
86	2019/5/21	A18	35.12	16.9	69.0	38	17	0.55	360	297	906
Others											
57	2019/5/18	NS-6A	34.26	13.3	63.4	23	14	1.00	258	1,905	539
58	2019/5/18	EW-7	33.34	11.3	62.9	35	8	0.62	357	1,180	561
60	2019/5/18	EW-9	34.33	13.3	62.3	28	9	0.90	368	980	817
67	2019/5/19	NS-10	34.41	13.3	68.6	29	11	0.91	446	1,126	1,206

SSS = sea surface salinity; SST = sea surface temperature; PAR_s = surface photosynthetically active radiation; Z_{eu} = euphotic zone depth; Z_{mix} = mixed layer depth; Chl a = mean euphotic zone depth chlorophyll a; PP_1 = primary productivity estimated from the vertically resolved productivity model; PP_2 = primary productivity estimated from ^{14}C-incubations; PP_3 = primary productivity estimated from surface variables.

Any frontal enhancement in RB1904 could not be resolved due to the limited number of ^{14}C-incubations completed inshore. During TN368 productivity decreased from inshore to offshore as determined by all three estimates (**Figures 6**, **7**) and paralelled the chlorophyll distribution (**Figure 5**). During early spring, primary productivity of the inshore area was low likely due to the relatively weak stratification, although a bloom of the haptophyte *Phaeocystis* occurred and increased productivity slightly (Smith et al., 2021). During late spring productivity was greatest in the deep, warmer waters influenced by the Gulf Stream intrusions and short productivity pulses driven by Ekman restratification (Oliver et al., 2022), and in summer was greatest on the continental shelf.

The spatial distribution of primary productivity estimated by the vertically resolved productivity model of each transect in the three cruises indicated that there was a slight primary productivity enhancement in many of the transects (**Figures 6**, **7**), but the increase was only statistically significant in two of the 24 transects. Specifically, there was a statistically significant increase in productivity in 1 of 11 transects in AR29, 1 of 6 transects in RB1904, and none in TN368 ($P < 0.05$; *t*-test), although slight increases at the shelf break locations occurred within five transects in each cruise. This suggests that a productivity enhancement can and does occur in the shelf-break region, but is not consistent through time; furthermore, its magnitude is such that it is difficult to clearly identify unless specifically targeted by mesoscale sampling. Such modest spatial intensifications may not last for extended periods of time. That is, two consecutive transects showed different patterns of productivity, and if it was enhanced at the front in one, it was rarely enhanced in one sampled immediately before or after (usually a matter of 48 h). As a result, such increases will not be apparent in satellite composites of chlorophyll or productivity estimates.

The Relationship Among the Three Methods

To understand the relationship between the two models and the ^{14}C-method, we examined productivity relationships among all three estimates (**Figure 8**). We observed that the primary

TABLE 4 | Primary productivity during TN368.

Cast	Date	Station Location	SSS	SST (°C)	PAR_s (mol photons m^{-2} d^{-1})	Z_{eu} (m)	Z_{mix} (m)	Chl *a* (μg L^{-1})	PP_1 (mg C m^{-2} d^{-1})	PP_2 (mg C m^{-2} d^{-1})	PP_3 (mg C m^{-2} d^{-1})
Inshore											
41	2019/7/9	A5	31.92	17.27	71.3	25	5	1.35	340	947	813
43	2019/7/9	A6	31.97	17.01	69.1	21	7	1.45	285	1,071	498
46	2019/7/9	A9	32.16	19.80	68.2	26	6	0.73	189	276	350
77	2019/7/12	A7	31.96	21.42	68.3	28	6	0.59	176	331	396
79	2019/7/12	A6	31.94	19.67	69.8	26	5	0.87	210	239	423
80	2019/7/12	A5	31.98	19.47	69.7	34	7	0.76	334	1,046	632
Front											
11	2019/7/6	A14	32.53	20.47	63.9	37	5	0.67	333	536	658
13	2019/7/6	A15	32.26	21.87	51.1	39	5	0.41	316	351	637
26	2019/7/7	A14	32.84	22.17	53.4	35	6	0.65	339	847	546
30	2019/7/7	A12	32.78	21.37	54.2	30	8	0.67	251	357	415
83	2019/7/13	A12	32.32	21.30	70.7	39	10	0.44	259	592	429
84	2019/7/13	A13	32.32	21.35	70.6	52	8	0.61	270	821	559
94	2019/7/14	A11	32.19	21.36	68.6	31	7	0.88	277	451	475
Offshore											
14	2019/7/6	A16	32.20	21.09	50.3	28	5	0.61	195	191	331
28	2019/7/7	A16	32.11	21.27	62.0	30	5	0.80	247	110	451
Others											
32	2019/7/8	S1	34.29	23.79	41.5	36	7	0.50	269	216	338
34	2019/7/8	S2	33.63	22.78	47.4	38	7	0.58	286	143	483
35	2019/7/8	S3	32.69	20.96	52.4	38	7	0.59	332	536	661
53	2019/7/10	AC2	31.96	20.16	64.0	37	5	0.92	433	226	752
56	2019/7/10	SSF2	35.37	25.22	63.9	61	16	0.39	222	304	416
63	2019/7/11	AL3	32.49	20.96	63.8	28	10	0.46	180	312	458
64	2019/7/11	AC2	31.97	19.53	56.1	31	5	0.61	247	315	536
82	2019/7/13	HS1	34.82	24.31	70.7	40	14	0.68	144	274	360

SSS = sea surface salinity; SST = sea surface temperature; PAR_s = surface photosynthetically active radiation; Z_{eu} = euphotic zone depth; Z_{mix} = mixed layer depth; Chl a = mean euphotic zone depth chlorophyll a; PP_1 = primary productivity estimated from the vertically resolved productivity model; PP_2 = primary productivity estimated from ^{14}C-incubations; PP_3 = primary productivity estimated from surface variables.

productivity of all three estimates increased and decreased at the same time, which is not surprising as all are largely a function of chlorophyll, irradiance and temperature (despite the fact that the surface variable estimates do not include photoinhibition, and the ^{14}C-incubations could be impacted by factors such as the change of temperature of flowing seawater during incubations and the changing meteorological patterns (clouds) in space as the ship moved). There were significant differences between the productivity estimated by bio-optical model and ^{14}C-uptake ($P < 0.05$, *t*-test), but no significant difference in all three cruises between the productivity measured via the surface variable estimates and ^{14}C-incubations. We believe the estimates derived by bio-optical model may be more representative of the true productivity, although some substantial variations at selected stations remain unexplained.

DISCUSSION

The ^{14}C-incubation method is highly sensitive and historically has been the preferred method for measuring productivity in the ocean. However, there are still uncertainties and biases due to a lack of agreement on standardized methods. Some of the concerns and uncertainties include the different size of incubation bottles (usually not larger than 250 ml), the use of trace-metal clean sampling, the incubation technique, the various lengths of incubations (up to 48 h), and the different post-incubational treatment of samples. It has been suggested that the ^{14}C-method may overestimate primary production (Peterson, 1978), and that isotopic measurements underestimate total productivity unless they include the release of dissolved organic carbon during incubations (Gosselin et al., 1997). However, until satellite estimates of chlorophyll, surface temperatures and PAR became available, there was no way to compare independent estimates with the isotopic incubations.

Given the potential influence of temperature on ^{14}C-rates, we hypothesized that the rates measured were either over- or under-estimates (depending on the initial sampling location). To some extent, we found that the vertically resolved bio-optical model gave results that appear to be more robust; furthermore, they clearly resolved productivity at smaller vertical and horizontal scales, and appeared to be less impacted by some of the uncertainties in ^{14}C-measurements.

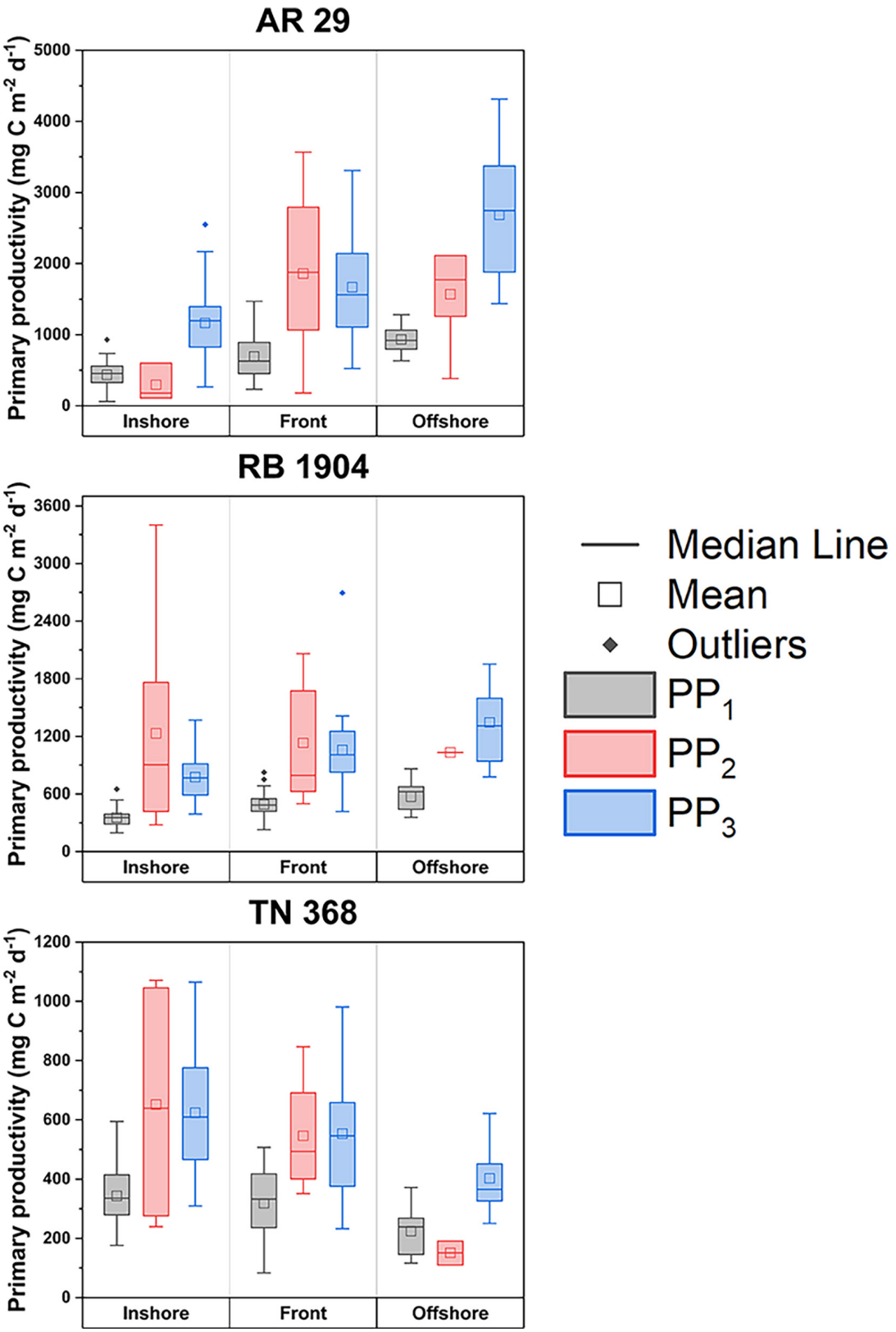

FIGURE 6 | The distribution of average primary productivity at stations inshore of the front, near the front, and offshore of the front within the three cruises. The dots outside of the boxes are extreme values that were not included in the means. Error bars represent the standard deviations.

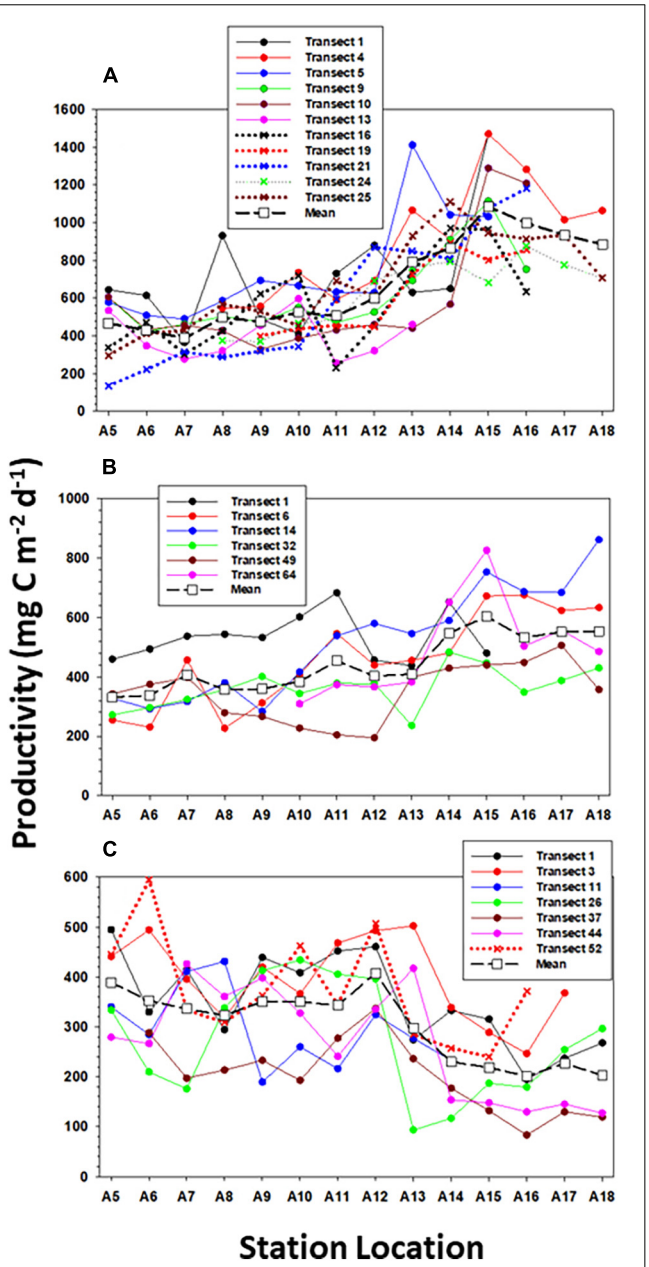

FIGURE 7 | The distribution of primary productivity determined by the vertically resolved productivity model along all transects occupied within **(A)** AR29, **(B)** RB1904, and **(C)** TN368.

Oliver et al. (2021) found very thin layers of diatoms in offshore waters, and by using a vertically resolved model determined that these thin layers (ca. 3 m in thickness) contributed up to 30% of the integrated productivity at individual stations. Both methods demonstrate that the New England waters are highly productive due to a variety of biological and physical processes occurring at different times of the year, and there exists some short-term productivity enhancements at the shelf break on short time scales. These increases are unlikely to be captured by radioisotope measurements due to the logistics of conducting these types of measurements and usually do not persist long enough to influence satellite chlorophyll determinations, but are included within the vertically resolved model.

Assessing the Impact of Temperature on ^{14}C-Measurements

Temperature is an important factor influencing primary productivity. However, the ^{14}C-incubations experienced a wide temperature variation during the 24-h incubations, as the ship moved between cold and warm waters frequently. Also, temperature varied vertically within the euphotic zone, and these vertical variations were not accounted for during the incubations (that is, all depths were incubated at surface temperatures). We attempted to quantify the vertical and horizontal impacts in two ways. Vertical influences were estimated from the vertically resolved model, where we arbitrarily set the temperatures of all depths to the surface value (temperature directly influencing the optimal productivity depth as per Behrenfeld and Falkowski (1997a) seven-order polynomial relationship). Because the mixed layer and euphotic zone depths were relatively similar, we did not expect a large influence of vertical changes. This proved to be correct for AR29 and RB1904, as the mean change in productivity was ca. 1% (**Supplementary Table 2**). The vertical temperature effect was greater in TN368, and the overestimate for locations A5 to A12 ranged from 15 – 28% (**Supplementary Table 2**). These changes largely resulted from the cooler temperatures at the inshore stations at depth, resulting in increases in ^{14}C-productivity due to increased temperatures during incubation of deeper samples.

For estimates of temperature effects driven by horizontal variations, we estimated the time that each ^{14}C-sample was in an altered temperature (one different from its original sampling depth) and calculated the change (increase or decrease) in productivity by estimating the photosynthetic rate at each temperature using the photosynthesis-temperature relationship (Behrenfeld and Falkowski, 1997a). We then estimated the degree of under- or over-estimate for each incubation (**Supplementary Table 3**). We hypothesized that the ^{14}C-values would be overestimates at inshore stations in AR29 and RB1904 due to the temperature effect, since those cruises had the largest spatial gradients in temperature, and that ^{14}C-uptake rates from offshore stations would be reduced. This was partially correct, in that the change was a function of the direction that the ship moved (offshore into warmer waters, or inshore into colder waters). ^{14}C-productivity during AR29 was likely overestimated at locations A2-A6 by ca. 27%; offshore locations (Stations A14-A18) likely had the productivity reduced by ca. 13%. A similar pattern was observed in RB1904: at inshore locations (A5-A7) ^{14}C-productivity was increased by 19%, and offshore stations had the productivity reduced by 8%, although substantial variability was introduced by the direction of ship movement (**Supplementary Table 3**). Changes within TN368 were less pronounced, as surface temperatures were more uniform. Productivity changes in that cruise ranged from a 1.7% increase to a decrease of 12.5%. Temperature effects on incubations can be significant and need

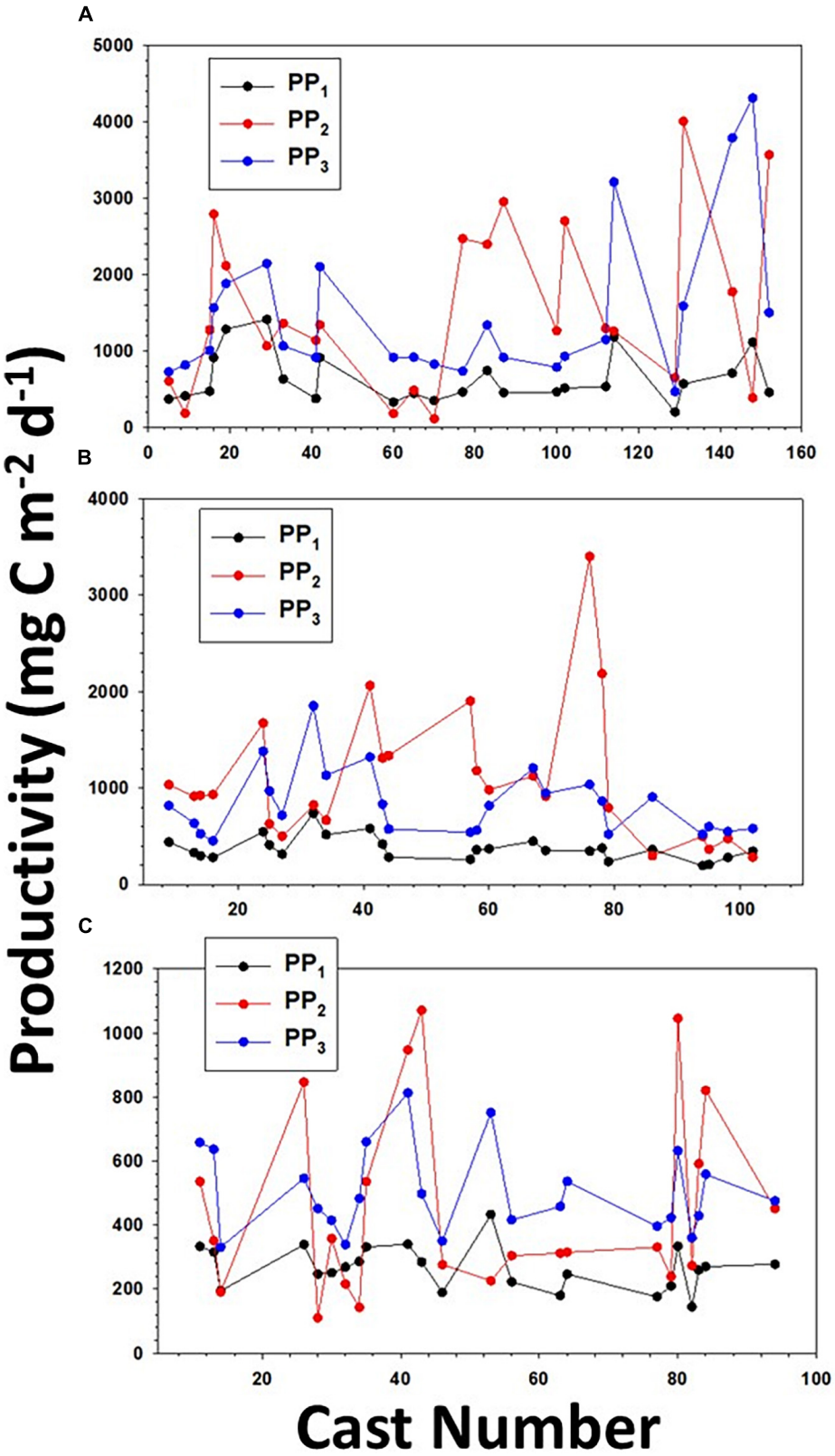

FIGURE 8 | The distribution of primary productivity determined by the vertically resolved productivity model (PP_1), ^{14}C-uptake (PP_2), and by the surface variable productivity model (PP_3) along **(A)** AR29, **(B)** RB1904, and **(C)** TN368.

to be considered using traditional isotopic procedures, especially in regions with marked in situ temperature gradients.

Is the Shelf Break a Site of Enhanced Productivity?

Our composite data do not reveal an enhancement of primary production at the shelf break, although at certain times there does appear to be a slight increase (**Figure 7**). Zhang et al. (2013) using a simple NPZ model suggested that there should be an enhancement at the shelf break during spring and summer based on increased nutrient fluxes from the slope water into the euphotic zone. They also noted that such increases in biomass were not apparent in the satellite or observational data, a finding confirmed by Oliver et al. (2022). Oliver et al. (2022) did find ephemeral increases in biomass at the shelf break due to Ekman restratification driven by winds, but that event was short-lived, as the winds that stimulated the bloom were in the opposite direction as the prevailing winds. Our results from the vertically resolved productivity model suggested that during certain transects there appeared to be a slight enhancement near the shelf break. Indeed, during AR29 five out of 11 transects showed an increase at the shelf break from the vertically resolved model results; during RB1904 and TN368 five (out of 6) and five out of seven showed a shelf-break increase. However, during three cruises only 1, 1, and 0 transects manifested a significant increase. Furthermore, those enhancements were modest, and as a result, productivity at the shelf break is not increased relative to the rates observed on the shelf and slope (**Figure 6**) in either the ^{14}C-uptake rates or those modeled from surface variables.

Summary

While numerous physical mechanisms potentially can increase nutrient fluxes into the euphotic zone at the shelf break in the Mid-Atlantic Bight (e.g., Linder et al., 2004; Zhang et al., 2013), extensive surveys using multiple methods were able to define limited periods of enhanced productivity – consistent with the ephemeral increases found by Oliver et al. (2022). Our results do not address the physical forcing of the system and only assess the results of these physical processes. The region is clearly a site of substantial fisheries and higher trophic level accumulations, but the food web likely does not benefit substantially from any increased productivity based on shelf-break features. To understand the underlying causes of such a large system productivity, a full food-web analysis is needed with sampling at small (<10 km) horizontal scales. The continental shelf is being influenced by large-scale processes that in turn are being driven by climate change (e.g., increased interactions with warm core rings, bringing nutrients onto the shelf and compensatory flows of high biomass waters offshore; Gawarkiewicz et al., 2019; Zhang et al., in prep), so the impact of the shelf break on the regional food web and biogeochemical cycles may increase in coming decades.

DATA AVAILABILITY STATEMENT

The datasets presented in this study can be found in online repositories. The names of the repository/repositories and accession number(s) can be found below: All data used in these analyses can be obtained from the BCO-DMO data repository (https://www.bco-dmo.org/project/748894).

AUTHOR CONTRIBUTIONS

JM wrote the manuscript and analyzed the data. WS conducted the field work, helped analyze the data, and wrote the manuscript. Both authors contributed to the article and approved the submitted version.

FUNDING

This research was supported by the National Science Foundation (Grant No. 1657855) and Shanghai Jiao Tong University.

SUPPLEMENTARY MATERIAL

The Supplementary Material for this article can be found online at: https://www.frontiersin.org/articles/10.3389/fmars.2022.824303/full#supplementary-material

REFERENCES

Behrenfeld, M. J., and Falkowski, P. G. (1997a). Photosynthetic rates derived from satellite-based chlorophyll concentration. *Limnol. Oceanogr.* 42, 1–20. doi: 10.4319/lo.1997.42.1.0001

Behrenfeld, M. J., and Falkowski, P. G. (1997b). A consumer's guide to phytoplankton primary productivity models. *Limnol. Oceanogr.* 42, 1479–1491. doi: 10.4319/lo.1997.42.7.1479

Campbell, J., Antoine, D., Armstrong, R., Arrigo, K., Balch, W., Barber, R., et al. (2002). Comparison of algorithms for estimating ocean primary production from surface chlorophyll, temperature, and irradiance. *Glob. Biogeochem. Cycles* 16, 9–1. 9-1-9-15, doi: 10.1029/2001gb001444

Gardner, W. D., Richardson, M. J., and Smith, W. O. Jr. (2000). Seasonal patterns of water column particulate organic carbon and fluxes in the Ross Sea, Antarctica. *Deep Sea Res. II* 47, 3423–3449. doi: 10.1016/S0967-0645(00)00074-6

Gawarkiewicz, G., Todd, R. E., Zhang, W., Partida, J., Gangopadhyay, A., Monim, M.-U.-H., et al. (2019). The changing nature of shelf-break exchange revealed by the OOI Pioneer Array. *Oceanography* 31, 60–70. doi: 10.5670/oceanog.2018.110

Gosselin, M., Levasseur, M., Wheeler, P. A., Horner, R. A., and Booth, B. C. (1997). New measurements of phytoplankton and ice algal production in the Arctic Ocean. *Deep Sea Res. II* 44, 1623–1644. doi: 10.1016/S0967-0645(97)00054-4

Houghton, R. W., Aikman, F., and Ou, H. W. (1988). Shelf-slope frontal structure and cross-shelf exchange at the New England shelf-break. *Cont. Shelf. Res.* 8, 687–710. doi: 10.1016/0278-4343(88)90072-6

Knap, A. H., Michaels, A., Close, A. R., Ducklow, H., and Dickson, A. G. (1996). *Protocols for the Joint Global Ocean Flux Study (JGOFS) Core Measurements*. Paris: UNESCO.

Linder, C. A., and Gawarkiewicz, G. (1998). A climatology of the shelfbreak front in the Middle Atlantic Bight. *J. Geophys. Res.* 103, 18,405–18,423. doi: 10.1029/98JC01438

Linder, C. A., Gawarkiewicz, G. G., and Pickart, R. S. (2004). Seasonal characteristics of bottom boundary layer detachment at the shelfbreak front in the Middle Atlantic Bight. *J. Geophys. Res.* 109:C03049. doi: 10.1029/2003JC002032

Lozier, M. S., and Gawarkiewicz, G. (2001). Cross-frontal exchange in the Middle Atlantic Bight as evidenced by surface drifters. *J. Phys. Oceanogr.* 31, 2498–2510. doi: 10.1175/1520-048520010312.0.CO;2

Marra, J., and Barber, R. T. (2004). Phytoplankton and heterotrophic respiration in the surface layer of the ocean. *Geophys. Res. Lett.* 31:L09314. doi: 10.1029/2004GL019664

Marra, J., Dickey, T., Chamberlin, W. S., Ho, C., Granata, T., Kiefer, D. A., et al. (1992). Estimation of seasonal primary production from moored optical sensors in the Sargasso Sea. *J. Geophys. Res.* 97, 7399–7412. doi: 10.1029/92JC00408

Marra, J., Houghton, R. W., Boardman, D. C., and Neale, P. J. (1982). Variability in surface chlorophyll-a at a shelf-break front. *J. Mar. Res.* 40, 575–591.

Marra, J., Houghton, R. W., and Garside, C. (1990). Phytoplankton growth at the shelf-break front in the Middle Atlantic Bight. *J. Mar. Res.* 48, 851–868. doi: 10.1357/002224090784988665

Marra, J. F., Barber, R. T., Barber, E., Bidigare, R. R., Chamberlin, W. S., Goericke, R., et al. (2021). A database of ocean primary productivity from the 14C method. *Limnol. Oceanogr. Lett.* 1, 107–111. doi: 10.1002/lol2.10175

Oliver, H., Zhang, W. G., Smith, W. O. Jr., Alatalo, P., Chappell, P. D., Hirzel, A. J., et al. (2021). Diatom hotspots driven by western boundary current instability. *Geophys. Res. Lett.* 48:e2020GL091943. doi: 10.1029/2020GL091943

Oliver, H., Zhang, W. G., Smith, W. O. Jr., Archibald, K., Hirzel, A., Sosik, H. M., et al. (2022). Ephemeral surface chlorophyll enhancement at the New England shelf break driven by Ekman restratification. *J. Geophys. Res.* 127, e2021JC017715. doi: 10.1029/2021JC017715

O'Reilly, J. E., and Busch, D. A. (1984). Phytoplankton primary production on the northwestern Atlantic shelf. *Rapp. P.V. Reun. Cons. Int. Explor. Mer.* 183, 255–268. doi: 10.1016/j.ecss.2014.12.047

Peterson, B. J. (1978). Radiocarbon uptake: its relation to net particulate carbon production. *Limnol. Oceanogr.* 23, 179–184. doi: 10.4319/lo.1978.23.1.0179

Platt, T., and Jassby, A. D. (1976). The relationship between photosynthesis and light for natural assemblages of coastal marine phytoplankton. *J. Phycol.* 12, 421–430. doi: 10.1111/j.1529-8817.1976.tb02866.x

Ryan, J. P., Yoder, J. A., Barth, J. A., and Cornillon, P. C. (1999a). Chlorophyll enhancement and mixing associated with meanders of the shelf break front in the Mid-Atlantic Bight. *J. Geophys. Res.* 104, 23,479–23,493. doi: 10.1029/1999JC900174

Ryan, J. P., Yoder, J. A., and Cornillon, P. C. (1999b). Enhanced chlorophyll at the shelfbreak of the Mid-Atlantic Bight and Georges Bank during the spring transition. *Limnol. Oceanogr.* 44, 1–11. doi: 10.4319/lo.1999.44.1.0001

Smith, W. O. Jr., Marra, J., Hiscock, M. R., and Barber, R. T. (2000). The seasonal cycle of phytoplankton biomass and primary productivity in the Ross Sea, Antarctica. *Deep Sea Res. II* 47, 3119–3140. doi: 10.1016/S0967-0645(00)00061-8

Smith, W. O. Jr., Zhang, W. G., Hirzel, A., Stanley, R. H. R., Meyer, M. G., Sosik, H. M., et al. (2021). A regional, early spring bloom of Phaeocystis pouchetii on the New England continental shelf. *J. Geophys. Res.* 126:e2020JC016856. doi: 10.1029/2020JC016856

Townsend, D. W., Thomas, A. C., Mayer, L. M., Thomas, M. A., and Quinlan, J. A. (2006). "Oceanography of the Northeast Atlantic continental shelf," in *The Sea: The Global Coastal Ocean: Interdisciplinary Regional Studies and Syntheses 14*, eds A. R. Robinson and K. H. Brink (Boston, MA: Harvard University Press), 119–168.

Xu, Y., Chant, R., Gong, D., Castelao, R., Glenn, S., and Schofield, O. (2011). Seasonal variability of chlorophyll a in the Mid-Atlantic Bight. *Cont. Shelf Res.* 31, 1640–1650. doi: 10.1016/j.csr.2011.05.019

Yoder, J. A., McClain, C. R., Feldman, G. C., and Esaias, W. E. (1993). Annual cycles of phytoplankton chlorophyll concentrations in the global ocean: a satellite view. *Glob. Biogeochem. Cycles* 7, 181–193. doi: 10.1029/93GB02358

Yoder, J. A., Schollaert, S. E., and O'Reilly, J. E. (2002). Climatological phytoplankton chlorophyll and sea surface temperature patterns in continental shelf and slope waters off the northeast U.S. coast. *Limnol. Oceanogr.* 47, 672–682. doi: 10.4319/lo.2002.47.3.0672

Yoder, O., Reilly, J. E., Barnard, A. H., Moore, T. S., and Ruhsam, C. M. (2001). Variability in coastal zone color scanner (CZCS) chlorophyll imagery of ocean margin waters off the US East Coast. *Cont. Shelf Res.* 21, 1191–1218. doi: 10.1016/s0278-4343(01)00009-7

Zhang, W. G., and Gawarkiewicz, G. G. (2015). Length scale of the finite-amplitude meanders of shelfbreak fronts. *J. Phys. Oceanogr.* 45, 2598–2620. doi: 10.1175/jpo-d-14-0249.1

Zhang, W. G., Gawarkiewicz, G. G., McGillicuddy, D. J. M. Jr., and Wilkin, J. L. (2011). Climatological mean circulation at the New England Shelf Break. *J. Phys. Oceanogr.* 41, 1874–1893. doi: 10.1175/2011jpo4604.1

Zhang, W. G., McGillicuddy, D. J., and Gawarkiewicz, G. G. (2013). Is biological productivity enhanced at the New England shelfbreak front? *J. Geophys. Res.* 118, 517–535. doi: 10.1002/jgrc.20068

Zhang, W. G., McGillicuddy, D. J., Smith, W. O. Jr., Sosik, H. R., and Stanley, R. H. R. (in prep). *Characterization of the Cross-Shelf Exchange Associated with a Shelf-Water Streamer at the Mid-Atlantic Bight Shelf Edge.*

Conflict of Interest: The authors declare that the research was conducted in the absence of any commercial or financial relationships that could be construed as a potential conflict of interest.

Publisher's Note: All claims expressed in this article are solely those of the authors and do not necessarily represent those of their affiliated organizations, or those of the publisher, the editors and the reviewers. Any product that may be evaluated in this article, or claim that may be made by its manufacturer, is not guaranteed or endorsed by the publisher.

Copyright © 2022 Ma and Smith. This is an open-access article distributed under the terms of the Creative Commons Attribution License (CC BY). The use, distribution or reproduction in other forums is permitted, provided the original author(s) and the copyright owner(s) are credited and that the original publication in this journal is cited, in accordance with accepted academic practice. No use, distribution or reproduction is permitted which does not comply with these terms.

frontiers in Marine Science

ORIGINAL RESEARCH
published: 17 February 2022
doi: 10.3389/fmars.2022.796187

Effects of the Coastal Uplift on the Kuroshio Ecosystem, Eastern Taiwan, the Western Boundary Current of the North Pacific Ocean

Chung-Chi Chen[1,2], Chun-Yi Lu[1], Sen Jan[3]*, Chih-hao Hsieh[3] and Chih-Ching Chung[4]*

[1] Department of Life Science, National Taiwan Normal University, Taipei, Taiwan, [2] College of Marine Sciences, National Dong Hwa University, Hualien, Taiwan, [3] Institute of Oceanography, National Taiwan University, Taipei, Taiwan, [4] Institute of Marine Environment and Ecology, National Taiwan Ocean University, Keelung, Taiwan

The Kuroshio is the western boundary current of the North Pacific Ocean. In the subtropical region of eastern Taiwan, a coastal uplift of the isotherms has occurred. To explore its impact on this oligotrophic ecosystem, hydrographic data along the transect line at 23.75°N were measured between September 2012 and September 2014. Results show that the intensity of coastal uplift was positively correlated to the flow volume transport of the Kuroshio. Significant dissolved inorganic nutrients were uplifted to the sunlit zone, especially in the onshore. For example, compared to the offshore, nitrate concentration increased 0.49 μM (or ∼178%) in the upper 100 m of the onshore. The increased nutrients thereafter enhanced the growth of phytoplankton; for instance, the Chl *a* concentration increased 88.3%, compared to offshore, in the upper 100 m of the onshore. Phytoplankton community was mostly composed of picophytoplankton (<2 μm in size), which were dominated, in terms of relative abundance, by *Prochlorococcus* (83.6%), followed by *Synechococcus* (13.8%) and picoeukaryotes (2.7%). The relative abundance of *Prochlorococcus* increased from onshore toward offshore, but the trend was reversed for *Synechococcus* and picoeukaryotes, which may be affected by the coastal uplift. The results also suggest that the coastal uplift may support more energy transferred to higher tropical levels in this oligotrophic Kuroshio ecosystem.

Keywords: coastal uplift, dissolved inorganic nutrients, picoeukaryotes, picoplankton, *Prochlorococcus*, *Synechococcus*, the Kuroshio

OPEN ACCESS

Edited by:
William Savidge, University of Georgia, United States

Reviewed by:
Takeyoshi Nagai, Tokyo University of Marine Science and Technology, Japan
Yuqiu Wei, Yellow Sea Fisheries Research Institute, Chinese Academy of Fishery Sciences (CAFS), China

****Correspondence:***
Sen Jan
senjan@ntu.edu.tw
Chung-Chi Chen
ccchen@ntnu.edu.tw

Specialty section:
This article was submitted to Coastal Ocean Processes, a section of the journal Frontiers in Marine Science

Received: *16 October 2021*
Accepted: *12 January 2022*
Published: *17 February 2022*

Citation:
Chen C-C, Lu C-Y, Jan S, Hsieh C-h and Chung C-C (2022) Effects of the Coastal Uplift on the Kuroshio Ecosystem, Eastern Taiwan, the Western Boundary Current of the North Pacific Ocean. Front. Mar. Sci. 9:796187. doi: 10.3389/fmars.2022.796187

INTRODUCTION

The Kuroshio is the western boundary current in the North Pacific Ocean and is the counterpart of the Gulf Stream in the North Atlantic Ocean. It originates from the North Equatorial Current and becomes a pronounced current that crosses the Luzon Strait and flows along the east coast of Taiwan, and the shelf break of the East China Sea (ECS), before reaching the southeastern coast of Japan (Nitani, 1972). The Kuroshio is oligotrophic water with low biological productivity (Guo, 1991). However, several physical processes bring nutrient-rich subsurface Kuroshio water to the surface, such as upwelling, vertical mixing induced by typhoons, vertical nutrient flux induced by Kelvin–Helmholtz billows, strong northeast winter monsoons, and cyclonic mesoscale eddies (Hsu et al., 2010; Hung and Gong, 2011; Sukigara et al., 2014; Chen et al., 2015; Acabado et al., 2021). Primary production may therefore be enhanced by this uplifted nutrient-rich subsurface Kuroshio

water. These subsurface nutrients uplift processes are, however, local (e.g., upwelling in northeast Taiwan) and/or episodic and seasonal dependent events; thereafter, their impact on ecosystems may be confined spatiotemporally (e.g., Chen et al., 2015).

Another process, turbulent vertical mixing, has also been reported for the diffusion of subsurface nutrients to the sunlit layer in shelf slope along the Kuroshio (Nagai et al., 2019). Interestingly, the subsurface water uplift to shallow water has been observed on the east coast of Taiwan along Kuroshio's path (Chen et al., 2017). This suggests that its impact is in the broadened geographic range of this narrow-shelf subtropical Kuroshio ecosystem along the east coast of Taiwan. This coastal uplift effect on this oligotrophic ecosystem is, however, rarely being evaluated, especially on its biogeochemical responses (e.g., dissolved inorganic nutrient dynamics, biological production, phytoplankton composition. . .) on the shore side of the Kuroshio (Lai et al., 2021).

In the oligotrophic subtropical northwest Pacific, primary productivity is mainly contributed by the most abundant phytoplankton, e.g., *Prochlorococcus* and *Synechococcus* (Buitenhuis et al., 2012; Endo and Suzuki, 2019). During the uplift, the cold and nutrient-rich deep waters shoal to shallow water and enhance phytoplankton growth (Rochford, 1984; Roughan and Middleton, 2002). The shoaled nutrient-rich waters may be important for biological production and plankton dynamics (e.g., picoplankton composition) in oligotrophic ecosystems, such as the Kuroshio (Kobari et al., 2020; Lai et al., 2021). Using temperature modulated dilution experiments, Liu et al. (2020) have demonstrated that nutrient-dependent temperature sensitivities of picophytoplankton in the subtropical Kuroshio, one of the warmest regions of the global ocean (Wu et al., 2012); It suggests the importance of nutrient availability in evaluating the response of primary productivity to the projected ocean warming, especially in the oligotrophic ocean. The coastal uplift along the subtropical Kuroshio, off the east coast of Taiwan may therefore provide as a suitable nature ecosystem to examine those assumptions.

In addition, as stated above, the impact of the coastal uplift is rarely evaluated in the Kuroshio ecosystem, not even to elucidate the potential forces for the coastal uplift in this system. In this study, we therefore intend to reveal the potential mechanism for the causes of uplifting and its impact on the Kuroshio ecosystem, including the dynamics of nutrient and picoplankton, especially at the eastern coast of Taiwan.

MATERIALS AND METHODS

Study Area and Sampling

To understand the coastal uplift effect on the Kuroshio ecosystem, eight stations (K101–K108) along a transect (KTV1) between 121.72° and 123° E at 23.75° N were repeatedly surveyed across the Kuroshio, east of Taiwan (**Figure 1**). Samples were collected from six shipboard measurements taken from the R/V *Ocean Researcher I* between September of 2012 and 2014: September and November 2012, June and September 2013, and July and September 2014 (**Table 1**). At each station, seawater was sampled at eight depths (2–5, 10, 30, 50, 100, 150, 200, and 250 m), using Teflon-coated Go-Flo bottles (20 l, General Oceanics Inc., Miami, FL, United States) mounted on a General Oceanic rosette assembly. Sub-samples were taken for analyses of dissolved inorganic nutrients [e.g., nitrate (NO_3^-; N), phosphate (PO_4^{3-}; P), and silicate (SiO_3^{2-})], chlorophyll *a* (Chl *a*), autotrophic picoplankton (e.g., *Synechococcus*, *Prochlorococcus*, and picoeukaryotes), and heterotrophic bacteria (Bact), as described below. Please refer to Chen et al. (2017, 2021) for a detailed description of the methods used to collect the hydrographic data and analyze the aforementioned response variables. For reference, additional temperature profiles up- and downstream of the KTV1 transect along the Kuroshio were also measured in September 2013 and March 2006, respectively (**Figure 1**).

Physical, Chemical Hydrographics, and Uplift Magnitude

Temperature and salinity were recorded to a depth of 250 m in the water column using a SeaBird CTD (SBE 9/11 puls, SBE Inc., Barre, VT, United States). Photosynthetically active radiation (PAR) was also measured to a depth of 250 m in the water column using an irradiance sensor (4π; QSP-200L). The depth of the euphotic zone (Z_E) was taken as the penetration depth of 1% of the surface light. The depth of the mixed layer (M_D) was based on the potential density criterion of 0.125 kg m^{-3} (Levitus, 1982). To evaluate and estimate the uplift magnitude, the uplift area (U_A) was applied to the area where the water temperature $\leq$ 21°C for the upper 100 m depth along the KTV1 transect. The gridding methods of Surfer 11 (Golden Software, Inc., Golden, CO, United States) were used for this area estimation.

The velocity was measured with a shipboard 75-kHz acoustic Doppler current profiler (ADCP) in roughly the upper 600 m along the cruise track while underway. The velocity at each station was also measured from the sea surface to near the seafloor using a pair of lowered AD comprising two 300-kHz, self-contained ADCPs with a downward-looking "master" and an upward-looking "slave." The lowered ADCP data were processed using the velocity inversion method with the bottom tracking mode (Visbeck, 2002; Thurnherr, 2010). The water volume transport (Q_{250}; $S_V = 10^6$ m^3 s^{-1}) in the upper 250 m across the KTV1 was then calculated using positive normal velocities (i.e., $v > 0$ m s^{-1}) on a grid 10-km wide by 8-m thick over the transect. Portions of the dataset assessed herein (i.e., water volume transport, temperature, salinity, and normal velocity) were published (Jan et al., 2015; Chen et al., 2017).

Water samples for dissolved inorganic nitrate, phosphate, and silicate analysis were collected from each sampling depth in 100 ml polypropylene bottles. The samples were immediately frozen in liquid nitrogen. A custom-made flow-injection analyzer was used for the nitrate, phosphate, and silicate analysis, and they were characterized by detection limits of 0.3, 0.01, and 0.5 μM, respectively (Gong et al., 2003).

Biological Variables and Data Analyses

The water samples (2 L) taken for Chl *a* analysis were immediately filtered through GF/F filter paper (Whatman, 47 mm) and stored in liquid nitrogen. The Chl *a* retained on the

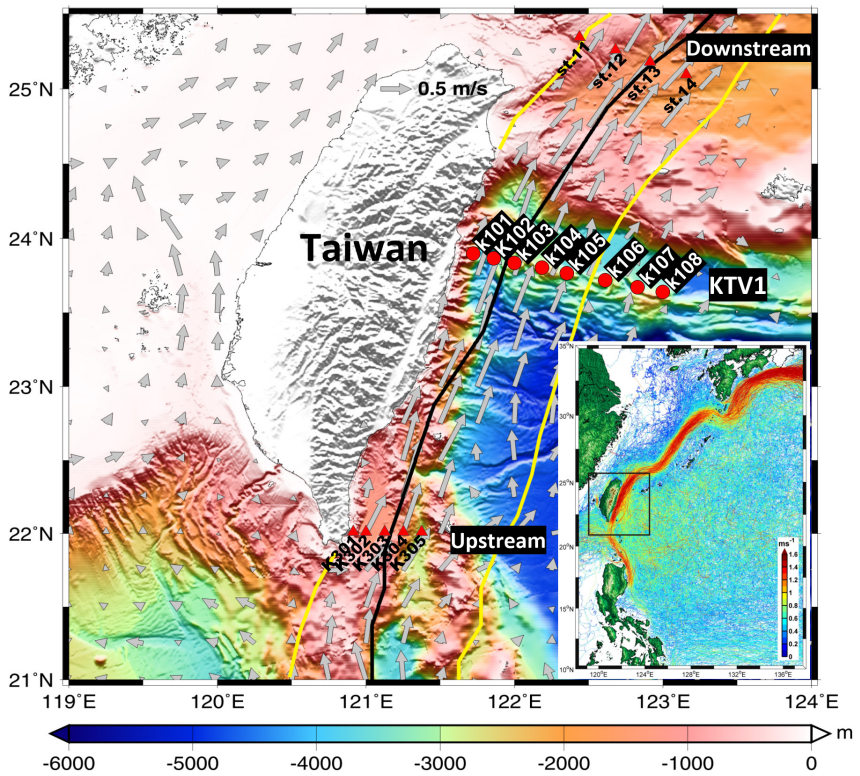

FIGURE 1 | Sampling stations (K101–K108) along the KTV1 transect of the Kuroshio, east of Taiwan. The climatological current velocity (gray arrows) at a depth of 30 m was computed from the historical ADCP dataset available from Taiwan's Ocean Data Bank. The bold black line indicates the maximum velocity axis at 15 m depth obtained from the surface drifter data. The solid yellow line indicates the 0.2 m s^{-1} isotach at 30 m depth obtained from the historical ADCP dataset (Jan et al., 2015). The path of the Kuroshio with velocity > 1 m s^{-1} is indicated by surface drifter trajectories and speeds (data available at http://www.coriolis.eu.org/Data-Products/Data-Delivery/Data-selection) in the lower right inset where the black dotted rectangle marks the map area.

GF/F filters was quantified fluorometrically (Turner Design 10-AU-005), as in Parsons et al. (1984). When applicable, Chl *a* was converted to carbon units using a C:Chl ratio of 65.9, which was estimated from the integrated value over the upper 200 m of the Kuroshio waters (KW; Furuya, 1990).

Water samples for picoplankton enumeration were fixed in seawater-buffered paraformaldehyde at a final concentration of 0.2% (w/v) in the dark (Liu et al., 1997); they were subsequently frozen and stored in liquid nitrogen until further analysis. They were then identified and enumerated using a flow cytometer (FACSAria, Becton-Dickinson, Franklin Lakes, NJ, United States). The different picophytoplankton were distinguished based on cell size (forward- and side-scattering) and autofluorescence in the ranges of orange from phycoerythrin (575 ± 15 nm, for *Synechococcus*) and red from divinyl chlorophyll (>670 nm, for *Prochlorococcus* and photosynthetic picoeukaryotes) under excitation at 488 nm (Chan et al., 2020). The heterotrophic bacteria were stained with the nucleic acid-specific dye SYBR® Green I (emission = 530 ± 30 nm) in a 10^4-fold-diluted commercial solution (Molecular Probes, Eugene, OR, United States; Liu et al., 2002). Known numbers of fluorescent beads (TruCOUNT Tubes, Becton-Dickinson, Franklin Lakes, NJ, United States) were simultaneously used as an instrument internal standard (Chung and Gong, 2019; Chan et al., 2020). When applicable, cell abundances were converted to carbon units using the factors widely applied, including 53 fg C $cell^{-1}$ for *Prochlorococcus*, 250 fg C $cell^{-1}$ for Synechococcus, 2100 fg C $cell^{-1}$ for picoeukaryotes, and 20 fg C $cell^{-1}$ for heterotrophic bacteria (Lee and Fuhrman, 1987; Morel et al., 1993; Campbell et al., 1994; Buck et al., 1996).

For comparison, the depth-integrated value of chemical and biological variables for the upper 100 m (down to the photic layer depth; see below for details) water depth were estimated using the trapezoidal method for each station. The mean depth-integrated value of variables was averaged over all stations of the KTV1 transect for each sampling period. The depth-integrated and its mean values were applied for further comparison and

TABLE 1 | The estimated coastal uplift area (U_A; km^2), water volume transport (Q_{250}; S_V = 10^6 m^3 s^{-1}) in the upper 250 m of water depth at different sampling periods.

Date Variables	2012/09	2012/11	2013/06	2013/09	2014/07	2014/09
U_A	0.0	6.2	61.6	0.2	33.0	9.5
Q_{250}	20.1	18.4	22.9	15.7	19.9	18.8

Please refer to the "Materials and Methods" section for a detailed estimation of the uplift area.

analysis. SigmaStat (ver. 3.5, Systat Software, Inc., Chicago, IL, United States) was used for simple and multiple linear regression analyses and for analysis of variance (ANOVA).

RESULTS

Physical and Chemical Hydrographics in the Kuroshio

Physical Hydrographic

In the Kuroshio, east of Taiwan, high surface temperature and salinity were observed with the mean values ± standard deviation (SD; for this and all parameters discussed henceforth) in the range of 26.1 (± 0.2)–30.2 (± 0.8)°C and 33.77 (± 0.17)–34.37 (± 0.32) over each sampling period, respectively. Vertically, seawater temperature displayed a coastal uplift (i.e., onshore uplifting and offshore deepening) of the isotherms along the KTV1 transect using data from July 2014 as a typical example (**Figure 2a**). As for the M_D depth, it was shallower in the summer and deeper in other seasons, and its average value over each sampling period ranged from 12.9 (±3.9) to 72.4 (± 25.6) m. The Z_E was however more consistent with an average depth of 103.2 (±12.3) m.

To evaluate the coastal uplift magnitude, the uplift area is estimated and serves as an index (see methods for details), and its area ranged from 0.0 to 61.6 km^2 at different sampling periods (**Table 1**). Interestingly, the uplift area was linear, in the significant margin, related to the water volume transport (Q_{250}; **Figure 3**). The mean values of Q_{250} over each sampling period were in the range of 15.7–22.9 S_V (**Table 1**). Additionally, the coastal uplift phenomenon was not only observed in the KTV1 transect; it was also found in its upstream and downstream (**Supplementary Figure S1**).

Chemical Hydrographic

In the oligotrophic Kuroshio, the nutrient concentrations in the surface water were not as low as expected; for example, its nitrate and phosphate values were 0.69 μM (St. K103) and 0.08 μM (St. K102), respectively, in July 2014 (**Figures 2b,c**). This phenomenon was also observed at other sampling periods. On average, the values for nitrate, phosphate, and silicate in the surface water were in the range of 0.00 (±0.00)–0.28 (±0.23) μM, 0.02 (±0.00)–0.10 (±0.02) μM, and 0.44 (±0.22)–3.19 (±1.30) μM over each sampling period, respectively. The mean depth-integrated (i.e., the upper 100 m water depth) nutrient concentrations were in the range of 0.22 (±0.28)–2.06 (±0.89) μM for nitrate, 0.05 (±0.02)–0.21 (±0.04) μM for phosphate, and 0.32 (±0.15)–4.68 (±1.08) μM for silicate over each sampling period. Additionally, the molar ratio of nitrate to phosphate (the N/P ratio) was in the range of 9.6–29.5 over each sampling period, with an average value of 10.4 (**Supplementary Figure S2**). Corresponding to the isotherms uplifting, nutrient concentrations (i.e., nitrate and phosphate) also demonstrated a coastal uplift pattern along the KTV1 transect (**Figures 2a–c**). For example, both nitrate (≥1.0 μM) and phosphate (≥0.1 μM) concentration contours could shoal to 30 m in the onshore stations; however, this depth could deepen to 150 and 250 m in the offshore stations (**Figures 2b,c**). A positive linear relationship was also significantly evidenced between the mean depth-integrated nitrate (or phosphate) concentration and the uplift area over each sampling period (all $p < 0.05$; **Figure 4a**), but not for silicate. The coastal uplift trend was also observed but not statistically significant between the uplift area vs. the difference between the average depth-integrated nitrate value of onshore Sts. (K101–104), and offshore, Sts. (K105–108) stations over each sampling period ($p = 0.06$; **Figure 5a**).

Biological Variables in the Kuroshio

Chl *a* Distribution

In this oligotrophic Kuroshio ecosystem, the mean Chl *a* concentration in the surface water ranged from 0.07 (±0.03) to 0.33 (±0.25) μg Chl L^{-1} over each sampling period. The mean depth-integrated Chl *a* value was in the range of 0.19 (±0.05) to 0.49 (±0.23) μg Chl L^{-1} over each sampling period. Furthermore, a significant linear relationship was evidenced between the depth-integrated values of Chl *a* and nutrients (e.g., nitrate, phosphate, or silicate) using all pooled data over each sampling station (all $p < 0.01$; **Table 2**).

The spatial and vertical distributions of Chl *a* may represent a variable response to nutrient uplifting impact on the Kuroshio ecosystem. The coastal uplift was also observed in the Chl *a* distribution pattern; for example, its value at the subsurface Chl *a* maximum (SCM) was higher and located shallower in the onshore compared to that of offshore in the KTV1 (**Figure 2d**). A similar coastal uplift pattern was also demonstrated in other sampling periods, and the SCM with a value could reach 2.03 μg Chl L^{-1} located at 30 m water depth in June 2013 (**Supplementary Figure S3**). A significant linear relationship was also evidenced between the uplift area and the mean depth-integrated Chl *a* concentration over each sampling period ($p < 0.05$; **Figure 4b**). The difference between the average depth-integrated Chl *a* value of onshore (Sts. K101–104) and offshore (Sts. K105–108) stations significantly and linearly increased with increasing of the uplift area ($p \leq 0.01$; **Figure 5b**).

Picoplankton Abundance and Distribution

In this study, the Chl *a* concentration was significantly and linearly regressed with total autotrophic picoplankton abundances using the depth-integrated values for the upper 100 m depth of all sampling stations ($p < 0.05$; **Figure 6a**). As for autotrophic picoplankton, it was dominated by *Prochlorococcus*, followed by *Synechococcus* and then picoeukaryotes, with an average relative abundance of 83.6 (±12.5)%, 13.8 (±11.1)%, and 2.7 (±1.6)%, respectively. The mean depth-integrated abundances of *Prochlorococcus*, *Synechococcus*, and picoeukaryotes were in the range of 21.34 (±8.62)–93.64 (±26.61) × 10^3 cells mL^{-1}, 2.87 (±1.71)–21.51 (±18.22) × 10^3 cells mL^{-1}, and 0.80 (±0.55)–2.89 (±2.28) × 10^3 cells mL^{-1} over each sampling period, respectively (**Figure 7**); its biomass was in the range of 1.13 (±0.46)–4.96 (±1.14) μg C L^{-1}, 0.72 (±0.43)–5.38 (±4.56) μg C L^{-1}, and 1.68 (±1.15)–6.08 (±4.79) μg C L^{-1}, respectively. The depth-integrated abundance of autotrophic picoplankton was significantly related to the depth-integrated nutrient concentration (e.g., nitrate, phosphate, or silicate), in most cases, with negative slope for *Prochlorococcus* and positive

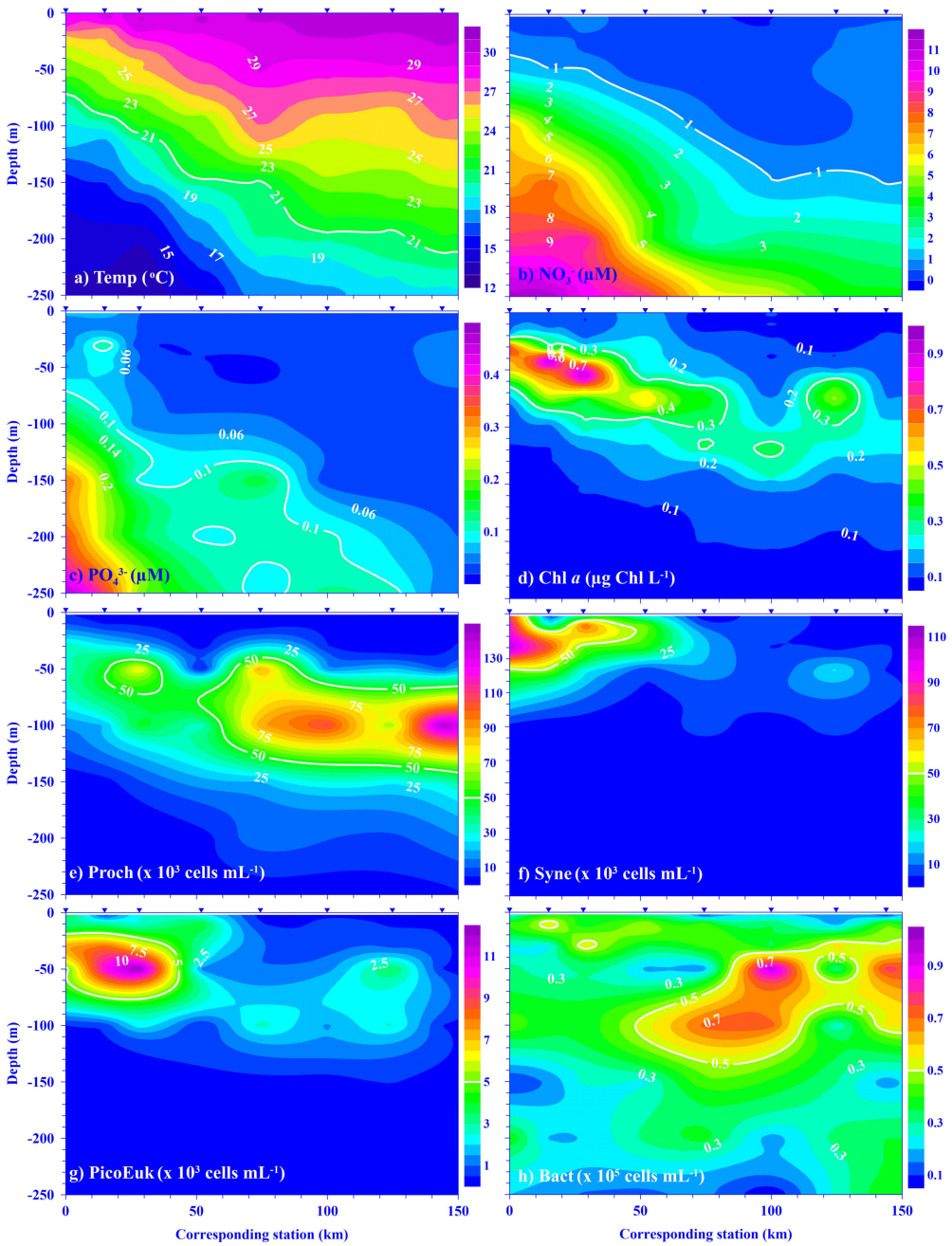

FIGURE 2 | Typical depth profile contour plots of **(a)** temperature (Temp; °C), **(b)** nitrate (NO_3^-; μM), and **(c)** phosphate (PO_4^{3-}; μM), **(d)** chlorophyll *a* (Chl *a*; μg Chl L^{-1}), **(e)** *Prochlorococcus* (Proch; $\times 10^3$ cells mL^{-1}), **(f)** *Synechococcus* (Syne; $\times 10^3$ cells mL^{-1}), **(g)** picoeukaryotes (PicoEuk; $\times 10^3$ cells mL^{-1}), **(h)** heterotrophic bacteria (Bact; $\times 10^3$ cells mL^{-1}) within 250 m water depth along sampling stations in July 2014. Contour lines in white bold are guidelines including: temperature (21°C), nitrate (1 μM), phosphate (0.1 μM), Chl *a* (0.3 μg Chl L^{-1}), Proch (50 × 10^3 cells mL^{-1}), Syne (50 × 10^3 cells mL^{-1}), PicoEuk (5 × 10^3 cells mL^{-1}), and Bact (0.5 × 10^5 cells mL^{-1}). The inverse triangles at the top of each panel indicate the locations of Stations K101–K108 along the KTV1 transect (**Figure 1**).

slope for *Synechococcus* and picoeukaryotes using all pooled data at each sampling station (**Table 2**); the linear relationships were also significantly evidenced for the N/P ratio (all $p < 0.001$; **Table 2**). The relative abundance of autotrophic picoplankton to total autotrophic picoplankton was significantly and linearly regressed with the N/P ratio, but not for nutrient concentrations, for values over each sampling period (**Supplementary Figure S4**); its slope was negative for *Prochlorococcus* ($p < 0.01$) but positive for *Synechococcus* ($p < 0.01$) and picoeukaryotes ($p < 0.05$; **Supplementary Figure S4**). The result also indicates that abundances of *Prochlorococcus* decreased, but *Synechococcus* and picoeukaryotes increased with increasing of the N/P ratio or

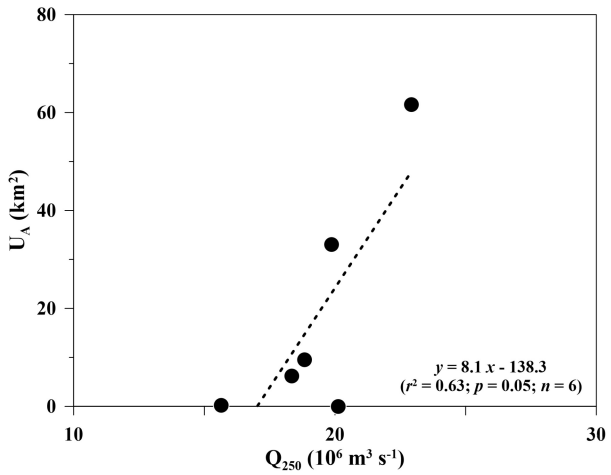

FIGURE 3 | Relationship between the uplift area (U_A; km^2) and volume transport (Q_{250}; S_V; 10^6 m^3 s^{-1}) at different sampling periods. The slope and r^2 of the linear regression (dashed lines) are shown and also applied to **Figures 4**–**6**.

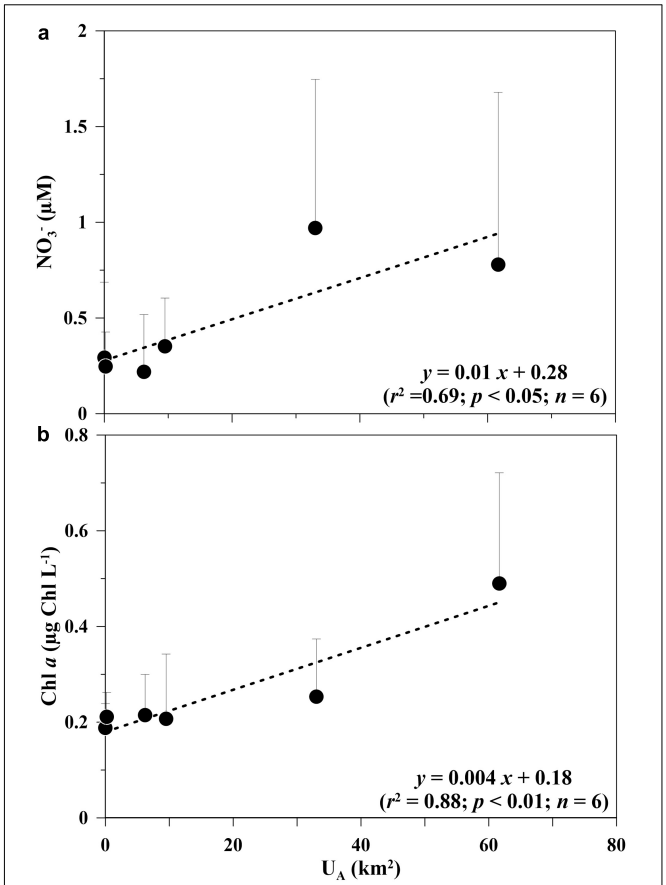

FIGURE 4 | Relationships between the uplift area (U_A; km^2) versus the mean depth-integrated values of **(a)** nitrate (NO_3^-; μM) and **(b)** chlorophyll *a* (Chl *a*; μg Chl L^{-1}) over each sampling period. SD (vertical lines with caps) is also illustrated and applied to **Figure 8**.

nitrate concentration. This phenomenon could also be evidenced in the spatial, both vertical and horizontal, distribution of autotrophic picoplankton. Generally, the abundances of *Synechococcus* and picoeukaryotes were higher in the shallow water at onshore stations (**Figures 2f,g**), but a higher abundance of *Prochlorococcus* was observed in the deeper water at offshore stations (**Figure 2e**). The relative abundance of *Prochlorococcus* increased from onshore toward offshore, ranging from 71.8 (±18.2) to 93.5 (±3.22)% for the upper 100 m depth (**Figure 8**). However, the trend was inverse for *Synechococcus*; that is, its relative abundance decreased from onshore toward offshore, with a range from 23.9 (±15.9) to 5.1 (±2.5)%. Even though the relative abundance was small for picoeukaryotes, it also demonstrated a trend similar to that of *Synechococcus*' and with values ranging from 4.3 (±2.8) to 1.4 (±1.3)% (**Figure 8**).

The abundance of heterotrophic picoplankton (e.g., heterotrophic bacteria) was approximately one to two orders of magnitude higher than autotrophic picoplankton in this study. Its mean depth-integrated abundance ranged from 0.42 (±0.13) to 4.80 (±0.94) × 10^5 cells mL^{-1} or biomass is in the range of 0.84 (±0.25)–9.60 (±1.89) μg C L^{-1} over each sampling period (**Figure 7**). Generally, the spatial distribution of higher heterotrophic bacteria abundance was like that of *Prochlorococcus* (**Figures 2e,h**). The depth-integrated abundance of heterotrophic bacteria was also significantly, positively and linearly regressed with *Prochlorococcus* at all sampling stations (r^2 = 0.61; p < 0.001); but its relationship with *Synechococcus* abundance was negative (r^2 = 0.10; p < 0.05; data not shown). Its depth-integrated value was also significantly, negatively and linearly related to nutrient (nitrate and silicate) concentrations and the N/P ratio, which was similar to relationships observed between *Prochlorococcus* abundance and nutrient concentrations (**Table 2**). Additionally, a linear relationship was significantly evidenced between the depth-integrated abundances (or carbon biomass) of heterotrophic bacteria and total autotrophic picoplankton using all pooled data of each sampling station (p < 0.001; **Figure 6b**).

DISCUSSION

The Coastal Uplift and Its Impact on Chemical Hydrographics in the Kuroshio

The typical characteristic of KW is high salinity and high temperature, as it originates from the Northern Equatorial Current with modification from South China Sea water and West Philippine Sea water (also called North Pacific water) (Mensah et al., 2014, 2015). During its downstream transport, a tremendous amount of oligotrophic water, heat, and salt is delivered northward from its origin (Nitani, 1972). High surface temperature (>26.1°C) and salinity (>33.77) were observed in this study. Vertically, seawater temperature displayed an onshore lifting and offshore deepening of the isotherms (i.e., tilting isotherms) across the Kuroshio in the KTV1 transect (**Figures 1**, **2a**). This westward (shoreward)

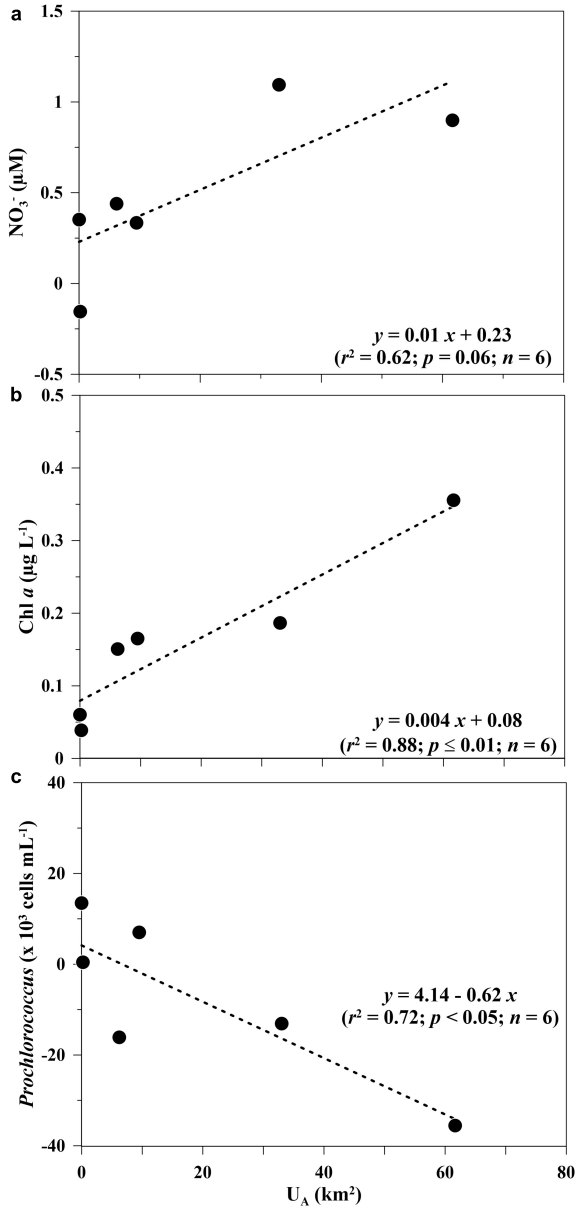

FIGURE 5 | Relationships between the uplift area (U_A; km^2) versus: **(a)** nitrate concentration (NO_3^-; μM), **(b)** chlorophyll *a* value (Chl *a*; μg Chl L^{-1}), and **(c)** *Prochlorococcus* abundance (×10^3 cells mL^{-1}), and the values are the difference between the average depth-integrated nitrate concentration of onshore, Sts. (K101–104), and offshore, Sts. (K105–108) stations over each sampling period.

TABLE 2 | The slopes, r^2 and *p*-values of linear regressions between the depth-integrated values of variables vs. nutrient concentrations (μM) [e.g., nitrate (NO_3^-; N), phosphate (PO_4^{3-}; P), silicate (SiO_3^{2-})] or the N/P molar ratio for the upper 100 m depth of all sampling stations.

Nutrients Variables	$[NO_3^-]$	$[PO_4^{3-}]$	$[SiO_3^{2-}]$	The N/P ratio
Chl *a* (*n* = 48)	Slope = 0.15 r^2 = 0.41***	Slope = 1.86 r^2 = 0.47***	Slope = 0.04 r^2 = 0.17**	Slope = 0.01 r^2 = 0.03
Proch (*n* = 47)	Slope = –13.02 r^2 = 0.08*	Slope = 110.91 r^2 = 0.04	Slope = –13.16 r^2 = 0.41***	Slope = –2.46 r^2 = 0.39***
Syne (*n* = 47)	Slope = 12.81 r^2 = 0.70***	Slope = 47.90 r^2 = 0.07	Slope = 4.03 r^2 = 0.34***	Slope = 1.05 r^2 = 0.54***
PicoEuk (*n* = 47)	Slope = 1.59 r^2 = 0.58***	Slope = 8.47 r^2 = 0.12*	Slope = 0.57 r^2 = 0.36***	Slope = 0.12 r^2 = 0.40***
Bact (*n* = 47)	Slope = –0.69 r^2 = 0.08*	Slope = 11.54 r^2 = 0.16**	Slope = -0.80 r^2 = 0.53***	Slope = –0.18 r^2 = 0.65***

Variables include chlorophyll a (Chl a; μg L^{-1}) concentration, abundances (×10^3 cells mL^{-1}) of Prochlorococcus (Proch) Synechococcus (Syne), picoeukaryotes (PicoEuk), as well as heterotrophic bacteria (Bact; ×10^5 cells mL^{-1}).
n, sampling number.
****p < 0.001; **p < 0.01; *p ≤ 0.05.*

elevated sloping isotherm (and isopycnal) is typical in the western boundary current, such as the Kuroshio, off the east coast of Taiwan (Jan et al., 2011; Chen et al., 2017). Even though this pattern is a normal characteristic of a geostrophic current, its uplifting magnitude of cold water mass, biological responses, and associated variation of these variables due to the strengthening/weakening of the geostrophic current have rarely been calculated with *in situ* data, not to mention its impact on the ecosystem. To estimate the uplifting magnitude in the vertical, the uplift area was quantified, applied, and served as an index (see "Materials and Methods" for details; **Table 1**).

In our statistical analysis of the six cruise observations, the isotherm slope and associated uplift area on the onshore side of the Kuroshio is linearly correlated to the volume transport in the upper 250 m Q_{250} with r^2 = 0.63 (p = 0.0059; **Figure 3**). The increase of uplift area at a certain depth in the upper layer suggests the support of cold water and nutrients from lower layers, which potentially brings biological influences to the upper layer, as observed during our cruise surveys. Within the seasonal time scale (i.e., the intraseasonal time scale), the variability of the isotherm (and isopycnal) slope and associated volume transport across the Kuroshio east of Taiwan is closely related to the impingement of mesoscale eddies, which has been demonstrated and discussed using observations from moored pressure sensor-equipped inverted echo sounder (PIES) array, moored 75-kHz acoustic Doppler current profilers, ship-based hydrography surveys, and satellite altimeter data (Jan et al., 2015, 2017; Chang et al., 2018; Mensah et al., 2020). Based on the theory of geostrophic balance and the corresponding thermal wind relation of a large-scale, stratified ocean current (e.g., the Kuroshio), the increase (or decrease) of isotherm slope across the Kuroshio causes an increase (or decrease) of volume transport in the Kuroshio and vice versa (Jan et al., 2017). The thermal wind relation states a balance between geostrophic velocity shear and horizontal density gradient perpendicular to the velocity shear (e.g., Cushman-Roisin, 1994): $\frac{\partial v_G}{\partial z} = -\frac{g}{\rho_0 f}\frac{\partial \rho}{\partial x}$ (where v_G is the northward geostrophic velocity, g is gravitational acceleration, ρ_0 is reference seawater density, f is the Coriolis parameter calculated as 2Ωsin (latitude), Ω is the angular velocity of earth rotation, and ρ is density). As the velocity in the upper layer increases and consequently leads to the increase of the velocity shear, the density gradient is therefore adjusted to increase the isopycnal (or isotherm) slope across the current. The physical process typically causes the uplift of the isotherm/isopycnal in the onshore side of the Kuroshio, which corresponds to the increase of upward vertical velocity near the coast and consequently

creates a net nutrient flux in the vertical. As the upper layer velocity decreases, the aforementioned processes reverse. Note that the across-Kuroshio isotherm/isopycnal slope could also be influenced by the hydrography of an impinging mesoscale eddy (Jan et al., 2017). The impingement of a cyclonic eddy from the east could heave (depress) isotherms/isopycnals on the offshore (onshore) side of the Kuroshio and lead to the weakening of Kuroshio transport east of Taiwan, as illustrated in the Figure 1A of Jan et al. (2017). As an anticyclonic eddy impinges on the Kuroshio, the processes in the eddy-Kuroshio interaction reverse and the isotherm/isopycnal slope and associated Kuroshio transport increases as illustrated in the Figure 1B of Jan et al. (2017). The positive linear correlation of the onshore uplift area and Q_{250} obtained from the six of our observations can be plausibly attributed to the aforementioned dynamics. Additionally, this coastal uplift was also found in the upstream and downstream of the KTV1 transect along the Kuroshio-influenced regions (**Supplementary Figure S1**; Lai et al., 2021). It suggests that this coastal uplift may occur year-round in a broad-scale region on the onshore side of Kuroshio, eastern Taiwan. This also indicates that its impact on the Kuroshio ecosystem may be more profound than expected.

Despite the swift downstream advection of any variability in the Kuroshio, the frontogenesis and frontolysis occurring when mesoscale eddies of both signs impinge onto the Kuroshio and associated submesoscale processes created during the impingement (e.g., Nagai et al., 2006; McWilliams et al., 2009), particularly on the offshore side, and its potential biological influences merit a further study. Note that the mesoscale eddy influence and corresponding eddy-Kuroshio interaction is not the only cause of the uplift area and Q_{250} variability described herein. The entrainment of colder water (e.g., South China Sea water from the Luzon Strait or riverine waters from the east coast of Taiwan) to the onshore flank of the Kuroshio in the upper 200 m could also result in the change of density gradient across the Kuroshio through isotherm heaving, resulting in the increase of northward flow volume transport (Mensah et al., 2014; Jan et al., 2015). The southwesterly wind burst-induced seaward Ekman transport along the east coast and typhoons that pass across or nearby Taiwan could also contribute to the uplift of nearshore isotherms (or colder subsurface water) and the associated nutrient concentration in the upper 100–200 m, which merits a future study. It should also be noted that a decreased Q_{250} may be accompanied by the depression of isotherms on the onshore side of the upper layer Kuroshio. This downward moving process will not have a positive effect on the increase of nutrient concentration near the eastern coast of Taiwan.

Even though the KW carries oligotrophic water, the nutrient concentration is normally close to zero in the surface water (e.g., Chen et al., 1995; Kodama et al., 2014). In this study, nitrate concentration in the surface reached 0.69 μM at St. K103, an onshore station (**Figure 2b**); this relatively high nutrient value in the surface water was also found at onshore stations in other sampling periods. This phenomenon might be caused by the coastal uplift. Corresponding to the isotherms coastal uplifting, nutrient distribution also demonstrated a coastal uplift pattern; that is, an onshore lifting and offshore deepening of the nutrient concentration contours along the KTV1 transect (**Figures 2b,c**). This pattern could be significantly evidenced by the negative linear relationships between nutrients (nitrate or phosphate) and water temperature using all pooled data in

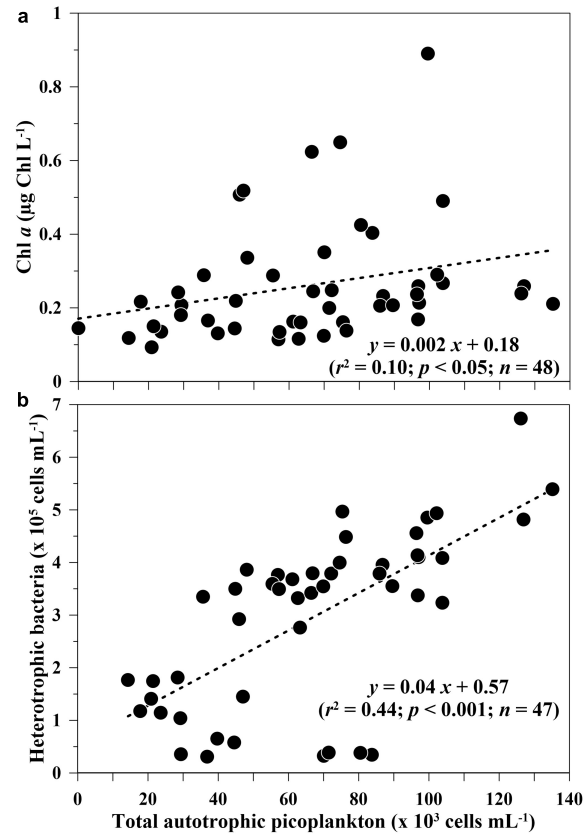

FIGURE 6 | Relationships between the depth-integrated values of total autotrophic picoplankton abundance (×10^3 cells mL^{-1}) versus **(a)** chlorophyll *a* value (Chl *a*; μg Chl L^{-1}) and **(b)** heterotrophic bacteria abundance (×10^5 cells mL^{-1}) for the upper 100 m depth of all sampling stations.

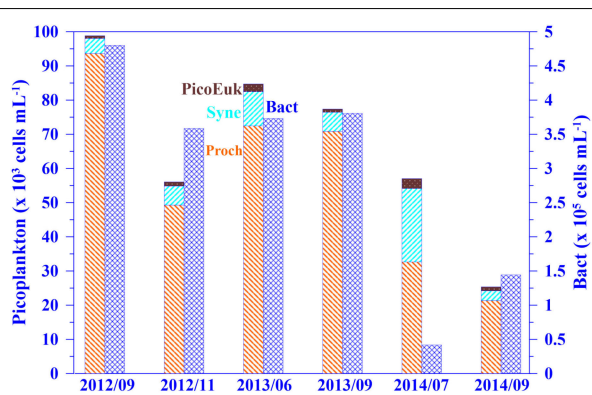

FIGURE 7 | The depth-integrated abundances of heterotrophic bacteria (Bact; ×10^5 cells mL^{-1}) and autotrophic picoplankton (×10^3 cells mL^{-1}), e.g., *Prochlorococcus* (Proch), *Synechococcus* (Syne), and picoeukaryotes (PicoEuk), for the upper 100 m depth over each sampling period.

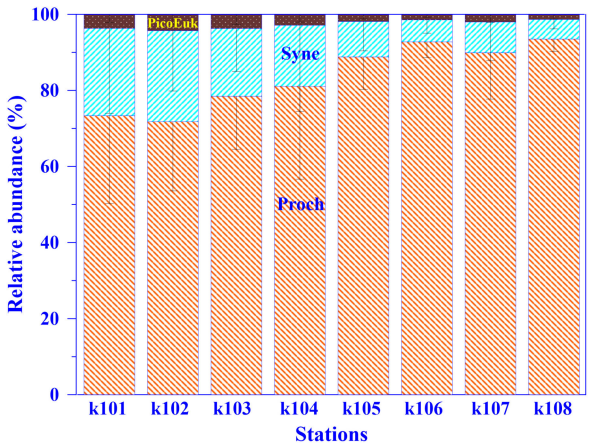

FIGURE 8 | The relative abundances of different autotrophic picoplankton, including *Prochlorococcus* (Proch), *Synechococcus* (Syne), and picoeukaryotes (PicoEuk), to total autotropic picoplankton (Proch + Syne + PicoEuk) for the upper 100 m depth over each sampling station.

this study; The trend was also significant for nutrients and water density but with the positive linear relationships (all $p < 0.001$; data not shown). This assumption was also supported by the significant linear relationship between the nutrient concentrations and the uplift area (**Figure 4a**). Additionally, there was also a trend displayed that the difference of average nutrient value between onshore and offshore stations increased with increasing of the uplift magnitude, even though it was not statistically significant (**Figure 5a**). In addition to dissolved inorganic nutrient concentration/availability, the N/P ratio also has important implications for marine plankton (Wal et al., 1994; Agawin et al., 2004). The average N/P ratio was small, with a value of 10.4 in this study (**Supplementary Figure S2**). This ratio is consistent with the KW properties characterized by a low N/P ratio (e.g., <16; Kodama et al., 2014). Noticeably, the N/P ratio varied spatiotemporally in this study, and this might result in variant responses on marine plankton (**Supplementary Figure S2**). The results all suggest that the pelagic ecosystem across the Kuroshio mainstream (e.g., onshore to offshore) may have different responses due to its horizontal and spatial nutrient distribution and/or the variant N/P ratio.

Coastal Uplift Impact on Biological Variables in the Kuroshio

Phytoplankton growth mostly depends on nutrient availability in oligotrophic KW (Lin et al., 2020; Liu et al., 2020). Light availability might not be a limited factor for phytoplankton growth in this subtropical Kuroshio region since its Z_E consistently reached 103 m water depth in this study. The nutrient availability limitation could be indirectly supported by the significant linear relationship between the values of Chl *a* and nutrients (**Table 2**). The coastal uplift not only enhanced the upward nutrient concentration, but it also increased phytoplankton biomass (used Chl *a* as proxy) in the shallow water of the Kuroshio. Generally, the SCM was located shallower onshore and became deeper toward the offshore, and its value even reached 2.03 μg Chl L^{-1} (**Figure 2d** and **Supplementary Figure S3**). The depth-integrated Chl *a* concentration also increased with an increase in the uplift magnitude (**Figure 4b**). Spatially, the average Chl *a* concentration was higher in the onshore than in the offshore, and the difference between onshore and offshore stations was also significantly related to the uplift magnitude (**Figure 5b**). This suggests that the coastal uplift of nutrients may enhance the growth of phytoplankton in the onshore stations, and its enhancement increased with an increase in the uplift magnitude in the Kuroshio, eastern Taiwan.

Additionally, phytoplankton composition may also vary due to nutrient availability and/or the N/P ratio (Agawin et al., 2004; Mouriño-Carballido et al., 2016; Liu et al., 2020). In the oligotrophic ocean, plankton is dominated by picoplankton, which includes both autotrophic and heterotrophic picoplankton (Marañón et al., 2001; Calvo-Díaz et al., 2011). The composition of picoplankton, especially picophytoplankton, may vary with environmental factors, such as light intensity, nutrient availability, turbulent mixing, and temperature (Smayda and Reynolds, 2001; Mouriño-Carballido et al., 2016; Liu et al., 2020). The abundance of autotrophic picoplankton was dominated by *Prochlorococcus* (83.6%), followed by *Synechococcus* (13.8%) and then picoeukaryotes (2.7%) in this study. Similar dominance of picophytoplankton abundance was also observed in the Kuroshio and the subtropical northwest Pacific. There, it was mostly dominated by *Prochlorococcus* and *Synechococcus* (Jiao and Yang, 2002; Li et al., 2017; Endo and Suzuki, 2019; Liu et al., 2020). The picoeukaryotes abundance was relatively low in a similar region, and its majority was composed of Alveolata, Haptophyta, and Stramenopiles (Chan et al., 2020). The abundance of total autotrophic picoplankton (*Prochlorococcus* + *Synechococcus* + picoeukaryotes) was significantly related to the Chl *a* concentration (**Figure 6a**). This suggests that phytoplankton might be dominated by autotrophic picoplankton in the Kuroshio. In oceanic waters, picophytoplankton is responsible for 46–89% of the bulk Chl *a* (Jiao and Yang, 2002). This assumption could also be supported by the high proportion of carbon biomass of picophytoplankton to phytoplankton; its proportion was approximately 50.4 (±18.2)% in this study. Picophytoplankton tend to dominate the phytoplankton biomass in the oligotrophic ocean, where their high surface-to-volume ratio makes them the best competitors for low nutrient concentrations (Raven, 1998; Alvain et al., 2005; Buitenhuis et al., 2012).

The relative contribution of different picophytoplankton to its composition, however, varied spatiotemporally. Spatially, the contribution of *Prochlorococcus* to total picophytoplankton abundance increased from onshore to offshore, but the pattern was inverse for *Synechococcus* and picoeukaryotes. Additionally, the difference in *Prochlorococcus* abundance between onshore and offshore decreased with an increase in the coastal uplift magnitude (**Figure 5c**). This suggests that the increasing nutrient concentrations caused by the coastal uplift might decrease and/or increase the growth of *Prochlorococcus* and other picophytoplankton (e.g.,

Synechococcus or picoeukaryotes) onshore, respectively. This assumption could be supported by the significant linear relationship between different picophytoplankton and nutrient concentrations (e.g., nitrate and silicate), which have negative and positive slopes for *Prochlorococcus* and other picophytoplankton (e.g., *Synechococcus* or picoeukaryotes), respectively (**Table 2**); Mouriño-Carballido et al. (2016) have also observed similar trends. The negatively linear relationship was also evidenced between phosphate concentration versus the difference between onshore and offshore stations of *Prochlorococcus* abundance over each sampling period (data not shown; $r^2 = 0.81$; $p \leq 0.01$). The difference in *Synechococcus* abundance between onshore and offshore stations also significantly increased with increasing nitrate concentration (data not shown; $r^2 = 0.67$; $p < 0.05$). Similar to previous relationships between nitrate concentrations and picophytoplankton, the regressions were also significantly evidenced between the N/P molar ratio and picophytoplankton (**Table 2** and **Supplementary Figure S4**). Phytoplankton species composition has also been observed and shifted with the N/P molar ratio (Agawin et al., 2004).

As for heterotrophic picoplankton (or heterotrophic bacteria), it dominates the picoplankton in oligotrophic oceans, such as the Kuroshio (**Figure 7**; Calvo-Díaz et al., 2011). In this study, heterotrophic bacteria were positively regressed with total autotrophic picoplankton in terms of abundance and biomass (**Figure 6b**). On average, the ratio of autotrophic to heterotrophic picoplankton biomass in carbon units was 1.13 ± 0.54 over this study if the extremely high ratio of the July 2014 data was excluded from this estimation. This ratio was at the high end of observed values (0.81–1.21) in the North Atlantic subtropical gyre (Calvo-Díaz et al., 2011). The distribution of heterotrophic bacteria was similar to that of *Prochlorococcus,* even though its abundance was one to two orders of magnitude higher than *Prochlorococcus*. This assumption could be supported by the significant relationship found between abundances of heterotrophic bacteria and *Prochlorococcus*. The relationships between heterotrophic bacteria and nutrient concentrations or the N/P ratio were also significant and similar to that of *Prochlorococcus* (**Table 2**). Even though an inverse pattern was observed between biomass of heterotrophic bacteria and *Prochlorococcus* in the downstream Kuroshio (Jiao and Yang, 2002). The results suggest that heterotrophic bacteria might be partially dependent on resources derived from picophytoplankton.

Implication of the Coastal Uplift Effect on the Kuroshio Ecosystem

The coastal uplift occurred in the onshore region with approximately 50 × 400 km (width × length) along the Kuroshio, east of Taiwan (**Figures 1**, **2** and **Supplementary Figure S1**). Coastal uplift enhanced and increased nutrient concentration in the shallow water of this onshore region; the nutrient concentration also increased with the uplift magnitude increasing (**Figure 4a**). Compared to the offshore region, on average, nitrate concentration increased approximately 0.49 μM over 100 m water depth (or 0.69 g N m^{-2}) in the onshore region; the total amount of nitrate increased approximately 1.37 × 10^4 T of N in the onshore region along the Kuroshio. Primary production will therefore be promoted by the enhanced nutrients in the sunlit layer, approximately 100 m in the oligotrophic Kuroshio. Unfortunately, primary production was not measured in this study. Phytoplankton biomass, however, not only increased with increasing uplift magnitude: its value was higher in the onshore than that of the offshore regions for an average value of 0.16 μg Chl L^{-1} (or 1.06 g C m^{-2}); the total amount of phytoplankton biomass increased approximately 2.11 × 10^4 T of C in the onshore region along the Kuroshio, east coast of Taiwan. High phytoplankton biomass can provide and transfer energy to higher trophic levels in the pelagic ecosystem of Kuroshio. This implies that the coastal uplift may play one of the key roles in resolving the "Kuroshio paradox" (Nagai, 2019).

Picoplankton is highly susceptible to environmental changes, including altering its community compositions and/or nutrition strategy to respond (Worden et al., 2015; Chung and Gong, 2019). In addition to increasing nutrient concentrations and phytoplankton biomass, the relative abundances and composition of picophytoplankton also changed due to the coastal uplift. For example, the relative abundances of *Synechococcus* and picoeukaryotes increased toward onshore but decreased for *Prochlorococcus* (**Figure 8**). This implied that the organic carbon content should increase and be higher in the onshore than in the offshore regions, even if similar Chl *a* concentrations are found in both regions. Growth of *Synechococcus* and picoeukaryotes is more favorable in high nutrient availability environments, such as the onshore region of the Kuroshio (Mouriño-Carballido et al., 2016; Liu et al., 2020). The growth of *Prochlorococcus* is, however, less susceptible to nutrient depletion (or availability) but more vulnerable to higher temperature (Olson et al., 1990; Liu et al., 2020). This may explain why the higher abundance of *Prochlorococcus* was normally observed at water column where water temperature < 30°C, i.e., generally, at the shallow layer onshore and deeper layer offshore (**Figure 2e** and **Supplementary Figure S5b**; Jiao and Yang, 2002). The results also suggest that this phenomenon (e.g., decreasing *Prochlorococcus* abundance) should be enhanced in the Kuroshio due to water temperature increases caused by global warming. In the subtropical Kuroshio ecosystem, surface-warming rates have been suggested approximately two to three times faster than other subtropical regions in the past decades (Wu et al., 2012). This accelerated warming may subsequently change the flow velocity of the Kuroshio Current (Wu et al., 2012, 2016; Yang et al., 2016). This implies that the previously observed phenomena (e.g., the coastal uplift magnitude and its subsequent changes in nutrient dynamics and picoplankton composition) may be intensified and enhanced by future global warming.

Growth of heterotrophic bacteria may be limited by substrate supply (e.g., organic carbon) and/or temperature in the shelf region and in the Kuroshio (Jiao and Yang, 2002; Shiah et al., 2003; Lai et al., 2021). As stated above, heterotrophic bacteria were significantly related to autotrophic picoplankton. In the coastal uplift onshore region, picophytoplankton (e.g., *Synechococcus* and picoeukaryotes) with higher organic carbon content may favor the growth of heterotrophic bacteria; its abundance was averagely higher, ca. 0.17 × 10^5 cells mL^{-1}, in the onshore than offshore regions in this study.

CONCLUSION

The Kuroshio is oligotrophic and low productivity, but it supports a high abundance of fish population. This is called the "Kuroshio paradox." In this study, a coastal uplift was observed in the subtropical Kuroshio, off the east coast of Taiwan. Vertically, seawater temperature displayed an onshore lifting and offshore deepening of the isotherms across the Kuroshio. This coastal uplift occurs year-round and approximately covers the area along the Kuroshio, eastern Taiwan. Interestingly, the coastal uplift intensity (or magnitude) was significantly related to the volume transport of the upper 250 m depth in the Kuroshio. Its magnitude (e.g., isotherm slope) variation could be associated with the adjustment of the pressure gradient force and the Coriolis force, which is not balanced in the cross-stream direction. A large amount of dissolved inorganic nutrients was uplifted to the sunlit zone, and it promoted primary production especially in the onshore region; in total, it is estimated to increase approximately 1.37×10^4 T of N and 2.11×10^4 T of C in the onshore from that of offshore regions along the Kuroshio, eastern Taiwan. The relative abundance of picophytoplankton also changed due to the coastal uplift; the relative abundances of *Synechococcus* and picoeukaryotes increased toward onshore, but it decreased for *Prochlorococcus*. This phenomenon can be explained by the fact that the growth of *Synechococcus* and picoeukaryotes is more favorable in high nutrient availability environments, but the growth of *Prochlorococcus* is less susceptible to nutrient depletion but more vulnerable to higher temperatures. The results all suggest the coastal uplift supports more energy transferred to higher tropical levels, and it may play a key element in mapping the puzzle of the "Kuroshio paradox."

DATA AVAILABILITY STATEMENT

The datasets presented in this study can be found in online repositories. The names of the repository/repositories and accession number(s) can be found below: doi.org/10.5061/dryad.bzkh1899p.

AUTHOR CONTRIBUTIONS

C-CChen contributed to designing of the research, analyzing data, and writing the manuscript. C-YL performed the research (Chl *a*, dissolved inorganic nutrients) and analyzed the data. SJ performed the research (water volume transport), analyzed the data, and wrote part of the manuscript. C-hH performed the research (picoplankton abundance) and analyzed data. C-CChung performed the research (picoplankton abundance) and analyzed the data. All authors contributed to manuscript revision and approved the submitted version.

FUNDING

This study is part of the multidisciplinary "Plankton Ecological Processes in Subtropical-shelf Ecosystems" (PEPSE) and "The Observations of the Kuroshio Transports and their Variability" (OKTV) programs, which are supported by the Ministry of Science and Technology, Taiwan (MOST; 107-2611-M-003-001-MY3 and 110-2611-M-003-002 to C-CChen). SJ was supported by the MOST grant no. 101-2611-M-002-018-MY3, 103-2611-M-002-011, and 105-2119-M-002-042.

ACKNOWLEDGMENTS

We are indebted to the officers and crew of the *Ocean Researcher I* for their assistance during the research cruise. This article was subsidized by National Taiwan Normal University (NTNU).

SUPPLEMENTARY MATERIAL

The Supplementary Material for this article can be found online at: https://www.frontiersin.org/articles/10.3389/fmars.2022.796187/full#supplementary-material

REFERENCES

Acabado, C. S., Cheng, Y.-H., Chang, M.-H., and Chen, C.-C. (2021). Vertical nitrate flux induced by Kelvin-Helmholtz billows over a seamount in the Kuroshio. *Front. Mar. Sci.* 8:680729. doi: 10.3389/fmars.2021.680729

Agawin, N. S., Duarte, C., Agustí, S., and Vaqué, D. (2004). Effect of N:P ratios on response of Mediterranean picophytoplankton to experimental nutrient inputs. *Aquat. Microb. Ecol.* 34, 57–67. doi: 10.3354/ame034057

Alvain, S., Moulin, C., Dandonneau, Y., and Breon, F. M. (2005). Remote sensing of phytoplankton groups in case 1 waters from global SeaWiFS imagery. *Deep-Sea Res. Part I-Oceanogr. Res. Pap.* 52, 1989–2004. doi: 10.1016/j.dsr.2005.06.015

Buck, K. R., Chavez, F. P., and Campbell, L. (1996). Basin-wide distributions of living carbon components and the inverted trophic pyramid of the central gyre of the north Atlantic Ocean, summer 1993. *Aquat. Microb. Ecol.* 10, 283–298. doi: 10.3354/ame010283

Buitenhuis, E. T., Li, W. K. W., Vaulot, D., Lomas, M. W., Landry, M. R., Partensky, F., et al. (2012). Picophytoplankton biomass distribution in the global ocean. *Earth Syst. Sci. Data* 4, 37–46. doi: 10.5194/essd-4-37-2012

Calvo-Díaz, A., Díaz-Pérez, L., Suárez, L. Ñ, Morán, X. A. G., Teira, E., and Marañón, E. (2011). Decrease in the autotrophic-to-heterotrophic biomass ratio of picoplankton in oligotrophic marine waters due to bottle enclosure. *Appl. Environ. Microbiol.* 77, 5739–5746. doi: 10.1128/AEM.00066-11

Campbell, L., Nolla, H. A., and Vaulot, D. (1994). The importance of *Prochlorococcus* to community structure in the central North Pacific Ocean. *Limno. Oceanogr.* 39, 954–961. doi: 10.4319/lo.1994.39.4.0954

Chan, Y. F., Chung, C. C., Gong, G. C., and Hsu, C. W. (2020). Spatial variation of abundant picoeukaryotes in the subtropical Kuroshio Current in winter. *Mar. Ecol.* 41:e12579. doi: 10.1111/maec.12579

Chang, M.-H., Jan, S., Mensah, V., Andres, M., Rainville, L., Yang, Y. J., et al. (2018). Zonal migration and transport variations of the Kuroshio east of Taiwan induced by eddy impingements. *Deep-Sea Res. Part I-Oceanogr. Res. Pap.* 131, 1–15. doi: 10.1016/j.dsr.2017.11.006

Chen, C. T. A., Liu, C. T., and Pai, S. C. (1995). Variations in oxygen, nutrient and carbonate fluxes of the Kuroshio Current. *La Mer* 33, 161–176.

Chen, C.-C., Gong, G.-C., Chiang, K.-P., Shiah, F.-K., Chung, C.-C., and Hung, C.-C. (2021). Scaling effects of a eutrophic river plume on organic carbon consumption. *Limnol. Oceanogr.* 66, 1867–1881. doi: 10.1002/lno.11729

Chen, C.-C., Hsu, S.-C., Jan, S., and Gong, G.-C. (2015). Episodic events imposed on the seasonal nutrient dynamics of an upwelling system off northeastern Taiwan. *J. Mar. Syst.* 141, 128–135. doi: 10.1016/j.jmarsys.2014.07.021

Chen, C.-C., Jan, S., Kuo, T. H., and Li, S. Y. (2017). Nutrient flux and transport by the Kuroshio east of Taiwan. *J. Mar. Syst.* 167, 43–54. doi: 10.1016/j.jmarsys.2016.11.004

Chung, C.-C., and Gong, G.-C. (2019). Attribution of the growth of a distinct population of *Synechococcus* to the coverage of lateral water on an upwelling. *Terr. Atmos. Ocean. Sci.* 30, 575–587. doi: 10.3319/tao.2018.09.26.01

Cushman-Roisin, B. (1994). *Introduction to Geophysical Fluid Dynamics*. Hoboken, NJ: Prentice-Hall.

Endo, H., and Suzuki, K. (2019). "Spatial variations in community structure of haptophytes across the Kuroshio front in the Tokara Strait," in *The Kuroshio-induced Nutrient Supply in the Shelf and Slope Region off the Southern Coast of Japan*, eds T. Nagai, H. Saito, K. Suzuki, and M. Takahashi (Hoboken, NJ: John Wiley & Sons, Inc), 207–221. doi: 10.1002/9781119428428.ch13

Furuya, K. (1990). Subsurface chlorophyll maximum in the tropical and subtropical western Pacific Ocean: vertical profiles of phytoplankton biomass and its relationship with chlorophyll a and particulate organic carbon. *Mar. Biol.* 107, 529–539. doi: 10.1007/BF01313438

Gong, G.-C., Wen, Y.-H., Wang, B.-W., and Liu, G.-J. (2003). Seasonal variation of chlorophyll a concentration, primary production and environmental conditions in the subtropical East China Sea. *Deep-Sea Res. II Top. Stud. Oceanogr.* 50, 1219–1236. doi: 10.1016/S0967-0645(03)00019-5

Guo, Y. J. (1991). The Kuroshio, Part II. Primary productivity and phytoplankton. *Oceanogr. Mar. Bio. Ann. Rev.* 29, 155–189.

Hsu, S. C., Wong, G. T. F., Gong, G. C., Shiah, F. K., Huang, Y. T., Kao, S. J., et al. (2010). Sources, solubility, and dry deposition of aerosol trace elements over the East China Sea. *Mar. Chem.* 120, 116–127. doi: 10.1016/j.marchem.2008.10.003

Hung, C. C., and Gong, G. C. (2011). Biogeochemical responses in the Southern East China Sea after Typhoons. *Oceanography* 24, 42–51. doi: 10.5670/oceanog.2011.93

Jan, S., Chen, C. C., Tsai, Y. L., Yang, Y. J., Wang, J., Chern, C. S., et al. (2011). Mean structure and variability of the cold dome Northeast of Taiwan. *Oceanography* 24, 100–109. doi: 10.5670/oceanog.2011.98

Jan, S., Mensah, V., Andres, M., Chang, M.-H., and Yang, Y. J. (2017). Eddy-Kuroshio interactions: local and remote effects. *J. Geophys. Res. Oceans* 122, 9744–9764. doi: 10.1002/2017JC013476

Jan, S., Yang, Y. J., Wang, J., Mensah, V., Kuo, T.-H., Chiou, M.-D., et al. (2015). Large variability of the Kuroshio at 23.75°N east of Taiwan. *J. Geophys. Res. Oceans* 120, 1825–1840. doi: 10.1002/2014jc010614

Jiao, N., and Yang, Y. (2002). Ecological studies on *Prochlorococcus* in China seas. *Chinese Sci. Bull.* 47, 1243–1250. doi: 10.1360/02tb9276

Kobari, T., Honma, T., Hasegawa, D., Yoshie, N., Tsutsumi, E., Matsuno, T., et al. (2020). Phytoplankton growth and consumption by microzooplankton stimulated by turbulent nitrate flux suggest rapid trophic transfer in the oligotrophic Kuroshio. *Biogeosciences* 17, 2441–2452. doi: 10.5194/bg-17-2441-2020

Kodama, T., Shimizu, Y., Ichikawa, T., Hiroe, Y., Kusaka, A., Morita, H., et al. (2014). Seasonal and spatial contrast in the surface layer nutrient content around the Kuroshio along 138°E, observed between 2002 and 2013. *J. Oceanogr.* 70, 489–503. doi: 10.1007/s10872-014-0245-5

Lai, C.-C., Wu, C.-R., Chuang, C.-Y., Tai, J.-H., Lee, K.-Y., Kuo, H.-Y., et al. (2021). Phytoplankton and bacterial responses to monsoon-driven water masses mixing in the Kuroshio off the east coast of Taiwan. *Front. Mar. Sci.* 8:707807. doi: 10.3389/fmars.2021.707807

Lee, S., and Fuhrman, J. A. (1987). Relationship between biovolume and biomass of naturally derived marine bacterioplankton. *Appl. Environ. Microbiol.* 53, 1298–1303. doi: 10.1016/0198-0254(87)96080-8

Levitus, S. (1982). *Climatological Atlas of the Word Ocean, NOAA Professional Paper No. 13*. Silver Spring, Md: US Government Printing Office.

Li, J., Jiang, X., Li, G., Jing, Z., Zhou, L., Ke, Z., et al. (2017). Distribution of picoplankton in the northeastern South China Sea with special reference to the effects of the Kuroshio intrusion and the associated mesoscale eddies. *Sci. Total Environ.* 589, 1–10. doi: 10.1016/j.scitotenv.2017.02.208

Lin, F. S., Ho, P. C., Sastri, A. R., Chen, C. C., Gong, G. C., Jan, S., et al. (2020). Resource availability affects temporal variation of phytoplankton size structure in the Kuroshio east of Taiwan. *Limmol. Oceanogr.* 65, 236–246. doi: 10.1002/lno.11294

Liu, H. B., Suzukil, K., Minami, C., Saino, T., and Watanabe, M. (2002). Picoplankton community structure in the subarctic Pacific Ocean and the Bering Sea during summer 1999. *Mar. Ecol. Prog. Ser.* 237, 1–14. doi: 10.3354/Meps237001

Liu, H., Nolla, H. A., and Campbell, L. (1997). Prochlorococcus growth rate and contribution to primary production in the equatorial and subtropical North Pacific Ocean. *Aquat. Microb. Ecol.* 12, 39–47. doi: 10.3354/ame012039

Liu, K., Suzuki, K., Chen, B., and Liu, H. (2020). Are temperature sensitivities of *Prochlorococcus* and *Synechococcus* impacted by nutrient availability in the subtropical northwest Pacific? *Limnol. Oceanogr.* 66, 639–651. doi: 10.1002/lno.11629

Marañón, E., Holligan, P. M., Barciela, R., González, N., Mouriño, B., Pazó, M. J., et al. (2001). Patterns of phytoplankton size structure and productivity in contrasting open-ocean environments. *Mar. Ecol. Prog. Ser.* 216, 43–56. doi: 10.3354/meps216043

McWilliams, J. C., Colas, F., and Molemaker, M. J. (2009). Cold filamentary intensification and oceanic surface convergence lines. *Geophys. Res. Lett.* 36:L18602. doi: 10.1029/2009GL039402

Mensah, V., Jan, S., Andres, M., and Chang, I. H. (2020). Response of the Kuroshio east of Taiwan to mesoscale eddies and upstream variations. *J. Oceanogr.* 76, 271–288. doi: 10.1007/s10872-020-00544-8

Mensah, V., Jan, S., Chang, M. H., and Yang, Y. J. (2015). Intraseasonal to seasonal variability of the intermediate waters along the Kuroshio path east of Taiwan. *J. Geophys. Res. Oceans* 120, 5473–5489. doi: 10.1002/2015jc010768

Mensah, V., Jan, S., Chiou, M.-D., Kuo, T. H., and Lien, R.-C. (2014). Evolution of the Kuroshio Tropical water from the Luzone Strait to the east of Taiwan. *Deep-Sea Res. Part I-Oceanogr. Res. Pap.* 86, 68–81. doi: 10.1016/j.dsr.2014.01.005

Morel, A., Ahn, Y.-H., Partensky, F., Vaulot, D., and Claustre, H. (1993). *Prochlorococcus* and *Synechococcus*: a comparative study of their optical properties in relation to their size and pigmentation. *J. Mar. Res.* 51, 617–649. doi: 10.1357/0022240933223963

Mouriño-Carballido, B., Hojas, E., Cermeño, P., Chouciño, P., Fernández-Castro, B., Latasa, M., et al. (2016). Nutrient supply controls picoplankton community structure during three contrasting seasons in the northwestern Mediterranean Sea. *Mar. Ecol. Prog. Ser.* 543, 1–19. doi: 10.3354/meps11558

Nagai, T. (2019). *The Kuroshio Current: Artery of Life*. Washington, DC: John Wiley & Sons.

Nagai, T., Durán, G. S., Otero, D. A., Mori, Y., Yoshie, N., Ohgi, K., et al. (2019). How the Kuroshio current delivers nutrients to sunlit layers on the continental shelves with aid of near-internal waves and turbulence. *Geophys. Res. Lett.* 46, 6726–6735. doi: 10.1029/2019GL082680

Nagai, T., Tandon, A., and Rudnick, D. L. (2006). Two-dimensional ageostrophic secondary circulation at ocean fronts due to vertical mixing and large-scale deformation. *J. Geophys. Res.* 111:C09038. doi: 10.1029/2005JC002964

Nitani, H. (1972). "Beginning of the Kuroshio," in *Kuroshio: Its Physical Aspects*, eds H. Stommel and K. Yoshida (Tokyo: University of Tokyo Press), 129–163.

Olson, R. J., Chisholm, S. W., Zettler, E. R., Altabet, M. A., and Dusenberry, J. A. (1990). Spatial and temporal distributions of prochlorophyte picoplankton in the North Atlantic Ocean. *Deep-Sea Res. Part I-Oceanogr. Res. Pap.* 37, 1033–1051. doi: 10.1016/0198-0149(90)90109-9

Parsons, T. R., Maita, Y., and Lalli, C. M. (1984). *A Manual of Chemical and Biological Methods for Seawater Analysis*. Oxford, NY: Pergamon Press.

Raven, J. A. (1998). The twelfth tansley lecture. small is beautiful: the picophytoplankton. *Funct. Ecol.* 12, 503–513. doi: 10.1046/j.1365-2435.1998.00233.x

Rochford, D. J. (1984). Nitrates in eastern Australian coastal waters. *Aust. J. Mar. Freshwater Res.* 35, 385–397. doi: 10.1071/MF9840385

Roughan, M., and Middleton, J. H. (2002). A comparison of observed upwelling mechanisms off the east coast of Australia. *Cont. Shelf Res.* 22, 2551–2572. doi: 10.1016/S0278-4343(02)00101-2

Shiah, F. K., Gong, G. C., and Chen, C. C. (2003). Seasonal and spatial variation of bacterial production in the continental shelf of the East China Sea: possible

controlling mechanisms and potential roles in carbon cycling. *Deep-Sea Res. II Top. Stud. Oceanogr.* 50, 1295–1309. doi: 10.1016/S0967-0645(03)00024-9

Smayda, T. J., and Reynolds, C. S. (2001). Community assembly in marine phytoplankton: application of recent models to harmful dinoflagellate blooms. *J. Plankton Res.* 23, 447–461. doi: 10.1093/plankt/23.5.447

Sukigara, C., Suga, T., Toyama, K., and Oka, E. (2014). Biogeochemical responses associated with the passage of a cyclonic eddy based on shipboard observations in the western North Pacific. *J. Oceanogr.* 70, 435–445. doi: 10.1007/s10872-014-0244-6

Thurnherr, A. M. (2010). A practical assessment of the errors associated with full-depth LADCP profiles obtained using teledyne RDI workhorse acoustic doppler current profilers. *J. Atmos. Ocean. Tech.* 27, 1215–1227. doi: 10.1175/2010jtecho708.1

Visbeck, M. (2002). Deep velocity profiling using lowered acoustic doppler current profilers: bottom track and inverse solutions. *J. Atmos. Ocean. Tech.* 19, 794–807. doi: 10.1175/1520-0426(2002)019<0794:dvpula>2.0.co;2

Wal, P. V. D., Kraay, G. W., and Meer, J. V. D. (1994). Community structure and nutritional state of phytoplankton growing in mesocosms with different initial N:P ratios studied with high performance liquid chromatography. *Sarsia* 79, 409–416. doi: 10.1080/00364827.1994.10413572

Worden, A. Z., Follows, M. J., Giovannoni, S. J., Wilken, S., Zimmerman, A. E., and Keeling, P. J. (2015). Rethinking the marine carbon cycle: factoring in the multifarious lifestyles of microbes. *Science* 347:1257594. doi: 10.1126/science.1257594

Wu, C.-R., Wang, Y.-L., Lin, Y.-F., Chiang, T.-L., and Wu, C.-C. (2016). Weakening of the Kuroshio intrusion into the South China Sea under the global warming hiatus. *IEEE J. Sel. Top. Appl. Earth Obs. Remote Sens.* 9, 5064–5070. doi: 10.1109/JSTARS.2016.2574941

Wu, L. X., Cai, W. J., Zhang, L. P., Nakamura, H., Timmermann, A., Joyce, T., et al. (2012). Enhanced warming over the global subtropical western boundary currents. *Nat. Clim. Change* 2, 161–166. doi: 10.1038/Nclimate1353

Yang, H., Lohmann, G., Wei, W., Dima, M., Ionita, M., and Liu, J. (2016). Intensification and poleward shift of subtropical western boundary currents in a warming climate. *J. Geophys. Res. Oceans* 121, 4928–4945. doi: 10.1002/2015JC011513

Conflict of Interest: The authors declare that the research was conducted in the absence of any commercial or financial relationships that could be construed as a potential conflict of interest.

Publisher's Note: All claims expressed in this article are solely those of the authors and do not necessarily represent those of their affiliated organizations, or those of the publisher, the editors and the reviewers. Any product that may be evaluated in this article, or claim that may be made by its manufacturer, is not guaranteed or endorsed by the publisher.

Copyright © 2022 Chen, Lu, Jan, Hsieh and Chung. This is an open-access article distributed under the terms of the Creative Commons Attribution License (CC BY). The use, distribution or reproduction in other forums is permitted, provided the original author(s) and the copyright owner(s) are credited and that the original publication in this journal is cited, in accordance with accepted academic practice. No use, distribution or reproduction is permitted which does not comply with these terms.

frontiers in Marine Science

ORIGINAL RESEARCH
published: 03 March 2022
doi: 10.3389/fmars.2022.815348

Impact of Mesoscale Circulation on the Structure of River Plumes During Large Rainfall Events Inshore of the East Australian Current

Junde Li[1]*, *Moninya Roughan*[1], *Colette Kerry*[1] and *Shivanesh Rao*[2]

[1] School of Biological Earth and Environmental Sciences, University of New South Wales, Sydney, NSW, Australia, [2] Science, Economics and Insights Division, Department of Planning, Industry and Environment, Sydney, NSW, Australia

OPEN ACCESS

Edited by:
Toru Kobari,
Kagoshima University, Japan

Reviewed by:
Laurent Marcel Cherubin,
Florida Atlantic University,
United States
Zhiqiang Liu,
Southern University of Science and Technology, China
Hui Wu,
East China Normal University, China

***Correspondence:**
Junde Li
junde.li@unsw.edu.au

Specialty section:
This article was submitted to Coastal Ocean Processes, a section of the journal Frontiers in Marine Science

Received: 15 November 2021
Accepted: 27 January 2022
Published: 03 March 2022

Citation:
Li J, Roughan M, Kerry C and Rao S (2022) Impact of Mesoscale Circulation on the Structure of River Plumes During Large Rainfall Events Inshore of the East Australian Current. Front. Mar. Sci. 9:815348. doi: 10.3389/fmars.2022.815348

Estuarine outflow can have a significant impact on physical and ecological systems in the coastal ocean. Along southeastern Australia, inshore of the East Australian Current, the shelf is narrow, the coastal circulation is advection dominated, and river estuarine outflow tends to be low, hence river plumes have largely been ignored. For these reasons, we lack an understanding of the spatial and temporal evolution of river plumes during large rainfall events (which are projected to increase in frequency and intensity), and the interaction of the mesoscale circulation with the estuarine outflow remains to be explored. Using a high-resolution (750 m) hydrodynamic model, we simulate idealized plumes from 4 estuaries during three different mesoscale circulation scenarios and investigate the spatial and temporal evolution of the estuarine outflow under two contrasting rainfall events (normal and large). We explore the plume from the largest of the 4 rivers, the Hawkesbury River, to understand the impact of the mesoscale circulation. During the first EAC mode, the plume spreads both northward and southeastward. The offshore spread of the plume is the largest in this scenario (~12.5 km east of the river mouth) in the wet event. In the second EAC mode, this plume dispersal is toward the north and east, driven by the proximity of a cyclonic eddy on the shelf, with an eastward extension of 11 km. In the third EAC mode, most of this river plume spreads southward with some to the north, again dictated by the position of the cyclonic eddy. The cross-shelf dispersal is a minimum of 9.5 km from the river mouth. It takes around 6 days for the freshwater spatial extent of the plume in the wet event to return to the base case. These results show the importance of mesoscale EAC circulation on the shelf circulation when considering river plumes dispersal. Knowledge of the ultimate fate of riverborne material, dilution and cumulative effects will enable better environmental management of this dynamic region for the local government.

Keywords: East Australian Current, dye tracers, Hawkesbury Shelf bioregion, Regional Ocean Modeling System, river plume, large rainfall, Hawkesbury River, Sydney estuary

1. INTRODUCTION

Freshwater flow is a critical landscape process that influences the coastal marine ecosystems (Skreslet, 1986). River discharge stimulates phytoplankton and subsequently zooplankton assemblages by providing high nutrient concentrations (Schlacher et al., 2008). River plumes form biogeochemical hot spots in coastal seas worldwide and rank amongst the most productive regions of the world's oceans (Schlacher et al., 2008). Natural variation in freshwater flowing from rivers strongly influences the distribution and abundance of fish and invertebrates through changes in growth, survival, and recruitment (Gillson, 2011; Gillson et al., 2012). Freshwater flow is also a powerful forcing agent in coastal ecosystems (Schlacher et al., 2008). Freshwater flow has a pivotal role in determining fisheries production due to its effects on environmental conditions (Grimes, 2001; Lloret et al., 2004). Episodic flood events maintain and enhance biological productivity and modify the species composition of landings by altering rates of estuarine immigration and emigration due to changes in salinity altering habitat availability (Gillson, 2011). Gillson et al. (2012) showed that flood events can influence commercial fisheries by modifying landings composition, fishers' harvesting behavior, and revenue generation. Severe flood events cause widespread mortalities of fish due to the production of unfavorable water quality characteristics in estuarine and coastal systems, which have been documented in the Richmond, Clarence, and Mcleay River estuaries in eastern Australia (Dawson, 2002; Eyre et al., 2006; Kroon and Ludwig, 2010). Therefore, understanding the spatial and temporal evolution of river plumes, particularly during flood events, is an important issue in fisheries ecology.

It is recognized that the estuarine zone is an important site for physico-chemical processes (Covelli et al., 2007), where flood river plumes are important pathways for materials from terrestrial to the sea and dominant sources of coastal pollutants (Warrick et al., 2004). Jaffe et al. (1995) showed that the Tuy River plume effectively transports a variety of pollutants derived from anthropogenic activities, such as heavy metals and organic contaminants, into the coastal zone. By studying the chemical composition of suspended particulate matter, Kannan et al. (2012) identified the water masses and movement of Yangtze River plumes to the Yellow Sea in the transport of sediments and contaminants. The river discharge of wastewater which contains macronutrients and micropollutants, are known to cause various deleterious effects in the coastal environment (Lawrence, 2010). There is a growing need to understand the dispersion of river plumes across coastal marine systems, which is essential to drive catchment management actions in protecting our coastal environment.

The East Australian Current (EAC) a major western boundary current flows poleward along southeastern Australia and typically separates from the coast, between 31°S and 32.5°S (Cetina-Heredia et al., 2014). When the current separates, it typically sheds large anti-cyclonic eddies. Additionally, eddy dipoles can form, associated with cyclonic eddies (Malan et al., 2020). The cyclonic eddies either form as frontal eddies on the inside edge of the EAC jet (Roughan et al., 2017; Schaeffer et al., 2017) or as westward propagating cyclones that interact with the EAC jet (Roughan et al., 2017; Li et al., 2022).

The Hawkesbury Shelf region is located downstream of the EAC separation, which has been identified as a region of high productivity (Oke and Middleton, 2001). The shelf circulation in this region is dominated by three prominent circulation patterns, which are associated with the poleward along-shore flow of the EAC jet, the eddies and the eddy dipoles downstream of the typical EAC separation region (33°S) (Malan et al., 2020; Ribbat et al., 2020b; Roughan et al., 2022). The circulation modes are largely dictated by where the EAC separates and the presence (or absence) of anticyclonic and cyclonic eddies as described in Roughan et al. (2022). The three modes are shown clearly in the schematic diagram of Ribbat et al. (2020b), their Figure 12. While the circulation patterns have been studied in some detail, little is known about the impact of the mesoscale circulation over the Hawkesbury Shelf region. Moreover, this is the first study to explore the spatial and temporal evolution of the river plumes.

Most estuaries in the Hawkesbury Shelf region are drowned river valleys with strong oceanic influence. The rainfall is typically low with small river outflows, and their impacts have largely been neglected by many studies, for example, recent modeling studies of this region assume freshwater inflow is negligible (Kerry et al., 2016; Ribbat et al., 2020b). However, the river discharges dramatically increase during sporadic large rainfall events, which is three times larger than the mean inflow in the Hawkesbury River region (Gillson et al., 2012). In this case, their impact will become significant to coastal and shelf ecosystems.

Previous studies have used numerical models to trace the riverine freshwater by releasing dyes into the rivers in many coastal regions, such as the New York Bight (Zhang et al., 2010), the Rhine Region (Rijnsburger et al., 2021), the South Brazilian Bight (Marta-Almeida et al., 2021), the Yangtze River estuary (Yu et al., 2020; Wu et al., 2021), and the Great Barrier Reef (Colberg et al., 2020). Three-dimensional structure and evolution of the river plumes have been presented in these numerical simulations. However, the knowledge of the spatial and temporal evolution of river plumes in the Hawkesbury Shelf region is limited, especially with large river discharges during high rainfall events.

In this study, we use a high-resolution numerical model to understand the dilution of estuarine outflow during large rainfall events and the influence of the mesoscale circulation patterns on river plume structure inshore of the EAC. Section 2 describes the numerical model configuration and sensitivity experiments. The model simulations of the spatial and temporal evolution of the river plumes are presented in Section 3. In Sections 4, 5, we provide a further discussion and summary of the results.

2. MATERIALS AND METHODS

2.1. Model Configuration

We use a series of nested configurations of the Regional Ocean Modeling System (ROMS) for the EAC system (**Figure 1**), building on configurations of Kerry and Roughan (2020); Li et al. (2021b, 2022); Ribbat et al. (2020b). ROMS is an open-source

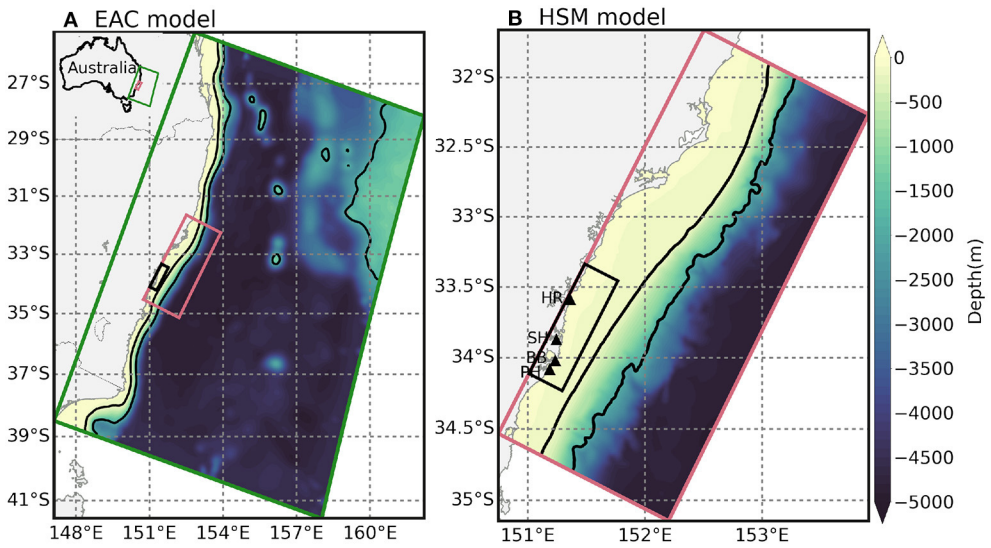

FIGURE 1 | Schematic diagram showing the model bathymetry (color shading) in the study site along the east coast of Australia in the model domains. **(A)** The EAC-ROMS parent model, and **(B)** the nested HSM model. The locations of the 4 rivers are indicated by the black triangles: Hawkesbury River (HR), Sydney Harbor (SH), Botany Bay (BB), and Port Hacking (PH). The black rectangle indicates the region covers the plumes from the four rivers.

hydrodynamic model which is widely used (Shchepetkin and McWilliams, 2005) for coastal and shelf seas applications.

We use a high-resolution ROMS configuration of the Hawkesbury Shelf region, hereafter referred to as the Hawkesbury Shelf Model (HSM) model, with a model domain is shown in **Figure 1B**. The HSM model has a horizontal resolution of 750 × 750 m (Ribbat et al., 2020a,b) and 30 vertical s-layers, with a higher resolution in the upper ocean to resolve the wind-driven and estuarine outflow circulation and near the bottom for improved resolution of the bottom boundary layer. The model bathymetry was obtained from the 50-m high resolution Multibeam Dataset for Australia from Geoscience Australia (Whiteway, 2009). We use atmospheric forcing from the Bureau of Meteorology Atmospheric high-resolution Regional Reanalysis for Australia (BARRA-R) (Su et al., 2019) and include barotropic tidal forcing at the open boundaries that were extracted from the TPXO8 global tidal model solutions with a 1/30° resolution (Egbert and Erofeeva, 2002). We use the MPDATA horizontal advection scheme for dye tracers (Smolarkiewicz, 1984). The Mellor and Yamada (1982) level-2.5, second-moment turbulence closure scheme (MY2.5) is used in parameterizing vertical turbulent mixing of momentum and tracers. The HSM model is one-way nested inside a coarser resolution (2.5–6 km) EAC-ROMS model (**Figure 1A**), with the same configuration as Li et al. (2021a,b, 2022).

The EAC-ROMS model is well-validated and widely used for example by Kerry and Roughan (2020), Malan et al. (2020), Schilling et al. (2020), and Li et al. (2021b, 2022), for exploring ocean dynamics and biological connectivity. This model is nested inside the newest Australian national Bluelink reanalysis product version BRAN2020 (Chamberlain et al., 2021), with a horizontal resolution of 10 × 10 km. The EAC-ROMS covers a 25+ years (1994–2019) simulation, using the same bathymetry, atmospheric and tide forcing products as those in the HSM model. This nested site of models provides a highly resolved representation of the regional circulation regime encompassing the EAC along the southeastern Australian Coast from 26–39°S.

In the model nesting, the EAC-ROMS model provides initial and boundary conditions for the HSM model. The downscaling ratio was between 3:1 and 5:1, varying due to the varying cross-shelf resolution of the EAC-ROMS model. To avoid depth mismatches between the parent (EAC-ROMS) and child (HSM model) grids, the bathymetries are gradually merged over the regional baroclinic Rossby Radius of 19 km (25 grid cells) along the eastern, northern, and southern boundaries (Ribbat et al., 2020b).

2.2. EAC Scenarios

The daily satellite observations of geostrophic current velocities are obtained from Archiving, Validation and Interpretation of Satellite Oceanographic (AVISO) (Ducet et al., 2000), which are distributed by the Copernicus Marine and Environment Monitoring Service (https://marine.copernicus.eu/). The AVISO daily data used here spans a 25-year period from January 1994 to February 2019, with a horizontal resolution of 1/4°. AVISO daily geostrophic current velocities are interpolated onto the model grid, and Empirical Orthogonal Functions (EOFs) were applied to the velocity fields for the whole 25-year period.

Previous work in the HSM region by Ribbat et al. (2020b) and Roughan et al. (2022) showed that there are 3 dominant oceanographic scenarios associated with the separation of the EAC and its eddy field. We use EOF analysis to extract the dominant modes that represent these EAC scenarios from our multi-decadal EAC-ROMS model run, which has been interpolated onto the HSM model grid.

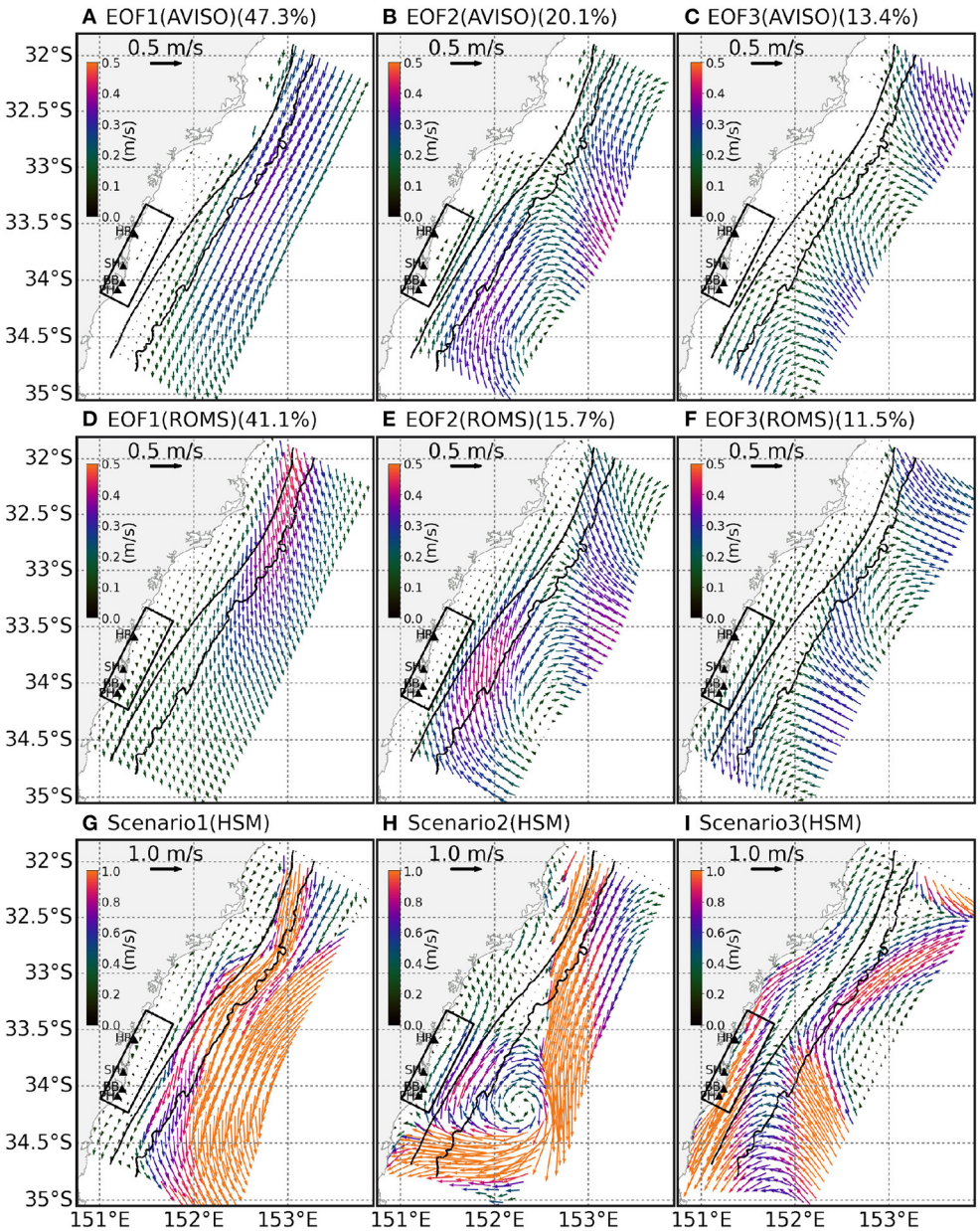

FIGURE 2 | EOF analysis of daily velocities from the EAC-ROMS simulations and AVISO observations for the period of 1994–2019, and mean velocities of the chosen EAC scenarios from the HSM model simulations. **(A–C)** Spatial patterns of the three dominate EOF modes in geostrophic velocities from AVISO observations. Percentages of the explained variances for each mode are indicated. **(D–F)** Same as **(A–C)**, but for surface velocities from the EAC-ROMS simulations. Panels **(G–I)** show the snapshots of the mean circulation patterns in the HSM model that reproduce each EAC scenario as shown in the EOF modes.

The results of the EOF analysis of daily-averaged geostrophic velocity fields from AVISO observations and the multi-decadal EAC-ROMS simulations are shown in **Figure 2**. These results show the first three leading modes that represent the EAC scenarios as follows:

1. Mode 1 (**Figures 2A,D**) represents 47.3% (AVISO) and 41.1% (ROMS) of the variability and is described as an "EAC mode" (EAC scenario 1), where southward circulation dominates the flow through the entire HSM domain, and the along-shore current in the Hawkesbury Shelf bioregion is southward but relatively weak.
2. Mode 2 (**Figures 2B,E**) represents 20.1% (AVISO) and 15.7% (ROMS) of the variability and is described as an "EAC eddy mode" (EAC scenario 2), where southward circulation dominates the flow in the north of the domain, and a cyclonic flow dominates in the southern half of the HSM domain.

3. Mode 3 (**Figures 2C,F**) represents 13.4% (AVISO) and 11.5% of (ROMS) the variability and is described as an "EAC eddy dipole mode" (EAC scenario 3), where southward circulation dominates the flow in the northern third of the domain, a small cyclone dominates the central third of the domain, and an anticyclone dominates in the southern third of the domain, forming an eddy dipole downstream of the EAC jet.

These three scenarios closely resemble the three modes identified by Ribbat et al. (2020b) in a 2-year simulation and defined by Roughan et al. (2022) to explore shelf transport pathways. However, as the modes presented here are identified from a multi-decadal (25-year) observation and simulation, we consider them to be more robust because EOF analysis can capture more time-scale variability in a longer time series.

2.3. Freshwater Inflow Scenarios

To investigate the dilution and dispersion of estuarine outflow, we add river discharges into the HSM model to represent two rainfall scenarios, provided by the Department of Planning, industry and Environment (DPIE), referred to as the "Base Case" and the "Wet event" scenarios as shown in **Figure 3** and **Table 1**. The base case scenario represents the "base flow" and is the annual mean discharge across the estuary entrance as derived from respective calibrated models from Sydney Water Corporation. These were further verified using the observed tidal prism. The wet case scenario is an idealization representation of the "1 in 100 year" extreme flood starting on 18th March 2021 rainstorm event. This representation is superimposed on top of the base case to give the wet event.

TABLE 1 | The river discharges (m^3 s^{-1}) and salinity (psu) applied at each of the four river mouths during the two rainfall scenarios "Base case" and "Wet event."

Rivers	Base case		Wet event	
	Discharge	Salinity	Maximum discharge	Minimum salinity
Hawkesbury River (HR)	4,100	34.6	14,100	19.4
Sydney Harbor (SH)	2,400	35.1	2,670	21.3
Botany Bay (BB)	2,600	34.9	3,545	24.2
Port Hacking (PH)	650	35.0	731	33.74

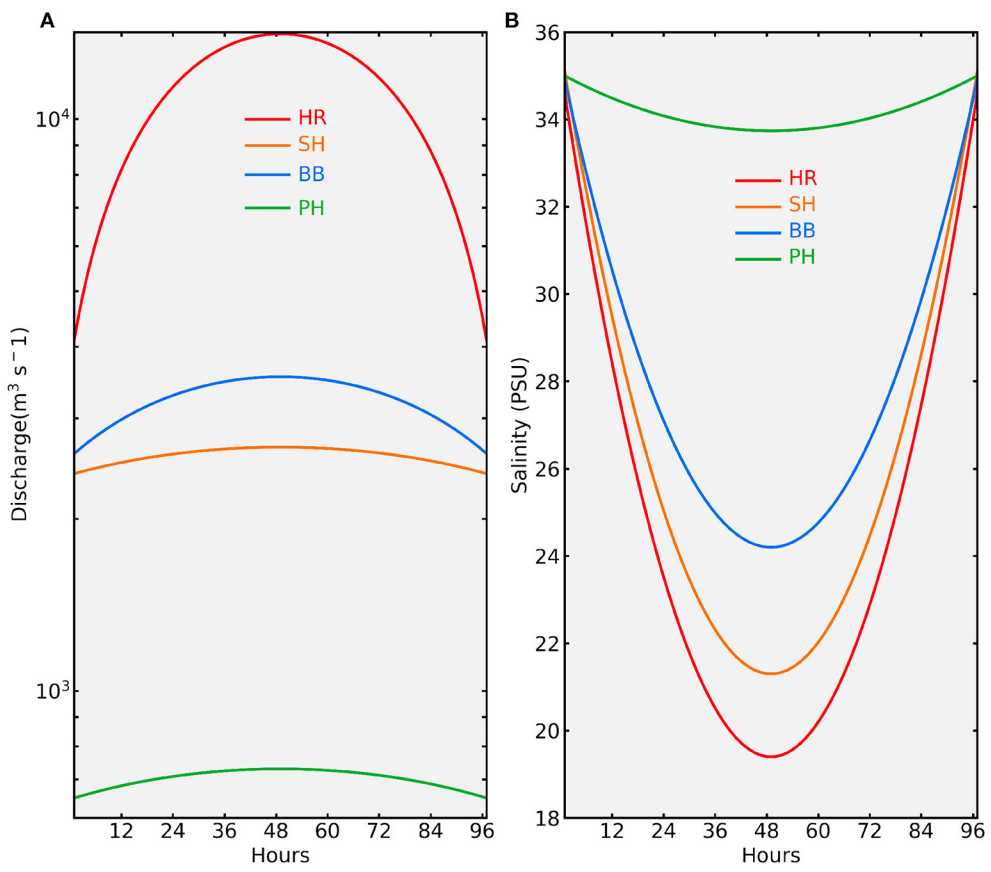

FIGURE 3 | River discharges and salinity at the river mouths during the wet event scenarios. **(A)** Time series of river discharges during the wet event, the discharges return to the same constant value as base case 96 h later. Discharges of HR, SH, BB, and PH rivers are indicated with red, orange, blue, green, and black lines, respectively. **(B)** Same as **(A)**, but for the salinity.

The estuarine outflow salinity is the mean salinity observed at the DPIE Beachwatch sites near their respective estuary entrances. The four estuaries of interest are the Hawkesbury River (HR), Sydney Harbor (SH), Botany Bay (BB), and Port Hacking (PH). In the base case scenario, the river transports are constant at four river mouths, with values of 4,100 m^3 s^{-1} (HR), 2,400 m^3 s^{-1} (SH), 2,600 m^3 s^{-1} (BB), and 650 m^3 s^{-1} (PH). We also use constant surface salinity at the river mouths, with values of 34.6 (HR), 35.1 (SH), 34.9 (BB), and 35.0 (PH). In the wet events, the river transports increase rapidly and peak after 48 h, with values of 14,100 m^3 s^{-1} (HR), 2,670 m^3 s^{-1} (SH), 3,545 m^3 s^{-1} (BB), and 731 m^3 s^{-1} (PH) (**Figure 3A**). The surface salinity at the river mouths also decreases rapidly to 19.4 (HR), 21.3 (SH), 24.2 (BB), and 33.7 (PH) (**Figure 3B**). Four days later, both the river transports and salinity return to normal, with the same constant transport and salinity as the base case.

The volume flux discharges in **Table 1** are the sum of the modeled mean estuarine outflows (provided by Sydney Water Corporation) and the mean freshwater catchment flow observations from the WaterNSW online database (https://realtimedata.waternsw.com.au). Estuaries such as Sydney Harbor, Botany Bay, and Port Hacking did not have a complete monitoring network, so a multiplicative factor of 2 is applied to the WaterNSW observations. This factor is estimated based on the percentage of creeks/rivers not monitored. The Hawkesbury River flow was derived from the Manly Hydraulics Laboratory (MHL) velocity observations and was not modified. The 4 day peak flow duration for the wet event is estimated from the peak flow duration for the monitored creeks.

2.4. Sensitivity Experiments

To investigate the river outflows during three dominant EAC scenarios, we choose snapshots based on the principal component of each EAC mode that represent the oceanographic circulation pattern identified by the EOF modes. As shown in **Figures 2G–I**, these snapshots show the mean surface velocities within the first 4 days in the HSM model simulation during the base case rainfall scenarios and represent Modes 1–3, respectively. It is clear that the chosen snapshots well represent the "EAC mode", "EAC eddy mode", and "EAC eddy dipole mode", providing us the confidence to use them to simulate the impact of the EAC scenarios on the temporal and spatial evolution of the river plumes. In this study, we perform two sensitivity experiments in each EAC scenario, as described below.

To examine the different evolution of estuarine outflow between the base case and wet event, we add the dye tracers in the HSM model simulation with transports and salinity in the base case and wet event scenarios. The initial dye concentration is set to 1 kg m^{-3}. The temperature profiles at the river mouths are extracted from the monthly climatology of the EAC-ROMS multi-decadal simulations. We also use climatological salinity in the bottom 20 layers at the river mouths, but the salinity linearly increases with depth in the top 10 layers. The river discharge decreases with depth at the river mouths, with 55% of the outflow are in the top 10 layers.

In each EAC scenario, the initial and boundary conditions for the HSM model are taken from the parent EAC-ROMS model during the time period identified in each of the representative scenarios. To get a more realistic simulation, we spin up the HSM model with base case river outflows and salinity for 7 days before adding the dye tracer. This short period of spin up allows the low salinity water to mix with shelf water and spread out of the river mouth. After the initial spin up, we perform two model runs of 15 days duration with river transports and salinity representing the two rainfall scenarios. The simulations in the first 4 days are used for comparison.

3. RESULTS

3.1. Spatial Distributions of River Plume

To compare the difference of river plumes between the base case and wet event, we averaged the surface dye concentration over the first 4 days in the Hawkesbury Shelf bioregion (**Figure 4**). The mean dye concentration around the river mouth is much larger in the wet event than in the base case, particularly in the Hawkesbury River region (**Figures 4G–I**). In this study, we focus on the evolution of the river plume around the Hawkesbury River because it has the largest discharge among four rivers (**Figure 3A**), which is more than four times larger than the other rivers. In the base case, the river plume dispersal varies in different EAC scenarios (**Figures 4A–C**). In EAC scenario 1 (**Figure 4A**), the river plume spreads both northward and southeastward near the coast. However, in EAC scenario 2 (**Figure 4B**), the river plume dispersal is toward the north due to the impact of the cyclonic eddies on the shelf. In EAC scenario 3 (**Figure 4C**), most of the river plume spreads southward, with some to the north. In the wet event, the evolution of river plumes shows the same spatial patterns as that in the base case (**Figures 4D–F**), but with a much larger area due to the increase in river discharges. The river plume spreads further southeast in EAC scenario 1, but more onshore in EAC scenario 3. The largest differences appear east, south and north of the river mouth in EAC scenario 1 and EAC scenario 3 (**Figures 4G,I**), but east and north of the river mouth in EAC scenario 2 (**Figure 4H**).

The evolution of the river plume also relies on the initial salinity at the river mouths because the salinity contributes to the density structure, which affects the background currents. Compared to the spatial distributions of dye concentration, the low sea surface salinity (SSS) has consistent patterns in all EAC scenarios of both the base case and wet event (**Figure 5**). This suggests that the SSS we used here at the river mouth can well represent the evolution of the river plume, which can be captured in both the low salinity freshwater and dye concentration. This gives us confidence that the sensitivity experiments in this study can be used to understand the dilution of estuarine outflow during large rainfall events.

Due to the large outflow at the Hawkesbury River, this region has the largest dye concentration and lowest salinity. As the dye concentration was 1 for the freshwater and 0 for the pure sea water, to identify the vertical penetration of the river plume, we estimate the freshwater thickness induced by the rivers as $T_{freshwater} = \int_{-H}^{\eta} c \ dz$. H is the water depth, η is the sea

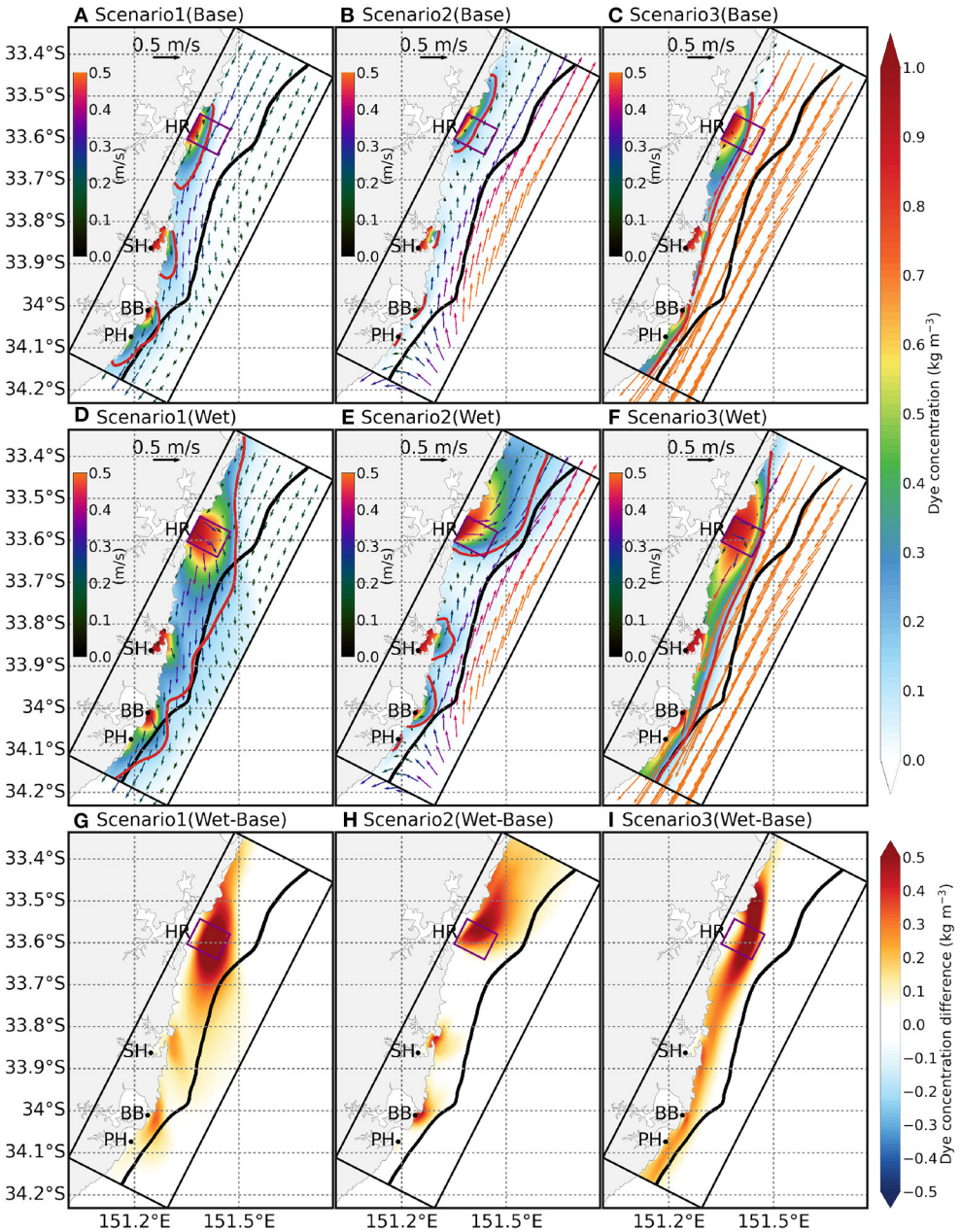

FIGURE 4 | Spatial distributions of dye concentration averaged over the first 4 days for each EAC scenario and their differences between the wet event and the base case. **(A–C)** Spatial distributions of dye concentration for EAC scenario 1, EAC scenario 2, and EAC scenario 3 in the base case. The solid black line shows the 100 m isobath, and the red line indicates the contour of 0.15 dye concentration. The vectors show the mean surface velocities. **(D–F)** Same as **(A–C)**, but for the wet event. **(G–I)** Differences of dye concentration for three EAC scenarios between the wet event **(D–F)** and the base case **(A–C)**.

surface height, and c is the dye concentration. As shown in **Figure 6**, freshwater thickness is larger than 10 m within the dye concentration of 0.15 around the river mouth in the base case. We also found the freshwater thickness of ∼3 m south of the river mouth in EAC scenario 1 and EAC scenario 3 (**Figures 6A,C**) and north of the river mouth in EAC scenario 2 (**Figure 6B**). In the wet event, large discharges increase the area of freshwater thickness as indicated by the dye concentration of 0.15 in **Figures 6D–F**. In EAC scenario 1 and EAC scenario 3, large freshwater thickness difference between the base case and wet event can be found east, south and north of the river mouth (**Figures 6G–I**). In EAC scenario 2, the freshwater thickness difference is much smaller and appears north of the river mouth (**Figure 6H**).

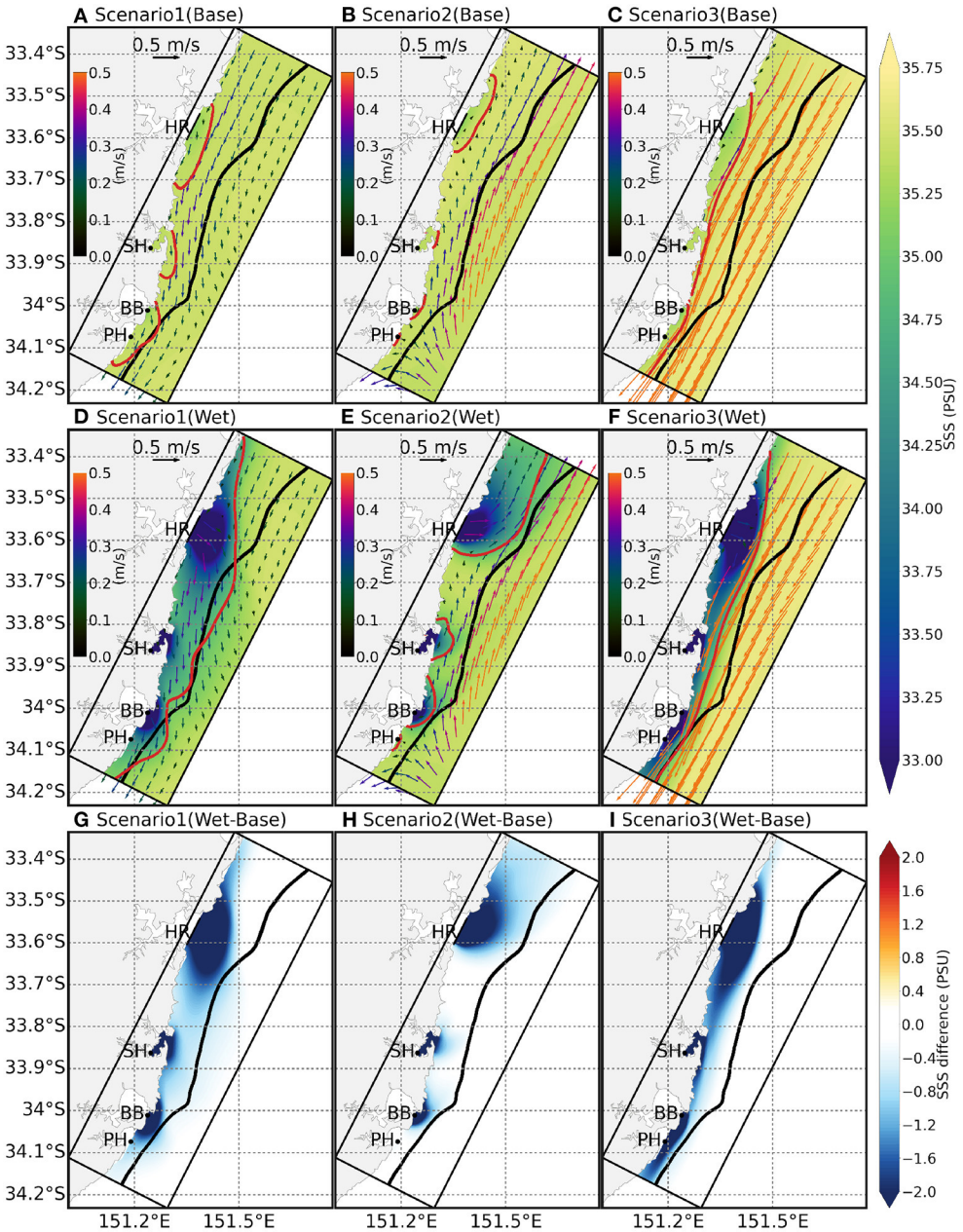

FIGURE 5 | Spatial distributions of SSS averaged over the first 4 days for each EAC scenario and their differences between the wet event and the base case. **(A–C)** spatial distributions of SSS for EAC scenario 1, EAC scenario 2, and EAC scenario 3 in the base case. The solid black line shows the 100 m isobath, and the red line indicates the contour of 0.15 dye concentration. The vectors show the mean surface velocities. **(D–F)** Same as **(A–C)**, but for the wet event. **(G–I)** Differences of SSS for three EAC scenarios between the wet event **(D–F)** and the base case **(A–C)**.

3.2. Cross-Section of the Plume at Hawkesbury River

As discussed in section 3.1, the largest difference of dye concentration, SSS and freshwater thickness between the base case and wet event can be found in the purple box in **Figure 6**. To investigate the vertical evolution and eastward dispersal of the river plume, we calculate the averaged dye concentration, salinity, along-shore and cross-shore velocities within the purple box.

Figure 7 shows the cross-section of dye concentration east of the river mouth. As indicated by the red line, the maximum eastward extension can reach around 4 km in EAC scenario 2 (**Figure 7B**), with a high dye concentration (0.5) about 2 km away from the river mouth. The river plume spreads much farther in EAC scenario 1 and EAC scenario 3 (**Figures 7A,C**). The vertical impact reaches about 20 m in EAC scenario 2, but is only 15 m and 13 m in EAC scenario 1 and EAC scenario 3, respectively.

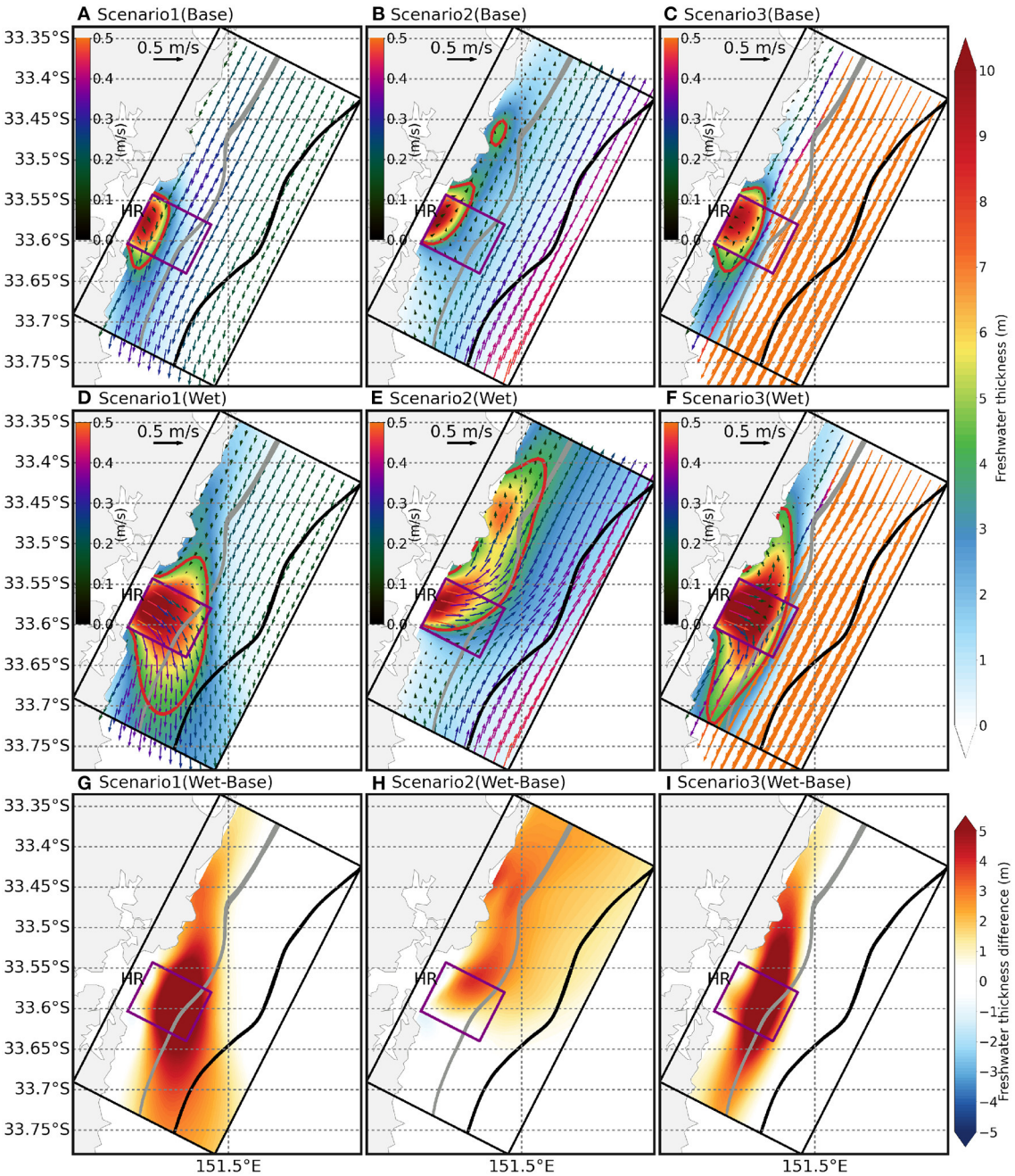

FIGURE 6 | Spatial distributions of freshwater thickness averaged over the first 4 days for each EAC scenario in the HR region and their differences between the wet event and the base case. **(A–C)** spatial distributions of freshwater thickness for EAC scenario 1, EAC scenario 2, and EAC scenario 3 in the base case. The solid gray and black lines show the 50 and 100 m isobath, respectively. The red line indicates the freshwater thickness contour of 4 m, and the purple box shows the location used in the following **Figures 7**, **8**, **10**. The vectors show the mean surface velocities. **(D–F)** Same as **(A–C)**, but for the wet event. **(G–I)** Differences of freshwater thickness for three EAC scenarios between the wet event **(D–F)** and the base case **(A–C)**.

In the wet event, the eastward velocities increase significantly at the river mouth in three EAC scenarios. the maximum eastward extension is about 12.5, 11.5, and 9.5 km in EAC scenario 1, EAC scenario 2 and EAC scenario 3, respectively (**Figures 7D–F**). High dye concentration also spreads farthest in EAC scenario 1, but nearest in EAC scenario 2. The vertical penetration of high dye concentration is the deepest in EAC scenario 3 but the shallowest in EAC scenario 2. The differences of dye concentration between the wet event and base case are constrained within 2–12 km away from the river mouth and

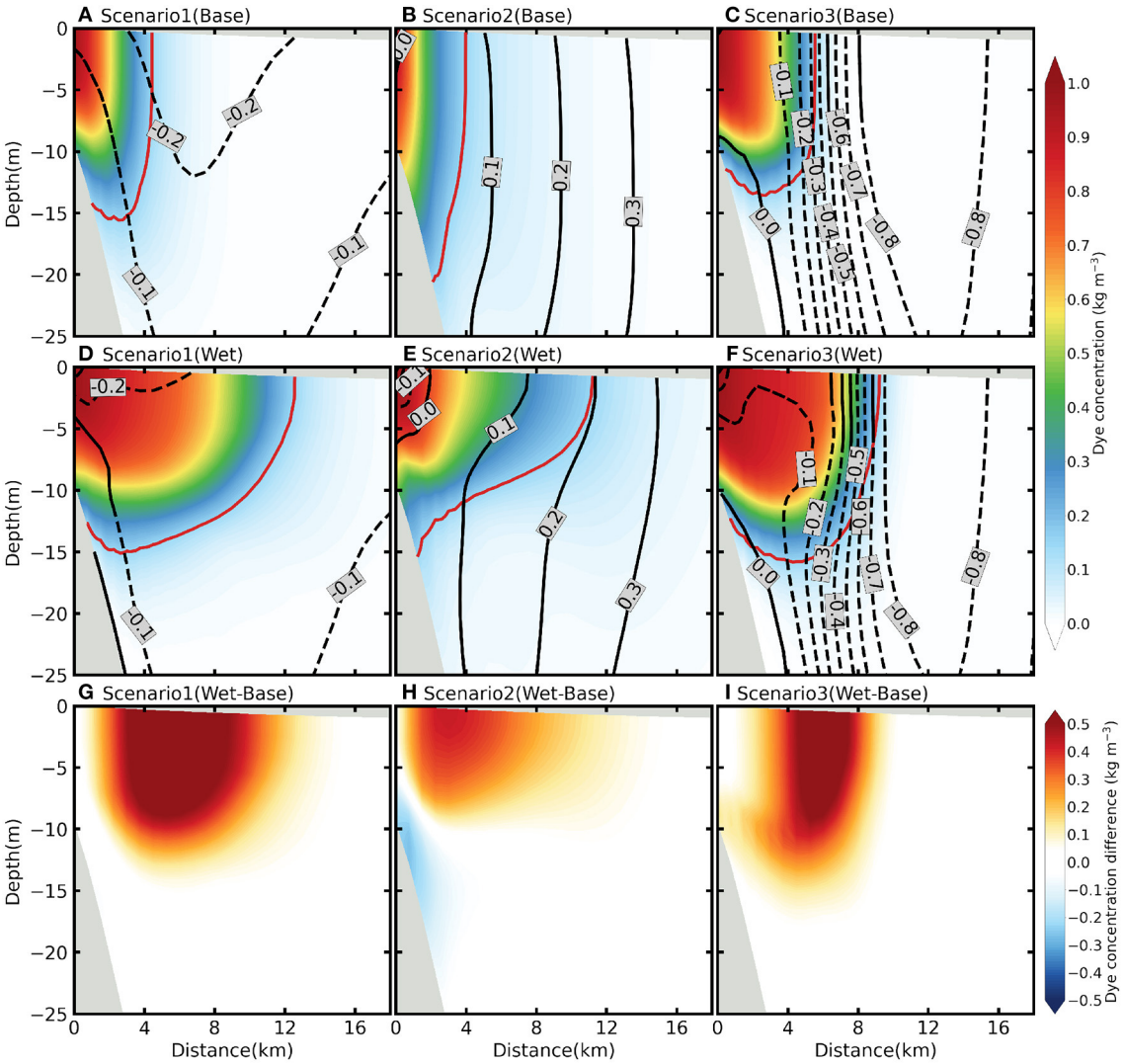

FIGURE 7 | Cross-section profiles of dye concentration averaged over the first 4 days within the purple box in **Figure 6** for each EAC scenario and their differences between the wet event and the base case. **(A–C)** Cross-sections profiles of dye concentration for EAC scenario 1, EAC scenario 2, and EAC scenario 3 in the base case. The solid and dashed black lines show the northward and southward velocities, respectively. The red line indicates the contour of 0.15 dye concentration. **(D–F)** Same as **(A–C)**, but for the wet event. **(G–I)** Differences of dye concentration for three EAC scenarios between the wet event **(D–F)** and the base case **(A–C)**. Only the dye concentration profiles less than 18 km from the river mouth are shown.

12 m depth in EAC scenario 1 (**Figure 7G**). Compared to EAC scenario 1, the difference is much smaller in EAC scenario 2 (**Figure 7H**). In EAC scenario 3, the difference appears within 2–9 km away from the river mouth but reach about 15 m depth (**Figure 7I**).

The vertical profiles of salinity show similar patterns to dye concentration (**Figure 8**). The salinity differences of salinity near the river mouth and offshore water are very small in the base case (**Figures 8A–C**). However, in the wet event, the salinity decreases significantly due to the increase in river discharges (**Figures 8D–F**). The difference of salinity between wet event and base case starts from the river mouth to 8–21 km (**Figures 8G–I**).

3.3. Temporal Evolution of River Plume

To investigate the horizontal dispersion of the river plume, we estimate the freshwater area as

$$A_{freshwater} = \int c\, dxdy. \quad (1)$$

Following the method in Duran-Matute et al. (2014) and Yu et al. (2020), we can also calculate the amount of freshwater volume and the transport through a transect as follows:

$$V_{freshwater} = \int c\, dxdydz \quad (2)$$

$$Q_{freshwater} = \int_A c * u_n\, dA \quad (3)$$

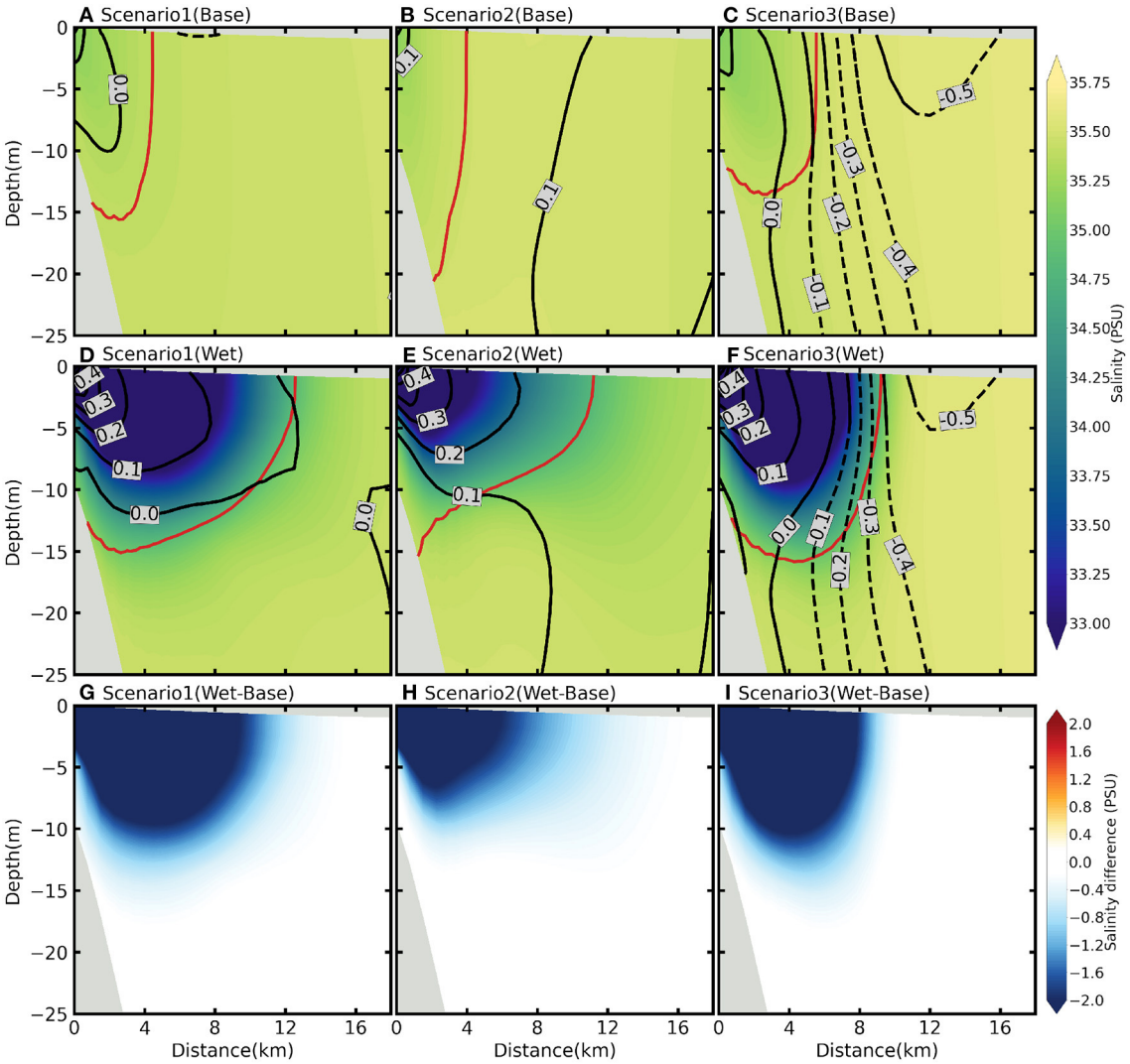

FIGURE 8 | Cross-section profiles of salinity averaged over the first 4 days within the purple box in **Figure 6** for each EAC scenario and their differences between the wet event and the base case. **(A–C)** Cross-section profile of salinity for EAC scenario 1, EAC scenario 2, and EAC scenario 3 in the base case. The solid and dashed black lines show the eastward and westward velocities, respectively. The red line indicates the contour of 0.15 dye concentration. **(D–F)** Same as **(A–C)**, but for the wet event. **(G–I)** Differences of salinity for three EAC scenarios between the wet event **(D–F)** and the base case **(A–C)**. Only the salinity profiles less than 18 km from the river mouth are shown.

where u_n is the velocity component normal to the transect.

Figure 9A shows the temporal evolution of the river plume around the Hawkesbury River. The difference in the freshwater area between the wet event and base case increase with time in the first 2 days due to increased river discharges, with the largest difference in the EAC scenario 1. It takes around 6 days for the freshwater area in the wet event to return to the same level as the base case. The freshwater areas in the wet event averaged within the first 4 days are much larger than those in the base case (**Figure 9C**). The EAC scenario 1 in the wet event has the largest freshwater area of 6.10×10^8 m^2. The smallest freshwater area can be found in the EAC scenario 2 in the base case, which is 1.99×10^8 m^2. The freshwater volume shows consistent temporal variation with the freshwater area (**Figures 9A,B**), that the EAC scenario 1 has the largest difference. Within the first 4 days, the freshwater volumes in the wet event are larger than those in the base case for three EAC scenarios (**Figures 9B,D**).

To examine the along-shore and cross-shore extension of the river plumes at the Hawkesbury River, we calculate the freshwater transport across the east, north and south faces of the purple box in **Figure 10**. Large river discharges at the river mouth increase the eastward velocities, which facilitate the eastward extension of the river plume. As shown in **Figure 10A**, the eastward extension of the river plume varies with the discharge, with large transport within the first 4 days. The eastward transports in EAC scenario 1 and EAC scenario 2 indicate that the river plume flows out of the box from the east face (**Figure 10D**). However, the transport is westward in EAC scenario 3 across

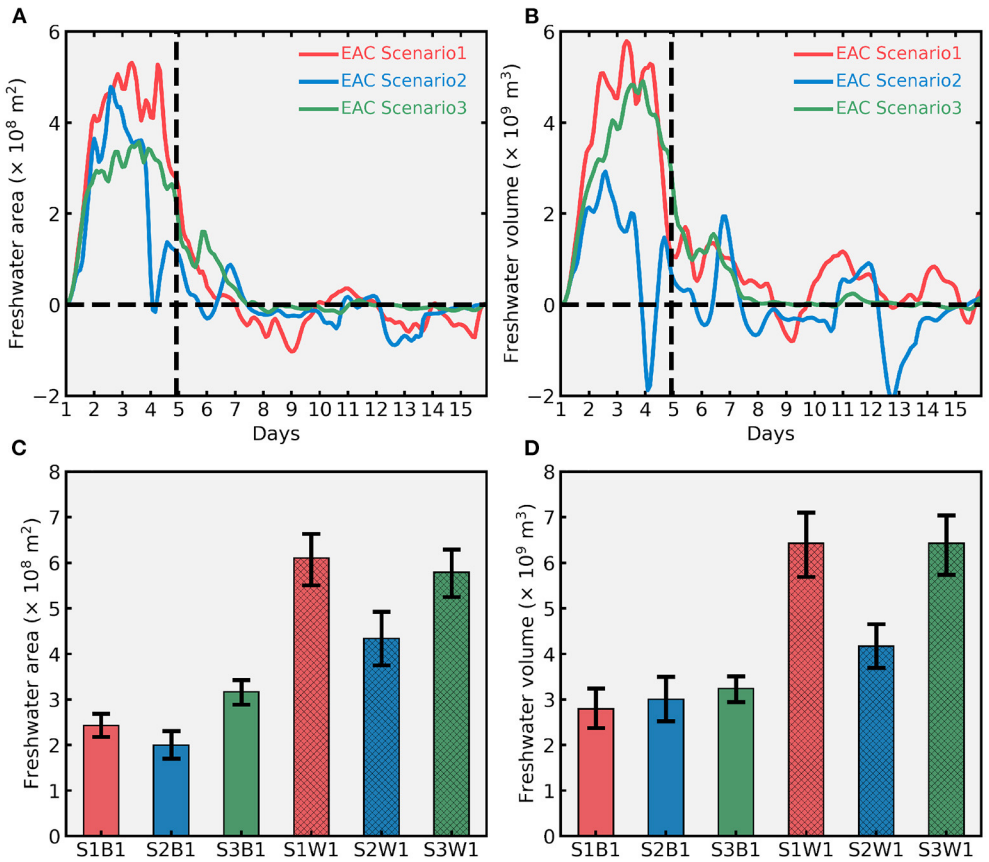

FIGURE 9 | Time series of freshwater area and volume difference between the base case and wet event for each EAC scenario during the whole simulation period. **(A)** Time series of freshwater area. The solid (dashed) red, blue, and green lines indicate EAC scenario 1, EAC scenario 2, and EAC scenario 3 in the base case (wet event), respectively. **(B)** Same as **(A)**, but for the freshwater volume. **(C)** Freshwater area averaged within the first 4 days for the base case (unhatched bars) and wet event (hatched bars). The red, blue, and green bars indicate EAC scenario 1, EAC scenario 2, EAC scenario 3, respectively. **(D)** Same as **(C)**, but for the freshwater volume.

the east face, implying that the background current impedes the river plume extends further east. The along-shore transports are more variable (**Figures 10B,C**), the freshwater flows into and out of the box from both the north and south faces. Time series of northward and southward transports also show the along-shore extension are much farther in the wet event when river discharges are larger. Within the first 4 days, the along-shore extension is mainly northward in EAC scenario 2 due to the existence of the cyclonic eddies (**Figure 10E**), and it is poleward in EAC scenario 1 and EAC scenario 3 because of the EAC jet and the eddy dipoles (**Figure 10F**).

4. DISCUSSION

4.1. Role of Mesoscale Circulation on River Plumes

In the Hawkesbury Shelf marine bioregion, the circulation is influenced by the onshore encroachment of the EAC (Roughan and Middleton, 2004; Archer et al., 2017; Malan et al., 2020; Xie et al., 2020, 2021) and the western branch of both mesoscale anticyclonic and cyclonic eddies (Oke and Griffin, 2011; Schaeffer et al., 2013). As the EAC jet and the anticyclonic eddies encroach upon the coast, their shoreward movements accelerate the poleward along-shore current. However, the intrusion of cyclonic eddies result in a northward flow on the shelf (Kerry et al., 2020; Ribbat et al., 2020b; Roughan et al., 2022). Therefore, the variability of the EAC jet and the eddy field play a role in the evolution of the river plumes near the coast. Here we show different spatial patterns of the main river plumes in the Hawkesbury Shelf bioregion influenced by the 3 dominant mesoscale circulation modes, the "EAC mode", "EAC eddy mode", and "EAC eddy dipole mode". Our results indicate that the spatial structure and dispersion of the river plumes are associated with the mesoscale circulation.

Malan et al. (2020) examined individual eddy dipole events from satellite altimetry observations and found that the cyclonic eddy often co-occurs during the shedding of the anticyclonic eddy from the EAC jet, which sets up a large horizontal shear field between the north branch of the eddy and the EAC flowing offshore to the east. Li et al. (2021b, 2022) showed that both the upstream EAC volume transport and westward

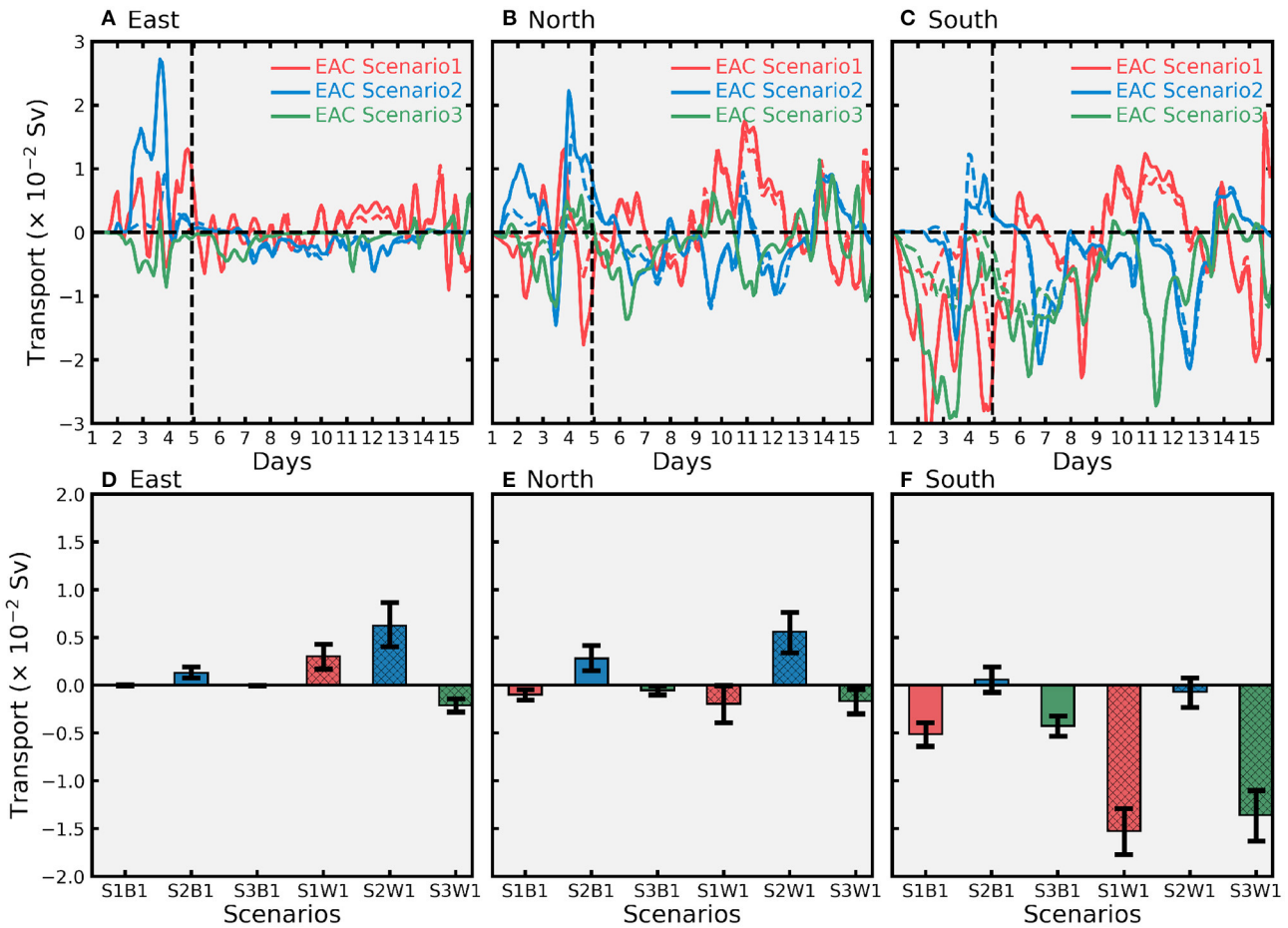

FIGURE 10 | Time series of freshwater transport to the north, south and east for each EAC scenario in the base case and wet event during the whole simulation period. **(A)** Time series of freshwater transport along the east side of the purple box in **Figures 4**, **6**. The solid (dashed) red, blue, and green lines indicate EAC scenario 1, EAC scenario 2, EAC scenario 3 in the wet event (base case), respectively. **(B,C)** Same as **(A)**, but for the north and south side of the box. **(D)** Freshwater transport averaged within the first 4 days for the base case (unhatched bars) and wet event (hatched bars). **(E,F)** Same as **(D)**, but for the north and south side of the box.

propagation of Rossby waves modulate the latitude of the EAC separation and further control the formation and position of mesoscale eddies and eddy dipoles. Here we showed the links between the mesoscale ocean dynamics and the regional river plume extensions, and the dynamics and underlying controlling mechanisms of these mesoscale features will be the topic of future work.

Our results show that the low salinity fresh water from the river mouth extends northward and southeastward in EAC scenario 1, disperses northward and eastward in EAC scenario 2, and spreads southward with some to the north in EAC scenario 3. Each scenario is dictated by the position of the EAC jet in relation to the cyclonic and anticyclonic eddy. In EAC scenario 1, the EAC jet dominates the flow, driving the plume poleward and offshore in the southern part of the domain. In EAC scenario 2, the cyclonic eddy is located directly adjacent to the Hawkesbury Shelf region, driving a northward flow, and some shelf export to the north. Offshore transport (**Figure 7**) is the largest in EAC scenario 1 and 2. In EAC scenario 3, the plume is dictated by the location of the anticyclonic eddy, which traps the plume by the coast.

In the South Brazilian Bight and South Brazil, a permanent continuous Brazil Current flows southward along the slope. By releasing passive dyes together with the river discharge in the hydrodynamical model, Marta-Almeida et al. (2021) showed that the local river plumes are confined to the inner shelf because the strong and persistent large-scale Brazil Current flowing southward over the slope prevents the river plumes from interaction with offshore oceanic mesoscale dynamics. The effect of mesoscale eddies on river plumes was conducted in the Agulhas Mozambique Channel region (Malauene et al., 2018), where the circulation is dominated by trains of intermittent, passing mesoscale eddies. They showed that offshore passing eddies modulate river plumes direction and spread depends on their strength and proximity to the shelf. The Zambezi River plume is bi-directional, which is associated with mesoscale eddies. The southward-directed plume was clearly detached from the coast and directly related to offshore anticyclonic eddies

which were able to induce a southward current over most of the shelf. They suggested that offshore mesoscale eddies should be taken into account when studying the river plumes of the Sofala Bank. The Hawkesbury Shelf region is located downstream of the EAC separation, where the shelf circulation is dominated by three prominent EAC modes. Here we showed that both the large-scale EAC and mesoscale eddies play roles in modulating the river plumes.

Interestingly, a study of the interaction of loop current eddies with the Mississippi River plume also showed that eddy pairs (what we term an eddy dipole) controlled offshore export pathways of riverine material (Schiller et al., 2011). As in the EAC system, eddy dipoles can generate coherent cross-shelf flows. These results demonstrate that the configuration of eddy dipoles and proximity of eddies to the shelf break strongly determines the characteristics of offshore freshwater transport. The three EAC scenarios and the position of the cyclonic eddy dictate the variability in the along-shore and offshore pathways that the plume may take.

Our study supports the findings of Schiller et al. (2011), who show that in order to obtain a complete picture of the dynamics impacting river plume dispersal, mesoscale circulation must be considered. In this case, it is necessary to downscale larger domain coarser models that resolve the mesoscale circulation properly in higher resolution nested models that better resolve shelf circulation. Nesting within a data assimilating model (e.g., Kerry et al., 2020) will ensure realistic connections between the shelf and the deep ocean if specific case studies are to be explored as per (Roughan et al., 2022).

4.2. Impact of River Discharge on the Shelf Circulation

On the one hand, the mesoscale circulation can influence the spatial and temporal evolution of river plumes. On the other hand, the river discharge also affects the stratification, instabilities, shelf circulation and dynamics at the submesoscale over the shelf, which is relevant to the ecosystem and biogeochemical processes. Large river plume plays a significant role in regulating the shelf circulation, which intensifies the cross-shelf exchange (Wu et al., 2021). River outflow can also enhance the submesoscale currents by increasing lateral buoyancy gradients but suppresses them by decreasing the boundary layer depth (Barkan et al., 2017). As this study focuses on the response of river plumes to the mesoscale circulation, all the above critical processes are neglected. In future work, we aim to focus on the effects of the river discharge on the shelf circulation and dynamics, and we will take advantage of the high-resolution model to understand the critical duration and river discharge of transport that is required to affect the shelf dynamics at submesoscale.

4.3. Secondary Drivers of Plume Structure

Downstream of the EAC separation point, coastal wind stress is the secondary driver of shelf circulation through Ekman transport mechanisms (Schaeffer et al., 2013). In this region, (Rossi et al., 2014) showed that prolonged downwelling favorable winds (for greater than 5 days) occur up to 31% of the year, where as upwelling winds (for greater than 5 days) only occur for 4% of the year. Downwelling favorable winds (from the south) act to mix the water column and result in northward flow close to the coast. Periods of heavy rainfall are often associated with winds from the south, which could act to drive the plumes to the north. An upwelling favorable wind (from the north) combined with EAC encroachment leads to the strongest poleward along-shore velocities on the shelf and offshore cross-shelf surface transport, but the downwelling favorable winds play an opposite role (Schaeffer et al., 2013; Archer et al., 2017). The impact of coastal winds on the dispersion of river plumes in each EAC scenario deserves further exploration, particularly the coupled effect of strong winds that drive storms, heavy rainfall and waves.

In addition to mesoscale circulation and local wind forcing, tides can also impact the river plume structure. In large river plumes, tidal currents act to stabilize the offshore growth of river-plume bulges in the coastal and shelf region (Isobe, 2005; Li and Rong, 2012) or enhance the downstream along-shore freshwater transport by compressing the bulge shoreward against the coast (Chen, 2014). At the northern side of the Changjiang River mouth, the tidal forcing can increase the vertical mixing, resulting in the formation of a strong along-coast salinity gradient that restricts the northward extension of the plume (Wu et al., 2011). At the Berau River mouth, tides cause vertical mixing and suppress the cross-shelf spreading of the river plume (Tarya et al., 2015). Although tidal forcing was included in our simulation, as both the river outflow and tidal circulation are "weak" in our region we expect the effect of tidal forcing to be small. Future studies could improve our understanding of the impact of tides on river plumes adjacent to the EAC.

4.4. Multi-Scale Variability of the River Plumes

The EAC flow and its associated eddy field vary on seasonal and interannual timescales, which may also impact river plume evolution. Previous studies have demonstrated the seasonality of the EAC flow, where it is stronger in Austral summer (Dec-Feb) than in Austral winter (Jun-Aug) (Ridgway, 1997; Archer et al., 2017; Kerry and Roughan, 2020). As discussed in Li et al. (2021b), there is strong interannual variability of eddy activity around the typical EAC separation region, which is related to the EAC transport upstream. As such, the frequency and magnitude of the chosen EAC scenarios in the present study (that well represent the three dominant EAC modes) may vary across seasons and longer timescales.

4.5. Sensitivity to Freshwater Inflow

Historic observations of plume extents by Kingsford and Suthers (1994) showed that Botany Bay plumes could range in offshore extension from 2 km during a dry spell to 11 km during large rainfall events. They also noted that the plumes were shallow ranging 2–8 m deep above higher density coastal waters. These values agree well with the plume dimensions presented here (9.5–12 km in horizontal, 13–20 m in vertical). Hence our sensitivity studies with idealized river discharges provide the best estimate on the middle and upper limit of the river plume dispersal over

the Hawkesbury Shelf under the three circulation scenarios. This means the results can be used to explore a range of ecological impacts of the river plumes and their offshore extents.

4.6. Ecological Implications

The contrasting river plume structures presented in the three EAC scenarios will have differing impacts on the local hydrodynamics, water environment and ecological processes. Firstly, river plumes can drive the distribution and dispersion of material (e.g., sediment, marine litter, or metals) coming out of the estuaries (Jaffe et al., 1995; Warrick et al., 2004). We also know that eddies impact the transport and distribution of larval fish (Roughan et al., 2011) and crustacea in the region (Cetina-Heredia et al., 2019).

Large rainfall events can maintain and enhance biological productivity due to lower salinity water altering habitat availability. Locally, Kingsford and Suthers (1994) found major differences in larval fish and zooplankton distributions and abundance in the Botany Bay plume. It has been shown that fresh water can affect the distribution of commercially fished prawns (Gammelsrød, 1992), and it is thought that river plumes may impact fish activity (Gillson, 2011; Gillson et al., 2012). This implies that the flood events may produce different fish distribution and abundance in the three dominant EAC scenarios, thereby having a commercial fisheries impact. Hence each of these mesoscale circulations combined with the river plume scenarios may also affect the population dynamics of marine organisms.

Here we showed that the river plume has the largest freshwater area and eastward extension (12.5 km) during the large rainfall event in the "EAC mode". The salinity around the river mouth decreases rapidly in this EAC scenario, which likely creates a physical barrier to the recruitment of marine taxa and reduces available nursery habitat both north, southeast and east of the river mouth. In the "EAC eddy mode", the impact of the river plumes on the local ecological system mainly covers the north and east of the river mouth because the freshwater driven by the proximity of the cyclonic eddy carries large quantities of suspended sediment toward these directions. In the "EAC dipole mode", the river plume mainly spreads southward driven by the western branch of the anticyclonic eddy, decreasing the salinity south of the river mouth.

5. CONCLUSION

Using a high-resolution (750 m) hydrodynamic model, we simulate four idealized river plumes in the Hawkesbury bioregion during three dominant mesoscale circulation scenarios and investigate the spatial and temporal evolution of river plumes in the base case and wet event. We compare the spatial patterns of river plumes during each EAC scenario and explore the impact of the mesoscale circulation on the plume dispersion. We focus on the Hawkesbury River plume as it has the largest discharge among the four rivers examined. We find the river plumes have significantly different 3 dimensional structures in response to the mesoscale circulation scenarios. In all scenarios, the plume remains trapped by the coast with an offshore extent of less than 12 km. In the "EAC mode", the plume spreads both northward and southeastward. The offshore spread in this scenario is the largest, which is around 12.5 km to the east of the river mouth in the wet event. In the "EAC eddy mode", this plume dispersal is toward the north and east, driven by the proximity of a cyclonic eddy on the shelf, with an eastward extension of 11.5 km. In the "EAC eddy dipole mode", most of this river plume spreads southward with some to the north, again dictated by the position of the cyclonic eddy. The cross-shelf dispersal is a minimum of 9.5 km from the river mouth. The difference of the freshwater spatial extent of the plume between the wet event and base case is the largest in EAC scenario 1 and the smallest in EAC scenario 2. Our results have far-reaching implications for the understanding of ecological systems and provide guidance for the local and state government bodies. Knowledge regarding the ultimate fate of riverborne material, dilution and cumulative effects (e.g., over long times and from multiple sources) will enable better environmental management of this dynamic region.

DATA AVAILABILITY STATEMENT

EAC-ROMS model initial and boundary conditions are provided by CSIRO Australia BRAN2020 and available at https://research.csiro.au/bluelink/outputs/data-access/. The atmospheric forcing BARRA-R data are obtained from http://www.bom.gov.au/research/projects/reanalysis/. The tide forcing is obtained from https://www.tpxo.net/global/tpxo8-atlas. The AVISO products are downloaded from https://resources.marine.copernicus.eu/product-detail/SEALEVEL_GLO_PHY_L4_MY_008_047/INFORMATION. The EAC-ROMS model output (https://doi.org/10.26190/TT1Q-NP46) is available at https://researchdata.edu.au/high-resolution-22-version-20/1676421 and should be cited as (Li et al., 2021a).

AUTHOR CONTRIBUTIONS

MR, SR, and JL conceived the study and developed the conceptual framework. CK configured and validated the EAC-ROMS model. JL ran the EAC-ROMS and HSM model and analyzed the model results. All authors contributed to interpreting the results and writing and editing the manuscript. All authors contributed to the article and approved the submitted version.

FUNDING

This research was partially supported by the New South Wales Department of Planning, Industry and Environment. Former model development was partially supported by the Australian Research Council grants LP120100592, DP140102337, LP160100162, and LP170100498. This research was undertaken with the assistance of resources and services from the National Computational Infrastructure (NCI), which is supported by the Australian Government. This research also includes computations using the computational cluster Katana https://doi.org/10.26190/669X-A286, supported by Research Technology Services at UNSW Sydney.

REFERENCES

Archer, M. R., Roughan, M., Keating, S. R., and Schaeffer, A. (2017). On the variability of the east Australian current: jet structure, meandering, and influence on shelf circulation. *J. Geophys. Res. Oceans* 122, 8464–8481. doi: 10.1002/2017JC013097

Barkan, R., McWilliams, J. C., Shchepetkin, A. F., Molemaker, M. J., Renault, L., Bracco, A., et al. (2017). Submesoscale dynamics in the northern Gulf of Mexico. Part I: Regional and seasonal characterization and the role of river outflow. *J. Phys. Oceanogr*. 47, 2325–2346. doi: 10.1175/JPO-D-17-0035.1

Cetina-Heredia, P., Roughan, M., Liggins, G., Coleman, M. A., and Jeffs, A. (2019). Mesoscale circulation determines broad spatio-temporal settlement patterns of lobster. *PLoS ONE* 14, e0211722. doi: 10.1371/journal.pone.0211722

Cetina-Heredia, P., Roughan, M., Sebille, E. V., and Coleman, M. A. (2014). Long-term trends in the East Australian Current separation latitude and eddy driven transport. *J. Geophys. Res. Oceans* 119, 4351–4366. doi: 10.1002/2014JC010071

Chamberlain, M. A., Oke, P. R., Fiedler, R. A. S., Beggs, H. M., Brassington, G. B., and Divakaran, P. (2021). Next generation of bluelink ocean reanalysis with multiscale data assimilation: Bran2020. *Earth Syst. Sci. Data* 13, 5663–5688. doi: 10.5194/essd-13-5663-2021

Chen, S. N. (2014). Enhancement of alongshore freshwater transport in surface-advected river plumes by tides. *J. Phys. Oceanogr*. 44, 2951–2971. doi: 10.1175/JPO-D-14-0008.1

Colberg, F., Brassington, G. B., Sandery, P., Sakov, P., and Aijaz, S. (2020). High and medium resolution ocean models for the Great Barrier Reef. *Ocean Modell*. 145:101507. doi: 10.1016/j.ocemod.2019.101507

Covelli, S., Piani, R., Acquavita, A., Predonzani, S., and Faganeli, J. (2007). Transport and dispersion of particulate Hg associated with a river plume in coastal Northern Adriatic environments. *Mar. Pollut. Bull*. 55, 10–12. doi: 10.1016/j.marpolbul.2007.09.006

Dawson, K. (2002). Fish kill events and habitat losses of the Richmond River, NSW Australia: an overview. *J. Coast. Res*. 36, 216–221. doi: 10.2112/1551-5036-36.sp1.216

Ducet, N., Le Traon, P. Y., and Reverdin, G. (2000). Global high-resolution mapping of ocean circulation from TOPEX/Poseidon and ERS-1 and -2. *J. Geophys. Res. Oceans* 105, 477–498. doi: 10.1029/2000JC900063

Duran-Matute, M., Gerkema, T., De Boer, G. J., Nauw, J. J., and Gräwe, U. (2014). Residual circulation and freshwater transport in the Dutch Wadden Sea: a numerical modelling study. *Ocean Sci*. 10, 611–632. doi: 10.5194/os-10-611-2014

Egbert, G. D., and Erofeeva, S. Y. (2002). Efficient inverse modeling of barotropic ocean tides. *J. Atmos. Ocean. Technol*. 19, 183–204. doi: 10.1175/1520-0426(2002)019<0183:EIMOBO>2.0.CO;2

Eyre, B. D., Kerr, G., and Sullivan, L. A. (2006). Deoxygenation potential of the Richmond river estuary floodplain, northern NSW, Australia. *River Res. Appl*. 22, 981–992. doi: 10.1002/rra.950

Gammelsrød, T. (1992). Variation in shrimp abundance on the Sofala Bank, Mozambique, and its relation to the Zambezi River runoff. *Estuar. Coast. Shelf Sci*. 35, 91–103. doi: 10.1016/S0272-7714(05)80058-7

Gillson, J. (2011). Freshwater flow and fisheries production in estuarine and coastal systems: where a drop of rain is not lost. *Rev. Fish. Sci*. 19, 168–186. doi: 10.1080/10641262.2011.560690

Gillson, J., Suthers, I., and Scandol, J. (2012). Effects of flood and drought events on multi-species, multi-method estuarine and coastal fisheries in eastern Australia. *Fish. Manage. Ecol*. 19, 54–68. doi: 10.1111/j.1365-2400.2011.00816.x

Grimes, C. B. (2001). Fishery production and the Mississippi River discharge. *Fisheries* 26, 17–26. doi: 10.1577/1548-8446(2001)026<0017:FPATMR>2.0.CO;2

Isobe, A. (2005). Ballooning of river-plume bulge and its stabilization by tidal currents. *J. Phys. Oceanogr*. 35, 2337–2351. doi: 10.1175/JPO2837.1

Jaffe, R., Leal, I., Alvarado, J., Gardinali, P., and Sericano, J. (1995). Pollution effects of the Tuy River on the central Venezuelan coast: anthropogenic organic compounds and heavy metals in Tivela mactroidea. *Mar. Pollut. Bull*. 30, 820–825. doi: 10.1016/0025-326X(95)00087-4

Kannan, N., Kim, M., Hong, S. H., Jin, Y., Yim, U. H., Ha, S. Y., et al. (2012). Chemical tracers, sterol biomarkers and satellite imagery in the study of a river plume ecosystem in the Yellow Sea. *Continent. Shelf Res*. 33, 29–36. doi: 10.1016/j.csr.2011.10.001

Kerry, C., Powell, B., Roughan, M., and Oke, P. (2016). Development and evaluation of a high-resolution reanalysis of the East Australian Current region using the Regional Ocean Modelling System (ROMS 3.4) and Incremental Strong-Constraint 4-Dimensional Variational (IS4D-Var) data assimilation. *Geosci. Model Dev*. 9, 3779–3801. doi: 10.5194/gmd-9-3779-2016

Kerry, C., and Roughan, M. (2020). Downstream evolution of the east Australian current system: mean flow, seasonal, and intra-annual variability. *J. Geophys. Res. Oceans* 125, e2019JC015227. doi: 10.1029/2019JC015227

Kerry, C., Roughan, M., and Powell, B. (2020). Predicting the submesoscale circulation inshore of the East Australian current. *J. Mar. Syst*. 204, 103286. doi: 10.1016/j.jmarsys.2019.103286

Kingsford, M. J., and Suthers, I. M. (1994). Dynamic estuarine plumes and fronts: importance to small fish and plankton in coastal waters of NSW, Australia. *Continent. Shelf Res*. 14, 655–672. doi: 10.1016/0278-4343(94)90111-2

Kroon, F. J., and Ludwig, J. A. (2010). Response and recovery of fish and invertebrate assemblages following flooding in five tributaries of a sub-tropical river. *Mar. Freshw. Res*. 61, 86–96. doi: 10.1071/MF08357

Lawrence, M. G. (2010). Detection of anthropogenic gadolinium in the Brisbane River plume in Moreton Bay, Queensland, Australia. *Mar. Pollut. Bull*. 60, 1113–1116. doi: 10.1016/j.marpolbul.2010.03.027

Li J, Roughan M, Kerry C. Variability and drivers of ocean temperature extremes in a warming western boundary current. *J Clim.* (2022) 35:1097–111. doi: 10.1175/JCLI-D-21-0622.1

Li, J., Kerry, C., and Roughan, M. (2021a). *A High-Resolution, 22-Year, Free-Running, Hydrodynamic Simulation of the East Australia Current System Using the Regional Ocean Modeling System (Version 2.0)*. UNSW.dataset.

Li, J., Roughan, M., and Kerry, C. (2021b). Dynamics of interannual eddy kinetic energy modulations in a western boundary current. *Geophys. Res. Lett*. 48, e2021GL094115. doi: 10.1029/2021GL094115

Li, M., and Rong, Z. (2012). Effects of tides on freshwater and volume transports in the Changjiang River plume. *J. Geophys. Res. Oceans* 117, 6027. doi: 10.1029/2011JC007716

Lloret, J., Palomera, I., Salat, J., and Sole, I. (2004). Impact of freshwater input and wind on landings of anchovy (*Engraulis encrasicolus*) and sardine (*Sardina pilchardus*) in shelf waters surrounding the Ebre (Ebro) River delta (north-western Mediterranean). *Fish. Oceanogr*. 13, 102–110. doi: 10.1046/j.1365-2419.2003.00279.x

Malan, N., Archer, M., Roughan, M., Cetina-Heredia, P., Hemming, M., Rocha, C., et al. (2020). Eddy-driven cross-shelf transport in the east Australian current separation zone. *J. Geophys. Res. Oceans* 125, e2019JC015613. doi: 10.1029/2019JC015613

Malauene, B. S., Moloney, C. L., Lett, C., Roberts, M. J., Marsac, F., and Penven, P. (2018). Impact of offshore eddies on shelf circulation and river plumes of the Sofala Bank, Mozambique Channel. *J. Mar. Syst*. 185, 1–12. doi: 10.1016/j.jmarsys.2018.05.001

Marta-Almeida, M., Dalbosco, A., Franco, D., and Ruiz-Villarreal, M. (2021). Dynamics of river plumes in the South Brazilian Bight and South Brazil. *Ocean Dyn*. 71, 59–80. doi: 10.1007/s10236-020-01397-x

Mellor, G. L., and Yamada, T. (1982). Development of a turbulence closure model for geophysical fluid problems. *Rev. Geophys*. 20, 851–875. doi: 10.1029/RG020i004p00851

Oke, P. R., and Griffin, D. A. (2011). The cold-core eddy and strong upwelling off the coast of New South Wales in early 2007. *Deep Sea Res. II Top. Stud. Oceanogr*. 58, 574–591. doi: 10.1016/j.dsr2.2010.06.006

Oke, P. R., and Middleton, J. H. (2001). Nutrient enrichment off Port Stephens: the role of the east Australian current. *Continent. Shelf Res*. 21, 6–7. doi: 10.1016/S0278-4343(00)00127-8

Ribbat, N., Roughan, M., Powell, B., Kerry, C., and Rao, S. (2020a). *A High-Resolution (750m) Free-Running Hydrodynamic Simulation of the Hawkesbury Shelf Region off Southeastern Australia (2012-2013) Using the Regional Ocean Modeling System*. UNSW.dataset.

Ribbat, N., Roughan, M., Powell, B., Rao, S., and Kerry, C. G. (2020b). Transport variability over the Hawkesbury Shelf (31.5-34.5°S) driven by the east Australian current. *PLoS ONE* 15:e0241622. doi: 10.1371/journal.pone.0241622

Ridgway, K. R. (1997). Seasonal cycle of the east Australian current. *J. Geophys. Res. C Oceans* 102, 22921–22936. doi: 10.1029/97JC00227

Rijnsburger, S., Flores, R. P., Pietrzak, J. D., Horner-Devine, A. R., Souza, A. J., and Zijl, F. (2021). The evolution of plume fronts in the Rhine region of freshwater influence. *J. Geophys. Res. Oceans* 126:e2019JC015927. doi: 10.1029/2019JC015927

Rossi, V., Schaeffer, A., Wood, J., Galibert, G., Morris, B., Sudre, J., et al. (2014). Seasonality of sporadic physical processes driving temperature and nutrient high-frequency variability in the coastal ocean off southeast Australia. *J. Geophys. Res. Oceans* 119, 445–460. doi: 10.1002/2013JC009284

Roughan, M., Cetina-Heredia, P., Ribbat, N., and Suthers, I. M. (2022). Shelf transport pathways adjacent to the east Australian current reveal sources of productivity for coastal reefs. *Front. Mar. Sci*. 8, 789687. doi: 10.3389/fmars.2021.789687

Roughan, M., Keating, S. R., Schaeffer, A., Cetina Heredia, P., Rocha, C., Griffin, D., et al. (2017). A tale of two eddies: the biophysical characteristics of two contrasting cyclonic eddies in the east Australian current system. *J. Geophys. Res. Oceans* 122, 2494–2518. doi: 10.1002/2016JC012241

Roughan, M., Macdonald, H. S., Baird, M. E., and Glasby, T. M. (2011). Modelling coastal connectivity in a western boundary current: seasonal and inter-annual variability. *Deep Sea Res. II Top. Stud. Oceanogr*. 58, 628–644. doi: 10.1016/j.dsr2.2010.06.004

Roughan, M., and Middleton, J. H. (2004). On the east Australian current: variability, encroachment, and upwelling. *J. Geophys. Res. C Oceans* 109:C07003. doi: 10.1029/2003JC001833

Schaeffer, A., Gramoulle, A., Roughan, M., and Mantovanelli, A. (2017). Characterizing frontal eddies along the east Australian current from HF radar observations. *J. Geophys. Res. Oceans*, 122, 3964–3980. doi: 10.1002/2016JC012171

Schaeffer, A., Roughan, M., and Morris, B. D. (2013). Cross-shelf dynamics in a western boundary current regime: implications for upwelling. *J. Phys. Oceanogr*. 43, 1042–1059. doi: 10.1175/JPO-D-12-0177.1

Schiller, R. V., Kourafalou, V. H., Hogan, P., and Walker, N. D. (2011). The dynamics of the Mississippi River plume: impact of topography, wind and offshore forcing on the fate of plume waters. *J. Geophys. Res. Oceans* 116:C06029. doi: 10.1029/2010JC006883

Schilling, H. T., Everett, J. D., Smith, J. A., Stewart, J., Hughes, J. M., Roughan, M., et al. (2020). Multiple spawning events promote increased larval dispersal of a predatory fish in a western boundary current. *Fish. Oceanogr*. 29, 309–323. doi: 10.1111/fog.12473

Schlacher, T. A., Skillington, A. J., Connolly, R. M., Robinson, W., and Gaston, T. F. (2008). Coupling between marine plankton and freshwater flow in the plumes off a small estuary. *Int. Rev. Hydrobiol*. 93, 641–658. doi: 10.1002/iroh.200711050

Shchepetkin, A. F., and McWilliams, J. C. (2005). The regional oceanic modeling system (ROMS): a split-explicit, free-surface, topography-following-coordinate oceanic model. *Ocean Modell*. 9, 347–404. doi: 10.1016/j.ocemod.2004.08.002

Skreslet, S. (1986). *The Role of Freshwater Outflow in Coastal Marine Ecosystems*, Vol. 7. Berlin: Springer-Verlag. doi: 10.1007/978-3-642-70886-2

Smolarkiewicz, P. K. (1984). A fully multidimensional positive definite advection transport algorithm with small implicit diffusion. *J. Comput. Phys*. 54, 325–362. doi: 10.1016/0021-9991(84)90121-9

Su, C. H., Eizenberg, N., Steinle, P., Jakob, D., Fox-Hughes, P., White, C. J., et al. (2019). BARRA v1.0: the bureau of meteorology atmospheric high-resolution regional reanalysis for Australia. *Geosci. Model Dev*. 12, 2049–2068. doi: 10.5194/gmd-12-2049-2019

Tarya, A., Van Der Vegt, M., and Hoitink, A. J. (2015). Wind forcing controls on river plume spreading on a tropical continental shelf. *J. Geophys. Res. Oceans* 120, 16–35. doi: 10.1002/2014JC010456

Warrick, J. A., Mertes, L. A., Washburn, L., and Siegel, D. A. (2004). Dispersal forcing of southern California river plumes, based on field and remote sensing observations. *Geomar. Lett*. 24, 46–52. doi: 10.1007/s00367-003-0163-9

Whiteway TG. *Australian Bathymetry and Topography Grid*. Canberra, ACT: Geoscience Australia (2009). Available online at: https://data.gov.au/data/dataset/australian-bathymetry-andtopography-grid-june-2009

Wu, H., Zhu, J., Shen, J., and Wang, H. (2011). Tidal modulation on the Changjiang River plume in summer. *J. Geophys. Res. Oceans* 116:C08017. doi: 10.1029/2011JC007209

Wu, R., Wu, H., and Wang, Y. (2021). Modulation of shelf circulations under multiple river discharges in the east China Sea. *J. Geophys. Res. Oceans* 126:e2020JC016990. doi: 10.1029/2020JC016990

Xie, S., Huang, Z., and Wang, X. H. (2021). Remotely sensed seasonal shoreward intrusion of the east australian current: implications for coastal ocean dynamics. *Remote Sens*. 13, 854. doi: 10.3390/rs13050854

Xie, S., Huang, Z., Wang, X. H., and Leplastrier, A. (2020). Quantitative mapping of the east Australian current encroachment using time series Himawari-8 sea surface temperature data. *J. Geophys. Res. Oceans* 125:e2019JC015647. doi: 10.1029/2019JC015647

Yu, Y., Chen, S. H., Tseng, Y. H., Guo, X., Shi, J. I., Liu, G., et al. (2020). Importance of diurnal forcing on the summer salinity variability in the east China sea. *J. Phys. Oceanogr*. 50, 633–653. doi: 10.1175/JPO-D-19-0200.1

Zhang, W. G., Wilkin, J. L., and Schofield, O. M. (2010). Simulation of water age and residence time in New York Bight. *J. Phys. Oceanogr*. 40, 965–982. doi: 10.1175/2009JPO4249.1

Conflict of Interest: The authors declare that the research was conducted in the absence of any commercial or financial relationships that could be construed as a potential conflict of interest.

Publisher's Note: All claims expressed in this article are solely those of the authors and do not necessarily represent those of their affiliated organizations, or those of the publisher, the editors and the reviewers. Any product that may be evaluated in this article, or claim that may be made by its manufacturer, is not guaranteed or endorsed by the publisher.

Copyright © 2022 Li, Roughan, Kerry and Rao. This is an open-access article distributed under the terms of the Creative Commons Attribution License (CC BY). The use, distribution or reproduction in other forums is permitted, provided the original author(s) and the copyright owner(s) are credited and that the original publication in this journal is cited, in accordance with accepted academic practice. No use, distribution or reproduction is permitted which does not comply with these terms.

frontiers in Marine Science

ORIGINAL RESEARCH
published: 09 March 2022
doi: 10.3389/fmars.2022.855183

Cross-Shelf Exchange in the Southwestern Atlantic Shelf: Climatology and Extreme Events

Giuliana Berden[1,2,3]*, *Alberto R. Piola*[1,2,3,4] *and Elbio D. Palma*[2,5]

[1] *Facultad de Ciencias Exactas y Naturales, Universidad de Buenos Aires, Buenos Aires, Argentina,* [2] *Consejo Nacional de Investigaciones Científicas y Técnicas (CONICET), Buenos Aires, Argentina,* [3] *Departamento Oceanografía, Servicio Hidrografía Naval, Buenos Aires, Argentina,* [4] *Unidad Mixta Internacional - Instituto Franco-Argentino Sobre Estudios del Clima y sus Impactos, Buenos Aires, Argentina,* [5] *Departamento de Física, Universidad Nacional del Sur and Instituto Argentino de Oceanografía/CONICET, Bahía Blanca, Argentina*

The variability and drivers of the cross-shelf exchanges between the Southwestern Atlantic shelf and the open ocean from 30 to 40°S are analyzed using a high-resolution ocean model reanalysis at daily resolution. The model's performance was first evaluated using altimetry data, and independent mooring and hydrographic data collected in the study area. Model transports are in overall good agreement with all other estimates. The record-mean (1993–2018) cross-shore transport is offshore, 2.09 ± 1.60 Sv. 73% of the shelf-open ocean exchange occurs in the vicinity of Brazil-Malvinas Confluence (∼38°S) and 20% near 32°S. This outflow is mostly contributed by northward alongshore transport through 40°S (63%) and the remaining by southward transport through 30°S (37%). The cross-shore flow presents weak seasonal variations, with a maximum in austral summer, and high variability at subannual and weekly time scales. The latter is mainly associated with abrupt wind changes generated by synoptic atmospheric systems. Alongshore wind variations set up sea-level changes in the inner shelf which in turn drive large anomalies in the associated geostrophic alongshore flow. The difference in inner shelf sea-level anomalies at 30 and 40°S is a good indicator of cross-shelf exchange at seasonal and shorter time scales. Episodes of extreme offshore transport that reach up to 9.45 Sv and last about 2 days are driven by convergence of these alongshore flows over the shelf. Large exports of shelf waters lead to freshening of the upper open ocean as revealed by *in-situ* and satellite observations. In contrast, onshore extreme events drive open ocean water intrusions of up to 6.53 Sv and last <4 days. These inflows, particularly the subtropical waters from the Brazil Current, induce a substantial salinification of the outer shelf.

Keywords: cross-shelf exchange, western boundary current, Brazil-Malvinas Confluence, continental shelf, high frequency variability, extreme events

OPEN ACCESS

Edited by:
William Savidge, University of Georgia, United States

Reviewed by:
Ryan McCabe, National Oceanic and Atmospheric Administration (NOAA), United States
Dorleta Orue-Echevarria, Institut de Ciéncies del Mar (CSIC), Spain

***Correspondence:**
Giuliana Berden
giuliberden@gmail.com

Specialty section:
This article was submitted to Coastal Ocean Processes, a section of the journal Frontiers in Marine Science

Received: *14 January 2022*
Accepted: *07 February 2022*
Published: *09 March 2022*

Citation:
Berden G, Piola AR and Palma ED (2022) Cross-Shelf Exchange in the Southwestern Atlantic Shelf: Climatology and Extreme Events. Front. Mar. Sci. 9:855183. doi: 10.3389/fmars.2022.855183

1. INTRODUCTION

Continental shelves account for <10% of the global ocean surface, yet they host 20–30% of the ocean's primary production (de Haas et al., 2002) and 90% of the global fish catch (Gattuso et al., 1998). In addition, continental shelves play a key role in the biogeochemical cycling of the ocean due to the continental discharge of organic matter and nutrients. Consequently, 80% of organic carbon

is buried in continental shelves (Rabouille et al., 2001; Chen et al., 2003) and these are important sites for denitrification (Christensen et al., 1987; Rabouille et al., 2001). The Southwestern Atlantic Shelf (SWAS) hosts one of the most productive marine ecosystems of the southern hemisphere due to the supply of nutrients from continental discharge, shelf currents, and open ocean sources. The high primary productivity over the shelf and its subsequent fate might have a significant biogeochemical impact on the open ocean.

Bounding the SWAS, the Malvinas Current (MC) flows northeastward carrying relatively low-salinity, cold and nutrient-rich waters from the Antarctic Circumpolar Current. The MC reaches approximately 38°S where it collides with the Brazil Current (BC), which advects warm and salty waters southward (Gordon and Greengrove, 1986, **Figure 1**). The latitudinal position of the Brazil/Malvinas Confluence (BMC) varies seasonally, shifting southward during the austral fall and northward during the austral spring (Combes and Matano, 2014a). There is also a southward shift of the BMC position in the past decades associated with a longer-term oscillation (Lumpkin and Garzoli, 2011).

Diluted subantarctic waters referred to as Subantarctic Shelf Waters (SASW) enter the SWAS near 54°S (Piola et al., 2018). These cold, relatively low-salinity (∼33.8) and nutrient-rich waters flow northward and reach the Southern Brazilian Shelf at 34°S to 32°S, where they meet a southwestward flow of warm-salty Subtropical Shelf Waters (STSW), forming the Subtropical Shelf Front (STSF, Piola et al., 2000). The STSF is a subsurface front capped by low-salinity waters derived from the Río de la Plata (RDP). The RDP is the major contributor of continental nutrients and organic matter to the central portion of the SWAS (Braga et al., 2008; see Figure 1 in Piola et al., 2018; Bordin et al., 2019; Berden et al., 2020). On average, the RDP discharges around 25,000 $m^3.s^{-1}$ of freshwater over the shelf

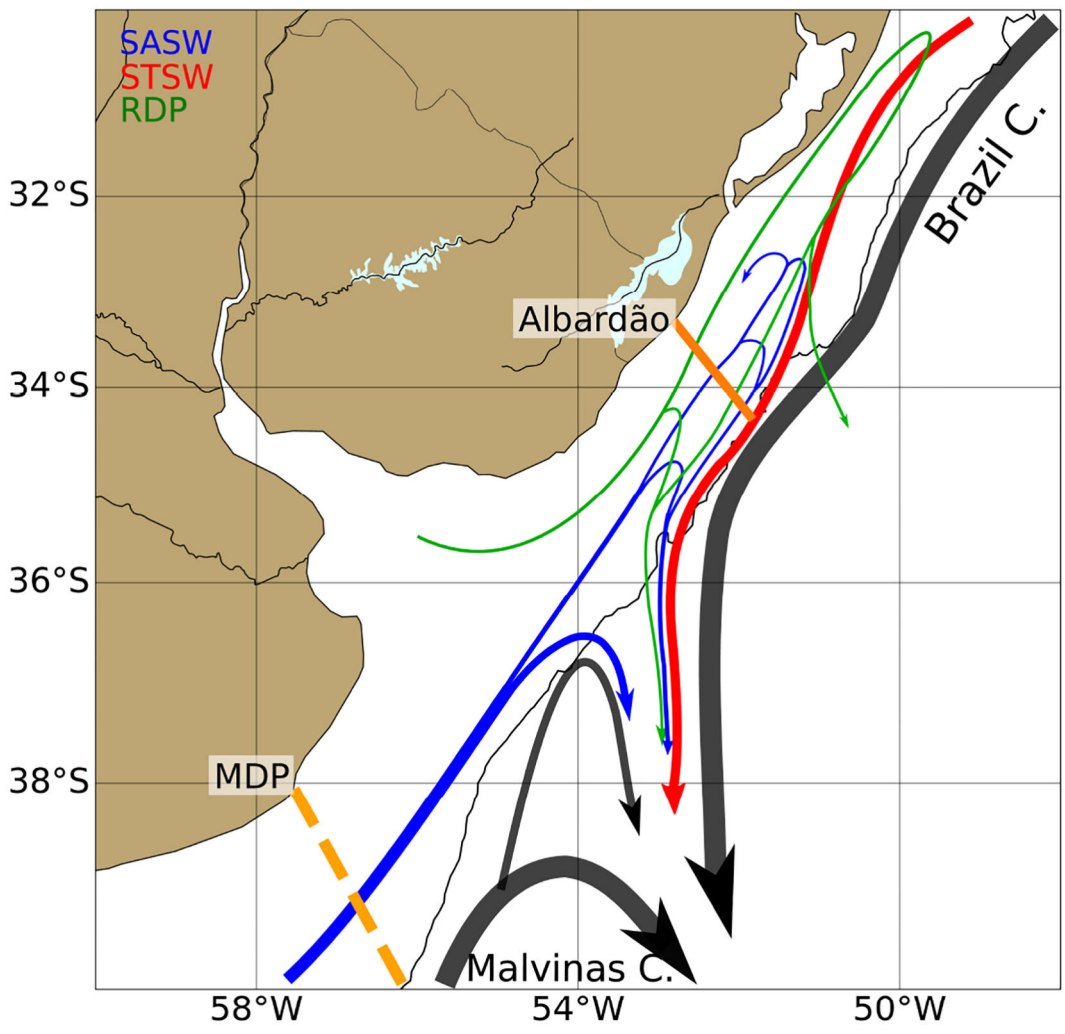

FIGURE 1 | Schematic circulation diagram of the Southwestern Atlantic Shelf between 30 and 40°S. The Mar del Plata (MDP) and Albardão transects are indicated by an orange dashed and solid line, respectively. The gray line indicates the 200 m isobath. SASW, Subantarctic Shelf Water (blue); STSW, Subtropical Shelf Water (red); RDP, Río de la Plata water (green). Adapted from Berden et al. (2020) with permission.

(Borús et al., 2017). From April to September south of 30°S the continental shelf is dominated by southwesterly winds, while northeasterly winds prevail from October to March (e.g., Matano et al., 2014). These seasonal reversals in alongshore winds have a profound effect on the shelf circulation, leading to northeastward extensions of the RDP low salinity waters to 28°S in fall-winter, and retraction to 32°S en spring-summer (Piola et al., 2000, 2005). Direct current meter observations near 40°S indicate a mean northeastward transport of SASW of 2.65 Sv, with large variability, including transport reversal events lasting a few days, which are closely associated with alongshore winds variability (Lago et al., 2021). Numerical models suggest that the transport over the shelf is modulated by the intensity of the MC, which sets up the cross-shore pressure gradient (Matano et al., 2010). However, altimetry-derived velocity fields and more recent numerical simulations indicate this influence is limited to a few tens of kilometers over the outer shelf (Combes and Matano, 2018; Lago et al., 2021). The influence of the tides north of 39°S is very limited except in the inner portion of the RDP (Palma et al., 2004).

Strong western boundary currents (WBCs), including the BC and the MC, are thought to act as barriers to exchanges between the shelf and the open ocean (Roughan et al., 2011; Franco et al., 2017; Malan et al., 2020). However, *in-situ* and satellite observations, and numerical simulations indicate that the BMC is an effective conduit of shelf waters toward the deep adjacent ocean (Guerrero et al., 2014; Matano et al., 2014; Berden et al., 2020). Synoptic hydrographic observations suggest that the STSF is nearly density-compensated (Piola et al., 2000, 2008) allowing the necessary baroclinicity for cross-isobaths exchanges (Berden et al., 2020). The slight changes in isopycnal depth on either side of the STSF and its partial cross-shore orientation allow cross-isobath movements suggesting the STSF may be a path of export of shelf waters to the open ocean. Combes et al. (2021) suggest that between 22.2 and 35°S the mean cross-isobath transport is modulated by the bathymetry and its variability is determined by the local wind and the internal variability of the BC. In addition, onshore intrusions of South Atlantic Central Waters (SACW) in the bottom layer of the outer shelf north of the BMC have been reported in several studies (Braga et al., 2008; Möller et al., 2008; Piola et al., 2008; Palma and Matano, 2009; Berden et al., 2020). These SACW intrusions are a significant nutrient source to the shelf region (e.g., Ciotti et al., 1995 and references therein).

Analyses of *in-situ* observations provided a synoptic characterization of the water exchange between the SWAS and the open ocean (Berden et al., 2020) estimating an offshore transport of 3.44 Sv between 32.1 and 37.7°S. Analyses of altimetry data indicate a maximum off-shelf transport in January–June between 35 and 38°S, and a minimum in July to December (Strub et al., 2015). Matano et al. (2010) and Combes and Matano (2014b) study the interaction between the WBCs and the shelf in the South Brazil Bight and Patagonia based on numerical models. North of 29°S, the circulation is driven by the interaction between intrusions of the BC over the middle and outer-shelf and upwelling favorable wind stress in the inner-shelf. Between 30 and 40°S, the STSF seems to be a preferential path for the ejection of shelf waters. Matano et al. (2014) use 10-day averaged outputs from a high-resolution model (1/24°) to analyze the exchanges of shelf-waters focusing on the sea surface salinity variability. The model suggests that low-salinity waters of the RDP are exported in the vicinity of the BMC. A Lagrangian particle analysis with a similar model indicates that the export of SASW occurs primarily along two different paths (Franco et al., 2018). The waters following a fast path (<2 months) are exported near the BMC and those following a slow path (>130 days), flow northward over the shelf beyond the latitude of the BMC, describe a cyclonic loop near 32°S and subsequently follow the shelf-break southward to the BMC. Likewise, other numerical simulations (1/12°, 10-day average) suggest that the location of the BMC determines the position of the largest offshore transport, but not its magnitude (Combes and Matano, 2018). Recent analyses based on a high-resolution nested model (1/36°, 5-day average) indicate an offshore transport of ∼1.6 Sv between 35 and 25.2°S (Combes et al., 2021).

In this article, we extend previous studies analyzing the export of shelf waters to the open ocean between 30 and 40°S and its time and space variability using daily outputs from a global high-resolution ocean model reanalysis. Given the recent observational evidence of large-amplitude alongshore transport fluctuations at a synoptic time scale near 40°S (Lago et al., 2021) we also analyze the model results to determine if such changes may impact the offshore transport. The daily resolution of the reanalysis allows us to study the temporal variability at high frequencies, which has not been discussed hitherto.

2. DATA AND METHODS

2.1. Reanalysis GLOBAL_REANALYSIS_PHY_001_030

This study is based on the analysis of the Copernicus Marine Environment Monitoring Service (CMEMS) global ocean reanalysis (GLORYS12V1) during 1993–2018. GLORYS12V1 is based on the NEMOv3.1 ocean model, described in Madec et al. (2017). The model is driven at the surface by the ERA-interim atmospheric reanalysis from the European Centre for Medium-Range Weather Forecasts. Satellite-derived along-track sea level anomaly (SLA, Pujol et al., 2016), sea surface temperature (SST) from NOAA's Optimum Interpolation Sea Surface temperature (0.25°, Reynolds et al., 2007), sea ice concentration from CERSAT and *in situ* vertical profiles of temperature (T) and salinity (S) from the CORA4.1 database (Cabanes et al., 2013) are jointly assimilated. The assimilation procedure employs a reduced-order Kalman filter with a 3D multivariate modal decomposition of the background error. The assimilation procedure includes an adaptive-error estimate and a localization algorithm. In addition, a 3D-VAR scheme corrects for the slowly-evolving large-scale biases in temperature and salinity (Lellouche et al., 2018). The reanalysis does not incorporate tidal forcing. The model output is provided daily on a standard regular grid at 1/12° (∼8 km) and on 50 standard vertical levels, with 22 levels in the upper 100 m. Consequently, the vertical resolution is 1 m at the surface, decreases to 33 m at the bottom of the continental shelf (200 m), and reaches 450 m near the bottom in the deep ocean (5,700 m).

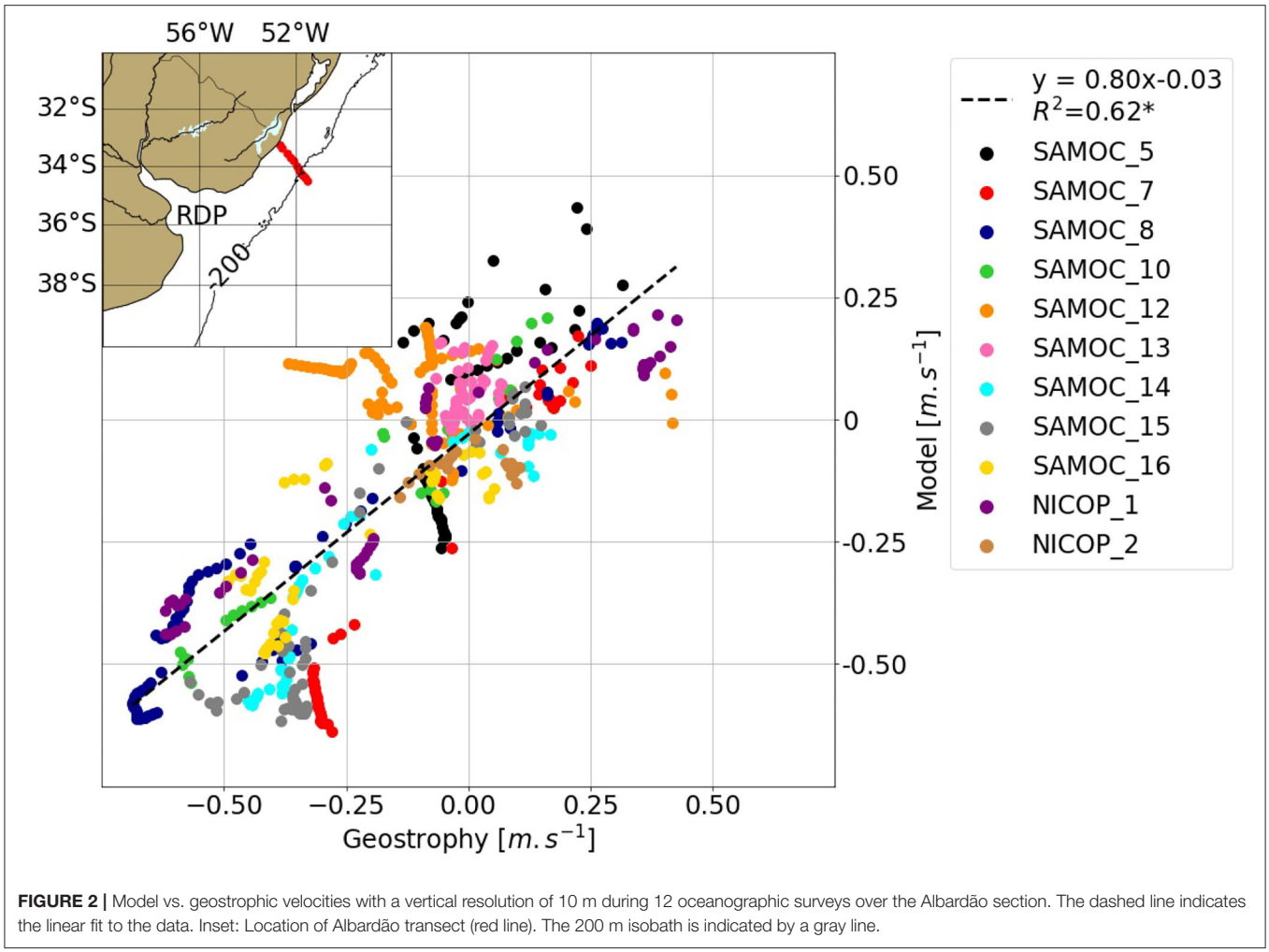

FIGURE 2 | Model vs. geostrophic velocities with a vertical resolution of 10 m during 12 oceanographic surveys over the Albardão section. The dashed line indicates the linear fit to the data. Inset: Location of Albardão transect (red line). The 200 m isobath is indicated by a gray line.

2.2. *In-situ* Data

To evaluate the model performance, the model was compared with *in-situ* data collected during 12 hydrographic surveys over a cross-shelf transect off southern Brazil, hereafter referred to as the Albardão transect (**Figure 2** and **Table 1**). The data consists of high-resolution, cross-shore sections of conductivity-temperature-depth (CTD) profiles occupied between August 2003 and October 2018. In addition, the alongshore volume transport between the coast and the 200 m isobath near 39°S (hereafter referred to as the MDP transect, location shown by the orange dashed line in **Figure 1**) has been recently estimated, hereafter referred to as T_{Obs}, based on direct current observations during 11 months from December 2014 to November 2015. Details of these transport estimates are provided in Lago et al. (2021). Note that the *in-situ* observations used herein were not assimilated to the ocean reanalysis.

TABLE 1 | Hydrographic surveys along the Albardão transect.

Cruise	Dates	Vessel	Country
NICOP _1	26–27 August 2003	Puerto Deseado	Argentina
NICOP _2	9–10 February 2004	Antares	Brazil
SAMOC _5	5–6 July 2011	Puerto Deseado	Argentina
SAMOC _7	9 July 2012	Puerto Deseado	Argentina
SAMOC _8	10 Dec 2012	Alpha-Crucis	Brazil
STSF	7–8 October 2013	Puerto Deseado	Argentina
SAMOC _10	14 October 2014	Puerto Deseado	Argentina
SAMOC _12	17–18 September 2016	Alpha-Crucis	Brazil
SAMOC _13	29 October 2016	Puerto Deseado	Argentina
SAMOC _14	29–30 September 2017	Puerto Deseado	Argentina
SAMOC _15	25 April 2018	Alpha-Crucis	Brazil
SAMOC _16	26 October 2018	Puerto Deseado	Argentina

2.3. Satellite Data

The altimetry data (sea level anomalies and associated geostrophic currents) used in this analysis were the delayed-time merged all satellites Global Ocean Gridded SSALTO/DUACS Sea Surface Height L4 product from Copernicus Marine (Pujol et al., 2016). The gridded product has a spatial resolution of 1/4° on a regular grid and a daily temporal resolution.

2.4. Wind Data

Wind stress data was obtained from the ERA5 global atmospheric reanalysis (Hersbach et al., 2020), which covers 1979–2022, produced by the European Center of Middle-range Weather Forecast (ECMWF). This product is available hourly over a regular grid of 1/4°. Daily averages were used in this work.

2.5. Methods

Since the WBCs may act as barriers to exchanges between the shelf and the open ocean, the possible impact of the BC and MC intensity is studied. The analysis of the BC variability is based on the depth-averaged model velocity in the upper 0–200 m at 34.5°S projected in the local along-slope direction (orientation of 36° from the true north). Likewise, the MC velocity was defined at 42°S, where the model velocity is projected to 45° from the true north. Since the BC presents substantial mesoscale variability (see Chidichimo et al., 2021), it is difficult to determine its precise position in the cross-shore direction along 34.5°S in the daily model outputs. Therefore, the position of the current was determined using the mean velocity field between 1993 and 2018 considering the current as a uniform flow with intensity $>10\ cm.s^{-1}$. Once the position of the current is established, the along-slope velocity component is averaged horizontally to obtain a single velocity time series. The same procedure is followed to determine the MC intensity. The sensitivity of the definition of both currents to changes in the velocity threshold and depth over which the velocity is integrated was analyzed (**Supplementary Figure 1**). The resulting velocity magnitude is not significantly sensitive to changes in depth of integration considering a range of 200–400 m. Although the velocity magnitude displays variations associated with changes in the threshold used to define the BC and MC, tested in the range of 5–20 $cm.s^{-1}$, these changes are small and the resulting velocities are highly correlated ($R^2 > 0.85^*$). The significance of the statistical correlations was calculated at a 95% confidence level. Hereafter, significant correlations are indicated with an asterisk (*), and correlations with $R^2 < 0.15$ will not be addressed. In addition, the BMC location was analyzed as a possible driver of cross-shelf exchange. The position of the BMC is determined daily as the latitude where the 10°C isotherm at 200 m intersects the 1,000 m isobath (Goni and Wainer, 2001; Matano et al., 2014).

3. RESULTS AND DISCUSSION

3.1. Evaluation of Model Performance

In this section, we evaluate the model's ability to capture the patterns of the shelf circulation and its time variability. To this end, we compare the model outputs with available *in-situ* and satellite observations.

3.1.1. Currents

The currents extracted from the model over the continental shelf were first compared with *in-situ* data collected in the Albardão transect (**Figure 2**). Alongshore geostrophic velocities relative to the sea surface were estimated from the hydrographic data with a vertical resolution of 10 m. Absolute velocities were then computed by adjusting the relative geostrophic profiles to the surface geostrophic velocity derived from the gridded altimetry data. Model velocities were projected in the alongshore direction and low-passed filtered with a 5-day window. Model and observations are in relatively good agreement based on the linear correlation ($R^2 = 0.62^*$).

3.1.2. Comparison With Satellite Altimetry

To further evaluate the model performance, we compared the standard deviation of the sea level anomaly (SLA) from the model and the gridded satellite data. It is important to note that the model assimilates altimetry derived along-track sea level. The spatial structures of the standard deviation of SLA (**Figure 3**) are very similar at offshore locations and present the largest differences over the RDP estuary and coastal regions northeast of the RDP mouth. To analyze the temporal evolution of SLA we selected a location on the mid-shelf close to the climatological latitude of the BMC (36.9°S), which is a preferential location of export of shelf-waters to the open ocean (black dot in **Figures 3A,B**). The 10-day filtered time series of SLA shows a significant correlation ($R^2 = 0.72^*$) between the model and the altimeter data. This correlation decreases considering daily data ($R^2 = 0.50^*$) because the model output contains more high-frequency variability than the altimeter data. These differences between altimetry and model results are expected because of the comparatively poor space and time resolution of the altimeter data. Although the gridded altimetry product is available daily, the most frequent (Jason 3) revisits occur at 10-day intervals. Therefore, the gridded altimetric product has an effective spatial and temporal resolution of 280 km and 21 days (see **Figures 2B**, **3** in Ballarotta et al., 2019) and cannot appropriately resolve estuarine and nearshore features, nor small mesoscale features (Pujol et al., 2016) generated by the model's internal dynamics.

3.1.3. Comparison With *in-situ* Alongshore Transports

Alongshore transport over the MDP transect between the coast and the 200 m isobath near 39°S was recently estimated by Lago et al. (2021) using *in-situ* data (T_{Obs}). The analyses of Lago et al. (2021) reveal the barotropic nature of the circulation and a close agreement between geostrophic and direct transport estimates. To evaluate the model performance, we computed the alongshore component of model transport across the same line, hereafter referred to as T_{Model} (**Figure 4**). The time-averaged T_{Obs} is 2.68 Sv and its standard deviation is 2.13 Sv. Meanwhile, T_{Model} presents lower mean and standard deviations; 2.13 and 1.32 Sv, respectively. In addition, flow reversal events were analyzed by Lago et al. (2021). Particularly, an event observed in early May 2015 shows a flow reversal from −2.57 to 5.84 Sv in T_{Obs} and from −1.46 to 5.15 Sv in T_{Model}.

T_{Model} explains 79% of the variance of T_{Obs} (**Figure 4C**). However, the mean difference of 0.55 Sv represents a relative error of 0.55 Sv/2.68 Sv = 0.20, or 20% less than the observed transport. T_{Model} has less energy than T_{Obs}, at periods shorter than ∼ 30 days. However, both transport time series present peaks at similar frequencies at around 5.8, 7.4, 10, 16, 28, and 85 days (**Figure 4D**). T_{Obs} displays higher energy in almost all peaks except at 85 days where both model and *in-situ* transports

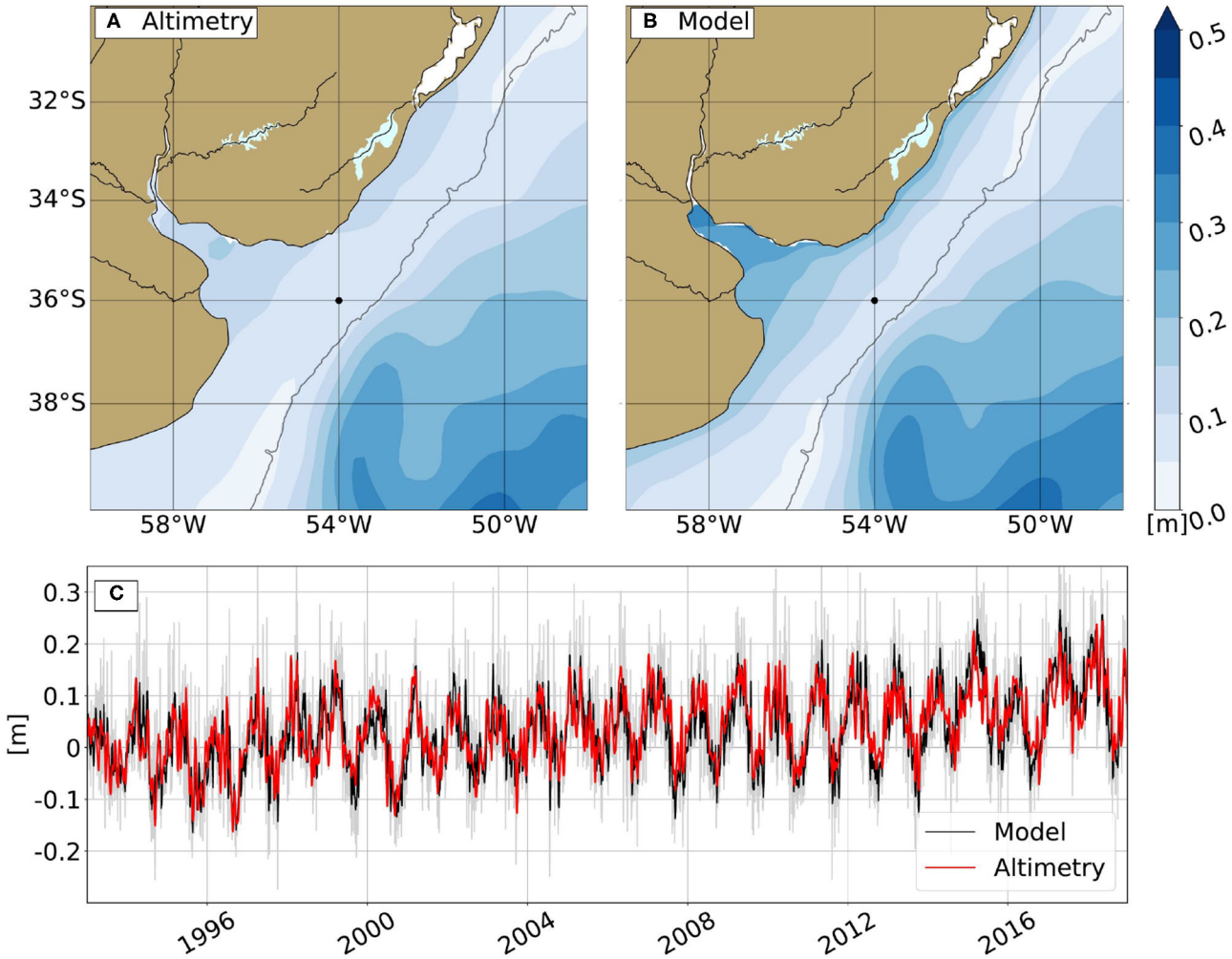

FIGURE 3 | Standard deviation of sea level anomaly based on satellite altimetry **(A)** and the model **(B)**. The 200 m isobath is indicated by a gray line. **(C)** Ten-day filtered time series of SLA at 36°S, 54°W (black dot in **A,B**). Altimetry data is shown in red and model data in black. The daily (unfiltered) model output is shown in gray.

are in much better agreement. Hence, the model reproduces the regional dynamics but it contains lower energy at shorter periods.

Additionally, Lago et al. (2021) estimated the alongshore transport using altimeter data (T_{Sat}). Their mean T_{Sat} is 2.42 ± 0.64 Sv, thus matching quite well the 2.13 ± 1.32 Sv from the model during the same period. Since the model assimilates along-track altimeter sea level anomaly, this agreement is not surprising.

3.2. Cross-Shore Transport Variability

To study the cross-shore transport between 30 and 40°S and its temporal and spatial variability, the 200 m isobath was divided into 20 zonal bands each spanning 0.5° of latitude (**Figure 5**). The time-averaged offshore transport through each outer shelf segment was estimated as the sum of the transports entering through the northern and southern boundaries of each zonal band. The total offshore transport between 30 and 40°S, hereafter referred to as T_{Cross} (**Figure 6C**), is defined as the sum of the transports entering through the northern boundary at 30°S (T_N, positive southward, i.e., entering the domain; **Figure 6A**) and the southern boundary at 40°S (T_S, positive entering the domain; **Figure 6B**). We estimated the changes in the volume of shelf water based on the changes in the model-derived SLA. The resulting rate of daily volume change has a standard deviation of 0.16 Sv, which is an order of magnitude smaller than the typical daily mass convergence between 30 and 40°S. Thus, we assumed the mass storage plays a minor role in the cross-shore transports estimated based on mass conservation. We also investigate extreme events which are defined as those periods when the transport is higher/lower than the record-mean ±2 standard deviations. In addition, possible physical mechanisms modulating the variability of the cross-shore transport such as the intensity of the BC and the MC, the BMC location, the alongshore transport variability, and the winds are analyzed.

The variability of the shelf transports (T_N, T_S, and T_{Cross}) can be caused by circulation changes occurring on a variety of

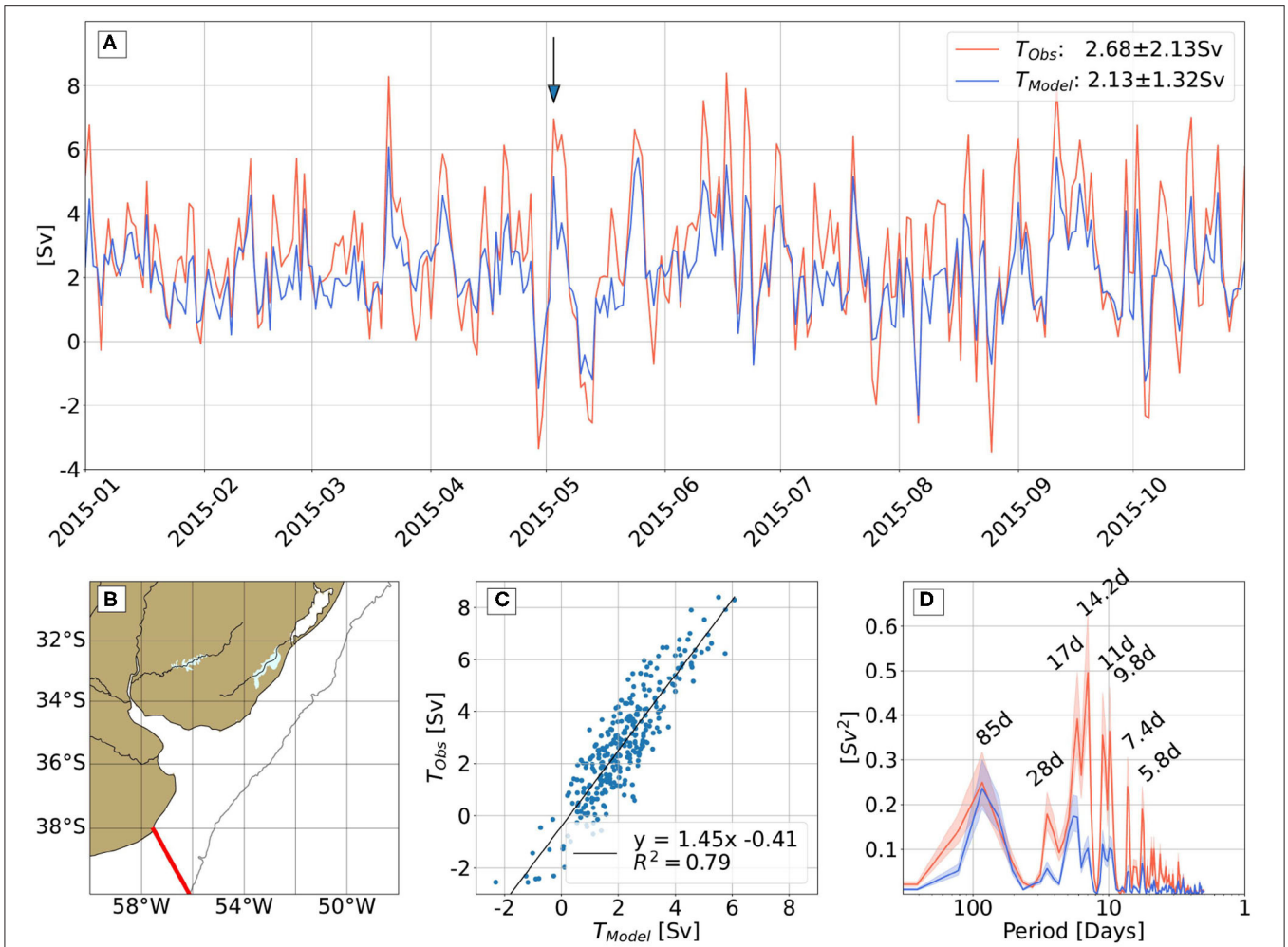

FIGURE 4 | (A) Daily observational (T_{Obs}, red) and model-derived (T_{Model}, blue) shelf transport (Sv) across the red line shown in **(B)**. **(C)** T_{Obs} vs. T_{Model}, and linear regression (black line). **(D)** Power spectrum of T_{Obs} (red line) and T_{Model} (blue line) with bands of 95% confidence levels (shadings).

time scales. Thus, it is useful to split the model-derived transport variability by filtering the daily transport signals as follows:

$$T = T_{mean} + T_{weekly} + T_{subannual} + T_{seasonal} + T_{interannual} \quad (1)$$

where T_{mean} is the record-mean transport and T_{weekly}, $T_{subannual}$, $T_{seasonal}$, and $T_{interannual}$ are associated with weekly (<10 days), subannual (10 days–5 months), seasonal (5–23 months), and interannual (>23 months) time scales, respectively (Hirschi et al., 2007). To compute each component the daily transport time series is filtered with a Butterworth window of order 5. The weekly scale is included to study the high-frequency variability, which is particularly relevant to understand the extreme offshore transport anomaly events. **Table 2** shows the standard deviation of each transport and for each of the above-defined time scales. The larger variability is concentrated on the subannual and weekly time scales, with the latter being the largest. Although the transport power spectrum shows a marked peak around 1 year (2.7–9.2% of energy), there is a substantial amount of energy (>85%) distributed in the high frequencies (subannual and weekly), without a characteristic frequency (**Figure 6D**).

3.2.1. Mean, and Low-Frequency Variability (Interannual and Seasonal)

The record-length mean offshore transport [mean ± 1 standard deviation] between 30 and 40°S (T_{Cross}) is 2.09 ± 1.60 Sv (**Table 3**). Sixty-three percent (1.31 ± 1.16 Sv) of T_{Cross} is contributed by T_S and the remaining 37% (0.78 ± 1.36 Sv) by T_N. The contribution of continental discharge from the RDP is <1% of the offshore transport variability. Previous estimates of the mean off-shelf transport based on the analyses of a high-resolution regional model show a mean offshore transport of 1.21 Sv between 34 and 38°S (Matano et al., 2014). This is in relatively good agreement with the GLORYS12V1 offshore transport computed over the same latitude range (1.72 ± 1.35 Sv).

The offshore flow across the 200 m isobath is not uniform. Most of the flow (1.53 ± 0.74 Sv or 73%, **Table 3**) occurs in the vicinity of the BMC (between 35.5 and 37.5°S, hereinafter

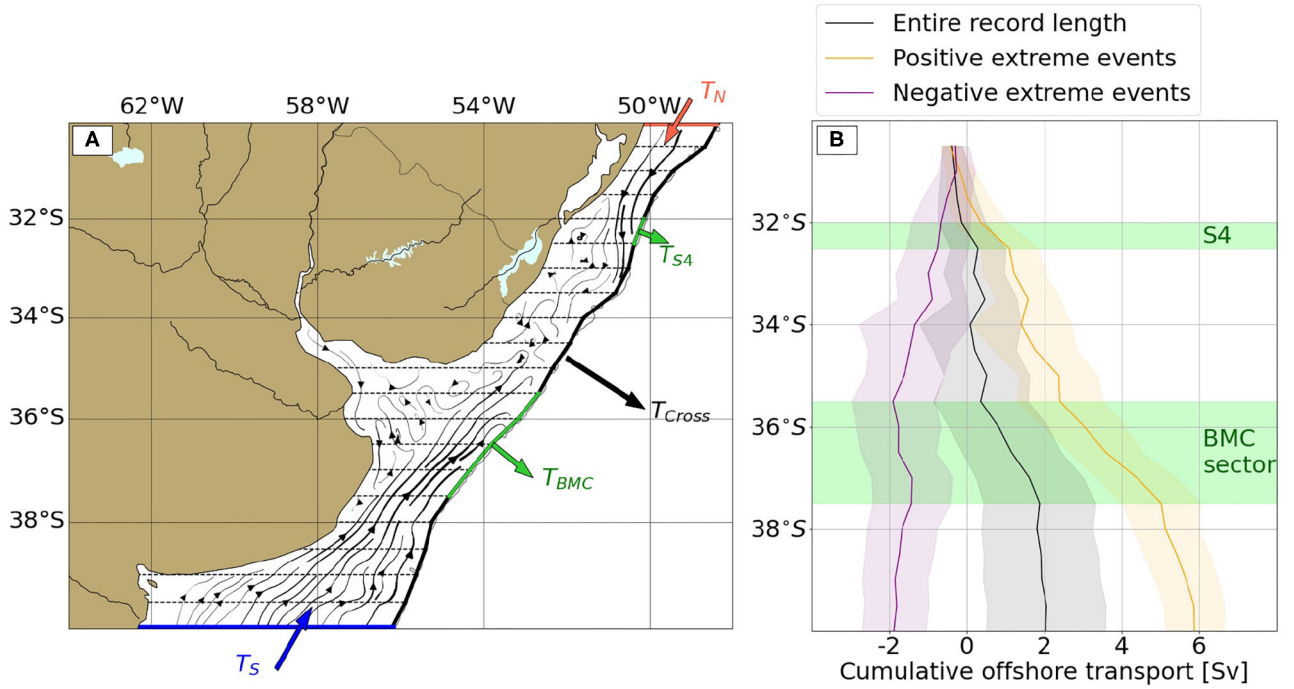

FIGURE 5 | (A) Streamlines over the shelf show time-mean flow structure for the entire record length. Zonal strips used to estimate cross-shore transports (dashed lines). The 200 m isobath is indicated by a heavy black line. **(B)** Cumulative offshore transport through the 200 m isobath from 30°S across the 20 outer shelf segments. Mean offshore transport during the entire model run period (1993–2018, black), positive (orange, offshore) and negative (purple, onshore) extreme events. The transport standard deviations are indicated by the background shading. The BMC sector and S4 are indicated in green.

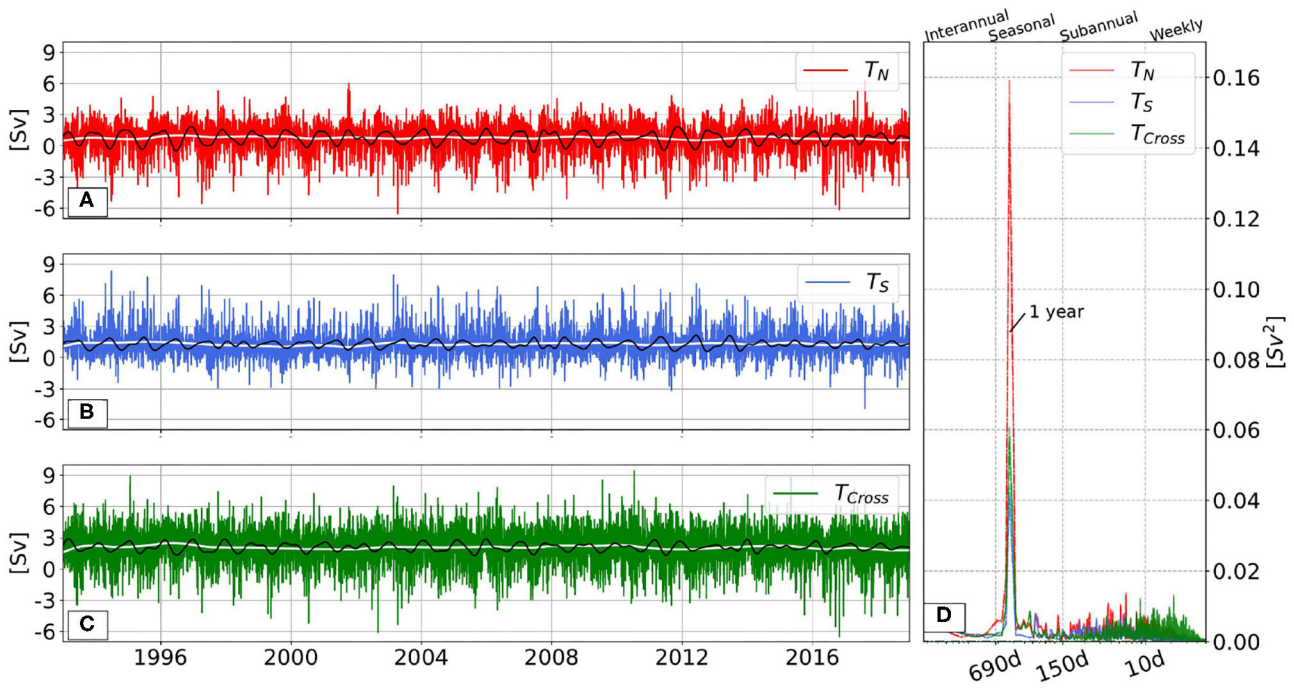

FIGURE 6 | Transports (Sv) over the continental shelf through 30°S (**A**, red, T_N), 40°S (**B**, blue, T_S), and cross-shore (**C**, green, T_{Cross}). Also shown are $T_{seasonal}$ plus T_{mean} (black) and $T_{interannual}$ plus T_{mean} (white). **(D)** Transport power spectra through the same sections. Vertical lines at 10, 150, and 690 days represent the breaks between time scales.

referred to as "BMC sector") and about 20% of T_{Cross} occurs in the vicinity of 32°S (0.42 ± 0.31 Sv, hereinafter referred to as "S4"; **Figure 5**).

The record-mean circulation pattern (**Figure 5A**) is in agreement with Matano et al. (2014), Combes and Matano (2018), and Combes et al. (2021). It shows that water entering from the north of the domain is exported through S4 while water entering from the south of the domain is mostly exported in the vicinity of BMC. Transport variations at the interannual scale present a low standard deviation (<0.15 Sv, **Table 2**) and display similar spectral amplitudes throughout this time scale. The preferential export routes at interannual time scales do not show significant relationships with T_N and T_S.

Although T_N, T_S, and T_{Cross} do not show high standard deviation at the seasonal time scales (**Table 2**), they all have high spectral energy around 1 year (**Figure 6D**). The annual cycle of T_N presents a minimum transport (<0.43 ± 0.40 Sv) from April to July and a maximum transport (1.26 ± 0.34 Sv) in October (**Figure 7**), in agreement with Strub et al. (2015) and Combes and Matano (2018). In contrast, T_S presents a maximum from April to July (>1.46 ± 0.35 Sv) and a minimum (0.95 ± 0.31 Sv) in October. The above-described annual cycle of T_S is in good agreement with Strub et al. (2015) and Combes and Matano (2018) and the altimetry-derived transport through a cross-shelf section at around 39°S recently reported by Lago et al. (2021). The annual cycles of T_N and T_S are partially compensated. Consequently, T_{Cross} shows a maximum of 2.40 ± 0.37 Sv in January and a minimum of 1.74 ± 0.34 Sv in June.

When analyzing the predominant export locations, the cross-shore transport through the BMC sector (T_{BMC}) presents subtly higher seasonal variability than T_{Cross} and similar spectral energy concentrated around one year (**Supplementary Figure 2**). The annual cycle of T_{BMC} (**Figure 7B**) shows a maximum (1.82 ± 0.49 Sv) in January and a minimum (1.20 ± 0.37 Sv) in August. The cross-shore transport through S4 (T_{S4}) also presents an annual cycle with a maximum (0.54 ± 0.18 Sv) in October and a minimum (0.28 ± 0.12 Sv) in June. At the seasonal scale, significant and positive correlations between T_{Cross} and T_{BMC} (0.55*) and between T_{Cross} and T_{S4} (0.77*) are observed (**Figure 8J**). Most of the variability of T_{S4} is associated with T_N ($R^2 = 0.71$*, not shown). However, T_{BMC} presents no relationship with T_S (not shown). The seasonal component of T_S presents a negative correlation with T_{S4} ($R^2 = 0.30$*, not shown). However, it is difficult to identify a physical process that may explain this correlation.

The climatology of the vertical temperature and salinity structure of the outer shelf averaged over the BMC sector is shown in **Figure 7C**. Note that on average the transport through this sector is offshore (positive) throughout the year (**Figure 7B**). Low salinity waters (S < 33.5), characteristic of shelf waters diluted by the RDP discharge, are present in the upper layer (z < 25 m) throughout the year, except in winter (JJA) when saltier and colder waters (S∼33.8, <11°C), associated with SASW are observed. Below this near-surface layer, waters with salinities between 33.8 and 35 are observed throughout the year. These waters represent mixtures of SASW with TW (Tropical Waters)/SACW. The salinity and temperature maxima observed during April–May and November are associated with a higher proportion of TW/SACW. On average the transport through S4 is also offshore (positive) throughout the year (**Figure 7B**). The vertical temperature and salinity structures are shown in **Figure 7D**. Low-salinities (S < 33.5) RDP waters are exported in the upper layer (z < 25 m) during July–October. During this period, at about 60 m depth, waters are warmer (>19°C) and saltier (>34) than in the upper layer. The rest of the year, saltier waters (S > 34) with surface temperatures ranging from 25.6 °C in March to 16.4 °C in July associated with STSW are exported to the open ocean through S4.

TABLE 2 | Standard deviation of transport (Sv) through selected sections, estimated over the entire model period (1993–2018).

	Interannualy	Seasonal	Subannual	Weekly
T_N	0.11	0.54	0.82	0.90
T_S	0.11	0.32	0.71	0.79
T_{Cross}	0.15	0.36	0.72	1.32
T_{BMC}	0.20	0.39	0.39	0.43
T_{S4}	0.06	0.15	0.19	0.18

*Section locations are shown in **Figure 5A**.*

3.2.1.1. Drivers of Low Frequency (Interannual and Seasonal) Cross-Shore Transport Variability

In this section, we analyze the physical mechanisms driving offshore transport at low frequencies. At interannual scales,

TABLE 3 | Mean transport (Sv) through selected sections for the entire model run (1993–2018), during extreme cross-shore transport events, and during the large transport reversal observed in early May 2015 (see section 4.4).

	Record length (Sv, mean ± SD)	Positive extreme events T_{Cross} (Sv, mean ± SD)	Negative extreme events T_{Cross} (Sv, mean ± SD)	2015-04-29 (Sv)	2015-05-03 (Sv)
T_N	0.78 ± 1.36	2.02 ± 1.57	−2.16 ± 1.42	0.80	3.44
T_S	1.31 ± 1.16	4.03 ± 1.69	0.14 ± 1.28	−1.82	5.36
T_{Cross}	2.09 ± 1.60	6.05 ± 0.74	−2.02 ± 0.87	−1.03	8.80
T_{BMC}	1.53 ± 0.74	2.62 ± 0.71	0.48 ± 0.64	0.99	3.11
T_{S4}	0.42 ± 0.31	0.74 ± 0.34	−0.08 ± 0.25	0.31	1.10

*Section locations are shown in **Figure 5A**.*

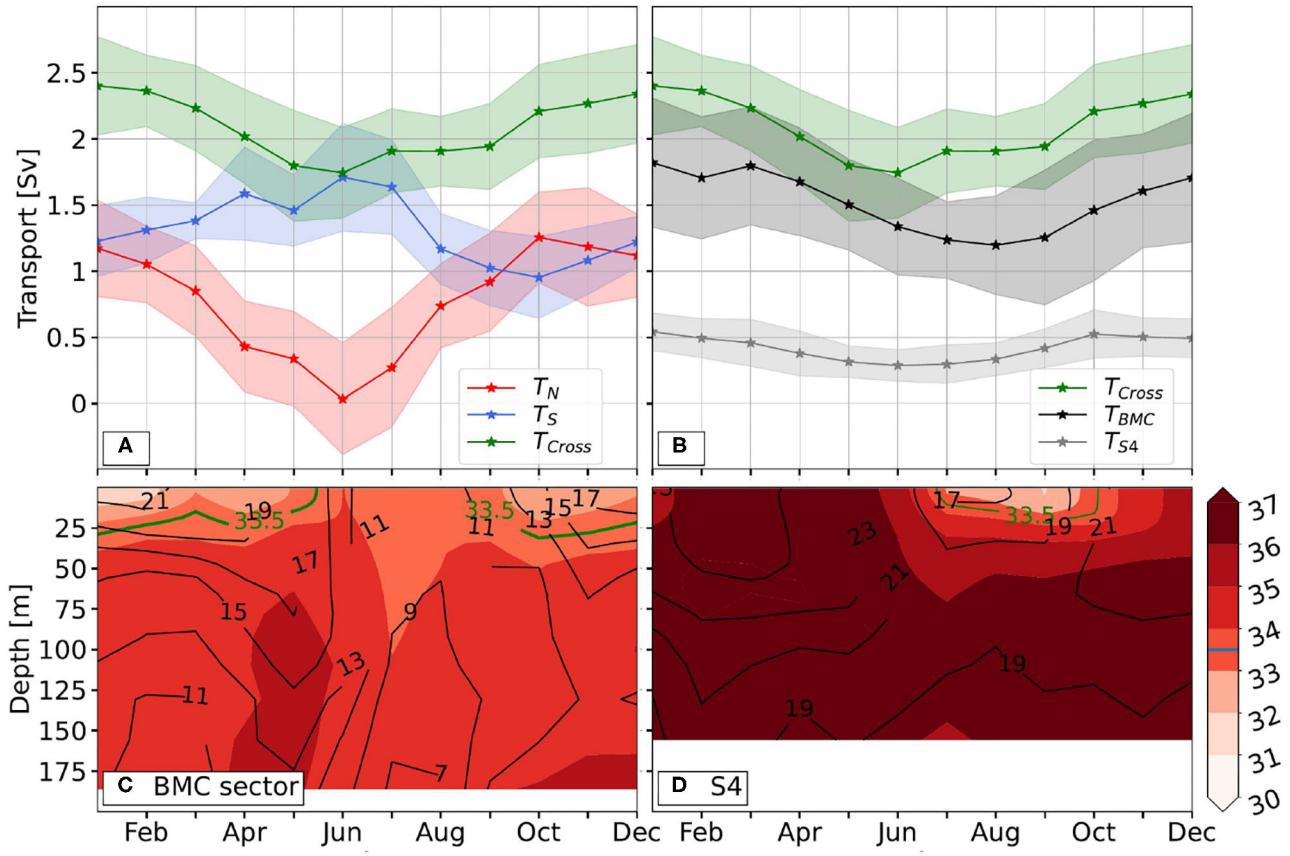

FIGURE 7 | (A,B) Record length monthly mean transports (Sv, solid line) and standard deviation (shading), through 30°*S* (T_N, red), 40°*S* (T_S, blue), the shelf break between 30 and 40°*S* (T_{Cross}, green), the BMC (T_{BMC}, black), and S4 (T_{S4}, gray) segments. **(C,D)** Vertical distribution of the annual cycle of temperature (black contours, with 2°C contour interval) and salinity (background colors, with 1 contour interval, 33.5 shown by green line) averaged over the shelf break BMC **(C)** and S4 **(D)** sectors.

T_{Cross} is positively correlated with T_N and T_S, with R^2 = 0.40* and 0.51*, respectively (**Supplementary Figure 3**). Therefore, T_S has more control of T_{Cross} than T_N at this time scale in agreement with Combes and Matano (2018). The BMC location and T_{Cross} are not significantly correlated. To better understand the interannual variability of T_{Cross}, the T_S and T_N variability are further explored. To study the possible impact of the variability of the WBCs (Brazil and Malvinas currents), as suggested by numerical simulations (e.g., Matano et al., 2010), we compute the correlation between T_S and the intensity of the MC (I_{MC}) and between T_N and the intensity of the BC (I_{BC}). Another likely driver of T_{Cross} is the local alongshore wind defined as the wind stress vector at the boundary sections projected on the alongshore direction (38° from true North for both transects following the coastline). Local alongshore wind stress over the northern and southern sections was analyzed with southwesterly wind stress defined as positive. In the southern boundary, positive correlations at the interannual scale are observed between T_S and I_{MC}, with R^2 = 0.34* (**Supplementary Figure 3B**) and T_S and alongshore wind stress with R^2 = 0.27 (not significant, **Supplementary Figure 3C**). At the northern boundary, T_N does not show a significant correlation with I_{BC} and alongshore wind stress.

At the seasonal scale, T_{Cross} variability presents a high positive correlation with T_N (R^2 = 0.77*) and a negative correlation with T_S (R^2 = 0.22*; **Figure 8A**). Thus, although the record-length mean T_{Cross} is mostly contributed by T_S, the variability at the seasonal scale is driven by variations in T_N. The BMC location and T_{Cross} are not correlated. These results are in agreement with Combes and Matano (2018). As the variability of the offshore transport is set by the variability of T_N and T_S, it is useful to further analyze the processes that determine the variations of the alongshore transports. The WBCs intensity was analyzed finding a low positive correlation between I_{BC} and T_N with R^2 0.15* and no correlation between I_{MC} and T_S (**Figure 8D**). T_N presents a strong and negative correlation with the alongshore wind stress (R^2 = 0.88*, **Figure 8G**) in agreement with Combes et al. (2021). Therefore, high positive (southward) T_N is associated with northeasterly wind stress that sets up a negative SLA along the coast over the northern transect. The resulting cross-shore pressure gradient leads to a southwestward geostrophic flow through 30°S. Likewise, T_S

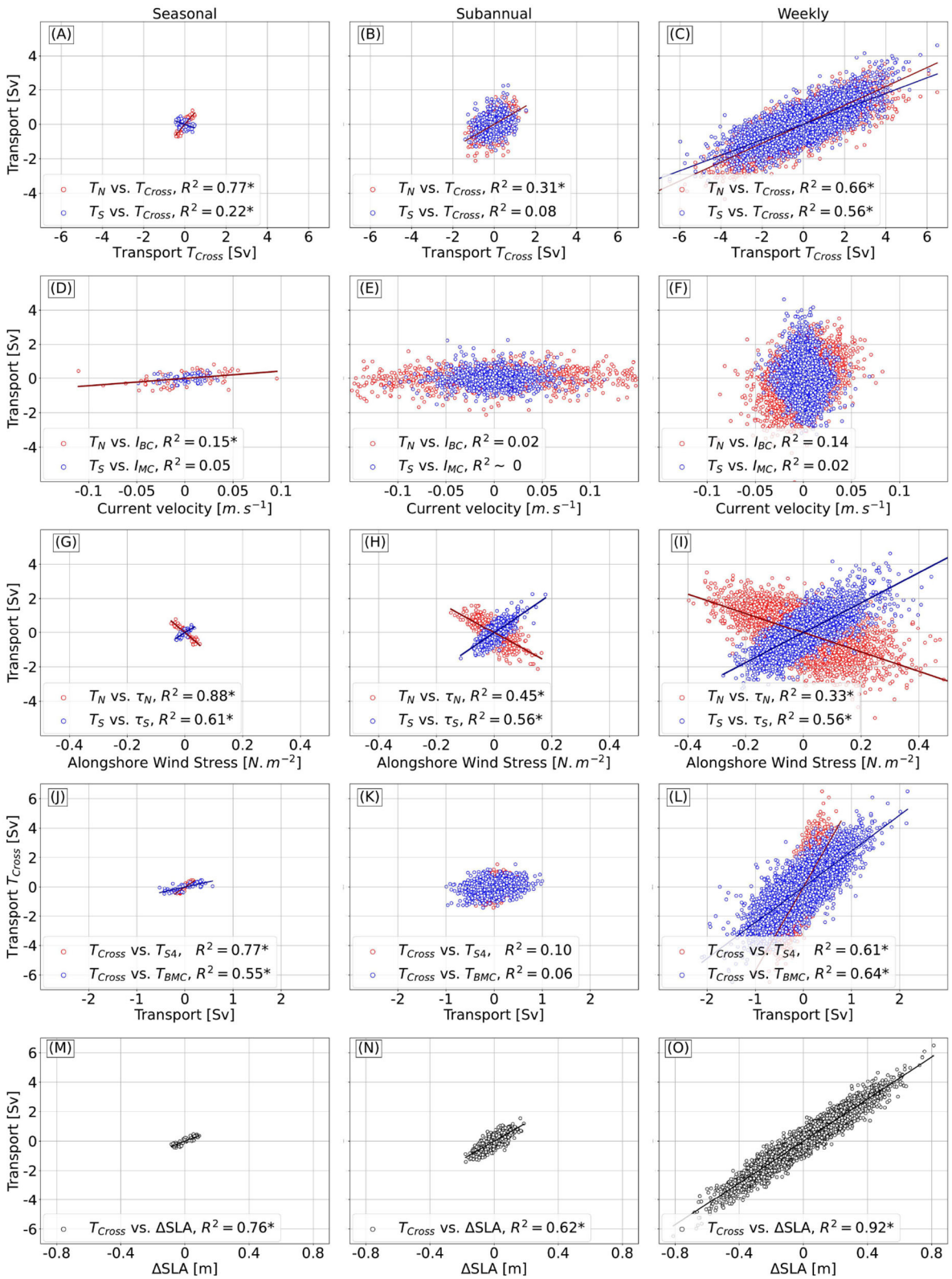

FIGURE 8 | (A–C) T_N (red) and T_S (blue) vs. T_{Cross}. **(D–F)** T_N vs. I_{BC} (red) and T_S vs. I_{MC} (blue). **(G–I)** T_N vs. alongshore wind stress at 30°S (red) and T_S vs. alongshore wind stress at 40°S (blue). **(J–L)** T_{Cross} vs. T_{S4} (red) and T_{BMC} (blue). **(M–O)** T_{Cross} vs. the difference of inner shelf SLA between 40 and 30°S. **(A,D,G,J,M)** Seasonal scale, **(B,E,H,K,N)** subannual scale and **(C,F,I,L,O)** weekly scale.

presents a positive correlation with the alongshore wind stress (R^2 = 0.61*, **Figure 8G**). Therefore, high T_S are associated with southwesterly wind stress that generates a positive SLA along the coast over the southern transect. The resulting cross-shore pressure gradient is related to a northeastward geostrophic flow through 40°S. The subtraction of the inner shelf SLA between the southern and northern boundaries represents 76% of the seasonal T_{Cross} variability (**Figure 8M**). In summary, the inner-shelf SLA variability at the boundaries (40 and 30°S) is a good indicator of the T_{Cross} variability at seasonal time scales.

3.2.2. High-Frequency Variability (Subannual and Weekly)

At the subannual scale, the variability of T_N, T_S, and T_{Cross} is larger than at low frequencies, with standard deviations of 0.82, 0.71, and 0.72 Sv, respectively (**Table 2**). The power spectra of transport variations show substantial energy (38.5, 40.4, and 22.5%, respectively) over a wide range of frequencies (**Figure 6D**). T_{S4} and T_{BMC} are very weakly correlated with the transport variations at the northern and southern boundaries (R^2 < 0.15, **Figure 8K**).

At the weekly time scale, the standard deviations of T_N, T_S, and T_{Cross} increase to 0.90, 0.79, and 1.32 Sv, respectively (**Table 2**). The power spectra of the transport variability at the weekly time scale present high energy (47.0, 51.6, and 71.9%, respectively) over the entire frequency range (<10 days, **Figure 6D**). The transports through the preferential export routes are clearly related to the intensity of T_{Cross} with R^2 = 0.61* and 0.64* through the S4 and BMC sectors, respectively (**Figure 8L**). The T_{S4} variability is more closely associated with the T_N variability (R^2 = 0.71*, not shown) than to T_S (R^2 = 0.25*, not shown), while the T_{BMC} variability is more closely associated with T_S variability (R^2 = 0.58*, not shown) than to T_N (R^2 = 0.11, not shown).

3.2.2.1. Drivers of High-Frequency (Subannual and Weekly) Cross-Shore Transport Variability

Following the analysis of the low-frequency variability, the possible physical mechanisms modulating the high frequencies variability of T_{Cross} are analyzed. We investigate the possible relationship between the high-frequency variability of T_{Cross} and the location of the BMC, the shelf and WBCs transports, and the wind stress patterns. At the subannual scale, there is no significant correlation between T_{Cross} and T_S (**Figure 8B**) or with the location of the BMC (not shown). In contrast, T_{Cross} is primarily controlled by T_N (R^2 = 0.31*, **Figure 8B**). T_N and T_S are driven by the local alongshore wind stress (R^2 = 0.45* and 0.56*, **Figure 8H**) and not by the WBCs (**Figure 8E**). As pointed out earlier, since local alongshore wind stress sets up SLA variations over the coast and similar to our findings at the seasonal time scale, the inner shelf SLA variations at the northern and southern boundaries are a good indicator of the T_{Cross} at subannual time scales. Changes in the inner shelf SLA difference at the southern and northern boundaries represent 62% of the T_{Cross} variability at subannual time scales (**Figure 8N**).

Numerical analyses indicate that although the location of the BMC does not modulate the magnitude of the export of shelf waters between 30 and 40°S, it does determine the position over the shelf break where the largest offshore transport occurs (Combes and Matano, 2018). Satellite and *in-situ* observations suggest that mesoscale eddies can induce the export of shelf waters (e.g., Guerrero et al., 2014; Manta et al., 2022). As these features have a typical time scale of 10–200 days, they could modulate the T_{BMC} at the subannual scale. The role of eddies in the cross-shore transports is further suggested by the significant decrease in correlation between the cross-shore (T_{Cross}) and the alongshore transports (T_N and T_S) at the subannual time scale (compare **Figures 8A–C**), and between T_{Cross} and the transport across the BMC sector (**Figure 8K**).

At the weekly time scale, there is no significant correlation between T_{Cross} and the BMC location (not shown). In contrast, T_{Cross} is closely associated with T_N and T_S (R^2 = 0.66* and 0.56*, respectively, **Figure 8C**). These alongshore transports are modulated by local alongshore wind stress over the northern and southern boundaries (R^2 = 0.33* and 0.56*, respectively, **Figure 8I**) and not by the intensity of WBCs (**Figure 8F**). These transport fluctuations are associated with the inner shelf SLA at 30 and 40°S. Similar to our findings at the seasonal and subannual time scales, the difference between inner shelf SLA at the southern and northern boundaries is a good proxy of T_{Cross} variability, representing 92% of the weekly variability (**Figure 8O**). These results are in agreement with Lago et al. (2021) who show that the alongshore transport can be estimated based on the difference in SLA between the coast and the shelf. Wind-forced coastal-trapped waves are an additional source of SLA variability at the weekly time scale (Brink, 1991; de Freitas et al., 2021). However, the details of the dynamics of processes leading to the model variability are deferred to a future study.

3.3. Analysis of Extreme Transport Events

In this section, the extreme cross-shore transport events are studied based on the daily, unfiltered T_N, T_S, and T_{Cross}. The monthly distribution of the number of positive extreme events is shown in **Figure 9A**. Recall positive transports imply northward flow over the shelf through 40°S (T_S), southward flow through 30°S (T_N), and offshore flow through the outer shelf between 30 and 40°S (T_{Cross}). Extreme southward (positive) T_N events (red bars in **Figure 9A**) occur more frequently in spring, last <3 days, and reach 6.32 Sv, eight-fold the mean value (0.78 Sv; **Table 4**). Extreme northward (positive) T_S events (blue bars in **Figure 9A**) are more frequent in austral winter (June–July) and infrequent in summer. Typically, the extreme transport events across the southern boundary last <4 days and reach transports of up to 8.36 Sv (**Table 4**), six-fold the mean value (1.31 Sv). The occurrence of positive T_{Cross} extreme events (green bars in **Figure 9A**) has two maxima, in fall and spring, and are less frequent in summer. The extreme export events have a shorter duration (<2 days) and present a maximum export transport of 9.45 Sv (more than four-fold the mean export transport, 2.09 Sv). During the entire period, the offshore transports across the BMC sector and S4 account for 73 and 20% of the total transport across the 200 m isobath between 30 and 40°S, respectively. However, during the extreme events, the transports across BMC and S4 decrease to 43 and 12% of the record-mean T_{Cross}. Therefore, the

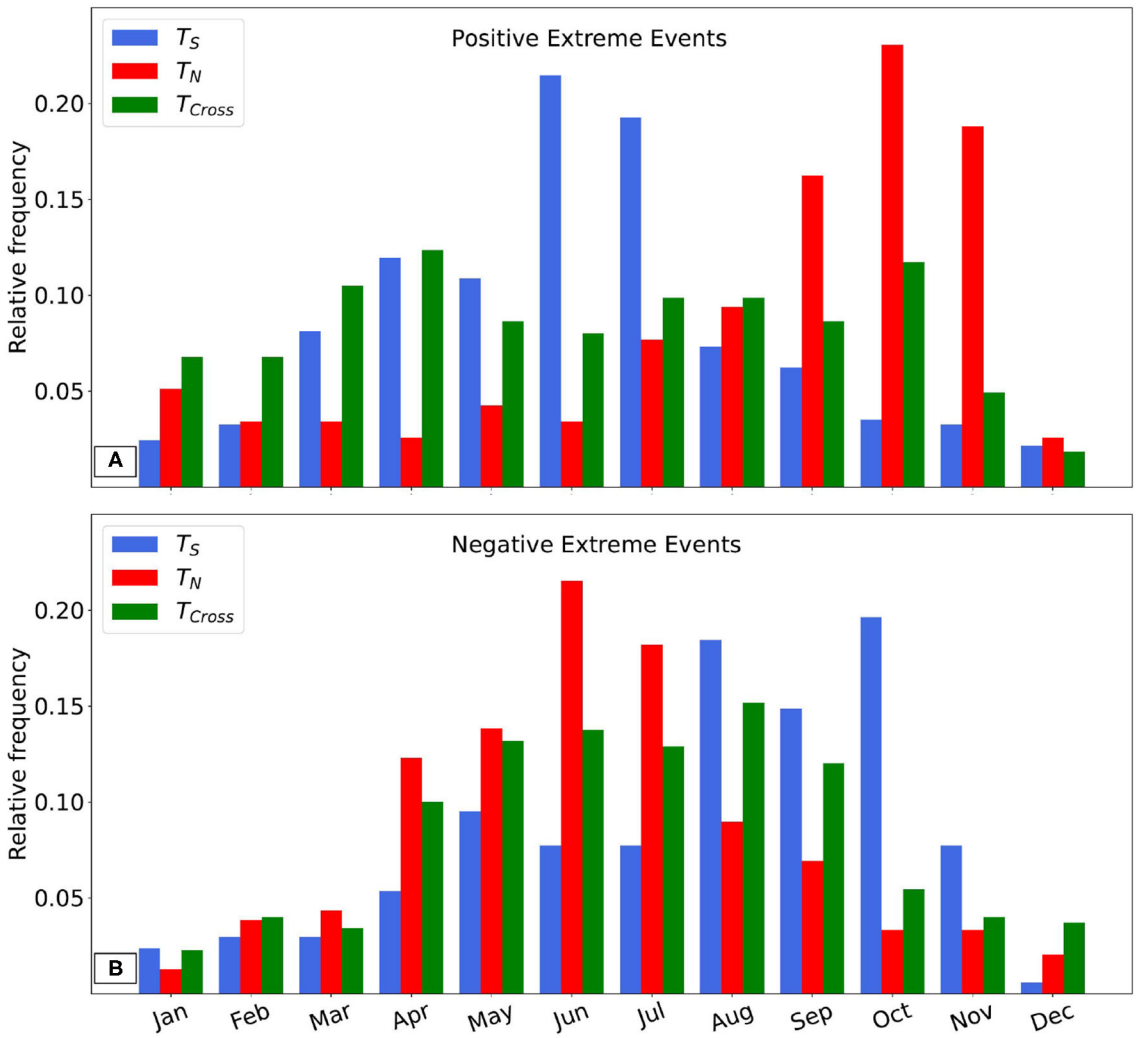

FIGURE 9 | Histogram of monthly binned extreme transport events through 40°S (T_S, blue), 30°S (T_N, red), and cross-shore (T_{Cross}, green). **(A)** Positive extreme events. **(B)** Negative extreme events.

TABLE 4 | Statistics of extreme transport events through selected sections.

	30°S	40°S	Shelf break
Number of positive events	81 (1.2%)	262 (3.8%)	142 (1.7%)
Duration [min/max][days]	1/3	1/4	1/2
Transport [min/max][Sv]	3.51/6.32	3.63/8.36	5.31/9.45
Number of negative events	246 (4.1%)	129 (1.7%)	255 (3.6%)
Duration [min/max][days]	1/6	1/3	1/4
Transport [min/max][Sv]	−6.54/−1.94	−4.92/−1.00	−6.53/−1.11

Number of extreme events (days) and percent (relative to the total number of model days). Transports in Sv.

offshore transport during the extreme export events is spatially more uniformly distributed. During the average positive T_{Cross} export event (T_{Cross} mean of 6.08 Sv), 4.27% of the total volume of shelf waters between 30 and 40°S is exported to the open ocean.

The monthly distribution of the number of negative extreme events is shown in **Figure 9B**. Negative (northward) extreme T_N events are more frequent in June–July and uncommon in summer, last <6 days, and reach −6.54 Sv. Negative (southward) extreme T_S events occur more frequently between August and October and infrequently in summer, last <3 days, and reach transports of up to −4.92 Sv. The occurrence of negative extreme T_{Cross} events is maximum during winter and minimum during summer. The extreme cross-shore transport events have a short duration (between 1 and 4 days) and the maximum onshore transport reaches −6.53 Sv. During these negative cross-shore transport events the BMC sector continues to be an export location with offshore transports of shelf waters of 0.48 ± 0.64 Sv (**Table 3**). Therefore, the on-shelf intrusion of open ocean water is distributed over the remaining of the shelf break domain (**Figure 5B**), including S4. These negative extreme events represent on average 1.79% of the total shelf volume between 30 and 40°S.

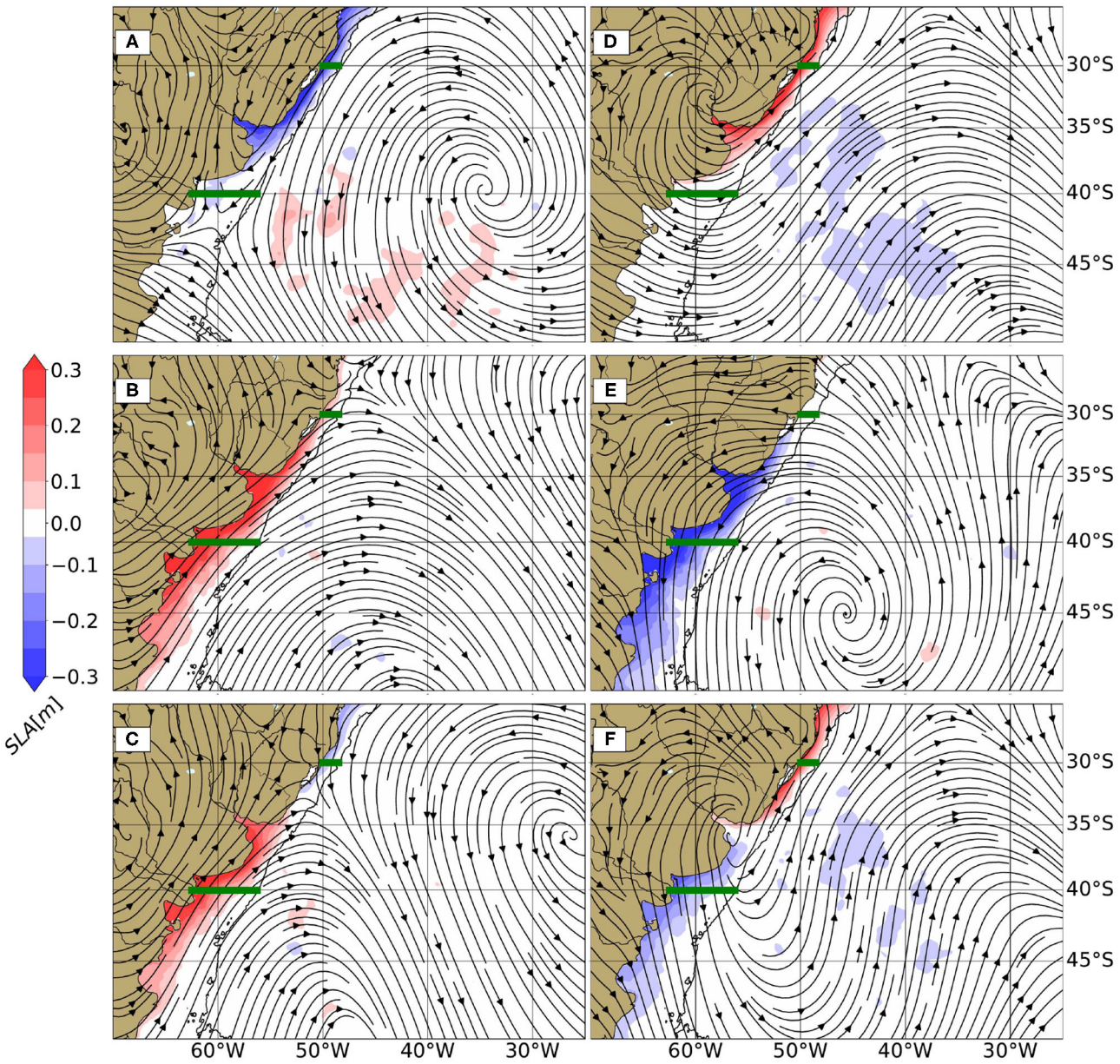

FIGURE 10 | Composite of model derived sea level anomaly (background color shading) and black streamlines show surface wind patterns during positive **(A)** and negative **(D)** extreme T_N events. **(B)** and **(E)**, same as **(A,D)** for T_S. **(C)** and **(F)**, same as **(A,D)** for T_{Cross}. The 200 m isobath is indicated by a gray line.

The extreme events have a typical duration in the weekly time scale. As discussed in section 3.2.2.1, the variability on this scale is mostly driven by the local alongshore wind stress. Therefore, it is useful to further explore the possible association between variations in regional wind patterns and extreme transport events. Recall that southwesterly wind stress is referred to as positive and northeasterly wind stress as negative. A composite (average fields during extreme events) of positive T_N extreme events is characterized by negative (northeasterly) local alongshore wind stress ($\sim -0.27\ N.m^{-2}$) at 30°S associated with a high atmospheric pressure center located near 40°S–35°W (**Figure 10A**). Consequently, a negative SLA develops along the coast, which is most intense north of the RDP estuary. The resulting cross-shore pressure gradient leads to a southwestward geostrophic flow north of 38°S. The negative SLA and the associated geostrophic flow weaken near the southern boundary. The negative T_N extreme events are characterized by positive local alongshore wind stress ($\sim 0.16\ N.m^{-2}$) at 30°S, associated with a high atmosphere pressure center located near 32.5°S–59.5°W (**Figure 10D**). Consequently, a positive SLA develops along the coast north of 38°S, which leads to a northeastward geostrophic flow at 30°S.

The positive extreme events in T_S are associated with positive (southwesterly) local alongshore wind stress ($\sim$0.21 $N.m^{-2}$) at 40°S, associated with a low atmospheric pressure center located south of 50°S (**Figure 10B**), that generates southwesterly wind stress over the continental shelf south of 30°S. This intense wind stress creates a positive SLA along the coast in the entire domain, which leads to a relatively strong northeastward geostrophic flow at 40°S. This northeastward flow extends northeastward, also leading to northeastward (negative) flow across the northern boundary. Conversely, negative T_S extreme events are associated with negative (northeasterly) local alongshore wind stress at 40°S (~-0.13 $N.m^{-2}$) associated with a high atmospheric pressure center located at 45°S–47.5°W (**Figure 10E**). In response to this wind stress pattern, there is a negative inner shelf SLA south of 30°S and an associated southwestward flow across the southern boundary (**Figure 10E**).

The positive T_{Cross} extreme events are characterized by southwesterly wind stress at 40°S ($\sim$0.22 $N.m^{-2}$) and northeasterly wind stress at 30°S (~-0.08 $N.m^{-2}$). A low atmospheric pressure center located near 50°S–50°W (**Figure 10C**) generates southwesterly wind stress over the continental shelf south of 40°S and a positive SLA along the coast south of 34°. Thus, this atmospheric circulation pattern leads to relatively intense northeastward transport (4.03 $\pm$ 1.69 Sv, **Table 3**) over the shelf across the southern boundary (T_S, 40°S). Conversely, a high atmospheric pressure center located near 35°S–28°W generates northeasterly wind stress over the continental shelf north of 30°S. In response to this wind stress pattern, a weak negative SLA develops in the inner shelf north of 33°S, this negative anomaly leads to southwestward transport (2.02 $\pm$ 1.57 Sv, **Table 3**) over the shelf across the northern boundary (T_N, 30°S). The resulting mass convergence over the shelf between 30 and 40°S is compensated by a strong offshore flow of shelf waters. The negative extreme events of T_{Cross} are associated with a high atmospheric pressure center located over the RDP (**Figure 10F**). This feature leads to northwesterly wind stress at 40°S (~-0.04 $N.m^{-2}$) that generates a negative SLA over the coast south of the RDP and southwesterly wind stress at 30°S ($\sim$0.14 $N.m^{-2}$) that generates a positive SLA north of RDP. As a result, a weakening of northeastward flow across the southern boundary (T_S, 0.14 $\pm$ 1.28 Sv) and a northeastward transport across the northern boundary are observed (T_N, -2.16 $\pm$ 1.42 Sv). Analogous to the positive extreme events, the mass divergence over the shelf between 30 and 40°S is compensated by an influx of deep-ocean waters to the shelf. These import events can have an important biogeochemical impact on the shelf.

Intense Malvinas Current intrusions over the shelf, causing substantial cooling, increased salinity, and elevated surface chlorophyll concentrations have been reported near 41°S (Piola et al., 2010). A recent analysis of *in-situ* observations collected in late April 2016 between 34 and 38°S presents relatively cold, salty, and high-nutrient waters in the outer shelf near 36.5°S (Manta et al., 2022, their **Figures 2C,F**, **5C**). These observations suggest onshore flow of subantarctic water from the Malvinas Current. Our model analysis indicates that T_{Cross} reached -2.55 Sv in the previous days. About 30% of this inflow occurred across the BMC (T_{BMC} ~-0.81 Sv). As might be expected, on average T_{BMC} is positive and peaks in the BMC sector of the shelf-break (**Supplementary Figure 4**). However, there are a few instances (about 2.20% of the time) when T_{BMC} is negative (onshore), as observed in late April 2016. In the model, the relatively intense import of slope waters was associated with northeastward flows of -4.09 Sv across 30°S and 1.54 Sv across 40°S, which peaked on 27 April 2016. Thus, the model circulation is consistent with the observation of subantarctic waters in the outer shelf south of the BMC reported by Manta et al. (2022). Moreover, the model results suggest that the onshelf flow observed in late April 2016 between 30 and 40° was a response to divergence of the along-shore circulation, which was mostly driven by the pattern of alongshore winds. However, in agreement with the observations of Manta et al. (2022), mesoscale eddies that approach the outer shelf may create a fine scale structure of relatively intense cross-shore flows (see **Supplementary Figure 5**). In addition, highly non-linear submesoscale features of characteristic scale <10 km, not resolved by the GLORYS reanalysis, are ubiquitous in the Brazil/Malvinas Confluence (Orúe-Echevarría et al., 2019), and may further contribute to cross-shelf exchanges.

3.3.1. The T_{Cross} Event of Early May 2015

From 29 April to 3 May 2015 the model produces large transport anomalies across 40°S. This event is of interest because it was also clearly detected by direct current observations close to 40°S (see section 3.1.3 and Lago et al., 2019, 2021). On 29 April 2015, the circulation is characteristic of an extreme negative T_S event, with northeasterly wind stress (**Figure 11A**) generating a negative inner shelf SLA associated with southwestward flow over the shelf south of 33°S (**Figure 11C**). At that time the flow over much of the shelf is southward, reaching -1.82 Sv across 40°S and +0.8 Sv across 30°S. Recall that we have defined southward flow at 30°S as positive. In response to the divergence of the alongshore circulation, T_{Cross} presents a negative (onshore) transport (-1.03 Sv) (**Table 3**). The flow structure indicates intrusions of slope waters: relatively cold-salty waters from the MC south of 37°S and warm-salty waters from the BC near 31°S (**Figure 11B**). On 3 May, the circulation has evolved to one that is characteristic of extreme offshore transport events with T_{Cross} reaching 8.80 Sv (**Table 3**). This very large export of relatively fresh shelf waters (**Figure 11E**) is mediated by strong convergence of the alongshore circulation over the shelf (**Figure 11F**). At that time the flow across 40°S reverses to northward, with T_S reaching 5.36 Sv in response to a positive SLA over the inner shelf generated by local southwesterly/westerly wind stress (**Figure 11D**). In contrast, the flow at 30°S is still southwestward (positive), with T_N reaching 3.44 Sv, in response to a negative SLA over the inner shelf which in turn results from local northeasterly wind stress at that location. Shelf water export during extreme events does not necessarily follow the most frequently observed pathways across the BMC and S4 segments, it occurs across most of the shelf break, with a maximum export occurring between 32 and 36.5°S.

4. SUMMARY AND CONCLUSIONS

The variability and drivers of the cross-shelf exchanges between the Southwestern Atlantic shelf between 30 and 40°S and the open ocean have been analyzed using a high-resolution

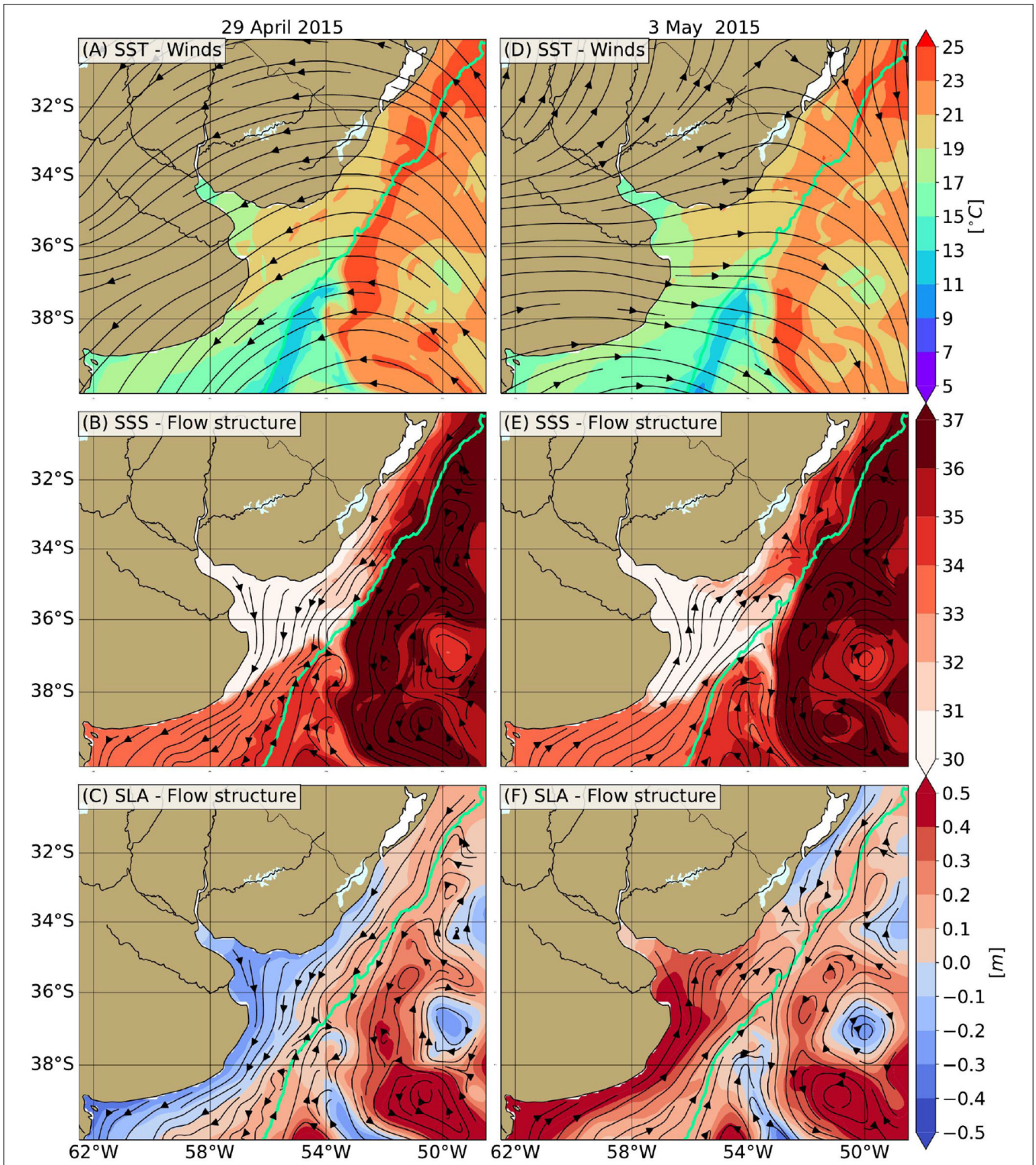

FIGURE 11 | SST (°C, **A,D**), SSS **(B,E)**, SLA (m, **C,F**) are shown in colors (color scale at right). Black streamlines show the flow structure over the upper 200 m **(B,C,E,F)** and surface wind patterns from ERA5 **(A,D)**. The left panels **(A–C)** present the fields on 29 April 2015 and the right panels **(D–F)** on 3 May 2015. The 200 m isobath is indicated by a green line.

ocean reanalysis. Independent hydrographic data from 12 oceanographic surveys carried out on the shelf near 34°S between 2003 and 2018, 24 years of gridded altimetry data (note that GLORYS12V1 assimilates along-track altimetry), and an independent estimate of alongshore transport near 39°S based on mooring data were used to evaluate the model performance. There is a substantial agreement near 39°S between daily alongshore shelf transports from observations and the model. The model also shows similar patterns of SLA variability to the altimetry derived data, although with somewhat larger differences over the Río de la Plata. The relatively low spatial and temporal resolution of the gridded altimetric product does not allow the representation of mesoscale, high-frequency processes (3–10 day periods) which are generated by the model's internal dynamics. In addition, the model presents an overall good agreement with geostrophic velocities calculated from the hydrographic data over the shelf near 34°S.

Once the reanalysis performance was assessed, we analyzed the cross-shore transport and its temporal and spatial variability. The record length mean cross-shore transport [mean ± standard deviation] between 30 and 40°S (T_{Cross}) is 2.09 ± 1.60 Sv, with positive transport representing offshore flow. Sixty-three percent of the mean T_{Cross} was contributed by northward transport across 40°S (T_S) and the remaining 37% by southward transport across 30°S (T_N). Most of the offshore flow (73%) occurs in the vicinity of the BMC and about 20% in the vicinity of 32°S. T_{Cross} presents more variability at high frequencies, 71.9 and 22.5% of energy in the weekly and subannual scales, respectively than at low frequencies, 4.9 and 0.7% of energy in the seasonal and interannual scales, respectively.

At the interannual scale, the cross-shore transport variability (T_{Cross}) is more controlled by the alongshore transport over the shelf across 40°S (T_S, 51%) than across 30°S (T_N, 40%) and T_S is moderately modulated by the intensity of the Malvinas Current. At the annual scale, there is high spectral energy in all transports. In the mean, T_N and T_S are positive throughout the year. T_N presents a maximum (southwestward) transport in October and a minimum from April to July while T_S has the opposite behavior, though with somewhat weaker amplitude. Consequently, T_{Cross} is positive (offshore) throughout the year, and presents a maximum in January and a minimum in June. The alongshore transports over the shelf are driven by local alongshore wind stress. T_{Cross} variability is mostly driven by T_N variability. At the subannual scale, T_N and T_S are driven by the local alongshore wind stress and T_{Cross}, particularly near 32°S, is primarily controlled by T_N. At the weekly time scale, both T_N and T_S are also strongly modulated by the local alongshore wind stress. T_S has control over the export of shelf waters across the BMC, while T_N is more closely associated with cross-shore fluxes at 32°S.

Extreme alongshore transport events across 30 and 40°S have been analyzed using the model's daily output. These events are closely associated with local wind stress with a duration of <6 and 4 days, respectively. During positive events, defined as convergence of alongshore flow over the shelf, transports reach 6 and 8 times their long-term averages, respectively. Extreme offshore transport events reach up to 9.45 Sv. These high export events last <2 days and are more frequent during fall and spring. Despite the short duration of intense export events, 4.3% of the total volume of shelf water between 30 and 40°S is exported to the adjacent deep ocean during the average event (6.05 Sv). These large exports of shelf waters must lead to freshening of upper ocean waters as revealed by *in-situ* and satellite observations. In contrast, negative extreme events drive open ocean water intrusions of up to 6.53 Sv. These onshore flow events last <4 days and are more frequent in winter. During the average onshore flow event, 1.8% of the total volume of shelf water is replaced by slope water. The inflows of open ocean waters, particularly those of salty subtropical waters from the Brazil Current, must cause a substantial salinification of outer shelf waters and those from the Malvinas Currents contribute with nutrients.

Alongshore winds over the shelf generate SLAs over the inner shelf. The associated cross-shore pressure gradient leads to alongshore geostrophic flows. Southwesterly winds over the southern boundary (40°S) drive a positive SLA on the inner shelf and northeasterly winds over the northern boundary (30°S) generate a negative SLA on the inner shelf. The resulting cross-shore pressure gradients drive convergent alongshore geostrophic flows over the shelf and export of shelf waters to the open ocean. Conversely, opposite winds generate divergent alongshore geostrophic flows over the shelf and drive the import of slope water to the shelf. These SLA variations on the inner shelf, mostly controlled by alongshore wind variations, exert an important control on alongshore circulation, and cross-shelf exchange, on seasonal, subannual, and weekly scales and also on the extreme events.

DATA AVAILABILITY STATEMENT

Publicly available datasets were analyzed in this study. These data can be found at: GLORYS12V1 ocean reanalysis (https://resources.marine.copernicus.eu/documents/QUID/CMEMS-GLO-QUID-001-030.pdf); ERA5 atmospheric reanalysis (https://www.ecmwf.int/en/forecasts/datasets/reanalysis-datasets/era5); and altimetry data from Copernicus Marine https://resources.marine.copernicus.eu/product-detail/SEALEVEL_GLO_PHY_L4_MY_008_047/INFORMATION). *In situ* data located near 39° used to evaluate the model performance can be found in public SE-ANOE public data repository at: https://www.seanoe.org/data/00403/51492/ and https://www.seanoe.org/recordview. Hydrographic data near 34° used to evaluate the model performance can be found in public data repository at ftp://ftp.aoml.noaa.gov/phod/pub/SAM/hydrographic_data/, in this in-text data citation references: Charo et al. (2020).

AUTHOR CONTRIBUTIONS

GB processed the hydrographic and the model data and did the model performance evaluation and the transport calculations and prepared the manuscript with contributions from all co-authors. All authors participated in the scientific interpretation of the results. All authors contributed to the article and approved the submitted version.

FUNDING

This work was partially funded by the Inter-American Institute for Global Change Research (IAI) grants CRN3070 (US National Science Foundation grant GEO-1128040) and SGP-HW 017. Additional funding was provided by IAI/CONICET grant RD3347, FONCYT grant PICT2016-0557, and SECYT-UNS grant 24-F079.

ACKNOWLEDGMENTS

GB was supported by a doctoral fellowship from Consejo Nacional de Investigaciones Científicas y Técnicas (Argentina). The hydrographic data were collected as part of the South Atlantic Meridional Overturning Circulation initiative (https://www.aoml.noaa.gov/phod/SAMOC_international/). We thank the science parties and crews of the NICOP/Plata, SAM, and STSF cruises that collected the data in the Albardão transect. We particularly thank Marcela Charo (SHN, Argentina) for data calibration and processing and Loreley Lago (CIMA, Argentina) for providing the observational transport time series shown in **Figure 4**.

SUPPLEMENTARY MATERIAL

The Supplementary Material for this article can be found online at: https://www.frontiersin.org/articles/10.3389/fmars.2022.855183/full#supplementary-material

REFERENCES

Ballarotta, M., Ubelmann, C., Pujol, M.-I., Taburet, G., Fournier, F., Legeais, J.-F., et al. (2019). On the resolutions of ocean altimetry maps. *Ocean Sci.* 15, 1091–1109. doi: 10.5194/os-15-1091-2019

Berden, G., Charo, M., Möller O. O. Jr, and Piola, A. R. (2020). Circulation and hydrography in the western south Atlantic shelf and export to the deep adjacent ocean: 30°S to 40°S. *J. Geophys. Res.* 125, e2020JC016500. doi: 10.1029/2020JC016500

Bordin, L. H., Machado, E. d. C., Carvalho, M., Freire, A. S., and Fonseca, A. L. (2019). Nutrient and carbon dynamics under the water mass seasonality on the continental shelf at the South Brazil Bight. *J. Mar. Syst.* 189, 22–35. doi: 10.1016/j.jmarsys.2018.09.006

Borús, J., Uriburu Quirno, M., and Calvo, D. (2017). *Evaluación de Caudales Mensuales Descargados por los Grandes ríos del Sistema del Plata al Estuario del Río de la Plata*. Ezeiza: Alerta Hidrológico-Instituto Nacional del Agua y el Ambiente.

Braga, E. S., Chiozzini, V. C., Berbel, G. B., Maluf, J. C., Aguiar, V. M., Charo, M., et al. (2008). Nutrient distributions over the Southwestern South Atlantic continental shelf from Mar del Plata (Argentina) to Itajaí(Brazil): winter-summer aspects. *Contin. Shelf Res.* 28, 1649–1661. doi: 10.1016/j.csr.2007.06.018

Brink, K. (1991). Coastal-trapped waves and wind-driven currents over the continental shelf. *Annu. Rev. Fluid Mech.* 23, 389–412. doi: 10.1146/annurev.fl.23.010191.002133

Cabanes, C., Grouazel, A., von Schuckmann, K., Hamon, M., Turpin, V., Coatanoan, C., et al. (2013). The CORA dataset: validation and diagnostics of *in-situ* ocean temperature and salinity measurements. *Ocean Sci.* 9, 1–18. doi: 10.5194/os-9-1-2013

Charo, M., Guerrero, R., and Piola, A. (2020). *Subtropical Shelf Front cruise-Conductivity-Temperature-Depth (CTD) Data*. Harvard Dataverse.

Chen, C.-T. A., Liu, K.-K., and Macdonald, R. (2003). "Continental margin exchanges," in *Ocean Biogeochemistry*, Fasham MJR, editor (Berlin: Springer), 53–97. doi: 10.1007/978-3-642-55844-3_4

Chidichimo, M., Piola, A., Meinen, C., Perez, R., Campos, E., Dong, S., et al. (2021). Brazil current volume transport variability during 2009-2015 from a long-term moored array at 34.5°S. *J. Geophys. Res.* 126, e2020JC017146. doi: 10.1029/2020JC017146

Christensen, J. P., Murray, J. W., Devol, A. H., and Codispoti, L. A. (1987). Denitrification in continental shelf sediments has major impact on the oceanic nitrogen budget. *Glob. Biogeochem. Cycles* 1, 97–116. doi: 10.1029/GB001i002p00097

Ciotti, Á. M., Odebrecht, C., Fillmann, G., and Moller O. O. Jr (1995). Freshwater outflow and Subtropical Convergence influence on phytoplankton biomass on the southern Brazilian continental shelf. *Cont. Shelf Res.* 15, 1737–1756. doi: 10.1016/0278-4343(94)00091-Z

Combes, V., and Matano, R. P. (2014a). Trends in the Brazil/Malvinas confluence region. *Geophys. Res. Lett.* 41, 8971–8977. doi: 10.1002/2014GL062523

Combes, V., and Matano, R. P. (2014b). A two-way nested simulation of the oceanic circulation in the southwestern Atlantic. *J. Geophys. Res.* 119, 731–756. doi: 10.1002/2013JC009498

Combes, V., and Matano, R. P. (2018). The Patagonian shelf circulation: drivers and variability. *Prog. Oceanogr.* 167, 24–43. doi: 10.1016/j.pocean.2018.07.003

Combes, V., Matano, R. P., and Palma, E. D. (2021). Circulation and cross-shelf exchanges in the northern shelf region of the southwestern Atlantic: kinematics. *J. Geophys. Res.* 126, e2020JC016959. doi: 10.1029/2020JC016959

de Freitas, P. P., de Moraes Paiva, A., Cirano, M., Mill, G. N., da Costa, V. S., Gabioux, M., et al. (2021). Coastal trapped waves propagation along the southwestern Atlantic continental shelf. *Cont. Shelf Res.* 226, 104496. doi: 10.1016/j.csr.2021.104496

de Haas, H., van Weering, T. C., and de Stigter, H. (2002). Organic carbon in shelf seas: sinks or sources, processes and products. *Cont. Shelf Res.* 22, 691–717. doi: 10.1016/S0278-4343(01)00093-0

Franco, B. C., Palma, E. D., Combes, V., Acha, E. M., and Saraceno, M. (2018). Modeling the offshore export of Subantarctic Shelf Waters from the Patagonian shelf. *J. Geophys. Res.* 123, 4491–4502. doi: 10.1029/2018JC013824

Franco, B. C., Palma, E. D., Combes, V., and Lasta, M. L. (2017). Physical processes controlling passive larval transport at the Patagonian Shelf Break Front. *J. Sea Res.* 124, 17–25. doi: 10.1016/j.seares.2017.04.012

Gattuso, J.-P., Frankignoulle, M., and Wollast, R. (1998). Carbon and carbonate metabolism in coastal aquatic ecosystems. *Annu. Rev. Ecol. Syst.* 29, 405–434. doi: 10.1146/annurev.ecolsys.29.1.405

Goni, G. J., and Wainer, I. (2001). Investigation of the Brazil Current front variability from altimeter data. *J. Geophys. Res.* 106, 31117–31128. doi: 10.1029/2000JC000396

Gordon, A. L., and Greengrove, C. L. (1986). Geostrophic circulation of the Brazil-Falkland confluence. *Deep Sea Res. Part A.Oceanogr.* 33, 573–585. doi: 10.1016/0198-0149(86)90054-3

Guerrero, R. A., Piola, A. R., Fenco, H., Matano, R. P., Combes, V., Chao, Y., et al. (2014). The salinity signature of the cross-shelf exchanges in the Southwestern Atlantic Ocean: satellite observations. *J. Geophys. Res.* 119, 7794–7810. doi: 10.1002/2014JC010113

Hersbach, H., Bell, B., Berrisford, P., Hirahara, S., Horányi, A., Mu noz-Sabater, J., et al. (2020). The era5 global reanalysis. *Q. J. R. Meteorol. Soc.* 146, 1999–2049. doi: 10.1002/qj.3803

Hirschi, J. J., Killworth, P. D., and Blundell, J. R. (2007). Subannual, seasonal, and interannual variability of the North Atlantic meridional overturning circulation. *J. Phys. Oceanogr.* 37, 1246–1265. doi: 10.1175/JPO3049.1

Lago, L. S., Saraceno, M., Martos, P., Guerrero, R. A., Piola, A. R., Paniagua, G. F., et al. (2019). On the wind contribution to the variability of ocean currents over wide continental shelves: a case study on the northern Argentine continental shelf. *J. Geophys. Res.* 124, 7457–7472. doi: 10.1029/2019JC015105

Lago, L. S., Saraceno, M., Piola, A. R., and Ruiz-Etcheverry, L. A. (2021). Volume transport variability on the northern argentine continental shelf from *in situ* and satellite altimetry data. *J. Geophys. Res.* 126, e2020JC016813. doi: 10.1029/2020JC016813

Lellouche, J.-M., Greiner, E., Le Galloudec, O., Garric, G., Regnier, C., Drevillon, M., et al. (2018). Recent updates to the Copernicus Marine Service global ocean monitoring and forecasting real-time 1/12° high-resolution system. *Ocean Sci.* 14, 1093–1126. doi: 10.5194/os-14-1093-2018

Lumpkin, R., and Garzoli, S. (2011). Interannual to decadal changes in the western South Atlantic's surface circulation. *J. Geophys. Res.* 116, 1–10. doi: 10.1029/2010JC006285

Madec, G., Bourdallé-Badie, R., Bouttier, P.-A., Bricaud, C., Bruciaferri, D., Calvert, D., et al. (2017). *Nemo Ocean Engine. Note du Pôle de Modélisation de l'Institut Pierre-Simon Laplace, No. 27*. Institut Pierre-Simon Laplace.

Malan, N., Archer, M., Roughan, M., Cetina-Heredia, P., Hemming, M., Rocha, C., et al. (2020). Eddy-driven cross-shelf transport in the East Australian Current separation zone. *J. Geophys. Res.* 125, e2019JC015613. doi: 10.1029/2019JC015613

Manta, G., Speich, S., Barreiro, M., Trinchin, R., De Mello, C., Laxenaire, R., et al. (2022). Shelf water export at the brazil-malvinas confluence evidenced from combined *in-situ* and satellite observations. *Front. Marine Sci.* doi: 10.3389/fmars.2022.857594. [In Press].

Matano, R., Palma, E. D., and Piola, A. R. (2010). The influence of the Brazil and Malvinas Currents on the Southwestern Atlantic Shelf circulation. *Ocean Sci.* 6, 983–995. doi: 10.5194/os-6-983-2010

Matano, R. P., Combes, V., Piola, A. R., Guerrero, R., Palma, E. D., Ted Strub, P., et al. (2014). The salinity signature of the cross-shelf exchanges in the Southwestern Atlantic Ocean: numerical simulations. *J. Geophys. Res.* 119, 7949–7968. doi: 10.1002/2014JC010116

Möller, O. O. Jr, Piola, A. R., Freitas, A. C., and Campos, E. J. (2008). The effects of river discharge and seasonal winds on the shelf off southeastern South America. *Cont. Shelf Res.* 28, 1607–1624. doi: 10.1016/j.csr.2008.03.012

Orúe-Echevarría, D., Castellanos, P., Sans, J., Emelianov, M., Vallés-Casanova, I., and Pelegrí, J. L. (2019). Temperature spatiotemporal correlation scales in the Brazil-Malvinas Confluence from high-resolution *in situ* and remote sensing data. *Geophys. Res. Lett.* 46, 13234–13243. doi: 10.1029/2019GL084246

Palma, E., Matano, R., and Piola, A. (2004). A numerical study of the Southwestern Atlantic Shelf circulation: Barotropic response to tidal and wind forcing. *J. Geophys. Res.* 109, C08014. doi: 10.1029/2004JC002315

Palma, E. D., and Matano, R. P. (2009). Disentangling the upwelling mechanisms of the south Brazil bight. *Cont. Shelf Res.* 29, 1525–1534. doi: 10.1016/j.csr.2009.04.002

Piola, A. R., Campos, E. J., Möller, O. O. Jr, Charo, M., and Martinez, C. (2000). Subtropical shelf front off eastern South America. *J. Geophys. Res.* 105, 6565–6578. doi: 10.1029/1999JC000300

Piola, A. R., Martínez Avellaneda, N., Guerrero, R. A., Jardon, F. P., Palma, E. D., and Romero, S. I. (2010). Malvinas-slope water intrusions on the northern Patagonia continental shelf. *Ocean Sci.* 6, 345–359. doi: 10.5194/os-6-345-2010

Piola, A. R., Matano, R. P., Palma, E. D., Moller, O. O., and Campos, E. J. D. (2005). The influence of the Plata River discharge on the western South Atlantic shelf. *Geophys. Res. Lett.* 32, 1–4. doi: 10.1029/2004GL021638

Piola, A. R., Möller, O. O. Jr, Guerrero, R. A., and Campos, E. J. (2008). Variability of the subtropical shelf front off eastern South America: Winter 2003 and summer 2004. *Cont. Shelf Res.* 28, 1639–1648. doi: 10.1016/j.csr.2008.03.013

Piola, A. R., Palma, E. D., Bianchi, A. A., Castro, B. M., Dottori, M., Guerrero, R. A., et al. (2018). "Physical oceanography of the SW Atlantic Shelf: a review," in *Plankton Ecology of the Southwestern Atlantic–From the Subtropical to the Subantarctic Realm*, eds M. Hoffmeyer, M. E. Sabatini, F. Brandini, D. Calliari, and N. Santinelli (Cham: Springer), 37–56. doi: 10.1007/978-3-319-77869-3_2

Pujol, M.-I., Faugére, Y., Taburet, G., Dupuy, S., Pelloquin, C., Ablain, M., et al. (2016). Duacs DT2014: the new multi-mission altimeter data set reprocessed over 20 years. *Ocean Sci.* 12, 1067–1090. doi: 10.5194/os-12-1067-2016

Rabouille, C., Mackenzie, F. T., and Ver, L. M. (2001). Influence of the human perturbation on carbon, nitrogen, and oxygen biogeochemical cycles in the global coastal ocean. *Geochim. Cosmochim. Acta* 65, 3615–3641. doi: 10.1016/S0016-7037(01)00760-8

Reynolds, R. W., Smith, T. M., Liu, C., Chelton, D. B., Casey, K. S., and Schlax, M. G. (2007). Daily high-resolution-blended analyses for sea surface temperature. *J. Clim.* 20, 5473–5496. doi: 10.1175/2007JCLI1824.1

Roughan, M., Macdonald, H. S., Baird, M. E., and Glasby, T. M. (2011). Modelling coastal connectivity in a Western Boundary Current: Seasonal and inter-annual variability. *Deep Sea Res. Part II Top. Stud. Oceanogr.* 58, 628–644. doi: 10.1016/j.dsr2.2010.06.004

Strub, P. T., James, C., Combes, V., Matano, R. P., Piola, A. R., Palma, E. D., et al. (2015). Altimeter-derived seasonal circulation on the Southwest Atlantic shelf: 27° − 43°S. *J. Geophys. Res.* 120, 3391–3418. doi: 10.1002/2015JC010769

Conflict of Interest: The authors declare that the research was conducted in the absence of any commercial or financial relationships that could be construed as a potential conflict of interest.

Publisher's Note: All claims expressed in this article are solely those of the authors and do not necessarily represent those of their affiliated organizations, or those of the publisher, the editors and the reviewers. Any product that may be evaluated in this article, or claim that may be made by its manufacturer, is not guaranteed or endorsed by the publisher.

Copyright © 2022 Berden, Piola and Palma. This is an open-access article distributed under the terms of the Creative Commons Attribution License (CC BY). The use, distribution or reproduction in other forums is permitted, provided the original author(s) and the copyright owner(s) are credited and that the original publication in this journal is cited, in accordance with accepted academic practice. No use, distribution or reproduction is permitted which does not comply with these terms.

frontiers in Marine Science

ORIGINAL RESEARCH
published: 16 March 2022
doi: 10.3389/fmars.2022.835656

Wind-Controlled Transport of Saltwater in the Southeastern Baltic Sea: A Model Study

Victor Zhurbas[1] *and Germo Väli*[2]*

[1] Shirshov Institute of Oceanology, Russian Academy of Sciences, Moscow, Russia, [2] Department of Marine Systems, Tallinn University of Technology, Tallinn, Estonia

We hypothesized that the saltwater transport in a system of the southeastern Baltic basins including the Gdańsk and Gotland deeps connected by the Hoburg Channel, is greatly controlled by wind forcing, which has a clear physical explanation. Namely, the westerly winds develop the Ekman transport in the upper layer to the south from the Gotland Deep to the Gdańsk Deep which causes a compensatory saltwater countercurrent in the deep layer to the north from the Gdańsk Deep toward the Gotland Deep, and, vice versa, the easterly winds develop the Ekman transport to the north from the Gdańsk Deep toward the Gotland Deep causing a compensatory saltwater countercurrent in the deep layer to the south from the Gotland Deep to the Gdańsk Deep. To confirm the hypothesis, results of numerical modeling of the Baltic Sea circulation for a 10-year period (2010–2019) are applied. The daily saltwater transport to the northeast through a cross-section of the Hoburg Channel is found to be highly correlated with the wind stress component toward southeast (the correlation coefficient is 0.812) which can be considered as a straightforward confirmation of the hypothesis indicating the strong wind-driven circulation also in the deep layers of the Baltic Sea. Estimates of the daily saltwater transport through the above-mentioned and several other cross-sections of the southeastern Baltic Sea basins confirm a rule stating that the maximum correlation takes place between the saltwater transport and a wind stress component directed perpendicularly to the right relative to the direction of saltwater transport.

Keywords: Baltic Sea, wind-controlled saltwater transport, Ekman transport, compensatory flow, numerical modeling, GETM

OPEN ACCESS

Edited by:
William Savidge, University of Georgia, United States

Reviewed by:
Terry Whitledge, Retired, Fairbanks, Alaska, United States
Laura Tuomi, Finnish Meteorological Institute, Finland
Heiner Dietze, GEOMAR Helmholtz Center for Ocean Research Kiel, Helmholtz Association of German Research Centres (HZ), Germany

***Correspondence:**
Germo Väli
germo.vali@taltech.ee

Specialty section:
This article was submitted to Coastal Ocean Processes, a section of the journal Frontiers in Marine Science

Received: *14 December 2021*
Accepted: *24 February 2022*
Published: *16 March 2022*

Citation:
Zhurbas V and Väli G (2022) Wind-Controlled Transport of Saltwater in the Southeastern Baltic Sea: A Model Study. Front. Mar. Sci. 9:835656. doi: 10.3389/fmars.2022.835656

INTRODUCTION

The Baltic Sea is a semi-enclosed sea, the water exchange of which with the North Sea of the Atlantic Ocean is hampered by the presence of quite narrow and shallow straits—the Great and Little Belts and Öresund. The water balance of the Baltic Sea is made up of the inflow of saline water from the North Sea and the outflow of freshened water back, formed by mixing the incoming saline water with freshwater river runoff and precipitation. An overturning water-mass circulation in the Baltic Sea created in this way is referred to as the Baltic haline conveyor belt (Döös et al., 2004). As a result, the deep layer of the Baltic Sea below approx. 40–70 m depth is filled with saline water constituting

permanent halocline, and the only way to effectively ventilate it is by the lateral replacement with newly inflowing oxygenated saline water of the North Sea origin which is vital for the ecosystem functioning. Ventilation of the deepest layers of the Baltic Sea takes place only with very strong barotropic inflows called the Major Baltic Inflows (MBIs) which are quite rare and irregular (e.g., Matthäus and Frank, 1992; Mohrholz, 2018).

In fact, the Baltic Proper is a chain of basins connected by straits, and the depth of the basins and straits basically increases eastward and northward with distance from the transit area with the North Sea. The saline water of the North Sea origin spreads along the chain of basins and straits in the form of a bottom gravity current. An important link in this chain of basins is the Słupsk Furrow (SF), an elongated, channel-like topographic constriction between the Bornholm Basin in the west and the Eastern Gotland/Gdańsk basins in the east (**Figure 1**). The SF is the only pathway for saltwater of the North Sea origin to enter the deep basins of the eastern and northern Baltic Proper.

Keeping in mind the bottom topography (see **Figure 1**), the saltwater, leaving SF for the east, supposedly has two options to go. First, it can turn to the southeast toward the Gdańsk Basin and then, having made a cyclonic loop, rush north to the Gotland Deep through the Hoburg Channel. Second, it can turn to the northeast to rush directly to the Hoburg Channel and further enter the Gotland Deep. Which route is actually implemented is largely determined by dynamic processes in the bottom gravity currents. The first route (to the southeast to the Gdańsk Deep) is supported by the presence of a geostrophic balance of forces in the direction transverse to the gravitational current (e.g., Borenäs et al., 2007). Indeed, due to the geostrophic balance, the salty and dense water will flow eastward along the southern slope of SF and, after leaving it, will have to turn southeast and rush to the Gdańsk Deep along the southwestern slope of the basin. The second route (to the northeast directly to the Hoburg Channel and further to the Gotland Deep) is supposedly supported by a secondary circulation formed in a gravity current passing through a rotating channel (Johnson and Sanford, 1992). Namely, the Ekman transport to the north is formed in the bottom boundary layer beneath the eastward-flowing gravity current which moves the densest and saltiest water to the northern slope of SF (Zhurbas et al., 2012). As a result, the densest and saltiest water leaving SF gets a chance (at least a speculative one) to rush northeast directly to the Hoburg Channel.

In addition to the gravity current dynamics, the saltwater transport in the Baltic Sea is greatly influenced by the wind forcing. Numerical modeling of circulation in the Baltic Sea shows that the northerly and easterly winds promote transport of saltwater to the east in the lower layer of SF (Krauss and Brügge, 1991; Zhurbas et al., 2010, 2012). And vice versa, the southerly and westerly winds, promote a compensatory flow to the west in the lower layer of SF which weaken the eastward transport of saltwater, and, given a sufficiently strong southerly / westerly wind, can completely block it (Zhurbas et al., 2012).

Krauss and Brügge (1991) explained the above-mentioned feature of the wind-controlled saltwater transport through SF by a reasoning that the dominant wind-produced circulation is characterized by coastal jets in the wind direction and countercurrents in the central region, deflected by bottom topography. The water exchange between Bornholm and Eastern Gotland / Gdańsk basins occurs through SF, which is close to the center of the Baltic Sea at this longitude. Accordingly, bottom currents opposite to the wind direction prevail, which can explain the saltwater transport in SF to the east at easterly winds but cannot at northerly winds. However, in addition to the Krauss and Brügge (1991) explanation, one can hypothesize that the saltwater transport in SF to the east at northerly winds is caused by the wind-driven Ekman transport to the west in the upper layer which develops compensatory countercurrents in the lower layer.

Keeping in mind an analogy between the bottom topography configurations of the Bornholm Basin—SF—deep basins east of SF and the Gdańsk Deep—Hoburg Channel—Gotland Deep, one would expect that the easterly winds will contribute to the transport of saltwater coming from the SF to the southeast toward the Gdańsk Deep, and, vice versa, the westerly winds to the northeast toward the Hoburg Channel and Gotland Deep.

The objective of this study is to investigate the saltwater exchange between the basins of the southeastern Baltic Sea, including the Słupsk Furow, the Gdańsk Deep, the Hoburg Channel, and the Gotland Deep, depending on wind forcing based on multi-year numerical simulations and decide which effect, the wind-driven coastal jets or wind-driven Ekman transport in the open sea, prevails.

MATERIALS AND METHODS

Model Setup and Validation

The General Estuarine Transport Model (GETM; Burchard and Bolding, 2002) is applied to simulate thermohaline fields, salinity, currents, and overall dynamics in the southeastern Baltic Sea. GETM is a primitive equation, 3-dimensional, free surface, hydrostatic model with the embedded vertically adaptive coordinate scheme (Hofmeister et al., 2010; Gräwe et al., 2015; Klingbeil et al., 2018). The vertical mixing is parameterized by two equation k-ε turbulence model coupled with an algebraic second-moment closure (Burchard and Bolding, 2001; Canuto et al., 2001), and the implementation of the turbulence model is performed via General Ocean Turbulence Model (GOTM) (Umlauf and Burchard, 2005).

The model domain includes the entire Baltic Sea with an open boundary in the Kattegat (see **Figure 1A**) and has the horizontal grid spacing of 0.5 nautical miles (926 m) and 60 adaptive layers in the vertical direction. The digital topography of the Baltic Sea is obtained from the Baltic Sea Bathymetry Database.[1] The model run is started from 1 April 2010 with initial thermohaline conditions taken from the Baltic Sea reanalysis for the 1989–2015 by the Copernicus Marine service. The atmospheric forcing is adopted from HIRLAM (High Resolution Limited Area Model) version maintained by the Estonian Weather Service with the spatial resolution of 11 km (Männik and Merilain, 2007). For the lateral boundary conditions, time-series of observed sea

[1] http://data.bshc.pro/

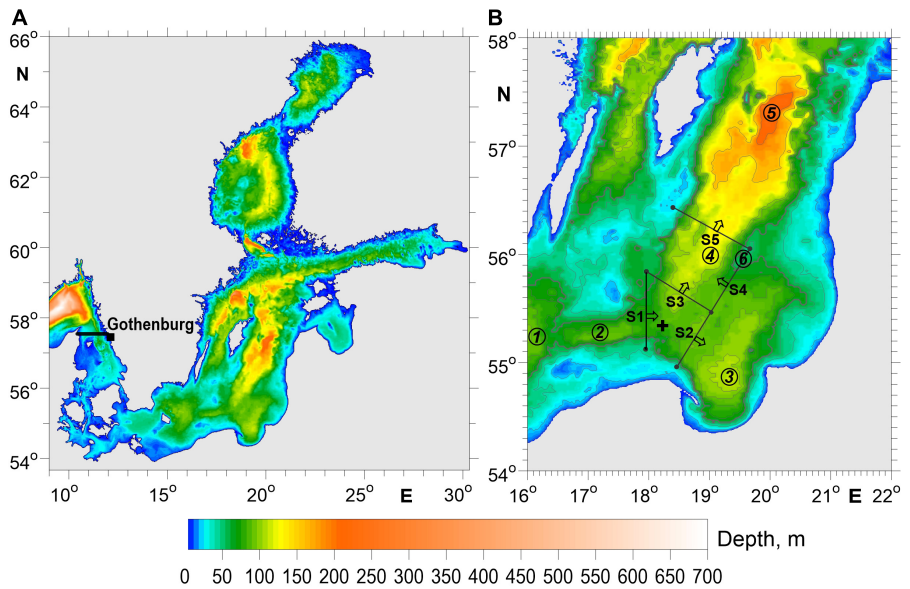

FIGURE 1 | (A) Bathymetric map of the Baltic Sea. The model domain has an open boundary close to Gothenburg (the bold black line). **(B)** Close-up of the southeastern Baltic Sea. The encircled numbers *1–6* point at the Bornholm Basin (*1*), the Słupsk Furrow (*2*), the Gdańsk Basin (*3*), the Hoburg Channel (*4*), the Gotland Deep (*5*), and the Klaipeda Bank (6). The black lines labeled S1–S5 are the locations of 5 cross-sections through which the saltwater transport is calculated. The arrows at the cross-sections show the direction corresponding to the positive value of the saltwater transport. The black cross points at the location of the IOW monitoring station TF0256.

surface height from Gothenburg Torshamnen coastal station and climatological profiles of temperature and salinity (Janssen et al., 1999) along the transect between Denmark and Sweden are used. More detailed information about the model setup is available in Zhurbas et al. (2018) and Liblik et al. (2020).

The model has been thoroughly tested by means of comparison of the simulated and observed current velocity variance and time series of sea-level fluctuations, temperature and salinity in the surface and bottom layers for a number of monitoring stations of the Baltic Sea including those of Bornholm and Gotland deeps (see Zhurbas et al., 2018 for details). Since this study is focused on the salt water transport in a transit area between the Bornholm, Gdańsk, and Gotland deeps where the salinity values in the permanent halocline are extremely variable, it seems reasonable to provide a specific, additional validation of the model based on the comparison of the measured and simulated bottom salinities in the area of interest. Time-series of salinity in the bottom and near-surface layers, measured at the IOW monitoring station TF0256 (18.246°E, 55.326°N), seem to be suitable empirical data for this purpose. This station is located at the eastern exit of the Słupsk Furrow where the saltwater pathway forks out into a southeastern branch toward the Gdańsk Deep and a northeastern branch toward the Gotland Deep (see **Figure 1**). Also we use for model validation the *in situ* salinity time-series in the permanent halocline of the Gotland Deep (monitoring station BY15, 100 m depth level). The time-series of salinity measured at TF0256 and BY15 during 10-year period of 2010–2019 show a reasonably good correspondence with the modeled time series in 2010–2017 and some positive bias of the modeled salinity in 2018–2019 (**Figure 2**).

Definition of the Saltwater Transport and Wind Stress

In order to characterize the saltwater transport in the transit area between the Bornholm, Gdańsk, and Gotland deeps, five cross-sections S1–S5 are chosen (see **Figure 1B**). The cross-sections are implied to be basically perpendicular to the sea depth contours while the saltwater flow in the deep / bottom layer follows basically the sea depth contours in view of topographic steering (e.g., Wåhlin, 2002). The cross-section chosen are:

- S1 is a cross cross-section through the SF outlet;
- S2+S4 is a transect from the Cape Rozewie, Poland, to the Klaipeda Bank, which is conditionally considered as the northwest boundary of the Gdańsk Basin;
- S2 is a cross-section through which the saltwater from SF supposedly enters the Gdańsk Basin;
- S3 is a cross-section through which the saltwater from SF supposedly goes directly to the Hoburg Chanel and further to the Gotland Deep;
- S4 is a cross-section through which the saltwater from SF having made a cyclonic loop in the Gdańsk Basin enters the Hoburg Channel;
- S5 is a cross cross-section though the Hoburg Channel.

Before calculating saltwater transport through cross-sections S1–S5, one has to define a salinity threshold dividing the freshened, upper layer water and the saltwater occupying the permanent halocline. Keeping in mind that the surface salinity in the area of interest is not constant but varies considerably (e.g., within 7.0–7.7 PSU for station TF0256 in accordance to

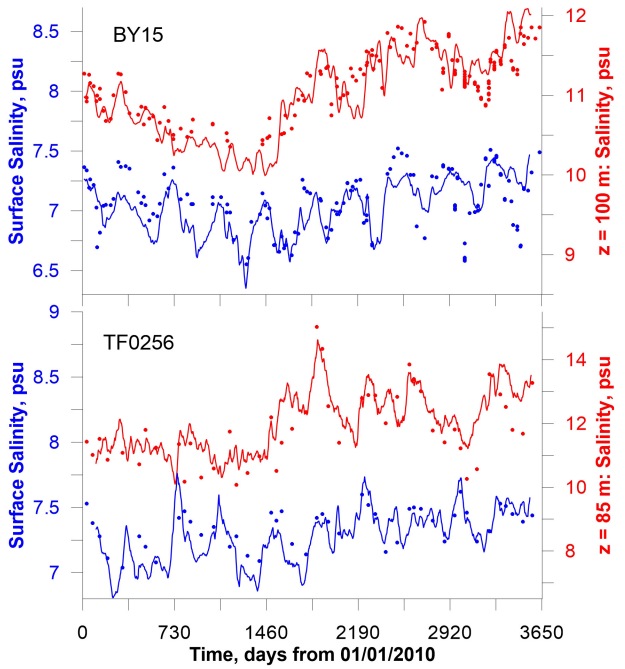

FIGURE 2 | Salinity time series at the sea surface (blue) and the permanent halocline / bottom layer (red) measured in the IOW monitoring station TF0256 (18.236°E, 55.326°N) and monitoring station BY15 in the Gotland Deep (dots) and simulated by the model (lines). The *in situ* data were taken from https://www.io-warnemuende.de/ (last access: 5 July 2021) and the Nest Institute's BED (Baltic Environmental Database) database.

Figure 2), we decided to choose for the salinity threshold not a constant value but a variable value which exceeds the surface salinity $S_{surface}$ by some constant surplus, namely by 1 PSU. Thus, we calculate saltwater transport through cross-section S1 (and similarly for S2–S5) as

$$T_{sal}(t) = \int_{S1}\int_{-H}^{0} S_{ex} u_N dz\, dl,\ S_{ex} = \begin{cases} S \text{ if } S \geq S_{surface} + 1 \\ 0 \text{ if } S < S_{surface} + 1 \end{cases}, \quad (1)$$

where S is salinity, H is the sea depth, dz and dl are increments along the vertical (z) axis and horizontally along the cross-section, respectively, u_N is the horizontal velocity component normal to the cross-section and positive in the direction shown by the arrows in **Figure 1**. Basically T_{sal} was calculated from the model output once a day using daily mean values of u_N, and, therefore, the T_{sal} time-series to be analyzed are the daily values of the saltwater transport.

Keeping in mind the goal to relate saltwater transports with the wind forcing, the proper parameter for the comparison seems to be the wind stress $\boldsymbol{\tau} = (\tau_x, \tau_y)$ rather than wind velocity at 10 m level $\boldsymbol{V}_{10} = (U_{10},\ V_{10})$. Indeed, the Ekman transport in the surface layer, T_E, is expressed as $T_E = |\boldsymbol{\tau}|/(\rho_0 f)$, where ρ_0 is the reference water density and f is the Coriolis parameter, and, therefore, the saltwater, transport being treated as compensatory flow in the bottom layer, is expected to depend linearly on the wind stress value $|\boldsymbol{\tau}|$.

To characterize effect of wind forcing on saltwater transport, the hourly time series of the 10-m level wind velocity from HIRLAM interpolated to the mid-point of cross-sections S1–S5 were used to calculate the wind stress time series as follows:

$$(\tau_x, \tau_y) = \rho_a c_D (U_{10}, V_{10}) |\boldsymbol{V}_{10}|, \quad (2)$$

where $\rho_a = 1.28\ \text{kg}\cdot\text{m}^{-3}$ is the air density and c_D is the drag coefficient which can be found from the empirical formula (Large and Pond, 1981).

$$c_D = 1 \cdot 10^{-3} \begin{cases} 1.14 \text{ at } |\boldsymbol{V}_{10}| < 10\ \text{m}\cdot\text{s}^{-1} \\ 0.49 + 0.065 \cdot |\boldsymbol{V}_{10}| \text{ at } |\boldsymbol{V}_{10}| \geq 10\ \text{m}\cdot\text{s}^{-1} \end{cases}. \quad (3)$$

Further, the arithmetic average of 24 consecutive terms of the hourly series of $\boldsymbol{\tau}$ was found to obtain a time series of daily mean values of the wind stress, $\langle\boldsymbol{\tau}\rangle$.

Note that the GETM model uses a more advanced parameterization of momentum flux through the air-sea interface which is based on a wider set of input parameters including U_{10}, V_{10}, precipitation, sea surface temperature, as well as temperature, pressure and humidity of the air (Kondo, 1975). We prefer to use a simple formulation such as Eq. (2)–(3) because it is easier to implement due to the fact that it is based on wind data alone.

RESULTS

The wind driven Ekman transport in a relatively deep, open sea, $T_E = |\boldsymbol{\tau}|/(\rho_0 f)$, is proportional to the wind stress and directed perpendicularly to the right (in the Northern Hemisphere) from the direction of the wind (and the direction of wind stress defined by Eq. 2–3). Therefore, in order to statistically access the azimuthal distribution and the most probable direction of the Ekman transport, we calculated the distribution of the cumulative wind stress (in percent) for a 10-year period (2010–2019) depending on the wind vector direction (**Figure 3**).

The azimuthal distribution of the wind stress is found to be strongly anisotropic with 45% of the total within a narrow range of the wind velocity vector angle [0°, 60°] (the angle is counted counterclockwise from the east). Therefore, 45% of the total wind-driven Ekman transport in the southeastern Baltic Sea goes to the south-southeast within the angle range [–90°, –30°]. We do not present the distribution of the cumulative wind stress depending on the direction of the wind velocity vector for sections S2–S5, since it is similar to that for section S1 shown in **Figure 3**. This is not surprising, since all sections S1–S5 are located in the open sea at a distance of no more than 100 km, which is not large enough to provide significant differences in long-term wind statistics.

In accordance to our hypothesis presented in the Abstract and Introduction, the saltwater transport though SF is expected to be negatively correlated with the y-component of the wind stress τ_y defined by Eq. (2). This expectation is clearly confirmed by **Figure 4** where a scatter plot of the daily saltwater transport T_{sal} through cross-section S1 vs. the daily mean of the y-component of the normalized wind stress $\langle\tau_y/\rho_0\rangle$ is presented.

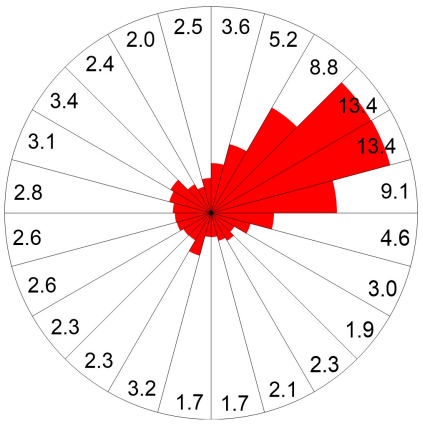

FIGURE 3 | Distribution of the cumulative wind stress (in percent) in the mid-point of cross-section S1 for a 10-year period (2010–2019) depending on direction of the wind velocity vector.

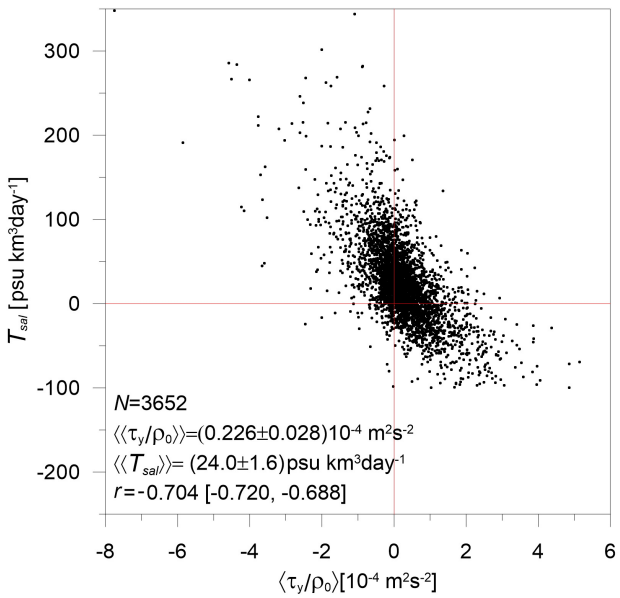

FIGURE 4 | A scatter plot of the daily saltwater transport T_{sal} through cross-section S1 vs. the daily mean of the y-component of wind stress $\langle\tau_y/\rho_0\rangle$; $\langle\langle\ldots\rangle\rangle$ is the 10-year mean value. The numbers in the square brackets and next to the ± sign quantify the 95% confidence limits.

The correlation coefficient for the 10-year time series of T_{sal} and $\langle\tau_y/\rho_0\rangle$ is $r = 0.704$. Note that the 10-year mean values of $\langle\tau_y/\rho_0\rangle$ and T_S are $\langle\langle\tau_y/\rho_0\rangle\rangle = (0.226 \pm 0.028)\cdot10^{-4}$ m^{2}s^{-2} (which confirms the prevalence of southerly winds in accordance to **Figure 3**) and $\langle\langle T_{sal}\rangle\rangle = 24.5 \pm 1.6$ psu·km^{3}day^{-1} (which corresponds to the transport of salt water to the east through the SF on average).

To obtain statistical estimates of saltwater transport through cross-sections S1–S5 depending on the wind force and wind direction, a partial mean $\langle T_{sal}\rangle$ of the daily saltwater transport T_{sal} was calculated for 12 ranges of the wind vector direction and 4 ranges of the daily mean friction velocity $u_* = \sqrt{\langle\tau_x/\rho_0\rangle^2 + \langle\tau_y/\rho_0\rangle^2}$ based on the 10-year time series (**Figure 5**).

At light to moderate winds of any direction, the partial mean saltwater transport $\langle T_{sal}\rangle$ through cross-section S1 (i.e., through SF) remains positive (eastward) being maximum for winds blowing to the south and minimum for winds to the north. For strong winds blowing to the north, the $\langle T_{sal}\rangle$ through S1 has reversed to the west (becomes negative). If the wind increases to stormy, then the reverse transport of saltwater to the west in SF becomes stronger and takes place in a wider range of wind vector angle from 0 to 150°.

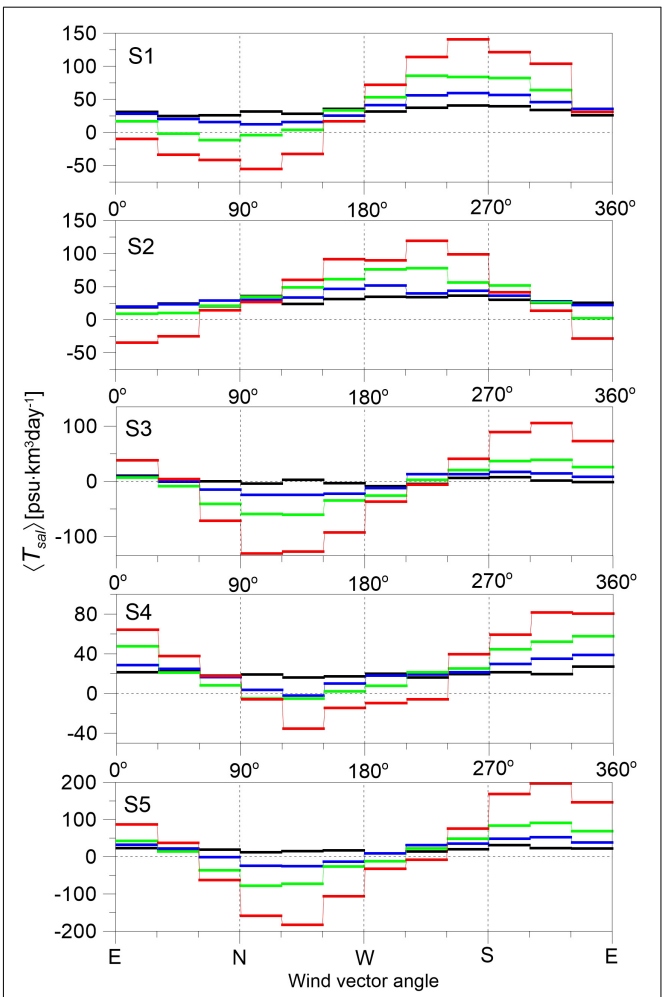

FIGURE 5 | The partial mean value $\langle T_{sal}\rangle$ of the daily saltwater transport T_{sal} through the five cross-sections S1–S5 for 12 ranges of the wind velocity vector angle and 4 ranges of the daily mean friction velocity u_* estimated from the 10-year time series. The friction velocity ranges are $0 \le u_* < 0.25$ cm · s^{-1} (light wind, $|V_{10}| \le 4$ m · s^{-1})—black segments, 0.25 cm · s^{-1} $\le u_* < 0.75$ cm · s^{-1} (moderate wind, 4 m · s^{-1} $\le |V_{10}| < 7$ m · s^{-1})—blue segments, 0.75 cm · s^{-1} $\le u_* < 1.5$ cm · s^{-1} (fresh wind, 7 m · s^{-1} $\le |V_{10}| < 10$ m · s^{-1})—green segments, $u_* \ge 1.5$ cm · s^{-1} (storm wind, $|V_{10}| \ge 10$ m · s^{-1})—red segments.

Dependence of $\langle T_{sal}\rangle$ on u_* and the wind vector angle for cross-sections S2, S3, S4, and S5 has the shape similar to that for S1, but the maximum positive value of $\langle T_{sal}\rangle$ is located in the wind vector angle range (150°, 270°), (270°, 360°), (300°, 360°), and (270°, 360°), respectively, and the minimum negative value is shifted approx. by 180° relative to the maximum positive value. A remarkable difference of the saltwater transport through S3 is that for vanishing wind forcing ($u_* \to 0$) the $\langle T_{sal}\rangle$ approx. vanishes too, while for the rest of cross-sections (S1, S2, S4, and S4), $\langle T_{sal}\rangle$ tends to a definitely positive value.

To learn which wind direction is most / less favorable for saltwater transport through cross-sections S1–S5, the correlation coefficient between T_{sal} and the projection of the wind stress vector $\tau_\varphi = \langle\tau_x\rangle\cos(\varphi) + \langle\tau_y\rangle\sin(\varphi)$, where φ is the angle counting counterclockwise relative to the x-axis (eastward), was calculated from the 10-year time series of daily values of T_{sal} and τ_φ (**Figure 6**). The correlation is maximum at $r_{max} =$ 0.704, 0.701, 0.739, 0.612, and 0.812 for $\varphi(r_{max}) =$ 269, 197, 316, 339, and 320° for the cross-sections S1–S5, respectively, and, evidently, is minimum $r_{min} = -r_{max}$ for the opposite wind vector direction $\varphi(r_{min}) = \varphi(r_{max}) + 180°$. The maximum correlation between T_{sal} and τ_φ was found to be relatively high, $r_{max} =$ 0.612–0.812, showing that the local wind forcing variability can be responsible for $r^2_{max} =$ 0.403–0.659 of the variance in T_{sal} time series, while the rest of T_{sal} variance is probably caused by inflow pulses which have no direct relation to the local wind variability. Like **Figure 5**, **Figure 6** confirms that the most favorable wind direction increasing saltwater transport through the cross-sections S1–S5 is when the wind vector is directed perpendicularly to the right relative to the saltwater flow. For example, the eastward saltwater flow through cross-section S1 is maximally correlated with the southward wind stress component ($\varphi(r_{max}) =$ 269°) and the northeast saltwater transport through the cross-sections S3 and S5 is maximally correlated with the southeastward wind stress component ($\varphi(r_{max}) =$ 316 and 320°, respectively). Note that the values of $\varphi(r_{max})$ are in full correspondence with rougher estimates of the wind vector angle range at which the partial mean value $\langle T_{sal}\rangle$ of the daily saltwater transport T_{sal} through the five cross-sections S1–S5 is maximum (cf. **Figures 5**, **6**).

If we take $\varphi =$ 180, 135, 225, 315, 225° for sections S1–S5, respectively, which is in correspondence with the Krauss and Brügge (1991) hypothesis on the wind-driven coastal jets at the wind direction opposite to the saltwater flow through the sections, the correlation coefficient between T_{sal} and the projection of the wind stress vector will be $r =$ 0.201, 0.376, –0.171, 0.544, –0.250. The latter values of r are considerably smaller than r_{max} except for section S4 where $r_{max} = 0.612$.

Figures 5, **6** characterize in different ways the daily saltwater transport through cross-sections S1–S5 depending on the wind vector angle which may differ much from the total (cumulative) saltwater transport through cross-sections S1–S5 depending on the wind vector angle, because the azimuthal distribution of the cumulative wind stress is strongly anisotropic with the overwhelming dominance of winds from the west-southwest (see **Figure 3**). The percentage of the positive cumulative saltwater transport through cross-sections S1–S2 for a 10-year period of 2010–2019 depending on the wind vector direction (**Figure 7**) displays an obvious similarity with the respective daily saltwater transports vs. the wind vector direction. Namely, the maximum cumulative transport, like the daily transports, takes place at wind vectors directed toward the south for cross-section S1

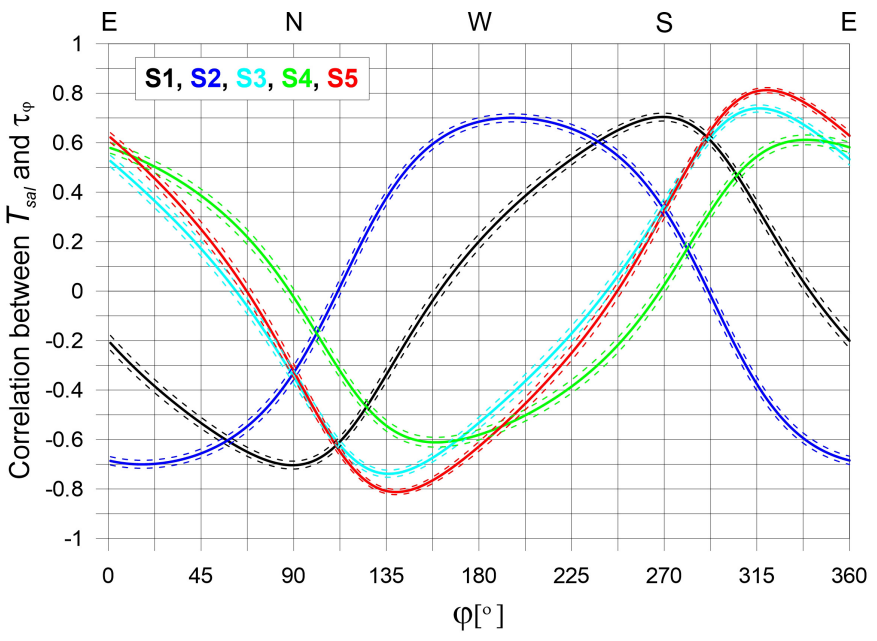

FIGURE 6 | Correlation between the daily saltwater transport T_{sal} through cross-sections S1–S5 and the projection of the wind stress vector $\tau_\varphi = \langle\tau_x\rangle\cos(\varphi) + \langle\tau_y\rangle\sin(\varphi)$ vs. angle φ. The dotted lines are the 95% confidence limits.

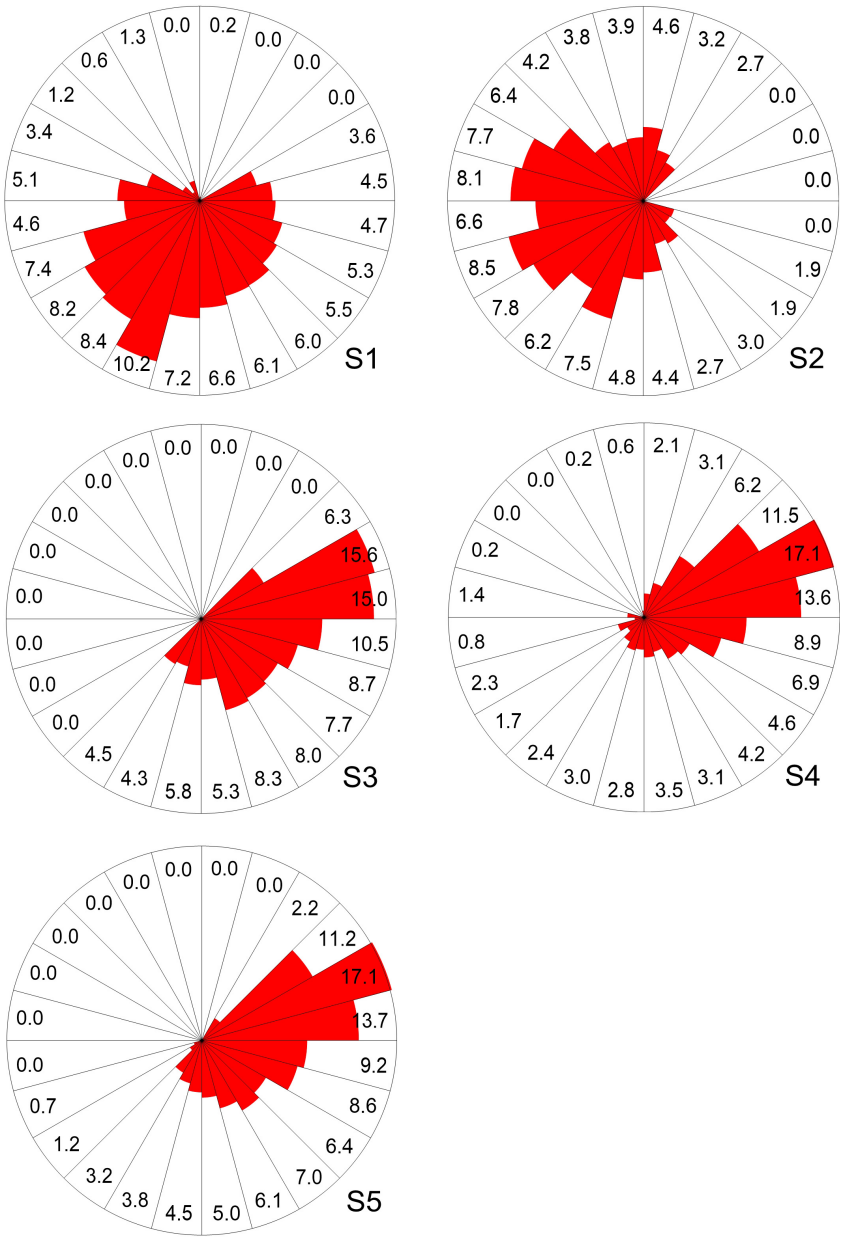

FIGURE 7 | Percentage of the positive cumulative saltwater transport through cross-sections S1–S5 for a 10-year period of 2010–2019 depending on the wind velocity vector direction.

and toward the west-southwest for cross-section S2. However, for cross-sections S3–S5 the cumulative and daily saltwater transports vs. wind vector direction behave differently. Namely, the maximum cumulative saltwater transport takes place at wind vectors directed toward east-northeast, while the maximum daily saltwater transport at wind vectors toward southeast. The discrepancy between the cumulative and daily saltwater transports vs. wind vector angle for cross-sections S3 and S5 is caused by strong anisotropy of the cumulative wind stress: The latter has a strong petal toward the east-northeast direction of the wind vector (see **Figure 3**) which provides a relatively large, positive wind stress component to the southeast favoring the saltwater transport to the north-northeast though cross-sections S3 and S5.

Correlation between daily saltwater transport T_{sal} for cross-section S1 and other four cross-sections S2–S5 is found to be positive varying between $r_{S1,S4} = 0.187$ (for cross-sections S1 and S4) and $r_{S1,S3} = 0.488$ (for cross-sections S1 and S3; **Table 1**). The positiveness of the correlation in this case can be intuitively explained by the fact that the positive fluctuation of T_{sal} through the SF (cross-section S1) leads to an increase of T_{sal} through the other cross-sections S2–S5, and the correlation will be minimal

TABLE 1 | Correlation coefficient r between daily saltwater transports T_{sal} through cross-sections S1–S5 calculated from the 10-year time series.

S1	S2	S3	S4	S5	
$r_{S1,S1} = 1$	$r_{S1,S2} = 0.394$[0.367, 0.420]	$r_{S1,S3} = 0.488$[0.464, 0.512]	$r_{S1,S4} = 0.187$[0.157, 0.218]	$r_{S1,S5} = 0.405$[0.378, 0.431]	S1
	$r_{S2,S2} = 1$	$r_{S2,S3} = -0.401$[–0.427,–0.374]	$r_{S2,S4} = -0.442$[–0.467, –0.416]	$r_{S2,S5} = -0.455$[–0.479, –0.429]	S2
		$r_{S3,S3} = 1$	$r_{S3,S4} = 0.415$[0.389, 0.441]	$r_{S3,S5} = 0.862$[0.853, 0.870]	S3
			$r_{S4,S4} = 1$	$r_{S4,S5} = 0.662$[0.644, 0.679]	S4
				$r_{S5,S5} = 1$	S5

Numbers in square brackets are the 95% confidence intervals.

for cross-sections S1 and S4, since the saltwater from the cross-section S1 reaches cross-section S4 along the longest route with an cyclonic bypass of the Gdańsk Basin.

Correlation between daily saltwater transport T_{sal} for cross-section S2 and cross-sections S3–S5 is negative varying within (–0.455, –0.401). Negative correlation in this case is quite expected because the saltwater transport to the north (south) corresponds to the positive (negative) fluctuation of T_{sal} through cross-sections S3–S5 but negative (positive) fluctuation of T_{sal} through cross-sections S2 (see **Figure 1** and the caption to it).

The fact that the saltwater transport to the north (south) corresponds to the positive (negative) fluctuation of T_{sal} through cross-sections S3–S5 causes the positive correlation between saltwater transports through pair of cross-sections S3–S4 ($r_{S3,S4} = 0.415$), S3–S5 ($r_{S3,S5} = 0.862$), and S4–S5 ($r_{S4,S5} = 0.662$). The highest correlation, $r_{S3,S5} = 0.862$, is found for daily saltwater transports through cross-sections S3 and S5, since these two cross-sections are equally oriented (from southeast to northwest), and the saltwater transport through them describes the same process of the northeast saltwater flow toward the Gotland Deep.

The mean value $\langle\langle T_{sal}\rangle\rangle$ and standard deviation σ of the daily saltwater transport T_{sal} through cross-sections S1–S5 calculated from the 10-year time series (2010–2019) of T_{sal} (**Table 2**) show that $\langle\langle T_{sal}\rangle\rangle$ for cross-section S1 is approximately equal to the sum of $\langle\langle T_{sal}\rangle\rangle$ for cross-sections S2 and S3. This is a consequence of the balanced salt water transport, namely, the salt water leaving SF for the east has only two options: it can go either to the southeast through cross-section S2 toward the Gdańsk Basin or to the northeast through cross-section S3 directly toward the Hoburg Channel and further the Gotland Deep. Similarly, the mean daily transport through cross-section S2, $\langle\langle T_{sal}\rangle\rangle = 25.50$ psu·km^3·day^{-1}, is approximately equal to that of S4 ($\langle\langle T_{sal}\rangle\rangle = 25.24$ psu·km^3·day^{-1}) which is in accordance with the long-term constancy of the salt content and anticyclonic circulation of saltwater flow in the Gdańsk Basin. However, the mean value of daily saltwater transport through cross-section S5 is definitively less than that of the cross-section S1 ($\langle\langle T_{sal}\rangle\rangle = 18.57$ and 23.95 psu·km^3·day^{-1} for S5 and S1, respectively), and the difference is probably balanced by a salinity loss due to vertical (diapycnal) mixing. An argument in favor of the role of diapycnal mixing in the balance of salt water transport though cross-sections S1 and S5 is the existence of a hotspot of diapycnal mixing in the eastern slope of the Hoburg Channel to the south of cross-section S5 caused by the effect of "bottle neck" for the northeast saltwater flow created by a topography constriction associated with the Klaipeda Bank (Paka et al., 2019; see **Figure 1**). Standard deviation σ of T_{sal} through cross-sections S1, S2, S4, and S5 is 1.7–4.1 times more than the mean value $\langle\langle T_{sal}\rangle\rangle$ which indicates the frequent alteration in the T_{sal} time series caused by the wind forcing variability. For cross-section S3, $\langle\langle T_{sal}\rangle\rangle = -3.32$ psu·km^3·day^{-1} is negative with the absolute value much smaller (practically nil) than that for the rest of the cross-sections. In view of this and recalling that the partial mean value $\langle T_{sal}\rangle$ for weak winds vanishes for cross-section S3 (see **Figure 5**), we conclude that unaffected by wind forcing, net gravity flow of saltwater leaving SF turns to the southeast toward the Gdańsk Deep and has no chance to turn to the northeast directly toward the Hoburg Channel.

TABLE 2 | Mean value $\langle\langle T_{sal}\rangle\rangle$ and standard deviation σ of the daily salt water transport T_{sal} through cross-sections S1–S5 calculated from the 10-year time series (2010 –2019) of T_{sal}.

Cross-section	$\langle\langle T_{sal}\rangle\rangle$ [psu·km^3·day^{-1}]	σ [psu·km^3·day^{-1}]
S1	23.95 ± 1.63	50.22
S2	25.50 ± 1.52	47.04
S3	–3.32 ± 1.76	54.43
S4	25.29 ± 1.39	42.86
S5	18.57 ± 2.44	75.22

Numbers next to the ± sign determine the 95% confidence intervals of $\langle\langle T_{sal}\rangle\rangle$.

DISCUSSION AND CONCLUSION

The objective of this study is to investigate the saltwater exchange between the basins of the southeastern Baltic Sea, such as the Słupsk Furrow, the Gdańsk Deep, the Hoburg Channel, and the Gotland Deep, depending on wind forcing based on numerical simulations. We hypothesized that the saltwater transport in a system of basins including the Gdańsk and Gotland deeps connected by the Hoburg Channel, is greatly controlled by wind forcing. Wind-driven Ekman transport in the upper layer directed to the south from the Gotland Deep to the Gdańsk Deep develops a compensatory saltwater countercurrent in the deep layer directed to the north from the Gdańsk Deep to the Gotland Deep, and, vice versa, the wind-driven Ekman transport directed to the north develops a compensatory saltwater flow to the south from the Gotland Deep to the Gdańsk Deep. This hypothesis is based on an analogy between the bottom topography configurations of the Bornholm Basin—SF—deep basins east of SF and the Gdańsk Deep—Hoburg

Channel—Gotland Deep and the results of numerical modeling by Krauss and Brügge (1991) showed that the saltwater transport to the east through SF is enhanced by northerly and easterly winds and weakened by southerly and westerly winds. Note that the hypothesis stating that the wind-driven Ekman transport in the upper layer drives saltwater countercurrent in the lower layer, differs from the original hypothesis by Krauss and Brügge (1991) stating that coastal jets in the wind direction drive countercurrents in the central region, deflected by bottom topography, including saltwater countercurrent in the lower layer. To our mind, both hypothesis are robust, and the results of modeling give an opportunity to resolve which effect, the wind-driven coastal jets or wind-driven Ekman transport in the open sea, prevails. If the effect of wind-driven coastal jets prevails, the maximum saltwater transport to the east through SF and to the northeast through the Hoburg Channel will take place at easterly and northeasterly winds, respectively. If the effect of wind-driven Ekman transport in the open sea prevails, the maximum saltwater transport to the east through SF and to the northeast through the Hoburg Channel will take place at northerly and northwesterly winds, respectively.

To resolve between the hypotheses, results of numerical modeling of the Baltic Sea circulation for a 10-year period 2010–2019) are applied. The model setup is based on GETM with 0.5 nautical mile grid (Zhurbas et al., 2018; Liblik et al., 2020). Validation of the model was performed by the comparison of salinity time series in the surface and bottom layers measured at the IOW monitoring station TF0256, located at the eastern exit of SF, with the simulated time series.

If the wind forcing is weak or absent, the simulated saltwater flow leaving SF for the east turns to the southeast in accordance to the gravity current dynamics and having made a cyclonic detour in the Gdańsk Basin heads north toward the Hoburg Channel and further the Gotland Deep. The mean value of the daily saltwater transport through SF, $\langle\langle T_{sal}\rangle\rangle = 23.95$ psu·km^3·day^{-1}, calculated for the 10-year simulation period, exceeds similar estimate for the Hoburg Channel, $\langle\langle T_{sal}\rangle\rangle = 18.57$ psu·km^3·day^{-1}, and the difference is probably balanced by a salinity loss due to vertical (diapycnal) mixing. An argument in favor of the role of diapycnal mixing in the balance of salt water transport though cross-sections S1 and S5 is the existence of a hotspot of diapycnal mixing in the eastern slope of the Hoburg Channel to the south of cross-section S5 caused by the effect of "bottle neck" for the northeast saltwater flow created by a topography constriction associated with the Klaipeda Bank (Paka et al., 2019).

The daily saltwater transport to the east through SF is found to be highly correlated with the wind stress component toward south (the correlation coefficient is 0.704) which is in accordance with the Krauss and Brügge (1991) findings. Even a higher correlation, $r = 0.812$, is found for the daily saltwater transport to the northeast through the Hoburg Channel (cross-section S5) and the wind stress component toward southeast, which confirm the above mentioned hypothesis on the prevalence of the effect of open-sea Ekman transport rather than that of the coastal jets. More confirmation of the hypothesis yields similar calculations for cross-sections S2 and S3: maximum correlation of $r = 701$ and 0.739 was found between the saltwater transport to the southeast and northeast and the wind stress component to the southwest and southeast for cross-sections S2 and S3, respectively. However, the rule saying that the maximum correlation between the saltwater transport through a cross-section and a wind stress component directed perpendicularly to the right relative to the direction of saltwater transport being exactly satisfied for cross-sections S1, S2, S3, and S5, is violated to some extent for cross-section S4 where the maximum correlation, $r = 0.612$, takes place for the saltwater transport to the northwest and the wind stress component toward the east (instead of the northeast in accordance to the rule). A violation of the rule in the case of cross-section S4 can be intuitively explained by a well pronounced curvature of the deep layer isobaths steering the flow caused by the proximity of the Klaipeda Bank which provides a drastic change of the saltwater flow direction nearby cross-section S4.

However, the fact that the wind velocity vector directed to the southeast is the most favorable for the saltwater transport to the northeast through the Hoburg Channel does not guarantee that the cumulative saltwater transport through cross-section S5 is maximum for the same wind velocity vector direction. Actually, the maximum cumulative saltwater transport takes place at wind velocity vectors directed toward east-northeast, while the maximum daily saltwater transport at wind velocity vectors toward southeast. The discrepancy between the cumulative and daily saltwater transports vs. wind velocity vector angle for cross-section S5 (as well as for cross-section S3) is caused by strong anisotropy of the cumulative wind stress: the latter has a strong petal toward the east-northeast direction of the wind velocity vector (see **Figure 3**) which provides a relatively large, positive wind stress component to the southeast favoring the saltwater transport to the northeast though the Hoburg Channel.

DATA AVAILABILITY STATEMENT

The raw data supporting the conclusions of this article will be made available by the authors, without undue reservation.

AUTHOR CONTRIBUTIONS

VZ proposed the idea of the work, developed the approach needed, performed statistical processing of the model output, participated in interpreting the results, and prepared the manuscript with contributions from both authors. GV developed the model setup, performed numerical modeling and primary processing of the model output, participated in interpreting the results.

FUNDING

VZ was supported by budgetary financing of the Shirshov Institute of Oceanology RAS (Project No. 149-2019-0003). GV was supported by the Estonian Research Council (grant no. PRG602).

ACKNOWLEDGMENTS

An allocation of computing resources on High Performance Computing cluster by the Tallinn University of Technology and the University of Tartu was gratefully acknowledged. The GETM community in Leibniz Institute of Baltic Sea Research (IOW) was greatly acknowledged for maintaining and developing the model code along with their user support.

REFERENCES

Borenäs, K., Hietala, R., Laanearu, J., and Lundberg, P. (2007). Some estimates of the Baltic deep-water transport through the Stolpe trench. *Tellus A* 59, 238–248. doi: 10.1111/j.1600-0870.2006.00221.x

Burchard, H., and Bolding, K. (2001). Comparative analysis of four second-moment turbulence closure models for the oceanic mixed layer. *J. Phys. Oceanogr.* 31, 1943–1968. doi: 10.1175/1520-04852001031<1943:CAOFSM<2.0.CO;2

Burchard, H., and Bolding, K. (2002). *GETM – A General Estuarine Transport Model, Scientific Documentation, Technical Report EUR 20253 EN*. Ispra: European Commission.

Canuto, V. M., Howard, A., Cheng, Y., and Dubovikov, M. S. (2001). Ocean turbulence. Part I: one-point closure model—momentum and heat vertical diffusivities. *J. Phys. Oceanogr.* 31, 1413–1426. doi: 10.1175/1520-04852001031<1413:OTPIOP<2.0.CO;2

Döös, K., Meier, H. E. M., and Döscher, R. (2004). The Baltic haline conveyor belt or the overturning circulation and mixing in the Baltic. *Ambio* 33, 261–266. doi: 10.1579/0044-7447-33.4.261

Gräwe, U., Holtermann, P., Klingbeil, K., and Burchard, H. (2015). Advantages of vertically adaptive coordinates in numerical models of stratified shelf seas. *Ocean Model.* 92, 56–68. doi: 10.1016/j.ocemod.2015.05.008

Hofmeister, R., Burchard, H., and Beckers, J. M. (2010). Non-uniform adaptive vertical grids for 3D numerical ocean models. *Ocean Model.* 33, 70–86.

Janssen, F., Schrum, C., and Backhaus, J. O. (1999). A climatological data set of temperature and salinity for the Baltic Sea and the North Sea. *Deutsche Hydrogr. Z.* 51:5. doi: 10.1007/BF02933676

Johnson, G. C., and Sanford, T. B. (1992). Secondary circulation in the Faroe Bank channel outflow. *J. Phys. Oceanogr.* 22, 927–933. doi: 10.1175/1520-04851992022<0927:SCITFB<2.0.CO;2

Klingbeil, K., Lemarié, F., Debreu, L., and Burchard, H. (2018). The numerics of hydrostatic structured-grid coastal ocean models: state of the art and future perspectives. *Ocean Model.* 125, 80–105. doi: 10.1016/j.ocemod.2018.01.007

Kondo, J. (1975). Air-sea bulk transfer coefficients in diabatic conditions. *Boundary Layer Meteorol.* 9, 91–112. doi: 10.1007/BF00232256

Krauss, W., and Brügge, B. (1991). Wind-produced water exchange between the deep basins of the Baltic Sea. *J. Phys. Oceanogr.* 21, 373–384. doi: 10.1175/1520-04851991021<0373:WPWEBT<2.0.CO;2

Large, W. G., and Pond, S. (1981). Open ocean momentum flux measurements in moderate to strong winds. *J. Phys. Oceanogr.* 11, 324–336. doi: 10.1175/1520-04851981011<0324:OOMFMI<2.0.CO;2

Liblik, T., Väli, G., Lips, I., Lilover, M.-J., Kikas, V., and Laanemets, J. (2020). The winter stratification phenomenon and its consequences in the Gulf of Finland, Baltic Sea. *Ocean Sci.* 16, 1475–1490. doi: 10.5194/os-16-1475-2020

Männik, A., and Merilain, M. (2007). Verification of different precipitation forecasts during extended winter-season in Estonia. *HIRLAM Newslett.* 52, 65–70.

Matthäus, W., and Frank, H. (1992). Characteristics of major Baltic inflows – a statistical analysis. *Cont. Shelf Res.* 12, 1375–1400. doi: 10.1016/0278-4343(92)90060-W

Mohrholz, V. (2018). Major Baltic inflow statistics – revised. *Front. Mar. Sci.* 5:384. doi: 10.3389/fmars.2018.00384

Paka, V. T., Zhurbas, V. M., Golenko, M. N., Korzh, A. O., Kondrashov, A. A., and Shchuka, S. A. (2019). Innovative closely spaced profiling and current velocity measurements in the southern Baltic Sea in 2016–2018 with special reference to the bottom layer. *Front. Earth Sci.* 7:111. doi: 10.3389/feart.2019.00111

Umlauf, L., and Burchard, H. (2005). Second-order turbulence closure models for geophysical boundary layers. A review of recent work. *Cont. Shelf Res.* 25, 795–827. doi: 10.1016/j.csr.2004.08.004

Wåhlin, A. K. (2002). Topographic steering of the dense currents with application to submarine canyons. *Deep Sea Res. I* 49, 305–320. doi: 10.1016/S0967-0637(01)00058-9

Zhurbas, V., Elken, J., Paka, V., Piechura, J., Väli, G., Chubarenko, I., et al. (2012). Structure of unsteady overflow in the Słupsk Furrow of the Baltic Sea. *J. Geophys. Res. Oceans* 117:C04027. doi: 10.1029/2011JC007284

Zhurbas, V., Elken, J., Väli, G., Kuzmina, N., and Paka, V. (2010). Pathways of suspended particles transport in the bottom layer of the southern Baltic Sea depending on the wind forcing (Numerical Simulation). *Oceanology* 50, 841–854. doi: 10.1134/S0001437010060032

Zhurbas, V., Väli, G., Golenko, M., and Paka, V. (2018). Variability of bottom friction velocity along the inflow water pathway in the Baltic Sea. *J. Mar. Syst.* 184, 50–58. doi: 10.1016/j.jmarsys.2018.04.008

Conflict of Interest: The authors declare that the research was conducted in the absence of any commercial or financial relationships that could be construed as a potential conflict of interest.

Publisher's Note: All claims expressed in this article are solely those of the authors and do not necessarily represent those of their affiliated organizations, or those of the publisher, the editors and the reviewers. Any product that may be evaluated in this article, or claim that may be made by its manufacturer, is not guaranteed or endorsed by the publisher.

Copyright © 2022 Zhurbas and Väli. This is an open-access article distributed under the terms of the Creative Commons Attribution License (CC BY). The use, distribution or reproduction in other forums is permitted, provided the original author(s) and the copyright owner(s) are credited and that the original publication in this journal is cited, in accordance with accepted academic practice. No use, distribution or reproduction is permitted which does not comply with these terms.

frontiers in Marine Science

ORIGINAL RESEARCH
published: 17 March 2022
doi: 10.3389/fmars.2022.841900

Offshore Freshwater Pathways in the Northern Gulf of Mexico: Impacts of Modeling Choices

Guangpeng Liu[1,2], Annalisa Bracco[1] and Daoxun Sun[1,3]*

[1] School of Earth and Atmospheric Sciences, Georgia Institute of Technology, Atlanta, GA, United States, [2] Department of Oceanography, University of Hawai'i at Manoa, Honolulu, HI, United States, [3] Deep Sea Research Center, Pilot National Laboratory for Marine Science and Technology, Qingdao, China

The Gulf of Mexico is a very productive and economically important system where riverine runoff acts as a linkage between the continental shelf and the open ocean, providing nutrients in addition to freshwater. This work investigates the three-dimensional transport and pathway structure of this river runoff offshore the continental shelf using ensembles of numerical simulations with different configurations regarding grid resolution (mesoscale resolving and submesoscale permitting) and river setup using suites of 5-months long integrations covering nearly 3 years. The riverine forcing is applied only at the surface over an area around the river mouth, a strategy often adopted in numerical studies, or as a meridional flux with a vertical extension. The simulated flow captures the southward offshore transport of river runoff driven by its interaction with the largest mesoscale circulations in the basin, the Loop Current and Loop Current eddies. This pathway is strong and well-document during summer but also active and relevant in winter, despite a less obvious surface signature. The most intense transport occurs primarily at the peripheries of the Loop Current and the detached eddies, and the freshwater is subducted as deep as 600 m around the mesoscale anticyclonic eddies. Submesoscale motions strengthen slightly the spread of freshwater plumes in summer but their contribution is negligible, if not negative, in winter. Differences in the freshwater distribution and transport volume among runs are small and generally less than 10% among ensembles, with overall slightly higher volume of freshwater transported off-shore and at depth in submesoscale permitting runs that include a velocity flux in their riverine input representation.

Keywords: Gulf of Mexico, freshwater offshore pathways, regional modeling, submesoscales, riverine modeling

OPEN ACCESS

Edited by:
Alejandro Jose Souza, Center for Research and Advanced Studies - Mérida Unit, Mexico

Reviewed by:
Alejandro Orfila, Spanish National Research Council (CSIC), Spain
Hui Wu, East China Normal University, China

***Correspondence:**
Annalisa Bracco
abracco@gatech.edu

Specialty section:
This article was submitted to Coastal Ocean Processes, a section of the journal Frontiers in Marine Science

Received: *22 December 2021*
Accepted: *23 February 2022*
Published: *17 March 2022*

Citation:
Liu G, Bracco A and Sun D (2022) Offshore Freshwater Pathways in the Northern Gulf of Mexico: Impacts of Modeling Choices. Front. Mar. Sci. 9:841900. doi: 10.3389/fmars.2022.841900

INTRODUCTION

Understanding the pathway and transport of freshwater input into an ocean basin is key for estimating land-ocean linkages, the contribution of coastal areas to the oceanic carbon cycling and one component of the anthropogenic pressure on marine ecosystems. In coastal areas, riverine inflow influences oceanic physical and biogeochemical properties. On the physical side, the inflow of low salinity waters modifies stratification, stability and at times circulation (e.g., in the South

China Sea, Cai and Gan, 2017; Zeng et al., 2021), while on the biogeochemical side algal blooms, hypoxia, eutrophication and pollutants accumulation result from nutrient and sediment loading by the riverine water, often modified by anthropogenic stressors (e.g., Krug, 1993).

The Gulf of Mexico (GoM, **Figure 1A**) is a semi-enclosed region highly impacted by several large rivers and is an ideal testbed for studies on river discharge, plume formation, and freshwater transport. The Mississippi River and the neighboring Atchafalaya River (MARS, **Figure 1B**) are the first and second-largest freshwater inputs into the GoM, with an average rate of more than 14,000 m^3/s, and constitute the biggest river system in North America (Morey et al., 2003; Hu et al., 2005; Schiller et al., 2011). They contribute freshwater and abundant nutrients to the semienclosed basin, and this input also enriches microbial diversity (Mason et al., 2016). Rivers smaller than the MARS also drain in the GoM, and their contribution cannot be neglected because of their specific input locations or seasonality. For example, the Mobile River System (confluence of Alabama and Tombigbee rivers) and the Texas Gulf Coast Hydrologic Region (Sabine, Brazos, Trinity, etc.) can contribute to the GoM as much as 3,500 m^3/s and 1,400 m^3/s discharge in March and May–June, respectively (Fournier et al., 2019).

Many studies have shown that the advection of riverine water offshore into the northern GoM is modulated by the seasonally varying wind patterns (Walker et al., 1994; Schiller et al., 2011) and by entrainment events due to occasional intrusions of the Loop Current (LC) into De Soto Canyon and the accompanying LC eddies (Morey et al., 2003; Hu et al., 2005; Schiller and Kourafalou, 2014; Androulidakis et al., 2019; Brokaw et al., 2019). These studies are predominantly focused on the interaction of the river plume and the local mesoscale LC eddies during late spring and summer, when the riverine contribution is generally at its maximum, and the impact of submesoscale currents has not been explored in detail.

Global studies have investigated how representing rivering fluxes as bogus volume fluxes imposed at the ocean surface or point sources may impact global salinity budgets (Feng et al., 2021) but less is known for enclosed basins, where models can be run at high resolution to better represent the dynamics responsible for the offshore and vertical spreading of the freshwater anomalies. Among these dynamics, in the past two decades the oceanographic community has paid particular attention to submesoscale circulations. In the GoM, for example, mesoscale structures and rivering inputs have been shown to jointly contribute to the juxstaposition of water masses with different densities and therefore to the development of frontal and baroclinic instabilities. The end result is the formation of submesoscale lateral convergence zones (Luo et al., 2016; Barkan et al., 2017a,b) where fresh water, nutrients, and pollutants accumulate (Huntley et al., 2015; Choi et al., 2017; Bracco et al., 2019; Justic et al., 2021).

Here, we focus on the representation of the freshwater contribution in an ocean model aiming to answer two questions in the context of regional submesoscale permitting and mesoscale resolving high resolution simulations:

(1) Do submesoscale circulations contribute to the pathway and transport characteristics of the freshwater plume in conjunction with the LC system (LCS), and if so how much?

and

(2) Is there a significant difference in the model representation of this pathway whenever the freshwater input is imposed as a volume flux at the river mouths or more simply as an additional passive contribution at the ocean surface (i.e., is treated similarly to a precipitation term)? We stress that some ocean models use the second, simpler strategy, also when run for prediction and predictability studies.

To answer them, we use ensembles of ocean model runs at two horizontal grid resolutions and with different river configurations, and we examine the three-dimensional structure of river discharges from ten major rivers in the GoM (**Figure 1A**). The integrations cover the period December 2013 – August 2016, allowing us to explore the variability of the MARS-LCS interactions under different conditions (**Figure 1B**). This time interval covers a year of relative low discharge in 2014 (medium winter and low summer discharges), a year of typical discharge in 2015 (low winter, high late spring/early summer discharge), and a year characterized by extreme flooding conditions in January-February due to the influence of the El Niño event in 2016 (very high winter and spring discharge).

MATERIALS AND METHODS

To solve the fine-scale, regional circulation, we use the primitive-equation, free-surface, split-explicit Regional Ocean Modeling System (ROMS) in its Coastal and Regional Ocean COmmunity model version (CROCO; Shchepetkin and McWilliams, 2003, 2011; Debreu et al., 2008, 2012). The model domain covers the GoM north of 24°N (**Figure 1A**), with open boundaries to the south and east. K-profile parameterization (KPP) is used for vertical mixing of tracers and momentum (Large et al., 1994). The 3rd-order upstream biased advection scheme and the split and rotated 3rd-order upstream biased advection scheme are used for lateral momentum and tracer advection, respectively. Analysis products of the Hybrid Coordinate Ocean Model-Navy Coupled Ocean Data Assimilation (HYCOM-NCODA) experiment 31.0 (before April 4th, 2014) and experiment 32.5 (after April 4th, 2014) at 1/25° resolution are used as initial and boundary conditions (Cummings, 2005; Cummings and Smedstad, 2013). The boundary conditions are updated every 3 h. All forcing fields (i.e., 10 m wind, surface shortwave radiation, surface downward long wave radiation, precipitation, 2 m air temperature and relative humidity) are from the NAVy Global Environmental Model (NAVGEM), which are also used in HYCOM-NCODA analysis. Atmospheric forcing is employed in our simulations with bulk parameterization, as in HYCOM-NCODA. The topography is derived from 2-min Gridded Global Relief Data (ETOPO2) (Smith and Sandwell, 1997) and is smoothed with a maximum slope factor of 0.25 to reduce horizontal pressure gradient errors caused by sigma-coordinates

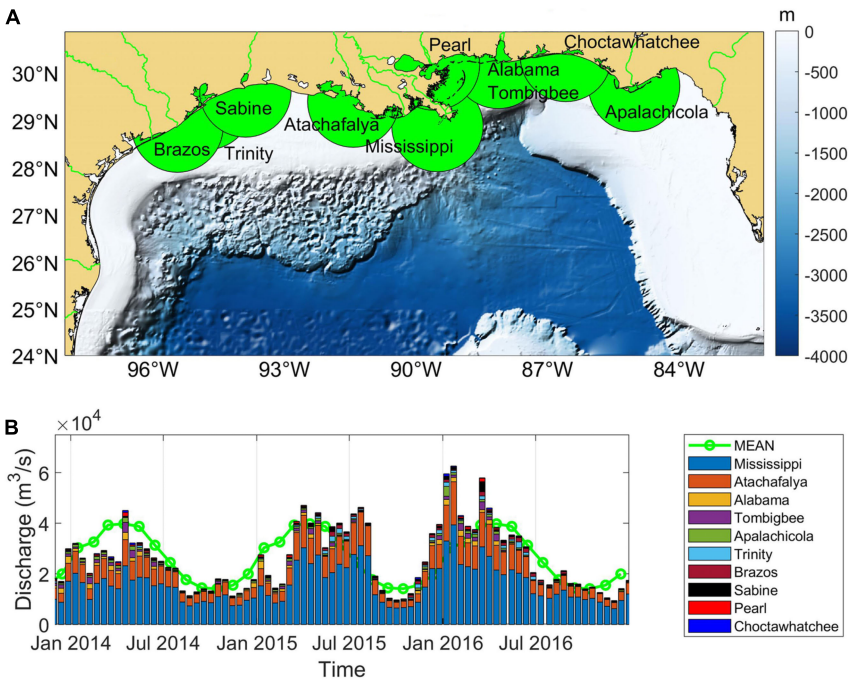

FIGURE 1 | (A) Bathymetry of the Gulf of Mexico with indicated the river mouth of the rivers considered in the simulations (green dots) and major shelves. Rivers Alabama and Tombigbee share the same river mouth in our model setup. The dots cover the region where the bogus freshwater fluxes are applied in the passive configuration. **(B)** Freshwater discharge rate of each river from December 2013 to August 2016. Vertical dash lines show the 1st day of January and July during this period. Green dotted line indicates the mean discharge rate, calculated as monthly means over the 11-year period Jan 2010 – Nov 2021.

(Sikirić et al., 2009). The configuration choices insure that the Loop Current dynamics do not diverge significantly from the analysis in all runs and that overall the model follows the dynamical evolution of the HYCOM-NCODA system.

River discharges of ten major rivers (**Figure 1**), collected daily by the U.S. Geological Service (USGS) and the U.S. Army Corps of Engineers (USACE), are imposed in the simulations in an active or passive manner. In the active configuration, the discharges are imposed as a southward volume flux at the river mouths. The river salinity is set to 4 psu, and the temperature is set at the local air temperature value. The freshwater flux decays exponentially away from the surface toward the ocean bottom. In the passive river configuration, which is commonly preferred because easier to implement, the river discharge is simulated as a bogus flux that is added to precipitation around the river mouth, with the amplitude of the flux decreasing according to a Gaussian function with an e-folding length of 50 km. (see **Figure 1**) to ensure that the freshwater reaches realistically far offshore (Barkan et al., 2017a).

The December 2013 – August 2016 period is divided into 8 intervals, each 5 months long. For each interval, the model is run freely (without any data assimilation) starting on December, April and August 1st, 2nd, and 3rd of each year from the HYCOM analysis. The three-member ensembles allow for quantifying the internal variability, while the re-starting every 5 months assures that the runs do not diverge much from the observed conditions in their LCS representation. At the same time, the set-up choices limit us to investigating subseasonal to (at most) seasonal changes associated with the riverine fluxes representation. Two ensembles (active and passive) are run at 1 km (submesoscale-permitting, SP) and two at 3.5 km (mesoscale-resolving, MR) horizontal resolution, with 70 sigma layers in all cases. In the SP case a two-member ensemble is run also without riverine discharge except for that contained in the initial conditions; in those no-river runs the surface salinity continues to be modified by evaporation and precipitation.

RESULTS

The predictability of surface fields – sea surface temperature (SST), salinity (SSS), relative vorticity and height (SSH) — is described in terms of variability, climatology and ensemble spread in Sun et al. (2021), thereafter SBL21, and is not repeated here. In this work, we focus on salinity pattern at and below the surface, paying closer attention to the 3D distribution of riverine waters as they move offshore into the open ocean. A configuration close to that adopted here has been validated in various fields in previous studies (see e.g., Cardona et al., 2016; Luo et al., 2016, and Liu et al., 2021). Overall the model reproduces well the stratification and mesoscale variability, but LC structures (the LC and the detached eddies) are often stronger than observed in terms of their eddy kinetic energy. This is a common problem in ocean-only model. Renault et al. (2016), for example, assessed the role of atmospheric coupling using ocean-atmosphere coupled and uncoupled simulations, and showed that

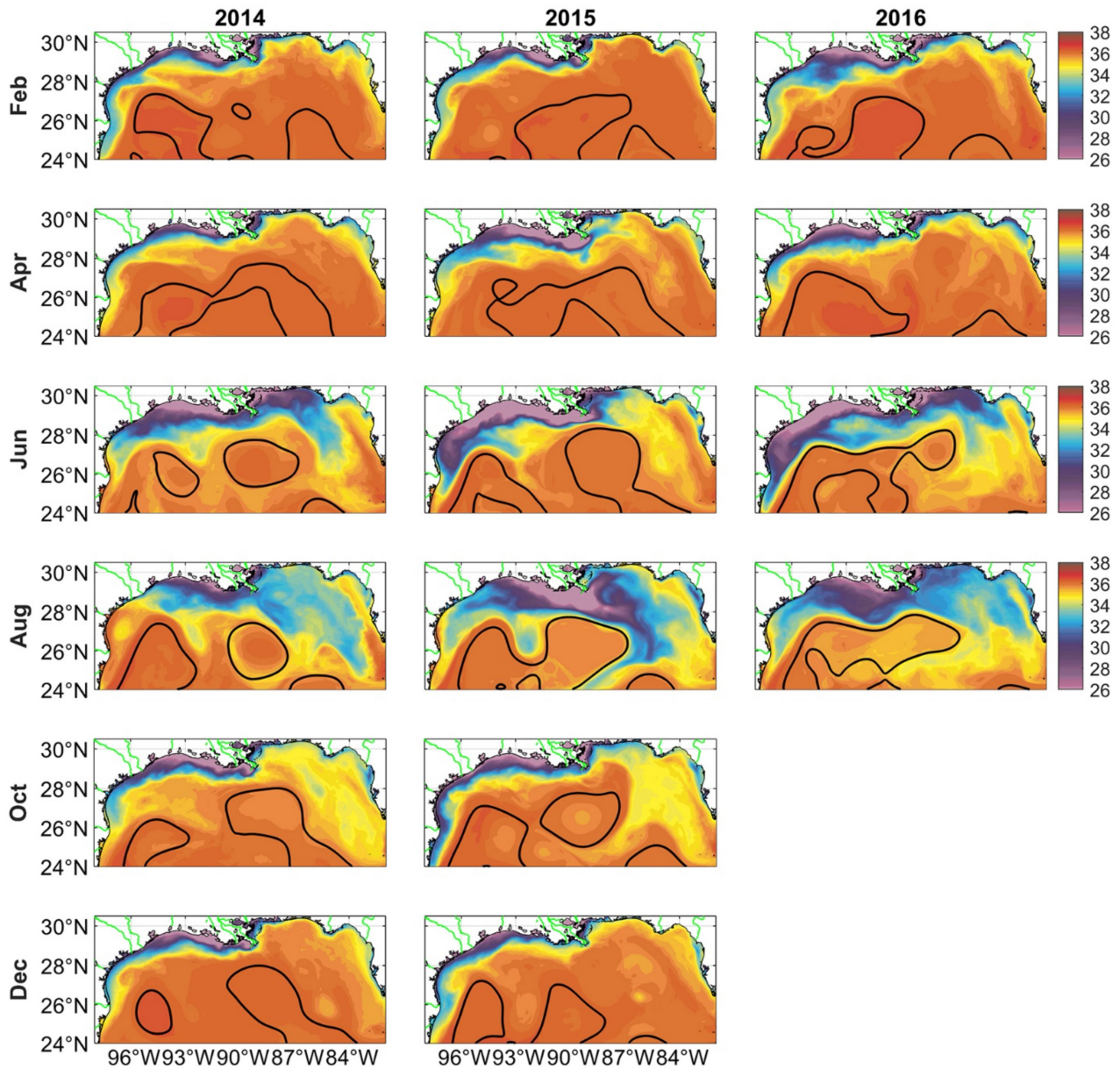

FIGURE 2 | Monthly averaged surface salinity in the first member (initialized on the 1st of the month) of the SP active case shown in the third (February, June, and October) and fifth (April, August, and December) months of the (free) simulation. Black contour indicates 0.17 m sea surface height anomaly (SSHa) and broadly follow the LCS and the Rings, following Leben and Born (1993).

the current-wind feedback in coupled simulation attenuates the mean transfer of energy from the atmosphere to the ocean, and consequently decreases the level of eddy kinetic energy in the ocean by nearly 30%.

Modeled Salinity and Circulation Features in the Gulf of Mexico

Figure 2 shows the monthly mean sea surface salinity (SSS) in the 3rd and 5th months of each model period for the first member of the SP active ensemble. The SSS field varies greatly across years because of the freshwater input, the variations in wind pattern as well as the position of the LC and the Rings (Morey et al., 2003; Schiller et al., 2011; Schiller and Kourafalou, 2014; da Silva and Castelao, 2018). Winds in the GoM are typically southeasterly in summer and northerly and northeasterly during fall and winter (Morey et al., 2003) and drive the seasonal circulation over the shallow inner shelf. In the multi-year average, in February –April low-salinity waters are confined to the Louisiana-Texas (LATEX) continental shelf, and extend offshore in summer (June to August), with a major branch of freshwater spreading to the east of the Mississippi Delta,

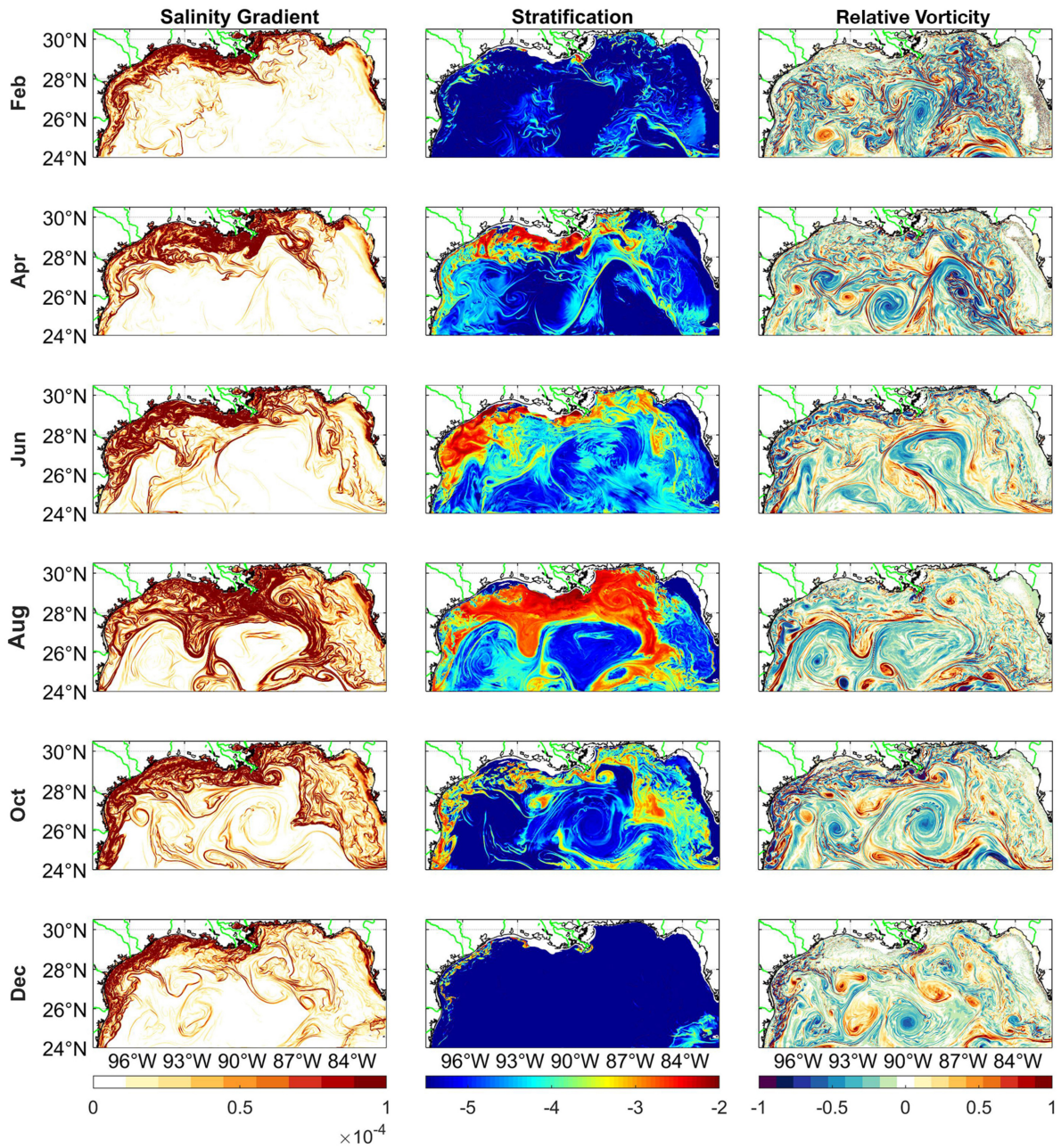

FIGURE 3 | Instantaneous fields of surface salinity gradient (m^{-1}), stratification in the upper 10 m of the water column (log scale, s^{-2}), and normalized surface relative vorticity ζ/f (unitless) in Feb, Apr, Jun, Aug, Oct, and Dec 2015. The patterns are obtained from the first ensemble member of each SP active case in the 3rd and 5th months of the (free) simulation and exemplify the dynamical characteristics of the flow field in the various seasons.

along the coast of the Mississippi-Alabama-Florida (MAFLA) and toward the West Florida shelf. The shape and extension of this branch are linked to the position of the LC. In fall the fresh SSS retracts toward the shelf, with remnants around the LCS, and in winter (November to January) only the shelf areas are occupied by low salinity waters near the surface.

In the period considered, low-salinity waters (identified by salinity less than 34 psu) were mainly limited to the coastal areas in August 2014 because the discharge in April-July was anomalously low, but extended well offshore to as far as 26°N in 2015, when the late spring/summer discharge was highest among the 3 years (**Figure 1B**) and the LC was in an extended position for most of the time.

During winter and spring, the El Niño Southern Oscillation (ENSO) is an important driver of interannual variability in salinity and coastal circulation (Gomez et al., 2019). ENSO indeed

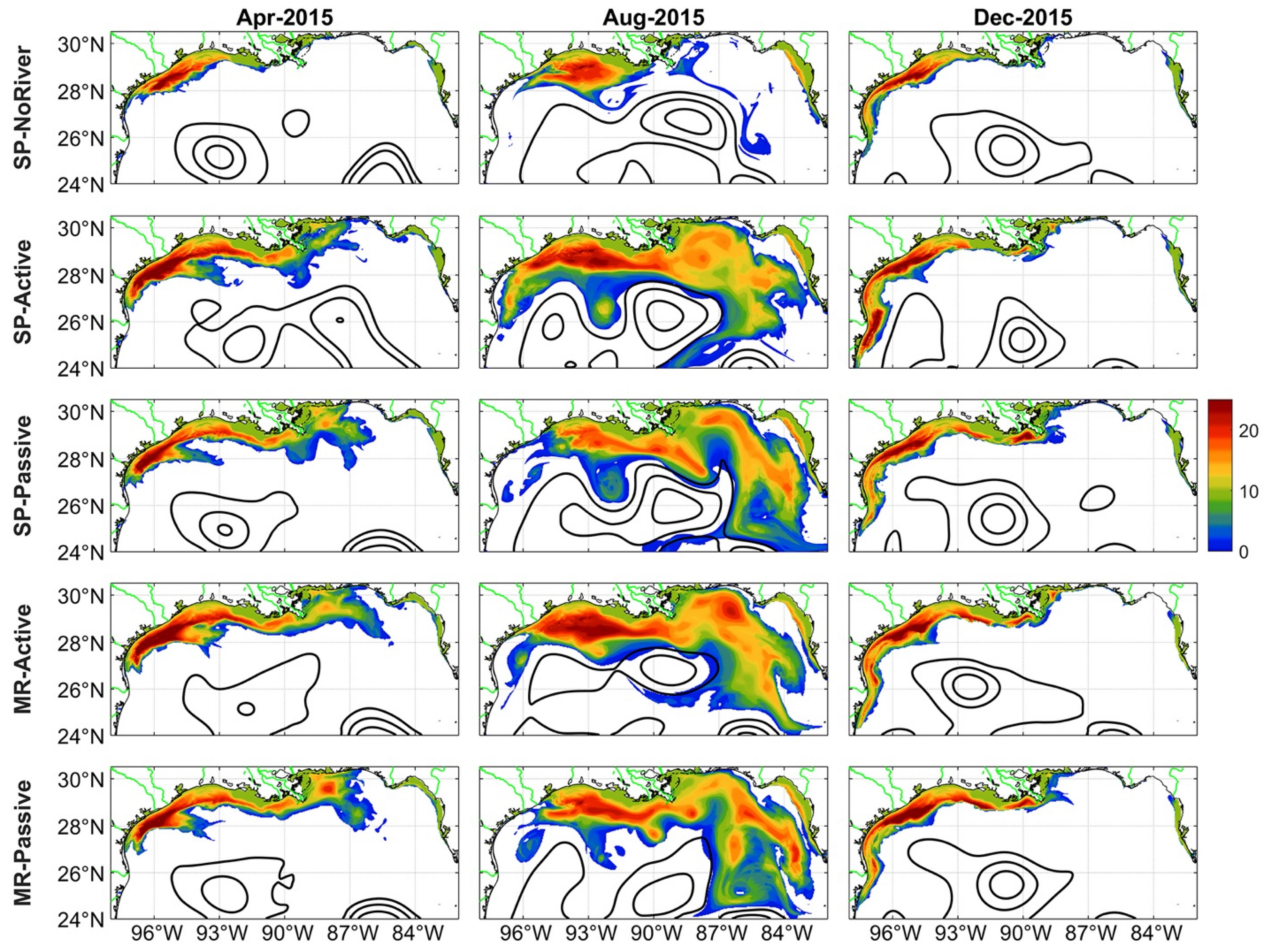

FIGURE 4 | Monthly and vertically averaged freshwater (=34 psu) extension in Apr, Aug, and Dec 2015 with different model setup. Color shading denotes the thickness of the freshwater patches in meters. SSHa contours (0.17, 0.4, and 0.6 m) are also shown.

modulates the global precipitation patterns over the continental United States that feed the Mississippi River basin and the wind anomalies that control the alongshore currents over the LATEX shelf *via* the thermal wind relation (Childers et al., 1990; Schimidt et al., 2001). This modulation results in flooding conditions and wider than normal offshore spreading of low-salinity waters in winter and early spring during El Niño events, as verified in 2016 from February to April.

As mentioned, the GoM circulation in the upper 600–800 m of the water column is dominated by the anticyclonic Loop Current (LC), which is relatively warm and salty, and its detached eddies or Rings (Hamilton, 2009). The LC and the Rings can extend to 200 – 300 km in diameter (Gordon, 1967). Whenever a Ring is formed, and through its westward drift, smaller mesoscale eddies, spinning both cyclonically and anticyclonically, are also generated. Around and within the large mesoscale structures, submesoscale circulations have been observed year-round (Poje et al., 2014; D'Asaro et al., 2018) at horizontal scales from hundreds of meters to few kilometers. They emerge from the conversion of available potential energy from the mixed layer to kinetic energy and are fueled by the density gradients associated with the energetic mesoscale structures (McWilliams, 2008) and the river discharge (Barkan et al., 2017a).

Figure 3 presents the surface salinity gradient field, the surface relative vorticity $\zeta = \partial v/\partial \times - \partial u/\partial y$ normalized by the Coriolis parameter *f,* and the near-surface stratification, or the squared Brunt–Väisälä frequency $N^2 = -\frac{g}{\rho}\frac{d\rho}{dz}$, where ρ is the potential density, in 2015 for one of the SP active runs. Similar patterns are detectd in other cases but with relatively weaker magnitude or less extension for all fields. For relative vorticity, in the offshore portion of the basin – offshore the shallow continental slope – submesoscale circulations in the form of small eddies are most energetic in winter when the mixed layer is deepest and submesoscale fronts prevail in summer, due to the river-induced submesoscale enhancement, as shown in previous studies (Luo et al., 2016; Barkan et al., 2017b). Over the shelf, submesoscale eddies are more commonly observed from late spring to early fall (Horner-Devine et al., 2015; Kobashi and Hetland, 2020). Focusing on stratification, very weakly stratified waters can be seen inside the LC and Rings extending to the shelves in

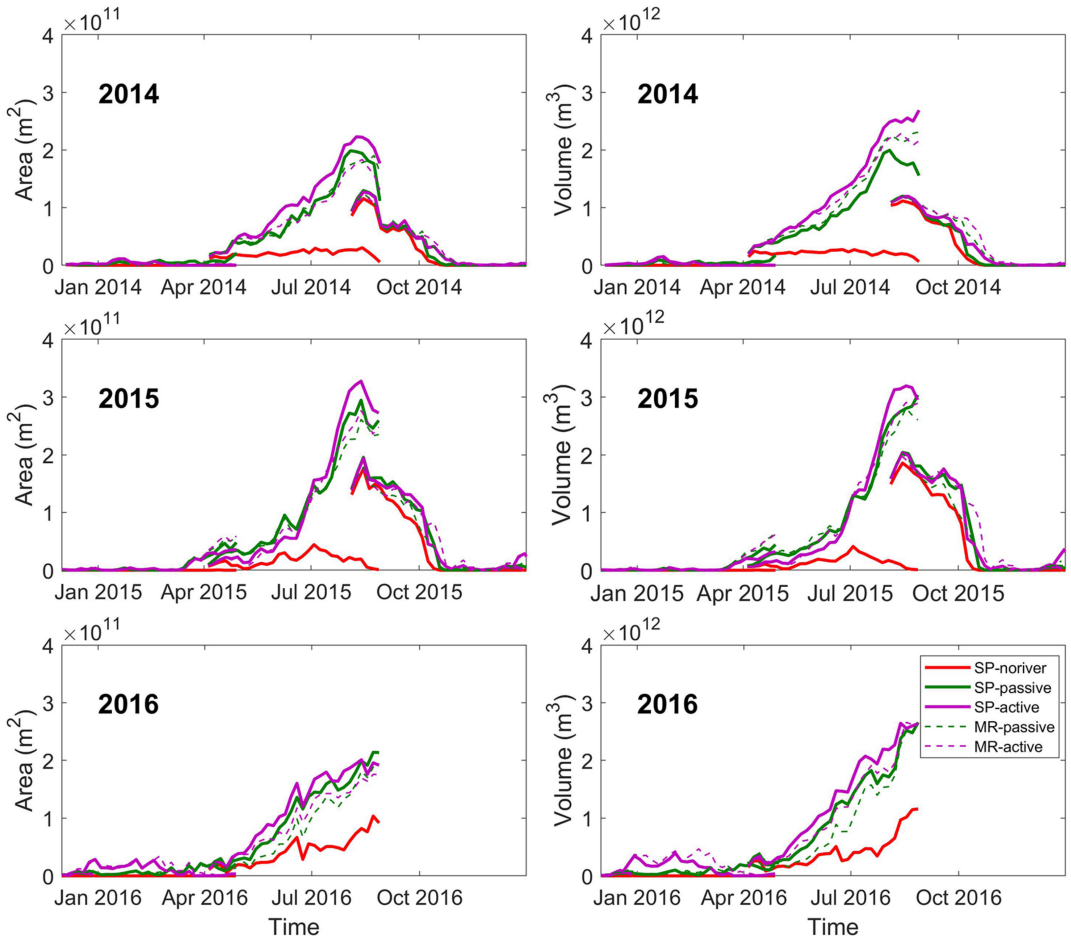

FIGURE 5 | Time evolution of the ensemble mean area **(left)** and volume **(right)** of freshwater (psu < 34) in 2014, 2015, and 2016 in waters with depth greater than 100 m. The standard deviation is always much less than one order of magnitude of the mean value and is not shown for clarity.

winter, since the nearshore temperature is low throughout the shallow water column and winds strongest at the coast. On the other hand, waters are strongly stratified in summer whenever impacted by the abundant riverine output (Morey et al., 2003).

Patterns of salinity gradients, stratification and vorticity at the mesoscales remain considerably similar across ensembles, as seen in **Supplementary Figure 1** for the corresponding quantities in the MR ensembles, and in SBL21 for further comparisons of predictability skills.

Spatial Patterns of Low-Salinity Waters

Figure 4 shows the monthly averaged spatial patterns of the freshwater spreading area and normalized volume, or thickness in 2015, together with the sea surface height anomaly (SSHa) contours across the different ensembles. Again, the freshwater is identified by 34 psu isohaline. Sea SSHa contours of 0.17, 0.4, and 0.6 m outline major anticyclonic features, and the 0.17 m threshold is assumed to identify the boundary of the LC and LC eddies in the GoM following previous literature (Leben and Born, 1993; Donohue et al., 2016; Hamilton et al., 2016). In winter, westward/southward wind-driven coastal currents carry low salinity water over the LATEX shelf. During the summer, two branches of low salinity water can be present and transported eastward in the northern GoM. The first branch represents the portion of pre-existing waters on the LATEX shelf transported along-shore, which is also present in the no-river case. The second branch originates mainly from the MARS and moves eastward onto the MAFLA shelf, the West Florida shelf or is advected into the Gulf interior by the intrusion of the LC and the Rings. Finally, in August parcels of low salinity waters can be seen trapped in the cyclonic recirculation between the large anticyclonic patters (LC and Rings) and they are more relevant in the SP-active case than in the other ensembles. The trapping of low salinity waters between two mesoscale anticyclonic structures has been pointed by Androulidakis et al. (2019) as a secondary mechanism of freshwater removal by the LC eddies. The SSHa patterns are overall similar among different ensembles. Quantification of the differences is presented in SBL21, where it is found that the LC has a statistically significant lower probability to extend northward of 28°N in the SP integrations with an active river configuration, compared to the other cases.

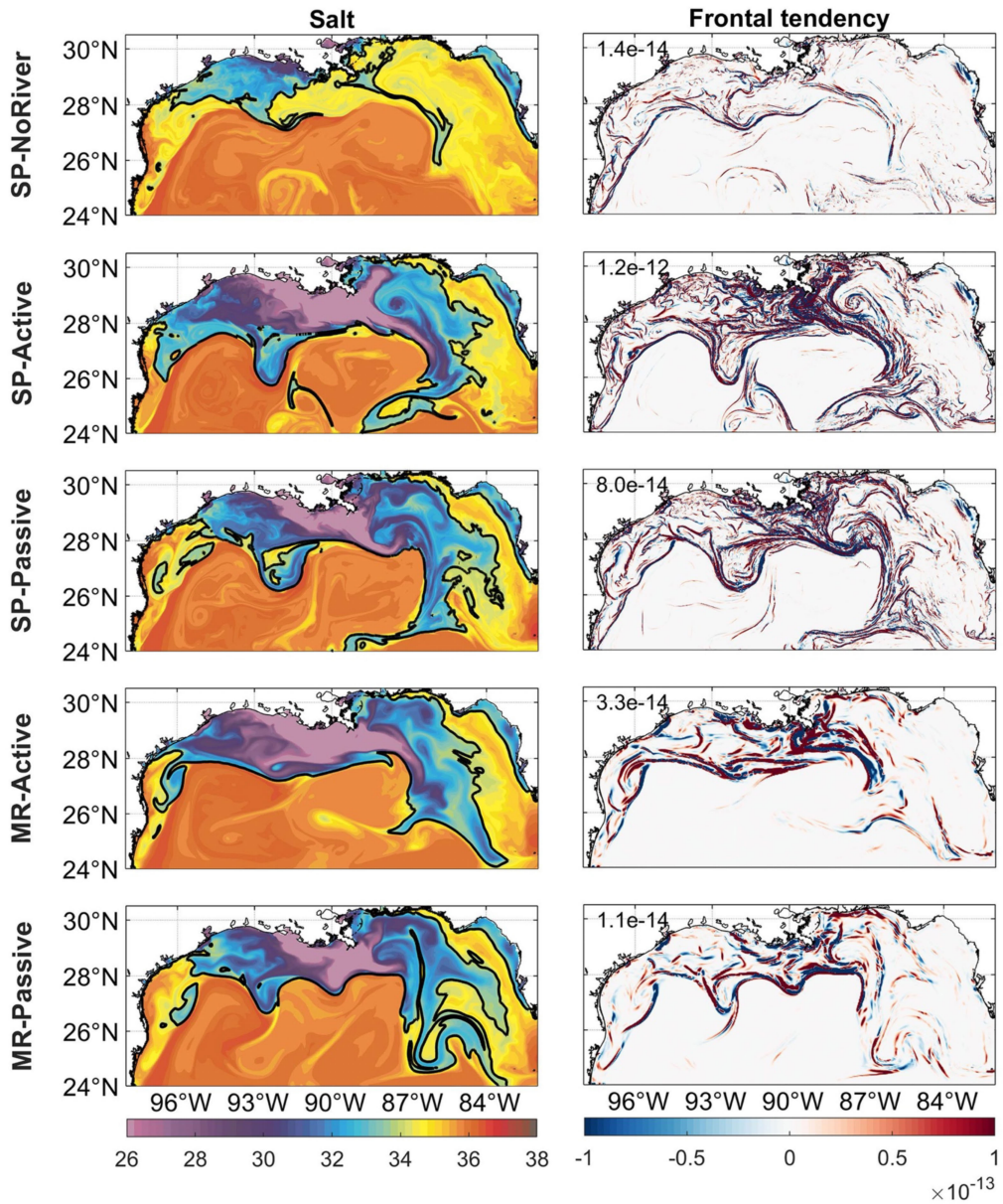

FIGURE 6 | Instantaneous surface salinity and frontal tendency on August 05, 2015 in the first member of each of the 5 ensembles 5 months after initialization. Domain-averaged values for *F* are indicated in each plot. Black contours in salinity fields indicate 34 psu.

In terms of salinity, the modeled freshwater spatial distribution is modestly affected by the setup of river forcing. This is the case although Morey et al. (2003) have demonstrated that the variability in river discharge does not control, but only modulate, the seasonal salinity patterns in the GoM, with the LCS being a player at least as important. In our simulations, both the spreading area and volume are small in the no-river case, as to be expected, and maximum values are achieved in the active river simulations. The role of small differences in LCS are most evident in comparing the SP passive and active cases and their salinity distribution in August 2015. The extension of the LC, which is slightly different among the two cases, modifies the pathway of the Mississippi River water pushing it further east in the passive case.

Interannual and Seasonal Variability in Freshwater Plume

To quantify the different behaviors in the transport pathways and transport efficiency, we calculated the time-series of freshwater spreading area and volume, shown in **Figure 5**. We excluded from the calculation coastal areas where the water column depth is less than 100 m given that differences could be driven by river

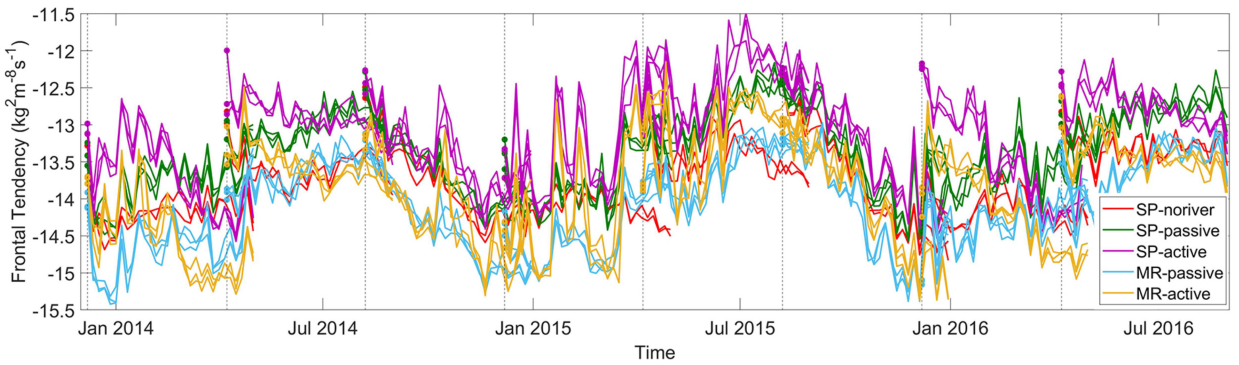

FIGURE 7 | Time series of frontal tendency (in log scale) over the 8 integration periods in all the members of the 5 ensembles averaged over the model domain for which the water column is deeper than 100 m.

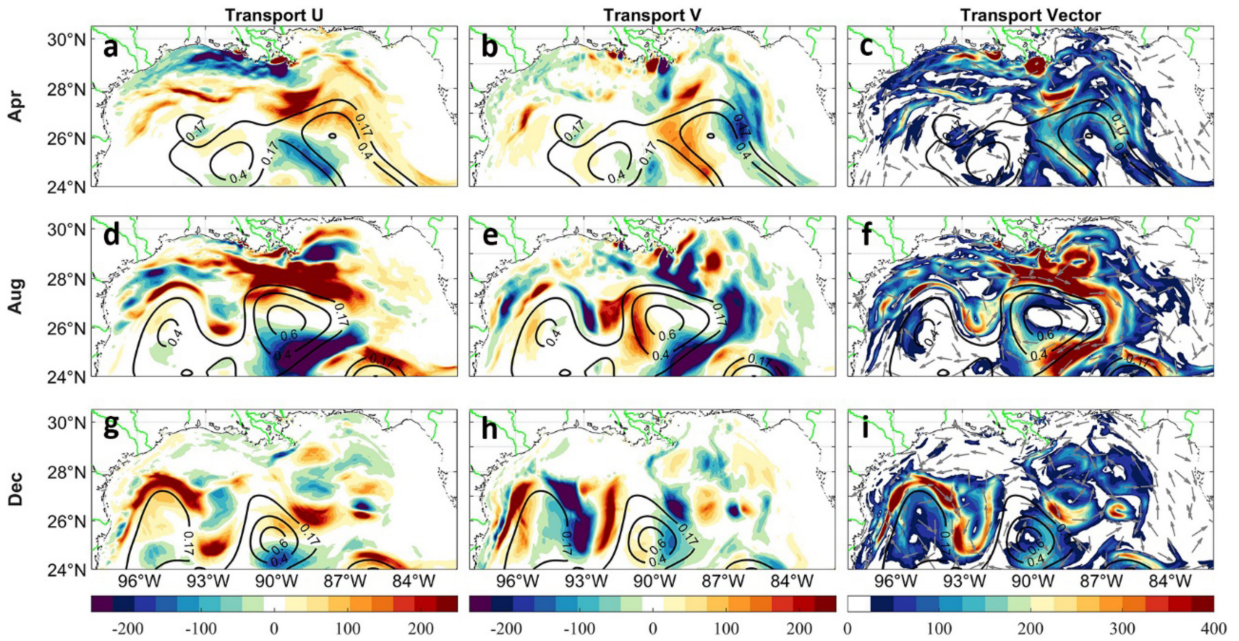

FIGURE 8 | Monthly averaged freshwater zonal **(a,d,g)** and meridional **(b,e,h)** transport, as well as the transport vector **(c,f,i)** integrated over the upper 100 m in April, August, and December, 2015. The fields are obtained from the first member of the SP active ensemble. Units: m^3/s. Contours show monthly averaged SSHa.

configuration choices in the immediate surrounding of the river mouths. This arbitrary threshold excludes all areas impacted by the modified precipitation fluxes where waters may stagnate in conditions of low winds. The Mississippi River mouth represents the exception, but its freshwater is rapidly transported offshore or to the west in both passive and active cases. We varied the threshold and tested values between 50 and 200 m and results do not change qualitatively.

Interannual changes are generally larger than the differences among different ensembles. As a reminder, for each 5-months long simulation period, the integrations share the atmospheric forcing and start from similar initial conditions (1-day apart). The freshwater area coverage tends to be low in winter, except for 2016, reaches $\sim$2–3 $\times$ 10^{11} m^2 during summer, and drops to less than 10^{11} m^2 in November of 2014 and 2015. The freshwater volume follows an analogous evolution with comparable seasonality. The largest area and volume of low-salinity waters occur in the summer of 2015. Moreover, relatively lower freshwater coverage but comparable to 2015 freshwater volume is found in August 2016, implying that low salinity waters reached deeper than in other summers, because the larger fluxes occurred earlier in the year (**Figure 1**), when the MLD was deeper. In the 2016 summer the introduction of freshwater in the basin due to extreme precipitation events, which is illustrated by the increasing freshwater area and volume in the no-river case, is also a noticeable occurrence.

Differences among ensembles are small. The MR and SP runs have similar LCS representations and identical river forcing,

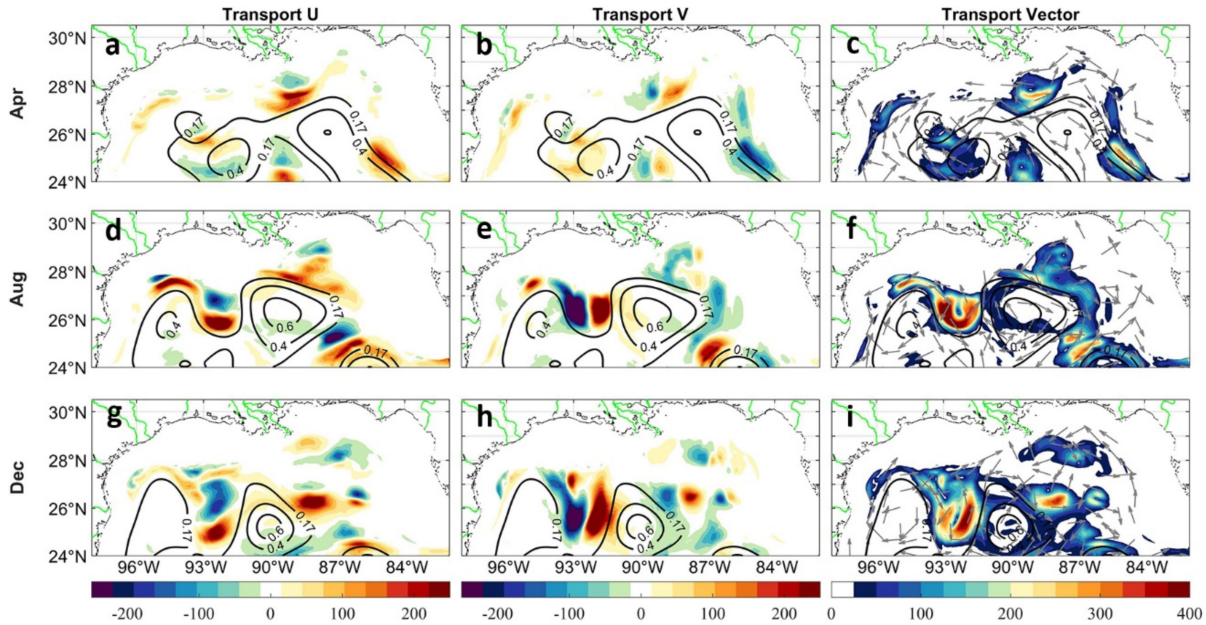

FIGURE 9 | Monthly averaged freshwater zonal **(a,d,g)** and meridional **(b,e,h)** transport, as well as the transport vector **(c,f,i)** integrated between 100 and 200 m in April, August, and December 2015. The fields are obtained from the first member of the SP active ensemble. Units: m^3/s.

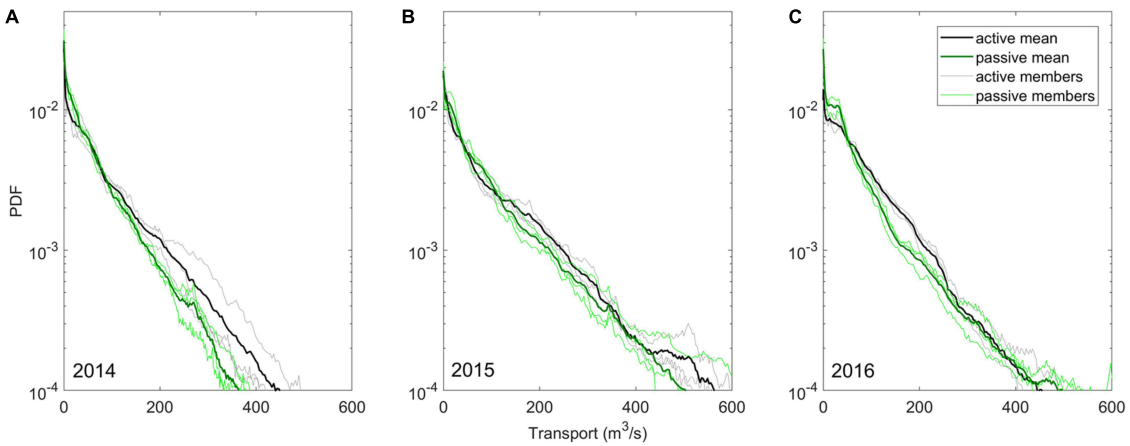

FIGURE 10 | Probability density functions (PDFs) of active and passive transport ensembles for August of 2014 **(A)**, 2015 **(B)**, and 2016 **(C)**.

and the freshwater spreading evolves similarly over time. In the active river configuration the velocity flux associated with the freshwater input contributes to a slightly greater spread compared to the passive set-up. Differences are larger whenever the freshwater discharge is high, as verified during winter/spring 2016 and more generally in the summer season.

The freshwater spreading is a near-surface process strongly affected by the upper-layer circulation dynamics. During late spring and summer the submesoscale circulations tend to further aid spreading in the SP simulations. In these seasons the prevailing submesoscale features are in the form of density fronts with horizontal advective tendency induced by confluence and convergence (Wang et al., 2021) that contribute to the transport of the riverine water. Indeed, in summer the discrepancy between SP and MR simulations is consistent among years. The lateral convergence zones in the submesoscale frontal structures that abound around the LCS (Zhong et al., 2012; D'Asaro et al., 2018) accumulate and distribute freshwater, contributing to the wider extension of riverine inputs. The summer submesoscale contribution is highlighted comparing the instantaneous distributions of surface salinity and frontogenetic tendency, F, defined as $F = \frac{D|\nabla_h \rho|}{Dt} = Q \cdot \nabla_h \rho$ where $\frac{D}{Dt}$ is the total derivative and represents the rate of change ($\frac{Da}{Dt} = \frac{\partial a}{\partial t} + u\frac{\partial a}{\partial x} + v\frac{\partial a}{\partial y}$) and $Q = (Q1, Q2) = -(\frac{\partial u}{\partial x}\frac{\partial \rho}{\partial x} + \frac{\partial v}{\partial x}\frac{\partial \rho}{\partial y}, \ \frac{\partial u}{\partial y}\frac{\partial \rho}{\partial x} + \frac{\partial v}{\partial y}\frac{\partial \rho}{\partial y})$ (Hoskins, 1982;

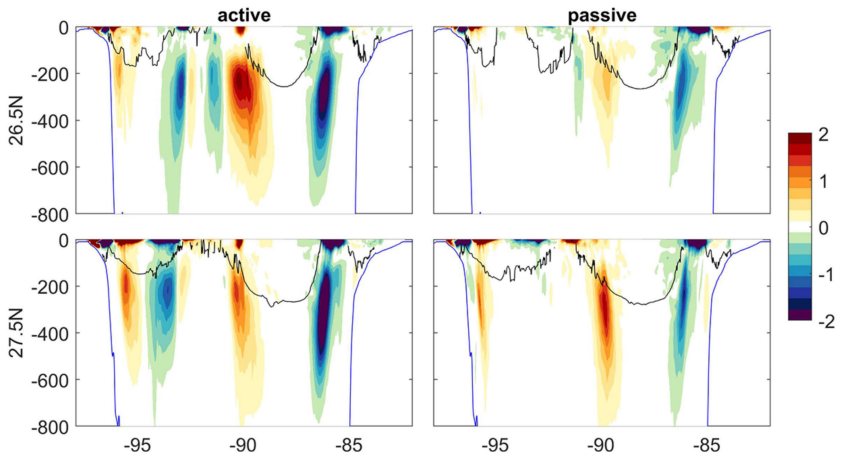

FIGURE 11 | Monthly averaged meridional freshwater transport across different sections in June 2015 in the SP runs, active, and passive. Black line indicates the depth of density 1,026 kg/m^3. Blue line provides the bathymetry information. Units: m^3/s.

Capet et al., 2008) for a day in August 2015 (**Figure 6**). *F*, which is two orders of magnitude greater in the SP-active case compared to the MR-passive one, follows closely the freshwater pathways in all cases.

From late fall to early spring, on the other hand, the mixed-layer is deeper and offshore the continental shelf fronts and filaments can be more easily fragmented by submesoscale instabilities that extract energy from the mixed-layer and generate eddies that restratify the upper water column (Luo et al., 2016). The time evolution of *F* over waters deeper than 100 m is shown in **Figure 7**, where is also evident that within each given ensemble the internal variability is small even at the submesoscales. Given the conbined annual cycle of *F* and mixed-layer depth, the prevailing submesoscale circulations converge material at their interior (D'Asaro et al., 2018), stretching the freshwater patches in filaments less effectively than in summer. Furthermore, in these seasons low-salinity waters flow mostly along the LATEX shelve, due to the prevailing northeasterly and northerly winds and more limited river discharge. The submesoscale eddies and fragmented fronts that occupy waters with a depth greater than $\sim$ 100 m, have negligible impact on the freshwater spread in "normal" winters (2014 and 2015). On the other hand, in 2016, when the river runoff was very abundant and was pushed offshore by the anomalous winds, the submesoscale circulations cause a slight reduction in volume spread compared to the MR case by limiting the mixed-layer extention (Barkan et al., 2017b).

Horizontal and Vertical Transport of Riverine Waters

We next analyze the freshwater transport, *T*, highlighting the riverine water pathways. We do so by adopting the methodology introduced by Schiller et al. (2011) and applied to the GoM in subsequent works (Schiller and Kourafalou, 2014; Androulidakis et al., 2019; Brokaw et al., 2019). The freshwater transport is defined as $T = V \times fw \times dx \times dz$ where *V* is the horizontal velocity with its zonal or meridional components, *dx* is the corresponding space distance, *dz* is the vertical thickness, and *fw* is the freshwater anomaly calculated as $fw = (S_b - S) / S_b$. Here S_b is the background salinity field without the added river discharge (i.e., the mean salinity in no-river cases in this work) and *S* is the salinity field in each of the active or passive runs without any threshold applied. Since *V* and *fw* can be both positive and negative, positive zonal transport can be interpreted as either freshwater moving to the east (both positive) or saltier water moving westward (both negative). In the following we modify *fw* by setting all the negative values to zero in order to select the transport of freshwater. The difference between setting the negative *fw* to zero and considering freshwater anomalies of both signs is shown in **Supplementary Figure 2**, while **Figure 2** and **Supplementary Figure 3** display monthly salinity fields in one of the SP no-river and SP-active members, respectively. We stress that the mesoscale patterns are similar, but necessarily not identical among the runs (see also SBL21), and that the SP no-river ensemble includes contributions from precipitation anomalies in its freshwater budget.

The spatial patterns of freshwater transport integrated over the upper 100 m of the water column in the last month of the 5-month long runs in 2015 are shown in **Figure 8** for the first member of the SP active-river ensemble. Positive values correspond to eastward and northward transport. Anticyclonic (clockwise) freshwater transport greater than 100 m^3/s is detected at the periphery of large anticyclones in summer, especially near the north, east and south boundaries of the LC eddy (**Figure 8**, transport vector). A similar pattern is also observed in winter but with reduced transport associated with it. A small cyclonic eddy (**Figure 3**) with opposite transport can indeed be seen at about 94°W, 25°N during February.

Previous studies on the offshore pathways of freshwater transport in the GoM have focused on the interactions between the LCS and MARS in summer (Schiller and Kourafalou, 2014; Androulidakis et al., 2019; Brokaw et al., 2019), following the peak of riverine discharge. Brokaw et al. (2019) identified three main

pathways in summer by analyzing the surface salinity transport from 2010 to 2018, two of which are captured here and are realized by the relative positions of the LC and LC eddies with respect to the river plume. According to the first pathway, the freshwater is advected eastward from the MAFLA shelf, then southward and finally exits the GoM from the Florida Straits. The second pathway is characterized by narrow freshwater bands surrounding the LC eddies or the LC extension. This recirculation pattern advects the low-salinity waters offshore to the south, then westward and back north toward its source. The third pathway describes conditions when the Rings and the LC do not reach north enough to interact with the river plumes and no detectable interactions between the LCS and the MARS are found. This condition was relevant to portions of 2010 and 2012, when the freshwater remained distributed in the northern part of the basin with decreasing concentrations moving southward and a nearly homogenous gradient, but in the period considered here this third condition is never observed or simulated. On the other hand, a west-to-east offshore transport characterizes the summer of 2015 when two large Rings occupy the central GoM. The smaller cyclonic circulation found at about 93°W and 26°N in August acts as a bridge connecting these two anticyclones and contributes to the lateral transport of nearshore freshwaters from west to east. A similar redistribution pattern is observed also in the other two summers (**Supplementary Figures 4**, **5**).

Our analysis indicates that the influence of the LC system on the offshore transport of freshwater extends to the winter seasons, despite its surface signature being significantly reduced. As mentioned, in winter the surface river discharge is confined to the western coastal regions due to the prevailing northerly and northeasterly winds. The low-salinity waters surrounding the LC and central LC eddies mainly originate from the confluence regions of downcoast inner shelf currents and upcoast outer shelf currents between 26 and 28°N, west of 96°W (Walker et al., 1996; Zavala-Hidalgo, 2003). The offshore transport is sustained by the jet associated with the decaying eddy or a pair of eddies usually found near the coast in this season (Zavala-Hidalgo, 2003), and seen, for example, between 93° and 96°W in **Figure 3**. This long-distance transport mechanism of nearshore, river-influenced waters is evident in April 2015 (**Figure 8**) and occurs also in 2014 and 2016 (**Supplementary Figures 4**, **5**). Another important contribution to winter transport comes from summer coastal waters transported offshore that continue to be advected by the mesoscale field.

To expand our analysis to greater depths and fully encompass the GoM deep chlorophyll maximum located at around 100 m (e.g., Pasqueron de Fommervault et al., 2017) and the whole euphotic layer, we extended the computation of the integrated freshwater transport between 100 and 200 m (**Figure 9**). This calculation is relevant for the primary productivity of the basin being riverine water the main contributor to its nitrogen and phosphorus balance. Below 100 m the freshwater transport follows the boundary of the Rings and LC, with a pattern similar to that of the upper layer but overall decreased magnitude. Significantly enhanced values occur also inside/around cyclonic structures that are part of the LCS, which in August 2015 can be seen at about 94°W and 25°N in February and 93°W and 26°N.

Transport patterns and overall intensity are slightly greater in active runs than in passive configurations. This is quantified in **Figure 10**, where the probability density function of the transport vector is plotted for the month of August in all 3 years and two SP ensembles. Differences are small but robust, and corroborate the volume differences in low salinity waters quantified in **Figure 5**. Indeed, if the tails of the distributions are similar once the ensemble variability is accounted for, the core indicates greater transport in the active ensemble in the 50–300 m^3/s in all members and all years. In addition, the largest transport rate identified by the flattest slope is detected in 2015 for both active and passive cases, while in 2014, the overall transport rate stays at the lowest level among all 3 years.

Finally, the LCS controls not only the horizontal but also the vertical distribution of freshwater. In the passive configuration, the strength of the subduction around the LC and the Rings is reduced compared to the active runs. This is exemplified in **Figure 11**, where transects taken at latitudes ranging from 26 to 28°N are shown for June 2015. Here the choice of the month is due to the very strong similarity in the LCS in the two members considered. The contour of 1026 kg/m^3 density is used to outline the position of different circulation features. The freshwater can penetrate to depths close to 600 m during summer, approaching the vertical scale of the LCS structures. The most intense vertical penetration is found at the periphery of the Rings. This feature, combined with the fact that meridional currents weaken with depth, contributes to a strong downwelling/subduction of freshwater into the deep ocean. In the northern portion of the basin, where the LC and the Rings do not intrude, the freshwater transport below the mixed layer is modest or null.

CONCLUSION

In this work we investigated the three-dimensional pathway and offshore transport of low-salinity riverine outflow in the GoM over a nearly 3-year period, using regional ocean simulations at mesoscale resolving and submesoscale permitting resolution. We extended previous studies that focused on the offshore removal process of near-surface freshwater from the MARS by exploring the intraseasonal variability of the offshore water transport. We considered simulations with different river configurations, ranging from no river inflow (no-river), to a passive configuration in which the riverine fluxes are converted to precipitation and are applied to an area extending offshore about 50 km from the river mouth, and finally to an active configuration with a point-source southward volume flux added at the mouth of each river. The passive configuration is usually preferred and has been used in several recent works showing realistic offshore extension of low-salinity waters in the GoM (Barkan et al., 2017a; Liu et al., 2021). However, the active configuration proves that converting the river discharge to a vertically decaying volume flux can increase the amount of riverine water that reaches offshore in the model runs, and its vertical extent.

It is well documented that river discharge that originated from the MARS interacts with the LC system in the summer season (Morey et al., 2003; Schiller et al., 2011;

Schiller and Kourafalou, 2014; Androulidakis et al., 2019; Brokaw et al., 2019). During summer, the intrusions of the anticyclonic LC eddies entrain at their periphery freshwater from the river-influenced regions and move it toward the Gulf interior. These low-salinity waters are then transported either eastward by the LC and can exit through the Florida Straits, or westward to the central Gulf by the LC eddies. We showed that in winter the lateral transport of nearshore waters from confluence regions over the western shelf is the dominant pathway, but the southward transport of MARS waters by the LC eddies remains significant while less notable since the mixed-layer is deeper, the surface signature consequently less evident, and the amount of involved freshwater generally smaller (**Figure 7**).

Our analysis also provides evidence that the freshwater transport surrounding the LC and LC eddies penetrates as deep as $\sim$ 600 m. The low-salinity subduction processes are most prominent around the Rings and in the cyclonic circulations commonly generated when the LC eddies detach from the main current (**Figures 8**, **10**).

On interannual timescales, the rainfall over the continental United States and the LC dynamics modulate the offshore reach of the riverine input in spring to fall, while the ENSO-induced co-variability of salinity and coastal currents in the northern GoM (Gomez et al., 2019) is the major player in winter (Munoz and Dee, 2017). Particularly, El Niño events are linked to large positive precipitation anomalies in late fall and winter, and declining values from spring onward (Lee et al., 2014, 2018). This rainfall anomaly and the associated storminess tendency that co-occur with strong El Niños, contributed to the extensive three-dimensional spread of low-salinity waters in the winter of 2016. The waters of riverine origin were more abundant and also transported to greater depths in spring 2016 compared to the spring in the other 2 years.

In addition to the dominant mesoscale LC circulations, we discussed the role of submesoscale motions in modulating the transport and distribution of freshwater in the GoM. Generally, the intensified submesoscale fronts accumulate, stretch and advect the freshwater plume (Zhong et al., 2012; D'Asaro et al., 2018). Given their abundance in the summer season, higher values of freshwater spreading area and volume are found in the SP cases in summer, following the maximum river runoff, when both mesoscale and submesoscale currents have the strongest influence on the distribution of low-salinity waters. The difference, however, is contained between 3 and 14% in area, and between 0 and 10% in volume for the offshore portion of the domain. In 2016, when the riverine inflow was large also in winter, the restratification by submesoscale eddies had a small but negative impact on the freshwater spreading, so that the overall freshwater volume found offshore is greater in the mesoscale resolving run.

In the vertical direction, submesoscale dynamics can significantly increase the vertical velocity and mixing rate within the mixed layers (Thomas and Ferrari, 2008; Thomas et al., 2008; Zhong and Bracco, 2013; Callies et al., 2015; Liu et al., 2018, 2021), and accelerate the subduction process of low-salinity waters as a result. Their offshore contribution, however, is limited in summer by the mixed-layer depth (Liu et al., 2021). As a result, the subduction in this season is mostly driven by the mesoscale circulations with comparable efficiency in the MR and SP ensembles.

Overall, differences are robust but small, with the submesoscale permitting resolution and the active river configuration contributing to the offshore spreading by making it slightly more efficient and deep reaching in most seasons. On the other hand, the predictability of offshore spreading of riverine water in all years considered is intrinsically linked to the internal (modeled) variability of the LCS and does not change significantly among ensembles. This is good news for biogeochemistry studies. While submesoscale circulations may impact the distribution and availability of nutrients, their contribution to the offshore redistribution of riverine waters remains small even in presence of very large outflows as in the case of the MARS.

DATA AVAILABILITY STATEMENT

The datasets presented in this study can be found in online repositories. The names of the repository/repositories and accession number(s) can be found below: https://www.dropbox.com/sh/g5sywqcyqog0i8v/AAD2LvGMlCy2rHk-t1zQzHA8a?dl=0.

AUTHOR CONTRIBUTIONS

AB conceived the work. DS performed the simulations. GL conducted the analyses and wrote the first draft. All authors contributed to the interpretation of the results and to the writing of the article, to the article and approved the submitted version.

FUNDING

This work was supported by the Gulf Research Program (GRP) of the National Academies of Sciences, Engineering, and Medicine through its Understanding Gulf Ocean Systems 2 (UGOS-2) Grant "The Loop Current and the Mississippi-Atchafalaya River System: Interactions, Variability, and Modeling Requirements." GL and AB were partially supported by the National Science Foundation (OCE - 1658174).

SUPPLEMENTARY MATERIAL

The Supplementary Material for this article can be found online at: https://www.frontiersin.org/articles/10.3389/fmars.2022.841900/full#supplementary-material

REFERENCES

Androulidakis, Y., Kourafalou, V., Le Hénaff, M., Kang, H., Sutton, T., Chen, S., et al. (2019). Offshore spreading of Mississippi Waters: pathways and vertical structure under eddy influence. *J. Geophys. Res.* 124, 5952–5978. doi: 10.1029/2018jc014661

Barkan, R., McWilliams, J. C., Shchepetkin, A. F., Molemaker, M. J., Renault, L., Bracco, A., et al. (2017a). Submesoscale dynamics in the Northern Gulf of Mexico. Part I: Regional and seasonal characterization and the role of river outflow. *J. Phys. Oceanogr.* 47, 2325–2346. doi: 10.1175/jpo-d-17-0035.1

Barkan, R., McWilliams, J. C., Molemaker, M. J., Choi, J., Srinivasan, K., Shchepetkin, A. F., et al. (2017b). Submesoscale dynamics in the Northern Gulf of Mexico. Part II: Temperature–salinity relations and cross-shelf transport processes. *J. Phys. Oceanogr.* 47, 2347–2360. doi: 10.1175/jpo-d-17-0040.1

Bracco, A., Liu, D., and Sun. (2019). Mesoscale-submesoscale interactions in the Gulf of Mexico: From oil dispersion to climate. *Chaos Solitons Fract.* 119, 63–72.

Brokaw, R. J., Subrahmanyam, B., and Morey, S. L. (2019). Loop Current and eddy-driven salinity variability in the Gulf of Mexico. *Geophys. Res. Lett.* 46, 5978–5986. doi: 10.1029/2019gl082931

Cai, Z., and Gan, J. (2017). Formation and dynamics of a long-lived eddy train in the South China Sea: a modeling study. *J. Phys. Oceanogr.* 47, 2793–2810. doi: 10.1175/JPO-D-17-0002.1

Callies, J., Ferrari, R., Klymak, J. M., and Gula, J. (2015). Seasonality in submesoscale turbulence. *Nat. Commun.* 6:6862. doi: 10.1038/ncomms7862

Capet, X., McWilliams, J. C., Molemaker, M. J., and Shchepetkin, A. F. (2008). Mesoscale to submesoscale transition in the California Current System. Part II: Frontal processes. *J. Phys. Oceanogr.* 38, 44–64. doi: 10.1175/2007JPO3672.1

Cardona, Y., Ruiz-Ramos, D. V., Baums, I. B., and Bracco, A. (2016). Potential connectivity of coldwater black coral communities in the northern Gulf of Mexico. *PLoS One* 11:e0156257. doi: 10.1371/journal.pone.015625

Childers, D. L., Day, J. W., and Muller, R. A. (1990). Relating climatological forcing to coastal water levels in Louisiana estuaries and the potential importance of El Nino-Southern Oscillation events. *Clim. Res.* 1, 31–42.

Choi, J., Bracco, A., Barkan, R., Shchepetkin, A. F., McWilliams, J. C., and Molemaker, J. (2017). Submesoscale dynamics in the northern Gulf of Mexico. Part III: Lagrangian implications. *Phys. Ocean* 47, 2361–2376.

Cummings, J. A. (2005). Operational multivariate ocean data assimilation. *Q. J. Roy. Meteorol. Soc.* 131, 3583–3604. doi: 10.1256/qj.05.105

Cummings, J. A., and Smedstad, O. M. (2013). "Variational data assimilation for the global ocean," in *Data Assimilation for Atmospheric, Oceanic and Hydrologic Applications (Vol. II)*, eds S. K. Park and L. Xu (Berlin: Springer Berlin Heidelberg), 303–343. doi: 10.1007/978-3-642-35088-7_13

da Silva, C. E., and Castelao, R. M. (2018). Mississippi River plume variability in the Gulf of Mexico from SMAP and MODIS-Aqua observations. *J. Geophys. Res.* 123, 6620–6638. doi: 10.1029/2018JC014159

D'Asaro, E. A., Shcherbina, A. Y., Klymak, J. M., and Molemaker, J. (2018). Ocean convergence and the dispersion of flotsam. *Proc. Natl. Acad. Sci. U.S.A.* 115:1162. doi: 10.1073/pnas.1718453115

Debreu, L., Marchesiello, P., Penven, P., and Cambon, G. (2012). Two-way nesting in split-explicit ocean models: Algorithms, implementation and validation. *Ocean Model.* 4, 1–21. doi: 10.1016/j.ocemod.2012.03.003

Debreu, L., Vouland, C., and Blayo, E. (2008). AGRIF: Adaptive grid refinement in Fortran. *Comput. Geosci.* 34, 8–13. doi: 10.1016/j.cageo.2007.01.009

Donohue, K. A., Watts, D. R., Hamilton, P., Leben, R., and Kennelly, M. (2016). Loop Current Eddy formation and baroclinic instability. *Dynam. Atmosph. Oceans* 76, 195–216. doi: 10.1016/j.dynatmoce.2016.01.004

Feng, Y., Menemenlis, D., Xue, H., Zhang, H., Carroll, D., Du, Y., et al. (2021). Improved representation of river runoff in Estimating the Circulation and Climate of the Ocean Version 4 (ECCOv4) simulations: implementation, evaluation, and impacts to coastal plume regions. *Geosci. Model. Dev.* 14, 1801–1819. 2021 doi: 10.5194/gmd-14-1801-2021,

Fournier, S., Reager, J. T., Dzwonkowski, B., and Vazquez-Cuervo, J. (2019). Statistical mapping of freshwater origin and fate signatures as land/ocean "regions of influence" in the Gulf of Mexico. *J. Geophys. Res. Oceans* 124, 4954–4973. doi: 10.1029/2018jc014784

Gomez, F. A., Lee, S. K., Hernandez, F. J. Jr., Chiaverano, L. M., Muller-Karger, F. E., Liu, Y., et al. (2019). ENSO-induced co-variability of salinity, plankton biomass and coastal currents in the Northern Gulf of Mexico. *Scient. Rep.* 9:178. doi: 10.1038/s41598-018-36655-y

Gordon, A. (1967). Circulation of the Caribbean Sea. *J. Geophys. Res.* 72, 6207–6223.

Hamilton, P. (2009). Topographic Rossby waves in the Gulf of Mexico. *Progr. Oceanogr.* 82, 1–31. doi: 10.1016/j.pocean.2009.04.019

Hamilton, P., Lugo-Fernández, A., and Sheinbaum, J. (2016). A Loop Current experiment: Field and remote measurements. *Dynam. Atmosph. Oceans* 76, 156–173. doi: 10.1016/j.dynatmoce.2016.01.005

Horner-Devine, A. R., Hetland, R. D., and MacDonald, D. G. (2015). Mixing and transport in coastal river plumes. *Annu. Rev. Fluid Mech.* 47, 569–594.

Hoskins, B. J. (1982). The Mathematical theory of frontogenesis. *Annu. Rev. Fluid Mech.* 14, 131–151. doi: 10.1146/annurev.fl.14.010182.001023

Hu, C., Nelson, J. R., Johns, E., Chen, Z., Weisberg, R. H., and Müller-Karger, F. E. (2005). Mississippi River water in the Florida Straits and in the Gulf Stream off Georgia in summer 2004. *Geophys. Res. Lett.* 32:14. doi: 10.1029/2005gl022942

Huntley, H. S., Lipphardt, B. L., Jacobs, G., and Kirwan, A. D. (2015). Clusters, deformation, and dilation: Diagnostics for material accumulation regions. *J. Geophys. Res.* 120, 6622–6636. 1002/ 2015j c0110 36 doi: 10

Justic, D., Kourafalou, V., Mariotti, G., He, S., and Weisberg, R. (2021). A review of transport processes in the Gulf of Mexico along the river-estuary-shelf-ocean continuum: a synthesis of research from the Gulf of Mexico Research Initiative. *Estuar. Coasts.* 5, 1–37. doi: 10.1007/s12237-021-01005-1

Kobashi, D., and Hetland, R. (2020). Reproducibility and variability of submesoscale frontal eddies on a broad, low-energy shelf of freshwater influence. *Ocean Dynam.* 70, 1377–1395.

Krug, A. (1993). Drainage history and land use pattern of a Swedish river system – their importance for understanding nitrogen and phosphorus load. *Hydrobiologia* 251, 285–296.

Large, W. G., McWilliams, J. C., and Doney, S. C. (1994). Oceanic vertical mixing: A review and a model with a nonlocal boundary layer parameterization. *Rev. Geophys.* 32, 363–403. doi: 10.1029/94RG01872

Leben, R. R., and Born, G. H. (1993). Tracking Loop Current eddies with satellite altimetry. *Adv. Space Res.* 13, 325–333. doi: 10.1016/0273-1177(93)90235-4

Lee, S.-K., Lopez, H., Chung, E.-S., DiNezio, P., Yeh, S.-W., and Wittenberg, A. T. (2018). On the fragile relationship between El Niño and California rainfall. *Geophys. Res. Lett.* 45, 907–915. doi: 10.1002/2017GL076197

Lee, S.-K., Mapes, B. E., Wang, C., Enfield, D. B., and Weaver, S. J. (2014). Springtime ENSO phase evolution and its relation to rainfall in the continental U.S. *Geophys. Res. Lett.* 41, 1673–1680. doi: 10.1002/2013GL059137

Liu, G., Bracco, A., and Passow, U. (2018). The influence of mesoscale and submesoscale circulation on sinking particles in the northern Gulf of Mexico. *Elementa* 6:36. doi: 10.1525/elementa.292

Liu, G., Bracco, A., and Sitar, A. (2021). Submesoscale mixing across the mixed layer in the Gulf of Mexico. *Front. Mar. Sci.* 8:615066. doi: 10.3389/fmars.2021.615066

Luo, H., Bracco, A., Cardona, Y., and McWilliams, J. C. (2016). The submesoscale circulation in the Northern Gulf of Mexico: Surface processes and the impact of the freshwater river input. *Ocean Model.* 101, 68–82. doi: 10.1016/j.ocemod.2016.03.003

Mason, O. U., Canter, E. J., Gillies, L. E., Paise, T. K., and Roberts, B. J. (2016). Mississippi River Plume Enriches Microbial Diversity in the Northern Gulf of Mexico. *Front. Microbiol.* 7:1048. doi: 10.3389/fmicb.2016.01048

McWilliams, J. C. (2008). Fluid dynamics at the margin of rotational control. *Environ. Fluid Mech.* 8, 441–449. doi: 10.1007/s10652-008-9081-8

Morey, S. L., Martin, P. J., O'Brien, J. J., Wallcraft, A. A., and Zavala-Hidalgo, J. (2003). Export pathways for river discharged fresh water in the northern Gulf of Mexico. *J. Geophys. Res.* 108:3303. doi: 10.1029/2002jc001674

Munoz, S. E., and Dee, S. G. (2017). El Niño increases the risk of lower Mississippi River flooding. *Scient. Rep.* 7:1772. doi: 10.1038/s41598-017-01919-6

Pasqueron de Fommervault, O., Perez-Brunius, P., Damien, P., Camacho-Ibar, V. F., and Sheinbaum, J. (2017). Temporal variability of chlorophyll distribution in the Gulf of Mexico: bio-optical data from profiling floats. *Biogeosciences* 14, 5647–5662. doi: 10.5194/bg-14-5647-2017

Poje, A. C., Özgökmen, T. M., Lipphardt, B. L. Jr., and Haus, B. K. (2014). Submesoscale dispersion in the vicinity of the Deepwater Horizon spill. *Proc. Natl. Acad. Sci. U.S.A.* 111:12693. doi: 10.1073/pnas.1402452111

Renault, L., Molemaker, M. J., Gula, J., Masson, S., and McWilliams, J. C. (2016). Control and stabilization of the Gulf Stream by oceanic current interaction with the atmosphere. *J. Phys. Oceanogr.* 11, 3439–3453.

Schiller, R. V., and Kourafalou, V. H. (2014). Loop Current impact on the transport of Mississippi River Waters. *J. Coastal Res.* 298, 1287–1306. doi: 10.2112/jcoastres-d-13-00025.1

Schiller, R. V., Kourafalou, V. H., Hogan, P., and Walker, N. D. (2011). The dynamics of the Mississippi River plume: Impact of topography, wind and offshore forcing on the fate of plume waters. *J. Geophys. Res.* 116:C06029. doi: 10.1029/2010jc006883

Schimidt, N., Lipp, E. K., Rose, J. B., and Luther, M. E. (2001). ENSO influences on seasonal rainfall and river discharge in Florida. *J. Clim.* 14, 615–628.

Shchepetkin, A. F., and McWilliams, J. C. (2003). A method for computing horizontal pressure-gradient force in an oceanic model with a nonaligned vertical coordinate. *J. Geophys. Res.* 108:3090. doi: 10.1029/2001JC001047

Shchepetkin, A. F., and McWilliams, J. C. (2011). Accurate Boussinesq oceanic modeling with a practical, "Stiffened" Equation of State. *Ocean Model.* 38, 41–70. doi: 10.1016/j.ocemod.2011.01.010

Sikirić, M. D., Janeković, I., and Kuzmić, M. (2009). A new approach to bathymetry smoothing in sigma-coordinate ocean models. *Ocean Model.* 29, 128–136. doi: 10.1016/j.ocemod.2009.03.009

Smith, W. H. F., and Sandwell, D. T. (1997). Global sea floor topography from satellite altimetry and ship depth soundings. *Science* 277, 1956–1962. doi: 10.1126/science.277.5334.1956

Sun, D., Bracco, A., and Liu, G. (2021). The role of freshwater forcing on surface predictability in the Gulf of Mexico. *J. Geoph. Res. Oceans* arXiv:2112.10309 [preprint].

Thomas, L., and Ferrari, R. (2008). Friction, frontogenesis, and the stratification of the surface mixed layer. *J. Phys. Oceanogr.* 38, 2501–2518. doi: 10.1175/2008jpo3797.1

Thomas, L., Tandon, A., and Mahadevan, A. (2008). Submesoscale processes and dynamics. Ocean Modeling in an Eddying Regime, Geophys. Monogr. *A. Geophys.* 177, 17–38. doi: 10.1029/177GM04

Walker, N. D., Huh, O. K., Rouse, L. J. Jr., and Murray, S. P. (1996). Evolution and structure of a coastal squirt off the Mississippi River delta: Northern Gulf of Mexico. *J. Geophys. Res.* 101, 20643–20655. doi: 10.1029/96JC00919

Walker, N. D., Rouse, L. J. Jr., Fargion, G. S., and Biggs, D. C. (1994). The Great Flood of summer 1993: Mississippi River discharge studied, *Eos. Transact. Am. Geophys.* 75, 409–415. doi: 10.1029/94EO01045

Wang, T., Barkan, R., McWilliams, J. C., and Molemaker, M. J. (2021). Structure of submesoscale fronts of the Mississippi River Plume. *J. Phys. Oceanogr.* 51, 1113–1131. doi: 10.1175/JPO-D-20-0191.1

Zavala-Hidalgo, J. (2003). Seasonal circulation on the western shelf of the Gulf of Mexico using a high-resolution numerical model. *J. Geophys. Res.* 108:3389. doi: 10.1029/2003jc001879

Zeng, X., Bracco, A., and Tagklis, F. (2021). Dynamical impact of the Mekong River plume in the South China Sea. *Oceans*. Available as arXiv:2112.11252 [preprint].

Zhong, Y., and Bracco, A. (2013). Submesoscale impacts on horizontal and vertical transport in the Gulf of Mexico. *Oceans* 118, 5651–5668. doi: 10.1002/jgrc.20402

Zhong, Y., Bracco, A., and Villareal, T. A. (2012). Pattern formation at the ocean surface: Sargassum distribution and the role of the eddy field. *Limnol. Oceanogr.* 2, 12–27. doi: 10.1215/21573689-1573372

Conflict of Interest: The authors declare that the research was conducted in the absence of any commercial or financial relationships that could be construed as a potential conflict of interest.

Publisher's Note: All claims expressed in this article are solely those of the authors and do not necessarily represent those of their affiliated organizations, or those of the publisher, the editors and the reviewers. Any product that may be evaluated in this article, or claim that may be made by its manufacturer, is not guaranteed or endorsed by the publisher.

Copyright © 2022 Liu, Bracco and Sun. This is an open-access article distributed under the terms of the Creative Commons Attribution License (CC BY). The use, distribution or reproduction in other forums is permitted, provided the original author(s) and the copyright owner(s) are credited and that the original publication in this journal is cited, in accordance with accepted academic practice. No use, distribution or reproduction is permitted which does not comply with these terms.

frontiers in Marine Science

ORIGINAL RESEARCH
published: 21 March 2022
doi: 10.3389/fmars.2022.857594

Shelf Water Export at the Brazil-Malvinas Confluence Evidenced From Combined *in situ* and Satellite Observations

Gaston Manta[1,2], Sabrina Speich[1], Marcelo Barreiro[2], Romina Trinchin[2], Camila de Mello[2], Rémi Laxenaire[1,3] and Alberto R. Piola[4,5,6,7]*

[1] Laboratoire de Météorologie Dynamique, LMD-IPSL, UMR 8539, École Polytechnique, ENS, CNRS, Paris, France, [2] Departamento de Ciencias de la Atmósfera, Facultad de Ciencias, Universidad de la Repuíblica, Montevideo, Uruguay, [3] Laboratoire de L'Atmosphére et des Cyclones (LACy), UMR 8105 CNRS, Météo-France, Université de La Réunion, Paris, France, [4] Facultad de Ciencias Exactas y Naturales, Universidad de Buenos Aires, Buenos Aires, Argentina, [5] Consejo Nacional de Investigaciones Científicas y Técnicas (CONICET), Buenos Aires, Argentina, [6] Departamento Oceanografía, Servicio Hidrografía Naval, Buenos Aires, Argentina, [7] Unidad Mixta Internacional: Instituto Franco-Argentino Sobre Estudios del Clima y sus Impactos, Buenos Aires, Argentina

OPEN ACCESS

Edited by:
William Savidge, University of Georgia, United States

Reviewed by:
Tamaryn Morris, South African Weather Service, South Africa
Anna Rubio, Technology Center Expert in Marine and Food Innovation (AZTI), Spain

***Correspondence:**
Gaston Manta
gaston.manta@lmd.ipsl.fr

Specialty section:
This article was submitted to Coastal Ocean Processes, a section of the journal Frontiers in Marine Science

Received: *18 January 2022*
Accepted: *07 February 2022*
Published: *21 March 2022*

Citation:
Manta G, Speich S, Barreiro M, Trinchin R, de Mello C, Laxenaire R and Piola AR (2022) Shelf Water Export at the Brazil-Malvinas Confluence Evidenced From Combined in situ and Satellite Observations. Front. Mar. Sci. 9:857594. doi: 10.3389/fmars.2022.857594

The Brazil-Malvinas Confluence (BMC) is the region where opposing and intense western boundary currents meet along the Southwestern Atlantic slope at about 38°S, generating one of the most energetic mesoscale regions of the global ocean. Based on shipborne observations acquired within the Uruguayan Economic Exclusive Zone (EEZ), combined with satellite data and an eddy tracking algorithm, we analyze the cross-shelf exchanges during May 2016, when the BMC was in an anomalous northern position. Two types of shelf water export were observed triggered by mesoscale dynamics: one was the export of shallow Rio de la Plata Plume waters driven off-shelf by the retroflection of the Brazil Current. This export formed a 70 km wide, 20 m deep filament that propagated offshore at 0.3 m s^{-1}, with a transport of 0.42 Sv. It lasted about 10 days before being mixed with ambient Confluence waters by strong winds. An additional type of off-shelf transport consisted of a subsurface layer of Subantarctic Shelf Waters (SASW) about 60 m thick that subducted at the BMC reaching 130 m deep and transporting 0.91 ± 0.91 Sv. We show that geostrophic currents derived from satellite altimetry over the slope can be useful to track this subsurface off-shelf export as they are significantly correlated with absolute velocity measurements at this depth. Argo temperature and salinity profiles show evidence of these two types of shelf water export occurring between the BMC front and the separation of the Brazil Current from the shelf-break, suggesting this is a relatively frequent phenomenon, in agreement with previous observations.

Keywords: subsurface shelf water export, cross-shelf exchanges, mesoscale eddies, satellite altimetry, Argo floats, western boundary currents

INTRODUCTION

Western boundary currents (WBCs) and adjacent continental shelves display two distinct circulation regimes separated by a strong vorticity barrier and therefore exhibit distinct water-mass properties and ecosystem composition (Roughan et al., 2011; Franco et al., 2018). Nevertheless, at the separation of WBCs from the shelf-break, the instabilities of the currents generate meanders and eddies that induce strong interactions between the shelf and the deep ocean generating intense cross-shelf exchanges (Arruda and da Silveira, 2019; Ismail and Ribbe, 2019; Malan et al., 2020; Roughan et al., 2022). These cross-shelf exchanges have important consequences for marine life, as they provide nutrients to the oligotrophic deep ocean and offshore advection of larvae from species that live on the shelf (Franco et al., 2017, 2018). Historically, these systems have been difficult to model accurately, due to a combination of numerical constraints such as small-scale highly energetic dynamics over steep and complex topography, and also due to the lack of observations to compare with, making the sampling of these sporadic events very valuable.

In the South Atlantic, the WBCs are the poleward flowing warm and salty south Brazil Current (BC), which is a relatively weak western boundary current associated with the subtropical gyre, and the cold and relatively fresh northward-flowing Malvinas Current (MC), which is a branch of the Antarctic Circumpolar Current (Gordon, 1989). While the BC extends down to about 500 m, the MC presents a predominantly barotropic structure and extends to the bottom (e.g., Vivier and Provost, 1999). Both currents converge along the South American slope at about 38°S at the so-called Brazil-Malvinas Confluence (BMC), generating one of the most energetic mesoscale regions of the global ocean (Chelton et al., 1990). On average, the BC begins to separate from the shelf break at 36.5°S, and the main core of the MC retroflects at about 38.8°S where the 200 and 1,000 m isobaths diverge at Ewing terrace. At that point, the MC is no longer constrained by the topographic steering and retroflects, while a shallow branch of the MC continues northward over the shelf-break (Matano et al., 2010). Between 36.5 and 38.8°S, the ocean area over the slope is characterized by high eddy kinetic energy with changes in current speed and direction (**Figure 1A**). Satellite-derived salinity, *in situ* observations, and modeling studies suggest that this region is also where most of the cross-shelf exchanges in the Southwestern Atlantic take place (Guerrero et al., 2014; Matano et al., 2014; Franco et al., 2018; Berden et al., 2020; Orúe-Echevarría et al., 2021).

The Uruguayan Economic Exclusive Zone (EEZ) is located in the northwestern edge of the Argentine Basin covering the slope between 34.6 and 37.3°S. The EEZ spans an area of about 140×10^3 km^2 (**Figure 1**) and includes part of the region of high kinetic energy and intense cross-shelf exchanges (e.g., Guerrero et al., 2014; Matano et al., 2014; Franco et al., 2018; Berden et al., 2020). The water column over the slope region is characterized by at least six water masses from various sources, a micro-tidal regime, and large seasonal variability. Sea surface temperature (SST) variability presents a seasonal amplitude of 12°C and the wind stress curl reverses seasonally (Piola et al., 2018). Most prominent in the shelf circulation is the northward flow of Subantarctic Shelf Water (SASW) originating from the Patagonia continental shelf (Piola et al., 2000). The northeastward flow of SASW is dynamically controlled by the along-shore wind stress variability (Lago et al., 2021) and in the outer shelf by variations of the intensity of the MC (Matano et al., 2010; Artana et al., 2019). Numerical simulations indicate that in early summer and early winter about 1 Sv of SASW is exported offshore close to the BMC (Franco et al., 2018), while the mid-shelf portion of SASW continues flowing northeastward up to near 32°S. There, SASW meets the subtropical shelf waters (STSW), forming a density compensated front referred to as the Subtropical Shelf Front (Piola et al., 2000). This frontal system extends from the inner shelf at 32°S to the outer shelf near 38.5°S, at the initiation of the BMC (**Figure 1B**; Gordon, 1989; Piola et al., 2000).

A distinct characteristic of the regional shelf circulation is the influence of the discharge of the Rio de la Plata (RdlP) estuary, which drains the second largest hydrological basin in South America (Framiñan et al., 1999; Piola et al., 2005). With a mean outflow of about 25,000 m^{3}s^{-1}, the RdlP significantly dilutes and supplies nutrients to the neighboring shelf waters (Piola et al., 2000). The RdlP buoyant plume, associated with absolute salinities lower than 33.65 g kg^{-1}, presents a strong seasonal variability, with northeastward spreading in austral fall-winter, and southward retraction in summer (Piola et al., 2000). These waters spread over the entire Uruguayan shelf and are often exported to the deep ocean (e.g., Provost et al., 1996; Guerrero et al., 2014). Large interannual variability has also been observed mainly driven by a positive relationship between El Niño Southern Oscillation (ENSO) and precipitation in the RdlP basin during spring, summer and fall (e.g., Grimm et al., 2000; Barreiro, 2010).

The Uruguayan EEZ, although known to be highly variable, is poorly sampled, with historically no national oceanographic research vessel capable of performing full-depth CTD profiles nor underway velocity measurements. During April and May 2016, the Spanish R/V Sarmiento de Gamboa conducted 82 full-depth CTD stations in the Uruguayan EEZ, covering along-slope transects, thus providing ideal measurements to study cross-shelf exchanges. Here we analyze the cruise data, together with other *in situ* and satellite observations and an eddy tracking algorithm, to provide a full water column description of the water masses and circulation, with particular focus on the intense mesoscale variability and cross-shelf exchanges.

DATA

We analyzed the hydrographic data collected by the Spanish R/V Sarmiento de Gamboa cruise conducted between 9 April and 10 May 2016 (henceforth "the cruise"). The sampling consisted of 12 along-shelf transects, separated by approximately 25 km, and a nominal distance between stations of 50 km. The sections were occupied from the deep ocean toward the coast. In this way, an almost regular grid was created over ∼320 km along-slope and 370 km across-slope polygon. In total, 82 full-depth stations (between 18 and 4,147 m) were occupied using a Sea Bird Electronics (SBE) 32 Carousel Water Sampler rosette and a SBE

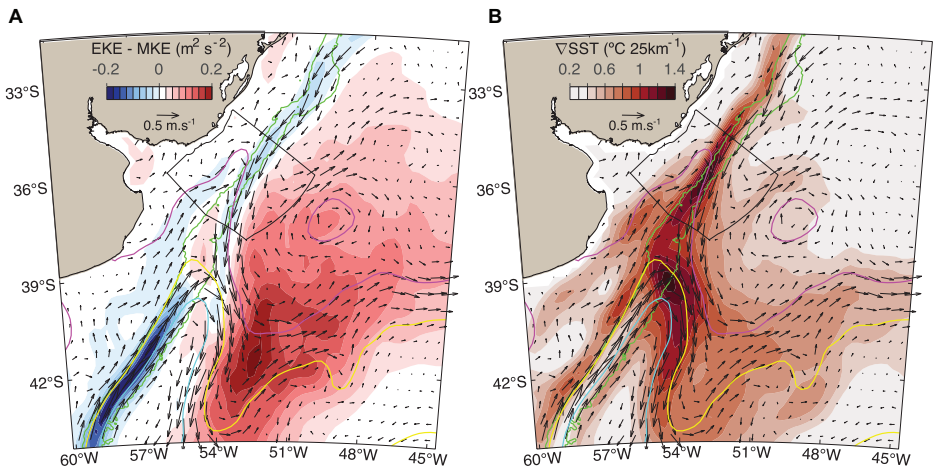

FIGURE 1 | Long-term mean conditions in the Southwestern Atlantic Ocean derived from satellite observations. Both panels show the mean surface geostrophic currents displayed as black arrows, the green lines show the 500 and 2,500 m isobaths, and the 0 m (cyan), 0.25 m (yellow), and 0.5 m (magenta) Absolute Dynamic Topography contours which indicate the retroflection of the main core of the Malvinas Current, the mean confluence position and the separation of the Brazil Current from the shelf-break, respectively. The black polygon delimits the Uruguayan Exclusive Economic Zone (EEZ). Background colors show the long-term daily mean of **(A)** eddy kinetic energy (EKE) minus mean kinetic energy (MKE) and **(B)** SST gradient.

911 plus Conductivity, Temperature and Depth (CTD) profiler, fitted with a SBE43 oxygen sensor and an ECO-AFL/FL Wet Labs Fluorometer. The CTD was fitted with dual temperature and conductivity sensors. Water samples for salinity, dissolved oxygen, nutrients and chlorophyll-a determination were taken in all odd-numbered transects at 5 m depth, and at additional depths depending on the maximum station depth. Two additional water samples were collected within the euphotic depth for chlorophyll-a, and for nutrients at 100, 500, 1,000, and 1,500 m, and near the bottom when the station depth allowed it. At stations shallower than 100 m, a mid-depth sample was collected. The CTD sensors were laboratory calibrated in April 2015. In addition, salinity and dissolved oxygen were calibrated based on the water samples collected during the cruise.

Additionally, underway measurements of temperature, salinity and fluorescence were sampled at 1 min intervals using a Sea-Bird SEACAT SBE 21 Thermosalinograph (TSG) and a Turner 10 fluorescence system. Temperature and salinity from the TSG were calibrated with the nearest CTD measurements. Wind measurements, air temperature, and humidity were also collected underway at about 10 m above the sea surface with a Geonica Meteodata automatic weather station. A hull-mounted Teledyne RD Ocean Surveyor Acoustic Doppler Current Profiler (ADCP) operating at a frequency of 75 and 150 kHz recorded underway ocean currents with 16 m and 8 m depth bins, starting at 10 m and reaching up to 700 and 400 m depth, respectively. The ADCP was operated at 75 kHz over the deep ocean and at 150 kHz over the shelf, recording one profile approximately every 1 min.

Turbidity from water samples was determined on board with a Multiparameter Senso Direct 150 Lovibond. *In situ* chlorophyll-a was also determined on board by acetone extraction and fluorometer reading following Yentsch and Menzel (1963). Fluorescence values from the TSG were calibrated using 32 measurements of chlorophyll-a from water samples collected at 5 m depth by empirically computing a scale factor to minimize the root square mean error. Fluorescence values from the CTD were previously adjusted with a "dark offset" calculation for each profile, by subtracting the mean value of the aphotic zone in values deeper than 200 m to each profile. The adjusted chlorophyll-a data compare well and are significantly correlated (**Supplementary Figure 1**), although absolute values of chlorophyll-a are out of the scope of this study, which focuses on identifying low and high-productivity regions. Water samples for nutrients were fixed on board and measured at the Institute of Marine Sciences (ICM-CSIC) in Barcelona, Spain. At the laboratory nitrate, nitrite, and phosphate concentration were determined using a Seal Analytical MT19 Auto Analyzer with the colorimetric technique and an automated system by continuous flow analysis applying the methodology of Grasshoff et al. (2009).

To complement the cruise hydrographic data we used all Argo profiles available for the Southwestern Atlantic between 32–42°S and 58–49°W (Argo, 2021). Moreover, to gather more information on the regional dynamics, we use satellite data sets with daily resolution: (I) (SST with 0.25° horizontal resolution from the National Oceanic and Atmospheric Administration Optimum Interpolation Sea Surface Temperature for analyzing the long-term characteristics between 1993 and 2019 (OI SST V2; Reynolds et al., 2007), (II) The Multi-scale Ultra-high Resolution (MUR) SST analysis (Chin et al., 2017). This data set has a horizontal resolution 0.01°, making it more useful to identify (sub) mesoscale structures. These data are only available since 2002 and were therefore only used to study the variability of SST within the period of the cruise; (III) Surface chlorophyll-a concentration L4 (gridded and gap-filled) product from Marine Copernicus (CMEMS) with 4 km resolution (Garnesson et al., 2019) within the period of the cruise; (IV) L4 Sea Surface Salinity (SSS) v03.21 from the European Space Agency Sea Surface

Salinity Climate Change Initiative consortium at 50 km and a weekly resolution, spatially sampled on a 25 km EASE (Equal-Area Scalable Earth) grid and 1 day of time sampling. This dataset combines the satellite measurements from SMOS, SMAP, and Aquarius covering the period January 2010–September 2020 (see Boutin et al., 2021); (V) Ssalto/Duacs Multimission Altimeter derived absolute dynamic topography (ADT) and derived surface geostrophic velocity fields at a 0.25° horizontal grid for the period 1993–2019 distributed by CMEMS (Capet et al., 2014; Pujol et al., 2016). This latter dataset is also used as input for the Tracked Ocean Eddies (TOEddies) automatic detection algorithm developed by Chaigneau et al. (2011), Pegliasco et al. (2015) and Laxenaire et al. (2018, 2019, 2020). The TOEddies algorithm detects eddies as ADT extrema, corresponding to the center of an eddy, within closed ADT contours. By restricting the detection to eddies large enough to be in geostrophic equilibrium, these ADT contours correspond to streamlines and the largest closed contour is identified as the eddy boundary. Eddies are then tracked over time by computing their surface overlap over time taking advantage of their large size relative to their daily displacement. A detailed description of TOEddies can be found in Laxenaire et al. (2018).

Furthermore, we used ETOPO1 bathymetry with 1 min (about 2 km) horizontal resolution (Amante and Eakins, 2009). Finally, we also accounted for the daily discharges of the Rio de la Plata between 1988 and 2019 from Borús et al. (2017) and ERA5 reanalysis (Hersbach et al., 2020) hourly surface winds and sea level pressure from 1993 to 2019 in the Southwestern Atlantic (32–42°S 60–45°W) with 0.25° horizontal resolution to study the climatological context during the period of the cruise. **Table 1** summarizes the datasets used.

TABLE 1 | Datasets and main characteristics related to this study.

Dataset	Main characteristic
***In situ* observations of the cruise**	
Termosalinograph (TSG)	Underway continuous surface measurements of temperature, salinity and fluorescence
Hull-mounted acoustic doppler current profiler (ADCP)	Underway continuous measurements of water velocity between 28 and 500 m of depth
Conductivity-temperature-Depth (CTD)	82 full water depth profiles of temperature, salinity, pressure, oxygen and fluorescence
Water samples	Discrete samples taken from the rosette of the CTD at 32 of the 82 stations at 5 m depth
Other *in situ* observations	
Argo profiles	Temperature, salinity and pressure profiles between surface and at least 1,000 m
Rio de la Plata (RdlP) discharges	Daily time series between 1988 and 2019
Satellite observations	
Absolute dynamic topography (ADT) and derived geostrophic currents	Estimate the surface geostrophic flow, identify the Brazil-Malvinas Confluence, the separation of Brazil Current from the shelf break and the retroflection of Malvinas Current. Spatio-temporal resolution: Daily, 25 km.
TOEddies	Identify the surface extension of mesoscale eddies. Spatio-temporal resolution: Daily, 25 km.
Sea surface temperature (SST)	Combined with ADT, provides information about the surface water mass distribution and circulation. Spatio-temporal resolution: Daily, 1–25 km.
Sea surface salinity (SSS)	Tracking low salinity surface shelf waters in the deep ocean. Spatio-temporal resolution: Weekly, 50 km.
Chlorophyll-a	Study spatial evolution of highly productive waters that might be related to shelf water export. Spatio-temporal resolution: Daily, 4 km.
Other datasets	
ERA 5 reanalysis	Understand the mean and the anomalous conditions of the winds during the period of the cruise in the entire basin. Spatio-temporal resolution: Hourly, 25 km.
ETOPO 1 bathymetry	Bottom depth. Horizontal resolution: 2 km

MATERIALS AND METHODS

CTD profiles were generated in 1 dbar bin average. All the gridded fields were linearly interpolated and previously smoothed with a 5 dbar centered moving average to remove spiciness from the plots. ADCP data was processed with Cascade V7.2 (Le Bot et al., 2011) with tide correction and a 16 m vertical resolution. Along and across slope velocities were computed by assuming a 40° inclination of the slope with respect to the zonal axis. Conservative temperature (Θ, °C) and absolute salinity (S_A, g kg^{-1}) were calculated from observations from the Thermodynamic Equation of SeaWater 2010 (McDougall and Barker, 2011) and used for the water mass characterization. Water masses in the deep ocean were classified based on neutral density (γn) ranges and thermohaline properties following Valla et al. (2018). Mixing of SACW and TW with shelf waters leads to substantial freshening over a wide neutral density range and are labeled as "others." On the shelf (stations shallower than 200 m depth) thermohaline properties were used to identify shelf water masses following Berden et al. (2020; specified in **Table 2**). The data were sorted as shelf (0–200 m) and the slope (500–2,500 m) based on interpolated ETOPO1 bathymetry (Amante and Eakins, 2009), and retaining only the values within the desired ranges. In the case of Argo floats, we also filtered duplicated profiles and retained only those with good quality (flagged as 1 or 2), and the co-localized values between 1,000 and 2,500 m. To study the vertical distribution of the shelf waters with Argo floats, we interpolated the irregular sampling to a regular 10 m interval, which is the coarser resolution of the Argo profiles, in order to get the same number of observations per profile. For all the observations, we colocalized each measurement to obtain the closest satellite measurement in space and time to compare.

Using satellite altimetry, we followed the criteria proposed by Lumpkin and Garzoli (2011) to detect the location of the confluence over the slope "*as the latitude where the surface current vectors interpolated to the 1,000 m isobath change direction from southward (Brazil Current) to northward (Malvinas Current) in 77 day low−passed velocity fields.*" However, we modified it as follows. Instead of interpolating the meridional velocity to a

TABLE 2 | Water masses mean characteristics in the Uruguayan Economic Exclusive Zone.

Water mass	RDPPW	SASW	STSW[a]	TW	SACW	AAIW	UCDW	NADW	LCDW	AABW
γ^n (kg m^{-3})	S_A < 33.65	33.65 < S_A < 34 6 < Θ < 17	S_A > 33.65	< 26.35	26.35-27.10	27.10–27.60	27.60–27.90	27.90–28.10	28.10–28.27	> 28.27
Pressure (dbar)	19	70	84	103	332	821	1,560	2,431	3,349	3,847
Θ (°C)	17.78	10.87	14.67	19.72	11.12	4.05	2.98	2.60	0.87	-0.06
S_A (g kg^{-1})	30.77	33.84	34.81	36.38	35.14	34.42	34.78	35.02	34.9	34.85
S_P (psu)	30.63	33.68	34.64	36.21	34.97	34.25	34.61	34.85	34.73	34.67

Columns show the name of the water mass, and the associated neutral density ranges (γ^n, kg m^{-3}) in the deep ocean. The remaining lines show the characteristics of each water mass averaged over all stations: pressure (dbar), conservative temperature (Θ, °C), absolute salinity (S_A, g kg^{-1}), and practical salinity (S_P, psu). Acronyms correspond to RDPPW, Rio de la Plata Plume Water; SASW, Subantarctic Shelf Water; STSW, Subtropical Shelf Water; TW, Tropical Water; SACW, South Atlantic Central Water; AAIW, Antarctic Intermediate Water; UCDW, Upper Circumpolar Deep Water; NADW, North Atlantic Deep Water; LCDW, Lower Circumpolar Deep Water; and AABW, Antarctic Bottom Water.

[a]*STSW was restricted to the shelf.*

unique latitudinal point over the 1,000 m isobath, we localized the change in the meridional currents averaged between the 500 and 2,500 m isobaths over the slope. Though no substantial differences are found in the results, our indicator is less sensitive to slight zonal displacements of the currents.

Following earlier work (e.g., Barré et al., 2011; Ferrari et al., 2017) we used three specific ADT contours as (i) a proxy for the position of the BMC (ADT 0.25 m; correlated with R^2 = 0.94; p < 0.001), (ii) the retroflection of MC (ADT 0 m), and (iii) the separation of BC from the shelf-break (ADT 0.5 m). Note that ADT is not a useful tool to study long-term variations because both, steric height and shift in the currents have induced variations (e.g., Fang and Zhang, 2015; Ruiz-Etcheverry and Saraceno, 2020), but it can be a useful tool to identify fronts in the past decade.

RESULTS

Results are divided into four subsections. First, we describe the interannual contextualization of the period of the cruise and show that 2016 was a period of strong anomalous circulation conditions. Secondly, we analyze the oceanic variability during the period of the cruise. Then, we present a general description of the *in situ* observations, followed by the characterization of the shelf water export to the adjacent deep ocean and its relationship with the position of the BMC and mesoscale activity. Finally, based on extended Argo profiles and satellite observations, we explore the frequency of the shelf water distribution over the slope and the utility of altimetry to identify the shelf water export events.

Interannual Contextualization of the Period of the Cruise

To put the observations collected during the 2016 cruise into a long-term context we calculated the BMC index (BMCi) for the period 1993–2020. The BMCi is an indicator of the meridional fluctuations of the confluence. The seasonal amplitude of the BMCi is about 1° latitude (Lumpkin and Garzoli, 2011), reaching the southernmost and northernmost locations at the end of the summer and winter, respectively. A striking feature found in the BMCi is the trend of about 1° during the study period, or about 0.3° decade^{-1}. This trend represents a meridional shift from a mean position at about 38–39°S. This trend has been reported earlier both for the BMC and the separation of the BC from the shelf-break (e.g., Goni et al., 2011; Ruiz-Etcheverry and Saraceno, 2020; Bodnariuk et al., 2021) and is less than half of the trend reported by Lumpkin and Garzoli (2011) during the period 1992–2007. The reduction in linear trend when considering the past decade appears to be associated with larger amplitude meridional fluctuations observed after 2010 compared with the preceding decade (**Figure 2A**).

During 2016, the BMC was in an anomalous northern position that lasted from the beginning of January until September, being in a record northern position relative to the climatology during the majority of the summer and at the end of autumn (**Figure 2A**). During the cruise, the BMC was located on average at the 82th percentile of its latitude distribution (increasing toward lower latitude), 92th after removing the seasonal cycle. The anomalous northward position of the BMC coincided with intense SST and ADT anomalies of about 5°C and 0.5 m when comparing inshore and offshore positions at the 2,500 m isobath (**Figures 2B,C**). It is also remarkable that the negative anomalies of SST and ADT, associated with the recirculation of the MC, with negative SST and ADT anomalies from 40°S 52°W up to the Uruguayan slope at 37°S 54°W (**Figures 2C–E**). In the entire Southwestern Atlantic basin, ERA5 data shows persistent anomalous southwesterly winds during April and May 2016, particularly during May (Wind roses in **Figures 2B,C**).

Likewise, mean RdlP discharges were above 95th percentile during the first half of 2016, probably related to extreme discharges associated with the ENSO "Godzilla" event that peaked during the previous summer (Schiermeier, 2015). In particular, the previous 30-day running-mean discharge, a gross estimation of the available RDPPW over the shelf, was 56,670 m^3 s^{-1}, more than twice the climatological mean of 25,000 m^3 s^{-1}, corresponding to the 98th percentile in a 32-year daily time series from Borús (2017; **Supplementary Figure 2**).

Variability Within the Period of the Cruise and Shelf Water Export

The period of the cruise was characterized by changing atmospheric and oceanic synoptic conditions. Intensification of a

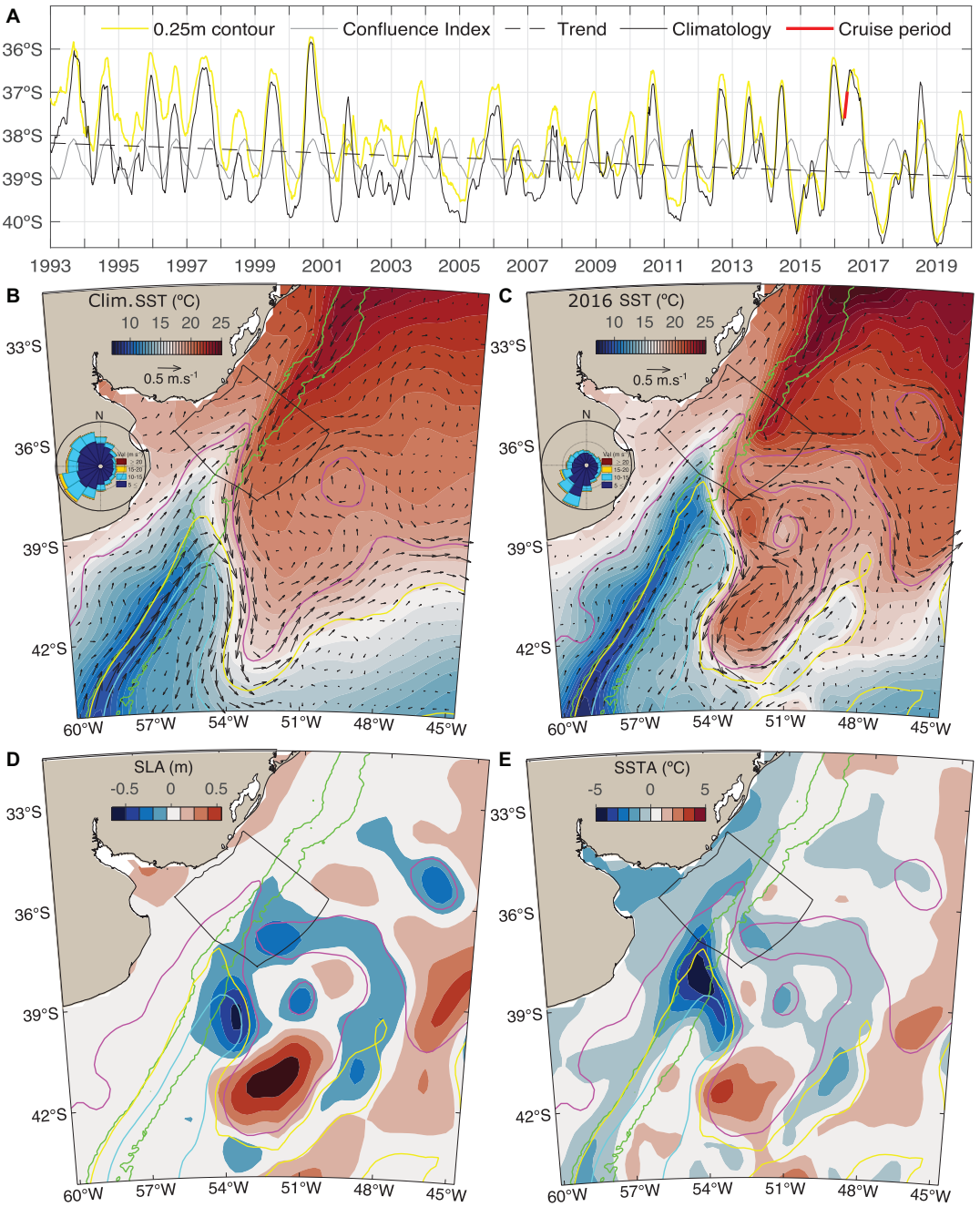

FIGURE 2 | (A) Time series of the Brazil-Malvinas Confluence mean latitudinal position over the slope (black line). The position during the cruise is shown in red. Gray and dotted lines show the seasonal cycle and long-term linear trend, respectively. The yellow line shows the 0.25 m contour of ADT over the slope. **(B)** Climatological SST (°C, background color) and surface geostrophic currents (m s^{-1}, vectors) for April-May. All panels show the mean surface geostrophic currents displayed as black vectors, the green lines show the 500 and 2,500 m isobaths. Also shown are the 0 m (cyan), 0.25 m (yellow), and 0.5 m (magenta) ADT contours, which indicate the MC retroflection, the mean confluence position over the slope and the separation of the BC from the shelf-break, respectively. The windrose for the same period and taking all grid points is also plotted over land. **(C)** Same as b, but for April-May 2016. **(D)** Sea level anomalies (SLA, m) for April-May 2016. **(E)** Sea surface temperature anomalies (SSTA, °C) for April-May 2016.

low-pressure system in the South Atlantic generated strong winds (up to 23.5 m s^{-1} on 25 April) and forced the vessel to return to the port of Montevideo between 26 and 29 April. The persistent southwesterly winds induced a drop in the air temperature and a large oceanic heat loss (not shown). Moreover, there was advection of cold waters under intense northeastward currents on the shelf that persisted until the end of the cruise and even longer (Proença et al., 2017). Thus, unplanned, this resulted in an 18-day

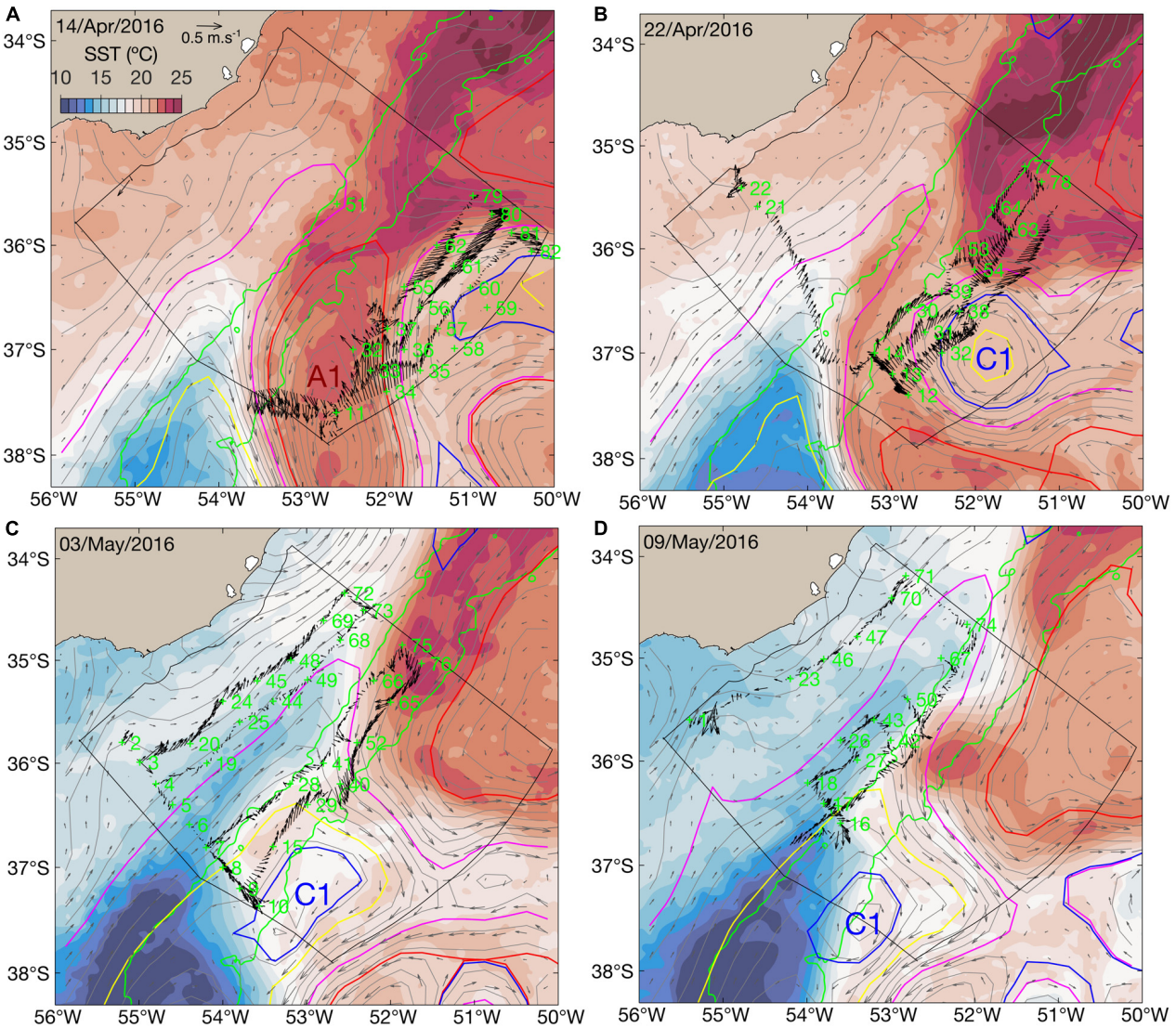

FIGURE 3 | Representative snapshots of the oceanic synoptic situations during the cruise for **(A)** 14 April 2016, **(B)** 22 April 2016, **(C)** 3 May 2016, **(D)** 9 May 2016. Background colors represent SST (°C), while gray contours and vectors represent ADT and associated geostrophic currents, respectively. Black vectors represent the ADCP measurements averaged over the upper 100 m, which represents better the upper geostrophic circulation than the shallowest measurement, and green numbers indicate the CTD stations occupied during approximately that week. The green lines show the 500 and 2,500 m isobaths, and the 0 m (cyan), 0.25 m (yellow), and 0.5 m (magenta) ADT contours which indicate the retroflection of the main core of the Malvinas Current, the mean confluence position and the separation of the BC from the shelf-break, respectively.

sampling of the deep ocean stations (from 9 to 26 April) and a 12-day sampling of the shelf and slope stations (from 29 April to 10 May) separated by a 2 day stop in between. Henceforth we dubbed these spatio-temporal grouping of stations as the first "half" and second "half" of the cruise, respectively.

Each half of the cruise can also be split into two parts based on the mesoscale dynamical state of the ocean, lasting about a week each. During the first 10 days of the cruise, the open-ocean area south of 36°S was mostly occupied by a large anticyclonic eddy (A1) that detached from BC and moved southward (**Figure 3A**). Subsurface salinities up to 37 g kg^{-1} were measured within A1 and the BC, and the most intense currents were observed at the periphery of A1, with speeds larger than 1 m s^{-1} and reaching depths as deep as 300 dbar. As a consequence of the eddy shedding, the BC retroflection was located north of 36°S. During the following 8 days, a cyclonic eddy (C1) entered the region from the east and occupied part of the area where A1 was located the previous week, with the retroflection of the BC displacing slightly southward (**Figure 3B**; see also **Supplementary Video 1**). The second half of the cruise was characterized by the southward displacement of C1 out of the study area followed by a southward extension of BC reaching 37°S (**Figure 3C**). This period can also be divided into two different mesoscale dynamical regimes: from 29 April to 3 May C1 persisted as a coherent structure

(**Figure 3C**), whereas, from 4 to 9 May, C1 displaced toward the MC (**Figure 3D**).

In situ Observations in the Uruguayan Economic Exclusive Zone During April–May 2016

Underway surface temperature and salinity were both extremely variable in space and time during the cruise. Extreme temperature values were associated with variability from WBCs over the slope, with coldest waters (10°C) south of the Uruguayan EEZ related to the MC, and warmest waters (25°C) associated with the mesoscale activity of the BC (**Figure 4B**). The SST over the shelf cooled about 6°C between the beginning and the end of the cruise (**Figures 4A,D**). The air temperature was lower than SST during most of the cruise, up to 8°C cooler than the SST over the BC and 5°C in some parts of the shelf (**Figure 4B**). Surface salinity varied from 0.5 g kg^{-1} close to the RdlP and 37.0 g kg^{-1} in the deep ocean, with also large variations through time. The position at [35.3°S, 55°W] near station 1 close to the RdlP mouth was crossed three times 9 and 26 April, and 10 May, and the TSG salinity and temperature observations were 26.1, 26.7, and 8.5 g kg^{-1}, and 21.0, 18.9, and 14.6°C, respectively (**Figure 4A**). Due to the extreme discharges of the RdlP, MODIS Aqua image during 9 May shows the muddy RdlP water more than 100 km away from its climatological position off Montevideo (not shown; Maciel et al., 2021). This was also reflected in the anomalous low salinity water (S_A < 2 g kg^{-1}) observed at station 1 conducted on 9 May inshore of the RdlP turbidity front. At this station, turbidity concentration was at least one order of magnitude higher than at other stations (**Figure 4C**). Nitrate and phosphate were maximum also at this station, 23.42 and 2.77 μmol kg^{-11}, respectively. Overall, nutrients were high over the shelf and in the cold waters over the southern portion of the slope, with maximum values close to the RdlP and in the southern shelf break covered by MC, and low over the deep ocean stations (**Figure 4F**).

Surface chlorophyll-a was mostly positively correlated with the nutrient distribution, decreasing toward the deep ocean. Maximum values were measured near the coast immediately offshore from the turbidity front (10 < S_A < 25 g kg^{-1}), although they did not peak at station 1 in the RdlP waters, where nutrient values were maximum, due to the effect on light attenuation in muddy waters (e.g., Carreto et al., 2003; Kruk et al., 2015; Martínez and Ortega, 2015). High surface fluorescence and chlorophyll-a were also observed in the southernmost area of the Uruguayan EEZ, at stations 7 and 9 over the outer shelf and slope, over the Ewing Terrace and Rio de la Plata canyon under the influence of the MC retroflection at about 37°S 54°W. These stations showed the coldest surface waters and high concentration of nutrients (**Figures 4D–F**), and also the highest integrated fluorescence in the CTD profile (3.15 mg m^{-3}) in the upper 50 m (**Figure 4D**), as these stations were occupied at the end of a chlorophyll bloom that took place 10–25 April according to satellite observations (**Supplementary Video 1**). The intense front observed in this region, and the mixing with shelf waters probably triggered this bloom. In contrast, a band of high nutrient low chlorophyll was formed in the outer shelf from 26 April until the end of the cruise, probably due to the fully mixed water column by strong southwesterly winds (wind rose from ship measurements in **Figure 4B**) and intense northeastward currents.

In agreement with satellite geostrophic observations, observed upper-ocean currents (averaged over the upper 100 m) displayed two clearly different regimes in the shelf and deep ocean (**Figures 1**, **4D**). Despite the stations over the shelf being occupied over a period of nearly 1 month, northeastward surface velocities prevailed in this region, while velocities over the deep ocean were higher and with different directions due to mesoscale eddies and the retroflection of the major currents. The BC appeared as a southward flow in the northern half of the Uruguayan EEZ over the 2,000 m isobath with Θ > 23°C and S_A > 36 g kg^{-1}, respectively, and very low chlorophyll-a and nutrient concentration. A retroflection of the BC, usually referred to as "overshoot," was observed at about [36.5°S, 52°W] between the 3,000 and 4,000 m isobaths (**Figure 4D**).

Below the surface, the full-depth CTD profiles showed three different water masses on the shelf and seven water masses in the deep ocean (see **Table 2** for acronyms and mean properties). From the coast to the 50 m isobath (about 80–100 km), the study area was mostly filled with RDPPW. With S_A < 33.65 g kg^{-1}, it is the most nutrient-rich and high-chlorophyll-a water mass. SASW prevailed toward the outer shelf, narrowing considerably toward the north as the shelf also narrows as it tends to be replaced by STSW. A very small fraction of the shelf was occupied with STSW which was mainly found in the outermost stations in the northern part of the shelf (**Figure 5A**). The observed transition between SASW and STSW agrees with the location of the Subtropical Shelf Front determined from historical data (Piola et al., 2000).

The deep ocean exhibited TW and SACW in the upper layers. The data display evidence of intrusions of SASW and STSW at several vertical levels within the relatively warm and salty TW and SACW. Large amplitude thermohaline intrusions observed in this region are ubiquitous of the confluence region (e.g., Piola and Georgi, 1982; Bianchi et al., 1993; Orúe-Echevarría et al., 2021), and are indicative of intense isopycnal mixing between the adjacent water masses with contrasting thermohaline properties (**Figure 5B**). Water masses found at deeper depths were those characteristics of the region: UCDW, NADW, LCDW, and AABW, respectively (Maamaatuaiahutapu et al., 1992, 1994; Provost et al., 1995; Valla et al., 2018; **Table 2** and **Figure 5B**).

Surface Water Export

In this subsection we describe the evidence suggesting the export of shelf waters to the adjacent open ocean and discuss the processes involved. A well-known process exporting surface shelf water consists of brackish RDPPW and mixtures of shelf waters being advected offshore by the mesoscale activity of the BC. These have been detected by satellite SSS observations (Guerrero et al., 2014) and in numerical simulations (Matano et al., 2014). Export of low-salinity shelf waters is also apparent in hydrographic observations from the BC and near the confluence (Gordon, 1989; Provost et al., 1996; Piola et al., 2008; Berden et al., 2020). The high-resolution UEEZ observations reported here provide valuable information from the region of detachment of shelf

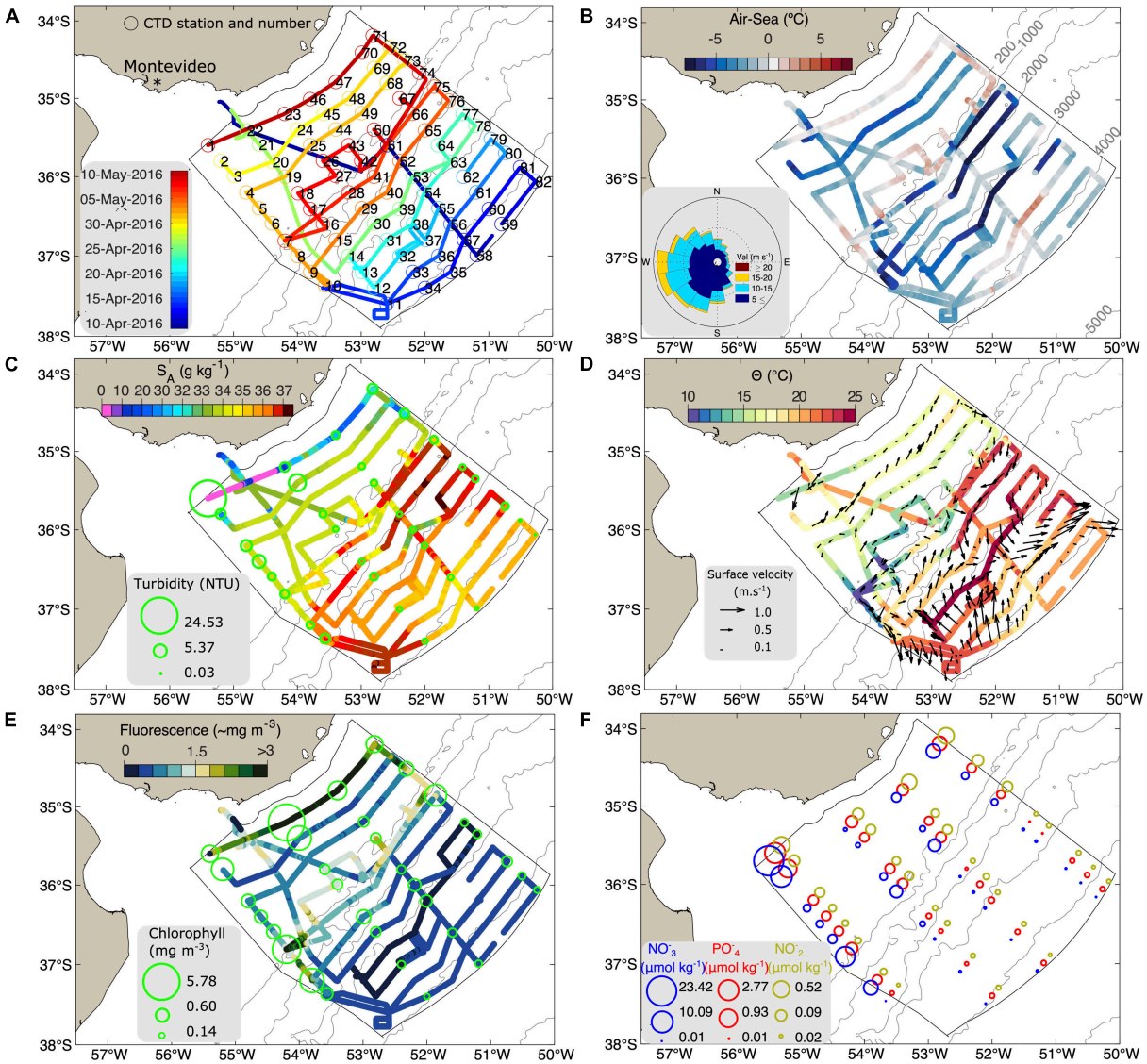

FIGURE 4 | Near-surface observations during April-May 2016. **(A)** Cruise track and station numbers. **(B)** Difference between air and sea surface temperature (°C). Wind rose from ship measurements (m s^{-1}) during the cruise period is also shown. **(C)** Absolute Salinity (S_A, g kg^{-1}). The size of the green circle represents specific turbidity measurements (NTU). **(D)** Sea surface temperature (°C) and currents (m s^{-1}) from the ADCP averaged over the upper 100 m (black vectors). **(E)** Chlorophyll-a from fluorescence. The symbol size represents the *in situ* chlorophyll-a measurements (mg m^{-3}). **(F)** Nitrates (NO^-_3, µmol kg^{-1}, blue symbols), Phosphates (PO^-_4, µmol kg^{-1}, red symbols), and Nitrites (NO^-_2, µmol kg^{-1}, green symbols) concentration at 5 m depth.

waters. We identified an export event during the first half of the cruise, although only the initial part of the low salinity plume detaching from the shelf was detected in satellite SSS (**Supplementary Figure 3C**), suggesting that the coarse satellite observations cannot properly resolve it. Nevertheless, satellite chlorophyll-a provides useful information about the spatial structure of the export due to the contrasting values between shelf and the open ocean waters (such as during 24 April at 36°S 52.5°W, **Figure 6**). The high chlorophyll-a filament consisted of a brackish water filament detached from the shelf along the BC retroflection (**Figure 6A**). The TSG measurements across the filament and 2 CTD profiles occupied that day display the 3-D structure of the low salinity RDPPW filament. The filament was 70 km wide and 20 m deep according to the TSG and the CTD profiles inside the filament, respectively (**Figures 6B,C**). Within the 70 km wide filament and the ADCP measurements in the upper 60 m, which better represent the filament, the mean across-slope velocity was 0.30 m s^{-1} (**Figures 6B,C**), and the off-shore estimated transport 0.42 Sv.

The northern edge of the filament showed very sharp gradients. In 20 km, S_A decreased from 36.45 to 32.34 g kg^{-1}, temperature from 23.75 to 20.1°C, and fluorescence increased from 0.2 to 0.4 mg m^{-3}. Also, very close to the front, a local maximum of 0.7 m s^{-1} in the across-slope velocity was observed

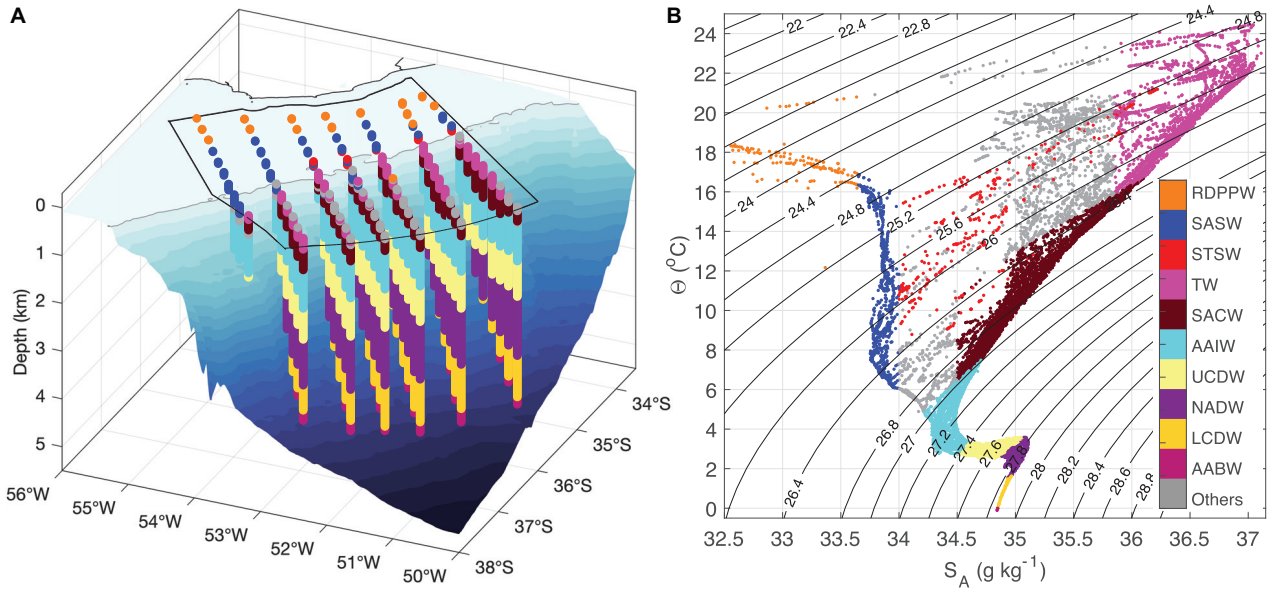

FIGURE 5 | (A) 3-D visualization of the CTD profiles occupied during the cruise. Each vertical line represents a CTD profile and the colors within each line a specific water mass as shown in **(B)**. The black polygon at the surface shows the Uruguayan EEZ and the gray line shows the 200 m isobath. **(B)** Θ-S_A diagram of the CTD profiles shown in **(A)** and water masses whose hydrographic characteristics are described in **Table 2**.

(**Figure 6C**). The southern side of the filament showed a less intense fluorescence gradient, probably because the region north of the filament was occupied by oligotrophic BC water, while cold-core (< 19.5°C), high-fluorescence (> 0.35 mg m^{-3}) eddy C1 was located south of the filament. The CTD profile occupied within the filament showed that the brackish water extended downward to about 20 m depth, characterized by RDPPW properties (S_A < 33.65 g kg^{-1}; **Figure 6D**) and high fluorescence (> 0.45 mg m^{-3}). It is remarkable also that the vertically integrated fluorescence in the upper 140 m was higher in the CTD profile outside the filament, but the peak was below 40 m of depth and it was not apparent in satellite observations (**Figure 6B**).

Subsurface Water Export

The *in situ* data also showed evidence of subsurface shelf-water export over the slope located at the BMC during the second half of the cruise. The gridded absolute salinity field from CTD profiles averaged between 40 and 120 m depth shows a low salinity tongue of SASW (S_A < 34 g kg^{-1}; < 12°C) being exported offshore up to the outer slope, approximately over the 2,000 m isobath (**Figure 7A**). Most of the CTD profiles over the slope were occupied within the first week of May 2016. Hence, the altimetry map of 3 May might be taken as representative of the regional circulation during that week (**Figure 7B**). The SASW tongue was located between the BMC and the BC separation from the shelf (yellow and magenta contours in **Figure 7B**, respectively), with geostrophic velocities oriented perpendicular to the slope toward the open ocean. The Θ-S_A diagram of that section shows a clear transition from subantarctic waters within the MC to subtropical waters from the BC (**Figure 7C**). Three CTD profiles showed the presence of SASW. The freshest SASW variety was observed at the BMC (station 40 at 36.2°S 52.6°W), with a homogeneous layer of 33.76 g kg^{-1} found between 70 and 130 m of depth (**Figures 7C,F**). The next CTD profile to the south showed evidence of SASW located between 160 and 230 m of depth. Here, SASW properties showed evidence of mixing with saltier waters with a relative maximum of 34.45 g kg^{-1} at 200 m of depth. Finally, the third profile with SASW was located in the southernmost CTD profile (station 9), which displayed a Θ-S_A structure typical from the MC over the slope (**Figures 7B,C**).

We next constructed an along-slope section over the main core of the WBCs, occupied during the period 3–5 May, when eddy C1 was merging with the MC. We did so from continuous ADCP velocity measurements and seven CTD profiles occupied along the 285 km section (stations 9, 15, 29, 40, 53, 65, and 76 from south to north, respectively; **Figures 7D–G**). The CTD profile containing the homogeneous layer of SASW at the BMC (station 40) was separated from the two closest stations by about 40 km. Therefore, we assumed that the horizontal extension of this layer was 40 km, half the distance between the two closest stations and approximately the extension of the low salinity surface signature from the TSG, with an uncertainty of 40 km. The mean across-slope velocity measured from the ADCP within the representative 40 km of the CTD station and the 70–130 m depth containing the homogenous SASW layer was 0.38 m s^{-1}. Hence, our estimate of the offshore export of SASW at the BMC is 0.91 ± 0.91 Sv.

An across-slope CTD transect allowed us to identify and track the core of the SASW from the shelf to the deep adjacent ocean, although it must be interpreted with caution because the transect is a collection of non-synoptic data. The profiles showing the

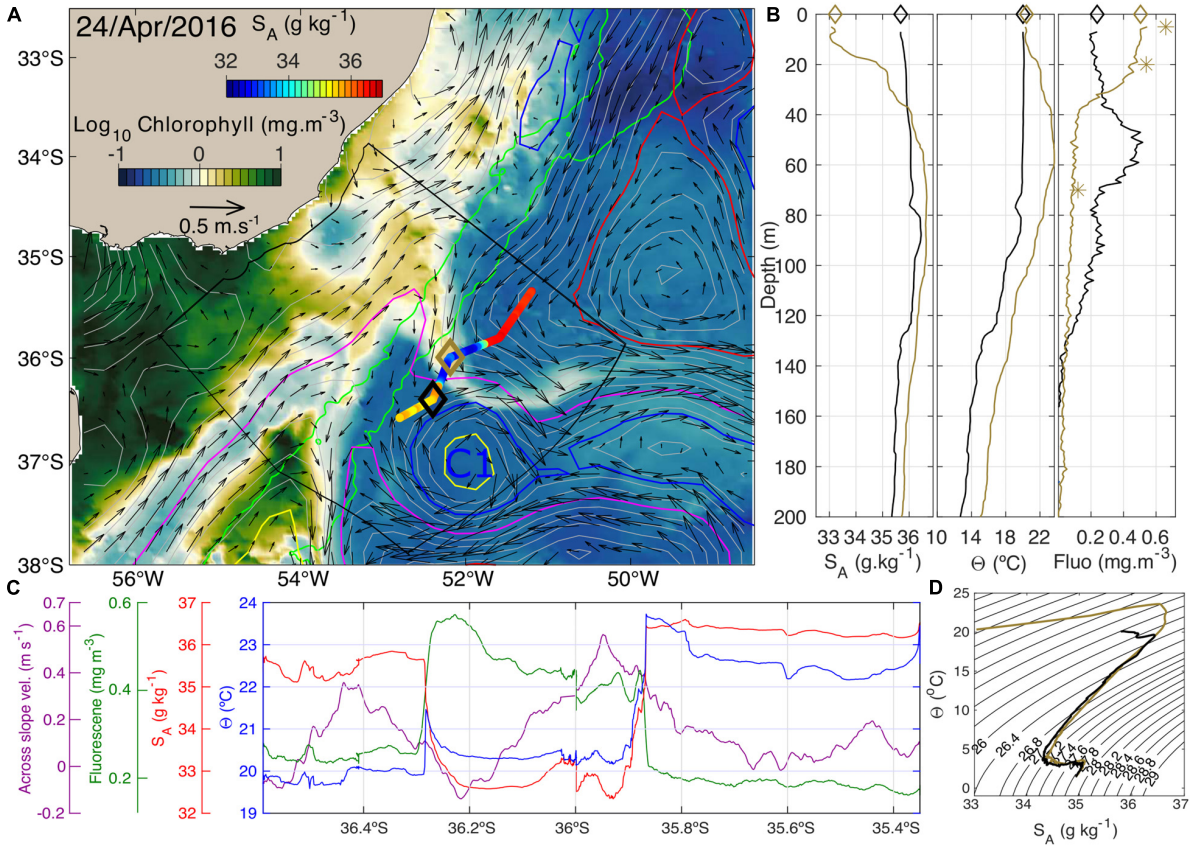

FIGURE 6 | (A) Satellite chlorophyll-a and surface geostrophic currents on 24 April 2016. Gray lines show ADT contours. Underway near-surface salinity measurements are indicated along the cruise track across the filament, color-coded by SSS (color scale above). Black and brown diamonds indicate the location of the CTD profiles 39 and 53 collected that day. The green lines show the 500 and 2,500 m isobaths. Yellow and magenta colors represent the 0.25, and 0.5 m ADT contours, respectively. Red and blue contours refer to anticyclonic and cyclonic eddies, respectively. **(B)** Upper 200 m profiles of Absolute Salinity (S_A, g kg^{-1}), Conservative temperature (Θ, °C), and fluorescence (mg m^{-3}) from the CTDs 39 and 53. Brown and black lines correspond to stations 53 and 39 carried out within and outside the low-salinity filament, respectively. Asterisks show the laboratory chlorophyll-a measurement from the water samples collected at station 53. **(C)** Underway TSG measurements on the transect occupied across the low-salinity filament shown in **(A)**. The panel shows: Upper 60 m across-shore velocities from the ADCP (magenta, m s^{-1}, and absolute salinity (red, S_A, g kg^{-1}), conservative temperature (blue, Θ,°C), and fluorescence (green, mg m^{-3}). **(D)** Θ^-S_A diagram of stations 53 and 39 in brown and black, respectively.

layer of SASW immediately outside the shelf were conducted on 4 and 6 May 2016. The reconstructed transect shows a 60 m thick layer of SASW (Θ between 6–12°C and S_A 33.75–34 g kg^{-1}) flowing below the γ = 25.7 kg m^{-3} isopycnal. This vein of SASW left the surface at the shelf break where it subducted, reaching 130 m of depth at the 2,300 m isobath (**Figure 8A**). The exported SASW might have reached deeper levels, but this cannot be assessed with the cruise data as the following offshore CTD profiles along this transect were collected 10 days earlier (**Figures 8A,B**).

In this case, no low salinity signature was identified in satellite SSS (**Supplementary Figure 3D**). Chlorophyll-a showed a relative maximum at the same location where the SASW offshore export is apparent in the observations. However, the signal was very weak and might have also been locally generated instead of being advected (**Supplementary Video 1**). On the other hand, geostrophic currents derived from satellite altimetry show a high correlation and the lowest root mean square error (RMSE) with ADCP measurements at a depth of 110 m ($p < 0.01$; R^2 0.82 and 0.35; RMSE 0.25 and 0.23 m s^{-1}, for along and across slope velocities, respectively; **Supplementary Figure 4**). Therefore, although satellite observations cannot directly detect the subsurface export of SASW, satellite altimetry might be used as an indicator of where and when such export events take place.

Shelf Waters Detection From Argo Floats and Satellite Observations

In this section, we explore the frequency of RDPPW and SASW over the slope and their relationship with altimetry using long-term Argo floats and satellite observations. The Hovmoller diagram constructed from satellite geostrophic currents and SSS in the zonally averaged slope shows that most of the observed across-slope positive (offshore) velocities occur between the BMC and the separation of the BC from the shelf break,

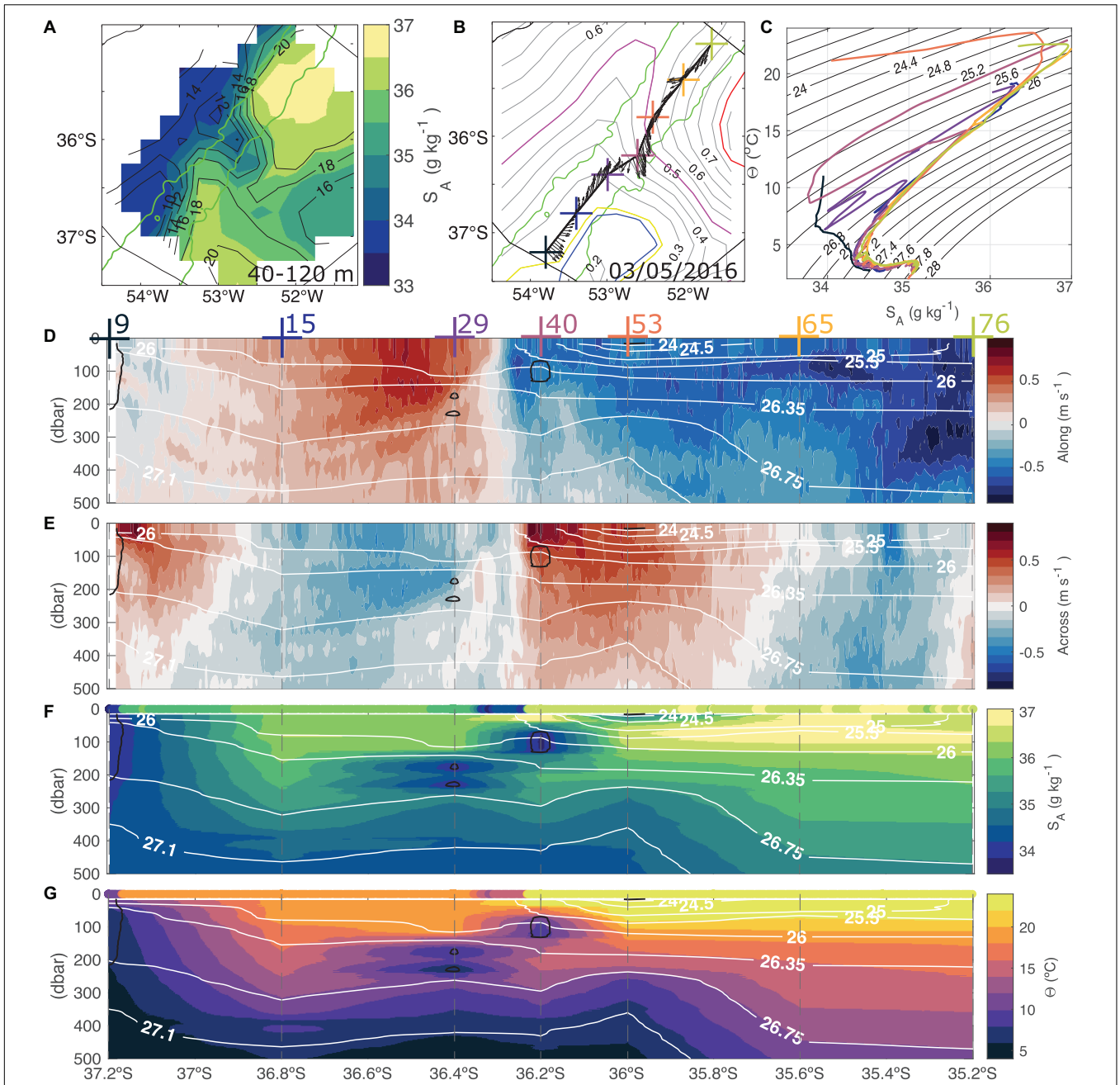

FIGURE 7 | Overview of the export of Subantarctic Shelf Waters at the Brazil-Malvinas Confluence during the first week of May 2016. **(A)** Mean absolute salinity (shades) and conservative temperature (contours) averaged over the 40–120 m depth interval. **(B)** Location of CTD stations occupied over the main BC and MC on 2 and 3 May 2016 approximately over the 1,600 m isobath. Vectors show the upper 100 m velocity field from the ADCP, and gray contours the ADT, with the yellow and magenta lines representing the BMC and the separation of BC from the shelf break, respectively, and blue and red contours the cyclonic and anticyclonic eddies, respectively. Colored crosses indicate the profiles in the Θ-S_A diagram in **(C)**. The panels below show: **(D)** Along slope velocity (m s^{-1}). **(E)** Across slope velocity (m s^{-1}). **(F)** Absolute salinity (g kg^{-1}), and **(G)** Conservative Temperature (°C), respectively. TSG underway measurements are also plotted above panels **(F,G)**. Black contours enclose shelf water (S_A < 34 g kg^{-1}), gray lines are contours of constant neutral density, and dotted lines the CTD profiles location in all panels.

following the described seasonal migration of the BMC (see black and magenta contours in **Figures 9A,B**). It is also remarkable that a local maximum in across-slope velocity (0.3–0.4 m s^{-1}) is observed when the BMC reaches its extreme highest and lowest latitude. Also, across-slope velocities higher than 0.1 m s^{-1} are observed during winter north of the separation of the BC from the shelf break at about 33°S (**Figure 9A**).

Satellite SSS with shelf water characteristics (S_A < 34 g kg^{-1}) are observed over the slope north of the BMC in most of the

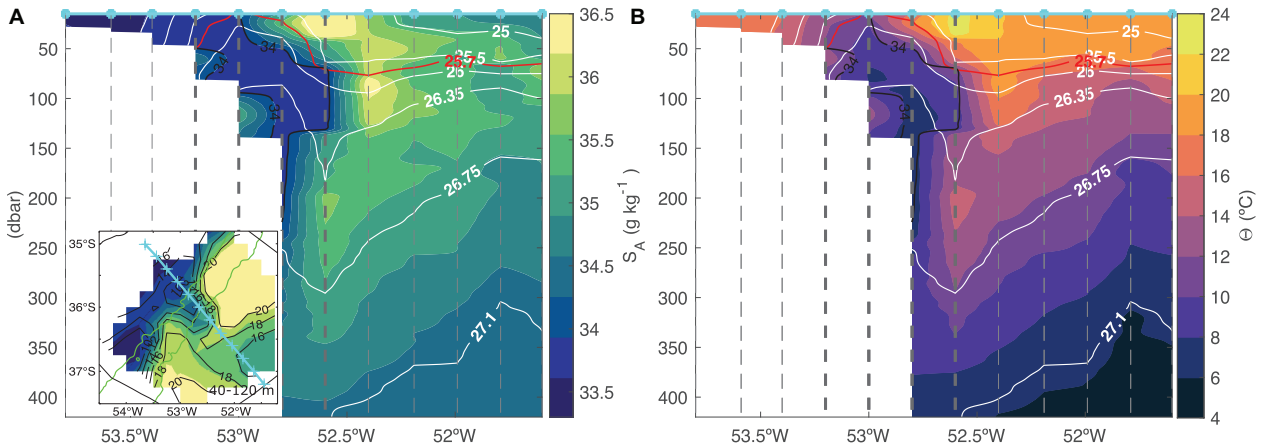

FIGURE 8 | Across-slope section. **(A)** Absolute salinity (S_A, g kg^{-1}). The inset shows the S_A field averaged over the 40–120 m depth interval, and the cyan line shows the transect. **(B)** Conservative temperature (Θ,°C). The 34 g kg^{-1} contour delimiting Subantarctic Shelf Waters is drawn in black. Neutral density contours are shown in gray, with the 25.7 kg m^{-3} shown in red. Dotted lines show the location of the CTD profiles used to make the section, and the bold dotted lines correspond to those stations considered as synoptic conducted between the 4 and 8 May.

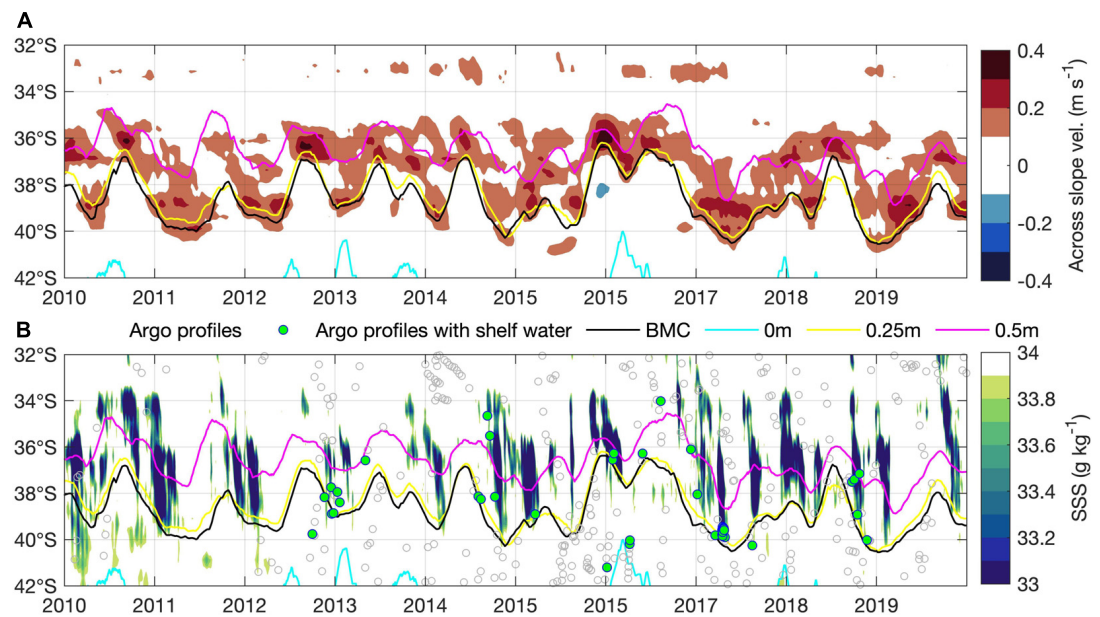

FIGURE 9 | Hovmoller plots of latitude vs. time over the zonally averaged slope in the Southwestern Atlantic. In both panels, the black contours represent the BMC position, and the 0, 0.25, and 0.5 m contours of ADT are shown in cyan, yellow, and magenta, respectively. **(A)** Surface across-slope velocity (m s^{-1}). **(B)** Sea Surface Salinity (SSS, g kg^{-1}). Gray circles show Argo profiles located over the slope, and green circles indicate data from Argo profiles in which shelf waters were observed. Note that only the period where SSS is available is plotted.

cases. They display a clear seasonal cycle, mostly determined by the southward extension of the BMC, reaching higher latitudes at the end of the summer (**Figure 9B**). From the 431 Argo profiles located between the 1,000 and 2,500 m isobaths and from 32 to 42°S over the southwestern Atlantic slope, 59 (12%) contained shelf waters, while 32 (7%) contained exclusively RDPPW. Most of the profiles containing shelf waters were located north or at the BMC, in particular between the BMC and the separation of BC from the shelf-break (Yellow and magenta contours in **Figure 9B**, respectively). The shallowest salinity observations from the 427 Argo profiles were significantly correlated with satellite SSS ($p < 0.01$; $R^2 = 0.64$). Co-localized Satellite SSS measurements showed less variance than *in situ* observations, as expected from its coarse space-time resolution. Nevertheless, the RMSE was 0.78 g kg^{-1}, which might be an acceptable value to identify RDPPW, yet too large to correctly single out SASW. While shelf water ($S_A < 34$ g kg^{-1}) was detected in the shallowest measurement (1–10 m) of 54 of

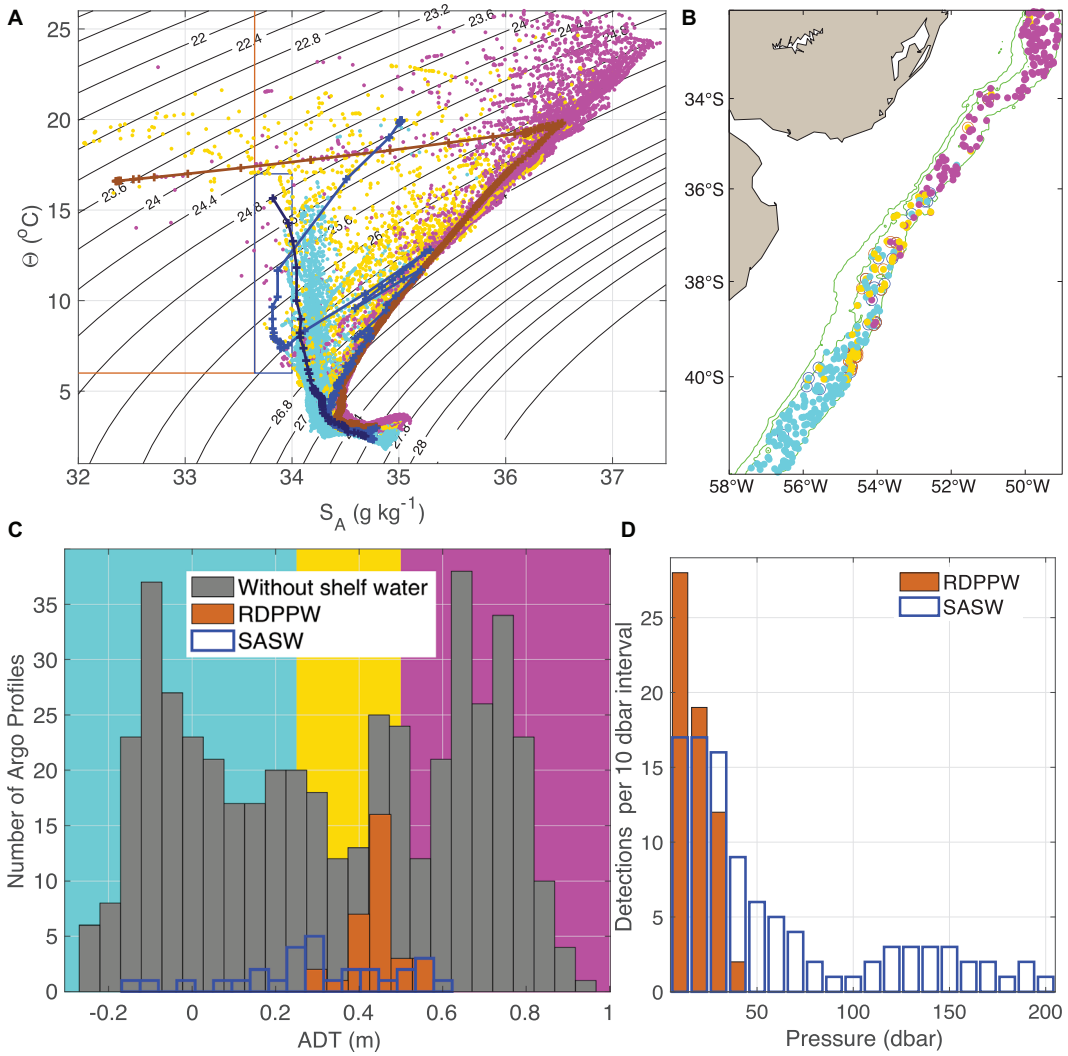

FIGURE 10 | (A) Θ-S_A diagram of Argo profiles over the Southwestern Atlantic slope co-localized with ADT values. Colors represent ADT values < 0.25 m in sky-blue (MC), > 0.5 m in magenta (BC), and yellow in between (BMC) in panels **(A,B)**. Blue and brown polygons represent the thermohaline intervals for Rio de la Plata Plume Water (RDPPW) and Subantarctic Shelf Water (SASW), and the three colored Θ-S_A diagrams are example profiles similar to those containing shelf water observed in the deep ocean during the 2016 cruise. **(B)** Argo profiles locations following the same color code as in **(A)**. **(C)** Histogram of the Argo profiles co-localized with ADT over the slope. **(D)** Histogram of the pressure at which Rio de la Plata Plume Waters (RDPPW, brown) and Subantarctic Shelf Waters (SASW, blue) are found in Argo profiles located over the slope.

the 427 Argo profiles, the corresponding co-localized satellite SSS detected 58.

Argo profiles in the slope co-localized with ADT show values ranging between -0.25 and 0.96 m, with remarkable differences in the Θ-S_A signature depending on which side of the fronts the floats were localized (**Figures 10A,B**). **Figure 10A** also shows three Θ-S_A diagrams from Argo floats containing shelf waters similar to CTD stations occupied during the 2016 cruise (station 53 in **Figure 6D** and stations 9 and 40 in **Figure 7C**). The histogram in **Figure 10C** displays the number of Argo profiles as a function of ADT. The maximum frequencies are observed in the −0.1 to −0.05 m and 0.6–0.65 m intervals. Argo profiles containing SASW spread over a wide range of ADTs (−0.15 and 0.6 m), while the profiles containing exclusively RDPPW are restricted to the 0.25 and 0.6 m range, thus falling between the BMC and the separation of the BC from the shelf break. In particular, ADT ranges between 0.35 and 0.45 m contain the majority of Argo profiles with RDDPW, with 23 out of 38 profiles (∼60%) within these two class intervals (**Figure 10C**). Inspection of the vertical distribution of shelf waters in the Argo profiles, both RDPPW and SASW are most frequently observed in the upper ocean interval (10–20 dbar). However, while RDPPW is exclusively restricted to the upper 40 dbar, these data show that SASW can reach depths of 200 dbar (**Figure 10D**).

SUMMARY AND CONCLUSION

The hydrographic cruise that took place in April–May 2016 in the Uruguayan EEZ provided an unprecedented dataset to

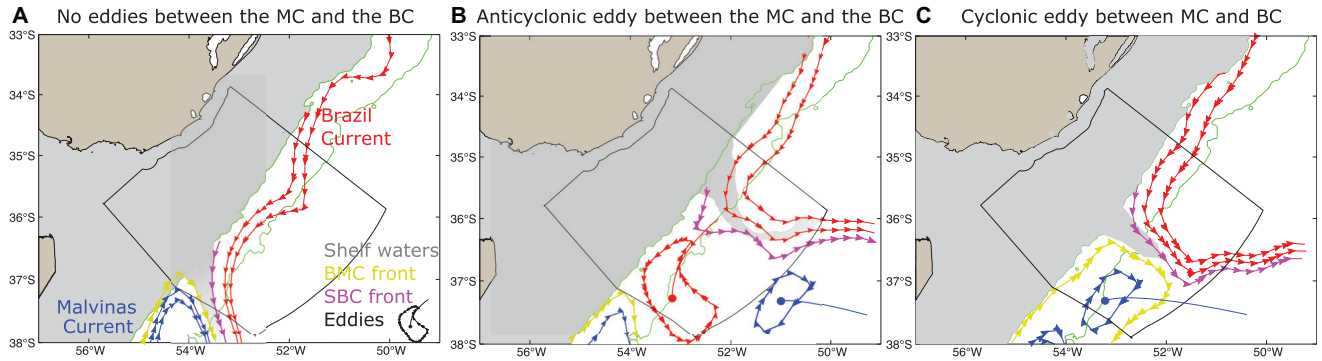

FIGURE 11 | Schematic circulation patterns of 3 shelf water export situations in the Uruguayan EEZ. BMC stands for Brazil-Malvinas Confluence and SBC for Separation of Brazil Current from the shelf-break. Shelf waters (S_A < 34 g kg^{-1}) are shown in gray. Green lines show the 500 and 2,500 m isobaths. **(A)** Without eddies between the Brazil Current and Malvinas Current. **(B)** With an anticyclonic **(C)** cyclonic eddy between the main currents, respectively.

investigate local water masses, ocean dynamics, and cross-shelf exchanges at the Brazil Malvinas Confluence. Despite the survey covering a relatively small area, our study shows that it is characterized by a highly variable and dynamic environment. Water properties can fluctuate from below 0°C to over 25 °C in conservative temperature and from almost freshwater to over 37 g kg^{-1} in absolute salinity. The region hosts intense western boundary currents and mesoscale activity developing offshore, displaying large oceanic space-time variability at all scales (from synoptic, to interannual and interdecadal) driving cross-shore exchanges.

The first half of 2016 was an anomalous period in the southwestern Atlantic in terms of atmospheric and oceanic circulation. It was characterized by intense southwesterly winds, negative SST anomalies, and large Rio de la Plata discharges. By extending the Brazil Malvinas Confluence latitudinal position index of Lumpkin and Garzoli (2011), we showed that the confluence was located anomalously north during the first half of 2016, occupying the Uruguayan EEZ when the *in situ* survey was conducted.

In this work, we focused on cross-shelf exchanges as they have important consequences for carbon export, water masses transformations, and marine biodiversity. Previous studies provide evidence that, regionally, shelf water export is closely related to the confluence position (e.g., Matano et al., 2014; Berden et al., 2020; Orúe-Echevarría et al., 2021; **Figure 11A**). This control is somehow expected since the Brazil and Malvinas currents generate a barotropic pressure gradient that extends into the shelf controlling the outer shelf circulation (Palma et al., 2008; Matano et al., 2010). Our analyses provide evidence of the 3-D structure and evolution of two different kinds of shelf water export associated with the BMC dynamics: one related to Rio de la Plata waters that remain confined to the surface layers; the other involves SASWs that subducts under the subtropical thermocline while crossing the slope. To understand the dynamical setting associated with these processes and to assess their significance in time we used a combination of different observations that include the cruise hydrographic data, Argo profiles, satellite maps of SSS, SST, ADT, and chlorophyll-a, and a recently developed eddy detection algorithm.

A near-surface export of shelf water consisted of a thin off-shelf layer of Rio de la Plata waters following the path of the retroflection of the Brazil Current after an anticyclonic eddy shedding that dissipated after 10 days due to strong winds that mixed the stratified plume (**Figure 11B**). In addition, the hydrographic observations reveal a subsurface export of SASW. In this case, the driving mechanism also appears to be associated with mesoscale dynamics triggered by the merging of a cyclonic eddy with the Malvinas Current at the confluence with Brazil Current (**Figure 11C**). This generated intense off-shelf velocities at the shelf break. Evidence of subsurface export of shelf waters based on hydrographic and lowered ADCP observations near the BMC has been recently reported by Berden et al. (2020, their Figures 4C, 8E). The novelty of this study relies on the availability of closely spaced along-slope sections which reveal the detailed structure of the cross-shelf fluxes. Combining these *in situ* and satellite observations we reconstruct the 3-D field, quantify the export, and associate mesoscale ocean dynamics as the driving mechanism.

Using numerical simulations, Matano et al. (2014) showed that a time-averaged convergence of volume of about 1.21 Sv in the along-shore flow of SASWs (1.15 Sv) and STSW (0.038 Sv) and the inflow of Rio de la Plata waters (0.024 Sv) between 34 and 38°S must be exported offshore. The 1.21 Sv could hardly be achieved by the exported low salinity RdlP plumes, but the sum of both surface and subsurface export as observed in this work is closer to. In addition, Franco et al. (2018) using numerical simulations showed that released neutrally buoyant particles equally distributed in the vertical at 38°S over the shelf were exported all along the shelf-break between the retroflection of the Malvinas Current and the Subtropical Shelf Front at about 32°S. Most of the neutrally buoyant particles were exported at the BMC, in particular within the 50–200 m layers. They also showed that as SASW was exported, it rapidly became saltier. The intense mixing observed over the slope together with the fact that the difference between SASWs and the surrounding ocean waters can be less than 0.2 g kg^{-1}, makes it difficult to detect this water mass based

only on salinity differences with the surrounding waters, as the shelf water freshwater signature rapidly fades as shown by Franco et al. (2018).

By using Argo profiles located within the southwestern Atlantic slope, we provide evidence of the presence of Rio de la Plata waters and SASWs between the separation of the Brazil Current from the shelf-break and the confluence and at the same depths as observed during the 2016 cruise. At specific values of absolute dynamic topography of 0.35–0.45 m, we found shelf waters over the slope in more than half of the Argo profiles, further suggesting the export of shelf waters at this location is relatively frequent. Also, by inspecting Argo profiles together with satellite surface salinity we show that SASWs is often found over the slope, especially within the shallow branch of the Malvinas Current. Because of the similarity between SASWs and surrounding waters thermohaline properties and the intense mixing taking place over the slope, detection of shelf waters within this current is challenging. Nonetheless, by combining *in situ* water velocity measurements and concomitant satellite altimetry observations we found evidence of SASWs along the BMC. In contrast, Rio de la Plata waters are more easily detectable in the open ocean due to their low salinity characteristics.

We also provided evidence that, although satellite surface salinity reveals shelf water exports (Guerrero et al., 2014), the coarse resolution of satellite data limits the ability to detect the fine structure and temporal evolution of the exported waters. This suggests that several export events might not be properly captured by satellite surface salinity. Chlorophyll-a, which has higher resolution especially under clear sky conditions, could be a complementary tool to detect these freshwater export events, but need to be contrasted with other salinity observations, as high chlorophyll-a filaments could be associated with several other processes not related to shelf-waters. Combination of different observations in the future (e.g., satellite Chlorophyll-a and salinity observations) could provide more insights on detecting and characterizing shelf water export events.

Another useful approximation to study shelf water export processes are high-resolution numerical models, as they reproduce the shelf-water export, especially when the confluence and the separation of the Brazil Current from the shelf break are along the same front (Berden et al., 2020; Orúe-Echevarría et al., 2021), but probably also to better simulate the impact of mesoscale eddies, like those observed during the 2016 cruise (**Figure 11**). Recent numerical simulations highlight the role of along-shelf winds in modulating the magnitude of along-shelf transports and the resulting shelf-open ocean exchanges (Berden et al., in press). In agreement with our findings, the numerical models indicate that a majority of the cross-shore flow occurs close to the confluence. Our retrospective analysis indicates seasonal fluctuations of the export location between 35.5 and 40°S which are modulated by displacements of the confluence, and also suggest a secondary export route near 33°S. This latter export location is also apparent in ocean reanalyses (Berden et al., in press). One of the several advantages of studying cross-shelf exchanges with numerical models is the ability to be able to track the water being exported (Franco et al., 2018; Combes et al., 2021).

Finally, our analyses suggest that geostrophic currents derived from satellite altimetry are a robust indicator for the regional dynamics and a useful tool to track cross-shore water export events. By providing relatively accurate steric height estimates, satellite altimetry shows a high correlation with absolute velocities at 100 m of depth. Hence, satellite altimetry seems to be more useful than satellite surface salinity to identify subsurface shelf water export events. As altimetry is relatively accurate in identifying the location of the confluence (ADT contour 0.25 m over the slope) and the separation of Brazil Current from the shelf-break (ADT contour 0.5 m), across-slope velocity maxima confined between the 0.25 and 0.5 m ADT contours over the shelf break might be a good indicator for subsurface shelf water export occurrences. However, satellite altimetry does not resolve smaller scales than the largest mesoscale. Hence, several filaments of a few tens of km and small eddy-like structures near the BMC (diameter about 50 km) such as the merging of eddy C1 with the MC are not well-resolved as suggested by Ferrari et al. (2017). In addition, intense (> 1Sv) wind-driven high frequency (1–3 days) cross-shelf exchanges were detected by Berden et al. (in press) from high-resolution reanalyses not properly resolved by altimetry.

In conclusion, *in situ* hydrographic and ADCP observations combined with long-term satellite observations, an eddy detection algorithm, and Argo float profiles allowed us to identify and characterize the 3-D structure and evolution of surface and subsurface shelf water export to the adjacent deep ocean. The two types of shelf water export pathways may contribute to balancing the mass convergence associated with along-shore flows. Future oceanographic surveys covering the entire width of the continental slope and achieving high-resolution synoptic along-slope sections at the BMC might help to better constrain the structure of subsurface shelf water export.

DATA AVAILABILITY STATEMENT

The full processed data necessary to reproduce the reported finding is available at https://doi.org/10.17882/86206. Raw TSG and meteorological underway measurements are available at http://data.utm.csic.es/viewer/?vessel=sdg&cruise=20160408&dataset=tss. Raw CTD and ADCP data is available for research under the previous authorization of the Uruguayan national oil company (https://www.ancap.com.uy). ADT and chlorophyll-a data were downloaded from http://marine.copernicus.eu/, SST from https://psl.noaa.gov/, SSS from https://catalogue.ceda.ac.uk/uuid/fad2e982a59d44788eda09e3c67ed7d5 and eddy tracking from https://vesg.ipsl.upmc.fr/thredds/catalog/IPSLFS/rlaxe/catalog.html?dataset=DatasetScanIPSLFS/rlaxe/Database_South_Atl.zip.

AUTHOR CONTRIBUTIONS

GM processed the hydrographic data and made the transport calculations, and prepared the manuscript with contributions

from all co-authors. All authors participated in the scientific interpretation of the results.

FUNDING

This work was supported by the European Union's Horizon 2020 research and innovation program under grant agreements no. 817578 (TRIATLAS), the TOEddies CNES-TOSCA research grant. We also acknowledge the mesoscale calculation server CICLAD (http://ciclad-web.ipsl.jussieu.fr) dedicated to Institut Pierre Simon Laplace modeling effort for technical and computational support. GM received funding from bourse ANII-Campus France (POS_CFRA_2017_1_146868). AP acknowledges the support from the Inter-American Institute for Global Change Research/CONICET (Argentina) grant RD3347.

ACKNOWLEDGMENTS

We deeply acknowledge all the people behind the cruise planning and sampling processing, especially those on board RV Sarmiento de Gamboa, as well as all the open access datasets. GM acknowledges Uruguayan law No. 18.381 (exp No. 2018/14000/020893) and Phillip Miller for the very useful discussions. We also acknowledges William Sadvige, Tamaryn Morris, and Anna Rubio for their constructive comments and suggestions that greatly improved the manuscript.

SUPPLEMENTARY MATERIAL

The Supplementary Material for this article can be found online at: https://www.frontiersin.org/articles/10.3389/fmars.2022.857594/full#supplementary-material

REFERENCES

Amante, C., and Eakins, B. W. (2009). *ETOPO1 1 Arc-Minute Global Relief Model: Procedures, Data Sources and Analysis. NOAA Technical Memorandum NESDIS NGDC-24*. Washington, DC: NOAA, doi: 10.7289/V5C8276M

Argo (2021). *Argo Float Data and Metadata From Global Data Assembly Centre (Argo Gdac)*. France: SEANOE doi: 10.17882/42182

Arruda, W. Z., and da Silveira, I. C. A. (2019). Dipole-induced Central Water extrusions south of Abrolhos Bank (Brazil, 20.5 os). *Continental Shelf Res.* 188:976. doi: 10.1016/j.csr.2019.103976

Artana, C., Provost, C., Lellouche, J. M., Rio, M. H., Ferrari, R., and Senneìchael, N. (2019). The Malvinas Current at the Confluence with the Brazil Current: Inferences from 25 years of Mercator Ocean reanalysis. *J. Geophys. Res.: Oceans* 124, 7178–7200. doi: 10.1029/2019JC015289

Barré, N., Provost, C., Renault, A., and Sennéchael, N. (2011). Fronts, meanders and eddies in Drake Passage during the ANT-XXIII/3 cruise in January–February 2006: A satellite perspective. *Top. Stud. Oceanogr.* 58, 2533–2554. doi: 10.1016/j.dsr2.2011.01.003

Barreiro, M. (2010). Influence of ENSO and the South Atlantic Ocean on climate predictability over Southeastern South America. *Clim. Dyn.* 35, 1493–1508. doi: 10.1007/s00382-009-0666-9

Berden, G., Charo, M., Möller, O. O. Jr., and Piola, A. R. (2020). Circulation and Hydrography in the Western South Atlantic Shelf and Export to the Deep Adjacent Ocean: 30° S to 40° S. *J. Geophys. Res. Oceans* 125:e2020JC016500.

Berden, G., Piola, A. R., and Palma, E. D. (in press). *Cross-Shelf Exchange in the South Western*. Atlantic shelf: Climatology and extreme events. *Front. Mar. Sci.* doi: 10.3389/fmars.2022.855183

Bianchi, A. A., Giulivi, C. F., and Piola, A. R. (1993). Mixing in the Brazil-Malvinas confluence. *Oceanogr. Res. Papers* 40, 1345–1358.

Bodnariuk, N., Simionato, C. G., Saraceno, M., Osman, M., and Diaz, L. B. (2021). Interannual variability of the Latitude of Separation of the Brazil Current: Teleconnections and Oceanic Rossby Waves Propagation. *J. Geophys. Res. Oceans* 126:e2021JC017557. doi: 10.1029/2021JC017557

Borús, J. (2017). *Evaluación de Caudales Diarios Descargados por los Grandes Ríos del Sistema del Plata al Río de la Plata*. Argentina: Dirección de Sistemas de Información y Alerta Hidrológico Instituto Nacional del Agua.

Borús, J., UriburuQuirno, M., and Calvo, D. (2017). *Evaluación de Caudales Mensuales Descargados por los Grandes ríos del Sistema del Plata al Estuario del Río de la Plata*. Ezeiza: Alerta Hidrológico-Instituto Nacional del Agua y el Ambiente.

Boutin, J., Reul, N., Köhler, J., Martin, A. C., Catany, R., Guimbard, S., et al. (2021). Satellite-based Time-Series of Sea Surface Salinity designed for Ocean and Climate Studies. *ESSOAr* 1–47. doi: 10.1002/essoar.10507337.1

Capet, A., Mason, E., Rossi, V., Troupin, C., Faugère, Y., Pujol, I., et al. (2014). Implications of refined altimetry on estimates of mesoscale activity and eddy-driven offshore transport in the Eastern Boundary Upwelling Systems. *Geophys. Res. Lett.* 41, 7602–7610. doi: 10.1002/2014GL061770

Carreto, J. I., Montoya, N. G., Benavides, H. R., Guerrero, R., and Carignan, M. O. (2003). Characterization of spring phytoplankton communities in the Río de La Plata maritime front using pigment signatures and cell microscopy. *Marine Biol.* 143, 1013–1027. doi: 10.1007/s00227-003-1147-z

Chaigneau, A., Le Texier, M., Eldin, G., Grados, C., and Pizarro, O. (2011). Vertical structure of mesoscale eddies in the eastern South Pacific Ocean: A composite analysis from altimetry and Argo profiling floats. *J. Geophys. Res.* 116:C11025. doi: 10.1029/2011JC007134

Chelton, D. B., Schlax, M. G., Witter, D. L., and Richman, J. G. (1990). Geosat altimeter observations of the surface circulation of the Southern Ocean. *J. Geophys. Res.* 95, 17877–17903. doi: 10.1029/JC095iC10p17877

Chin, T. M., Vazquez-Cuervo, J., and Armstrong, E. M. (2017). A multi-scale high-resolution analysis of global sea surface temperature. *Remote Sens. Environ.* 200, 154–169. doi: 10.1016/j.rse.2017.07.029

Combes, V., Matano, R. P., and Palma, E. D. (2021). Circulation and cross-shelf exchanges in the northern shelf region of the southwestern Atlantic: Kinematics. *J. Geophys. Res.* 126:e2020JC016959. doi: 10.1029/2020JC016959

Fang, M., and Zhang, J. (2015). Basin-scale features of global sea level trends revealed by altimeter data from 1993 to 2013. *J. Oceanogr.* 71, 297–310. doi: 10.1007/s10872-015-0289-1

Ferrari, R., Artana, C., Saraceno, M., Piola, A. R., and Provost, C. (2017). Satellite altimetry and current-meter velocities in the Malvinas current at 41°S: Comparisons and modes of variations. *J. Geophys. Re. Oceans* 122, 9572–9590. doi: 10.1002/2017jc013340

Framiñan, M. B., Etala, M. P., Acha, E. M., Guerrero, R. A., Lasta, C. A., and Brown, O. B. (1999). "Physical characteristics and processes of the Río de la Plata estuary," in *Estuaries of South America* (Heidelberg: Springer), 161–194. doi: 10.1007/978-3-642-60131-6_8

Franco, B. C., Palma, E. D., Combes, V., Acha, E. M., and Saraceno, M. (2018). Modeling the offshore export of Subantarctic Shelf Waters from the Patagonian shelf. *J. Geophys. Res.* 123, 4491–4502. doi: 10.1029/2018JC013824

Franco, B. C., Palma, E. D., Combes, V., and Lasta, M. L. (2017). Physical processes controlling passive larval transport at the Patagonian Shelf Break Front. *J. Sea Res.* 124, 17–25. doi: 10.1016/j.seares.2017.04.012

Garnesson, P., Mangin, A., Fanton, d'Andon, O., Demaria, J., and Bretagnon, M. (2019). The CMEMS GlobColour chlorophyll a product based on satellite observation: multi-sensor merging and flagging strategies. *Ocean Sci.* 15, 819–830. doi: 10.5194/os-15-819-2019

Goni, G. J., Bringas, F., and DiNezio, P. N. (2011). Observed low frequency variability of the Brazil Current front. *J. Geophys. Res.* 116:198. doi: 10.1029/2011JC007198

Gordon, A. L. (1989). Brazil-Malvinas Confluence–1984. *Deep Sea Res. Part A. Oceanogr. Res. Papers* 36, 359–384. doi: 10.1016/0198-0149(89)90042-3

Grasshoff, K., Kremling, K., and Ehrhardt, M. (eds) (2009). *Methods of Seawater Analysis*. New Jersey, NJ: John Wiley & Sons.

Grimm, A. M., Barros, V. R., and Doyle, M. E. (2000). Climate variability in southern South America associated with El Niño and La Niña events. *J. Clim.* 13, 35–58. doi: 10.1175/1520-04422000013

Guerrero, R. A., Piola, A. R., Fenco, H., Matano, R. P., Combes, V., Chao, Y., et al. (2014). The salinity signature of the cross-shelf exchanges in the Southwestern Atlantic Ocean: Satellite observations. *J. Geophys. Res. Oceans* 119, 7794–7810. doi: 10.1002/2014JC010113

Hersbach, H., Bell, B., Berrisford, P., Hirahara, S., Horányi, A., Muñoz-Sabater, J., et al. (2020). The ERA5 global reanalysis. *Q. J. Roy. Meteorol. Soc.* 146, 1999–2049. doi: 10.1002/qj.3803

Ismail, M. F. A., and Ribbe, J. (2019). On the cross-shelf exchange driven by frontal eddies along a western boundary current during austral winter 2007. *Estuarine* 227:106314. doi: 10.1016/j.ecss.2019.106314

Kruk, C., Martínez, A., Nogueira, L., Alonso, C., and Calliari, D. (2015). Morphological traits variability reflects light limitation of phytoplankton production in a highly productive subtropical estuary (Río de la Plata South America). *Mar. Biol.* 162, 331–341. doi: 10.1007/s00227-014-2568-6

Lago, L. S., Saraceno, M., Piola, A. R., and Ruiz-Etcheverry, L. A. (2021). Volume Transport Variability on the Northern Argentine Continental Shelf from In Situ and Satellite Altimetry Data. *J. Geophys. Res.* 126:e2020JC016813. doi: 10.1029/2020JC016813

Laxenaire, R., Speich, S., Blanke, B., Chaigneau, A., Pegliasco, C., and Stegner, A. (2018). Anticyclonic eddies connecting the western boundaries of Indian and Atlantic oceans. *J. Geophys. Res.* 123, 7651–7677. doi: 10.1029/2018JC014270

Laxenaire, R., Speich, S., and Stegner, A. (2019). Evolution of the Thermohaline Structure of One Agulhas Ring Reconstructed from Satellite Altimetry and Argo Floats. *J. Geophys. Res.* 124, 8969–9003. doi: 10.1029/2018JC014426

Laxenaire, R., Speich, S., and Stegner, A. (2020). Agulhas Ring Heat Content and Transport in the South Atlantic Estimated by Combining Satellite Altimetry and Argo Profiling Floats Data. *J. Geophys. Res.* 125:e2019JC015511. doi: 10.1029/2019JC015511

Le Bot, P., Kermabon, C., Lherminier, P., and Gaillard, F. (2011). *CASCADE V6. 1: Logiciel de Validation et de Visualisation des Mesures ADCP de Coque. OPS/LPO 11-01*. Available online at: https://archimer.ifremer.fr/doc/00342/45285/ (accessed January 27, 2021).

Lumpkin, R., and Garzoli, S. (2011). Interannual to decadal changes in the western South Atlantic's surface circulation. *J. Geophys. Res.* 116:C01014. doi: 10.1029/2010JC006285

Maamaatuaiahutapu, K., Garçon, V. C., Provost, C., Boulahdid, M., and Bianchi, A. A. (1994). Spring and winter water mass composition in the Brazil-Malvinas Confluence. *J. Mar. Res.* 52, 397–426. doi: 10.1357/0022240943077064

Maamaatuaiahutapu, K., Garçon, V. C., Provost, C., Boulahdid, M., and Osiroff, A. P. (1992). Brazil-Malvinas confluence: Water mass composition. *J. Geophys. Res.* 97, 9493–9505. doi: 10.1029/92JC00484

Maciel, F. P., Santoro, P. E., and Pedocchi, F. (2021). Spatio-temporal dynamics of the Río de la Plata turbidity front; combining remote sensing with in-situ measurements and numerical modeling. *Cont. Shelf Res.* 213:104301. doi: 10.1016/j.csr.2020.104301

Malan, N., Archer, M., Roughan, M., Cetina-Heredia, P., Hemming, M., Rocha, C., et al. (2020). Eddy-driven cross-shelf transport in the East Australian Current separation zone. *J. Geophys. Res.* 125:e2019JC015613. doi: 10.1029/2019JC015613

Martínez, A., and Ortega, L. (2015). Delimitation of domains in the external Río de la Plata estuary, involving phytoplanktonic and hydrographic variables. *Braz. J. Oceanogr.* 63, 217–227. doi: 10.1590/s1679-87592015086106303

Matano, R. P., Combes, V., Piola, A. R., Guerrero, R., Palma, E. D., Strub, P. T., et al. (2014). The salinity signature of the cross-shelf exchanges in the Southwestern Atlantic Ocean: Numerical simulations. *J. Geophys. Res.* 119, 7949–7968. doi: 10.1002/2014JC010116

Matano, R. P., Palma, E. D., and Piola, A. R. (2010). The influence of the Brazil and Malvinas Currents on the Southwestern Atlantic Shelf circulation. *Ocean Sci.* 6, 983–995. doi: 10.5194/os-6-983-2010

McDougall, T. J., and Barker, P. M. (2011). *Getting Started with TEOS-10 and the Gibbs Seawater (GSW) Oceanographic Toolbox Version 3.06.12. SCOR/IAPSO WG127*.

Orúe-Echevarría, D., Pelegrí, J. L., Alonso-González, I. J., Benítez-Barrios, V. M., Emelianov, M., García-Olivares, A., et al. (2021). A view of the Brazil-Malvinas confluence, March 2015. *Deep Sea Res. Part I Oceanogr. Res. Papers* 172: 103533.

Palma, E. D., Matano, R. P., and Piola, A. R. (2008). A numerical study of the Southwestern Atlantic Shelf circulation: Stratified ocean response to local and offshore forcing. *J. Geophys. Res. Oceans* 109, 1–17. doi: 10.1029/2007JC004720

Pegliasco, C., Chaigneau, A., and Morrow, R. (2015). Main eddy vertical structures observed in the four major Eastern Boundary Upwelling Systems. *J. Geophys. Res. Oceans* 120, 6008–6033. doi: 10.1002/2015JC010950

Piola, A. R., Campos, E. J., Möller, O. O. Jr., Charo, M., and Martinez, C. (2000). Subtropical shelf front off eastern South America. *J. Geophys. Res. Oceans* 105, 6565–6578. doi: 10.1029/1999JC000300

Piola, A. R., and Georgi, D. T. (1982). Circumpolar properties of Antarctic intermediate water and Subantarctic Mode Water. *Deep Sea Res. Part A. Oceanogr. Res. Papers* 29, 687–711. doi: 10.1016/0198-0149(82)90002-4

Piola, A. R., Matano, R. P., Palma, E. D., Möller, O. O. Jr., and Campos, E. J. (2005). The influence of the Plata River discharge on the western South Atlantic shelf. *Geophys. Res. Lett.* 32, 1–4. doi: 10.1029/2004GL021638

Piola, A. R., Möller, O. O. Jr., Guerrero, R. A., and Campos, E. J. (2008). Variability of the subtropical shelf front off eastern South America: winter 2003 and summer 2004. *Cont. Shelf Res.* 28, 1639–1648. doi: 10.1016/j.csr.2008.03.013

Piola, A. R., Palma, E. D., Bianchi, A. A., Castro, B. M., Dottori, M., Guerrero, R. A., et al. (2018). Physical oceanography of the SW Atlantic Shelf: a review. *Plankton Ecol. South. Atlantic* 2018, 37–56. doi: 10.1007/978-3-319-77869-3_2

Proença, L. A., Schramm, M. A., Alves, T. P., and Piola, A. R. (2017). "The extraordinary 2016 autumn DSP outbreak in Santa Catarina, Southern Brazil, explained by large-scale oceanographic processes," in *Marine and Fresh-Water Harmful Algae. Proceedings of the 17th International Conference on Harmful Algae*, eds L. A. O. Proença and G. M. Hallegraeff (Washington, DC: International Society for the Study of Harmful Algae)

Provost, C., Gana, S., Garçon, V., Maamaatuaiahutapu, K., and England, M. (1995). Hydrographic conditions in the Brazil-Malvinas Confluence during austral summer 1990. *J. Geophys. Res.* 100, 10655–10678. doi: 10.1029/94JC02864

Provost, C., Garçon, V., and Falcon, L. M. (1996). Hydrographic conditions in the surface layers over the slope-open ocean transition area near the Brazil-Malvinas confluence during austral summer 1990. *Cont. Shelf Res.* 16, 215–235.

Pujol, M.-I., FaugeÌre, Y., Taburet, G., Dupuy, S., Pelloquin, C., Ablain, M., et al. (2016). DUACS DT2014: the new multi-mission altimeter data set reprocessed over 20 years. *Ocean Sci.* 12, 1067–1090. doi: 10.5194/os-12-1067-2016

Reynolds, R. W., Smith, T. M., Liu, C., Chelton, D. B., Casey, K. S., and Schlax, M. G. (2007). Daily high-resolution-blended analyses for sea surface temperature. *J. Clim.* 20, 5473–5496. doi: 10.1175/2007JCLI1824.1

Roughan, M., Cetina-Heredia, P., Ribbat, N., and Suthers, I. M. (2022). Shelf Transport Pathways Adjacent to the East Australian Current Reveal Sources of Productivity for Coastal Reefs. *Front. Mar. Sci.* 8:789687.

Roughan, M., Macdonald, H. S., Baird, M. E., and Glasby, T. M. (2011). Modelling coastal connectivity in a Western Boundary Current: Seasonal and inter-annual variability. *Deep Sea Res. Part II* 58, 628–644. doi: 10.1016/j.dsr2.2010.06.004

Ruiz-Etcheverry, L. A., and Saraceno, M. (2020). Sea Level Trend and Fronts in the South Atlantic Ocean. *Geosciences* 10:218. doi: 10.3390/geosciences10060218

Schiermeier, Q. (2015). Hunting the Godzilla El Niño. *Nat. News* 526:490.

Valla, D., Piola, A. R., Meinen, C. S., and Campos, E. (2018). Strong mixing and recirculation in the northwestern Argentine Basin. *Oceans* 123, 4624–4648.

Vivier, F., and Provost, C. (1999). Volume transport of the Malvinas Current: Can the flow be monitored by TOPEX/POSEIDON? *Oceans* 104, 21105–21122. doi: 10.1029/1999JC900056

Yentsch, C. S., and Menzel, D. W. (1963). A method for the determination of phytoplankton chlorophyll and phaeophytin by fluorescence. *Deep*

Sea Res. Oceanogr. Abstracts 10, 221–231. doi: 10.1016/0011-7471(63)90358-9

Conflict of Interest: The authors declare that the research was conducted in the absence of any commercial or financial relationships that could be construed as a potential conflict of interest.

Publisher's Note: All claims expressed in this article are solely those of the authors and do not necessarily represent those of their affiliated organizations, or those of the publisher, the editors and the reviewers. Any product that may be evaluated in this article, or claim that may be made by its manufacturer, is not guaranteed or endorsed by the publisher.

Copyright © 2022 Manta, Speich, Barreiro, Trinchin, de Mello, Laxenaire and Piola. This is an open-access article distributed under the terms of the Creative Commons Attribution License (CC BY). The use, distribution or reproduction in other forums is permitted, provided the original author(s) and the copyright owner(s) are credited and that the original publication in this journal is cited, in accordance with accepted academic practice. No use, distribution or reproduction is permitted which does not comply with these terms.

frontiers in Marine Science

ORIGINAL RESEARCH
published: 24 March 2022
doi: 10.3389/fmars.2022.841364

Distribution of Harmful Algae (*Karenia* spp.) in October 2021 Off Southeast Hokkaido, Japan

Hiroshi Kuroda, Yukiko Taniuchi, Tsuyoshi Watanabe, Tomonori Azumaya and Natsuki Hasegawa*

Fisheries Resources Institute (Kushiro Station), Japan Fisheries Research and Education Agency, Kushiro, Japan

An unprecedented large-scale outbreak of harmful algae, including *Karenia selliformis* and *Karenia mikimotoi*, was reported in mid-September 2021 in the northwest Pacific Ocean off southeastern Hokkaido, Japan. It inflicted catastrophic damage on coastal fisheries in the ensuing months. To understand the spatiotemporal distribution of *Karenia* spp. abundance, we conducted extensive ship-based surveys across several water masses during 4–14 October, 2021 and analyzed *in-situ* data in combination with Sentinel-3-derived ocean color imagery with a horizontal resolution of 300 m. High chlorophyll-*a* concentrations (exceeding 10 mg m^{-3}) were identified mainly in coastal shelf–slope waters of <1,000-m water depth occupied by Surface Coastal Oyashio Water or Modified Soya Warm Current Water. *Karenia* spp. abundance was strongly correlated with chlorophyll-*a* concentration, which typically had a shallow vertical maximum within the surface mixed layer. Large- and small-scale distributions of *Karenia* spp. abundance at the ocean surface were estimated from two satellite-imagery products: maximum line height and red-band difference. Maps generated of *Karenia* spp. abundance revealed snapshots of dynamic *Karenia* bloom distributions. Specifically, the cores of *Karenia* blooms were located on continental shelves, sometimes locally exceeded 10^4 cells mL^{-1}, and seemed to be connected intermittently to very nearshore waters. Relatively high-abundance areas (>10^3 cells mL^{-1}) of *Karenia* spp. on the shelf were characterized by submesoscale (i.e., 1–10 km) patch- or streak-like distributions, or both. Within a roughly 24-h period from 12 to 13 October, *Karenia*-spp. abundances averaged over the shelf abruptly increased more than doubled; these abundance spikes were associated with the combined effects of physical advection and algal growth. The obtained maps and features of *Karenia* spp. abundance will provide basic estimates needed to understand the processes and mechanisms by which algal blooms can inflict damage on regional fisheries.

Keywords: harmful algal bloom, *Karenia*, northwestern Pacific Ocean, *in-situ* measurement, Sentinel 3

OPEN ACCESS

Edited by:
Hiroaki Saito,
The University of Tokyo, Japan

Reviewed by:
Eko Siswanto,
Japan Agency for Marine-Earth Science and Technology (JAMSTEC), Japan
Po Teen Lim,
University of Malaya, Malaysia

****Correspondence:***
Hiroshi Kuroda
kurocan@affrc.go.jp

Specialty section:
This article was submitted to Coastal Ocean Processes, a section of the journal Frontiers in Marine Science

Received: *22 December 2021*
Accepted: *01 February 2022*
Published: *24 March 2022*

Citation:
Kuroda H, Taniuchi Y, Watanabe T, Azumaya T and Hasegawa N (2022) Distribution of Harmful Algae (Karenia spp.) in October 2021 Off Southeast Hokkaido, Japan. Front. Mar. Sci. 9:841364. doi: 10.3389/fmars.2022.841364

INTRODUCTION

Harmful algal blooms (HABs) are a critical global problem, and their increasing frequency and severity may be tied to climate change (e.g., Wells et al., 2015, 2020; Frölicher and Laufkötter, 2018; IPCC [Intergovernmental Panel on Climate Change], 2019; Trainer et al., 2019). Over the last decade, many incidents that have inflicted devastating damage on marine ecosystems and

human well-being across the world's oceans have been attributed to HABs of record-breaking scale; the HABs have been associated with basin-scale ocean and atmospheric variability, particularly anomalously high temperatures (i.e., marine heatwaves) (Lefebvre et al., 2016; McCabe et al., 2016; Ryan et al., 2017; León-Muñoz et al., 2018; Roberts et al., 2019; Bondur et al., 2021).

An unfortunate feature of large-scale HABs along open coastlines is that even if natural, healthy marine environments are maintained without artificial eutrophication, HABs can develop and progress without initially being noticed by human observers and can bloom abruptly to uncontrollable levels (e.g., Anderson et al., 2008; Vargo et al., 2008; White et al., 2014; Du et al., 2016; Crawford et al., 2021). Even in places where harmful algal species have been rarely observed, once a harmful outbreak occurs, further outbreaks can occur repeatedly in subsequent years (e.g., Kim et al., 2007; Onitsuka et al., 2010; Feki et al., 2014). Hence, it is essential to retroactively understand this spatiotemporal transition, including the development, maintenance, and decay of specific HABs, in order to mitigate the impacts of HABs on human well-being as much as possible. An important challenge that needs to be addressed before we tackle this problem is how to precisely estimate the spatiotemporal distribution of HABs by combining information from several data types.

Unprecedented large-scale HABs occurred in Pacific coastal waters off southeastern Hokkaido, Japan, in mid-September 2021, about a month after the subsidence of the most intense and extensive marine heatwaves ever recorded over the northwest Pacific Ocean (Kuroda and Setou, 2021). There had been no previous reports of large-scale events attributed to HABs over the whole of this study region, where the marine environment has largely been maintained in its natural, healthy condition. The HABs consisted of *Karenia* and other species and included *Karenia selliformis*, *Karenia longicanalis*, and *Karenia mikimotoi* (Iwataki et al., 2022). As a result, serious potential impacts on coastal ecosystems and fisheries were reported for southeast Hokkaido (see the bold magenta line in **Figure 1A**): sea urchins experienced mass die-offs, chum salmon died in fixed nets, and juvenile fishes died in rearing facilities. Although is unclear what level of *Karenia* spp. abundance causes mortality in these species, the order of magnitude of *Karenia* spp. abundance observed in our study ($>10^2$–10^4 cells mL^{-1}) might be sufficient to cause ecological damage according to previous toxicity assessments (e.g., Shi et al., 2012; Basti et al., 2015).

Kuroda et al. (2021a) provided an initial report on the HABs, in which they described the development of the HABs from August to September 2021 and inferred potential source areas by combining three analyses: satellite-derived chlorophyll *a* concentrations (SCCs) at the sea surface, a realistic high-resolution (1/50°) ocean circulation model, and particle-tracking simulations. The HABs occurred in a crossroad-like confluence zone of subarctic and subtropical waters. The areal extent of SCCs exceeding 5 or 10 mg m^{-3} in the study region started to slowly increase after 20 August, when the marine heatwaves subsided, intermittently exceeded the climatological daily maximum after late August, and reached record-breaking extremes in mid-to-late September (**Figure 2**). About 70% of the SCCs that exceeded 10 mg m^{-3} occurred in places where water depths were <300 m (i.e., coastal shelf waters), where small-scale submesoscale variations are expected to dominate. The high SCCs were tightly linked with low-salinity water (e.g., subarctic Oyashio and river-influenced waters), whereas high-salinity subtropical water appeared to suppress the occurrence of HABs.

It should be emphasized that the analysis presented by Kuroda et al. (2021a) has some limitations. One limitation is that the study dealt only with the HAB developmental stage (i.e., up to late September) and did not describe the transition to full-blown HABs. The second limitation is that the study was based primarily on remote sensing and simulations, with little analysis of *in-situ* measurements. For instance, the use of ocean circulation model outputs entails some degree of uncertainty, and although high-SCC areas were analyzed as a metric of HAB extent, the validity of this metric needs to be verified by *in-situ* observations. Another limitation is that the study focused on the overall distribution of SCCs; the spatiotemporal transition of *Karenia* blooms in coastal shelf waters is often characterized by small-scale structures, and is difficult to understand on the basis of the overall SCC distribution.

To address these limitations, here, we analyzed the results from ship surveys conducted on 4–14 October, 2021 and spanning a wide area across several water masses in the Pacific Ocean off southeast Hokkaido. The study aimed to describe the distribution of *Karenia* spp. blooms together with chlorophyll-*a* concentrations in relation to oceanographic conditions. Moreover, to understand both large- and small-scale distributions of *Karenia* spp. blooms, we generated maps of *Karenia* spp. abundances by combining *in situ* measurements with Sentinel-3-derived ocean color imagery with a horizontal resolution of 300 m.

MATERIALS AND METHODS

Field Measurements From Aboard a Research Vessel

In-situ Measurements

We performed extensive ship surveys from aboard R/V *Hokko-maru* (international gross tonnage, 1246 t; designed draft, 4.5 m) from 4 to 14 October, 2021 in the northwest Pacific off southeastern Hokkaido, Japan (**Figure 1**). During the surveys, we took measurements with conductivity–temperature–depth (CTD) sensors, collected water samples with a bucket and Niskin bottles, and obtained a continuous recording of near-surface temperature, salinity, and chlorophyll-*a* concentration along the ship track.

Surveys were first carried out along the A Line during 4–10 October (**Figure 1B**, closed red circles) and then along the L lines during 10–14 October (**Figure 1B**, closed blue circles). The A Line, which extends about 500-km southeast from the Hokkaido coast, is a regular monitoring transect that has been used by the Japan Fisheries Research and Education Agency to monitor the state of the Oyashio (with a focus on its mesoscale variability) since 1987 (e.g., Kuroda et al., 2017, 2019). For our study, CTD measurements were obtained at 28 stations along

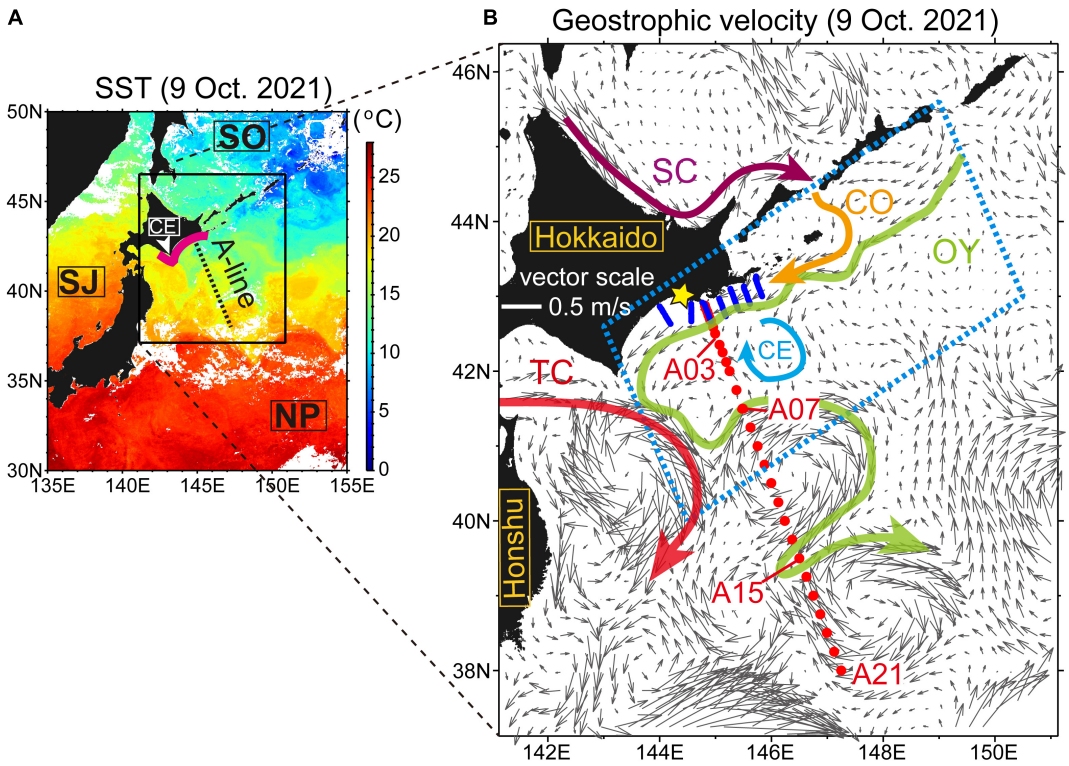

FIGURE 1 | (A) Himawari-8-derived sea surface temperatures around Japan on 9 October, 2021. White areas denote clouds. Geographic names are enclosed in rectangles: SJ, Sea of Japan; SO, Sea of Okhotsk; NP, North Pacific; and CE, Cape Erimo. The bold magenta line roughly indicates coastal waters where fisheries experienced devastating damages that were attributable to harmful algal blooms after mid-September 2021. **(B)** Absolute geostrophic velocity at the sea surface, estimated from near-real-time gridded altimetry products. Closed red and blue circles indicate conductivity–temperature–depth (CTD) stations along the A Line and L lines, respectively. The star symbol indicates the location of the Katsurakoi fishery harbor. Schematic flow patterns are depicted by colored vectors: SC, Soya Warm Current; CO, Coastal Oyashio; OY, Oyashio; TC, Tsugaru Warm Current; and CE, clockwise eddy. Positions where the Oyashio crossed the A Line were determined on the basis of 5°C isotherms at 100-m depth. Daily areal extents of satellite-derived chlorophyll-*a* concentrations were estimated within the blue dashed square (**Figure 2**).

the A Line (i.e., in order from north to south, Stns. B01, A01, B02–B04, A02, A025, A03, A035, A04, A045, and A05–A21). The L-lines consist of seven cross-shelf transects (i.e., lines L1–L7 in order from east to west), each with 15–17 stations spaced about 2 km apart and located mainly on the Pacific shelf; these transects have been used to capture submesoscale variability in association with the Coastal Oyashio on the shelf (e.g., Sakamoto et al., 2010; Kusaka et al., 2016; Kuroda et al., 2021b). It should be noted that the ship survey was not used to observe very nearshore waters of depth <20 m, where low-salinity river discharge is expected to dominate (e.g., Kuroda et al., 2021a), because the research vessel could not enter shallow waters without significant risk of stranding.

Conductivity–Temperature–Depth sensors combined with dissolved oxygen, fluorescence, and turbidity sensors were lowered to the vicinity of the seafloor or to 3,100 dbar for the A Line, and to 490 dbar for the L lines. At all CTD stations, a bucket was also used to sample water from a depth of a few dozen centimeters, and the temperature, salinity, and chlorophyll-*a* concentration of the sampled water were also obtained. Subsurface waters at standard depths (10, 20, 30, 40, 50, 60, 80, 100, 125, 150, 200, 300, 400, 500, 600, 800, 1,000, 1,250, 1,500, 2,000, 2,500, and 3,000 dbar in the case of the A Line) were also sampled by using Niskin bottles on a CTD–rosette sampler system. The sampled water was aliquoted into smaller bottles on deck for transport to a shore-based laboratory, where we obtained measurements of conductivity/salinity (in 200- or 250-mL subsamples), chlorophyll *a* concentration (100 mL from the standard depths above 200 m), and *Karenia* spp. abundance (250 mL for the L lines at 10-m depth or 1,000 mL for the A Line).

Moreover, along the track of R/V *Hokko-maru*, near-surface temperatures, salinities, chlorophyll-*a* concentrations, and geolocations were continuously recorded at intervals of 1 min by digital sensors and a global positioning system receiver. Ship speeds ranged from 0.0 to 14.9 knots during the period of analysis; the mean was 4.9 knots. The spatial resolution of the ship-track data therefore changed from 0 to 460 m, with an average of 151 m; this indicated that the ship-track data could be used to capture submesoscale variations with a typical scale of 0.1–10 km (McWilliams, 2016; Kuroda and Toya, 2020).

Shore-Based Measurements

In a shore-based laboratory of Fisheries Resources Institute (Kushiro Station), salinity/conductivity was measured with high

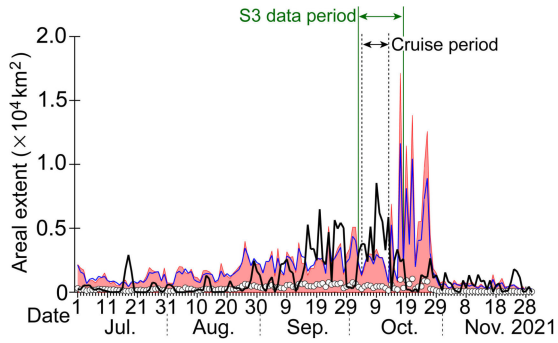

FIGURE 2 | Daily areal extent of high satellite-derived chlorophyll-*a* concentrations exceeding 10 mg m^{-3} across the study region (i.e., within the blue dashed square in **Figure 1B**). The original time series published by Kuroda et al. (2021a) was extended to 30 November, 2021. The black bold line indicates the daily areal extent in 2021. White circles denote climatological daily means calculated over the previous 23 years (1998–2020), and the blue line indicates the climatological daily mean plus three standard deviations. Red shading shows the range between the lowest daily minimums and highest daily maximums recorded over the previous 23 years. Horizontal double-headed arrows represent the periods of the ship survey (black) and the Sentinel-3 data (green) that were analyzed in this study. Chlorophyll-*a* concentrations were based on near-real-time and reprocessed L4 products of global daily datasets with a horizontal grid of about 4 km that were created by merging sensor data from SeaWiFS, MODIS, MERIS, VIIRS-SNPP, and JPSS1 and downloaded from the European Union's Copernicus Marine Service.

accuracy by using a Guildline Model 8400B "Autosal" Laboratory Salinometer, Smith Falls, ON, Canada.

Chlorophyll-*a* concentrations were measured manually by using the procedures described by Kasai et al. (1998). Water samples were filtered onto 25-mm Whatman GF/F glass fiber filters immediately after sampling and preserved in *N*, *N*-dimethylformamide as described by Suzuki and Ishimaru (1990). Samples and filters were frozen onboard R/V *Hokko-maru* and stored in the dark until they could be measured with a fluorometer (Model 10AU, Turner Designs, San Jose, CA, United States) in a shore-based laboratory.

For enumeration of *Karenia* spp., water samples of 250 or 1,000 mL were fixed and preserved with acid Lugol's solution (final concentration, 4%) at 5°C. Samples were concentrated to a volume of 25–50 mL by reverse filtration through 2-μm pore-size filters (Dodson and Thomas, 1964). A 0.2–0.5-mL sample of the concentrated algal cells was settled in a chamber (SCS N04, Matsunami, Osaka, Japan) and counted under an inverted microscope (ECLIPSE TE300, Nikon, Tokyo, Japan). *Karenia* spp. were taxonomically identified on the basis of the results of Iwataki et al. (2022).

Correction of Sensor Values

Conductivity–Temperature–Depth-derived raw data were processed and averaged at 1-dbar intervals. Profiles of CTD-based salinity and chlorophyll *a* were corrected by using a linear regression between CTD-based sensor values and values manually measured from sampled waters. Moreover, erroneous temperature, salinity, and chlorophyll-*a* values recorded at depths of 0–4 m by the CTD were replaced by values obtained by linear interpolation between the 0-m bucket sample and a CTD measurement at 5-m depth. Interpolation errors were mostly negligible because the surface mixed layer was formed near the sea surface (typically, 20–25 m) throughout the period of our ship survey.

Near-surface temperature, salinity, and chlorophyll-*a* concentration along the ship track were corrected by using a linear regression against the temperature (R^2 = 0.995), salinity (R^2 = 0.996), and chlorophyll *a* concentration (R^2 = 0.737) of the bucket-sampled water.

Field Measurements From a Harbor

After mid-September 2021 (when *Karenia* blooms were first observed), surface water samples were collected daily around the Katsurakoi fishery harbor (144°26.77′E, 42°56.81′N; indicated by the star symbol in **Figure 1B**). Samples were collected from three fixed sites within a few hundred meters of the harbor. Buckets were used for sample collection at two of the sites, and an automated seawater intake to our shore-based laboratory was used at the other site. Water samples were filtered onto 25-mm Whatman GF/F glass fiber filters immediately after sampling to measure chlorophyll-*a* concentrations with a fluorometer. For enumeration of *Karenia* spp., water samples were fixed and preserved at 5°C with acid Lugol's solution (final concentration, 4%) for measurements conducted prior to 28 September, and with Hepes-buffered paraformaldehyde and glutaraldehyde (Katano et al., 2009) for subsequent measurements. *Karenia* spp. abundances (cells mL^{-1}) were estimated from 46 randomly selected samples collected during 21 September–22 October, 2021.

Satellite Measurements

Ocean color imagery based on Sentinel-3A/3B Ocean and Land Color Imager Level-2 Full Resolution were downloaded from Copernicus Online Data Access. The horizontal resolution was about 300 m, and the time interval between images was near-daily. The data period analyzed was from 3 October to 18 October, 2021 (**Supplementary Table 1**), roughly corresponding to the time period of the ship survey. For analysis, we selected imagery with a relatively small ratio of cloud coverage (< 20%) over the shelf off southeastern Hokkaido. We used normalized water-leaving reflectance ($\rho_w[\lambda]$) for a wavelength band centered at λ and chlorophyll-*a* concentrations that were derived from one of two algorithms: a neural network-based approach (hereafter, "NN") for optically complex waters (Doerffer and Schiller, 2007) and a maximum band ratio semi-analytical algorithm (hereafter, "OC4ME") for open oceans (Morel et al., 2007; Cherif et al., 2021; Moutzouris-Sidiris and Topouzelis, 2021).

Chlorophyll-*a* estimates obtained from NN and OC4ME had limited accuracy on the Pacific shelf (see section "Maps of Chlorophyll-*a* Concentration" for details), where there was considerable submesoscale variability in areas of high chlorophyll-*a* concentration (>20 mg m^{-3}). Therefore, reflectance-based maximum line height (MLH; Smith and Bernard, 2020) was used instead of NN and OC4ME to estimate chlorophyll-*a* concentrations at the sea surface.

Surface abundances of *Karenia* spp. were estimated from satellite-derived reflectance-based variables by using two methods. One method directly estimated *Karenia* spp. abundances through a combination of reflectance-based red band difference (RBD; Jordan et al., 2021) and *in-situ Karenia* spp. abundance. The other method entailed two steps: in the first step, chlorophyll-*a* concentrations were estimated by using a combination of MLH and *in-situ* chlorophyll *a* concentrations, as mentioned above, and in the second step, chlorophyll-*a* concentrations were converted into *Karenia* spp. abundances by using an observed relationship between them.

RBD and MLH are defined as follows:

$$RBD = \rho_w(681) - \rho_w(665)$$
$$MLH = \max[LH(681), LH(709)],$$

where $LH(\lambda)$ is defined as follows:

$$LH(\lambda) = \rho_w(\lambda) - \rho_w(665) - \left\{[\rho_w(753) - \rho_w(665)] \times \left(\frac{\lambda - 665}{753 - 665}\right)\right\}.$$

Relationships between the spectral properties of *Karenia* spp. and the Sentinel-3 spectral bands are illustrated in the schematic diagram in **Supplementary Figure 1**. Calculations of RBD and MLH were both based on the 665–753-nm spectral band, as opposed to OC4ME, which is based on the 443–560-nm spectral band. The 665–753-nm spectral band has an important advantage over the spectral band used in OC4ME in that the former is not strongly influenced by the absorption associated with colored dissolved organic matter (e.g., at around 440 nm), which is frequently found in the coastal waters of our study area (e.g., Isada et al., 2021).

Red band difference is frequently used for detecting and monitoring *Karenia* spp. blooms (e.g., Amin et al., 2009; Wolny et al., 2020; Jordan et al., 2021). $LH(\lambda)$, which is similar to fluorescence line height (Gower et al., 1999), with a baseline formed by the reflectance between 665 and 753 nm, was applied to all spectra (Smith and Bernard, 2020). MLH was expected to be appropriate for detecting both low (<about 20 mg m^{-3}) chlorophyll-*a* concentrations and the high (>about 20 mg m^{-3}) chlorophyll-*a* concentrations associated with red tides, because the reflectance peak at 681 nm is generally related to chlorophyll-*a* fluorescence emissions; however, at higher biomass this peak shifts to longer wavelengths owing to the combined effects of increased phytoplankton absorption and backscattering, as well as pure water absorption (e.g., Gower et al., 1999, 2005; Gower, 2016).

Finally, after generating maps of *Karenia* spp. abundance, we estimated specific rates of change (hereafter, "growth rate"), assuming exponential algal growth, from two maps of satellite-derived *Karenia* spp. abundance. Specifically, growth rate was estimated as $r = \left[\ln(K_{t2}) - \ln(K_{t1})\right]/\triangle t$, where $\triangle t$ is the time interval between satellite images and K_{t1} and K_{t2} represent *Karenia* spp. abundances estimated in a given region at times $t1$ and $t2$, respectively (i.e., $\triangle t = t2 - t1$). This estimation method was based on the work of Stumpf et al. (2008), who developed the method for satellite-derived chlorophyll-*a* imagery.

RESULTS

Overview of Oceanographic Conditions

The oceanographic conditions in our study area during the cruise can be seen from satellite-based data captured on 9 October, 2021 (**Figure 1**). The northern part of the A Line was occupied by cold waters, and the southern part was occupied by warm waters (**Figure 1A**). In the cold-water area, the Oyashio flowed southwestward along the continental slope off southeastern Hokkaido, came in contact with the Tsugaru Warm Current south of Cape Erimo, formed a sharp thermal front, and then flowed along the edge of anticyclonic mesoscale eddies, with several meanders (**Figure 1B**). A part of the Oyashio then crossed the A Line again near Stn. A15.

Inshore of the Oyashio, the Coastal Oyashio flowed along the Pacific shelf off southeastern Hokkaido as a downstream extension of the Soya Warm Current in the Sea of Okhotsk. The Coastal Oyashio crossed several L lines. As explained in the subsequent section "Field Measurements," the Coastal Oyashio transported Modified Soya Warm Current Water, which is formed by the mixing of a subtropical water mass referred to as Soya Warm Current Water that outflows from the Sea of Okhotsk with surrounding subarctic waters on the Pacific shelf.

Transition of Algal Blooms

In terms of large-scale variability along the shelf (i.e., on a scale of ∼500 km), as briefly mentioned in the section "Introduction," the areal extent of SCCs exceeding 10 mg m^{-3} around the study region (**Figure 1B**, blue dashed square) reached a record-breaking level in mid-to-late September 2021 (**Figure 2**), which was roughly comparable to the climatological mean plus six standard deviations. During the first half of our study period (i.e., 3–18 October), this record-breaking level was further maintained. The maximum areal extent of SCCs in 2021 was observed on 9 October. However, during the second half of our study, the areal extent decreased rapidly. Hence, we examined both the maintenance and decay periods of algal blooms.

Field Measurements

Along the ship track, temperatures, salinities, and chlorophyll-*a* concentrations changed dramatically as the research vessel repeatedly crossed subarctic and subtropical water masses, as well as water masses created by mixture of the two (**Figure 3**). Roughly speaking, cold (warm) waters corresponded to low-salinity (high-salinity) waters. Cold low-salinity subarctic (warm high-salinity subtropical) waters corresponded to high (low) concentrations of chlorophyll *a* with high (low) spatial variability. Along the ship track around the L lines on the Pacific shelf during 10–14 October, chlorophyll-*a* concentrations reached particularly high values, typically >10 mg m^{-3}, intermittently exceeded 20 mg m^{-3}, and even reached up to 35 mg m^{-3}. High chlorophyll-*a* concentrations >20 mg m^{-3} were distributed as patch-like local maxima along the ship track (**Figure 4**).

The spatial scale of local maxima >20 mg m^{-3} was not more than about a few kilometers and was therefore associated with submesoscale variability (**Figure 4B**). In addition, high chlorophyll-*a* concentrations roughly corresponded to high abundances of *Karenia* spp., as is described below.

On the Pacific shelf around the L lines, salinities were persistently lower than 33.6, and temperatures were in the range 11.0–17.0°C (**Figure 3**). These water masses were classified as Modified Soya Current Water (generally defined by temperatures >7.0°C and salinities of 33.0–33.7 on the Pacific shelf off southeastern Hokkaido) and Surface Coastal Oyashio Water (temperatures >2.0°C and salinities of 32.0–33.0) (Oguma et al., 2008; Kusaka et al., 2013). Hence, subarctic water masses and modified subtropical waters with particularly high chlorophyll-*a* concentration were present simultaneously on the Pacific shelf.

Surface chlorophyll-*a* concentrations were examined in relation to three environmental variables: water depth, sea surface salinity, and temperature (**Figure 5**). Some 83% of chlorophyll-*a* concentration measurements exceeding 10 mg m^{-3} were obtained in places where the water depth was <1,000 m, i.e., primarily coastal shelf–slope waters (**Figures 5A,B**). These high chlorophyll-*a* concentrations were also associated with two different surface salinities (**Figure 5C**), with local peaks at salinities of 32.9–33.0 and 33.4–33.5. The lower and higher salinity peaks corresponded to Surface Coastal Oyashio Water and Modified Soya Warm Current Water, respectively. However,

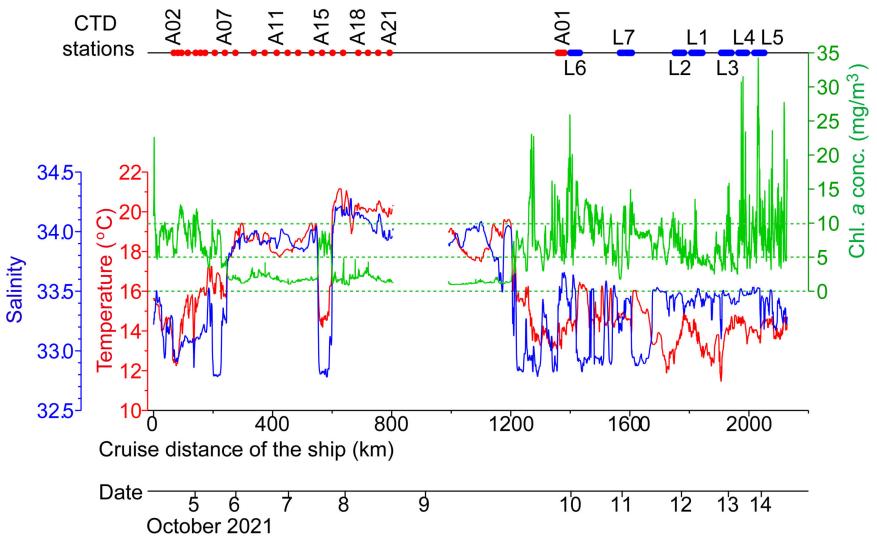

FIGURE 3 | Sea-surface temperatures (red line, corresponding to the red left-hand axis), salinities (blue line, corresponding to the blue left-hand axis), and chlorophyll-*a* concentrations (green line, corresponding to the green right-hand axis) along the ship track during 4–14 October, 2021. The upper horizontal axis denotes the timing of conductivity–temperature–depth (CTD) measurements.

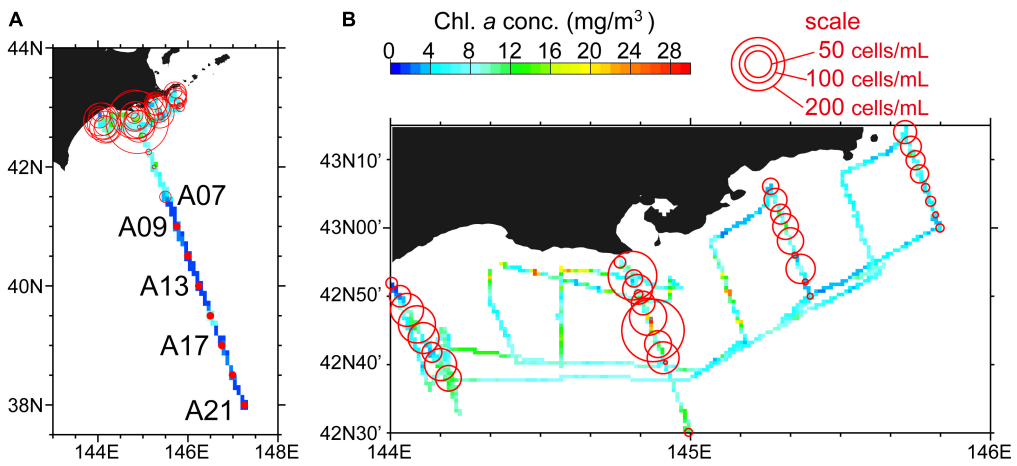

FIGURE 4 | Surface chlorophyll-*a* concentrations (colored grid cells) along the ship track during 4–14 October, 2021. Grid cells shows averages across **(A)** 5′ (longitude) × 5′ (latitude) (i.e., an approximately 7 × 9 km rectangle) and **(B)** 45″ (longitude) × 30″ (latitude) (i.e., an approximately 1 × 1 km rectangle). *Karenia* spp. abundance at a depth of 10 m is also shown by the area of red circles. Red closed circles indicate that *Karenia* spp. were not found.

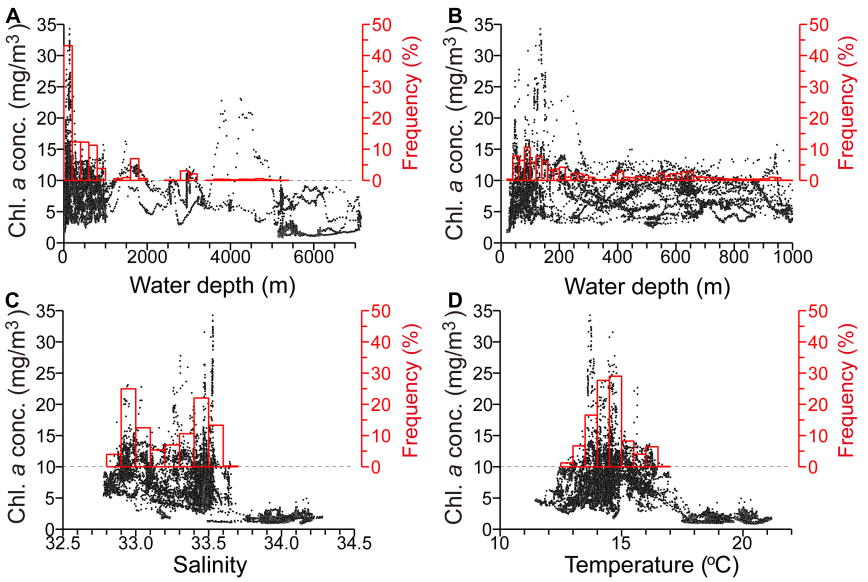

FIGURE 5 | Scatter plots of surface chlorophyll-*a* concentration along the ship track versus **(A)** water depth (for all measured depths), **(B)** water depth (for depths <1,000 m), **(C)** sea-surface salinity, and **(D)** sea-surface temperature. For each panel, frequency distributions of chlorophyll-*a* concentrations exceeding 10 mg m^{-3} are denoted by red bars, corresponding to the red right-hand axis (%).

the high chlorophyll-*a* concentrations in the two water masses were not associated with different sea-surface temperatures (i.e., the frequency distribution of temperature showed a single mode) (**Figure 5D**). Chlorophyll-*a* concentrations for salinities >33.7 and temperatures >17.5°C were mostly lower than 3 mg m^{-3}, which suggests that massive algal blooms were much less common in pure subtropical waters. The above relationships were qualitatively consistent with those of SSCs as a function of simulated variables (Kuroda et al., 2021a), except for the marked *in-situ* discrimination between Surface Coastal Oyashio Water and Modified Soya Warm Current Water, and missing measurements of river-discharge-influenced waters with salinity <32.0 near the coast.

At CTD stations, vertical profiles of chlorophyll-*a* concentration tended to show a vertical maximum at the surface (**Figure 6A**). Also, at most of the CTD stations, the surface mixed-layer depth ranged from 1 to 54 m (**Figure 6B**). The modal mixed-layer depth was 20–25 m. Namely, algal blooms were not homogeneous within the surface mixed layer but were intensified at the sea surface. Mixed-layer depths were weakly correlated with the surface chlorophyll-*a* concentration (**Figure 6C**). This indicates that satellite measurements of the sea surface could appropriately capture the distribution of algal blooms during the period of the ship survey, despite the seasonal development of a surface mixed layer.

Interestingly, chlorophyll-*a* concentrations at depths of 0 and 10 m were correlated with each other (**Figure 6D**). The ratio of chlorophyll *a* at 0 m to that at 10 m was averaged over all profiles and estimated as 2.4 (**Figure 6A**); this value was used to scale *Karenia* spp. abundances that were sampled at 10-m depth.

Karenia spp. abundance at 10-m depth was examined in relation to the surface chlorophyll-*a* concentration along the ship track (**Figure 4**, open red circles). Measured abundances ranged from 0 to 277 cells mL^{-1} during the period of the ship survey. High *Karenia* spp. abundance was most common in the

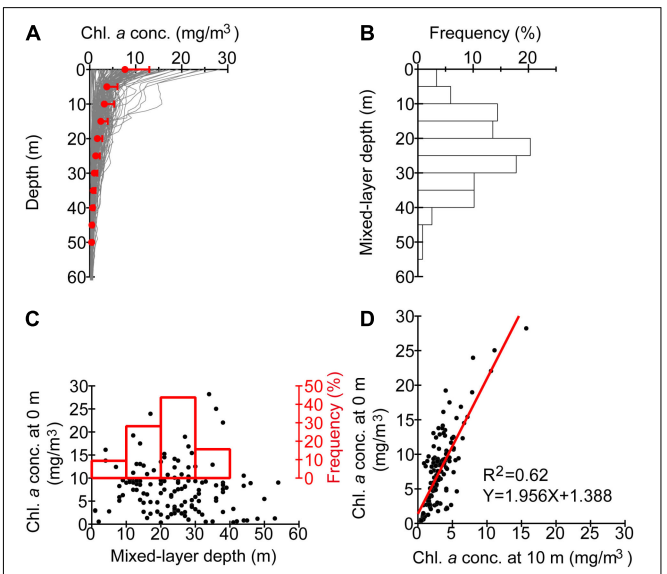

FIGURE 6 | (A) Profiles of chlorophyll-*a* concentrations based on conductivity–temperature–depth (CTD) measurements. Bin-averages and standard deviations are indicated by closed red circles and horizontal bars, respectively. **(B)** Frequency distribution of mixed-layer depths based on CTD measurements. **(C)** The same as **Figure 5**, but for chlorophyll-*a* concentrations as a function of mixed-layer depths at CTD stations. **(D)** Scatter plots of chlorophyll-*a* concentrations at 0 versus 10 m at CTD stations.

northern part of the A Line and along sections of the L lines with high chlorophyll-*a* concentrations. Meanwhile, *Karenia* spp. were wholly absent in the southern A Line (i.e., Stns. A09–A21), which was occupied by subtropical waters, except at Stn. A15. At 10-m depth, *Karenia* spp. abundance was positively correlated with the chlorophyll-*a* concentration (**Figure 7**, closed red circles) after $\log_{10}(x + 0.1)$ transformation of both variables. This indicates that, to a first-order approximation, chlorophyll-*a* concentration can be regarded as an index of *Karenia* spp. abundance off southeastern Hokkaido, at least during autumn 2021.

To obtain a more robust statistical relationship between chlorophyll-*a* concentration and *Karenia* spp. abundance, we also examined the data collected from the Katsurakoi fishery harbor (**Figure 7**, closed blue circles). *Karenia* spp. abundances (chlorophyll-*a* concentrations) from the harbor ranged from 0 to 9,600 cells mL^{-1} (1.75–123.20 mg m^{-3}), which was markedly higher than those obtained from the ship survey. By combining the two data sources, we obtained a robust log–log regression line spanning a wide range of values of both variables ($R^2 = 0.75$).

Combination of *in-situ* and Satellite Measurements

Maps of Chlorophyll-*a* Concentration

To estimate maps of chlorophyll-*a* concentration as accurately as possible, we first compared satellite-derived variables measured at 0029–0035 coordinated universal time (UTC) on 9 October with *in-situ* chlorophyll-*a* concentrations at the sea surface along the ship track during 0300–2,400 (UTC) on the same day (**Figure 8**). On that day, the research vessel traversed a considerable distance along the A Line from south to north (**Figure 8A**, magenta line). OC4ME-based chlorophyll-*a* concentrations were most-closely correlated to *in-situ* measurements, although the original OC4ME estimates included some noise around clouds as well as overestimated chlorophyll-*a* concentrations ($R^2 = 0.78$; **Figure 8B**). Estimates of NN more frequently included noise around clouds and were strongly polarized, but there was still a strong correlation with *in-situ* measurements ($R^2 = 0.57$; **Figure 8C**). MLH and RBD estimates were quite similar and were strongly correlated with *in-situ* measurements (**Figures 8D,E**). These large positive correlations (**Figures 8B–E**) were attributed to the large-scale differences in chlorophyll-*a* concentrations between coastal-shelf and offshore waters; i.e., the presence of algal blooms in the subarctic northern A Line and the absence of blooms in the subtropical southern stations (**Figures 8A**, **9A**). However, for areas of relatively low chlorophyll-*a* concentration (<3 mg m^{-3}), chlorophyll *a* derived from RBD and MLH were positively biased and noisier than those derived from OC4ME; this reduced the correlations obtained (**Figure 9A**).

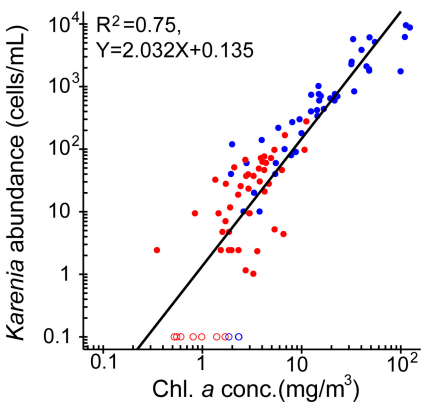

FIGURE 7 | Scatter plots of *Karenia* spp. abundance versus chlorophyll-*a* concentration based on *in-situ* observations. The two variables were transformed by $log_{10}(x + 0.1)$. Red and blue closed circles indicate data points from the ship survey at 10-m depth and from the vicinity of the Katsurakoi fishery harbor at the sea surface, respectively. Open circles denote that abundance is equal to zero. The thick black line shows the log–log regression line.

To test the validity of satellite-derived estimates on the shelf (where harmful blooms were most intense) at the submesoscale, we compared satellite-based variables measured at 0052–0055 (UTC) on 12 October and 0025–0028 (UTC) on 13 October with *in-situ* surface chlorophyll-*a* concentrations along the ship track that were measured during the above time periods ±4 h (**Figures 9B,C**). Chlorophyll-*a* concentrations based on MLH and RBD changed most synchronously with those obtained from *in-situ* measurements, whereas OC4ME-based estimates were less representative of small-scale variations in chlorophyll *a* (**Figure 10**), particularly on 13 October (**Figure 9C**), when small-scale noise was apparent. Therefore, we concluded that MLH and RBD were best suited to describing the spatial variability of chlorophyll-*a* concentrations on the Pacific shelf. We also estimated regression lines between satellite-derived variables and *in-situ* chlorophyll-*a* concentrations for the combined data obtained on 9, 11–12, and 12–13 October (**Table 1**).

Note that MLH and RBD tended to overestimate chlorophyll-*a* concentrations on the shelf (**Figures 9B,C**). For the ±4 h relative to the satellite observation time on 12 and 13 October, mean chlorophyll-*a* concentrations based on MLH and RBD were estimated as 10.7 and 6.6 mg m^{-3}, respectively—higher than the 5.6 mg m^{-3} measured *in situ*. Moreover, correlations declined if the time window was expanded beyond ±4 h of the satellite observation time (data not shown). This suggests that algal-bloom frontal structures changed rapidly spatiotemporally at the submesoscale, as is indicated by a previous analysis of thermal fronts on the Pacific shelf (Kuroda and Toya, 2020).

Maps of *Karenia* spp. Abundance

First, we generated maps of surface *Karenia* spp. abundance by combining satellite-derived surface RBD with *in-situ Karenia* spp. abundance at a depth of 10 m. *In-situ Karenia* spp. abundance was positively correlated with satellite-derived RBD once the abundance was log-transformed (**Figure 11**). Satellite-derived RBD was converted to *Karenia* spp. abundance by using a log–linear regression (**Figure 11**). We assumed that the average ratio (i.e., 2.4) of chlorophyll-*a* concentrations between the two depths (**Figure 6A**) was identical to that of *Karenia* spp. abundances, and estimated *Karenia* spp. abundance at a depth of 10 m was converted to that at the surface.

Second, we also generated maps of *Karenia* spp. abundance from maps of chlorophyll-*a* concentration. We used MLH

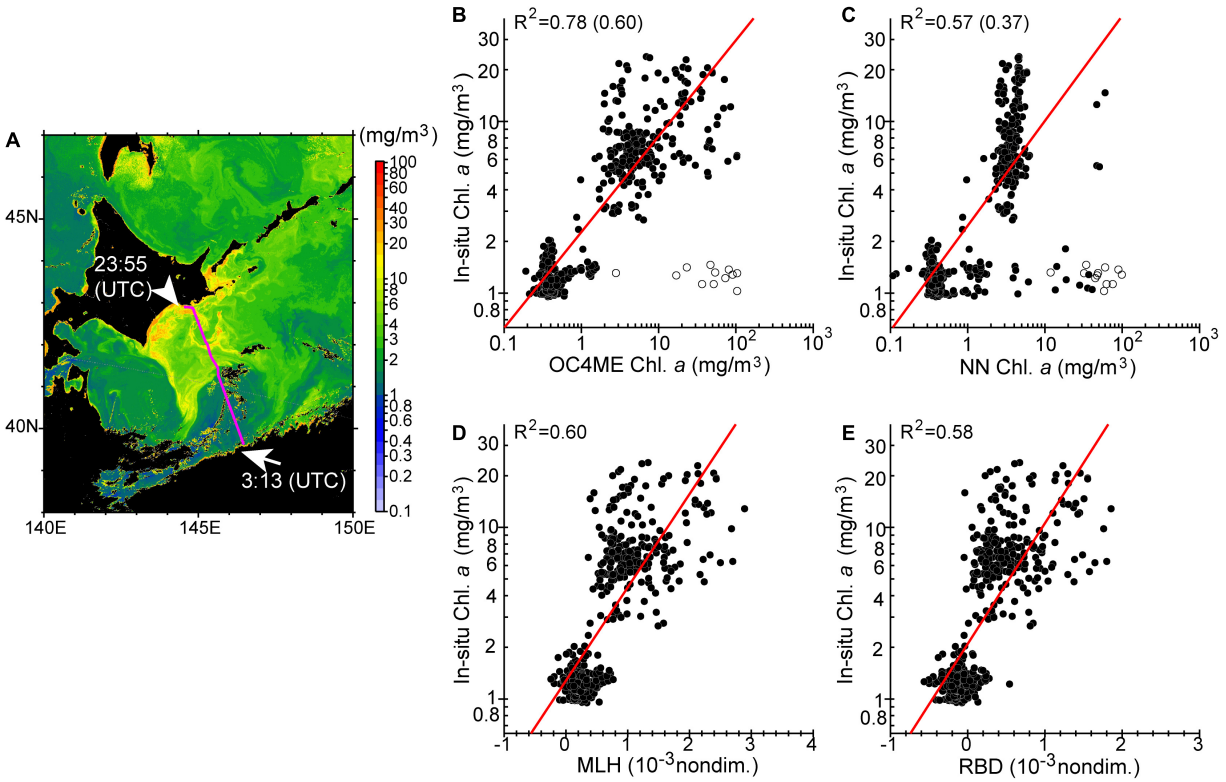

FIGURE 8 | (A) Chlorophyll-*a* concentrations on 9 October, 2021, derived from the maximum band ratio semi-analytical algorithm (OC4ME) and corrected by the regression equation shown in **Table 1**. The magenta line represents the ship track from 0313 (UTC) to 2355 (UTC) on the same day. Scatter plots show surface chlorophyll-*a* concentrations along the ship track versus **(B)** OC4ME-derived chlorophyll-*a* concentrations, **(C)** Neural network (NN)-derived chlorophyll-*a* concentrations, **(D)** maximum line height (MLH), and **(E)** red-band difference (RBD). Coefficients of determination are shown in the top left-hand corner of each panel. For **(B,C)**, coefficients of determination shown in parenthesis were estimated when data points with large deviations around the edges of clouds (indicated by open circles) were not excluded.

to estimate chlorophyll-*a* concentration for this analysis, mainly because MLH performed well in matching the spatial variability of chlorophyll-*a* concentrations on the Pacific shelf (see the preceding section "Maps of Chlorophyll-*a* Concentration") and MLH was most prone to underestimating chlorophyll-*a* concentrations in coastal waters where harmful algal blooms were not reported. This suggested that MLH-based chlorophyll-*a* concentrations most reduced contamination associated with colored dissolved organic matter in coastal waters (**Supplementary Figure 2**).

Maximum line height-derived chlorophyll-*a* concentrations were estimated by using the regression equation in **Table 1** and converted into *Karenia* spp. abundances by using the regression equation in **Figure 7**. We assumed that *Karenia* spp. were absent at chlorophyll-*a* concentrations <2.2 mg m^{-3}, a threshold that corresponds to the maximum *in-situ* surface chlorophyll-*a* concentration at which *Karenia* spp. were not identified (**Figure 7**).

Maps generated by using the two methods for 9 October, 2021 were largely consistent with each other, particularly for large- and small-scale structures of *Karenia* spp. abundance. However, the second method tended to generate higher estimates (**Figures 12A,B**). The bias was about 0.3 $\log_{10}$(cells mL^{-1}) over the whole study region, which means that there was an approximately 2-fold difference in estimated *Karenia* abundances between the first and second methods. Possible reasons for this bias are discussed in section "Uncertainties of Estimated *Karenia* spp. Abundance."

Spatiotemporal Distribution of *Karenia* spp.

On 9 October, the core of the *Karenia* bloom appears to have been primarily located on the shelf (**Figure 12C**); *Karenia* abundances exceeding 10^3 cells mL^{-1} on the shelf (**Figure 12C**, yellow colors) tended to exhibit streak-like structures of width <10 km, which were associated with submesoscale filaments. The streak-like filaments extended roughly in parallel to the coastline, rather than normal to it. Moreover, particularly high abundances exceeding 10^4 cells mL^{-1} (**Figure 12C**, red colors) were distributed in a patch-like manner on the shelf. These small, surface-level structures are also identifiable in the ship-track data as patch-like localized chlorophyll-*a* maxima of up to a few kilometers in scale (**Figure 4B**).

Karenia spp. abundances on the continental slope were lower overall than those on the shelf. However, relatively high abundances on the slope ($\sim 10^2$ cells mL^{-1}; **Figure 12C**, green colors) occurred along the edge of a mesoscale

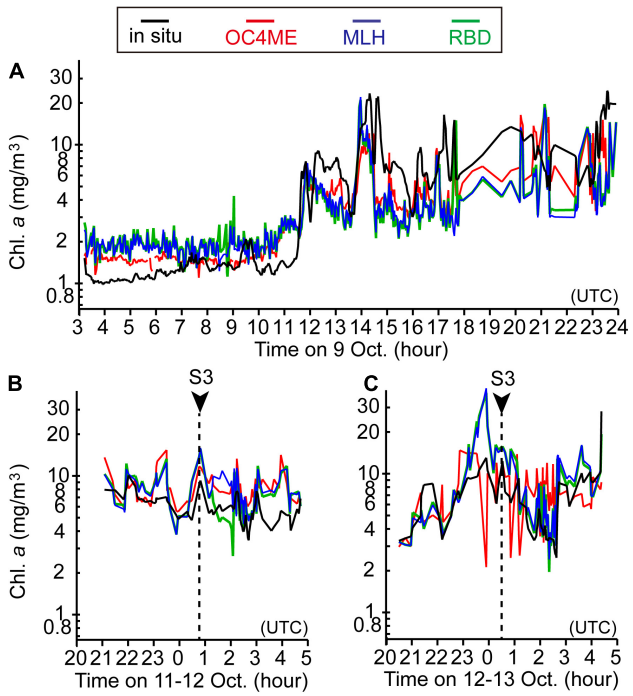

FIGURE 9 | Time series of surface chlorophyll-*a* concentrations based on *in-situ* measurements (black lines), maximum band ratio semi-analytical algorithm (OC4ME)-derived estimates (red lines), maximum line height (MLH)-derived estimates (blue lines), and red-band difference (RBD)-derived estimates (green lines) that were corrected by using the regression equations listed in **Table 1**. The Sentinel-3 data shown in panels **(A–C)** correspond to images obtained on 9 October 0029–0032 (UTC), 12 October 0052–0055, and 13 October 0025–0028, respectively. For panels **(B,C)**, *in-situ* chlorophyll-*a* concentrations were compared during the 4 h before or after the Sentinel-3 observations.

clockwise eddy with a diameter of about 100 km (**Figure 1B**, light blue eddy).

Karenia spp. abundances in very nearshore waters were typically on the order of $<10^1$ cells mL^{-1} (**Figure 12C**, white) and were clearly lower than those on the shelf. However, this might have been caused by estimation biases in the data from Sentinel 3. Despite this possible bias, high abundances exceeding 10^3 cells mL^{-1} were distributed locally near the coast (**Figure 12C**, light purple arrows) and were connected to high-abundance patches on the shelf by streak-like filaments.

On the basis of the RBD-derived *Karenia* spp. abundances for 3–18 October, the above-described features were common throughout our study period, although the spatiotemporal distribution of *Karenia* spp. blooms changed greatly (**Figure 13**). In particular, dynamic changes became apparent within a single day from 12 to 13 October (**Figures 13C,D**). *Karenia* spp. abundances on the shelf increased abruptly, and high-abundance patches also expanded to the vicinity of the coastline. Streak-like structures with high abundances exceeding 10^3 cells mL^{-1} were more apparent on 13 October, particularly in the western half of the study region. When *Karenia* spp. abundances were averaged over the shelf (**Figure 13A**, pink polygon), the rate of increase in abundance was estimated to be 2.1- and 2.6-fold per day for RBD- and MLH-derived estimates (**Figure 13F**), respectively. The rate of increase of *Karenia* abundance exceeded that of chlorophyll-*a* concentrations (∼1.5-fold per day). Moreover, on 18 October, when algal blooms over the Pacific shelf decayed gradually (**Figure 2**), a streak-like structure became highly intensified along the coastline just east of Cape Erimo, where *Karenia* abundances exceeded 10^4 cells mL^{-1} (**Figure 13E**). Hence, a western-intensified structure became more apparent during the decay period of the algal blooms over the shelf.

DISCUSSION

Uncertainties of Estimated *Karenia* spp. Abundance

In this study, we generated maps of estimated *Karenia* spp. abundance by using two methods, the first based on RBD and the second on MLH. The MLH-derived abundances were about twice as high as those derived from RBD. First, we discuss the possible reasons for this difference below.

There are at least three weaknesses associated with the RBD-based estimation, in which RBD was directly converted into *Karenia spp.* abundance. First, *in-situ Karenia* spp. abundances measured during our ship survey ranged from 0 to 277 cells mL^{-1} (**Figure 11**). Therefore, RBD-derived estimates of abundance >277 cells mL^{-1} (before conversion to abundance at 0-m depth) were determined by extrapolating the regression line between RBD and *in-situ Karenia* spp. abundance (**Figure 11**). This extrapolation is likely associated with some degree of error. Second, the sample size (n = 68) used to estimate the regression line itself was somewhat small (**Figure 11**), especially in comparison with the sample size of surface chlorophyll-*a* concentrations along the ship track (**Figures 8**, **10**). Third, the period of observation differed between *Karenia* spp. abundances determined from water samples and those determined from satellite measurements. We permitted a maximum time difference of 6.9 days for the A Line and 1 day for the L lines (**Figure 11**); if we had used a smaller maximum time difference, the number of data points available would have been further reduced.

Likewise, there are at least two weaknesses associated with the MLH-based estimation, in which MLH was used indirectly to estimate *Karenia* spp. abundance. First, although small-scale variations of chlorophyll-*a* concentrations on the shelf were reasonably well reproduced by MLH-derived estimates, MLH-based chlorophyll-*a* concentrations on the Pacific shelf were positively biased in comparison with *in-situ* chlorophyll-*a* concentrations (**Figures 9B,C**). This bias could be attributable to centimeter-scale vertical heterogeneities of chlorophyll *a* near the sea surface, which are captured differently by satellite imagery and *in-situ* surveys (e.g., Harvey, 1966; Mitchell and Fuhrman, 1989). Second, as with RBD, very high MLH-derived chlorophyll-*a* concentrations (exceeding 123.20 mg m^{-3}) were determined by extrapolation of a regression line (**Table 1**). The threshold of 123.20 mg m^{-3} corresponds to an abundance of $10^{4.4}$ (∼25,000) cells mL^{-1} (**Figure 7**).

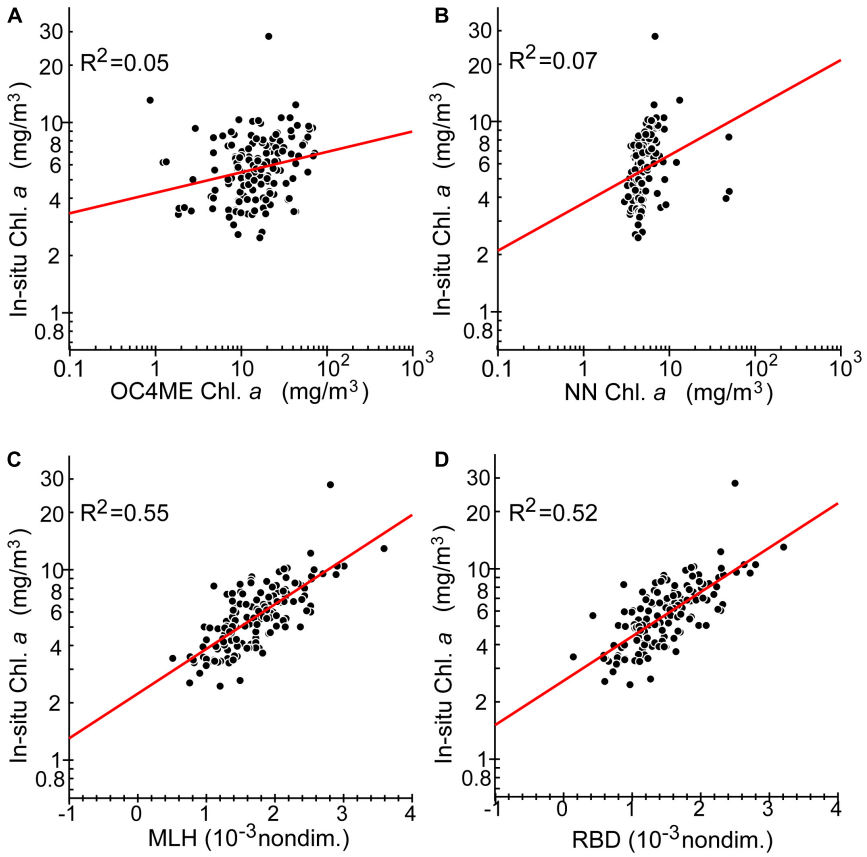

FIGURE 10 | Panels **(A–D)** are the same as **Figures 8B–E**, respectively, but only for data points collected during the 4 h before or after the Sentinel-3 observations on 12 and 13 October, 2021.

At present, it is difficult to determine which of the two methods more closely matched the actual *Karenia* spp. abundances. We therefore chose to apply both methods and evaluate the two resultant sets of *Karenia* spp. abundances while taking the uncertainties of each method into account. In future work, these weaknesses could be mitigated by increasing the sample size for the regressions used in each method. This could be accomplished by incorporating *in-situ* measurements of *Karenia* spp. abundance obtained by other organizations.

TABLE 1 | Equations and determination coefficients of regression lines for *in-situ* chlorophyll-*a* concentrations and satellite-derived variables.

Variables	Regression line equations	R^2
OC4ME	$Y = 0.444X+0.346$	0.68
NN	$Y = 0.570X+0.385$	0.57
MLH	$Y = 401.984X+0.171$	0.56
RBD	$Y = 422.452X+0.226$	0.54

OC4ME, maximum band ratio semi-analytical algorithm; NN, neural network-based approach; MLH, maximum line height; RBD, red band difference. To estimate statistical values in this table, satellite-derived variables measured on 9, 12, and 13 October were compared with in-situ chlorophyll-a concentrations obtained during 0300–2400 (UTC) on 9 October and during the ±4 h around the observation time of Sentinel 3 on 12 and 13 October, respectively (see ***Figure 9****). X and Y represent satellite-derived variables and in-situ chlorophyll-a concentrations, respectively.*

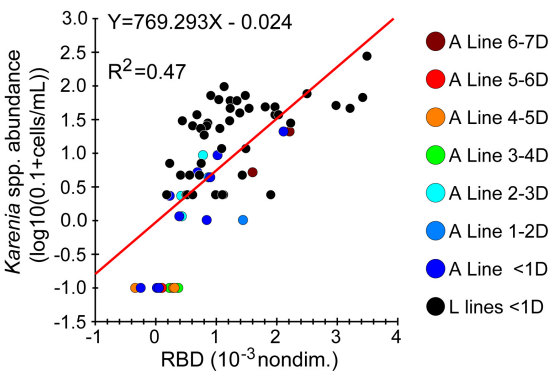

FIGURE 11 | Scatter plots of *Karenia* abundance at 10-m depth along the A Line and L lines. Data collected from the L lines (black closed circles) were measured within 1 day ("<1D") of an observation by Sentinel 3. Data collected from the A Line are colored according to time interval (in days) between the abundance measurement and an observation by Sentinel 3, where the longest interval was 7 day.

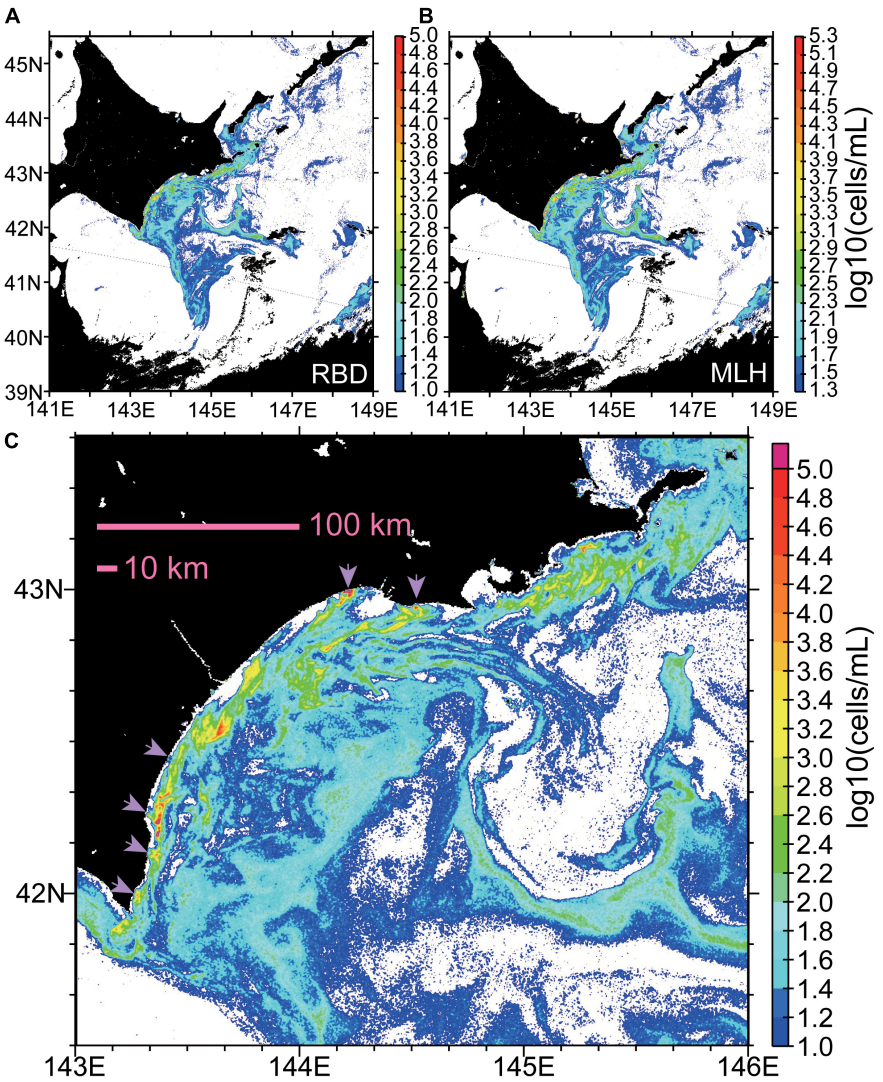

FIGURE 12 | Maps of *Karenia* abundance ($\log_{10}$[cells mL^{-1}]) on 9 October 2021, estimated **(A)** directly from red-band difference (RBD) or **(B)** indirectly from maximum line height (MLH) and estimated chlorophyll-*a* concentrations. The color scale of panel **(B)** is offset from that of panel **(A)** by 0.3, which corresponds to about a 2-fold difference [i.e., $10^{0.3}\sim2$]. **(C)** The same as panel **(A)**, but for a smaller area. Light purple arrows indicate high abundances in very nearshore waters.

There were large uncertainties in RBD- and MLH-derived abundances near the southeast coast of Hokkaido, and these methods may have underestimated *in-situ Karenia* spp. abundances in this region. To examine this in more detail, we extended the analysis period of Sentinel-3 data and extracted RBD- and MLH-derived *Karenia* spp. abundances from the 300-m grid cell that was closest to the Katsurakoi fishery harbor. On 21 September, when the second-largest *in-situ Karenia* spp. abundance ($10^{3.9}$ cells mL^{-1}) was recorded, RBD- and MLH-derived abundances were estimated to be 10^{3} and $10^{3.9}$ cells mL^{-1}, respectively. Although the MLH-derived value was reasonable, the RBD-derived value underestimated the *in-situ* abundance by about one order of magnitude. Interestingly, *in-situ Karenia* spp. abundances from the fishery harbor differed greatly among the three monitoring sites established at that location, which were all within a few hundred meters of each other. On 23 September, when Sentinel-3 imagery and *in-situ Karenia* spp. abundances from all three sites were available, we obtained *in-situ* abundances of $10^{3.4}$, $10^{2.9}$, and $10^{2.4}$ cells mL^{-1} from the three harbor sites and RBD- and MLH-derived abundances of $10^{2.3}$ and $10^{2.6}$ cells mL^{-1}, respectively. Thus, satellite-derived estimates failed to reproduce the highest observed *in-situ* abundance on that day. This indicates that the spatial distribution of *in-situ Karenia* spp. abundances near the coast can change drastically, even within a few hundred meters. Hence, further work is needed to evaluate the accuracy of satellite-derived abundances near the coast by examining very-nearshore *in-situ Karenia* spp. abundances from additional coastal sites. Simultaneously, it will be important to use ocean-color images with a finer spatial resolution. Although Sentinel-2

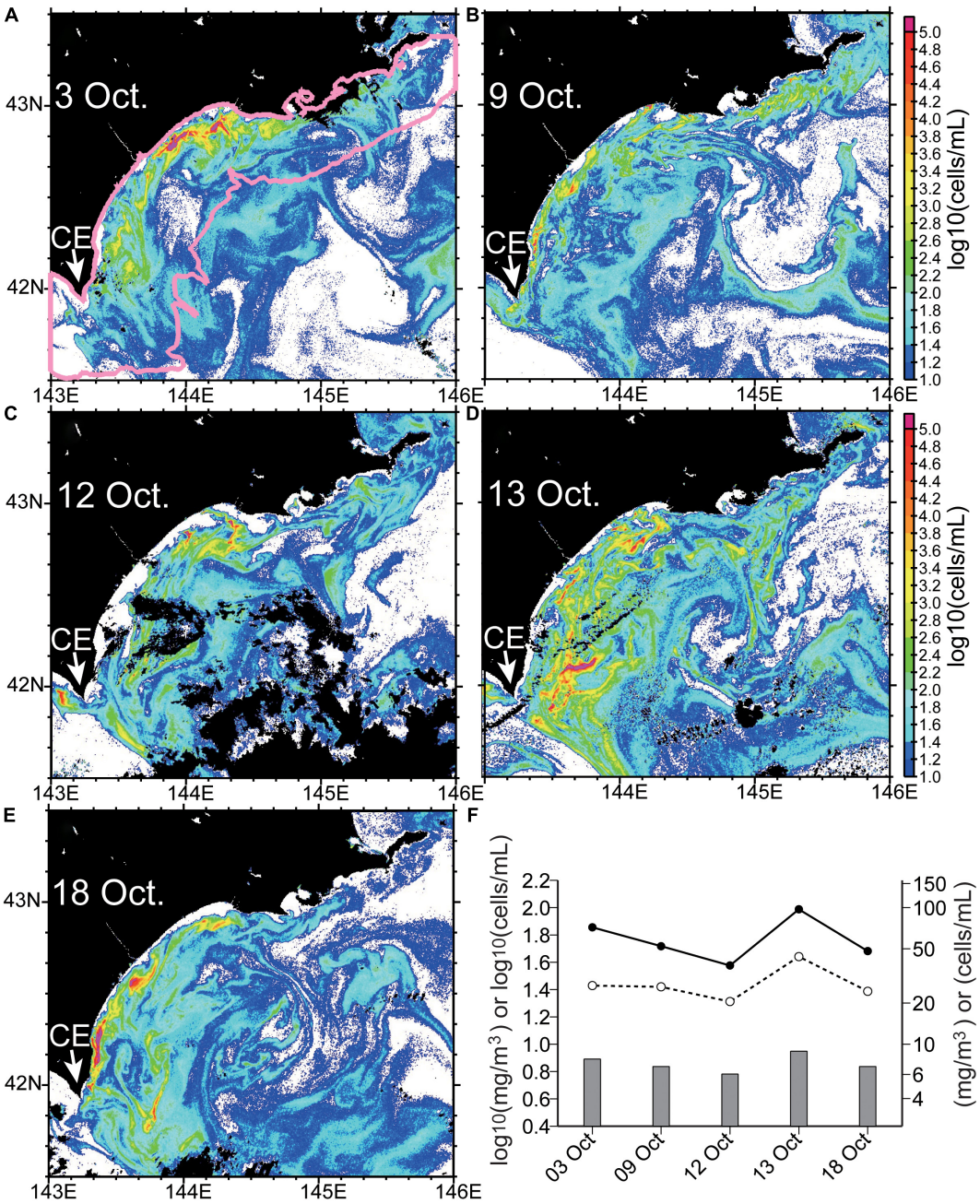

FIGURE 13 | (A–E) The same as **Figure 12C** (units: $\log_{10}$[cells mL^{-1}]), but for **(A)** 3, **(B)** 9, **(C)** 12, **(D)** 13, and **(E)** 18 October, 2021. CE, Cape Erimo. **(F)** *Karenia* abundance (lines) and chlorophyll-*a* concentration (bars) averaged over shelf–slope regions with water depth <1,000 m [i.e., the pink polygon in panel **(A)**] and derived from red-band difference (dashed line, open circles) and maximum line height (solid line, closed circles). Estimated chlorophyll-*a* concentrations were based on maximum line height and a regression equation (**Table 1**).

ocean-color imagery (which has a horizontal resolution of 10, 20, or 60 m) might be feasible (e.g., Caballero et al., 2020), some methodological changes will be required because Sentinel 2 does not capture the 681-nm spectral band.

It is noteworthy that the satellite-derived *Karenia* spp. abundances estimated in this study are still imperfect; they will need to be refined to accurately monitor the presence or absence of *Karenia* spp. or to precisely detect signs of impending *Karenia* spp. blooms from weak reflectance signals. A preliminary evaluation of these use cases was conducted by using Sentinel-3 images from July 2017 to October 2021 (**Supplementary Figure 3**). Our tentative results indicate that MLH-derived *Karenia* spp. abundances overestimated the true abundances in some cases, despite the likely absence of *Karenia*

blooms in 2017–2020, particularly during massive spring diatom blooms and autumn blooms off the southeast coast of Hokkaido (e.g., Okamoto et al., 2010; Suzuki et al., 2011; Isada et al., 2019; Kuroda et al., 2019). This overestimation was likely caused by the fact that the MLH-based estimate relates *Karenia* spp. abundances to chlorophyll-*a* concentrations. A similar pattern of overestimation in spring and autumn was also identified for RBD-derived *Karenia* spp. abundance, although the estimated abundances during 2017–2020 never exceeded the record-breaking abundances reached in October 2021. Hence, more sophisticated algorithms are still needed to precisely discriminate harmful *Karenia* blooms from non-harmful algal blooms by using satellite data, e.g., Siswanto et al. (2013), El-Habashi et al. (2016), El-Habashi et al. (2019), and Martinez-Vicente et al. (2020).

To identify *Karenia* blooms more precisely, it is necessary to estimate the reflectance spectral properties of *Karenia* spp. (in particular, *K. selliformis*, the properties of which have not yet been reported) and the other dominant species in our study area. It should be remembered that the RBD method that we employed was originally proposed by Amin et al. (2009) for *Karenia brevis* and non-*K. brevis* species (mainly diatoms) along the west coast of Florida (**Supplementary Figure 1**). In fact, our cell enumeration data (not shown) revealed that diatoms existed in mixture with *Karenia* spp. off the Hokkaido coast and that the abundance of diatoms relative to *Karenia* spp. tended to increase as *Karenia* spp. abundance declined. This tendency can be also seen in **Figure 7**; deviations of *Karenia* spp. abundance from the log–log regression line tended to decrease as *in-situ* chlorophyll-*a* concentrations increased (i.e., as *Karenia* spp. abundance increased). Moreover, note that the dominant diatom species and their spectral properties probably differ between the west coast of Florida and our study area. Hence, further work is needed to identify the dominant diatom species from long-term monitoring data along the A Line and to precisely measure the spectral properties of *Karenia* spp. and non-*Karenia* spp. associated with the dominant diatoms in our study area.

The Rapid Increase in *Karenia* spp. Abundance

We successfully generated maps of *Karenia* spp. abundance and described the spatiotemporal variations in abundance from 3 to 18 October, 2021 (**Figure 13**). However, the possible physico-biochemical dynamics responsible for spatiotemporal changes in *Karenia* spp. abundance remain largely unexamined. Here, we focus on the 24-h period from 12 to 13 October, when *Karenia* spp. abundances averaged over the shelf abruptly increased over 2-fold (**Figures 13C,D**). Throughout this period, as is indicated in **Figures 13C,D**, our study area had few clouds along the shelf, suggesting that light conditions were favorable for algal growth.

In general, any enhancement of algal abundance can be caused by biological growth, physical advection, or a combination of the two (e.g., Richardson, 1997; Stumpf et al., 2008; Thyng et al., 2013). If the abrupt increase of *Karenia* app. abundance from 12 to 13 October were caused solely by algal growth, the growth rate would have been 0.74 and 0.96 day^{-1} for RBD- and MLH-derived abundances, respectively. These growth rates exceed the growth rates or maximum growth rates of *Karenia* species reported by previous studies, which range from 0.04 to 0.41 day^{-1} for *K. selliformis* (Medhioub et al., 2009; Mardones et al., 2020), and from 0.216 to 0.727 day^{-1} for *K. mikimotoi* (Shen et al., 2016; Zhao et al., 2017). This discrepancy indicates that physical advection might also have contributed to the abrupt abundance increase, as suggested by the interpretation of Stumpf et al. (2008).

Physical advection can occur on a variety of spatiotemporal scales. At the shelf scale (defined here by the pink polygon in **Figure 13A**), horizontal onshore-offshore advection probably had a negligible effect on the abrupt increase in *Karenia* spp. abundance during the 24-h period, because *Karenia* spp. abundances were higher on the shelf than on the offshore slope. At the shelf scale, therefore, we need to primarily consider sources of vertical advection such as wind-induced upwelling, which might uplift pre-existing *Karenia* spp. populations from the subsurface or concentrate *Karenia* spp. near the sea surface through a shoaling of the mixed layer/pycnocline (e.g., Pitcher et al., 1998). However, high-resolution mesoscale model data from the Japan Meteorological Agency's weather forecast system (Saito et al., 2006) indicate that northeasterly winds with a velocity of 3.2–6.2 m s^{-1} predominated at 2 m above the sea surface over the shelf throughout 12 October. This wind regime would have favored coastal downwelling, rather than upwelling. Therefore, *Karenia* spp. abundance increased at the sea surface in spite of gentle downwelling-favorable winds, particularly on the western shelf.

Regarding physical advection at finer scales, the streak- and patch-like submesoscale structures we observed are likely to be among the key elements for understanding any physical-biological coupling that occurred. Streak-like filaments are also frequently identified in maps of satellite-derived chlorophyll-*a* concentration (e.g., Malanotte-Rizzoli et al., 2014; Shulman et al., 2015; Lehahn et al., 2017). Filamentary structures are generally interpreted as Lagrangian coherent structures, which are attributed mainly to horizontal advection (Lehahn et al., 2007; Hernández-Carrasco et al., 2018, 2020). However, this interpretation is likely to be complicated in our case, because *Karenia* spp. growth could have been superimposed on purely Lagrangian transport processes, and strong vertical advection induced by submesoscale variations could have contributed to the abrupt shelf-scale increase of *Karenia* spp. abundance (e.g., Meng et al., 2020). Further research will be needed to examine how small-scale submesoscale variations combined with algal growth contributed to the abrupt shelf-scale increase of *Karenia* spp. abundance, including the observed western intensification of *Karenia* blooms. Unfortunately, although clarification of these physical–biochemical processes is urgently needed, this is beyond the scope of our study.

CONCLUSION

Unprecedented outbreaks of harmful *Karenia* algae were reported in mid-September 2021 in the northwest Pacific Ocean off of southeastern Hokkaido, Japan, and inflicted

catastrophic damage on coastal fisheries in the ensuing months. To understand the distribution of *Karenia* spp. blooms, we conducted extensive ship surveys and analyzed *in-situ* data in combination with Sentinel-3-derived ocean-color imagery. High chlorophyll-*a* concentrations (exceeding 10 mg m^{-3}) were detected mainly in coastal shelf–slope waters <1,000 m deep that were occupied by Surface Coastal Oyashio Water and Modified Soya Warm Current Water, and *Karenia* blooms occurred around the confluence of subtropical and subarctic waters. Abundances of *Karenia* spp. were correlated with chlorophyll-*a* concentrations, which typically had a vertical maximum at the surface within the homogeneous surface mixed layer (typical mixed-layer depths were around 20–25 m). Moreover, large- and small-scale distributions of *Karenia* spp. abundances at the ocean surface were estimated by using two methods based on Sentinel-3-derived MLH and RBD. The two methods provided consistent spatial maps of *Karenia* spp. abundances, except in very nearshore waters. In addition, MLH-derived abundances were about twice as high as RBD-derived abundances, primarily because of uncertainties attributable to limited sample ranges and sample sizes of *in-situ Karenia* spp. abundances, which can be improved by the addition of more *in-situ Karenia* abundance data to our regression models.

Our estimates of *Karenia* spp. abundance revealed the spatiotemporal distributions and dynamic features of *Karenia* blooms on the Pacific shelf off southeastern Hokkaido. The cores of *Karenia* blooms (typically > 10^3 cells mL^{-1}) were generally confined to the shelf. High-abundance areas were characterized by streak-like structures (>10^3 cells mL^{-1}) associated with submesoscale filaments that tended to be oriented parallel to the coastline, as well as by patch-like structures (>10^4 cells mL^{-1}). In very nearshore waters, *Karenia* spp. blooms were local, intermittent, and connected to blooms in shelf waters by streak-like structures. We also observed a greater-than 2-fold increase in *Karenia* spp. abundance within roughly 24 h from 12 to 13 October; this was associated with the combined effects of physical advection and algal growth. Our findings illustrate the impossibility of using ship surveys to capture the overall spatial structure of *Karenia* blooms, which change on an hour-to-hour basis, off southeastern Hokkaido. Hence, the maps of RBD- and MLH-derived *Karenia* spp. abundances generated in our study can provide the basic information needed to understand the processes and mechanisms by which harmful algal blooms during late summer–autumn 2021 caused damage to regional fisheries.

DATA AVAILABILITY STATEMENT

The gridded level-4 chlorophyll concentration data from ocean color sensors used for **Figure 2** were downloaded from the Copernicus Marine Environment Monitoring Service (CMEMS) (ftp://my.cmems-du.eu and https://nrt.cmems-du.eu, accessed on 2 December 2021). The near-real-time absolute dynamic topography used for **Figure 1B** was also downloaded from CMEMS (ftp://nrt.cmems-du.eu, accessed on 1 November 2021). Sea-surface temperatures based on Himawari 8 data for **Figure 1A** were obtained from the Japan Aerospace Exploration Agency P-tree system (ftp://ftp.ptree.jaxa.jp, accessed on 1 November 2021). Sentinel-3A/3B Ocean and Land Color Imager Level-2 data were obtained from Copernicus Online Data Access (https://coda.eumetsat.int, accessed on 1 November 2021). For hydrographic data obtained during *in situ* surveys, please contact the corresponding author.

AUTHOR CONTRIBUTIONS

HK summarized the ideas and wrote the manuscript through discussions with co-authors. YT conducted ship surveys and sampling and analyzed measurements. TW and NH conducted sampling around the Katsurakoi fishery harbor and analyzed water samples. TA checked and modified the manuscript with respect to physical oceanography. NH also led the project. All authors contributed to the article and approved the submitted version.

FUNDING

This study was supported by funds provided by the Japan Fisheries and Education Agency.

ACKNOWLEDGMENTS

We express our deepest gratitude to the captains, officers, and crew of R/V *Hokko-maru*, as well as to our collaborators during the monitoring of the A and L lines.

SUPPLEMENTARY MATERIAL

The Supplementary Material for this article can be found online at: https://www.frontiersin.org/articles/10.3389/fmars.2022.841364/full#supplementary-material

REFERENCES

Amin, R., Zhou, J., Gilerson, A., Moshary, F., and Ahmed, S. (2009). Novel optical techniques for detecting and classifying toxic dinoflagellate *Karenia brevis* blooms using satellite imagery. *Opt. Express* 17, 9126–9144. doi: 10.1364/oe.17.009126

Anderson, D. M., Burkholder, J. M., Cochlan, W. P., Glibert, P. M., Gobler, C. J., Heil, C. A., et al. (2008). Harmful algal blooms and eutrophication: examining linkages from selected coastal regions of the United States. *Harmful Algae* 8, 39–53. doi: 10.1016/j.hal.2008.08.017

Basti, L., Nagai, S., Go, J., Okano, S., Nagai, K., Watanabe, R., et al. (2015). Differential inimical effects of *Alexandrium* spp. and *Karenia* spp. on cleavage, hatching, and two larval stages of Japanese pearl oyster *Pinctada fucata* martensii. *Harmful Algae* 43, 1–12. doi: 10.1016/j.hal.2014.12.004

Bondur, V., Zamshin, V., Chvertkova, O., Matrosova, E., and Khodaeva, V. (2021). Detection and analysis of the causes of intensive harmful algal bloom in

Kamchatka based on satellite data. *J. Mar. Sci. Eng.* 9:1092. doi: 10.3390/jmse9101092

Caballero, I., Fernández, R., Eccalante, O. M., Mamán, L., and Navarro, G. (2020). New capabilities of Sentinel-2A/B satellites combined with in situ data for monitoring small harmful algal blooms in complex coastal waters. *Sci. Rep.* 10:8743. doi: 10.1038/s41598-020-65600-1

Cherif, E. K., Mozetič, P., Francé, J., Flander-Putrle, V., Franeli-Pucer, J., and Vodopivec, M. (2021). Comparison of in-situ chlorophyll-*a* time series and Sentinel-3 Ocean and Land Color Instrument data in Slovenia national waters (Gulf of Trieste, Adriatic Sea). *Water* 13:1903. doi: 10.3390/w13141903

Crawford, D. W., Montero, P., and Daneri, G. (2021). Blooms of *Alexandrium catenella* in coastal waters of Chilean Patagonia: is subantarctic surface water involved? *Front. Mar. Sci.* 8:612628. doi: 10.3389/fmars.2021.612628

Dodson, A. N., and Thomas, W. H. (1964). Concentrating plankton in a gentle fashion. *Limnol. Oceanogr.* 9, 455–456. doi: 10.4319/lo.1964.9.3.0455

Doerffer, R., and Schiller, H. (2007). The MERIS Case 2 water algorithm. *Int. J. Remote Sens.* 28, 517–535. doi: 10.1080/01431160600821127

Du, X., Peterson, W., Fisher, J., Hunter, M., and Peterson, J. (2016). Initiation and development of a toxic and persistent *pseudo-nitzschia* bloom off the Oregon coast in spring/summer 2015. *PLoS One* 11:e0163977. doi: 10.1371/journal.pone.0163977

El-Habashi, A., Ahmed, S., Ondrusek, M. E., and Lovko, V. (2019). Analyses of satellite ocean color retrievals show advantage of neural network approaches and algorithms that avoid deep blue bands. *J. Appl. Remote Sen.* 13:024509. doi: 10.1117/1.JRS.13.024509

El-Habashi, A., Ioannou, I., Tomlinson, M. C., Stumpf, R. P., and Ahmed, S. (2016). Satellite retrievals of *Karenia brevis* harmful algal blooms in the West Florida Shelf using neural networks and comparisons with other techniques. *Remote Sens.* 8:377. doi: 10.3390/rs8050377

Feki, W., Hamza, A., Frossard, V., Abdennadher, M., Hannachi, I., Jacquot, M., et al. (2014). What are the potential drivers of blooms of the toxic dinoflagellate *Karenia selliformis*? A 10-year study in the Gulf of Gabes, Tunisia, southwestern Mediterranean Sea. *Harmful Algae* 23, 8–18. doi: 10.1016/j.hal.2012.12.001

Frölicher, T. L., and Laufkötter, C. (2018). Emerging risks from marine heat waves. *Nat. Commun.* 9:650. doi: 10.1038/s41467-018-03163-6

Gower, J. (2016). On the use of satellite-measured chlorophyll fluorescence for monitoring coastal waters. *Int. J. Remote Sens.* 37, 2077–2086. doi: 10.1080/01431161.2015.1111542

Gower, J. F. R., Doerffer, R., and Borstad, G. A. (1999). Interpretation of the 685 nm peak in water-leaving radiance spectra in terms of fluorescence, absorption and scattering, and its observation by MERIS. *Int. J. Remote Sens.* 20, 1771–1786. doi: 10.1080/014311699212470

Gower, J., King, S., Borstad, G., and Brown, L. (2005). Detection of intense plankton blooms using the 709nm band of the MERIS imaging spectrometer. *Int. J. Remote Sens.* 26, 2005–2012. doi: 10.1080/01431160500075857

Harvey, G. W. (1966). Microlayer collection from the sea surface: a new method and initial results. *Limnol. Oceanogr.* 11, 608–613. doi: 10.4319/lo.1966.11.4.0608

Hernández-Carrasco, I., Alou-Font, E., Dumont, P.-A., Cabornero, A., Allen, J., and Orfila, A. (2020). Lagrangian flow effects on phytoplankton abundance and composition along filament-like structures. *Prog. Oceanogr.* 189:102469. doi: 10.1016/j.pocean.2020.102469

Hernández-Carrasco, I., Orfila, A., Rossi, V., and Garçon, V. (2018). Effect of small scale transport processes on phytoplankton distribution in coastal seas. *Sci. Rep.* 8:8613. doi: 10.1038/s41598-018-26857-9

IPCC [Intergovernmental Panel on Climate Change] (2019). *IPCC Special Report on the Ocean and Cryosphere in a Changing Climate*. Geneva: IPCC.

Isada, T., Abe, H., Kasai, H., and Nakaoka, M. (2021). Dynamics of nutrients and colored dissolved organic matter absorption in a wetland-influenced subarctic coastal region of northeastern Japan: contributions from mariculture and eelgrass meadows. *Front. Mar. Sci.* 8:711832. doi: 10.3389/fmars.2021.711832

Isada, T., Hattori-Saito, A., Saito, H., Kondo, Y., Nishioka, J., Kuma, K., et al. (2019). Responses of phytoplankton assemblages to iron availability and mixing water masses during the spring bloom in the Oyashio region, NW Pacific. *Limnol. Oceanogr.* 64, 197–216. doi: 10.1002/lno.11031

Iwataki, M., Lum, W. M., Kuwata, K., Takahashi, K., Arima, D., Kuribayashi, T., et al. (2022). Morphological variation and phylogeny of *Karenia selliformis* (Gymnodiniales, Dinophyceae) in an intensive cold-water algal bloom in eastern Hokkaido, Japan in September–November 2021. *bioRxiv* [Preprint] doi: 10.1101/2021.12.13.472515

Jordan, C., Cusack, C., Tomlinson, M. C., Meredith, A., McGeady, R., Salas, R., et al. (2021). Using the red band difference algorithm to detect and monitor a *Karenia* spp. bloom off the south coast of Ireland, June 2019. *Front. Mar. Sci.* 8:638889. doi: 10.3389/fmars.2021.638889

Kasai, H., Saito, H., and Tsuda, A. (1998). Estimation of standing stock of chlorophyll *a* and primary production from remote-sensed ocean color in the Oyashio region, the western subarctic Pacific, during the spring bloom in 1997. *J. Oceanogr.* 54, 527–537. doi: 10.1007/BF02742454

Katano, T., Yoshida, M., Lee, J., Han, M.-S., and Hayami, Y. (2009). Fixation of *Chattonella antiqua* and *C. marina* (Raphidophyceae) using Hepes-buffered paraformaldehyde and glutaraldehyde for flow cytometry and light microscopy. *Phycologia* 48, 473–479. doi: 10.2216/08-102.1

Kim, C.-J., Kim, H.-G., Kim, C.-H., and Oh, H.-M. (2007). Life cycle of the ichthyotoxic dinoflagellate *Cochlodinium polykrikoides* in Korean coastal waters. *Harmful Algae* 6, 104–111. doi: 10.1016/j.hal.2006.07.004

Kuroda, H., and Setou, T. (2021). Extensive marine heatwaves at the sea surface in the northwestern Pacific Ocean in summer 2021. *Remote Sens.* 13:3989. doi: 10.3390/rs13193989

Kuroda, H., and Toya, Y. (2020). High-resolution sea surface temperatures derived from Landsat 8: a study of submesoscale frontal structures on the Pacific shelf off the Hokkaido coast, Japan. *Remote Sens.* 12:3326. doi: 10.3390/rs12203326

Kuroda, H., Azumaya, T., Setou, T., and Hasegawa, N. (2021a). Unprecedented outbreak of harmful algae in Pacific coastal waters off southeast Hokkaido, Japan, during late summer 2021 after record-breaking marine heatwaves. *J. Mar. Sci. Eng.* 9:1335. doi: 10.3390/jmse9121335

Kuroda, H., Taniuchi, Y., Kasai, H., Nakanowatari, T., and Setou, T. (2021b). Co-occurrence of marine extremes induced by tropical storms and an ocean eddy in summer 2016: anomalous hydrographic conditions in the Pacific shelf waters off southeast Hokkaido, Japan. *Atmosphere* 12:888. doi: 10.3390/atmos12070888

Kuroda, H., Toya, Y., Watanabe, T., Nishioka, J., Hasegawa, D., Taniuchi, Y., et al. (2019). Influence of Coastal Oyashio water on massive spring diatom blooms in the Oyashio area of the North Pacific Ocean. *Prog. Oceanogr.* 175, 328–344. doi: 10.1016/j.pocean.2019.05.004

Kuroda, H., Wagawa, T., Kakehi, S., Shimizu, Y., Kusaka, A., Okunishi, T., et al. (2017). Long-term mean and seasonal variation of altimetry-derived Oyashio transport across the A-line off the southeastern coast of Hokkaido, Japan. *Deep Sea Res. I* 121, 95–109. doi: 10.1016/j.dsr.2016.12.006

Kusaka, A., Azumaya, T., and Kawasaki, Y. (2013). Monthly variations of hydrographic structures and water mass distribution off the Doto area, Japan. *J. Oceanogr.* 69, 295–312. doi: 10.1007/s10872-013-0174-8

Kusaka, A., Shimizu, Y., Sato, T., and Yoshida, J. (2016). Temporal variations in the current structure and volume transport of the Coastal Oyashio revealed by direct current measurement. *J. Oceanogr.* 72, 601–615.

Lefebvre, K. A., Quakenbush, L., Frame, E., Huntington, K. B., Sheffield, G., Stimmelmayr, R., et al. (2016). Prevalence of algal toxins in Alaskan marine mammals foraging in a changing arctic and subarctic environment. *Harmful Algae* 55, 13–24. doi: 10.1016/j.hal.2016.01.007

Lehahn, Y., d'Ovidio, F., and Koren, I. (2017). A satellite-based Lagrangian view on phytoplankton dynamics. *Ann. Rev. Mar. Sci.* 10, 99–119. doi: 10.1146/annurev-marine-121916-063204

Lehahn, Y., d'Ovidio, F., Lévy, M., and Heifetz, E. (2007). Stirring of the northeast Atlantic spring bloom: a Lagrangian analysis based on multisatellite data. *J. Geophys. Res.* 112:C08005. doi: 10.1029/2006JC003927

León-Muñoz, J., Urbina, M. A., Garreaud, R., and Iriarte, J. L. (2018). Hydroclimatic conditions trigger record harmful algal bloom in western Patagonia (summer 2016). *Sci. Rep.* 8:1330. doi: 10.1038/s41598-018-19461-4

Malanotte-Rizzoli, P., Artale, V., Borzelli-Eusebi, G. L., Brenner, S., Crise, A., Gacic, M., et al. (2014). Physical forcing and physical/biochemical variability of the Mediterranean Sea: a review of unresolved issues and directions for future research. *Ocean Sci.* 10, 281–322. doi: 10.5194/os-10-281-2014

Mardones, J. I., Norambuena, L., Paredes, J., Fuenzalida, G., Dorantes-Aranda, J. J., Lee Chang, K. J., et al. (2020). Unraveling the *Karenia selliformis* complex with the description of a non-gymnodimine producing Patagonian phylotype. *Harmful Algae* 98:101892. doi: 10.1016/j.hal.2020.101892

Martinez-Vicente, V., Kurekin, A., Sá, C., Brotas, V., Amorim, A., Veloso, V., et al. (2020). Sensitivity of a satellite algorithm for harmful algal bloom

discrimination to the use of laboratory bio-optical data for training. *Front. Mar. Sci.* 7:582960. doi: 10.3389/fmars.2020.582960

McCabe, R. M., Hickey, B. M., Kudela, R. M., Lefebvre, K. A., Adams, N. G., Bill, B. D., et al. (2016). An unprecedented coastwide toxic algal bloom linked to anomalous ocean conditions. *Geophys. Res. Lett.* 43, 10366–10376. doi: 10.1002/2016GL070023

McWilliams, J. C. (2016). Submesoscale currents in the ocean. *Proc. Math. Phys. Eng. Sci.* 472:20160117. doi: 10.1098/rspa.2016.0117

Medhioub, A., Medhioub, W., Amzil, Z., Sibat, M., Bardouil, M., Benneila, I., et al. (2009). Influence of environmental parameters on *Karenia selliformis* toxin content in culture. *Cah. Biol. Mar.* 50, 333–342.

Meng, Q., Xuan, J., Zhang, W., Zhou, F., Hao, Q., Zhao, Q., et al. (2020). Impact of submesoscale vertical advection on primary productivity in the southern East China Sea. *J. Geophys. Res. Biogeosci.* 125:e2019JG005540. doi: 10.1029/2019JG005540

Mitchell, J. G., and Fuhrman, J. A. (1989). Centimeter scale vertical heterogeneity in bacteria and chlorophyll *a*. *Mar. Ecolo. Prog. Ser.* 54, 141–148. doi: 10.3354/meps054141

Morel, A., Gentili, B., Claustre, H., Babin, M., Bricaud, A., Ras, J., et al. (2007). Optical properties of the "clearest" natural waters. *Limnol. Oceanogr.* 52, 217–229. doi: 10.1364/AO.20.000177

Moutzouris-Sidiris, I., and Topouzelis, K. (2021). Assessment of chlorophyll-a concentration from Sentinel-3 satellite images at the Mediterranean Sea using CMEMS open source in situ data. *Open Geosci.* 13, 85–97. doi: 10.1515/geo-2020-0204

Oguma, S., Ono, T., Kusaka, A., Kasai, H., Kawasaki, Y., and Azumaya, T. (2008). Isotopic tracers for water masses in the coastal region of eastern Hokkaido. *J. Oceanogr.* 64, 525–539. doi: 10.1007/s10872-008-0044-y

Okamoto, S., Hirawake, T., and Saitoh, S. (2010). Interannual variability in the magnitude and timing of the spring bloom in the Oyashio region. *Deep Sea Res. II* 57, 1608–1617. doi: 10.1016/j.dsr2.2010.03.005

Onitsuka, G., Miyahara, K., Hirose, N., Watanabe, S., Semura, H., Hori, R., et al. (2010). Large-scale transport of *Cochlodinium polykrikoides* blooms by the Tsushima Warm Current in the southwest Sea of Japan. *Harmful Algae* 9, 390–397. doi: 10.1016/j.hal.2010.01.006

Pitcher, G. C., Boyd, A. J., Horstman, D. A., and Mitchell-Innes, B. A. (1998). Subsurface dinoflagellate populations, frontal blooms and the formation of red tide in the southern Benguela upwelling system. *Mar. Ecol. Prog. Ser.* 172, 253–264. doi: 10.3354/meps172253

Richardson, K. (1997). "Harmful or exceptional phytoplankton blooms in the marine ecosystem," in *Advances in Marine Biology*, eds J. H. S. Blaxter and A. J. Southward (Cambridge, MA: Academic Press), 301–385. doi: 10.1016/S0065-2881(08)60225-4

Roberts, S. D., Van Ruth, P. D., Wilkinson, C., Bastianello, S. S., and Bansemer, M. S. (2019). Marine heatwave, harmful algae blooms and an extensive fish kill event during 2013 in South Australia. *Front. Mar. Sci.* 6:610. doi: 10.3389/fmars.2019.00610

Ryan, J. P., Kudela, R. M., Birch, J. M., Blum, M., Bowers, H. A., Chavez, F. P., et al. (2017). Causality of an extreme harmful algal bloom in Monterey Bay, California, during the 2014–2016 northeast Pacific warm anomaly. *Geophys. Res. Lett.* 44, 5571–5579. doi: 10.1002/2017GL072637

Saito, K., Fujita, T., Yamada, Y., Ishida, J., Kumagai, Y., Aranami, K., et al. (2006). The operational JMA nonhydrostatic mesoscale model. *Mon. Wea. Rev.* 134, 1266–1298. doi: 10.1175/MWR3120.1

Sakamoto, K., Tsujino, H., Nishikawa, S., Nakano, H., and Motoi, T. (2010). Dynamics of the Coastal Oyashio and its seasonal variation in a high-resolution western North Pacific Ocean model. *J. Phys. Oceanogr.* 40, 1283–1301. doi: 10.1175/2010JPO4307.1

Shen, A., Ma, Z., Jiang, K., and Li, D. (2016). Effects of temperature on growth, photophysiology, rubisco gene expression in *Prorocentrum donghaiense* and *Karenia mikimotoi*. *Ocean Sci. J.* 51, 581–589. doi: 10.1007/s12601-016-0056-2

Shi, F., McNabb, P., Rhodes, L., Holland, P., Webb, S., Adamson, J., et al. (2012). Toxic effects of three dinoflagellate species from the genus *Karenia* on invertebrate larvae and finfish. *N. Z. J. Mar. Freshw. Res.* 46, 149–165. doi: 10.1080/00288330.2011.616210

Shulman, I., Penta, B., Richman, J., Jacobs, G., Anderson, S., and Sakalaukus, P. (2015). "Are the satellite-observed narrow, streaky chlorophyll filaments locally intensified by the submesoscale processes?," in *Proceedings of the SPIE 9459 (Ocean Sensing and Monitoring VII) 94590K* (Baltimore, MD), doi: 10.1117/12.2177569

Siswanto, E., Ishizaka, J., Tripathy, S. C., and Miyamura, K. (2013). Detection of harmful algal blooms of *Karenia mikimotoi* using MODIS measurements: a case study of Seto-Inland Sea, Japan. *Remote Sen. Environ.* 129, 185–196. doi: 10.1016/j.rse.2012.11.003

Smith, M. E., and Bernard, S. (2020). Satellite ocean color based harmful algal bloom indicators for aquaculture decision support in the southern Benguela. *Front. Mar. Sci.* 7:61. doi: 10.3389/fmars.2020.00061

Stumpf, R. P., Litaker, R. W., Lanerolle, L., and Tester, P. A. (2008). Hydrodynamic accumulation of *Karenia* off the west coast of Florida. *Cont. Shelf Res.* 28, 189–213. doi: 10.1016/j.csr.2007.04.017

Suzuki, K., Kuwata, A., Yoshie, N., Shibata, A., Kawanobe, K., and Saito, H. (2011). Population dynamics of phytoplankton, heterotrophic bacteria, and viruses during the spring bloom in the western subarctic Pacific. *Deep Sea Res. I* 58, 575–589. doi: 10.1016/j.dsr.2011.03003

Suzuki, R., and Ishimaru, T. (1990). An improved method for the determination of phytoplankton chlorophyll using N, N-dimethylformamide. *J. Oceanogr. Soc. Japan* 46, 190–194. doi: 10.1007/BF02125580

Thyng, K. M., Hetland, R. D., Ogle, M. T., Zhang, X., Chen, F., and Campbell, L. (2013). Origins of *Karenia brevis* harmful algal blooms along the Texas coast. *Limnol. Oceanogr. Fluid Environ.* 3, 269–278. doi: 10.1215/21573689-2417719

Trainer, V. L., Moore, S. K., Hallegraeff, G., Kudela, R. M., Clement, A., Mardones, J. I., et al. (2019). Pelagic harmful algal blooms and climate change: lessons from nature's experiments with extremes. *Harmful Algae* 91:101591. doi: 10.1016/j.hal.2019.03.009

Vargo, G. A., Heil, C. A., Fanning, K. A., Dixon, L. K., Neely, M. B., Lester, K., et al. (2008). Nutrient availability in support of *Karenia brevis* blooms on the central West Florida Shelf: what keeps *Karenia* blooming? *Cont. Shelf Res.* 28, 73–98. doi: 10.1016/j.csr.2007.04.008

Wells, M. L., Karlson, B., Wulff, A., Kudela, R., Trick, C., Asnaghi, V., et al. (2020). Future HAB science: directions and challenges in a changing climate. *Harmful Algae* 91:101632. doi: 10.1016/j.hal.2019.101632

Wells, M. L., Trainer, V. L., Smayda, T. J., Karlson, B. S. O., Trick, C. G., Kudela, R. M., et al. (2015). Harmful algal blooms and climate change: learning from the past and present to forecast the future. *Harmful Algae* 49, 68–93. doi: 10.1016/j.hal.2015.07.009

White, A. E., Watkins-Brandt, K. S., McKibben, S. M., Wood, A. M., Hunter, M., Forster, Z., et al. (2014). Large-scale bloom of *Akashiwo sanguinea* in the Northern California current system in 2009. *Harmful Algae* 37, 38–46. doi: 10.1016/j.hal.2014.05.004

Wolny, J. L., Tomlinson, M. C., Schollaert Uz, S., Egerton, T. A., McKay, J. R., Meredith, A., et al. (2020). Current and future remote sensing of harmful algal blooms in the Chesapeake Bay to support the shellfish industry. *Front. Mar. Sci.* 7:337. doi: 10.3389/fmars.2020.00337

Zhao, Y., Tang, X., Zhao, X., and Wang, Y. (2017). Effect of various nitrogen conditions on population growth, temporary cysts and cellular biochemical compositions of *Karenia mikimotoi*. *PLoS One* 12:e0171996. doi: 10.1371/journal.pone.0171996

Author Disclaimer: The A Line monitoring program was supported by the Fisheries Agency, Japan, but the content of this study does not necessarily reflect the views of the Fisheries Agency.

Conflict of Interest: The authors declare that the research was conducted in the absence of any commercial or financial relationships that could be construed as a potential conflict of interest.

Publisher's Note: All claims expressed in this article are solely those of the authors and do not necessarily represent those of their affiliated organizations, or those of the publisher, the editors and the reviewers. Any product that may be evaluated in this article, or claim that may be made by its manufacturer, is not guaranteed or endorsed by the publisher.

Copyright © 2022 Kuroda, Taniuchi, Watanabe, Azumaya and Hasegawa. This is an open-access article distributed under the terms of the Creative Commons Attribution License (CC BY). The use, distribution or reproduction in other forums is permitted, provided the original author(s) and the copyright owner(s) are credited and that the original publication in this journal is cited, in accordance with accepted academic practice. No use, distribution or reproduction is permitted which does not comply with these terms.

frontiers | Frontiers in Marine Science

ORIGINAL RESEARCH
published: 04 April 2022
doi: 10.3389/fmars.2022.836469

Variability and Intensity of the Sea Surface Temperature Front Associated With the Kuroshio Extension

Jingyuan Xi[1], *Yuntao Wang*[1*], *Zhixuan Feng*[1,2], *Yang Liu*[1,3] *and Xinyu Guo*[1,4]

[1] State Key Laboratory of Satellite Ocean Environment Dynamics, Second Institute of Oceanography, Ministry of Natural Resources, Hangzhou, China, [2] State Key Laboratory of Estuarine and Coastal Research, School of Marine Sciences, and Institute of Eco-Chongming, East China Normal University, Shanghai, China, [3] Laboratory of Fisheries Oceanography, Ocean University of China, Qingdao, China, [4] Center for Marine Environmental Studies, Ehime University, Matsuyama, Japan

OPEN ACCESS

Edited by:
William Savidge,
University of Georgia, United States

Reviewed by:
Sophie Clayton,
Old Dominion University, United States
Lequan Chi,
University of Georgia, United States

***Correspondence:**
Yuntao Wang
yuntao.wang@sio.org.cn

Specialty section:
This article was submitted to Coastal Ocean Processes, a section of the journal Frontiers in Marine Science

Received: *15 December 2021*
Accepted: *08 March 2022*
Published: *04 April 2022*

Citation:
Xi J, Wang Y, Feng Z, Liu Y and Guo X (2022) Variability and Intensity of the Sea Surface Temperature Front Associated With the Kuroshio Extension. Front. Mar. Sci. 9:836469. doi: 10.3389/fmars.2022.836469

Seventeen years of satellite observational data are used to describe the variability in sea surface temperature (SST) fronts and associated features, e.g., frontal intensity and probability, in the northwestern Pacific Ocean. Compared with the SST gradient and frontal probability, the frontal intensity is less impacted by background noise in satellite observations and precisely represents the variability in frontal patterns. The seasonal variability in frontal intensity is prominent, and the corresponding seasonality varies spatially. Fronts are more common during winter in the northern region around the Oyashio Current but are most common during spring in the Kuroshio Current and to the south of the Kuroshio Extension. The meridional migration of fronts is associated with the seasonal movement of the North Pacific subtropical gyre. Though overall averaged frontal intensity along the Kuroshio Extension is most prominent in the northwestern Pacific Ocean, the associated variability in fronts is highly complex. The current study reveals that seasonality itself cannot capture the whole picture of frontal features because eddy-induced intraseasonal variability and basin-scale signal-induced interannual variability can modulate frontal dynamics. In particular, the monthly frontal intensity in regions where the seasonal cycle is not significant depends on the Pacific Decadal Oscillation and North Pacific Gyre Oscillation. Furthermore, the oscillation of the Kuroshio Extension and associated mesoscale eddies can impact its intraseasonal variability. The comprehensive analysis of frontal intensity in the Kuroshio Extension is helpful for delineating regional dynamics and has the potential to improve our understanding of controls on marine primary production.

Keywords: sea surface temperature front, Kuroshio Extension, seasonal cycle, frontal intensity, interannual variability

INTRODUCTION

Oceanic fronts delineate the boundaries between different water masses that are characterized by distinctive parameters, such as temperature, salinity, and chlorophyll (Yoder et al., 1994). A front is a narrow band where the water mass properties change rapidly; thus, the horizontal gradient in water parameters is largely applied for front identification (Castelao and Wang, 2014). In particular, with the development of remote sensing, satellite measurements of ocean color have been used to identify oceanic fronts (Wang et al., 2015). Due to the global coverage and high spatiotemporal resolution of satellite observations for sea surface temperature (SST), SST fronts are widely adopted to investigate frontal features and underlying frontogenesis (Wang et al., 2021a). Fronts are important for understanding regional dynamics and the associated impact on productivity (Ribalet et al., 2010). For instance, phytoplankton biomasses tend to be elevated near fronts where positive vertical flux supplies more nutrients (Clayton et al., 2014; Nagai and Clayton, 2017), leading to a productive zone (Hashioka and Yamanaka, 2007) and feeding grounds for fishes (Kitagawa et al., 2004). Under the scenario of climate change, an improved understanding of fronts is important to forecast and predict marine production and fisheries in the future (Woodson and Litvin, 2015).

The first global survey for SST fronts was conducted by Legeckis in 1978 using visual identification (Legeckis, 1978). Automatic detection algorithms were developed to identify fronts using the horizontal gradient in SST, and fronts were defined as those with high gradient values (Canny, 1986; Simpson, 1990). Recently, the gradient-based method has been successfully applied in many regions, e.g., the Eastern Boundary Currents (Wang et al., 2015) and South China Sea (Wang et al., 2020). An alternative algorithm was developed based on the histogram of SST, and the front is defined as the location where the fewest pixels with intermediate SST values separate the majority of pixels with higher and lower SSTs (Cayula and Cornillon, 1996). The histogram method was used to identify fronts in large global marine ecosystems (Belkin et al, 2009). A comparison between the methods indicates that more false fronts were identified with the gradient method and more fronts were missing when using the histogram method (Ullman and Cornillon, 2000). Both algorithms have been further improved, for example, by further examining sea surface height to incorporate mesoscale dynamics (Miller, 2009), and their applications are important for understanding oceanic dynamics.

Previous studies have revealed that SST fronts are ubiquitous in global oceans, although their frequencies and intensities vary greatly (Kartushinsky and Sidorenko, 2013). The frequency of fronts is usually defined as the frontal probability during a predefined period (Wang et al., 2015), while the intensity of fronts is usually obtained as the magnitude of the SST gradient associated with an identified front (Sugimoto et al., 2014). The frontal probability is useful to depict spatial distributions and temporal variabilities in fronts (Lorenzzetti et al., 2009). Fronts are more prevalent in coastal regions than in open oceans (Belkin, 2021). The presence of fronts is mainly determined by ocean dynamics, and fronts in coastal regions are related to orography-induced instability (Gan and Allen, 2002) and coastal upwelling and mixing (Wang et al., 2020), among other mechanisms. For instance, changes in coastlines or the presence of islands can induce instability, and fronts are persistently generated between coastal and offshore waters (Wang et al., 2021a). In comparison, high frontal probability only occurs in the open ocean when associated with strong boundary currents (Ullman and Cornillon, 2000) and substantial mesoscale eddies (Ji et al., 2018). For example, there is a high frontal probability in the western boundary current systems, e.g., the Kuroshio Current, the Brazil Current and the Gulf Stream, where the fronts delineate the boundary between the warm current and surrounding water (Parfitt et al., 2016; Chen et al., 2019). Additionally, oscillation of the boundary current induces meanders and mesoscale eddies that can generate fronts (Yuan and Castelao, 2017). Fronts are generally dominated by seasonal variability due to the underlying frontogenesis (Belkin et al, 2009). In the Brazil Current, upwelling-favorable winds mainly occur during local summer and drive offshore Ekman transport, which brings subsurface water to the surface (Chen et al., 2019). When this subsurface cold water crops out at the surface, an SST front is generated between coastal water and offshore warm water. In other seasons, when the wind changes direction, fronts are much less pronounced (Wang et al., 2021a). Similar seasonal fronts are also identified in some typical monsoon-dominated systems, e.g., the western boundary of the South China Sea (Wang et al., 2020), where the summer monsoon induces coastal upwelling and fronts. The seasonal cycle, as the dominating signal for most of time, is generally used to delineate the major variance in frontal patterns (Ullman and Cornillon, 2000).

The spatial-temporal variability in fronts is usually depicted by two methods, e.g., seasonal averaging of the frontal probability and empirical orthogonal function (EOF) decomposition (Cayula and Cornillon, 1996; Wang et al., 2020). The former method can show the evolution of fronts in space and time (Wang et al., 2021b). For example, the seasonal fronts, calculated with seasonal (monthly) climatology, in the South China Sea are characterized by high frontal probabilities off the coast of Vietnam in summer and off the coast of China in winter (Wang et al., 2020). To further resolve the interannual variability or trend in fronts, the EOF method decomposes complex signals into multiple modes, and the first few modes can describe the majority of the variance in frontal features (Wang et al., 2015). Because of the noisy nature of fronts, the explained variance in the EOF is usually small in comparison with SST and other factors (Yu et al., 2019). The first two EOF modes explained less than 20% of frontal variability in the Eastern Boundary Current Systems (Wang et al., 2015) and South China Sea (Wang et al., 2020), but they are still important for assessing frontal features, as the explained local variance can be larger than 50%. The EOF captures the region with prominent frontal variation in space and the associated temporal evolution, e.g., seasonal and interannual variability (Chen et al., 2019). For example, the EOF can describe the

seasonal variability in fronts in the South China Sea, where fronts are distributed along the coast due to monsoon-induced upwelling or coastal currents (Yu et al., 2020). After removing the seasonal climatology, the remaining interannual variability shows that the fronts are modulated by basin-scale signals, e.g., the El Niño-Southern Oscillation (ENSO) (Wang et al., 2021a).

The intensity of the front is another factor used to describe frontal features. The Antarctic polar front varies little in position as it is forced by orography, and the frontal probability is persistently high over a year (Graham and De Boer, 2013). However, the corresponding intensity of fronts changes greatly between different seasons due to regional changes in SST and wind (Freeman et al., 2016). Indeed, the intensity of the front is determined by the underlying dynamics that drive the front (Kostianoy et al., 2004), and its variations are important for understanding frontogenesis. In regions where fronts are associated with eddies and the meanders of currents, the movement of eddies and currents induces large variance in the front position; thus, the intensity of fronts is generally weak (Wang et al., 2021b). In areas where fronts are generated by wind-induced coastal upwelling, the intensity of the front is related to the wind stress that increases with the magnitude of wind (Wang et al., 2015). Furthermore, the intensity of the front can modify the wind stress in return and subsequently determine the wind-front interactions (Chen et al., 2019). Specifically, the wind stress is reduced over the cooler side of the front, e.g., the upwelling region; consequently, there will be less coastal upwelling, and the front is hard to preserve (Yu et al., 2020). Thus, in addition to the spatiotemporal variability in fronts, it is also important to further explore frontal intensity to gain a comprehensive understanding of the major features and underlying mechanisms.

The northwestern Pacific Ocean is characterized by prominent dynamical energy due to the Kuroshio Current and Oyashio Current (Miyazawa et al., 2009). As the poleward-flowing Kuroshio and equatorward-flowing Oyashio currents converge, their confluence zone, namely, the Kuroshio-Oyashio Interfrontal Zone (KOIZ), is highly dynamic and associated with high instability and eddies (Yasuda, 2003). The two currents have distinctive properties; in particular, the Kuroshio Current is much warmer and saltier than the Oyashio Current (Watanabe, 2009; Vivier et al., 2020). Correspondingly, there are prominent frontal features, such as the previously reported large SST gradients (Wang et al., 2021b). The KOIZ and the associated frontal zone extends eastward from 140°E to 180°E (Qu et al., 2001). In this study, the KOIZ and its extension zone are referred as the Kuroshio Extension following Qiu and Chen (2010). The Kuroshio Current and Oyashio Current transport comparable nutrients to the KOIZ *via* their respective nutrient streams (Guo et al., 2012; Long et al., 2019), fueling the biological activities in the Kuroshio Extension (Clayton et al., 2021). Interannual variability of dynamical status in the Kuroshio Extension has mostly been studied during the past few decades (Seo et al., 2014). The system can be distinguished as stable and unstable dynamical modes, and it is more energetic during the unstable mode (Qiu et al., 2014). These dynamic modes are modulated by the Pacific Decadal Oscillation (PDO) and North Pacific Gyre Oscillation (NPGO) (Qiu and Chen, 2010). In particular, during the positive phase of the PDO, negative SST anomalies in the eastern Pacific Ocean are transported westward *via* baroclinic Rossby waves (Seo et al., 2014). The depressed ocean surface interacts with the Shatsky Ridge and generates instability, resulting in an unstable mode and leading to a larger SST gradient (Wang et al., 2021b). The long-term trend in the front shows a poleward shift of the front due to the expansion of the trade winds, which causes more warm water to move northward by Ekman transport under the impact of the Atlantic Multidecadal Oscillation (AMO) (Wu et al., 2020). Thus, the unstable mode of the Kuroshio Extension is favorable for generating regional fronts (Wang et al., 2021b), which gradually move northward in association with the meridional movement of the trade winds (Wu et al., 2019). Since the occurrence of the Kuroshio Large Meander in 2017, the instability has been promptly elevated in the Kuroshio Extension (Sugimoto et al., 2021) and can potentially impact the regional fronts.

The variability in fronts in the Kuroshio Extension is simultaneously impacted by multiple dynamic processes, e.g., the migration of the Kuroshio and Oyashio currents, mesoscale eddies and interannual variability (Shan et al., 2020). However, a comprehensive description of frontal intensity and its variability is still lacking. In this study, 17 years of satellite data are applied to identify the daily distribution of the SST fronts, and the associated frontal intensity is applied to investigate their spatiotemporal variability and underlying dynamics. The study improves the understanding of fronts in strong western boundary currents and has important implications for assessing the impact of climate change on regional dynamics.

DATA AND METHODS

Satellite observations of SST spanning 17 years from September 2002 to August 2019 at daily intervals are used in this study to identify fronts. SST was measured by the Moderate Resolution Imaging Spectroradiometer (MODIS) onboard National Aeronautics and Space Administration's (NASA) satellite Aqua. Level-3 data are applied in the current study, and their spatial resolution is equal to 1/24°, which is approximately 4.5 km. The data within 5 km of the coast and clouds are discarded to avoid cloud and land contamination. Additionally, the SST is further replaced with a 3-day average at daily intervals to reduce the impact of clouds. Because the water masses maintain their location in space over short periods, e.g., a few days, the averaging method reduces cloud coverage without being impacted by frontal migration (Yu et al., 2020). Three-day averaged SST are applied throughout the entire study. The SST gradient, e.g., magnitude and direction, is further calculated from the SST at daily intervals for each pixel following Wang et al. (2015). In the direction crossing the front, only one pixel is used to depict the front location, while the front can stretch for a few to hundreds of pixels along the front. Though fronts are generally

narrow in width, e.g., much less than 5km, the identified fronts are always defined as 5 km in width following the spatial resolution of the satellite observations. The study region is selected as 130°E to 174°E and 28°N to 45°N, focusing on the Kuroshio Current to the south of Japan, Oyashio Current to the northeast of Japan and the Kuroshio Extension.

The daily distribution of fronts is derived from the gradient of SST using an improved edge-detection method (Wang et al., 2020). Briefly, the algorithm seeks the local maximum of SST gradient magnitude, and the pixels with a gradient magnitude larger than threshold T_1 are flagged as potential frontal pixels. The same front is found by searching the surrounding three pixels perpendicular to the direction of the SST gradient, and the one with the largest gradient magnitude is identified as the frontal pixel. The entire front is identified until the magnitude of the gradient decreases to below a lower threshold, T_2. The employed thresholds, T_1 and T_2, are 2.8°C per 100 km and 1.4°C per 100 km, respectively. The selection of thresholds depends on the spatial resolution and smoothness of the dataset, and these values were adopted from Wang et al. (2015) because the comparable SST gradients. The applied method can effectively capture the daily distribution of the SST front.

Because of the impact of cloud coverage, monthly averages are calculated for satellite datasets. The Kuroshio Extension region is not persistently impacted by clouds; thus, the monthly average can effectively fill the gaps and obtain continuous time series. As the average is obtained only over the period when the data are free of clouds, the averaging method effectively reduces the impact of cloud coverage without introducing bias due to varying sampling size. The monthly composite of frontal patterns, e.g., SST gradient, frontal probability and frontal intensity, is applied in this study to describe the major frontal features in the Kuroshio Extension. Specifically, the frontal intensity is obtained as the magnitude of the SST gradient over the location where the front is identified to quantify the frontal feature. The monthly frontal intensity (MFI) is applied by averaging the daily frontal intensity for each month using the cloud-free period. The corresponding monthly frontal probability is calculated as the number of times the pixel is identified as a front divided by the number of times the pixel is cloud free during the corresponding month (Wang et al., 2015). The monthly climatology of MFI is calculated by averaging the corresponding monthly values over 17 years, while the anomaly is obtained by removing the monthly climatology (Wang et al., 2020).

The frontal patterns are further analyzed to determine their spatial and temporal variability and their dependence on basin-scale interannual indices. The EOF method is applied to capture the major variability using the monthly time series of frontal intensity. Due to the noisy nature of the fronts, the original dataset was first linearly interpolated into a coarse grid with a spatial resolution equal to 1/8°. The overall average of MFI is removed at each pixel before conducting EOF analysis. The seasonal cycle and its significance are assessed using the time series of MFI. The seasonal cycle is obtained with the least square regression by fitting a sinusoidal function with a period of 12 months. The seasonal cycle is included in the seasonal variability, which also delineates signals with other seasonal changes, such as semi-seasonal cycle. The obtained seasonal cycle is further tested to determine whether the regression is significant at the 95% confidence level. The anomaly time series is used to calculate the dependence between frontal intensity and interannual indices. In particular, the anomaly time series is obtained by removing the overall average for the corresponding month. The Pearson correlation coefficient is calculated between the anomaly field and different indices, e.g., NPGO, PDO, ENSO, among others.

RESULTS

Demonstration of Front Identification and Associated Features

A demonstration is shown in **Figure 1** for the procedure of front identification. Because of cloud coverage, there are still remaining gaps in satellite observations after the 3-day average that may interfere with the demonstration of frontal identification. Thus, the front is identified using the 11-day averaged data to reflect a continuous pattern. The SST, SST gradient and identified SST front in the Kuroshio Extension region are shown from September 4, 2002, to October 18, 2002, at 11-day intervals as an example. The identified front (**Figure 1** third column) is in good agreement with the SST gradient (**Figure 1** second column) and delineates the boundary between water masses with different SSTs (**Figure 1** first column).

The monthly frontal features, including the averaged SST gradient magnitude (**Figure 2A**), frontal probability (**Figure 2B**) and frontal intensity (**Figure 2C**), in August 2008 are shown. The MFI shows high frontal intensity to the east of Japan in the zonal band at approximately 39°N (**Figure 2C**). The corresponding monthly frontal probability (**Figure 2B**) also shows high values in the same region. In comparison to a direct average of the gradient magnitude, the MFI is less noisy and is able to delineate high values in the SST gradient magnitude (**Figure 2A**). Because the frontal intensity is defined as zero if no fronts are identified during a certain month, the regions without fronts have a value close to zero (**Figure 2C**). In contrast, there is a persistent SST gradient value regardless of whether fronts are present (**Figure 2A**). Thus, the frontal intensity can effectively eliminate the influence of the background SST gradient by highlighting the front-associated features.

Average Frontal Features in the Kuroshio Extension

The frontal features in the Kuroshio Extension region are associated with prominent spatial and temporal variability. The spatial patterns of the overall SST gradient (**Figure 3A**), frontal probability (**Figure 3B**) and frontal intensity (**Figure 3C**) are highly similar. They are characterized by high values near the coast of Japan, particularly at approximately 40°N, and extend eastward, although the value generally decreases with offshore distance. As one of the strongest western boundary currents, the highest frontal probability and frontal intensity in the Kuroshio

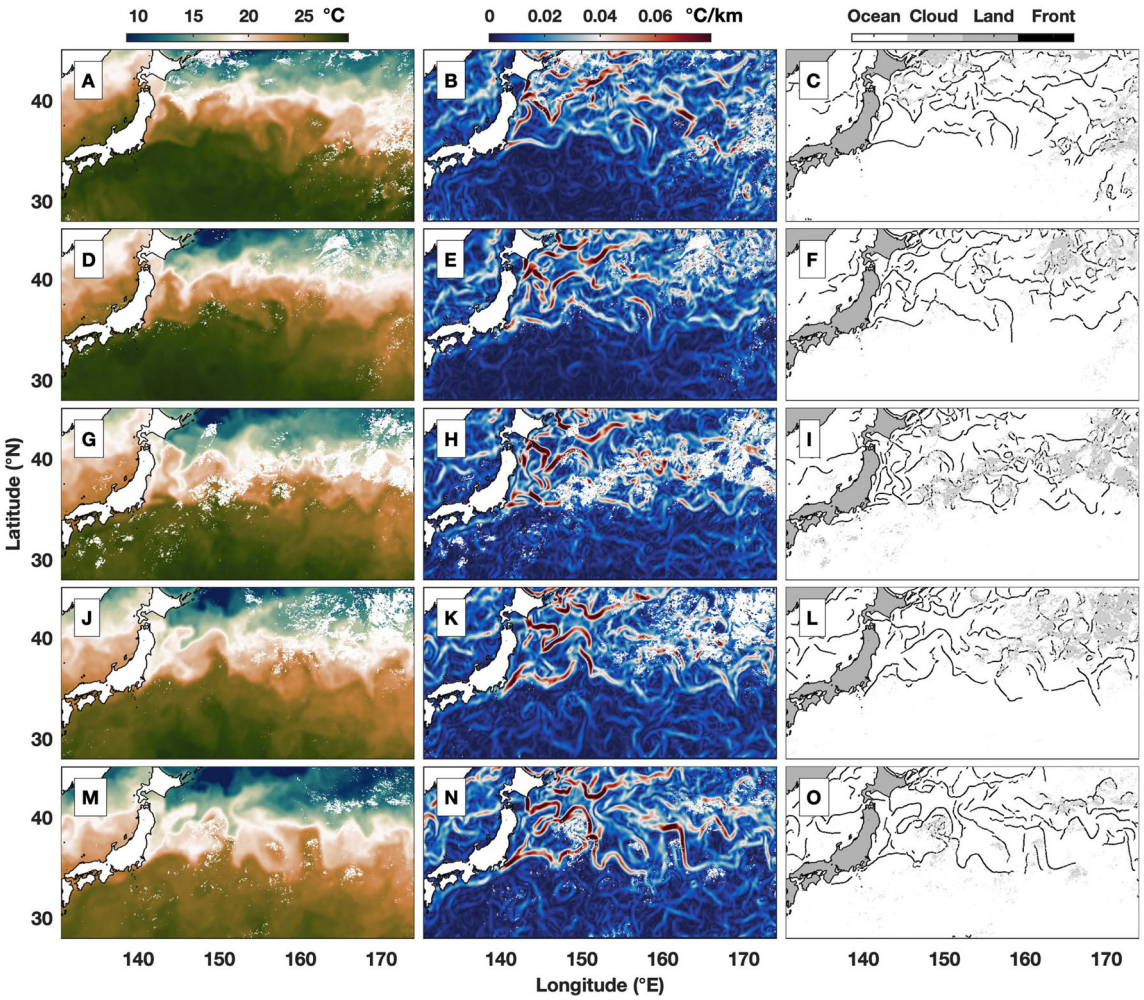

FIGURE 1 | Example of sea surface temperature (SST) front detection using 11-day averaged **(A, D, G, J, M)** SST (°C), **(B, E, H, K, N)** SST gradient magnitude (° C/km), and **(C, F, I, L, O)** identified SST front. The middle time of average is **(A–C)** September 4, **(D–F)** September 15, **(G–I)** September 26, **(J–L)** October 7, and **(M–O)** October 18, 2002.

Extension are more than 9% and 0.03°C/km, respectively. These values are higher than those of eastern boundary currents (Wang et al., 2015) and some coastal upwelling regions (Wang et al., 2020), which are usually identified as the regions with prominent fronts (Belkin et al, 2009).

There are also differences among the SST gradients, frontal probabilities and frontal intensities that were revealed in their overall distribution. For example, a large SST gradient, e.g., 0.04°C/km, exists in the entire Kuroshio Extension, while a high frontal probability, e.g., 8%, occupies an even larger area. In contrast, a high frontal intensity, e.g., 0.03°C/km, is concentrated in a small area characterized by a large SST gradient and high frontal probability. A large band of frontal intensity clearly delineates the KOIZ, where a high-value band can be found extending from the eastern coast of Japan, i.e., 35°N and 140°E, toward the northeast (**Figure 3C**). Thus, the frontal intensity can be used as a precise proxy that is little impacted by background SST gradients and fronts to describe frontal features and is further applied in the following analysis.

Seasonal Variability in Frontal Intensity

The seasonal averages of frontal intensity (where winter, spring, summer and fall are defined as December to February, March to May, June to August and September to November, respectively) show prominent differences (**Figure 4**). In winter, the region with a high frontal intensity is centralized in a small coastal area located directly to the east of Japan at approximately 35°N (**Figure 4A**). The corresponding value of frontal intensity is greater than 0.05°C/km, which is the highest of the year across the entire study region. In contrast, the fronts in the open ocean are much less pronounced, and the intensity values are generally close to zero. The frontal intensity in the Kuroshio Extension region is greatly enhanced in spring; in particular, frontal intensities greater than 0.03°C/km occupy the entire coastal area

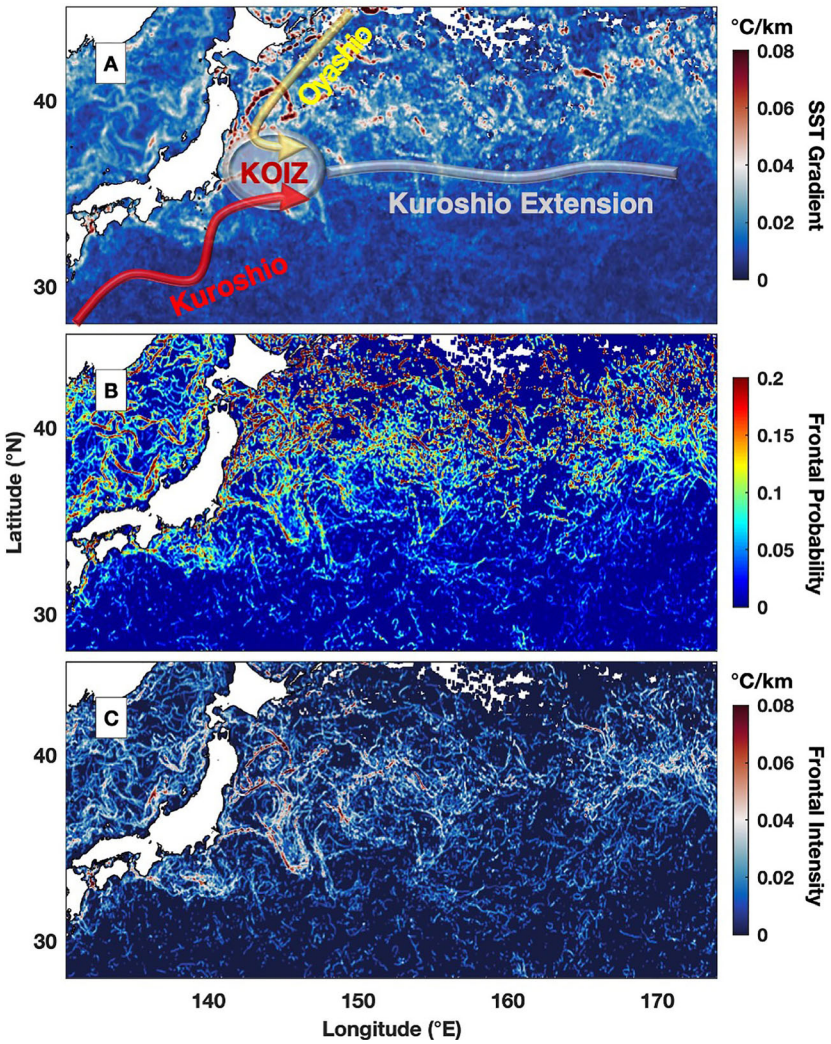

FIGURE 2 | An example of monthly averaged **(A)** SST gradient (°C/km), **(B)** frontal probability and **(C)** frontal intensity (°C/km) in August 2008 for the Kuroshio Extension region. The blank area over the ocean indicates that the region is persistently obstructed by clouds during the month. The Kuroshio Current, Oyashio Current, Kuroshio-Oyashio Interfrontal Zone (KOIZ) and Kuroshio Extension are schematically shown in panel **(A)**.

between 35°N and 41°N and extend approximately 400 km offshore (**Figure 4B**). The weakest frontal intensity occurs in summer, when the frontal intensity value is universally less than 0.02°C/km (**Figure 4C**), although weak fronts are distributed throughout the entire region. The frontal intensity greatly increases in the northern section, e.g., to the north of 35°N, during fall, and the corresponding value is approximately 0.03°C/km near the coastal region (**Figure 4D**). Simultaneously, the fronts are reduced in the southern region. There is also prominent seasonal variability in frontal intensity in the area to the west of Japan in the East Sea/Sea of Japan (Park et al., 2007); however, the underlying frontogenesis is related to eddies and the marginal sea circulation system, which is very different from the Kuroshio Extension, and the region is excluded from the current study.

The variability in MFI in the Kuroshio Extension is further investigated *via* EOFs. The first three modes explain approximately 15% of the total variance in the frontal intensity, e.g., 7.0%, 5.1% and 3.2% for EOF1, EOF2 and EOF3, respectively. The value is lower than many former studies that focused on frontal probability, where the first one or two modes usually explain 15% of the total variance (Wang et al., 2015). This finding is due to the complex dynamics in the Kuroshio Extension region, and the MFI has larger variation than frontal probability; thus, multiple modes are required to describe the variability in the MFI. The first EOF shows high intensity in the entire southern section of the study region, especially along the Kuroshio Current and Kuroshio Extension to the east of Japan (**Figure 5A**). The corresponding monthly average of the temporal EOF of MFI is dominated by a prominent seasonal variability, peaking in spring,

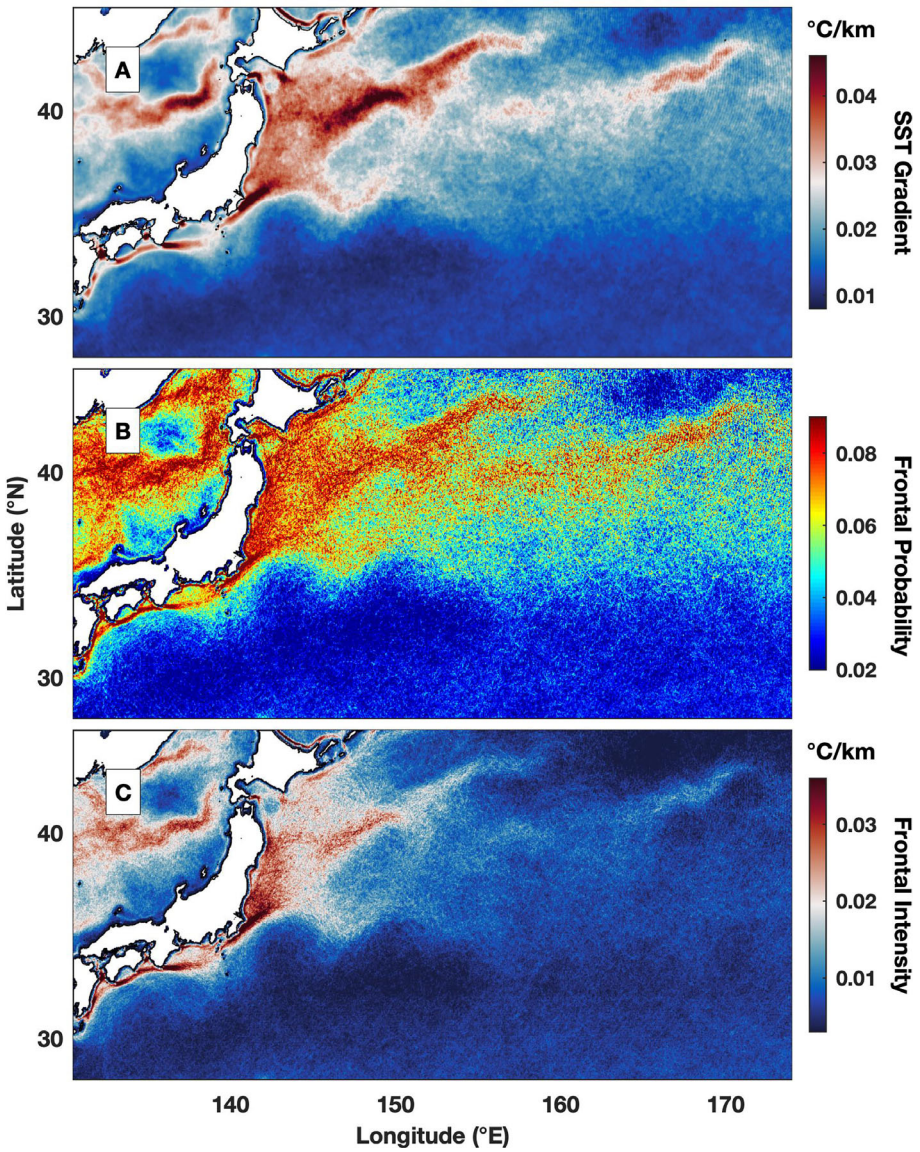

FIGURE 3 | Seventeen-year averaged **(A)** SST gradient (°C/km), **(B)** frontal probability and **(C)** frontal intensity (°C/km) from September 2002 to August 2019.

e.g., March to May, and troughing in winter, e.g., December to February (**Figure 5B**). The enhancement in the MFI is highly consistent with the high seasonal average in spring (**Figure 4B**). The monthly average time series (**Figures 5B, D, F**) starts in December for easier comparison with **Figure 4**. Monthly average is near zero for the period from June to October, indicating the frontal intensity during this period is persistently close to the corresponding overall average. The second EOF mostly focuses on the northern section around the Oyashio Current (**Figure 5C**). The associated seasonal variability shows high frontal intensity in fall, e.g., September to November, and low intensity in summer, e.g., May to July (**Figure 5D**). The third mode of EOF delineates the frontal variability off the entire coast of Japan (**Figure 5E**). The corresponding time series shows elevated frontal intensity in winter and early spring, e.g., December to April, whereas depressed values occur in summer and early fall, e.g., June to October (**Figure 5F**). During winter, the temperature in the Kuroshio Current is much higher than that in the surroundings, thus generating stronger fronts (Seo et al., 2014). In contrast, almost the whole region features high temperatures during summer, and the horizontal gradient in SST is small, showing fewer fronts.

The seasonality of frontal intensity varies among different regions, e.g., a fall peak in the northern section but a spring peak in the southern section (**Figure 4**), indicating that the underlying dynamics for frontogenesis are different or the seasonality varies. In **Figure 6A**, the regions with large variability in MFI, e.g., the coastal regions near Japan, Kuroshio Extension and branch of the

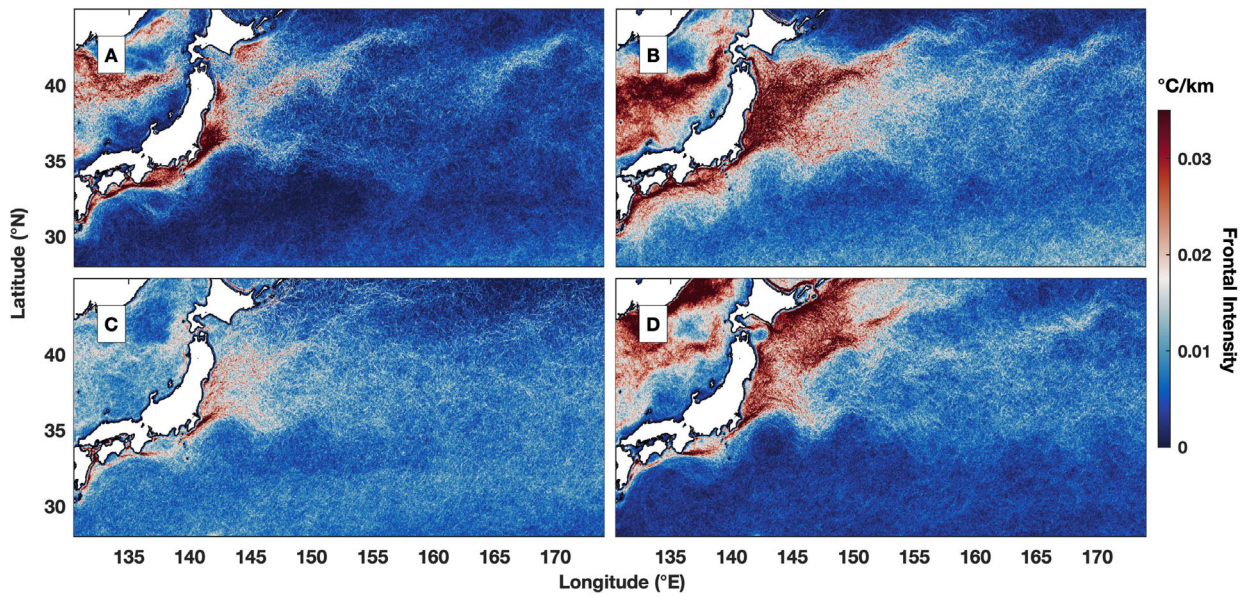

FIGURE 4 | Seasonal averaged frontal intensity (°C/km) for **(A)** winter (December to February), **(B)** spring (March to May), **(C)** summer (June to August) and **(D)** fall (September to November).

Oyashio Current, are generally found in regions with high averages of frontal intensity (**Figure 3C**). A detailed comparison shows that there is actually large variability along the Kuroshio Current located south of Japan (31°N, 138°E). The area is highly consistent with the path of the Kuroshio Current (Qiu and Chen, 2010). The large variability indicates that multiple dynamics drive the variability in the front, which was formerly revealed by the EOFs in the Kuroshio Extension. However, the small amount of explained variance and large standard deviation in each month (**Figures 5B, D, F**) indicate that the temporal evolution also includes complex variability, such as noise in the MFI and interannual and intraseasonal variability. Thus, the MFI variance and the importance of the seasonal cycle at each location should be assessed first. The seasonal cycle is found to be important for the southern and northern regions, and their phases show maxima over the year in spring and fall, respectively, while the phase of annual maximum mainly occurs between May and July in the coastal region. Indeed, the identified seasonal cycles are consistent with the spatiotemporal features captured by EOFs (**Figure 5**). In comparison, the seasonal cycle in the majority of the region, especially around the Kuroshio Extension, e.g., between 32°N and 42°N, is not significant. This region is roughly the same region where a high magnitude of EOF1 was identified (**Figure 5A**), although the time series is mostly dominated by seasonal variation (**Figure 5B**). Thus, this finding can help to explain the low variance explained by the EOFs, as there are also signals characterized by other frequencies, e.g., interannual and intraseasonal variabilities.

The percentage of variance explained by the seasonal cycle shows a significant dominance of the variability in MFI in the northern region (**Figure 6B**), and the corresponding phase of maximum in MFI happens in fall (**Figure 6C**). The southern region is also characterized by significant seasonal cycle, though the explained variance is only around 30%. The phase of maximum happens in winter in the eastern region and gradually change to later time of a year towards the west. Seasonal cycle contributes less than 20% of variance for majority of the Kuroshio Extension where the regression is not significant. Note the low value of explained seasonal cycle doesn't imply the seasonal variability is not important, but the seasonal changes are not fitting well with the sinusoidal function. For example, the EOF1 captures the MFI is remaining a similar value around zeros for almost half year (**Figure 5B**), which cannot be reproduced with seasonal cycle. To further illustrate the significance of the seasonal cycle in MFI variation, two locations denoted in **Figure 6C** are selected as examples, and the corresponding seasonal cycles are obtained by fitting a sinusoidal function (**Figure 7**). In the northern region (denoted by the blue dot), the correlation between the seasonal cycle regression and the original time series is only 0.35 (**Figure 7A**), and the seasonal cycle is not significant at the 95% confidence level. The monthly average MFI actually captures two peaks, i.e., in April and October (**Figure 7B**). Simultaneously, there is large variance for each month, which is revealed by the high standard deviation. In comparison, the seasonal cycle is prominent in the southern region (denoted by the red dot), and its correlation with the original time series reaches 0.79 (**Figure 7C**), which is significant at the 95% confidence level. Additionally, the seasonal variability is clearly revealed by monthly averages, although the variation in each month is still high (**Figure 7D**) due to interannual variability; for example, lower magnitudes of the MFI are identified from 2010

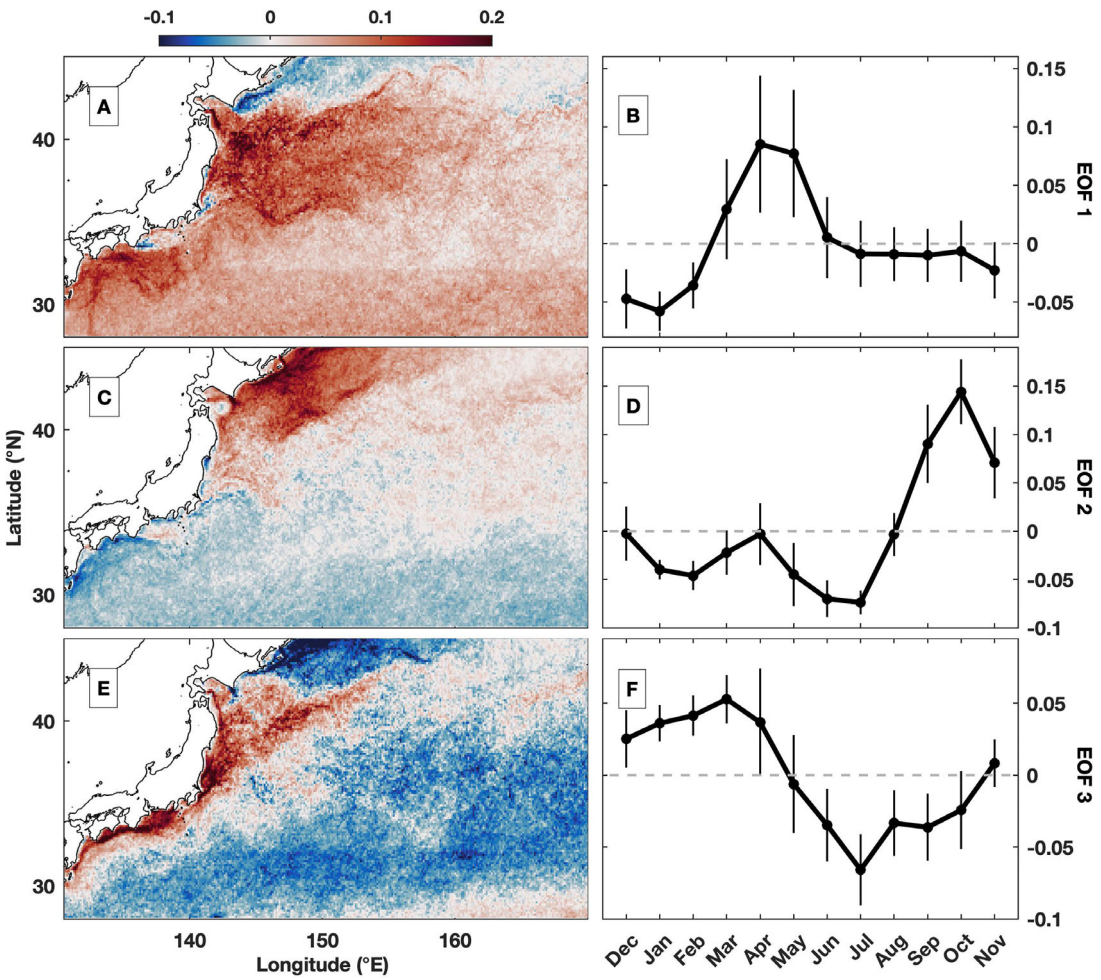

FIGURE 5 | **(A, C, E)** Spatial magnitude and **(B, D, F)** temporal amplitude of monthly averaged frontal intensity (°C/km) using the empirical orthogonal function (EOF). The vertical bars in **(B, D, F)** indicate the standard deviation for corresponding months. The **(A, B)** first mode, **(C, D)** second mode and **(E, F)** third mode of EOFs. The monthly averaged time series in **(B, D, F)** is set to start in December for easier comparison with **Figure 4**.

to 2011, and higher magnitudes are identified in 2013 and from 2017 to 2019.

Interannual Variability in Frontal Intensity

To investigate the migration and interannual variability in frontal intensity, the zonally averaged MFI is calculated between 166°E and 171°E (**Figure 8A**). The Hovmöller diagram shows that the fronts are first generated in the southern region and gradually develop in the northern region. This feature is better revealed in the field of monthly climatological averages (**Figure 8B**), in which fronts are generated in the southern region, e.g., 29°N, during spring and rapidly extend northward to 35°N until summer. The frontal intensity between 35°N and 41°N is simultaneously elevated in summer, while the frontal intensity in the northern section, e.g., at approximately 42°N, is generally high. The frontal intensity monotonically decreases from south, e.g., 0.015°C/km, to north, e.g., 0.008°C/km. Although the meridional migration of fronts is prominent, the value is much lower than that in coastal regions (**Figure 3C**). There is also clear interannual variability in the anomaly field, which is quantified by spatially averaging the MFI after removing the monthly climatological average (**Figure 8C**). The frontal intensity is low between mid-2006 and mid-2009 and between mid-2012 and 2015, while high values are found since. It is interesting to note that the negative anomalies are generally associated with the period when the Kuroshio Extension is characterized by an unstable mode (Qiu et al., 2014). This feature is quite different in the upstream of Kuroshio Extension where the variability in MFI is much larger during unstable mode (**Figure 7C**) associated with higher frontal probability (Wang et al., 2021b), but the underlying dynamic requires future investigation. The elevated frontal intensity after 2016 can be related to the occurrence of the Kuroshio Large Meander (Sugimoto et al., 2021), associated with the Kuroshio Extension switches to the unstable mode (Qiu et al., 2020), which introduces high instability (Nagano et al., 2019). Thus, fronts are

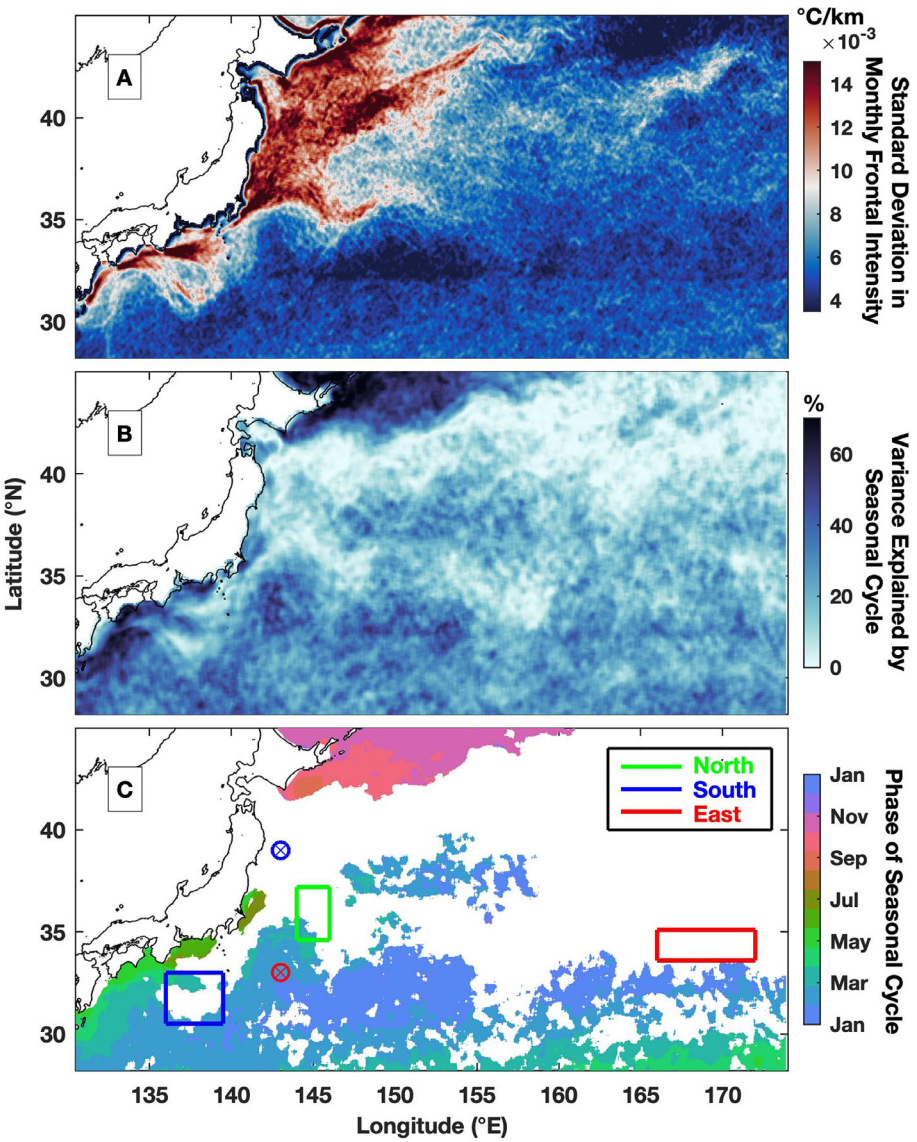

FIGURE 6 | **(A)** Standard deviation of the monthly time series of MFI (°C/km). **(B)** Percentage of the variance explained by seasonal cycle. **(C)** Phase of the annual seasonal cycle of MFI; only the region with significant regression is shown. In panel **(C)**, two locations denoted by blue and red circles are investigated in **Figure 7**, as the blue (red) location is dominated by a significant (nonsignificant) seasonal cycle. Three designated regions with nonsignificant seasonal cycles, i.e., north, south and east, are further applied to investigate interannual variability in **Figure 9**.

characterized by complex dynamics, including seasonal and interannual variabilities. Similar enhancements in MFI after 2016 are also identified upstream of the Kuroshio Extension (**Figure 7**).

The interannual variability in front is largely impacted by basin-scale signals, e.g., PDO and NPGO, especially in regions where the seasonal cycle is not significant (**Figures 7A, B**). Three regions with nonsignificant seasonal cycles are selected to investigate their interannual variability in frontal intensity (**Figure 6C**). The MFI in the northern region has a correlation of 0.59 with the NPGO, which leads the interannual variability in the MFI by 13 months. The positive phase of the NPGO enhances the frontal intensity along the Kuroshio Extension after roughly one year, and the negative NPGO depresses the frontal intensity (**Figure 9A**). The timing between the NPGO and MFI represents the time required for the signal to propagate from the eastern Pacific to the Kuroshio Extension (Lin et al., 2014). The MFIs in the southern and eastern regions are negatively correlated with the PDO, and the corresponding correlation coefficients are -0.55 (**Figure 9B**) and -0.65 (**Figure 9C**), respectively. All the acquired correlations are significant at the 95% confidence level. Notably, there is a difference in the time when the highest coefficients occur. The largest coefficient between frontal intensity and PDO occurs

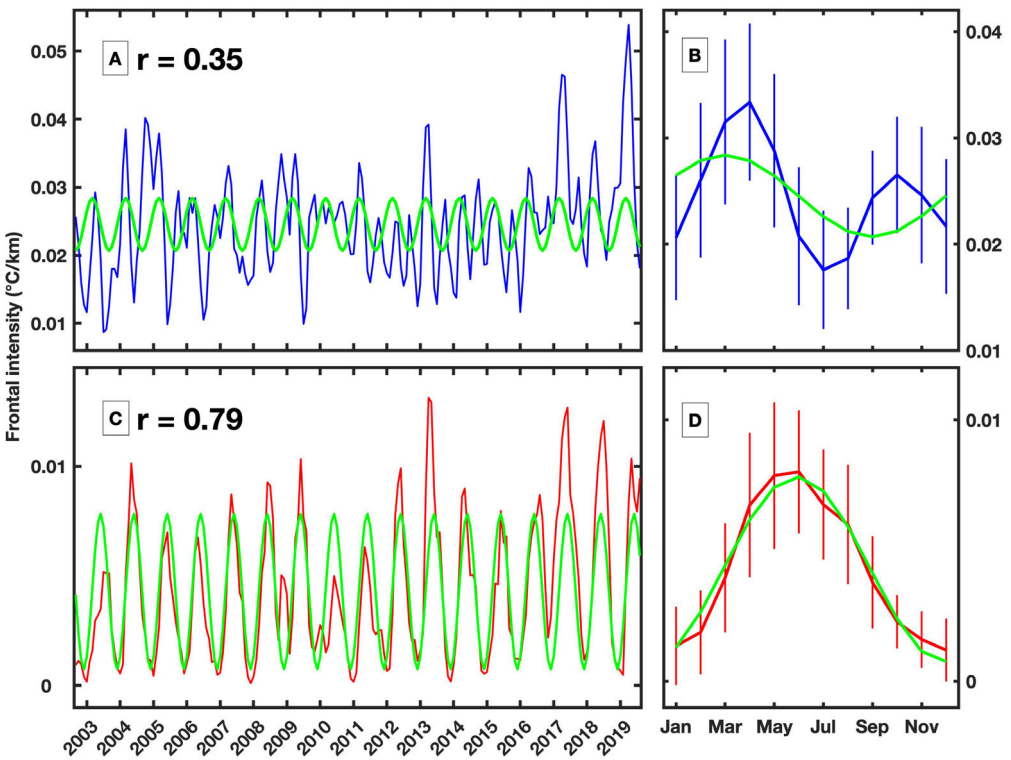

FIGURE 7 | **(A)** Monthly time series of MFI in the blue region shown in **Figure 6C**. The green line shows the obtained seasonal cycle of the time series. The correlation coefficient between the monthly time series and seasonal cycles is shown in the figure. **(B)** Climatological monthly average and associated standard deviation. Panels **(C, D)** are similar to panels **(A, B)**, respectively, but for the red region shown in **Figure 6C**.

simultaneously in the south, but frontal intensity leads the PDO by 6 months in the east. The timing indicates a westward propagation of frontal intensities that initiates in the east around the Kuroshio Extension and propagates west toward the Kuroshio Current. A similar westward propagation signal was identified in previous studies that found that the interannual variability in the SST gradient is modulated by the PDO signal, and its different phases induce changes in the stability of the Kuroshio Extension (Wang et al., 2021b). Other interannual signals are also investigated, such as ENSO and AMO, but no significant dependence is found between these signals and the frontal intensity.

DISCUSSION

Seventeen years of satellite observations of SST are applied to detect oceanic fronts and the associated features, i.e., frontal intensity, in the region of the Kuroshio Extension. During the front detection procedure, the SST gradient is first calculated, and the front is identified based on the direction and value of the SST gradient (Wang et al., 2020). The applied method can successfully capture the location of fronts (**Figure 1**), which are mainly distributed along the Kuroshio Extension and the region to the north. Due to the contrasting features of the Kuroshio Current and Oyashio Current, their confluence is characterized by strong dynamics (Miyazawa et al., 2009). Indeed, prominent frontal intensities are identified in the region of the KOIZ (Vivier et al., 2020). The large frontal intensities in the northern region (**Figure 3**) are related to the strong mesoscale eddies (Ji et al., 2018) and oscillation in the path of the Oyashio Current (Wu et al., 2019). In particular, the two identified bands, e.g., 40°N, 150°E and 40°N, 168°E, distributed toward the northeast are in good agreement with the persistent anticyclonic eddy and the flow of the subarctic current, which flows toward the northeast between 40°N and 43°N (Ohshima et al., 2005).

In comparison, frontal intensities are much less prominent in the southern section, with sparse and weaker fronts occurring during spring and summer (**Figure 4**). The region is a part of the North Pacific subtropical gyre (McClain et al., 2004), where the surface water is uniformly high in temperature (Kobashi and Kubokawa, 2012). Frontal intensities are elevated in the region located further south at the subtropical front between 20°N and 25°N (Yuan and Talley, 1996), but this feature is not included in the current study. During spring and summer, the North Pacific subtropical gyre shifts northward in association with the presence of fronts in the southern section of the study region. The meridional migration of fronts is also observed in **Figures 8A, B**, spanning from spring to summer.

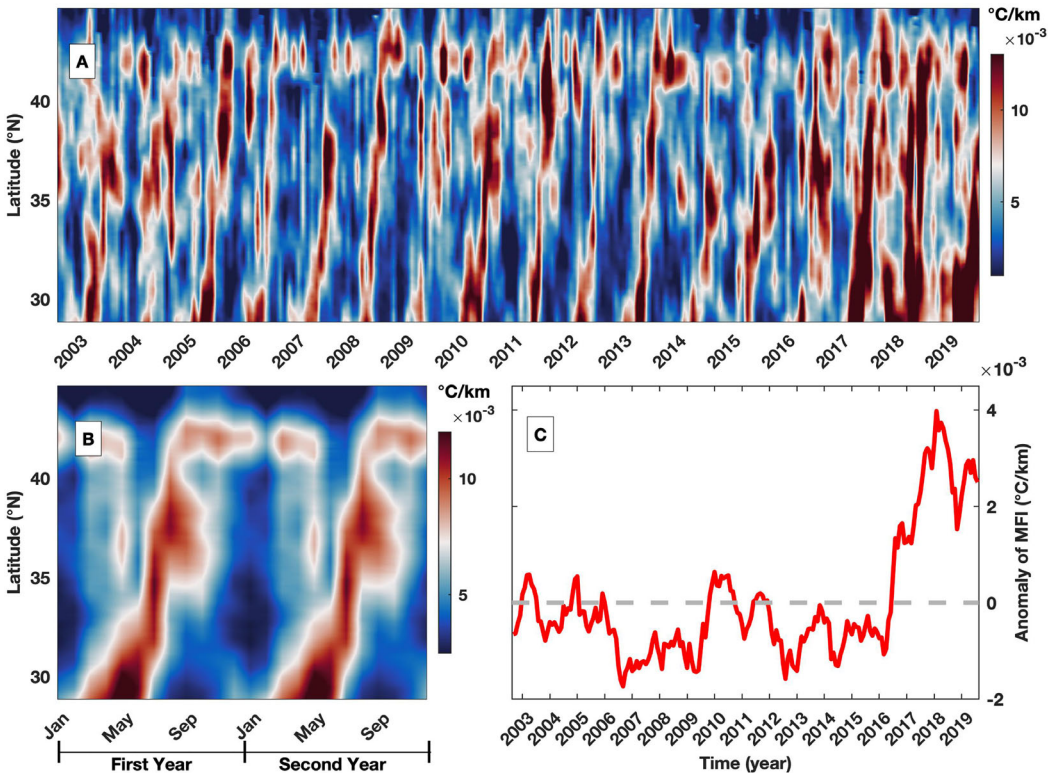

FIGURE 8 | **(A)** Hovmöller diagram of MFI in the meridional direction for the region between 166°E and 171°E; **(B)** corresponding monthly climatology but repeated twice; **(C)** the time series of anomaly in MFI, which is obtained with the difference between the time series and corresponding climatology by averaging over the region.

Previous studies have focused on frontal distribution and probability (Yuan and Talley, 1996); however, some fronts are distributed persistently at certain positions, and the location provides limited information for describing the frontal features (Freeman et al., 2016). A similar phenomenon is identified when the confluence of the Kuroshio Current and Oyashio Current introduces a persistent front in the Kuroshio Extension region. Thus, frontal intensity offers new insight for understanding frontal features and for investigating underlying frontogenesis. For example, the background SST gradient exists universally in the ocean and can be interpreted as many weak fronts (**Figure 2A**). In comparison, the frontal intensity is defined only when the location is identified as a front; thus, the background SST gradient is greatly reduced, and the frontal features are more prominent (**Figure 2C**).

The first three EOF modes all reveal prominent seasonal variability in the MFI (**Figure 5**). The region with the highest frontal intensity shifts meridionally during different seasons (**Figure 4**) due to the trade wind's expansion and migration of the confluence zone (Wu et al., 2020). Although most former studies describe frontal variability using seasonal cycles (Chen et al., 2019), the current study shows that there are also other forms of variance, such as intraseasonal (**Figure 7**) and interannual variabilities (**Figure 8**). The seasonal cycle is not a significant pattern for the MFI in the Kuroshio Extension (**Figure 6C**). A detailed investigation found that the variability is much more complex and that the seasonal cycle does not explain the total variability. Because of the influence of interannual signals on modulating frontal variability (Wang et al., 2020), the MFI in the region with a nonsignificant seasonal cycle (**Figure 6C**) is characterized by complex variability (**Figure 7A**).

Due to the complex dynamics in the Kuroshio Extension region, it is difficult to delineate the frontal intensity with simplified signals. Moreover, fronts are actually three-dimensional features (Wu et al., 2019), and the subsurface information is also important to describe the comprehensive features of fronts. With the development of automatic oceanic observation platforms, e.g., unmanned surface vehicles, Argo floats, and gliders (Chai et al., 2020), the vertical section on both sides of the front can be measured to better describe the differences in oceanic features across the front and associated dynamics (Shao et al., 2019).

The convergence associated with fronts aggregates and elevates nutrient levels, which can subsequently induce ecosystem responses (Woodson and Litvin, 2015). Clear dependence was previously identified between fronts and marine phytoplankton in response to both seasonal and interannual variabilities (Kouketsu et al., 2016). The Kuroshio

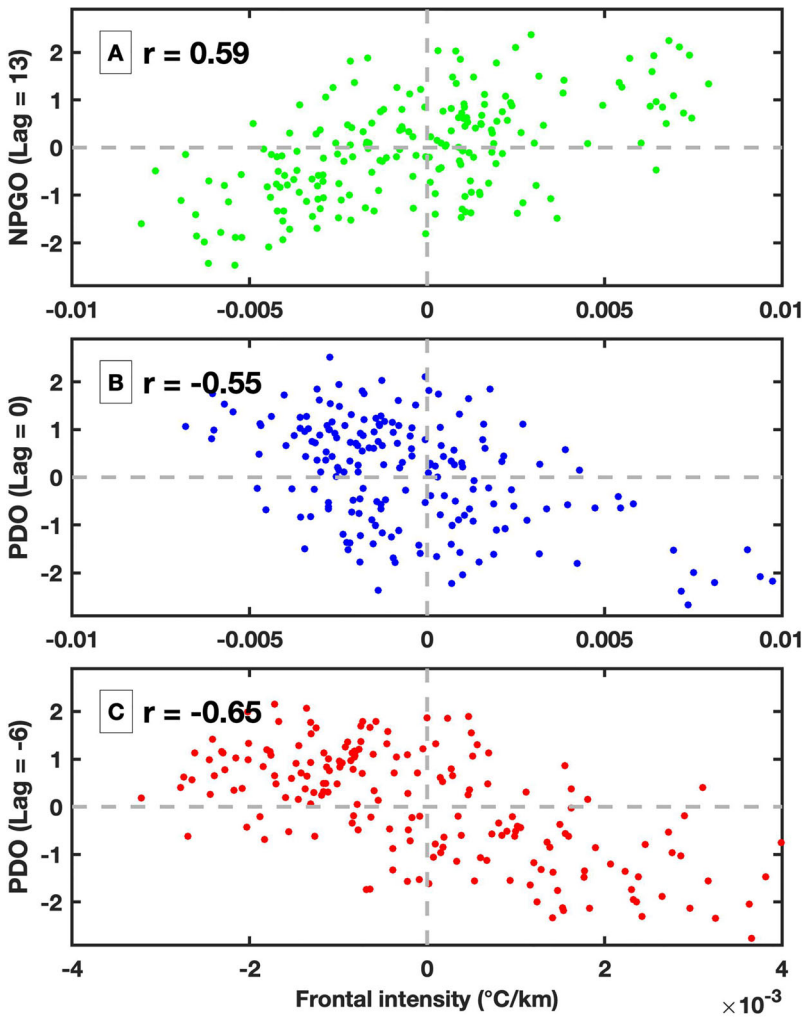

FIGURE 9 | Scatterplot between **(A)** MFI in the northern region and NPGO index where the NPGO is leading by 13 months; **(B)** MFI in the southern region and PDO index without lagging; **(C)** MFI in the eastern region and PDO index where the MFI is leading by 6 months. The applied lag is selected to obtain the largest correlation between two time series. All the correlations are significant at the 95% confidence level. The regions are denoted in **Figure 6C**.

Extension has been an important fishing ground due to its high productivity (Watanabe, 2009). Thus, an improved knowledge of oceanic fronts is helpful to understand the variability in marine primary production and the carbon cycle.

CONCLUSION

Satellite-derived frontal features are investigated in the Kuroshio Extension region. Seasonal cycles are generally a critical component for all geophysical features, i.e., SST, SST gradients and fronts; thus, they are widely applied to describe signals. However, our study indicates that it is important to evaluate whether the seasonal cycle is significant beforehand (**Figure 6**), as the variability in signals can be much more complex (**Figure 7**). A simplified seasonal cycle can be misleading when the signal is influenced at different scales, i.e., intraseasonal and interannual variability. The MFI is a good parameter to delineate the spatial and temporal variability in fronts that can reduce the background noise in the SST gradient field.

A major focus is to describe the seasonal and interannual variability in frontal intensity in the Kuroshio Extension and investigate the underlying dynamics that drive the corresponding variability. The seasonal variability in the MFI is mostly impacted by the confluence of the Kuroshio and Oyashio currents (Kida et al., 2015) and associated mesoscale dynamics, such as eddies (Itoh and Yasuda, 2010; Chelton et al., 2011). The interannual variability is impacted by basin-scale signals, such as the PDO and NPGO (Wang et al., 2021b). Due to the importance of the Kuroshio Extension in driving the carbon cycle and fisheries (Kitagawa et al., 2004; Yatsu et al., 2013; Sutton et al., 2017), an improved understanding of frontal intensity is crucial

for predicting the changes in ocean dynamics and ecosystems under the scenario of future climate change.

DATA AVAILABILITY STATEMENT

The original contributions presented in the study are included in the article. Further inquiries can be directed to the corresponding author.

AUTHOR CONTRIBUTIONS

Data curation, JX. Writing, YW and JX. Review of the manuscript, ZF, YL, and XG. Visualization, YL. Funding, YW. All authors have read and agreed to the published version of the manuscript.

FUNDING

The study is funded by the National Natural Science Foundation of China (42176013, 41730536 and 41890805).

ACKNOWLEDGMENTS

We are very thankful to the National Aeronautics and Space Administration (NASA) for producing and distributing the sea surface temperature dataset (NASA, 2014).

REFERENCES

Belkin, I. M. (2021). Remote Sensing of Ocean Fronts in Marine Ecology and Fisheries. *Remote Sens.* 13, 883. doi: 10.3390/rs13050883

Belkin, I. M., Cornillon, P. C., and Sherman, K. (2009). Fronts in Large Marine Ecosystems. *Prog. Oceanogr.* 81, 223–236. doi: 10.1016/j.pocean.2009.04.015

Canny, J. A. (1986). Computational Approach to Edge Detection. *IEEE Trans. Pattern Anal. Mach. Intell.* 8, 679–698. doi: 10.1109/TPAMI.1986.4767851

Castelao, R. M., and Wang, Y. (2014). Wind-Driven Variability in Sea Surface Temperature Front Distribution in the California Current System. *J. Geophys. Res. Oceans* 119, 1861–1875. doi: 10.1002/2013JC009531

Cayula, J., and Cornillon, P. (1996). Cloud Detection From a Sequence of SST Images. *Remote Sens. Environ.* 55, 80–88. doi: 10.1016/0034-4257(95)00199-9

Chai, F., Kenneth, J., Claustre, H., Xing, X., Wang, Y., Boss, E., et al. (2020). Monitoring Ocean Biogeochemistry With Autonomous Platforms. *Nat. Rev. Earth Environ.* 1 (6), 315–326. doi: 10.1038/s43017-020-0053-y

Chelton, D. B., Gaube, P., Schlax, M. G., Early, J. J., and Samelson, R. M. (2011). The Influence of Nonlinear Mesoscale Eddies on Near-Surface Oceanic Chlorophyll. *Science* 334 (6054), 328–332. doi: 10.1126/science.1208897

Chen, H. H., Qi, Y., Wang, Y., and Chai, F. (2019). Seasonal Variability of SST Fronts and Winds on the Southeastern Continental Shelf of Brazil. *Ocean Dyn.* 69 (11), 1387–1399. doi: 10.1007/s10236-019-01310-1

Clayton, S., Nagai, T., and Follows, M. J. (2014). Fine Scale Phytoplankton Community Structure Across the Kuroshio Front. *J. Plankton Res.* 36 (4), 1017–1030. doi: 10.1093/plankt/fbu020

Clayton, S., Palevsky, H. I., Thompson, L., and Quay, P. D. (2021). Synoptic Mesoscale to Basin Scale Variability in Biological Productivity and Chlorophyll in the Kuroshio Extension Region. *J. Geophys. Res. Oceans* 126, e2021JC017782. doi: 10.1029/2021JC017782

Freeman, N. M., Lovenduski, N. S., and Gent, P. R. (2016). Temporal Variability in the Antarctic Polar Front, (2002–2014). *J. Geophys. Res. Oceans* 121, 7263–7276. doi: 10.1002/2016JC012145

Gan, J., and Allen, J. S. (2002). A Modeling Study of Shelf Circulation Off Northern California in the Region of the Coastal Ocean Dynamics Experiment: Response to Relaxation of Upwelling Winds. *J. Geophys. Res. Oceans* 107, 3123. doi: 10.1029/2000JC000768

Graham, R. M., and De Boer, A. M. (2013). The Dynamical Subtropical Front. *J. Geophys. Res. Oceans* 118, 5676– 5685. doi: 10.1002/jgrc.20408

Guo, X., Zhu, X.-H., Wu, Q.-S., and Huang, D. (2012). The Kuroshio Nutrient Stream and its Temporal Variation in the East China Sea. *J. Geophys. Res.* 117, C01026. doi: 10.1029/2011JC007292

Hashioka, T., and Yamanaka, Y. (2007). Seasonal and Regional Variations of Phytoplankton Groups by Top-Down and Bottom-Up Controls Obtained by a 3D Ecosystem Model. *Ecol. Modell.* 202 (1–2), 68–80. doi: 10.1016/j.ecolmodel.2006.05.038

Itoh, S., and Yasuda, I. (2010). Characteristics of Mesoscale Eddies in the Kuroshio-Oyashio Extension Region Detected From the Distribution of the Sea Surface Height Anomaly. *J. Phys. Oceanogr.* 40 (5), 1018–1034. doi: 10.1175/2009JPO4265.1

Ji, J., Dong, C., Zhang, B., Liu, Y., Zou, B., King, G. P., et al. (2018). Oceanic Eddy Characteristics and Generation Mechanisms in the Kuroshio Extension Region. *J. Geophys. Res. Oceans* 123, 8548–8567. doi: 10.1029/2018JC014196

Kartushinsky, A. V., and Sidorenko, A. Y. (2013). Analysis of the Variability of Temperature Gradient in the Ocean Frontal Zones Based on Satellite Data. *Adv. Space Res.* 52 (8), 1467–1475. doi: 10.1016/j.asr.2013.07.023

Kida, S., Mitsudera, H., Aoki, S., Guo, X., Ito, S. I., Kobashi, F., et al. (2015). Oceanic Fronts and Jets Around Japan: A Review. *J. Oceanogr.* 71, 469–497. doi: 10.1007/978-4-431-56053-1_1

Kitagawa, T., Kimura, S., Nakata, H., and Yamada, H. (2004). Diving Behavior of Immature, Feeding Pacific Bluefin Tuna (Thunnus Thynnus Orientalis) in Relation to Season and Area: The East China Sea and the Kuroshio-Oyashio Transition Region. *Fish. Oceanogr.* 13 (3), 161–180. doi: 10.1111/j.1365-2419.2004.00282.x

Kobashi, F., and Kubokawa, A. (2012). Review on North Pacific Subtropical Countercurrents and Subtropical Fronts: Role of Mode Waters in Ocean Circulation and Climate. *J. Oceanogr.* 68 (1), 21–43. doi: 10.1007/s10872-011-0083-7

Kostianoy, A. G., Ginzburg, A. I., Frankignoulle, M., and Delille, B. (2004). Fronts in the Southern Indian Ocean as Inferred From Satellite Sea Surface Temperature Data. *J. Mar. Syst.* 45 (1–2), 55–73. doi: 10.1016/j.jmarsys.2003.09.004

Kouketsu, S., Kaneko, H., Okunishi, T., Sasaoka, K., Itoh, S., Inoue, R., et al. (2016). Mesoscale Eddy Effects on Temporal Variability of Surface Chlorophyll a in the Kuroshio Extension. *J. Oceanogr.* 72 (3), 439–451. doi: 10.1007/s10872-015-0286-4

Legeckis, R. (1978). A Survey of Worldwide Sea Surface Temperature Fronts Detected by Environmental Satellites. *J. Geophys. Res. Oceans* 83 (C9), 4501–4522. doi: 10.1029/JC083iC09p04501

Lin, P., Chai, F., Xue, H., and Xiu, P. (2014). Modulation of Decadal Oscillation on Surface Chlorophyll in the Kuroshio Extension. *J. Geophys. Res. Oceans* 119, 187–199. doi: 10.1002/2013JC009359

Long, Y., Zhu, X.-H., and Guo, X. (2019). The Oyashio Nutrient Stream and its Nutrient Transport to the Mixed Water Region. *Geophys. Res. Lett.* 46, 1513–1520. doi: 10.1029/2018GL081497

Lorenzzetti, J. A., Stech, J. L., Mello Filho, W. L., and Assireu, A. T. (2009). Satellite Observation of Brazil Current Inshore Thermal Front in the SW South Atlantic: Space/time Variability and Sea Surface Temperatures. *Conti. Shelf Res.* 29 (17), 2061–2068. doi: 10.1016/j.csr.2009.07.011

McClain, C. R., Signorini, S. R., and Christian, J. R. (2004). Subtropical Gyre Variability Observed by Ocean-Color Satellites. *Deep Sea Res. Part II Top. Stud. Oceanogr.* 51 (1–3), 281–301. doi: 10.1016/j.dsr2.2003.08.002

Miller, P. I. (2009). Composite Front Maps for Improved Visibility of Dynamic Sea-Surface Features on Cloudy SeaWiFS and AVHRR Data. *J. Mar. Syst.* 78, 327–336. doi: 10.1016/j.jmarsys.2008.11.019

Miyazawa, Y., Zhang, R., Guo, X., Tamura, H., Ambe, D., Lee, J. S., et al. (2009). Water Mass Variability in the Western North Pacific Detected in a 15-Year Eddy Resolving Ocean Reanalysis. *J. Oceanogr.* 65 (6), 737–756. doi: 10.1007/s10872-009-0063-3

Nagai, T., and Clayton, S. (2017). Nutrient Interleaving Below the Mixed Layer of the Kuroshio Extension Front. *Ocean Dyn.* 67 (8), 1027–1046. doi: 10.1007/s10236-017-1070-3

Nagano, A., Yamashita, Y., Hasegawa, T., Ariyoshi, K., Matsumoto, H., and Shinohara, M. (2019). Characteristics of an Atypical Large–Meander Path of the Kuroshio Current South of Japan Formed in September 2017. *Mar. Geophys. Res.* 40, 525–539. doi: 10.1007/s11001-018-9372-5

NASA (2014). *Goddard Space Flight Center, Ocean Ecology Laboratory, Ocean Biology Processing Group. Moderate-Resolution Imaging Spectroradiometer (MODIS) Aqua 11μm Day/Night Sea Surface Temperature Data* (Greenbelt, MD, USA: NASA OB.DAAC).

Ohshima, K. I., Wakatsuchi, M., and Saitoh, S. I. (2005). Velocity Field of the Oyashio Region Observed With Satellite-Tracked Surface Drifters During 1999–2000. *J. Oceanogr.* 61 (5), 845–855. doi: 10.1007/s10872-006-0004-3

Parfitt, R., Czaja, A., Minobe, S., and Kuwano-Yoshida, A. (2016). The Atmospheric Frontal Response to SST Perturbations in the Gulf Stream Region. *Geophys. Res. Lett.* 43, 2299–2306. doi: 10.1002/2016GL067723

Park, K. A., Ullman, D. S., Kim, K., Chung, J. Y., and Kim, K. R. (2007). Spatial and Temporal Variability of Satellite-Observed Subpolar Front in the East/Japan Sea. *Deep Sea Res. Part I: Oceanogr. Res. Pap.* 54 (4), 453–470. doi: 10.1016/j.dsr.2006.12.010

Qiu, B., and Chen, S. (2010). Eddy-Mean Flow Interaction in the Decadally Modulating Kuroshio Extension System. *Deep Sea Res. Part II Top. Stud. Oceanogr.* 57 (13–14), 1098–1110. doi: 10.1016/j.dsr2.2008.11.036

Qiu, B., Chen, S., Schneider, N., Oka, E., and Sugimoto, S. (2020). On the Reset of the Wind-Forced Decadal Kuroshio Extension Variability in Late 2017. *J. Clim.* 33, 10813–10828. doi: 10.1175/JCLI-D-20-0237.1

Qiu, B., Chen, S., Schneider, N., and Taguchi, B. (2014). A Coupled Decadal Prediction of the Dynamic State of the Kuroshio Extension System. *J. Clim.* 27 (4), 1751–1764. doi: 10.1175/JCLI-D-13-00318.1

Qu, T., Mitsudera, H., and Qiu, B. (2001). A Climatological View of the Kuroshio/Oyashio System East of Japan. *J. Phys. Oceanogr.* 31, 2575–2589. doi: 10.1175/1520-0485(2001)031<2575:ACVOTK>2.0.CO;2

Ribalet, F., Marchetti, A., Hubbard, K., Brown, K., Durkin, C., Morales, R., et al. (2010). Unveiling a Phytoplankton Hotspot at a Narrow Boundary Between Coastal and Offshore Waters. *Proc. Natl. Acad. Sci. U.S.A.* 107, 16571–16576. doi: 10.1073/pnas.1005638107

Seo, Y., Sugimoto, S., and Hanawa, K. (2014). Long-Term Variations of the Kuroshio Extension Path in Winter: Meridional Movement and Path State Change. *J. Clim.* 27, 5929–5940. doi: 10.1175/JCLI-D-13-00641.1

Shan, X., Jing, Z., Gan, B., Wu, L., Chang, P., Ma, X., et al. (2020). Surface Heat Flux Induced by Mesoscale Eddies Cools the Kuroshio-Oyashio Extension Region. *Geophys. Res. Lett.* 47 (1), e2019GL086050. doi: 10.1029/2019GL086050

Shao, M., Ortiz-Suslow, D. G., Haus, B. K., Lund, B., Williams, N. J., Özgökmen, T. M., et al. (2019). The Variability of Winds and Fluxes Observed Near Submesoscale Fronts. *J. Geophys. Res. Oceans* 124 (11), 7756–7780. doi: 10.1029/2019JC015236

Simpson, J. J. (1990). On the Accurate Detection and Enhancement of Oceanic Features Observed in Satellite Data. *Remote Sens. Environ.* 33 (1), 17–33. doi: 10.1016/0034-4257(90)90052-N

Sugimoto, S., Kobayashi, N., and Hanawa, K. (2014). Quasi-Decadal Variation in Intensity of the Western Part of the Winter Subarctic SST Front in the Western North Pacific: The Influence of Kuroshio Extension Path State. *J. Phys. Oceanogr.* 44, 2753–2762. doi: 10.1175/JPO-D-13-0265.1

Sugimoto, S., Qiu, B., and Schneider, N. (2021). Local Atmospheric Response to the Kuroshio Large Meander Path in Summer and Its Remote Influence on the Climate of Japan. *J. Clim.* 34 (9), 3571–3589. doi: 10.1175/JCLI-D-20-0387.1

Sutton, A. J., Wanninkhof, R., Sabine, C. L., Feely, R. A., Cronin, M. F., and Weller, R. A. (2017). Variability and Trends in Surface Seawater Pco2 and CO2 Flux in the Pacific Ocean. *Geophys. Res. Lett.* 44 (11), 5627–5636. doi: 10.1002/2017GL073814

Ullman, D. S., and Cornillon, P. C. (2000). Evaluation of Front Detection Methods for Satellite-Derived SST Data Using *in Situ* Observations. *J. Atmos. Ocean. Technol.* 17 (12), 1667–1675. doi: 10.1175/1520-0426(2000)017<1667:EOFDMF>2.0.CO;2

Vivier, F., Kelly, K., and Thompson, L. (2020). Heat Budget in the Kuroshio Extension Region: 1993–99. *J. Phys. Oceanogr.* 32, 3436–3454. doi: 10.1175/1520-0485(2002)032<3436:HBITKE>2.0.CO;2

Wang, Y., Castelao, R. M., and Yuan, Y. (2015). Seasonal Variability of Alongshore Winds and Sea Surface Temperature Fronts in Eastern Boundary Current Systems. *J. Geophys. Res. Oceans* 120, 2385–2400. doi: 10.1002/2014JC010379

Wang, Y., Liu, J., Liu, H., Lin, P., Yuan, Y., and Chai, F. (2021a). Seasonal and Interannual Variability in the Sea Surface Temperature Front in the Eastern Pacific Ocean. *J. Geophys. Res. Oceans* 126, e2020JC016356. doi: 10.1029/2020JC016356

Wang, Y., Tang, R., Yu, Y., and Ji, F. (2021b). Variability in the Sea Surface Temperature Gradient and Its Impacts on Chlorophyll-A Concentration in the Kuroshio Extension. *Remote Sens.* 13 (5), 888. doi: 10.3390/rs13050888

Wang, Y., Yu, Y., Zhang, Y., and Chai, F. (2020). Distribution and Variability of Sea Surface Temperature Fronts in the South China Sea. *Estuar. Coast. Shelf Sci.* 240, 106793. doi: 10.1016/j.ecss.2020.106793

Watanabe, Y. (2009). Recruitment Variability of Small Pelagic Fish Populations in the Kuroshio-Oyashio Transition Region of the Western North Pacific. *J. North Atl. Fish. Sci.* 41, 197–204. doi: 10.2960/J.v41.m635

Woodson, C., and Litvin, S. (2015). Ocean Fronts Drive Marine Fishery Production and Biogeochemical Cycling. *Proc. Natl. Acad. Sci. U.S.A.* 112 (6), 1710–1715. doi: 10.1073/pnas.1417143112

Wu, B., Lin, X., and Qiu, B. (2019). On the Seasonal Variability of the Oyashio Extension Fronts. *Clim. Dyn.* 53 (11), 7011–7025. doi: 10.1007/s00382-019-04972-1

Wu, B., Lin, X., and Yu, L. (2020). North Pacific Subtropical Mode Water is Controlled by the Atlantic Multidecadal Variability. *Nat. Clim. Change* 10 (3), 238–243. doi: 10.1038/s41558-020-0692-5

Yasuda, I. (2003). Hydrographic Structure and Variability in the Kuroshio-Oyashio Transition Area. *J. Oceanogr.* 59 (4), 389–402. doi: 10.1023/A:1025580313836

Yatsu, A., Chiba, S., Yamanaka, Y., Ito, S., Shimizu, Y., Kaeriyama, M., et al. (2013). Climate Forcing and the Kuroshio/Oyashio Ecosystem. ICES. *J. Mar. Sci.* 70, 922–933. doi: 10.1093/icesjms/fst084

Yoder, J. A., Ackleson, S. G., Barber, R. T., Flament, P., and Balch, W. M. (1994). A Line in the Sea. *Nature* 371, 689–692. doi: 10.1038/371689a0

Yuan, Y., and Castelao, R. M. (2017). Eddy-Induced Sea Surface Temperature Gradients in Eastern Boundary Current Systems. *J. Geophys. Res. Oceans* 122 (6), 4791–4801. doi: 10.1002/2017jc012735

Yuan, X., and Talley, L. D. (1996). The Subarctic Frontal Zone in the North Pacific: Characteristics of Frontal Structure From Climatological Data and Synoptic Surveys. *J. Geophys. Res. Oceans* 101 (C7), 16491–16508. doi: 10.1029/96JC01249

Yu, Y., Wang, Y., Cao, L., and Chai, F. (2020). The Ocean-Atmosphere Interaction Over a Summer Upwelling System in the South China Sea. *J. Mar. Syst.* 208, 103360. doi: 10.1016/j.jmarsys.2020.103360

Yu, Y., Xing, X., Liu, H., Yuan, Y., Wang, Y., and Chai, F. (2019). The Variability of Chlorophyll-a and its Relationship With Dynamic Factors in the Basin of the South China Sea. *J. Mar. Syst.* 200, 103230. doi: 10.1016/j.jmarsys.2019.103230

Conflict of Interest: The authors declare that the research was conducted in the absence of any commercial or financial relationships that could be construed as a potential conflict of interest.

Publisher's Note: All claims expressed in this article are solely those of the authors and do not necessarily represent those of their affiliated organizations, or those of the publisher, the editors and the reviewers. Any product that may be evaluated in this article, or claim that may be made by its manufacturer, is not guaranteed or endorsed by the publisher.

Copyright © 2022 Xi, Wang, Feng, Liu and Guo. This is an open-access article distributed under the terms of the Creative Commons Attribution License (CC BY). The use, distribution or reproduction in other forums is permitted, provided the original author(s) and the copyright owner(s) are credited and that the original publication in this journal is cited, in accordance with accepted academic practice. No use, distribution or reproduction is permitted which does not comply with these terms.

frontiers | Frontiers in Marine Science

ORIGINAL RESEARCH
published: 07 April 2022
doi: 10.3389/fmars.2022.831262

Prediction of Long-Term Beach Profile Evolution Due to Episodic Wave Incidence Under Tidal Environment

Sahong Lee[1], *Changbin Lim*[1] *and Jung-Lyul Lee*[2*]

[1] School of Civil, Architecture and Environmental System Engineering, Sungkyunkwan University, Suwon, South Korea,
[2] Graduate School of Water Resources, Sungkyunkwan University, Suwon, South Korea

Recently, studies have been conducted that long-term changes in shoreline position can be sufficiently interpreted using an ordinary differential equation that includes only erosion and recovery processes. Here, the erosion process term is given as a function of the breaking wave energy, which causes the shoreline to retreat to the ultimate erosion position by the incoming wave energy. The recovery process term is given as a function of the concentration of suspended sediment and allows it to recover to its shoreline position. Therefore, in this study, we propose a numerical technique that simulates long-term changes in the beach profile by extending the ordinary differential equation to be applied to the change in seabed constituting the beach profile by applying the parabolic equation of the equilibrium beach profile of the surf zone. This model also consists of a term that allows the beach profile to converge to the equilibrium beach profile due to the breaking wave energy and another term that allows it to converge back to the linear shoaling profile when the wave is extinguished. Therefore, it is possible to simulate the repeated formation and disappearance of scarp and berm whenever a storm wave passes, and it can also be applied to the morphological change at the beach with a large tidal range. The validity of the proposed methodology was verified by comparing the long-term shoreline observation data of Tairua Beach, New Zealand, where the tidal difference is about 2 m, with the results of the long-term beach section convergence model of this study. In addition, short-term observation data were also compared and analyzed to investigate the ability to simulate morphological changes due to episodic erosion and recovery processes. The results of this study are expected to be applied not only to the beach profile but also to the three-dimensional morphology change of the beach, and it is expected that it will serve as a cornerstone for a more detailed topographic change prediction study due to sea level rise.

Keywords: numerical model, equilibrium beach profile, beach response, beach scale factor, bar migration

OPEN ACCESS

Edited by:
Juan Jose Munoz-Perez, University of Cádiz, Spain

Reviewed by:
Zhaoqing Yang, Pacific Northwest National Laboratory (DOE), United States
Pushpa Dissanayake, University of Kiel, Germany

***Correspondence:**
Jung-Lyul Lee
jllee6359@hanmail.net

Specialty section:
This article was submitted to Coastal Ocean Processes, a section of the journal Frontiers in Marine Science

Received: *08 December 2021*
Accepted: *04 March 2022*
Published: *07 April 2022*

Citation:
Lee S, Lim C and Lee J-L (2022) Prediction of Long-Term Beach Profile Evolution Due to Episodic Wave Incidence Under Tidal Environment. Front. Mar. Sci. 9:831262. doi: 10.3389/fmars.2022.831262

INTRODUCTION

The rise of wave height and sea level due to climate change has increased the need for awareness of the importance of long-term changes in beaches for sustainable coastal conservation and research supporting long-term change prediction. Although the prevalence of predictive models based on morphodynamic modeling is increasing (Pender and Karunarathna, 2013), existing beach profile change models cannot simulate long-term sedimentation. Fang and Ron (2013) and Montaño et al. (2020) highlighted that no individual model is currently capable of simulating beach recovery and erosion processes over a long period. For that reason, it seems to be impossible to simulate long-term beach profile changes, including tidal effects, in the macro-environment.

Long-term morphological changes are a phenomenon that can only be achieved by simulating storm wave erosion and mild wave deposition. In particular, since it is not easy to simulate the sedimentation process, at present only the numerical model of shoreline position change that is less affected by the magnitude of wave energy and can include the sedimentation process is applied only to long-term topographic change simulation. The shoreline position change model, which was first suggested by Wright et al. (1985), is a bulk-type ordinary differential equation (ODE) model that does not allow numerical divergence (Wright et al., 1985; Miller and Dean, 2004; Yates et al., 2009). Recently, Lim et al. (2021) applied the concept of the horizontal behavior of suspended sediment to solidify the topographical and physical basis of this type of shoreline position change model and showed adequate similarity despite a long-term simulation.

The bulk-type model has a term given as the equilibrium erosion width or equilibrium beach profile, which is a target variable (shoreline position or beach profile) that retreats and ultimately converges due to the continuous breaking wave action. Several empirical formulae have been proposed for the study of the shape of the beach profile, starting with the equilibrium beach profile (EBP) suggested by Brunn (1954) and Dean (1977; 1991). Thereafter, several studies on the EBP (Larson, 1991; Bodge, 1992; Komar and McDougal, 1994) have been conducted. It is generally accepted that the empirical formula fits relatively well with the actual beach profile (Wang and Kraus, 2005). These studies established a series of formulae to simulate the configuration of the EBP and used mathematical models to predict beach profile behavior (Thieler et al., 2000). A study on the profile of the offshore region outside the surf zone was also performed. The so-called shoaling profile zone is considered a static region balanced by the continuous wave incidence (Bernabeu et al., 2003). There is no definite curve equation for this region; however, it can be considered a parabolic equation similar to the wave profile region (Bernabeu et al., 2003; Requejo et al., 2006).

In addition to these studies on the equilibrium beach profile since the first attempt by Wang et al. (1975), several numerical model development studies to predict the change in the beach profile for 45 years have been made. These studies have led to the development of a three-dimensional model that includes almost all physical phenomena, such as waves, currents, and topography changes. For example, Margvelashvili et al. (2008) developed one-dimensional vertical and three-dimensional fine-resolution numerical models of sediment transport. Nam et al. (2009) proposed a two-dimensional numerical model of nearshore waves, currents, and sediment transport. Hanson et al. (2010) presented a mathematical approach and numerical model that simulates beach and dune changes in response to cross-shore processes of dune growth by wind, dune erosion by storms, and gradients in longshore sand transport that will alter shoreline position. It is also useful to refer to Callaghan et al. (2006), who reviewed numerical models of sediment conservation. However, although existing models faithfully include all physical processes, they can only predict short-term erosion, and few models can simulate beach recovery and sedimentation processes over a long period (Swart, 1974; Wang et al., 1975; Larson and Kraus, 1989; Larson et al., 1999; Lesser et al., 2004; Roelvink et al., 2009; Fang and Ron, 2013; Deltares, 2018).

Although the existing beach profile change model has the advantage of including various physical phenomena of sediment transport, it also has drastic limitations. First, unlike the observation trend in the lab, where the beach section converges at the certain time point, it is continuously eroded. Second, when the waves become calm, it cannot be seen that it recovers to the original beach before the storm wave, as seen one or two months later with the development of berms in the natural beach. A method to solve this problem is to include a physical process in which the suspended sand particles are restored to their original position according to the horizontal movement of the shoreward. In this study, we propose a model that converges to the storm beach when the waves are high and converges to the normal beach when the waves are calm again by determining the EBP to converge introducing the concept of wave phase potential.

Figure 1 summarizes the contents of this study and explains the components and process of the study: The prediction of long-term beach profile evolution is derived based on the shoreline response model (SLRM), which simulates the temporal change in shoreline position as shown in the research process. Using the equilibrium beach profile, the governing equation of the beach profile convergence model (BPCM) with water depth as a variable was derived, and a numerical model was developed in which the target beach profile to converge by applying the wave phase potential was determined so that the water depth gradually converges to it. The long-term simulation validity of the model was verified using the wave and shoreline observation data taken at Tairua Beach in New Zealand by Montaño et al. (2020) to the BPCM of this study. The validity of whether detailed beach profile changes, such as bar migration, can be simulated was reviewed through a comparison with the short-term observed beach profile.

MODEL DESCRIPTION

Governing Equation of the Shoreline Response Model (SLRM)

The generation and deposition of suspended sediment is considered horizontal behavior in the direction of the wave force along the cross-shore rather than vertical behavior in the

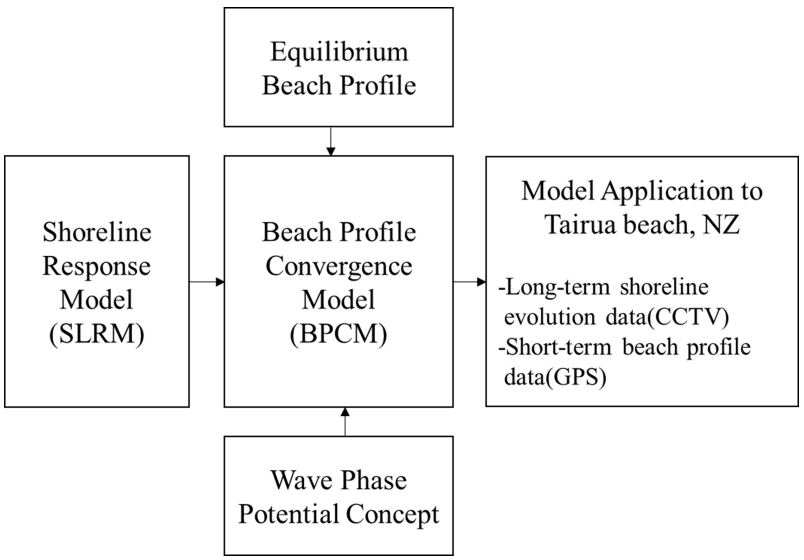

FIGURE 1 | Research processes.

direction of gravity. Therefore, the temporal change in the shoreline is expressed by Eq. (1) (Lim et al., 2021):

$$D_s \frac{dy}{dt} = q_D^c - q_E^c \tag{1}$$

where D_s is the vertical height limit at which the suspended sediment occurs, defined as the sum of the berm height and closure depth; q_E^c is the erosion rate of the beach (per unit length of the shore) caused by suspension from the original location of the sediment, and q_D^c is the rate of sedimentation (per unit length of the coast) that occurs by returning to the original position. When the wave height is reduced, the process of returning to the original shoreline is simulated as a sedimentation phenomenon in which the sand returns to its original position and is superior to that of erosion.

As shown in Eq. (2), the equation governing the change in shoreline position is derived from the horizontal behavior characteristics of the suspension and recovery of sediment proposed by Lim et al. (2021) as follows:

$$\frac{dy}{dt} = k_r(y_{eq} - y) \tag{2}$$

where k_r is the beach recovery factor, which is the rate at which the suspended sand returns to the shore, which can vary depending on the characteristics of the sand.

The shoreline position reaching equilibrium y_{eq}in an environment where a constant wave is continuously incident is expressed in terms of wave energy at the starting point of wave breaking E_b and beach response factor a_r as shown in Eq. (3) below.

$$y_{eq} = \frac{q_E^c}{k_r D_s} = \frac{mE_b}{k_r \rho_s (1-p)} = \frac{E_b}{a_r} \tag{3}$$

In this study, a_r is a beach response factor obtained from a field experiment by Yates et al. (2009) and is regarded as a value determined according to beach characteristics regardless of wave energy.

The physical basis of the ODE equation was first empirically proposed by Miller and Dean (2004) and established by Lim et al. (2021). Kim et al. (2021) and Lim et al. (2021) conducted studies on the estimation of the beach response factor a_r. Lim et al. (2021) obtained their results by applying the Tairua beach wave and shoreline observation data from Montaño et al. (2020) to Eq. (6). Compared to the blind test result found by Montaño et al. (2020), the correlation coefficient was 0.74, which was satisfactory even though it was compared with the long-term observation data for approximately 11 years.

Governing Equation of the Beach Profile Convergence Model (BPCM)

The EBP formula (Eq. 4) presented by Bruun (1954) and Dean (1977) was used to extend the ODE equation (Eq. 2), which simulates the shoreline position change with beach profile change.

$$h = Ay^{2/3} \tag{4}$$

where h is the depth of the water, and A is the beach scale factor, which is a coefficient dependent on the median grain size (D_{50}), which can be calculated using Dean's table (Dean, 1987). Furthermore, y is the seaward distance from the shoreline. If differentiation is considered in the EBP equation, (Eq. 4), the following relational equation (Eq. 5) is obtained:

$$dh = \frac{2}{3} Ay^{-1/3} dy \tag{5}$$

Applying Eq. (4), we get

$$dh = \frac{2}{3} A^{3/2} h^{-1/2} dy \tag{6}$$

If the EPB equation (Eq. 4) is applied to the right side of the SLRM governing equation (Eq. 2) and Eq. (6) is applied to the left side, the following equation is obtained:

$$\frac{3h^{1/2}}{2}\frac{dh}{dt} = q_r(h_{eq}^{3/2} - h^{3/2}) \tag{7}$$

where q_r is the convergence factor that allows the water depth to converge to the equilibrium water depth. The same value as the beach recovery factor k_r, which was applied to the shoreline position equation (Eq. 2), is applied. However, this result is obtained under the assumption that Eq. (4) holds the relationship between the distance y from the shoreline and the water depth h.

Eq. (7) is rearranged by $dh^m = mh^{m-1}\,dh$ to the 3/2 power of h as shown in Eq. (8).

$$\frac{dh^{3/2}}{dt} = q_r(h_{eq}^{3/2} - h^{3/2}) \tag{8}$$

This equation becomes a governing equation that simulates temporal changes in the beach profile.

The formula for the equilibrium beach profile given in Eq. (4) corresponds to a shallow water region. However, for storm beaches that follow Eq. (4) formed by storm waves, when the wave period is shortened, the shallow water region to which the equilibrium beach cross-section is applied becomes narrow. And as formed on the offshore, the straight beach profile converges to the normal beach as the slope gradually becomes steeper (**Figure 2**).

To realize this phenomenon, the concept of wave phase potential is introduced and briefly summarized as follows. The wave phase potential can be expressed as the integral of the wave phase, which decreases as the wave advances from its point of origin. This mechanism is similar to the Earth's gravitational field, the potential of which decreases from the distant atmosphere towards the center of the Earth (the center of gravity). Therefore, the wave phase potential for waves entering the shore is expressed by wave number k as follows:

$$\psi_p = \int k(h)dy \tag{9}$$

Here, the wave number is defined by the angular frequency σ, and phase celerity C as follows:

$$k(h) = \sigma / C \tag{10}$$

By applying the wave number of shallow water to Eq. (10), the following equilibrium water depth is obtained in terms of the wave phase potential:

$$\psi_p = \frac{3\sigma}{2\sqrt{g}A^{3/2}} \text{ and } h_{eq} = \frac{2\sqrt{g}A^{3/2}}{3\sigma}\psi_p \tag{11}$$

where the wave phase potential is defined as seaward from the shoreline (as wave phase decreases towards shoreline). Therefore, the wave phase potential ψ_p has a linear proportional relationship with the equilibrium depth h_{eq} and thus providing information on important physical properties that enable the simulation of morphological evolution such as scarp or berm converging to the equilibrium state by estimating the wave phase potential.

Numerical Scheme and Performance Test

As shown in **Figure 3**, the water depth h converges to the equilibrium water depth h_e. Thereafter, the governing equation (Eq. 12) is numerically analyzed by a simple finite difference with respect to time at each y point where the grid is located, as shown in Eq. (12).

$$\dot{h}_i^{n+1} = \dot{h}_i^n + dtq_r(\dot{h}_{eq,i} - \dot{h}_i^n) \tag{12}$$

where $\dot{h}$ is $h^{3/2}$. Through this, it is possible to simulate the convergence from the initial water depth to the equilibrium depth based on the temporal change in the water depth using wave information.

The most difficult and important part of the model for changing the beach profile is to simulate the retreat or advance of the shoreline. In this study, when the shoreline retreat caused by erosion was steeper than the critical slope 1:m_{cr}, the berm collapsed, and a new calculation grid was created. The numerical scheme is as follows:

$$h_l^{n+1} = h_w^n - \frac{\Delta y}{m_{cr}} \text{ for } m = \frac{\Delta y}{h_w^n - h_l^n} < m_{cr} \tag{13}$$

where Δy is the grid size, and h_l and h_w are the water depths on the land side and the water side with the shoreline in between, respectively. When the water depth increased and the shoreline moved seaward, the berm height formula outlined by Sunamura (1975) was applied to ensure that the berm height rose only to the level given as a function of the breaking wave height H_b.

$$h_B = 1.1H_b \tag{14}$$

Figures 4 shows the simulated results obtained by applying the storm wave scenario function suggested by Kim et al. (2021). To extract the high wave scenario, Kim et al. (2021) non-dimensionalized the wave height data before and after the occurrence of the maximum wave height of the NOAA wave data across 40 years (1979–2018) by the peak wave height and period value. A storm wave scenario function (SWSF) that fits well by taking dimensionless values with respect to the peak wave height was proposed. The SWSF for the peak wave height (H_p) of 4.5 m and peak period (T_p) of 11.1 sec were applied following the shoreline response (**Figure 4A**) and the corresponding beach profile change result (**Figure 4B**) according to the high wave incidence. From the simulation results, it can be confirmed that the occurrence of scarp due to high waves and the formation of berms after the extinction of high waves can be reproduced.

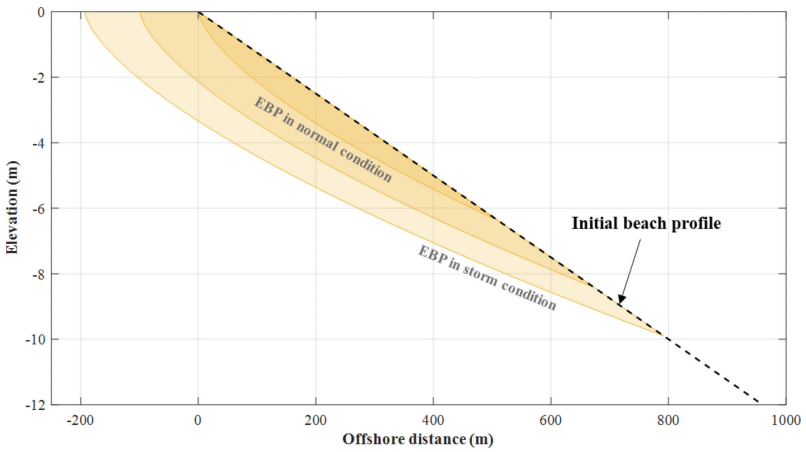

FIGURE 2 | Diagram of EBP change according to wave condition.

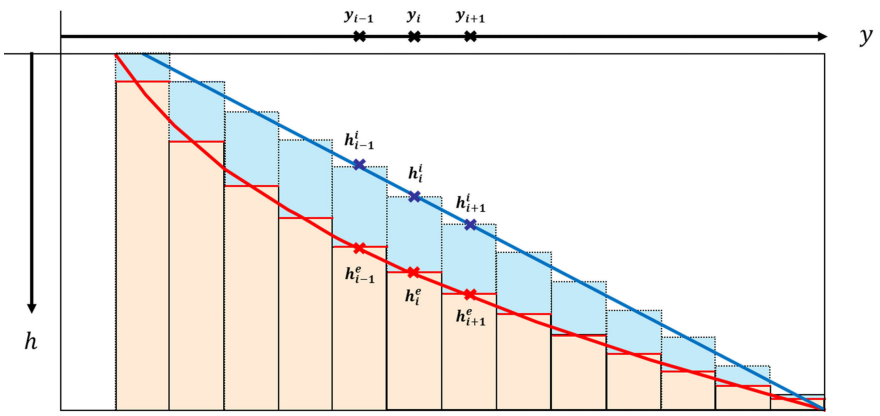

FIGURE 3 | Diagram of numerical calculation system in BPCM.

VERIFICATION OF LONG-TERM PERFORMANCE OF THE MODEL

Study Site for Model Validation

To investigate the practical field applicability, the results of this model were compared with long-term shoreline evolution data (Montaño et al., 2020) and short-term beach profile evolution data (van Maanen et al., 2008) obtained from Tairua Beach, New Zealand (**Supplementary Figure 1**). The data were extracted from video images acquired using a CCTV camera system installed on Tairua Beach.

Tairua Beach is located on the eastern coast of the northern island of New Zealand (36°5945″S, 17.5°5140″E) (**Supplementary Figure 1A**). It has a length of 1.2 km, and topographically, it is a relatively stable pocket beach that sits between Pumpkin Hill to the north and Paku Hill to the south (**Supplementary Figure 1B**). According to Wright and Short (1984), Tairua Beach is classified as an intermediate beach (Bogle et al., 1999) and frequently exhibits a transverse-bar-rip morphology.

Incident Wave Data

The long-term wave input data of this model were provided by MetOcean (Montaño et al., 2020), and were extracted from wave hindcast data between January 1, 1979, and December 31, 2016, at a depth of 10 m using a hydrodynamic model (SWAN), as shown in **Supplementary Figure 1B**. Further, **Supplementary Figure 2** shows the time series change of wave information (wave height, period, wave direction) provided from "Shoreshop" (https://coastalhub.science/data).

Long-Term Shoreline Evolution Data

The Waikato Regional Council and the National Institute of Water and Atmospheric Research (NIWA) produced shoreline evolution data for the Tairua beach through image processing

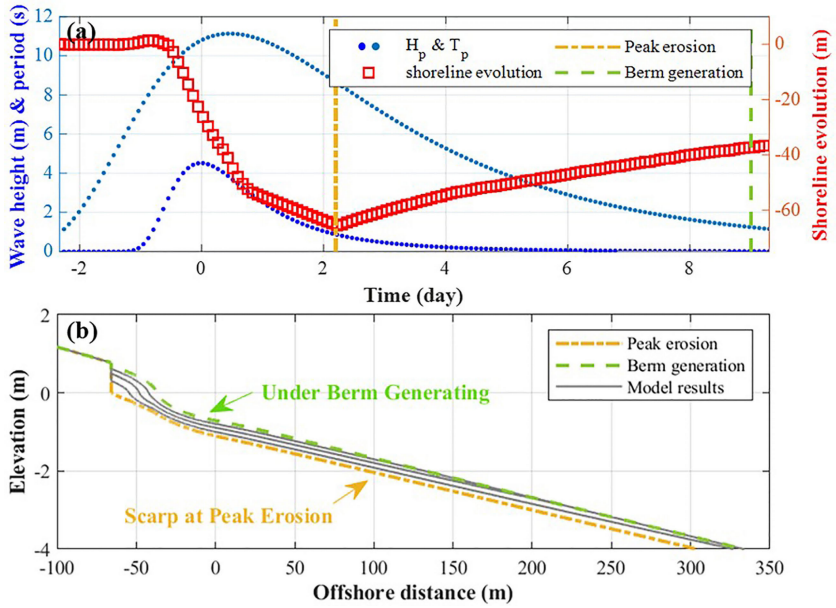

FIGURE 4 | **(A)** Time evolution of SWSF (blue dots) and shoreline retreat width (red square) for H_p = 4.5 m and T_p = 11.1sec. **(B)** Beach profile change results applying SWSF (peak erosion and berm generation).

from 1999 to 2017 (Montaño et al., 2020). Shoreline data were extracted using a camera system installed on a hill (at an elevation of approximately 60 m) at the north end of the beach, and values were produced once a day from time-averaged images for 10 min. Although Tairua Beach is a microtidal environment (tidal range is between 1.2 and 2 m), the images taken at the time when the tide levels are 0.45 and 0.55 m were selected to exclude the effect of tidal waves as much as possible. **Figure 5** shows the tidal fluctuations and historical tide data (only astronomical tide) of Tairua beach provided by "Shoreshop" (https://coastalhub.science/data). To compare the shoreline position results of the SLRM, the values between 0.45 m and 0.55 m which correspond to the shoreline are indicated by a red line in **Figure 5**.

Figure 6 shows the temporal changes in shoreline evolution at the time of comparison. The validity of the model was verified by comparing it with the numerical results of the BPCM proposed in this study.

Determination of Input Data

It has been reported that the median grain size of the sand composing Tairua beach is between 0.3–0.6 mm, whereas the low tidal terrace (LTT) and upper beach face (UBF) are 0.02 mm and 0.2 mm, respectively (van Maanen et al., 2008; Blossier et al., 2016; Blossier et al., 2017; Montaño et al., 2020 and Smith and Bryan, 2007). However, the area with a median particle diameter of 0.3–0.6 mm is considered the upper beach face because of the relatively coarse median grain size. The point where the shoreline position data obtained through the shoreline image was extracted was presumed to be the LTT, where the particle size was finer.

Supplementary Figure 3 shows the results of the equilibrium beach profile plotted on the beach profile data provided by "Shoreshop" (https://coastalhub.science/data) and shows the validity of the beach scale factor. Beach profile data were observed at four baselines (P1–P4) on March 15, 2001. By taking the average of the beach profile data, an EBP (h_{eq}) that best fits the beach scale factor of 0.094 $m^{1/3}$ was obtained, as

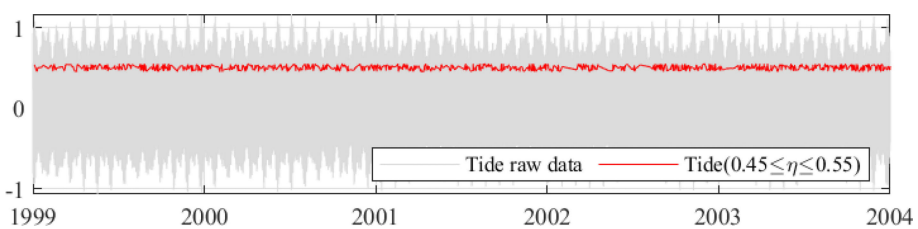

FIGURE 5 | Tide raw data (gray line) and tide data at the time of shoreline observation data (red line).

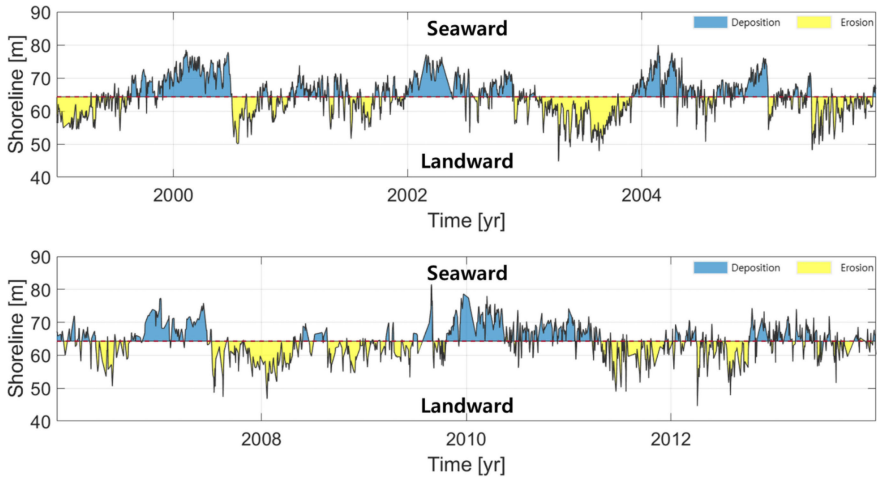

FIGURE 6 | Temporal series of shoreline change on Tairua Beach, New Zealand (Montaño et al., 2020).

shown in **Figure 7**. Beach scale factor A of 0.094 $m^{1/3}$ was applied to the LTT, which can represent the tidal environment, the beach scale factor A of 0.094 $m^{1/3}$ was applied. This corresponds to median grain size (D_{50}) of 0.18 mm.

Normal waves generally produce planar beach profiles. When high waves flow onto a planar beach, it naturally converges towards an equilibrium beach profile. The initial slope is determined using Eq. (14), which was proposed by Suh and Dalrymple (1988).

$$m_i = \frac{5}{6}\frac{\sqrt{h_b}}{A^{3/2}} \tag{15}$$

where h_b is the breaking depth. The initial slope m_i is set to 41, assuming h_b = 2 m in consideration of the tidal range.

This BPCM can reproduce scarp and berm formation, for which the foreshore slope must be set. Kim et al. (2014) proposed an empirical formula for the equilibrium foreshore slope as a function of the wave period, and the median grain size as:

$$m_f = CT^m D_{50}^n \tag{16}$$

Furthermore, by applying experimental data performed on three indoor wave flumes, similar to Watanabe et al. (1980); Kajima et al. (1982), and Wise et al. (1996), the three parameters C, m, and n in Eq. (16) were determined to be 3.012, 0.416, and 0.122, respectively. Therefore, the foreshore slope (m_f) can be conveniently estimated using only the information of the wave period and the sand median grain size (D_{50}) in the foreshore as follows:

$$m_f = 3.012\frac{T^{0.416}}{D_{50}^{0.122}} \tag{17}$$

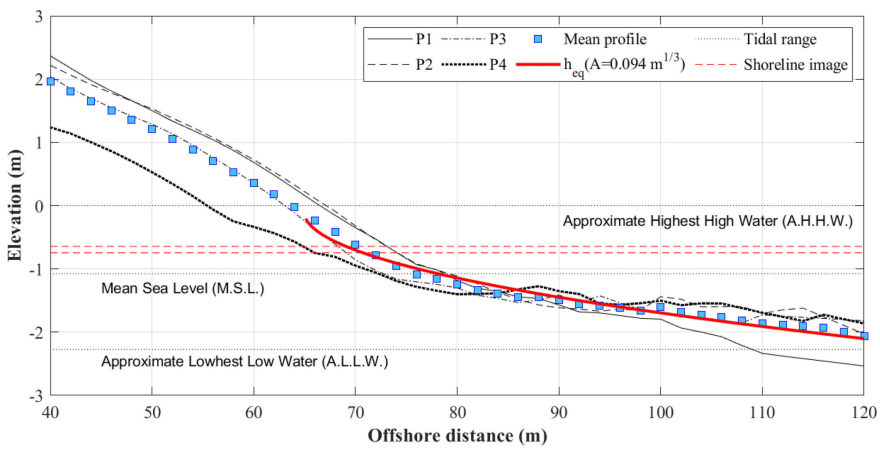

FIGURE 7 | Equilibrium beach profile (red line) for estimating the beach scale factor.

The convergence factor q_r given in Eq. (12) is estimated using Eq. (18), which was proposed by Lim et al. (2021), to estimate the beach recovery factor using the beach scale factor.

$$q_r = \frac{2.3A^{3/2}}{(1 + 14A^{3/2})} \tag{18}$$

The convergence factor q_r = 0.047/day was estimated from a beach scale factor (A) of 0.094 $m^{1/3}$. However, this is a calculation formula obtained for the eastern coast of Korea (tidal range <30 cm), which is a microtidal environment with little effect from tides; therefore, there may be errors in the tidal environment. **Table 1** summarizes the input data used to simulate long-term shoreline response.

Comparison With Shoreline Position Data Extracted From CCTV

To compare the numerical results with the observed data, the BPCM was performed for six years from 1999 to 2004, and the effect of changes in the beach scale factor A, on the numerical results was investigated. **Figure 8** shows a comparison with the observed results for four different A values of 0.063 $m^{1/3}$, 0.080 $m^{1/3}$, 0.094 $m^{1/3}$, and 0.106 $m^{1/3}$; suggesting that the numerical results change depending on the factor. The model is divided into three time periods (1999–2000, 2001–2002, and 2003–2004) with 2-year intervals. It can be confirmed that as the beach scale factor decreases, the range of shoreline fluctuation becomes more severe (**Figure 8**).

The only factor that affects the numerical values is the beach scale factor (A). The correlation coefficient (R_{xy}), root mean square error (RMSE), and slope θ of the fitting line were used as evaluation indicators to determine the level of similarity between the observed value and the numerical calculation value. **Figure 9** shows the correlation distribution between the results of the shoreline position and the observed data according to four different beach scale factors and the fitting curves between them. The higher the correlation coefficient (R_{xy}), the lower the RMSE and the relative error; the closer the fitting curve slope is to 45°, the greater the similarity.

The results suggest that at the smallest RMSE and relative error of approximately 3.7 m and 2.6 m, respectively, the beach scale factor is 0.094 $m^{1/3}$, whereas the beach scale factor showing the closest fitting line slope to 45° is 0.063 $m^{1/3}$. And as the beach scale factor increased, the correlation also tended to increase, with the largest value at 0.063 $m^{1/3}$. **Figure 10** compares the results observed alone for the beach scale factor of 0.094 $m^{1/3}$ with the numerical results (the smallest RMSE and relative error case).

DISCUSSION

Bar Migration

Short-term beach profile data observed by van Maanen et al. (2008) were used to investigate the validity of the numerical model results for morphological changes along the beach cross-section from March 13 to 16, 2001. The measured bed elevation profiles show that the rate of onshore migration of the bar crest averaged 3.5 m/day. During the experiment, a beach profile was repeatedly measured up to a depth of 7 m below the mean sea level using an instrumented sea sled (**Supplementary Figure 4A, B**).

A pressure sensor deployed approximately 900 m offshore at a water depth of 10 m provided the offshore wave data necessary to force the model. The sensor measured the water pressure every 4 h for a 1 h period at a sampling frequency of 2 Hz. **Supplementary Figure 5** shows the values of the root-mean-square wave height H_{rms} and zero-crossing wave period T_{m02}, which were only available every 4 h (**Supplementary Figures 5A, B**). Tidal elevation data were also recorded at a water depth of 10 m and were available every 30 min (**Supplementary Figures 5C**). The H_{rms} increased slowly from approximately 4.3 m to 0.65 m during observation, and T_{m02} decreased from approximately 10 sec to 7 sec. The tide is a semidiurnal tide with a range of approximately 1.5 m. Simultaneously the video images taken at Tairua Beach showed waves breaking on the bar to be limited to low-tide conditions. The field site was monitored by a video camera mounted at the south end of the beach (70.5 m above the chart datum). The camera provided a snapshot and a 10-min time-exposure image every daylight hour (van Maanen et al., 2008).

Convergent Curves for Scarp and Bar Formation

The beach profile data observed by van Maanen et al. (2008) show a UBF zone and an LTT zone, as shown in **Figure 11**, similar to the beach profile in any other tidal environment. The growth of the bar in **Supplementary Figure 5** shows that as the waves become relatively calm after the storm event, coarse sands suspended from the UBF and moving seaward were deposited in the LTT, forming a bar, and growing toward the UBF. The beach scale factors of the beach profile that dominate UBF and LTT were evaluated to be 0.13 $m^{1/3}$ and 0.094 $m^{1/3}$, respectively (**Supplementary Figure 5**). These scale factors correspond to median particle diameters (D_{50}) of 0.32 mm and 0.18 mm, respectively, in the table presented by Dean (1977). Based on the results, although there is a tidal range, the

TABLE 1 | Input conditions for prediction result of shoreline evolution.

Factor	Unit	Value
Median grain size, D_{50}	*mm*	0.18
Beach scale factor, A	$m^{1/3}$	0.094
Initial slope, m_i	1: m_i	37
Beach face slope, m_f	1: m_f	7.94
Convergence factor, q_r	1/day	0.047

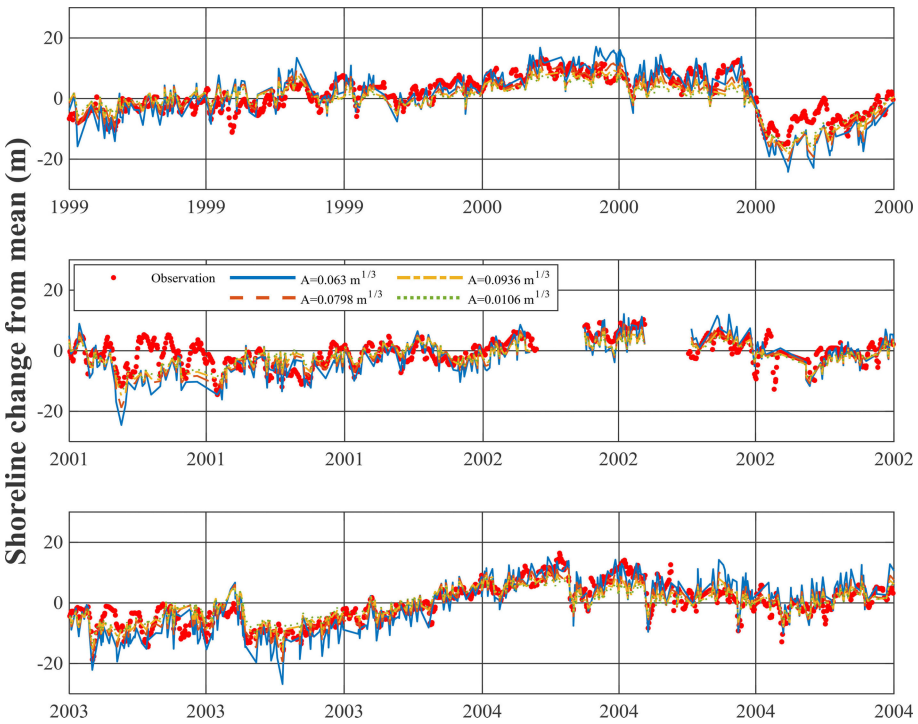

FIGURE 8 | Model outputs compared to observations (red dot) for 4 different values of *A*.

equilibrium beach profile can be applied from the approximate highest high water (A.H.H.W.). In addition, it also shows that the beach scale factor still follows the table of Dean (1977). This result is also applied to the west coast of Korea, where the tidal range is 5–10 m.

The bar that grows from LTT to UBF is similar to the process of developing the berm, which is formed by re-accumulating the suspended sand on the foreshore as the waves become calm, in contrast to the bar growing at the breaking point under the influence of the undertow in a no-tide environment. Therefore, the beach scale factor of the beach profile that dominates the shape of the bar follows 0.13 $m^{1/3}$ corresponding to the UBF value rather than the beach scale factor A of the LTT, as shown in **Figure 11**.

Among the major local tidal constituents, the principal lunar semi-diurnal tide (M_2) and the principal solar semi-diurnal tide (S_2) are factors that affect 99% of tides (Defant, 1961; MacMillan, 1966; Neumann and Pierson, 1966). Therefore, tide fluctuations can be expressed as M_2 and S_2 constituents (Hardisty, 2007). An M_2 of 1.9 m and S_2 of 0.4 m were reported at Tairua Beach (Green, 1994; Zhi, 2014).

Numerical Results

Using the BPCM, it was simulated that a steep slope UBF is generated while converging to an equilibrium beach profile under storm duration from an initial slope of 1:41, and a bar is formed similar to the process in which a berm is formed toward the corresponding EBF as the wave condition becomes milder. **Table 2** summarizes the input data required for BPCM simulation.

Figure 12A shows the BPCM results assuming that the storm and normal wave conditions in **Table 2** are continuously applied. It shows the model result in which a double slope is formed under the storm wave condition before the bar is created. The double slopes of the UBF and LTT were reproduced by varying the beach scale factors.

Owing to the storm wave incidence, the intersection where the double slope appears is formed at a lower level than the MSL. However, the reproduction of the longshore bar formed at the breaking point of the storm beach under a storm wave cannot be reproduced in the BPCM model. However, it is difficult to observe this in a tidal environment. **Figure 12A** also shows the model results at the observation starting on March 13, as an environment was created in which the sands escaping from the UBF were deposited while the milder wave condition continued. However, the model result shows a berm formation rather than a bar shape, possibly due to excessive deposition.

In Eq. 12, $h^{3/2}$ was taken for $\dot{h}$; however, the deposition amount can be adjusted by taking the nth power, which is a different value from the $(3/2)^{th}$ power, and satisfactory results were obtained when n=5. **Figure 12B** shows the model results simulated with the 5th power, showing results similar to the bar shape at the time of the observation starting on March 13. It was found that the bar shape measured on Mar 13th was simulated relatively well by applying a beach scale factor of 0.13 $m^{1/3}$ on the

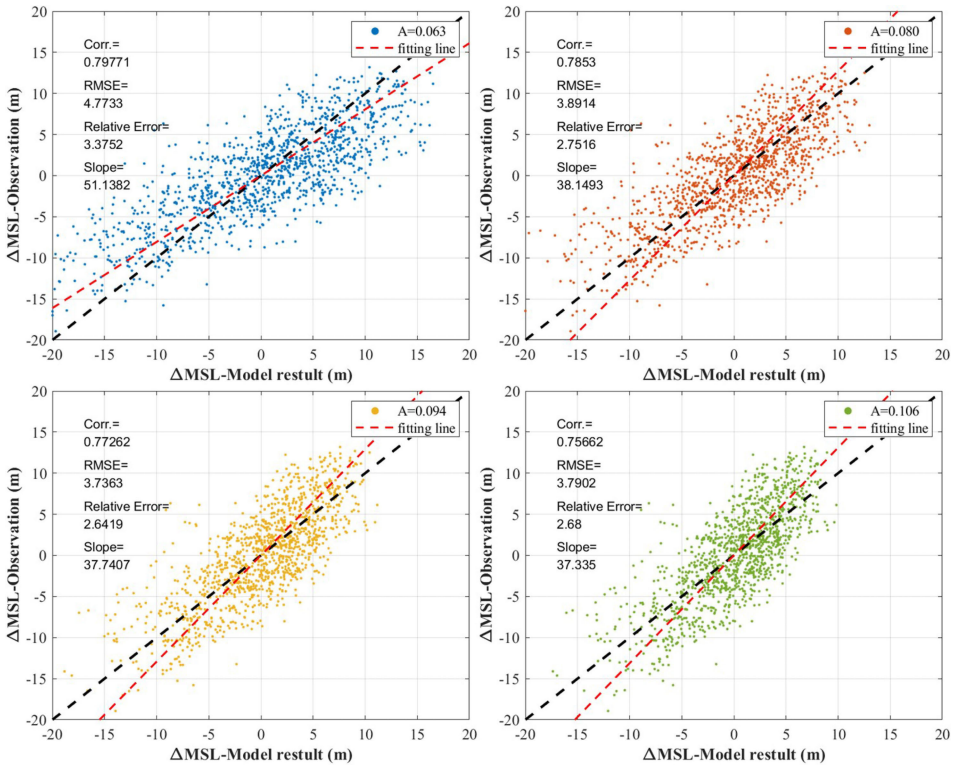

FIGURE 9 | Concordance analysis for 4 different values of *A*.

LTT zone. **Figure 12C** shows the shape of the bar that varies according to the value of *n*. As *n* increased, the dominant depth zone for generating the bars was limited.

The reproducibility of this water depth change model was verified using data observed from March 13 to 16, 2001 at Tairua Beach, whereas the initial depth was obtained from a beach profile observed on March 13, 2001. **Figure 13** shows a comparison of the numerical results with the observed beach profiles. The numerical model simulates bar migration shoreward over time. The front side of the bar moved forward to the shore; however, the speed was underestimated differently from the observed results. In addition, the seaward berm formation on the UBF appears to be well reproduced. The model results were obtained using the 5th power in Eq. (12).

CONCLUSIONS

A model has been established that can simulate changes in the beach profile over several decades with time steps from several seconds to several hours, regardless of the time interval of wave information. This provides a means to predict the long-term changes in the beach profile if there is a predicted scenario of the model input data for the rise in wave height or sea level due to climate change.

This study applied this model, with results showing a correlation of 77% and an RMSE of 3.7 m when comparing the observed data of shoreline position at Tairua Beach in New Zealand, which had a tidal range of 2–3 m, with the model results proposed in this study. Compared to the shoreline response model of Lim et al. (2021), which ignores the influence of the berm and tides, the present model requires a slightly longer computing time and shows higher reproducibility of model results.

The model presented in this study is based on the shoreline position response model of the ODE governing equation, which converges to the equilibrium erosion width, which is the maximum erosion width ideally formed by the continuous incidence of the same wave energy as the shoreline position as a variable. However, in contrast to the ODE governing equation, the governing equation of the model presented in this study uses water depth as a variable and converges to the equilibrium beach profile set in the surf zone according to the breaking wave height. This idea is consistent with the fact that the beach response coefficient a_r, as suggested by Yates et al. (2009), can be derived from the equilibrium beach profile formula, as revealed by Kim et al. (2021) and Lim et al. (2021).

The unique beach convergence coefficient (q_r) in BPCM is related to the beach recovery coefficient (k_r), one of the two coefficients in the shoreline response model, and is a constant that can be extracted from the sand grain size. However, it is

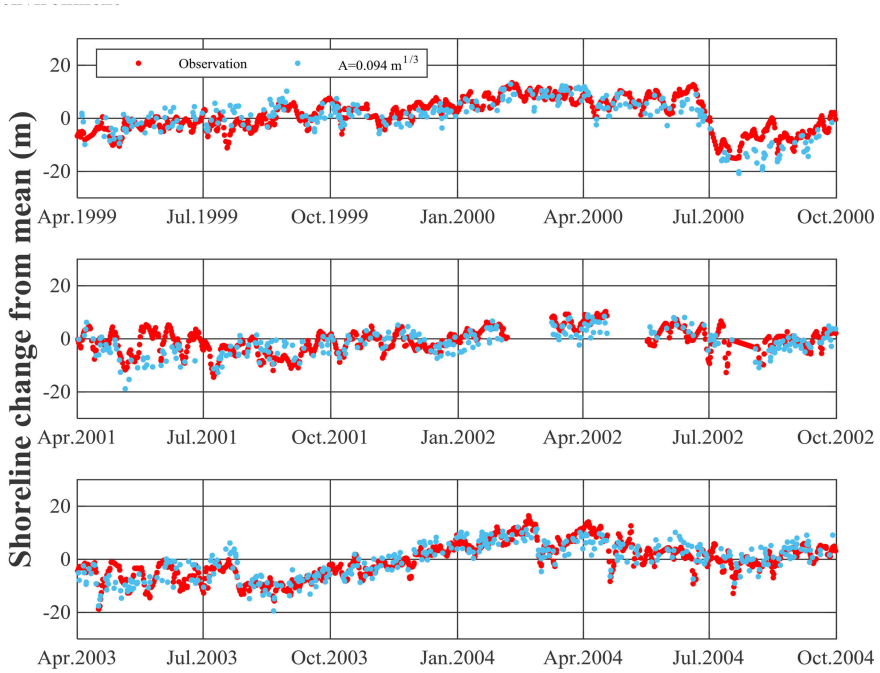

FIGURE 10 | Model outputs (blue dot) compared to observations (red dot).

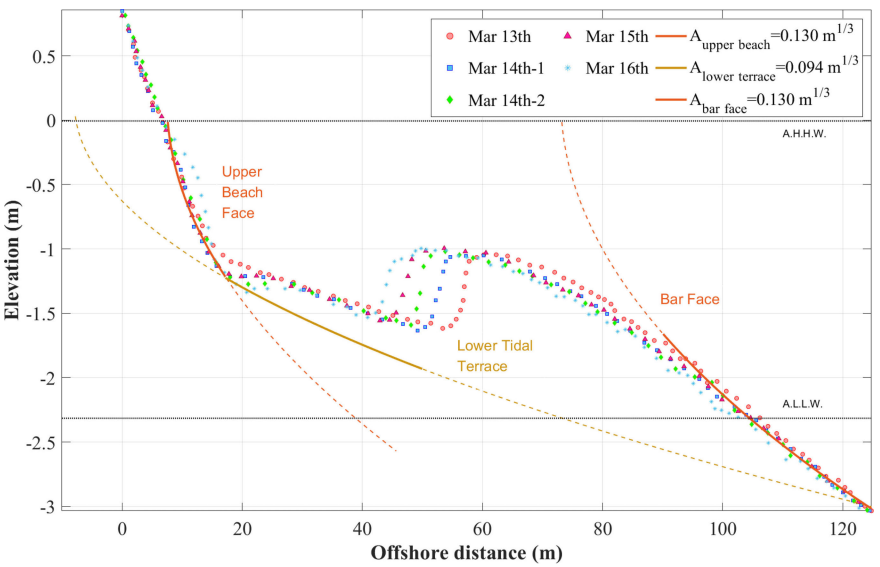

FIGURE 11 | Equilibrium beach profile for estimating the beach scale factor.

assumed that the same value is applied only within the surf zone and decreases with water depth in the offshore area outside the breaking zone. The beach recovery factor is a constant whose unit is the reciprocal of time-related to the property of the suspended sediment to return to its original location. The role of the other beach response coefficients is replaced by allowing the water depth to converge to an equilibrium beach profile in the surf zone.

Satisfactory results were obtained by comparing shoreline observation data at Tairua Beach, New Zealand, which has a micro-tidal range, with the long-term shoreline response model of this study. In addition, we comparatively analyzed short-term

TABLE 2 | Input conditions for prediction result of beach profile change.

Factor		Unit	Value
Beach scale factor, A	UBF	$m^{1/3}$	0.130
	LTT		0.094
Initial slope, m_i	UBF&LTT	1: m_i	41.0
Convergence factor, q_r	UBF	day^{-1}	0.065
	LTT		0.047
Mean significant wave height	Under Storm	m	1.0
	After storm		0.5
Mean wave period	Under Storm	sec	12.0
	After storm		8.0
Tidal ranges	M_2	m	1.9
	S_2		0.4

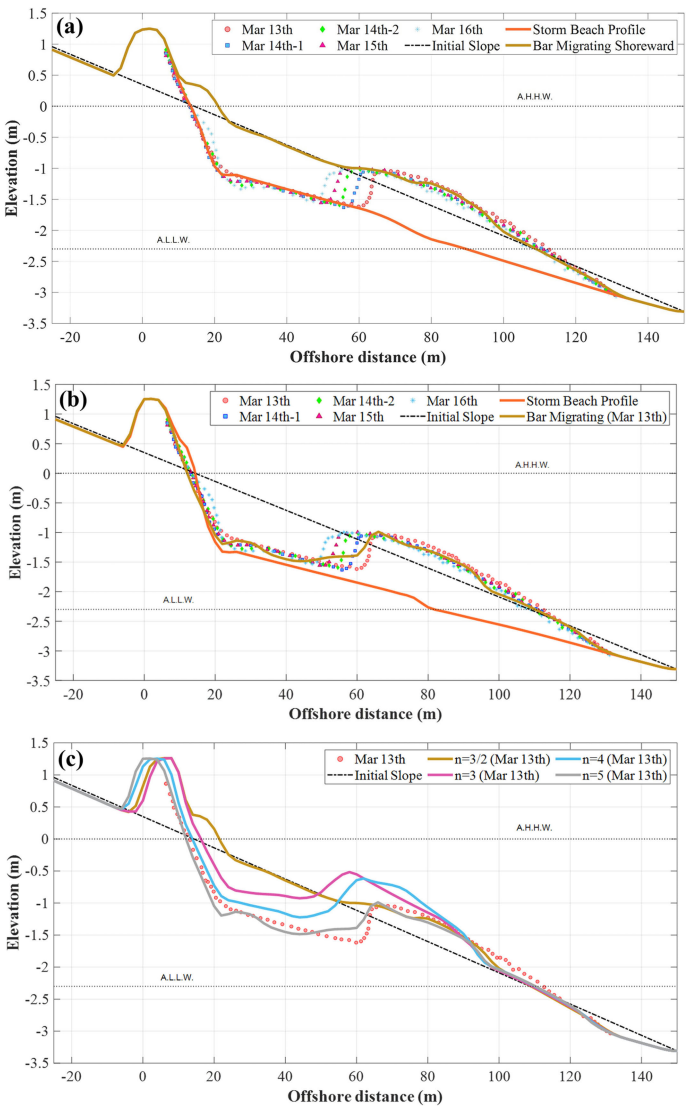

FIGURE 12 | **(A)** Model results of scarp and bar formation from initial slope, **(B)** model results simulated with 5th power in Eq. (12) and **(C)** variation of bar shape according to n value.

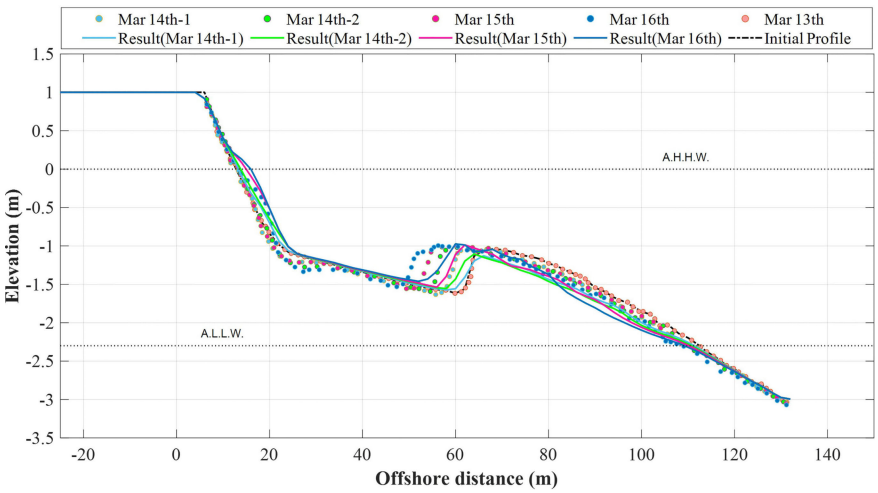

FIGURE 13 | Observed data (symbols) and model (solid line) of beach profile versus cross-shore distance.

observational data to examine our ability to simulate changes in beach profiles more closely. In the tidal environment, it was confirmed that a double slope was formed under the storm wave condition before the bar was created, and the reinforcing bar migrated by the recovery process of sediments suspended from the UBF as the wave height became mild.

DATA AVAILABILITY STATEMENT

Publicly available datasets were analyzed in this study. This data can be found here: https://coastalhub.science/data.

AUTHOR CONTRIBUTIONS

SL: conceptualization, acquisition of data, visualization, and writing – original draft and editing. CL: acquisition of data, visualization, and writing – editing. J-LL: conceptualization, supervision, validation, and writing – original draft and review. All authors contributed to the article and approved the submitted version.

FUNDING

This research was part of the "Practical Technologies for Coastal Erosion Control and Countermeasure" project supported by the Ministry of Oceans and Fisheries, Korea (Grant No. 20180404).

SUPPLEMENTARY MATERIAL

The Supplementary Material for this article can be found online at: https://www.frontiersin.org/articles/10.3389/fmars.2022.831262/full#supplementary-material

Supplementary Figure 1 | Study site. **(A)** Location of Tairua, New Zealand North Island **(B)** detail of Tairua Beach. Pressure sensor (S4_N) location used for SWAN model validation (Montaño et al., 2020).

Supplementary Figure 2 | Input conditions. **(A)** Significant wave height **(B)** mean wave period **(C)** wave direction (Montaño et al., 2020).

Supplementary Figure 3 | Information related to beach profile observation data (https://coastalhub.science/data).

Supplementary Figure 4 | **(A)** Instrumented sled used during the experiment at Tairua Beach. **(B)** Time averaged video image of Tairua Beach during the experiment. Measurements were taken in the cross-shore transect as indicated by the black line (van Maanen et al., 2008).

Supplementary Figure 5 | Measured **(A)** wave height H_{rms} and offshore zero crossing **(B)** wave period T_{m02}, and **(C)** tidal elevation during the experiment (van Maanen et al., 2008).

REFERENCES

Bernabeu, A. M., Raúl, M., and Cesar, V. (2003). An Equilibrium Profile Model for Tidal Environments. *Sci. Marina* 66 (4), 177–198. doi: 10.3989/scimar.2002.66n4325

Blossier, B., Bryan, K. R., Daly, C. J., and Winter, C. (2016). Nearshore Sandbar Rotation at Single-Barred Embayed Beaches. *J. Geophys. Res. Ocean* 121, 2286–2313. doi: 10.1002/2015JC011031

Blossier, B., Bryan, K. R., Daly, C. J., and Winter, C. (2017). Shore and Bar Cross-Shore Migration, Rotation, and Breathing Processes at an Embayed Beach. *J. Geophys. Res. Earth Surf.* 122, 1745–1770. doi: 10.1002/2017JF004227

Bodge, K. R. (1992). Representing Equilibrium Beach Profiles With an Exponential Expression. *J. Coastal Res.* 8 (1), 47–55.

Bogle, J. A., Bryan, K. R., Black, K. P., Hume, T. M., and Healy, T. R. (1999). "Observations of Geomorphic Parameters Using Video Images. Coasts and Ports '99," in *Proceedings of the 14th Australasian Coastal and Ocean Engineering conference and the 7th Australasian Port and Harbour Conference*, , April 14–16, Vol. vol I. 70–75(Perth, Australia).

Bruun, P. (1954). *Coast Erosion and the Development of Beach Profiles, Beach Erosion Board Technical Memorandum. No. 44. U.s* (Vicksburg, MS: Army Engineer Waterways Experiment Station).

Callaghan, D. P., Saint-Cast, F., Nielsen, P., and Baldock, T. E. (2006). Numerical Solutions of the Sediment Conservation Law; a Review and Improved Formulation for Coastal Morphological Modeling. *Coastal Eng.* 53 (7), 557–571. doi: 10.1016/j.coastaleng.2006.03.001

Dean, R. G. (1977). *Equilibrium Beach Profiles: U.s. Atlantic and Gulf Coasts, Technical Report No. 12, Newark, DE: Department of Civil Engineering* (University of Delaware).

Dean, R. G. (1987). *Coastal Sediment Processes: Toward Engineering Solutions. Proceedings of the Specialty Conference on Coastal Sediments '87* (New York: American Society of Civil Engineers), 1–24.

Dean, R. G. (1991). Equilibrium Beach Profiles: Characteristics and Applications. *J. Coastal Res.* 7 (1), 53–84.

Defant, A. (1961). *Physical Oceanography*. Vol. 2 (New York: Pergamon Press), 598.

Deltares (2018). *Delft3D-FLOW User Manual: Simulation of Multidimensional Hydrodynamic Flows and Transport Phenomena Including Sediments* (The Netherlands: Deltares).

Fang, Y., and Ron, J. C. (2013). *Modelling Coastal Process for Long-Term Shoreline Change, Proceeding of Coast and Ports 2013 Conference*. (Sydney: National Committee for Coastal and Ocean Engineering).

Green, J. P. B. (1994). "Estuarine Enclosed Beaches and the Geomorphic Processes Affecting Their Morphology," in *Master of Science (Geography) Thesis* (Tairua Estuary, New Zealand: University of Auckland).

Hanson, H. H., Larson, M., and Kraus, N. C. (2010). Calculation of Beach Change Under Interacting Cross- Shore and Longshore Processes. *Coastal Eng.* 57 (6), 610–919. doi: 10.1016/j.coastaleng.2010.02.002

Hardisty, J. (2007). *Estuaries: Monitoring and Modelling the Physical System* (Oxford: Blackwell Publishing).

Kajima, R., Shimizu, T., Maruyama, K., and Saito, S. (1982). "Experiments on Beach Profile Change With a Large Wave Flume," in *International Conference on Coastal Engineering*. (Cape Town: ASCE) 1385–1404.

Kim, H., Kevin, H., Jin, J. Y., Park, G. S., and Lee, J. (2014). Empirical Estimation of Beach-Face Slope and its Use for Warning of Berm Erosion. *J. Meas. Eng.* 2 (1), 29–42.

Kim, T. K., Lim, C., and Lee, J. L. (2021). Vulnerability Analysis of Episodic Beach Erosion by Applying Storm Wave Scenarios to a Shoreline Response Model. *Front. Mar. Sci.* 8. doi: 10.3389/fmars.2021.759067

Komar, P. D., and McDougal, W. G. (1994). The Analysis of Exponential Beach Profiles. *J. Coastal Res.* l0 (l), 56–69.

Larson, M. (1991). "Equilibrium Profile of a Beach With Varying Grain Size," in *Sediments '91* (New York: American Society of Civil Engineers), 905–919.

Larson, M., and Kraus, N. C. (1989). "SBEACH: Numerical Model for Simulating Storm-Induced Beach Change," in *Report 1 Empirical Foundation and Model Development, Technical Report, CERC-89(9)* (Vicksburg: US Army Corps of Engineering).

Larson, M., Kraus, N. C., and Byrnes, M. R. (1999). "SBEACH: Numerical Model for Simulating Storm-Induced Beach Change," in *Report 2 Numerical Formulation and Model Tests. Technical Report. CERC-89(9)*, 116.

Lesser, G. R., Roelvink, J. A., van Kester, J. A. T. M., and Stelling, G. S. (2004). Development and Validation of a Three-Dimensional Morphological Model. *Coastal Eng.* 51, 883–915. doi: 10.1016/j.coastaleng.2004.07.014

Lim, C., Kim, T. K., and Lee, J. L. (2021). Evolutionary Response of Shoreline Position Inferred by Horizontal Behavior of Suspension and Recovery Processes of Wave-Driven Sediments Shoreline Response Induced by Spatial Suspension and Recovery Processes of Wave-Induced Sediments. *Geomorphology*. Submitted for review.

MacMillan, D. H. (1966). *Tides* (New York: American Elsevier).

Margvelashvili, N., Saint- Cast, F., and Condie, S. (2008). Numerical Modeling of the Suspended Sediment Transport in Torres Strait. *Cont. Shelf Res.* 28 (16), 2241–2256. doi: 10.1016/j.csr.2008.03.037

Miller, J. K., and Dean, R. G. (2004). A Simple New Shoreline Change Model. *Coastal Eng.* 51 (7), 531–556. doi: 10.1016/j.coastaleng.2004.05.006

Montaño, J., Coco, G., Antolnez, J. A. A., Beuzen, T., Bryan, K. R., Castelle, L., et al. (2020). Blind Testing of Shoreline Evolution Models. *Sci. Rep.* 10, 2137. doi: 10.1038/s41598-020-59018-y

Nam, P. T., Larson, M., Hanson, H., and Hoan, L. X. (2009). Numerical Model of Nearshore Waves, Currents, and Sediment Transport. *Coastal Eng.* 56 (11-12), 1084–1096. doi: 10.1016/j.coastaleng.2009.06.007

Neumann, G., and Pierson, W. J. (1966). *Principles of Physical Oceanography* (Englewood Cliffs: Prentice-Hall), 230–233.

Pender, D., and Karunarathna, H. (2013). A Statistical Process-Based Approach for Modelling Beach Profile Variability. *Coastal Eng.* 81 (2013), 19–29. doi: 10.1016/j.coastaleng.2013.06.006

Requejo, S., Medina, R., and González, M. (2006). "Equilibrium Beach Profile for Refraction-Diffraction Areas," in *Coastal Dynamics 2005: State of the Practice*. (Barcelona: ASCE) 1–13.

Roelvink, D., Reniers, A., van Dongeren, A., Van Thiel de Vries, J., McCall, R., and Lescinsky, J. (2009). Modelling Strom Impacts on Beaches, Dunes and Barrier Islands. *Coastal Eng.* 56, 1133–1152. doi: 10.1016/j.coastaleng.2009.08.006

Smith, R. K., and Bryan, K. R. (2007). Monitoring Beach Face Volume With a Combination of Intermittent Profiling and Video Imagery. *J. Coast. Res.* 234, 892–898. doi: 10.2112/04-0287.1

Suh, K. D., and Dalrymple, R. A. (1988). Expression for Shoreline Advancement of Initially Plane Beach. *J. Waterw. Port Coastal Ocean Eng.* 114 (6), 770–777. doi: 10.1061/(ASCE)0733-950X(1988)114:6(770)

Sunamura, T. (1975). A Study of Beach Ridge Formation in Laboratory. *Geog. Rev. Jpn.* 48 (11), 761–767. doi: 10.4157/grj.48.761

Swart, D. H. (1974). "A Schematization of Onshore- Offshore Transport," in *Proceedings of the Fourteenth International Conference on Coastal Engineering* (Copenhagen: American Society of Civil Engineers), 884.

Thieler, E. R., Pilkey, O. H., Young, R. S., Bush, D. M., and Chai, F. (2000). The Use of Mathematical Models to Predict Beach Behavior for U.s. Coastal Engineering: A Critical Review. *J. Coastal Res.* 16 (1), 48–70.

van Maanen, B., de Ruiter, P. J., Coco, G., Bryan, K. R., and Ruessink, B. G. (2008). Onshore Sandbar Migration at Tairua Beach (New Zealand): Numerical Simulations and Field Measurements. *Mar. Geol.* 253, 99–106. doi: 10.1016/j.margeo.2008.05.007

Wang, H., Dalrymple, R. A., and Shiau, J. C. (1975). "Computer Simulation of Beach Erosion and Profile Modification Due to Waves," in *Proceedings of the 2nd. Annual Symp. Of Waterways, Harbours and Coastal Eng. Div. ASCE on Modeling Techniques(Modeling '75, San Franc)*, vol. 2. (San Francisco: ASCE) 1369–1384.

Wang, P., and Kraus, N. C. (2005). Beach Profile Equilibrium and Patterns of Wave Decay and Energy Dissipation Across the Surf Zone Elucidated in a Large-Scale Laboratory Experiment. *J. Coastal Res.* 21 (3), 522–534. doi: 10.2112/03-003.1

Watanabe, A., Riho, Y., and Horikawa, K. (1980). "Beach Profiles and on-Offshore Sediment Transport," in *International Conference on Coastal Engineering*. (Sydney: ASCE) 1106–1121.

Wise, R. A., Smith, S. J., and Larson, M. (1996). "SBEACH: Numerical Model for Simulating Storm-Induced Beach Change: Report 4 Cross-Shore Transport Under Random Waves and Model Validation With Supertank and Field Data," in *Coastal Engineering Technical Report Cerc-89-9*. (Vicksburg: US Army Corps of Engineering)

Wright, L. D., and Short, A. D. (1984). Morphodynamic Variability of Surf Zones and Beaches: A Synthesis. *Mar. Geol.* 56, 93–118. doi: 10.1016/0025-3227(84)90008-2

Wright, L. D., Short, A. D., and Green, M. O. (1985). Short-Term Changes in the Morphologic Statses of Beaches and Surf Zones: An Empirical Model. *Mar. Geol.* 62, 339–364. doi: 10.1016/0025-3227(85)90123-9

Yates, M. L., Guza, R. T., and O'Reilly, W. C. (2009). Equilibrium Shoreline Response: Observations and Modeling. *J. Geophys. Res.* 114 (C9), C09014. doi: 10.1029/2009JC005359

Zhi, L. (2014). "Hydrodynamic and Sediment Transport Numerical Modelling and Applications," in *Doctor of Philosophy (Earth and Ocean Sciences) Thesis* (Tairua Estuary, New Zealand: The University of Waikato).

Conflict of Interest: The authors declare that the research was conducted in the absence of any commercial or financial relationships that could be construed as a potential conflict of interest.

Publisher's Note: All claims expressed in this article are solely those of the authors and do not necessarily represent those of their affiliated organizations, or those of the publisher, the editors and the reviewers. Any product that may be evaluated in this article, or claim that may be made by its manufacturer, is not guaranteed or endorsed by the publisher.

Copyright © 2022 Lee, Lim and Lee. This is an open-access article distributed under the terms of the Creative Commons Attribution License (CC BY). The use, distribution or reproduction in other forums is permitted, provided the original author(s) and the copyright owner(s) are credited and that the original publication in this journal is cited, in accordance with accepted academic practice. No use, distribution or reproduction is permitted which does not comply with these terms.

frontiers | Frontiers in Marine Science

ORIGINAL RESEARCH
published: 07 April 2022
doi: 10.3389/fmars.2022.843549

Seasonal Distributions of Methane in a Populous Urban Coastal Sea Area

Hsiao-Chun Tseng[1,2*], *Chia-Chia Lin*[1], *Hui-Juan Pan*[3], *Yokie Tai Yuh Han*[1] *and Gwo-Ching Gong*[1,2*]

[1] Institute of Marine Environment and Ecology, National Taiwan Ocean University, Keelung, Taiwan, [2] Center of Excellence for the Oceans, National Taiwan Ocean University, Keelung, Taiwan, [3] Institute of Earth Sciences, College of Ocean Science and Resource, National Taiwan Ocean University, Keelung, Taiwan

Methane (CH_4) is an important greenhouse gas, and its concentrations in aquatic areas are heavily influenced by anthropogenic activities, especially human-induced eutrophication, polluted river discharge and wastewater treatment plant (WWTP) effluents. Although coastal areas and estuaries contribute large amounts of global oceanic CH_4 emissions, the relative contributions of different sources have not been well determined. The Tamsui River located in northern Taiwan is an urban river flowing through populated cities and thus likely carries large amounts of contaminants, such as nutrients and organic matter to the estuary. In this study, we characterized the spatial distribution and seasonal variations in CH_4 in the Tamsui River estuary adjacent marine areas. The sea-to-air CH_4 fluxes were also estimated to quantify the strength of the study area as an atmospheric CH_4 source. Our results showed that CH_4 concentrations in coastal sea areas were influenced by WWTP effluents, sediment and freshwater inputs. Thus, river discharge and nutrient levels as well as strong vertical mixing and disturbances might increase CH_4 concentrations and emissions. The seasonal surface CH_4 concentrations and sea-to-air CH_4 fluxes were 13.7 ± 18.7 nM and 41.7 ± 68.0 μmol m^{-2} d^{-1} in autumn; 29.3 ± 19.8 nM and 61.3 ± 44.6 μmol m^{-2} d^{-1} in spring; 21.8 ± 13.9 nM and 37.0 ± 26.2 μmol m^{-2} d^{-1} in summer; and 27.0 ± 21.4 nM and 85.9 ± 75.4 μmol m^{-2} d^{-1} in winter.

Keywords: methane, WWTP effluents, nutrients, Tamsui River, greenhouse gases

OPEN ACCESS

Edited by:
William Savidge, Odum School of Ecology, University of Georgia, United States

Reviewed by:
Stefano Bonaglia, University of Gothenburg, Sweden
Masahiro Suzumura, National Institute of Advanced Industrial Science and Technology (AIST), Japan

***Correspondence:**
Hsiao-Chun Tseng
h.c.jean.tseng@gmail.com
Gwo-Ching Gong
gcgong@mail.ntou.edu.tw

Specialty section:
This article was submitted to Coastal Ocean Processes, a section of the journal Frontiers in Marine Science

Received: *26 December 2021*
Accepted: *02 March 2022*
Published: *07 April 2022*

Citation:
Tseng H-C, Lin C-C, Pan H-J, Han YTY and Gong G-C (2022) Seasonal Distributions of Methane in a Populous Urban Coastal Sea Area. Front. Mar. Sci. 9:843549. doi: 10.3389/fmars.2022.843549

INTRODUCTION

Methane (CH_4), the second most important greenhouse gas after carbon dioxide (CO_2), has global warming potential over a 20-year time frame (GWP_{20}) that is 86 times as high as that of CO_2 (IPCC, 2013). It accounts for 16–25% of atmospheric warming to date (Etminan et al., 2016). The global atmospheric CH_4 concentration has increased significantly from a preindustrial value of 722 ± 25 ppb in 1750 to 1803 ± 2 ppb in 2011, and the most plausible cause of the increase in CH_4 concentration is human activities (IPCC, 2013). Kirschke et al. (2013) estimated that the global surface-to-air CH_4 emissions from 2000 to 2009 were 678 Tg CH_4 yr^{-1}, with a large range of 542-852 Tg CH_4 yr^{-1}. Jackson et al. (2020) also reported that the average global CH_4 emissions for 2017 were 596 Tg CH_4 yr^{-1}, with a range of 572–614 Tg CH_4 yr^{-1}. The open ocean is a modest source of

CH_4 to the atmosphere at a rate of less than 2 Tg CH_4 yr^{-1} (Rhee et al., 2009). A large fraction of marine-originated CH_4 in the atmosphere is produced in oxygenated surface waters that are oversaturated with CH_4 in relation to atmospheric equilibrium (Karl et al., 2008; Repeta et al., 2016), an unexplained phenomenon referred to as the marine methane paradox (Reeburgh, 2007; Repeta et al., 2016). Previous research has revealed that most CH_4 found in the euphotic zone was released during zooplankton grazing (de Angelis and Lee, 1994) or in anoxic microenvironments within zooplankton fecal pellets (Tilbrook and Karl, 1994). Recent research has determined that the formation of CH_4 in oxic environments can occur *via* methylphosphonate cycling (Karl et al., 2008) and by dimethylsulfide (DMS) cycling (Damm et al., 2010; Florez-Leiva et al., 2013; Zindler et al., 2013). Moreover, Bogard et al. (2014) suggested a possible link between CH_4 concentration and phytoplankton standing stock (i.e., chlorophyll *a*), which implies that factors influencing phytoplankton standing stock, such as grazing, nutrient availability and the physical structure of the water column, have a strong bearing on pelagic CH_4 dynamics.

Coastal regions are more intense sources of CH_4 to the atmosphere, which contribute approximately 75% of global oceanic CH_4 emissions (Bange et al., 1994). Continental shelves emit approximately 13 Tg CH_4 yr^{-1} (Bange et al., 1994), whereas estuaries emit between 1 and 7 Tg CH_4 yr^{-1} (Bange et al., 1994; Upstill-Goddard et al., 2000). The high CH_4 concentrations in the surface waters of continental shelves are due to direct CH_4 inputs from estuaries and sediments where methanogenesis is sustained by abundant organic matter sedimentation (Bange et al., 1994; Rehder et al., 1998; Upstill-Goddard et al., 2000; Middelburg et al., 2002; Borges et al., 2018). In addition, the impacts of human activities on coastal CH_4 emissions, such as dam construction (Chen et al., 2008), eutrophication (Beaulieu et al., 2019), wastewater discharge into coastal areas (Du et al., 2018), changes in hydrology (Pekel et al., 2016) and climate feedbacks, such as microbial responses to warming (Yvon-Durocher et al., 2014), are not well understood and have been poorly quantified. Beaulieu et al. (2019) and Nijman et al. (2021) also reported that future CH_4 emissions from lakes and impoundments worldwide may increase due to increases in nutrients and water temperature. Borges et al. (2018) also found that productivity and temperature are drivers to seasonal and spatial variations of dissolved methane in the Southern Bight of the North Sea. In addition, Myllykangas et al. (2019) addressed that eutrophication and climate change may accelerate CH_4 emissions from estuaries, causing positive feedbacks with global warming.

The scope of this study is to investigate seasonal distributions of methane in a populous urban coastal sea area. Estuaries transfer terrestrial matter and human impacts (nutrients, organic matter etc.) from land to ocean. The Tamsui River is a populous urban river, and the highest regional population density in its catchment reaches 38,607 people per km^2 (Yonghe district). Recent research (Borges et al., 2016; Gelesh et al., 2016; Borges et al., 2018; Humborg et al., 2019) has found massive CH_4 emissions in estuaries and coastal water during summertime, which might be due to temperature controlling methanogenesis in organic matter rich sediments. Since the seawater temperature was higher in tropical/subtropical areas than in temperate regions, the CH_4 concentrations in the water might also be higher, especially under future climate change. Seasonal data collection is needed for a comprehensive view of the situation. This research aims to understand the seasonal variations in CH_4 concentrations as well as their interaction with other environmental factors that may be influenced by human activities in a populous urban coastal area.

MATERIALS AND METHODS

Study Area

The Tamsui River is located in northern Taiwan (**Figure 1**) and has a total length of 159 km. The catchment area of the Tamsui River is 2,726 km^2, and it covers the whole metropolitan area of Taipei, the capital city of Taiwan. The drainage basin includes several regions along the main tributaries where large amounts of nutrients, resulting from industrial and agricultural activities, enter the river (Wen et al., 2008). The Tamsui River delivers materials, including suspended particles, nutrients, organic matter, and pollutants, from land into its estuary and adjacent marine areas. There were 7.13 million people living in the catchment, and approximately 60% of the population utilized the sanitary sewers in 2019 (Tseng et al., 2021). The largest wastewater treatment plant (WWTP) in Taiwan is located near the Tamsui River estuary (**Figure 1**), and its ocean outfall pipe extends from the shore and enters the ocean. The outlet of the ocean outfall pipe of the WWTP was located near sampling station 11 (**Figure 1**) and its diffuser tubes are 3 km from shore at water depths between 30 m and 40 m.

The regional climate is subtropical, with temperatures varying between 10 and 35 °C and annual precipitation ranging between 1500 and 2500 mm (Wen et al., 2008). The dry season ranges from November to April, and the wet season ranges from May to October. According to the historical data from the Tamsui weather station (**Figure 1**) over the past 25 years (1995-2020), the average rainfall is 776 ± 269 mm during the dry season, while it is 1322 ± 440 mm during the wet season (Central Weather Bureau: https://www.cwb.gov.tw/eng/).

Cruise Information and Sampling Instruments

Seasonal samples were taken in the Tamsui River estuary adjacent sea area (**Figure 1**) during four cruises onboard R/V Ocean Researcher 2 and R/V New Ocean Researcher 2: OR2-2390 (November 2019), NOR2-0004 (May 2020), NOR2-0009 (August 2020), and NOR2-0027 (January 2021). Discrete water samples were taken at various depths at 16 sampling stations in autumn (November 2019) and 20 sampling stations in spring (May 2020) and summer (August 2020). Due to the adverse weather conditions in winter (January 2021), discrete water samples were taken at various depths at 6 sampling stations, and surface water samples were taken at 10 sampling stations.

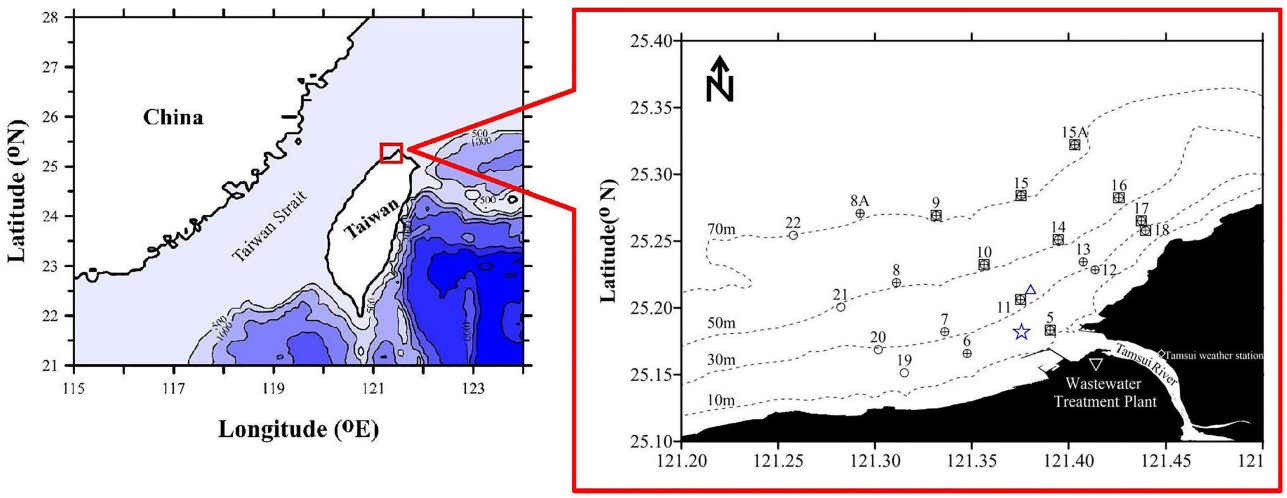

FIGURE 1 | Study area and station locations. +: OR2-2390 (November 2019); ○: NOR2-0004 (May 2020) and NOR2-0009 (August 2020); □: NOR2-0027 (January 2021). Δ: ocean outfall pipe of wastewater treatment plant. ☆: Wind station.

The vertical profiles of seawater temperature and salinity were measured with a conductivity–temperature–depth instrument (CTD; SBE 9/11, Seabird Scientific, USA). Seawater samples from various depths were collected using a carousel water sampler (SBE32, Seabird Scientific, USA) that was fitted with 20 L Teflon-coated Go-Flo bottles (General Oceanic, USA) mounted on a CTD assembly.

Chemical Analysis

Water samples for nutrient analysis were placed in 100 mL polypropylene bottles and immediately frozen with liquid nitrogen. The methods employed for nitrate (NO_3-) and phosphate PO_4^{3-} analysis are described in detail elsewhere (Gong et al., 1996; Gong et al., 2000), and the precision was ±0.3 and ±0.01 μmol L^{-1}, respectively. Dissolved oxygen (DO) was measured by spectrophotometry (Pai et al., 1993) with a precision of approximately ± 0.32% at the 190 μmol L^{-1} level. Water samples for chlorophyll *a* (Chl *a*) analysis were immediately filtered through GF/F filter paper (Whatman, 47 mm) and stored at -20°C. A Turner Designs model 10-AU-005 fluorometer (Turner Inc., USA) was utilized to measure the Chl *a* concentration following extraction by 90% acetone (Strickland and Parsons, 1972; Gong et al., 1993; Gong et al., 1995).

Water samples for CH_4 concentration were collected in 120 mL dark borosilicate serum bottles. The bottles were rinsed three times with the sampled water. After a 2-fold bottle volume was allowed to overflow the bottle, 0.2 mL saturated $HgCl_2$ was added. It was then sealed with a butyl stopper and crimped with an aluminum cap. The samples were stored in a dark box and kept at 4°C. All the water samples were transferred to a laboratory and analyzed within three months of collection. Measurements were made with the headspace technique (Weiss, 1981) and a gas chromatograph (GC; Agilent 7890) with a flame ionization detector (FID). The GC-FID had a 1.8 m long stainless steel column with a diameter of 3.2 mm, which was filled with a 60/80 mesh molecular sieve 5A. The FID was calibrated with pure N_2 (Yeong Her, Taiwan) and three commercial gas mixtures with CH_4 mixing ratios of 1.16 ppmv (MESA Specialty Gas, USA), 3.02 ppmv (Yeong Her, Taiwan) and 9.60 ppmv (Yeong Her, Taiwan).

CH_4 Saturation Ratio and Fluxes

The saturation (R, %) and sea-to-air flux (F, μmol·m^{-2}·d^{-1}) of CH_4 were calculated using the following formulas:

$$R = \left(C_{obs}/C_{eq}\right) * 100$$

$$F \quad \left(\mu mol \quad m^{-2} \quad d^{-1}\right) \quad = k\left(C_{obs} - C_{eq}\right)$$

C_{obs} represents the observed concentration of gas dissolved in water, and C_{eq} is the expected equilibrium water concentration. The expected equilibrium water concentration was calculated using the solubility equation of (Wiesenburg and Norman, 1979), together with the *in situ* temperature, salinity and molar fraction of CH_4 in the air. The atmospheric CH_4 concentrations were taken from the NOAA/ESRL *in situ* program (http://www.esrl.noaa.gov/gmd). The monthly average atmospheric CH_4 concentrations at Mauna Loa (Hawaii, United States station) in November, 2019, May 2020, August 2020 and December 2020 were 1900, 1901, 1878 and 1912 ppb, respectively. (The data for Jan. 2021 have not yet come out; therefore, December 2020 monthly average atmospheric CH_4 concentrations were used).

Fluxes (μmol·m^{-2}·d^{-1}) of CH_4 across the air-water interface were determined by C_{obs}–C_{eq} and the gas exchange coefficient *k*. The value of *k* is a specific function of the properties of the gas, the temperature (°C) and turbulence and is frequently parameterized as a function of the wind speed. In this study, wind speed at a height of approximately 15 m above the sea

surface from a meteorological platform (121.3758°E 25.1817°N; **Figure 1**) was used. Daily wind speed data were provided by the Harbor and Marine Technology Center (https://www.ihmt.gov.tw/). We calculated k by using the equation established by Wanninkhof (2014). A positive flux indicates gas transfer from the water to the atmosphere.

RESULTS

Marine hydrographic and chemical data as well as Chl *a* and CH_4 were measured during four seasonal cruises in the Tamsui River estuary adjacent marine area. Detailed information on the seasonal cruises and the average hydrographic data, nutrient concentrations, and Chl *a* and CH_4 concentrations are listed in **Table 1**. **Figure 2** presents cross-sectional studies of the Tamsui River estuary adjacent marine area in autumn, spring and summer.

Marine Environmental Conditions and Methane Concentrations in the Dry Season (Autumn and Winter)

In autumn, the seawater temperature and salinity ranged from 18.9 to 24.0°C and 33.45 to 34.30 (**Table 1**), respectively. The seawater temperature gradually decreased with depth (**Figure 2A**), and the lowest salinity values were observed near shore (**Figure 2B**). The PO_4^{3-} and NO_3^- concentrations ranged from 0.26 to 0.78 μM and 2.9 to 9.4 μM (**Table 1**), respectively. The nutrient concentrations increased with depth and from offshore to inshore (**Figures 2C, D**). Chl *a* concentrations ranged between 0.15 and 1.50 mg m^{-3} (**Table 1**) and gradient descent from the surface water (**Figure 2E**). DO concentrations ranged between 186.7 and 228.9 μM (**Table 1**) and had the same pattern as the Chl *a* distributions (**Figure 2F**). CH_4 concentrations ranged from 1.4 to 78.0 nM (**Table 1**), and high CH_4 concentrations were observed near station 11, where the outlet of the ocean outfall pipe which discharged the WWTP effluents was located (**Figure 2G**). The average surface seawater CH_4 concentration was 13.7 ± 18.7 nM. Long-term wind speed data from the meteorological platform were used, and the average wind speed in November between 2005 and 2019 was 7.9 ± 0.8 m/s. The sea-to-air CH_4 flux was 46.3 ± 75.4 μmol m^{-2} d^{-1} (**Table 2**).

In winter, only surface water was taken between stations 5 and 9 so there was no cross-sectional figure due to the adverse weather conditions caused by the prevailing northeast monsoon. According to the data from 10 sampling stations, the seawater temperature and salinity ranged from 18.4 to 19.4°C and 33.06 to 34.35 (**Table 1**), respectively. Although nutrient concentrations were comparably high, with PO_4^{3-} and NO_3^- concentrations ranging from 0.44 to 0.85 μM and 6.0 to 8.5 μM, the Chl *a* concentrations were low, ranging between 0 and 0.30 mg m^{-3} (**Table 1**). DO concentrations were comparably high and ranged between 227.7 and 252.4 μM (**Table 1**), which might be caused by low temperature and high wind ventilation. Wind speed data between 2005 and 2019 from the meteorological platform were used, and the average wind speed in January was 8.0 ± 0.8 m/s. CH_4 concentrations ranged from 5.4 to 69.6 nM, and the average surface CH_4 concentration was 27.0 ± 21.4 nM. With a comparably high wind speed, the sea-to-air CH_4 flux was as high as 90.4 ± 79.3 μmol m^{-2} d^{-1} (**Table 2**).

Marine Environmental Conditions and Methane Concentrations in the Wet Season (Spring and Summer)

In spring, the seawater temperature and salinity ranged from 26.0 to 27.2°C and 31.68 to 34.46 (**Table 1**), respectively. The seawater temperature was homogeneous throughout the water column (**Figure 2H**). The PO_4^{3-} and NO_3^- concentrations ranged from 0.12 to 0.87 μM and 0 to 3.7 μM (**Table 1**), respectively. Low salinity and high nutrient concentrations were observed in the surface water and near the shore (**Figures 2I–K**) due to heavy precipitation on the sampling date. Chl *a* concentrations ranged between 0 and 0.77 mg m^{-3} (**Table 1**) and had higher concentrations nearshore (**Figure 2L**). DO concentrations ranged between 193.1 and 216.0 μM (**Table 1**) and had a similar pattern as the Chl *a* distributions (**Figure 2M**). CH_4 concentrations ranged from 4.3 to 77.4 nM (**Table 1**), and high CH_4 concentrations were observed near the shore (**Figure 2N**). The average surface seawater CH_4 concentration was comparably high at 29.3 ± 19.8 nM. The average wind speed in May 2005 and 2019 from the meteorological platform was 5.0 ± 0.6 m/s. The sea-to-air CH_4 flux was 47.2 ± 34.3 μmol m^{-2} d^{-1} (**Table 2**).

In summer, the seawater temperature and salinity ranged from 27.0 to 30.8°C and 33.62 to 34.20 (**Table 1**), respectively. The seawater temperature gradually decreased with depth (**Figure 2O**), and low salinity values were observed near shore (**Figure 2P**). The PO_3^- and NO_3^- concentrations ranged from 0.09

TABLE 1 | The seasonal average hydrographic data, nutrients, Chl *a* and CH_4 concentrations.

Sampling Date		Temperature (°C)	Salinity	CH_4 (nM)	DO (μM)	PO_4^{3-} (μM)	NO_3^- (μM)	DIN (μM)	Chl_*a* (mg m^{-3})
Autumn	Range	18.9-24.0	33.45-34.30	1.4-78.0	186.7-228.9	0.26-0.78	2.9-9.4	3.58-10.15	0.15-1.50
Nov. 2019	Mean	23.4 ± 0.9	33.72 ± 0.20	13.0 ± 16.6	217.7 ± 7.4	0.38 ± 0.10	4.3 ± 1.1	5.66 ± 1.51	0.72 ± 0.25
Spring	Range	26.0-27.2	31.68-34.46	4.3-77.4	193.1-216.0	0.12-0.87	0-3.7	0.50-17.33	0-0.77
May 2020	Mean	26.8 ± 0.2	34.14 ± 0.47	20.2 ± 16.7	206.1 ± 4.5	0.26 ± 0.14	0.6 ± 0.6	3.09 ± 2.64	0.36 ± 0.15
Summer	Range	27.0-30.8	33.62-34.20	5.0-58.5	185.0-209.4	0.09-0.49	0-4.7	0.52-6.76	0.15-1.6
Aug. 2020	Mean	29.6 ± 0.9	34.00 ± 0.14	17.5 ± 13.1	190.8 ± 4.6	0.26 ± 0.10	1.1 ± 0.9	3.01 ± 1.61	0.56 ± 0.29
Winter	Range	18.4-19.4	33.06-34.35	5.4-69.6	227.7-252.4	0.44-0.85	6.0-8.5	6.83-13.14	0-0.30
Jan. 2021	Mean	18.6 ± 0.3	34.06 ± 0.37	20.4 ± 13.8	224.7 ± 7.9	0.59 ± 0.08	6.8 ± 0.6	8.49 ± 1.37	0.12 ± 0.07

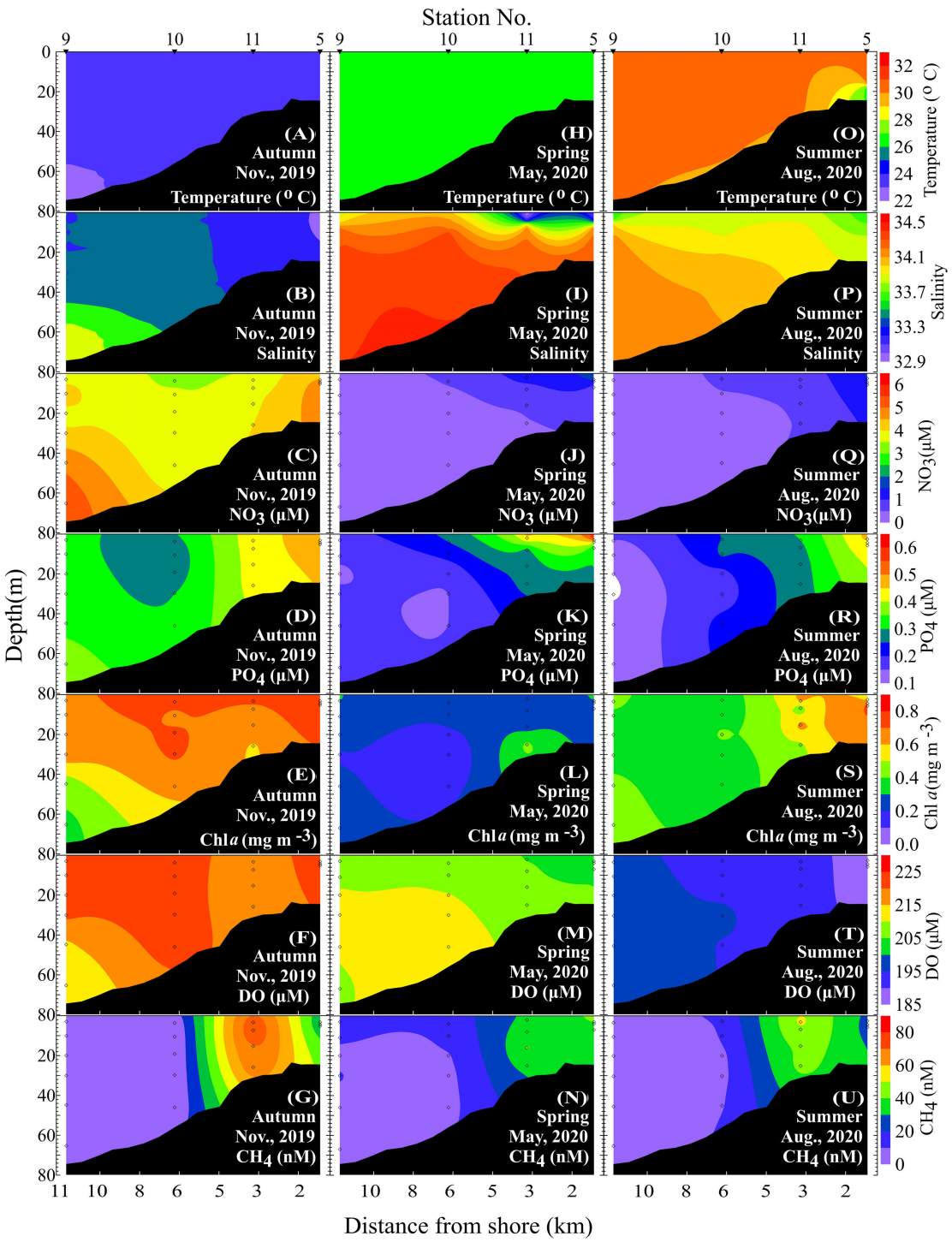

FIGURE 2 | Cross-section of temperature, salinity, NO_3, PO_4, Chl *a*, DO and CH_4 **(A–G)** in autumn, **(H–N)** in spring, and **(O–U)** in summer.

to 0.49 μM and 0 to 4.7 μM (**Table 1**), respectively. Chl *a* and DO concentrations ranged from 0.15 to 1.60 mg m^{-3} and 185.0 to 209.4 μM (**Table 1**), respectively. High nutrient and Chl *a* concentrations appeared nearshore (**Figures 2Q-S**) with low salinity (**Figure 2P**), which indicated freshwater input from the shore. CH_4 concentrations ranged from 5.0 to 58.5 nM (**Table 1**), and high CH_4 concentrations were observed near the outlet of the ocean outfall pipe (**Figure 2U**). The average surface seawater

TABLE 2 | The seasonal average surface hydrographic data, CH_4 concentrations, air CH_4 concentrations, wind speed and sea-to-air CH_4 fluxes.

Season	Sampling Date	Temperature (°C)	Salinity	Air CH_4 concentrations (ppm)	surface CH_4 concentrations (nM)	CH_4 saturation (%)	Monthly wind speed ($m\ s^{-1}$)	Sea-to-air CH_4 fluxes ($\mu mol\ m^{-2}\ d^{-1}$)
Autumn	Nov. 2019	23.8 ± 0.2	33.63 ± 0.10	1.90 ± 0.01 [a]	13.7 ± 18.7	615 ± 840	7.9 ± 0.8	46.3 ± 75.4
Spring	May 2020	26.8 ± 0.2	33.71 ± 0.78	1.90 ± 0.02 [a]	29.3 ± 19.8	1383 ± 930	5.0 ± 0.6	47.2 ± 34.3
Summer	Aug. 2020	29.9 ± 0.7	33.89 ± 0.16	1.88 ± 0.01 [a]	21.8 ± 13.9	1095 ± 702	5.0 ± 0.7	37.0 ± 26.2
Winter	Jan. 2021	18.8 ± 0.4	33.75 ± 0.53	1.91 ± 0.02 [a]	27.0 ± 21.4	1104 ± 878	8.0 ± 0.8	90.4 ± 79.3

[a]*Air CH_4 concentrations were from the monthly average data at Mauna Loa, Hawaii, United States.*

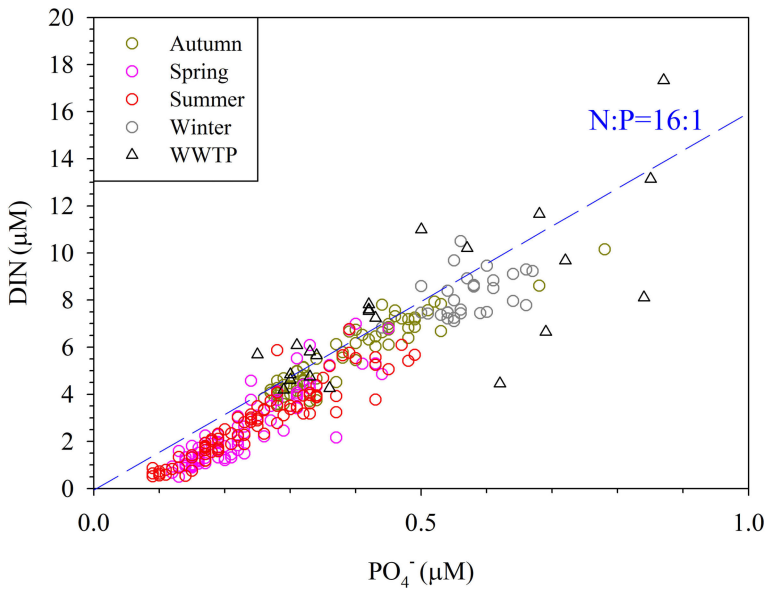

FIGURE 3 | The DIN concentration (μM) versus PO_4 concentration (μM), obtained at 66 stations during four cruises from November 2019 to January 2021. Δ presents the data influenced by ocean outfall pipe of wastewater treatment plant.

CH_4 concentration was 21.8 ± 13.9 nM. The average wind speed in August between 2005 and 2019 from the meteorological platform was 5.0 ± 0.7 m/s. The sea-to-air CH_4 flux was 37.0 ± 26.2 $\mu mol\ m^{-2}\ d^{-1}$ (**Table 2**).

DISCUSSION

One of the effective options for mitigating rapid climate change is to reduce CH_4 emissions due to its shorter lifetime than CO_2 (Shindell et al., 2012), which leads to an urgent need to understand the natural or anthropogenic factors influencing CH_4 concentrations and emissions. The aim of this research is to understand the seasonal variations and possible sources of CH_4 concentrations as well as their interaction with other environmental factors in a populous urban coastal sea area.

Inputs from WWTP Effluents

Wastewater is a major anthropogenic source of CH_4 and one of the fastest growing sources of CH_4 emissions (Kirschke et al., 2013). According to the IPCC (2013), the wastewater CH_4 emissions from 2000 to 2009 represented 22.7% of all anthropogenic CH_4 emissions. Du et al. (2018) reported that CH_4 emissions from wastewater in China increased from 1349.01 Gg in 2000 to 3430.03 Gg in 2014, and the highest proportion of emissions was from WWTPs. Cotovicz et al. (2016) found that high CH_4 concentrations could be sustained by allochthonous sources, such as sewage networks and polluted rivers, especially under high accumulated precipitation conditions. Yu et al. (2017) also pointed out that high CH_4 concentrations are frequently found in the water of urban drainage systems, composed of sewer systems, and WWTPs. According to **Figure 2**, CH_4 concentrations were high from the bottom to the surface water near station 11, where the outlet of the ocean outfall pipe of the WWTP was located. In addition, most of the water samples near the ocean outfall pipe of the WWTP did not follow the Redfield ratio (**Figure 3**) and were high in surface CH_4 concentrations (**Figure 4**). Moreover, the highest CH_4 concentrations in the water column were found near the ocean outfall pipe of the WWTP (**Figures 2G, N, U**). The inputs from WWTP effluents contributed to the increase in the CH_4

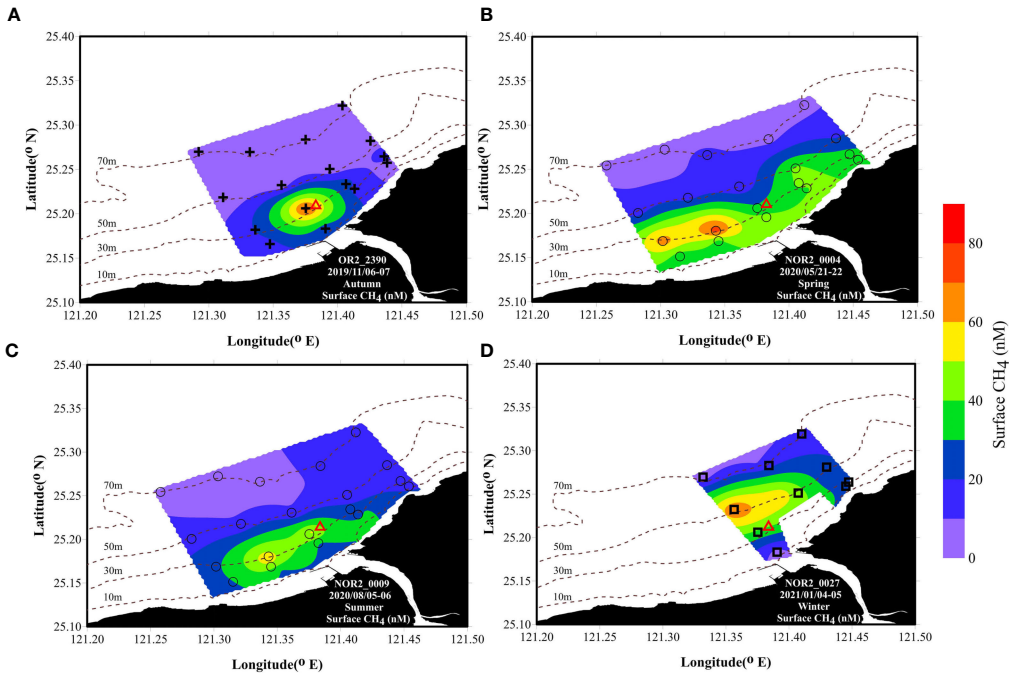

FIGURE 4 | CH_4 (nM) distributions of the surface water in the Tamsui River estuary and its adjacent marine area in **(A)** autumn, **(B)** spring **(C)** summer and **(D)** winter. Δ: ocean outfall pipe of ocean outfall pipe of wastewater treatment plant.

concentrations in the study area. The average seasonal surface CH_4 concentrations were 13.7 ± 18.7, 29.3 ± 19.8, 21.8 ± 13.9 and 27.0 ± 21.4 nM in autumn, spring, summer and winter, respectively. If water samples near the ocean outfall pipe of the WWTP were excluded, the average seasonal surface CH_4 concentrations then became 9.6 ± 8.9, 21.5 ± 13.2, 18.0 ± 8.2 and 15.4 ± 9.1 nM in autumn, spring, summer and winter, respectively. This finding shows that approximately 17-43% of the surface CH_4 concentrations in the study area were influenced by the WWTP effluents. The average annual sea-to-air CH_4 flux was 56.5 ± 22.3 μmol m^{-2} d^{-1} and reached 35.2 ± 8.4 μmol m^{-2} d^{-1} when excluding the water samples near the ocean outfall pipe of the WWTP. This result indicated that WWTP effluents influenced approximately one-third of the CH_4 emissions in the study area.

Inputs From Freshwater

In addition to the inputs from WWTP effluents, freshwater also contributed to the CH_4 concentrations in the Tamsui River estuary adjacent marine area. The Tamsui River is a small mountain river with an average flow rate of approximately 210 m^3/s. Although the Tamsui River transferred a comparably small amount of water mass to its adjacent marine areas, it brought high concentrations of CH_4 and nutrients. **Figure 2** shows high concentrations of CH_4 and nutrients with slightly low salinity nearshore. Dissolved inorganic nitrogen (DIN) concentrations represented the nitrogen level in the water and were well correlated with CH_4 concentrations (**Figure 5A**). CH_4 and PO_4^{3-} concentrations also showed a positive correlation (**Figure 5B**). According to Nijman et al. (2021), nutrients increased methane-oxidizing bacterial (MOB) abundance and methane oxidation potential, while warming only increased MOB abundance without altering methane oxidation potential. Thus, the differences of seawater temperature might result in different linear regressions between wet and dry seasons (**Figures 5A, B**).

CH_4 Emissions From Sediment

Seasonal variations of CH_4 concentration in the Tamsui River ranged between 362 and 2961nM (unpublished data). Rivers brought high concentrations of CH_4 and organic matter to coastal water (Chen et al., 2008; Zhang et al., 2008; Tseng et al., 2017; Sun et al., 2018). Coastal sediment which is rich in organic matter has been proposed to be the origin of CH_4 (Borges and Abril, 2011; Tseng et al., 2017). In addition, high CH_4 concentrations are frequently attributed to sedimentary methanogenesis in coastal environments (Bange, 2006; Zhou et al., 2009), especially in shallower waters. Borges et al. (2018) also found a seasonal peak of CH_4 in the nearshore and shallow seep areas in the Belgian coastal zone during summer, which was related to sediment organic matter content. **Figure 6** shows that CH_4 concentrations in the bottom water gradually decreased with the bottom depth. This result might be related to low abundance of methanotrophs in shallow coastal zones so more CH_4 seeps escaping from the sediment and higher CH_4 concentrations in the bottom water (Broman et al., 2020). According to our results, the CH_4 concentration in the bottom water did not influenced by the sediment input when the depth

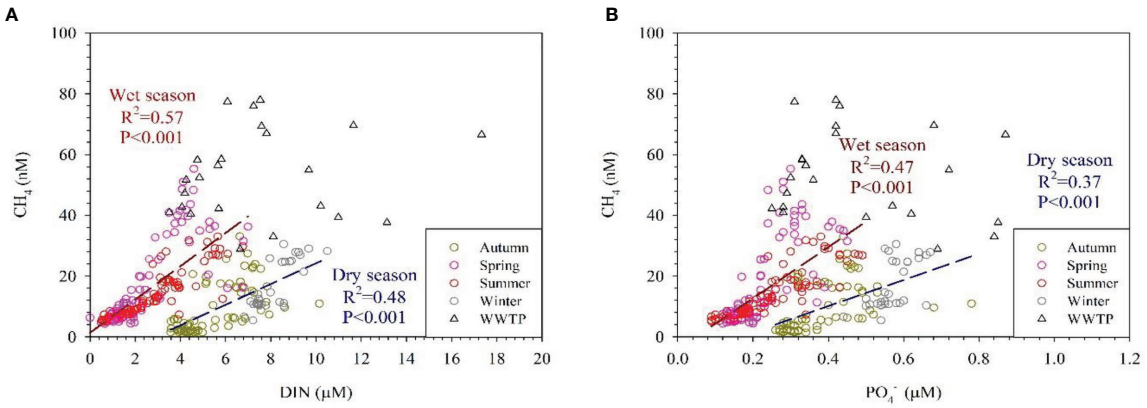

FIGURE 5 | CH_4 concentration (nM) versus **(A)** DIN (μM) **(B)** PO_4 (μM) in the dry season and in the wet season, obtained at 66 stations during four cruises from November 2019 to January 2021. Δ presents the data influenced by ocean outfall pipe of wastewater treatment plant, which has been excluded in the correlation.

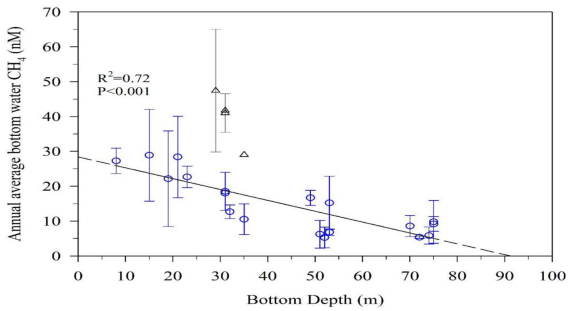

FIGURE 6 | The annual average bottom water CH_4 concentrations (nM) versus bottom depths (m), obtained at 62 stations during four cruises from November 2019 to January 2021. Δ presents the data influenced by ocean outfall pipe of wastewater treatment plant, which has been excluded in the correlation.

deeper than 90m. This might be due to CH_4 oxidized in the sediment before it released to the bottom water. According to the Sewerage Systems Office of the Public Works Department of the Taipei City Government, the ocean outfall pipe of a WWTP extends from shore, and its diffuser tubes are at water depths between 30 m and 40 m. Samples in the bottom water near the diffuser tubes were high in CH_4 concentrations (**Figure 6**).

Seasonal Variations in CH_4 and Sea-to-Air CH_4 Fluxes

Except for four individual observations in autumn, the surface water was supersaturated in CH_4 with respect to the atmosphere at most stations in the Tamsui River estuary adjacent marine area during the four cruises, which indicated that the study area was a net source of atmospheric CH_4. The average surface seawater CH_4 concentration varied between 13.7 and 29.3 nM (**Table 2**). The average surface seawater CH_4 concentrations were higher in spring, summer and winter (29.3, 21.8 and 27.0 nM) and lower in autumn (13.7 nM). In spring and summer (wet seasons), river discharge was more due to high precipitation and brought high concentrations of nutrients and CH_4 from land to sea. In addition, relatively strong vertical mixing and disturbances might bring high CH_4 concentrations from the bottom to the surface water in winter.

Figure 7 shows the average 15-year (2005-2019) monthly wind speed from the meteorological platform. In autumn, low river discharge and the wind speed was just picking up after October so the vertical mixing was relatively weak comparing with that in winter, which resulted in the lowest average surface seawater CH_4 concentrations. The wind speeds were higher in autumn and winter than in spring and summer (**Table 2**). The sea-to-air CH_4 flux variability was within the range of -3.0–308.9 μmol m^{-2} d^{-1}. The average sea-to-air CH_4 flux was the highest in winter (90.4 μmol m^{-2} d^{-1}), followed by spring and autumn (47.2 and 46.3 μmol m^{-2} d^{-1}) and was lowest in summer (37.0 μmol m^{-2} d^{-1}).

When compared globally, the Scheldt estuary in the North Sea has the highest surface CH_4 concentrations in its adjacent marine area, followed by the Tamsui River, Changjiang, and

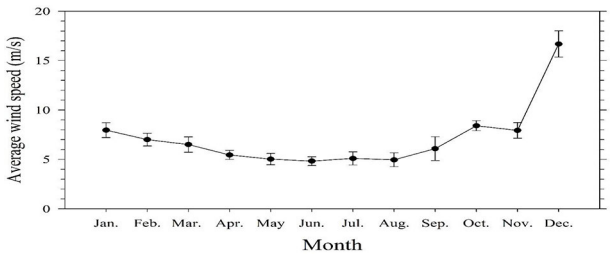

FIGURE 7 | The average 15-year (2005-2019) monthly wind speed at a height of approximately 15 m above the sea surface from the meteorological platform.

Pearl River (**Table 3**). In regard to the sea-to-air CH_4 fluxes, the adjacent marine areas of Scheldt and Tamsui River are the highest. Extremely high CH_4 was observed near the Scheldt estuary adjacent marine area due to gassy sediments (Borges et al., 2016), and its emission may be increased when the ocean warms (Borges et al., 2018). Furthermore, inputs from WWTP effluents increased CH_4 concentrations in the Tamsui River estuary adjacent marine area, and this situation may be worsened when the population grows.

CONCLUSIONS

In this study, we characterized the spatial distribution and seasonal variations in CH_4 in the Tamsui River estuary adjacent marine area as well as estimated sea-to-air CH_4 fluxes to quantify the strength of the study area as an atmospheric CH_4 source. The Tamsui River estuary adjacent marine area were active sites for CH_4 emissions. Our research results showed that CH_4 concentrations in coastal areas were influenced by WWTP effluents, sediment and freshwater inputs. In addition, CH_4 concentrations increased with the nutrient levels. Moreover, strong vertical mixing and disturbances might also increase CH_4 emissions, especially in coastal areas.

Climate change may increase precipitation in tropical/subtropical areas and transfer more nutrients and organic matter from land to ocean. Extreme weather events, such as typhoons and cyclones, can increase CH_4 emissions in coastal areas due to sediment disturbance. Anthropogenic conditions, such as high coastal populations, sewage, and WWTP effluents, also influence coastal CH_4 emissions. Escalating a feedback loop continues to circle between greenhouse gas emissions and climate change might increase extreme weather events. Nevertheless, preventing unthinkable events from happening takes tremendous time and effort. Accelerating the process from the root through scientific

TABLE 3 | Compilation of surface CH_4 concentrations, saturations and fluxes from the several estuaries and their adjacent marine areas.

Area	Regional Sea	Sampling Date	n	Salinity	CH_4 concentrations (nM)	CH_4 saturation (%)	Wind speed (m s^{-1})	Sea-to-airCH_4 fluxes (μmol m^{-2} d^{-1})	References
Scheldt estuary adjacent marine area	North sea	2016 monthly	108	30.5-34.2	47.4 ± 44.5		5.5 ± 2.1[a]	60 ± 112[e]	Borges et al., 2018
Changjiang estuary and its adjacent marine area	East China Sea	May 2011	8	S<30	12.6 ± 8.1	505 ± 323	5.0 ± 3.6[b]	20.2 ± 22.7[f]	Sun et al., 2018
		Aug. 2011	18		10.4 ± 7.7	480 ± 356	5.8 ± 1.7[b]	21.7 ± 28.0[f]	
		Oct. 2011	2		8.9 ± 6.5	371 ± 264	7.1 ± 2.3[b]	27.5 ± 33.6[f]	
		Mar. 2011	36	S>30	4.6 ± 4.4	161 ± 149	7.6 ± 3.8[b]	4.33 ± 8.86[f]	
		May 2011	37		5.2 ± 4.4	218 ± 179	8.4 ± 3.9[b]	13.4 ± 28.6[f]	
		Aug. 2011	16		6.0 ± 1.8	289 ± 90	6.2 ± 1.5[b]	11.6 ± 7.57[f]	
		Oct. 2011	31		4.7 ± 1.1	216 ± 48	7.4 ± 3.0[b]	10.7 ± 8.26[f]	
		Dec. 2011	29		4.3 ± 1.2	174 ± 41	8.7 ± 2.8[b]	9.34 ± 7.96[f]	
		May 2002	18	S>30	5.05 ± 2.49	216 ± 101	4.9 ± 1.8[b]	5.8 ± 7.3[e]	
		June 2006	10		6.22 ± 3.52	289 ± 180	6.8[c]	18.1 ± 17.1[e]	Zhang et al., 2008
		Aug. 2005	5		6.85 ± 3.77	348 ± 187	7.6[c]	26.2 ± 23.1[e]	
		Oct. 2006	24		7.09 ± 3.62	350 ± 179	5.9 ± 2.5[b]	14.4 ± 12.0[e]	
		Nov. 2002	12		3.53 ± 0.68	161 ± 32	7.6[c]	7.3 ± 3.8[e]	
Pearl River estuary adjacent marine area	South China Sea	Sep. 2003	22	33.68 ± 0.24	4.4 ± 2.2	233 ± 115	6.73[d]	8.3 ± 7.2[f]	Tseng et al., 2017
		Jul. 2005	19	32.54 ± 1.35	6.2 ± 1.5	323 ± 75	6.73[d]	14.5 ± 4.9[f]	
Tamsui River estuary adjacent marine area	Taiwan Strait	Nov. 2019	16	33.63 ± 0.10	13.7 ± 18.7	615 ± 840	7.9 ± 0.8[c]	46.3 ± 75.4[f]	This study
		May 2020	20	33.71 ± 0.78	29.3 ± 19.8	1383 ± 930	5.0 ± 0.6[c]	47.2 ± 34.3[f]	
		Aug. 2020	20	33.89 ± 0.16	21.8 ± 13.9	1095 ± 702	5.0 ± 0.7[c]	37.0 ± 26.2[f]	
		Jan. 2021	10	33.75 ± 0.53	27.0 ± 21.4	1104 ± 878	8.0 ± 0.8[c]	90.4 ± 79.3[f]	

[a]*Wind speed from the Westhinder Platform in the Belgian Coastal Zone.*
[b]*Wind speed from the ship based in situ wind speeds.*
[c]*Averaged monthly wind speeds obtained from the weather monitoring station.*
[d]*Average monthly wind speeds were from the National Aeronautics and Space Administration (NASA) QuikSCAT satellite platform.*
[e]*Fluxes were calculated by Wanninkhof (1992) equation.*
[f]*Fluxes were calculated by Wanninkhof (2014) equation.*

findings that identifying possible CH_4 sources is the pivotal information required to mitigate the crisis in time.

DATA AVAILABILITY STATEMENT

The original contributions presented in the study are included in the article/supplementary material, further inquiries can be directed to the corresponding authors.

AUTHOR CONTRIBUTIONS

H-CT and G-CG co-developed the idea of the study. H-CT leaded the research cruises and did the sampling. C-CL, H-JP, and YTYH did the sampling and data analysis. H-CT wrote the first draft of the article and all authors contributed equally to the interpretation of the results and in writing the final manuscript.

FUNDING

This research was supported by Ministry of Science and Technology of the ROC, Taiwan (MOST 108-2611-M-019-021-MY3).

ACKNOWLEDGMENTS

The authors wish to thank the Ministry of Science and Technology of the ROC, Taiwan for supporting this research, and the captain and crews of Ocean Researcher 2 and New Ocean Researcher 2 for their assistance.

REFERENCES

Bange, H. W. (2006). Nitrous Oxide and Methane in European Coastal Waters. *Estuarine Coastal Shelf Sci.* 70, 361–374. doi: 10.1016/j.ecss.2006.05.042

Bange, H. W., Bartell, U. H., Rapsomanikisa, S., and Andreae, M. O. (1994). Methane in the Baltic and North Seas and a Reassessment of the Marine Emissions of Methane. *Glob. Biogeochem. Cycles* 8, 465–480. doi: 10.1029/94GB02181

Beaulieu, J. J., DelSontro, T., and Downing, J. A. (2019). Eutrophication Will Increase Methane Emissions From Lakes and Impoundments During the 21st Century. *Nat. Commun.* 10, 1375. doi: 10.1038/s41467-019-09100-5

Bogard, M. J., del Giorgio, P. A., Boutet, L., Chaves, M. C. G., Prairie, Y. T., Merante, A., et al. (2014). Oxic Water Column Methanogenesis as a Major Component of Aquatic CH4 Fluxes. *Nat. Commun.* 5, 5350. doi: 10.1038/ncomms6350

Borges, A. V., and Abril, G. (2011). "5.04 - Carbon Dioxide and Methane Dynamics in Estuaries," in *Treatise on Estuarine and Coastal Science*. Eds. E. Wolanski and D. McLusky (Waltham: Academic Press), p. 119–161.

Borges, A. V., Champenois, W., Gypens, N., Delille, B., and Harlay, J. (2016). Massive Marine Methane Emissions From Near-Shore Shallow Coastal Areas. *Sci. Rep.* 6, 27908. doi: 10.1038/srep27908

Borges, A. V., Speeckaert, G., Champenois, W., Scranton, M. I., and Gypens, N. (2018). Productivity and Temperature as Drivers of Seasonal and Spatial Variations of Dissolved Methane in the Southern Bight of the North Sea. *Ecosystems* 21, 583–599. doi: 10.1007/s10021-017-0171-7

Broman, E., Sun, X., Stranne, C., Salgado, M. G., Bonaglia, S., Geibel, M., et al. (2020). Low Abundance of Methanotrophs in Sediments of Shallow Boreal Coastal Zones With High Water Methane Concentrations. *Front. Microbiol.* 11, 1536. doi: 10.3389/fmicb.2020.01536

Chen, C.-T. A., Wang, S.-L., Lu, X.-X., Zhang, S.-R., Lui, H.-K., Tseng, H.-C., et al. (2008). Hydrogeochemistry and Greenhouse Gases of the Pearl River, its Estuary and Beyond. *Quat. Int.* 186, 79–90. doi: 10.1016/j.quaint.2007.08.024

Cotovicz, L. C., Knoppers, B. A., Brandini, N., Poirier, D., Costa Santos, S. J., and Abril, G. (2016). Spatio-Temporal Variability of Methane (CH4) Concentrations and Diffusive Fluxes From a Tropical Coastal Embayment Surrounded by a Large Urban Area (Guanabara Bay, Rio De Janeiro, Brazil). *Limnol. Oceanogr.* 61, S238–S252. doi: 10.1002/lno.10298

Damm, E., Helmke, E., Thoms, S., Schauer, U., N¨othig, E., Bakker, K., et al. (2010). Methane Production in Aerobic Oligotrophic Surface Water in the Central Arctic Ocean. *Biogeosciences* 7, 1099–1108. doi: 10.5194/bg-7-1099-2010

de Angelis, M. A., and Lee, C. (1994). Methane Production During Zooplankton Grazing on Marine Phytoplankton. *Limnol. Oceanogr.* 39 (6), 1298–1308. doi: 10.4319/lo.1994.39.6.1298

Du, M., Zhu, Q., Wang, X., Li, P., Yang, B., Chen, H., et al. (2018). Estimates and Predictions of Methane Emissions From Wastewater in China From 2000 to 2020. *Earth's Future* 6, 252–263. doi: 10.1002/2017EF000673

Etminan, M., Myhre, G., Highwood, E. J., and Shine, K. P. (2016). Radiative Forcing of Carbon Dioxide, Methane, and Nitrous Oxide: A Significant Revision of the Methane Radiative Forcing. *Geophys. Res. Lett.* 43. doi: 10.1002/2016GL071930

Florez-Leiva, L., Damm, E., and Farías, L. (2013). Methane Production Induced by Dimethylsulfide in Surface Water of an Upwelling Ecosystem. *Prog. Oceanogr.* 112-113, 38–48. doi: 10.1016/j.pocean.2013.03.005

Gelesh, L., Marshall, K., Boicourt, W., and Lapham, L. (2016). Methane Concentrations Increase in Bottom Waters During Summertime Anoxia in the Highly Eutrophic Estuary, Chesapeake Bay, U.S.A. *Limnol. Oceanogr.* 61, S253–S266. doi: 10.1002/lno.10272

Gong, G. C., Chen, L. Y. L., and Liu, K. K. (1996). Chemical Hydrography and Chlorophyll a Distribution in the East China Sea in Summer: Implications in Nutrient Dynamics. *Cont. Shelf Res.* 16, 1561–1590. doi: 10.1016/0278-4343(96)00005-2

Gong, G.-C., Shiah, F.-K., Liu, K.-K., Wen, Y.-H., and Liang, M.-H. (2000). Spatial and Temporal Variation of Chlorophyll a, Primary Productivity and Chemical Hydrography in the Southern East China Sea. *Cont Shelf Res.* 20, 411–436. doi: 10.1016/S0278-4343(99)00079-5

Gong, G.-C., Yang, W.-R., and Chang, J. (1995). *In Vivo* Fluorescence-Derived Chlorophyll a Concentrations in the Southern East China Sea. *Acta. Oceanogr. Taiwanica* 34, 73–85.

Gong, G.-C., Yang, W.-R., and Wen, Y.-H. (1993). Correlation of Chlorophyll a Concentration and Sea Tech Fluorometer Fluorescence in Seawater. *Acta. Oceanogr. Taiwanica* 31, 117–126.

Humborg, C., Geibel, M. C., Sun, X., McCrackin, M., Mörth, C.-M., Stranne, C., et al. (2019). High Emissions of Carbon Dioxide and Methane From the Coastal Baltic Sea at the End of a Summer Heat Wave. *Front. Marine Sci.* 6. doi: 10.3389/fmars.2019.00493

IPCC (2013). Climate Change 2013: The Physical Science Basis. Contribution of Working Group I to the Fifth Assessment Report of the Intergovernmental Panel on Climate Change, in: T.F. Stocker, D. Qin, G.-K. Plattner, M. Tignor, S.K. Allen, J. Boschung, A. Nauels, et al. (Ed.), C.2; C.6; C.8, pp. 159–254; pp. 473–552; pp. 677–731, Cambridge, United Kingdom and New York, NY, USA.

Jackson, R. B., Saunois, M., Bousquet, P., Canadell, J. G., Poulter, B., Stavert, A. R., et al. (2020). Increasing Anthropogenic Methane Emissions Arise Equally From Agricultural and Fossil Fuel Sources. *Environ. Res. Lett.* 15, 071002. doi: 10.1088/1748-9326/ab9ed2

Karl, D. M., Beversdorf, L., Björkman, K. M., Church, M. J., Martinez, A., and Delong, E. F. (2008). Aerobic Production of Methane in the Sea. *Nat. Geosci.* 1, 473–478. doi: 10.1038/ngeo234

Kirschke, S., Bousquet, P., Ciais, P., Saunois, M., Canadell, J. G., Dlugokencky, E. J., et al. (2013). Three Decades of Global Methane Sources and Sinks. *Nat. Geosci.* 6, 813–823. doi: 10.1038/ngeo1955

Middelburg, J. J., Nieuwenhuize, J., Iversen, N., Høgh, N., Dewilde, H., Helder, W., et al. (2002). Methane Distribution in European Tidal Estuaries. *Biogeochemistry* 59, 95–119. doi: 10.1023/A:1015515130419

Myllykangas, J.-P., Hietanen, S., and Jilbert, T. (2019). Legacy Effects of Eutrophication on Modern Methane Dynamics in a Boreal Estuary. *Estuaries Coasts* 43, 189–206. doi: 10.1007/s12237-019-00677-0

Nijman, T. P. A., Davidson, T. A., Weideveld, S. T. J., Audet, J., Esposito, C., Levi, E. E., et al. (2021). Warming and Eutrophication Interactively Drive Changes in the Methane-Oxidizing Community of Shallow Lakes. *ISME Commun.* 1, 32. doi: 10.1038/s43705-021-00026-y

Pai, S.-C., Gong, G.-C., and Liu, K.-K. (1993). Determination of Dissolved Oxygen in Seawater by Direct Spectrophotometry of Total Iodine. *Marine Chem.* 41, 343–351. doi: 10.1016/0304-4203(93)90266-Q

Pekel, J. F., Cottam, A., Gorelick, N., and Belward, A. S. (2016). High-Resolution Mapping of Global Surface Water and its Long-Term Changes. *Nature* 540, 418–422. doi: 10.1038/nature20584

Reeburgh, W. S. (2007). Oceanic Methane Biogeochemistry. *Chem. Rev.* 107, 486–513.

Rehder, G., Keir, R. S., Suess, E., and Pohlmann, T. (1998). The Multiple Sources and Patterns of Methane in North Sea Waters. *Aquat. Geochem.* 4, 403–427. doi: 10.1023/A:1009644600833

Repeta, D. J., Ferrón, S., Sosa, O. A., Johnson, C. G., Repeta, L. D., Acker, M., et al. (2016). Marine Methane Paradox Explained by Bacterial Degradation of Dissolved Organic Matter. *Nat. Geosci.* 9, 884–887. doi: 10.1038/ngeo2837

Rhee, T. S., Kettle, A. J., and Andreae, M. O. (2009). Methane and Nitrous Oxide Emissions From the Ocean: A Reassessment Using Basin-Wide Observations in the Atlantic. *J. Geophys Res.* 114, D12304. doi: 10.1029/2008JD011662

Shindell, D., Kuylenstierna, J. C., Vignati, E., van Dingenen, R., Amann, M., Klimont, Z., et al. (2012). Simultaneously Mitigating Near-Term Climate Change and Improving Human Health and Food Security. *Science* 335, 183–189. doi: 10.1126/science.1210026

Strickland, J. D. H., and Parsons, T. R. (1972). *A Practical Handbook of Seawater Analysis* (Ottawa, Canada: Fisheries Research Board of Canada), p. 310.

Sun, M. S., Zhang, G. L., Ma, X., Cao, X. P., Mao, X. Y., Li, J., et al. (2018). Dissolved Methane in the East China Sea: Distribution, Seasonal Variation and Emission. *Marine Chem.* 202, 12–26. doi: 10.1016/j.marchem.2018.03.001

Tilbrook, B. D., and Karl, D. M. (1994). Dissolved Methane Distributions, Sources, and Sinks in the Western Bransfield Strait, Antarctica. *J. Geophys. Res.* 99, 16383–16393. doi: 10.1029/94JC01043

Tseng, H.-C., Chen, C.-T. A., Borges, A. V., DelValls, T. A., and Chang, Y.-C. (2017). Methane in the South China Sea and the Western Philippine Sea. *Cont. Shelf Res.* 135, 23–34. doi: 10.1016/j.csr.2017.01.005

Tseng, H.-C., Newton, A., Gong, G.-C., and Lin, C.-C. (2021). Social–Environmental Analysis of Estuary Water Quality in a Populous Urban Area. *Elem: Sci. Anth.* 9, 1. doi: 10.1525/elementa.2020.00085

Upstill-Goddard, R. C., Barnes, J., Frost, T., Punshon, S., and Owens, N. J. P. (2000). Methane in the Southern North Sea: Low-Salinity Inputs, Estuarine Removal, and Atmospheric Flux. *Glob. Biogeochem. Cycles* 14, 1205–1217. doi: 10.1029/1999GB001236

Wanninkhof, R. (1992). Relationship Between Wind Speed and Gas Exchange Over the Ocean. *J. Geophys. Res.* 97, 7373–7382. doi: 10.1029/92JC00188

Wanninkhof, R. (2014). Relationship Between Wind Speed and Gas Exchange Over the Ocean Revisited. *Limnol. Oceanogr: Methods* 12, 351–362. doi: 10.4319/lom.2014.12.351

Weiss, R. F. (1981). Determinations of Carbon Dioxide and Methane by Dual Catalyst Flame Ionization Chromatography and Nitrous Oxide by Electron Capture Chromatography. *J. Chromatogr. Sci.* 19, 611–616. doi: 10.1093/chromsci/19.12.611

Wen, L.-S., Jiann, K.-T., and Liu, K.-K. (2008). Seasonal Variation and Flux of Dissolved Nutrients in the Danshuei Estuary, Taiwan: A Hypoxic Subtropical Mountain River. *Estuarine Coastal Shelf Sci.* 78, 694–704. doi: 10.1016/j.ecss.2008.02.011

Wiesenburg, D. A., and Norman, L. G. J. (1979). Equilibrium Solubilities of Methane,Carbon Monoxide, and Hydrogen in Water and Sea Water. *J. Chem. Eng. Dafa* 24, 356–360. doi: 10.1021/je60083a006

Yu, Z., Wang, D., Li, Y., Deng, H., Hu, B., Ye, M., et al. (2017). Carbon Dioxide and Methane Dynamics in a Human-Dominated Lowland Coastal River Network (Shanghai, China). *J. Geophys. Res.: Biogeosci.* 122, 1738–1758. doi: 10.1002/2017JG003798

Yvon-Durocher, G., Allen, A. P., Bastviken, D., Conrad, R., Gudasz, C., St-Pierre, A., et al. (2014). Methane Fluxes Show Consistent Temperature Dependence Across Microbial to Ecosystem Scales. *Nature* 507, 488–491. doi: 10.1038/nature13164

Zhang, G., Zhang, J., Liu, S., Ren, J., Xu, J., and Zhang, F. (2008). Methane in the Changjiang (Yangtze River) Estuary and its Adjacent Marine Area: Riverine Input, Sediment Release and Atmospheric Fluxes. *Biogeochemistry* 91, 71–84. doi: 10.1007/s10533-008-9259-7

Zhou, H., Yin, X., Yang, Q., Wang, H., Wu, Z., and Bao, S. (2009). Distribution, Source and Flux of Methane in the Western Pearl River Estuary and Northern South China Sea. *Marine Chem.* 117, 21–31. doi: 10.1016/j.marchem.2009.07.011

Zindler, C., Bracher, A., Marandino, C. A., Taylor, B., Torrecilla, E., Kock, A., et al. (2013). Sulphur Compounds, Methane, and Phytoplankton: Interactions Along a North–South Transit in the Western Pacific Ocean. *Biogeosciences* 10, 3297–3311. doi: 10.5194/bg-10-3297-2013

Conflict of Interest: The authors declare that the research was conducted in the absence of any commercial or financial relationships that could be construed as a potential conflict of interest.

Publisher's Note: All claims expressed in this article are solely those of the authors and do not necessarily represent those of their affiliated organizations, or those of the publisher, the editors and the reviewers. Any product that may be evaluated in this article, or claim that may be made by its manufacturer, is not guaranteed or endorsed by the publisher.

Copyright © 2022 Tseng, Lin, Pan, Han and Gong. This is an open-access article distributed under the terms of the Creative Commons Attribution License (CC BY). The use, distribution or reproduction in other forums is permitted, provided the original author(s) and the copyright owner(s) are credited and that the original publication in this journal is cited, in accordance with accepted academic practice. No use, distribution or reproduction is permitted which does not comply with these terms.

frontiers | Frontiers in Marine Science

ORIGINAL RESEARCH
published: 02 May 2022
doi: 10.3389/fmars.2022.842155

Elevated Nutrient Supply Caused by the Approaching Kuroshio to the Southern Coast of Japan

Gloria Silvana Durán Gómez and Takeyoshi Nagai*

Department of Ocean Sciences, Tokyo University of Marine Science and Technology, Minatoku, Japan

Although the Kuroshio Current has been well-known for being nutrient poor in its upper layers, it sustains a great biodiversity within its region, including the Kuroshio Extension. Previous studies reported that the Kuroshio carries a large amount of nutrients in its dark subsurface layers, yet, the mechanisms of how these nutrients are brought to sunlit layers remain unclear. In a previous observational study, it is shown that when the Kuroshio flows near the shelf break, very strong turbulence with dissipation rates of O (10^{-7} W kg $^{-1}$), caused by trapped near-inertial internal waves, leads to the generation of large diffusive nitrate fluxes of 1-10 mmol N m $^{-2}$ day $^{-1}$. Nevertheless, since these results were obtained from just one transect survey, questions remain, such as how long the enhanced turbulent diffusive nitrate flux extends downstream, and how the Kuroshio path modulations affect this nutrient injection. In this study, observed features were reproduced by using a high-resolution nested simulation coupled with a N_2PZD_2 ecosystem model. The results show that when the model Kuroshio flows closely to the coast, it hits a small bump in the upstream region of the Hyuganada Sea producing negative potential vorticity. At the same time, trapped near-inertial internal waves in a streak of lowered lowest internal wave frequencies are reproduced near the area with low PV values, generating strong vertical mixing similar to the observations. Since more nitrate is brought upward on the continental shelf when the Kuroshio approaches to the coast, the enhanced vertical mixing effectively diffuses up the nitrate from subsurface to surface layers at a rate of ~*O*(1 mmol N m $^{-2}$ day $^{-1}$) toward 50-100 km downstream along the Kuroshio. Further analyses on how the distance between the model Kuroshio and the southeastern coast of Kyushu affects the nutrient supply, suggest that when the Kuroshio flows closer to the coast, the internal wave kinetic energy, the nitrate concentration, its vertical gradients and vertical diffusive flux increase.

Keywords: Kuroshio, Hyuganada Sea, ROMS, continental shelf, turbulence, nutrient supply

OPEN ACCESS

Edited by:
Chin-Chang Hung, National Sun Yat-sen University, Taiwan

Reviewed by:
Terry Whitledge, Retired, Fairbanks, United States
Takahiro Tanaka, Japan Fisheries Research and Education Agency, Japan

****Correspondence:***
Gloria Silvana Durán Gómez
silvanadg20@hotmail.com

Specialty section:
This article was submitted to Coastal Ocean Processes, a section of the journal Frontiers in Marine Science

Received: *23 December 2021*
Accepted: *28 March 2022*
Published: *02 May 2022*

Citation:
Durán Gómez GS and Nagai T (2022) Elevated Nutrient Supply Caused by the Approaching Kuroshio to the Southern Coast of Japan. Front. Mar. Sci. 9:842155. doi: 10.3389/fmars.2022.842155

1 INTRODUCTION

The Kuroshio is a strong western boundary current of the North Pacific. It has been considered nutrient poor in its surface layers, that contradicts the implications that the Kuroshio regions accommodate a large variety of marine organisms, possessing the highest biodiversity of the world ocean (Saito, 2019). Several recent studies have reported that the Kuroshio carries a large amount of

nutrients in its deep layers that are transported downstream (Guo et al., 2012), similar to the Gulf Stream in the North Atlantic (Pelegrí and Csanady, 1991; Palter et al., 2011). The amounts of nutrients carried laterally along these nutrient streams are found to be increased by current mergers, e.g., between the Gulf Stream and other current branches (Palter and Lozier, 2008), and between the Kuroshio and its recirculation gyre (Guo et al., 2013). In addition to these along stream variations, several studies have pointed out that nutrient concentrations on the density surfaces are elevated along the Gulf Stream (Pelegrí et al., 1996; Palter and Lozier, 2008; Whitt, 2019) and the Kuroshio (Komatsu and Hiroe, 2019; Nagai et al., 2019), in comparison to those on the shore and offshore side of the streams. The mechanism of how these elevated nutrient concentrations are formed has been under debate. Pelegrí et al. (1996) speculated diapycnal mixing, caused by the geostrophic vertical shear, as a mechanism to bring up nutrients to shallow layers and form the elevated nutrient concentrations on the density surfaces, which then increases the nutrient lateral transport near the surface to the downstream. On the contrary, Palter and Lozier (2008) analyzed the historical hydrographic dataset and concluded that the elevated concentrations are advected laterally, maintaining the characteristics of the tropical origin, and that the advected transport is much greater than that caused by the diapycnal mixing processes (Whitt, 2019).

However, a recent numerical study showed that when the upstream Gulf Stream near the Bahamas Banks interacts with a topography on its anticyclonic side, it generates negative potential vorticity and associated forward energy cascade (Gula et al., 2016). Likewise, it has been reported that when the Kuroshio encounters topographic features, such as islands, seamounts and ridges, it can induce strong turbulence and elevated vertical mixing (Hasegawa et al., 2004; Chang et al., 2016; Nagai et al., 2017; Tsutsumi et al., 2017; Hasegawa, 2019; Nagai et al., 2021a; Tanaka et al., 2019). The enhanced mixing can modify the water masses in the surroundings, and diffuse tracers vertically including nutrients. Nagai et al. (2021b) reported that the elevated turbulence in the Kuroshio flowing over the Izu Ridge induces a large nutrient diffusive flux, accompanied by the subsurface increase in chlorophyll-a concentrations. Since the Kuroshio encounters topographic features in many other regions, the topography-induced diapycnal mixing within the Kuroshio could be the cause to supply a large amount of nutrients to the euphotic zone. If this is the case, the Kuroshio nutrient stream enriches not only its downstream region, but also the southern coast of Japan, sustaining the biological productivity over the continental shelf. Nevertheless, whether and how the subsurface nutrients can be injected in the regions of the continental shelf remain unclear. A previous observational study by Nagai et al. (2019) showed that in the Hyuganada Sea, southeast of Kyushu, turbulence caused by trapped near-inertial internal waves in the Kuroshio can diffuse up subsurface nutrients to sunlit surface layers. Since this previous study was conducted for only one transect survey, questions remain as to how long this enhanced turbulent diffusive nitrate flux extends downstream along the Kuroshio. Although several studies have pointed out that the Kuroshio variabilities, such as modulations of its path and strength, can affect the biological productivity and fish catches (Oey et al., 2018; Durán Gómez et al., 2020; Lizarbe Barreto et al., 2021), how these modulations may influence on the nutrient supply along the southern coast of Japan is still unknown.

In this study, we seek to complement by setting two working hypotheses: 1) a large amount of subsurface nitrate from the Kuroshio nutrient stream is brought upward when the Kuroshio approaches to the coast, leading to an increase in nitrate concentrations and its vertical gradient on the continental shelf; 2) anticyclonic vorticity and geostrophic vertical shear in the Kuroshio can cause the trapping of near-inertial internal waves, that induce strong turbulence and vertical mixing, thus, increasing the nitrate vertical diffusive flux. These inherent characteristics of the Kuroshio, the subsurface nutrient stream and the elevated mixing, may work together, leading to an efficient agent to supply nutrients, which could temporarily be modulated depending on how close the Kuroshio flows to the shelf break. To this end, a high-resolution nested numerical simulation, coupled with a N_2PZD_2 ecosystem model, is used to reproduce the Kuroshio, near-inertial internal waves and enhanced nitrate diffusive flux over the continental shelf. The objectives of this study are to elucidate how far the elevated nutrient supply persists downstream along the Kuroshio, and to understand how the elevated nutrient flux is related to the model Kuroshio path transitions in the region off east of Kyushu. Section 2 shows the methodology to reproduce the observations with a numerical model, and the equations for the parameters to examine the hypotheses. Section 3 presents the comparisons made between the numerical simulations and the observations taken onboard in November 2018 (Nagai et al., 2019), the analyses for the continuance of the elevated nitrate diffusive flux to the downstream, and the nutrient flux modulations due to the Kuroshio path variabilities. Discussions follow in Section 4, and lastly, conclusions are given in Section 5.

2 METHODOLOGY

2.1 Numerical Model

In this study, the Regional Oceanic Modeling System (ROMS) is used. The ROMS is an ocean circulation model developed for global and regional simulations, that solves incompressible hydrostatic primitive equations under the Boussinesq approximation with a so called s-coordinate vertical grid and a horizontal curvilinear grid (Shchepetkin and McWilliams, 2005). 4-level nested grids are used for the simulation, with a finest grid of ~500 m resolution, that is nested in the ~1.5 km resolution grid off Kyushu and Shikoku. The selected area for the finest grid is located within the ranges 30.9-32.6°N and 130.9-132.4°E.

A nitrogen based N_2PZD_2 ecosystem model, including nitrate, ammonium, phytoplankton, zooplankton, large and small detritus (Gruber et al., 2006; Nagai and Clayton, 2017), is coupled with a physical model to reproduce nitrate

distributions and its diffusive flux. The nested ecosystem simulation was started from model October year 8 with interpolated initial conditions taken from the coarse resolution (10-15 km) model outputs in the North Pacific. The COADS monthly climatology wind, heat and freshwater fluxes are forced at the surface (da Silva et al., 1994), and lateral boundary conditions for the coarse North Pacific model are given from Levitus climatology (Levitus, 1982). Bottom drag was modeled with the quadratic bottom friction with a drag coefficient of 0.004. The model vertical diffusivity K_v was parameterized with the K-Profile Parameterization (KPP) (Large et al., 1994), and the lateral Laplacian viscosity was parameterized using the Smagorinsky scheme in the finest grid (Smagorinsky, 1993). The bottom depths for these grids are generated using JODC 500-m mesh topography data (J-EGG500). Due to the lack of field observations in the study area, except for our high-resolution data obtained in November 2018, the validation of the ROMS results was made through comparisons with the available reanalysis data from COPERNICUS Marine Service (MERCATOR GLORYS12V1, http://www.mercator-ocean.fr). More details have been added in the Supplementary Material.

2.2 Potential Vorticity PV

For the vertical section obtained onboard in November 2018, two-dimensional PV_{2D} is computed neglecting gradients normal to the observation line as follows,

$$fPV_{2D} = \frac{1}{g}\left[f\left(f + \frac{\partial v_g}{\partial x_a}\right)\frac{\partial b}{\partial z} - f^2\left(\frac{\partial v_g}{\partial z}\right)^2\right] \quad (1)$$

where f is Coriolis parameter, V_g geostrophic velocity normal to the observation line, x_a the coordinate along the observation line, $b = -g\rho/\rho_o$ is buoyancy with ρ density, ρ_o reference density, and g gravitational acceleration.

On the other hand, three-dimensional PV is computed using the horizontal flow in the simulation according to the following form, neglecting the small vertical velocity,

$$PV = -\frac{1}{\rho}\left[-\frac{\partial v}{\partial z}\frac{\partial \rho}{\partial x} + \frac{\partial u}{\partial z}\frac{\partial \rho}{\partial y} + \left(f + \frac{\partial v}{\partial x} - \frac{\partial u}{\partial y}\right)\frac{\partial \rho}{\partial z}\right] \quad (2)$$

where u and v are zonal and meridional velocities, and x and y, respective coordinates with z vertical coordinate.

2.3 Non-geostrophic Shear

Assuming that density perturbations caused by the near-inertial waves are small, the non-geostrophic shears (u_z^a and v_z^a) are obtained by subtracting the geostrophic shear ($-b_y/f$ and b_x/f) from the total shear (u_z and v_z),

$$\begin{aligned}\frac{\partial u_a}{\partial z} &= \frac{\partial u}{\partial z} + \frac{1}{f}\frac{\partial b}{\partial y}\\ \frac{\partial v_a}{\partial z} &= \frac{\partial v}{\partial z} - \frac{1}{f}\frac{\partial b}{\partial x}.\end{aligned} \quad (3)$$

2.4 Internal Wave Kinetic Energy

Since the Kuroshio is a strong current, it can induce Doppler-shift to the model variables recorded on the Eulerian frame. With this strong current, the finest grid domain is too small to employ the Lagrangian temporal filter by using numerous passive particles to extract internal wave energy flux, avoiding the Doppler shift (e.g., Nagai et al., 2015). Instead, the non-geostrophic shear is used to extract the internal wave velocities and the kinetic energy without the Doppler smearing effects. First, the surface mixed layer, which is defined as the layer with a density difference within 0.001 kg m^{-3} from the surface, is excluded for the analysis. Second, the non-geostrophic shear (3) is demeaned and detrended vertically to reduce the influences from the subinertial submesoscale shear. Finally, the modified non-geostrophic shear is integrated vertically to obtain the internal wave velocity (u_{IW}, v_{IW}). The estimated internal wave velocity exhibits baroclinic wave structures with vertical phase transitions consistent with the internal waves. Then, the obtained horizontal velocity of internal waves is used to compute the internal wave kinetic energy, $IWKE = (u_{IW}^2 + v_{IW}^2)/2$.

2.5 The Lowest Internal Wave Frequency

The lowest internal wave frequency ω_{min} is computed using the vertical component of the relative vorticity $\zeta = v_x - u_y$, Coriolis parameter f, the geostrophic vertical shear (u_z^g, v_z^g), and the buoyancy frequency square $N^2 = db/dz$ as follows,

$$\omega_{min} = \sqrt{f(f+\zeta) - f^2\frac{\left(\frac{\partial u_g}{\partial z}\right)^2 + \left(\frac{\partial v_g}{\partial z}\right)^2}{N^2}}. \quad (4)$$

The geostrophic shear is obtained from model density horizontal gradient using the thermal-wind relation, $f\partial ug/\partial z = -\partial b/\partial y$, $f\partial vg/\partial z = \partial b/\partial x$.

2.6 Averaged Variables Over the Continental Shelf

To investigate how the approaching model Kuroshio path influences on the environment of the continental shelf, several variables are averaged over the shelf, such as nitrate concentration, nitrate vertical gradient, nitrate vertical diffusive flux, and IWKE. The continental shelf is defined as the area with model depths shallower than 200 m. The 200 m criterion is used since internal waves are allowed in the stratified layers, and appear only below the mixed layer depth (50-100 m), leaving a layer of 150 m depth for their propagation at most.

The nitrate diffusive flux F (mmol $m^{-2}s^{-1}$) is obtained using $F = K_v d\mathrm{Nut}/dz$, where Nut is the nitrate concentration (mmol m^{-3}), z vertical coordinate, dNut/dz vertical nitrate gradient, and K_v KPP vertical diffusivity (m^2s^{-1}). These nitrate related parameters are interpolated at 100 m depth, just above the nutrient stream core (σ_θ = 26-26.5 kg m^{-3}, Guo et al., 2012) where the water of high nitrate concentrations starts climbing up the slope when the Kuroshio flows closer to the coast (**Supplementary Animation Anime S1**).

Then, the nitrate parameters and IWKE are averaged zonally to construct the quantities over the continental shelf as a function of latitude and time. Along the latitudinal direction, a 2.5 km running average is performed for these zonally averaged parameters.

2.7 The Minimum Distance From the Shore

To investigate the influences of the Kuroshio path modulations on the IWKE, nitrate concentration, nitrate vertical gradient, and nitrate diffusive flux, the minimum distance between the Kuroshio and the coast as a function of latitude and time are computed. First, the model Kuroshio axis is defined by the contour of the sea surface height (SSH) at 0.2 m. The SSH = 0.2 m is selected because the fastest part of the Kuroshio is found to be aligned parallel to this contour on average, although it is sometimes misaligned due to effects of land and islands on the sea surface height gradients of the Kuroshio. Second, the coastline is determined excluding small bays with convoluted shoreline. Finally, the minimum distance to the Kuroshio is obtained at each point along the defined coastline.

2.8 Lagrangian Particle Tracking

To determine the frequency of the fluctuating internal wave velocity shear in the simulation, avoiding the Doppler effect, Lagrangian particles passive to three-dimensional flow are released in the finest grid model domain during December. The passive 3000 particles are released three times every 5 days from December 1st between 15 and 200 m depth, within the ranges of 131.1-131.45°E and 30.9-31.18°N in the upstream region. The vertical shear of zonal and meridional velocities is interpolated along the trajectories of each particle and written as hourly averages in the output file. The released particle trajectories are shown as an Animation In **Supplementary Animation Anime S2**.

3 RESULTS

3.1 Physical and Biological Conditions in the Hyuganada Sea

Sea surface temperature (SST) and sea surface height (SSH) satellite observations from Himawari-8 and AVISO (Archiving, Validation, and Interpretation of Satellite Oceanographic data), respectively, are obtained on November 25th, 2018, same period when observations were taken onboard by Nagai et al. (2019), to be compared with the model results (**Figure 1**). Besides, the simulation results on November 11th and December 20th are compared to contrast the different Kuroshio path states (**Figures 1B, C**). From these comparisons, it is found that the model results in December are more consistent with the satellite observations during the November 2018 cruise, since the model Kuroshio (defined at SSH = 0.2 m contour) flows northeastward off Kyushu, reaches the latitude 31.45°N, and sets a warm temperature boundary up to 24°C in front of the coast, similar to the observations. Slightly colder SST on the model December 20th (**Figure 1C**) than the satellite SST on November 25th (**Figure 1A**) is attributed to a more active wintertime cooling in late December. Simultaneously, December model nitrate distributions present a tongue of high concentration near the bottom that runs along the shoaled isopycnal toward the coast (**Figure 2A**). Although the detailed nitrate distribution is not perfectly reproduced by the model, the relation between the nitrate concentrations and the water density is consistent with the observations. For example, nitrate concentrations of $NO_3^- \sim 10 - 12\mu M$ and ~14 – 16μ M can be found along isopycnals σ_θ = 25.5 and 26 kg m^{-3}, respectively, for both in the observations and the model. The difference of nitrate distributions between the observations in November and the model December arises from the slightly different density distributions. Since the hydrographic vertical structures are rapidly changing, as shown in the supplementary animations (**Supplementary Animation Anime S1**), and observations took 8 hours to complete, the differences can be caused not only by spatial distribution mismatches but also by the temporal aliasing in the observations. The detailed comparisons of the ROMS results with the reanalysis given in the Supplementary Material (**Supplementary Figures S1–S8**) suggest that the hydrographic vertical structures are fairly well reproduced by ROMS as long as the Kuroshio flows similarly with respect to the coast.

On the contrary, the model Kuroshio in November flows away from the coast, being observed at the southern edge of the

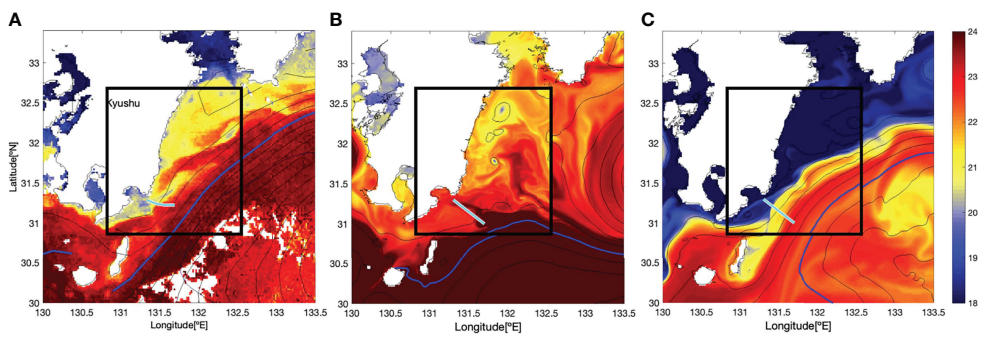

FIGURE 1 | Sea Surface Temperature °C for **(A)** satellite observation by Himawari-8 on Nov25th, 2018, and for the ROMS simulation on **(B)** November 11th and **(C)** December 20th. Thin black contours represent Sea Surface Height (SSH), and the Kuroshio axis is represented as the blue contour at SSH = 1.1 m for **(A)** the observation (COPERNICUS Marine Service) and at SSH = 0.2 m for **(B, C)** the simulations. Cyan lines represent where the vertical sections are computed, and black squares enclose the finest grid region of ROMS.

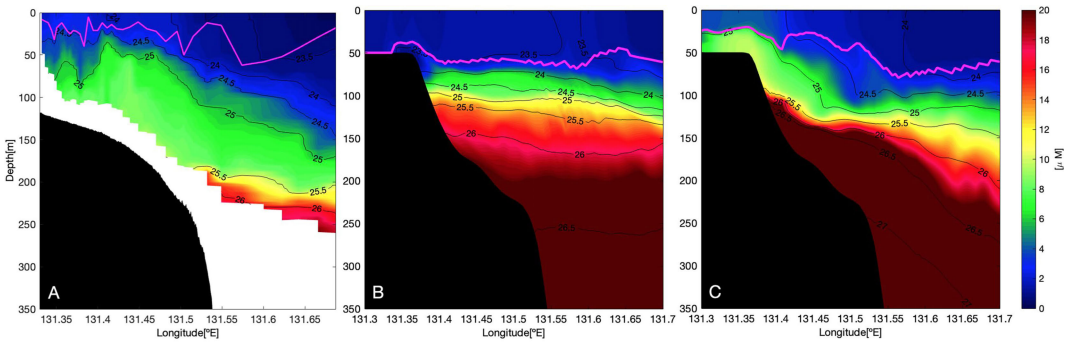

FIGURE 2 | Vertical sections, computed along the cyan line in **Figure 1**, of nitrate concentration (μM) for **(A)** *in-situ* data taken onboard in November 2018 (Nagai et al., 2019), for ROMS numerical simulation on **(B)** November 11th and **(C)** December 20th at hour 18:00. The black contours represent isopycnals, and the magenta line represents the mixed layer depth (MLD) where density difference is 0.125 kg m^{-3} from the surface. Black shapes near the bottom represent **(A)** acoustically detected bottom depth and **(B, C)** model topography.

finest model domain (inside the black square in **Figure 1**) at the position of 31.1°N, 131.8°E. The vertical section of the model density shows that less dense water ($\sigma_\theta < 24$ kg m^{-3}) is located at the surface layers, above 50 m depth, except near longitude 131.6°E, in which relatively dense water appears (**Figure 2**). Further, isopycnals are nearly flat below 50 m depth with the contours of $\sigma_\theta = 26$ kg m^{-3} and $\sigma_\theta = 26.5$ kg m^{-3} located at depths of 150 m and 270 m, respectively, suggesting that there is no frontal structure and nitrate rich water is kept in darker and deeper layers.

Note that the model bottom topography (black shape in **Figure 2B**) is shallower near the coast than the acoustically detected ones in the observations that is around 150 m depth (black shape in **Figure 2**), that likely blocks the model onshore flow. However, as shown in the **Supplementary Material** (**Supplementary Figures S9, S10**), the model topography near the coast is generally deeper by 10-50 m and smoother than the topographic source data (J-EGG500). This suggests that the contrast in the topography between the model and the acoustically detected one is due to high resolution lateral *in-situ* depth changes that are not resolved in J-EGG500 and does not represent the average difference between the model and the real topography, i.e., the model has much deeper and milder bottom slope compared to the real topography, which would allow more onshore flows rather than blocking them.

The mixed layer depth (MLD) across the Kuroshio during November 2018 observations, defined at the depth where the density differs 0.125 kg m^{-3} from the surface, is as shallow as ~30 m on the onshore side, and it deepens slightly offshore between longitudes 131.58-131.61 °E with a convex downward structure down to ~60 m (**Figure 2**). Similarly, the model MLD in December remains shallower on the onshore side (~50 m) than that on the offshore side from longitude 131.55°E, where the MLD deepens to ~100 m depth, with a convex downward structure centered at 131.6°E (**Figure 2**). Although the spatial patterns of the MLD in the observation and the model are consistent, the model MLD during December is roughly 50 m deeper than that in the observation. Yet, as it was explained previously, the December model nitrate concentration NO_3^- presents more similar distributions to the *in-situ* data with a high concentration tongue running over the slope, probably caused by the tilted pycnocline of the Kuroshio approaching to the coast for both observations and December model results. Below the model MLD, the nitrate concentrations are brought upward onshore side, resulting in higher concentrations between 50 and 100 m depth over the continental shelf.

To compare the model Kuroshio with the observations quantitatively, the mean distance between the Kuroshio axis and the coastline within the latitude range of 31.0-31.45°N is computed. This range is selected since the model Kuroshio in December (SSH = 0.2 m) flows away from the coast at latitude 31.45°N, as it is observed in the finest grid of the ROMS (inside the black square in **Figure 1C**). The computed mean distance to the Kuroshio is 92 km from the coastline. On the other hand, the distance obtained for the observations considers the Kuroshio axis as the contour at SSH = 1.1 m, since the SSH contour from satellite sea surface height AVISO data at this value is located within the highest SSH gradient band along the Kuroshio (**Supplementary Figure S11**). The calculated distance with respect to the coastline within the same latitude range is 93 km. The similarity in these distances and the SSH spatial patterns, between the observations in November and the model December, allows us to consider that the model December results are closer to the observed ones for further analyses.

However, even though both the observation and the model results present similar spatial distribution patterns for chlorophyll-a (**Figure 3**), with higher concentrations on the shore side in upper 50 m depth, the model chlorophyll-a overestimates the *in-situ* data by threefold.

3.2 Shear-Bands and Potential Vorticity in the Hyuganada Sea

To compare the model velocities with the observations, velocities are decomposed into along and across front components with respect to the mean Kuroshio Current direction for both the

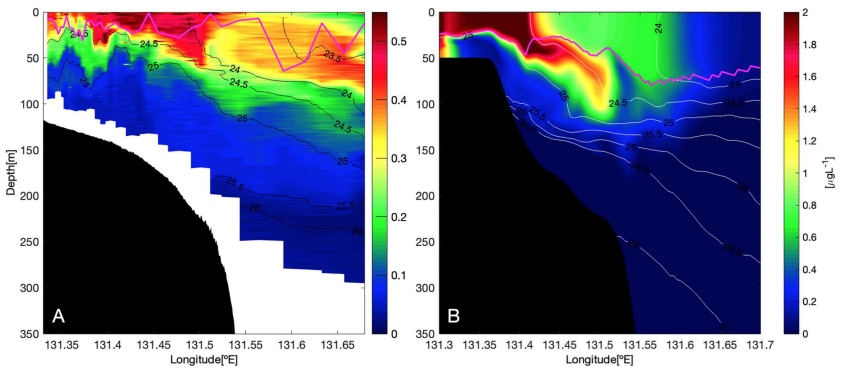

FIGURE 3 | Vertical sections, computed along the cyan line in **Figure 1**, of chlorophyll-a concentration (μg L^{-1}) for **(A)** *in-situ* data taken onboard in November 2018 (Nagai et al., 2019), and for **(B)** ROMS numerical simulation on December 20th at hour 18:00. The black and white contours in A and B, respectively, represent isopycnals and the magenta line represents the MLD.

observations and the model (**Figure 4**). A core of large positive along-frontal velocities are directed northeastward above 120 m depth in the observation (**Figure 4A**), while the fast current of ~1 ms^{-1} in the model reaches down to 250 m depth on the offshore side from the longitude 131.63°E, associated with a deeper baroclinic isopycnal structure (**Figure 4B**). Additionally, the observations suggest the presence of a counter current near the sloping bottom of the continental shelf, with negative values of the along-front current velocity within the depth ranges of 50-125 m and 175-250 m. Although this counter current is also seen in the model but with a deeper extent, the model across-front current presents larger spatial structures than the observations with offshore-ward and onshore-ward currents separated around 131.6°E. Both the model and the observations show banded structures of alternating positive and negative signs, that are suggestive of internal waves (**Figures 4C, D**). Thus, the model velocity fields are in fairly good agreement with the observations.

From the observation data, two-dimensional potential vorticity (PV_{2D}) is computed using (1), with measured density and the velocity across the Kuroshio (**Figure 5A**). Note, however, that as the geostrophic flow with the level of no motion at 300 m depth at most is not reliable, the ADCP lateral velocity gradient is used for the geostrophic lateral velocity shear, instead. Negative values of PV_{2D} appear on the core of the along-frontal flow in the upper 75 m depth

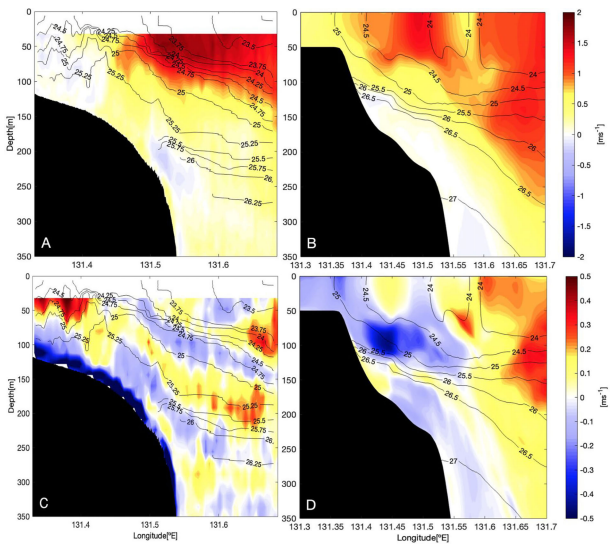

FIGURE 4 | Vertical sections of **(A, B)** along and **(C, D)** across-frontal velocities (ms^{-1}). **(A, C)** are from *in-situ* observations taken onboard in November 2018 (Nagai et al., 2019); **(B, D)** are from ROMS numerical simulation on December 20th at hour 08:00. Positive velocity indicates the flow toward the Kuroshio downstream in **(A, B)** and toward offshore in **(C, D)**. The black contours represent isopycnals. Note there are marked differences in the density structures at 50-100 m between isopycnals σ_θ = 24.5 and 25 kg m^{-3} after 10 hours that are shown in **Figure 3**, illustrating how rapidly the hydrographic structures change over time.

at longitude 131.55°E. These negative PV_{2D} values coincide with intense turbulent kinetic energy (TKE) dissipation rates (**Figure 5B**), suggesting that submesoscale inertial and symmetric instability could be the cause of the strong turbulence over the shelf. It should be noted that these negative values are also found in some other regions, such as around 50 m depth at longitude 131.4°E; however, since these locations are in well-stratified layers without large TKE dissipation rates, it is suspected that the missing nonmeasurable along-frontal gradients produce these erroneous negative values. Those neglected gradients in the two-dimensional assumption are probably caused by internal waves.

On the other hand, three-dimensional PV is computed using (2) in the numerical model. The plane view of the model PV, interpolated at 100 m depth, shows its highest values of $4 \times 10^{-9} m^{-1} s^{-1}$ along the cyclonic side of the model Kuroshio axis (the blue contour at SSH = 0.2 m), which extends closely to the coast. More importantly, the northeastward flowing model Kuroshio generates negative PV at the shallow bump in the upstream region, located within the range of 30.9-31.4°N, 131.1-131.5°E, forming a streak of low PV in the southwestern region of the domain (**Figure 6A**). The vertical section of the model PV presents large positive values along the pycnocline, while the negative PV values are above the pycnocline at 131.55°E, similar to the observation (**Figures 6B**, **5A**). Furthermore, banded shear with positive and negative signs along the tilted isopycnals of the Kuroshio front are reproduced by the model, presenting larger amplitudes over the continental shelf (**Figure 6C**). The shear banding nearly along density surfaces is suggestive of propagating near-inertial internal waves, which can be trapped within the Kuroshio by its large anticyclonic vorticity and geostrophic vertical shear (Whitt and Thomas, 2013). In addition, the negative PV, accompanied by sharp lateral density gradient, can induce submesoscale instability, such as inertial and symmetric instability, followed by secondary Kelvin-Helmholtz (K-H) instability and strong turbulence (Molemaker et al., 2015; Gula et al., 2016; Nagai et al., 2021a), although these instabilities are not fully resolved in the present simulation of 500-m resolution.

3.3 Internal Waves and Nutrient Flux

Aside from the similarity of the nitrate tongue in the model December result and in the observations, which extends from dark subsurface layers toward upper layers in the onshore region (**Figures 2A, C**), elevated subsurface nitrate diffusive flux also appears within the density range of σ_θ = 24.5-26 kg m^{-3}, that is consistent with the observations (**Figure 7**). Since the core of the model Kuroshio nutrient stream is found at σ_θ= 26-26.5 kg m^{-3} (**Supplementary Animation Anime S1**), as it has been found by Guo et al. (2012), the elevated diffusive flux could inject nitrate from the upper part of the nutrient stream to shallower layers. However, the isopycnal σ_θ = 26 kg m^{-3} is found at approximately 50 m deeper in the observation than the simulation because of a much thicker pycnostad of σ_θ=25-25.5 kg m^{-3} in the observations, probably caused by tidal mixing and/or the mixing induced by the Kuroshio intrusion in the upstream region. Consequently, the isopycnal σ_θ = 26.5 kg m^{-3} cannot be seen in the observations (**Figure 7A**), since its depth is too close to the bottom or exceeds the tow-yo instrument reachable depth. Although the depths of denser water than σ_θ = 25.5 kg m^{-3} in the model are approximately 50 m shallower than the observations, the large nitrate diffusive flux of 1-10 mmol $m^{-2} day^{-1}$ is found within the density range of 24.5-26 kg m^{-3}, similar to the observation, demonstrating that the model does capture the elevated diffusive nitrate flux from the upper core of the Kuroshio nutrient stream.

The generation of negative PV on the slope of the shallow bump in the upstream region, revealed by the observation and the model (**Figures 5A**, **6A**), implies that the observed intense turbulence can be attributed to secondary K-H instability associated with inertial and symmetric instability. Nonetheless, Nagai et al. (2019) interpreted that the strong turbulence and associated elevated nitrate diffusive flux are caused by trapped near-inertial internal waves within the Kuroshio. To elucidate whether trapped near-inertial waves influence on the nitrate flux, the model internal wave kinetic energy (IWKE) is investigated. In the region of the latitudes 31-31.5°N, the computed IWKE shows two bands of high values that form a V-shaped

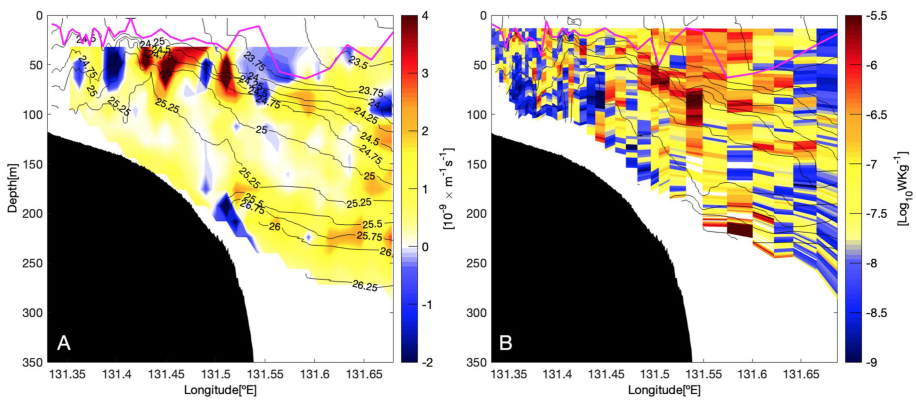

FIGURE 5 | Observations taken onboard in November 2018 (Nagai et al., 2019) for **(A)** two-dimensional potential vorticity (1) and **(B)** turbulent kinetic energy (TKE) dissipation rate (WKg^{-1}). The black contours represent isopycnals and the magenta line represents the MLD.

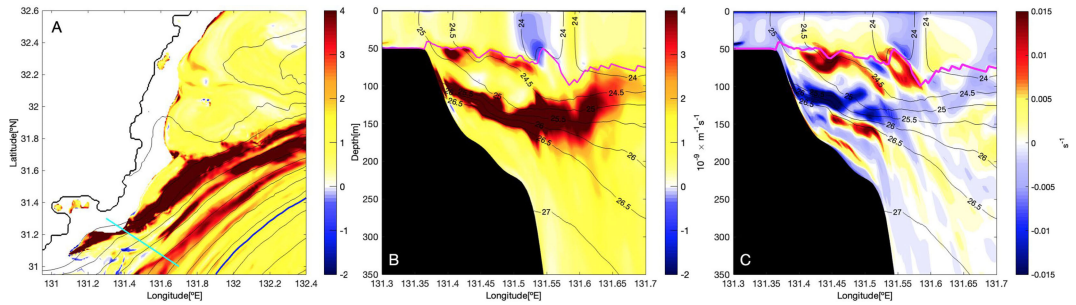

FIGURE 6 | Potential vorticity and vertical shear from the simulation on December 20th at hour 08:00 for **(A)** plane view of potential vorticity (2) interpolated at 100 m depth, vertical sections computed along the cyan line in **(A)** for **(B)** potential vorticity ($m^{-1}s^{-1}$) and **(C)** zonal shear (s^{-1}). Blue contour in **(A)** represents the model Kuroshio axis at SSH = 0.2 m, and magenta line in **(B, C)** is the MLD.

distribution (**Figure 8A**). One of these branches runs offshore region, while the other one spreads closer to the coast. The latter one coincides with a narrow band of lowered lowest internal wave frequency ω_{min} (4), suggesting that these internal waves are near their minimum frequencies and they may have gotten trapped in the region with lowered ω_{min} (**Figure 8B**). It should be noted that the high IWKE coastal branch goes through the region where the vertical sections have been shown previously in **Figures 2–4** and **6**, **7**.

Regions of high IWKE with relatively high ω_{min}, especially in the offshore region, are found probably because internal waves could have broadband frequencies, but they are still near the local ω_{min}, which varies spatially because of the geostrophic shear. For instance, high IWKE regions with $\omega_{min}/f \sim 1$, surrounded by $\omega_{min}/f > 1.1$, can still be attributed to trapped internal waves with super-inertial frequencies, yet these frequencies are still near the lowest local internal wave frequency (Whitt et al., 2018). These trapped near-lowest-frequency internal waves, in a region with lowered ω_{min}, could induce strong turbulence caused by their large amplitude vertical shear with high vertical wavenumbers. Lastly, the model diffusive NO_3^- flux clearly shows large values of O(1 mmol $m^{-2}day^{-1}$) that persist downstream over ~100 km along the Kuroshio (**Figure 8C**). This band of elevated nitrate diffusive flux is found near and within the region of high IWKE band and lowered ω_{min}, that is close to the coast. Likewise, there is an even larger nitrate diffusive flux O(10 mmol $m^{-2}day^{-1}$), which can be clearly seen in the upstream region where the Kuroshio flows over the shallow bump, that coincides with the locations of negative and near zero PV values (**Figure 6A**). From the December model results, it has been shown that the approaching Kuroshio to the coast leads to generations of low and negative PV and to the near-lowest-frequency internal wave trapping, which in turn elevate the nitrate diffusive flux. This simulated nitrate diffusive flux of 1-10 mmol $m^{-2}day^{-1}$ over the tilted thermocline of the Kuroshio, within 50-120 m depth, is qualitatively and quantitatively consistent with the observations, whereas the elevated flux above the model mixed layer depth is inconsistent with the observations (**Figures 7A, B**).

3.4 Temporal Changes of Internal Waves and Nitrate Flux Caused by the Kuroshio Path Variability

Although observations made by Nagai et al. (2019) revealed that the elevated nitrate diffusive flux occurs when the Kuroshio flows

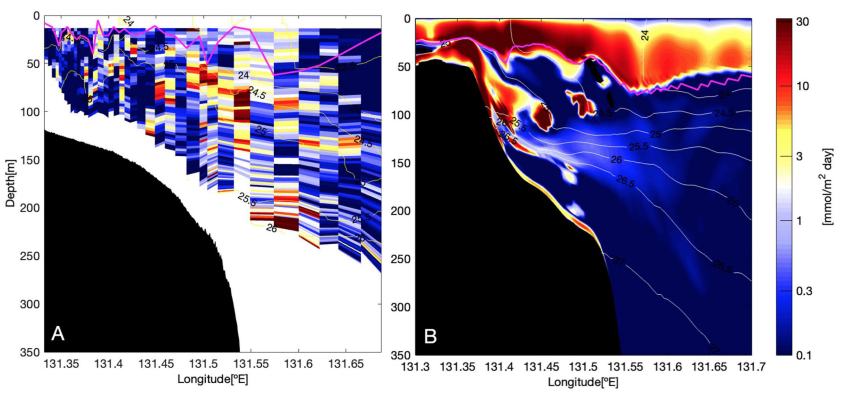

FIGURE 7 | Vertical sections of nitrate diffusive flux (mmol $m^{-2}day^{-1}$) for **(A)** *in-situ* data in November 2018 (Nagai et al., 2019) and for **(B)** numerical simulation on December 20th at hour 18:00. Magenta line represents the MLD.

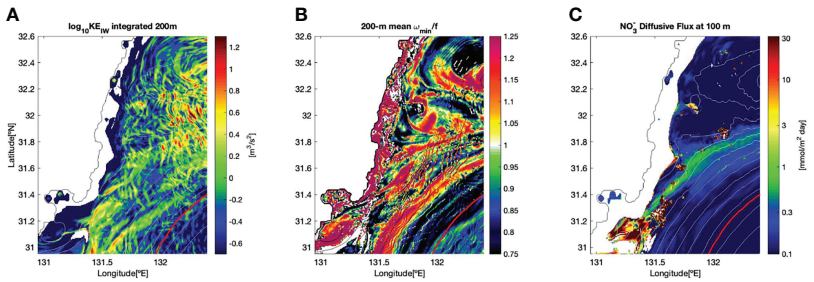

FIGURE 8 | Plane views on December 20th at hour 18:00 of **(A)** internal wave kinetic energy integrated over 200 m depth (m^3s^{-2}), **(B)** the minimum internal wave frequency divided by Coriolis parameter ωmin/f averaged within upper 200 m, and **(C)** nitrate diffusive flux (mmol $m^{-2}day^{-1}$) interpolated at 100 m depth. Red line represents the Kuroshio axis at SSH = 0.2 m.

close to the coast, as the observations were conducted just once, it remains unclear how the elevated mixing and the nitrate flux are modulated by the Kuroshio path variations. To analyze these temporal variations, the averaged IWKE and nitrate flux over the continental shelf are computed as a function of latitude and time (**Figures 9**, **10**). The integrated IWKE over 200 m depth on the continental shelf presents high values in the upstream latitudes from the end of October to the beginning of November. Then, low IWKE values appear in all through November, that are followed by an increase from the beginning of December. After the IWKE decreases from early-middle December, an increase is clearly seen toward the downstream, reaching up to 31.8°N, to the end of December. In parallel, the averaged nitrate flux at 100 m depth presents an increasing trend from the end of November through December (**Figure 10C**). The averaged NO_3^- concentration shows a first moderate increase in the second half of November, up to ~O(1μM), but it does not extend further north. In contrast, from the beginning of December high NO_3^- concentrations of ~O(10 μM) extend along the coast getting as far as latitude 32°N. Right before the start of this increase, the vertical gradient of nitrate concentration is intensified, which is accompanied by an increase of nitrate diffusive flux that reaches values of O(10 mmol $m^{-2}day^{-1}$).

The minimum distance between the coast and the model Kuroshio (SSH = 0.2 m) is found to be shortened more frequently in December (**Figure 11**). While the *in-situ* observations are conducted during November when the Kuroshio flows relatively close to the coast, the model Kuroshio in November presents an opposite figure by flowing away from the coast. Even though the model distance is very small (~30 km) at the beginning of November, it is limited only for the lower latitude range, presenting larger distances of 140 km in the downstream latitudes. The minimum distance shows gradual decreases from the middle to the end of November. It is in this period when the averaged nitrate concentration over the continental shelf shows a moderate increase (**Figure 10A**). After

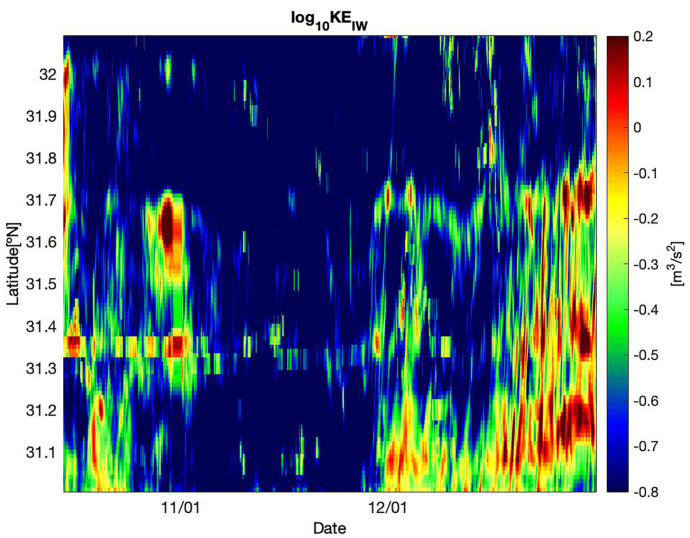

FIGURE 9 | Hovmoeller plot of internal wave kinetic energy integrated over 200 m depth (m^3s^{-2}) and averaged zonally over the continental shelf, where depth is less than 200 m depth, as a function of latitude and time.

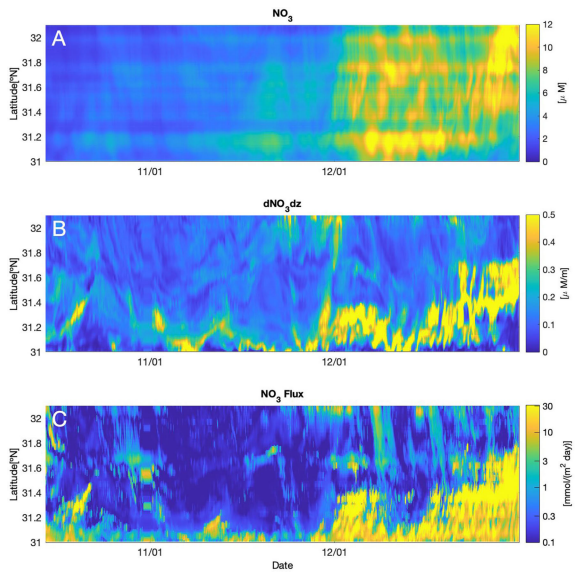

FIGURE 10 | Hovmoeller plot of **(A)** nitrate concentration (μM), **(B)** nitrate vertical gradient (μMm^{-1}) and **(C)** nitrate diffusive flux (mmol $m^{-2}day^{-1}$) interpolated at 100 m depth and averaged zonally over the continental shelf, where depth is less than 200 m depth, as a function of latitude and time.

this gradual decrease in the minimum distance, it drops abruptly from the upstream to the downstream in the beginning of December, presenting values less than 60 km at latitude 31.4°N and less than 120 km at latitude 32°N. In response to this decrease of the minimum distance in a wider latitude range caused by the approaching Kuroshio to the coast, the nitrate concentration and its diffusive flux increase in the beginning of December in comparison to those in November (**Figures 10A, C**). In the mid-December, the minimum distance increases again and it is accompanied by a decrease of the nitrate vertical gradient and the nitrate diffusive flux (**Figures 10B, C**). Yet, in the end of December, the model Kuroshio approaches to the coast once more, reducing the minimum distance that is again accompanied by increases of all these nitrate related variables (**Figures 10**, **11**).

Interestingly, the IWKE is also inversely proportional to the minimum distance, presenting larger values when shorter distances appear at the end of October, at the beginning of December, and from the middle to the end of December (**Figure 9**). These results suggest that enhanced diffusive nitrate flux is caused by the approaching Kuroshio to the coast, which leads to an increase in the nitrate concentration, its vertical gradient, and in the IWKE followed by elevated vertical mixing. It is noteworthy that the increase in nitrate concentration cannot be simply attributed to a seasonal mixed layer deepening since the model monthly mean MLDs for both months remain shallower than 100 m depth (**Figure 12**). As in **Figures 2C** and **3B**, the December MLD is shallower near the coast with a band of relatively deeper MLD on the northwestern side of the model Kuroshio axis (magenta line in **Figure 12B**). The latter deep MLD band corresponds to the convex downward MLD found in the vertical section of the model December (**Figure 3B**).

4 DISCUSSION

A number of previous studies have shown that when the Kuroshio bumps into topographic features, strong turbulence and vertical mixing are induced (Nagai et al., 2017; Tsutsumi et al., 2017; Hasegawa, 2019; Nagai et al., 2019; Nagai et al., 2021a). Besides, a recent high-resolution numerical study conducted by Gula et al. (2016) demonstrated that when the Gulf Stream interacts with a topography, it generates negative PV that leads to inertial instability. The results in the present study show that when the model Kuroshio approaches to the coast, in the Hyuganada Sea, it leads to a large nitrate diffusive flux of 1-10

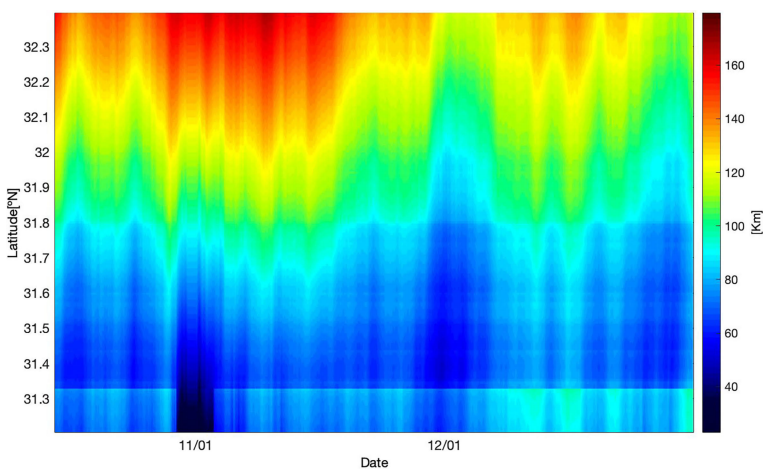

FIGURE 11 | Hovmoeller plot of the minimum distance between the eastern coast of Kyushu and the model Kuroshio axis, defined as the contour of SSH = 0.2 m, as a function of latitude and time.

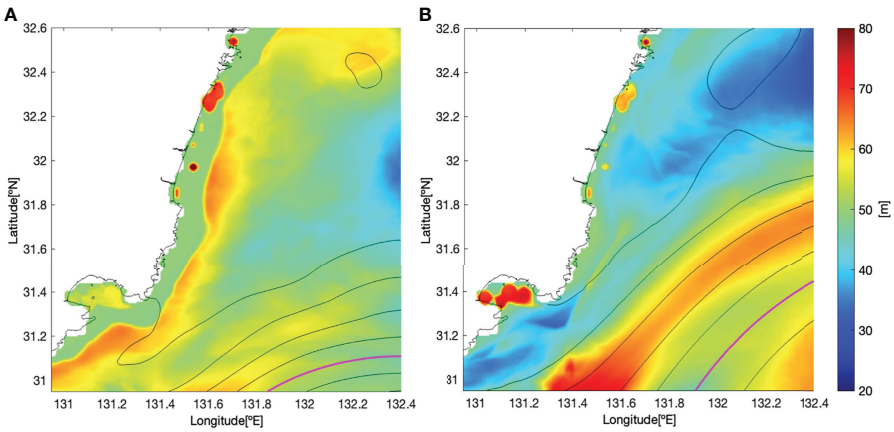

FIGURE 12 | Monthly averaged model mixed layer depth (m), where the density difference is 0.125 kg m^{-3} from the surface, for **(A)** November and **(B)** December. Black contours represent monthly mean SSH and magenta line represents the monthly mean model Kuroshio axis at SSH = 0.2 m.

mmol m^{-2}day^{-1} by flowing over a bump located in the upstream region of the model domain. The most intense nitrate diffusive flux of O(10 mmol m^{-2}day^{-1}) occurs in the vicinity of negative PV water generated on the northwestern slope of the bump. The large flux of O(1 mmol m^{-2}day^{-1}) continues further downstream over 100 km along the Kuroshio in a narrow band of lowered $\omega_{\min}$ with high IWKE. Although the resolution of the numerical model in the present study is not fine enough to fully resolve submesoscale instabilities, negative PV would correspond to a small Richardson number. This can be illustrated with the two-dimensional PV after rewriting it with the geostrophic shear as it has been shown in (1). When PV_{2D} is negative, the following condition needs to be satisfied for the geostrophic Richardson number (Thomas et al., 2013; Tandon and Nagai, 2019),

$$Ri_g = \frac{\frac{\partial b}{\partial z}}{\left(\frac{\partial v_g}{\partial z}\right)^2} < \frac{f}{\left(\frac{\partial v_g}{\partial x_a} + f\right)} \tag{5}$$

Considering that the vertical component of relative vorticity can only be smaller or equivalent to f in magnitude, the negative PV_{2D} corresponds to a small geostrophic Richardson number $Ri_g <$ O(1). Accordingly, the negative PV generated in the simulation leads to a large eddy diffusivity by using the interior KPP scheme (Large et al., 1994), which depends on the gradient Richardson number. Although the amplitude of the enhanced diffusivity may not be accurate, it can mimic the enhanced vertical tracer mixing caused by the generation of negative PV.

The disturbances in the geostrophic flows, including internal lee waves and turbulence produced by these currents themselves, e.g., by flowing over a bump, can result in inertial oscillation (Nikurashin and Ferrari, 2011; Wenegrat et al., 2020). Then, the near-inertial internal waves can propagate in the stratified layers above and below. It should be noted that the positive but low PV values, generated over the slope of the bump, can allow internal waves and lower their minimum frequency, ω_{min}, that may trap the near-inertial internal waves. This can be shown by rewriting the ω_{min} with the geostrophic Richardson number,

$$\omega_{min} = \sqrt{f(f+\zeta) - f^2 Ri_g^{-1}} \tag{6}$$

Because of low PV corresponds to a small geostrophic Richardson number (5), the magnitude of the second term of (6) becomes larger with a smaller Ri_g, which in turn reduces the ω_{min}. Moreover, lateral shear caused by the flow separation behind the bump can induce relative vorticity with both signs, being the negative relative vorticity on the northwestern slope of the bump able to lower the ω_{min} as well. Correspondingly, the low PV generation caused by the geostrophic current, the Kuroshio flowing over topographic features, leads to an intense vertical diffusive flux of nitrate not only through the submesoscale instability, but also by confining generated/propagating near-inertial internal waves. These tightly connected mixing mechanisms, associated with low PV, could make the lee sides of topographic obstacles to geostrophic currents as very efficient nutrient injection hotspots.

As it is shown in **Figure 8B**, relatively large internal wave kinetic energy (IWKE), located in a confined thin layer of the lowered ω_{min} near the coast, would suggest the presence of trapped near-inertial waves within a region of strong geostrophic lateral and vertical shear (Kunze, 1985; Whitt and Thomas, 2013), which may enhance local mixing (Kunze et al., 1995; Li et al., 2019). The vertical section of the model vertical shear shows large amplitude banded shear structures roughly along the isopycnals in the tilted Kuroshio thermocline, when the model Kuroshio approaches the coast (**Figure 6C**), supporting the above explanations that the banded shear in the model is caused by near-inertial internal waves (Rainville and Pinkel, 2004; Nagai et al., 2017). To determine the frequencies of these waves in a strong current avoiding the Doppler-shift, passive 3000 Lagrangian particles were released three times into the model Kuroshio every 5 days from December 1st (**Supplementary Animation Anime S2**). The peaks in the obtained mean Lagrangian frequency spectra of zonal and meridional shear appear near near–inertial frequency, $f/2\pi$, suggesting that vertical shear in the model is mostly associated with near-inertial internal waves (**Figure 13**). However, the peaks appear in a little wide

wavenumber range, suggesting that the modulations of the lowest internal wave frequency ω_{min} are caused by the geostrophic shear. When there is strong anticyclonic background vorticity and/or vertical geostrophic shear, the ω_{min} can be modified, decreasing the lower-frequency bound for internal waves (Mooers, 1975; Kunze, 1985; Li et al., 2019). Due to this modification, waves with a frequency of ω_{min} can propagate freely in regions where the ω_{min} has been lowered further. At the same time, they can not propagate into other regions where the local ω_{min} is higher than the wave frequencies. Thus, when they are bounded by a higher ω_{min} wall, these near-inertial internal waves get trapped. The trapped waves could work as mixers, by inducing turbulence (Kunze et al., 1995), resulting in elevated nitrate diffusive flux from subsurface layers to shallow layers along the Kuroshio and increasing the biological production (Nagai et al., 2017; Kobari et al., 2020).

As shown in the temporal variations over the continental shelf (**Figures 9**, **10**), when the model Kuroshio approaches to the coast in December, the IWKE, the nitrate concentration, and its vertical gradient show increasing trends, accompanied by the intensification of the nitrate diffusive flux to 1-10 mmol $m^{-2}day^{-1}$. **Supplementary Animation Anime S1** illustrates that the Kuroshio approach to the coast during the model December is indeed accompanied by approach of the subsurface nutrient stream core. Therefore, the approaching Kuroshio and its subsurface nutrient stream to the coast provide a very efficient nutrient supply route to the continental shelf, associated with the combination of the onshore nutrient advection, enhanced vertical gradient of nutrient concentrations, and elevated vertical mixing caused by the submesoscale instability and trapped near-inertial internal waves, which are associated with low PV.

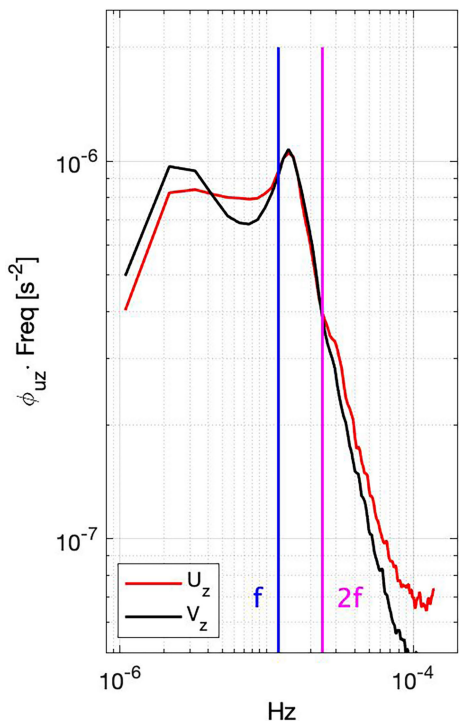

FIGURE 13 | Mean Lagrangian shear spectra for (black) meridional and (red) zonal velocity shear. The vertical lines (blue and magenta) indicate the range between *f* and 2*f*, where *f* is Coriolis frequency. Note that spectra is in variance preserved form (s^{-2}). The 1835 particles out of 9000, with mean speeds more than 0.45 m s^{-1} and last more than 58 hours in the nested model domain, are chosen to compute the mean spectra.

On the other hand, it was shown that the model chlorophyll-a was overestimated compared to the observations by threefold on the shore side (**Figure 3**). This overestimation could be due to the use of a single phytoplankton functional group in the model. As it is explained by Gruber et al. (2006), one of the deficiencies of the modeled chlorophyll-a is its overestimation in the eutrophic nearshore regions. And, since the Kuroshio regions are often dominated by small size plankton communities (Clayton et al., 2014; Endo and Suzuki, 2019), the model carbon to chlorophyll-a ratio is most likely underestimated in the offshore region. Moreover, as nitrate and chlorophyll-a are not conservative parameters, the fast biogeochemical response can easily induce these differences in the chlorophyll-a concentrations. For example, the ecosystem model in the present study may not be able to reproduce the rapid zooplankton grazing on phytoplankton in the oligotrophic environment (Kobari et al., 2020), that can induce the chlorophyll-a overestimation on the shore side. In addition, the model isopycnal of σ_θ = 25 kg m^{-3} outcrops on the shore side, accompanied by water of relatively high nitrate concentration ($NO_3^- \sim 6-8\mu M$, **Figure 2C**), whereas in the observation it lies below 50 m depth, keeping the nitrate concentrations near the surface relatively low (**Figure 2A**). The model MLD on December 20th is roughly 50 m deeper than that of the observations during November 2018. This deeper MLD, caused by more active entrainment and deepening of the MLD during model December than that of the observation in November 2018, could explain the reason of denser water outcropping in the model as well as the large model diffusive nitrate flux within the mixed layer, which is not seen in the observations (**Figure 7**). Thus, the more active MLD entrainment of denser and nutrient rich water to the surface layers in the model December could also be one of the reasons for the overestimated model chlorophyll-a concentrations.

Although this study is focused on how the submesoscale instability and trapped near-inertial waves influence on the vertical mixing, it should be noted that other processes can also occur simultaneously and have some effects on the mixing. Previous studies reported that the formation and propagation of a small cyclonic eddy in the southern region of Kyushu induce a small meander of the Kuroshio, that may trigger the Kuroshio Large Meander (KLM). It is speculated that the cyclonic eddy advects the subsurface nitrate-rich-water downstream to the trough of the meander, leading to an increase in surface phytoplankton (Lizarbe Barreto et al., 2021), while the southwestward returning flow along the coast can produce strong turbulence above the topographic features. If the cyclonic eddy is present between the Kuroshio and the coast, the nutrient diffusive flux could be even larger since shoaled nutrients at the center of the cyclonic eddy are more susceptible

to the surface mixing processes. In this manner, when the cyclonic eddy is present, our results that show the enhanced nutrient flux with a shorter minimum distance between the Kuroshio and the coast would not be applicable. Moreover, Li et al. (2018) showed that the large amplitude nonlinear internal waves generated from the Luzon Strait in South China Sea induce diffusive nitrate flux of 0.635-2.54 mmol $m^{-2}day^{-1}$, which is in similar order of magnitude of the flux found in this study. Recent studies have also pointed out that the turbulent mixing in the Kuroshio over the topographic features is more consistent with the shear instability caused by large amplitude high vertical modes nonlinear internal waves of wavelengths ~100 m in proximity to the seamounts (Tsutsumi et al., 2017; Takahashi et al., 2022). These large amplitude nonlinear internal waves can neither be fully resolved nor well parameterized in the present numerical model, suggesting that the model diffusive flux could be most likely underestimated. Our analyses in the present study are limited only to the simulation period, in which the Kuroshio flows close to or away from the coast without a propagating cyclonic eddy. Further, the model resolution and the KPP parameterization do not allow highly nonlinear internal wave induced mixing processes. In this regard, to clarify the robustness of the results in the present study, analyses of the influences of the Kuroshio on the continental shelf with the presence of the small cyclonic meander and the effects of highly nonlinear internal wave phenomena should be addressed by using models with higher resolutions and proper internal wave mixing parameterizations as future investigations.

5 CONCLUSIONS

In this study, a numerical simulation was conducted to reproduce previously observed nitrate supply processes through vertical mixing, which are considered to be caused by trapped near-inertial internal waves within the Kuroshio in the Hyuganada Sea, southeast of Kyushu. Our focus is to elucidate how far the elevated nutrient supply persists downstream along the Kuroshio, and to understand how the elevated nutrient flux is related to the model Kuroshio path transitions.

Based on the simulation results, it is found that when the model Kuroshio approaches to the coast of Kyushu, it encounters a shallow bump at the southwestern region of the Hyuganada Sea, generating low and negative PV values over the slope. The negative PV, which corresponds to a low Richardson number, leads to an intense model diffusive nitrate flux. On top of that, the topography-induced disturbances seem to produce near-inertial waves, which get trapped in a streak of lowered lowest internal wave frequency ω_{min} due to the strong anticyclonic vorticity field and the large vertical shear created in the lee side of the bump. These trapped near-inertial internal waves enhance the eddy diffusivity within this streak of lowered ω_{min}. Simultaneously, during this approach, the Kuroshio brings a large amount of nitrate in its subsurface layer, increasing the nitrate vertical gradients, thus, leading to a higher potential for the diffusive flux. Ultimately, the enhanced diffusivity, caused by the negative PV and the trapped near-inertial internal waves, elevates the nitrate diffusive flux from subsurface to shallow layers, providing a very efficient route to supply subsurface nutrients from the upper core of the Kuroshio nutrient stream over the continental shelf. While the intense nitrate diffusive flux of O(10 mmol m^{-2} day^{-1}) is limited only near the region of negative PV in the upstream region of the model domain, the large diffusive flux of O(1 mmol m^{-2} day^{-1}) extends downstream over ~ 100 km along the Kuroshio.

Although the Kuroshio Current has been well-known for being nutrient poor, the high nutrient concentration located in its subsurface layers can be the reason for its major biodiversity. By elevating the nutrient diffusive flux associated with submesoscale instabilities and the trapping of generated/propagating near-inertial internal waves in the vicinity of the topographic features, bringing up these subsurface nutrients to surface layers is considered to be a very important mechanism which consists of co-working multiscale mixing processes. Along its path, the Kuroshio is known to flow through a great deal of topographic features, such as I-Lan Ridge east of Taiwan, seamounts in the Tokara Strait, and the islands in the Izu-Ridge, where several recent studies have reported elevated nutrient supply. This study showed that the Kuroshio approaching to the southern coast of Japan, in the Hyuganada Sea, can also enhance the nutrient supply, promoting primary production, hence, increasing the biological production along the coast (**Supplementary Animation Anime S3**).

DATA AVAILABILITY STATEMENT

The observation data in the manuscript is available at https://doi.pangaea.de/10.1594/PANGAEA.902182. The ROMS code is available from https://www.myroms.org/. The original contributions presented in the study are included in the article/Supplementary Material. Further inquiries can be directed to the corresponding author.

AUTHOR CONTRIBUTIONS

GSDG analyzed model results, created the figures, and edited the manuscript. TN run the numerical models, and edited the manuscript. All authors contributed to the article and approved the submitted version.

FUNDING

SKED (JPMXD0511102330), OMIX (KAKENHI16H01590 and 18H04914) and KAKENHI (19H01965 and 20K20634).

ACKNOWLEDGMENTS

GSDG thanks MEXT and JASSO for their financial support for studying in Japan. GSDG and TN thank Prof. Nakamura, Prof.

Nishina, Prof. Kobari from Kagoshima University, Capt. Uchiyama and crew members of R.T.V. Kagoshima-Maru for the observations and ship operations, and Prof. Yoshie from Ehime University for the nutrient analysis. GSDG and TN thank Perro Guardián del cielo.

SUPPLEMENTARY MATERIAL

The Supplementary Material for this article can be found online at: https://www.frontiersin.org/articles/10.3389/fmars.2022.842155/full#supplementary-material

REFERENCES

Chang, M.-H., Jheng, S.-Y., and Lien, R.-C. (2016). Trains of Large Kelvin-Helmholtz Billows Observed in the Kuroshio Above a Seamount. *Geophys. Res. Lett.* 43, 8654–8661. doi: 10.1002/2016GL069462

Clayton, S., Nagai, T., and Follows, M. J. (2014). Fine Scale Phytoplankton Community Structure Across the Kuroshio Front. *J. Plankton. Res.* 36, 1017–1030. doi: 10.1093/plankt/fbu020

da Silva, A., Young, A. C., and Levitus, S. (1994). "Atlas of Surface Marine Data 1994," in *Algorithms and Procedures Tech. Rep. 6* (Florida, USA: Department of Commerce, NOAA, NESDIS).

Durán Gómez, G. S., Nagai, T., and Yokawa, K. (2020). Mesoscale Warm-Core Eddies Drive Interannual Modulations of Swordfish Catch in the Kuroshio Extension System. *Front. Mar. Sci* 7, 680. doi: 10.3389/fmars.2020.00680

Endo, H., and Suzuki, K. (2019). "Spatial Variations in Community Structure of Haptophytes Across the Kuroshio Front in the Tokara Strait," in *Kuroshio Current: Physical, Biogeochemical, and Ecosystem Dynamics*. Eds. T. Nagai, H. Saito, K. Suzuki and M. Takahashi (Washington, D.C., USA:AGU-Wiley).

Gruber, N., Frenzel, H., Doney, S. C., Marchesiello, P., McWilliams, J. C., Moisan, J. R., et al. (2006). Eddy-Resolving Simulation of Plankton Ecosystem Dynamics in the California Current System. *Deep. Sea. Res. Part I: Oceanog. Res. Pap.* 53, 1483–1516. doi: 10.1016/j.dsr.2006.06.005

Gula, J., Molemaker, M. J., and McWilliams, J. C. (2016). Topographic Generation of Submesoscale Centrifugal Instability and Energy Dissipation. *Nat. Commun.* 7, 1–7. doi: 10.1038/ncomms12811

Guo, X., Zhu, X.-H., Long, Y., and Huang, D. (2013). Spatial Variations in the Kuroshio Nutrient Transport From the East China Sea to South of Japan. *Biogeosciences* 10, 6403–6417. doi: 10.5194/bg-10-6403-2013

Guo, X., Zhu, X.-H., Wu, Q.-S., and Huang, D. (2012). The Kuroshio Nutrient Stream and its Temporal Variation in the East China Sea. *J. Geophys. Res.: Ocean.* 117, C01026. doi: 10.1029/2011JC007292

Hasegawa, D. (2019). "Island Mass Effect. Kuroshio Current: Physical, Biogeochemical, and Ecosystem Dynamics," in *Kuroshio Current: Physical, Biogeochemical, and Ecosystem Dynamics*. Eds. T. Nagai, H. Saito, K. Suzuki and M. Takahashi, Washington, D.C., USA: AGU-Wiley. 163–174.

Hasegawa, D., Yamazaki, H., Lueck, R., and Seuront, L. (2004). How Islands Stir and Fertilize the Upper Ocean. *Geophys. Res. Lett.* 31, 16303. doi: 10.1029/2004GL020143

Kobari, T., Honma, T., Hasegawa, D., Yoshie, N., Tsutsumi, E., Matsuno, T., et al. (2020). Phytoplankton Growth and Consumption by Microzooplankton Stimulated by Turbulent Nitrate Flux Suggest Rapid Trophic Transfer in the Oligotrophic Kuroshio. *Biogeosciences* 17, 2441–2452. doi: 10.5194/bg-17-2441-2020

Komatsu, K., and Hiroe, Y. (2019). "Structure and Impact of the Kuroshio Nutrient Stream," in *Kuroshio Current: Physical, Biogeochemical, and Ecosystem Dynamics*. Eds. T. Nagai, H. Saito, K. Suzuki and M. Takahashi (Washington, D.C., USA: AGU-Wiley). doi: 10.1002/9781119428428.ch5

Kunze, E. (1985). Near-Inertial Wave Propagation in Geostrophic Shear. *J. Phys. Oceanog.* 15, 544–565. doi: 10.1175/1520-0485(1985)015<0544:NIWPIG>2.0.CO;2

Kunze, E., Schmitt, R. W., and Toole, J. M. (1995). The Energy Balance in a Warm-Core Ring's Near-Inertial Critical Layer. *J. Phys. Oceanog.* 25, 942–957. doi: 10.1175/1520-0485(1995)025<0942:TEBIAW>2.0.CO;2

Large, W. G., McWilliams, J. C., and Doney, S. C. (1994). Oceanic Vertical Mixing: A Review and a Model With a Nonlocal Boundary Layer Parameterization. *Rev. Geophys.* 32, 363–403. doi: 10.1029/94RG01872

Levitus, S. (1982). *Climatological Atlas of the World Ocean* Vol. 13 (Florida, USA: Algorithms and procedures NOAA/ERL GFDL Professional Paper). NTIS PB83-184093.

Li, D., Chou, W.-C., Shih, Y.-Y., Chen, G.-Y., Chang, Y., Chow, C. H., et al. (2018). Elevated Particulate Organic Carbon Export Flux Induced by Internal Waves in the Oligotrophic Northern South China Sea. *Sci. Rep.* 8, 2045–2322. doi: 10.1038/s41598-018-20184-9

Li, Q., Mao, X., Huthnance, J., Cai, S., and Kelly, S. (2019). On Internal Waves Propagating Across a Geostrophic Front. *J. Phys. Oceanog.* 49, 1229–1248. doi: 10.1175/JPO-D-18-0056.1

Lizarbe Barreto, D. A., Chevarria Saravia, R., Nagai, T., and Hirata, T. (2021). Phytoplankton Increase Along the Kuroshio Due to the Large Meander. *Front. Mar. Sci.* 8. doi: 10.3389/fmars.2021.677632

Molemaker, M. J., McWilliams, J. C., and Dewar, W. K. (2015). Submesoscale Instability and Generation of Mesoscale Anticyclones Near a Separation of the California Undercurrent. *J. Phys. Oceanog.* 45, 613–629. doi: 10.1175/JPO-D-13-0225.1

Mooers, C. N. (1975). Several Effects of a Baroclinic Current on the Cross-Stream Propagation of Inertial-Internal Waves. *Geophys. Astroph. Fluid. Dynam.* 6, 245–275. doi: 10.1080/03091927509365797

Nagai, T., and Clayton, S. (2017). Nutrient Interleaving Below the Mixed Layer of the Kuroshio Extension Front. *Ocean. Dynam.* 67, 1027–1046. doi: 10.1007/s10236-017-1070-3

Nagai, T., Durán Gómez, G. S., Otero, D. A., Mori, Y., Yoshie, N., Ohgi, K., et al. (2019). How the Kuroshio Current Delivers Nutrients to Sunlit Layers on the Continental Shelves With Aid of Near-Inertial Waves and Turbulence. *Geophys. Res. Lett.* 46, 6726–6735. doi: 10.1029/2019GL082680

Nagai, T., Hasegawa, D., Tanaka, T., Nakamura, H., Tsutsumi, E., Inoue, R., et al. (2017). First Evidence of Coherent Bands of Strong Turbulent Layers Associated With High-Wavenumber Internal-Wave Shear in the Upstream Kuroshio. *Sci. Rep.* 7, 1–14. doi: 10.1038/s41598-017-15167-1

Nagai, T., Hasegawa, D., Tsutsumi, E., Nakamura, H., Nishina, A., Senjyu, T., et al. (2021). The Kuroshio Flowing Over Seamounts and Associated Submesoscale Flows Drive 100-km-Wide 100-1000-Fold Enhancement of Turbulence, *Commun. Earth Environ.* 2, 170. doi: 10.1038/s43247-021-00230-7

Nagai, T., Rosales Quintana, G. M., Durán Gómez, G. S., Hashihama, F., and Komatsu, K. (2021b). Elevated Turbulent and Double-Diffusive Nutrient Flux in the Kuroshio Over the Izu Ridge and in the Kuroshio Extension. *J Oceanog*, 77(1), 55–74. doi: 10.1007/s10872-020-00582-2

Nagai, T., Tandon, A., Kunze, E., and Mahadevan, A. (2015). Spontaneous Generation of Near-Inertial Waves by the Kuroshio Front. *J. Phys. Oceanog.* 45, 2381–2406. doi: 10.1175/JPO-D-14-0086.1

Nikurashin, M., and Ferrari, R. (2011). Global Energy Conversion Rate From Geostrophic Flows Into Internal Lee Waves in the Deep Ocean. *Geophys. Res. Lett.* 38, L08610. doi: 10.1029/2011GL046576

Oey, L.-Y., Wang, J., and Lee, M.-A. (2018). Fish Catch is Related to the Fluctuations of a Western Boundary Current. *J. Phys. Oceanog.* 48, 705–721. doi: 10.1175/JPO-D-17-0041.1

Palter, J. B., and Lozier, M. S. (2008). On the Source of Gulf Stream Nutrients. *J Geophys Res.* 113, C06018. doi: 10.1029/2007JC004611

Palter, J. B., Lozier, M. S., Sarmiento, J. L., and Williams, R. G. (2011). The Supply of Excess Phosphate Across the Gulf Stream and the Maintenance of Subtropical Nitrogen Fixation. *Glob. Biogeochem. Cycles* 25, GB4007. doi: 10.1029/2010GB003955

Pelegrí, J. L., and Csanady, G. T. (1991). Nutrient Transport and Mixing in the Gulf Stream. *J. Geophys. Res.* 96, 2577–2583. doi: 10.1029/90JC02535

Pelegrí, J., Csanady, G., and Martins, A. (1996). The North Atlantic Nutrient Stream. *J. Oceanog.* 52, 275–299. doi: 10.1007/BF02235924

Rainville, L., and Pinkel, R. (2004). Observations of Energetic High-Wavenumber Internal Waves in the Kuroshio. *J. Phys. Oceanog.* 34, 1495–1505. doi: 10.1175/1520-0485(2004)034<1495:OOEHIW>2.0.CO;2

Saito, H. (2019). "The Kuroshio: Its Recognition, Scientific Activities and Emerging Issues," in *Kuroshio Current: Physical, Biogeochemical, and Ecosystem Dynamics*. Eds. T. Nagai, H. Saito, K. Suzuki and M. Takahashi (Washington, D.C., USA: AGU-Wiley).

Shchepetkin, A. F., and McWilliams, J. C. (2005). The Regional Oceanic Modeling System (ROMS): A Split-Explicit, Free-Surface, Topography-Following-Coordinate Oceanic Model. *Ocean. Model.* 9, 347–404. doi: 10.1016/j.ocemod.2004.08.002

Smagorinsky, J. (1993). "Some Historical Remarks on the Use of non-Linear Viscosities," in *Large Eddy Simulation of Complex Engineering and Geophysical Flows* (Cambridge, UK: Cambridge University Press).

Takahashi, A., Lien, R.-C., Kunze, E., Nakamura, H., Inoue, R., and Tsutsumi, E. (2022). "Energetic turbulence and nonlinear internal waves in Tokara Strait," in *Presented at 2022 Ocean Sci. Meet., Virtual, Feb. 24 - March 4, Abstract, in Session PS11-01-03* Hawaii, USA.

Tanaka, T., Hasegawa, D., Yasuda, I., Tsuji, H., Fujio, S., Goto, Y., et al. (2019). Enhanced Vertical Turbulent Nitrate Flux in the Kuroshio Across the Izu Ridge. *J. Oceanog.* 75, 195–203. doi: 10.1007/s10872-018-0500-2

Tandon, A., and Nagai, T. (2019). "Mixing Associated With Submesoscale Processes," in *Encyclopedia of Ocean Sciences*, *3rd ed.* Eds. H. K. Cochran, H. J. Bokuniewicz and P. L. Yger (Cambridge, Massachusetts, USA:Elsevier).

Thomas, L. N., Taylor, J. R., Ferrari, R., and Joyce, T. M. (2013). Symmetric Instability in the Gulf Stream. *Deep-Sea. Res. II* 91, 96–110. doi: 10.1016/j.dsr2.2013.02.025

Tsutsumi, E., Matsuno, T., Lien, R.-C., Nakamura, H., Senjyu, T., and Guo, X. (2017). Turbulent Mixing Within the Kuroshio in the Tokara Strait. *J. Geophys. Res.: Ocean.* 122, 7082–7094. doi: 10.1002/2017JC013049

Wenegrat, J. O., Thomas, L. N., Sundermeyer, M. A., Taylor, J. R., D'Asaro, E. A., Klymak, J. M., et al. (2020). Enhanced Mixing Across the Gyre Boundary at the Gulf Stream Front. *Proc. Natl. Acad. Sci.* 117, 17607–17614. doi: 10.1073/pnas.2005558117

Whitt, D. B. (2019). "On the Role of the Gulf Stream in the Changing Atlantic Nutrient Circulation During the 21st Century," in *Kuroshio Current: Physical, Biogeochemical, and Ecosystem Dynamics*. Eds. T. Nagai, H. Saito, K. Suzuki and M. Takahashi (Washington, D.C., USA: AGU-Wiley).

Whitt, D. B., and Thomas, L. N. (2013). Near-Inertial Waves in Strongly Baroclinic Currents. *J. Phys. Oceanog.* 43, 706–725. doi: 10.1175/JPO-D-12-0132.1

Whitt, D. B., Thomas, L. N., Klymak, J. M., Lee, C. M., and D'Asaro, E. A. (2018). Interaction of Superinertial Waves With Submesoscale Cyclonic Filaments in the North Wall of the Gulf Stream. *J. Phys. Oceanog.* 48, 81–99. doi: 10.1175/JPO-D-17-0079.1

Conflict of Interest: The authors declare that the research was conducted in the absence of any commercial or financial relationships that could be construed as a potential conflict of interest.

Publisher's Note: All claims expressed in this article are solely those of the authors and do not necessarily represent those of their affiliated organizations, or those of the publisher, the editors and the reviewers. Any product that may be evaluated in this article, or claim that may be made by its manufacturer, is not guaranteed or endorsed by the publisher.

Copyright © 2022 Durán Gómez and Nagai. This is an open-access article distributed under the terms of the Creative Commons Attribution License (CC BY). The use, distribution or reproduction in other forums is permitted, provided the original author(s) and the copyright owner(s) are credited and that the original publication in this journal is cited, in accordance with accepted academic practice. No use, distribution or reproduction is permitted which does not comply with these terms.

frontiers | Frontiers in Marine Science

ORIGINAL RESEARCH
published: 13 May 2022
doi: 10.3389/fmars.2022.869285

Enhanced Cross-Shelf Exchange Between the Pacific Ocean and the Bungo Channel, Japan Related to a Heavy Rain Event

Akihiko Morimoto[1]*, *Menghong Dong*[1], *Mahiro Kameda*[1], *Taiga Shibakawa*[2], *Makiko Hirai*[3], *Kouhei Takejiri*[4], *Xinyu Guo*[1] and *Hidetaka Takeoka*[5]

[1] Center for Marine Environmental Studies, Ehime University, Matsuyama, Japan, [2] Graduate School of Science, Kyoto University, Kyoto, Japan, [3] Fisheries Research Center, Ehime Research Institute of Agriculture, Forestry and Fisheries, Uwajima, Japan, [4] Fisheries Promotion Division, Oita Prefectural Government, Oita, Japan, [5] South Ehime Fisheries Research Center, Ehime University, Minamiuwa-gun, Japan

OPEN ACCESS

Edited by:
Wei-Bo Chen,
National Science and Technology Center for Disaster Reduction (NCDR), Taiwan

Reviewed by:
Fajin Chen,
Guangdong Ocean University, China
Qinghua Ye,
Deltares, Netherlands
Zhixuan Feng,
East China Normal University, China

***Correspondence:**
Akihiko Morimoto
morimoto.akihiko.cl@ehime-u.ac.jp

Specialty section:
This article was submitted to Coastal Ocean Processes, a section of the journal Frontiers in Marine Science

Received: 04 February 2022
Accepted: 20 April 2022
Published: 13 May 2022

Citation:
Morimoto A, Dong M, Kameda M, Shibakawa T, Hirai M, Takejiri K, Guo X and Takeoka H (2022) Enhanced Cross-Shelf Exchange Between the Pacific Ocean and the Bungo Channel, Japan Related to a Heavy Rain Event. Front. Mar. Sci. 9:869285. doi: 10.3389/fmars.2022.869285

A heavy rain event occurred in early July 2018 near the Seto Inland Sea. Despite clear weather after the heavy rain, the water temperature at 5 m depth on the eastern coast of the Bungo Channel decreased by approximately 3°C. Postulating that the water temperature decrease was related to the heavy rain event, we analyzed observed data during and after the heavy rain and conducted numerical experiments. We found that the surface water temperature decrease was caused by vertical mixing of cold water supplied from the Pacific Ocean in the bottom layer. Numerical experiments revealed that the bottom cold water from the Pacific Ocean was not controlled by the heavy rain event but was intensified by the heavy rain event. The lower salinity (lower water density) due to the heavy rain lasted until the end of August. This lower density intensified the gravitational circulation in the Bungo Channel for 2 months, which led to a 17.5% increase in inflow from the Pacific Ocean in the bottom layer and a 20% increase in the dissolved inorganic nitrogen flux to the Bungo Channel.

Keywords: cross-shelf exchange, bottom intrusion, heavy rain, nutrient supply, gravitational circulation

1 INTRODUCTION

Ocean currents such as the Kuroshio and Gulf Stream are geostrophic currents that result from a balance between the Coriolis and pressure gradient forces. A geostrophic current flows along continental shelf isobaths because the horizontal divergence should be zero. Since the Kuroshio and Gulf Stream have ageostrophic components in the real ocean, flow across the continental shelf occurs at times. Generally, the cross-shelf flow is much slower than an alongshore flow such as the Kuroshio. However, cross-shelf flow in the bottom layer contributes strongly to material exchange between the open ocean and coastal sea, especially the nutrient supply from the open ocean into coastal seas. The nutrient flux across the shelf increases despite the slower cross-shelf flow because the horizontal gradient in the nutrient concentration in the bottom layer around the shelf slope is larger. Nutrients supplied from the open ocean related to the cross-shelf flow are thought to contribute largely to primary production in coastal seas. Therefore, many studies have examined the

variation in the cross-shelf flow in the presence of a strong current. Atkinson (1977) firstly reported a bottom intrusion of relatively cooler and high-density Gulf Stream water into the south Atlantic Bight shelf in the Gulf Stream region. And then several studies were carried out in terms of the cross-shelf flow in the Gulf Stream region (Lee et al., 1981; Lents, 2003; Castelao, 2011; Ullman et al., 2014). In the Eastern Australian Current region, Schaeffer et al. (2013) analyzed 2 years of mooring data and revealed forcing mechanisms for cross-shelf exchange through the momentum balance. Recently, Brink (2016) reviewed cross-shelf exchange research and pointed out the difficulty with observing cross-shelf flow and the need for further studies of physical mechanisms and quantitative prediction of cross-exchange. He also described the importance of understanding ecosystem responses to cross-shelf exchange.

The Bungo Channel is located in southwestern Japan between Shikoku and Kyushu Islands and connects the Pacific Ocean to the Seto Inland Sea (**Figure 1A**). It is approximately 50 km wide and 100 km long, and it has a mean water depth of 80 m (**Figure 1B**). There is a continental shelf slope south of the Bungo Channel along which the Kuroshio flows. The marine environment in the Bungo Channel is influenced by perturbations of the Kuroshio, such as the Kuroshio meander and frontal eddies, and surface and bottom intrusions occur from early summer to autumn (Kaneda et al., 2002a). The surface intrusion of a warm water mass in the Pacific Ocean is called the Kyucho, which is Japanese for a sudden strong current (**Figure 1C**). The Kyucho can increase the water temperature in the Bungo Channel by 4–5°C within a day as warm water in the Kuroshio intrudes into the Bungo Channel at speeds of 0.3–0.5 m s^{-1} (Takeoka and Yoshimura, 1988; Takeoka et al., 1993; Takeoka et al., 1995). Several studies have investigated this phenomenon and its mechanism (Akiyama and Saito, 1993; Takeoka et al., 1993; Isobe et al., 2010; Nagai and Hibiya, 2012). In the bottom layer, the bottom intrusion of cold, nutrient-rich water from the shelf slope into the Bungo Channel. Koizumi (1999) showed that relatively cool water (< 20°C) entered the channel for approximately 10 days. Kaneda et al. (2002a) analyzed water temperature time-series data for 2 years at a depth of 68 m along the east coast of the Bungo Channel and revealed that bottom intrusions occurred repeatedly from early summer to late autumn, especially during neap tides. Since there are few large rivers in the Bungo Channel, the nutrient supply associated with a bottom intrusion is thought to be crucial for the Bungo Channel ecosystem (Kaneda et al, 2002b; Katano et al., 2005).

Both the Kyucho and bottom intrusions occur during summer neap tides, albeit irregularly (Kaneda et al., 2002a). However, there is a strong correlation between the intensities of the Kyucho and bottom intrusions on a monthly scale (Takeoka et al., 2000), and the intensities of both were correlated with the distance of the Kuroshio axis from the Bungo Channel; when the Kuroshio approaches the Bungo Channel, both Kyucho and bottom intrusions tend to occur (Kaneda et al., 2002c). Therefore, the Kuroshio variation might influence the occurrence of bottom intrusions, but we do not know what triggers a bottom intrusion. Based on a numerical model, Arai (2005) proposed a mechanism for bottom intrusions in the Bungo Channel. However, there is no observational evidence of upwelling southeast of the Bungo Channel. Therefore, the mechanism of bottom intrusions remains controversial.

The vertical circulation in the Bungo Channel during summer tends to be a gravitational circulation such as an estuary circulation; low density surface water flows from the Seto Inland Sea southward into the Pacific Ocean, while high density bottom water flows from south to north (Chang et al., 2009). Therefore, a bottom intrusion might be enhanced by decreasing water density in the Seto Inland Sea. In Japan, heavy rain events are frequent during the rainy season (June and July), and the maximum hourly rainfall is increasing (Fujibe, 2015). Heavy rain events occurred 15 times since 1938 around the Seto Inland Sea area, and 7 of 15 of heavy rain events occurred after 2010. In recent years, the water density in the Seto Inland Sea is thought to have decreased. In early July 2018, a heavy rain event

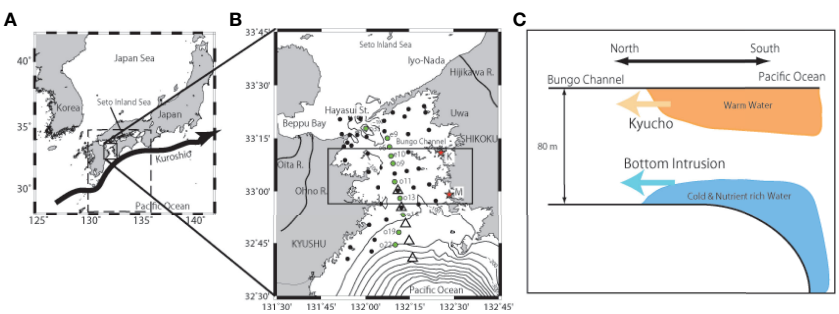

FIGURE 1 | **(A)** Map of Japan. The dashed square indicates the numerical model domain; the solid square is enlarged in **(B)**. **(B)** Topography around the Bungo Channel and observed points. Contour lines denote the bottom topography every 100 m of depth. Both black and green dots show the Ehime and Oita Prefecture hydrographic observation stations. **Figure 5** uses the hydrographic data of green dots stations. The temporal variation in water temperature was measured at stations marked with red stars. Triangles show nutrient observation points. The black square indicates the area of control volume. **(C)** Schematic of intrusion phenomena in the Bungo Channel.

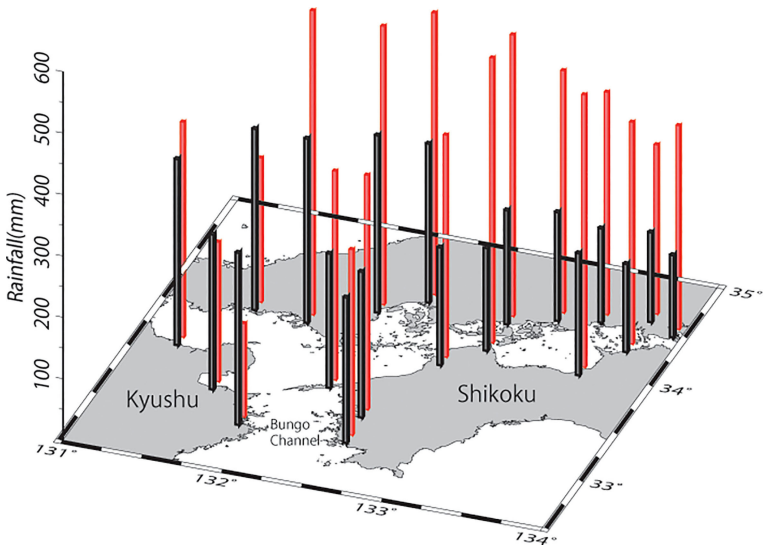

FIGURE 2 | Integrated precipitation for July 5–8, 2018 (red bars) and monthly integrated precipitation in July of a normal year (black bars) around the Seto Inland Sea.

occurred near the Seto Inland Sea, causing flooding and landslides. The integrated precipitation during the 4-day event greatly exceeded the monthly integrated rainfall in a normal July (**Figure 2**). The maximum integrated rain fall during the heavy rain event was 965 mm which was the highest integral rain fall during a heavy rain event after 2010. The precipitation and river discharge supplied an enormous amount of freshwater during a short period. During the heavy rain, the precipitation exceeded 500 mm in the northern part of the Bungo Channel, dramatically decreasing the water density there. A few days after the heavy rain event, the surface water temperature decreased in the eastern part of the Bungo Channel, despite the clear weather and warm season. This required a supply of cooler water, possibly a bottom intrusion. Therefore, we examined whether there was an enhanced bottom intrusion from the Pacific Ocean to the Bungo Channel related to the heavy rain event using observed data and a numerical model. Section *Analyzed Data and Numerical Model Description* describes the observed data and numerical model. Section *Water Temperature Variation During and After the Heavy Rain Event* presents the data analysis. Section *Numerical Experiments* shows the results of the numerical model for both a heavy-rain case (RC) and a no-rain case (NRC). Section *Discussion* discusses the results, and Section *Summary* summarizes the findings.

2 ANALYZED DATA AND NUMERICAL MODEL DESCRIPTION

Water temperature was measured from the surface to bottom at two stations on the eastern coast of the Bungo Channel (**Figure 1B**). Water temperature at 1, 5, 10, 20, 30, and 40 m depth was measured every hour at Station K by using a thermistor-chain (Nichiyu Co., Ltd.) with an accuracy of ±0.1°C and at 5, 20, 30, 40, and 55 m depth at Station M every 10 min by using water temperature meters (JFE advantec Co., Ltd.) with an accuracy of ±0.02°C. The tide killer filter (Hanawa and Mitsudera, 1985) was applied to the water temperature data to remove high-frequency signals associated with tidal variation. The tide killer filter can eliminate the signals with less than 48-hour variability. We used the Level 3 hourly sea surface temperature (SST) data of the Himawari-8 geostationary meteorological satellite obtained from the Japan Aerospace Exploration Agency. The Himawari-8 SST data have a spatial resolution of 2 km. We used only the night-time SST data to remove outlying values. The Fisheries Research Centers of Ehime and Oita Prefectures conducted hydrographic observations from research vessels just after the heavy rain event. Both Fisheries Research Centers measured vertical profiles of water temperature and salinity at 51 stations using CTD (JFE Advantec Co., Ltd.) with an accuracy of ±0.01°C for water temperature and ±0.01 mS cm^{-1} for conductivity (**Figure 1B**). Oita Prefecture covered the western side of the Bungo Channel from July 10 to 12, and Ehime Prefecture covered the eastern side from July 11 to 13. We used nutrient data observed on a transect in the southern part of the Bungo Channel in July from 1994 to 2005. Nitrate, nitrite, ammonium, phosphate, and silicate were analyzed by an auto-analyzer (TRAACS 800, Bran Luebbe Co., Ltd.).

The three-dimensional, sigma-coordinate numerical model used here is the model that Chang et al. (2009) developed based on the Princeton Ocean Model (Blumberg and Mellor, 1987). The horizontal and vertical mixing coefficients are calculated using the Smagorinsky (1963) formulation and Mellor and Yamada (1982) turbulent closure scheme, respectively. The model calculation domain is from 129.9875°E to 136.0125°E

and 28.125°N to 34.8083°N (**Figure 1A**); it has a horizontal resolution of approximately 1 km (1/120° in the meridional and 1/80° in the zonal direction) and 31 vertical layers. The bottom topography was prepared using Japan Oceanographic Data Center and ETOPO1 datasets. The minimum water depth in the model was set to 5 m. Open boundary conditions for water temperature, salinity, and current velocity were applied from the Japan Coastal Ocean Experiment 2 reanalysis data (Miyazawa et al., 2009). The model considered tidal constituents (M_2, S_2, O_1, and K_1) and applied sea level variation from the harmonic constants of tide model NAO.99b (Matsumoto et al., 2000) at the open boundaries. Heat flux and wind stress every 6 h calculated by the Grid Point Value of Mesoscale Model (GPV-MSM) of the Japan Meteorological Agency were applied at the sea surface. Precipitation calculated using GPV-MSM was applied at the sea surface, except during the heavy rain event in July 2018. Precipitation data observed by meteorological radar were applied at the sea surface before and during the heavy rain event (from June 25 to July 10, 2018) because the distribution and intensity of rainfall calculated by GPV-MSM differed from observations around the northern part of the Bungo Channel. The model considered 37 rivers and obtained river discharge data from the Ministry of Land, Infrastructure, Transport and Tourism database. The model was integrated from January 1, 2015 to September 15, 2018.

3 WATER TEMPERATURE VARIATION DURING AND AFTER THE HEAVY RAIN EVENT

The daily precipitation at Uwa, on the northeastern coast of the Bungo Channel, from July 5 to 8, 2018 was 70.5, 178.0, 229.0, and 62.0 mm, respectively. There was no precipitation from July 9 to 20. Therefore, we define the period of the heavy rain event studied as July 5 to 8. **Figure 2** shows the integrated precipitation during the heavy rain event. The averaged integrated precipitation on the eastern coast during the heavy rain event was 409.8 mm. Since there are no large rivers in the Bungo Channel, the main supply of freshwater from rivers to Iyo-Nada was from the Hijikawa River, and that to Beppu Bay was from the Oita and Ohno Rivers (**Figure 1B**). Those river basins have areas almost equal to the area of the Bungo Channel. Precipitation over the Bungo Channel during the heavy rain event might account for a large portion of the freshwater in the sea.

Figure 3 shows the temporal variation in water temperature at Stations K and M (see **Figure 1B**) from July 5 to 15. The water temperature at 5 m depth decreased from July 11 at Station K and from July 13 at Station M. This water temperature decrease started 3 or 5 days after the heavy rain event, with decreases of 3.53°C and 1.48°C at Stations K and M, respectively. The water temperature at 40 m depth at Station K started decreasing during

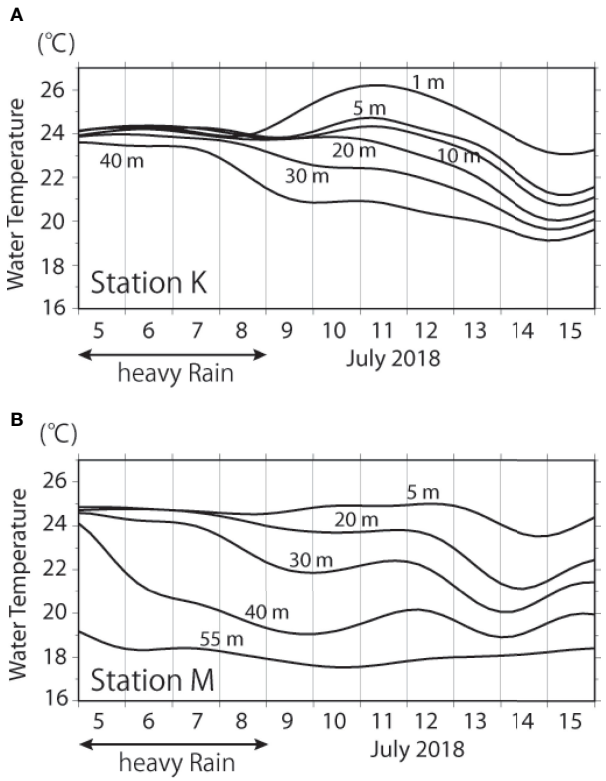

FIGURE 3 | Temporal variation in water temperature from July 5 to 15 **(A)** at 1, 5, 10, 20, 30, and 40 m depth at Station K and **(B)** 5, 20, 30, 40, and 55 m depth at Station M.

the heavy rain event on July 7 and reached a minimum on July 15, with a total decrease of 5.18°C. The water temperature at 40 m depth at Station M started decreasing before the heavy rain event on July 5 and reached a minimum on July 9, with a total decrease of 4.42°C. In both stations, the water temperature decrease started in the lower layer and then the decrease propagated to the upper layers. The fact suggests that water mass with lower temperature intruded into the small bays where water temperature monitored through bottom layer. To examine the horizontal distribution of the water temperature decrease at the sea surface after the heavy rain event, we calculated the difference in the satellite SST between July 10 and 15 (**Figure 4**). The water temperature decreased in the northern part, along the west coast, and in the middle of the east coast of the Bungo Channel, where the topography is relatively complex with islands and small peninsulas. By contrast, SST increased in the central and northeastern parts of the Bungo Channel. **Figure 5** shows north–south cross-sections of water temperature and salinity on July 11 and 12 observed by Ehime and Oita Prefectural Fisheries Research Centers in the central part of the Bungo Channel. The water mass was mixed in the north and stratified in the south. Low-salinity water (< 32.2 psu) was seen from Stations o35 to o13, with a high-temperature water mass from o13 to o22 in the surface layer. In the bottom layer, the water from the shelf slope to Station o6 in the northern part of the Bungo Channel was cooler than 19°C and had a salinity > 34.0 psu. The distribution of the water mass in the surface and bottom layers suggests that low-salinity water flows out from the Bungo Channel in the surface layer and below, while saline water enters the Bungo Channel from the shelf slope in the bottom layer, *via* bottom intrusion. **Figure 6** shows the horizontal distribution of surface

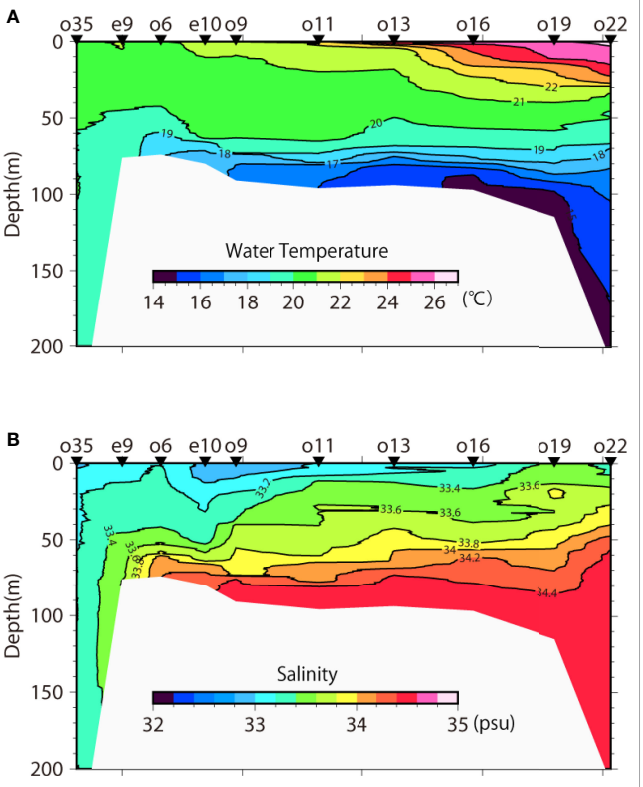

FIGURE 5 | Observed north–south cross-sections of **(A)** water temperature and **(B)** salinity from July 11 to 12 at the stations shown as green dots in **Figure 1B**.

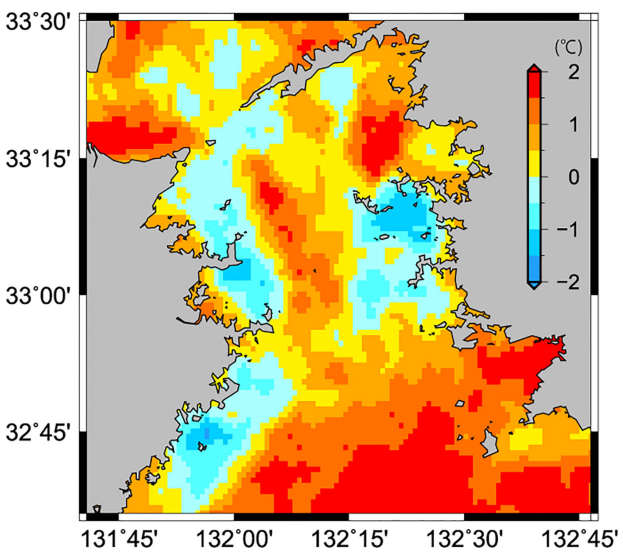

FIGURE 4 | Sea surface temperature (SST) difference between July 10 and 15. Negative values denote a water temperature decrease from July 10.

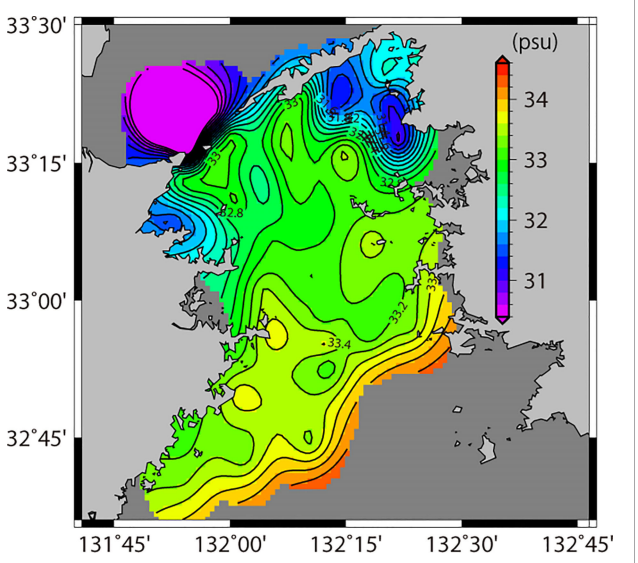

FIGURE 6 | Horizontal distribution of sea surface salinity observed during July 10–13, 2018.

salinity from July 10 to 13 according to both the Ehime and Oita Fisheries Research Centers. There was low-salinity water (< 30 psu) north of the Hayasui Strait, with a salinity front there. The low-salinity water might have come from Beppu Bay, to which two large rivers supply freshwater. More low-salinity water was present in the northeastern part of the Bungo Channel. This might have been caused by the heavy rainfall over the sea and freshwater from two small rivers. High-salinity water (> 33.8 psu) was present in the southern part of the Bungo Channel.

The data analysis indicated that the bottom intrusion in the southern part of the Bungo Channel occurred before the heavy rain event, and a cooler water mass moved northward in the bottom layer. This was shown by the temporal variation in the water temperature at Stations M and K (**Figure 3**). The cooler water mass reached the northern part of the Bungo Channel 3–4 days after the heavy rain event (**Figure 5**). The SST near regions with complex topography decreased on July 15, 7 days after the heavy rain event (**Figure 4**). The water column might be mixed vertically by the strong tidal current in narrow straits and around peninsulas because July 15 was a spring tide. Since a cooler water mass was present in the bottom layer due to the bottom intrusion, the strong vertical mixing of the spring tide might have lowered the SST on July 15. The occurrence of the bottom intrusion appeared to be independent of the heavy rain event. However, it is possible that the heavy rain event intensified the bottom intrusion by supplying low-salinity water (causing buoyancy) in the northern part of the Bungo Channel (**Figure 6**), which resulted in a large north–south horizontal density gradient, which might have enhanced gravitational circulation: low-salinity water (low water density) in the northern part of the Bungo Channel flows to southward in the surface layer, while dense water around shelf slope flows to northward in the bottom layer. Hereafter, we describe this current pattern (Southward flow in the surface layer and northward flow in the bottom layer) as "gravitational circulation". The distribution of lower-salinity water implies a southward current in the upper layer (**Figure 6**). Considering mass conservation, the northward current in the lower layer should be intensified. As a result, the bottom intrusion would be enhanced.

4 NUMERICAL EXPERIMENTS

To confirm our hypothesis and understand how the heavy rain event influenced the cross-shelf material exchange, we conducted two sets of numerical experiments using a three-dimensional physical model. One experiment applied realistic river discharges, precipitation, wind forcing, and heat flux (RC), and the other had no river discharge or precipitation during or after the heavy rain event (NRC), while the other conditions were the same as those in the RC. In the NRC, river discharge and precipitation from July 1 to 15 were set to zero.

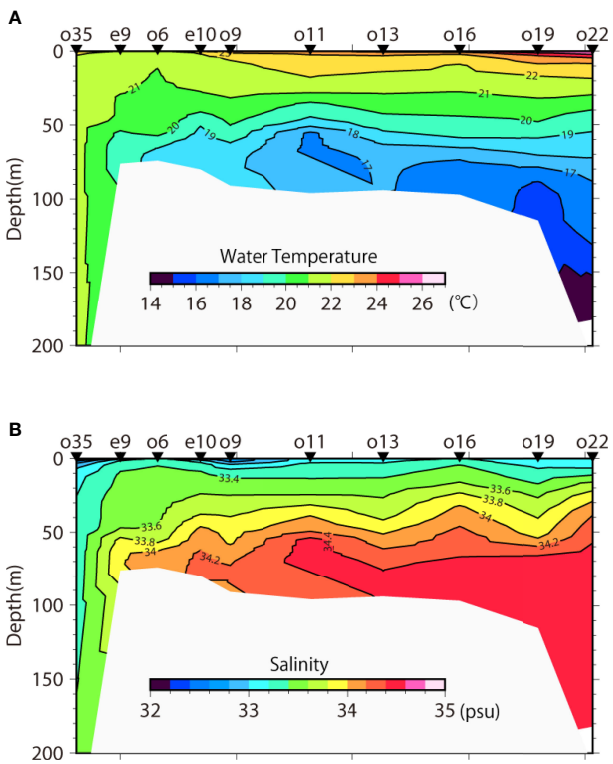

FIGURE 7 | North–south cross-sections of **(A)** water temperature and **(B)** salinity calculated using the numerical model. Calculated values used in these figures are compared with the observations at the same location and time from **Figure 5**.

4.1 Validation of the Numerical Model

We tried to reproduce the water temperature and salinity distributions in the Bungo Channel just after the heavy rain event (RC). **Figure 7** shows the north–south cross-sections (see **Figure 1B**) of water temperature and salinity calculated by the numerical model. For comparison, calculated values were compared with observations at the same time and location to plot the cross-section. Compared with **Figure 5**, the model reproduced the vertical mixing in the northern part, warm surface layer in the southern part, and intrusion of a cooler high-salinity water mass in the bottom layer. However, the bottom cold water was thicker than observed, and the mixed layer in the upper layer was thinner than observed. Although there were some differences, the overall features of the north–south structure were reproduced. **Figure 8** shows the calculated horizontal distribution of surface salinity where calculated values used only at observation points shown in **Figure 1B**. Although the distribution of the low-salinity water around the Hayasui Strait is a little different from the observations, and the salinity in the northeastern part of the Bungo Channel is a little higher (**Figure 6**), the model reproduced the surface salinity distribution well. Since we demonstrated the reproducibility of the model, the NRC was examined using the same parameters and boundary conditions as those for the RC, except for river discharge and precipitation from July 1 to 15.

4.2 Enhanced Bottom Intrusion Related to the Heavy Rain Event

We compared the results of the RC and NRC to determine the influence of the heavy rain event in early July 2018 on the intensity of a bottom intrusion and cross-shelf exchange for 2 months. **Figure 9** shows the temporal variation in the surface salinity of RC and NRC in the Hayasui Strait from July 1 to August 31, 2018. The variation was smaller in the NRC than in the RC; the surface salinity decreased drastically from 33.8 psu on July 5 to 33.0 on July 10 because of the heavy rain event. Subsequently, the salinity increased slightly on July 12 and stayed essentially constant until July 22, before decreasing suddenly by 0.6 psu due to the horizontal advection of lower salinity water originating from fresh water discharged from rivers inside the Seto Inland Sea during the heavy rain event. Since a southerly wind blew after the heavy rain event, the freshwater discharged from the Hijikawa River was transported northward and then advected to the Hayasui Strait by a surface residual current (not shown in figure). The salinity in the Hayasui Strait was much lower in RC than in NRC until the end of August. This suggests that the north–south horizontal density gradient of RC is much larger than that of NRC, and that the gravitational circulation of RC is stronger than that of NRC. As a result, the bottom intrusion is more intense in RC than in NRC.

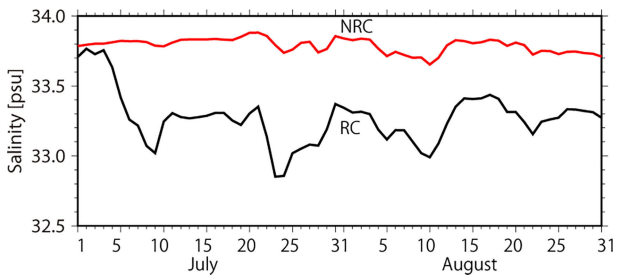

FIGURE 9 | Temporal variation in the calculated sea surface salinity at the Hayasui Strait in the northern Bungo Channel from July 1 to August 31. Black and red lines show the variation in the rain (RC) and no-rain (NRC) cases, respectively.

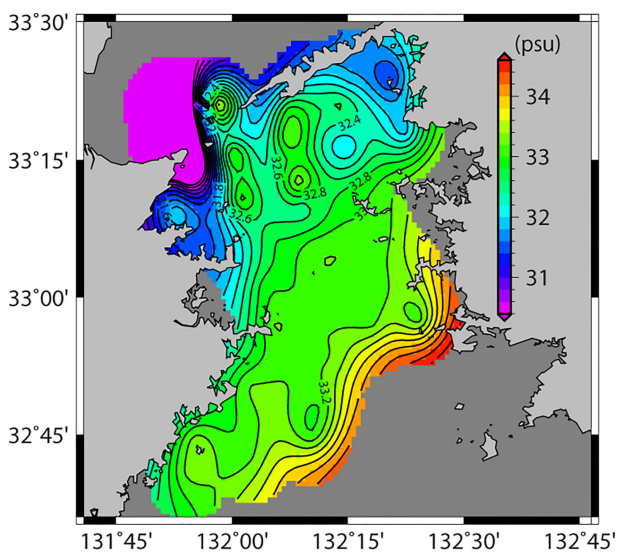

FIGURE 8 | Horizontal distribution of sea surface salinity calculated by the numerical model for the observations at the same location and time as those in **Figure 6**.

Figure 10A shows the temporal variation in water temperature below 50 m depth in RC and NRC averaged in an area, shown in **Figure 1B** as a black square. Based on cross-sections of water temperature and salinity shown in **Figures 5** and **7**, we define below 50 m depth as bottom layer and above 50 m depth as surface layer. Both RC and NRC showed similar variations. The water temperature decreased on July 4–8, July 22–29, August 1–6, and August 12–21. The decreases during July 4–8 and August 1–6 were sudden. The temporal variation in water temperature below 50 m in RC and NRC was the same until July 12. Subsequently, the water temperature was lower in RC than in NRC, with especially large differences from July 14 to August 2 and from August 17 to 21 (**Figure 10A**). The volume transports in the surface layer V_s (above 50 m depth) and the bottom layer V_b (below 50 m depth) at 32.92°N (southern boundary of the black square shown in **Figure 1B**) in RC and NRC were calculated by following equations (**Figure 10B**).

$$V_s = \int_{A_{upper}} v da, \quad V_b = \int_{A_{lower}} v da, \tag{1}$$

where v is north-southward component of current velocity at 32.92°N, and A_{upper} and A_{lower} are section area of surface layer

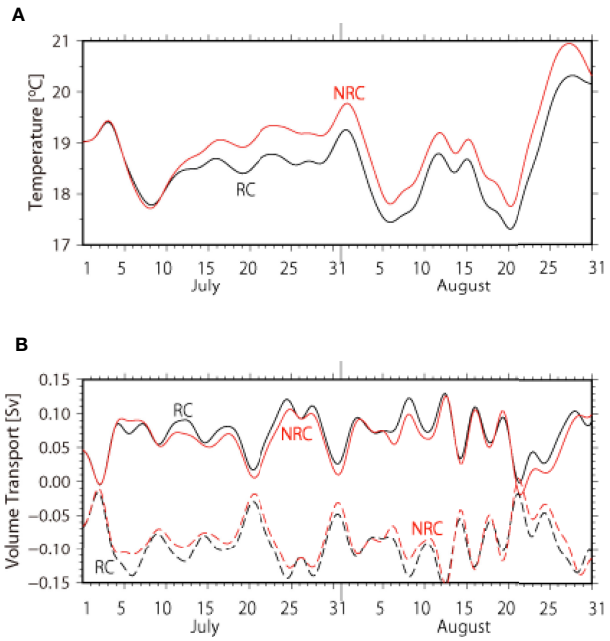

FIGURE 10 | Temporal variation in the **(A)** calculated water temperature below 50 m depth averaged in the control volume shown in **Figure 1B** as a black square, and **(B)** calculated volume transports above 50 m depth and below 50 m depth across 32.92°N. Black and red lines show the variation in the rain (RC) and no-rain (NRC) cases, respectively.

and bottom layer, respectively. Here, positive values mean northward transport. The volume transport at both bottom and surface layers in RC and NRC at 32.92°N showed similar variability for 2 months (**Figure 10B**). The volume transport was mostly positive in the bottom layer and negative in the surface layer, *i.e.*, water was transported from the Pacific Ocean to the Bungo Channel in the bottom layer and from the Bungo Channel to the Pacific Ocean in the surface layer. In both RC and NRC, the volume transport variation across 32.92°N were similar until July 12 in both layers, after which the volume transport tended to be larger in RC. The average volume transports in the surface and bottom layers for 2 months were -0.956 Sv for RC and -0.813 Sv for NRC, and 0.738 Sv for RC and 0.628 Sv for NRC, respectively, being 17.5% larger in RC. When the water temperature decreased, the northward volume transport in the bottom layer across 32.92°N also increased suddenly, except during August 12–21 (**Figure 10B**). This suggests that a cooler water mass was transported from the shelf region, and that at least three bottom intrusions occurred over the 2 months. Except in early July, the volume transport during the bottom intrusions were larger in RC than in NRC and the water temperature in the bottom layer was lower in RC than in NRC. The bottom intrusion in RC supplied more water from the shelf slope to the Bungo Channel.

The larger volume of transport at 32.92°N in RC suggests that the heavy rain event in early July enhanced the gravitational circulation in the Bungo Channel for at least 2 months. In order to compare intensity of gravitational circulation between RC and NRC, we calculated water budget in a control volume shown in **Figures 1B**, **11A** shows averaged water budget from July 1 to

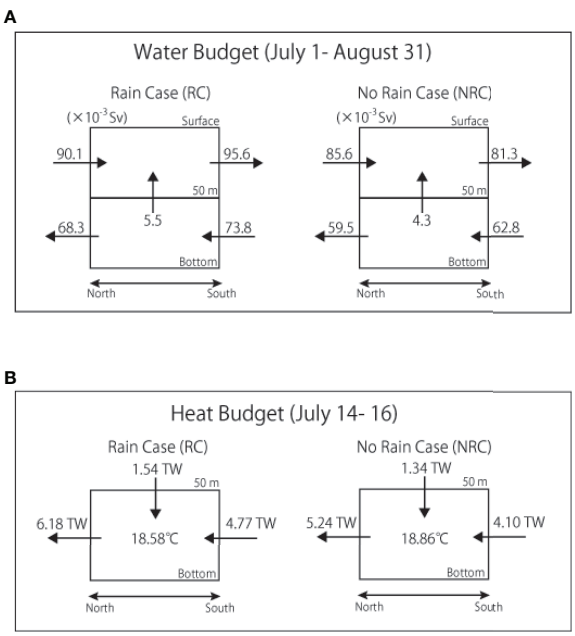

FIGURE 11 | Budget in a control volume shown in **Figure 1B** as a black square. **(A)** Water budget from July 1 to August 31 in the control volume and numbers indicate volume transport. Unit is in 10^{-3} Sv. **(B)** Heat budget below 50 m depth in the control volume from July 14 to 16 and numbers on the arrows indicate heat transport with a unit in TW. Numbers in the boxes show average water temperature below 50 m depth from July 14 to 16.

August 31. Southward volume transport (Bungo Channel to the Pacific Ocean) in the surface layer at northern and southern boundaries in RC is larger than that in NRC, and northward volume transport in the bottom layer in RC is also larger than that in NRC. The result clearly indicates that the gravitational circulation in the Bungo Channel was intensified by the heavy rain event. Difference of water temperature in the bottom layer between RC and NRC appeared on July 12 and gradually increased its difference until July 16, and after that the difference became almost stable (**Figure 10A**). We examined averaged heat budget in bottom layer of the control volume shown in **Figure 1B** from July 14 to 16 to see the cause of water temperature difference between RC and NRC just after the heavy rain event (**Figure 11B**). Mean water temperature in the bottom layer of the control volume from July 14 to 16 in RC and NRC were 18.58°C and 18.86°C, respectively. Horizontal heat transports were northward in RC and NRC due to northward volume transport shown in **Figure 11A**. The horizontal heat transports at southern and northern boundary in RC were larger than those in NRC. This is because volume transport in RC is larger than that in NRC. Horizontal heat budgets in the control volume in RC and NRC were -1.41 TW and -1.14 TW, respectively. It is found that intensification of the gravitational circulation related to the heavy rain event supplied much cooler water mass into the bottom layer of the Bungo Channel from shelf edge region.

5 DISCUSSION

We examined the decrease in surface water temperature after a heavy rain event in mid-July (**Figure 3**). Observations indicated that a cold water mass in the shelf slope region intruded into the bottom layer of the Bungo Channel when the heavy rain started. In the numerical experiment, the bottom intrusion in early July occurred at the same time and magnitude in both RC and NRC. This suggests that the heavy rain event did not influence the occurrence of the bottom intrusion in early July. However, the northward volume transport below 50 m depth across 32.92°N after July 11 was larger in RC than in NRC (**Figure 10B**), while the water temperature in the bottom layer of the control volume was lower in RC than in NRC (**Figure 10A**). Namely, the heavy rain event enhanced the shelf slope water mass supply to the bottom layer of the Bungo Channel. The water temperature in the surface layer decreased in the area with complex topography (**Figure 4**), and the minimum water temperature at 5 m depth occurred during a spring tide. It is thought that the surface water temperature decrease during the spring tide in mid-July was caused by strong tidal vertical mixing of cold water, which was supplied by the bottom intrusion. Therefore, the surface water temperature decrease in mid-July was not related to the heavy rain event in early July. However, since the cold water mass supply from the shelf slope region was larger in RC than in NRC, the heavy rain event might have influenced the magnitude of the surface water temperature decrease in mid-July.

The numerical experiments showed that the lower-salinity condition in the Hayasui Strait lasted until the end of August in RC, and bottom intrusions after mid-July in RC supplied much cold water to the bottom layer of the Bungo Channel compared with NRC. The lower density in the Bungo Channel due to the heavy rain event did not influence the occurrence of the bottom intrusion, because bottom intrusions occurred after mid-July in both RC and NRC. However, the bottom intrusion supplied more cold water in RC than in NRC; *i.e.*, the heavy rain event in early July intensified the cross-shelf exchange between the Bungo Channel and Pacific Ocean for approximately 2 months (**Figure 11A**). This intensified cross-shelf exchange was thought to cause the following. Since the density in the Bungo Channel decreased for 2 months, the horizontal density gradient between the Bungo Channel and Pacific Ocean was larger. As a result, northward volume transport in the lower layer related to gravitational circulation increased, and bottom intrusions were intensified by the northward flow, and much cold water was supplied to the Bungo Channel.

Although the Bungo Channel faces the Pacific Ocean, the lower-salinity condition continued for 2 months. The heavy rain event in early July 2018 occurred over the entire Seto Inland Sea area (**Figure 2**), supplying an enormous volume of freshwater to the Seto Inland Sea as precipitation and river discharge. Since the density in the Seto Inland Sea in summer is lower than that in the Pacific Ocean, sea water in the Seto Inland Sea is transported to the Pacific Ocean (Chang et al., 2009). As the mean residence time of sea water in the Seto Inland Sea is 7.7 months (Takeoka, 1984), the freshwater supplied to the Seto Inland Sea by the heavy rain might gradually be transported to the Bungo Channel. In addition, the less saline water in the Seto Inland Sea is mixed by the strong tidal current in the narrow Hayasui Strait, located in the northern part of the Bungo Channel. Therefore, the lower-salinity condition lasted for 2 months for the one heavy rain event.

Recently, the numbers of heavy rain events and tropical cyclones approaching the south coast of Japan have increased (Yamaguchi and Maeda, 2020). The resulting increase in precipitation could decrease the water density (decrease salinity) in the Seto Inland Sea. The numerical experiments showed that the density decrease in the Bungo Channel did not trigger the bottom intrusion but did intensify the bottom intrusion. Increases in heavy rain and tropical cyclones around the Seto Inland Sea might enhance the transport of cold water from the shelf slope to the Bungo Channel, increasing the nutrient supply to the Bungo Channel. **Figure 12A** shows characteristics of water mass and dissolved inorganic nitrogen (DIN) concentration of the water mass in the southern part of the Bungo Channel in July. In the surface layer (low water density), salinity were lower and DIN were low as well. DIN concentration increased with water density below 24 σt. Therefore, enhancement of cold water transport from the shelf slope might supply much DIN to the Bungo Channel. In order to estimate DIN transport from shelf slope region, we calculated a liner empirical equation between water temperature and DIN concentration. **Figure 12B** shows the correlation between water

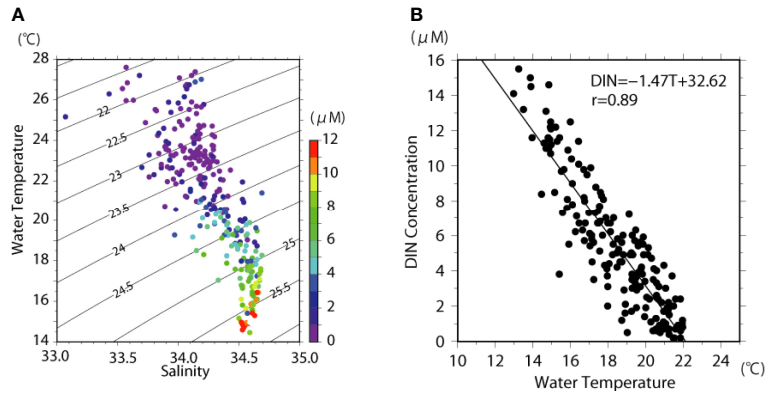

FIGURE 12 | **(A)** T-S diagram with dissolved inorganic nitrogen (DIN) concentration observed in the southern part of the Bungo Channel. Observation points are shown as triangles in **Figure 1B**. **(B)** Scatterplot of water temperature and DIN observed in the southern part of the Bungo Channel. The line in the figure is the regression line.

temperature lower than 22°C and the DIN concentrations at five stations in the southern part of the Bungo Channel; the correlation coefficient was 0.89 and relation between water temperature T and DIN concentration was DIN=-1.47T+32.62. We calculated the DIN flux, NT, across 32.92°N using a following equation.

$$\mathrm{NT} = \int_A DINvda, \tag{2}$$

where *DIN* is DIN concentration calculated from water temperature using above linear empirical equation, *v* is north-southward component of current velocity at 32.92°N, and *A* is section area of 32.92°N. Positive value of NT indicate northward DIN flux. The DIN flux shown in **Figure 13** was positive, *i.e.*, DIN is transported to the Bungo Channel from the Pacific Ocean. The DIN flux was higher when a bottom intrusion occurred. The 2-month DIN flux averaged 0.42 kmol s^{-1} in RC and 0.35 kmol s^{-1} in NRC, being 20% higher in RC. Since no large rivers enter the Bungo Channel, the increase in DIN flux related to an enhanced gravitational circulation would change primary productivity. Hayami et al. (2005) showed that the chlorophyll-a concentration was high when an intense bottom intrusion occurred. An increased nutrient supply to the Bungo Channel from the Pacific Ocean might affect nutrient conditions in the western part of the Seto Inland Sea, as more than 60% of the nutrients in the Seto Inland Sea originate from the Pacific Ocean (Yanagi and Ishii, 2004; Hayami et al., 2005). Gravitational circulations and bottom intrusions in the Bungo Channel are thought to be the main mechanisms supplying nutrients from the Pacific Ocean to the Seto Inland Sea. Therefore, intensification of the gravitational circulation in the Bungo Channel could affect the Bungo Channel and Seto Inland Sea ecosystems. The nutrient supply *via* rivers also increases with heavy rain events (Higashino and Stefan, 2014). The occurrence of heavy rain events near the Seto Inland Sea might increase the nutrient supply from both oceanic and terrestrial sources.

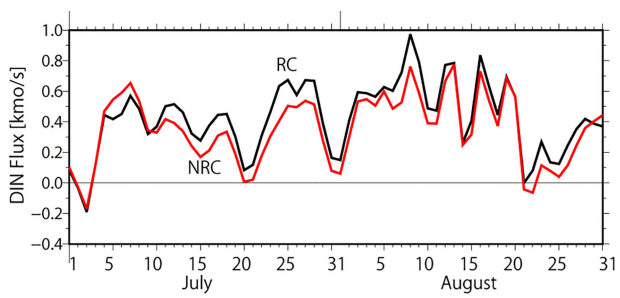

FIGURE 13 | Temporal variation in the DIN flux across 32.92°N shown by the red line in **Figure 1B**. Black and red lines in show the variation in the rain (RC) and no-rain (NRC) cases, respectively.

6 SUMMARY

A water temperature decrease in the surface layer on the eastern coast of the Bungo Channel was observed a few days after a heavy rain event in July 2018. We hypothesized that the heavy rain event influenced the water temperature decrease by intensifying inflow from the Pacific Ocean to the Bungo Channel in the bottom layer, thereby transporting cold water from the shelf slope region to the bottom layer of the Bungo Channel. To examine this hypothesis, we analyzed observed water temperatures and salinity during and after the heavy rain event and conducted numerical experiments.

The water temperature decrease in the surface layer after the heavy rain event was caused by strong vertical mixing of the cold water mass in the bottom layer supplied by a bottom intrusion, during a spring tide. Numerical experiments showed that the heavy rain event did not affect the occurrence of the bottom intrusion but did intensify the bottom intrusion. The numerical experiments also showed that the heavy rain event in early July gave rise to a lower water density in the Bungo Channel for 2

months, which intensified the gravitational circulation in the Bungo Channel. As a result, the inflow from the Pacific Ocean to the Bungo Channel below 50 m depth increased 17.5% after the heavy rain event.

It was suggested that the intensified gravitational circulation in the Bungo Channel increased the nutrient supply from the Pacific Ocean. The DIN flux across the southern part of the Bungo Channel was 20% larger in the RC than in the NRC in the numerical experiment. The heavy rain event also increased the nutrient supply *via* rivers. Therefore, heavy rain events near the Seto Inland Sea might increase the nutrient supply from both land and the open ocean.

DATA AVAILABILITY STATEMENT

The original contributions presented in the study are included in the article/supplementary material. Further inquiries can be directed to the corresponding author.

AUTHOR CONTRIBUTIONS

MD developed a physical numerical model. MK and TS analyzed outputs of numerical model. MH and KT conducted hydrographic observation. XG and HT made a basic idea of the present study. All authors contributed to the article and approved the submitted version.

FUNDING

This research was financially supported by the Japan Society for the Promotion of Science, Grant-in-Aid for Scientific Research on Innovative Areas (Research in a proposed research area) (19H05696) and Grant-in-Aid for Scientific Research (B) (20H01972). Research product of Sea Surface Temperature produced from Himawari-8 that was used in this paper was supplied by the P-Tree System, Japan Aerospace Exploration Agency.

ACKNOWLEDGMENTS

The authors are grateful to anonymous reviewers for their critical reading and useful comments.

REFERENCES

Akiyama, H., and Saito, S. (1993). The *Kyucho* in Sukumo Bay Induced by Kuroshio Warm Filament Intrusion. *J. Oceanogr.* 49, 667–682. doi: 10.1007/BF02276751

Arai, M. (2005). Numerical Study of a Kyucho and a Bottom Intrusion in the Bungo Channel, Japan: Disturbances Generated by the Kuroshio Small Meanders. *J. Oceanogr.* 61, 953–971. doi: 10.1007/s10872-006-0012-3

Atkinson, L. P. (1977). Modes of Gulf Stream Intrusion Into the South Atlantic Bight Shelf Waters. *Geophys. Res. Lett.* 4, 583–586. doi: 10.1029/GL004i012p00583

Blumberg, A. F., and Mellor, G. L. (1987). "A Description of a Three Dimensional Coastal Ocean Circulation Model," in *In Three-Dimensional Coastal Ocean Models, Coastal Estuarine Stud*, Vol. 4 . Ed. N. Heaps (AGU, Washington, D.C: American Geophysical Union), 1–16.

Brink, K. H. (2016). Cross-Shelf Exchage. *Annu. Rev. Mar. Sci.* 8, 59–78. doi: 10.1146/annurev-marine-010814-015717

Castelao, R. (2011). Intrusion of Gulf Stream Waters Onto the South Atlantic Bight Shelf. *J. Geophys. Res.* 116, C10011. doi: 10.1029/2011JC007178

Chang, P. H., Guo, X., and Takeoka, H. (2009). A Numerical Study of the Seasonal Circulation in the Seto Inland Sea, Japan. *J. Oceanogr.* 65, 721–736. doi: 10.1007/s10872-009-0062-4

Fujibe, F. (2015). Relationship Between Interannual Variations of Extreme Hourly Precipitation and Air/Sea-Surface Temperature in Japan. *SOLA* 201511, 5–9. doi: 10.2151/sola.2015-002

Hanawa,, and Mitsudera, (1985). On the Data Processings of Daily Mean Values of Oceanographical Data: Note on the Daily Mean Sea-Level Data. *Bull. Coast. Oceanogr.* 23 (1), 79–87. doi: 10.32142/engankaiyo.23.1_79

Hayami, Y., Ougiyama, S., Yamada, M., Yamada, M., Takemura, K., and Takeoka, H. (2005). Seasonal and Inter-Annual Variation in Chlorophyll a Concentration in Kitanada Bay, Uwa Sea. *Bull. Jpn. Soc Fish. Oceanogr.* 69, 1–9.

Higashino, M., and Stefan, H. G. (2014). Modeling the Effect of Rainfall Intensity on Soil-Water Nutrient Exchange in Flooded Rice Paddies and Implications for Nitrate Fertilizer Runoff to the Oita River in Japan. *Water Resour. Res.* 50 (11), 8611–8624. doi: 10.1002/2013WR014643

Isobe, A., Guo, X., and Takeoka, H. (2010). Hindcast and Predictability of Sporadic Kuroshio-Water Intrusion (*Kyucho* in Bungo Channel) Into the Shelf and Costal Waters. *J. Geophys. Res.* 115, C04023. doi: 10.1029/2009JC005818

Kaneda, A., Norimatsu, K., Watanabe, K., Koizumi, Y., and Takeoka, H. (2002c). Influence of Onshore/Offshore Movement of the Kuroshio on the Water Temperature in the Bungo Channel, Japan. *Bull. Coast. Oceanogr.* 39 (2), 181–188. doi: 10.32142/engankaiyo.39.2_181

Kaneda, A., Takeoka, H., and Koizumi, Y. (2002b). Periodic Occurrence of Diurnal Signal of ADCP Backscatter Strength in Uchiumi Bay. *Estuar. Coast. Shelf. Sci.* 55, 323–330. doi: 10.1006/ecss.2001.0908

Kaneda, A., Takeoka, H., Nagaura, E., and Koizumi, Y. (2002a). Periodic Intrusion of Cold Water From the Pacific Ocean Into the Bottom Layer of the Bungo Channel, Japan. *J. Oceanogr.* 58, 547–556. doi: 10.1023/A:1021262609923

Katano, T., Kaneda, A., Takeoka, H., and Nakano, S. (2005). Seasonal Changes in Abundance and Composition of Picophytoplankton in Relation to Occurrence of Kyucho and Bottom Intrusion in Uchiumi Bay, Japan. *Mar. Ecol. Prog. Ser.* 298, 59–67. doi: 10.3354/meps298059

Koizumi, Y. (1999). *Kyucho Events and the Mechanism of Phytoplankton Growth in the Eastern Coast of the Bungo Channel* (University of Tokyo: Doctoral Thesis), 145 pp.

Lee, T. N., Atkinson, P. A., and Legeckis, R. (1981). Observations of a Gulf Stream Frontal Eddy on the Georgia Continental Shelf, April 1977. *Deep-Sea. Res.* 28, 347–378. doi: 10.1016/0198-0149(81)90004-2

Lents, S. J. (2003). A Climatology of Salty Intrusions Over the Continental Shelf From Georges Bank to Cape Hatteras. *J. Geophys. Res.* 108 (C10), 3326. doi: 10.1029/2003JC001859

Matsumoto, K., Takanezawa, T., and Ooe, M. (2000). Ocean Tide Models Developed by Assimilation TOPEX/POSEIDON Altimeter Data Into Hydorodynamical Model: A Global Model and a Regional Model Around Japan. *J. Oceanogr.* 56 (5), 567–581. doi: 10.1023/A:1011157212596

Mellor, G. L., and Yamada, T. (1982). Development of a Turbulence Closure Model for Geophysical Fluid Problems. *Rev. Geophys.* 20, 851–875. doi: 10.1029/RG020i004p00851

Miyazawa, Y., Zhang, R., Guo, X., Tamura, H., Ambe, D., Lee, J.-S., et al. (2009). Water Mass Variability in the Western North Pacific Detected in a 15-Year Eddy Resolving Ocean Reanalysis. *J. Oceanogr.* 65, 737–756. doi: 10.1007/s10872-009-0063-3

Nagai, T., and Hibiya, T. (2012). Effects of Tidally Induced Eddies on Sporadic Kuroshio-Water Intrusion (*Kyucho*). *J. Oceanogr.* 69, 369–377. doi: 10.1007/s10872-013-0179-3

Schaeffer, A., Roughan, R., and Wood, J. E. (2013). Observed Bottom Boundary Layer Transport and Uplift on the Continental Shelf Adjacent to a Western

Boundary Current. *J. Geophys. Res. Ocean.* 119, 4922–4939. doi: 10.1002/2013JC009735

Smagorinsky, J. S. (1963). General Circulation Experiments With the Primitive Equations. I. The Basic Experiment. *Mon. Wea. Rev.* 91, 99–164. doi: 10.1175/1520-0493(1963)091<0099:GCEWTP>2.3.CO;2

Takeoka, H. (1984). Fundamental Concepts of Exchange and Transport Time Scales in a Coastal Sea. *Cont. Shelf. Res.* 3 (3), 311–326. doi: 10.1016/0278-4343(84)90014-1

Takeoka, H., Akiyama, H., and Kikuchi, T. (1993). The *Kyucho* in the Bungo Channel, Periodic Intrusion of Oceanic Warm Water. *J. Oceanogr.* 49, 369–382. doi: 10.1007/BF02234954

Takeoka, H., Koizumi, Y., and Kaneda, A. (2000). "Year-To-Year Variation of a Kyucho and a Bottom Intrusion in the Bungo Channel, Japan," in *Interaction Between Estuaries, Coastal Seas and Shelf Seas*. Ed. T. Yanagi (Tokyo: Terra Scientific Publishing Company), 192–215.

Takeoka, H., Tanaka, Y., Ohno, Y., Hisaki, Y., Nadai, A., and Kuroiwa, H. (1995). Observation of the Kyucho in the Bungo Channel by HF Radar. *J. Oceanogr.* 51, 699–711. doi: 10.1007/BF02235460

Takeoka, H., and Yoshimura, T. (1988). The *Kyucho* in Uawjima Bay. *J. Oceanogr. Soc Jap.* 44, 6–16. doi: 10.1007/BF02303146

Ullman, D. S., Codiga, D. L., Pfeiffer-Herbert, A., and Kincaid, C. R. (2014). An Anomalous Near-Bottom Cross-Shelf Intrusion of Slop Water on the Southern New England Continental Shelf. *J. Geophys. Res. Ocean.* 119, 1739–1753. doi: 10.1002/2013JC009259

Yamaguchi, M., and Maeda, S. (2020). Increase in the Number of Tropical Cyclones Approaching Tokyo Since 198. *J. Meteor. Soc Jap.* 98, 775–786. doi: 10.2151/jmsj.2020-039

Yanagi, T., and Ishii, D. (2004). Open Ocean Originated Phosphorus and Nitrogen in the Seto Inland Sea. *J. Oceanogr.* 60, 1001–1005. doi: 10.1007/s10872-005-0008-4

Conflict of Interest: The authors declare that the research was conducted in the absence of any commercial or financial relationships that could be construed as a potential conflict of interest.

Publisher's Note: All claims expressed in this article are solely those of the authors and do not necessarily represent those of their affiliated organizations, or those of the publisher, the editors and the reviewers. Any product that may be evaluated in this article, or claim that may be made by its manufacturer, is not guaranteed or endorsed by the publisher.

Copyright © 2022 Morimoto, Dong, Kameda, Shibakawa, Hirai, Takejiri, Guo and Takeoka. This is an open-access article distributed under the terms of the Creative Commons Attribution License (CC BY). The use, distribution or reproduction in other forums is permitted, provided the original author(s) and the copyright owner(s) are credited and that the original publication in this journal is cited, in accordance with accepted academic practice. No use, distribution or reproduction is permitted which does not comply with these terms.

frontiers | Frontiers in Marine Science

ORIGINAL RESEARCH
published: 18 May 2022
doi: 10.3389/fmars.2022.853847

Differences in the Composition of Abundant Marine Picoeukaryotes in the Marginal Sea Derived from Flooding

Chih-Ching Chung[1,2*], *Gwo-Ching Gong*[1,2], *Yun-Chi Lin*[1] and *Ching-Wei Hsu*[1]

[1] Institute of Marine Environment and Ecology, National Taiwan Ocean University, Keelung, Taiwan, [2] Center of Excellence for the Oceans, National Taiwan Ocean University, Keelung, Taiwan

OPEN ACCESS

Edited by:
Hiroaki Saito,
The University of Tokyo, Japan

Reviewed by:
Shunyan Cheung,
University of California, Santa Cruz, United States
Yasuhide Nakamura,
Shimane University, Japan

***Correspondence:**
Chih-Ching Chung
chungcc@mail.ntou.edu.tw

Specialty section:
This article was submitted to Coastal Ocean Processes, a section of the journal Frontiers in Marine Science

Received: 13 January 2022
Accepted: 11 April 2022
Published: 18 May 2022

Citation:
Chung C-C, Gong G-C, Lin Y-C and Hsu C-W (2022) Differences in the Composition of Abundant Marine Picoeukaryotes in the Marginal Sea Derived from Flooding. Front. Mar. Sci. 9:853847. doi: 10.3389/fmars.2022.853847

The transient impact of flooding on the community composition of marine picoeukaryotes (PEs, cell size ≤5 μm) in the East China Sea (ECS) was revealed in this study. In a summer without flooding (i.e., July 2009), photosynthetic picoeukaryotes (PPEs) were more abundant in the area covered by the Changjiang River diluted water (CDW, salinity ≤31) than in the non-CDW affected area. According to the 18S ribosomal RNA phylogeny, Alveolata (all from the superclass Dinoflagellata) was the main community component accounting for 72 to 99% of the community at each sampling station during the nonflooded summer. In addition to Dinoflagellata, diatoms or Chlorophyta also contributed a considerable proportion to the PE assemblage at the stations close to the edge of CDW coverage. In July 2010, an extreme flooding event occurred in the Changjiang River basin and led to the CDW covering nearly half of the ECS. In the flooded summer, the abundance of PPEs in the CDW-covered area decreased significantly to less than 1×10^4 cells ml^{-1}. Compared to that during the nonflooded summer, the diversity of the PE composition was increased. While Dinophyceae still dominated the surface waters, Syndiniophyceae, which were represented by the uncultured Marine Alveolata Group (MALV)-I and MALV-II, accounted for a substantial amount in the Dinoflagellata superclass relative to this community composition in the nonflooded summer. Furthermore, a variety of plankton, including Cryptophyta, Haptophyta, Picobiliphyta, the uncultured Marine Stramenopiles (MASTs) and heterotrophic nanoflagellates, were observed. The nutrition modes of these PEs have been reported to be mixotrophic or heterotrophic. Therefore, it was inferred that the potentially mixotrophic and heterotrophic PE compositions might be favored in the marginal sea in the flooded summer.

Keywords: picoeukaryote, 18S rRNA phylogeny, flooding, global climate change, East China Sea

INTRODUCTION

The distribution and succession of picoplankton (cell size ≤2 μm; recent studies defined it as ≤5 μm) are easily affected by abrupt environmental events because of their tiny cell sizes and various physiological characteristics. According to the existence of a cell nucleus, picoplankton can be divided into prokaryotic picoplankton and eukaryotic picoplankton (also known as picoeukaryotes, PEs). Picocyanobacteria (mainly *Synechococcus* and *Prochlorococcus*) are important prokaryotic picoplankton in the ocean. There have been many studies describing their responses to sudden environmental changes. For example, it has been reported that sudden environmental events, such as the passage of tropical cyclones, heavy atmospheric deposition associated with dust storms, or abundant terrestrial material inputs derived from flooding events, not only promote the transient growth of *Synechococcus* species but also alter their community assemblage (Chang et al., 1996; Herut et al., 2005; Chen et al., 2009; Chung et al., 2011; Chung et al., 2014; Chung et al., 2015). However, there is still a lack of relevant field studies on the relationship between PE assemblage composition and sudden environmental changes. The taxonomic assemblages of PEs are more diverse than those of picocyanobacteria. In addition, PEs exhibit versatile nutritional strategies (i.e., phototrophy, mixotrophy, and heterotrophy), allowing them to cope with changes in the surrounding environment (Worden et al., 2015). Regarding the phototrophic mode, photosynthetic picoeukaryotes (PPEs) and picocyanobacteria are important primary producers in the microbial carbon cycle in marine ecosystems. The abundance of PPEs is usually lower than that of picocyanobacteria by approximately one to two orders of magnitude; however, their contributions to total primary production are almost equivalent (Worden et al., 2004; Jardillier et al., 2010). Another large group of PEs are heterotrophic and play the role of primary consumers in the microbial food web (Stoeck et al., 2010; McKie-Krisberg and Sanders, 2014; Unrein et al., 2014; Worden et al., 2015; Leles et al., 2018). In addition to PPEs and heterotrophic PEs, mixotrophic PEs exhibit a dual nutritional strategy within single cells. These organisms shift their trophic mode from phototrophy to bacterivory when the environment is inappropriate for photosynthesis or when the cells lack nutrients (McKie-Krisberg and Sanders, 2014; Worden et al., 2015). In response to environmental changes, alterations in the composition of PEs or the conversion of their nutritional modes might further affect the microbial carbon cycle and the biogeochemical cycles of marine ecosystems (Hoegh-Guldberg and Bruno, 2010; Stoeck et al., 2010; Hilligsøe et al., 2011; Worden et al., 2015; Leles et al., 2018).

Rivers input considerable amounts of fresh water and terrestrial materials into the ocean, providing an important source of nutrients for phytoplankton growth in estuaries and adjacent oceanic areas (Justić et al., 1995; Gong et al., 2006). The Changjiang River (aka. the Yangtze River) is the longest river in Asia, and its input substantially affects the biogeochemical processes of the East China Sea (ECS) shelf. However, the completion and commissioning of the Changjiang River Dam have led to a significant decrease in the supply of fresh water and terrestrial materials to the ECS. The deficiency of the terrestrial supply of nutrients (e.g., silicate) has not only led to a decline in primary productivity but has also caused the dominant phytoplankton to shift from diatoms to dinoflagellates (Gong et al., 2006). However, the injection of large amounts of freshwater and riverine materials derived from a flood that occurred in the Changjiang River Basin stimulated a temporary massive growth of diatoms in the ECS (Gong et al., 2011). Under increasing human activities and the scenario of global environmental change, floods and droughts will likely occur often, especially in Eastern Asia (IPCC, 2021). More dynamic river discharge and loading of terrestrial materials will result in greater impacts on the marine ecosystem. Compared to microplankton (cell size ≥20 μm, e.g., diatoms), picoplankton show a relatively fast response to environmental changes due to their tiny cell size. Previous studies examining the influence of terrigenous substances on marine picoplankton ecology have often been conducted in estuaries (e.g., Paerl et al., 2020), and information from shelf and open ocean areas is still lacking. In the ECS, Tsai et al. (2010) and Lee et al. (2018) both proposed that the abundance and distribution of picoplankton were determined by the degree of the expansion of Changjiang discharge water over the shelf of the ECS. However, the community assemblages of picoplankton and their dynamics during flooding periods have not been comprehensively described.

In the summer of 2010, a devastating flood occurred in the Changjiang River Basin. The consequent freshwater inputs resulted in the expansion of the Changjiang River discharge to over half of the ECS. We have examined the influence of flooding on the ecology of prokaryotic picoplankton in our previous studies (Chung et al., 2014; Chung et al., 2015). Although PEs are larger than prokaryotic picoplankton, the PE community assemblage is difficult to determine based on microscopic observation alone due to the tiny size of these organisms. Recently, phylogenetic analyses of 18S ribosomal RNA genes have been well developed to examine PEs in the oceans at a fine taxonomic resolution (Moon-van der Staay et al., 2001; Massana, 2011). Phylogenetic information combined with hydrographic data will be of great utility in addressing the ecological roles of different PEs and inferring the impacts of environmental changes on their niches in the oceans. This study, combined with our previous findings, will provide more comprehensive information on how floods affect the succession of picoplankton in the ocean.

MATERIALS AND METHODS

Sample Collection

Two voyages aboard R/V *Ocean Researcher I* were conducted in the ECS during the periods from 29 June to 13 July 2009 and 6 July to 17 July 2010 (**Figure 1A**). Temperature and salinity were measured with a conductivity/temperature/depth recorder (CTD) (SBE911 plus, Sea-Bird Electronics, Washington, USA). Water samples for determining the concentrations of nutrients and chlorophyll *a* and the abundance of picoplankton were

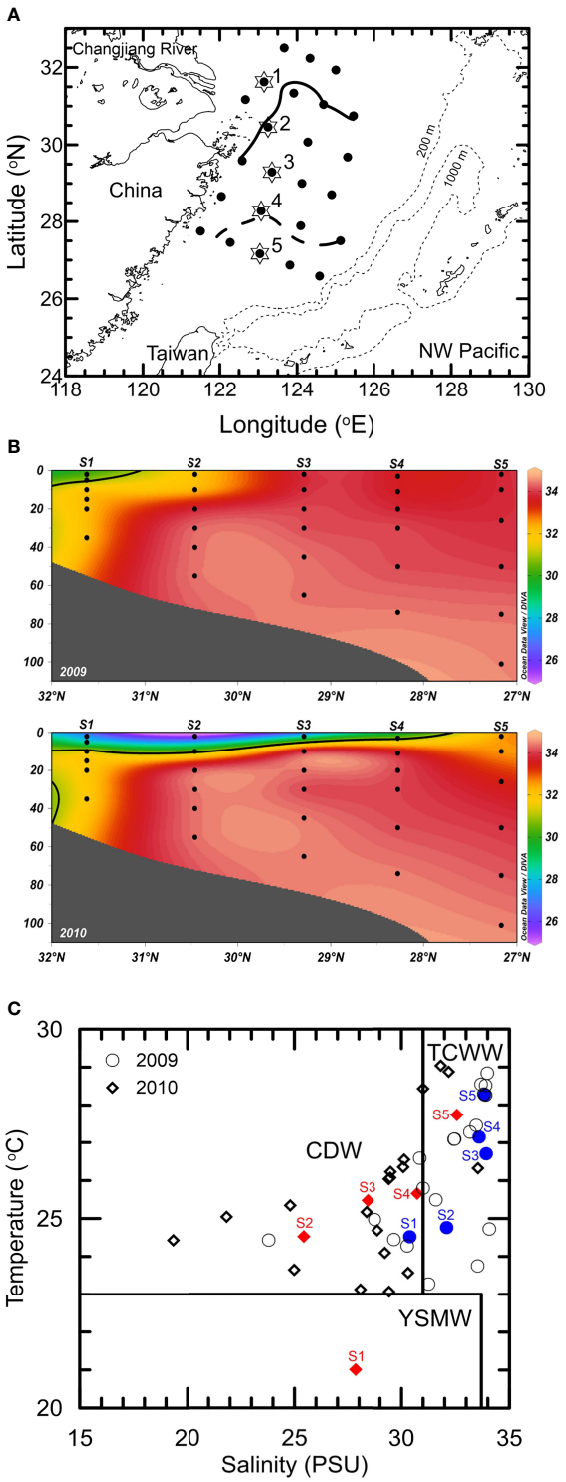

FIGURE 1 | **(A)** Locations of observation stations in the East China Sea. The solid and dashed lines represent the isohaline of 31 in the summers of 2009 and 2010, respectively. A total of 24 stations were visited during the 2 cruises. The phylogenetic analysis of 18S rRNA genes was performed based on the surface samples of Stations 1 to 5 denoted by star symbols. **(B)** Vertical distribution of salinity at Stations 1 to 5 in the summers of 2009 and 2010. The isohaline of 31 is indicated by the solid line. **(C)** Temperature-salinity diagram. Characterization of different water masses, including the Changjiang diluted water (CDW), the Taiwan strait current warm water (TCWW) and the Yellow Sea mixed water (YSMW), was in accordance with the definitions of Gong et al. (1996).

collected using Teflon-coated 20-liter Niskin bottles (General Oceanics, Florida, USA) mounted on a CTD rosette sampler. A total of 24 stations located on the ECS shelf were visited. DNA samples collected from the surface (depth=5 m) at the 5 stations (S1 to S5) (**Figure 1A**) were used to analyze the phylogenetic diversity of 18S rRNA genes.

Determination of Chlorophyll *a* and Nutrient Concentrations

One liter of water to be used for chlorophyll *a* analysis was immediately filtered through a GF/F class filter (Whatman, Maidstone, UK), and the filter was stored at -20°C until analysis. Chlorophyll *a* preserved on the filter was extracted in pure acetone at 4°C overnight in the dark and was measured with a fluorometer (10-AU-005, Turner Design, California, USA) (Welschmeyer, 1994; Gong et al., 1996). To determine the concentrations of dissolved inorganic nutrients, the water sample was placed in a polypropylene bottle and immediately frozen with liquid nitrogen onboard the survey vessel. Nitrite (NO_2) and nitrate (NO_3) concentrations were measured *via* the pink azo dye method with a self-designed flow injection analyzer (Strickland and Parsons, 1972; Gong et al., 1996). The concentration of phosphate (PO_4) was determined by the molybdenum blue method (Pai et al., 1990; Gong et al., 1996).

Counting of Picoplankton

Samples for picoplankton counting were fixed in seawater-buffered paraformaldehyde at a final concentration of 0.2% (w/v), frozen in liquid nitrogen and kept at -80°C until analysis. Flow cytometry (FACSAria, Becton-Dickinson Co., New Jersey, USA) was applied to distinguish different populations of picoplankton. For picocyanbacteria (i.e., *Synechococcus* and *Prochlorococcus*) and small PPEs, abundance estimates and counts were determined according to their cell size (forward- and side-scattering) and their autofluorescence in the orange (from phytoerythrin, 575 ± 15 nm) and red (from chlorophyll, >670 nm) ranges. Heterotrophic bacteria were counted in a separate subsample stained with SYBR-Green I dye (Molecular Probes Inc., Oregon, USA). A known number of fluorescent beads (TruCOUNT Tubes, Becton-Dickson Co., New Jersey, USA) was simultaneously counted to convert the flow rates for determining picoplankton abundance in the sample (Liu et al., 2002; Chung et al., 2015).

DNA Extraction From Small Planktonic Cells

Five liters of the surface water was subsequently filtered through 20 μm-pore size nylon mesh (Sefar, Heiden, Switzerland) and 5 μm-pore size polycarbonate membranes (47 mm diameter) (Nuclepore, Whatman, Maidstone, UK) to remove larger plankton. The cells in the filtrate were harvested using 0.8 μm-pore size polycarbonate membranes (47 mm diameter) (Nuclepore, Whatman, Maidstone, UK) under gentle vacuum (≤100 mmHg). The membranes were frozen in liquid nitrogen and kept at -80°C until DNA extraction. Cells (cell size between 0.8 and 5 μm) retained on the membranes were disrupted by glass beads (0.1 mm diameter) using a bead beater (BioSpec Products, Oklahoma, USA) and then treated with lysis buffer containing 0.1 M EDTA (pH 8.0), 1 mM Tris-HCl (pH 8.0), 0.25% sodium dodecyl sulfate and 0.1 mg ml^{-1} proteinase K (Roche, Penzberg, Germany) at 55°C overnight. After the removal of detritus and residual polysaccharides by treatment with 1% hexadecyltrimethylammonium bromide (Sigma-Aldrich, Missouri, USA), followed by chloroform extraction and an additional round of phenol/chloroform/isoamyl alcohol (v:v:v=25:24:1) extraction, DNA was precipitated by adding isopropanol. The DNA pellet was dissolved in Tris-EDTA buffer (pH 8.0), and its concentration and purity were determined using a spectrophotometer (NanoDrop, Thermo Scientific, Delaware, USA) at wavelengths of 260 and 280 nm (Chung et al., 2015).

Pyrosequencing

Variable region 4 (V4) of the 18S rRNA gene was amplified by polymerase chain reaction (PCR) with 50 ng DNA as the template. The PCR mixture contained Phusion High-Fidelity DNA polymerase (New England Biolabs, Massachusetts, USA), 1× Phusion HF buffer, a 200 μM deoxynucleotide solution mixture, and both the forward fusion primer "Primer A-MID-TAReukFWD" (5'-Primer A-MID-CCAGCASCYGCG GTAATTCC-3', MID=multiplex identifier, S=G or C, Y=C or T) and the reverse primer "TAReukREV" (5'-ACTTTCGTT CTTGATYA-3', Y=C or T, R=A or G) (Stoeck et al., 2010; Tamaki et al., 2011). Unidirectional pyrosequencing was performed only with Primer A (Tamaki et al., 2011). The MIDs were used to assist in sample identification after pyrosequencing. To increase specificity and sensitivity in PCR amplification, touchdown PCR was performed in a thermocycler (Model 9700, Applied Biosystems, New York, USA) under the following conditions: 1 cycle of 98°C for 30 sec; followed by 10 cycles of 98°C for 10 sec, 53°C for 30 sec, and 72°C for 30 sec; then 20 cycles of 98°C for 10 sec, 48°C for 30 sec, and 72°C for 30 sec; and finally, 1 cycle of 72°C for 10 min. The amplicons were subjected to agarose gel electrophoresis and purified using a QIAquick Gel Extraction Kit (Qiagen, California, USA). The concentrations of the purified amplicons (495 base pairs) were measured using a Qubit dsDNA High Sensitive Assay Kit (Thermo Fisher Scientific, Massachusetts, USA) and a fluorometer (Qubit 2.0) (Thermo Fisher Scientific, Massachusetts, USA). Equal molar amounts of all amplicons were combined for pyrosequencing on a Roche 454 Genome Sequencer FLX+ Instrument (454 Life Sciences, Connecticut, USA).

Sequence Processing, Operational Taxonomic Unit (OTU) Definition, and Diversity Analysis

Raw sequences were processed using the algorithms AmpliconNoise (Quince et al., 2011) and PyroNoise (Quince et al., 2009) to reduce the pyrosequencing error rates. Any sequence with more than one mismatch with the MID, more than two mismatches with the primers, or a PCR one-base error was excluded. Chimeras were detected and removed with UCHIME (Edgar et al., 2011). All the

resultant sequences were aligned to the SILVA rRNA SEED database (release 138) and clustered into OTUs at a cutoff level of 3% divergence based on the pairwise alignment distance. The taxonomy of each OTU was annotated by the SILVA rRNA reference dataset (release 138) with the Ribosomal Database Project Classifier (Wang et al., 2007) and was subsequently confirmed using BLASTN searches against the GenBank database. The OTUs that were not classified as eukaryotic 18S rRNA genes or affiliated with larger protozoans (i.e., ciliates and radiolarians) and metazoans (e.g., copepods) were excluded from further analysis. The OTUs comprising less than 2 reads (i.e., singletons and doubletons) were also removed. The resultant OTUs were applied for the assessment of richness and diversity indices. Additionally, the OTUs with a relative contribution greater than 0.1% of the total reads in any sample were regarded as abundant OTUs and were applied to investigate the assemblage composition of PEs (Wu et al., 2017). All of the above and α- and β-diversity analyses were implemented using the Mothur software package (version 1.47.0) (Schloss et al., 2009). The phylogenetic relationship between the abundant OTUs in a taxon was interpreted by the maximum likelihood (ML) algorithm with the Kimura two-parameter model (Kimura, 1980). The effects of sampling error on tree inference and the stability of branch nodes were tested by bootstrap analyses with 1,000 repetitions. The software IQ-TREE (version 1.4.4) were used for the phylogeny-related analysis and tree construction (Nguyen et al., 2014). The vegan package in R was used in the ordination analysis.

Data Availability

All of the sequences of 18S rRNA V4 gene fragments were deposited in the Sequence Read Archive (SRA) database with accession numbers SAMN10089074 to SAMN10089083.

RESULTS

Hydrographic Characteristics

The plume of the Changjiang River was small during the summer without flooding in 2009. The Changjiang River diluted water (CDW), which has been defined as water with a temperature ≥23°C and salinity ≤31 (Gong et al., 1996), was restricted to the inshore region of the northwestern ECS (approximately 0.4×10^5 km^2). Most surfaces in the ECS were covered with high-temperature, oligotrophic waters from northward-flowing Taiwan Current Warm Water (TCWW) and the intrusion of the Kuroshio Current (**Table 1**, **Figure 1**). These conditions represent the typical hydrography of the ECS in nonflooded summers (Gong et al., 2011). In contrast, extreme flooding occurred in the Changjiang River Basin in summer 2010 and led to a large amount of fresh water being injected into the ECS. Through the extension of CDW coverage to the southern ECS (approximately 1.7×10^5 km^2), more than half of the surface ECS was fertilized with terrestrial nutrients, resulting in a subsequent increase in the chlorophyll *a* concentration (**Table 1**, **Figure 1**).

Distribution of Photosynthetic Picoeukaryotes

Among PEs, only PPEs can be detected and counted by flow cytometry due to the presence of chlorophyll. The distribution of PPEs in both summers is presented in **Figure 2**. Regardless of whether flooding occurred, PPEs were mainly distributed in the coastal areas covered by the CDW. However, the highest count of PPEs in the nonflooded summer was greater than 2.5×10^4 cells ml^{-1}, which was approximately twice as high as the maximum PPE count in the flooded summer. Overall, the abundance of PPEs within the CDW-influenced area in the nonflooded summer was significantly greater than that in the flooded summer (p<0.001) (**Figure 2**).

Diversity of Picoeukaryotes

According to a previous study of hydrography in the ECS (Gong et al., 1996), we defined Station 1 and Station 2 as CDW-influenced stations and Station 5 as an oceanic station. In addition to Stations 1, 2 and 5, the hydrography of Stations 3 and 4 was susceptible. In the nonflooded summer, Stations 3 and 4 were usually covered with salty, higher-temperature water. Nevertheless, during the

TABLE 1 | The hydrographic properties and the cell numbers of phycoerytherin-rich *Synechococcus* (PE-rich *Syn*), photosynthetic picoeukaryotes (PPE) and heterotrophic bacteria (Bac) in the surface waters (depth=5 m) of environmental DNA sampling stations in the summers of 2009 and 2010.

Station	T (°C)	S	TM (%)	DIN (μM)	DIP (μM)	SiO_3 (μM)	Chl. *a* (mg m^{-3})	PE-rich *Syn* (cells ml^{-1})	PPE (cells ml^{-1})	Bac (cells ml^{-1})
2009										
1	24.52	30.38	62.0	4.1	0.28	12.84	5.13	481,500	38,400	1,599,800
2	24.76	32.10	77.2	2.9	0.06	4.32	1.82	657,000	6,200	527,300
3	26.70	33.93	84.8	0	0.10	3.82	0.19	94,500	7,500	992,700
4	27.14	33.60	85.6	0	0.04	2.55	0.17	233,000	6,200	1,310,300
5	28.26	33.85	82.5	0	0.04	2.77	0.24	56,800	3,200	988,000
2010										
1	21.01	27.84	75.4	16.3	0.16	10.85	2.25	62,500	2,200	1,520,200
2	24.52	25.44	75.0	21.1	0.24	13.67	3.36	239,800	10,200	519,600
3	25.47	28.42	79.7	13.9	0.30	2.27	1.71	169,700	6,600	964,600
4	25.66	30.73	81.2	2.4	0.32	4.21	1.30	73,300	4,200	1,018,600
5	27.73	32.57	83.5	0	0.02	1.88	0.66	81,800	11,700	287,900

Hydrographic parameters listed are temperature (T), salinity (S), turbidity (TM), and the concentrations of dissolved inorganic nitrogen (DIN, NO_2+NO_3), dissolved inorganic phosphate (DIP), silicate (SiO_3) and chlorophyll a (Chl. a).

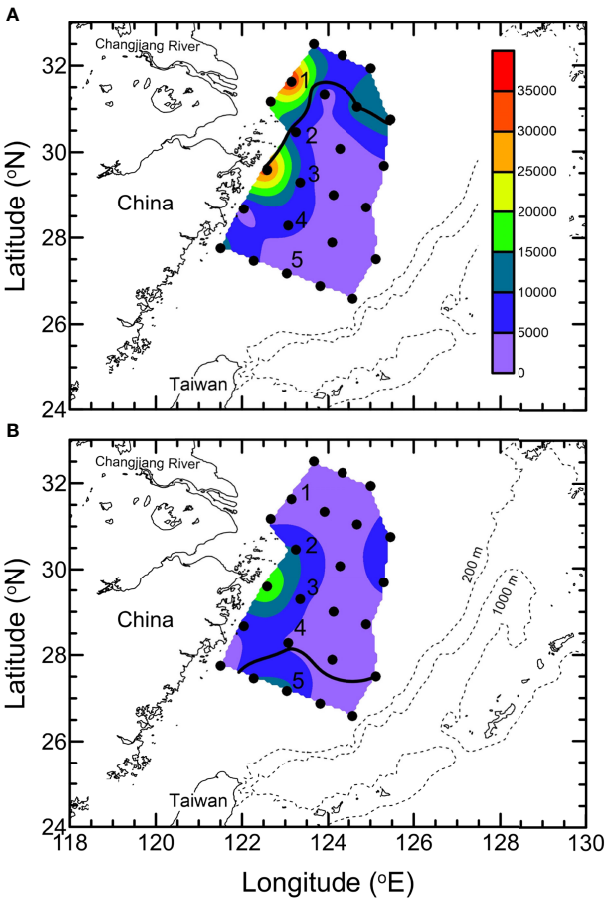

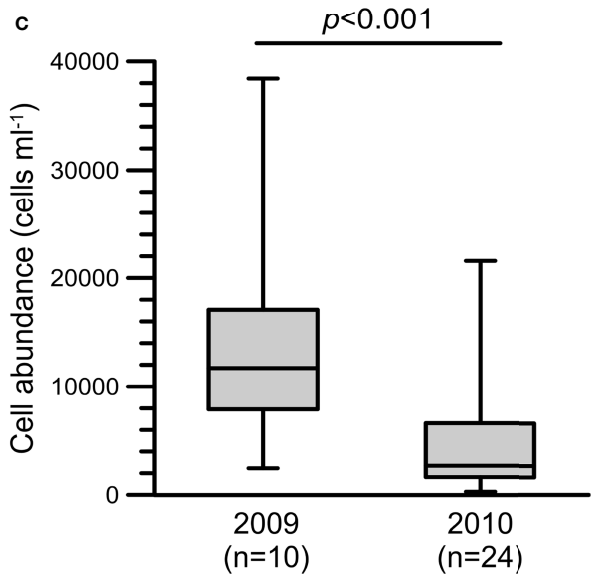

FIGURE 2 | Distribution of photosynthetic picoeukaryotes (PPEs) (cells ml^{-1}) at the surface on the East China Sea shelf in the summers of **(A)** 2009 and **(B)** 2010. The solid lines indicate the isohaline of 31. **(C)** Whisker plot of PPE abundance in the surface waters of the stations confined to the area within the isohaline of 31 (i.e., 10 stations in 2009 and 24 stations in 2010).

flooded summer of 2010, the surfaces of Stations 3 and 4 were overlaid by the extended CDW (**Table 1** and **Figure 1**). Compared to the nonflooded summer of 2009, the hydrographic conditions of the five stations were significantly affected by the occurrence of flooding in the summer of 2010. Therefore, these five stations were selected to further study the impact of flooding on the diversity of the small eukaryotic plankton assemblage.

After the removal of chimeras, singletons, doubletons, and reads belonging to larger protozoans (e.g., ciliates and radiolarians) and metazoans (e.g., copepods), we obtained a total of 960,541 high-quality reads for the 18S rRNA gene phylogenetic analysis. According to the criterion of 3% sequence divergence, these reads were categorized into 2,616 OTUs (**Table 2**). The rarefaction curves, except for that of Station 2, almost reached a plateau phase, indicating that the sampling efforts were enough to analyze 18S rRNA gene diversity (**Supplementary Figure 1**). Based on the ACE, Shannon and Pielou indices, the species richness and divergence of PEs in the flooded summer were greater than those in the nonflooded summer overall. The diversity was more pronounced at the CDW-influenced stations (i.e., Stations 1 and 2) than at the other three offshore stations (i.e., Stations 3, 4 and 5) (**Table 2**, **Figure 3**).

To clarify the impact of floods on the ecology of PEs, a total of 240 abundant OTUs were selected for the subsequent analysis of the community composition. While the abundant OTUs accounted for only approximately one-tenth of the total OTUs, they comprised 902,380 reads, which accounted for 94% of the total reads (**Table 2**). During the nonflooded summer, the PEs at each station were almost entirely composed of the Alveolata species, except at Station 2 (**Figure 4A**). In this study, 63 OTUs were grouped into Alveolata. They all belonged to the phylum Dinoflagellata. Among these OTUs, 18 OTUs were grouped into the class Dinophyceae. They were all affiliated with *Gymnodinium*. OTU-001 accounted for the highest proportion of the community at all stations and was the most important member. The other 45 OTUs were categorized into the class Syndiniophyceae, among which 7 OTUs were affiliated with *Euduboscquella* spp. (the uncultured Marine Alveolata Group I, MALV-I). In addition to OTU-001, OTU-002 (i.e., *Euduboscquella* sp.) contributed considerable read numbers, and this group was also suggested to be the major PE at all stations (**Figure 5**). *Euduboscquella* sp. is already known to be an intracellular parasite of tintinnid ciliates (Jung et al., 2016). The uncultured Marine Alveolata Group II (MALV-II), which comprised 38 OTUs, was another dominant group within Dinoflagellata. Its abundance accounted for less than 10% of all dominant OTU sequences (**Figures 4A**, **5**). All of the OTUs in MALV-II were *Amoebophyra* sp., which are syndinean dinoflagellates that parasitize free-living dinoflagellates, such as *Gymnodinium* (Yih and Coats, 2000). In contrast to the other 3 stations, although Dinoflagellata still accounted for most of the community assemblage at Stations 2 and 3, their proportions declined to 81% and 74%, respectively. Instead, at Station 2, Stramenopiles, mainly represented by two diatoms *Fragilariopsis dollolus* (OTU-49) and *F. kerguelensis* (OTU-101) and one uncultured Marine Stramenopile Group 13 (MAST-13) (*Bicosoeca vacillans*, OTU-316), jointly accounted for approximately 15% of the total reads (**Figures 4A**, **6**). At Station 3, Chlorophyta contributed 25% of the total reads and were primarily composed of *Picochlorum* sp. (OTU-005) and *Chloropicon roscoffensis* (OTU-013), which accounted for 20% and 4%, respectively (**Figures 4A**, **7**).

The community composition of PEs in the flooded summer was more diverse than that in the nonflooded summer. The proportion of Alveolata declined at all stations except Station 4, falling to 80% at Stations 1 and 5 and approximately 50% at Station 2 (**Figure 4B**). Although the composition of the Alveolata to that in the nonflooded summer was similar, the ratio of MALV-II at each station increased to 10% (**Figure 5**). In addition to Alveolata, the other phyla found at all stations were Stramenopiles, Chlorophyta, Haptophyta and Picobiliphyta. Chlorophyta were mainly composed of *Tetraselmis subcordiformis* (OTU-059), *Mamiella* sp. (OTU-187), *Micromonas bravo* (OTU-05) and *Ostreococcus* sp. (OTU-068). They were widely distributed in various stations with a proportion of less than 10%. *Picochlorum* and *Chloropicon*, which were found at Station 3 in the nonflooded summer, almost disappeared in the flooded summer. Moreover,

TABLE 2 | Summary of pyrosequencing result of 18S ribosomal RNA gene V4, and the indices of richness estimate (ACE), diversity (Shannon) and evenness (Pielou) in the East China Sea in the summers of 2009 and 2010 (**Figure 1**).

Station	Total Reads	OTU	Coverage	ACE	Shannon	Pielou
2009						
S1	131,383 (122,861)	308 (11)	1.00	444	0.93	0.19
S2	13,819 (13,466)	280 (28)	1.00	581	2.79	0.48
S3	336,527 (320,163)	1,025 (38)	1.00	878	2.45	0.41
S4	26,495 (23,887)	587 (50)	0.99	973	3.04	0.49
S5	110,761 (98,676)	1,111 (69)	1.00	1,218	3.42	0.52
2010						
S1	85,742 (78,946)	902 (63)	1.00	1,002	3.21	0.51
S2	41,037 (36,698)	762 (92)	1.00	996	4.29	0.67
S3	64,079 (59,449)	704 (64)	1.00	825	2.80	0.46
S4	124,462 (114,080)	1,175 (93)	1.00	1,274	3.70	0.57
S5	32,077 (27,801)	976 (81)	0.99	1,224	4.31	0.64

The numbers in parentheses represent the number of dominant OTUs and the total read number they have in each station.

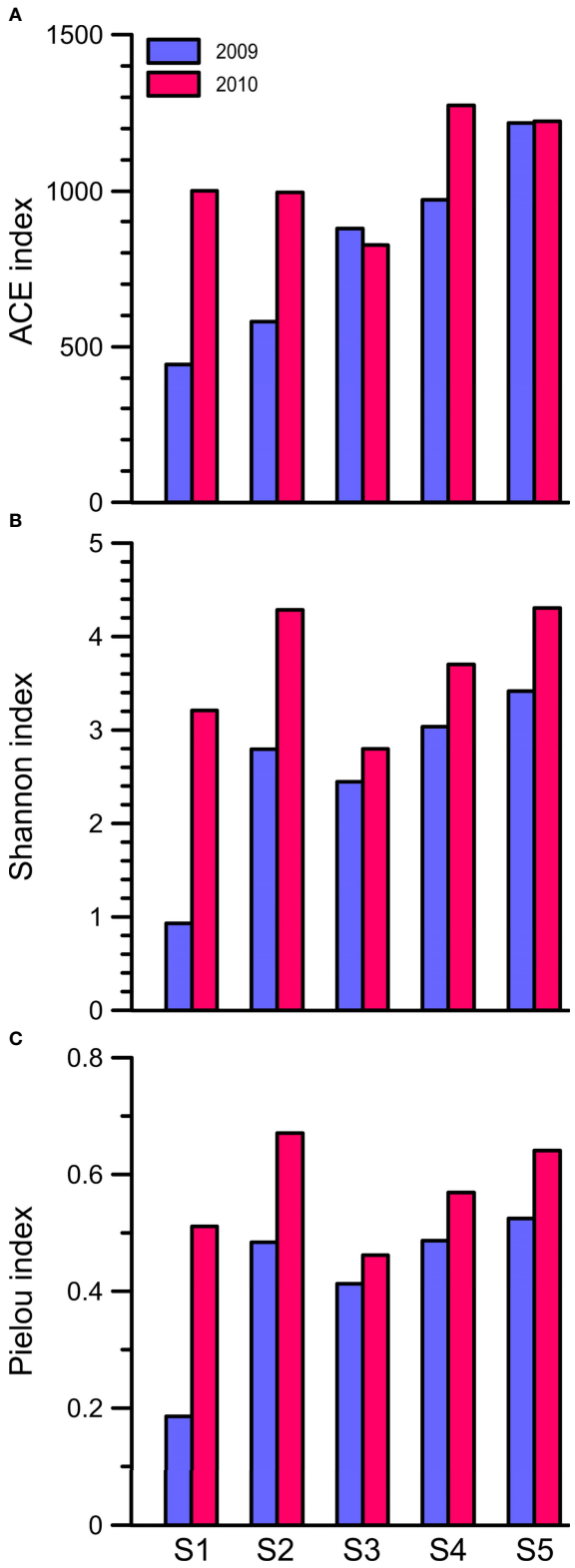

FIGURE 3 | The **(A)** ACE, **(B)** Shannon diversity and **(C)** Pielou evenness indices of the community assemblages of picoeukaryotes, which were inferred from the OTU composition, at Stations 1 to 5 in the summers of 2009 and 2010.

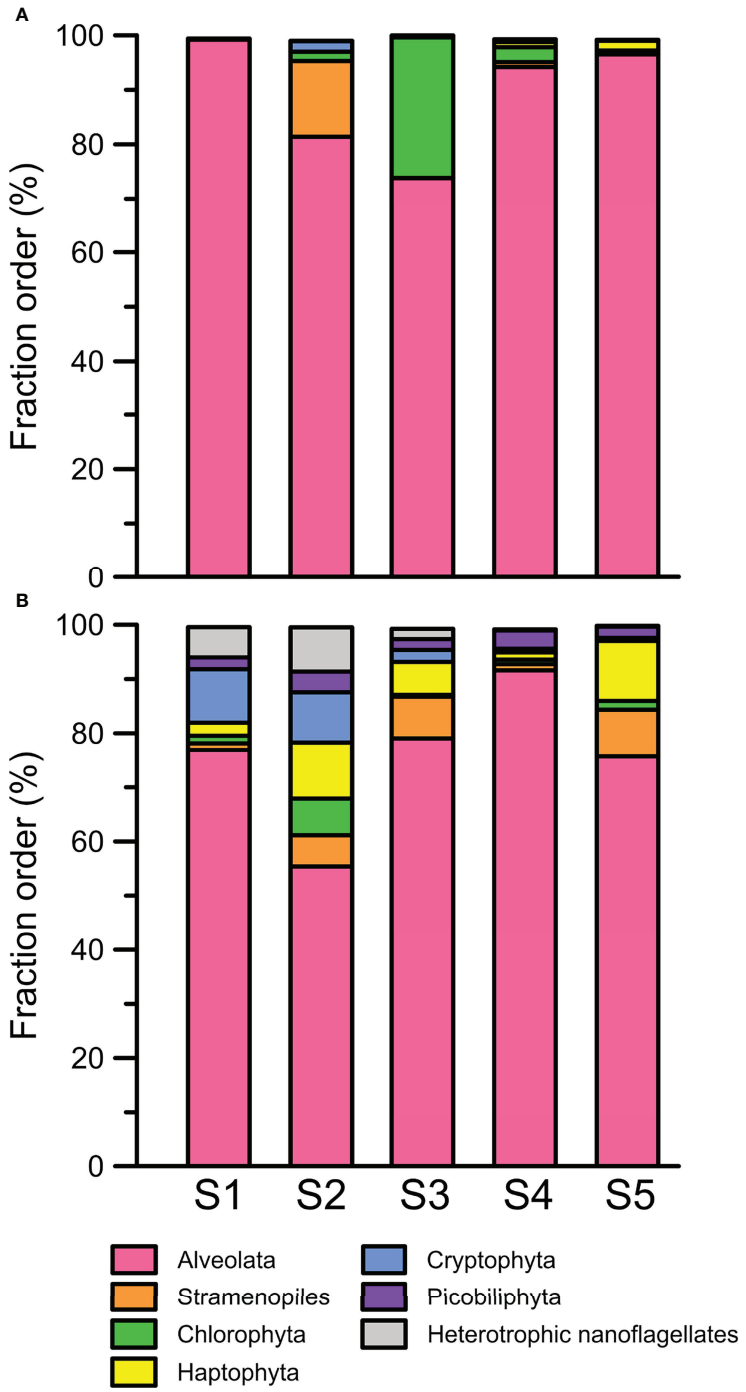

FIGURE 4 | Community compositions of abundant picoeukaryotes indicated at the phylum level at Stations 1 to 5 in the summers of **(A)** 2009 and **(B)** 2010.

Cryptophyta and heterotrophic nanoflagellates only appeared at the CDW-influenced stations (i.e., Stations 1 and 2) (**Figure 4B**). Regarding nutritional strategies, the PEs that were found in the flooded summer were suggested to be heterotrophic or mixotrophic. For example, OTU-036 (*Chrysochromulina simplex*, Haptophyta) (**Figure 8**) and OTU-019 and OTU-032 (*Teleaulax amphioxeia*, Cryptophyta) (**Figure 9**) were mixotrophic. OTU-250 (*Picomonas judraskeda*, Picobiliphyta) (**Figure 10**) and several nanoflagellates, such as OTU-063 (*Protaspis grandis*) and OTU-113 (*Cryothecomonas aestivalis*) (**Figure 11**), were heterotrophic. Additionally, OTU-078 (*Pirsonia verrucose*, MAST-1C, Stramenopiles) and OTU-244

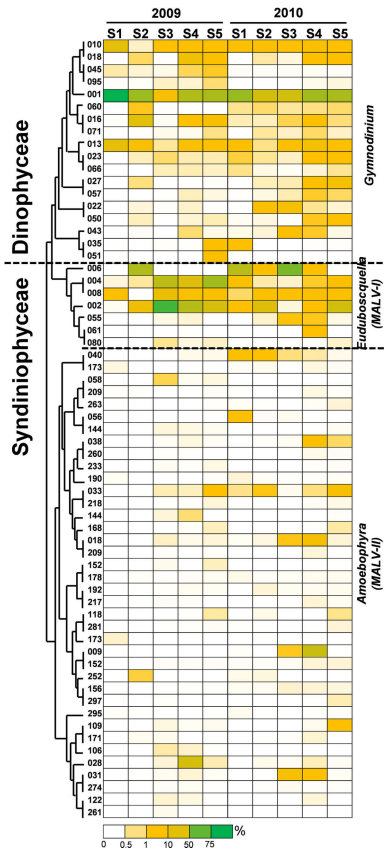

FIGURE 5 | Heatmap representing the relative contribution of each abundant OTU of Alveolata during the summers of 2009 and 2010. All of the abundant OTUs of Alveolata identified in this study were grouped into the phylum Dinoflagellata. After phylogenetic analysis, these OTUs were further assigned to the classes Dinophyceae and Syndiniophyceae. This figure shows that the OTUs of the Dinophyceae were all affiliated with *Gymnodinium*. The other OTUs of the Syndiniophyceae belonged to *Eudubosquella* (MALV-I) and *Amoebophyra* (MALV-II). The relative contribution indicates the percentage of the number of 18S rRNA gene V4 sequences in each OTU. The phylogenetic tree in the left position was constructed using the maximum likelihood algorithm. The labels at the bottom position indicate the color codes of the different percentages.

(*Incisomonas marina*, MAST-3, Stramenopiles) were suggested as parasites for hosting centric diatoms (**Figure 6E**). The new appearance of heterotrophic and mixotrophic PEs in the flooded summer implied that the microbial cycle should be different from that in the summer without flooding.

DISCUSSION

The clustering analysis of the PE assemblage composition at each station and the correlation with environmental parameters are shown in **Figure 12**. The correlation results indicate that salinity reduction and the input of terrestrial dissolved inorganic nitrogen (DIN) were possible factors promoting the transient growth of Cryptophyta and HNFs at the inshore stations (i.e., Stations 1 and 2). The rise in turbidity resulted in increases in Picobiliphyta and MALV-II at the offshore stations (i.e., Stations 3, 4 and 5). Moreover, the abundance of Stramenopiles (e.g., MAST-1C) and Haptophyta (e.g., *Chrysochromulina simplex*) both increased to account for considerable proportions of the total PE composition at each station in the flooded summer. Although there were obvious differences in the species composition at each station in the nonflooded and flooded summers, no consistent inference was obtained based on the correlation analysis between the species composition and various environmental factors (**Figure 12**). The term "picoeukaryotes" generally refers to eukaryotic plankton with cell sizes smaller than 2 or 5 μm. Their community composition is very complicated, and each species possesses unique biological characteristics. It is still difficult to elucidate the relationships among their succession, nutritional modes and ambient parameters (Worden et al., 2015). Our results in this study also supported this interpretation. The combination of systematic studies of single species with more comprehensive sampling of marine PE biodiversity in diverse marine environments will enable significant progress in the comparison and clarification of the relationships between PE activities and environmental factors (Worden et al., 2015).

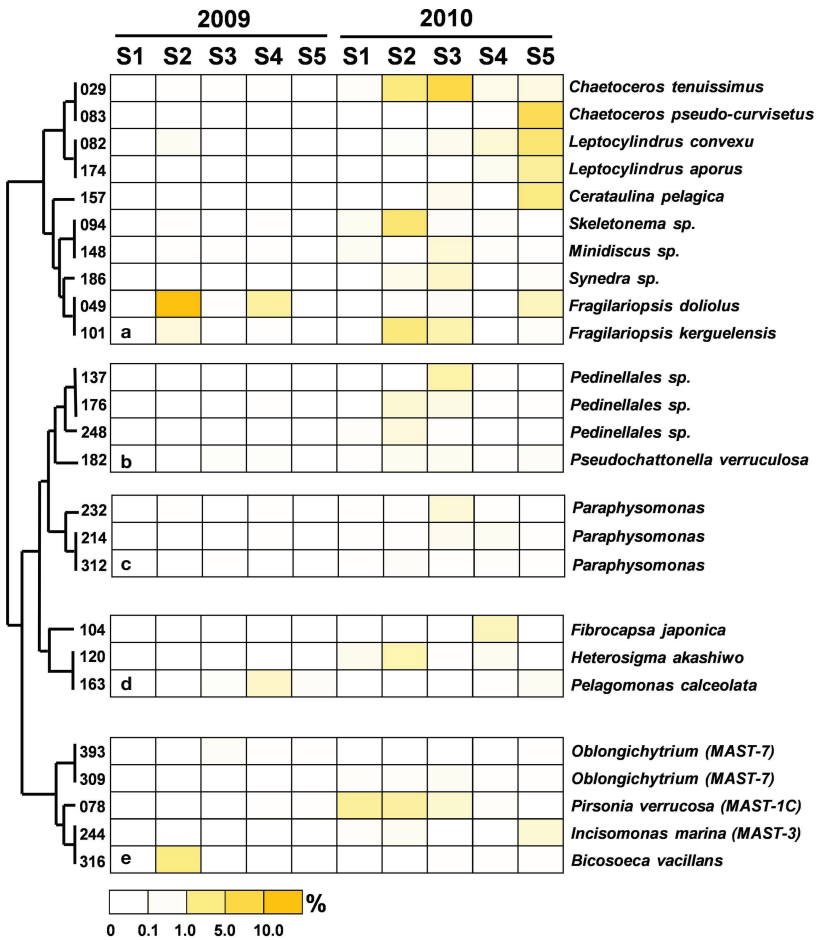

FIGURE 6 | Heatmap representing the relative contribution of each abundant OTU of Stramenopiles during the summers of 2009 and 2010. All of the abundant Stramenopile OTUs identified in this study were grouped into **(A)** Bacillariophyceae, **(B)** Dictyochophyceae, **(C)** Chryosophyceae, **(D)** other (i.e., *F. japonica* belonged to Chloromonadophyceae, *H. akashiwo* belonged to Raphidophyceae, and *P. caceolata* belonged to Pelagophyceae) or **(E)** marine Stramenopile lineages (MAST). The relative contribution indicates the percentage of the number of 18S rRNA gene V4 sequences in each OTU. The phylogenetic tree in the left position was built using the maximum likelihood algorithm. The labels at the bottom position indicate the color codes of the different percentages.

Picoplankton succession responds quickly to changes in the environment. Therefore, when a sudden environmental event occurs, picoplankton composition shows a temporarily higher degree of divergence (e.g., Herut et al., 2005; Chen et al., 2009; Chung et al., 2011; Chung et al., 2015). The newly emerging PE populations in the flooded summer were more diverse and possessed versatile nutrition modes, mostly tending toward heterotrophy or mixotrophy. We found that *Teleaulax amphioxeia* was the main member of Cryptophyta at the inshore stations after the flood (**Figure 9**). It has been reported that *T. amphioxeia* is a mixotroph that shifts its nutritional mode from photosynthesis to predation when the abundance of *Synechococcus* or bacteria increases (Yoo et al., 2017). Accordingly, grazing by *T. amphioxeia* was one of the possible factors contributing to the decrease in the number of *Synechococcus* in the flooded summer (Chung et al., 2014; Chung et al., 2015). *T. amphioxeia* also served as an excellent prey for nanoflagellates and ciliates (Nishitani et al., 2010; Hernández-Urcera et al., 2018). Compared to that occurring in the nonflooded summer, the PE niches in the microbial food web were more differentiated, and the process of the pelagic ecosystem should have been more complicated when the flooding occurred.

Mixotrophic haptophytes have been considered important bacterivores in oligotrophic coastal waters (Unrein et al., 2014; Chan et al., 2018). We found that haptophytes occupied a significant proportion of the picoplankton assemblage at each station in the flooded summer. Among them, *Chrysochromulina* spp. were the major members. *Chrysochromulina* have been identified as mixotrophic haptophytes and showed high phagotrophic ability in phosphate-starved or low-irradiance conditions (Kawachi et al., 1991; Jones et al., 1993).

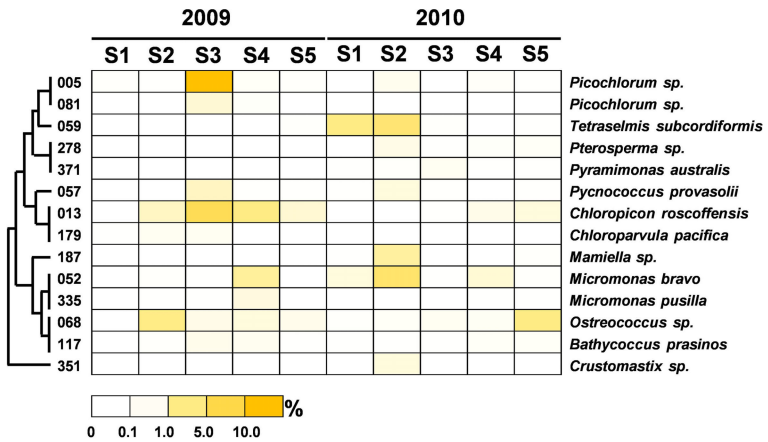

FIGURE 7 | Heatmap representing the relative contribution of each abundant OTU of Chlorophyta during the summers of 2009 and 2010. The relative contribution indicates the percentage of the number of 18S rRNA gene V4 sequences in each OTU. The phylogenetic tree in the left position was built using the maximum likelihood algorithm. The labels at the bottom position indicate the color codes of the different percentages.

Søgaard et al. (2021) reported that an under-ice algal bloom dominated by mixotrophic haptophytes (i.e., *Chrysochromulina* and *Prymnesium*) occurred in the early spring in the Arctic. The authors deduced that freshwater input derived from the melting ice, subsequently resulting in nutrient dilution and low light intensity, jointly led to the thriving of *Chrysochromulina* and *Prymnesium*. However, previous studies on *Chrysochromulina* were all carried out in high-latitude areas. Relevant research works on these species have not been performed in subtropical oceans. Based on the results of the correlation analysis (**Figure 12**) and the previous studies mentioned above, it was inferred that the salinity decline derived from the flooding led to the emergence of *Chrysochromulina* spp.

The operation of the Three Gorges Dam drastically decreased territorial silicate loading into the ECS, resulting in a regime shift in the dominant phytoplankton species from diatoms to dinoflagellates (Gong et al., 2006). A similar distribution of phytoplankton was observed in this study. Regarding the relationship between Stramenopiles distribution and flooding, during the nonflooded period, only a higher proportion of diatoms could be found at Station 2. By contrast, diatoms prevailed at every station in the flooded summer. 18S rRNA sequences from large chain-form diatoms (e.g., *Chaetoceros tenuissimus*, *Leptocylindrus convexu* and *Cerataulins pelagica*, etc.) found in our picoplankton dataset might be attributed to cell rupture during filtration. However, this also suggested that more diatoms should be present in the waters after the input of terrestrial materials (Chung et al., 2012). In addition to diatoms, some heterotrophic lineages of MAST (i.e., MAST-1C, MAST-3 and MAST-7) (Logares et al., 2012; Labarre et al., 2021) were found after flooding. Among them, *Pirsonia verrucosa* (OTU-076) (MAST-1C) and the diatom *C. tenuissimus* appeared

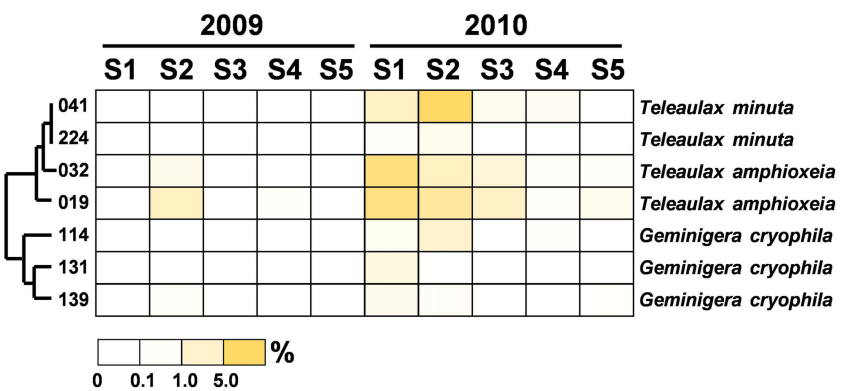

FIGURE 8 | Heatmap representing the relative contribution of each abundant OTU of Haptophyta during the summers of 2009 and 2010. The relative contribution indicates the percentage of the number of 18S rRNA gene V4 sequences in each OTU. The phylogenetic tree in the left position was built using the maximum likelihood algorithm. The labels at the bottom position indicate the color codes of the different percentages.

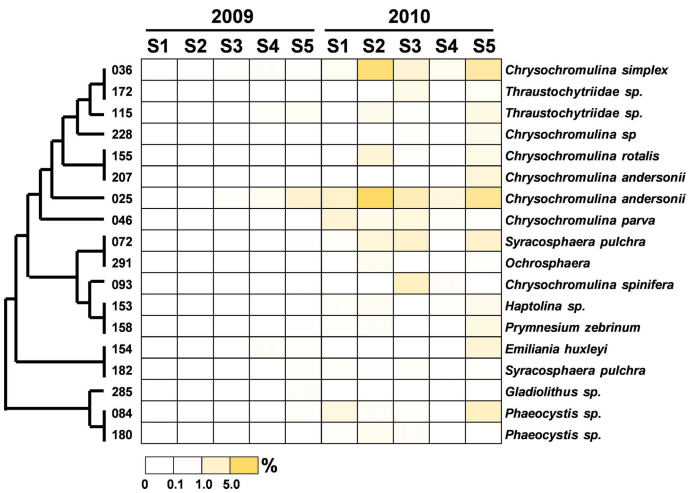

FIGURE 9 | Heatmap representing the relative contribution of each abundant OTU of the Cryptophyta during the summers of 2009 and 2010. The relative contribution indicates the percentage of the number of 18S rRNA gene V4 sequences in each OTU. The phylogenetic tree in the left position was built using the maximum likelihood algorithm. The labels at the bottom position indicate the color codes of the different percentages.

concurrently at Stations 1 to 3 (**Figure 6**). *Pirsonia* are parasitic flagellates that are specifically hosted by marine-centric diatoms (Kühn et al., 1996; Kühn et al., 2004). A similar co-occurrence of MAST-3 and diatoms was observed at Station 5 (**Figure 6**). MAST-3 has poor mobility, and it was speculated that epiphytism or parasitism should be one of its lifestyles (Cavalier-Smith and Scoble, 2013; Gómez et al., 2010; Massana et al., 2014; Seeleuthner et al., 2018). *Solenicola setigera* (MAST-3I) has been confirmed to be parasitic to diatoms (Gómez et al., 2011). Although relative evidence is still lacking, *Incisomonas marina* (OTU-244) (MAST-3J) was suggested to also follow the same life strategy (Cavalier-Smith and Scoble, 2013; Seeleuthner et al., 2018). The cooccurrence of MAST-1C or MAST-3 accompanied diatoms implied that diatom abundance in the flooded summer should be controlled by these parasitic flagellates at this time.

Due to its high growth rate and tolerance to environmental changes, *Picochlorum* (Chlorophyta) has been widely used in the algae-related biotechnology industry (Foflonker et al., 2018; Gonzalez-Esquer et al., 2019; Krishnan et al., 2021). However, the ecology of *Picochlorum* in the oceans has not been studied. Genomic analysis conducted with multiple *Picochlorum* isolates

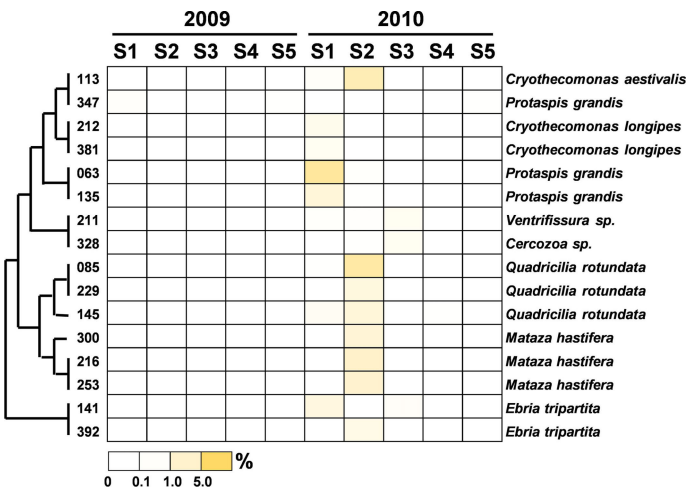

FIGURE 10 | Heatmap representing the relative contribution of each abundant OTU of Picobiliphyta during the summers of 2009 and 2010. The relative contribution indicates the percentage of the number of 18S rRNA gene V4 sequences in each OTU. The phylogenetic tree in the left position was built using the maximum likelihood algorithm. The labels at the bottom position indicate the color codes of the different percentages.

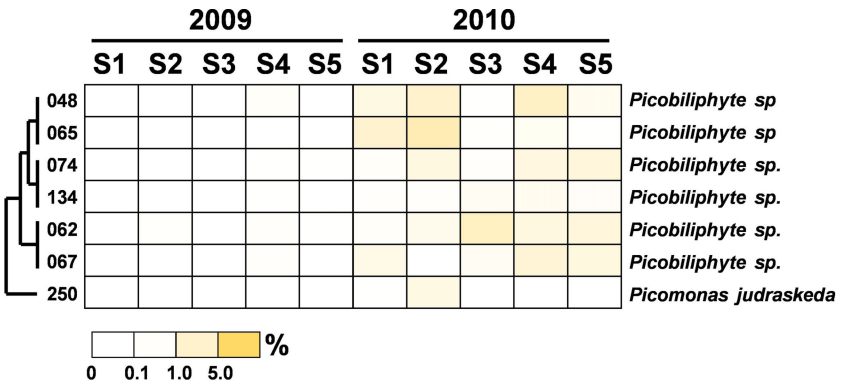

FIGURE 11 | Heatmap representing the relative contribution of each abundant OTU of the heterotrophic nanoflagellates during the summers of 2009 and 2010. The relative contribution indicates the percentage of the number of 18S rRNA gene V4 sequences in each OTU. The phylogenetic tree in the left position was built using the maximum likelihood algorithm. The labels at the bottom position indicate the color codes of the different percentages.

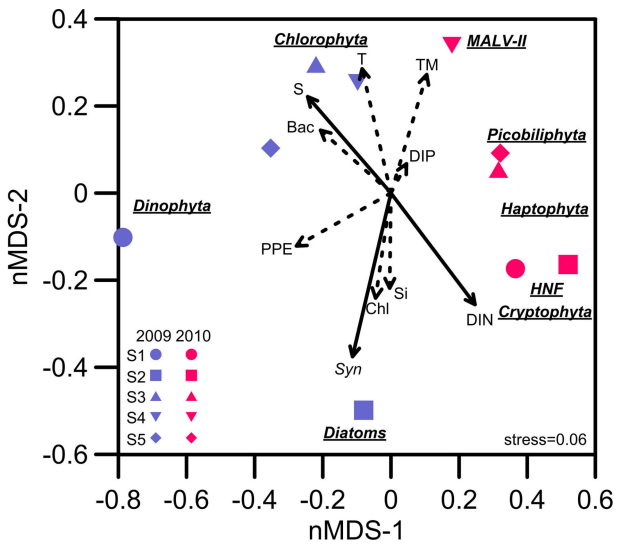

FIGURE 12 | Nonmetric multidimensional scaling (nMDS) ordination plot of the dominant picoeukaryote assemblages at Stations 1 to 5 in the summers of 2009 and 2010. The correlation relationships between the picoeukaryote assemblages and environmental factors among all stations were assessed with the function "envfit" (number of permutations=999) in the R package "vegan". The solid and dashed lines indicate significance (*p* value) at the ≤0.01 and ≤0.05 levels, respectively. S, salinity; T, temperature; TM, turbidity; DIP, dissolved inorganic phosphate; DIN, dissolved inorganic nitrogen (NO_2+NO_3); Si, silicate; Chl, chlorophyll *a*; Syn, *Synechococcus*; PPE, photosynthetic picoeukaryotes; Bac, bacteria.

revealed that allelic diversity and horizontal gene transfer might be the mechanisms for shaping their adaptation to variable environments (Foflonker et al., 2018). *Picochlorum* sp., occupied approximately 20% of the total reads at Station 3 in the nonflooded summer. A similar distribution of *Picochlorum* in the ECS was also found in summer 2019, when the Changjiang River plume was small. The emergence of *Picochlorum* should be attributed to the relatively stable hydrography (high temperature, high salinity and low DIN) in the summers without disturbances. This situation seems to be at odds with the high adaptability of *Picochlorum* to fluctuating environmental conditions. Pang et al. (2022) first confirmed that *Picochlorum* sp. (GLMF1 strain) was mixotrophic. Its bacterivory activity increased when the ambient conditions became more suitable for photosynthesis. The operation of a dual trophic strategy (phago-phototrophy) might benefit *Picochlorum* growth on the ECS shelf in the interference-free summer.

The development of high-throughput sequencing in the past decade has allowed us to comprehensively analyze 18S rRNA gene diversity so that we are able to explore the community composition of PEs in depth. However, with regard to protists, large differences in the copy numbers of rRNA genes among

various species may lead to deviations in the assessment of PE abundance and the contribution of various PEs to the ecosystem (Zhu et al., 2005). The cell debris of larger plankton or small particles attached to their nuclear DNA fragments mixed in the sample will contribute to mischaracterization of the PE composition (Sørensen et al., 2013; Chan et al., 2020). Moreover, it is difficult to determine the taxonomic identity of PEs and simultaneously evaluate their nutritional modes. In response to these problems, high-throughput 18S rRNA gene sequencing combined with fluorescent *in situ* hybridization (FISH) can more accurately assess PE assemblages in the field (Unrein et al., 2014). Alternatively, the application of other index genes (e.g., *rbcL*) provides a feasible way to assess the community composition of PEs in the field (Meakin and Wyman, 2011).

The quantity of nutrients and freshwater carried by river flows affects the phytoplankton composition and primary productivity in marginal seas (Smith and Demaster, 1966; Rabalais et al., 1996; Gong et al., 2006; Gong et al., 2011). Under the scenario of global warming and increasing human activities, the entry of riverine materials into seas will become more dynamic, in turn affecting biogeochemical cycles on the continental shelf (Gong et al., 2006; Gong et al., 2011; Chou et al., 2013; IPCC, 2021). While various *in situ* studies of the impact of extreme weather events on phytoplankton ecology in the northwest Pacific have been performed (Chang et al., 1996; Chen et al., 2009; Gong et al., 2011; Chung et al., 2014; Chung et al., 2015), our knowledge of how marine ecosystems respond to global climate changes and increasing human activities is still insufficient. During the flooded summer of 2010, we observed that PE diversity increased and that more 18S rRNA reads from bacterivores appeared, although the detailed mechanism still needs to be elucidated. It might be beneficial to deliver organic carbon from the microbial cycle to the grazing food chain (Tsai et al., 2010; Stibor et al., 2019; Gilbert and Mitra, 2022). Our findings provide insight into the change in the community composition of PEs between the dry period and flooding period over the large continental shelf system in the NW Pacific. This information will facilitate a complete assessment of the impact of freshwater discharge on changing the energy flow in the microbial food web.

DATA AVAILABILITY STATEMENT

All of the sequences of 18S rRNA V4 gene fragments were deposited in the Sequence Read Archive (SRA) Database with accession numbers SAMN10089074 to SAMN10089083.

AUTHOR CONTRIBUTIONS

C-CC and G-CG designed the cruises and the sampling work. C-CC and C-WH performed the high-throughput sequencing. C-CC, G-CG, and Y-CL analyzed the hydrographic and sequencing data. C-CC wrote the manuscript. All authors contributed to the article and approved the submitted version.

FUNDING

This study was supported by the Ministry of Science and Technology of Taiwan (MOST109-2611-M-019-004 and MOST110-2611-M-019-004) and the Center of Excellence for the Oceans of National Taiwan Ocean University. Y-CL was supported by the Research Scholar fellowship (MOST110-2611-M-019-018) from the Ministry of Science and Technology of Taiwan.

ACKNOWLEDGMENTS

We thank the captain and crew of R/V Ocean Researcher I for their assistance. We also thank the National Core Facility for Biopharmaceuticals (NCFB) and the National Center for High-performance Computing (NCHC) of National Applied Research Laboratories (NARLabs) for providing computational resources.

SUPPLEMENTARY MATERIAL

The Supplementary Material for this article can be found online at: https://www.frontiersin.org/articles/10.3389/fmars.2022.853847/full#supplementary-material

REFERENCES

Cavalier-Smith, T., and Scoble, J. M. (2013). Phylogeny of Heterokonta: *Incisomonas marina*, A Uniciliate Gliding Opalozoan Related to Solenicola (Nanomonadea), and Evidence That Actinophryida Evolved From Raphidophytes. *Eur. J. Protistol.* 49, 328–353. doi: 10.1016/j.ejop.2012.09.002

Chan, Y.-F., Chung, C.-C., Gong, G.-C., and Hsu, C.-W. (2020). Spatial Variation of Abundant Picoeukaryotes in the Subtropical Kuroshio Current in Winter. *Mar. Ecol.* 41, e12579. doi: 10.1111/maec.12579

Chan, Y.-F., Chiang, K.-P., Ku, Y., and Gong, G.-C. (2019). Abiotic and Biotic Factors Affecting the Ingestion Rates of Mixotrophic Nanoflagellates (Haptophyta). *Microb. Ecol.* 77, 607–615. doi: 10.1007/s00248-018-1249-2

Chang, J., Chung, C.-C., and Gong, G.-C. (1996). Influences of Cyclones on Chlorophyll a Concentration and *Synechococcus* Abundance in a Subtropical Western Pacific Coastal Ecosystem. *Mar. Ecol. Prog. Ser.* 140, 199–205. doi: 10.3354/meps140199

Chen, Y.-L. L., Chen, H.-Y., Jan, S., and Tuo, S.-H. (2009). Phytoplankton Productivity Enhancement and Assemblage Change in the Upstream Kuroshio After Typhoons. *Mar. Ecol. Prog. Ser.* 385, 111–126. doi: 10.3354/meps08053

Chou, C., Chiang, J. C. H., Lan, C.-W., Chung, C.-H., Liao, Y.-C., and Lee, C.-J. (2013). Increase in the Range Between Wet and Dry Season Precipitation. *Nat. Geosci.* 6, 263–267. doi: 10.1038/ngeo1744

Chung, C.-C., Chang, J., Gong, G.-C., Hsu, S.-C., Chiang, K.-P., and Liao, C.-W. (2011). Effects of Asian Dust Storms on *Synechococcus* Populaitons in the Subtropical Kuroshio Current. *Mar. Biotechnol.* 13, 751–763. doi: 10.1007/s10126-010-9336-5

Chung, C.-C., Gong, G.-C., Huang, C.-Y., Lin, J.-Y., and Lin, Y.-C. (2015). Changes in the *Synechococcus* Assemblage Composition at the Surface of the East China Sea Due to Flooding of the Changjiang River. *Microb. Ecol.* 70, 677–688. doi: 10.1007/s00248-015-0608-5

Chung, C.-C., Gong, G.-C., and Hung, C.-C. (2012). Effect of Typhoon Morakot on Microphytoplankton Population Dynamics in the Subtropical Northwest Pacific. *Mar. Ecol. Prog. Ser.* 448, 39–49. doi: 10.3354/meps09490

Chung, C.-C., Huang, C.-Y., Gong, G.-C., and Lin, Y.-C. (2014). Influence of the Changjiang River Flood on *Synechococcus* Ecology in the Surface Waters of the East China Sea. *Microb. Ecol.* 67, 273–285. doi: 10.1007/s00248-013-0299-8

Edgar, R. C., Haas, B. J., Clemente, J. C., Quince, C., and Knight, R. (2011). UCHIME Improves Sensitivity and Speed of Chimera Detection. *Bioinformatics* 27, 2194–2200. doi: 10.1093/bioinformatics/btr381

Foflonker, F., Mollegard, D., Ong, M., Yoon, H. S., and Bhattacharya, D. (2018). Genomic Analysis of *Picochlorum* Species Reveals How Microalgae may Adapt to Variable Environments. *Mol. Biol. Evol.* 35, 2702–2711. doi: 10.1093/molbev/msy167

Gilbert, P. M., and Mitra, A. (2022). From Webs, Loops, Shunts, and Pumps to Icrobial Multitasking: Evolving Concepts of Marine Microbial Ecology, the Mixoplankton Paradigm, and Implications for a Future Ocean. *Limnol. Oceanogr.* 67, 585–597. doi: 10.1002/lno.12018

Gómez, F., Moreira, D., Benzerara, K., and López-García, P. (2011). *Solenicola setigera* Is the First Characterized Member of the Abundant and Cosmopolitan Uncultured Marine Stramenopile Group MAST-3. *Environ. Microbiol.* 13, 193–202. doi: 10.1111/j.1462-2920.2010.02320.x

Gong, G.-C., Chang, J., Chiang, K.-P., Hsiung, T.-M., Hung, C.-C., Duan, S.-W., et al. (2006). Reduction of Primary Production and Changing of Nutrient Ratio in the East China Sea: Effect of the Three Gorges Dam? *Geophys. Res. Lett.* 33, L07610. doi: 10.1029/2006GL025800

Gong, G.-C., Chen, Y.-L. L., and Liu, K.-K. (1996). Chemical Hydrography and Chlorophyll a Distribution in the East China Sea in Summer: Implications in Nutrient Dynamics. *Cont. Shelf Res.* 16, 1561–1590. doi: 10.1016/0278-4343(96)00005-2

Gong, G.-C., Liu, K.-K., Chiang, K.-P., Hsiung, T.-M., Chang, J., Chen, C.-C., et al. (2011). Yangtze River Floods Enhance Coastal Ocean Phytoplankton Biomass and Potential Fish Production. *Geophy. Res. Lett.* 38, L13603. doi: 10.1029/2011GL047519

Gonzalez-Esquer, C. R., Wright, K. T., Sudasinghe, N., Carr, C. K., Sanders, C. K., Turmo, A., et al. (2019). Demonstration of the Potential of *Picochlorum soloecismus* as a Microalgal Platform for the Production of Renewable Fuels. *Algal Res.* 43, 101658. doi: 10.1016/j.algal.2019.101658

Hernández-Urcera, J., Rial, P., García-Portela, M., Lourés, P., Kilcoyne, J., Rodríguez, F., et al. (2018). Notes on the Cultivation of Two Mixotrophic Dinophysis Species and Their Ciliate Prey *Mesodinium Rubrum*. *Toxins* 10, 505. doi: 10.3390/toxins10120505

Herut, B., Zohary, T., Krom, M. D., Mantoura, R. F. C., Pitta, P., Psarra, S., et al. (2005). Response of East Mediterranean Surface Water to Saharan Dust: on-Board Microcosm Experiment and Field Observations. *Deep Sea Res. II* 52, 3024–3040. doi: 10.1016/j.dsr2.2005.09.003

Hilligsøe, K. M., Richardson, K., Bendtsen, J., Sørensen, L. L., Nielsen, T. G., and Lyngsgaard, M. M. (2011). Linking Phytoplankton Community Size Composition With Temperature, Plankton Food Web Structure and Sea-Air CO Flux. *Deep-Sea Res. I* 58, 826–838. doi: 10.1016/j.dsr.2011.06.004

Hoegh-Guldberg, O., and Bruno, J. F. (2010). The Impact of Climate Change on the World's Marine Ecosystems. *Science* 328, 1523–1528. doi: 10.1126/science.1189930

IPCC (2021). *Climate Change 2021: The Physical Science Basis. Contribution of Working Group I to the Sixth Assessment Report of the Intergovernmental Panel on Climate Change* In: V. Masson-Delmotte, P. A. Zhai, S.L. Pirani, C. Connors, S. Péan, N. Berger, et al. (Cambridge University Press).

Jardillier, L., Zubkov, M. V., Pearman, J., and Scanlan, D. J. (2010). Significant CO_2 Fixation by Small Prymnesiophytes in the Subtropical and Tropical Northeast Atlantic Ocean. *ISME J.* 4, 1180–1192. doi: 10.1038/ismej.2010.36

Jones, H. L. J., Leadbeater, B. S. C., and Green, J. (1993). Mixotrophy in Marine Species of *Chrysochromulina* (Prymnesiophyceae): Ingestion and Digestion of a Small Green Flagellate. *J. Mar. Biol. Assoc. U. K.* 73, 283–296. doi: 10.1017/S0025315400032859

Jung, J.-H., Choi, J. M., Coats, D. W., and Kim, Y.-O. (2016). *Euduboscquella Costata* N. Sp. (Dinoflagellata, Syndinea), an Intracellular Parasite of the Ciliate *Schmidingerella Arcuata*: Morphology, Molecular Phylogeny, Life Cycle, Prevalence, and Infection Intensity. *J. Eukaryot. Microbiol.* 63, 3–15. doi: 10.1111/jeu.12231

Justić, D., Rabalais, N. N., Turner, R. E., and Dortch, Q. (1995). Changes in Nutrient Structure of River-Dominated Coastal Waters: Stoichiometric Nutrient Balance and Its Consequences. *Estuar. Coast. Shelf Sci.* 40, 339–356. doi: 10.1016/S0272-7714(05)80014-9

Kawachi, M., Inouye, I., Maeda, O., and Chihara, M. (1991). The Haptonema as a Food-Capturing Device: Observations on *Chrysochromulina Hirta* (Prymnesiophyceae). *Phycologia* 30, 563–573. doi: 10.2216/i0031-8884-30-6-563.1

Kimura, M. (1980). A Simple Method for Estimating Evolutionary Rates of Base Substitutions Through Comparative Studies of Nucleotide Sequences. *J. Mol. Evol.* 16, 111–120. doi: 10.1007/BF01731581

Krishnan, A., Likhogrud, M., Cano, M., Edmundson, S., Melanson, J. B., Huesemann, M., et al. (2021). *Picochlorum Celeri* as a Model System for Robust Outdoor Algal Growth in Seawater. *Sci. Rep.* 11, 1–13. doi: 10.1038/s41598-021-91106-5

Kühn, S., Drebes, G., and Schnepf, E. (1996). Five New Species of the Nanoflagellate Pirsonia in German Bight, North Sea, Feeding on Planktic Diatoms. *Helgoländer meeresunters.* 50, 205–222. doi: 10.1007/BF02367152

Kühn, S., Medlinb, L., and Eller, G. (2004). Phylogenetic Position of the Parasitoid Nanoflagellate *Pirsonia* Inferred From Nuclear-Encoded Small Subunit Ribosomal DNA and a Description of *Pseudopirsonia* N. Gen. And *Pseudopirsonia mucosa* (Drebes) Comb. Nov. *Protist* 155, 143–156. doi: 10.1078/143446104774199556

Labarre, A., López-Escardó, D., Latorre, F., Leonard, G., Bucchini, ,. F., Obiol, A., et al. (2021). Comparative Genomics Reveals New Functional Insights in Uncultured MAST Species. *ISME J.* 15, 1767–1781. doi: 10.1038/s41396-020-00885-8

Lee, Y., Yang, E.-J., Youn, S., and Choi, J. K. (2018). Influence of the Changjiang Diluted Waters on the Nanophytoplankton Distribution in the Northern East China Sea. *J. Mar. Biolog. Assoc. U. K.* 98, 1535–1545. doi: 10.1017/S0025315417001163

Leles, S. G., Polimene, L., Bruggeman, J., Blackford, J., Ciavatta, S., Mitra, A., et al. (2018). Modelling Mixotrophic Functional Diversity and Implications for Ecosystem Function. *J. Plankton Res.* 40, 627–642. doi: 10.1093/plankt/fby044

Liu, H., Suzuki, K., Minami, C., Saino, T., and Watanabe, M. (2002). Picoplankton Community Structure in the Subarctic Pacific Ocean and the Bering Sea During Summer 1999. *Mar. Ecol. Prog. Ser.* 237, 1–14. doi: 10.3354/meps237001

Logares, R., Audic, S., Santini, S., Pernice, M. C., de Vargas, C., and Massana, R. (2012). Diversity Patterns and Activity of Uncultured Marine Heterotrophic Flagellates Unveiled With Pyrosequencing. *ISME J.* 6, 1823–1833. doi: 10.1038/ismej.2012.36

Massana, R. (2011). Eukaryotic Picoplankton in Surface Oceans. *Annu. Rev. Microbiol.* 65, 91–110. doi: 10.1146/annurev-micro-090110-102903

Massana, R., del Campo, J., Sieracki, M. E., Audic, S., and Logares, R. (2014). Exploring the Uncultured Microeukaryote Majority in the Oceans: Reevaluation of Ribogroups Within Stramenopiles. *ISME J.* 8, 854–866. doi: 10.1038/ismej.2013.204

McKie-Krisberg, Z. M., and Sanders, R. W. (2014). Phagotrophy by the Picoeukaryotic Green Alga Micromonas: Implications for Arctic Oceans. *ISEM J.* 10, 1953–1961

Meakin, N. G., and Wyman, M. (2011). Rapid Shifts in Picoeukaryote Community Structure in Response to Ocean Acidification. *ISME J.* 5, 1397–1405. doi: 10.1038/ismej.2011.18

Moon-van der Staay, S. Y., De Wachter, R., and Vaulot, D. (2001). Oceanic 18s rDNA Sequences From Picoplankton Reveal Unsuspected Eukaryotic Diversity. *Nature* 409, 607–610. doi: 10.1038/35054541

Nguyen, L.-T., Schmidt, H. A., von Haeseler, A., and Minh, B. Q. (2014). IQ-TREE: A Fast and Effective Stochastic Algorithm for Estimating Maximum-Likelihood Phylogenies. *Mol. Biol. Evol.* 32, 268–274. doi: 10.1093/molbev/msu300

Nishitani, G., Nagai, S., Baba, K., Kiyokawa, S., Kosaka, Y., Miyamura, K., et al. (2010). High-Level Congruence of *Myrionecta Rubra* Prey and Dinophysis Species Plastid Identities as Revealed by Genetic Analyses of Isolates From Japanese Coastal Waters. *Appl. Environ. Microbiol.* 76, 2791–2798. doi: 10.1128/AEM.02566-09

Paerl, R. W., Venezia, R. E., Sanchez, J. J., and Paerl, H. W. (2020). Picophytoplankton Dynamics in a Large Temperate Estuary and Impacts of Extreme Storm Events. *Sci. Rep.* 10, 22026. doi: 10.1038/s41598-020-79157-6

Pai, S.-C., Yang, C.-C., and Riley, J. P. (1990). Effects of Acidity and Molybdate Concentration on the Kinetics of the Formation of the Phosphoantimonylmolybdenum Blue Complex. *Anal. Chim. Acta* 229, 115–120. doi: 10.1016/S0003-2670(00)85116-8

Pang, M., Liu, K., and Liu, H. (2022). Evidence for Mixotrophy in Pico-Chlorophytes From a New *Picochlorum* (Trebouxiophyceae) Strain. *J. Phycol.* 58, 80–91. doi: 10.1111/jpy.13218

Quince, C., Lanzén, A., Curtis, T. P., Davenport, R. J., Hall, N., Head, I. M., et al. (2009). Accurate Determination of Microbial Diversity From 454 Pyrosequencing Data. *Nat. Methods* 6, 639–641. doi: 10.1038/nmeth.1361

Quince, C., Lanzen, A., Davenport, R. J., and Turnbaugh, P. J. (2011). Removing Noise From Pyrosequenced Amplicons. *BMC Bioinf.* 12, 38. doi: 10.1186/1471-2105-12-38

Rabalais, N. N., Turner, R. E., JustiĆ, D., Dortch, Q., Wiseman, W. J., and Sen Gupta, B. K. (1996). Nutrient Changes in the Mississippi River and System Responses on the Adjacent Continental Shelf. *Estuaries* 19, 386–407. doi: 10.2307/1352458

Søgaard, D. H., Sorrell, B. K., Sejr, M. K., Andersen, P., Rysgaard, S., Hansen, P. J., et al. (2021). An Under–Ice Bloom of Mixotrophic Haptophytes in Low Nutrient and Freshwater–Influenced Arctic Waters. *Sci. Rep.* 11, 2915. doi: 10.1038/s41598-021-82413-y

Sørensen, N., Daugbjerg, N., and Richardson, K. (2013). Choice of Pore Size can Introduce Artefacts When Filtering Picoeukaryotes for Molecular Biodiversity Studies. *Microb. Ecol.* 65, 964–968. doi: 10.1007/s00248-012-0174-z

Schloss, P. D., Westcott, S. L., Ryabin, T., Hall, J. R., Hartmann, M., Hollister, E. B., et al. (2009). Introducing Mothur: Open-Source, Platform-Independent, Community-Supported Software for Describing and Comparing Microbial Communities. *Appl. Environ. Microbiol.* 75, 7537–7541. doi: 10.1128/AEM.01541-09

Seeleuthner, Y., Mondy, S., Lombard, V., Carradec, Q., Pelletier, E., Wessner, M., et al. (2018). Single-Cell Genomics of Multiple Uncultured Stramenopiles Reveals Underestimated Functional Diversity Across Oceans. *Nat. Commun.* 9, 310. doi: 10.1038/s41467-017-02235-3

Smith, J. W. O., and Demaster, D. J. (1966). Phytoplankton Biomass and Productivity in the Amazon River Plume: Correlation With Seasonal River Discharge. *Cont. Shelf Res.* 16, 291–319. doi: 10.1016/0278-4343(95)00007-N

Stibor, H., Stockenreiter, M., Nejstgaard, J. C., Ptacnik, R., and Sommer, U. (2019). Trophic Switches in Pelagic Systems. *Curr. Opin. Syst. Biol.* 13, 108–114. doi: 10.1016/j.coisb.2018.11.006

Stoeck, T., Bass, D., Nebel, M., Christen, R., Jones, M. D. M., Breiner, H.-W., et al. (2010). Multiple Marker Parallel Tag Environmental DNA Sequencing Reveals a Highly Complex Eukaryotic Community in Marine Anoxic Water. *Mol. Ecol.* 19, 21–31. doi: 10.1111/j.1365-294X.2009.04480.x

Strickland, J. D. H., and Parsons, T. R. (1972). *A Practical Handbook of Seawater Analysis* (Ottawa, Canada: Fisheries Research Board of Canada).

Tamaki, H., Wright, C. L., Li, X., Lin, Q., Hwang, C., Wang, S., et al. (2011). Analysis of 16S rRNA Amplicon Sequencing Options on the Roche/454 Next-Generation Titanium Sequencing Platform. *PloS One* 6 (9), e25263–e25263. doi: 10.1371/journal.pone.0025263

Tsai, A.-Y., Gong, G.-C., Sanders, R. W., Wang, C.-J., and Chiang, K.-P. (2010). The Impact of the Changjiang River Plume Extension on the Nanoflagellate Community in the East China Sea. *Estuar. Coast. Shelf Sci.* 89, 21–30. doi: 10.1016/j.ecss.2010.05.005

Unrein, F., Gasol, J. M., Not, F., Forn, I., and Massana, R. (2014). Mixotrophic Haptophytes Are Key Bacterial Grazers in Oligotrophic Coastal Waters. *ISME J.* 8, 164–176. doi: 10.1038/ismej.2013.132

Wang, Q., Garrity, G. M., Tiedje, J. M., and Cole, J. R. (2007). Naive Bayesian Classifier for Rapid Assignment of rRNA Sequences Into the New Bacterial Taxonomy. *Appl. Environ. Microbiol.* 73, 5261–5267. doi: 10.1128/AEM.00062-07

Welschmeyer, N. A. (1994). Fluorometric Analysis of Chlorophyll *a* in the Presence of Chlorophyll B and Pheopigments. *Limnol. Oceanogra.* 39, 1985–1992. doi: 10.4319/lo.1994.39.8.1985

Worden, A. Z., Follows, M. J., Giovannoni, S. J., Wilken, S., Zimmerman, A. E., and Keeling, P. J. (2015). Rethinking the Marine Carbon Cycle: Factoring in the Multifarious Lifestyles of Microbes. *Science* 347, 1257594. doi: 10.1126/science.1257594

Worden, A. Z., Nolan, J. K., and Palenik, B. (2004). Assessing the Dynamics and Ecology of Marine Picophytoplankton: The Importance of the Eukaryotic Component. *Limnol. Oceanogra.* 49, 168–179. doi: 10.4319/lo.2004.49.1.0168

Wu, W., Logares, R., Huang, B., and Hsieh, C. h. (2017). Abundant and Rare Picoeukaryotic Sub-Communities Present Contrasting Patterns in the Epipelagic Waters of Marginal Seas in the Northwestern Pacific Ocean. *Environ. Microbiol.* 19, 287–300. doi: 10.1111/1462-2920.13606

Yih, W., and Coats, D. W. (2000). Infection of *Gymnodinium Sanguineum* by the Dinoflagellate *Amoebophrya* Sp.: Effect of Nutrient Environment on Parasite Generation Time, Reproduction, and Infectivity. *J. Eukary. Microbiol.* 47, 504–510. doi: 10.1111/j.1550-7408.2000.tb00082.x

Yoo, Y. D., Seong, K. A., Jeong, H. J., Yih, W., Rho, J.-R., Nam, S. W., et al. (2017). Mixotrophy in the Marine Red-Tide Cryptophyte *Teleaulax Amphioxeia* and Ingestion and Grazing Impact of Cryptophytes on Natural Populations of Bacteria in Korean Coastal Waters. *Harmful Algae* 68, 105–117. doi: 10.1016/j.hal.2017.07.012

Zhu, F., Massana, R., Not, F., Marie, D., and Vaulot, D. (2005). Mapping of Picoeucaryotes in Marine Ecosystems With Quantitative PCR of the 18S rRNA Gene. *FEMS Microb. Ecol.* 52, 79–92. doi: 10.1016/j.femsec.2004.10.006

Conflict of Interest: The authors declare that the research was conducted in the absence of any commercial or financial relationships that could be construed as a potential conflict of interest.

Publisher's Note: All claims expressed in this article are solely those of the authors and do not necessarily represent those of their affiliated organizations, or those of the publisher, the editors and the reviewers. Any product that may be evaluated in this article, or claim that may be made by its manufacturer, is not guaranteed or endorsed by the publisher.

Copyright © 2022 Chung, Gong, Lin and Hsu. This is an open-access article distributed under the terms of the Creative Commons Attribution License (CC BY). The use, distribution or reproduction in other forums is permitted, provided the original author(s) and the copyright owner(s) are credited and that the original publication in this journal is cited, in accordance with accepted academic practice. No use, distribution or reproduction is permitted which does not comply with these terms.

frontiers | Frontiers in Marine Science

ORIGINAL RESEARCH
published: 18 May 2022
doi: 10.3389/fmars.2022.829579

Shear Instability and Turbulent Mixing in the Stratified Shear Flow Behind a Topographic Ridge at High Reynolds Number

Jia-Lin Chen[1], Xiao Yu[2], Ming-Huei Chang[3], Sen Jan[3], Yiing Jang Yang[3] and Ren-Chieh Lien[4]*

[1] Department of Hydraulic and Ocean Engineering, National Cheng Kung University, Tainan City, Taiwan, [2] Department of Civil and Coastal Engineering, University of Florida, Gainesville, FL, United States, [3] Institute of Oceanography, National Taiwan University, Taipei, Taiwan, [4] Applied Physics Laboratory, University of Washington, Seattle, WA, United States

OPEN ACCESS

Edited by:
Hiroaki Saito,
The University of Tokyo, Japan

Reviewed by:
Takeyoshi Nagai,
Tokyo University of Marine Science and Technology, Japan
Alessandro Stocchino,
Hong Kong Polytechnic University, Hong Kong, SAR China

****Correspondence:***
Jia-Lin Chen
jialinchenps@gs.ncku.edu.tw

Specialty section:
This article was submitted to Coastal Ocean Processes, a section of the journal Frontiers in Marine Science

Received: *06 December 2021*
Accepted: *25 March 2022*
Published: *18 May 2022*

Citation:
Chen J-L, Yu X, Chang M-H, Jan S, Yang YJ and Lien R-C (2022) Shear Instability and Turbulent Mixing in the Stratified Shear Flow Behind a Topographic Ridge at High Reynolds Number. Front. Mar. Sci. 9:829579. doi: 10.3389/fmars.2022.829579

Observations on the lee of a topographic ridge show that the turbulence kinetic energy (TKE) dissipation rate due to shear instabilities is three orders of magnitude higher than the typical value in the open ocean. Laboratory-scale studies at low Reynolds number suggest that high turbulent dissipation occurs primarily within the core region of shear instabilities. However, field-scale studies indicate that high turbulence is mainly populated along the braids of shear instabilities. In this study, a high-resolution, resolving the Ozmidov-scale, non-hydrostatic model with Large Eddy Simulation (LES) turbulent closure is applied to investigate dominant mechanisms that control the spatial and temporal scales of shear instabilities and resulting mixing in stratified shear flow at high Reynolds number. The simulated density variance dissipation rate is elevated in the cusp-like bands of shear instabilities with a specific period, consistent with the acoustic backscatter taken by shipboard echo sounder. The vertical length scale of each cusp-like band is nearly half of the vertical length scale of the internal lee wave. However, it is consistent with instabilities originating from a shear layer based on linear stability theory. The model results indicate that the length scale and/or the period of shear instabilities are the key parameters to the mixing enhancement that increases with lateral Froude number Fr_L, i.e. stronger shear and/or steeper ridge.

Keywords: lee wave breaking, shear instability, flow topography interaction, LES simulation, turbulent mixing and diffusivity

INTRODUCTION

Understanding how turbulence leads to the enhanced mixing of heat and other scalars, such as salt and pollutants, in density-stratified fluids is a fundamental and central problem in geophysical and environmental fluid dynamics. Physical processes such as the topographically induced water intrusion, lee wave breaking, and shear instabilities are crucial to the spatial and temporal variation in biological productivity and biodiversity in ecosystems of the coastal ocean. Strong turbulent mixing could

enhance the mean nitrate flux and had a maximal value of 10.0 mmol m^{-2} day^{-1}, which was much higher than typical values for the open ocean (Tanaka et al., 2019; Acabado et al., 2021; Nagai et al., 2021). Field observations show that the high TKE dissipation rate enhances the vertical nitrate flux (Acabado et al., 2021). The mixing processes over topographic features along the Kuroshio are important agents for nutrient delivery to the primary producers and supporting migratory fish species in the Kuroshio Extension and subpolar regions. Because nutrients lie in the deep, dark subsurface layers, they are not immediately available for the photosynthesis process in the surface layer (Durán Gómez et al., 2020; Nagai et al., 2021). When ocean currents interact with seafloor topography, turbulent mixing may occur by breaking internal lee waves through shear instabilities (Farmer and Armi, 1999; Eiff and Bonneton, 2000). Lee-wave breaking provides a mechanism for extracting energy from the geostrophic flow and transferring energy to small-scale turbulence, which leads to a dissipative loss of mechanical energy and an irreversible transfer from kinetic energy to potential energy (Winters et al., 1995). Parameterizations based on a linear theory (Bell, 1975) for the energy flux into lee waves in the stratified flow have been implemented in global ocean models, highlighting the potential role of lee wave-driven mixing on overturning circulations. However, recent field observations in Drake Passage showed that turbulent dissipation rates are on average two to three times smaller than linear lee-wave generation predictions. This is because a greater fraction of high-frequency lee wave energy may be reabsorbed by the mean flow, and the reabsorption process influences the energy remaining for dissipation and mixing (Kunze and Lien, 2019). Hence, the nonlinear mechanisms leading to lee wave breaking and dictating turbulent dissipation processes still require adequate assessment (Legg, 2021).

The typical value of turbulent diffusivity in the open ocean pycnocline is O(10^{-5} m^2 s^{-1}) (Munk and Wunsch, 1998). Direct measurements of the TKE dissipation rate in the Tokara Strait, where the strong shear flow, Kuroshio interacts with a series of seamounts, demonstrate that the turbulent diffusivity reaches O (10^{-1} m^2 s^{-1}) in the lee of the seamount. The strong shear generated by the interaction of bathymetry and the geostrophic flow can result in instabilities at the interface of the lee wave and greatly enhance vertical mixing (Tsutsumi et al., 2017). Observations behind a topographic ridge near Green Island along the route of the Kuroshio also show that the TKE dissipation rate due to the observed shear instabilities is two orders of magnitude higher than other areas without topographic effects along the route of the Kuroshio (Mensah et al., 2014; Chang et al., 2016).

Field observations at high Reynolds number (Re ~ O(10^6), Re = Uδ/υ, where U, δ, and υ are the velocity scale, the half-thickness of the shear zone, and kinematic viscosity, respectively) suggest that the primary source for turbulent mixing in Kelvin-Helmholtz (KH) billows is not only within their convective overturning core but within the intensified shear layer, separating the cores, where secondary shear instabilities are present (Geyer et al., 2010; Chang et al., 2016). The 'zoo' of secondary instabilities within the braids is the important mechanism for turbulence generation (Mashayek and Peltier, 2012; Mashayek and Peltier, 2013). However, laboratory-scale studies at low Reynolds number (Re ~ 1000) demonstrate that the high TKE dissipation rate primarily occurs within the core region of shear instabilities, inconsistent with field observations at high-Re flows (Staquet, 1995; Smyth and Moum, 2000; Smyth et al., 2001; Smyth and Moum, 2012). A major challenge in estimating the amount of turbulent mixing in large-scale flow in the ocean, i.e., the parameterization, is the remarkably broad range of spatial and temporal scales involved, from those of smallest turbulent eddies (the submillimeter scale) to the largest scales of ocean circulations (thousands of kilometer scale). The Reynolds-averaged Navier–Stokes (RANS) model with k-ε turbulent closure has been used to study the characteristics of stratified flow in large-scale hydrodynamic model frameworks (e.g., ROMS, POMS) at high Reynolds number. In RANS models, all turbulent motions are modeled, and a scalar eddy viscosity is used to parameterize the turbulent mixing processes. Although the standard RANS k-ε model could produce the mean flow accurately, it produces large discrepancies in predicting the second-order flow characteristics such as shear instabilities (Shi et al., 2016) or convective overturning, which are important turbulence generation mechanisms for stratified flows at high Reynolds number, as demonstrated in field observations.

On the other hand, LES models resolve important large-scale turbulent eddies and can accurately capture the unsteadiness of coherent turbulent motions due to hydrodynamic instabilities. LES has been employed to study the development of shear instabilities and the transition from shear instabilities to turbulence at the edge of the river plume (Zhou et al., 2017; Shi et al., 2019). Therefore, LES is an ideal tool for investigating the dominant turbulent generation mechanism in stratified flows at high Reynolds number. In addition, the LES model can provide insights into the key parameters controlling KH billow properties, including the size, frequency, and propagation speed, when shear instability occurs.

In this study, a high-resolution LES model is implemented to explain the evolution of breaking lee waves in space and time and the resulting instabilities at high Reynolds number. The effect of density stratification on the strength and characteristics of turbulence is explored using a vertical grid resolution smaller than the Ozmidov length scale ($\ell_{Oz} = \varepsilon^{\frac{1}{2}}N^{-\frac{3}{2}}$, where ε is the TKE dissipation rate, and N is the buoyancy frequency) representing the outer scale of turbulence. The model governing equation and the model setup are described in Section 2. Model results are discussed in Section 3. A comparison with field measurements of acoustical backscatter intensity, acoustic Doppler current profiler (ADCP) velocity profiles, and conductivity-temperature-depth (CTD) profiles behind a topographic ridge along the route of the Kuroshio is discussed in Section 4. Finally, model experiments based on different upstream velocities, background stratifications, and topography structures are discussed to understand better the key parameters controlling the nonlinear mechanisms dictating turbulent generation and dissipation processes of flow-

topography interactions at high-Re flows. The dependence of the vertical mixing enhancement on the scale of shear instabilities will be discussed.

NUMERICAL MODEL

Governing Equation

In this study, the computational fluid dynamics (CFD) model OpenFOAM (Weller et al., 1998) is applied to investigate dominant mechanisms that control the variations in the strength and spatial/temporal scales of shear instabilities in stratified shear flow at high Reynolds number. The effect of density stratification on shear instability-induced turbulence is explored using LES models that resolve the unsteadiness of large-scale turbulent motions and parameterize subgrid turbulent motions at smaller scales. Turbulence generation mechanisms such as shear instabilities and convective instabilities are resolved using LES models with fine grid resolution (the vertical grid size is smaller than the Ozmidov scale). The governing equations for the LES model are:

$$\begin{gathered}\frac{\partial u_i}{\partial x_i} = 0,\\ \frac{\partial u_i}{\partial t} + \frac{\partial u_i u_j}{\partial x_j} = -\frac{1}{\rho}\frac{\partial p}{\partial x_i} + \frac{\partial \tau_{ij}}{\partial x_j} + \delta_{3i}\alpha sg,\\ \frac{\partial s}{\partial t} + \frac{\partial u_i s}{\partial x_i} = \frac{\partial}{\partial x_j}\left(\kappa \frac{\partial s}{\partial x_j}\right),\end{gathered} \tag{1}$$

where u_i is the i-th component of the resolved velocity, p is the resolved dynamic pressure, τ is the sum of the viscous stress and Reynolds stress, δ_{3i} is the Kronecker delta, and the coefficient $\alpha = (\rho-\rho_0)/s\rho_0$, in which ρ is the density of the fluid with a given tracer concentration s, and ρ_0 is the background density. When the density variation caused by tracer s is small, the Boussinesq approximation can be applied and a linear relation between the density ρ and tracer concentration s is $\rho = \rho_0\ (1 + \alpha s)$. In the momentum equation [the second equation in (1)], the last term represents the density stratification $\Delta\rho g/\rho_0$ by the scalar tracer s, where $\Delta\rho$ is the density difference between the top and bottom boundary. The third equation in (1) is the tracer transport equation for any conservative tracer s such as salinity or temperature where κ is the sum of the molecular diffusion coefficient and the subgrid diffusion coefficient.

In LES models, the turbulent stress term represents the momentum flux in the small-scale processes occurring at length scales that the computational grid cannot adequately resolve. We implemented the wall-adapting local eddy viscosity (WALE) subgrid closure model. The stress term is given by:

$$\tau_{ij} = 2(\nu + \nu_t)S_{ij}, \tag{2}$$

where ν is the kinematic viscosity of the fluid, ν_t is the eddy viscosity given by Ducros et al. (1998), and S_{ij} is the strain rate tensor of the resolved large scale, expressed as

$$\nu_t = \Delta_s^2 \frac{(S_{ij}^d S_{ij}^d)^{3/2}}{(S_{ij}S_{ij})^{5/2} + (S_{ij}^d S_{ij}^d)^{5/4}}, \tag{3}$$

with

$$\begin{gathered}\Delta_s = C_w V_c^{1/3},\\ S_{ij}^d = \frac{1}{2}\left(g_{ij}^2 + g_{ji}^2\right) - \frac{1}{3}\delta ij g_{kk}^2,\\ g_{ij} = \frac{\partial u_i}{\partial x_j},\end{gathered} \tag{4}$$

where $C_w = 0.325$ is a constant and V_c is the volume of the grid cell.

Model Setup

Observations behind a topographic ridge along the route of the Kuroshio demonstrate trains of shear instabilities characterized by strong shear flows and density gradients (Chang et al., 2016; Tsutsumi et al., 2017). Applying the Buckingham π theorem, the key dimensionless parameters for the system can be determined as

$$\mathrm{Re} = \frac{U_o \delta}{\nu},\ \mathrm{Ri_g} = \frac{N^2}{G^2},\ \mathrm{Fr} = \frac{U_o}{NH},\ \mathrm{S} = \frac{H}{L} \tag{5}$$

where Re is the Reynolds number, U_o is the freestream velocity of the layer, δ is the width of the shear zone, and ν is the kinematic viscosity of the fluid. Ri is the gradient Richardson number with buoyancy frequency $N = \sqrt{-\frac{g}{d}\frac{d\rho}{dz}}$ with g being the gravitational acceleration constant, and ρ being the potential density. The gradient Richardson number defined here is the ratio of the buoyancy term (represented by N^2) to the mean vertical shear term $G^2 = (\partial_z U)^2 + (\partial_z V)^2$. The Fr is the internal Froude number for a given seamount height H. The Froude number Fr defined in this study is the inverse of the Long number (Aguilar and Sutherland, 2006) or the steepness parameter (Nikurashin and Ferrari, 2010a). S is the steepness of the topographic ridge defined by the ratio of the height of a given seamount H and the corresponding width L.

Field observations along the route of Kuroshio indicate that strong currents are confined to the upper layers and rapidly weaken toward 400-m depth (Taniguchi et al., 2013; Jan et al., 2015). Therefore, the vertical length in the model domain is scaled down from 400 m to 100 m. Field measurements indicate that the maximum Kuroshio flow velocity, ranging between 0.5 m s^{-1} and 1.2 m s^{-1}, is modulated by tidal flows and internal waves. The tidally induced flow is weaker than the Kuroshio flow so that the flow direction is relatively steady, and total flow reversal does not occur (Chang et al., 2013). The freestream velocity at top the shear zone in the model inflow boundary is prescribed as U_0 =0.125-0.3 m s^{-1}, corresponding to one-fourth of the maximum observed flow velocity ranging between 0.5 m s^{-1} and 1.2 m s^{-1}.

The best available bathymetry data have a relatively low resolution for resolving the small-scale variations in topographic ridges. Therefore, similar to the approach used in previous studies (Klymak and Legg, 2010; Winters and Armi, 2012; Winters and Armi, 2014; Dossmann et al., 2016), the three-dimensional simulation was conducted over a two-dimensional topographic ridge parameterized by a Gaussian function:

$$z = H\exp\left(-\frac{(x - x_o)^2}{L^2}\right), \quad (6)$$

where x_0 is the center location of a topographic ridge, and L is the horizontal length scale.

In this study, a scaled-down turbulence resolving simulation was carried out in which both the length scale and velocity scale were chosen as one-fourth of the field conditions adapted to the constraint of the model grid resolution. The Ozmidov length scale can be estimated as $L_{oz} = \sqrt{\varepsilon/N^3} \approx O(1m)$ where ε is the TKE dissipation rate estimated by the Thorpe scale (Chang et al., 2016) and direct turbulence measurements (Tsutsumi et al., 2017). Therefore, a vertical grid resolution of 0.4 m is used in the model, which is smaller than the Ozmidov length scale. The simulation domain is a straight channel with a Gaussian seamount, in which the topographic ridge height from the bottom of the shear zone is scaled down from 200 m to 50 m and the horizontal length scale of the topographic ridge is scaled down from 800-1200 m to 200-300 m (**Figure 1**). The model is designed to keep the above nondimensional parameters the same as the field observations such that the resulting shear layer characteristics and shear instabilities are similar to the field observations. Initially, the background density field is prescribed by a linear function such that the buoyancy frequency is the same as the field observation. The shear rate and the time scale (calculated as the length scale divided by the velocity scale) is kept the same as the field observation because both the velocity and length scales are scaled by one-fourth. The density variation is therefore also scaled by one-fourth to have the same gradient Richardson number. The friction factor does not change significantly due to the scaling in the fully developed turbulent, high Reynolds number (Re~O(10^6)) flow (Moody, 1944). In the present model simulation, a linear velocity profile u(z) = Gz is prescribed at the inflow boundary. The maximum velocity of U_0 = 0.125-0.3 m s^{-1} is located at the top, and the velocity is zero at the bottom (the vertical length in the model domain is 100 m), which gives a constant shear rate G. For example, U_0 = 0.125 m s^{-1} gives $G = 1.25 \times 10^{-3}$ s^{-1}. Since the velocity and length are scaled-down by one-fourth, the velocity gradient is kept the same.

The free-slip boundary condition is used at the top and the bottom. The symmetric boundary condition is used for the two lateral boundaries, in which the velocity normal to the boundaries, and the gradients of density and velocity parallel to the wall are set to be zero. The outflow boundary condition is a mixed boundary condition. When the fluid flows out of the domain at the boundary, the velocity gradient is set to zero. When the fluid flows into the domain, the flow velocity is set to zero so there is no back flow at the outflow boundary. Initially, the background density is stably stratified with a linear distribution of density based on the observed buoyancy frequency N = 0.014-0.018 s^{-1} (**Table 1**). Therefore, the Froude

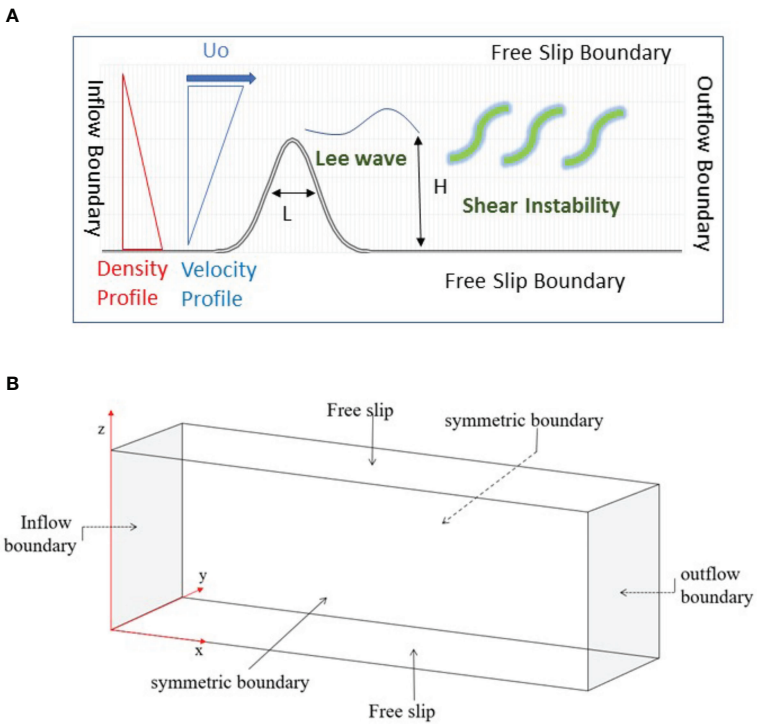

FIGURE 1 | **(A)** Model setup **(B)** A sketch of the computational domain. The inflow boundary condition implemented at the left and the outflow boundary condition at the right. A linear velocity profile is prescribed at the inflow boundary with the maximum velocity at the top and the minimum velocity at the bottom with a constant shear rate. Initially, the flow is stably stratified with a linear distribution of the density profile. The free-slip boundary condition is used at the top and the bottom.

TABLE 1 | In this study, model experiments with different intensities of shear flows and background stratification are conducted over narrow to wide ridges.

	Flow property	Geometry	Fr/Fr_L
Case A	U = 0.2 m s^{-1}	H = 50 m	Fr=0.250
	N = 0.016 s^{-1}	L = 300 m	Fr_L=0.042
Case B	U = 0.3 m s^{-1}	H = 50 m	Fr=0.375
	N = 0.016 s^{-1}	L = 300 m	Fr_L=0.063
Case C	U = 0.2 m s^{-1}	H = 50 m	Fr=0.250
	N = 0.016 s^{-1}	L = 200 m	Fr_L=0.063
Case D	U = 0.3 m s^{-1}	H = 50 m	Fr=0.375
	N = 0.016 s^{-1}	L = 200 m	Fr_L=0.094
Case E	U = 0.15 m s^{-1}	H = 50 m	Fr=0.188
	N = 0.016 s^{-1}	L = 200 m	Fr_L=0.047
Case F	U = 0.2 m s^{-1}	H = 50 m	Fr=0.222
	N = 0.018 s^{-1}	L = 200 m	Fr_L=0.056
Case G	U = 0.2 m s^{-1}	H = 50 m	Fr=0.286
	N = 0.014 s^{-1}	L = 200 m	Fr_L=0.071

The internal Froude number $Fr = \frac{U_0}{NH}$ ranges between 0.188-0.375, and the lateral Froude number $Fr_L = \frac{U_0}{NL}$ ranges between 0.047-0.083.

number of this study falls within the regime three of the regime diagram for lee waves in Legg (2021), suggesting the occurrences of blocking, hydraulic control, and lee wave saturation. Rotation effects set the lower bound frequency for internal lee wave and determine the internal wave ray propagation and critical layer. Therefore, rotation effects could also be important for inertial instabilities. When flow bifurcation occurs for Froude numbers below the critical value (see **Figure 1** from Perfect et al., 2020a), the top of the topography forms a region where the flow goes over the topographic ridge, hereafter referred to as the "cap". The flow over the cap is associated with the generation of internal lee waves (Voisin, 1991). When flow bifurcation occurs, the scale of internal lee waves and the resulting shear instabilities on the top of the topography is controlled by the corresponding width to the bifurcation cap when L<1km and the velocity of Kuroshio U_0 = 0.5- 1.2 m s^{-1} in our study site. The effect of the Coriolis force on the scale of internal lee waves and the resulting shear instabilities is less significant due to a relatively large Rossby number ($R_o = \frac{U}{fL}$) ~ O(10). The Burger number ($Bu = \frac{NH}{fL}$) ~ O(10) is greater than 1 so rotational effects are less significant comparing to stratification.

We used a body-fitting structured grid with uniform cells in each direction. The length of the computational domain is 2 km in the streamwise direction and 100 m in the spanwise direction, with a horizontal grid resolution of 1.25 m. The height of the computational domain in the vertical direction is 100 m with a vertical grid resolution of 0.4 m away from the topographic ridge. The smallest grid cells were at the peak of the ridge, which was 0.2 m, leading to the total number of grid points is 3.2×10^7. A second-order TVD scheme was chosen for spatial discretization, and the first-order Euler method was used for time marching. A fixed time step was chosen for each case based on the CFL condition (CFL < 0.5). All simulations were first run for 20,000 to 30,000 seconds (simulation time) to ensure that the flow reached a quasi-steady state. After the initial spin-up, each simulation was continued for another 20,000 seconds to obtain data for analysis.

The CFD model OpenFOAM has been validated with water tank experiments (Stiperski et al., 2017) in the stratified flow over Gaussian-shaped obstacles in a water flume in which the given salinity controlled the flow stratification. In recent years, many prior studies of internal waves (Eiff and Bonneton, 2000) and flow-topography interactions (Lacaze et al., 2013; Dossmann et al., 2014) have been carried out in this facility in the geophysical fluid dynamics laboratory in Toulouse, France. The size of the flume is 22 m long, 1 m high, and 3 m wide. The model is able to reproduce the horizontal and vertical scales of trapped lee waves (**Figure 2A**), long waves (**Figure 2B**), and hydraulic jump (**Figure 2C**) observed in the laboratory experiment.

THE TKE AND TRACER VARIANCE EQUATION

For any conservative tracer s and velocity u_j, the ensemble-mean and fluctuating components could be decomposed through Reynolds decomposition:

$$s = \langle s \rangle + s' \quad \text{and } u_j = \langle u_j \rangle + u_j' \tag{7}$$

We assume incompressible flow and denote the ensemble-averaged tracer as $\langle s \rangle$ with the mean of the fluctuation vanishing $\langle s' \rangle$ and $\langle uj' \rangle$=0.

TKE can be produced by shear flow or bottom friction, transferred through the process of turbulence energy cascade, and dissipated by viscous forces at the Kolmogorov scale. The process of production, transport and dissipation of TKE is expressed as:

$$\frac{\partial k}{\partial t} + \langle u_j \rangle \frac{\partial k}{\partial x_j} = -\frac{1}{\rho_o}\frac{\partial \langle u_i' p' \rangle}{\partial x_i} - \frac{1}{2}\frac{\partial \langle \overline{u_j' u_j' u_i'} \rangle}{\partial x_i} + \nu \frac{\partial^2 k}{\partial x_j^2} - \langle u_i' u_j' \rangle \frac{\partial u_i}{\partial x_j} - \nu \langle \frac{\partial u_i'}{\partial x_j}\frac{\partial u_i'}{\partial x_j} \rangle - \frac{g}{\rho_o} \langle \rho' u_i' \rangle \delta_{3i} \tag{8}$$

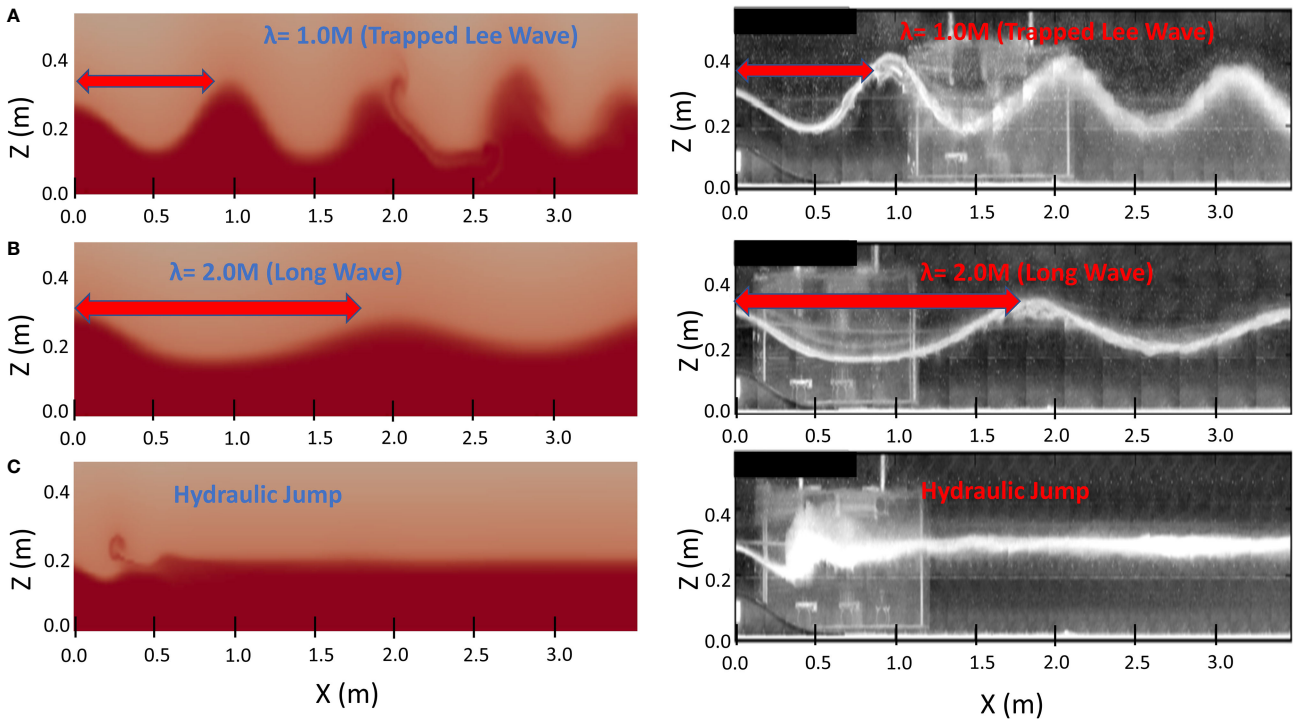

FIGURE 2 | The numerical model is validated with water tank experiments (Stiperski et al., 2017) in the stratified flow over a two dimensional Gaussian-shaped obstacle in a water flume in which the given salinity controlled the flow stratification. Model simulations (the left panels) show that the numerical model is able to reproduce the horizontal and vertical scales of **(A)** trapped lee waves, **(B)** long waves, and **(C)** hydraulic jump observed in the laboratory experiment (the right panels).

where k is the TKE, which is defined as one half of the sum of the velocity variance, with time t and the spatial coordinates x_i (x_1 = x, east westward, x_2 = y, north southward, and x_3 = z, up downward). The first term on the right-hand side (RHS) represents the pressure diffusion, the second term represents the turbulent transport, the third term represents molecular viscous transport, the fourth term represents turbulent production, the fifth term represents the turbulent dissipation, and the last term represents the buoyancy distraction.

In addition, the mass conservation can be described by the advection-diffusion equation for conservative tracer s without interior sinks or sources:

$$\frac{\partial s}{\partial t} + u_j \frac{\partial s}{\partial x_j} - \kappa_s \frac{\partial^2 s}{\partial x_j \partial x_j} = 0, \tag{9}$$

By applying several physically motivated mathematical rules (Pope, 2000), the conservation equation for the mean density $\langle s \rangle$ could also be derived as:

$$\frac{\partial \langle s \rangle}{\partial t} + \langle u_j \rangle \frac{\partial \langle s \rangle}{\partial x_j} + \frac{\partial \langle u_j' s' \rangle}{\partial x_j} - \kappa_s \frac{\partial^2 \langle s \rangle}{\partial x_j^2} = 0, \tag{10}$$

and a dynamic equation for the density variance $\langle s'^2 \rangle$ could be written as:

$$\frac{\partial \langle s'^2 \rangle}{\partial t} + \frac{\partial}{\partial x_j}\left(\langle u_j \rangle \langle s'^2 \rangle + \langle u_j' s'^2 \rangle - k_s \frac{\partial \langle s'^2 \rangle}{\partial x_j} \right) = -2 \langle u_j' s' \rangle \frac{\partial \langle s \rangle}{\partial x_j} - 2k_s \langle \frac{\partial s'}{\partial x_j} \frac{\partial s'}{\partial x_j} \rangle, \tag{11}$$

where k_s is the turbulent tracer eddy diffusivity and the first term on the RHS represents the density variance production, and the last term represents the density variance dissipation. The density variance equation, in which the time change rate of density variance is modulated by the interplay of density variance production and dissipation due to microstructure shear, provides a mean for quantifying the contributions of turbulent generation and dissipation to the mixing processes of the conservative tracer such as salinity, nutrient, or other biological properties (Pope, 2000; Burchard and Rennau, 2008; MacCready et al., 2018).

MODEL RESULTS

Lee Wave Breaking, Shear Instabilities, and Irreversible Mixing

The present numerical simulation with a spatial resolution close to the Ozmidov length scale successfully simulated three-

dimensional turbulent coherent structures behind the topographic ridge. **Figures 3**, **4** show an example of the model results with the internal Froude number, Fr = 0.25. The freestream velocity on the top of the shear zone in the model inflow boundary is given as U_0 =0.2 m s^{-1}, corresponding to the should delete max observed flow velocity of 0.8 m s^{-1}. When the energy flux ceases to increase due to topographic blocking effects, the saturated energy flux leads to the critical Froude number, Fr_c = 1 (Nikurashin and Ferrari, 2010b). A Froude number smaller than 1 implies downstream nonlinear internal lee waves and the blocking of flow upstream of the topography (Drazin, 1961; Aguilar and Sutherland, 2006; Winters and Armi, 2012). **Figure 3A** shows a snapshot of the simulation results of strong shear causing lee wave breaking and isopycnal heaving due to the involvement of irregular turbulent perturbations. Similar to the model results, the shipboard observation of echo sounder image also shows that the occurrence of lee waves and irregular oscillations in the lee of the topographic ridge (**Figure 3B**). The two-dimensional rollers and three-dimensional rib structures are shown in **Figure 3C** using the Q-method (Jeong and Hussain, 1995). At a high Reynolds number, shear instabilities evolve into turbulent coherent structures and break into smaller structures with local irregularities in terms of shapes and intensities.

Figure 4A shows the simulated instantaneous velocity model results along the spanwise direction's central transect. An accelerated jet-like layer formed over the ridge crest, and strong flow shear was induced in the boundary layer as the jet accelerated. The enhanced vertical shear and the return flow at the Z = 0-50 m (opposing the mean flow shown in blue in **Figure 4A**) appear downstream of the topography. Consequently, the strong shear flow between the jet and return flow leads to instabilities and mixing of the stratification (**Figure 4B**). The entrainment of denser fluid driven by shear-induced turbulent processes leads to an increase in the mixing layer thickness (Baines and Hoinka, 1985; Best, 2005; Talke et al., 2010; Klymak and Legg, 2010; Winters and Armi, 2013; Winters and Armi, 2014). The gradient Richardson number $Ri_G = \frac{N^2}{G^2}$ is computed to help identify the presence of shear instabilities (**Figure 4C**). The model results show that shear instabilities characterized by Ri_g < 0.25 occur below the interface of the lee wave (Farmer and Armi, 1999; Eiff and Bonneton, 2000). The vertical flow shear overcomes the stratification leading to Ri_g < 0.25 and initializes the generation of instabilities with strong spanwise vorticity (vortex rollers) near topography (strong blue color shown in **Figure 4D**).

The model result based on the three-dimensional topography parameterized by a Gaussian function $z = Hexp(-\frac{(x-x_o)^2+(y-y_o)^2}{L^2})$ is also discussed and compared with the results based on the simulations over two-dimensional topography shown in the above section. The return flow and lee wave generation are relatively weaker on the downstream side of the three-dimensional topography because of the flow splitting around the topographic ridge (**Figure 5A**). Model results show that the entrainment of

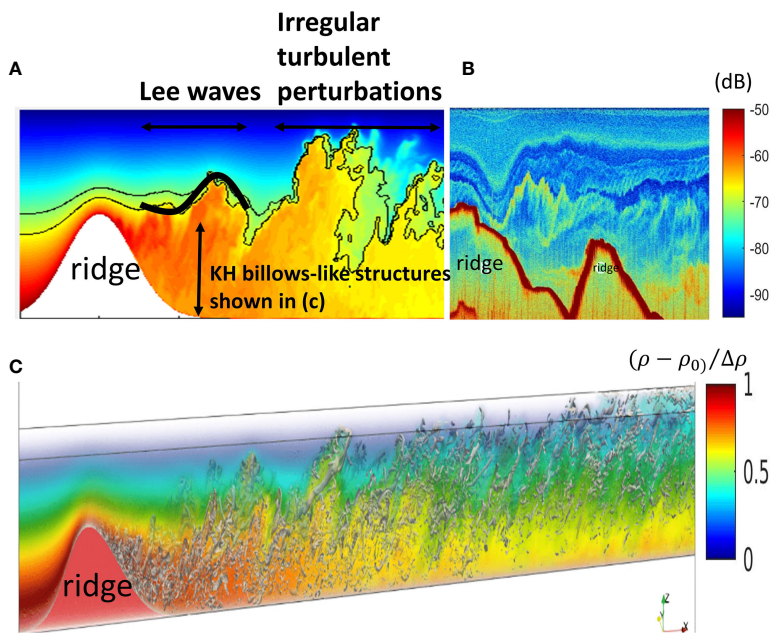

FIGURE 3 | **(A)** A schematic diagram shows the process of lee wave breaking and irregular turbulent perturbations in the lee of the topographic ridge. The color shows normalized density $(\rho - \rho_0)/\Delta\rho$, where $\Delta\rho$ is the density difference between the top and bottom boundary and ρ_0 is the background density [see the color legend in **(C)**]. **(B)** The shipboard observation of echo sounder intensity shows that the occurrence of lee waves and irregular oscillations in the lee of the topographic ridge. **(C)** Model results of KH billows-like structures. The coherent structures associated with shear instabilities are visualized by Q-method (Jeong and Hussain, 1995). The vertical coordinate is scale up five times for the visualization purpose.

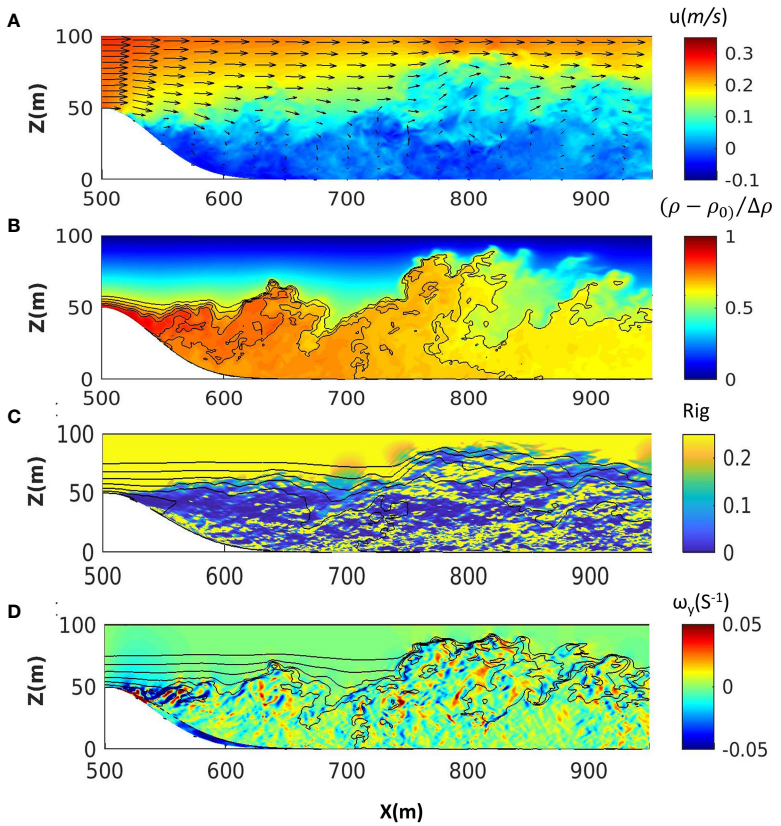

FIGURE 4 | Model simulations (*Fr*=0.25) of **(A)** streamwise velocity at the central transect of the spanwise direction, **(B)** normalized density $(\rho - \rho_0)/\Delta\rho$, where $\Delta\rho$ is the density difference between the top and bottom boundary and ρ_0 is the background density, **(C)** the gradient Richardson number calculated based on the spanwise averaged density gradient and velocity gradient (the spanwise averaged normalized density is shown as contour lines), and **(D)** the instantaneous spanwise vorticity ω_y=∂_z U+∂_x W (the instantaneous normalized density is shown as contour lines). The two-dimensional topography is parameterized by a Gaussian function.

denser fluid drives the mixing layer. An example of the entrainment of the denser fluid from the lower layer to the upper layer of the water column could be clearly seen between *x*=700-800 m in **Figures 4B** and **5B**. The mixing layer thickness indicated by the normalized density between 0.6 and 0.8 (the minimum and maximum value of the contour line) shows that the mixing layer thickness behind the two-dimensional topography (**Figure 4B**) is greater/thicker than that behind the three-dimensional topography (**Figure 5B**). The major difference between the model result based on the three-dimensional topography and the two-dimensional topography is the flow separation around the topography. Because deep flow does not go over the top of the three-dimensional topography, the effective topography height is smaller and the lee wave generation is weaker. In addition to breaking lee waves and shear instabilities shown in the *X*-*Z* plane, the turbulent wake is another process to generate horizontal instabilities in the *X*-*Y* plane (**Figure 5C**). The normalized density at *z*= 50 m in the *X*-*Y* plane is around 0.7, and is up to 0.8 at the side of the turbulent wake. The lighter fluid from the upper layer could be clearly seen along the central transect where the normalized density is as low as 0.3 (indicated by the black dash line in **Figure 5C**). It is noted that the focus of this study is the vertical mixing enhancement generated by lee wave breaking and shear instabilities along the central transect. Therefore, the three-dimensional simulation shown earlier in **Figure 4** was conducted over a two-dimensional topographic ridge with different ambient conditions, similar to the approach used for simulating flow over the west ridge of Luzon Strait (Jalali and Sarkar, 2017). The model result shows the snapshot of the simulated shear instabilities, which evolve into turbulent coherent structures and break into smaller structures with local irregularities in terms of shapes and intensities (**Figure 3C**). Horseshore vortex can be clearly identified, which characterizes the shear layer and is the main vortex structure. The vortex structure altering by different simulation parameters is analyzed by the characteristics of the turbulent shear layer in the next section.

The Simulated and Observed Core-Braid Structure of Shear Instabilities

The simulated time series of coherent structures behind the topographic ridge are further discussed with field observations. **Figure 6** shows the observed echo intensity measured behind a

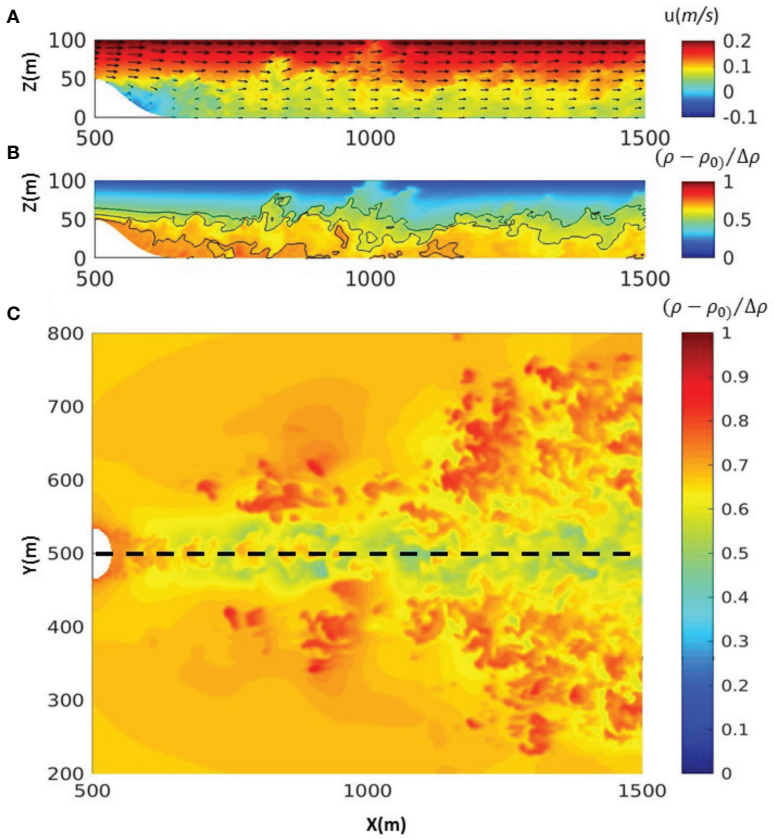

FIGURE 5 | Model simulations (*Fr*=0.25) of **(A)** streamwise velocity at the central transect of the spanwise direction, **(B)** normalized density $(\rho - \rho_0)/\Delta\rho$, where $\Delta\rho$ is the density difference between the top and bottom boundary and ρ_0 is the background density, and **(C)** the plane view of normalized density at *z*= 50m. The yellow dashed line indicates the central transect in the spanwise direction. The three-dimensional topography is parameterized by a Gaussian function.

topographic ridge along the route of the Kuroshio by a 120 kHz shipboard echo sounder (**Figure 6A**), density obtained from CTD profiling, velocity profiles obtained from a 150 kHz ADCP, and the gradient Richardson number, which provides a rough indication of shear instabilities (**Figure 6B**). The scattering of sound waves caused by the presence of a strong density gradient indicates that inclined, asymmetric, cusp-like bands form the temporal distribution of sound waves (Lavery et al., 2013; Chang et al., 2016). These patterns are different from the symmetric structure caused by an inflection point where a change in the horizontal velocity direction occurs at the middle of the water column (Chang et al., 2016). **Figure 7A** shows the observed time averaged density profile (red, original profile) and the density profile reordered as a function of depth (blue, reordered profile); **Figure 7B** shows the time averaged flow shear G^2 (red) and buoyancy frequency N^2 (blue). The gradient Richardson number falls between 0.2 and 0.25 at depths below the cusp-like band (depth< -140 m, indicated by the white dashed line in **Figure 6A**). The regime below the cusp-like band satisfies the condition of shear instability with $Ri_g < 0.25$, overlapping with the locations of density overturns (comparing the original and re-ordered density profiles in **Figure 7A**).

Previous literature shows that the distributions of the density variance dissipation rate clearly indicates that the mixing of tracer occurs exclusively in the braids of shear instabilities (Geyer et al., 2010). Therefore, the temporal distribution of the density variance dissipation [the second term of the RHS in the Equation (11)] provides a means to visualize the structure of shear instabilities and the resulting turbulent mixing. The simulated density variance dissipation at location *x*=800m (see **Figure 4** for the location) is compared with the temporal variation of acoustical backscatter intensity (see **Figure 8**). The observed echo intensity (**Figure 8A**) and the simulated density variance dissipation (**Figure 8B**) are considerably elevated in the braid mixing zone of shear instabilities with a specific period of 10 to 15 minutes ('M-B' indicates the location of the braid and the white circle indicates the core of shear instabilities in **Figure 8**). Correspondingly, each inclined cusp-like pattern has a horizontal length scale of 200 m and a vertical scale of 100 m. The vertical length scale of each inclined cusp-like pattern is nearly half of the vertical length scale of the internal lee wave (Klymak et al., 2010), but the wavelength is consistent with instabilities originating from a shear-layer based on the linear stability theory (Hazel, 1972). Therefore, the observed echo

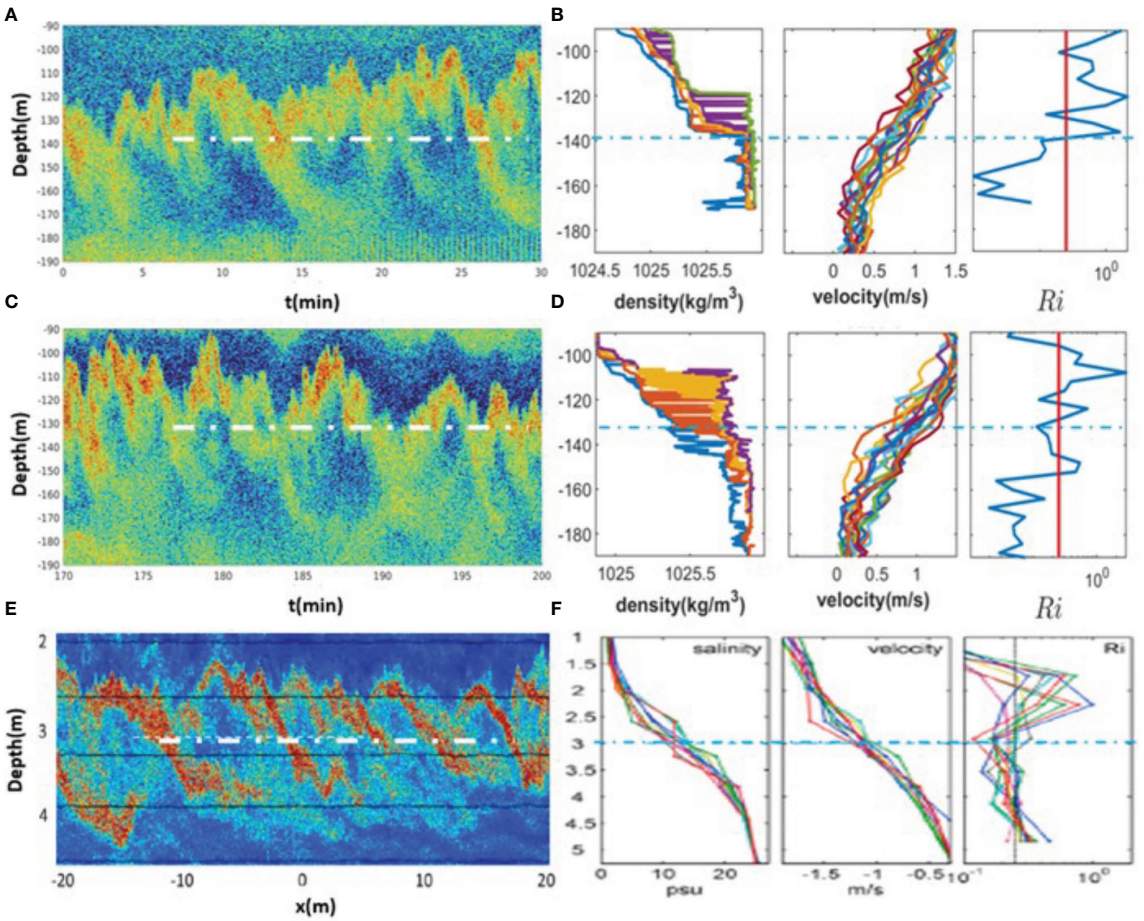

FIGURE 6 | **(A, C)** The observed echo sounder intensity, **(B, D)** density profiles, velocity profiles, and the gradient Richardson number (red solid lines indicate Ri_g=0.25) in the lee of a topographic ridge near the Green Island along the route of the Kuroshio. Observations were taken between **(A)** 03/22/2012 06:22:23-06:52:23AM and **(C)** between 03/22/2012 09:13:43-09:43:43AM. In the x axis t=0 is set as 03/22/2012 06:22:23. The white/blue dash lines separate the cusp-like band and the core of shear instabilities (indicated by white circles in **Figure 5A**) with Ri_g<0.25. **(E)** The observed echo sounder intensity, **(F)** salinity profiles, velocity profiles, and the gradient Richardson number in the Connecticut River, USA. The figure is adopted from Geyer et al. (2010).

intensity and the simulated density variance dissipation in the lee of a topographic ridge are relevant to KH billows-like structures of shear instabilities.

Figures 6C and D shows another example of the observed echo intensity, density profiles, and velocity profiles. The temporal variations in acoustic backscatter intensity exhibit a specific period of 5 to 8 minutes. The regimes with Ri_g < 0.25 overlap with the locations of density overturns (comparing the original and re-ordered density profiles in **Figure 7C**). The vertical flow shear is greater than the buoyancy frequency at depths greater than 130 m (**Figure 7D**). The pattern of the observed echo intensity is similar to previous field observations in the inner transect at the mouth of the Connecticut River, where strong shear flow is generated by the interaction of tidal currents and river plumes (Geyer et al., 2010). Strong density anomaly variance occurs mainly along the braids of shear instabilities indicated by high acoustic backscatter intensity (**Figures 6E, F**). The mixing zones appear more extensively in the upper limb of the braid due to the stronger vertical shear induced by the greater relative velocity in the upper water column.

DISCUSSION

Echo sounder images from shipboard observations suggest that both horizontal and vertical distribution of oscillation patterns could be modulated by the ambient conditions. For example, the horizontal scale of the braid shown in **Figure 6C** is smaller than the one shown in **Figure 6A** possibly due to the stronger shear rate (the maximum value of the red curve in **Figure 7D** is greater than that in **Figure 7B**). In this study, model experiments with different inflow velocities and background stratification is further discussed in this section. Prior laboratory experiments showed that the boundary layer separation and the source for turbulence generation downstream of the topographic ridge depend strongly

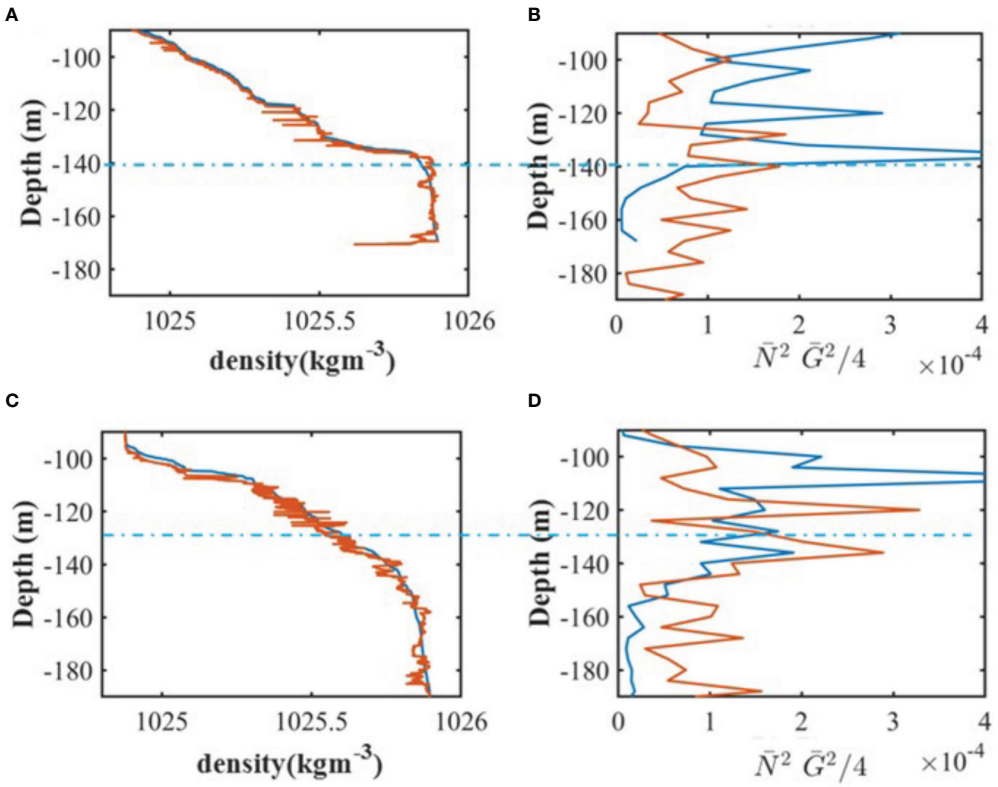

FIGURE 7 | **(A)** the left panel: the observed time averaged density profile (red, original profile) and **(B)** the density profile reordered as a function of depth (blue, reordered profile); the right panel: the time averaged flow shear $G^2 = (\partial_z U)^2 + (\partial_z V)^2$ (red) and buoyancy frequency $N^2 = -\frac{g}{\rho}\frac{d\rho}{dz}$ (blue) between 03/22/2012 06:22:23-06:52:23AM. The blue dash line separates the cusp-like band and the core of shear instabilities (indicated by white circles in **Figure 5A**) with Ri_g<0.25. **(C)** the left panel: the observed time averaged density profile; **(D)** the right panel: the time averaged flow shear and buoyancy frequency between 03/22/2012 09:13:43-09:43:43AM.

on the shape of the topography (Aguilar and Sutherland, 2006). In this study, numerical are conducted over narrow and wide ridges. The internal Froude number (F_r = Uo/NH) ranges between 0.188-0.375 and the lateral Froude number *Fr_L=Uo/NL* ranges between 0.047-0.094, where L is the width of the ridge (**Table 1**).

The Effect of the Ridge Geometry on Vertical Mixing Enhancement

The model result used to compare with the observed core-braid structure of shear instabilities is Case C with Fr = 0.25 and Fr_L = 0.063. The core of shear instabilities with Ri_g <0.25 is shown as white dashed circles under the braids of shear instabilities with the strong density variance dissipation (**Figures 8B**, **9**). The high-density variance dissipation rate [up to O(10^{-4} s^{-1})] are exclusively localized to the cusp-like band with a period of 10-15 minutes. The effect of the internal Froude number on down-stream nonlinear internal lee-waves has been discussed in previous studies (Drazin, 1961; Aguilar and Sutherland, 2006; Winters and Armi, 2012; Dossmann et al., 2016; Perfect et al., 2020b). In this section, the effect of the lateral Froude number on down-stream conditions is discussed based on numerical experiments over a wide and narrow ridge. **Figures 9**, **10** show the model results of flow shear, TKE dissipation, density variance dissipation, and eddy diffusivity of Case C and A at location x=800 m (see **Figure 4** for the location). Model results over a relatively wide ridge show that the shear instabilities have a period of 20-30 minutes (Case A with Fr = 0.25 and Fr_L = 0.043, **Figures 10A**). In addition to the changes in period and the horizontal length scale of shear instabilities, the thickness of the mixing layer (indicated by the stronger density variance shown in **Figure 12A**) also decreases in the case with the milder geometric slope. The TKE dissipation rate of Case C is up to 10^{-6} m^2 s^{-3} (**Figure 9C**) and the TKE dissipation rate of Case A is in the order of 10^{-7} m^2 s^{-3} (**Figure 10C**). Although regimes of Ri_g > 0.25 are found above z = 70 m in both cases, it is noted that the density variance dissipation of Case A is an order of magnitude smaller than the density variance dissipation of Case C (see **Figures 9D** and **Figure 10D**). Correspondingly, the vertical eddy viscosity is heterogeneously distributed over the water depth and the estimated eddy diffusivity of Case A is up to k_s= 10^{-3} m^2 s^{-1}, which is an order of magnitude smaller than the estimated eddy diffusivity of Case C (see **Figures 9E** and **Figure 10E**). The model results show that the vertical mixing enhancement due to flow topography interactions could be ten

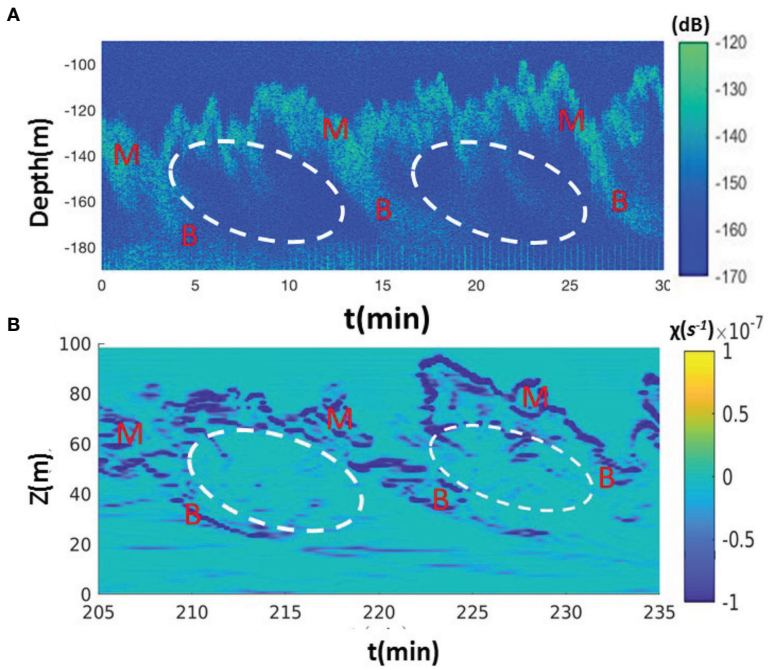

FIGURE 8 | **(A)** The observed echo intensity. 'M-B' indicates the location of the braid mixing zone and white circles indicate the core of shear instabilities. Observations were taken between 03/22/2012 06:22:23-06:52:23AM. In the x axis t=0 is set as 03/22/2012 06:22:23. **(B)** The patterns of the simulated density variance dissipation rate at x=800m (see **Figure 4** for the location).

times weaker when the flow goes over a relatively milder ridge and Fr_L decreases from 0.063 to 0.043.

The Intensity of Shear Flows on Vertical Mixing Enhancement

In this section, model experiments with different inflow velocities are discussed to characterize the intensity of turbulent mixing due to shear instabilities. The freestream velocity on the top of the shear zone is given as U_0 = 0.125-0.3 m s^{-1}, corresponding to the maximum observed flow velocity ranging from 0.5 m s^{-1} to 1.2 m s^{-1}, which represents the velocity of Kuroshio flow modulated by diurnal and semidiurnal tides and internal waves. Model results indicate that shear instabilities do not occur when the lower free stream velocity (U_0 = 0.15 $m\ s^{-1}$, Case E, with Fr = 0.188 and Fr_L = 0.047) is given in the inflow boundary. As the shear flow increases to 0.3 m s^{-1}, the simulated shear instabilities have a shorter period of 5 minutes (Case B, with Fr = 0.375 and Fr_L = 0.063, **Figure 11**). A diagram including the density variance of Cases A-C further indicates that the period of shear instabilities and the thickness of mixing layer is relevant to Fr or Fr_L (**Figures 12A**), and the braid mixing zone with a high TKE dissipation rate appears more frequently while the flow shear increases. The resulting depth-averaged density variance dissipation rate of Case B (U_0 = 0.3 m s^{-1}) is greater than O(10^{-5} s^{-1}) and the estimated eddy diffusivity k_s is up to 10^{-2} m^2 s^{-1}, which is one order magnitude greater than that of Case A (U_0 = 0.2 m s^{-1}, **Figure 11**). A diagram including model results of the depth-averaged mixing rate (the depth-averaged TKE dissipation rate and density variance dissipation rate) of Case A-G is summarized in **Figure 13**. Each dot represents the depth-averaged TKE dissipation rate or the density variance dissipation rate based on 30-minute average profiles at location x=800 m (see **Figure 4** for the location). The lowest depth-averaged TKE dissipation rate is shown in Case A (O(10^{-7} m^2 s^{-3})) with Fr_L=0.024, and the highest mixing rate is shown in Case D (O(10^{-5} m^2 s^{-3})) with Fr_L=0.094. The Fr_L values are the same for Case B and Case C, but the depth-averaged TKE dissipation rate of Case B (U_0 = 0.3 $m\ s^{-1}$) is slightly higher. The model results indicate that the depth-averaged TKE dissipation rate ranges between O(10^{-7} m^2 s^{-3}) and O(10^{-5} m^2 s^{-3}) and increases with the strength of shear flows.

The Effect of Background Stratification Variability on Vertical Mixing Enhancement

Previous studies in the upper equatorial ocean show that the period of shear instabilities depends on to the buoyancy frequency (Smyth and Moum, 2012). The laboratory study at moderate Reynolds number also shows that fluid parcels oscillate at the buoyancy frequency after passing over the ridge and strong mixing is generated during the buoyancy period (Klymak and Legg, 2010; Dossmann et al., 2016). In this section, numerical experiments with different background stratifications (Cases G, C, and F, N=0.014, 0.016, and 0.018 s^{-1} based on CTD measurements) are conducted to understand the effect of baroclinic variability on the observed temporal and spatial scales of shear instabilities induced by the flow-topography

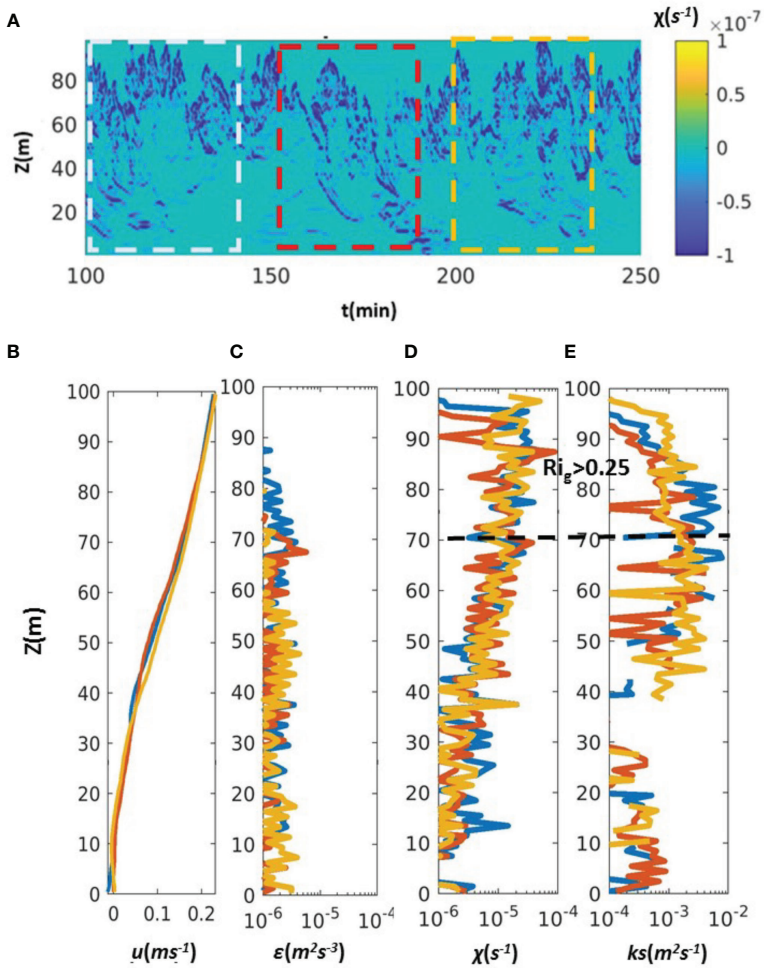

FIGURE 9 | Model results of Case C: the time series of **(A)** density variance dissipation. The blue, red, and orange lines indicate the interval for 30 minutes time average. **(B)** The time average profiles of flow shear, **(C)** TKE dissipation rate, **(D)** density variance dissipation, and **(E)** eddy diffusivity at location x=800 m (see **Figure 4** for the location).

interaction. The diagram including Cases A-G indicates that the thickness of the mixing layer is proportional to Fr_L (**Figure 12B**) and the period of shear instabilities is inversely proportional to the given Fr_L (**Figure 12C**). The depth averaged mixing rate slightly increases in the case with a lower buoyancy frequency (Case G, N=0.014 s^{-1} **Figures 13A, B**). Generally the depth-averaged TKE dissipation rate and the normalized density variance dissipation rate increase with Fr_L. However, the estimated eddy diffusivity (k_s = 10^{-3} m^2 s^{-1}) and the resulting mixing are on the same order of magnitude among the cases with different buoyancy frequencies. Model results indicate that the period of shear instabilities is not only relevant to the background stratification, as shown in previous literature but also relevant the ridge geometry and the intensity of the flow shear. The estimated eddy diffusivity and the resulting mixing are more sensitive to the intensity of the flow shear than the variation in density gradients in the stratified background.

Comparison with Model Parameterization of Eddy Diffusivity

Studying the nonlinear process of lee waves and the evolution of shear instabilities is crucial in understanding the turbulent process and of key interest in developing mixing parameterizations for ocean circulations and scalar transport models. Proper parameterization of small-scale physical processes, such as shear instabilities, is required in large-scale ocean circulation models with a horizontal grid resolution of kilometer scale. For example, in the vertical diffusivity in the Regional Ocean Modeling System (ROMS), the shear-generated mixing term is parameterized by a stability function of local buoyancy and flow shears. The viscosity coefficient is estimated by adding the effects of internal wave-generated mixing and shear mixing (Large et al., 1994).

$$\nu = \nu^{w} + \nu^{sh} \tag{12}$$

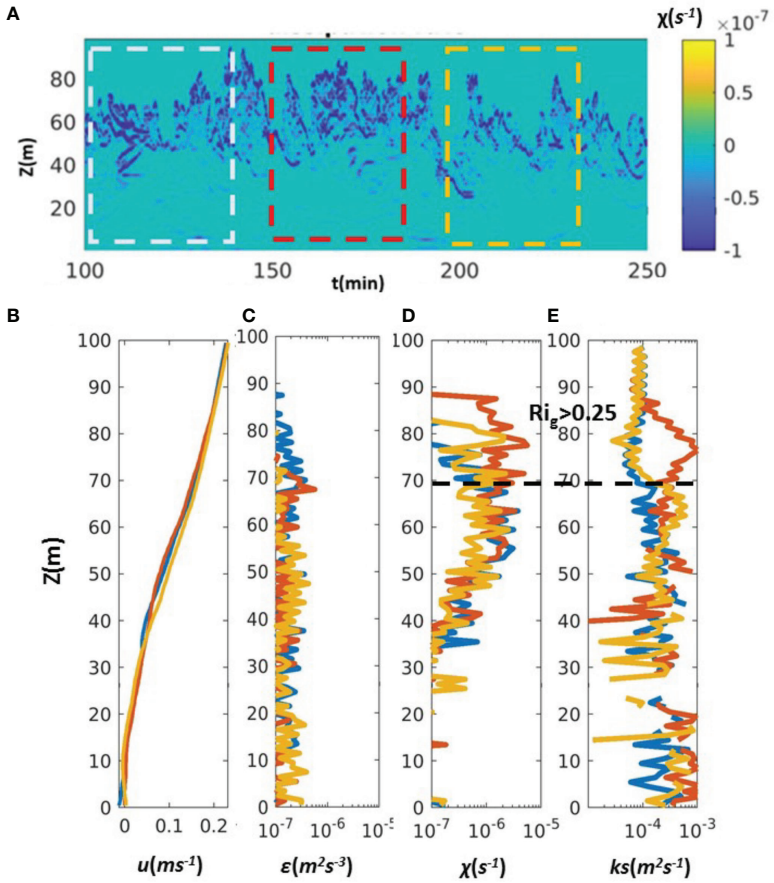

FIGURE 10 | Model results of Case A: the time series of **(A)** density variance dissipation. The blue, red, and orange lines indicate the interval for 30 minutes time average. **(B)** The time average profiles of flow shear, **(C)** TKE dissipation rate, **(D)** density variance dissipation, and **(E)** eddy diffusivity at location *x*=800 m (see **Figure 4** for the location).

where the eddy diffusivity due to the internal wave-generated mixing term v^w is 10^{-5}m^2 s^{-1} is estimated based on the data of Ledwell et al. (1993). The shear mixing term v^{sh} is calculated using a gradient Richardson number formulation with viscosity estimated as:

$$v^{sh} = \begin{cases} v_0 & \mathrm{Ri_g} < 0 \\ v_0\left[1 - \left(\mathrm{Ri_g}/\mathrm{Ri_0}\right)^2\right]^3 & 0 < \mathrm{Ri_g} < \mathrm{Ri_0} \\ 0 & \mathrm{Ri_g} > \mathrm{Ri_0} \end{cases} \quad (13)$$

where v_0 is 0.005 m^2 s^{-1}, Ri_0 =0.7. The maximum of v^{sh} = 0.005 m^2 s^{-1} can be obtained when shear instability occurs and Ri_g<0.25. Therefore, the maximum eddy diffusivity with the combination of internal wave and shear instability generated mixing is $O(10^{-3}$ m^2 s$^{-1})$, which is one to two orders of magnitude smaller than the observed eddy diffusivity under flow-topography interaction along the Kuroshio (Chang et al., 2016; Tsutsumi et al., 2017).

More recently, Klymak and Legg (2010) proposed eddy diffusivities related to the combination of the Ozmidov relation and the Osborn relation. Observational evidence indicates that the size of convectively unstable vertical displacements in a turbulent patch L_T is approximately equivalent to the Ozmidov scale ($Lt \approx Lo$) (Dillon, 1982; Wesson and Gregg, 1994; Moum, 1996). The Osborn relation related to the strength of the dissipation to the vertical eddy diffusivity is:

$$\mathrm{v} = \Gamma \in \mathrm{N}^{-2} \quad (14)$$

where the Ozmidov scale that defines the scale of turbulence overturning can be defined as:

$$\varepsilon = L_O^2 N^3 \quad (15)$$

Combining (14) and (15), the vertical diffusivity can be estimated as:

$$v = \Gamma L_O^2 N \quad (16)$$

where $\Gamma \approx 0.2$ and L_o is the size of the density overturns. Based on Equation (16), the estimation of vertical diffusivity due to internal wave-generated mixing is O(10^{-2} m^2 s^{-1}), which corresponds to the eddy diffusivity estimated based on the field observation under flow topography interactions along the

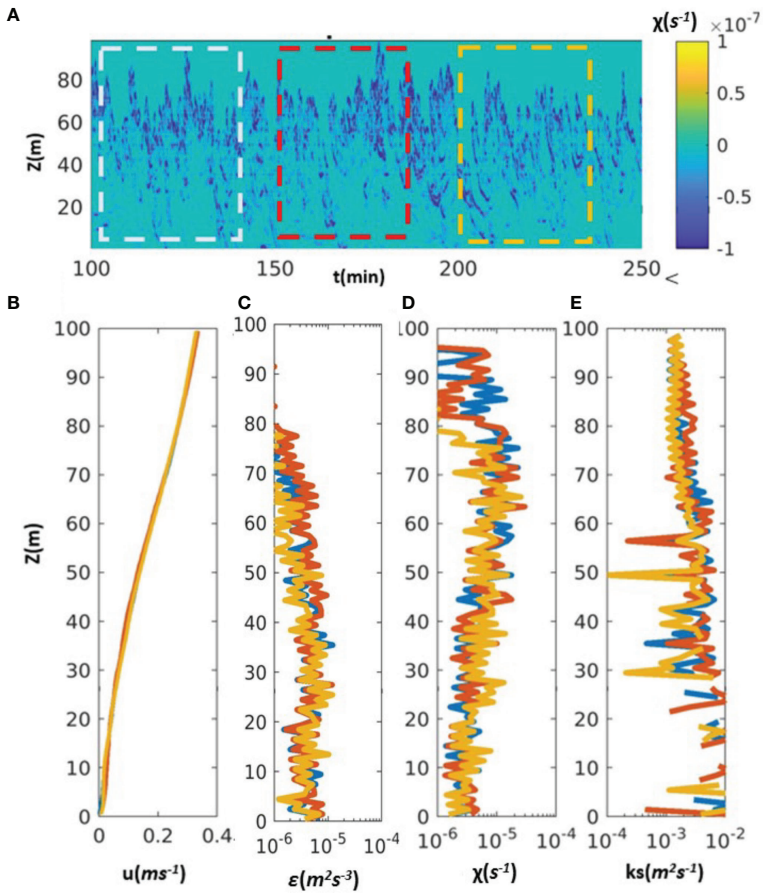

FIGURE 11 | Model results of Case B: the time series of **(A)** density variance dissipation. The blue, red, and orange lines indicate the interval for 30 minutes time average. **(B)** The time average profiles of flow shear, **(C)** TKE dissipation rate, **(D)** density variance dissipation, and **(E, C)** eddy diffusivity at location x=800 m (see **Figure 4** for the location).

Kuroshio. However, the dependence of eddy diffusivities on the intensity of flow shears and the ridge geometry is not considered in the existing model parameterization. Our study shows that high turbulence with vertical diffusivity up to O(10^{-2} m^2 s^{-1}) is populated primarily along the braids of shear instabilities with a specific period of 5 minutes (**Figure 11E**). The thickness of the mixing layer and the period of shear instabilities are modulated by the flow shear, background stratification, and ridge geometry. The difference in depth-averaged mixing rates can be up to two orders of magnitude. Therefore, it is suggested that the dependency of vertical mixing enhancement on Fr_L should be further considered in estimating the enhancement of eddy diffusivities and TKE dissipation rates under the circumstance of lee wave breaking.

CONCLUDING REMARKS

In this study, the CFD model OpenFOAM with LES turbulent closure is applied to investigate dominant mechanisms that control the spatial and temporal scales and intensities of shear instabilities and resulting mixing in the stratified shear flow at high Reynolds numbers. The model successfully reproduced the bulk properties of shear instabilities at high Reynolds numbers using a model spatial resolution close to the Ozmidov length scale. Both the observed echo intensity and model results of density variance dissipation show the spatial evolution of oscillations formed by inclined, asymmetric, cusp-like bands with high mixing in the braid. Strong mixing is located in the braids of shear instabilities above the core region with a greater Richardson number. These features have not been investigated in previous modeling and experimental studies at lower Reynolds numbers.

Observations under different ambient conditions conjecture that the frequency of shear instabilities and the elevated vertical mixing enhancement are modulated by inflow velocities and bouyancy frequencies. Model results show that the estimated eddy diffusivity and the resulting mixing are more sensitive to the flow shear rate than the variability of background stratification. The typical value of TKE dissipation rate in the open ocean is O (10^{-9} m^2 s^{-3}) (Munk and Wunsch, 1998) but the depth-averaged TKE dissipation rate can approach to O(10^{-5} m^2 s^{-3}) due to flow-topography interaction (**Figure 13**). The horizontal scale of shear

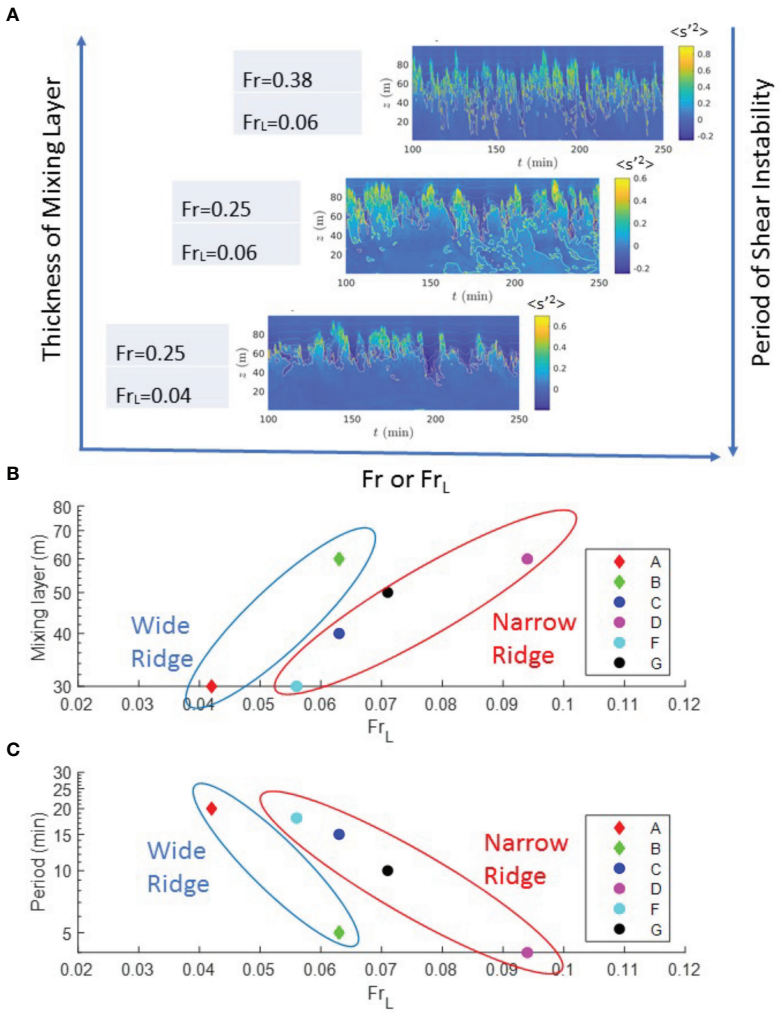

FIGURE 12 | **(A)** A diagram including the density variance of Case A-C shows the period of shear instabilities and the thickness of the mixing layer are relevant to *Fr* or Fr_L. Diagrams show the relationship of Fr_L versus **(B)** the thickness of the mixing layer (unit:meter) and **(C)** the period of shear instabilities (unit: minute).

instabilities and the resulting mixing enhancement behind the seamount are less significant when the shear flow is weaker or over milder seafloor topography. In contrast, the resulting mixing enhancement appears more frequently when Fr_L is greater. The frequency of mixing enhancement increases when shear flow becomes more intense or goes over relatively steeper seafloor topography (**Figure 14**).

The evolution of shear instabilities is of crucial importance in understanding the turbulent process and of key interest in developing mixing parameterizations for ocean circulation and scalar transport models (Smyth and Moum, 2012). Conventionally, the vertical diffusivity in the ocean circulation model is parameterized by a stability function of local buoyancy and flow shear (Large et al., 1994). The dependence of the eddy diffusivity on the intensity of flow shear and the ridge geometry is not considered in the existing model parameterization. The estimation of the eddy diffusivity coefficient with the combination of internal wave and shear instability generated mixing might be one to two order magnitude smaller than the actual eddy diffusivity under flow-topography interaction, incapable to capture the field observation of Chang et al. (2016); Tsutsumi et al. (2017). Our study indicates that the length scale or the period of shear instabilities are the keys to the mixing enhancement. Fr_L should be further considered under the circumstance of lee wave breaking dictating turbulent dissipation processes.

DATA AVAILABILITY STATEMENT

The data presented in this study are available through the corresponding author by request.

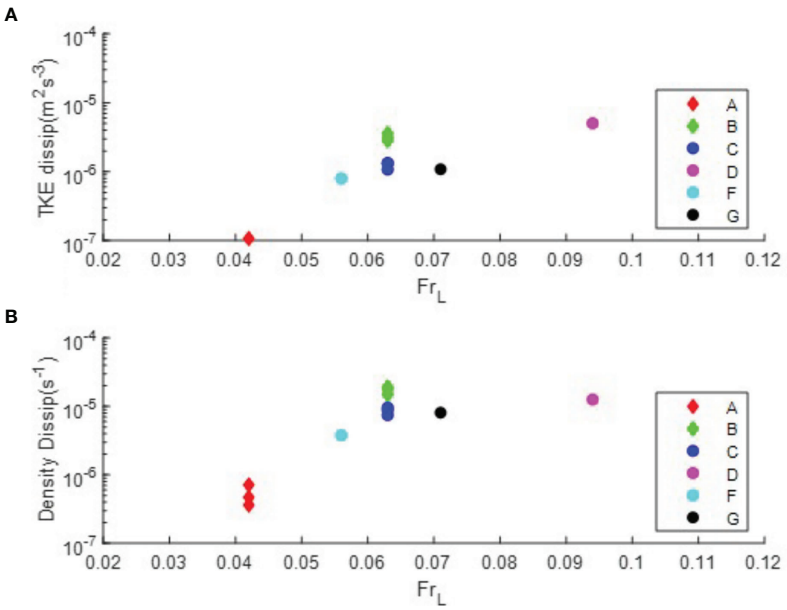

FIGURE 13 | Diagrams show Fr_L versus **(A)** the depth-averaged TKE dissipation rate (unit: $m^2\ s^{-3}$) and **(B)** the depth-averaged normalized density dissipation rate (unit: s^{-1}).

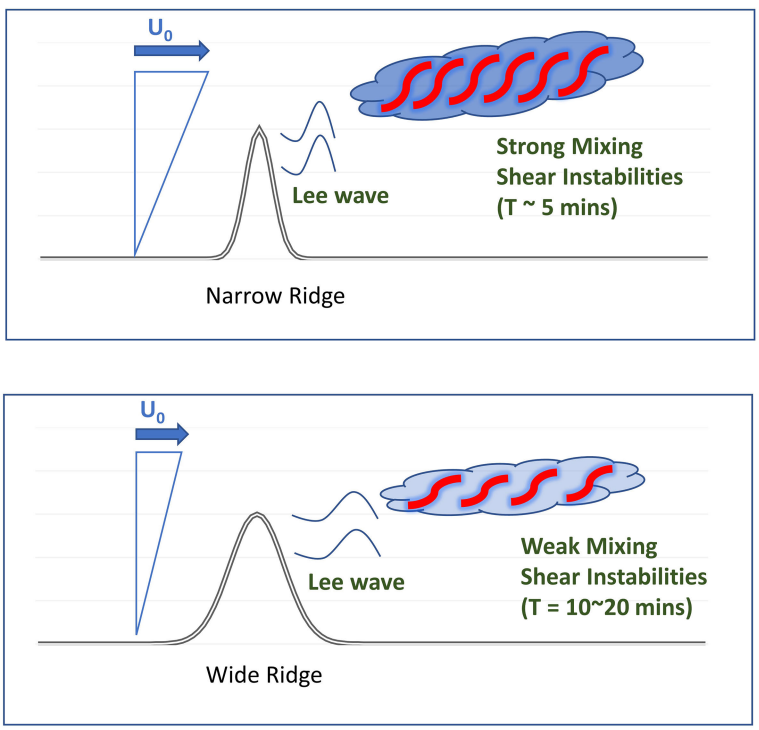

FIGURE 14 | A schematic diagram for the occurrence of mixing intensification due to flow-topography interaction. The typical value of turbulent in the open ocean is O(10^{-9} m^2 s^{-3}) (Munk and Wunsch, 1998) but the depth-averaged TKE dissipation rate is up to O(10^{-5} m^2 s^{-3}) due to flow-topography interaction. The frequency of mixing enhancement (red braids) and the thickness of mixing layer (blue clouds) are mainly modulated by the flow shear and the seafloor topography.

AUTHOR CONTRIBUTIONS

J-LC, XY, M-HC, and R-CL planned the research. J-LC, M-HC, SJ, and YY carried out the ship-based experiments with the assistance from marine technicians of NTU and crew members of R/Vs New Ocean Researcher 1, 2, and 3. J-LC wrote the manuscript with input from all co-authors. All authors contributed to the article and approved the submitted version.

FUNDING

Funding was provided by Taiwan's Ministry of Science and Technology (J-LC: MOST 110-2611-M-006-003, SJ: MOST 108-2611-M-002-019). XY contribution towards this research was also partly supported by the US National Science Foundation (NSF) under grant CMMI-2128895. R-CL contribution towards this research was supported by the US NSF under grant OCE-2048764.

ACKNOWLEDGMENTS

We thank Dr. Rocky Geyer, WHOI, for providing suggestions of the density variance analysis, and Shun-Yan Hsu, Sheng-De Tsai, Wei-Zhan Tsai, Cheng-Chien Hou, and Andhy Romdani for figure illustrations. Simulations were carried out on the HiperGator super computer at the University of Florida and MobyDick in National Cheng Kung University. Computer resources, technical expertise and assistance provided by the HiperGator and MobyDick staff are gratefully acknowledged. The CFD model OpenFOAM is developed primarily by OpenCFD Ltd and available at https://www.openfoam.com/.

REFERENCES

Acabado, C. S., Cheng, Y. H., Chang, M.-H., and Chen, C. C. (2021). Vertical Nitrate Flux Induced by Kelvin-Helmholtz Billows Over a Seamount in the Kuroshio. *Front. Mar. Sci.* doi: 10.3389/fmars.2021.680729

Aguilar, D. A., and Sutherland, B. R. (2006). Internal Wave Generation From Rough Topography. *Phys. Fluids* 18, 066603. doi: 10.1063/1.2214538

Baines, P. G., and Hoinka, K. P. (1985). Stratified Flow Over Two-Dimensional Topography in Fluid of Infinite Depth: A Laboratory Simulation. *J. Atmospheric Sci.* 42, 1614–1630. doi: 10.1175/1520-0469(1985)042<1614:SFOTDT>2.0.CO;2

Bell, T. H. (1975). Lee Waves in Stratified Flows With Simple Harmonic Time Dependence. *J. Fluid Mech.* 67, 705–722. doi: 10.1017/S0022112075000560

Best, J. (2005). The Fluid Dynamics of River Dunes: A Review and Some Future Research Directions. *J. Geophys. Res. Earth Surf.* 110, 1–21. doi: 10.1029/2004JF000218

Burchard, H., and Rennau, H. (2008). Comparative Quantification of Physically and Numerically Induced Mixing in Ocean Models. *Ocean Model.* 20, 293–311. doi: 10.1016/j.ocemod.2007.10.003

Chang, M.-H., Jheng, S.-Y., and Lien, R.-C. (2016). Trains of Large Kelvin-Helmholtz Billows Observed in the Kuroshio Above a Seamount. *Geophys. Res. Lett.* 43, 8654–8661. doi: 10.1002/2016GL069462

Chang, M.-H., Tang, T. Y., Ho, C.-R., and Chao, S.-Y. (2013). Kuroshio-Induced Wake in the Lee of Green Island Off Taiwan. *J. Geophys. Res. Oceans* 118, 1508–1519. doi: 10.1002/jgrc.20151

Dillon, T. M. (1982). Vertical Overturns: A Comparison of Thorpe and Ozmidov Length Scales. *J. Geophys. Res. Oceans* 87, 9601–9613. doi: 10.1029/JC087iC12p09601

Dossmann, Y., Paci, A., Auclair, F., Lepilliez, M., and Cid, E. (2014). Topographically Induced Internal Solitary Waves in a Pycnocline: Ultrasonic Probes and Stereo-Correlation Measurements. *Phys. Fluids* 26, 056601–056621. doi: 10.1063/1.4873202

Dossmann, Y., Rosevear, G., Griffiths, R. W., McC. Hogg, A., Hughes, G. O., and Copeland, M. (2016). Experiments With Mixing in Stratified Flow Over a Topographic Ridge. *J. Geophys. Res. Oceans* 121, 6961–6977. doi: 10.1002/2016JC011990

Drazin, P. G. (1961). On the Steady Flow of a Fluid of Variable Density Past an Obstacle. *Tellus* 13, 239–251. doi: 10.3402/tellusa.v13i2.9451

Ducros, F., Nicoud, F., and Poinsot, T. (1998). Wall-Adapting Local Eddy-Viscosity Models for Simulations in Complex Geometries. *Numerical Methods for Fluid Dynamics VI*. p. 1–7

Durán Gómez, G. S., Nagai, T., and Yokawa, K. (2020). Mesoscale Warm-Core Eddies Drive Interannual Modulations of Swordfish Catch in the Kuroshio Extension System. *Front. Mar. Sci.* 7. doi: 10.3389/fmars.2020.00680

Eiff, O. S., and Bonneton, P. (2000). Lee-Wave Breaking Over Obstacles in Stratified Flow. *Phys. Fluids* 12, 1073–1086. doi: 10.1063/1.870362

Farmer, D., and Armi, L. (1999). Stratified Flow Over Topography: The Role of Small-Scale Entrainment and Mixing in Flow Establishment. *Proc. R Soc. Lond. Ser. A* 455, 3221–3258. doi: 10.1098/rspa.1999.0448

Geyer, W. R., Lavery, A. C., Scully, M. E., and Trowbridge, J. H. (2010). Mixing by Shear Instability at High Reynolds Number. *Geophys. Res. Lett.* 37, 1–5. doi: 10.1029/2010GL045272

Hazel, P. (1972). Numerical Studies of the Stability of Inviscid Stratified Shear Flows. *J. Fluid Mech.* 51, 39–61.

Jalali, M., and Sarkar, S. (2017). Large Eddy Simulation of Flow and Turbulence at the Steep Topography of Luzon Strait. *Geophys. Res. Lett.* 44, 9440–9448. doi: 10.1002/2017GL074119

Jan, S., Yang, Y. J., Wang, J., Mensah, V., Kuo, T.-H., Chiou, M.-D., et al. (2015). Large Variability of the Kuroshio at 23.75°N East of Taiwan. *J. Geophys. Res. Oceans* 120, 1825–1840. doi: 10.1002/2014JC010614

Jeong, J., and Hussain, F. (1995). On the Identification of a Vortex. *J. Fluid Mech.* 332, 339–363.

Klymak, J. M., and Legg, S. M. (2010). A Simple Mixing Scheme for Models That Resolve Breaking Internal Waves. *Ocean Model.* 33, 224–234. doi: 10.1016/j.ocemod.2010.02.005

Klymak, J. M., Legg, S. M., and Pinkel, R. (2010). High-Mode Stationary Waves in Stratified Flow Over Large Obstacles. *J. Fluid Mech.* 644, 321–336. doi: 10.1017/S0022112009992503

Kunze, E., and Lien, R.-C. (2019). Energy Sinks for Lee Waves in Shear Flow. *J. Phys. Oceanogr.* 49, 2851–2865. doi: 10.1175/JPO-D-19-0052.1

Lacaze, L., Paci, A., Cid, E., Cazin, S., Eiff, O., Esler, J., et al. (2013). Wave Patterns Generated by an Axisymmetric Obstacle in a Two-Layer Flow. *Phys. Fluids* 54, 1–10. doi: 10.1007/s00348-013-1618-z

Large, W. G., McWilliams, J. C., and Doney, S. C. (1994). Oceanic Vertical Mixing: A Review and a Model With a Nonlocal Boundary Layer Parameterization. *Rev. Geophys.* 32, 363–403. doi: 10.1029/94RG01872

Lavery, A. C., Geyer, W. R., and Scully, M. E. (2013). Broadband Acoustic Quantification of Stratified Turbulence. *J. Acoust. Soc Am.* 134, 40–54. doi: 10.1121/1.4807780

Ledwell, J., Watson, A., and Law, C. (1993). Evidence for Slow Mixing Across the Pycnocline From an Open-Ocean Tracer-Release Experiment. *Nature* 364, 701–703. doi: 10.1038/364701a0

Legg, S. (2021). Mixing by Oceanic Lee Waves. *Annu. Rev. Fluid Mech.* 53, 173–201. doi: 10.1146/annurev-fluid-051220-043904

MacCready, P., Geyer, W. R., and Burchard, H. (2018). Estuarine Exchange Flow Is Related to Mixing Through the Salinity Variance Budget. *J. Phys. Oceanogr.* 48, 1375–1384. doi: 10.1175/JPO-D-17-0266.1

Mashayek, A., and Peltier, W. R. (2012). The 'Zoo' of Secondary Instabilities Precursory to Stratified Shear Flow Transition. Part 1 Shear Aligned Convection, Pairing, and Braid Instabilities. *J. Fluid Mech.* 708, 5–44. doi: 10.1017/jfm.2012.304

Mashayek, A., and Peltier, W. R. (2013). Shear-Induced Mixing in Geophysical Flows: Does the Route to Turbulence Matter to Its Efficiency? *J. Fluid Mech.* 725, 216–261. doi: 10.1017/jfm.2013.176

Mensah, V., Jan, S., Chiou, M.-D., Kuo, T. H., and Lien, R.-C. (2014). Evolution of the Kuroshio Tropical Water From the Luzon Strait to the East of Taiwan. *Deep Sea Res. Part Oceanogr. Res. Pap.* 86, 68–81. doi: 10.1016/j.dsr.2014.01.005

Moody, L. F. (1944). Friction Factors for Pipe Flow. *Trans. ASME* 66, 671–684.

Moum, J. N. (1996). Efficiency of Mixing in the Main Thermocline. *J. Geophys. Res. Oceans* 101, 12057–12069. doi: 10.1029/96JC00508

Munk, W., and Wunsch, C. (1998). Abyssal Recipes II: Energetics of Tidal and Wind Mixing. *Deep Sea Res. Part Oceanogr. Res. Pap.* 45, 1977–2010. doi: 10.1016/S0967-0637(98)00070-3

Nagai, T., Rosales Quintana, G. M., Durán Gómez, G. S., Hashihama, F., and Komatsu, K. (2021). Elevated Turbulent and Double-Diffusive Nutrient Flux in the Kuroshio Over the Izu Ridge and in the Kuroshio Extension. *J. Oceanogr.* 77, 55–74. doi: 10.1007/s10872-020-00582-2

Nikurashin, M., and Ferrari, R. (2010a). Radiation and Dissipation of Internal Waves Generated by Geostrophic Motions Impinging on Small-Scale Topography: Application to the Southern Ocean. *J. Phys. Oceanogr.* 40, 2025–2042. doi: 10.1175/2010JPO4315.1

Nikurashin, M., and Ferrari, R. (2010b). Radiation and Dissipation of Internal Waves Generated by Geostrophic Motions Impinging on Small-Scale Topography: Theory. *J. Phys. Ocean.* 40, 2025–2042. doi: 10.1175/2010JPO4315.1

Perfect, B., Kumar, N., and Riley, J. J. (2020a). Energetics of Seamount Wakes. Part II: Wave Fluxes. *J. Phys. Oceanogr.* 50, 1383–1398. doi: 10.1175/JPO-D-19-0104.1

Perfect, B., Kumar, N., and Riley, J. J. (2020b). Energetics of Seamount Wakes. Part I: Energy Exchange. *J. Phys. Oceanogr.* 50, 1365–1382. doi: 10.1175/JPO-D-19-0105.1

Pope, S. B. (2000). *Turbulent Flows* (Cambridge: Cambridge University Press). doi: 10.1017/CBO9780511840531

Shi, Z., Chen, J., and Chen, Q. (2016). On the Turbulence Models and Turbulent Schmidt Number in Simulating Stratified Flows. *J. Build. Perform. Simul.* 9, 134–148. doi: 10.1080/19401493.2015.1004109

Shi, J., Tong, C., Zhang, C., and Gao, X. (2019). Kelvin-Helmholtz Billows Induced by Shear Instability Along the North Passage of the Yangtze River Estuary, China. J. *Mar. Sci. Eng.* 7, 92. doi: 10.3390/jmse7040092

Smyth, W., and Moum, J. (2000). Length Scales of Turbulence in Stably Stratified Mixing Layers. *Phys. Fluids* 12, 1327–1342. doi: 10.1063/1.870385

Smyth, W., and Moum, J. (2012). Ocean Mixing by Kelvin-Helmholtz Instability. *Oceanography* 25, 140–149. doi: 10.5670/oceanog.2012.49

Smyth, W. D., Moum, J. N., and Caldwell, D. R. (2001). The Efficiency of Mixing in Turbulent Patches: Inferences From Direct Simulations and Microstructure Observations. *J. Phys. Oceanogr.* 31, 1969–1992. doi: 10.1175/1520-0485(2001)031<1969:TEOMIT>2.0.CO;2

Staquet, C. (1995). Two-Dimensional Secondary Instabilities in a Strongly Stratified Shear Layer. *J. Fluid Mech.* 296, 73–126. doi: 10.1017/S0022112095002072

Stiperski, I., Serafin, S., Paci, A., Ágústsson, H., Belleudy, A., Calmer, R., et al. (2017). Water Tank Experiments on Stratified Flow Over Double Mountain-Shaped Obstacles at High-Reynolds Number. *Atmosphere* 8, 1–19. doi: 10.3390/atmos8010013

Talke, S. A., Horner-Devine, A. R., and Chickadel, C. C. (2010). Mixing Layer Dynamics in Separated Flow Over an Estuarine Sill With Variable Stratification. *J. Geophys. Res. Oceans* 115, 1–17. doi: 10.1029/2009JC005467

Tanaka, T., Hasegawa, D., Yasuda, I., Tsuji, H., Fujio, S., Goto, Y., et al. (2019). Enhanced Vertical Turbulent Nitrate Flux in the Kuroshio Across the Izu Ridge. *J. Oceanogr.* 75, 195–203. doi: 10.1007/s10872-018-0500-2

Taniguchi, N., Huang, C.-F., Kaneko, A., Liu, C.-T., Howe, B. M., Wang, Y.-H., et al. (2013). Measuring the Kuroshio Current With Ocean Acoustic Tomography. *J. Acoust. Soc Am.* 134, 3272–3281. doi: 10.1121/1.4818842

Tsutsumi, E., Matsuno, T., Lien, R.-C., Nakamura, H., Senjyu, T., and Guo, X. (2017). Turbulent Mixing Within the Kuroshio in the Tokara Strait. *J. Geophys. Res. Oceans* 122, 7082–7094. doi: 10.1002/2017JC013049

Voisin, B. (1991). Internal Wave Generation in Uniformly Stratified Fluids. Part 1. Green's Function and Point Sources. *J. Fluid Mech.* 231, 439–480. doi: 10.1017/S0022112091003464

Weller, H. G., Tabor, G., Jasak, H., and Fureby, C. (1998). A Tensorial Approach to Computational Continuum Mechanics Using Object-Oriented Techniques. *Comput. Phys.* 12, 620–631. doi: 10.1063/1.168744

Wesson, J. C., and Gregg, M. C. (1994). Mixing at Camarinal Sill in the Strait of Gibraltar. *J. Geophys. Res. Oceans* 99, 9847–9878. doi: 10.1029/94JC00256

Winters, K. B., and Armi, L. (2012). Hydraulic Control of Continuously Stratified Flow Over an Obstacle. *J. Fluid Mech.* 700, 502–513. doi: 10.1017/jfm.2012.157

Winters, K. B., and Armi, L. (2013). The Response of a Continuously Stratified Fluid to an Oscillating Flow Past an Obstacle. *J. Fluid Mech.* 727, 83–118. doi: 10.1017/jfm.2013.247

Winters, K. B., and Armi, L. (2014). Topographic Control of Stratified Flows: Upstream Jets, Blocking and Isolating Layers. *J. Fluid Mech.* 753, 80–103. doi: 10.1017/jfm.2014.363

Winters, K. B., Lombard, P. N., Riley, J. J., and D'Asaro, E. A. (1995). Available Potential Energy and Mixing in Density-Stratified Fluids. *J. Fluid Mech.* 289, 115–128. doi: 10.1017/S002211209500125X

Zhou, Z., Yu, X., Hsu, T.-J., Shi, F., Rockwell Geyer, W., and Kirby, J. T. (2017). On Nonhydrostatic Coastal Model Simulations of Shear Instabilities in a Stratified Shear Flow at High Reynolds Number. *J. Geophys. Res. Oceans* 122, 3081–3105. doi: 10.1002/2016JC012334

Conflict of Interest: The authors declare that the research was conducted in the absence of any commercial or financial relationships that could be construed as a potential conflict of interest.

Publisher's Note: All claims expressed in this article are solely those of the authors and do not necessarily represent those of their affiliated organizations, or those of the publisher, the editors and the reviewers. Any product that may be evaluated in this article, or claim that may be made by its manufacturer, is not guaranteed or endorsed by the publisher.

Copyright © 2022 Chen, Yu, Chang, Jan, Yang and Lien. This is an open-access article distributed under the terms of the Creative Commons Attribution License (CC BY). The use, distribution or reproduction in other forums is permitted, provided the original author(s) and the copyright owner(s) are credited and that the original publication in this journal is cited, in accordance with accepted academic practice. No use, distribution or reproduction is permitted which does not comply with these terms.

frontiers | Frontiers in Marine Science

ORIGINAL RESEARCH
published: 30 May 2022
doi: 10.3389/fmars.2022.900299

Kuroshio Intrusion and Its Impact on Swordtip Squid (*Uroteuthis edulis*) Abundance in the Southern East China Sea

Yi-Chen Cheng[1], *Sen Jan*[1*] *and Chung-Chi Chen*[2]

[1] *Institute of Oceanography, National Taiwan University, Taipei, Taiwan,* [2] *Department of Life Science, National Taiwan Normal University, Taipei, Taiwan*

Swordtip squid (*Uroteuthis edulis*) is a primary target species of the commercial fishery in the southern East China Sea (ECS), and they normally migrate to a quasi-permanent upwelling zone (called a cold dome) off northeastern Taiwan for spawning and growth during spring (March–May) and fall (October–December) in a year. We examined the connection of the variability in its standardized annual catch per unit effort (CPUE) during 2009–2017 in regard to the physical processes on the southern shelf of the ECS using temperature and wind observations from an isle north of Taiwan (Peng-jia-yu) as well as satellite sea surface temperature and absolute geostrophic velocity. The annual CPUE is positively correlated with the daily temperature anomaly at Peng-jia-yu in the cold dome in October of the previous year and April of the year. A warmer environment favors the recruitment and consequently the catch of the swordtip squid. During the spawning periods of the 9 years, the warm water carried by the Kuroshio frequently intruded atop the cold dome, which benefited the growth of the larvae and consequently helped maintain a certain value of the standardized annual CPUE. The anomalously low CPUE in 2012 and 2016 is attributed to the blocking of the Kuroshio intrusion due to cold and less salty China Coastal Water atop the cold dome in the spring spawning of 2012 and 2016. Based on the velocity strength in the cold dome and in a specified shelf region together with the daily temperature anomaly at Peng-jia-yu, an occupation intensity factor is used to evaluate the dominance of warm Kuroshio water and cold shelf water in the cold dome, which could help predict annual catches.

Keywords: Kuroshio intrusion, cold dome, East China Sea Shelf, occupation intensity, swordtip squid resource, catch per unit effort (CPUE)

OPEN ACCESS

Edited by:
Kuoping Chiang, National Taiwan Ocean University, Taiwan

Reviewed by:
Meng-Hsien Chen, National Sun Yat-sen University, Taiwan
Zhixuan Feng, East China Normal University, China

***Correspondence:**
Sen Jan
senjan@ntu.edu.tw

Specialty section:
This article was submitted to Coastal Ocean Processes, a section of the journal Frontiers in Marine Science

Received: *20 March 2022*
Accepted: *28 April 2022*
Published: *30 May 2022*

Citation:
Cheng Y-C, Jan S and Chen C-C (2022) Kuroshio Intrusion and Its Impact on Swordtip Squid (Uroteuthis edulis) Abundance in the Southern East China Sea. Front. Mar. Sci. 9:900299. doi: 10.3389/fmars.2022.900299

INTRODUCTION

The swordtip squid (*Uroteuthis edulis*) has been a primary target species for commercial fisheries over the southern continental shelf of the East China Sea (ECS) since the 1950s (Chyn et al., 1998; Song et al., 2008; Wang et al., 2008; Wang et al., 2010; Liao et al., 2018). The swordtip squid supplies ~65% of the total cephalopod production in Taiwan (Liao et al., 2018), and the economic value of an annual

catch can reach tens of millions of US dollars (Wang et al., 2008; Fisheries Agency, 2016). Doubtlessly, a better understanding of the swordtip squid's spawning, maturation, and population, which have been investigated by Liao et al. (2006); Liao et al. (2018) and Wang et al. (2008); Wang et al. (2010); Wang et al. (2013), and their dependence on the environmental variables in the southern East China Sea is crucial to better managing swordtip squid resources regarding their commercial value.

The swordtip squid is a migratory species with a lifespan of approximately 9 months (Wang et al., 2008; Yamaguchi et al., 2015). This species primarily spawns and hatches in spring from March to May and also in fall from October to December each year and then migrates to the southern East China Sea shelf for feeding and growing (Wang et al., 2008; Wang et al., 2010; Wang et al., 2013). The fishing activity of swordtip squid occurs between the 100- and 200-m isobaths in the southern East China Sea (Liao et al., 2018). Wang et al. (2008) suggested that the swordtip squid spawning ground is in and around the coastal water off the northern coast of Taiwan. Liao et al. (2018) concluded that higher catch rates occurred in the front region and vicinity in areas with a sea surface temperature (SST) of ~20° C–26°C, chlorophyll-a of ~0.05–2.0 mg m^{-3}, and sea-level anomaly (SLA) of 0–2.0 m for an eddy-like sea-level feature. Chang K.-Y. et al. (2018) further found that a higher SST increases the growth rate of swordtip squid during the larval stage and hence helps shorten the prey period. The spawning, nursery, feeding, and fishing grounds of swordtip squid are shown in the inset in **Figure 1** (transparent purple shading area), which are from the northern coast of Taiwan, extending northeastward along 100–200-m isobaths to ~29°N in the central-eastern shelf of the ECS. The positive correlation between the swordtip squid abundance and catch and the oceanic variability was also addressed in the aforementioned papers. However, the underlying physical dynamics of swordtip squid catch-related, event-driven environmental variations have been less discussed in the open literature.

The hydrography on the shelf and shelf break of the southern ECS are subject to the intrusion of the Kuroshio (e.g., Chao, 1991; Hsueh et al., 1992; Chern and Wang, 1994; Chuang and Liang, 1994), the Taiwan Strait current coming from the southwest (e.g., Chern and Wang, 1992; Jan et al., 2002), the China coastal current in winter (e.g., Jan et al., 2002; Jan et al., 2006), the impingement of mesoscale eddies from the Philippine Sea (e.g., Yang et al., 1999; Johns et al., 2001; Zhang et al., 2001; Vélez-Belchí et al., 2013; Wu et al., 2014), barotropic and baroclinic tides (Hu et al., 2010; Lien et al., 2013), and quasi-permanent upwelling (named the "cold dome" after Chern and Wang, 1990). Atmospheric forcing, particularly the northeasterly monsoon in winter and typhoons in summer, also modifies the hydrography there (Chuang and Liang, 1994; Tsai et al., 2008; Morimoto et al., 2009). Importantly, in association with high biological production (Liu et al., 1992; Chen et al., 2021), the cold dome area and vicinity have been recognized as a primary swordtip squid spawning ground (Wang et al., 2010), and according to Chang K.-Y. et al. (2018), the surface temperature in and around the cold dome is a primary variable influencing species spawning and associated catches. We therefore focus on physical processes causing surface temperature variability on the southern shelf of the ECS, particularly in the cold dome region.

The formation of the cold dome has been attributed to quasi-permanent upwelling from upcanyon flows consisting of cold (<21°C) and saltier (>34.5) subsurface water of the Kuroshio

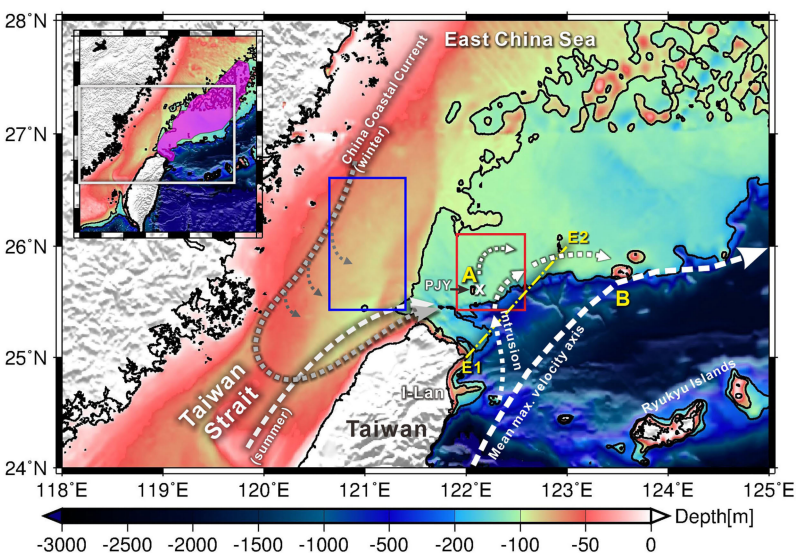

FIGURE 1 | Topography and schematic routes of major currents around northern Taiwan. "X" indicates the mean center position of relatively low-temperature surface water in the cold dome (Jan et al., 2011). The transparent purple shading region in the inset bounds the majority of vessel locations with swordtip squid catches. Red and blue rectangles are used to evaluate the velocity dominance of the Kuroshio intrusion and China Coastal Current, respectively, in the cold dome region. Points A and B are used to calculate the satellite SST difference between the Kuroshio's mean maximum velocity axis and the cold dome. The E1–E2 section (dotted yellow line) is used in the calculation of cross-shelf Ekman transport.

(Chern and Wang, 1990; Tang et al., 2000; Wu et al., 2008; Shen et al., 2011; Jan et al., 2011). It presents a cold patch with a cyclonic flow pattern in satellite SST and geostrophic velocity or is overlaid by warmer water from the Kuroshio intrusion (Tang et al., 2000; Jan et al., 2011; Chen et al., 2015). According to the summary in Jan et al. (2011), the mean center position of the cold surface water in the cold dome is 122.125°E, 25.625°N, with a length scale of ~100 km and a cyclonic flow pattern, particularly in summer. The Kuroshio intrusion could spread over the cold dome and thus reduce the surface appearance of the cold dome. A higher chlorophyll-*a* concentration sourced from the upwelled nutrient-rich subsurface water (e.g., Chen et al., 2017; Chen et al., 2021; Chen et al., 2022), and therefore higher primary productivity has been observed year-round in the cold dome region (Liu et al., 1992).

The Kuroshio intrusion is an important physical process affecting the hydrographic variability of the cold dome. Over the past three decades, the dynamics underlying the Kuroshio intrusion have been widely studied and attributed to winter monsoon-induced shoreward Ekman transport (Chao, 1991), surface water compensation-induced vortex stretching due to the subsidence of cold dense shelf water in winter (Chuang and Liang, 1994), the joint effect of baroclinicity and bottom relief (JEBAR) (Oey et al., 2010), the topographic beta (β, the planetary vorticity gradient) spiral induced by the upwelling created as the Kuroshio impinges onto the shelf break (Yang et al., 2018a; Yang et al., 2018b), and typhoons across northern Taiwan (Chern et al., 1990; Tang et al., 1999). In addition to these physical processes, an increasing amount of comprehensive *in situ* and satellite remote sensing data show that the impingement of westward-propagating eddies on the Kuroshio east of Taiwan and the associated dynamic adjustment contribute to the Kuroshio intrusion (Jan et al., 2015; Tsai et al., 2015; Yang et al., 2015; Andres et al., 2017; Jan et al., 2017; Chang, M.-H. et al., 2018; Mensah et al., 2020). On the other hand, the China Coastal Current could bring cold and brackish water to fill the cold dome in winter, and the warm but less saline Taiwan Strait current could occupy the cold dome in summer (Jan et al., 2011).

The primary objective of this study is thus to examine the dynamic processes causing the upper layer temperature anomaly and, in turn, the spawning and associated catch of swordtip squid in and around the cold dome. The standardized annual catch per unit effort (CPUE in kg day^{-1} per vessel) of swordtip squid over 2009–2017 obtained from Chang K.-Y. et al. (2018) is used to explore its relationship with the environmental variables. The dynamics related to the variability in these parameters are subsequently examined using field and satellite observations.

DATA AND METHODS

The CPUE is often positively related to the availability of fisheries and regarded as an indicator of fish abundance (Yu et al., 2018; Liu et al., 2019). Therefore, the catch and CPUE data were used to represent the abundance of swordtip squid in the southern ECS in study. The region covering most vessel locations of the catch is depicted in the inset in **Figure 1** (transparent purple shading area). The annual CPUE was calculated from the annual total catches and the total fishing days of the total fishing boats documented in the logbooks for the years from 2009 to 2017 (Wang et al., 2008; Chang K.-Y. et al., 2018) as

$$CPUE = Catch/Effort$$

The CPUE was further standardized by excluding the bonito fishing effort (Chang et al., 2015a), and hereafter, the standardized CPUE time series was used to find the correlation with the environmental parameters.

To understand the (temporal) serial correlation of swordtip squid resources, autocorrelation analysis was applied using the 9 years' standardized CPUE. Furthermore, to evaluate how the squid abundance (using the standardized annual CPUE as index) associates with the environmental variables, the Pearson correlation coefficient $\rho(X, Y)$ was used to quantify the correlations of the standardized annual CPUE and the monthly mean satellite chlorophyll-*a* concentrations in the cold dome or temperature at Peng-jia-yu, similar to that in Waluda et al. (1999) and Chang et al. (2015b). $\rho(X, Y)$ is calculated by

$$\rho(X, Y) = \frac{\mathrm{cov}(X, Y)}{\sigma_X \sigma_Y} = \frac{E[(X - \mu_X)(Y - \mu_Y)]}{\sigma_X \sigma_Y}$$

where cov(X, Y) is the covariance between variables X and Y; E is the expected value; μ is the mean value; and σ_X and σ_Y are the standard deviation of X and Y, respectively. The monthly mean chlorophyll-*a* concentration and temperature of July through December in the previous year (i.e., from 2008 to 2016) and of January through June in the year (i.e., from 2009 to 2017) was used to calculate the correlation coefficient with the standardized annual CPUE over the 9 years.

Sea level and seawater temperature observed at the Peng-jia-yu isle in the southern ECS (122.0792°E, 23.6283°N; **Figure 1**) since April 2008 were used to supplement the analysis of the relationship between the standardized annual CPUE and the physical processes over the southern shelf of the ECS. The sea level and temperature were measured every 10 min by a Sea-Bird SBE-39. The wind speed and direction were measured by the Central Weather Bureau of Taiwan at the Peng-jia-yu weather station and were obtained from https://e-service.cwb.gov.tw/HistoryDataQuery/index.jsp. The 10-min sea level and temperature data were time averaged every 60 min and resampled to hourly data. A low-pass filter with a cutoff frequency of 0.05 cycles per day (equivalent to a period of 20 days) was applied to the hourly resampled data to exclude tidally induced variability. The daily mean temperature at the Peng-jia-yu isle was also obtained by averaging the raw temperature data over 2008–2021 and was also 20-day low-pass filtered for the estimate of daily temperature anomaly.

The corresponding daily satellite remote-sensing products, including SST, sea surface height (SSH), sea-level anomaly (SLA), and chlorophyll-*a* concentrations, were collected from the Copernicus Marine Environment Monitoring Service (CMEMS, available at https://marine.copernicus.eu/) in the range of 118°E–128°E and 18°N–28°N. The horizontal

resolution is 0.05° (~6 km) in longitude and latitude for SST, 0.25° (~27.5 km) for SLA, and ~4 km for SSC. The daily SST anomaly (SSTa) is relative to the mean daily temperature calculated from SST during 2008–2018. The SLA was compared to the mean sea level calculated from SSH during 1993–2012. The absolute geostrophic velocity was further calculated from the satellite SSH and associated mean dynamic topography.

The Kuroshio intrusion in the southern ECS is identified by considering satellite SST, absolute geostrophic velocity, and the daily mean temperature anomaly at the Peng-jia-yu isle. Vélez-Belchí et al. (2013) defined an index using the difference in SST in the mean position of the non-intruding Kuroshio northeast of Taiwan and a point at 122.5°E and 26.75°N to evaluate the Kuroshio intrusion. The smaller the value is, the more likely the Kuroshio intrusion occurs because the intruding warm water on the ECS shelf decreases the temperature contrast between these two locations. A similar SST difference index was adopted, but the locations for the calculation of SST difference were shifted to points A (122.077°E, 25.629°N) in the cold dome and B (123.525° E, 25.525°N) in the mean maximum velocity axis of the Kuroshio (points A and B in **Figure 1**). The change in the shelf point directly evaluates whether the Kuroshio intrudes into the cold dome region. Wu et al. (2014) set a criterion to evaluate the Kuroshio intrusion by checking if the 0.2 m s^{-1} isotach of the satellite geostrophic velocity crosses the 200-m isobath on the southern shelf of the ECS. We adopt this idea but modify the criterion to indicate that the area average velocity, calculated by$(u^2 + v^2)^{1/2}$ as $v > 0$ in the red box in **Figure 1**, is larger than 0.2 m s^{-1} to indicate the Kuroshio intrusion. The two criteria are further supplemented with the maximum increase in the low-pass-filtered daily temperature anomaly at the Peng-jia-yu isle during the intrusion period (i.e., $\Delta T_{max} > 0.5$°C as the Kuroshio intrusion) to reduce the uncertainty in evaluating the Kuroshio intrusion.

To further analyze the potential dynamics for the Kuroshio intrusion, we integrated associated weather conditions from the Central Weather Bureau of Taiwan, satellite SSH, and geostrophic current and calculated wind-induced Ekman transport. The Ekman transport (Q_{Ek}) across the shelf break (yellow dotted line E1–E2 in **Figure 1**) is calculated by

$$Q_{Ek} = \int_{E1}^{E2} \rho_0^{-1} f^{-1} \tau dl \quad (1)$$

where ρ_o (1025 kg m^{-3}) is a reference density, f is the Coriolis parameter at 25.5°N (6.26×10^{-5} s^{-1}), and τ is the wind stress in the northeast and southwest directions. The wind data collected at the Peng-jia-yu weather station are used to calculate and represent τ along the E1–E2 line (**Figure 1**).

RESULTS

Variability of Temperature and Sea Level at Peng-jia-yu Over 2008–2021

Figure 2 shows the hourly temperature and sea level observed at the Peng-jia-yu isle from April 2008 to October 2021. The 20-day low-pass-filtered and linear regression of the temperature and sea-level observations are also shown in **Figure 2**. Note that the linear regressions of temperature and sea level suggest that the temperature increased by 0.71°C and sea level increased by 2 cm during the observation period. For a comparison between this temperature increasing rate and that of global temperature, the annual global mean SST anomalies during 2008 and 2018 were obtained from the National Centers for Environmental Information (https://www.ncdc.noaa.gov/cag/global/time-series). A similar linear regression was applied to the annual SST anomalies, and we obtained a 0.32°C increase over the 10-

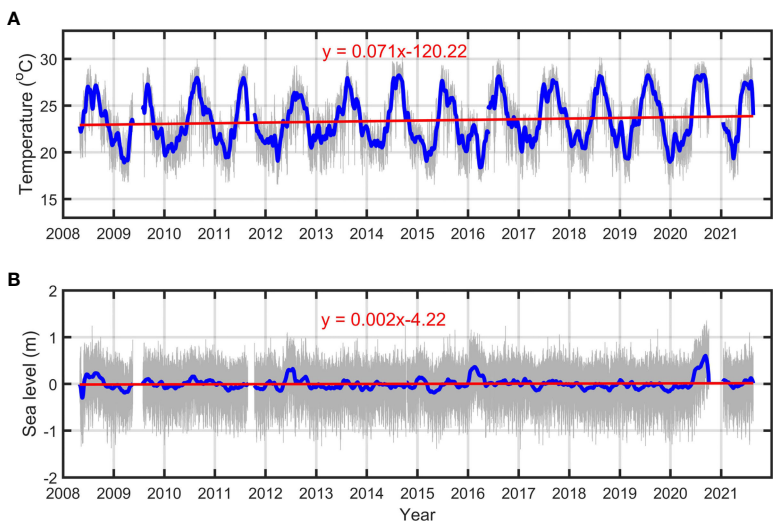

FIGURE 2 | **(A)** Temperature and **(B)** sea level measured at the Peng-jia-yu isle during 2008–2021. Gray, blue, and red lines represent hourly average and resampled data, 20-day low-pass-filtered data, and the linear regression of the data, respectively.

year dataset. A further discussion on the long-term changes in temperature and sea level at the Peng-jia-yu isle is not given here because this is not the central focus of this study. Additionally, the CPUE data used in this study are too short (9 years) to correlate with climate timescale temperature variability. Notably, there are intermittently missing data in the observations but the total time is less than 5% of the approximately 14 years of temperature and sea-level time series. These gaps in the time series have no significant influence on the results of low-pass filter and linear regression analyses.

The 20-day low-pass-filtered daily mean temperature illustrated in **Figure 3** is a base for calculating the daily mean temperature anomaly. The spawning periods of the swordtip squid in a year are marked in **Figure 3** for reference. The two periods correspond to the two low-temperature periods in the year.

Correlations of Standardized Annual CPUE and Environmental Variables

The standardized annual CPUE in **Figure 4** shows interannual variation with one peak in 2013 and two relative lows in 2012 and 2016. The highest CPUE (2013; ca. 260 kg day^{-1} per vessel) reached ~2 times the lowest CPUE (2016; ca. 125 kg day^{-1} per vessel) over the 9 years. The autocorrelation analysis of the standardized annual CPUE (**Supplementary Figure 1**), however, suggests that there was no significant correlation between the resources in the previous year and its coming years, which is consistent with that concluded by Chang K.-Y. et al. (2018). An insignificant correlation between the standardized annual CPUE is plausible because the swordtip squid is an annual species (Wang et al., 2008; Yamaguchi et al., 2015); therefore, it is known that its population abundance is primarily influenced by the variability of environmental variables on an approximately seasonal timescale. Physical processes possibly leading to this interannual variation are examined with available data collected at fixed stations and from satellite remote sensing later.

Results from further correlation analysis show that the variation in the standardized annual CPUE is positively correlated with the monthly mean temperature at Peng-jia-yu isle in the two main spawning seasons, i.e., October in the previous year (**Figure 5A**) and April in the year (**Figure 5B**). Generally, a higher temperature favors an increase in the growth rate of swordtip squid larvae during the spawning and incubation periods but could decrease their size and life during the adult stage. For the correlation between satellite chlorophyll-*a* concentrations in the cold dome and the standardized annual CPUE, the correlation coefficients were, however, mostly negative and not significant (data not shown), as discussed and concluded in Chang K.-Y. et al. (2018). Even so, notably, a satellite chlorophyll-*a* concentration peak was appeared in April in the cold dome with its value reaching over 0.55 mg Chl-*a* m^{-3} using mean daily values over 2008–2018 (**Supplementary Figure 2**).

Kuroshio Intrusions During Spawning Periods

Using the temperature and velocity criteria described in *Data and Methods* and considering only the 20 spawning periods from 2008 to 2017, 10 Kuroshio intrusion events were identified. The duration and ΔT_{max} of each intrusion event are summarized in

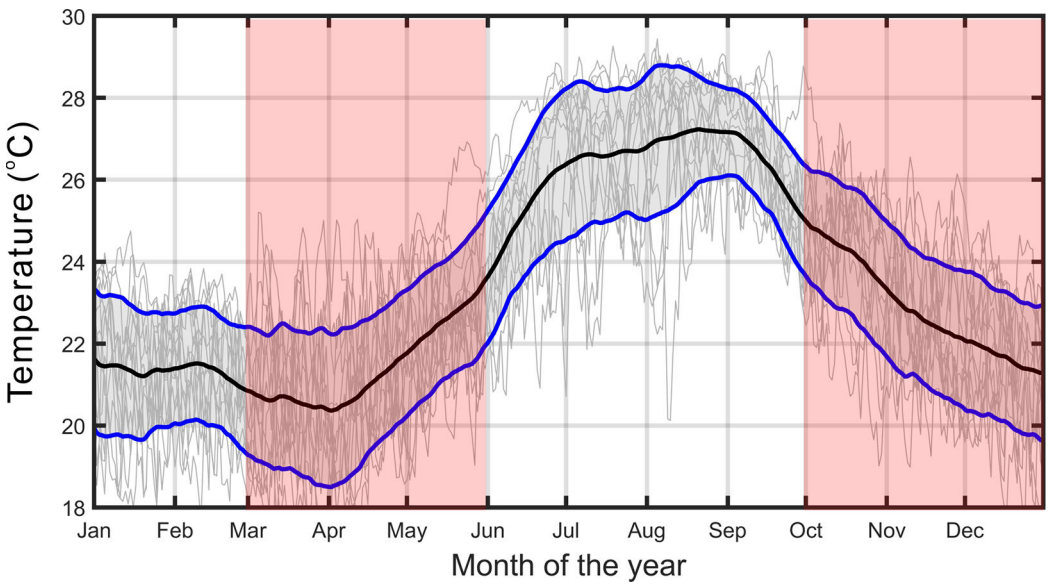

FIGURE 3 | The 20-day low-pass-filtered daily mean temperature (black line) calculated from the temperature observed at the Peng-jia-yu isle from 2008 to 2021. The ± one standard deviation from the mean value is bounded by the two blue lines. The gray lines are the raw temperature records of each year. Transparent pink shading indicates the spawning periods of the swordtip squid in the year.

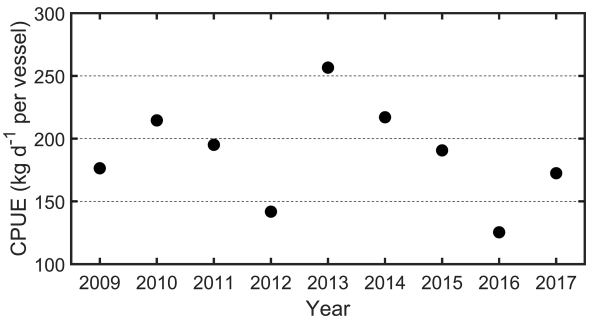

FIGURE 4 | Annual CPUE of swordtip squid (*Uroteuthis edulis*) from 2009 to 2017.

Table 1. The intrusion of the upper-layer Kuroshio frequently occurs off the northeastern coast of Taiwan, which is indeed a normal flow pattern that occurs when a stratified geostrophic current encounters a topographic rise. Considering the temporal evolution of impinging eddies east of Taiwan, satellite geostrophic currents in and around the cold dome, shoreward Ekman transport calculated by Eq. (1), and sea surface cooling due to winter atmospheric cold surges in association with spawning periods, the potential dynamics of the intrusions are attributed to three categories: 1) the joint influence of impinging eddies and shoreward Ekman transport for events 1, 4, and 8; 2) shoreward Ekman transport for events 2, 5, 6, 9, and 10; and 3) strong cold surge-induced shelf water cooling for events 3 and 7 (**Table 1**). The shortest period of intrusion was 42 days, and the longest was 84 days over 2008–2017. The typical flow field and temperature anomaly in the cold dome of the three dynamic regimes are discussed later.

DISCUSSION

Kuroshio Intrusion as a Normal Flow Pattern off Northeastern Taiwan

The warm surface water carried by the Kuroshio intrusion to the southern ECS benefits the spawning and incubation of the swordtip squid. The surface flow of the Kuroshio should intrude onto the southern shelf of the ECS if there is no blocking of excess flows from the ECS in winter or from the Taiwan Strait to the cold dome. The intrusion could be enhanced by onshore Ekman transport induced by northeasterly winds during the winter monsoon season (Chao, 1991), subsidence of surface water due to the atmospheric cooling of the winter cold surge (Chuang and Liang, 1994), winter cooling-caused JEBAR on the shelf break northeast of Taiwan (Oey et al., 2010), the topographic β spiral (Yang et al., 2018a), and the impingement of cyclonic eddies on the Kuroshio (Vélez-Belchí et al., 2013). Indeed, the Kuroshio intrusion should be a normal situation as this ~800-m-thick baroclinic geostrophic flow encounters the topographic rise northeast of Taiwan (**Figure 1**).

To verify this concept, the non-dimensional Burger number (Bu) is used to analyze the response when the Kuroshio encounters abrupt topography. Bu is defined as (Cushman-Roisin, 1994)

$$Bu = \frac{(NH)^2}{(fL)^2}$$

where $N = \left(-\frac{g}{\rho_0}\frac{\partial \rho}{\partial z}\right)^{1/2}$ is the buoyancy frequency in the stratified current (g = 9.8 m s^{-2} is the gravitational acceleration, ρ is density, and ρ_0 = 1025 kg m^{-3} is a reference density), H is the vertical scale of the topographic rise, f is the Coriolis parameter, and L is a geometrical horizontal length scale of the topography. As Bu ~1, the density stratification is as

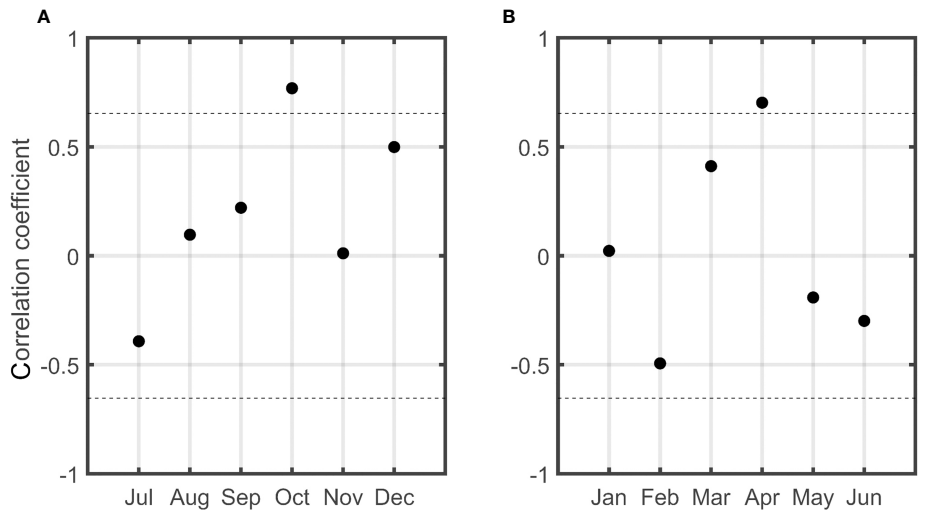

FIGURE 5 | Correlation coefficients of the standardized annual CPUE of swordtip squid over 2009–2017 and monthly mean seawater temperature at Peng-jia-yu isle for **(A)** July–December in the previous year over 2008–2016 and **(B)** January–June in the year over 2009–2017. The dashed lines mark the 95% confidence level.

TABLE 1 | Duration, period in days, maximum increase of low-pass-filtered temperature anomaly at the Peng-jia-yu isle (ΔT_{max}), and possible dynamics of Kuroshio intrusions during swordtip squid spawning periods over 2009–2017.

Intrusion event	Duration	Period (d)	ΔT_{max} (°C)	Potential dynamics
1	2008/09/28–2008/11/22	56	2.06	Eddy and shoreward Ekman transport
2	2009/11/18–2009/12/29	42	1.26	Shoreward Ekman transport
3	2010/03/19–2010/05/20	63	1.38	Strong cold surge-induced shelf water cooling
4	2010/10/28–2010/12/29	63	1.11	Eddy and shoreward Ekman transport
5	2011/04/05–2011/05/30	56	1.66	Shoreward Ekman transport
6	2012/10/01–2011/11/11	42	0.62	Shoreward Ekman transport
7	2013/03/11–2013/05/12	63	1.78	Strong cold surge-induced shelf water cooling
8	2013/10/01–2013/12/23	84	1.99	Eddy and shoreward Ekman transport
9	2014/03/04–2014/04/28	56	0.94	Shoreward Ekman transport
10	2016/11/03–2016/12/28	56	2.42	Shoreward Ekman transport

important as the Earth's rotation on the momentum balance of a stratified current (Cushman-Roisin, 1994), influencing the velocity field in the vertical direction. The vertical rigidity resulted from the rotating effect as the Rossby number $Ro << 1$ is weakened, and the flow directions of a stratified current tend to be decoupled in the vertical direction (Cushman-Roisin, 1994). The lighter surface current can flow directly over the topography, whereas the heavier current in the lower layer would be blocked by the topography and diverted following the isobath of the topography (Merkine, 1975; Merkine and Eugenia, 1976), similar to the situation in which a northward current encounters a zonal topographic rise in the central eastern Taiwan Strait (Jan et al., 1994). To estimate *Bu* in front of the steep shelf break off northeastern Taiwan, we set H ~200 m and $f = 6.03 \times 10^{-5}$ s^{-1} at 24.5°N. The baroclinic radius of deformation, calculated by $(g' H)^{1/2}/f$ (g' is reduced gravity calculated by $g\Delta\rho/\rho_o$), is adopted as the horizontal length scale L. The historical CTD data obtained from the Ocean Data Bank of Taiwan are used to calculate the mean density (σ_t) profiles across the Kuroshio at 24.5°N during the two spawning periods. According to the mean density profile at the section before the Kuroshio encounters the southern part of the ECS shelf (**Figure 6**), the density difference is ~2 kg m^{-3} over the upper 200 m in March–May (**Figure 6A**) and is even larger than this value in October–December (**Figure 6B**). The Rossby radius and buoyancy frequency N are ~36 km and ~0.98 $\times 10^{-2}$ s^{-1}, respectively. *Bu* is therefore ~1.16, suggesting that the surface intrusion of the Kuroshio is a normal situation off northeastern Taiwan. The strengthening of the northeastward outflow from the Taiwan Strait in summer and the southward-flowing China Coastal Water in winter and spring could impede the surface intrusion of the Kuroshio.

Kuroshio Intrusion Patterns

The three categories of dynamics underlying the Kuroshio intrusion (**Table 1**) are examined using satellite SSTa data, geostrophic currents, wind-induced Ekman transport, and daily mean temperature anomalies at the Peng-jia-yu isle. Taking event 4 in **Table 1** as an example, **Figure 7** illustrates typical flow patterns before and during the Kuroshio intrusion enhanced by both an impinging cyclonic eddy and winter northeasterly monsoon-induced shoreward Ekman transport across the E1–E2 section in **Figure 1**. Prior to this intrusion, the shoreward Ekman transport increased to ~2.5 $\times 10^6$ m^3 s^{-1} from early October 2010 (blue line in **Figure 7C**), and the daily mean temperature anomaly increased from mid-October 2010 (red line in **Figure 7C**). Meanwhile, a cyclonic eddy centered at ~124.5°E and 22.75°N was impinging on the offshore flank of the Kuroshio east of Taiwan (**Figure 7A**). The water mass carried by the westward-propagating cyclonic eddy gradually merged into the Kuroshio, and the satellite SSTa increased as time proceeded (**Figure 7B**). The intrusion flow, as indicated by current speeds larger than 0.2 m s^{-1}, reached 121.5°E to the west and 27°N to the north (black arrows in **Figure 7B**) and formed an anticyclonic loop over the southern shelf of the ECS. The daily mean temperature anomaly reached 2°C during the intrusion (red line in **Figure 7C**). The geostrophic velocity field in the southern ECS returned to the original pattern (not shown), and the temperature anomaly decreased (**Figure 7C**) after the intrusion event.

The typical geostrophic flow patterns, satellite SSTa, and daily mean temperature anomaly before and during the shoreward Ekman transport enhanced Kuroshio intrusion (event 2 in **Table 1**) are shown in **Figure 8**. The shoreward Ekman transport and associated daily mean temperature anomaly at the Peng-jia-yu isle increased from approximately early November 2009 (**Figure 8C**), and the satellite SSTa also increased during the intrusion (**Figure 8B**). The influence of an anticyclonic eddy centered at ~125°E and 23.25°N on the Kuroshio was likely inhibited by the Ryukyu Islands (**Figure 1**) during this event, and its influence on the flow pattern around the cold dome during the intrusion was not as clear as that in event 4 (**Figures 8A, B**).

The typical flow patterns and associated temperature anomaly shown in **Figure 9** represent the Kuroshio intrusion enhanced by unusually strong atmospheric cold surge-induced shelf water cooling during March–April 2013 (Event 7 in **Table 1**). There was no clear mesoscale eddy feature east of Taiwan (**Figures 9A, B**), and the wind-induced Ekman transport was relatively small across the E1–E2 transect (**Figure 9C**). The most likely cause for this event was cold surge-induced sea surface cooling, which created a zonal sea surface temperature gradient in the southern ECS before the intrusion (**Figure 9A**). Conceivably, the sinking of the cold dense surface water on the shelf could cause the warm surface water on the offshore side to extend westward, as shown by the satellite SSTa in **Figure 9B**. The associated dynamics were discussed in, e.g., Chuang and Liang (1994). The Kuroshio intrusion of this event caused a

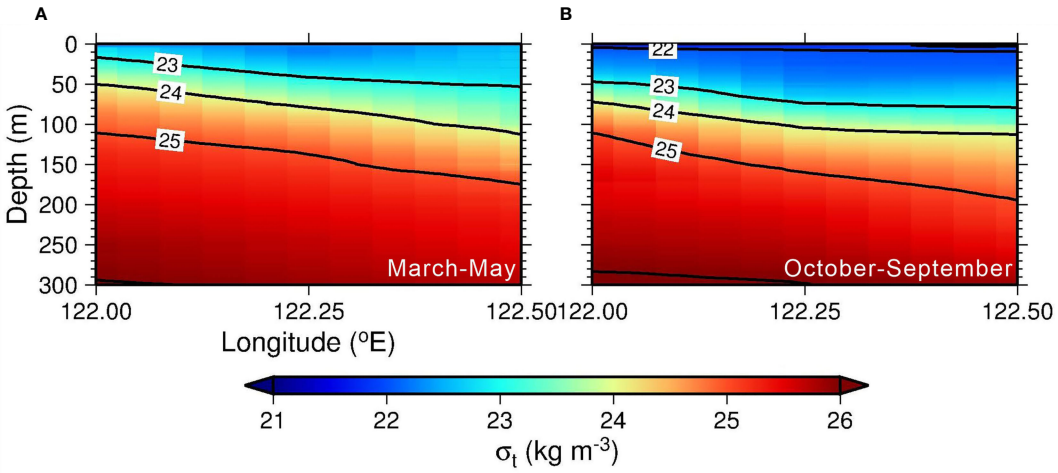

FIGURE 6 | Seasonal mean density (σ_t in kg m^{-3}) at a zonal section across the Kuroshio (24.5°N), which is immediately south of the ECS shelf. **(A)** March–May and **(B)** October–December.

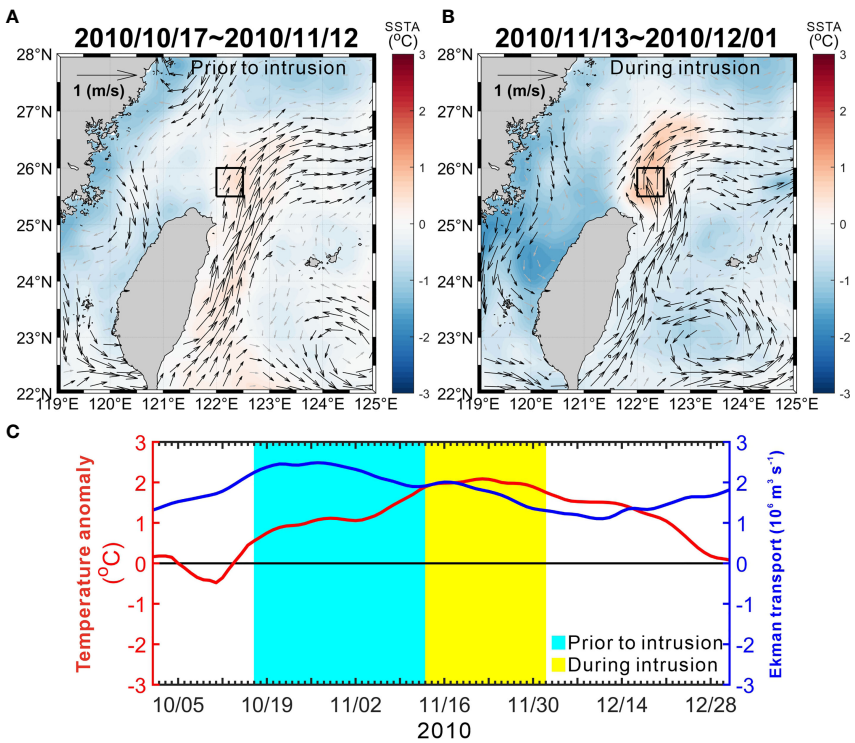

FIGURE 7 | The intrusion event dynamically contributed from the impinging eddy east of Taiwan and the northeasterly monsoon-induced northwestward (shoreward) Ekman transport. Satellite SSTa and SSH-derived geostrophic current **(A)** prior to the intrusion and **(B)** during the intrusion. Black arrows represent current speed ≥0.2 m s^{-1}, and gray arrows represent speed <0.2 m s^{-1}. **(C)** Twenty-day low-pass-filtered daily temperature anomaly at the Peng-jia-yu isle (red line) and the shoreward Ekman transport (blue line) across the E1–E2 transect as shown in **Figure 1**. The black box indicates a representative location for the cold dome.

1.78°C increase (from 0.83°C to 2.60°C) in the daily mean temperature anomaly at the Peng-jia-yu isle (**Table 1**, **Figure 9C**).

To summarize the aforementioned flow patterns of the Kuroshio northeast of Taiwan, the mean primary stream of the Kuroshio over 2008–2018, blocking (or cold shelf water intrusion), and intrusion into the cold dome (or warm intrusion) of the Kuroshio are as schematically shown in **Figures 10A–C**, respectively. The relative locations of the

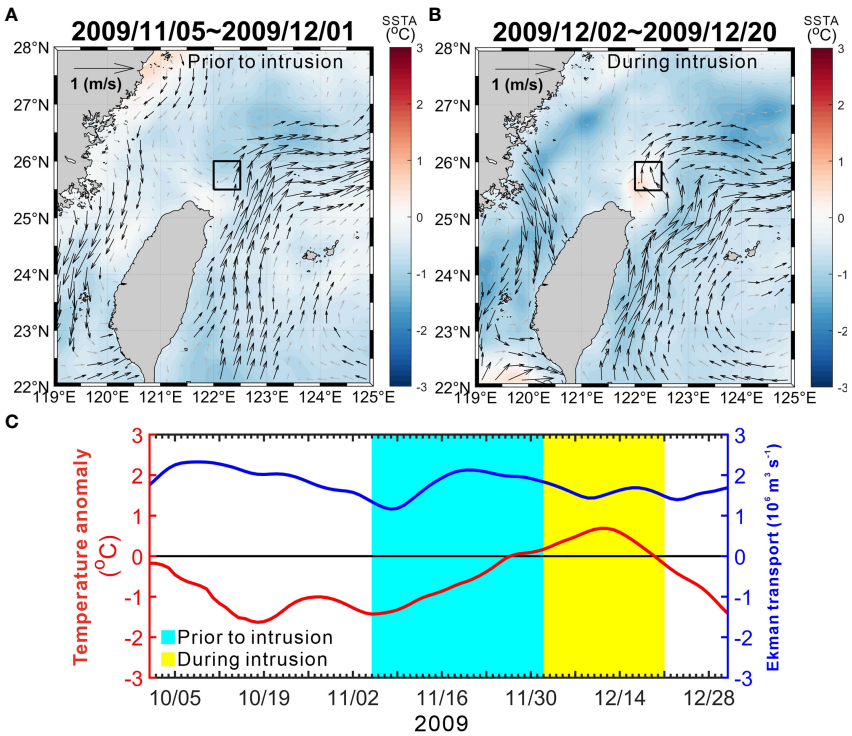

FIGURE 8 | The intrusion event dynamically contributed from the shoreward Ekman transport. Satellite SSTa and SSH-derived geostrophic current **(A)** prior to the intrusion and **(B)** during the intrusion. Black arrows represent current speed =0.2 m s-1, and gray arrows represent speed.

typical cold dome area, the maximum velocity axis, and the onshore flank of the Kuroshio are clearly seen from **Figure 10**. It should be noted that the topographic β spiral (Yang et al., 2018a; Yang et al., 2018b) plays a certain role in all of the Kuroshio intrusion. As the Kuroshio bumps onto the shelf break, the upslope flow creates upwelling and leads to the vortex compression over the continental shelf. This dynamic mechanism could drive the intruding Kuroshio to turn shoreward, making an anticyclonic loop on the southern shelf of the ECS.

Occupation Intensity Index for the Kuroshio and Shelf Water Intrusion

Considering the Kuroshio intrusion and with the primary purpose of this study in mind, we further find a dynamically related index rather than only velocity or temperature indicators for predicting the catch of swordtip squid around the shelf break of the southern ECS. The standardized annual CPUE was verified to be positively correlated with the SST anomaly in the cold dome during the spawning periods (Chang, K.-Y. et al., 2018; this study), and the SSTa in the cold dome is closely related to the vicinity shelf and shelf break processes. We therefore take the difference in area average velocity in the red and blue boxes in **Figure 1** as an indicator of occupation intensity for Kuroshio or shelf water. The daily mean temperature anomaly at the Peng-jia-yu isle is taken as an indicator of the strength of the temperature variability. The spawning and subsequent catch, particularly for abnormally low catches, could be expected by the two indicators. The dominance of the Kuroshio intrusion in and around the cold dome is determined by the area average geostrophic velocity, calculated $(u^2 + v^2)^{1/2}$ as $v > 0$ in the red box (121.875–122.625°E and 25.375–26.125°N) in **Figure 1**. Similarly, the dominance of the China Coastal Current and associated cold coastal water is determined by the area average geostrophic velocity as $u > 0$ in the blue box (120.625–121.375°E and 25.375–26.625°N) in **Figure 1**. The two boxes were selected by considering the swordtip squid spawning area reported in Chang et al. (2018) and the hydrographic characteristic of the southern ECS described in Chern and Wang (1989). The area average velocity was subsequently 20-day low-pass-filtered. **Figure 11A** shows the tendency of the Kuroshio (red line) and shelf water (blue line) intrusions during 2008–2017. The intensity of the shelf water intrusion (blue line in **Figure 11A**) is normally stronger than that of the Kuroshio intrusion (red line in **Figure 1**) in summer, which is mostly attributed to the occupation of strengthened northeastward throughflow in the Taiwan Strait in the cold dome area. Except for this seasonality, the dominance of the two parameters is mixed during the spawning periods indicated by the transparent pink shading in **Figure 11A**, which could be one of the causes of interannual variability in the standardized annual CPUE of swordtip squid.

We focus on the variability in the prevailing water mass in the cold dome during the spawning periods. The difference in the area average velocity in the red and blue boxes in **Figure 10A** normalized by the maximum absolute difference is defined as the occupation

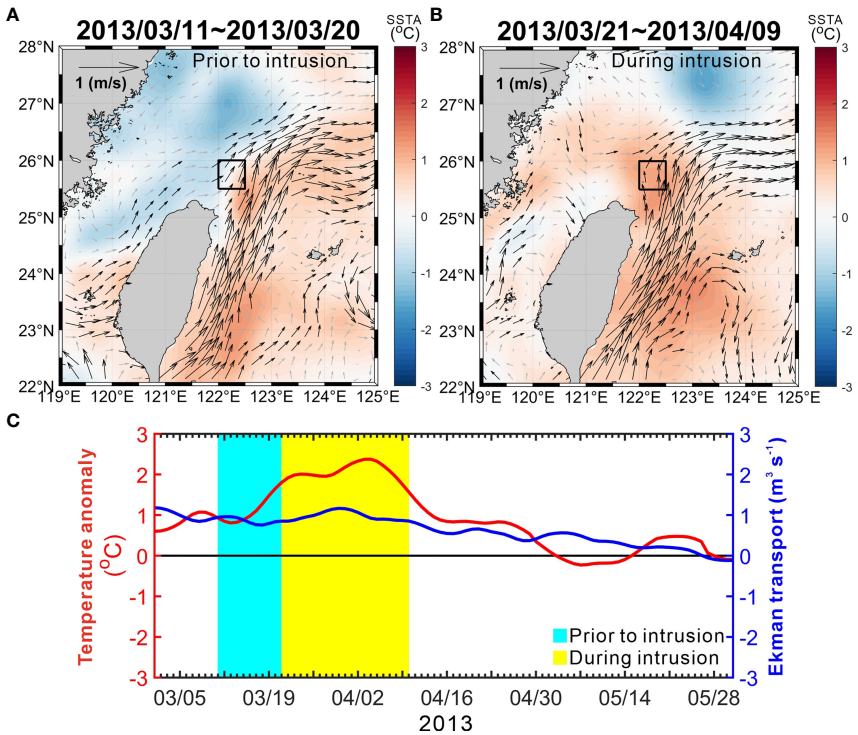

FIGURE 9 | The intrusion event dynamically contributed from strong winter cold surge-induced shelf water cooling. Satellite SSTa and SSH-derived geostrophic current **(A)** prior to the intrusion and **(B)** during the intrusion. Black arrows represent current speed =0.2 m s-1, and gray arrows represent speed.

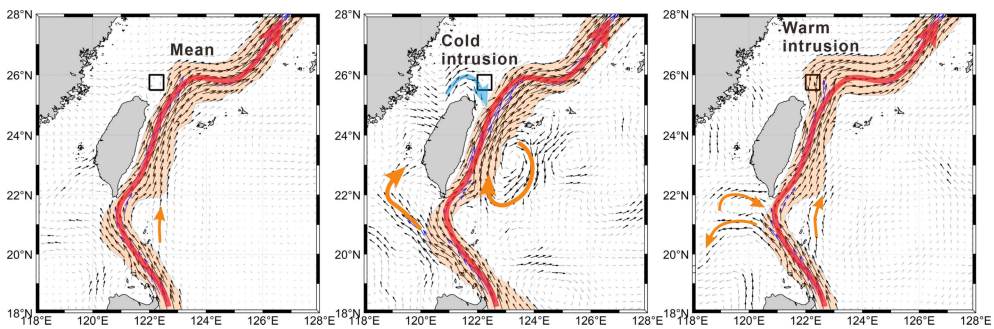

FIGURE 10 | A schematic showing **(A)** the mean primary stream over 2008–2018, **(B)** an example of blocking path, and **(C)** an example of intrusion path of the Kuroshio off the northeast coast of Taiwan. The black box represents the mean location of the cold dome as that in **Figure 7**. The red curve indicates the mean maximum velocity position of the Kuroshio. The absolute geostrophic velocity in the transparent orange shading region is ≥0.2 m s^{-1}.

intensity of the Kuroshio and shelf water in the cold dome. The results are illustrated in **Figure 11B**. A positive normalized occupation intensity in **Figure 11B** indicates that the hydrography is dominated by warm Kuroshio surface water (red filled areas) rather than cold shelf water (blue filled areas) and vice versa for a negative value in and around the cold dome region. The highest standardized CPUE in 2013 seemingly corresponds to the dominance of the Kuroshio intrusion and a higher daily mean temperature anomaly during spring spawning in 2013. The two low standardized CPUEs in 2012 and 2016 correspond to unusual dominances of cold shelf water in the cold dome during the spring spawning of the 2 years (blue filled areas in **Figure 11B**).

CONCLUDING REMARKS

This study examined possible connections of the standardized annual CPUE of swordtip squid (*Uroteuthis edulis*) over 2009–2017 and the physical processes on the southern shelf of the ECS.

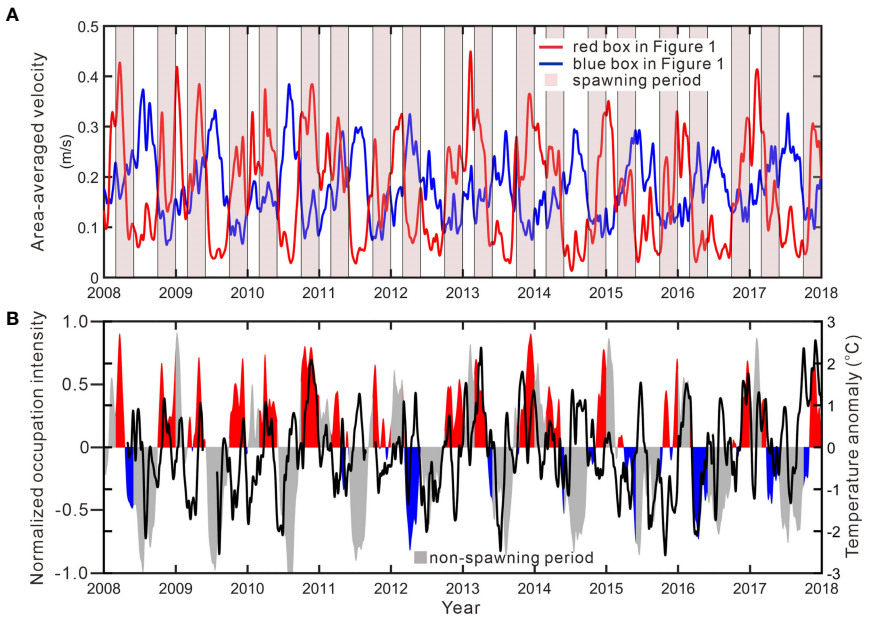

FIGURE 11 | **(A)** Twenty-day low-pass-filtered area average geostrophic velocity as $v > 0$ (red line) and $u > 0$ (blue line) in red and blue boxes, respectively, in **Figure 1**. Transparent pink shading represent spawning periods of the swordtip squid during 2008–2018. **(B)** Normalized occupation intensity of warm Kuroshio surface water (filled by red during spawning periods) and ECS shelf or Taiwan Strait water (filled by blue during spawning periods). The normalized occupation intensity is defined as the difference between the red and blue lines in **(A)** divided by the maximum absolute value of the difference. The difference during non-spawning periods is shown in gray.

Previous studies suggested that swordtip squid typically migrate to the cold dome off northern Taiwan for spawning during March–May and October–December each year, and higher seawater temperatures during the spawning and incubation periods are helpful for the growth rate and hence the recruitment and catch of swordtip squid. The standardized annual CPUE was positively correlated with the monthly mean temperature at the Peng-jia-yu isle in October in the previous year and April in the year over the 9 years. Through the analysis of satellite SSTa data, geostrophic velocity, and daily mean temperature anomalies at the Peng-jia-yu isle, we identified that the Kuroshio intrusion to the cold dome region caused 50% of the warm temperature anomaly during the spawning periods. Since the Kuroshio intrusion to the southern shelf of the ECS is a normal situation, as this stratified geostrophic current with *Bu* at O(1) encounters the steep shelf break northeast of Taiwan, the annual CPUE should also be maintained above a certain value. A higher daily mean temperature anomaly resulted in a higher standardized CPUE in 2013 over the 9 years. Conversely, the blocking of the Kuroshio intrusion due to the cold coastal water in winter is regarded as an abnormal situation in this study. The dominance of the cold and less salty China Coastal Water atop the cold dome in the spring spawning season impeded the warm Kuroshio surface water intrusion to the cold dome and conceivably caused the two anomalously low standardized CPUEs in 2012 and 2016.

Importantly, we introduced a normalized occupation intensity for evaluating the dominance of warm Kuroshio surface water and cold ECS shelf water as a proxy to predict standardized annual CPUE of the swordtip squid. The difference in area average geostrophic velocity in a representative area of the cold dome and a shelf region near the coast of China together with the daily mean temperature anomaly at Peng-jia-yu isle is used to indicate the dynamics dominating the temperature variability in the cold dome during the spawning periods. When the hydrography is dominated by the colder shelf water more than the Kuroshio water during the spawning period, we could expect a lower standardized annual CPUE for the year. The results of this study are hopefully useful for managing swordtip squid catches on the southern shelf of the ECS.

DATA AVAILABILITY STATEMENT

The temperature and sea level records at the Peng-jia-yu isle and the standardized annual CPUE of the swordtip squid used in this study are available at Mendeley Data http://dx.doi.org/10.17632/x5hf63kww4.1 and Mendeley Data http://dx.doi.org/10.17632/2z8t6c9brd.1, respectively. The daily meteorological data at the Peng-jia-ju weather station can be downloaded from Taiwan's Central Weather Bureau at https://e-service.cwb.gov.tw/HistoryDataQuery/index.jsp. The satellite SST, SSH, SLA, SSC, and geostrophic velocity data can be downloaded from the Copernicus Marine Environment Monitoring Service at http://marine.copernicus.eu/.

AUTHOR CONTRIBUTIONS

SJ provided the ideal and guided the data analysis of this study. Y-CC analyzed the correlation of the annual CPUE and

the environmental data. SJ, Y-CC, and C-CC organized the manuscript. SJ and C-CC wrote the first version of the manuscript. All authors contributed to the article and approved the submitted version.

FUNDING

This study was partially supported by the Ministry of Science and Technology (MOST) of Taiwan under grant MOST 105-2119-M-002-042.

ACKNOWLEDGMENTS

Dr. K.-Y. Chang kindly provided the annual CPUE data of swordtip squid to this study. Two reviewers provided constructive comments which clarified and strengthened the interpretation of this article. The daily meteorological dataset at Peng-jia-ju was downloaded from Taiwan's Central Weather Bureau at https://e-service.cwb.gov.tw/HistoryDataQuery/index.jsp. The satellite SST, SSH, SLA, SSC, and geostrophic velocity were downloaded from the Copernicus Marine Environment Monitoring Service at http://marine.copernicus.eu/.

SUPPLEMENTARY MATERIAL

The Supplementary Material for this article can be found online at: https://www.frontiersin.org/articles/10.3389/fmars.2022.900299/full#supplementary-material

REFERENCES

Andres, M., Mensah, V., Jan, S., Chang, M.-H., Yang, Y. J., Lee, C. M., et al. (2017). Downstream Evolution of the Kuroshio's Time-Varying Transport and Velocity Structure. *J. Geophys. Res. Oceans 122* 5, 3519–3542. doi: 10.1002/2016JC012519

Chang, K.-Y., Chen, C.-S., Wang, H.-Y., Kuo, C.-L., and Chiu, T.-S. (2015b). The Antarctic Oscillation Index as an Environmental Parameter for Predicting Catches of the Argentine Shortfin Squid (Illex Argentinus) Cephalopoda: Ommastrephidae) in Southwest Atlantic Waters. *Fish. Bull.* 113, 202–212. doi: 10.7755/FB.113.2.8

Chang, M.-H., Jan, S., Mensah, V., Andres, M., Rainville, L., Yang, Y. J., et al. (2018). Zonal Migration and Transport Variations of the Kuroshio East of Taiwan Induced by Eddy Impingements. *Deep-Sea Res. I* 131, 1–15. doi: 10.1016/j.dsr.2017.11.006

Chang, Y., Liao, H.-T., Lee, M.-A., Chan, J.-W., Shieh, W.-J., Lee, K.-T., et al. (2008). Multisatellite Observation on Upwelling After the Passage of Typhoon Hai-Tang in the Southern East China Sea. *Geophys. Res. Lett.* 35, L03612. doi: 10.1029/2007GL032858

Chang, K.-Y., Wang, K.-Y., and Liao, C.-H. (2018). Analyzing the Abundance Trend of Uroteuthis Edulis in Northern Taiwan Waters Using Generalized Linear Models. *J. Taiwan Fish. Res.* 26 (1), 1–12.

Chang, K.-Y., Wang, K.-Y., Liao, C.-H., and Wu, C.-L. (2015a). The Study on the Catch Per Unit Effort Standardization of Uroteuthis Edulis in the Northern Waters of Taiwan. *J. Taiwan Fish. Res.* 23 (2), 1–14.

Chao, S.-Y. (1991). Circulation of the East China Sea: A Numerical Study. *J. Oceanogr. Soc Japan* 46, 273–295. doi: 10.1007/BF02123503

Chen, C.-C., Hsu, S.-C., Jan, S., and Gong, G.-C. (2015). Episodic Events Imposed on the Seasonal Nutrient Dynamics of an Upwelling System Off Northeastern Taiwan. *J. Mar. Syst.* 141, 128–135. doi: 10.1016/j.jmarsys.2014.07.021

Chen, C.-C., Jan, S., Kuo, T.-S., and Li, S.-Y. (2017). Nutrient Flux and Transport by the Kuroshio East of Taiwan. *J. Mar. Syst.* 167, 43–54. doi: 10.1016/j.jmarsys.2016.11.004

Chen, C.-C., Lu, C.-Y., Jan, S., Hsieh, C.-H., and Chung, C.-C. (2022). Effects of the Coastal Uplift on the Kuroshio Ecosystem, Eastern Taiwan, the Western Boundary Current of the North Pacific Ocean. *Front. Mar. Sci.* 9, 796187. doi: 10.3389/fmars.2022.796187

Chen, C.-C., Shiah, F.-K., Gong, G.-C., and Chen, T.-Y. (2021). Impact of Upwelling on Phytoplankton Blooms and Hypoxia Along the Chinese Coast in the East China Sea. *Mar. Poll. Bull.* 167, 112288. doi: 10.1016/j.marpolbul.2021.112288

Chern, C.-S., and Wang, J. (1989). On the Water Masses at Northern Offshore Area of Taiwan. *Acta Oceanogr. Taiwanica* 22, 14–32.

Chern, C.-S., and Wang, J. (1990). On the Mixing of Waters at a Northern Offshore Area of Taiwan. *Terr. Atmos. Ocean. Sci.* 1 (3), 297–306. doi: 10.3319/TAO.1990.1.3.297(O)

Chern, C.-S., and Wang, J. (1992). The Influence of Taiwan Strait Waters on the Circulation of the Southern East China Sea. *La mer* 30, 223–228.

Chern, C.-S., and Wang, J. (1994). Influence of the Seasonal Thermocline on the Intrusion of Kuroshio Across the Continental Shelf Northeast of Taiwan. *J. Oceanogr.* 50, 691–711. doi: 10.1007/BF02270500

Chern, C.-S., Wang, J., and Wang, D.-P. (1990). The Exchange of Kuroshio and East China Sea Shelf Water. *J. Geophys. Res.* 95 (C9), 16017–16023. doi: 10.1029/JC095iC09p16017

Chuang, W.-S., and Liang, W.-D. (1994). Seasonal Variability of Intrusion of the Kuroshio Water Across the Continental Shelf Northeast of Taiwan. *J. Oceanogr.* 50, 531–542. doi: 10.1007/BF02235422

Chyn, S. S., Lee, K. T., and Liao, C. H. (1998). Aggregative Behavior of the Swordtip Squid (Loligo Edulis) Under Fishing Lights in the Coastal Waters of Northern Taiwan. *J. Fish. Soc Taiwan* 25, 1–15.

Cushman-Roisin, B. (1994). *Introduction to Geophysical Fluid Dynamics* (Hoboken: NJ: Prentice-Hall).

Fisheries Agency. (2016). *Annual Report of 2016* (Kaohsiung, Taiwan: Fisheries Agency, Council of Agriculture, Executive Yuan), 188.

Hsueh, Y., Wang, J., and Chern, C.-S. (1992). The Intrusion of the Kuroshio Across the Continental Shelf Northeast of Taiwan. *J. Geophys. Res. Oceans* 97 (C9), 14323–14330. doi: 10.1029/92JC01401

Hu, C.-K., Chiu, C.-T., Chen, S.-H., Kuo, J.-Y., Jan, S., and Tseng, Y.-H. (2010). Numerical Simulation of Barotropic Tides Around Taiwan, Terr. Atmos. *Ocean. Sci.* 21 (1), 71–84. doi: 10.3319/TAO.2009.05.25.02

Jan, S., Chen, C.-C., Tsai, Y.-L, Yang, Y. J., Wang, J., Chern, C.-S., et al (1994). Mean Structure and Variability of the Cold Dome Northeast of Taiwan. *Oceanography* 24 (4), 100–109. doi: 10.5670/oceanog.2011.98

Jan, S., Chern, C.-S., and Wang, J. (1994). A Numerical Study on Currents in the Taiwan Strait During Summertime. *La mer* 32, 225–234.

Jan, S., Mensah, V., Andres, M., Chang, M.-H., and Yang, Y. J. (2017). Eddy-Kuroshio Interactions: Local and Remote Effects. *J. Geophys. Res. Oceans* 122, 9744–9764. doi: 10.1002/2017JC013476

Jan, S., Sheu, D. D., and Kuo, H. M. (2006). Water Mass and Throughflow Transport Variability in the Taiwan Strait. *J. Geophys. Res. Oceans* 111, C12012. doi: 10.1029/2006JC003656

Jan, S., Wang, J., Chern, C.-S., Chao, S.-Y., et al. (2002). Seasonal Variation of the Circulation in the Taiwan Strait. *J. Mar. Syst.* 35 (3-4), 249–268. doi: 10.1016/S0924-7963(02)00130-6

Jan, S., Yang, Y. J., Wang, J., Mensah, V., Kuo, T.-H., Chiou, M.-D., et al. (2015). Large Variability of the Kuroshio at 23.75°N East of Taiwan. *J. Geophys. Res. Oceans* 120, 1825–1840. doi: 10.1002/2014JC010614

Johns, W. E., Lee, T. N., Zhang, D., Zantopp, R., Liu, C.-T., and Yang, Y. (2001). The Kuroshio East of Taiwan: Moored Transport Observations From the WOCE PCM-1 Array. *J. Phys. Oceanogr.* 31, 1031–1053. doi: 10.1175/1520-0485(2001)031<1031:TKEOTM>2.0.CO;2

Liao, C.-H., Lan, K.-W., Ho, H.-Y., Wang, K.-Y., and Wu, Y.-L. (2018). Variation in the Catch Rate and Distribution of Swordtip Squid Uroteuthis Edulis Associated With Factors of the Oceanic Environment in the Southern East China Sea. *Mar. Coast. Fish.* 10 (4), 452–464. doi: 10.1002/mcf2.10039

Liao, C.-H., Lee, M.-A., Lan, Y.-C., and Lee, K.-T. (2006). The Temporal and Spatial Change in Position of Squid Fishing Ground in Relation to Oceanic Features in the Northeastern Waters of Taiwan. *J. Fish. Soc Taiwan* 33, 99–113. doi: 10.29822/JFST.200606.0002

Lien, R.-C., Sanford, T. B., Jan, S., Yang, S., Chang, M.-H., Ma, B. B., et al. (2013). Internal Tides on the East China Sea Continental Slope. *J. Mar. Res.* 71 (1-2), 151–185. doi: 10.1357/002224013807343461

Liu, K. K., Gong, G.-C., Lin, S., Yang, C. Y., Wei, C. L., Pai, S.-C., et al. (1992). The Year-Round Upwelling at the Shelf Break Near the Northern Tip of Taiwan as Evidenced by Chemical Hydrography. *Terr. Atmos. Ocean. Sci.* 3, 243–275. doi: 10.3319/TAO.1992.3.3.243(KEEP)

Liu, S., Liu, Y., Fu, C., Yan, L., Xu, Y., Wan, R., et al. (2019). Using Novel Spawning Ground Indices to Analyze the Effects of Climate Change on Pacific Saury Abundance. *J. Mar. Syst.* 191, 13–23. doi: 10.1016/j.jmarsys.2018.12.007

Mensah, V., Jan, S., Andres, M., and Chang, M.-H. (2020). Response of the Kuroshio East of Taiwan to Mesoscale Eddies and Upstream Variations. *J. Oceanogr* 76, 271–288. doi: 10.1007/s10872-020-00544-8

Merkine, L.-O. (1975). Steady Finite-Amplitude Baroclinic Flow Over Long Topography in a Rotating Stratified Atmosphere. *J. Atmos. Sci.* 32 (10), 1881–1893. doi: 10.1175/1520-0469(1975)032<1881:SFABFO>2.0.CO;2

Merkine, L.-O., and Eugenia, K. R. (1976). Rotating Stratified Flow Over Finite Isolated Topography. *J. Atmos. Sci.* 33 (6), 908–922. doi: 10.1175/1520-0469(1976)033<0908:RSFOFI>2.0.CO;2

Morimoto, A., Kojima, S., Jan, S., and Takahashi, D. (2009). Movement of the Kuroshio Axis to the Northeast Shelf of Taiwan During Typhoon Events. *Estuar. Coast. Shelf Sci.* 82, 547–552. doi: 10.1016/j.ecss.2009.02.022

Oey, L.-Y., Hsin, Y.-C., and Wu, C.-R. (2010). Why Does the Kuroshio Northeast of Taiwan Shift Shelfward in Winter? *Ocean Dyn.* 60, 413–426. doi: 10.1007/s10236-009-0259-5

Shen, M.-L., Tseng, Y.-H., and Jan, S. (2011). The Formation and Dynamics of the Cold-Dome Off Northeastern Taiwan. *J. Mar. Sys.* 86, 1–2. doi: 10.1016/j.jmarsys.2011.01.002

Song, H., Ding, T., and Xu, K. (2008). The Quantity Distribution and Growth Characteristics of Loligo Edulis in the East China Sea. *J. Zhejiang Ocean Univ. (Natural Science)* 27, 115–118.

Tang, T.-Y., Hsueh, Y., Yang, Y. J., and Ma, J.-C. (1999). Continental Slope Flow Northeast of Taiwan. *J. Phys. Oceanogr.* 29, 1353–1362. doi: 10.1175/1520-0485(1999)029<1353:CSFNOT>2.0.CO;2

Tang, T.-Y., Tai, J.-H., and Yang, Y. J. (2000). The Flow Pattern North of Taiwan and the Migration of the Kuroshio. *Cont. Shelf Res.* 20, 349–371. doi: 10.1016/S0278-4343(99)00076-X

Tsai, C.-J., Andres, M., Jan, S., Mensah, V., Sanford, T. B., Lien, R.-C., et al. (2015). Eddy-Kuroshio Interaction Processes Revealed by Mooring Observations Off Taiwan and Luzon. *Geophys. Res. Lett.* 42, 8098–8105. doi: 10.1002/2015GL065814

Tsai, Y., Chern, C.-S., and Wang, J. (2008). Typhoon Induced Upper Ocean Cooling Off Northeastern Taiwan. Geophys. *Res. Lett.* 35, L14605. doi: 10.1029/2008GL034368

Vélez-Belchí, P., Centurioni, L. R., Lee, D.-K., Jan, S., and Niiler, P. P. (2013). Eddy Induced Kuroshio Intrusions Onto the Continental Shelf of the East China Sea. *J. Mar. Res.* 71 (1–2), 83–108. doi: 10.1357/002224013807343470

Waluda, C. M., Trathan, P. N., and Rodhouse, P. G. (1999). Influence of Oceanographic Variability on Recruitment in the Illex Argentinus (Cephalopoda: Ommastrephidae) Fishery in the South Atlantic. *Mar. Ecol. Prog. Ser.* 183, 159–167. doi: 10.3354/meps183159

Wang, K. Y., Chang, K. Y., Liao, C. H., Lee, M. A., and Lee, K. T. (2013). Growth Strategies of the Swordtip Squid, Uroteuthis Edulis, in Response to Environmental Changes in the Southern East China Sea–a Cohort Analysis. *Bull. Mar. Sci.* 89, 677–698. doi: 10.5343/bms.2012.1044

Wang, K.-Y., Lee, K.-T., and Liao, C.-H. (2010). Age, Growth and Maturation of Swordtip Squid (Photololigo Edulis) in the Southern East China Sea. *J. Mar. Sci. Tech.* 18 (1), 99–105. doi: 10.51400/2709-6998.1870

Wang, K.-Y., Liao, C.-H., and Lee, K.-T. (2008). Population and Maturation Dynamics of the Swordtip Squid (Photololigo Edulis) in the Southern East China Sea. *Fish. Res.* 90 (1–3), 178–186. doi: 10.1016/j.fishres2007.10.015

Wu, C.-R., Hsin, Y.-C., Chiang, T.-L., Lin, Y.-F., and Tsui, I.-F. (2014). Seasonal and Interannual Changes of the Kuroshio Intrusion Onto the East China Sea Shelf. *J. Geophys. Res. Oceans* 119, 5039–5051. doi: 10.1002/2013JC009748

Wu, C.-R., Lu, H.-F., and Chao, S.-Y. (2008). A Numerical Study on the Formation of Upwelling Off Northeast Taiwan. *J. Geophys. Res. Oceans* 113, C08025. doi: 10.1029/2007JC004697

Yamaguchi, T., Kawakami, Y., and Matsuyama, M. (2015). Migratory Routes of the Swordtip Squid Uroteuthis Edulis Inferred From Statolith Analysis. *Aquat. Biol.* 24, 53–60. doi: 10.3354/ab00635

Yang, D., Huang, R. X., Yin, B., Feng, X., Chen, H., Qi, J., et al. (2018a). Topographic Beta Spiral and Onshore Intrusion of the Kuroshio Current. *Geophys. Res. Lett.* 45, 287–296. doi: 10.1002/2017GL076614

Yang, Y. J., Jan, S., Chang, M. H., Wang, J., Mensah, V., Kuo, T. H., et al. (2015). Mean Structure and Fluctuations of the Kuroshio East of Taiwan From *in Situ* and Remote Observations. *Oceanogr* 28 (4), 74–83. doi: 10.5670/oceanog.2015.83

Yang, Y., Liu, C.-T., Hu, J.-H., and Koga, M. (1999). Taiwan Current (Kuroshio) and Impinging Eddies. *J. Oceanogr.* 55, 609–617. doi: 10.1023/A:1007892819134

Yang, D., Yin, B., Chai, F., Feng, X., Xue, H., Gao, G., et al. (2018b). The Onshore Intrusion of Kuroshio Subsurface Water From February to July and a Mechanism for the Intrusion Variation. *Prog. Oceanogr.* 167, 97–115. doi: 10.1016/j.pocean.2018.08.004

Yu, W., Zhang, Y., Chen, X., Yi, Q., and Qian, W. (2018). Response of Winter Cohort Abundance of Japanese Common Squid Todarodes Pacificus to the ENSO Events. *Acta Oceanol. Sin.* 37, 61–71. doi: 10.1007/s13131-018-1186-4

Zhang, D., Johns, W. E., Lee, T. N., Liu, C.-T., and Zantopp, R. (2001). The Kuroshio East of Taiwan: Modes of Variability and Relationship to Interior Meso-Scale Eddies. *J. Phys. Oceanogr.* 31, 1054–1074. doi: 10.1175/1520-0485(2001)031<1054:TKEOTM>2.0.CO;2

Conflict of Interest: The authors declare that the research was conducted in the absence of any commercial or financial relationships that could be construed as a potential conflict of interest.

Publisher's Note: All claims expressed in this article are solely those of the authors and do not necessarily represent those of their affiliated organizations, or those of the publisher, the editors and the reviewers. Any product that may be evaluated in this article, or claim that may be made by its manufacturer, is not guaranteed or endorsed by the publisher.

Copyright © 2022 Cheng, Jan and Chen. This is an open-access article distributed under the terms of the Creative Commons Attribution License (CC BY). The use, distribution or reproduction in other forums is permitted, provided the original author(s) and the copyright owner(s) are credited and that the original publication in this journal is cited, in accordance with accepted academic practice. No use, distribution or reproduction is permitted which does not comply with these terms.

frontiers | Frontiers in Marine Science

ORIGINAL RESEARCH
published: 16 June 2022
doi: 10.3389/fmars.2022.866075

A Cycle of Wind-Driven Canyon Upwelling and Downwelling at Wilmington Canyon and the Evolution of Canyon-Upwelled Dense Water on the MAB Shelf

Haixing Wang[1,2], *Donglai Gong*[1]*, *Marjorie A. M. Friedrichs*[1], *Courtney K. Harris*[1], *Travis Miles*[3], *Hao-Cheng Yu*[1] and *Yinglong Zhang*[1]

[1] Virginia Institute of Marine Science, William & Mary, Gloucester Point, VA, United States, [2] Berkshire Hathaway Specialty Insurance, Boston, MA, United States, [3] Department of Marine and Coastal Sciences, Rutgers University, New Brunswick, NJ, United States

OPEN ACCESS

Edited by:
Hiroaki Saito,
The University of Tokyo, Japan

Reviewed by:
Jesus Dubert,
University of Aveiro, Portugal
Hui Wu,
East China Normal University, China

***Correspondence:**
Donglai Gong
gong@vims.edu

Specialty section:
This article was submitted to Coastal Ocean Processes, a section of the journal Frontiers in Marine Science

Received: 30 January 2022
Accepted: 16 May 2022
Published: 16 June 2022

Citation:
Wang H, Gong D, Friedrichs MAM, Harris CK, Miles T, Yu H-C and Zhang Y (2022) A Cycle of Wind-Driven Canyon Upwelling and Downwelling at Wilmington Canyon and the Evolution of Canyon-Upwelled Dense Water on the MAB Shelf. Front. Mar. Sci. 9:866075. doi: 10.3389/fmars.2022.866075

Submarine canyons provide a conduit for shelf-slope exchange *via* topographically induced processes such as upwelling and downwelling. These processes in the Wilmington Canyon, located along the shelf-break of the Mid-Atlantic Bight (MAB), have not been previously studied, and the associated hydrographic variability inside the canyon and on the adjacent shelf are largely unknown. Observations from an underwater glider deployed in Wilmington Canyon (February 27 - March 8, 2016), along with wind and satellite altimetry data, showed evidence for a wind-driven canyon upwelling event followed by a subsequent downwelling event. Next, a numerical model of the MAB was developed to more fully represent these two events. Modeled results showed that under upwelling-favorable winds during February 25 - March 3, sea level increased seaward, shelf currents flowed northeastward, and canyon upwelling developed. Then under downwelling-favorable winds during March 4-7, sea level increased landward, shelf currents flowed southwestward, and canyon downwelling developed. Modeling experiments showed that canyon upwelling and downwelling were sub-tidal processes driven by winds and pressure gradients (associated with SSH gradients), and they would occur with or without tidal forcing. During the upwelling period, slope water originating from 150-215 m depths within the canyon (75 m below the canyon rim), was advected onto the shelf, forming a cold and dense canyon-upwelled slope-originated overflow water at the bottom of the outer shelf (75-150 m isobaths). The dense overflow current flowed was directed northeastward and expanded in the cross-shelf direction. It was 5-20 km wide and 10-30 m thick. The estimated volume of the plume overflow water exceeded 6×10^9 m^3 at peak. The density front at the shoreward side of the dense overflow water caused a subsurface baroclinic frontal jet, which flowed northeastward and along-shelf with maximum speed exceeding 0.5 m/s. In the ensuing downwelling event, a portion of the previously upwelled dense water was advected back to the canyon, and then flowed down-slope in the upper canyon in ~0.3 m/s bottom-

intensified currents. Dynamical investigation of the overflow current showed that its evolution was governed by unbalanced horizontal pressure gradient force in the cross-shelf direction and that the current was geostrophic.

Keywords: submarine canyon, shelf-slope exchange, upwelling, downwelling, wind-driven circulation, shelf-break dynamics, Mid-Atlantic Bight, frontal jet

1 INTRODUCTION

Shelf-break submarine canyons are common geomorphological features that incise the shelf-break, and they provide a conduit for shelf-slope exchange *via* topographically induced processes such as canyon upwelling and downwelling (Allen and Durrieu de Madron, 2009). Under similar upwelling- or downwelling-favorable conditions, the cross-isobath exchange flow in a canyon is stronger than that over a normal shelf-break (Klinck, 1996; She and Klinck, 2000; Kämpf, 2006). Thus, submarine canyons can drive enhanced shelf-slope exchanges of water masses (Kämpf, 2010; Connolly and Hickey, 2014). Canyon upwelling and downwelling occurs on the sub-inertial time scales and is associated with favorable conditions of along-shelf flows, which is driven by cross-shelf sea surface height gradients and winds. For canyons in the northern hemisphere, upwelling occurs under left-bounded along-shelf flows (flows with the coast to their left side; Klinck, 1996). Canyon upwelling and left-bounded along-shelf flows are often associated with seaward cross-shelf sea surface height gradients (∇SSH) that produce sea-level set-down at the coast (Freeland, 1982; Allen and Hickey, 2010), which in turn are often forced by upwelling-favorable winds (left-bounded along-shelf winds or seaward cross-shelf winds; Hickey, 1997; She and Klinck, 2000; Zhang and Lentz, 2017). Conversely, canyon downwelling in the northern hemisphere is associated with right-bounded along-shelf flows, SSH gradients that produce set-up at the coast, and downwelling-favorable winds.

Canyon upwelling and downwelling scenarios were considered separately in most previous canyon modeling studies. Often in these studies, separate upwelling and downwelling simulations were set up with opposite along-shelf flows (e.g., Klinck, 1996), or with winds blowing from opposite directions (e.g., Zhang and Lentz, 2017). They found that canyon circulation is stronger during upwelling than that during downwelling under conditions of equal strength but opposite directions. In addition, canyon upwelling can induce over 10 times more net cross-shelf-break transport than canyon downwelling (Spurgin and Allen, 2014). During canyon upwelling, substantial amounts of slope water can be channeled along the canyon towards the canyon head and upwelled onto the shelf (Allen and Hickey, 2010). The canyon-upwelled water forms a dense pool that expands on the bottom of the downstream shelf (e.g., Howatt and Allen, 2013). In this paper, we refer to this dense pool as a canyon-upwelled overflow, others have also referred to the feature as "canyon upwelling plume" and they have been reported in several process-oriented numerical modeling studies, such as Kämpf (2009, 2010, 2012), Howatt and Allen (2013); Ramos Musalem (2020) and Saldías and Allen (2020). They have also been produced in laboratory experiments by Ramos Musalem (2020). We chose to use the term "overflow" instead of "plume" because plume suggests lighter water than the surrounding, while overflow is a denser water than the surrounding. Notably, the scenario of a canyon downwelling event that immediately follows an upwelling event has not been investigated by previous canyon modeling studies. Thus, for a cycle of canyon upwelling and downwelling, it is unknown how the dense overflow water that has accumulated on the shelf during the upwelling phase would evolve during the ensuing downwelling event.

Studies of upwelling and downwelling in the shelf-break canyons of the Mid-Atlantic Bight (MAB; **Figure 1A**) are rare. A synoptic hydrographical survey in Wilmington Canyon by Church et al. (1984) observed slope water moving up along the canyon axis and shelf water moving seaward on the canyon's southwest flank. Mooring measurements of ocean currents in Baltimore Canyon (Hunkins, 1988) and Lydonia Canyon (Butman, 1986) showed that on the sub-tidal time scale, flows inside the canyons moved up-canyon and down-canyon when shelf currents were left-bounded and right-bounded, respectively. The above-mentioned studies were made before the dynamics of canyon upwelling and downwelling were well understood, however, all showed observations that could be explained by canyon upwelling or downwelling. Observational studies on near-bed circulation in Hudson Shelf Valley (which is the shoreward extension of Hudson Canyon) in wintertime 1999-2000, Harris et al. (2003) and Lentz et al. (2014) found that up-valley and down-valley currents were closely correlated with sea level set-down and set-up at the coast, respectively. An idealized modeling study by Zhang and Lentz (2017) confirmed that upwelling and downwelling in the Hudson Shelf Valley are correlated with seaward (positive) and shoreward (negative) cross-shelf ∇SSH on the continental shelf, respectively. For Wilmington Canyon (**Figure 1B**), upwelling and downwelling processes are still essentially unknown regarding the associated forcing conditions on the shelf and the hydrographic variability in and near the canyon.

Wilmington Canyon is the second largest shelf-break submarine canyon (after Hudson Canyon) in the southern MAB. The canyon has an approximately 55° axial bend (**Figure 1B**): the lower section from the canyon mouth to the bend orients towards the northwest and lays nearly perpendicular to the shelf break (~72°); the upper section from the bend to the canyon head veers to the northeast and lays nearly parallel to the shelf break (~17°). The canyon head intersects the continental shelf at around the 90 m isobath, and the canyon mouth intersects the shelf break at a depth of 150 m. On either side of the canyon axis, the canyon intersects with the continental

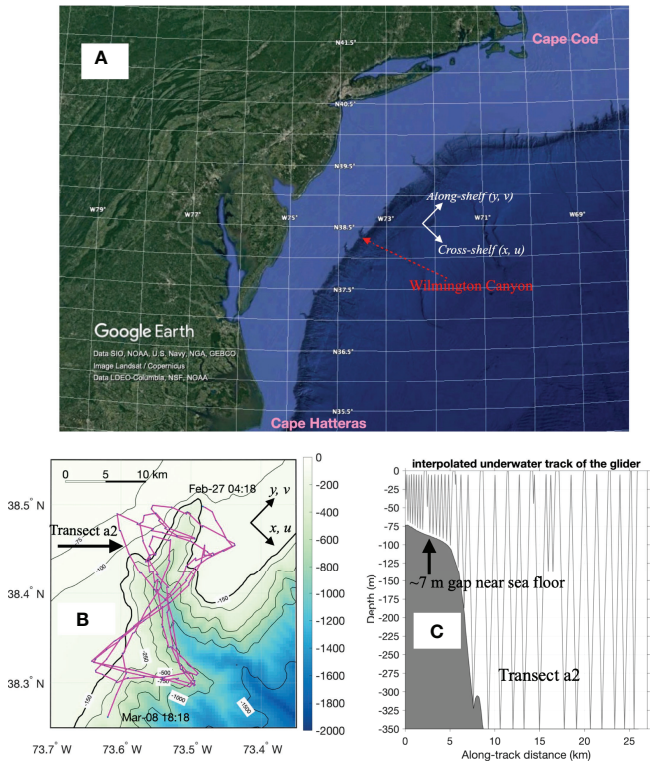

FIGURE 1 | **(A)** Location of Wilmington Canyon in the Mid-Atlantic Bight. **(B)** Wilmington Canyon bathymetry with glider survey track (magenta line) during 02/27-03/08/2016. **(C)** Underwater track taken by the glider at transect a2. The glider used in this study has a maximum diving depth of 350 m. At locations shallower than 350 m, the glider's altimeter sensor was used during diving to prevent the glider from hitting the seafloor. Thus, the water column within 7 m above the sea floor was generally not sampled.

shelf at the canyon rim. The canyon is approximately 20 km long from the canyon mouth to the canyon head, 10 km wide at the canyon mouth, and has a rim depth of 125 m at the head of the canyon. The depth change along the canyon thalweg from the canyon head to the canyon mouth is approximately 1000 m (www.geomapapp.org; Ryan et al., 2009). The roughly southeast-northwest lower canyon allows an along-shelf flow to interact with canyon topography in a way similar to those previously simulated by idealized numerical models (e.g., Klinck, 1996; Howatt and Allen, 2013). The roughly southwest-northeast alignment of the upper canyon means that canyon flows are channeled in the along-shelf direction. Thus, for Wilmington Canyon, a northeastward (southwestward) incoming along-shelf flow is not only upwelling-favorable (downwelling-favorable) in a classical sense due to the orientation of the lower canyon, but also can flow directly up-canyon (down-canyon) in the upper canyon.

In this study, an underwater glider was deployed in Wilmington Canyon during February 27 - March 8, 2016. During this time period, the MAB experienced nine days of upwelling-favorable winds followed by four days of downwelling-favorable winds. The glider fortuitously obtained hydrographic evidence of consecutive canyon upwelling and downwelling in Wilmington Canyon. To place the glider observations in a greater spatial and temporal context, we utilized a numerical model with realistic forcing and bathymetry. The model allowed us to investigate the cycle of upwelling and downwelling events and compare it with the glider observations. The rest of the paper is organized as follows. Section 2 includes a presentation of the glider survey design and glider configuration, as well as an outline of the numerical modeling system and model setup. In section 3, evidence of the consecutive occurrences of sub-tidal upwelling and downwelling is presented based on the glider observations (sections 3.1.1, 3.1.2.) and numerical simulation (sections 3.1.2, 3.1.3). Then, the development and receding of a canyon-upwelled dense water overflow is described based on model results (sections 3.2., 3.3). The results are discussed in section 4, and key findings are summarized in section 5.

2 METHODS

2.1 Glider Survey Design and Glider Configuration

A 350 m Slocum G2 glider "Amelia" was used to survey Wilmington Canyon during February 27 - March 8, 2016 (**Figure 1**). The glider repeated the "figure 8" shaped survey pattern 3 times (**Figure 1B**): a transect across the upper canyon, a

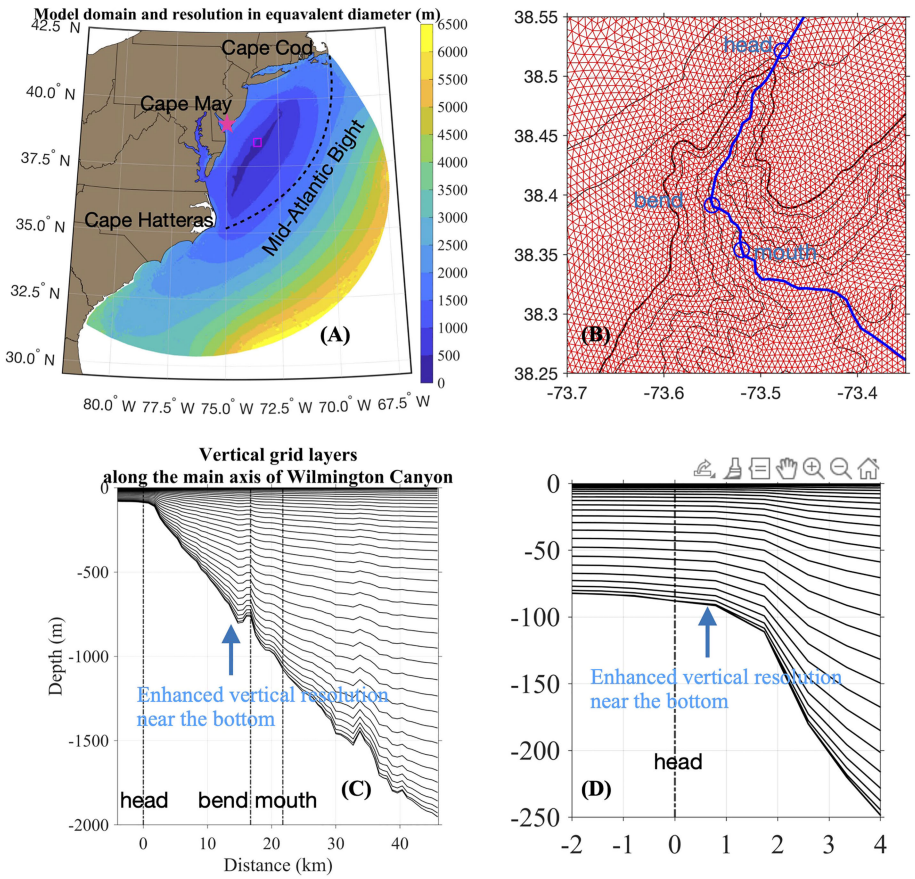

FIGURE 2 | **(A)** SCHISM model domain and horizontal resolution in equivalent diameter. The model uses >24,000 horizontal nodes, >48,000 unstructured triangular grids, with 350-1000 m resolution over the submarine canyons and adjacent shelf and slope. Location of Wilmington Canyon is indicated by the magenta box. **(B)** Model mesh over the Wilmington Canyon. Blue line indicates a transect along the canyon's main axis. Visualization of model vertical layers **(C)** along the axis of Wilmington Canyon, and **(D)** zoomed in near the canyon head. There are up to 55 vertical layers depending on water depth. Relatively high vertical resolution is set up for near the surface and bottom. The thickness of the bottom model layer is generally 0.1-5 m over the shelf, shelf-break, and canyon.

transect across the lower canyon, a transect parallel to the shelf break, then a transect along the lower canyon. The glider was equipped with the Sea-Bird Scientific's pumped glider conductivity temperature and depth (CTD) sensor. The CTD sensor was factory calibrated in June 2015 prior to deployment. After the glider was recovered, full resolution delayed-mode temperature, conductivity, and pressure data were extracted from the CTD sensor and thermal lag correction algorithms were applied following Garau et al. (2011). Absolute Salinity and potential density were calculated using Thermodynamic Equation of Seawater 2010 (TEOS-10) provided by the Gibbs SeaWater (GSW) Oceanographic Toolbox (McDougall and Barker, 2011). The glider was also equipped with the following sensors: Sea-Bird Scientific's EcoPUCK triplet fluorometer with chlorophyll-a, colored dissolved organic matter (CDOM), optical backscatter (700 nm) sensors, and an Aanderaa Optode for measuring dissolved oxygen. In this study, we used the temperature, salinity, and density data at the three repeated transects across the lower canyon, as well as those at the three repeated transects along the lower canyon.

An underwater glider dives and climbs in the water column by changing buoyancy while being propelled forward by the normal force acting on its wings (Webb et al., 2001). Typically, a Slocum glider dives and climbs at ~26° angle from the horizontal plane, at nominal vertical speeds of 0.15 ± 0.04 *m/s*, and horizontal speeds of 0.25 ± 0.06 *m/s* through the water. During a 350m deep "yo" consisting of one dive and one climb, which takes approximately 80 minutes, a glider moves laterally by ~1.4 km (assuming no currents) while making ~2400 measurements at a sampling rate of 0.5 Hz. At locations with bathymetry shallower than 350 m, the glider's downward facing altimeter sensor was used during the downcast to prevent the glider from hitting the seafloor. The glider would inflect from dive to climb at about 7 m above the sea floor. Thus, the water column within 7 m above the bottom was generally not sampled (**Figure 1C**).

2.2 Numerical Modeling Using the SCHISM Model

To place the observations in larger spatial and temporal contexts, we conducted numerical modeling experiments using the Semi-

implicit Cross-scale Hydroscience Integrated System Model (SCHISM, Zhang et al., 2016). SCHISM has been used in multiple studies of the coastal ocean of the U.S. east coast (e.g., Ye et al., 2019; Liu et al., 2020), as well as in a study of the submarine canyons in the Black Sea (Brovchenko and Maderich, 2011). SCHISM is based on unstructured horizontal grids and flexible vertical grids, thus it can represent the complex 3D topography while avoiding artifacts like "staircase-like" bathymetry (Zhang et al., 2016). The pressure gradient force error (Haney, 1991) is effectively reduced using the localized and hybridized vertical grid that lowers the coordinate slopes (Zhang et al., 2016). Other major characteristics of SCHISM include a hybrid finite element/volume formulation, semi-implicit time-stepping, implicit vertical advection scheme for transport (TVD^2; Ye et al., 2019), 3rd order Weighted Essentially Non-Oscillatory (WENO) transport in the horizontal dimension (Ye et al., 2019), an efficient and accurate Eulerian-Lagrangian algorithm for momentum advection, horizontal viscosity scheme (including bi-harmonic viscosity) to effectively remove inertial spurious modes without introducing excessive dissipation, etc. For detailed information about SCHISM, please refer to http://schism.wiki. The model implementation was designed to represent the hydrodynamical processes inside Wilmington Canyon, as well as the adjacent outer shelf, shelf-break, and continental slope regions. To achieve this, the model's domain size, bathymetry, horizontal resolutions, vertical layer configuration, boundary conditions, forcing conditions, simulation time, spin-up time, and time step were all considered.

The model domain covered the US east coast from Georgia to Massachusetts (**Figure 2A**) and used the GMRT (Ryan et al., 2009) v3.7 bathymetry data (which has 133 m gridded resolution) that has not been smoothed. Overall, the model grid included over 240,000 nodes and 480,000 triangular elements. The model's horizontal resolution was relatively uniform and high along the shelf-break in the southern and central MAB (**Figure 2A**). Along the shelf-break isobath (150 m) from ~50 km south of Norfolk Canyon to ~50 km north of Wilmington Canyon, the resolution was ~400 m (**Figures 2A, B**); in and around Hudson Canyon the resolution was ~1 km; in general, the resolution was 2-3 km at the coast (except in coastal estuaries such as the Chesapeake Bay where the resolution was increased) and 3-8 km at the open ocean boundary. In the vertical direction, depending on water depth, the model has up to 55 levels in the hybrid sigma-z (SZ) vertical grid with enhanced vertical resolutions at the surface and bottom (**Figures 2C, D**). The bottom layer thickness was generally 0.1-5 m over the continental shelf, shelf-break, slope, and canyons. The high horizontal resolution was designed to capture physical processes within and around the canyons. The intensified vertical resolution near the bottom was designed to capture topographical processes.

Our numerical simulation was subjected to relatively realistic atmospheric and oceanic conditions. It was initialized with conditions of temperature, salinity, and sub-tidal horizontal velocities from a data-assimilative global ocean model - the HYbrid Coordinate Ocean Model (HYCOM), Global Ocean Forecasting System (GOFS) 3.1. This HYCOM model had a 1/12-degree resolution which does not resolve the bathymetry of submarine canyons. At the open ocean boundary of our SCHISM model, a 1.5 degree nudging zone was set, and boundary conditions were forced by the temperature, salinity, and de-tided horizontal velocities from HYCOM, as well as by the tidal elevations and tidal currents from the FES2014 tides database (standard case with Tide). For atmospheric forcing, our implementation included winds, heat fluxes, precipitation, and evaporation from the North American Regional Reanalysis model (NARR, 32 km resolution). Finally, our model took inputs of daily freshwater discharge based on U.S. Geographical Survey (USGS) gauge data for the four major estuaries in the MAB, i.e., Chesapeake Bay, Delaware Bay, Hudson River, and Connecticut River. Altogether, these relatively realistic (as opposed to idealized) atmospheric and oceanic conditions allow us to simulate the hydrodynamics inside Wilmington Canyon and on the adjacent shelf during the study period. In addition, we performed a simulation that excluded tidal forcing at the open boundary (No-Tide case) to investigate how the sub-tidal wind-forced phenomena and tide-forced phenomena are superimposed, and whether the phenomena can be separated in time.

The SCHISM model simulations started on January 1 and ended on March 31, 2016. The spin up period was five days. Results representing February 24 - March 8, 2016, were used in this study. The model used a non-split time step of dt = 120 s. Each model day simulation took about 25 minutes using 300 cores (1324 Xeon "Broadwell" cores) on a High-Performance Computing system (the Bora cluster on SciClone at William & Mary). The model outputs were saved every 2 hours or 12 times daily. Altogether, the above configurations allowed us to investigate the hydrodynamics inside Wilmington Canyon and over the region surrounding the canyon.

3 RESULTS

Observed evidence for a cycle of upwelling and downwelling events is presented in section 3.1, including hydrographic transects within Wilmington Canyon from the glider survey, and the records of winds and water level at a coastal observation station. In section 3.2, we validate the SCHISM implementation by comparing the modeled hydrodynamics to observations. Then in section 3.3, the modeled results from within Wilmington Canyon are provided to examine how the hydrodynamics at the canyon responded to forcing conditions through different phases of the upwelling and downwelling cycle, and to visualize the upwelling and downwelling flows inside Wilmington Canyon. Lastly in section 3.4, the model results for a canyon-upwelled dens water overflow on the shelf, which was generated from the main head of Wilmington Canyon, are presented.

3.1 A Cycle of Upwelling and Downwelling in Wilmington Canyon Shown by Observations

We inferred that a cycle of canyon upwelling and downwelling occurred in Wilmington Canyon during February 27-March 8,

2016, based on repeated glider hydrographical transects. This inference was supported by the records of winds and water level at the NOAA station 8536110 at Cape May, NJ (~100 km shoreward of Wilmington Canyon).

3.1.1 *In Situ* Evidence From the Glider Survey

Three distinctive water masses comprising the upper 350 m of the water column in and around Wilmington Canyon were observed during the glider survey. To illustrate this, the temperature and salinity data, and associated T/S diagrams at a glider transect along the lower canyon are shown in **Figure 3**. From surface to bottom, we identified the low-temperature (~ 10 °C) and low-salinity (<34.5) winter shelf water (WSW), the high-temperature (~14 °C) and high-salinity (≥ 35.5) upper slope water (USW), and the low-temperature (~9°C) and high-salinity (~35.3) intermediate slope water (ISW).

By inspecting the spatial distribution of the three water masses at each glider transect and comparing the changes in water column structure between repeated transects (**Figure 4**), we could identify that a canyon upwelling event was immediately followed by a downwelling event. It is worth mentioning that a glider transect in this survey typically took 20-30 hours to complete, and the isopycnals below 150 m depth (e.g. σ_0 = 27.2 $kg\ m^{-3}$) within each glider transect showed semi-diurnal tidal time scale oscillations. Above 150 m, the water column in the canyon is more strongly influenced by surface and frontal processes and the tidally driven semi-diurnal variability is less obvious. While we cannot completely separate spatial variability from temporal variability in the glider observations, in section 3.3, we will use the SCHISM output at a fixed location to show the phases of the upwelling and downwelling events, and the daily mean (tidally averaged) spatial distributions of temperature and velocities across the entire canyon. Regardless of the phases of the tide, comparisons between repeated glider transects show that both the upwelling and downwelling events lasted for several days.

Temporal changes between the three cross-canyon transects across the lower canyon (**Figure 4A**) showed a sequence of water upwelling and downwelling. The transects c1, c2 and c3 were conducted February 27-28, March 2-3, and March 5, 2016, respectively. From transect c1 to transect c2, which were separated by about three days, the ISW layer rose by 50-70 m, consistent with upwelling. From transect c2 to transect c3, which were separated by about two days, the ISW layer fell by 50-70 m, consistent with downwelling.

Next, spatial and temporal varying water column structure at the three glider transects along the lower canyon (**Figure 4B**) also revealed the same sequence of upwelling and downwelling. The examination here focused on the water column below 100 m depth, especially on the σ_0 = 26.8-27.2 $kg\ m^{-3}$ isopycnals in the lower portion of USW and upper portion of ISW. In transects a1 (February 28-29) and a2 (March 3-4), the isopycnals tilted upward from the canyon mouth toward the shelf by about 80 m, indicative of upwelling. In transect a3 (March 6-7), the water layers tilted downward from the canyon mouth towards the shelf by about 80 m, indicative of downwelling.

3.1.2 Supporting Evidence From Records of Winds and Water Level at Cape May, NJ

Wind and water level data from the NOAA station 8536110 at Cape May, NJ (~100 km shoreward of Wilmington Canyon) were examined to characterize forcing conditions over the MAB coastal ocean (**Figure 5**). For most of the time during February 25 - March 3, winds were northwesterly or southwesterly (**Figure 5A**), i.e. upwelling-favorable. Corresponding to the upwelling winds, the measured water level was lower than predicted astronomical tide (**Figure 5B**), indicating a sea level

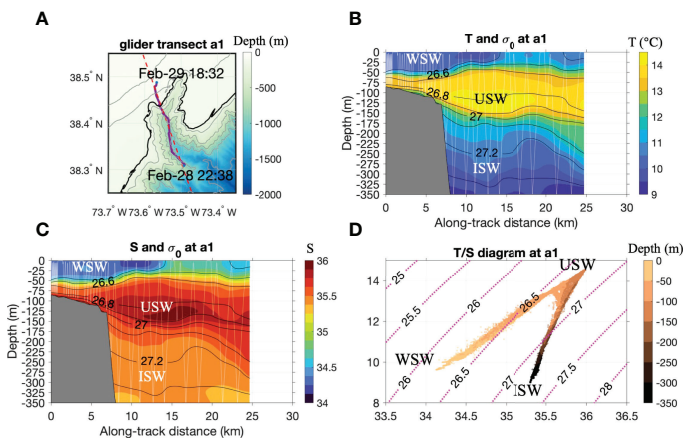

FIGURE 3 | Water masses in the upper 350 m in Wilmington Canyon shown by data at glider transect a1. **(A)** Purple line indicates glider transect a1. Red dashed line indicates where SCHISM model output was extracted in **Figure 6**. **(B, C)** Spatially interpolated fields of temperature and salinity, contours are isopycnals. **(D)** T/S diagram based on glider data. Three distinctive water masses comprised the upper 350 m of the water column in and around Wilmington Canyon during the glider survey. From surface downward, there were the low-temperature (~ 10°C) and low-salinity (<34.5) winter shelf water (WSW), the high-temperature (~14°C) and high-salinity (≥ 35.5) upper slope water (USW), and the low-temperature (~9°C) and high-salinity (~35.3) intermediate slope water (ISW). Each water mass is shown as an end member in the T/S diagram.

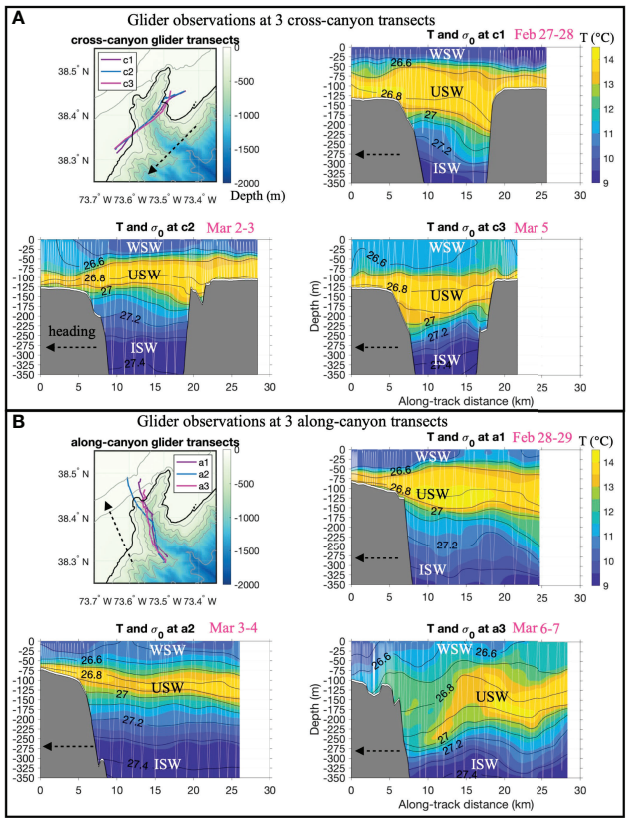

FIGURE 4 | Interpolated temperature (color) and density (contours) fields at **(A)** three repeated cross-canyon transects and **(B)** three repeated along-canyon transects from the glider survey. Typically in this mission, a glider transect took 20 to 30 hours to complete. Thin white lines in the temperature transects indicate glider tracks. Dashed black arrows indicate the glider's heading. The cross-canyon transects c1, c2 and c3 were conducted February 27-28, March 2-3, and March 5, 2016, respectively. The along-canyon transects In a1, a2 and a3 were conducted on February 28-29, March 3-4, and March 6-7 respectively.

set-down at the coast. Then during March 4-7, winds were northeasterly or northerly (**Figure 5A**), i.e. downwelling-favorable. Corresponding to the downwelling-favorable winds, measured water level was higher than predicted astronomical tide (**Figure 5B**), indicating a sea level set-up at the coast. The above temporal changes of wind directions and sea level suggest that forcing conditions over the MAB coastal ocean were upwelling-favorable when upwelling was observed in Wilmington Canyon by the glider, and forcing conditions changed to be downwelling-favorable when downwelling was observed in Wilmington Canyon. In section 3.3.1, we will use results from SCHISM to examine how the hydrodynamics at Wilmington Canyon responded to forcing conditions through different phases of the upwelling and downwelling events.

3.2 Model-Data Comparison

To validate the model, we first compared the modeled results from SCHISM with glider observations in terms of the T/S identities and spatial distribution of water masses within the canyon (**Figure 6A**). As an example, the modeled temperature and salinity data were extracted along the lower canyon to compare with observations. The model outputs were extracted at a straight transect which is roughly overlapping with but slightly longer than the glider transect, and at the halftime point between the beginning and end of the glider transect (**Figure 3A**). Compared to observations, the model underestimated the temperature and salinity of USW by about 0.8 °C and 0.4 respectively, and of ISW by about 1°C and 0.1 respectively (**Figure 6A**). Nonetheless, the model produced the same three distinctive water masses as observations. More importantly, the modeled spatial distribution pattern of the water masses, i.e. the water column structure, was consistent with that of observed: the WSW layer occupied the upper ~50 m of the water column over the outer shelf, and this layer became thinner, warmer, and saltier in farther offshore locations over the canyon; the ISW resided below 200 m within the canyon, but tilted upward from the canyon mouth towards the shelf; the USW was wedged between the WSW and ISW, and was thicker within the canyon, thinner over the shelf. Thus, the modeled results showed the same three water masses as observed, and the modeled spatial distribution of water masses was qualitatively similar to observed.

We also compared the modeled water level by SCHISM with the predicted (based on astronomical tides) and measured water level at the NOAA station 8536110 at Cape May, NJ (**Figure 6B**). The SCHISM model generally reproduced the measured water level in terms of tidal phases, and subtidal deviation from predicted water level. In particular, similar to the observed water level, the SCHISM water level was lower than the predicted water level during the upwelling period (e.g., on February 27), and higher than predicted during the downwelling period (e.g., on March 5). The above comparisons indicate that the modeled sea level response was consistent with observations.

The above validations gave us the confidence to use the SCHISM model to examine how the hydrodynamics at the canyon responded to forcing conditions through different phases of the upwelling and downwelling events, to visualize the upwelling and downwelling flows inside Wilmington Canyon, and to inspect the hydrodynamics on the adjacent shelf during the cycle of upwelling and downwelling event.

3.3 Modeled Upwelling and Downwelling Events Inside Wilmington Canyon

3.3.1 Temporal Evolution of the Upwelling and Downwelling Events

Time series of forcing conditions and flow responses at the canyon head (**Figure 7**) suggest that the canyon upwelling event lasted for 8.5 days from February 25 to March 4, 2016, persisted through multiple tidal cycles, and consisted of a 2-day ramp-up phase, a 5-day quasi-steady phase, and a 1.5-day relaxation phase when wind speeds were reduced. The ensuing downwelling event lasted for 3.5 days from March 4-7, and consisted of 1.5 days of ramp-up, followed by 2 days of relaxation when both winds and currents relaxed back toward zero.

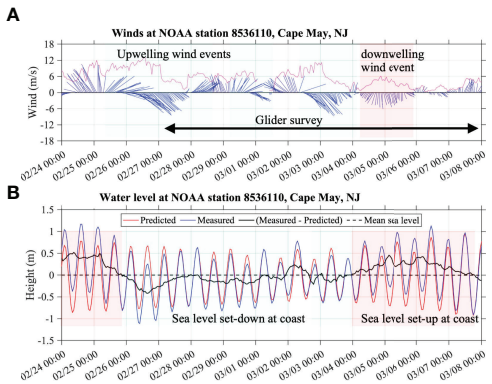

FIGURE 5 | **(A)** Wind and **(B)** water level data from the NOAA station 8536110 at Cape May, NJ (~100 km shoreward of Wilmington Canyon). For most of the time during February 25 - March 3, winds were northwesterly or southwesterly **(A)**, i.e. upwelling-favorable. Corresponding to the upwelling winds, the measured water level was lower than predicted, indicating a sea level set-down at the coast. Then during March 4-7, winds were northeasterly or northerly, i.e., downwelling-favorable. Corresponding to the downwelling-favorable winds, measured water level was higher than predicted, indicating a sea level set-up at the coast.

In the ramp-up phase of upwelling on February 25-26, winds turned from southerly to southwesterly and northwesterly with speeds of 10-15 *m/s*; during the same period the cross-shelf SSH gradient quickly increased (positive gradient is seaward, which corresponds to sea level set-down at the coast) from 0 to 3 ± 1.5 × 10^{-6} (**Figure 7A**). In response to the changing conditions of wind and SSH gradient, the near-bottom currents at the canyon head (extracted at 10 m above sea floor at the 110 m isobath), which were southwestward before, now turned to be northeastward (i.e. up-canyon), with speed accelerated to about 0.2 m/s (**Figure 7B**). The vertical flow velocity, *w*, turned from negative to positive (i.e. upward) at 4 ± 1 *mm/s*. In the same two days of upwelling ramp-up, water temperature decreased from 12.5 to 10.7 °C, and the water density anomaly increased from 26.7 to 27.2 *kg* m^{-3} (**Figure 7C**). In the following 5-day quasi-steady phase of upwelling, from February 27 to March 2, despite tidal oscillations, westerly winds sustained the positive cross-shelf SSH gradient (**Figure 7A**). During this phase, near-bottom currents at the canyon head continuously flowed up-canyon at 0.15-0.2 *m/s*, the vertical velocity remained upward at 3-5 *mm/s* (**Figure 7B**), water temperature and density anomalies remained steady at 10.5-11 °C, and 27.1-27.2 *kg* m^{-3}, respectively (**Figure 7C**).

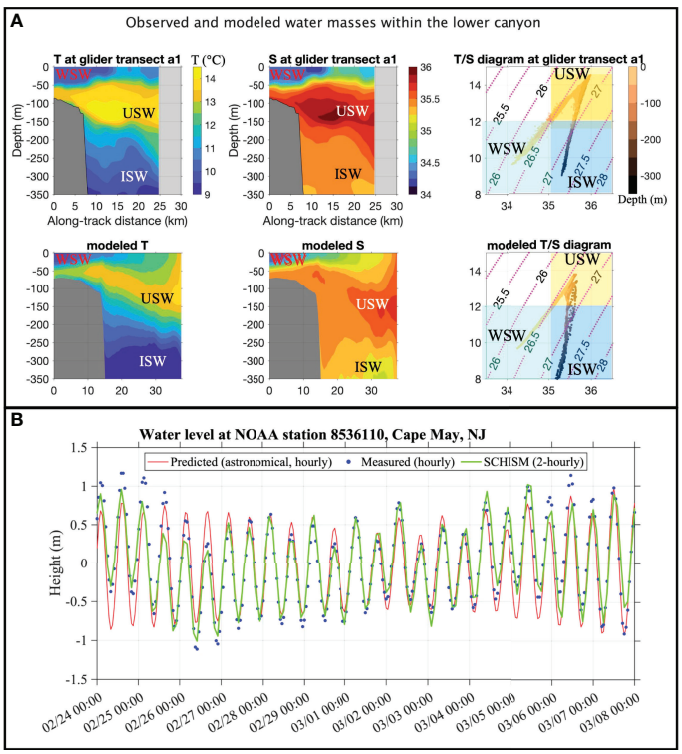

FIGURE 6 | **(A)** Comparison of the modeled results from SCHISM with glider observations in terms of the T/S identities and spatial distribution of water masses within the canyon. The locations of the glider transect and model transect are shown in **Figure 3A**. The glider transect was conducted from 22:38 Feb 28 - 18:32 Feb29 (GMT). The modeled results were averaged over 22:00 Feb 28 - 18:00 Feb 29. Bathymetry in glider transects was based on glider altimetry data. Bathymetry in modeled transects was based on GMRT data. **(B)** Comparison of the modeled water level by SCHISM with the predicted (based on astronomical tides) and measured water level at the NOAA station 8536110 at Cape May, NJ.

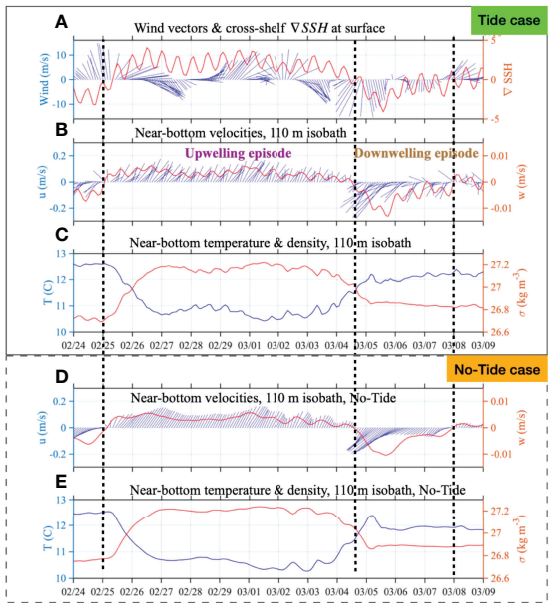

FIGURE 7 | Time series of forcing conditions and flow responses at the canyon head. The point from where the model outputs are extracted is located at about 10 m above bottom at 110 m isobath near the canyon head: **(A)** wind vectors and cross-shelf SSH gradient (positive is seaward), **(B)** near bottom velocities (full forcing with tides), **(C)** near bottom temperature and density, **(D)** near bottom velocities (no tides), and **(E)** near bottom temperature and density (no tides). The canyon upwelling event lasted for 8.5 days from February 25 to March 4, 2016, persisted through multiple tidal cycles, and consisted of a 2-day ramp-up phase, a 5-day quasi steady phase, and a 1.5-day relaxation phase. The ensuing downwelling event lasted for 3.5 days from March 4-7, and consisted of 1.5 days of ramp-up, and 2 days of relaxation.

Then during the relaxation phase of upwelling on March 3 and first half of March 4, northwesterly winds gave way to northeasterly winds, cross-shelf SSH gradient decreased to about 0 (**Figure 7A**), near-bottom flow and its vertical velocity both decreased to about 0 as well (**Figure 7B**), water temperature increased to 11.5 °C, and density anomaly decreased to 27.0 $kg\ m^{-3}$ (**Figure 7C**). In the transition phase between the upwelling event and downwelling event around 00:00 on March 4, the directions of winds and SSH gradient changed from being upwelling- to downwelling-favorable. Throughout March 4, northeasterly and northerly wind speeds continued to increase, and reached 10-16 m/s (**Figure 7A**) before decreasing on March 5 (**Figure 7A**).

In the second half of March 4 and first 18 hours of March 5, cross-shelf SSH gradient became increasingly negative from 0 to -4×10^{-6} (**Figure 7A**). At the same time, near the bottom at the canyon head (10 m above sea floor at the 110 m isobath), down-canyon currents increased from 0 to 0.35 *m/s*, vertical velocity accelerated from 0 to -13 *mm/s* (**Figure 7B**), temperature increased to about 12 °C, and the density anomaly decreased to 26.8 $kg\ m^{-3}$ (**Figure 7C**). From the end of March 5 to March 7, as wind speed gradually decreased, the cross-shelf SSH gradient and current velocities all gradually decreased, though the temperature and density anomalies roughly stayed constant.

3.3.2 Effect of Tides on Canyon Upwelling and Downwelling

The ocean's response to subtidal and tidal forces is a superimposition of various processes operating on different time scales. Due to the speed of glider's motion, their observations tend to convolve mesoscale spatial variability with temporal variability driven by tides. However, we can easily separate subtidal events and tidal variabilities in numerical models. Time series at the canyon head from the Tide and No-Tide simulations showed the same sub-tidal upwelling and downwelling events in response to changes in winds and cross-shelf SSH gradients. Tidal oscillations were superimposed on the sub-tidal events in the Tide case (**Figures 7B, C**) and were absent in the No-Tide case (**Figures 7D, E**).

In the Tide case, time series of near-bottom velocities, temperature, and density all displayed the sub-tidal events of upwelling and downwelling as well as tidal oscillations (**Figures 7B, C**). The sub-tidal upwelling event (February 25 - March 4) corresponded to 8.5 days of upwelling-favorable southwesterly and northwesterly winds and persistently positive cross-shelf SSH gradients (**Figure 7A**). The sub-tidal downwelling event (March 4-7) corresponded to 3.5 days of downwelling-favorable northerly and northeasterly winds and persistently negative cross-shelf SSH gradients. Tidal oscillations were mainly semi-diurnal, and superimposed on the sub-tidal signals (**Figures 7A–C**).

In the No-Tide case, where tidal forcing was turned off, the sub-tidal events of canyon upwelling and downwelling, demonstrated by the time series of velocities, temperature, and density, still occurred in the same periods and at nearly the same magnitudes (**Figures 7D, E**).

These results suggest that observed and modeled canyon upwelling and downwelling events were sub-tidal processes driven by winds and pressure gradients (associated with SSH gradients), and they would occur with or without tidal forcing.

3.3.3 Spatial Views of Upwelling and Downwelling Flows

The strongest flows during both upwelling and downwelling were located at the canyon head. During the upwelling event, upwelling flow delivered ISW and USW from 215-100 m depths through the canyon head onto the outer shelf; in the ensuing downwelling event, the previously upwelled water flowed down-slope inside the canyon in bottom-intensified currents.

The modeled horizontal velocity *hvel* and vertical velocity *w* at the shelf-break depth of z=150 m are shown in **Figure 8**. On March 1, at the peak of the upwelling period, maximum velocities (up-canyon *hvel* and upward *w*) were at the canyon head (**Figures 8A, C**). On March 5, at the peak of the downwelling period, the maximum velocities (down-canyon *hvel* and downward *w*) spread near the canyon head and along the northeast flank of the upper canyon (**Figures 8B, D**). Comparing the two scenarios (March 1 vs. March 5),

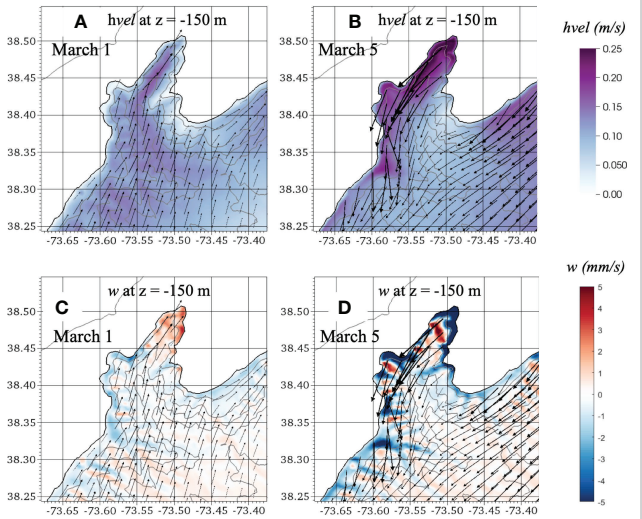

FIGURE 8 | Modeled fields of **(A, B)** horizontal velocity hvel and **(C, D)** vertical velocity w at the shelf-break depth of z = -150 m. hvel vectors were interpolated from unstructured model mesh (**Figure 2B**) to coarser structured grids for visualization. On March 1, at the peak of the upwelling period, maximum velocities (up-canyon hvel and upward w) were at the canyon head (**Figures 8A, C**). On March 5, at the peak of the downwelling period, the maximum velocities (down-canyon hvel and downward w) spread near the canyon head and along the northeast flank of the upper canyon (**Figures 8B, D**). Comparing the two scenarios (March 1 vs. March 5), downwelling had maximum hvel >0.3 m/s and maximum w >15 mm/s, both about twice those calculated during upwelling.

downwelling had maximum *hvel* >0.3 *m/s* and maximum *w* >15 *mm/s*, both about twice those calculated during upwelling.

Transect views of the along-canyon component of horizontal velocity, vertical velocity, and temperature for the transect along the main axis of Wilmington Canyon are shown in **Figure 9**. On March 1, in the quasi-steady maximum phase of the upwelling event, the canyon upwelling flow was characterized by up-canyon horizontal velocity (**Figure 9A**) and upward vertical velocity (**Figure 9C**). Near the canyon head, the flow's horizontal velocity reached 0.4-0.5 *m/s*, and vertical velocity reached about 5 mm/s. This canyon-upwelling flow delivered the lower layers of USW and upper layers of ISW from inside the canyon onto the outer continental shelf (**Figure 9E**). The deepest source of the upwelled water was from a depth of 215 m near the canyon mouth, which was about 50 m below the canyon rim at the canyon's mouth. On March 5, in the downwelling maximum phase, there were bottom-intensified currents flowing down-slope inside the canyon near the canyon head with horizontal velocity of 0.3 *m/s* (**Figure 9B**) and downward vertical velocity of 15 *mm/s* (**Figure 9D**). The previously upwelled dense slope water now fell to 200-350 m depths within the canyon (**Figure 9F**).

3.4 A Canyon-Upwelled Dense Water Overflow Revealed by the Model

The model simulation allowed us to study the fate, dynamics, and impact of the canyon-upwelled slope water on the shelf. As a result of upwelling at Wilmington Canyon, a dense water overflow made of relatively cold and dense ISW was found at the upper canyon and the bottom of the outer shelf northeast of the canyon. During the upwelling event, the overflow water was advected northeastward with shelf currents and grew wider in the cross-shelf direction. In the ensuing downwelling event, shelf currents changed to be southwestward, and the dense overflow water receded back into the canyon.

3.4.1 Development and Recession of the Canyon-Upwelled Dense Water

The development of a canyon-upwelled dense overflow water containing ISW is shown by the temperature and horizontal velocity vectors calculated for the model layer right above the sea floor (**Figure 10A**). Before the upwelling event on February 24, the bottom of the shelf was still occupied by USW (T>12°C). By day 2 of upwelling, on February 26, the canyon-upwelled ISW (T<12°C) was seen at the bottom of the shelf just north of the canyon head. This dense water was sustained on the shelf for the following six days of the upwelling event, during which time it flowed northeastward in the along-shelf direction and spread in the cross-shelf direction. As the dense water overflow developed, the bottom temperature on the downstream shelf between the 75-100 m isobaths cooled from 12-13 °C on February 24 to 10-11 °C on March 1. At the peak of upwelling on March 1, the cold overflow covered > 90% of the outer shelf between 75-150 m isobaths. The only shelf area that remained to be occupied by warmer USW (T>12°C) was located at the corner northeast of the canyon mouth.

The upwelling transported a substantial volume of ISW on to the shelf (**Figure 10B**). Within the area of outer shelf between 75-150 m isobaths and between Wilmington Canyon and Spencer Canyon, the volume of canyon-upwelled ISW with T<12 °C and S>35.2 increased from zero on February 24-25 to $4.5 \times 10^9 m^3$ on February 27, reached $>6 \times 10^9 m^3$ on March 1, and the volume of ISW on the shelf remained above $4.5 \times 10^9 m^3$ until the end of the upwelling period on March 4.

In the downwelling event (March 4-7) that directly followed the upwelling event (February 25 - March 4), the canyon-upwelled ISW receded from the shelf. During this period, the directions of winds and SSH gradients (**Figure 7A**) reversed to be downwelling-favorable, and the shelf currents flowed southwestward (Mar 5, **Figure 10**). Consequently, ISW was no longer being transported from within Wilmington Canyon onto the shelf, and the remaining ISW on the shelf was advected southwestward back towards the canyon. The dense ISW on the shelf decreased in terms of horizontal extent (**Figure 10A**) and total volume (**Figure 10B**).

3.4.2 Impact of Canyon-Upwelling Dense Water on Shelf Circulation

The canyon-upwelled dense water overflow induced an interesting velocity structure during the upwelling event. This is illustrated by the daily mean velocity distributions from March 1 (**Figure 11**). In terms of along-shelf velocity (**Figures 11C, D**), there was a northeastward-flowing frontal jet with speed > 0.5 *m/s* at the shoreward density front associated with the dense overflow (above 75 m isobath). Near the canyon head, the core of

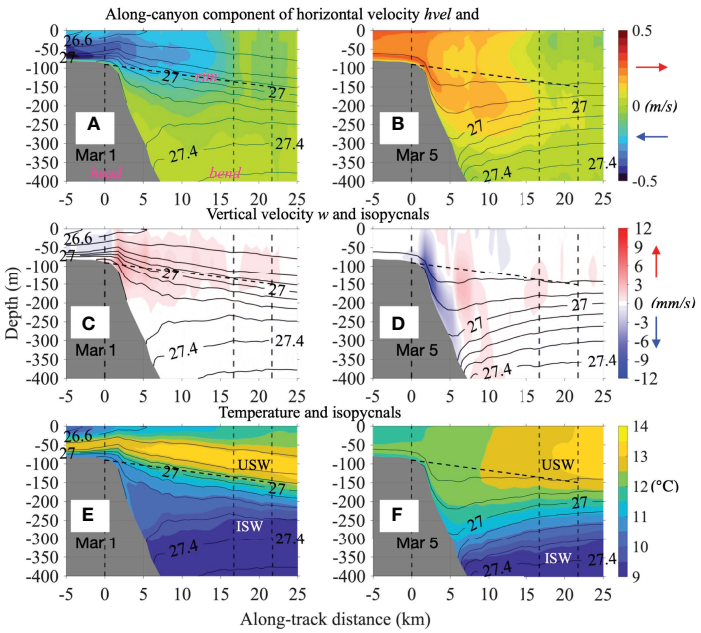

FIGURE 9 | Transect views of daily mean **(A, B)** along-canyon component of horizontal velocity, **(C, D)** vertical velocity w, and **(E, F)** temperature for the transect along the main axis of Wilmington Canyon (location of the transect is shown in **Figure 2B**). On March 1, during canyon upwelling, flow was characterized by up-canyon horizontal velocity and upward vertical velocity. The lower layers of USW and upper layers of ISW from inside the canyon upwelled onto the outer continental shelf. The deepest source of the upwelled water was from about 215 m depth near the canyon mouth, which was about 50 m below the canyon rim at the canyon's mouth. On March 5, during canyon downwelling, there were bottom-intensified currents flowing down-slope inside the canyon near the canyon head with horizontal velocity of 0.3 m/s and downward vertical velocity of 15 mm/s. The previously upwelled dense slope now fell to 200-350 m depths within the canyon.

this frontal jet was about 7 km wide in the cross-shelf direction and was about 30 m thick within the water column at 10-40 m above bottom (**Figure 11C**). Farther downstream (to the northeast), at 15 km away from the canyon, the core of the jet was approximately 10 km wide, and 10-15 m thick (**Figure 11D**). There was also secondary cross-shelf circulation that allowed the overflow water to expand both shoreward and seaward during the upwelling period. Near the canyon head, the daily mean cross-shelf circulation on March 1 was characterized by up to 0.1 *m/s* shoreward velocity on the shoreward and lower half of the overflow, and up to 0.05 *m/s* seaward velocity on the seaward and upper half of the overflow water (**Figure 11E**). Farther downstream, the cross-shelf circulation was characterized by <0.05 *m/s* shoreward velocity on the lower half of the overflow, and up to 0.2 *m/s* seaward velocity on the upper half of the overflow and in the water column above (**Figure 11F**). Both the along-shelf frontal jet and secondary cross-shelf circulation are indicative of density-driven dynamics by the canyon-upwelled overflow.

3.4.3 Dynamics Associated With the Dense Overflow Frontal Jet

To investigate the dynamical drivers of the frontal jet associated with the dense overflow, we focus on a cross-shelf transect just northeast of the canyon head labelled as "Northern-1". During upwelling on February 29, the Northern-1 cross-shelf transect's isopycnals domed at the head of the canyon due to upwelling of dense overflow water onto the shelf (**Figure 12**). Such a density distribution caused a shoreward baroclinic horizontal pressure gradient force (HPGF) to develop on the shoreward side of the canyon head, and seaward baroclinic HPGF to develop on the seward side of the canyon head (**Figure 12B**). Within the overflow water, the baroclinic HPGF was dominant and unbalanced in the cross-shelf direction, likely due to the ageostrophic advection up the canyon (**Figure 12F**), thus the overflow water spread seaward and shoreward from the canyon head by the cross-shelf baroclinic HPGF (**Figure 12F**).

Meanwhile, on the shoreward side of the canyon head both the baroclinic and barotropic HPGFs were in same direction toward the shore during upwelling; and on the seaward side of the canyon head, they opposed each other. Thus, the total HPGF was greater in magnitude on the shoreward side of the canyon head than the seaward side. Geostrophic balance required a greater Coriolis force on the shoreward side of the canyon head (**Figure 12C**). This implies that the along-shelf overflow current in the form of a northeastward subsurface baroclinic jet would develop on the shoreward flank of the canyon-upwelled dense water (**Figures 11C, D**). At the Northern-2 cross-shelf transect farther downstream of the canyon (**Figures 12G–L**), isopycnals were nearly parallel to the bottom, and the main force terms were in geostrophic balance (**Figure 12L**). However, the distribution of baroclinic HPGF was still shoreward on the shoreward flank of the dense water, and seaward on the seaward flank of the dense water (**Figure 12H**). Consequently, the Coriolis force was also

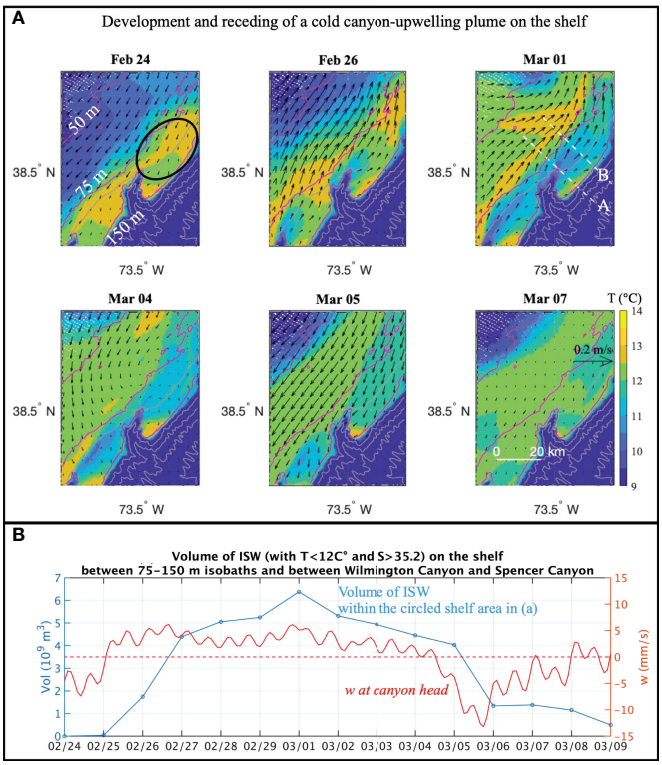

FIGURE 10 | **(A)** Daily mean temperature and horizontal velocity vectors calculated for the model layer right above the sea floor. A canyon-upwelled dense water overflow consisting of cold ISW developed on the shelf northeast of Wilmington Canyon during the upwelling phase, and the dense water receded from the shelf during the downwelling phase. **(B)** Daily mean volume of ISW (blue line) calculated within the circled shelf area northeast of Wilmington Canyon (between 75-m and 150-m isobaths). Red line is the 2-hourly vertical velocity at the canyon head.

greater on the shoreward flank of the dense water here (**Figure 12I**), thus there was the northeastward subsurface baroclinic jet.

4 DISCUSSION

4.1 Impact of Canyon-Upwelled Dense Water on the Canyon Flow During the Ensuing Downwelling Event

In this study, despite the speeds of shelf currents being about equal during the upwelling and downwelling events (March 1 & 5 in **Figure 10**), flows within Wilmington Canyon were stronger during the downwelling event than seen in the preceding upwelling event (March 1 & 5 in **Figures 8**, **9**). These results with angled canyon alignment and realistic bathymetry are different idealized modeling studies that showed canyon upwelling would be stronger than canyon downwelling (Klinck, 1996; Spurgin and Allen, 2014; Zhang and Lentz, 2017) under equal-strength background conditions. The parallel alignment of the upper canyon with the shelfbreak means there is a dynamical bias for enhanced gravity assisted down canyon flow. However, the details of such dynamical balances remain a topic of future investigation. In addition, our study of Wilmington Canyon investigated a real-world scenario in which a downwelling event immediately followed an upwelling event. In the upwelling phase, dense slope water was upwelled onto and sustained on the shelf. When the upwelling event ended, and conditions changed to be downwelling-favorable, the previously canyon-upwelled dense water that had been accumulated on the shelf was advected southwestward by the along-shelf shelf currents towards the canyon, which is oriented nearly along-shelf. The canyon-upwelled water then flowed down-slope toward deeper parts of the canyon causing bottom-intensified flow in the upper canyon. This receding of the previous upwelled water enhanced the effect of advection-driven canyon downwelling. As a result, the flow velocities in Wilmington Canyon in the downwelling event were stronger than seen in the preceding upwelling event.

4.2 Canyon Upwelled Dense Overflow Water in the MAB

The canyon-upwelled overflow from Wilmington Canyon resembled those reported in previous studies of canyon upwelling. These previous studies were based on either numerical simulations (e.g. Kämpf, 2009; Kämpf, 2010; Howatt and Allen, 2013; Ramos Musalem, 2020; Saldías and Allen, 2020) or laboratory models (Ramos Musalem, 2020) of idealized

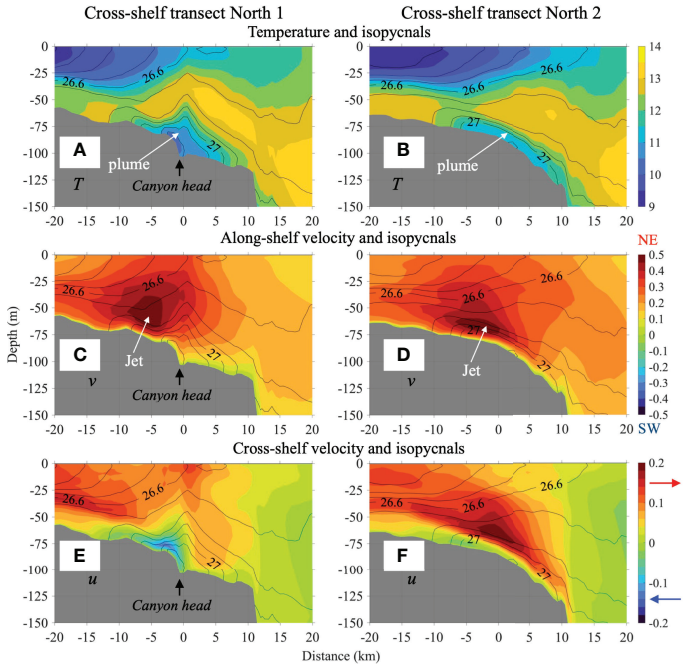

FIGURE 11 | Cross-shelf transect views of daily mean **(A, B)** temperature, **(C, D)** along-shelf velocity, and **(E, F)** cross-shelf velocity on March 1 during the upwelling event, contours are isopycnals. The locations of transects A and B are shown in **Figure 10** (Mar 1). The positive direction of along-shelf velocity is pointing northeastward, of cross-shelf velocity is pointing seaward. The cold and dense canyon-upwelled dense water overflow was seen at the canyon head. A subsurface along-shelf frontal jet was located at the shoreward flank of the canyon-upwelled overflow water. The frontal jet flowed towards northeast. At transect A, the dense water also expanded both shoreward and seaward in the cross-shelf direction.

straight and smooth canyons that were oriented perpendicular to the shelf-break. In contrast, our study represented Wilmington Canyon and the surrounding area using non-smoothed bathymetry (based on GMRT), and relatively realistic forcing conditions (with inputs of winds, tides, ocean currents, water column structure from data-assimilative models). Despite these differences, our modeling study and previous studies all showed a canyon-upwelled dense water developed on the continental shelf, and a near-bottom frontal jet on the shoreward flank of the upwelled dense water.

A canyon-upwelled dense water overflow consisting of ISW has not been reported in previous observational studies of the MAB. Although intrusions of the warm (>14 °C) USW at the outer shelf is a common feature in the MAB, the presence of colder and denser ISW on the shelf has been rarely observed. This discrepancy between modeling results and existing observations may be attributed to the fact that most hydrographic observations on the shelf avoid the bottom boundary layer (~0-10 m above bottom) and that continuous and high-resolution observations at the canyon heads and right downstream (northeast) of canyons during upwelling events are very rare. As a result, the presence of dense overflow water on the shelf resulting from canyon upwelling events may have consistently escaped previous observational efforts.

In this study, although a hint of ISW was observed on the outer shelf (**Figures 3**, **4**), the glider observations were insufficient to resolve the canyon upwelled overflow shown in the model. An operational reason was that the glider was programmed to avoid hitting the seafloor, therefore the bottom 5-10 m of the water column on the shelf was generally not well sampled. More importantly, the glider survey did not have sufficient spatial coverage on the outer shelf northeast of Wilmington Canyon where the dense water on the shelf would have resided.

In order to capture canyon-upwelled dense water from a shelf-break canyon in the MAB, we have the following recommendation for future observations: (1) high resolution hydrographic observations at the canyon head, especially the near-bottom 20 m northeast of a canyon; (2) conduct the study over a sustained period so that it can capture the episodic event when sub-tidal flows are northeastward over the outer shelf and shelf-break, especially during prolonged (>2 days) and strong (e.g. ≥10 *m/s*) upwelling-favorable wind events; (3) employ a complimentary set of moored array (profiler moorings capable of profiling from the bottom up to the surface, lined from the canyon head to the downstream shelf) and mobile platforms (gliders, AUVs or shipboard surveys for quick and high-resolution synoptic transects in both the along-overflow and across-overflow directions).

Canyon-upwelled dense overflows are likely important features that have the potential to supply significant quantities of water, salt, and nutrients from continental slope waters to the

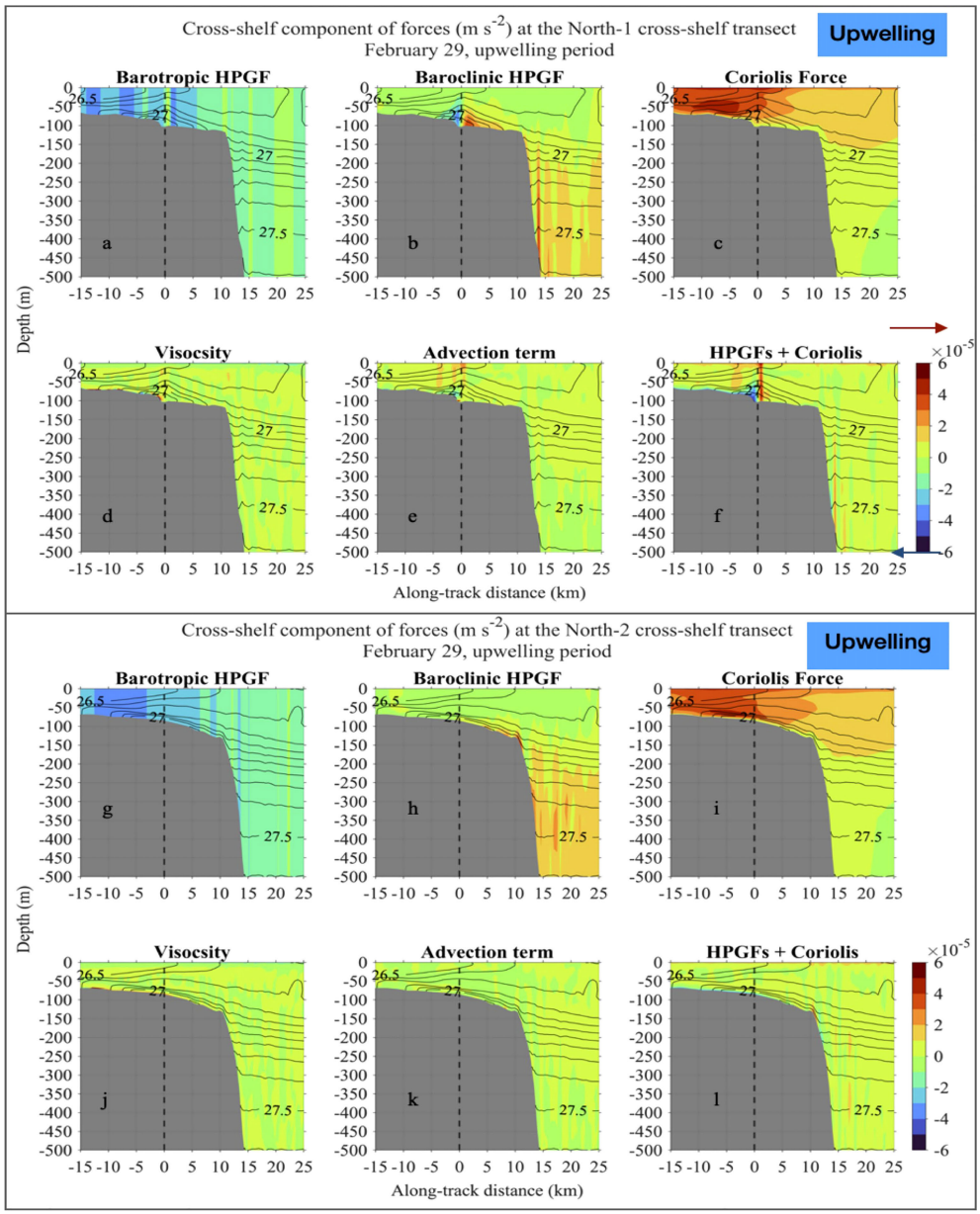

FIGURE 12 | Cross-shelf momentum balance for February 29, 2016 at the North-1 transect just northeast of the head of the canyon **(A–F)** and the North-2 transect 20 km northeast of the North-1 transect **(G–L)**. **(A, G)** Barotropic horizontal pressure gradient force. **(B, H)** Baroclinic horizontal pressure gradient force. **(C, I)** Coriolis Force. **(D, J)** Viscosity. **(E, K)** Advection. **(F, L)** HPGF + Coriolis.

continental shelf of the MAB. The overflow at Wilmington Canyon characterized in this study had its source water from the ISW, which were located roughly at 150 – 215 m depths. The peak volume of ISW contained in the overflow was estimated to be $> 6 \times 10^9 m^3$. Thus, it is reasonable to conclude that submarine canyons may supply a significant quantity of ISW onto the shelf during upwelling events. In addition, ISW is saltier than shelf waters, and has relatively high nutrient concentration (e.g. He et al., 2011), thus upwelled ISW may be a significant source of salt and nutrients from the slope sea to the shelf.

5 CONCLUSIONS

We used observations from a glider survey and a numerical model with relatively realistic bathymetry and forcing to analyze a cycle of wind-driven canyon upwelling and downwelling that occurred over Wilmington Canyon in the southern MAB. In this cycle of events, an upwelling event (February 25 - March 3, 2016) was immediately followed by a downwelling (March 4-7, 2016) event. During the upwelling event, winds were upwelling-favorable, sea level increased seaward, shelf currents flowed

northeastward, ISW originating from 150-215 m depths within the canyon was channeled onto the shelf, and formed a cold and dense canyon-upwelled overflow on outer continental shelf (75-150 m isobaths) northeast of the canyon. The overflow contained up to $6 \times 10^9 m^3$ of ISW, lowered the bottom temperature of the outer shelf by up to 2°C, and induced a near-bottom frontal jet with speeds over 0.5 *m/s*. In the ensuing downwelling event, winds were downwelling-favorable, sea level increased landward, shelf-currents were southwestward, and the previously upwelled ISW receded from the shelf to the canyon, causing 0.3 *m/s* bottom-intensified down-slope currents in the upper canyon near the canyon head. Canyon upwelled dense water overflows have not been reported in previous observational studies of the MAB due to their location specificity and episodic nature. However, they have the potential to supply and entrain significant quantities of water, salt, and nutrients from the slope sea to the continental shelf of the MAB.

DATA AVAILABILITY STATEMENT

The observational data and model outputs used in this study will be made available by the authors, without undue reservation.

AUTHOR CONTRIBUTIONS

HW conducted glider survey, numerical modeling, data analysis, data visualization, and writing. DG obtained funding, conducted glider survey, participated in data analysis and writing. MF participated in data analysis and writing. CH participated in data analysis and writing. TM participated in data analysis and writing. H-CY participated in numerical modeling and data analysis. YZ participated in numerical modeling, data analysis, and writing. All authors contributed to the article and approved the submitted version.

FUNDING

We thank the Mid-Atlantic Regional Association Coastal Ocean Observing System (MARACOOS, https://maracoos.org) for funding of this project. We thank the VIMS/SMS Office of Academic Studies for supporting Haixing Wang throughout his Ph.D. study. The work was supported by NOAA grant NA16NOS0120020/5940.

ACKNOWLEDGMENTS

We thank captains Sean Fate and PG Ross from the Virginia Institute of Marine Science (VIMS) Eastern Shore Lab, and David Aragon from Rutgers University for their assistance in the glider deployment. We thank William & Mary Research Computing for providing computational resources and technical support (https://www.wm.edu/it/rc). This paper is Contribution No.4102 of the Virginia Institute of Marine Science, William & Mary.

REFERENCES

Allen, S. E., and Durrieu de Madron, X. (2009). A Review of the Role of Submarine Canyons in Deep-Ocean Exchange With the Shelf. *Ocean Sci.* 5 (4), 607–620. doi: 10.5194/os-5-607-2009

Allen, S. E., and Hickey, B. M. (2010). Dynamics of Advection-Driven Upwelling Over a Shelf Break Submarine Canyon. *J. Geophys. Res. Oceans* 115 (C8). doi: 10.1029/2009JC005731

Brovchenko, I., and Maderich, V. (2011). Study of the Role of Underwater Canyons in Sediment Transport From the Black Sea East Coast. *Int. J. Comput. Civ. Struct. Eng.* 7 (2), 39–46.

Butman, B. (1986). *North Atlantic Slope and Canyon Study. Volume 2* (Woods Hole, MA (USA: Geological Survey).

Church, T. M., Mooers, C. N., and Voorhis, A. D. (1984). Exchange Processes Over a Middle Atlantic Bight Shelfbreak Canyon. *Estuar. Coast. Shelf Sci.* 19 (4), 393–411. doi: 10.1016/0272-7714(84)90093-3

Connolly, T. P., and Hickey, B. M. (2014). Regional Impact of Submarine Canyons During Seasonal Upwelling. *J. Geophys. Res. Oceans* 119 (2), 953–975. doi: 10.1002/2013JC009452

Freeland, H. J. (1982). A Topographically Controlled Upwelling Center Off Southern Vancouver Island. *J. Mar. Res.* 40, 1069–1093.

Garau, B., Ruiz, S., Zhang, W. G., Pascual, A., Heslop, E., Kerfoot, J., et al (2011). Thermal Lag Correction on Slocum CTD Glider Data. *J. Atmos. Ocean. Technol.* 28 (9), 1065–1071. doi: 10.1175/JTECH-D-10-05030.1

Haney, R. L. (1991). On The Pressure Gradient Force Over Steep Topography in Sigma Coordinate Ocean Models. *J. Phys. Ocean.* 21, 610–618.

Harris, C. K., Butman, B., and Traykovski, P. (2003). Winter-Time Circulation and Sediment Transport in the Hudson Shelf Valley. *Cont. Shelf Res.* 23 (8), 801–820. doi: 10.1016/S0278-4343(03)00025-6

He, R., Chen, K., Fennel, K., Gawarkiewicz, G. G., and McGillicuddy, D. J.Jr. (2011). Seasonal and Interannual Variability of Physical and Biological Dynamics at the Shelfbreak Front of the Middle Atlantic Bight: Nutrient Supply Mechanisms. *Biogeosciences* 8 (10), 2935. doi: 10.5194/bg-8-2935-2011

Hickey, B. M. (1997). The Response of a Steep-Sided, Narrow Canyon to Time-Variable Wind Forcing. *J. Phys. Oceanogr.* 27 (5), 697–726. doi: 10.1175/1520-0485(1997)027<0697:TROASS>2.0.CO;2

Howatt, T. M., and Allen, S. E. (2013). Impact of the Continental Shelf Slope on Upwelling Through Submarine Canyons. *J. Geophys. Res. Oceans* 118 (10), 5814–5828. doi: 10.1002/jgrc.20401

Hunkins, K. (1988). Mean and Tidal Currents in Baltimore Canyon. *J. Geophys. Res. Oceans* 93 (C6), 6917–6929. doi: 10.1029/JC093iC06p06917

Kämpf, J. (2006). Transient Wind Driven Upwelling in A Submarine Canyon: A Process Oriented Modeling Study. *J Geophys Res: Oceans* 111 (c11).

Kämpf, J. (2009). On the Interaction of Time-Variable Flows With a Shelfbreak Canyon. *J. Phys. Oceanogr.* 39 (1), 248–260. doi: 10.1175/2008JPO3753.1

Kämpf, J. (2010). On Preconditioning of Coastal Upwelling in the Eastern Great Australian Bight. *J. Geophys. Res. Oceans* 115 (C12). doi: 10.1029/2010JC006294

Kämpf, J. (2012). Lee Effects of Localized Upwelling in a Shelf-Break Canyon. *Cont. Shelf Res.* 42, 78–88. doi: 10.1016/j.csr.2012.05.005

Klinck, J. M. (1996). Circulation Near Submarine Canyons: A Modeling Study. *J. Geophys. Res. Oceans* 101 (C1), 1211–1223. doi: 10.1029/95JC02901

Lentz, S. J. (2010). The Mean Along-Isobath Heat and Salt Balances Over the Middle Atlantic Bight Continental Shelf. *J. Phys. Oceanogr.* 40 (5), 934–948. doi: 10.1175/2009JPO4214.1

Lentz, S. J., Butman, B., and Harris, C. (2014). The Vertical Structure of the Circulation and Dynamics in Hudson Shelf Valley. *J. Geophys. Res. Oceans* 119 (6), 3694–3713. doi: 10.1002/2014JC009883

Liu, Z., Wang, H. V., Zhang, Y., Magnusson, L., Loftis, J. D., and Forrest, D. (2020). Cross-Scale Modeling of Storm Surge, Tide, and Inundation in Mid-Atlantic Bight and New York City During Hurricane Sandy 2012. *Estuar. Coast. Shelf Sci.* 233. doi: 10.1016/j.ecss.2019.106544

McDougall, T. J., and Barker, P. M. (2011). Getting Started With TEOS-10 and the Gibbs Seawater (GSW) Oceanographic Toolbox 28.

Ramos Musalem, A. K. (2020). *Transport Through Submarine Canyons* (Doctoral dissertation, University of British Columbia).

Ryan, W. B. F., Carbotte, S. M., Coplan, J. O., O'Hara, S., Melkonian, A., Arko, R., et al (2009). Global Multi-Resolution Topography Synthesis. *Geochem. Geophys. Geosyst.* 10, Q03014. doi: 10.1029/2008GC002332

Saldías, G. S., and Allen, S. E. (2020). The Influence of a Submarine Canyon on the Circulation and Cross-Shore Exchanges Around an Upwelling Front. *J. Phys. Oceanogr.* 50 (6), 1677–1698. doi: 10.1175/JPO-D-19-0130.1

She, J., and Klinck, J. M. (2000). Flow Near Submarine Canyons Driven by Constant Winds. *J. Geophys. Res. Oceans* 105 (C12), 28671–28694. doi: 10.1029/2000JC900126

Spurgin, J. M., and Allen, S. E. (2014). Flow Dynamics Around Downwelling Submarine Canyons. *Ocean Sci.* 10, 799–819. doi: 10.5194/os-10-799-2014

Webb, D. C., Simonetti, P. J., and Jones, C. P. (2001). SLOCUM: An Underwater Glider Propelled by Environmental Energy. *IEEE J. Ocean. Eng.* 26 (4), 447–452. doi: 10.1109/48.972077

Ye, F., Zhang, Y., He, R., Wang, Z., Wang, H. V., and Du, J. (2019). Third-Order WENO Transport Scheme for Simulating the Baroclinic Eddying Ocean on an Unstructured Grid. *Ocean Model.* 143, 101466. doi: 10.1016/j.ocemod.2019.101466

Zhang, W., and Lentz, S. J. (2017). Wind-Driven Circulation in a Shelf Valley. Part I: Mechanism of the Asymmetrical Response to Along-Shelf Winds in Opposite Directions. *J. Phys. Oceanogr.* 47 (12), 2927–2947. doi: 10.1175/JPO-D-17-0083.1

Zhang, Y. J., Ye, F., Stanev, E. V., and Grashorn, S. (2016). Seamless Cross-Scale Modeling With SCHISM. *Ocean Model.* 102, 64–81. doi: 10.1016/j.ocemod.2016.05.002

Conflict of Interest: The authors declare that the research was conducted in the absence of any commercial or financial relationships that could be construed as a potential conflict of interest.

Publisher's Note: All claims expressed in this article are solely those of the authors and do not necessarily represent those of their affiliated organizations, or those of the publisher, the editors and the reviewers. Any product that may be evaluated in this article, or claim that may be made by its manufacturer, is not guaranteed or endorsed by the publisher.

Copyright © 2022 Wang, Gong, Friedrichs, Harris, Miles, Yu and Zhang. This is an open-access article distributed under the terms of the Creative Commons Attribution License (CC BY). The use, distribution or reproduction in other forums is permitted, provided the original author(s) and the copyright owner(s) are credited and that the original publication in this journal is cited, in accordance with accepted academic practice. No use, distribution or reproduction is permitted which does not comply with these terms.

frontiers | Frontiers in Marine Science

ORIGINAL RESEARCH
published: 17 June 2022
doi: 10.3389/fmars.2022.863227

Local And Deep-Ocean Forcing Effects on the West Florida Continental Shelf Circulation and Ecology

Robert H. Weisberg and Yonggang Liu*

College of Marine Science, University of South Florida, St. Petersburg, FL, United States

We review the evolution of knowledge on the forcing of the west Florida continental shelf by a combination of local winds and deep-ocean influences, and we provide application examples regarding the relationships between the shelf responses to these forcing functions and certain ecological phenomena, including blooms of the harmful alga, *Karenia brevis*, recruitment of gag juveniles and how Deepwater Horizon hydrocarbons may have affected west Florida reef fish and the shoreline. Our approach employs a coordinated set of observations and numerical circulation model simulations, wherein the observations, by providing reasonable veracity checks on the model simulations, allow for further dynamical analyses that would otherwise be unavailable from the observations alone. For the case of local forcing only, we provide two dynamically consistent definitions of the inner-shelf and outer-shelf regions, and for the case of deep-ocean forcing, we show how the west Florida shelf geometry (with regard to certain geophysical fluid dynamics principles) can result in the entire shelf region being impacted by the Gulf of Mexico Loop Current. Thus, we help to explain why the west Florida shelf experiences large inter-annual variations in shelf ecology, providing impetus for further interdisciplinary study.

Keywords: inner-shelf, outer-shelf, local forcing, deep-ocean forcing, ecological impacts, coastal upwelling, West Florida shelf

OPEN ACCESS

Edited by:
William Savidge,
University of Georgia, United States

Reviewed by:
Veronica Ruiz Xomchuk,
Florida Atlantic University, United States
Jeffrey W. Book,
United States Naval Research Laboratory, United States

***Correspondence:**
Robert H. Weisberg
weisberg@usf.edu

Specialty section:
This article was submitted to Coastal Ocean Processes, a section of the journal Frontiers in Marine Science

Received: *26 January 2022*
Accepted: *29 April 2022*
Published: *17 June 2022*

Citation:
Weisberg RH and Liu Y (2022) Local And Deep-Ocean Forcing Effects on the West Florida Continental Shelf Circulation and Ecology. Front. Mar. Sci. 9:863227. doi: 10.3389/fmars.2022.863227

1 INTRODUCTION

Generally considered as oligotrophic (e.g., Steidinger, 1975; Heil et al., 2001; Vargo et al., 2008; Dixon et al., 2014; O'Neil and Heil, 2014), the west Florida continental shelf (WFS) supports abundant fisheries and, on an inter-annual basis, may experience copious blooms of the toxic dinoflagellate, *Karenia brevis*. This dichotomy begs the question: How can an oligotrophic shelf have such a vibrant and varied ecosystem? The physics of the WFS circulation provides an answer.

Continental shelves, the regions between the shelf break and the shoreline, come in varying widths. Within this geometrical spectrum, the WFS (**Figure 1**) is relatively broad and gently sloping. Bounded in the south by the Florida Keys and in the northwest by the Florida Panhandle, and with the shelf break coinciding approximately with the 75 m isobath offshore from Tampa Bay, decreasing to about the 60 m isobath offshore from the Florida Big Bend, the width of the WFS

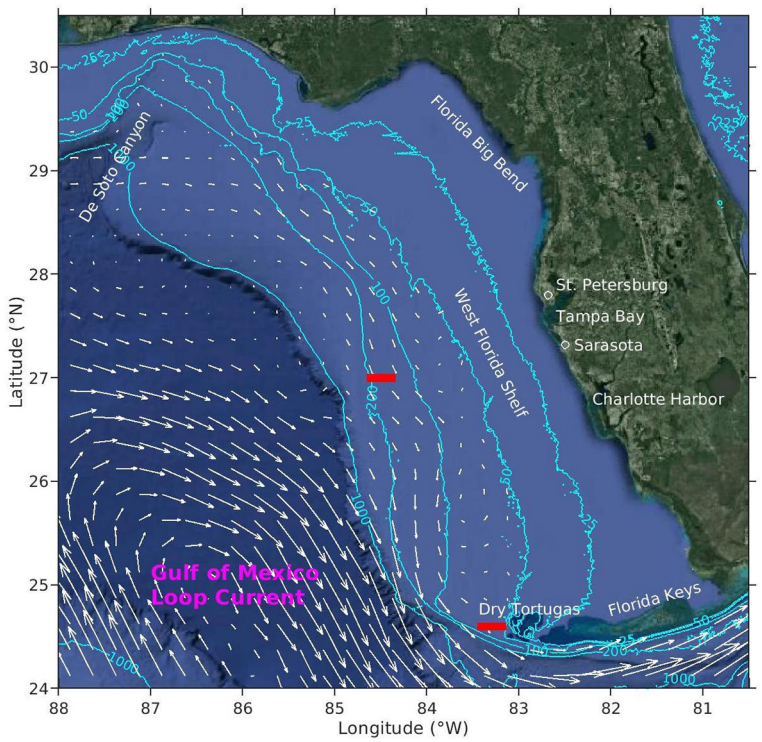

FIGURE 1 | The geometry of the WFS and the various locations referred to in the text. The red lines are of length equivalent to 30 km, the estimated WFS baroclinic, Rossby radius of deformation. Superimposed are surface geostrophic velocity vectors indicating the long-term mean position of the Gulf of Mexico Loop Current (adapted from Liu et al., 2016b).

varies from about 120 km offshore from Tampa Bay to about 180 km offshore from either the Florida Big Bend or the Charlotte Harbor estuary coasts. It then narrows in the Florida Panhandle, where the shelf break is at about the 40 m isobath at the DeSoto Canyon head. These dimensions, relative to the horizontal length scales over which new nutrients of either land or deep-ocean origins may extend, determine (under general conditions) the portions of the shelf that may be either deplete or replete with nutrients; hence oligotrophic, or not.

Separate horizontal length scales apply at the shelf break and the nearshore. At the shelf break, where the frictional boundary layers comprise only a small portion of the water column, the flow dynamics are largely geostrophic, rendering the appropriate horizontal length scale to be the baroclinic Rossby radius of deformation, or the scale over which the pressure gradient and Coriolis forces balance under stratified conditions. WFS observations show this to be about 30 km (He and Weisberg, 2003). The shallower nearshore, where friction is a dominant contributor, is more complex. There the salinity field is of use. Both estuarine and land-drainage inputs of fresh water result in lower nearshore salinity, rendering the salinity gradient region an indicator of how far offshore land-derived nutrients may extend. WFS observations and model simulations suggest some 10-20 km under general conditions (e.g., **Figure 2**).

Thus, if deep-ocean and land-drainage influences extend only 30 km and 10-20 km, respectively, then, with a width of between 120-180 km, there is a large, middle portion of the WFS that should (under general conditions) be deplete of nutrients. Three exceptions are noted. The first is along the Florida Panhandle coast, where the shelf, being only about 30 km wide at the Desoto Canyon head, may have its nutrients replenished regularly by adjacent, deeper ocean waters. The second is that under prolonged westerly wind and/or deep-ocean forcing conditions, Mississippi River water, with relatively high nutrient loads, may be advected to the WFS. Dowgiallo (1994) and Ortner et al. (1995) discuss one such event, Gilbes et al. (1996) shows how northern Florida rivers may add to this, He and Weisberg (2002) shows how the baroclinic structure during the spring transition may facilitate southward advection (as found by Gilbes et al., 1996), and Weisberg et al. (2005) provides three different scenarios by which river waters may transit south, one of which is described by both Morey et al. (2003) and Toner et al. (2003). The third, and the most interesting exception, is that owing to the partial closure of the WFS in the south by the Florida Keys, it is possible for the Gulf of Mexico Loop Current, if it contacts the west Florida escarpment near the Dry Tortugas, to set the entire WFS in motion (Hetland et al., 1999). When this occurs, and if it lasts long enough, then WFS waters may be replenished by deeper ocean waters with elevated inorganic nutrient concentrations that are upwelled and transported landward within the bottom Ekman layer. Such occurrence was observed in 1998 and

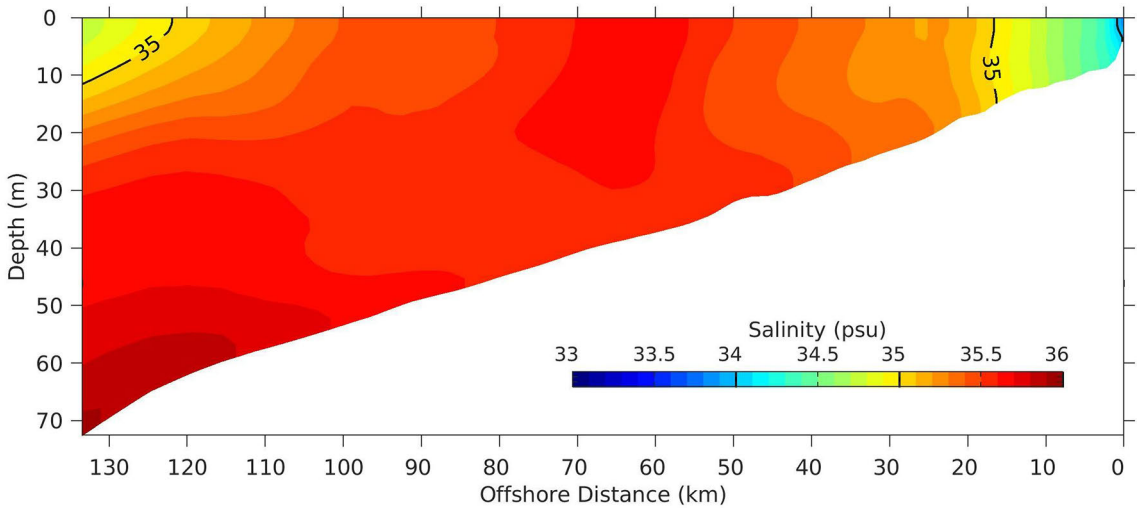

FIGURE 2 | A typical summer season salinity section sampled offshore from Sarasota, FL., as simulated using the West Florida Coastal Ocean Model (WFCOM).

described, along with the associated ecological impacts, by the companion papers of Weisberg and He (2003) and Walsh et al. (2003). This third exception, along with the shelf width, are what makes the WFS such an interesting region to study and what also accounts for the large inter-annual variations in circulation, water properties and ecological responses.

The remainder of the paper is organized as follows. Section 2 provides background information on both local and deep-ocean forcing for the WFS, including the origins and pathways for the new, deeper ocean fluid by which WFS water properties may be renewed through Loop Current-induced upwelling. Section 3 discusses applications to *K. brevis* harmful algae blooms (HABs), fisheries recruitment and harmful substance tracking. Concluding remarks follow in section 4.

2 BACKGROUND

In keeping with the theme of how the circulation may affect water properties and thence ecology, the fundamental dynamical question is how fluid may transit either way between the shelf break and the nearshore. Given the water column thickness that changes monotonically (by virtue of a nearly linearly sloping bottom) between these two shelf termini, background discussions begin with the concepts of mass and angular momentum conservation.

From a mass conservation perspective, it is difficult to move fluid from deeper to shallower water depths, for to do so requires the dislocation of water within a proportionately larger nearshore area to accommodate the volume of fluid coming from greater offshore depth. Conversely, to move fluid from shallower to deeper water, the area would have to shrink proportionately. How to accommodate such areal extent changes defies any simple physical conceptualization. Owing to the Earth's rotation, the changes in relative vorticity (fluid particle angular momentum) are even more difficult to accommodate. Taken together, these two conservation principles, which embody the conservation of potential vorticity, constrain the fluid to flow along lines of constant topography (isobaths). Crossing isobaths requires that these joint mass and angular momentum constraints be broken, either by friction or by the generation of energetic eddy-like motions. A more complete, deductive discussion of these constraints on the local wind, buoyancy and deep-ocean forcing effects for continental shelves may be found in Brink (1998a); Hill (1998), and Brink (1998b), respectively.

Whether moving fluid from deeper to shallower water, or conversely, frictional boundary layers are of primary importance. Ekman (1905) provides the basis for such understanding. A spatially uniform wind stress acting upon the sea surface will set the surface water in motion, and through friction, these surface waters will drive subsurface waters with speed decreasing with depth. The resulting vertical shear will tend to tilt the fluid's planetary vorticity vector, inducing relative vorticity, unless countered at the same rate by a frictional torque. To do this requires a vertical shear in the direction orthogonal to the wind stress, with this vertical shear also decreasing with depth. As a result, the wind-inducted velocity vector, while decreasing in magnitude, must also rotate to the right (in the northern hemisphere) with depth, the end result being the Ekman spiral that extends over a vertical length scale known as the Ekman depth. The Ekman depth is necessarily of relatively small length scale because the frictional dissipation must be large to avoid inducing too much relative vorticity. Thus, for deep regions that are unbounded by land, a uniform wind stress can only impact the near surface, and, when vertically integrated, causes a net water transport to the right of the wind stress (in the northern hemisphere) within this thin, surface (Ekman) layer. WFS observations and model simulations show the Ekman depth to be only a few to about 10-20 m (e.g., Weisberg et al., 2001). As

the water depth decreases toward land and approaches the Ekman depth, the stress of the moving fluid against the bottom modifies the flow, causing a more downwind-directed transport. The coastline further modifies this by allowing water to be set up or down by the Ekman transport divergence, supporting an across-shelf pressure gradient force and an associated geostrophic current that combines with the direct wind-driven current. The geostrophic current, by rubbing against the bottom, results in a bottom Ekman layer with a net transport driven to the left of the geostrophic current because of the pressure gradient. This process of a wind-driven surface flow, causing a geostrophic flow, leading a bottom Ekman layer flow is referred to the Ekman-geostrophic coastal ocean spin-up process (spin-up deriving from the Earth's rotation), and it occurs over a pendulum day, roughly a calendar day for the WFS. The geostrophic portion is along-isobath, whereas the surface and bottom Ekman layer portions have across-isobath directed components. Once established, the surface and bottom Ekman layers are what facilitate the across-shelf transport of fluid and the material properties (nutrients, phytoplankton, fish larvae, etc.) that are contained therein.

It should be noted that these concepts, rooted in Ekman (1905), are based on the parameterization of complex turbulent processes by a constant eddy coefficient. In reality, turbulence-induced friction is generally flow dependent. This, plus the stabilizing effects of stratification, may alter the evolution of the Ekman layers from the structure as originally presented. Lentz (1995) explored the effects of varying the vertical distribution of the eddy coefficient on the shelf response using a two-dimensional, constant density model. The along-shelf component was found to be insensitive relative to the across-shelf component, and it was the divergence of the across-shelf component that determined the extent of the inner shelf. Weisberg et al. (2000) provided a case study demonstrating the Ekman-geostrophic spin-up process for the WFS. Observed, in response to the sudden onset of upwelling favorable winds, was how the near surface velocity vector initially turned to the right of the wind stress before rotating to become more along-isobath as the geostrophic interior flow set in, and thence how the flow closer to the bottom turned toward the left as bottom friction induced a bottom Ekman layer response. This entire evolution, as observed over the full water column with a moored, Acoustic Doppler Current Profiler (ADCP), occurred over the course of a pendulum day.

2.1 Local Forcing

The WFS is forced regularly by synoptic scale weather systems, particularly in winter months. These generally entail southerly winds in advance of frontal passage, followed by northerly winds in the wake of frontal passage. Pioneering observations on WFS responses to such synoptic scale systems are given by Niiler (1976); Marmorino (1982; 1983) Mitchum and Sturges (1982); Cragg et al. (1983), and Weatherly and Thistle (1997), and pioneering numerical model simulations are given by Hsueh et al. (1982); Marmorino (1982), and Cooper (1987). As anticipated from the associated Ekman-geostrophic spin up discussion, these studies either observed or simulated coastal sea levels tending to rise as the front approaches and fall after the front passes. The observations also showed the Ekman and geostrophic velocity tendencies, but with limited temporal and spatial coverage. Further details had to await the advent of ADCPs for fuller water column sampling and increased computational resources for more realistic model domains and higher spatial resolutions.

Another insightful line of inquiry entailed a time-dependent analytical approach. Gill and Schumann (1974) developed a formalism for projecting wind forcing onto a set of continental shelf wave modes and integrating these in time and space to estimate the continental shelf response. Applications of such forced wave technique to the WFS for cases of idealized wind forcing, including the effects of friction on the wave modes, are given by Clarke and Van Gorder (1986) and Lopez and Clarke (1989), using the coastal boundary condition derived by Mitchum and Clarke (1986a). Mitchum and Clarke (1986b) then demonstrated the utility of this approach in accounting for both the coastal sea level variations associated with frontal passage and for estimating the vertically averaged along-shelf currents calculated geostrophically from the model pressure gradient field. A limitation, however, is that the analytical model effectively eliminates most of the inner-shelf by virtue of its coastal boundary condition being applied seaward of the region of overlapping surface and bottom Ekman layers (Mitchum and Clarke, 1986a) taken to be at about the 25 m isobath. Moreover, by only considering the vertically-averaged along-shelf geostrophic current between the 25m isobath and the shelf break, across-shelf exchanges are not included, nor is the response to major storm events such as hurricanes. Overcoming these limitations requires more complete, numerical circulation models.

In two related papers, Li and Weisberg (1999a; 1999b) applied the Princeton Ocean Model (POM) of Blumberg and Mellor (1987) with constant density, forced from rest by spatially uniform winds, to study the kinematics and dynamics, respectively, of the WFS responses to either upwelling or downwelling favorable winds. By applying a primitive equation model with realistic coastline and bathymetry, plus a flow dependent turbulence closure sub-model (Mellor and Yamada, 1982), the structure of the WFS responses to idealized wind stress and its spin-up was diagnosed, free from other simplifying assumptions.

Two different upwelling and downwelling cases were explored, the upwelling ones being for along-shelf winds (from the north-northwest) and offshore winds (from the east-northeast), and the downwelling ones being for along-shelf winds (from the south-southeast) and onshore winds (from the west-southwest). Under constant density, the along-shelf wind cases showed similar, but opposite responses for upwelling and downwelling. Spin-up occurred over a pendulum day, as expected, with sea levels set up or down by Ekman layer divergences, and an inner-shelf region was clearly definable from the momentum balance equations. As an example, **Figure 3** shows the terms in the vertically integrated along-shelf and across-shelf momentum equations sampled after the model simulation approached steady state for an across-shelf section offshore from Sarasota, FL (**Figure 1**). The across-shelf

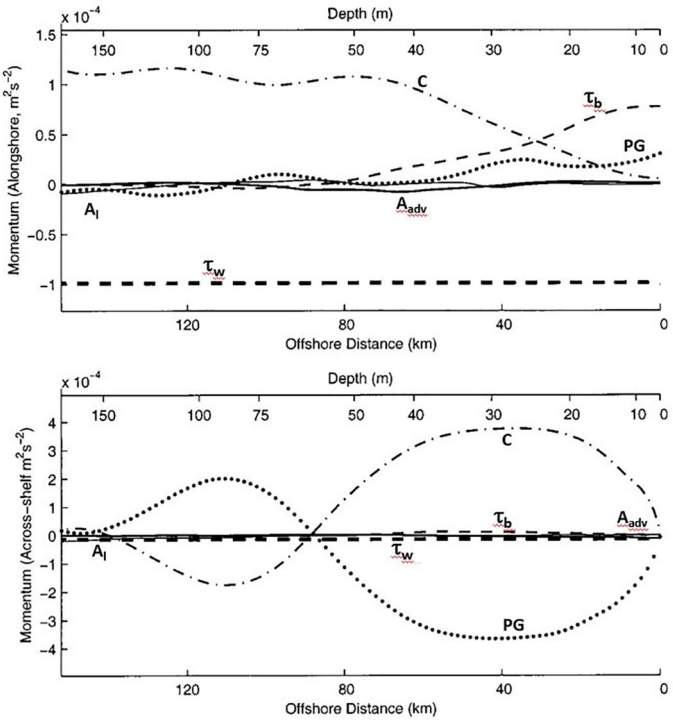

FIGURE 3 | Terms in the vertically integrated momentum balance at quasi-steady state for an initial value problem in which the WFS is forced from rest by an upwelling favorable wind stress in an application of the Princeton Ocean Model (from Li and Weisberg, 1999b). The top panel is for the along-shelf direction and the bottom panel is for the across-shelf direction. The dotted line is the pressure gradient term (PG), the dot-dashed line is the Coriolis term (C), the plain-dashed line is the bottom stress (τ_b), and the bold-dashed line is the surface stress (τ_w). The bold-solid and the plain solid lines are the advective (A_{adv}) and local (A_l) acceleration terms, respectively.

balance at quasi-steady state is quite simple, i.e., it is geostrophic, with the vertically integrated pressure gradient and Coriolis forces very nearly in balance. The change in sign at the outer edge of the inner-shelf is due to the complete closure (in the model) by the Florida Keys in the south and thus a reversal of flow. The organization of the inner-shelf is evidenced further by the along-shelf momentum balance terms. Seaward of approximately the 50 m isobath is a near balance between the wind stress and the vertically integrated Coriolis term, i.e., an Ekman balance, free from bottom effects. Landward from about the 50 m isobath is a gradual decrease in the vertically integrated Coriolis force, accompanied by a compensating increase in the bottom stress. The smaller increase in the pressure gradient term reflects the fact that the coastline is not straight; the isobaths do converge and diverge, as would be the case for any realistic continental shelf. The inner-shelf is therefore the transition zone in which bottom stress reduces from being a major to a minor contributor to the momentum balance when transiting away from the shoreline. Whether or not the surface and bottom Ekman layers overlap within this transition zone is not a major factor; instead, it is their interaction through divergence that determines the inner-shelf (as will be seen in the stratified case).

The onshore or offshore wind cases are also illuminating. Given realistic bottom bathymetry, onshore or offshore winds generate a nearshore pressure gradient force necessary to balance the wind stress in shallow water because the flow is directed downwind there, versus orthogonal to the wind farther offshore (as originally shown by Ekman, 1905); hence, coastal sea level is set up or down. This Li and Weisberg (1999a); Li and Weisberg (1999b) finding for the WFS was followed by subsequent studies such as Tilburg (2003) who performed a series of two-dimensional model simulations showing that across-shelf winds can result in across-shelf velocities in the upper few meters of the water column that are similar in magnitude to those induced by the along-shelf winds, Liu and Weisberg (2005a) who diagnosed in-situ observations to assess the role of across-shelf winds in the inner-shelf momentum balance and Fewings et al. (2008) who further considered the effects of waves to demonstrate an asymmetry in the inner-shelf responses to across-shelf wind forcing.

Stratification provides further nuance. Using the same model configuration [as in (Li and Weisberg 1999a; Li and Weisberg 1999b)], but with realistic stratification and time dependent wind forcing, Weisberg et al. (2001) provided detailed comparisons between observed and modeled sea level and velocity, along with dynamical analyses, for the month of April 1998. The sea level comparisons were at St. Petersburg, FL, and velocity comparisons were at the 20 m and 50 m isobaths offshore from Sarasota, FL. The velocity components were sampled across the entire water

column at 1 m intervals using moored ADCPs. A twin experiment performed with constant density enabled comparisons between simulations with and without stratification. April 1998 experienced a succession of three upwelling and downwelling favorable wind events, and the simulation with stratification agreed reasonably well with the sea level and velocity observations. Simulated sea level tracked nearly identically with observations for the stratified experiment and deviated somewhat for the constant density experiment. The velocity observations, when compared with the simulations, exhibited larger disparities between the stratified and constant density cases. Therefore, the inclusion of stratification was found to be quite important.

With stratification, both the observations and the model simulations showed reversals of the across-shelf and the along-shelf velocity components at the 20 m isobath with each reversal in wind forcing. For upwelling favorable winds, the observed near-bottom flows were directed onshore while the observed near-surface flows were directed offshore, and conversely for downwelling favorable winds. Interestingly, whereas the wind magnitudes were similar for these wind reversals, the observed upwelling responses were disproportionately larger and extended farther offshore than the observed downwelling responses. These observed asymmetric behaviors were also found in the simulations with stratification, but not in the constant density simulations. Thus, stratification caused an asymmetry in the upwelling/downwelling responses.

Explanations may be provided using either force or vorticity balance arguments. From a force balance perspective, the sea level response to downwelling favorable winds results in an offshore-directed pressure gradient force that drives an offshore-directed flow in the bottom Ekman layer. Isopycnals bending into the bottom result in an opposing buoyancy force. In contrast, the sea level response to upwelling favorable winds results in an onshore-directed pressure gradient force that drives an onshore-directed flow in the bottom Ekman layer. However, and opposite to the downwelling case, isopycnals bending into the bottom (across the bottom Ekman layer, as occurs by turbulence mixing and a zero normal heat flux constraint at the sediment/water interface) provide a buoyancy force that adds constructively to the surface slope induced pressure gradient force, thereby enhancing the upslope flow. The result is that the across-shelf flows within the bottom Ekman layer for upwelling winds are enhanced over that for downwelling winds. Simulation examples of the isopycnal slopes and their effect on the force balances are provided in Weisberg et al. (2001).

An equally compelling argument follows from the streamwise (along-shelf) component of vorticity equation (derived by cross differentiating and combining the across-shelf and the vertical momentum equations):

$$f\frac{\partial v}{\partial z}+\frac{g}{\rho_0}\frac{\partial \rho}{\partial x}+\frac{\partial^2}{\partial z^2}\left(K\frac{\partial u}{\partial z}\right)=\frac{\partial}{\partial t}\left(\frac{\partial u}{\partial z}\right)+R \qquad (1)$$

where the three terms on the left hand side of equation (1) are the tilting of planetary vorticity filaments by the vertical shear of the along-shelf jet, the buoyancy torque by the sloping isopycnals and the dissipation of relative vorticity by the vertical shear of the across-shelf flow, and the terms on the right hand side are the rate of change of relative vorticity, plus any residual (from horizontal friction or non-linearity). How these terms balance during peak downwelling and upwelling responses are illustrated in **Figure 4**. With isopycnals tending to slope into the bottom across the bottom Ekman layer for either upwelling (shown in **Figures 5**, **10**) or downwelling, we see that the associated buoyancy torque adds constructively in this layer with the planetary vorticity vector tilting term for upwelling, whereas it adds destructively for downwelling (e.g., see **Figure 4** along the sloping bottom between the surface and around 40m depth). Thus, the dissipation within the bottom Ekman layer must be larger under upwelling than under downwelling, which requires an expanded, more energetic bottom Ekman layer under upwelling than under downwelling (as evident by more closely packed isolines in **Figure 4** under upwelling) and hence the observed and simulated asymmetries.

Interestingly, this finding in observations and supported through model simulations is opposite to the expectation from the Lentz and Trowbridge (1991) observations and Trowbridge and Lentz (1991) analyses, wherein it was argued that by moving denser fluid upslope during upwelling, a more stable bottom boundary layer would suppress, versus enhance the flow, and conversely. We note, however, that the motivating observations of Lentz and Trowbridge (1991) are from a different dynamical regime, i.e., from an outer-shelf (90 m water depth), versus an inner-shelf location. Thus, the Ekman-geostrophic spin up process, whereby the evolving surface slope plays an important role in the preceding discussion would not have applied there. So, both finding are sensible, but for different reasons.

This seeming discrepancy provides segue for providing two different dynamical, albeit similar, definitions of the inner-shelf. Recall the Mitchum and Clarke (1986a) and Lentz (1994) definition of the inner-shelf as the region of overlapping surface and bottom Ekman layers. For the WFS, Weisberg et al. (2000) and Weisberg et al. (2001) showed that the Ekman layers do not have to overlap; they merely have to interact (through divergence). It is the divergence that tilts the sea surface to drive the inner-shelf geostrophic flow that, in turn, activates the bottom Ekman layer, and under stratified conditions, the surface and bottom Ekman layers may be separated from one another. This finding is evident in several of the other detailed dynamical analyses provided in Weisberg et al. (2001). It also appears in more recent simulations using the West Florida Coastal Ocean Model (WFCOM) introduced by Zheng and Weisberg (2012). Shown in **Figure 5** are across-shelf sections (sampled offshore from Sarasota, FL.) of the across-shelf component of velocity (top panel), the along-shelf component of velocity (middle panel) and salinity (bottom panel) for May, 9, 2018. Evident in the bottom panel is the upwelling of high salinity water with isolines bending into the bottom within the bottom Ekman layer. Evident in the top panel are an onshore flow within the bottom Ekman layer, an offshore flow within the surface Ekman layer and a general separation in-between. Evident in the middle panel is the (primarily geostrophic) inner-shelf jet centered in this case on about the 32 m isobath, all consistent with the prior discussions of **Figures 3**, **4**. Thus, one definition of the

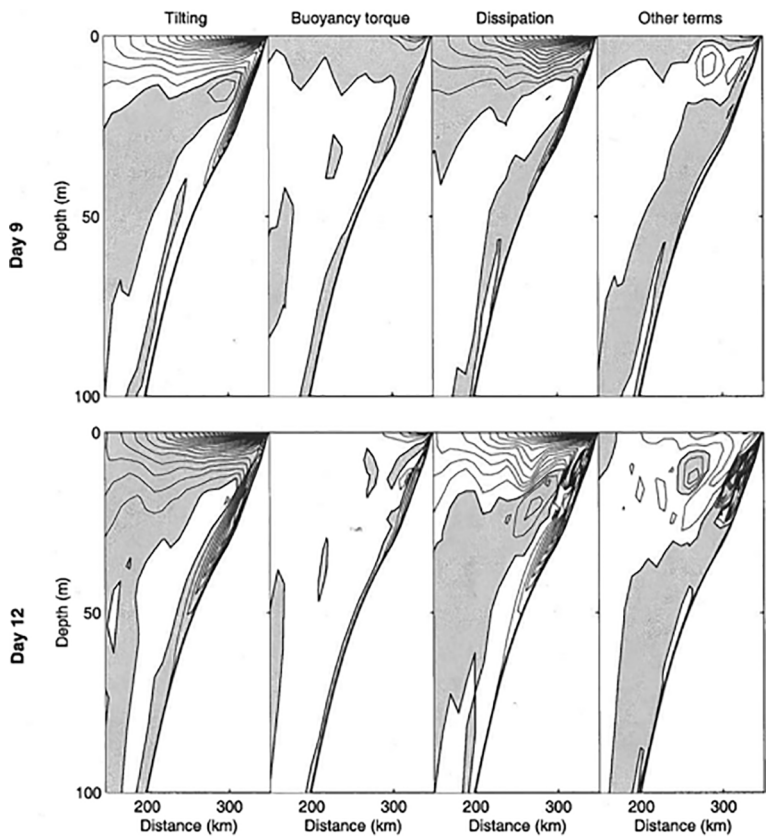

FIGURE 4 | Streamwise vorticity equation terms as functions of depth and offshore distance sampled at times of peak downwelling (upper panels) and upwelling (lower panels) in response to variable wind stress forcing from a Princeton Ocean Model simulation with realistic geometry, stratification and wind forcing (from Weisberg et al., 2001). The contour interval is 10^{-7} s^{-2}, clear regions are positive, shaded regions are negative, and the sloping bottom is the line that runs from the top right (the shoreline) to the bottom left of each panel. Note that the Tilting and Buoyancy torque terms have opposite sign for downwelling in the bottom Ekman layer, whereas they have the same sign for upwelling. Consequently, the bottom Ekman layer is thicker and more intensified (more contours) to provide more dissipation during upwelling than during downwelling.

inner-shelf is the region of interacting Ekman layers giving rise to a sea surface slope and an associated alongshore jet. With distinct surface and bottom Ekman layers separated by a largely geostrophic interior, instead of necessarily overlapping, these Ekman layers may interact through divergence (i.e., they may be connected *via* the vertical velocity component).

A second definition follows from the spatial distribution of terms comprising the vertically integrated vorticity balance. Using the formalism of Ezer and Mellor (1994), with non-linear and horizontal friction terms omitted, this balance may be expressed as:

$$\frac{\partial}{\partial t}\left(\frac{\partial M_y}{\partial x}-\frac{\partial M_x}{\partial y}\right)+\beta M_y = \frac{\partial P_b}{\partial x}\frac{\partial H}{\partial y}-\frac{\partial P_b}{\partial y}\frac{\partial H}{\partial x}+\frac{1}{\rho_0}\left[\frac{\partial(\tau_{y0}-\tau_{yb})}{\partial x}-\frac{\partial(\tau_{x0}-\tau_{xb})}{\partial y}\right] \quad (2)$$

where M_x and M_y are the volume transports per unit area in the along-shelf and across-shelf directions, β is the planetary vorticity gradient, P_b is the bottom pressure, H is the water depth and the τ's are the component surface wind (0) and bottom (b) stresses. Equation 2 states that when vertically integrated, the local rate of change of relative vorticity, plus the advection of planetary vorticity, are balanced by the bottom pressure torque and the differences between the surface wind stress and the bottom stress torques. By calculating these terms throughout the model domain, Weisberg et al. (2001) showed that the inner-shelf is the region where bottom pressure torque (in essence, vortex stretching by across-isobath flow) is balanced primarily by bottom stress torque, whereas the outer-shelf is the region where bottom pressure torque is balanced primarily by the rate of change of relative vorticity. This latter definition also explains why the inner-shelf tends to have a relatively orderly response to wind forcing with a well-defined coastal jet, whereas the outer-shelf tends to be more chaotic and eddy-like. One reason why the WFS is such an interesting study region is that the shelf is wide enough to distinguish between these inner-shelf and outer-shelf regions.

Further descriptions on the WFS inner-shelf responses to wind forcing over a three-year duration from an array of moored

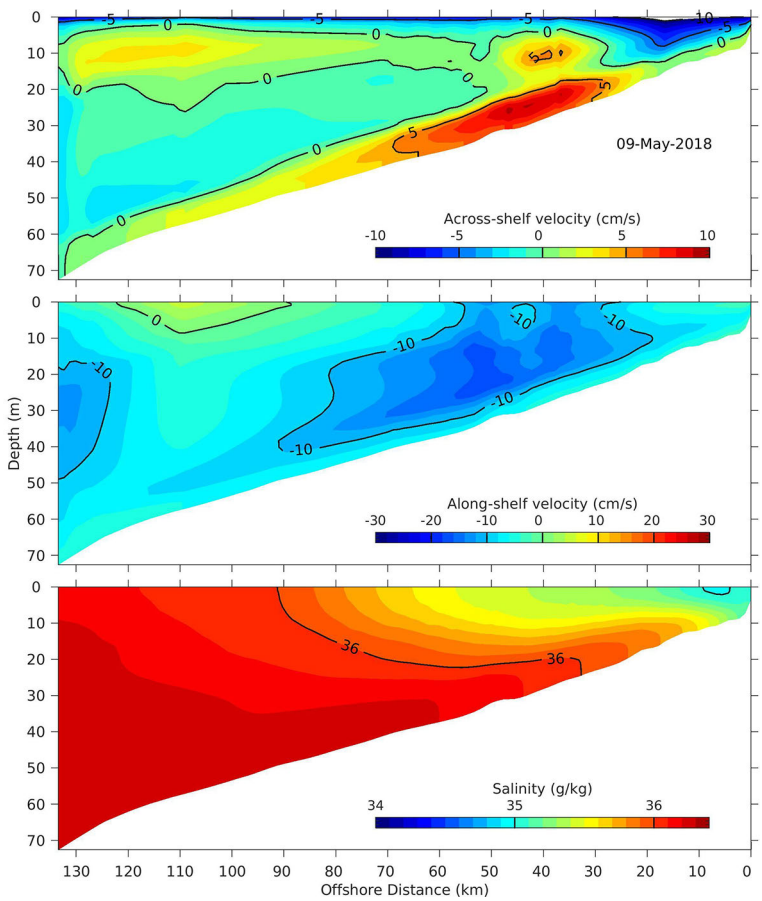

FIGURE 5 | Across-shelf sections sampled offshore from Sarasota, FL on May 9, 2018 from a West Florida Coastal Ocean Model simulation. From top to bottom are the across-shelf component of velocity, the along-shelf component of velocity and salinity, with contour intervals and units provided by the color bars in each panel.

ADCPs are provided by Liu and Weisberg (2005a); Liu and Weisberg (2005b). Using a Self-Organizing Map, an unsupervised learning, neural network analysis technique, **Figure 6** (from Liu and Weisberg, 2005a) shows how the surface, mid-water column and near-bottom velocity vectors organized over the October 1998 to September 2001 duration when 11 moorings were simultaneously deployed across the inner-shelf. By low-pass filtering to remove tides and inertial oscillations, the primarily synoptic weather induced fluctuations show upwelling and downwelling responses, each with a systematic left hand turning of the velocity vectors from surface to bottom as the surface and bottom Ekman layers interact with each other and with the geostrophic interior flow. Also observed are the upwelling flow patterns being larger in magnitude than the downwelling ones (the aforementioned and explained asymmetry), and with the inner-shelf jet (particularly for upwelling) having largest speeds at about the 25m to 30m isobaths.

Analyses regarding how coastal sea level variations may be related to the inner-shelf dynamics, plus contributions from farther offshore, using the same October 1998 to September 2001 data set as above, are provided by Liu and Weisberg (2007). One important finding is that to fully account for coastal sea level variations at synoptic weather scales, one needs to include both the inner-shelf barotropic and baroclinic current responses to along-shelf wind forcing as well as the frictional affects of the across-shelf winds because all of these may contribute similarly. Inner-shelf dynamics are also pertinent to both the long-term mean circulation and the seasonal variations found for the WFS (Weisberg et al., 2009b; Liu and Weisberg, 2012).

2.2 Deep-Ocean Forcing

The outer-shelf is forced primarily by the adjacent deeper ocean. Whether or not deep-ocean forcing along the shelf slope can project onto the shelf is governed in part by the process of geostrophic adjustment. The relevant parameter is the square of the ratio between the baroclinic Rossby radius of deformation evaluated at the shelf break and the shelf width. Studies by Janowitz and Pietrafesa (1980); Clarke and Brink (1985); Chapman and Brink (1987), and Kelly and Chapman (1988) address this topic. When this squared ratio (the Burger number) is small, the pressure gradient adjusts baroclinically in the vicinity of the shelf break such that flows imposed on the shelf

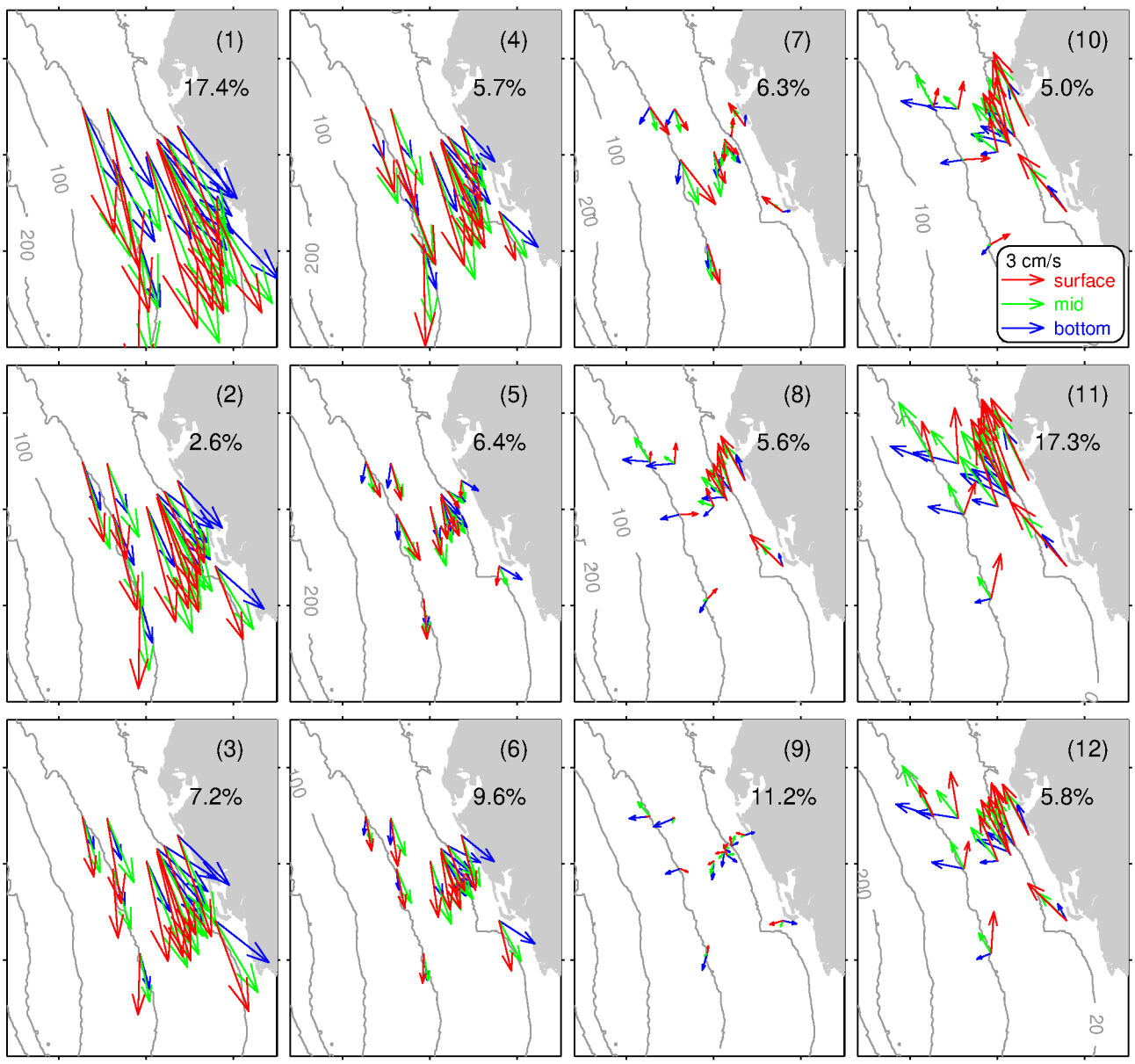

FIGURE 6 | A 3x4 Self Organizing Map array of velocity vector patterns spanning the inner-shelf. The input data set consisted of approximately three years of hourly 2-day low pass filtered velocity vectors sampled from near-surface (red), mid-water column (green) and near-bottom (blue) depths observed by ADCPs on a total of 11 moorings (from Liu and Weisberg, 2005a). The percentages provided in each pattern represents the percent of occurrence for each pattern. Note the systematic turning of the velocity vectors from near-surface to near-bottom, the asymmetry between upwelling and downwelling patterns, and, with the inner three isobaths (gray line) being 20 m, 50 m and 100 m depths, the largest vectors being located between the 20 m to 50 m isobaths and within this range, a little farther offshore for upwelling than for downwelling.

tend to be weak and barotropic. Similarly, flows locally forced on the shelf tend not to penetrate onto the shelf slope. These studies conclude (for small Burger number) that deep-ocean forcing should be relatively ineffective at generating shelf currents and that shelf forcing should be similarly ineffective at generating deep-ocean currents. Barotropic tides at higher frequency provide an exception, as does deep-ocean forcing when the Burger number is large. The west coast of the United States provides an example of the latter situation, where large eddies generated by shelf slope currents may affect water properties over most of the continental shelf.

Despite the WFS generally having small Burger number, there are locations where deep-ocean forcing may be controlling of shelf water properties. This may occur over the Panhandle coast and similarly near the Dry Tortugas where the Burger number at either of these locations is of order one, owing to the shelf width

being similar to the baroclinc Rossby radius of deformation (**Figure 1**). The Dry Tortugas takes on added importance because of the tendency for pressure perturbations to propagate along-isobath with shallow water to the right (in the northern hemisphere). Gill (1982) provides a geophysical fluid dynamical exposition, along with a lucid construct for why such topographic wave propagation is directionally-dependent. Thus, when the Gulf of Mexico Loop Current impacts the west Florida escarpment in the vicinity of the Dry Tortugas (the western-most islet of the Florida Keys chain), its pressure perturbation, by impacting all isobaths as shallow as 25 m, can establish a pressure gradient force that extends from the shelf break to the shoreline and that propagates northward over the entire WFS, even to the Florida Panhandle. Mitchum and Clarke (1986b) had this in mind when they added a sea level perturbation at Key West into their analytical model/data comparisons, Csanady (1978) provided the basis for how such perturbation could impact a shelf in the presence of frictional damping, and Hetland et al. (1999) expanded on these ideas for the WFS. Focusing on a jet formed along the edge of the WFS, these authors also demonstrated (*via* numerical model simulations) that if the Loop Current pressure perturbation contacted shallow isobaths near the Dry Tortugas, then the bulk of the shelf could be set in motion. Confirmation had to await new observations.

Here we provide two contrasting cases of deep-ocean forcing for the WFS, one for which the Loop Current did not result in a protracted state of upwelling, the other for which it did. The first case occurred in June 2000 when the Loop Current contacted the west Florida escarpment, but at a location to the north of the Dry Tortugas. As described by He and Weisberg (2003), shipboard hydrographic sections from June 6, 2000 and June 28, 2000, that extended across the WFS to the upper shelf slope, provided temperature and salinity data from which relative geostrophic velocity sections were computed. These, plus velocity data by moored ADCPs, provided a means by which barotropic and baroclinc components could be distinguished and also by which the flow field across the entire WFS could be described. These observations yielded a weak barotropic flow over the shelf and a stronger Loop Current related baroclinic flow limited to only a few tens of km landward from the shelf break, consistent with the aforementioned theory.

To demonstrate the near independence between the wind-driven, inner-shelf flows and the Loop Current-driven, outer-shelf flows, He and Weisberg (2003), using the POM, with an open boundary arcing from just west of the Mississippi River delta to the Florida Keys, imposed a sea level distribution along the open boundary to support a Loop Current inflow and outflow with a resulting contact at the west Florida escarpment, as observed. Results from constant density simulations with the Loop Current alone and with the Loop Current, together with either upwelling or downwelling favorable winds, are provided in **Figure 7**. These three cases showed the near independence between the shelf-wide responses to local wind and Loop Current forcing, and velocity vectors from nine moorings (with ADCPs) spanning the WFS further provided a general veracity check on the model simulation findings.

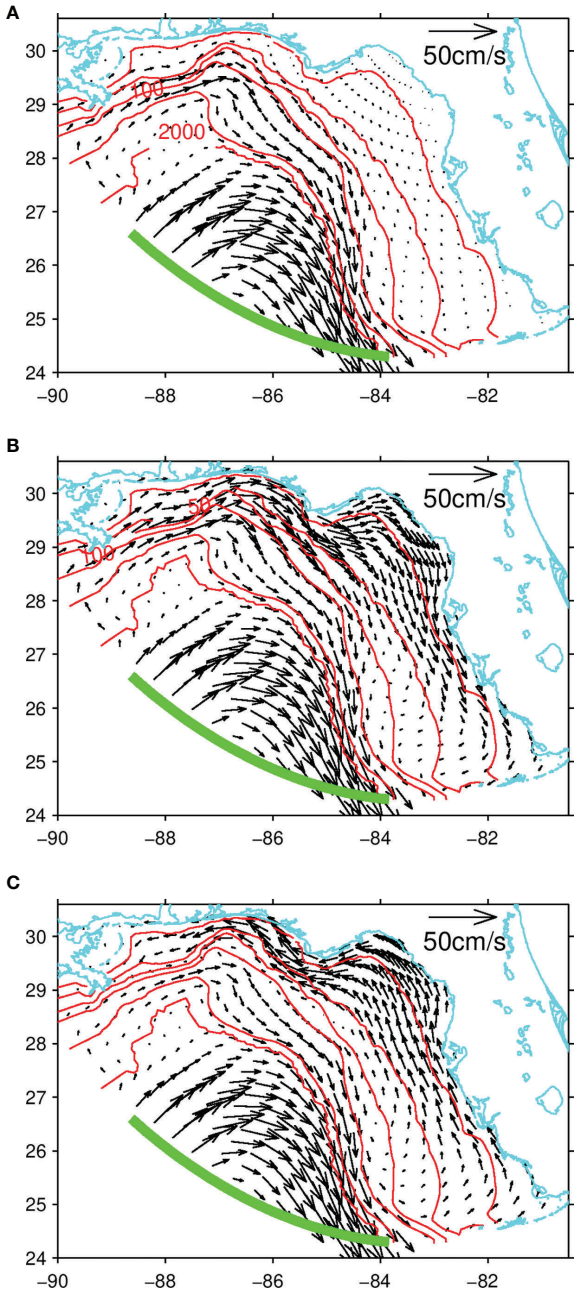

FIGURE 7 | Simulated WFS responses to Loop Current forcing alone **(A)**; Loop Current, plus upwelling favorable wind forcing **(B)**; and Loop Current, plus downwelling favorable wind forcing **(C)**. The green line denotes the region of Loop Current inflow and outflow (from He and Weisberg, 2003). The vectors are depth averaged currents, and the (red) depth contours are the 20 m, 50 m, 100 m, 200 m, 1000 m and 2000 m isobaths.

The second case harkens back to 1998 when the Loop Current did exhibit a prolonged contact with west Florida escarpment near the Dry Tortugas, for which the results on the circulation and ecology are documented by the companion papers of

Weisberg and He (2003) and Walsh et al. (2003), respectively. Given the He and Weisberg (2003) modeling technique as a precursor for estimating the Loop Current forcing, Weisberg and He (2003) made application to the anomalous conditions observed on the WFS in 1998. Two simulations were performed, one without and another with Loop Current contact. Snapshots of vertically (and daily) averaged velocity vectors for May 31, 1998 are shown in **Figure 8**. The left and right hand panels superimpose the velocity vectors on sea surface temperature and sea surface salinity, respectively. The top and bottom panels provide the cases with and without Loop Current forcing, respectively, with the local wind forcing being the same for each of these cases. It is noted that the winds in spring 1998 were also anomalously westerly so for the local forcing only case, we see an along-shelf transport along the Panhandle coast (even without the Loop Current) following the isobaths as they turn southward and continuing along the outer-shelf. Without Loop Current forcing at this time, the inner-shelf along Florida's west coast had relatively little current flow and even exhibited vectors pointing in the direction opposite to the outer-shelf flow direction. The addition of Loop Current forcing (bottom panels) changed the flow field markedly. The Loop Current forcing addition, by imposing a pressure gradient field with a relatively high along the shelf slope and low along the near-shore, energized the entire inner-shelf with a transport to the south that exited the WFS around the Dry Tortugas. Available velocity observations (again by moored ADCPs) demonstrated the general veracity of these model findings, and together, these observations and model simulations provided a confirmation of the Hetland et al. (1999) model-derived hypothesis. With the Loop Current forcing beginning in March, the observations and model simulations showed the Loop Current effects building toward the end of April with the entire WFS affected by May (Weisberg et al., 2004). Using a data assimilative model, Fan et al. (2004) then showed that such an upwelling circulation could also be obtained by assimilating surface drifter observations.

How this impacted water properties and phytoplankton ecology was advanced by Walsh et al. (2003). Water properties were sampled by a Minerals Management Service Northeastern Gulf of Mexico (NEGOM) Program (Nowlin et al., 1998; Jochens and Nowlin, 1999; Nowlin et al., 2000) and by a National Oceanic and Atmosphere Administration, Ecology of Harmful Algal Blooms (ECOHAB) regional field study. Observed in spring through fall of 1998 were increased nutrient levels (by virtue of upwelling of deeper ocean water across the shelf break) that tended to support the growth of diatoms, versus *K. brevis*

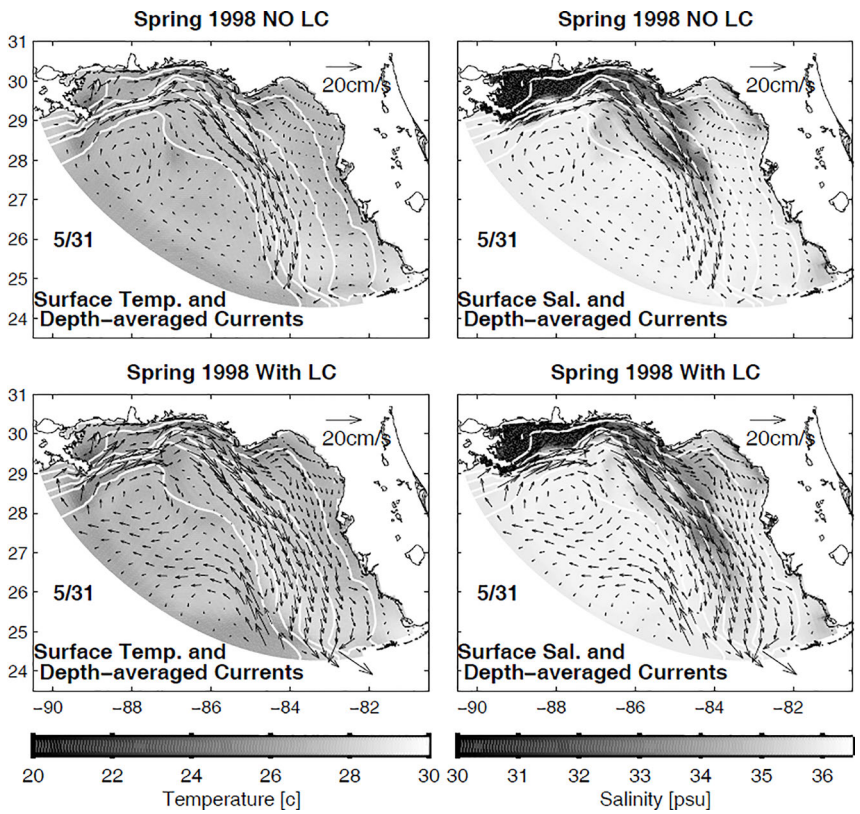

FIGURE 8 | Simulated WFS responses to local forcing alone (top panels) and local plus, Loop Current forcing (bottom panels) as sampled on May 31, 1998, a time when the Loop Current was in contact with west Florida escarpment near the Dry Tortugas. Shown are depth averaged currents superimposed on either surface temperature (left panels) or surface salinity (right panels). Note the full WFS responses with the inclusion of the Loop Current forcing (from Weisberg and He, 2003).

dinoflagellates; hence, the occurrence of a WFS red tide in 1998 was only nominal.

Nutrients upwelled from below the euphotic zone tend to be inorganic and conservatively advected. Thus, relative to nutrients sampled within the euphotic zone, these inorganic nutrients tend to correlate well with temperature and salinity. Weisberg and He (2003) provide such descriptions for phosphate, silicate and nitrate+nitrite using data from both the NEGOM program and from the western north Atlantic, WOCE A22 hydrographic section. Both of these data sources tend to give similar results for waters of potential temperature less than about 18°C, with such cooler waters showing steady increases in these nutrient levels with decreasing temperature down to the level of the Antarctic Intermediate Water. Thus, waters with potential temperatures of 18°C, or less, when upwelled onto the WFS, will tend to add nutrients to what may otherwise be an oligotrophic regime.

The year of 2010 provided another example of protracted upwelling by the Loop Current impacting the west Florida escarpment near the Dry Tortugas. This occurred from mid-May through December, documented observationally and with numerical circulation model simulations (e.g., Liu et al., 2011b; Weisberg et al., 2014a; Liu et al., 2016b). Consistent again with Hetland et al. (1999), the pressure perturbation by the Loop Current resulted in a pressure gradient with a relatively high along the upper slope/outer-shelf and low along the nearshore that propagated northward to set up an along-shelf (south-southeastward) geostrophic flow over the entire WFS. Left hand turning across the bottom Ekman layer resulted in an upwelling flow. Given the potential for such upwelling to alter the WFS nutrient state, Weisberg et al. (2016a) addressed the origin and pathways for deeper ocean water upwelled onto the WFS. The period of study was spring through summer of 2010, and the model used was the West Florida Coastal Ocean Model (WFCOM). WFCOM, introduced by Zheng and Weisberg (2012) and modified by Weisberg et al. (2014b), consists of the Finite Volume Community Model [FVCOM, e.g., Chen et al. (2003)] nested in the HYbrid Coordinate Model [HYCOM, e.g., Chassignet et al. (2009)]. Isopycnal particle tracking experiments were performed over three different 45-day intervals. Being that the Loop Current impact did not begin until mid-May, 2010, the first of these spanned April 1 through May 15, 2010, a period of time when the flow field was influenced by local, versus deep-ocean forcing. The second of these spanned May 1 through June 15, 2010, a period of time when persistent, deep-ocean forced upwelling added to local forcing for a portion of the time. The third experiment spanned June 1 through July 15, 2010, a period of time when persistent upwelling was always a factor. For each of these three experiments, particles were initiated near the bottom (in the lowest sigma (vertical) coordinate layer) along the 75 m, 100 m, 150 m, 200 m, 250 m and 300 m isobaths (i.e., isobaths between the shelf break and the upper portion of the shelf slope) from just west of Tampa Bay to the Mississippi River delta. The particles were then tracked three-dimensionally along isopycnals for 45 days. As expected, without protracted Loop Current-induced upwelling, the particles showed little directional preference. Once upwelling was in place, the translations were rectified shoreward, and when upwelling persisted for the entire integration, many of the particles were transported all of the way to the shoreline. Examples for particles initialized along the 100 m isobath are given in **Figure 9**. While not shown, many of the particles initialized along the 150 m isobath also translated to the shoreline, whereas fewer particles did so from the 200 m isobath. From the 250 m and the 300 m isobaths, the only particles to translate to the shoreline were those along the Florida Panhandle coast where the shelf is much narrower. The conclusions are that under persistent upwelling conditions, fluid (and material properties contained therein) may readily upwell across the shelf break and be transported over the entirety of the WFS from the upper region of the continental shelf slope (from depths between about 75 m to 200 m). With the potential temperatures of upper shelf water generally being about 15°C at 200 m depth, the observed temperature-nutrient relationships show that the WFS may be bathed in waters with elevated nutrient content under protracted Loop Current-induced upwelling conditions.

More recenty, Pan et al. (2017) and Kourafalou et al. (2018) demonstrated how these concepts apply to water properties observed and modeled along Pulley Ridge, a relatively deep reef track to the northwest of the Dry Tortugas.

Such Loop Current impacts upon the WFS are interannual occurrences, with about 10 of these observed by satellite altimetry from 1993 through the present time (Nickerson et al., 2022), the last sustained one being in 2018. In contrast with **Figure 5**, an upwelling situation under stratified conditions without significant Loop Current influence, **Figure 10** shows a similar across shelf section for September 29, 2018 with Loop Current influence. The salinity panel shows the upwelling of relatively high salinity water, with isohalines bending into the bottom across the bottom Ekman layer. The across-shelf velocity component panel shows onshore directed flow in the bottom Ekman layer, but a much lesser offshore directed flow at the surface because the winds were not the primary factor. The along-shelf velocity component shows the inner-shelf jet clearly separated from a region of similar sign farther offshore at the shelf break that is attributable to a mesoscale eddy observed in satellite imagery. This further demonstrates the role of deep-ocean forcing on WFS circulation when the Loop Current impacts the shelf slope near the Dry Tortugas.

3 APPLICATIONS

3.1 *Karenia Brevis* Red Tide

Already alluded to in section 2.2, by altering the nutrient state of the WFS, deep-ocean forcing may strongly influence the occurrence of *K. brevis* red tide on the WFS. With sufficient velocity and hydrographic observations for establishing model simulation veracity, Weisberg et al. (2014a) demonstrated why there was no red tide on the WFS in 2010 due to the protracted Loop Current-induced upwelling. Using similar reasoning, Weisberg et al. (2016b) was then able to explain why 2012

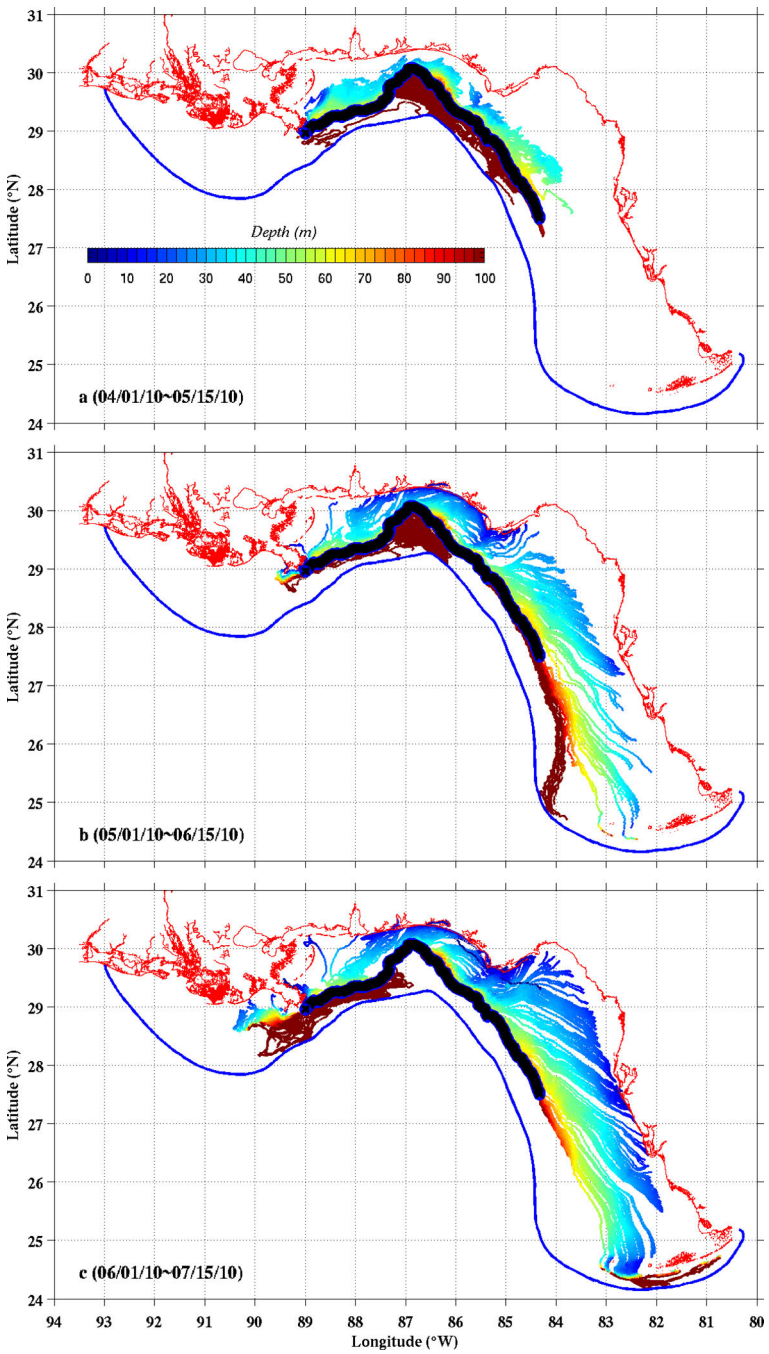

FIGURE 9 | WFCOM-simulated isopycnal water parcel trajectories, originating from the lowest model sigma layer and distributed at 1 km intervals (black dots) along the 100 m isobath. From top to bottom these span the 45-day intervals in 2010 of: **(A)** April 1 to May 15 (with no persistent upwelling), **(B)** May 1 to June 15 (with persistent upwelling occurring over the second half of the interval) and **(C)** June 1, to July 15 (with persistent upwelling throughout the interval), and the color-coding denotes particle depth (from Weisberg et al., 2016b).

experienced a pronounced red tide, whereas the subsequent one in 2013 was just nominal, again by virtue of Loop Current forcing effects. This latter paper also convincingly showed (*via* glider transects and satellite color imagery) the offshore origin for the *K. brevis* red tides found along the west Florida coast in a typical year, confirming the original supposition on offshore generation by Steidinger (1975) and Steidinger and Haddad (1981) and a previous case study by Weisberg et al. (2009a).

These findings motivated the Liu et al. (2016a) to examine major red tide occurrences along Florida's west coast with

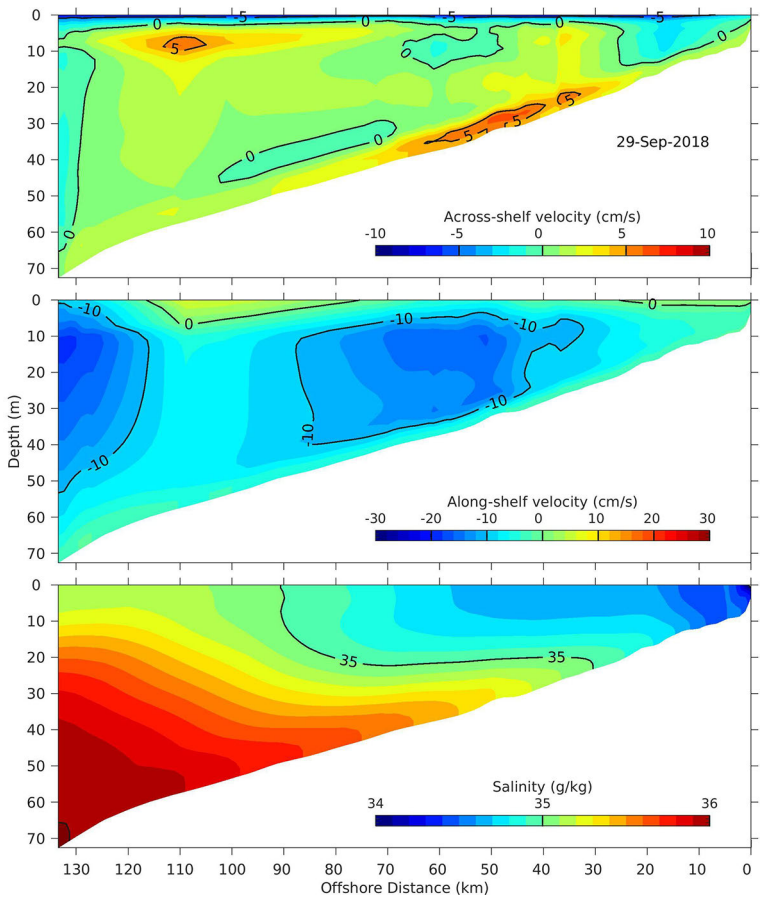

FIGURE 10 | Across-shelf sections sampled offshore from Sarasota, FL on September 29, 2018 from a West Florida Coastal Ocean Model simulation. From top to bottom are the across-shelf component of velocity, the along-shelf component of velocity and salinity, with contour intervals and units provided by the color bars in each panel.

respect to Loop Current behaviors, as evidenced in satellite altimetry records that began in 1993. The offshore origin hypothesis has its basis in **Figure 1**. Without deep-ocean forcing bringing a suite of new inorganic nutrients to the mid-shelf region, especially silicate, it is difficult for diatoms to outcompete dinoflagellates if phosphate and nitrogen compounds become available. Phosphate is generally not limiting (e.g., Lenes et al., 2008), and nitrogen compounds may be fixed by the cyanobacterium, *Trichodesmium* that may abound when the WFS is enriched with iron from Saharan dust transported in spring months by strengthening easterly winds (e.g., Lenes et al., 2001; Walsh et al., 2006; Lenes et al., 2008; Lenes and Heil, 2010; Heil et al., 2014). Thus, if a monospecific *K. brevis* bloom is able to form offshore in spring through summer months, to later be transported landward within the bottom Ekman layer by an upwelling circulation, either wind-driven, or by a combination of local wind and Loop Current forcing, then an intensifying *K. brevis* bloom may appear along the shoreline in fall, which is the typical onset time. Case studies showing this are documented for the WFS by Weisberg et al. (2009a; 2016b) and for the Florida Panhandle coast by McCulloch et al. (2013), and additional idealized modeling work for the Florida Panhandle coast is given by Janowitz et al. (2008).

Bloom intensification (major blooms have cell concentrations exceeding 10^6 cells per liter) may be accounted for in three different ways. The first is physical; cells originating over a deep water column will concentrate when advected to a shallow water column. Being that the shoreward advection occurs within the bottom Ekman layer, an evolving bloom is not visually detectable until the water column is shallow enough for the bloom to mix or migrate up to the surface, as was also evidenced in Weisberg et al. (2016b). The second is also physical; owing to lower nearshore salinities, cells may further concentrate by convergence along fronts (e.g., Janowitz and Kamykowski, 2006; Kamykowski et al., 2013). The third is bio-chemical; nearshore waters have higher nutrient concentrations, and these are further elevated by decaying fish that are killed by the *K. brevis* toxins (e.g., Walsh et al., 2009). This latter effect is what makes major red tide blooms so insidious; by killing fish, *K. brevis* induces its own nutrient supply.

Based on such bloom development concepts, if a mid-WFS origin is dependent upon oligotrophic conditions, and if these conditions are modified by prolonged Loop Current contacts

with the west Florida escarpment near the Dry Tortugas, then some correspondence between Loop Current behavior and major red tide occurrences would be expected. This motivated the Liu et al. (2016a) study in which the Self Organizing Map technique, was used to project snapshots of daily sea surface height and surface geostrophic currents (estimated from the satellite altimetry data) onto a discrete set of (20) patterns with an associated Best Matching Unit time series showing the temporal evolution of these patterns for the 23 year period, 1993 through 2015. Within this pattern evolution were instances when the Loop Current was in contact with the west Florida escarpment near the Dry Tortugas, the WFS "pressure point", as named by these authors. Upon comparing the Best Matching Unit time series with a weekly averaged, west Florida coast *K. brevis* cell count time series, a correspondence between pressure point contact and major red tide occurrences (or lack of) was found. This led to a qualitative scheme for hindcasting and forecasting. From a binary random variable perspective (i.e., did a major bloom occur, or not), this Occam's razor approach, while necessarily crude, did provide encouraging results. In hindcast, the success rate for the occurrence of no major *K. brevis* bloom in a given year (for the period 1993-2015) was 100% (6 out of 6 years), and for a major *K. brevis* bloom it was 76% (13 out of 17 years). Thus, Loop Current forcing (i.e., deep-ocean forcing) at the pressure point does impact the occurrence of major red tides on the WFS, which helps to explain why Florida red tides tend to have such large inter-annual variability.

Of course, there are exceptions to any simplistic scheme. The following year, 2016, was one for which a major red tide was not predicted, whereas one did occur. While pure speculation in the absence of any conclusive evidence, the 2016 red tide bloom onset was nearshore shortly after heavy rainfalls caused municipal sewage systems to be overwhelmed, resulting in large releases of partially treated effluent. Thus, whether or not human influence may be an exacerbating factor remains an open question, but one that must be tempered by the fact that *K. brevis* red tides have been a west Florida occurrence for as long as anecdotal records exist (e.g., https://myfwc.com/media/21885/bloom-historic-database.pdf).

Another interesting case occurred in 2018. The prior year (2017) red tide, which did adhere to the above scheme, persisted into 2018, but was limited in extent to the southern half of the WFS. The month of September 2018 then saw a major escalation in red tide extent and intensity, especially from Venice, FL to the Tampa Bay region and subsequently to both the Florida Panhandle and east coasts. Described by Weisberg et al. (2019), the Loop Current behavior for both 2017 and 2018 was conducive for major red tide initiation. The Loop Current, which had been situated far into the Gulf of Mexico, shed a Loop Current Ring in July 2018 and then retreated back to its more direct, inflow-outflow regime, making contact with the WFS pressure point and remaining in such contact through the end of the year. Thus, while the pressure point contact came too late to suppress offshore bloom generation, its timing ensured the transport of offshore-generated *K. brevis* cells to the nearshore. Water property observations by a glider deployment, optical measurements by satellite and WFCOM model simulations with particle tracking explained the *K. brevis* cell count distributions, as were first observed along the WFS shoreline and then simultaneously along the Panhandle and east coasts, all of which could be traced back to a mid-WFS origination zone roughly between the 30 m to 40 m isobaths.

3.2 Fish Recruitment

As an important recreational and commercial fish species in the low-latitude continental shelf waters of the Western Atlantic, gag (*Mycteroperca microlepis*) are known to spawn offshore and to settle near shore within seagrass meadows and other structured, post-settlement habitats (Keener et al., 1988; Levin and Hay, 2003; Casey et al., 2007. For the WFS, Fitzhugh et al. (2005) describe gag as belonging to a single population (see also Jue, 2006) that spawns from late winter to early spring at hard-bottom habitats between about the 40 m isobath and the shelf break. Early stage larvae have been collected from surface waters near the shelf break (Marancik et al., 2012), and juveniles are abundant enough within shallow, nearshore waters to be routinely surveyed (Casey et al., 2007; Switzer et al., 2012). Otoliths indicate that the time between spawning and settlement varies from roughly 30–50 days, and juvenile densities (juveniles caught per area sampled) tend to be the highest along the coast from the Tampa Bay to Charlotte Harbor estuaries, as compared with locations farther north and south, although there is substantial inter-annual and geographic variability in juvenile density (Fitzhugh et al., 2005; Switzer et al., 2012).

It was speculated that larval movement from spawning to settlement occurred in surface waters (e.g., Heppell et al., 2006; Adamski et al., 2013). However, Fitzhugh et al. (2005) found that the temporal and geographic trends in the mean fertilization and settlement dates of juvenile gag did not agree with seasonal changes in wind-driven surface currents. Thus, the conundrum of how gag larvae and juveniles get from spawning to settlement remained an issue.

This topic was addressed by Weisberg et al. (2014b) using both observations and WFCOM model simulations. Gag observations consisted of pre-settlement juveniles collected in the surf zone at Mullet Key (near the mouth of Tampa Bay) from April through June, 2007, with abundance peaking sharply on May 22nd and 23rd. The juvenile samples were co-located with drift algae of offshore, hard-bottom origin (e.g., Hanisak, 2001). Simultaneous WFS circulation observations consisted of full water column velocity records from moored ADCPs located on the 50 m isobath offshore from Tampa Bay, on the 20 m isobath offshore from Sarasota, Florida (just south from Tampa Bay) and on the 75 m isobath to the west-northwest of the Dry Tortugas (i.e., near the WFS pressure point).

During 2007, the Loop Current contacted the pressure point from about the end of March through the middle of May. A mooring near the pressure point clearly showed the response throughout this contact time, which closely matched the WFCOM simulation. Similarly, the velocity vectors observed and modeled at the other two mooring locations were in reasonably good agreements. Such veracity testing justified the

use of the model simulation to explore potential larvae transport routes. Based on the aforementioned spawning locations, spawning to settlement durations and the date of peak juvenile capture, these authors performed 45-day particle trajectory experiments, with particles initialized on the 40 m, 60 m, 80 m and 100 m isobaths between latitudes of 28^0 N to 29.5^0 N, with start times beginning on April 1 and at successive 2-day intervals thereafter. Two sets of experiments were performed, the first to test a surface transport hypothesis, the second to test a near bottom transport hypothesis, and results were shown for the April 7, April 9, April 11, April 13 and April 15 start times.

The surface transport hypothesis was rejected because none of the particles, regardless of their initial isobath locations, gained proximity to the nearshore. Instead, the surface trajectories tended southward over the outer-shelf. In contrast, particles initialized near the bottom tracked toward the nearshore, as expected for a bottom Ekman layer flow under upwelling conditions. As an example, results for the 40 m isobath initializations for four different start times are shown in **Figure 11**. Some of these trajectories even ended up at Mullet Key. More broadly, we see why the region from Tampa Bay to Charlotte Harbor tends to be such a prolific region for gag. Of secondary importance is the region around Apalachicola Bay, also recognized as a prolific area for gag. On this basis, and along with the co-location of the observed juveniles with algae of hard bottom origin and other geochemical analyses, the bottom transport hypothesis was accepted.

Just as is the case for *K. brevis* red tide, gag recruitment also appears related to the WFS circulation and the importance of deep-ocean forcing *via* Loop Current contact with the WFS pressure point. When this occurs in phase with spawning, and lasts long enough to facilitate transport form the spawning to settlement, then the expectation is for a very prolific gag year class.

3.3 Harmful Substance Tracking (e.g., The Deepwater Horizon Spill)

Not to belabor a point, but 2010, the year of the Deepwater Horizon oil spill was also a year when the Loop Current had prolonged contact with the WFS pressure point. We already discussed how this negated a red tide during that year, but how

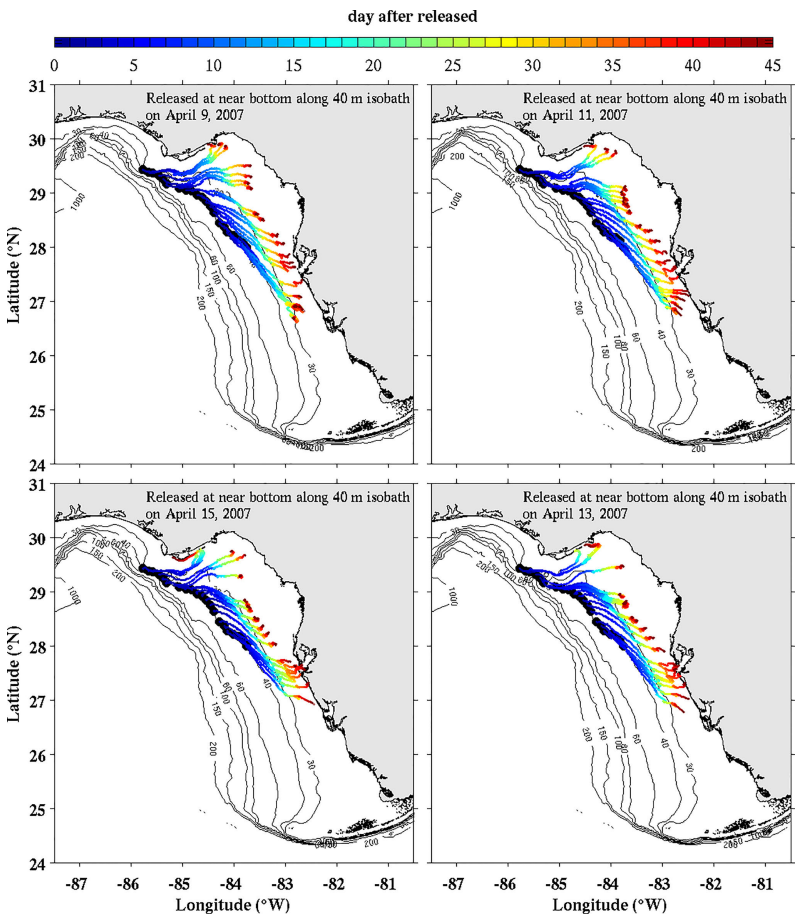

FIGURE 11 | WFCOM-simulated near-bottom particle trajectories for particles initialized on the 40 m isobath. Clockwise from the upper left hand panel are particles initialized on April 9, April 11, April 13 and April 15, 2007. Color-coding denotes particle age from initialization at day zero to 45 days (from Weisberg et al., 2014b).

might this pressure point contact also have affected the transport of hydrocarbons? Here we will consider two applications, the first of these addressing the question of subsurface hydrocarbon transport to the WFS, the second addressing the surface transport to the shoreline. Deep-ocean forcing on the continental shelf and slope is the common element in these.

Subsequent to the Deepwater Horizon oil spill that occurred from April 20 to July 15, 2010 (e.g., Liu et al., 2011a), anecdotal reports of fish lesions and other abnormalities began to emerge for the northern Gulf of Mexico. This prompted a study by Murawski et al. (2014) to investigate such occurrences, not only in the direct vicinity of where surface oil was documented, but also over the entire WFS where no surface oil had been evident. With bottom dwelling reef fish samples taken throughout the WFS from 2011 to 2012, these authors found ample evidence for fish lesions and further analyses of hydrocarbon compounds found in fish liver samples, when compared with Deepwater Horizon oil, further suggested that such hydrocarbons did make their way to the WFS.

Motivated by such findings, and in view of the Loop Current induced upwelling circulation that existed over the course of the oil spill, Weisberg et al. (2016c) applied the WFCOM to examine the possibility that Deep Water Horizon hydrocarbons were transported to the WFS sight unseen beneath the surface. Their approach consisted of an initial value problem, wherein a tracer, of normalized concentration, was uniformly distributed over the water column offshore from Panama City, FL. (in the northeastern sector of the Florida Panhandle coast) on June 19, 2010 in accordance with MODIS satellite ocean color observations and then allowed to evolve as a passive tracer whose concentration reduced over time by advection and turbulence mixing. **Figure 12** shows the near bottom tracer concentrations for July 15, July 30, August 15, and August 30, 2010. With the initial tracer value being 1.0, and with the tracer concentration color bar provided on a $\log_{10}$ scale, the green region corresponds to 0.40, the dark blue and mid-range magenta regions correspond to 0.12 and 0.05, respectively, and the gray region shows the lowest value retained and the extent of the WFCOM domain used in this experiment. Thus, even if the initial subsurface hydrocarbon concentrations were low, such values, reduced only by an order of magnitude, would have permeated most of the WFS's inner shelf, even as far south as the Dry Tortugas, providing a possible explanation for the Murawski et al. (2014) observations.

How Deepwater Horizon oil arrived on the northern Gulf of Mexico beaches also entailed a combination of deep-ocean and local forcing, further modified by wave effects *via* Stokes drift. Overviews on the fate of the Deepwater Horizon hydrocarbons are provided by Özgökmen et al. (2016) and Passow and Hetland (2016). Using WFCOM (a version that extended to west of the Mississippi River), Weisberg et al. (2017) considered surface particle trajectories (with particles initially distributed where surface oil was observed on May 24, 2010 and then further added at the well-head location with time through July 15, 2010) and tracked either with or without Stokes drift. Being that the well-head was outside of the WFCOM domain, a scheme was developed wherein HYCOM fields were used for particle tracking outside of the WFCOM domain that transitioned smoothly with WFCOM field tracking once the particles entered the WFCOM domain. Experiments were performed by nesting WFCOM in either the Gulf of Mexico HYCOM or the Global HYCOM, and the most realistic results were found when using Stokes drift and the Global HYCOM. These are shown in **Figure 13**, which provides the distribution of beached particles and their ages (days since initialized on May 24, 2010, or released at the well-head) on June 27, 2010 for the Global HYCOM/WFCOM case, either without (top panel), or with (bottom panel) Stokes drift. The number of beached particles, relative to the total number of particles released, and the percent of particles beached are provided in the upper right. An order of magnitude more particles were beached with the inclusion of Stokes drift than without, and their distribution along the northern gulf beaches closely matched the reported observations of tar balls and oil (http://gomex.erma.noaa.gov).

These authors concluded that the circulation was responsible for transporting the Deepwater Horizon oil to the vicinity of the shoreline, and that the waves, *via* Stokes drift, were responsible for the actual beaching of the oil. The explanation for the nearshore importance of the Stokes drift is that unlike the currents whose magnitude decreases toward, and whose direction tends to being parallel to, the shoreline, the Stokes drift, which occurs in the direction of wave propagation, may be normal to the shoreline. Thus, suitable models are required to get both the circulation and the waves correct. The HYCOM and merged HYCOM with WFCOM results further showed the importance of both horizontal and vertical resolution. Without horizontal resolution high enough to include an accurate coastline, complete with barrier islands, inlets and estuaries, it is not possible to replicate the observed beaching of oil. Without vertical resolution high enough to approximate how the surface Ekman layer combines with the geostrophic interior, it is necessary to include a wind factor to account for the surface oil not following the wind direction. For the DWH incident, earlier papers by Dietrich et al. (2012) and Le Henaff et al. (2012) provide examples wherein wind factors were applied. The ocean engineering and marine pollution literature also provides examples of both wind factors and Stokes drift inclusion, such as the works by Abascal et al. (2009a); Abascal et al. (2009b), and a study by Curcic et al. (2016) found that the addition of Stokes drift improved the tracking of surface drifters deployed in the northeast Gulf of Mexico during Hurricane Isaac in 2012.

With sufficiently high resolution, both horizontally and vertically, as achievable through downscaling, plus the addition of Stokes drift, it is possible to avoid the use of a wind factor. Downscaling, however, does not negate the necessity for the most accurate deep-ocean circulation, and in this Weisberg et al. (2017) case, the Global HYCOM actually provided better results than the Gulf of Mexico HYCOM. Similarly, observations sufficient for data assimilation and assessing the veracity of the model simulations (deep-ocean and coastal) are necessary.

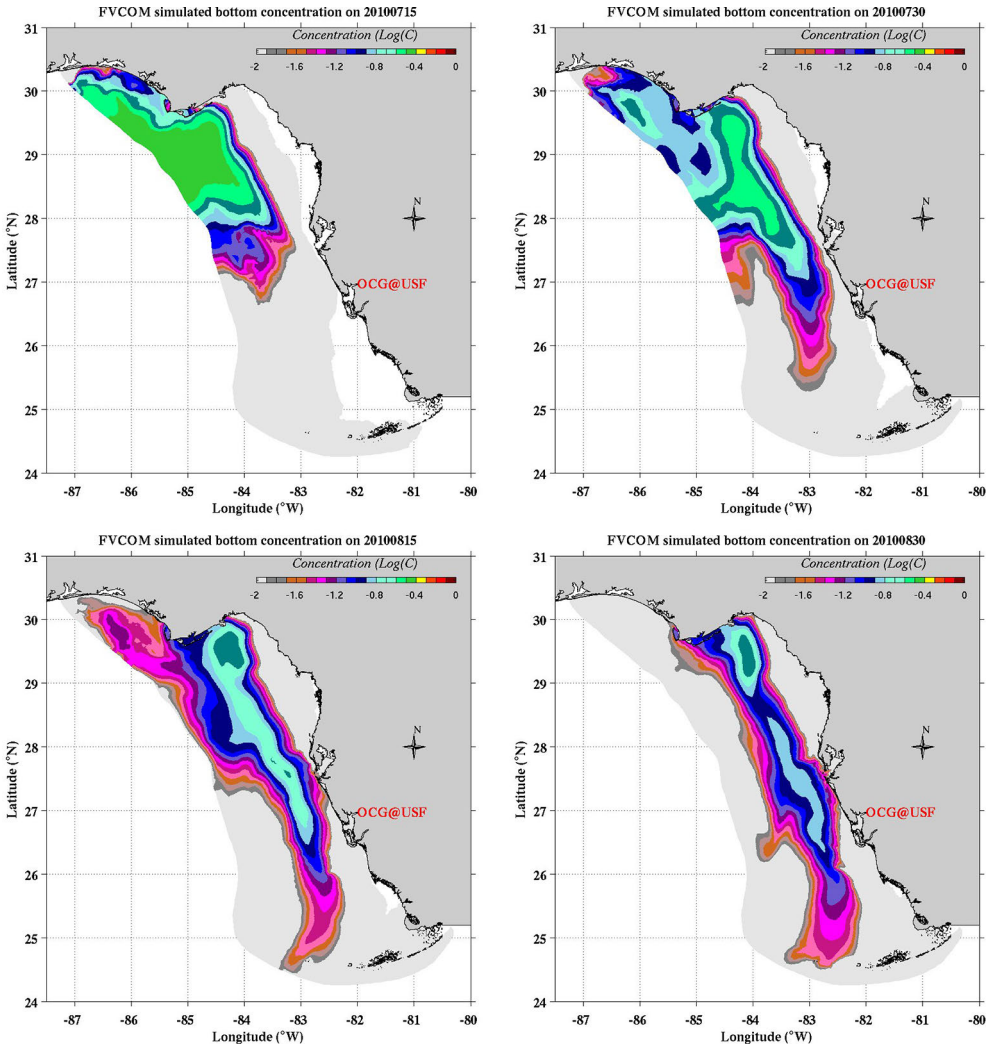

FIGURE 12 | WFCOM-simulated normalized near-bottom tracer concentration sampled on July 15, 2010; July 30, 2010; August 15, 2010; and August 30, 2010. With the initial value being 1.0, and the tracer concentration color bar provided on a $\log_{10}$ scale, the green region on the upper two panels corresponds to 0.40, and the dark blue and mid-range magenta regions on all panels correspond to 0.12 and 0.05, respectively. The gray region represents the lowest tracer concentration value plotted, and its location on the left-hand side demarks the offshore extent of the WFCOM domain used in this simulation (adapted from Weisberg et al., 2016c).

4 SUMMARY AND CONCLUSIONS

The coastal ocean, the region where society meets the sea, is driven by a combination of local and deep-ocean forcing. While all governed by the same physics, the responses of different coastal ocean regions to these two forcing agents is highly dependent upon shelf width and other geometrical considerations. Relative to narrow shelves, whose water properties may readily be influenced by both land drainage and the adjacent deep ocean, wide shelves tend to have mid-shelf regions that tend to be insolated from these effects and hence oligotrophic under general conditions. Here we examined the literature discussing the responses of the WFS to both local and deep-ocean forcing. Along with its width, that enables a separation between inner-shelf and outer-shelf regions, the partial closure of the WFS in the south by the Florida Keys chain, whose westernmost islet, the Dry Tortugas, is in close proximity to the Gulf of Mexico Loop Current, results in situations when protracted Loop Current interaction there can set the entire WFS in an upwelling motion. Such occurrence can alter the nutrient state of the WFS resulting in important ecological consequences.

Thus, we examined the physics of the WFS responses to both local wind and Loop Current forcing. For the case of local forcing only, and using a combination of velocity observations and numerical model simulations (shown to be in general agreement with the observations), we defined the inner-shelf in two ways. The first defines the inner-shelf as the region of interacting surface and bottom Ekman layers, where the linkage between these layers is by divergence. Surface

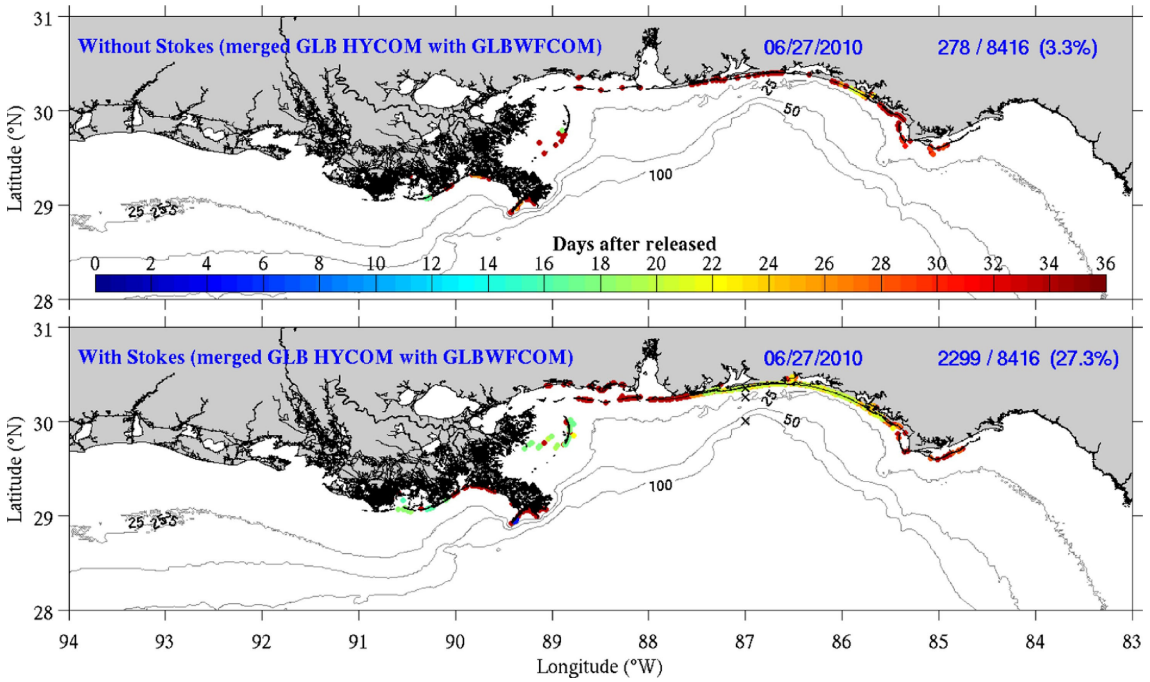

FIGURE 13 | Distribution of beached surface particles and their (color-coded) ages on June 27, 2010 for the case of the Global HYCOM merged with the WFCOM nested in the Global HYCOM, either without (top panel) or with (bottom panel) Stokes drift added. Bathymetric contours are in m. The number of beached particles, relative to the total number (8416) of particles released, and the percent of particles beached are provided in the upper right (from Weisberg et al., 2017).

convergence/divergence is what causes a sea surface slope, thereby establishing a geostrophic interior flow, which activates the bottom Ekman layer and its divergence/convergence. How these connect determines the offshore extent of the surface slope and hence of the inner-shelf, the dynamical balances of which are evident from the model simulations. The second definition follows from an analysis of the vertically integrated vorticity balance. Two regions emerge, one being the inner-shelf, where bottom pressure torque tends to be balanced by bottom friction torque and the other being the outer-shelf, where bottom pressure torque tends to be balanced by the rate of change of relative vorticity. The WFS is sufficiently wide to discern these two inner-shelf and outer-shelf regions. Such distinctly different balance tendencies explains why the inner-shelf responses appear to be relatively ordered with a well-defined coastal jet at some distance offshore, whereas the outer-shelf responses appear to be more chaotic and eddy-like.

Stratification adds nuance. Both observed and modeled is an asymmetry between the responses to upwelling and downwelling favorable winds, with the upwelling responses being disproportionately larger than the downwelling responses. Explanations are provided through discussion of the across-shelf force balance and through an analysis of the stream-wise vorticity equation. For both upwelling and downwelling responses, isopycnals tend to bend into the sloping bottom across the bottom Ekman layer. As a result, and first from a force balance perspective, the gradient buoyancy force adds constructive with the surface slope-induced pressure gradient force under upwelling, and conversely under downwelling. Next, from a vorticity perspective, the buoyancy torque adds constructively with the tilting of planetary vorticity under upwelling, whereas it tends to add destructive under downwelling. Consequently, there must be larger frictional dissipation within the bottom Ekman layer under upwelling than under downwelling; hence the response asymmetry. Additional momentum balance analyses show that the surface and bottom Ekman layers under stratified conditions may be separate from one another, even in relatively shallow, inner-shelf waters (the analysis shown in **Figure 4** is at the 20 m isobath).

The effects of deep-ocean forcing by Loop Current interaction with the west Florida escarpment depend upon where the interaction occurs. North from the Dry Tortugas, referred to as the pressure point, such effects are observed and modeled to be limited to within a baroclinic Rossby radius of deformation from the shelf break, about 30 km for the WFS, in essence the outer-shelf. At the pressure point, such effects are observed and modeled to extend over the entire WFS and even as far north as the Florida Panhandle coast. If such a Loop Current interaction with the pressure point is of protracted duration, then the nutrient state of the WFS may be altered by an infusion of inorganic nutrients upwelled across the shelf break from the upper slope region and advected shoreward, all within the bottom Ekman layer.

Protracted pressure point contact by the Loop Current is shown to have observable ecological consequences, and examples provided include impacts on harmful algae blooms, fisheries recruitment and the advection of harmful substances that, in

turn, have their own ecological impacts. These applications help to explain why the WFS exhibits large inter-annual variations in both water properties and biota.

In conclusion, by virtue of its width and geometry relative to geophysical fluid dynamics principles, the WFS provides an excellent natural laboratory for studying continental shelf responses to both local and deep-ocean forcing and their ecological consequences. Much remains to be learned about shelf ecology, why organisms organize spatially and temporally as they do, how to better forecast major red tide blooms, reef fish year class abundance and other matters of societal concern. Achieving such goals requires an increased recognition on the importance of the shelf circulation on shelf ecology, sustaining arrays of interdisciplinary observations and exercising appropriate models.

DATA AVAILABILITY STATEMENT

All of the information presented herein are available in cited refereed professional publications. Historical data from the COMPS program are stored on Research Workspace. Data may be accessed either from the COMPS web page (http://comps.marine.usf.edu:81/?mode=data), or directly from Research Workspace (https://www.researchworkspace.com/project/2692672/folder/2692680/manually-recovered). Time intervals of available data for individual moorings may be found in a table on the COMPS data Page (http://comps.marine.usf.edu:81/?mode=data). Model simulation outputs for WFCOM are available from our THREDDS server (http://ocgbackup.marine.usf.edu:8080/thredds/models.html) and are also shared daily with NOAA GOODS (https://gnome.orr.noaa.gov/goods). WFCOM simulations from January 2015 through the present time may be accessed at (http://ocgbackup.marine.usf.edu:8080/thredds/catalog/WFS_WFCOM_EXT_NF_model/catalog.html), and archives of hourly values from prior times may be obtained from the authors upon request.

AUTHOR CONTRIBUTIONS

RW and YL collaborate on all presently ongoing research, although some of the topics discussed herein preceded such collaboration. RW wrote the first draft of the manuscript with substantive inputs from YL. Both authors contributed to the article and approved the submitted version.

FUNDING

This research, spanning several decades, was previously funded by a variety of sources. Present support includes grants from NOAA-IOOS (through SECOORA), NA16NOS0120028, NOAA-ECOHAB (through Mote Marine Laboratory), NA19NOS4780183, NOAA Office of Coast Survey (through COMIT), NA20NOS4000227, the Florida Wildlife Commission-FWRI, PO # B609CF and Agreement # 20035, and NASEM UGOS1, NAS Grant # 2000009918. The NSF XSEDE Program, Contract #: OCE130015, also provides computer time, and some personnel support is through the USF College of Marine Science.

ACKNOWLEDGMENTS

The authors are indebted to various former PhD students whose dissertation work led to some of the findings cited herein. Moored velocity observations by the CMS-USF Ocean Circulation Lab had their origin in 1993 and subsequently expanded to a nearly continuous operation in 1998. Initial successes are owing to Mr. R. Cole the lead seagoing technician at that time followed over the past decade by Mr. J. Law who presently leads that sea-going effort, assisted with engineering expertise by Mr. R. Russell. Data management and computer support are owing to Mr. J. Donovan. We are also indebted to the various community modeling teams who over the years have facilitated the use of expertly developed codes; specifically, the POM, ROMS and FVCOM teams, and most notably Dr. C. Chen, the developer of FVCOM. The entire HYCOM group is also acknowledged. It is only through the sharing of such community models and model simulations that nested model codes such as WFCOM can be run by a broader group of scientists.

REFERENCES

Abascal, A. J., Castanedo, S., Medina, R., Losada, I. J., and Alvarez-Fanjul, E. (2009a). Application of HF radar currents to oil spill modeling. *Mar. Pollut. Bull.* 58, 238–248. doi: 10.1016/j.marpolbul.2008.09.020

Abascal, A. J., Castanedo, S., Mendez, F. J., Medina, R., and Losada, I. L. (2009b). Calibration of a Lagrangian transport model using drifting buoys deployed during the Prestige oil spill. *J. Coast. Res.* 25 (2009), 80–90. doi: 10.2112/07-0849.1

Adamski, K. M., Buckel, J. A., Martin, G. B., Ahrenholz, D. W., and Hare, J. A. (2013). Fertilization dates, pelagic larval durations, and growth in Gag (*Mycteroperca Microlepis*) from North Carolina, USA. *Bull. Mar. Sci.* 88, 971–986. doi: 10.5343/bms.2012.1003

Blumberg, A. F., and Mellor, G. L. (1987). "A description of a three-Dimensional coastal ocean circulation model," in *Three-Dimensional Coastal Ocean Models*, vol. Vol. 4 . Ed. N. Heaps (Washington, D.C: AGU), 208–233.

Brink, K. H. (1998a). *Wind-Driven Currents Over the Continental Shelf, in The Sea* Vol. 10. Eds. K. H. Brink and A. R. Robinson (N.Y: Wiley), 3–20.

Brink, K. H. (1998b). *Deep-Sea Forcing and Exchange Processes, in The Sea* Vol. 10. Eds. K. H. Brink and A. R. Robinson (N.Y: Wiley), 21–62.

Casey, J. P., Poulakis, G. R., and Stevens, P. W. (2007). Habitat use by juvenile Gag, *Mycteroperca Microlepis* (Pisces: Serranidae), in subtropical Charlotte Harbor, Florida (USA). *Gulf. Caribb. Res.* 19, 1–9. doi: 10.18785/gcr.1901.01

Chapman, D. C., and Brink, K. H. (1987). Shelf and slope circulation induced by fluctuating offshore forcing. *J. Geophys. Res.* 92, 11741–11759. doi: 10.1029/JC092iC11p11741

Chassignet, E. P., Hurlburt, H. E., Metzger, E. J., Smedstad, O. M., Cummings, J., Halliwell, G. R., et al. (2009). U.S. GODAE: Global ocean prediction with the HYbrid Coordinate Ocean Model (HYCOM). *Oceanography* 22, 48–59. doi: 10.5670/oceanog.2009.39

Chen, C. S., Liu, H., and Beardsley, R. C. (2003). An unstructured, finite-volume, three- dimensional, primitive equation ocean model: Application to coastal

ocean and estuaries. *J. Atmos. Oceanic Technol.* 20, 159–186. doi: 10.1175/1520-0426(2003)020<0159:AUGFVT>2.0.CO;2

Clarke, A. J., and Brink, K. H. (1985). The response of stratified, frictional flow of shelf and slope waters to fluctuating large-scale, low frequency wind forcing. *J. Phys. Oceanogr.* 15, 439–453. doi: 10.1175/1520-0485(1985)015<0439:TROSFF>2.0.CO;2

Clarke, A. J., and Van Gorder, S. (1986). A method for estimating wind-driven frictional, time-dependent, stratified shelf and slope water flow. *J. Phys. Oceanogr.* 16, 1013–1028. doi: 10.1175/1520-0485(1986)016<1013:AMFEWD>2.0.CO;2

Cooper, C. (1987). A numerical modeling study of low-frequency circulation on the West Florida Shelf. *Coast. Engin.* 11, 29–56. doi: 10.1016/0378-3839(87)90038-X

Cragg, J., Mitchum, G. T., and Sturges, W. (1983). Wind-induced sea surface slopes on the West Florida Shelf. *J. Phys. Oceanogr.* 13, 2201–2212. doi: 10.1175/1520-0485(1983)013<2201:WISSSO>2.0.CO;2

Csanady, G. T. (1978). The arrested topographic wave. *J. Phys. Oceanogr.* 8, 47–62. doi: 10.1175/1520-0485(1978)008<0047:TATW>2.0.CO;2

Curcic, M., Chen, S. S., and Ozgokmen, T. M. (2016). Hurricane-induced ocean waves and stokes drift and their impacts on surface transport and dispersion in the Gulf of Mexico. *Geophys. Res. Lett.* 43, 2773–2781. doi: 10.1002/2015GL067619

Dietrich, J. C., Trahana, C. J., Howard, M. T., Fleming, J. G., Weaver, R. J., Tanakae, D. S., et al. (2012). Surface trajectories of oil transport along the northern coastline of the Gulf of Mexico. *Cont. Shelf. Res.* 41, 17–47. doi: 10.1016/j.csr.2012.03.015

Dixon, L. K., Kirkpatrick, G. J., Hall, E. R., and Nissanka, A. (2014). Nitrogen, phosphorus and silica on the West Florida Shelf: Patterns and relationships with *Karenia* spp. occurrence. *Harmf. Algae.* 38, 8–19. doi: 10.1016/j.hal.2014.07.001

M. J. Dowgiallo (Ed.) (1994). "Coastal oceanographic effects of the summer 1993 Mississippi River flooding," in *Special NOAA Report.* (Silver Spring:Maryland, USA). 77pp.

Ekman, V. W. (1905). On the influence of the Earth's rotation on ocean-currents. *Arkiv. Matem. Astr. Fysik.* 2, 1–53.

Ezer, T., and Mellor, G.L (1994). Diagnostic and prognostic calculations of the North Atlantic circulation and sea level using a sigma coordinate ocean model. *J. Geophys. Research* 99(C7), 14159–171. doi: 10.1029/94JC00859

Fan, S., Oey, L.-Y., and Hamilton, P. (2004). Assimilation of drifter and satellite data in a model of the northwestern Gulf of Mexico. *Cont. Shelf. Res.* 24, 1001–1013. doi: 10.1016/j.csr.2004.02.013

Fewings, M., Lentz, S. J., and Fredericks, J. (2008). Observations of cross-shelf flow driven by cross-shelf winds on the inner continental shelf. *J. Phys. Oceanogr.* 38, 2358–2378. doi: 10.1175/2008JPO3990.1

Fitzhugh, G. R., Koenig, C. C., Coleman, F. C., Grimes, C. B., and Sturges, W. (2005). Spatial and temporal patterns in fertilization and settlement of young Gag (*Mycteroperca Microlepis*) Along the West Florida Shelf. *Bull. Mar. Sci.* 77, 377–396.

Gilbes, F., Tomas, C., Walsh, J. J., and Muller-Karger, F. E. (1996). An episodic chlorophyll plume on the West Florida Shelf. *Cont. Shelf. Res.* 16, 1201–1224. doi: 10.1016/0278-4343(95)00065-8

Gill, A. E. (1982). *Atmosphere-Ocean Dynamics* (San Diego, California, USA: Academic Press), p662.

Gill, A. E., and Schumann, E. H. (1974). The generation of long shelf waves by wind. *J. Phys. Oceanogr.* 4, 83–90. doi: 10.1175/1520-0485(1974)004<0083:TGOLSW>2.0.CO;2

Hanisak, M. D. (2001). Macroalgal blooms in Florida's coastal waters: *Codium Isthmocladum* (Abstract). *J. Phycol.* 37, 21.

Heil, C. A., Dixon, L. K., Hall, E., Garrett, M., Lenes, J. M., O'Neil, J. M., et al. (2014). Blooms of *Karenia brevis* (Davis) G. Hansen & O. Moestrup on the West Florida Shelf: Nutrient sources and potential management strategies based on a multi-year regional study. *Harmful Algae* 38, 127–140. doi: 10.1016/j.hal.2014.07.016

Heil, C. A., Vargo, G. A., Spence, D. A., Neely, M. B., Merkt, R., Lester, K. M., et al. (2001). "Nutrient stoichiometry of a *Gymnodinium Breve* bloom: What limits blooms in oligotrophic environments?," in *Harmful Algal blooms 2000*. Eds. G. M. Hallegraeff, S. I. Blackburn, C. J. Bolch and R. J. Lewis (Paris: UNESCO), 165–168.

Heppell, S. S., Heppell, S. A., Coleman, F. C., and Koenig, C. C. (2006). Models to compare management options for a protogynous fish. *Ecol. Appl.* 16, 238–249. doi: 10.1890/04-1113

Hetland, R. D., Hsueh, Y., Leben, R. R., and Niiler, P. P. (1999). A Loop Current-induced jet along the edge of the West Florida Shelf. *Geophys. Res. Lett.* 26, 2239–2242. doi: 10.1029/1999GL900463

He, R., and Weisberg, R. H. (2002). West Florida Shelf circulation and temperature budget for the 1999 spring transition. *Cont. Shelf. Res.* 22, 719–748. doi: 10.1016/S0278-4343(01)00085-1

He, R., and Weisberg, R. H. (2003). A Loop Current intrusion case study on the West Florida Shelf. *J. Phys. Oceanogr.* 33, 465–477. doi: 10.1175/1520-0485(2003)033<0465:ALCICS>2.0.CO;2

Hill, A. E. (1998). *Buoyant Effects in Coastal and Shelf Seas, in The Sea* Vol. 10. Eds. K. H. Brink and A. R. Robinson (N.Y: Wiley), 21–62.

Hsueh, Y., Marmarino, G. O., and Vansant, L. L. (1982). Numerical model studies of the winter storm response of the West Florida Shelf. *J. Phys. Oceanogr.* 12, 1037–1050. doi: 10.1175/1520-0485(1982)012<1037:NMSOTW>2.0.CO;2

Janowitz, G. S., and Kamykowski, D. (2006). Modeled *Karenia brevis* accumulation in the vicinity of a coastal nutrient front. *Mar. Ecol. Prog. Ser.* 314, 49–59. doi: 10.3354/meps314049

Janowitz, G. S., Kamykowski, D., and Liu, G. (2008). A three-dimensional wind and behaviorally driven population dynamics model for *Karenia brevis*. *Cont. Shelf. Res.* 28 (1), 177–188. doi: 10.1016/j.csr.2007.04.016

Janowitz, G. S., and Pietrafesa, L. J. (1980). A model and observations of time-dependent upwelling over the midshelf and slope. *J. Phys. Oceanogr.* 10, 1574–1583. doi: 10.1175/1520-0485(1980)010<1574:AMAOOT>2.0.CO;2

Jochens, A. E., and Nowlin, W. D. (1999). "Northeastern Gulf of Mexico Chemical Hydrography and Hydrography Study," in *Annual Report: Year 2, OCS Study MMS 99-0054*(New Orleans, La:Department of Interior, United States), 1–123.

Jue, N. K. (2006). Exploring the structure of genetic variation and the influences of demography on effective population size in the Gag grouper *Mycteroperca Microlepis* (Goode & Bean). *Jour. Fish. Biol.* 69, 217–224. doi: 10.1111/j.1095-8649.2006.01273.x

Kamykowski, D., Grabowski, K. M., Morrison, J. M., McCulloch, A. A., Nyadjro, E. S., Thomas, C. A., et al. (2013). Cold front induced changes on the Florida Panhandle shelf during October 2008. *Cont. Shelf. Res.* 54, 52–66. doi: 10.1016/j.csr.2012.12.006

Keener, P., Johnson, G. D., Stender, B. W., Brothers, E. B., and Beatty, H. R. (1988). Ingress of postlarval Gag, *Mycteroperca Microlepis* (Pisces, Serranidae), through a South-Carolina barrier-island Inlet. *Bull. Mar. Sci.* 42, 376–396.

Kelly, K. A., and Chapman, D. C. (1988). The response of stratified shelf and slope waters to steady offshore forcing. *J. Phys. Oceanogr.* 18, 906–925. doi: 10.1175/1520-0485(1988)018<0906:TROSSA>2.0.CO;2

Kourafalou, V. H., Androulidakis, Y. S., Kang, H., Smith, R. H., and Valle-Levinson, A. (2018). Physical connectivity between Pulley Ridge and Dry Tortugas coral reefs under the influence of the Loop Current/Florida Current system. *Prog. Oceanogr.* 165, 75–99. doi: 10.1016/j.pocean.2018.05.004

Le Henaff, M., Kourafalou, V. H., Paris, C. B., Helgers, J., Aman, Z. M., Hogan, P. J., et al. (2012). Surface evolution of the Deepwater Horizon oil spill patch: combined effects of circulation and wind-induced drift. *Environ. Sci. Technol.* 46, 7267–7273. doi: 10.1021/es301570w

Lenes, J. M., Darrow, B. P., Cattrall, C., Heil, C. A., Vargo, G. A., Callahan, M., et al. (2001). Iron fertilization and *Trichodesmium* response on the West Florida Shelf. *Limnol. Oceanogr.* 46, 1261–1277. doi: 10.4319/lo.2001.46.6.1261

Lenes, J. M., Darrow, B. A., Walsh, J. J., Prospero, M., He, R., Weisberg, R. H., et al. (2008). Saharan dust and phosphatic fidelity: A three-dimensional biogeochemical model of *Trichodesmium* as a nutrient source for red tides on the West Florida Shelf. *Cont. Shelf. Res.* 28, 1091–1115. doi: 10.1016/j.csr.2008.02.009

Lenes, J. M., and Heil, C. A. (2010). A historical analysis of the potential nutrient supply from the N2 fixing marine cyanobacterium Trichodesmium spp. To *Karenia brevis* in the eastern Gulf of Mexico. *J. Plankt. Res.* 32, 1421–1431. doi: 10.1093/plankt/fbq061

Lentz, S. (1994). Current dynamics over the northern California inner shelf. *J. Phys. Oceanogr.* 24, 2461–2478. doi: 10.1175/1520-0485(1994)024<2461:CDOTNC>2.0.CO;2

Lentz, S. (1995). Sensitivity of the inner shelf circulation to the form of the eddy viscosity profile. *J. Phys. Oceanogr.* 25, 19–28. doi: 10.1175/1520-0485(1995)025<0019:SOTISC>2.0.CO;2

Lentz, S. J., and Trowbridge, J. H. (1991). The bottom boundary layer over the northern California shelf. *J. Phys. Oceanogr.* 21, 1186–1202. doi: 10.1175/1520-0485(1991)021<1186:TBBLOT>2.0.CO;2

Levin, P. S., and Hay, M. E. (2003). Selection of estuarine habitats by juvenile Gags in experimental mesocosms. *Trans. Amer. Fish. Soc* 132, 76–83. doi: 10.1577/1548-8659(2003)132<0076:SOEHBJ>2.0.CO;2

Liu, Y., MacFadyen, A., Ji, Z.-G., and Weisberg, R. H. (Eds.) (2011a). "Monitoring and Modeling the Deepwater Horizon Oil Spill: A Record-Breaking Enterprise" *Geophys. Monogr. Ser*. vol. 195 (Washington, D.C., USA: AGU/geopress), 271 PP. doi: 10.1029/GM195

Liu, Y., and Weisberg, R. H. (2005a). Patterns of ocean current variability on the West Florida Shelf using the Self-Organizing Map. *J. Geophys. Res.* 110, C06003. doi: 10.1029/2004JC002786

Liu, Y., and Weisberg, R. H. (2005b). Momentum balance diagnoses for the West Florida Shelf. *Cont. Shelf. Res.* 25, 2054–2074. doi: 10.1016/j.csr.2005.03.004

Liu, Y., and Weisberg, R. H. (2007). Ocean currents and sea surface heights estimated across the West Florida Shelf. *J. Phys. Oceanogr.* 37, 1697–1713. doi: 10.1175/JPO3083.1

Liu, Y., and Weisberg, R. H. (2012). Seasonal variability on the West Florida Shelf. *Progr. Oceanogr.* 104, 80–98. doi: 10.1016/j.pocean.2012.06.001

Liu, Y., Weisberg, R. H., Hu, C., Kovach, C., and Riethmüller, R. (2011b). "Evolution of the Loop Current system during the *Deepwater Horizon* oil spill event as Observed With Drifters and Satellites," in *Monitoring and Modeling the Deepwater Horizon Oil Spill: A Record-Breaking Enterprise, Geophys. Monogr. Ser*, vol. 195 (Washington, D.C., USA: AGU/geopress), 91–101. doi: 10.1029/2011GM001127

Liu, Y., Weisberg, R. H., Lenes, J. M., Zheng, L., Hubbard, K., and Walsh, J. J. (2016a). Offshore forcing on the West Florida Shelf "Pressure Point" and its upwelling influence on harmful algal blooms. *J. Geophys. Res* 121, 5501–5515. doi: 10.1002/2016JC011938

Liu, Y., Weisberg, R. H., Vignudelli, S., and Mitchum, G. T. (2016b). Patterns of the Loop Current system and regions of sea surface height variability in the eastern Gulf of Mexico revealed by the Self-Organizing Maps. *J. Geophys. Res. Ocean.* 121, 2347–2366. doi: 10.1002/2015JC011493

Li, Z., and Weisberg, R. H. (1999a). West Florida Shelf response to upwelling favorable wind forcing, Part 1: Kinematics. *J. Geophys. Res.* 104, 13,507–13,527. doi: 10.1029/1999JC900073

Li, Z., and Weisberg, R. H. (1999b). West Florida Shelf response to upwelling favorable wind forcing, Part 2: Dynamics. *J. Geophys. Res.* 104, 23427–23442. doi: 10.1029/1999JC900205

Lopez, M., and Clarke, A. J. (1989). The wind-driven shelf and slope water flow in terms of a local and a remote response. *J. Phys. Oceanogr.* 19, 1091–1101. doi: 10.1175/1520-0485(1989)019<1091:TWDSAS>2.0.CO;2

Marancik, K. E., Richardson, D. E., Lyczkowski-Shultz, J., Cowen, R. K., and Konieczna, M. (2012). Spatial and temporal distribution of grouper larvae (*Serranidae: Epinephelinae: Epinephelini*) in the Gulf of Mexico and Straits of Florida. *Fish. Bull.* 110, 1–20.

Marmorino, G. O. (1982). Wind-forced sea level variability along the West Florida Shelf. *J. Phys. Oceanogr.* 12, 389–404. doi: 10.1175/1520-0485(1982)012<0389:WFSLVA>2.0.CO;2

Marmorino, G. O. (1983). Variability of current, temperature, and bottom pressure across the west Florida continental shelf, winter 1981-1982. *J. Geophys. Res.* 88, 4439–4457. doi: 10.1029/JC088iC07p04439

McCulloch, A. A., Kamykowski, D., Morrison, J. M., Thomas, C. J., and Pridgen, K. G. (2013). A physical and biological context for *Karenia brevis* seed populations on the northwest Florida shelf during July 2009. *Cont. Shelf. Res.* 63, 94–111. doi: 10.1016/j.csr.2013.05.001

Mellor, G. L., and Yamada, T. (1982). Development of a turbulence closure model for geophysical fluid problems. *Rev. Geophys. Spac. Phys.* 20, 851–875. doi: 10.1029/RG020i004p00851

Mitchum, G. T., and Clarke, A. J. (1986a). The frictional nearshore response to forcing by synoptic scale winds. *J. Phys. Oceanogr.* 16, 934–946. doi: 10.1175/1520-0485(1986)016<0934:TFNRTF>2.0.CO;2

Mitchum, G. T., and Clarke, A. J. (1986b). Evaluation of frictional wind-forced long waves theory on the West Florida Shelf. *J. Phys. Oceanogr.* 16, 1029–1037. doi: 10.1175/1520-0485(1986)016<1029:EOFWFL>2.0.CO;2

Mitchum, G. T., and Sturges, W. (1982). Wind-driven currents on the West Florida Shelf. *J. Phys. Oceanogr.* 12, 1310–1317. doi: 10.1175/1520-0485(1982)012<1310:WDCOTW>2.0.CO;2

Morey, S. L., Martin, P. J., O'Brien, J. J., Walcraft, A. A., and Zavala-Hidalgo, J. (2003). Export pathways for river discharged fresh water in the northern Gulf of Mexico. *J. Geophys. Res.* 108, C10, 3303. doi: 10.1029/2002JC001674

Murawski, S. A., Hogarth, W. T., Peebles, E. B., and Barbeiri, L. (2014). Prevalence of external skin lesions and polycyclic aromatic hydrocarbon concentrations in Gulf of Mexico fishes, post-*Deepwater Horizon*. *Trans. Am. Fish. Soc* 143 (4), 1084–1097. doi: 10.1080/00028487.2014.911205

Nickerson, A., Weisberg, R. H., and Liu, Y. (2022). On the evolution of the Gulf of Mexico Loop Current through its penetrative, ring shedding and retracted states. *Adv. Spac. Res* 69(11), 4058–4077. doi: 10.1016/j.asr.2022.03.039

Niiler, P. P. (1976). Observations of low-frequency currents on the west Florida continental shelf. *Mem. Soc R. Sci. Liege. X.* 6, 331–358.

Nowlin, W. D., Jochens, A. E., Howard, M. K., and DiMarco, S. F. (1998). "Nearshore bottom properties over the northeast shelves of the Gulf of Mexico as observed during early May 1998," in *TAMU Oceanography Technical Report No. 98-3-T*, vol. 77843. (College station TX: Dept. of Oceanography, Texas A&M university), 60pp.

Nowlin, W. D., Jochens, A. E., Howard, M. K., DiMarco, S. F., and Schroeder, W. W. (2000). Hydrographic properties and inferred circulation over the northeast shelves of the Gulf of Mexico During Spring to Midsummer of 1998. *Gulf. Mex. Sci.* 18, 40–54. doi: 10.18785/goms.1801.05

J. M. O'Neil and C. A. Heil (Eds.) (2014). "Nutrient dynamics of *Karenia brevis* red tide blooms in the Eastern Gulf of Mexico," in *Harmful Algae*, vol. 38 (New York, USA:Elsevier B.V.) 1–140 (special issue).

Ortner, P. B., Lee, T. N., Milne, P. J., Zika, R. G., Clarke, M. E., Podesta, G. P., et al. (1995). Mississippi River flood waters that reached the Gulf Stream. *J. Geophys. Res.* 100, 13595–13601. doi: 10.1029/95JC01039

Özgökmen, T. M., Chassignet, E. P., Dawson, C. N., Dukhovskoy, D., Jacobs, G., Ledwell, J., et al. (2016). Over what area did the oil and gas spread during the 2010 Deepwater Horizon oil spill? *Oceanography* 29, 96–107. doi: 10.5670/oceanog.2016.74

Pan, C., Jiang, M., Dalgleish, F. R., and Reed, J. K. (2017). Modeling the impacts of the Loop Current on circulation and water properties over the Pulley Ridge region on the southwest Florida shelf. *Ocean. Modell.* 112, 48–64. doi: 10.1016/j.ocemod.2017.02.009

Passow, U., and Hetland, R. D. (2016). What happened to all of the oil? *Oceanography* 29, 88–95. doi: 10.5670/oceanog.2016.73

Steidinger, K. A. (1975). Implications of dinoflagellate life cycles on initiation of *Gymnodinium brevis* red tides. *Environ. Letts.* 9, 129–139. doi: 10.1080/00139307509435842

Steidinger, K. A., and Haddad, K. (1981). Biologic and Hydrographic aspects of red tides. *Bioscience* 31 (11), 814–819. doi: 10.2307/1308678

Switzer, T. S., MacDonald, T. C., McMichael, R. H.Jr., and Keenan, S. F. (2012). Recruitment of juvenile gags in the eastern Gulf of Mexico and factors contributing to observed spatial and temporal patterns of estuarine occupancy. *Trans. Amer. Fish. Soc* 141, 707–719. doi: 10.1080/00028487.2012.675913

Tilburg, C. E. (2003). Across-shelf transport on a continental shelf: Do across-shelf winds matter? *J. Phys. Oceanogr.* 33, 2675–2688. doi: 10.1175/1520-0485(2003)033<2675:ATOACS>2.0.CO;2

Toner, M., Kirwan, A. D., Poje, C., Kantha, L. H., Muller-Karger, F. E., and Jones, C. K. P. T. (2003). Chlorophyll dispersal by eddy-eddy interactions in the Gulf of Mexico. *J. Geophys. Res.* 108 (C4), 3105. doi: 10.1029/2002JC001499

Trowbridge, J. H., and Lentz, S. J. (1991). Asymmetric behavior of an oceanic boundary layer above a sloping bottom. *J. Phys. Oceanogr.* 21, 1171–1185. doi: 10.1175/1520-0485(1991)021<1171:ABOAOB>2.0.CO;2

Vargo, G. A., Heil, C. A., Fanning, K. A., Dixon, L. K., Neely, M. B., and Lester, K. (2008). Nutrient availability in support of *Karenia brevis* blooms on the central West Florida Shelf: What keeps *Karenia* blooming ? *Cont. Shelf. Res.* 28 (1), 73–98. doi: 10.1016/j.csr.2007.04.008

Walsh, J. J., Jolliff, J., Darrow, B. P., Lenes, J. M., Milroy, S. P., Remsen, D., et al. (2006). Red tides in the Gulf of Mexico: where, when, and why. *J. Geophys. Res.* 111 (C11003). doi: 10.1029/2004JC002813

Walsh, J. J., Weisberg, R. H., Dieterle, D. A., He, R., Darrow, D. P., Jolliff, J. K., et al. (2003). The phytoplankton response to intrusion of slope water on the West Florida Shelf: Models and observations. *J. Geophys. Res.* 108 C6, 15. doi: 10.1029/2002JC001406

Walsh, J. J., Weisberg, R. H., Lenes, J. M., Chen, F. R., Dieterle, D. A., Zheng, L., et al. (2009). Isotopic evidence for dead fish maintenance of Florida red tides, with implications for coastal fisheries over both source regions of the West

Florida Shelf and Within Downstream Waters of the South Atlantic Bight. *Progr. Oceanogr.* 80, 51–73. doi: 10.1016/j.pocean.2008.12.005

Weatherly, G. L., and Thistle, D. (1997). On the wintertime currents in the Florida Big Bend region. *Cont. Shelf. Res.* 17, 1297–1319. doi: 10.1016/S0278-4343(97)00018-6

Weisberg, R. H., Barth, A., Alvera-Azcárate, A., and Zheng, L. (2009a). A coordinated coastal ocean observing and modeling system for the West Florida shelf. *Harmf. Algae.* 8, 585–598. doi: 10.1016/j.hal.2008.11.003

Weisberg, R. H., Black, B., and Li, Z. (2000). An upwelling case study on Florida's west coast. *J. Geophys. Res.* 105, 11459–11469. doi: 10.1029/2000JC900006

Weisberg, R. H., and He, R. (2003). Local and deep ocean forcing contributions to anomalous water Properties on the West Florida Shelf. *J. Geophys. Res.* 108, C6, 15. doi: 10.1029/2002JC001407

Weisberg, R. H., He, R., Kirkpatrick, G., Muller-Karger, F., and Walsh, J. J. (2004). Coastal ocean circulation influences on remotely sensed optical properties: A West Florida Shelf case study. *Oceanogr. (spec. iss. Coast. Ocean. Optic. Dynam.)* 17, 68–75. doi: 10.5670/oceanog.2004.49

Weisberg, R. H., He, R., Liu, Y., and Virmani, J. I. (2005). "West Florida Shelf circulation on synoptic, seasonal, and inter-snnual time scales, In: *Circulation in the gulf of Mexico observations and models, Geophys Monogr. Ser*, vol. 161 . Eds. W. Sturges and A. Lugo-Fernandez (Washington D.C: AGU), 325–347.

Weisberg, R. H., Li, Z., and Muller-Karger, F. E. (2001). West Florida Shelf response to local wind forcing: April 1998. *J. Geophys. Res.* 106 (C12), 31,239–31,262. doi: 10.1029/2000JC000529

Weisberg, R. H., Liu, Y., Lembke, C., Hu, C., Hubbard, K., and Garrett, M. (2019). The coastal ocean circulation influence on the 2018 West Florida Shelf *K. brevis* red tide bloom. *J. Geophys. Res. Ocean.* 124, 2501–2512. doi: 10.1029/2018JC014887

Weisberg, R. H., Liu, Y., and Mayer, D. A. (2009b). West Florida Shelf mean circulation observed with long-term moorings. *Geophys. Res. Lett.* 36, L19610. doi: 10.1029/2009GL040028

Weisberg, R. H., Zheng, L., and Liu, Y. (2016a). West Florida Shelf upwelling: origins and pathways. *J. Geophys. Res. - Ocean.* 121, 5672–5681. doi: 10.1002/2015JC011384

Weisberg, R. H., Zheng, L., and Liu, Y. (2017). On the movement of *Deepwater Horizon* oil to northern Gulf beaches. *Ocean. Modell.* 111, 81–97. doi: 10.1016/j.ocemod.2017.02.002

Weisberg, R. H., Zheng, L., Liu, Y., Corcoran, A., Lembke, C., Hu, C., et al. (2016b). *Karenia brevis* blooms on the West Florida Shelf: A comparative study of the robust 2012 Bloom and the nearly null 2013 event. *Cont. Shelf. Res.* 120, 106–121. doi: 10.1016/j.csr.2016.03.011

Weisberg, R. H., Zheng, L., Liu, Y., Lembke, C., Lenes, J. M., and Walsh, J. J. (2014a). Why a red tide was not observed on the west Florida continental shelf in 2010. *Harmf. Algae.* 38, 119–126. doi: 10.1016/j.hal.2014.04.010

Weisberg, R. H., Zheng, L., Liu, Y., Murawski, S., Hu, C., and Paul, J. (2016c). Did *Deepwater Horizon* hydrocarbons transit to the west Florida continental shelf? *Deep-Sea. Res. Part II.* 129, 259–272. doi: 10.1016/j.dsr2.2014.02.002

Weisberg, R. H., Zheng, L., and Peebles, E. (2014b). Gag grouper larvae pathways on the West Florida Shelf. *Cont. Shelf. Res.* 88, 11–23. doi: 10.1016/j.csr.2014.06.003

Zheng, L., and Weisberg, R. H. (2012). Modeling the west Florida coastal ocean by downscaling from the deep ocean, across the continental shelf and into the estuaries. *Ocean. Model.* 48, 10–29. doi: 10.1016/j.ocemod.2012.02.002

Author Disclaimer: All claims expressed in this article are solely those of the authors and do not necessarily represent those of their affiliated organizations, or those of the publisher, the editors and the reviewers. Any product that may be evaluated in this article, or claim that may be made by its manufacturer, is not guaranteed or endorsed by the publisher.

Conflict of Interest: The authors declare that the research was conducted in the absence of any commercial or financial relationships that could be construed as a potential conflict of interest.

Publisher's Note: All claims expressed in this article are solely those of the authors and do not necessarily represent those of their affiliated organizations, or those of the publisher, the editors and the reviewers. Any product that may be evaluated in this article, or claim that may be made by its manufacturer, is not guaranteed or endorsed by the publisher.

Copyright © 2022 Weisberg and Liu. This is an open-access article distributed under the terms of the Creative Commons Attribution License (CC BY). The use, distribution or reproduction in other forums is permitted, provided the original author(s) and the copyright owner(s) are credited and that the original publication in this journal is cited, in accordance with accepted academic practice. No use, distribution or reproduction is permitted which does not comply with these terms.

frontiers | Frontiers in Marine Science

ORIGINAL RESEARCH
published: 23 June 2022
doi: 10.3389/fmars.2022.867439

An Observation-Based Study of Gulf Stream Meander Kinematics Offshore of Cape Hatteras

Mike Muglia[1]*, *Harvey Seim*[2], *John Bane*[2] and *Patterson Taylor*[1]

[1] East Carolina University, Coastal Studies Institute, Wanchese, NC, United States, [2] Earth, Marine, and Environmental Sciences, University of North Carolina, Chapel Hill, NC, United States

Gulf Stream (GS) meander structure and propagation offshore of Cape Hatteras are investigated by integrating current measurements from a bottom-moored Acoustic Doppler Current Profiler (ADCP) with high-frequency radar (HFR) surface current measurements and satellite Sea Surface Temperature (SST) images during November 2014. The ADCP measurements provide well-resolved current observations throughout most of the water column, while hourly surface current measurements from HF radars and available satellite SST images provide spatial context to the GS orientation, meander propagation, circulation, and shear structure in the region of the ADCP mooring. The observations provide new insights about meander propagation and evolution in this important transition region. ADCP measurements observed that the increase and deepening intervals of the downstream current with approaching meander crests were typically longer than those for the decrease and shoaling of downstream current, consistent with prominent skewed crests near the surface. The transition time from trough to crest is much greater than that from crest to trough, reflecting the asymmetry in the downstream velocity structure. Vertical shears in the downstream and cross-stream velocity components are indicative of a cold dome centered downslope and offshore of the ADCP. Local maxima in downstream current and bottom temperature at the ADCP occur simultaneously, are accompanied by large vertical velocities, and are led by offshore currents in the upper water column. The mean meander phase speed estimated with HFRs is 48 km/day. Meander periods during the month are about 5-6 days. Where the maxima are seen in the water column, downstream currents reach 2.5 m/s, with current reversals sometimes in excess of 0.5 m/s. Downstream currents occupy an increasing portion of the water column as a crest approaches, and a decreasing fraction as a trough approaches. The deepening increase in downstream velocities with approaching crests is often accompanied by an increase in upstream velocities near the bottom.

Keywords: Gulf Stream, Cape Hatteras, meanders, western boundary current, observations

OPEN ACCESS

Edited by:
Alejandro Jose Souza, Center for Research and Advanced Studies - Mérida Unit, Mexico

Reviewed by:
Shin-ichi Ito, The University of Tokyo, Japan
Tal Ezer, Old Dominion University, United States

***Correspondence:**
Mike Muglia
muglia@gmail.com

Specialty section:
This article was submitted to Coastal Ocean Processes, a section of the journal Frontiers in Marine Science

Received: *01 February 2022*
Accepted: *23 May 2022*
Published: *23 June 2022*

Citation:
Muglia M, Seim H, Bane J and Taylor P (2022) An Observation-Based Study of Gulf Stream Meander Kinematics Offshore of Cape Hatteras. Front. Mar. Sci. 9:867439. doi: 10.3389/fmars.2022.867439

1 INTRODUCTION

The propagation and evolution of Gulf Stream (GS) meanders have been studied extensively both north and south of Cape Hatteras, with less attention given to the meander transition region near the cape. As a result, meander propagation past Cape Hatteras (**Figure 1**), and potential linkages between the two very different biogeophysical meander regimes to the south and north are not well understood. For example, meander decay downstream of the Charleston Bump may leave nutrient-rich upwelled water in meander troughs stranded south of Cape Hatteras (Savidge, 2004). Recent potential changes in the GS system make understanding these connections increasingly important. For example, indications of a recent westward shift of the GS destabilization point after it leaves the continental margin suggests enhanced exchange between the GS and the Slope Sea and increased high salinity warm water intrusions onto the Mid-Atlantic Bight (MAB) shelf and upper slope (Gawarkiewicz et al., 2012; Zhang and Gawarkiewicz, 2015; Andres, 2016). It has also been suggested that shifts in the GS destabilization point may influence coastal water levels (Ezer, 2019).

This paper presents observations that investigate GS meander properties and propagation offshore of Cape Hatteras by combining current measurements from a moored Acoustic Doppler Current Profiler (ADCP) with high frequency radar (HFR) surface current measurements and satellite Sea Surface Temperature images (SSTs) during November 2014. The ADCP measurements provide well-resolved current observations throughout most of the water column, while hourly surface current measurements from HF radars and available satellite SSTs provide spatial context to the GS orientation, meander propagation, and circulation in the region of the ADCP mooring. Together, these observations provide new insights about meander propagation and evolution in this important transition region.

2 BACKGROUND

Investigation of GS meander propagation has a rich history, with GS variability being recognized as far back as the sixteenth century (see Brooks and Bane, 1983). Meander evolution has been studied extensively both north and south of Cape Hatteras (Savidge, 2004). Upstream of Cape Hatteras, the GS is deflected seaward between 31° and 32 ° N latitude by the Charleston Bump (Brooks and Bane, 1978), a prominent topographic high on the Blake Plateau where water depth decreases from more than 700 m to less than 375 m (**Figure 1**) (Sedberry, 2010). Previous investigations have shown the deflection is bimodal, with both strongly and weakly deflected states typically occurring in the Fall/Winter and Spring/Summer, respectively. Both have been shown to have a significant downstream impact on Gulf Stream variability. Meanders when the GS is strongly deflected have periods between 14 and 20 days, with weakly deflected meanders having 4-8 day periods (Bane and Dewar, 1988). Meander lateral amplitudes are typically greatest (~50 km) at the initial deflection, and decrease downstream to a minimum of about 10 km at Cape Hatteras (Miller, 1994). Typical meander wavelengths are 100-250 km, with propagation speeds of 20-60 km/day (Brooks and Bane, 1981; Bane and Dewar, 1988). Both baroclinic (Oey et al., 1992) and barotropic processes contribute to meander growth and decay (Luther and Bane, 1985; Dewar and Bane, 1985; Gula et al., 2014), with energy exchanged between meanders and the mean flow (Kang and Curchitser,

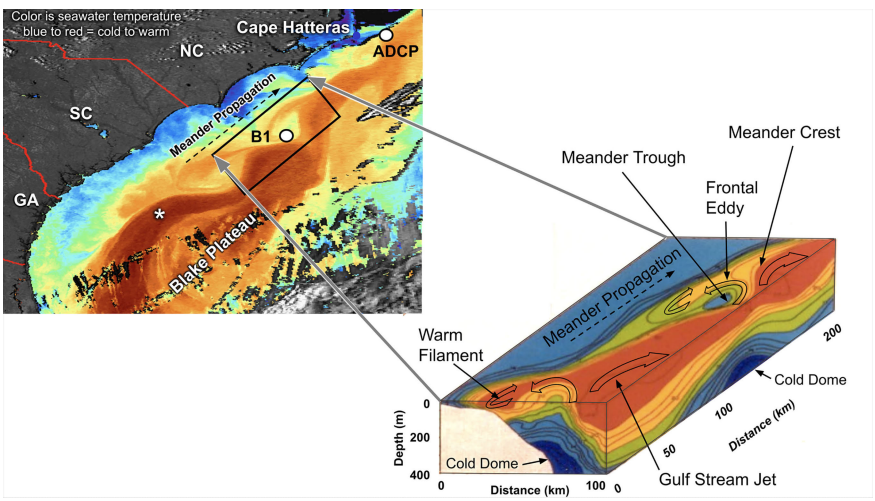

FIGURE 1 | Gulf Stream meander SST image (upper left) and associated 3-D volume view of meander features annotated (lower right). The location of mooring B1 (from Bane et al, 1981) is shown. Observed temperature and velocity time series from this mooring are shown schematically in **Figure 2**. The white asterisk shows the center of the area known at The Charleston Bump. The Blake plateau is the relatively level bathymetric region beneath and offshore of the Gulf Stream, and extending from the lower frame of this image northward to just offshore of Cape Hatteras.

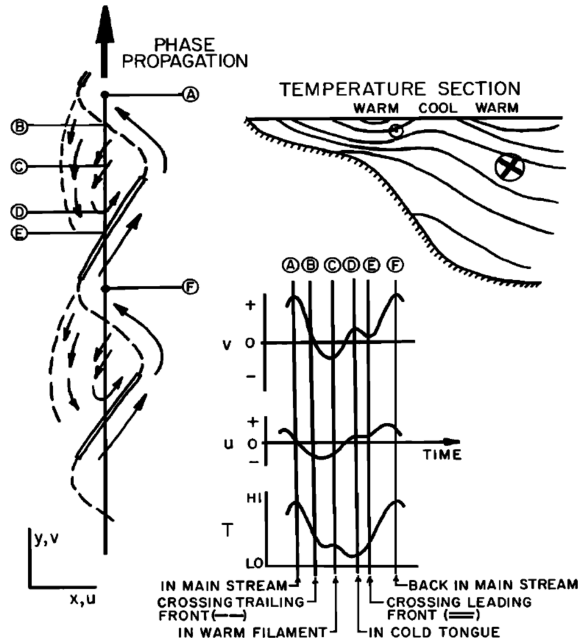

FIGURE 2 | Schematic meander structure and currents based on measurements made at location B1 shown in **Figure 1** and reported by Bane et al. (1981). The time series show alongstream (v) and cross-stream (u) velocity components and temperature (T) as a meander passes location B1.

2015) and lost by internal wave formation and near-bottom mixing (Todd, 2017).

Near Cape Hatteras, the GS leaves the continental margin and transitions from a topographically steered western boundary current to a free jet flowing in water depths that increase from 2000 m to 4500 m between 73° and 68° W. Some meanders increase in lateral amplitude to 100 km or more, and have periods of ~100 days. Propagation rates increase from about 14 km/d for longer periods and wavelengths of about 33 days and 460 km, to 45 km/d for shorter 4-day 180 km meanders (Tracey and Watts, 1986). In the region offshore of Cape Hatteras, the Deep Western Boundary Current (DWBC) passes beneath the GS, potentially contributing to meander growth (Dewar and Bane, 1989).

A depiction of 3-D meander structure along the Carolina coastline, derived from aircraft-launched expendable bathythermographs, is shown in **Figure 1** (adapted from Bane et al., 1981). Note the asymmetry of the meander crests and the associated skewness in the deepening of the warm isotherms as the meander crest propagates to the northeast. The deepening of the isotherms is analogous to the deepening of higher current speeds that also accompany the meander propagation.

The cool water in the meander trough, the "cold dome", is indicative of the upwelling that occurs in frontal eddies that form there and highlights the biogeochemical importance of these "nutrient pumps" (Yoder et al., 1983; Glenn and Ebbesmeyer, 1994a). A GS filament, which can form at a meander crest and is typically less than 100 m deep (Bane et al., 1981), is one mechanism for warm saline GS water to be advected onto the continental shelf.

Previous studies suggest GS variability upstream should affect downstream variability (Vazquez and Watts, 1985). Frontal eddies upstream of Cape Hatteras have been shown to propagate intact through this transition region by Glenn and Ebbesmeyer (1994b), without explicitly demonstrating the same for their accompanying meanders. The observations presented here provide evidence for meander propagation past Cape Hatteras, and thus suggest the importance of understanding their contribution to downstream variability.

3 OBSERVATION METHODS

Three types of observations made during November 2014 were used to observe GS meander evolution in the focus region (**Figure 3**): ADCP current measurements from a bottom mooring east of Cape Hatteras, HFR surface currents from the land based Southeast Coastal Ocean Observing Regional Association (SECOORA) network, and satellite SST images from the Rutgers University Coastal Ocean Observing Lab. ADCP and HFR data were quality controlled to Integrated Ocean Observing System (IOOS) standards (Integrated Ocean Observing System, 2021).

The ADCP mooring was maintained on the upper continental slope east of Cape Hatteras at 35.2°N and 75.1°W in a water depth of 260 m. The mooring contained a 150 kHz Teledyne Sentinel ADCP. The ADCP measures currents with 4-m vertical resolution over most of the water column every ten minutes, excluding only the bottom 8 m, and top ~28 m. The 10-minute measurements were hourly averaged. The ADCP currents were

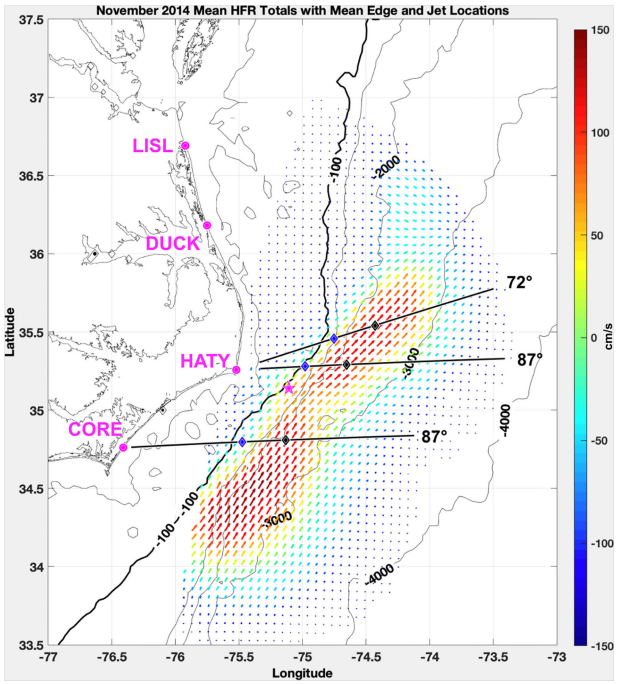

FIGURE 3 | A map of the study focus region. ADCP mooring is the pink star just offshore of the 100 m bold isobath. Land-based HF radars are located at the pink dots with their 4-letter identifiers. Mean GS edge and jet positions at blue diamonds and black diamonds respectively, along select HFR bearings from CORE and HATY for November 2014. The colored vector field shows the mean total surface current speeds from the radar network for November 2014.

rotated into a streamwise coordinate system such that the downstream direction was the depth-averaged and time-averaged velocity direction over the entire monthly record: 40° clockwise from True North in this case. The positive cross-stream direction (90°clockwise from the downstream direction) is nearly cross-isobath and offshore. Details of the mooring are further discussed in Muglia et al. (2020).

Hourly surface current measurements in the top 2.7 m of the water column, made from a land-based HFR network of 5 MHz Codar Ocean Sensors radars, were used to provide more frequent observations over a greater spatial region, thereby giving more context for surface processes than was available by satellite SST imagery alone (Roarty et al., 2010). Total surface currents are vector sums of radial surface current observations from four HFRs located on the Virginia and North Carolina coast. These consistently measure surface currents along the NC coast and provide measures of the GS as it transitions from a topographically-steered boundary current to a free jet. HFRs in the IOOS are given four letter identifiers: LISL is located in Little Island Park in Sandbridge VA, DUCK is at the Field Research Facility in Duck NC, HATY is located in Buxton NC on the north side of Cape Hatteras, and CORE is on the Core Banks of NC north of Cape Lookout at the National Parks Service's Great Island Campground. This study uses the HFRs to determine (1) GS position and width and orientation of the GS surface jet with individual radars, and (2) total surface currents from the combined HFR network on a 5.85 x 5.85 km grid. Radar and algorithm details are provided in Muglia et al. (2022). The method identifies hourly and mean locations of the GS edge and jet axis relative to the ADCP using radial velocities from individual monostatic HFRs HATY and CORE (**Figure 3**). The method was also used to estimate meander phase speed from several of the HFR currents over the entire time series. This average was derived by selecting the same prominent meander features in HFR currents six hours apart, and measuring distances between them on November: 7th from 12:00 to 18:00, 20th from 12:00 to 18:00, 27th from 00:00-06:00, and 30th 12:00-18:00. Estimates were 25.4 km/day, 55.2 km/day, 85.4 km/day, and 37.0 km/day, respectively. The reader is referred to Muglia et al. (2022) for a detailed explanation.

Satellite SSTs were provided courtesy of the Rutgers University Coastal Ocean Observing Lab (Rutgers Coastal Ocean Observing Lab, 2021). Products used for this work include the satellite sea surface temperature imagery collected from the National Oceanic and Atmospheric Association (NOAA) Advanced Very High Resolution Radiometer (AVHRR) and Terra Moderate Resolution Imaging Spectroradiometer (MODIS).

4 RESULTS

4.1 November 2014 Overview

The hourly HFR and ADCP current measurements provide consistent characterization of the current environment off Cape Hatteras during November 2014. This month was chosen because

of the concurrent availability of the observations presented and the higher quality of the HFR surface currents and GS estimates from them. It is informative to first characterize the GS environment during the month by exploring mean monthly surface currents, algorithm estimates of GS position and variability, and frequency and nature of GS meander events. With that foundation, the character of specific meander passages is determined by integrating available SST's, HFR surface currents, and ADCP current measurements throughout the water column.

HFRs provide consistent estimates of GS position and orientation, meander propagation, and circulation in the region of the ADCP mooring. **Figure 3** shows the November 2014 mean positions of the GS edge and jet axis along the three bearings closest to the ADCP mooring – one from CORE and two from HATY. The GS method selects the GS edge at the largest gradient in radial velocity, and the jet axis at the location of the maximum radial velocity along selected bearings. The CORE 72° bearing estimates are not included because of their high uncertainty caused by the estimates being made at great distance from the radar. Note that the ADCP, the red star offshore of the bold 100 m isobath in **Figure 3**, lies approximately along the same isobath as the upstream HFR mean GS edge locations where lateral shear in the cyclonic shear zone of the GS is greatest.

Monthly mean surface currents measured by the radar at the location of the ADCP are 0.8-0.9 m/s due to frequent GS incursions over the mooring (**Figure 3**).

The distribution of the algorithm's GS edge and jet axis picks (**Figure 4**) relative to the ADCP demonstrate the variability caused by frequent meander passages at the mooring. The frequent incursions of the GS edge landward of the 100 m isobath (**Figure 4**) along the HATY 87° bearing may explain the large mean current speeds near the ADCP (**Figure 3**).

Meander passages, identified as variations in GS edge and jet positions from the radar data near the ADCP, are apparent in the monthly time series of the ADCP downstream currents (**Figure 5**). Meander propagation over the mooring is recognizable in the alternating current increases, decreases, and occasional reversals. Deepening rapid downstream current in the water column indicates the approach of a meander crest, while decrease in downstream current indicates an approaching trough. Upstream-directed currents are the likely result of frontal eddy circulation in meander troughs (Bane et al., 1981; Glenn and Ebbesmeyer, 1994b). The skewness mentioned previously in the analogous deepening of warm isotherms with the meander passage in **Figure 1** can now be seen in the deepening of higher downstream current velocities measured by the ADCP over the time period of a meander passage. Indeed, several meander events in **Figure 5** are Eulerian depictions of a meander like that in **Figure 1** propagating past the mooring.

The downstream current time-series from the ADCP contains five or six meander passages over the mooring, identified by downstream current increases followed by decreases. There are four prominent meander passages during the month. Meander periods are about 5-6 days. Where the downstream-velocity maxima are seen in the water column, currents reach 2.5 m/s, with current reversals sometimes in excess of 0.5 m/s (**Figure 5**).

4.2 Current Structure From the ADCP

The measured currents are well resolved over most of the water column and provide rich current and shear structure detail in the

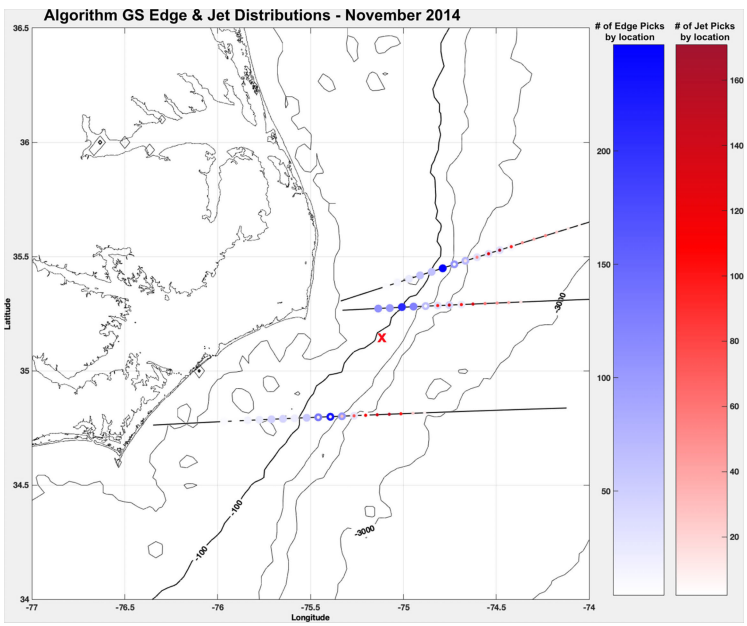

FIGURE 4 | The GS edge and jet location distributions from the algorithm for select CORE and HATY bearings during November 2014. The edge (jet) distributions are shown with blue (red) colorscale. The ADCP is located at the red 'x'.

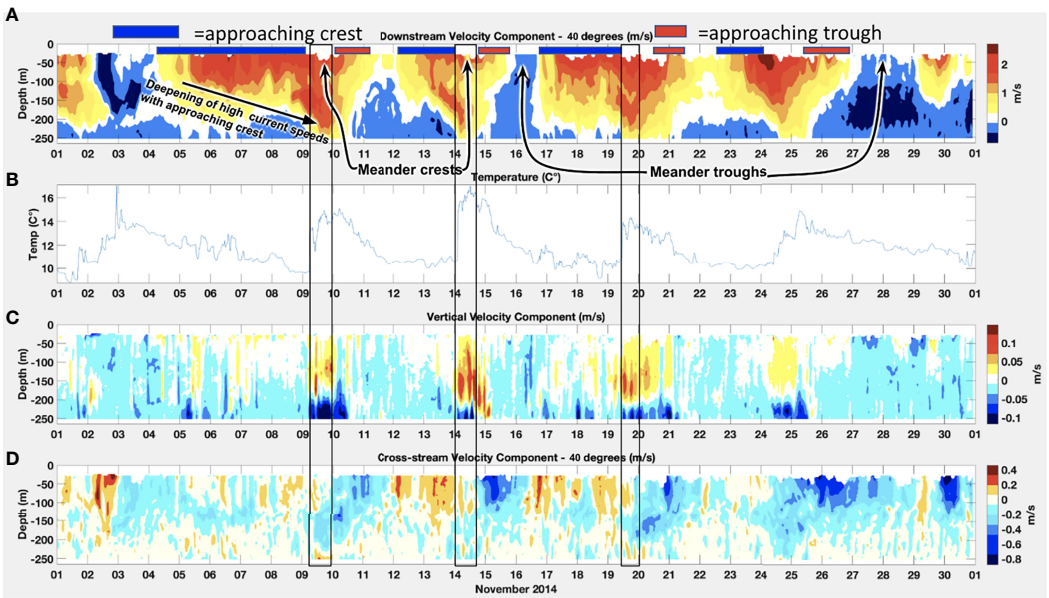

FIGURE 5 | ADCP measurements range limited to ~40 meters below the surface: downstream **(A)**, bottom temperature in °C **(B)**, vertical **(C)** and cross-stream **(D)** velocities in m/s. Three meander crests with similar characteristics are boxed. Positive downstream (cross-stream) velocity is northeastward (southeastward, or offshore).

downstream, cross-stream and vertical directions. It is useful to examine these current components with corresponding bottom temperature variations at the mooring to gain understanding of meander evolution and identify similarities and differences between events (**Figure 5**). Examining the velocity components' variability first is helpful to discern the more complicated associated shear profiles (**Figure 6**).

Several attributes appear repeatedly due to the alternating presence of meander crests and troughs over the ADCP. It is useful to explore the events that begin around November 5, 13 and 17 first. The changes that occur in the velocity components during these three events are consistent in character, and with the meanders depicted in **Figure 1**.

The transition time from trough to crest is greater than that from crest to trough, resulting in an asymmetry in the downstream velocity structure. Strong downstream currents occupy an increasing portion of the water column as a crest approaches, and a decreasing fraction as a trough approaches. The deepening of strengthening downstream velocities with approaching crests is often accompanied by an increase in upstream velocities near the bottom. The greater downstream velocities with the approaching crest that deepen beyond 100 m

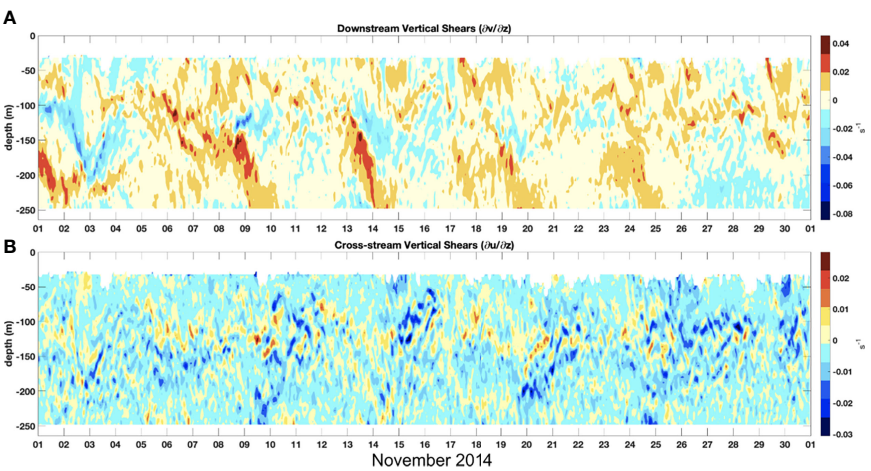

FIGURE 6 | ADCP downstream ∂v/∂z) **(A)** and cross-stream (∂u/∂z) **(B)** vertical shears, with zero current/shear contours in black.

bifurcate, causing high currents near the surface, slower flow beneath them, and a second maximum in downstream flow in the lower 100 m around the 9th, 13th, and 19th (**Figure 5**).

Cross-stream flow is offshore as a crest approaches, and transitions to onshore after a crest passes and a trough approaches. Note that this transition to onshore flow occurs first at depths of ~100-150 m, about ~12-24 hours prior to the change near the surface, and that the onshore flow at depth coincides with the deepening of downstream currents and increase in temperature at the ADCP (**Figure 5**, events outlined). The increase in upstream currents near the bottom with an approaching crest are often accompanied by onshore currents in the same region. Low bottom temperatures at the mooring, within the base of a cold dome, usually correspond with offshore flow in the top ~100 m of the water column, although offshore flow persists during the large increases in bottom temperature at the mooring that usually lead the transition to onshore flow following the passing trough.

Vertical velocities are generally small (~1 cm/s) except during the passage of a meander crest, when large vertical velocities (~10 cm/s) occur. From the surface to 200 m depth, the vertical currents are upward, while below 200 m they are downward. These large vertical velocities are coincident with the very abrupt arrival of warm (~15 C) water at the bottom, indicating the trailing edge of the cold dome of the frontal eddy is a strong thermal front.

Events at the beginning and end of the month, as well as the approaching crest on the 23rd have several aspects that differ from the three events that begin on the 5th, 13th, and 17th. The event from November 1st-4th is perhaps most dissimilar. Unlike the other crest-to-trough transitions discussed, large downstream currents persist at depth until the 2nd when the strongest upstream velocities occur in the upper 100 m, deepen, then slowly subside in the top 100 m while increasing at depth between 100-200 m. Also in stark contrast are the deepening upstream currents that coincide with the highest spike in temperature at the instrument. The bottom temperature increase is more gradual and vertical currents are limited. And, just before November 3rd the highest offshore currents of the time series, about 40 cm/s, coincide with the largest upstream velocities (**Figure 5**).

The increase and deepening in downstream current on November 23rd are accompanied by an increase in temperature at the mooring like the other events, but the depth profile of the high downstream currents is more symmetric over time. The switch to onshore currents occurs earlier during this event, coinciding with the increase in downstream flow, and like the other three events leads at depth before occurring in the top 100 m. Warming of bottom temperatures is less abrupt than for the events described earlier, and vertical currents are present but weaker than in the other events. The increase and deepening of the large downstream current on the 30th are much shallower, and thus results in little temperature increase at the mooring and no strong vertical currents. Rather than meander propagation along isobaths, the crest may be moving somewhat offshore in this instance.

4.3 Vertical Current Shear Structure From the ADCP

Having described the vertical structure of the current, it is informative to examine the shear profiles that result, in particular, the vertical shear of the downstream current $\partial v/\partial z$, called downstream shear) and the vertical shear of the cross-stream current ($\partial u/\partial z$ called cross-stream shear). Again, it is helpful to begin by considering the three similar events that begin on the 5th, 13th, and 17th, prior to exploring the events that differ. In all three, the deepening of the higher velocity current that occupies a greater portion of the water column during the meander crest approach is accompanied by deepening positive downstream shear from November 5th-10th, 12th-15th, and 17th-21st. The previously mentioned bifurcation in the deepening higher velocities causes associated positive shears near the surface that approach 0.02 s^{-1}. These then change to negative shears of the same magnitude beneath them, and return to positive shears below 100 m, sometimes reaching magnitudes of 0.04 s^{-1} (**Figure 6**). The largest shears observed during the time series accompany these events, and are all deeper than 100 m. The corresponding cross-stream shears also alternate from close to zero or negative near the surface, to positive, and back to negative again at about the same depth as the alternating downstream shears. The positive cross-stream shears near the middle of the water column are some of the highest during the time series, often approaching 0.02 s^{-1}. Although there is an apparent deepening of the positive cross-stream shear that accompanies the deepening downstream current with an approaching crest, the shear structure is often intricate, with shear profiles that can alternate from positive to negative up to six times over the water column as was the case on the 14th.

Decreases in downstream velocities, occasional reversals, and increasing onshore cross-stream currents that coincide with approaching troughs typically exhibit an increase in the proportion of the water column with negative shears. The troughs on November 11-12th, 16th, and 22-23rd are examples. The flow reversal on November 16th results in negative downstream shear over much of the water column. The shoreward velocity on the 16th produces more negative cross-stream shears over much of the water column that are still interleaved with positive shears (**Figure 6**).

The event at the beginning of the month, from November 1st-4th, that differs from the others has a shear profile that is nearly opposite that of an approaching meander crest. The deepening of the upstream currents from November 2nd to the 3rd from the surface to depths of 100 m are accompanied by negative downstream shear along their leading edge. Between November 3rd and 4th, when downstream velocities are slightly positive in the top 100 m, and upstream between about 100-200 m, the downstream shear profile is negative at the surface, positive near 100 m, negative between ~125-200 m, and positive again near the bottom. Cross-stream velocities switch from offshore to onshore over most of the water column between November 2nd and 3rd, with a switch from positive to negative cross-stream shears over much of the water column happening on the 3rd (**Figure 6**).

4.3.1 ADCP and HFR: Meander Event 1

Exploring the meander propagation from November 4-11, henceforth Event 1 (**Supplemental Material E1**), the longest in duration of the three events with similar characteristics, within the spatial context of the HFR surface currents provides a broader understanding of the event. Unfortunately, high quality SSTs are not available during this period. E1 provides HFR surface current snapshots at 20:00 Greenwich Mean Time (GMT) each day, with the ADCP location appearing as a pink dot on the left image. The radar times were chosen to reduce nighttime ionospheric interference that tends to limit range (Menelle et al., 2008). Beginning November 2nd, the end of daylight savings time, the local time was GMT-5, or 1500 Eastern Standard Time (EST). The ADCP surface current speeds are included in the HFR image title, and the associated downstream ADCP current time series figure on the right contains a green vertical line at the time corresponding to the HFR figure. On November 4th near-surface current speed at the ADCP is 0.92 m/s, and an approaching crest is apparent in the ADCP downstream currents (**Figure 5**) but isn't obvious in the HFR currents (E1). On November 5th, stronger downstream currents reach the ADCP, with surface currents increasing to 2.10 m/s, and deepening of the strong downstream currents in the water column. The meander crest becomes more apparent upstream of the ADCP in the surface current image (E1), but cross-stream currents are still small at the surface with offshore flow strongest at about 100 meters (**Figure 5**). On November 6th, strong downstream currents deepen with corresponding positive downstream shears at the velocity gradient and deepening onshore flow in the same region beneath 100 m (**Figure 6**). The meander crest is not prominent in the HFR image (E1), but ADCP near-surface speeds reach 2.10 m/s. The meander crest asymmetry is more visible in the radar currents on November 7th (E1). The ADCP near-surface speed is about 1.99 m/s, and strong positive shears are pervasive throughout the entire water column. Offshore flow exists in the region of strong downstream flow in the upper 100 m, with positive cross-stream shear at the base of the strong surface flow (**Figure 6**). On November 8th, again the crest is less prominent in the HFR surface currents (**Figure 7** and E1). The upstream flow indicative of the approaching crest develops near the bottom. Late on November 9th, the deepest downstream currents approach the bottom, ADCP surface currents are 1.79 m/s, and the meander crest is more pronounced in the HFR surface currents (E1). Offshore flow at the surface continues almost until November 10th, but onshore flow indicative of the approaching trough begins beneath 100 m. Strong positive downstream shears deepen to the bottom of the ADCP coverage along the edge of the strong downstream flow associated with the crest, and some of the strongest shears of the time series appear around 100 m.

On November 10th (E1) onshore currents shoal throughout the top 100 m and mark the passage of the meander crest over the mooring. Surface currents are still 0.99 m/s but are subsiding. Finally, on November 11th (E1), the trough with accompanying

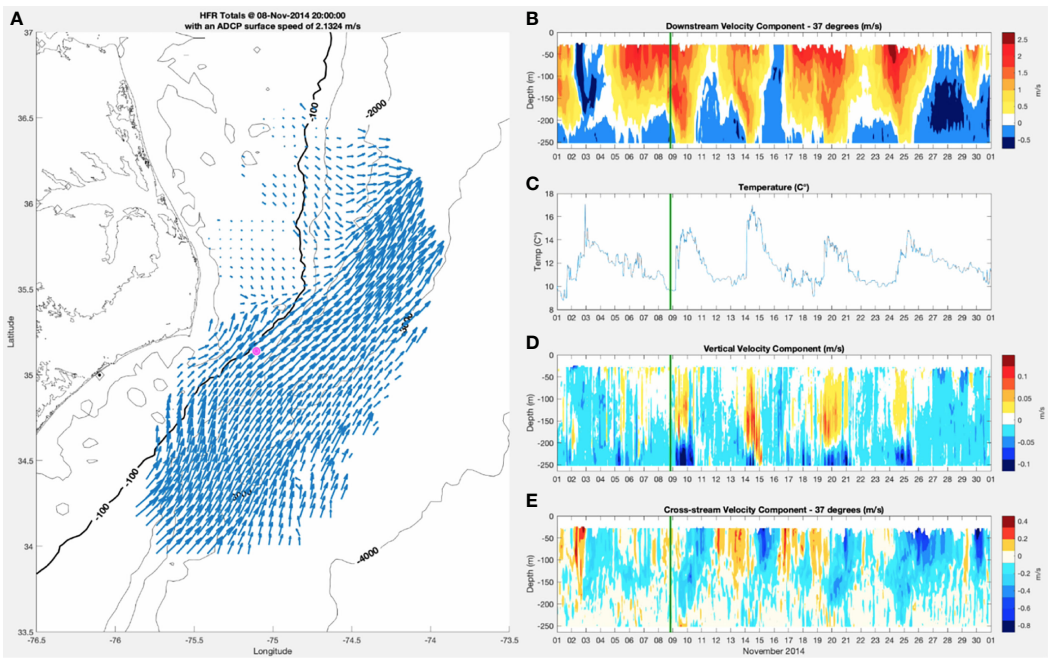

FIGURE 7 | Left: HFR surface currents **(A)** on November 8 at 20:00 GMT, with ADCP location at red asterisk, Right: ADCP downstream velocity contour **(B)**, bottom temperature **(C)**, vertical velocity contour **(D)**, and cross-stream velocity contour **(E)**, with green vertical line at November 8 at 20:00 GMT. See Event_1_.m4v for movie of meander passage from November 4 at 20:00 GMT to November 11 at 20:00 GMT.

strong onshore currents in the upper 100 m is over the mooring. Although the trough is prominent in the radar surface currents, there isn't reversal of the downstream flow in this case. Thus, either the center of the frontal eddy is onshore of the ADCP location or the frontal eddy is too weak to reverse the flow direction. Currents in the surface ADCP bin subside to about 0.76 m/s.

4.3.2 ADCP, HFR, and SST: Meander Event 2

What appears as a less developed meander event at the end of the month, November 26-30 at 18:00 GMT daily, henceforth Event 2 (**Supplemental Material E2**) in the downstream ADCP velocities is compelling to examine because all three types of observations are available. It includes pronounced cyclonic circulation and significant convergence in the HFR surface currents, and quality SST images on two of the days.

The spatial context provided by the SSTs and HFR currents provide insight not available from the ADCP observations alone. Beginning on November 26th, with the end of the meander crest passage at the ADCP, a large trough appears in the HFR currents southwest of the mooring with strong convergence at the southwest edge of the trough apparent in the surface currents near the 100 m isobath (**Figure 8** and E2). There is well established onshore flow, positive downstream shears, and negative cross-stream shears throughout most of the water column at the mooring (**Figure 6**). On November 27th, upstream currents begin to increase from the bottom to about 100 m below the surface. Shoreward flow over the entire water column is indicative of the approaching trough over the ADCP as seen in the HFR currents (E2). On November 28th, the trough is much less prevalent in the radar currents (E2). Strong shears develop at about 100 m in both the downstream and cross-stream velocities, where some shoaling of small offshore currents meet onshore flow there (**Figure 6**). The HFR currents from November 27th-29th appear to show the mooring at the edge of a trough which subsides as a couple of small wavelength features propagate past it, such that on November 29th the mooring is again on a crest edge (E2). The deepening in downstream currents on November 29th, and switch to offshore currents throughout much of the water column are also indicative of a crest over the ADCP as discussed in the other meander events (**Figure 6**). On November 30th, the crest appears to propagate downstream in all observations. Onshore currents appear at the ADCP late on November 29th at depth, and surface and increase on the 30th. Upstream currents begin to shoal from below (**Figure 6**). HFR currents (E2) indicate an approaching trough, and two SST images 3.5 hours apart (**Figure 11**) show downstream motion of the meander crest that brings the trough over the ADCP at 21:27 GMT.

The spatial context provided by the HFR currents over November 26th-30th contain some intriguing meander fluctuations that suggest a frontal eddy may be offshore of the ADCP causing a reversal in downstream currents. The meander crest and trough almost appear to shift temporarily upstream before propagating downstream at the end of the time series - in E2 on November 27th, the ADCP appears to be on the edge of the trough, but on November 29th in E2 it appears to be again on the edge of the crest. More likely, the ADCP is on the edge of two separate troughs over the period as the ADCP record suggests, with significant daily evolution in the meander pattern. For example,

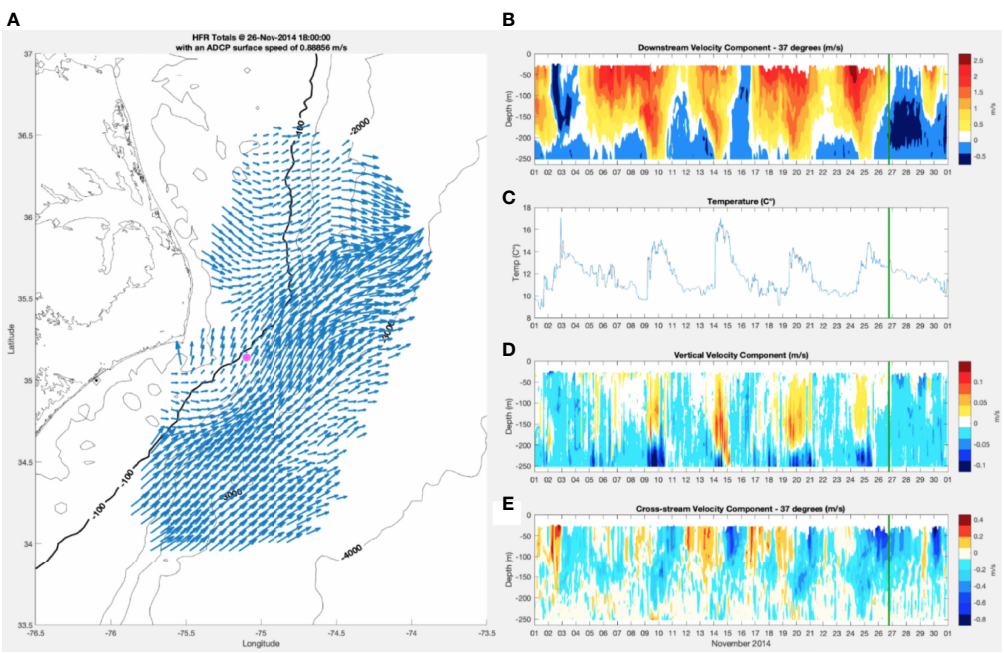

FIGURE 8 | Left: HFR surface currents **(A)** on November 26 at 18:00 GMT, with ADCP location at red asterisk. Right: ADCP downstream velocity contour **(B)**, bottom temperature **(C)**, vertical velocity contour **(D)**, and cross-stream velocity contour **(E)**, with green vertical line at November 26 at 18:00 GMT.

the meander crest and trough are well defined in several of the HFR surface current snapshots, but much less so on November 28th. The surface currents on November 27th and 29th have well defined troughs. Meanders may evolve over short time periods, relaxing and re-intensifying here. The Muglia et al., 2022 algorithm estimated averaged meander speeds of 48 km/day.

5 DISCUSSION

Observations off Cape Hatteras during November 2014 have both confirmed meander evolution characteristics seen in previous studies and revealed new details in this less studied GS meander transition region. Several meander attributes identified in these observations that agree with previous studies are as follows. At a fixed location, the time for an increase and deepening of the downstream current with an approaching crest is usually longer than that for the decrease and shoaling of the current after a crest passage, resulting in a skewed crest with the leading portion being longer than the trailing portion. Local maxima in current and temperature at the mooring occur simultaneously, are followed closely by remarkably strong vertical currents, and are usually led by offshore currents in the upper water column much like that presented by Bane et al. (1981) in their Figure 15, reproduced here in **Figure 1**. The average meander phase speed of ~48 km/day estimated from the HFR currents is slightly faster in this region than the 30-40 km/day seen earlier in Onslow Bay off southern North Carolina (Brooks and Bane, 1981), and is consistent with the 46-50 km/day observed for a frontal eddy propagating past Cape Hatteras by Glenn and Ebbesmeyer (1994a), the 40-55 km/day meander propagation reported by Savidge (2004), and the 40-70 km/day reported by Andres (2021).

Good agreement is found between the HFR-observed surface current pattern and modeled surface currents described by Miller and Lee (1995) and Gula et al. (2016). Moving upstream-to-downstream in **Figure 9**, note the offshore-then-onshore curving of the main GS jet (strongest current speeds) in each panel. This is the crest-trough-crest meander pattern. Adjacent to the main jet on the shoreward side is the cyclonic circulation of the frontal eddy that is located within the meander trough. Note the interesting area of near-zero flow along the shoreward side of the frontal eddy, which is due to the addition of the downstream propagation speed of the eddy with the upstream-directed cyclonic circulation, roughly adding together to be near zero.

Potential causes for the strong HFR surface-current convergence along the southwestern edge of the meander trough/frontal eddy in the November 26-30 event (**Figure 10**) have been discussed by other authors. On the frontal-eddy scale, there is generally upwelling (downwelling) within the leading (trailing) portion of a frontal eddy (Osgood et al, 1987; Bane et al, 2001). On the sub-mesoscale, Bower (1989); Thomas and Joyce (2010) and Gula et al. (2016) have shown that frontal jets tend to be confluent (diffluent) on the upstream (downstream) side of a meander trough. An additional contribution may come from shelf water export in the vicinity (Han et al., 2021). During the event, the wind at Diamond Shoals increased to 13 m/s out of the south, then swung more from the west/northwest on November 26th by about 18:00 GMT. It then subsided on November 27th before increasing again from the NW on November 28th. It blew from the NW at 10-12 m/s most of the day, then subsided again to less than 10 m/s on the 29th for the rest of the time period (US Dept. of Commerce, 2019). The increasing southerly winds shifting to northerly from the passage of a cold front, and the warm GS filament flooding Raleigh Bay may have caused convergence and export of shelf

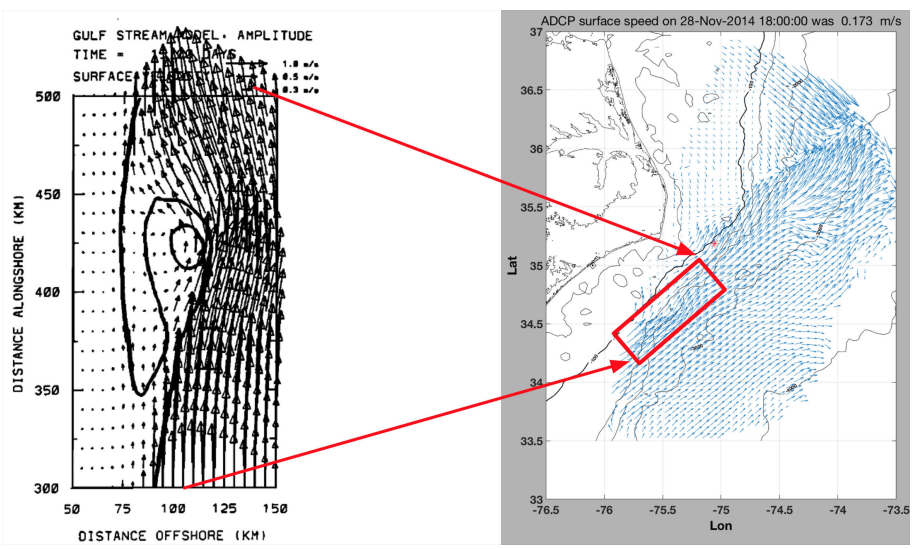

FIGURE 9 | Similar surface current circulation around a meander trough between modeled (left) and HFR observed currents (right). (Left is from Miller and Lee, 1995).

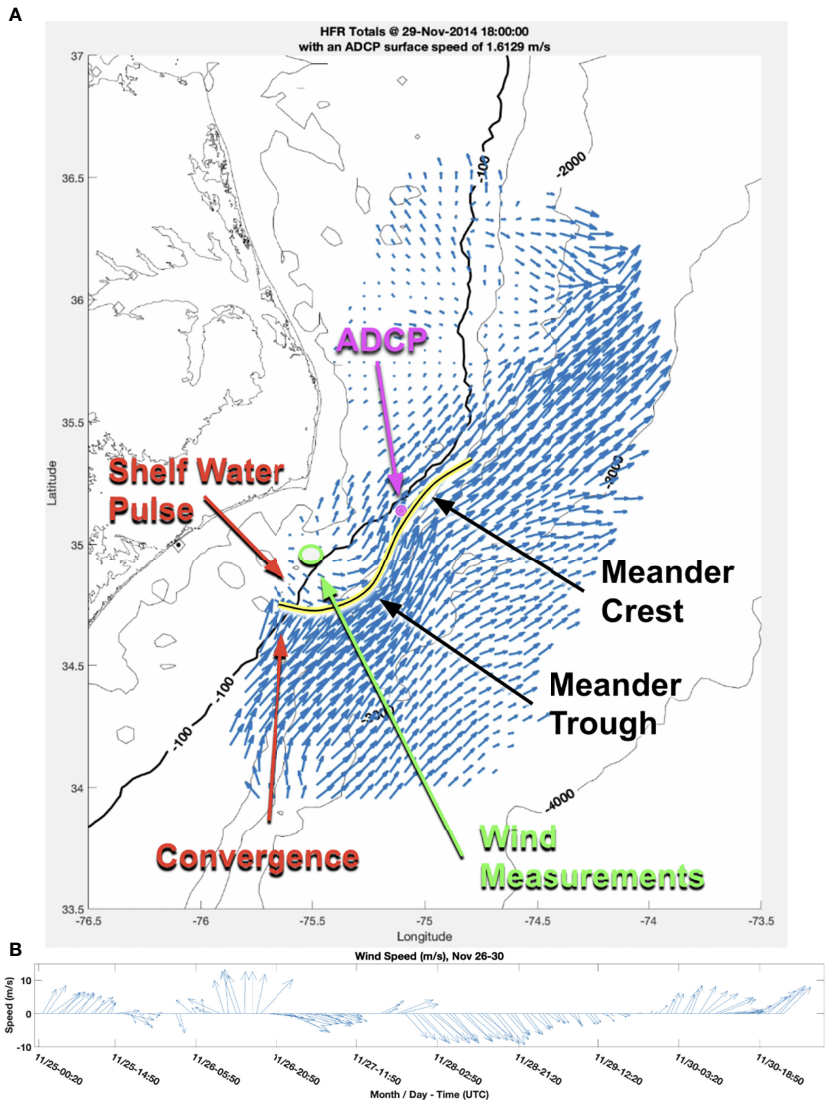

FIGURE 10 | HFR surface currents **(A)** on November 29th at 18:00 GMT with shelf water pulse, meander, and convergence, and location of wind measurements highlighted. Wind speed and direction timeseries **(B)** at the location noted in **(A)** from November 25th through November 30th.

water that enhanced the strong convergence at the meander trough (Churchill and Gawarkiewicz, 2012 and Han et al., 2021). Notable pulses of water from the shelf offshore, seen in the HFR currents, appear to contribute to the convergence at the trailing edge of the trough on the 26th (**Figure 10**), 27th (E2), and 29th (**Figure 11** and E2).

The combination of the well-resolved currents over the water column from the ADCP and higher frequency consistent spatial context from the HFR currents provide powerful tools to identify new details of the meander evolution here as well. The downstream current component from the ADCP exhibits much more exaggerated skewness in the upper 100 m of the water column during the November 5-11 and 17-22 events (**Figure 5**) than that established in Bane et al. (1981) (**Figure 2**). The increase in downstream currents in the top 100 m leads that at depth by several days in multiple instances, while crests depart at depth about a day before downstream currents subside at the surface. Onshore currents that precede troughs often begin just below 100 m prior to increasing at the surface. Also, the abrupt temperature increases and strong vertical currents at the mooring on November 9th, 14th, and 19th are unlike the gradual increase that coincides with increasing v in **Figure 2**, while the simultaneous occurrence of maxima in v and T are consistent.

Although three similar meander events occurred during the month, all were different in several ways including event duration, times for crest and trough approaches that defines the degree of skewness, amount of temperature increase at the

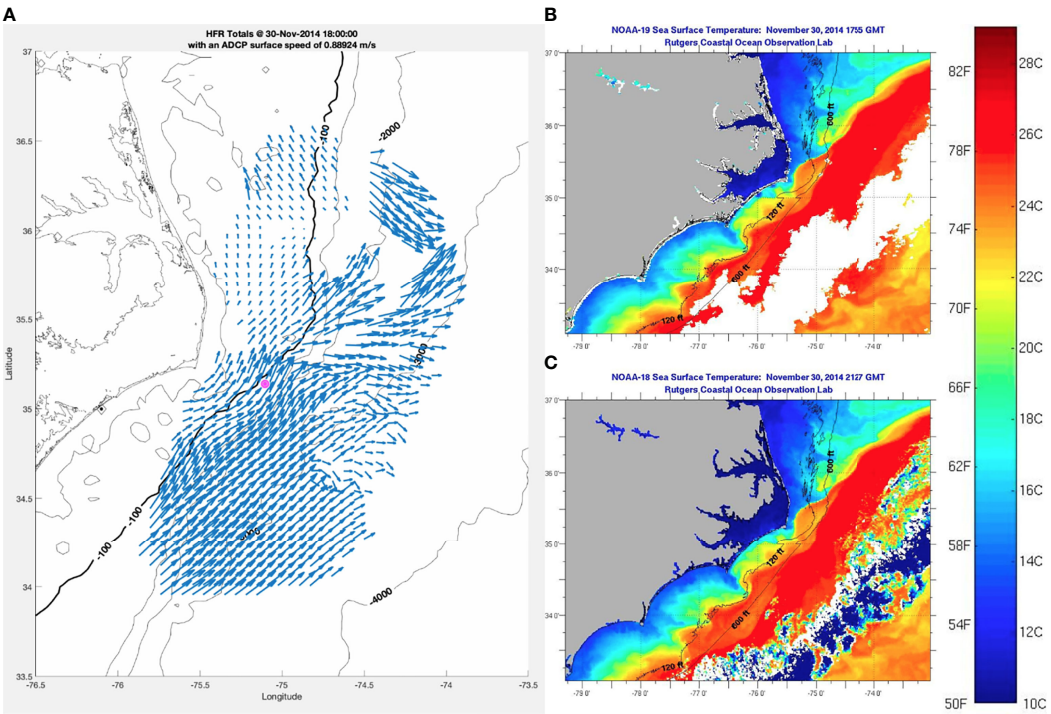

FIGURE 11 | **(A)**: HFR surface currents on November 30 at 18:00 GMT, with ADCP location at pink dot. **(B)** SST image on November 30th at 17:55 GMT. **(C)** SST image on November 30th at 21:27 GMT.

mooring, depth and magnitude of downstream and cross-stream velocity and associated shears. The degree to which the GS, particularly the center of the frontal eddy, is onshore or offshore of the mooring may contribute significantly to the differences. An example of the influence of GS position relative to the mooring is evident in the unique November 1-4 event. The GS position algorithm (Muglia et al., 2022) shows the GS moving offshore during this period along the HATY 87° bearing closest to the mooring. The strong upstream currents near the surface observed by the ADCP between November 2nd and 3rd coincide with the largest change in GS position along the 87° bearing (**Figure 12**). Quality SST's late on the 3rd and 4th (**Figure 13**) following the strong upstream flow near the surface on the ADCP, show a large filament pulling away from the ADCP that was possibly spawned by a strong frontal eddy, and contributed to the temperature spike at the mooring. Although, previous studies suggest filaments, or "shingles" (Von Arx et al., 1955), are surface-trapped features that don't extend downward to the mooring depth of 260 m (Bane et al., 1981).

The downstream and cross-stream shears also provide new information about the dynamics in this energetic region. Maxima in the vertical shear of the downstream velocity are nearly an order of magnitude greater than those observed in the stream just to the northeast after it parts from the continental margin (Whitt et al., 2018). The greatest shear magnitudes are often found well

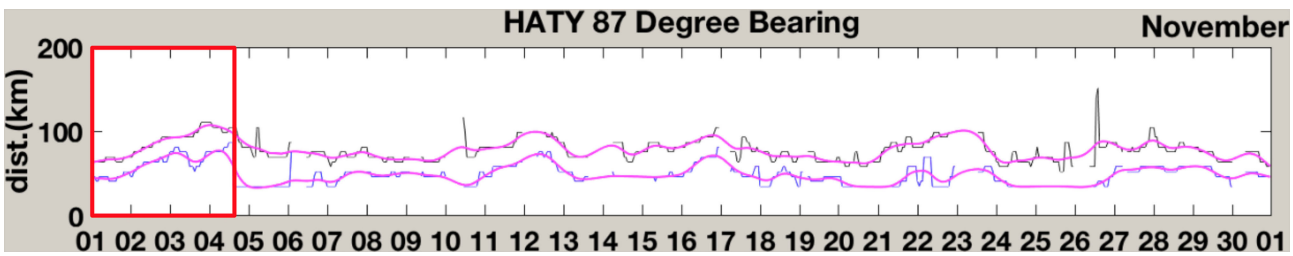

FIGURE 12 | Estimates of the range from the HATY HFR on the 87 degree bearing to the GS edge (blue) and jet (black), with magenta 28.5 hour low-pass cubic spline smoothing of all estimates.

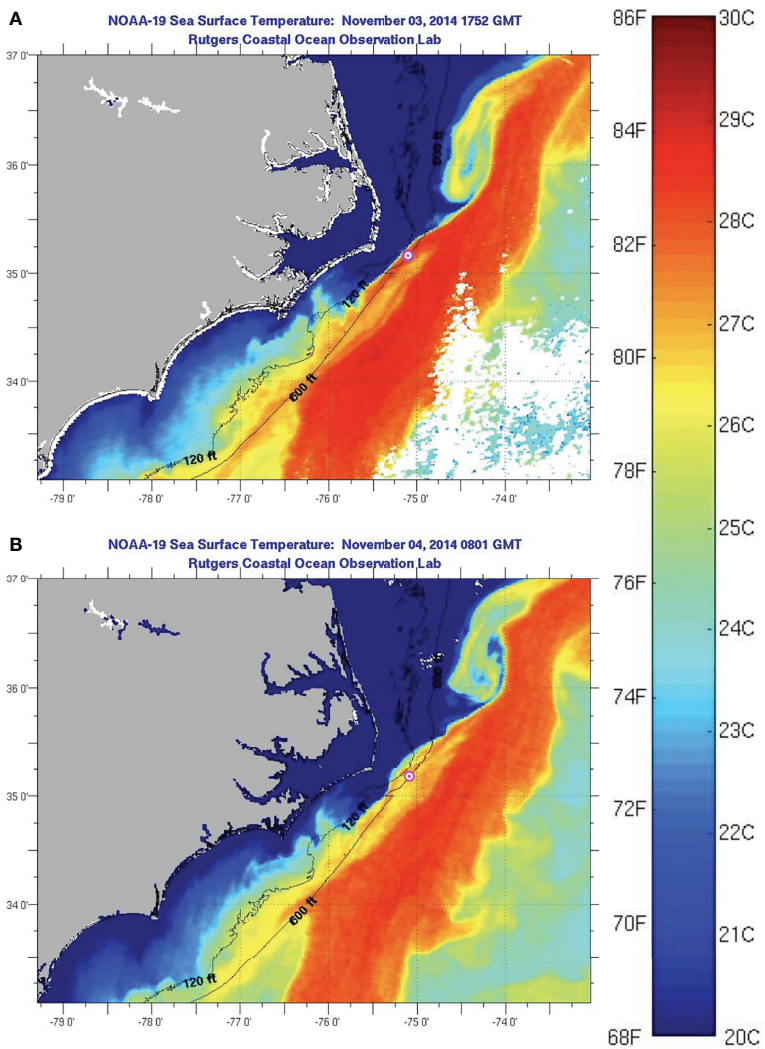

FIGURE 13 | SST image on November 3rd at 17:52 GMT and a day later on November 4th at 18:01 GMT. The ADCP location is marked with a pink dot.

below the velocity gradient beneath the GS jet axis (Muglia et al., 2020) and often persist to the bottom in the downstream direction (**Figure 6**). The bifurcation in the deepening increase in downstream velocity produces strong shears that alternate in sign, not consistent with the monotonic shoaling of the thermocline in typical depictions of the GS. The authors hypothesize that the center of a cold dome was downslope of the mooring causing the cross-slope density gradient to reverse sign for some portion of the water column inshore of the dome center. (A cold dome with this relative positioning was observed in November 1979 and reported by Brooks and Bane, 1983.) This may explain the unusual pattern in the downstream shears. It could also explain the second maximum in downstream velocity at depth. The slowdown below the second velocity maximum towards the seafloor is likely associated with a frictional bottom boundary layer. The presence of a cold-core frontal eddy offshore of the ADCP would cause isopycnals to slope in the opposite direction from the landward GS edge. Note the vertical shears in the cross-stream velocity are even more intricate, often changing sign more than four times throughout the water column.

Our interpretation is that the ADCP is in a region where departing crests have GS jet water flowing upward as the current flows toward the shelfbreak. When this occurs, the GS downstream velocity component is greater than the meander propagation speed in the upper portion of the water column, and water is moving upward along the GS's sloping thermocline as it makes its way northeastward. The water column is squashing, $\partial w/\partial z<0$, in the upper ~200 m and the vorticity is becoming more anti-cyclonic as water parcels flow through the curving meander crest, towards shore and then away from shore. Trough passages have associated cold domes (**Figure 14**), in which there are relatively smaller horizontal and vertical velocities, because the cooler water has less momentum than the faster and warmer GS jet water.

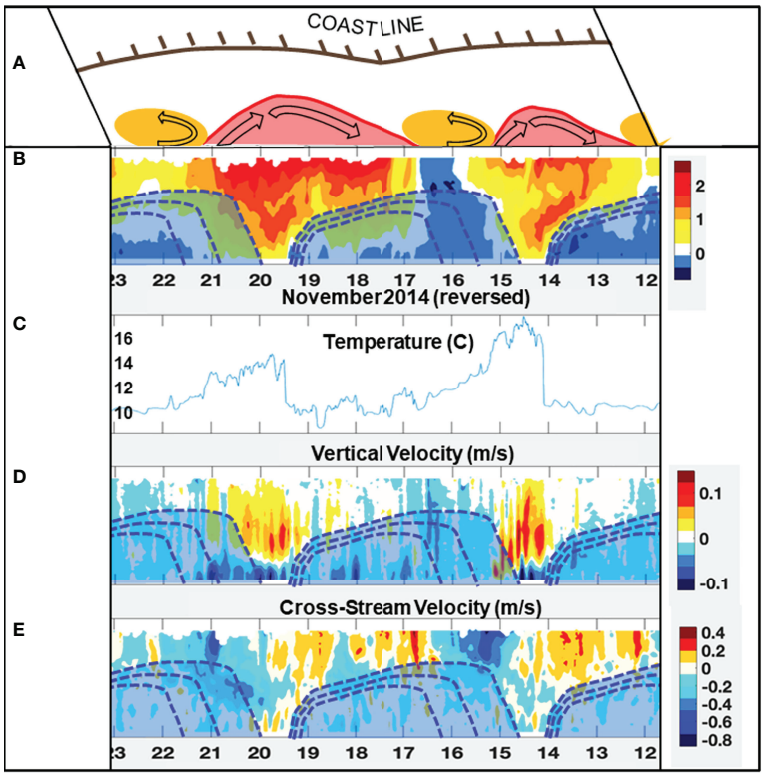

FIGURE 14 | A 3-D view of meander spatial structure, utilizing the ADCP time series from November 12 to 23. The time series have been reversed (right to left) to allow the data to be plotted as a function of downstream distance, assuming a constant downstream propagation speed. Two warm Gulf Stream meander crests and three cool cyclonic frontal eddies are shown schematically on the top horizontal surface **(A)**. Panel **(B)** is the downstream velocity component (positive to the right), **(C)** is bottom temperature (at the ADCP), **(D)** is the vertical velocity component, and E is the cross-stream velocity component (positive into the page, which is towards the coast). Three schematic cold domes in the meander troughs have been added (shaded light blue). The dashed contours are assumed isotherms.

6 CONCLUSIONS AND FUTURE WORK

The observations presented herein provide rich new information about meander structure and dynamics off Cape Hatteras. While they provide new understanding of meander evolution, they also expound upon the complexity and challenge of understanding the connections between the dynamics north and south of the cape in this important transition region. The observations suggest that meanders can persist through this transition region, may evolve substantially here, and contribute to meander evolution downstream after the GS leaves the continental margin (Andres, 2021). There are several factors that may contribute to this evolution. The large degree of skewness in several of the observed meander crests implies energy transfer from the meander to the mean flow (Bane et al., 1981). The steepening bottom slope tends to enhance the conversion of eddy kinetic energy back into the mean flow (Gula et al., 2016). The degree of this evolution, and its effect on GS meander evolution downstream is not well understood (Savidge, 2004).

Recent studies provide evidence of a significant velocity increase as the GS leaves the continental margin. Several cross-stream vessel transects measuring GS velocity both up and downstream of Cape Hatteras measured accelerations in near-surface velocities from 1.4 m/s at the southernmost transect to 2.5 m/s northeast of Cape Hatteras (Muglia et al., 2020 and Andres et al., 2018). Additional evidence for acceleration is provided by the HFR surface currents (Haines et al., 2017) and in their long-term means (Updyke, 2017), but whether meander evolution and decay here substantially contribute has not been quantified. Future work will utilize longer time series of the observations to attempt to quantify the connections up- and down-stream evident in Andres, 2021, and contributions to the mean flow.

DATA AVAILABILITY STATEMENT

The raw data supporting the conclusions of this article will be made available by the authors, without undue reservation.

AUTHOR CONTRIBUTIONS

MM wrote the initial manuscript. HS: advisor to MM, manuscript editor and science contributor. JB: committee for MM, manuscript editor and science contributor. PT: Research Scientist provided data collection, analysis, science contributions,

and figure wizardry. All authors contributed to the article and approved the submitted version.

FUNDING

NC Renewable Ocean Energy Program funding is provided by: General Assembly of North Carolina. An Act To Modify The Current Operations And Capital Improvements Appropriations Act of 2009 And For Other Purposes. Session Law 2010-31, Senate Bill 897. Session 2009. H. Rept. 131, pt. 1. Washington: GPO, 2001. The Library of Congress. Thomas. Web. 12 January 2012. Funding for operation of the HFR was provided as an award from the Southeast Coastal Ocean Observing Regional Association, which received funding from the Integrated Ocean Observing System under NOAA-NA11NOA0120033.

ACKNOWLEDGMENTS

The authors thank the North Carolina Renewable Ocean Energy Program, Southeast Atlantic Coastal Ocean Regional Association for funding and providing the observations used for this study, and Rutgers Coastal Ocean Observing Lab access to SST images. We are also grateful to our Processes driving Exchange At Cape Hatteras (PEACH) colleagues for providing the most recent insights and references relevant to the Cape Hatteras region and this study.

SUPPLEMENTARY MATERIAL

The Supplementary Material for this article can be found online at: https://www.frontiersin.org/articles/10.3389/fmars.2022.867439/full#supplementary-material

REFERENCES

Andres, M. (2016). On the Recent Destabilization of the Gulf Stream Path Downstream of Cape Hatteras. *Geophys. Res. Lett.* 43 (18), 9836–9842. doi: 10.1002/2016GL069966

Andres, M. (2021). Spatial and Temporal Variability of the Gulf Stream Near Cape Hatteras. *J. Geophys. Re.: Oceans* 126 (9). doi: 10.1029/2021JC017579

Andres, M., Muglia, M., Bahr, F., and Bane, J. (2018). Continuous Flow of Upper Labrador Sea Water Around Cape Hatteras. *Sci. Rep.* 8 (1), 1–8. doi: 10.1038/s41598-018-22758-z

Bane, J. M., Atkinson, L. P., and Brooks, D. A. (2001). "Gulf Stream Physical Oceanography at the Charleston Bump: Deflection, Bimodality, Meanders and Upwelling," in *Island in the Stream: Oceanography and Fisheries of the Charleston Bump*. Ed. G. R. Sedberry (American Fisheries Soc.), 25–36.

Bane, J. M., Brooks, D. A., and Lorenson, K. R. (1981). Synoptic Observations of the Three-Dimensional Structure and Propagation of Gulf Stream Meanders Along the Carolina Continental Margin. *J. Geophysic. Research: Oceans* 86 (C7), 6411–6425. doi: 10.1029/JC086iC07p06411

Bane, J. M., and Dewar, W. K. (1988). Gulf Stream Bimodality and Variability Downstream of the Charleston Bump. *J. Geophysic. Research: Oceans* 93 (C6), 6695–6710. doi: 10.1029/JC093iC06p06695

Bower, A. S. (1989). Potential Vorticity Balances and Horizontal Divergence Along Particle Trajectories in Gulf Stream Meanders East of Cape Hatteras. *J. Phys. Oceanog.* 19 (11), 1669–1681. doi: 10.1175/1520-0485(1989)019<1669:PVBAHD>2.0.CO;2

Brooks, D. A., and Bane, J. M. (1978). Gulf Stream Deflection by a Bottom Feature Off Charleston, South Carolina. *Science* 201 (4362), 1225–1226. doi: 10.1126/science.201.4362.1225

Brooks, D. A., and Bane, J. M. (1981). Gulf Stream Fluctuations and Meanders Over the Onslow Bay Upper Continental Slope. *J. Phys. Oceanog.* 11 (2), 247–256. doi: 10.1175/1520-0485(1981)011<0247:GSFAMO>2.0.CO;2

Brooks, D. A., and Bane, J. M. (1983). Gulf Stream Meanders Off North Carolina During Winter and Summer 1979. *J. Geophys Res.: Oceans* 88 (C8), 4633–4650. doi: 10.1029/JC088iC08p04633

Churchill, J. H., and Gawarkiewicz, G. G. (2012). Pathways of Shelf Water Export From the Hatteras Shelf and Slope. *J. Geophysic. Research: Oceans* 117 (C8), 133-145. doi: 10.1029/2012JC007995

Dewar, W. K., and Bane, J. M. (1985). Subsurface Energetics of the Gulf Stream Near the Charleston Bump. *J. Phys. oceanog.* 15 (12), 1771–1789. doi: 10.1175/1520-0485(1985)015<1771:SEOTGS>2.0.CO;2

Dewar, W. K., and Bane, J. M. (1989). Gulf Stream Dynamics. Pad II: Eddy Energetics at 73° W. *J. Phys. Oceanog.* 19 (10), 1574–1587. doi: 10.1175/1520-0485(1989)019<1574:GSDPIE>2.0.CO;2

Ezer, T. (2019). Regional Differences in Sea Level Rise Between the Mid-Atlantic Bight and the South Atlantic Bight: Is the Gulf Stream to Blame? *Earth's Future* 7 (7), 771–783. doi: 10.1029/2019EF001174

Gawarkiewicz, G. G., Todd, R. E., Plueddemann, A. J., Andres, M., and Manning, J. P. (2012). Direct Interaction Between the Gulf Stream and the Shelfbreak South of New England. *Sci. Rep.* 2, 553. doi: 10.1038/srep00553

Glenn, S. M., and Ebbesmeyer, C. C. (1994a). Observations of Gulf Stream Frontal Eddies in the Vicinity of Cape Hatteras. *J. Geophysic. Research: Oceans* 99 (C3), 5047–5055. doi: 10.1029/93JC02787

Glenn, S. M., and Ebbesmeyer, C. C. (1994b). The Structure and Propagation of a Gulf Stream Frontal Eddy Along the North Carolina Shelf Break. *J. Geophysic. Research: Oceans* 99 (C3), 5029–5046. doi: 10.1029/93JC02786

Gula, J., Molemaker, M. J., and McWilliams, J. C. (2014). Submesoscale Cold Filaments in the Gulf Stream. *J. Phys. Oceanog.* 44 (10), 2617–2643. doi: 10.1175/JPO-D-14-0029.1

Gula, J., Molemaker, M. J., and McWilliams, J. C. (2016). Submesoscale Dynamics of a Gulf Stream Frontal Eddy in the South Atlantic Bight. *J. Phys. Oceanog.* 46 (1), 305–325. doi: 10.1175/JPO-D-14-0258.1

Haines, S., Seim, H., and Muglia, M. (2017). Implementing Quality Control of High-Frequency Radar Estimates and Application to Gulf Stream Surface Currents. *J. Atmospheric Oceanic Technol.* 34.6, 1207–1224. doi: 10.1175/JTECH-D-16-0203.1

Han, L., Seim, H., Bane, J., Todd, R. E., and Muglia, M. (2021). A Shelf Water Cascading Event Near Cape Hatteras. *J. Phys. Oceanogr.* 51 (6), 2021–2033. doi: 10.1175/JPO-D-20-0156.1

Integrated Ocean Observing System (2021) *Quality Assurance/Quality Control of Real-Time Oceanographic Data*. Available at: https://ioos.noaa.gov/project/qartod/ (Accessed December 27, 2021).

Kang, D., and Curchitser, E. N. (2015). Energetics of Eddy–Mean Flow Interactions in the Gulf Stream Region. *J. Phys. Oceanog.* 45 (4), 1103–1120. doi: 10.1175/JPO-D-14-0200.1

Luther, M. E., and Bane, J. M. (1985). Mixed Instabilities in the Gulf Stream Over the Continental Slope. *J. Phys. oceanog.* 15 (1), 3–23. doi: 10.1175/1520-0485(1985)015<0003:MIITGS>2.0.CO;2

Menelle, M., Auffray, G., and Jangal, F. (2008). Full Digital High Frequency Surface Wave Radar: French Trials in the Biscay Bay. In *2008 International Conference on RADAR* (pp. 224-229). IEEE. doi: 10.1109/RADAR.2008.4653922

Miller, J. L. (1994). Fluctuations of Gulf Stream Frontal Position Between Cape Hatteras and the Straits of Florida. *J. Geophysic. Research: Oceans* 99 (C3), 5057–5064. doi: 10.1029/93JC03484

Miller, J. L., and Lee, T. N. (1995). Gulf Stream Meanders in the South Atlantic Bight: 1. Scaling and Energetics. *J. Geophysic. Research: Oceans* 100 (C4), 6687–6704. doi: 10.1029/94JC02542

Muglia, M., Seim, H., and Taylor, P. (2020). Gulf Stream Marine Hydrokinetic Energy Off Cape Hatteras, North Carolina. *Mar. Tech. Soc J.* 54 (6), 24–36. doi: 10.4031/MTSJ.54.6.4

Muglia, M., Seim, H., and Taylor, P. (2022). Gulf Stream Position, Width, and Orientation Estimated From HF Radar Radial Velocity Maps Off Cape

Hatteras, NC. *J. Atmospheric Oceanic Tech.* 39 (5), 689–705. doi: 10.1175/JTECH-D-21-0098.1

Oey, L. Y., Ezer, T., Mellor, G. L., and Chen, P. (1992). A Model Study of "Bump" Induced Western Boundary Current Variabilities. *J. Mar. Syst.* 3 (4-5), 321–342. doi: 10.1016/0924-7963(92)90009-W

Osgood, K., Bane, J. M., and Dewar, W. K. (1987). Vertical Velocities and Dynamical Balances in Gulf Stream Meanders. *J. Geophys. Res.* 92 (C12), 13,029–13,040. doi: 10.1029/JC092iC12p13029

Roarty, H., Glenn, S., Kohut, J., Gong, D., Handel, E., Rivera, E., et al. (2010). Operation and Application of a Regional High-Frequency Radar Network in the Mid-Atlantic Bight. *Mar. Technol. Soc. J.* 44 (6), 133–145. doi: 10.4031/MTSJ.44.6.5

Rutgers Coastal Ocean Oberving Lab (2019) *Satellite Imagery Seas Surface Temperature of East Coast*. Available at: https://marine.rutgers.edu/cool/sat_data/?product=sst&region=eastcoast&nothumbs=0 (Accessed December 27, 2021).

Savidge, D. K. (2004). Gulf Stream Meander Propagation Past Cape Hatteras. *J. Phys. Oceanogr.* 34 (9), 2073–2085. doi: 10.1175/1520-0485(2004)034<2073:GSMPPC>2.0.CO;2

Sedberry, G. R. (2010) *A Profile of the Charleston Bump*. Available at: https://oceanexplorer.noaa.gov/explorations/islands01/background/islands/sup11_bump.html (Accessed June 9th, 2019).

Thomas, L. N., and Joyce, T. M. (2010). Subduction on the Northern and Southern Flanks of the Gulf Stream. *J. Phys. oceanog.* 40 (2), 429–438. doi: 10.1175/2009JPO4187.1

Todd, R. E. (2017). High-Frequency Internal Waves and Thick Bottom Mixed Layers Observed by Gliders in the Gulf Stream. *Geophysic. Res. Lett.* 44 (12), 6316–6325. doi: 10.1002/2017GL072580

Tracey, K. L., and Watts, D. R. (1986). On Gulf Stream Meander Characteristics Near Cape Hatteras. *J. Geophysic. Research: Oceans* 91 (C6), 7587–7602. doi: 10.1029/JC091iC06p07587

Updyke, T. (2017). "An Update on Recent Work Involving HF Radar Data in the Mid-Atlantic," in *44th Mid Atlantic Bight Physical Oceanography and Meteorology meeting*, September 27th-29th (Wanchese, NC: Coastal Studies Institute, 850 NC 345).

US Department of Commerce, National Oceanic and Atmospheric Administration, National Weather Service, and National Data Buoy Center (1996) *NDBC Station Page*. Available at: https://www.ndbc.noaa.gov/station_page.php?station=41025 (Accessed June 4, 2019).

Vazquez, J., and Watts, D. R. (1985). Observations on the Propagation, Growth, and Predictability of Gulf Stream Meanders. *J. Geophysic. Research: Oceans* 90 (C4), 7143–7151. doi: 10.1029/JC090iC04p07143

Von Arx, W. S., Bumpus, D. F., and Richardson, W. S. (1955). On the Fine-Structure of the Gulf Stream Front. *Deep Sea Res. (1953)* 3 (1), 46–65. doi: 10.1016/0146-6313(55)90035-6

Whitt, D. B., Thomas, L. N., Klymak, J. M., Lee, C. M., and D'Asaro, E. A. (2018). Interaction of Superinertial Waves With Submesoscale Cyclonic Filaments in the North Wall of the Gulf Stream. *J. Phys. Oceanog.* 48 (1), 81–99. doi: 10.1175/JPO-D-17-0079.1

Yoder, J. A., Atkinson, L. P., Bishop, S. S., Hofmann, E. E., and Lee, T. N. (1983). Effect of Upwelling on Phytoplankton Productivity of the Outer Southeastern United States Continental Shelf. *Cont. Shelf Res.* 1 (4), 385–404. doi: 10.1016/0278-4343(83)90004-3

Zhang, W. G., and Gawarkiewicz, G. G. (2015). Dynamics of the Direct Intrusion of Gulf Stream Ring Water Onto the Mid-Atlantic Bight Shelf. *Geophys. Res. Lett.* 42 (18), 7687–7695. doi: 10.1002/2015GL065530

Conflict of Interest: The authors declare that the research was conducted in the absence of any commercial or financial relationships that could be construed as a potential conflict of interest.

Publisher's Note: All claims expressed in this article are solely those of the authors and do not necessarily represent those of their affiliated organizations, or those of the publisher, the editors and the reviewers. Any product that may be evaluated in this article, or claim that may be made by its manufacturer, is not guaranteed or endorsed by the publisher.

Copyright © 2022 Muglia, Seim, Bane and Taylor. This is an open-access article distributed under the terms of the Creative Commons Attribution License (CC BY). The use, distribution or reproduction in other forums is permitted, provided the original author(s) and the copyright owner(s) are credited and that the original publication in this journal is cited, in accordance with accepted academic practice. No use, distribution or reproduction is permitted which does not comply with these terms.

frontiers | Frontiers in Marine Science

ORIGINAL RESEARCH
published: 01 July 2022
doi: 10.3389/fmars.2022.912865

Delineation of Eastern Beaufort Sea Sub-regions Using Self-Organizing Maps Applied to 17 Years of MODIS-Aqua Data

Andrea Hilborn * *and Emmanuel Devred*

Bedford Institute of Oceanography, Fisheries and Oceans Canada, Dartmouth, NS, Canada

OPEN ACCESS

Edited by:
William Savidge,
University of Georgia, United States

Reviewed by:
Frano Matić,
Institute of Oceanography and Fisheries (IZOR), Croatia
Roy El Hourany,
UMR8187 Laboratoire d'océanologie et de géosciences (LOG), France
Keyhong Park,
Korea Polar Research Institute, South Korea

***Correspondence:**
Andrea Hilborn
Andrea.Hilborn@dfo-mpo.gc.ca

Specialty section:
This article was submitted to Coastal Ocean Processes, a section of the journal Frontiers in Marine Science

Received: *05 April 2022*
Accepted: *26 May 2022*
Published: *01 July 2022*

Citation:
Hilborn A and Devred E (2022) Delineation of Eastern Beaufort Sea Sub-regions Using Self-Organizing Maps Applied to 17 Years of MODIS-Aqua Data. Front. Mar. Sci. 9:912865. doi: 10.3389/fmars.2022.912865

Satellite observations are an integral component of long-term Arctic Ocean monitoring and help identifying changes resulting from climate warming. A Self-Organizing Maps (SOM) approach was applied to four-day composite satellite images of the Eastern Beaufort Sea (EBS) acquired by the MODerate resolution Imaging Spectroradiometer over the period 2003–2019. Using sea-surface temperature (SST), suspended particulate matter concentration (SPM) and chlorophyll-a concentration (Chl-a) as input the EBS was partitioned into six biogeochemical regions. The SOM approach revealed region-specific mean conditions and seasonal cycles for all properties, particularly for SPM and Chl-a. Three of the six regions, located on the continental shelf, had the highest SST, SPM and Chl-a with earlier maxima compared to the remaining three regions which comprised the shelf edge, Canada Basin and Amundsen Gulf. While mean and maximum SST did not exhibit significant trends over the 17 years of observations, the annual maximum SST in Amundsen Gulf was reached significantly earlier in recent years compared to the start of the time series. With the exception of Amundsen Gulf, sea-ice concentration (SIC) derived from microwave satellites declined throughout the study area; monthly trends showed dramatic SIC declines in regions on the shelf during May and June, and in Canada Basin during August. Correlation analysis of properties within and between regions showed that SST and SIC were driven by large scale processes while SPM and Chl-a showed regional features. SST and Chl-a in the regions nearest the Mackenzie River showed a strong relationship during seasonal warming. The SOM approach, applied to 17 years of satellite data, revealed spatially distinct marine units with unique characteristics, emphasizing the need for regional considerations when assessing the impact of climate warming in the Arctic Ocean.

Keywords: ocean colour, Beaufort Sea, chlorophyll-a concentration, suspended particulate matter, sea surface temperature, biogeochemical regions, self-organizing maps

1 INTRODUCTION

The Arctic is undergoing rapid changes as a result of climate forcing, including increasing air temperature [three to four times the rate of the Northern Hemisphere average; Serreze et al. (2009); Miller et al. (2010)], thawing of permafrost (Payette et al., 2004; Jorgenson et al., 2006), increasing cloudiness (Bélanger et al., 2013) and fall storminess (Ardyna et al., 2014). The Arctic Ocean, in particular, is experiencing major shifts to its sea ice regime, including a lengthening open-water season, reduction in sea ice thickness and extent, and disappearance of multi-year ice that propagate cascading effects on the entire marine ecosystem (Maslanik et al., 2011; Stroeve et al., 2012; Kwok and Cunningham, 2015). Due to the reduction in sea ice, the light field in the euphotic zone and conditions for phytoplankton growth have been impacted, with Arctic "spring" blooms starting earlier and ending later (Kahru et al., 2011; Kahru et al., 2016) at increasing latitudes (Renaut et al., 2018). As a result, an annual increase in net primary productivity of up to 30% over the period 1998 to 2012 in the Arctic has been documented (Arrigo and van Dijken, 2015). Furthermore, focusing on the Eastern Beaufort Sea (EBS) located in the western Canadian Arctic, the flux of SPM of terrestrial origin delivered by the Mackenzie River into the coastal ocean has dramatically increased in recent decades (Doxaran et al., 2015) driven by permafrost thaw, positive precipitation anomalies and increasing river discharge. These changes may also be delivering more contaminants into the EBS, which is concerning as polar environments, in particular, are very sensitive to changes (Macdonald et al., 1995; Macdonald et al., 2005).

Ocean colour satellite remote sensing is integral for monitoring climate change and its large-scale impacts occurring on the surface of the Arctic Ocean. Sensors mounted on satellites image a large spatial extent and allow long-term monitoring of particular biogeochemical and physical properties of the ocean surface. However, many studies are performed at the pan-Arctic scale (i.e., Ardyna and Arrigo (2020); Kahru et al. (2011); Kahru et al. (2016)) and may miss regional responses to local forcing, which lead to departures from trends recorded at large spatial scales. For instance, Screen (2017) discussed region-specific sea ice loss propagating errors when estimating loss of sea ice at large scales. Some studies have addressed this issue by partitioning the ocean into spatially discrete areas, also referred to as "ecological provinces" (Longhurst et al., 1995), using oceanographic data collected *in situ* or from satellite platforms. Ecological provinces were defined in the fundamental work of Longhurst et al. (1995), and in recent decades methods using satellite remote sensing of ocean colour and biogeochemical data have included delineation with dynamic boundaries (Devred et al., 2007; McIver et al., 2018; Reygondeau et al., 2018; Reygondeau et al., 2020), as well as objective and feature-based classifications (Martin Traykovski and Sosik, 2003; Oliver et al., 2004; Oliver and Irwin, 2008), principal component analysis (i.e., Hardman-Mountford et al., 2008), and neural gas methods (Taşdemir, 2011) to cite a few (see IOCCG, 2009).

The EBS and other areas of the Arctic Ocean have been neglected in previous ocean colour remote sensing studies delineating ecological provinces due to the challenges associated with remote sensing at high latitudes (IOCCG, 2015), such as sea ice cover, polar night, data loss from low sun angle, and poor performance of traditional ocean colour algorithms. In the current study, we focused on the EBS located in the Canadian Arctic to examine ecosystem characteristics and trends at a regional scale. Large geographic areas of the EBS have been designated Marine Protected Areas (MPAs) in recent years, with efforts to further classify hotspots and areas of ecological and biological significance using physical and biological data sources (DFO, 2015; Hodgson et al., 2015; Cobb et al., 2020). In the current study, we delineated biogeochemical regions using Self-Organizing Maps [SOMs; Kohonen (1984); Kohonen (1997)], a form of artificial neural network (ANN) well suited to non-linear datasets with missing data. SOMs have been applied in an extensive variety of studies from the medical field to biology and economics (Kaski et al., 1998) and in particular to study the ocean surface using satellite data to identify spatio-temporal patterns and relationships between variables (Ainsworth, 1999; Ainsworth and Jones, 1999; Hewitson and Crane, 2002; Richardson et al., 2003; El Hourany et al., 2019; Park et al., 2019; Xu et al., 2019), and estimate spatial fields (i.e., pCO_2 in Xu et al. (2019) and net community production in Park et al. (2019)). We applied the SOM methodology to a remote sensing dataset of three essential climate variables (WMO, 2016) spanning 17 years (2003–2019) acquired by the MODerate resolution Imaging Spectroradiometer (MODISA): sea-surface temperature (SST), suspended particulate matter concentration (SPM) and chlorophyll-a concentration (Chl-a, proxy for phytoplankton biomass). In addition, we used sea ice concentration (SIC) from the Advanced Microwave Scanning Radiometer - Earth Observing System sensors (AMSRE and AMSR2) to help interpret our findings. By constructing regions in this manner, using satellite data and finding "natural" spatio-temporal groupings, we demonstrate an effective and unsupervised methodology that can be further integrated into marine spatial planning and investigating biogeochemical regions in the Arctic Ocean. The long time series of properties, provided a means to derive climatologies, seasonal cycles and trends in each region, as well as allow investigation of connectivity between the regions.

2 MATERIALS AND METHODS

2.1 Study Area

The Beaufort Sea is a marginal sea of the Arctic Ocean spanning the coasts of the Yukon and Northwest Territories westward to northern Alaska (**Figure 1**). Our region of interest bounds the eastern (Canadian) portion of the Beaufort Sea, from 122° to 142° West and 68.5° to 72.5° North. There are two Marine Protected Areas (MPAs) in the area, namely the Tarium Niryutait MPA and Anguniaqvia Niqiqyuam MPA, along with terrestrial and coastal protected areas including the Kendall Island, Anderson River Delta and Banks Island No. 1 Migratory Bird Sanctuaries. At high latitudes during the summer the sun remains above the horizon from approximately May 19 to July 24 at the latitude of the

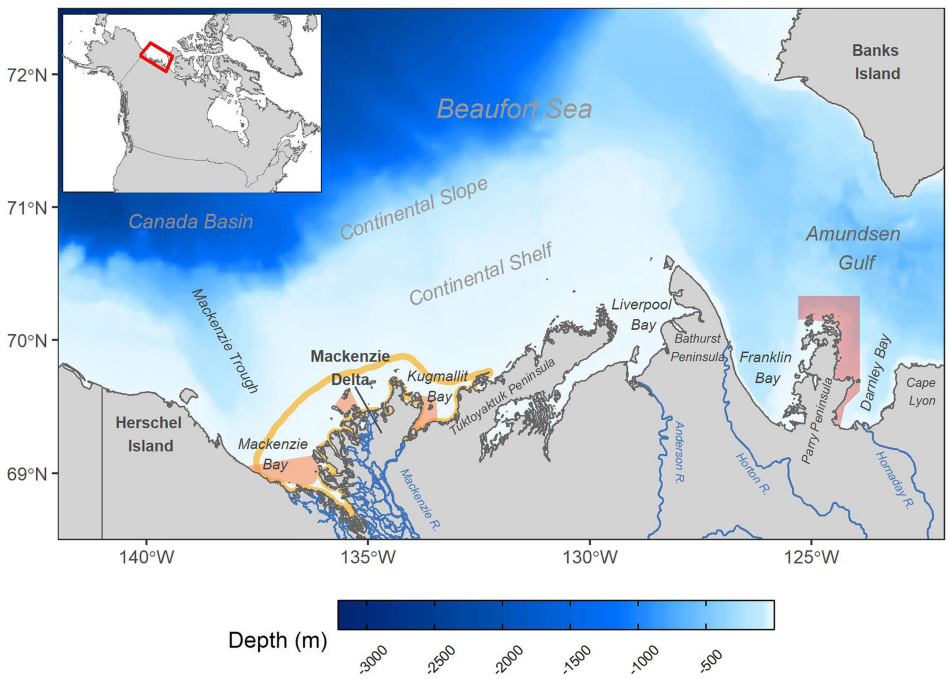

FIGURE 1 | Study area in the Eastern Beaufort Sea shown with bathymetry, notable physical features and freshwater inputs, Marine Protected Areas (MPAs) and location on inset map of Canada. The area of raised cloud albedo processing is shown as an orange outline around the Mackenzie Delta (see section 2.2.1). Tarium Niryutait MPA is indicated in orange, and Anguniaqvia Niqiqyuam MPA in red.

Mackenzie Delta, and from May 9 to August 4 at the latitude of Banks Island.

The region encompasses a large bathymetric range and variety of oceanographic conditions, and includes the Mackenzie Delta, the continental shelf and slope, the southern portion of the Canada Basin, and Amundsen Gulf. The Mackenzie River, the fourth largest Arctic river by discharge [mean annual discharge ~ 9,299 $m^3 s^{-1}$, ECCC (2021)], enters the ocean *via* the Mackenzie Delta on the western side of the shallow and expansive shelf. The river significantly impacts the physical and optical properties of the EBS, delivering suspended particles, nutrients and coloured-dissolved organic matter (CDOM) from its large watershed (drainage area of ~ 1.787 million km^2, Peucker-Ehrenbrink (2009)). The large freshwater input to the shelf (also referred to as "Mackenzie Shelf" due to its influence from and proximity to the Mackenzie River) makes it the most estuarine shelf in the Arctic (Macdonald et al., 1995). North of Mackenzie Bay the seafloor deepens into Mackenzie Trough, which extends north into Canada Basin, exceeding a depth of 3000 m, where the movement of water and ice are heavily influenced by the anti-cyclonic surface circulation of the Beaufort Gyre (Galley et al., 2013). The Bathurst Peninsula divides the eastern side of the continental shelf from Amundsen Gulf and physically impedes the eastward movement of the fresh, buoyant and sediment-laden plume from the Mackenzie River (Fissel et al., 2013).

The sea ice regime varies through the region, with perennial sea ice present in Canada Basin, while Amundsen Gulf has a variable inter-annual open water area (Arrigo and van Dijken, 2004). To the northeast of Cape Bathurst, as sea ice retreats in early June, a large open water area (flaw lead) expands and forms the Cape Bathurst polynya (Barber and Hanesiak, 2004). A landfast ice barrier forms in autumn on the Mackenzie Shelf within the 20-m isobath and persists through the winter. Leads form between this landfast ice and mobile offshore pack ice as ice movement is driven by winds, and ice ridges and rubble accumulate at the landfast interface ("stamukhi") physically trapping fluvial discharge to the coastal ocean (Giovando and Herlinveaux, 1981; Macdonald et al., 1995; Fissel et al., 2013). The barrier melts then breaks up typically in June as the temperature warms and the Mackenzie River discharge peaks, and the river plume is then free to expand up to hundreds of kilometers from shore (Macdonald et al., 1995).

2.2 Satellite Data and Processing

2.2.1 MODIS-Aqua SST, SPM and Chl-a

The *MODerate Resolution Imaging Spectroradiometer* is an optical sensor on the Aqua platform (referred to hereafter as MODISA) which has been collecting data at 36 wavebands since late 2002; nine bands image in the visible through near infrared wavelengths for ocean colour observation (i.e. signal-to-noise ratio of >400; Qi et al. (2017)). All but seven bands collect data at 1–km spatial resolution, with two collecting data at 250-m resolution (bands 1–2) and five collecting data at 500-m resolution (bands 3–7). Its polar orbit increases the number of times high latitude regions are imaged in a given day compared

to temperate regions; as solar elevation peaks during summer the Mackenzie Delta and EBS are imaged by MODISA up to seven times daily.

MODISA images intersecting the study region during the years 2003 through 2019 were acquired from the NASA Ocean Biology Processing Group website (OBPG; https://oceancolor.gsfc.nasa.gov) at Level-1A (L1A, unprocessed full-resolution instrument data). Due to low sun angles and the lack of daylight from late fall through boreal winter to early spring, combined with sea ice cover, images used in this study were confined from March 14th to October 1st of each year (year-day 73 to 274, 202 days per year), corresponding to dates with a noon solar zenith angle of <70° at 68.5°N (IOCCG, 2015). Images acquired prior to 16:30 UTC were removed to restrict the sun angle and the descending node. L1A images were processed to Level-2 (L2, derived geophysical variables) at 250-m spatial resolution to retrieve remote sensing reflectance (R_{rs}) and SST using the SeaWiFS Data Analysis System (SeaDAS v7.5.2.1, https://seadas.gsfc.nasa.gov, *l2gen* processor) with the Wang and Shi (2007) NIR-SWIR switching algorithm to correct for atmospheric signal. The 250-m resolution was used to ensure maximum spatial coverage near the Mackenzie Delta and to decrease the influence of sub-pixel ice floes on bio-optical retrievals.

A similar processing methodology to Doxaran et al. (2015) was used for retrieving additional pixels near the outlet of the Mackenzie River, where high sediment concentrations resulted in data loss when using standard atmospheric correction methods due to pixel brightness at infrared wavelengths which trigger ice and cloud masks. In brief, the area adjacent to the Mackenzie Delta was re-processed using a relaxed cloud albedo threshold (standard threshold of 0.027 replaced with 0.4; see orange contour on **Figure 1**), provided that a processed scene had sufficient valid ocean pixels (minimum 5000 pixels at 250-m resolution). We updated the area used in Doxaran et al. (2015), limiting this "high albedo region" to the 20 g m^{-3} contour identified from a climatology layer constructed with the SPM product from the standard albedo processing (see **Figure S1** for an example of improved spatial coverage).

The R_{rs} obtained from the standard and re-processed images were combined to calculate SPM and Chl-a, while daytime long-wave SST (11 μm) was calculated with *l2gen*. The SPM and Chl-a algorithms were implemented using python version 3.7.4 (Van Rossum and Drake, 2009).

2.2.2 Algorithms Used for SPM and Chl-a

Given the large dynamic range of SPM in the study area (i.e., < 1.0 g m^{-3} to > 100.0 g m^{-3}) we used the semi-analytical algorithm of Han et al. (2016), an algorithm parameterized with *in situ* data from the global ocean including 38 samples collected in the Beaufort Sea. The method relies on R_{rs} (667) where SPM is calculated as the weighted average of two algorithms (one for low-medium SPM and one for high SPM waters):

$$SPM = \frac{W_L SPM_L + W_H SPM_H}{W_L + W_H}, \quad (1)$$

where low (SPM_L) and high (SPM_H) SPM were calculated following:

$$SPM_L = \frac{404.4\rho_w(667)}{1 - \frac{\rho_w(667)}{0.5}}, \quad (2)$$

and

$$SPM_H = \frac{1214.669\rho_w(667)}{1 - \frac{\rho_w(667)}{0.3394}}. \quad (3)$$

When R_{rs} are between 0.03 and 0.04 sr^{-1} the following equations are used for the weights W_L and W_H:

$$W_L = log_{10}(0.04) - log_{10}[R_{rs}(667)] \quad (4)$$

and

$$W_H = log_{10}[R_{rs}(667)] - log_{10}(0.03) \quad (5)$$

If a pixel $R_{rs} \leq 0.03$ sr^{-1}, W_L is set to 1 and W_H is set to 0. If $R_{rs} \geq 0.04$ sr^{-1}, W_L is set to 0 and W_H is set to 1. Note that $\rho_w = \pi \times R_{rs}$.

Chlorophyll-a concentration (Chl-a, mg m^{-3}) was computed using the Arctic Ocean empirical band-ratio algorithm (AOEmp; Lewis and Arrigo (2020)), which relies on R_{rs} at 443, 488 and 547 nm. The algorithm was developed using the largest *in situ* dataset yet assembled for the Arctic Ocean from 34 expeditions that occurred between 1994 and 2016. Like the global OC3M Chl-a algorithm (O'Reilly et al., 1998), AOEmp is a band-ratio algorithm with updated coefficients [see Lewis and Arrigo (2020)]. In summary, Chl-a was calculated as the following:

$$Chl - a = 10^{\left(a + bR + cR^2\right)} \quad (6)$$

and

$$R = log_{10}\left(\frac{max(R_{rs}(443), R_{rs}(488))}{R_{rs}(547)}\right) \quad (7)$$

Where a = 0.0957, b = -2.7973, c = 0.6581 and R is the log_{10}-transformed blue-green maximum band ratio. In areas with high SPM, i.e., near the Mackenzie Delta, Chl-a may be over-estimated due to the large sediment load and high concentration of yellow substances.

Following calculation of SPM and Chl-a, additional steps were taken to ensure data quality and create temporal composites. Pixels with negative R_{rs} at 555 and 667 nm or with SST < -1.89°C were discarded. SPM range of variation was limited from 0.05 – 1000.00 g m^{-3} and Chl-a pixels were restricted to the range 0.05 – 40.00 mg m^{-3}. All SST, SPM and Chl-a images were projected on a 300-m regular grid using Generic Mapping Tools software (GMT, Wessel et al. (2013); https://www.generic-mapping-tools.org/). All individual scenes from a given day (including standard and raised cloud albedo processing) were combined into daily composite images by calculating the median value at each pixel. Finally, daily composite images were visually inspected to ensure that abnormal values were removed, then aggregated into four-day median composites (grouping by day of year, i.e., days 1 – 4, days

5 – 8, etc.) to reduce the impact of cloud cover while retaining an acceptable temporal resolution to resolve short term events.

A total of 13,325 L1A scenes from 2003 to 2019 were downloaded and processed among which 5006 were re-processed with a raised cloud albedo threshold near the outlet of the Mackenzie River. The resulting 2565 daily composites were aggregated into 740 four-day composites for each parameter. All analyses were performed using R software version 4.0.2 (R Core Team, 2019). ETOPO1 global relief data was used for bathymetry (Amante and Eakins, 2009), and hydrometric data from the Water Survey of Canada station at Arctic Red River [Station ID 10LC014; ECCC (2021)] during the study period were accessed using the *weathercan* R package LaZerte and Albers, 2018).

2.2.3 AMSRE and AMSR2 Sea Ice Concentration

SIC data from 2003 to 2019 were downloaded from the Universität Bremen website (https://seaice.uni-bremen.de/data; see **Table S1**) for two sensors: the *Advanced Microwave Scanning Radiometer - Earth Observing System* (AMSRE, 3.125-km resolution), which operated late 2002 to late 2011, and it's successor, the AMSR2 sensor, which began operations in late 2012.

The AMSRE and AMSR2 images were re-gridded using GMT to the 300-m grid corresponding to the SST, SPM and Chl-a data, and aggregated into four-day composites using the mean SIC at each grid cell. Pixels with SIC of <10% were discarded as in Perrette et al. (2011). We investigated bridging the gap in coverage between AMSRE and AMSRE2 (2011-10-03 to 2012-07-04) with data from the *Special Sensor Microwave Imager Sounder* (SSMIS, data at https://www.nsidc.org), but its coarse resolution (i.e., 25-km) prevented access to reliable data along the coast, so 2011 and 2012 were excluded from our SIC analysis.

2.3 Delineating Regions With Self-Organizing Maps

The *kohonen* R package (version 3.0.10, Wehrens and Buydens, 2007; Wehrens and Kruisselbrink, 2018), based on the original SOM methodology developed by Kohonen (1997), was used to partition the ESB into areas with similar temporal dynamics of SST, SPM and Chl-a using the four-day composites from all three parameters simultaneously as input. SOMs have been applied to a large variety of studies, and are well suited for pattern identification in large satellite datasets as they perform effectively even with a high percentage of missing data [i.e., Richardson et al. (2003)]. We implemented SOM processing using the *supersom()* function in the R *kohonen* package, resulting in a map showing pixels with high temporal similarity of concurrent SST, SPM and Chl-a assigned to the same groups.

Before running the SOM some pre-processing steps were taken. SPM and Chl-a were $\log_{10}$-transformed to obtain a normal distribution (Campbell, 1995), and the three input datasets were each centered and scaled (i.e. each value of each column had the column mean removed and were divided by the column standard deviation) to have a consistent range of values. Four-day composites with low spatial coverage (<5%) and individual pixels with valid data in less than 5% of the images were removed (see **Figure S2** for spatial and temporal coverage). Finally, to improve speed, reduce small gaps between pixels (i.e., Moiré pattern) and reduce ice-edge contamination of the SPM data due to straylight at the NIR wavelengths, we reduced the spatial resolution to 1.5-km, where each reduced pixel represented the median of at least five high resolution (i.e., 250-m) pixels. The SST, SPM and Chl-a datasets were arranged into three spatio-temporal matrices, which were concatenated together for SOM processing in order to consider all three parameters simultaneously (providing a final dataset of 98,844 rows corresponding to each pixel in the area of interest, and 635 columns corresponding to the time-series time step for all three parameters; **Figure 2**).

The first stage of processing was defining an appropriate number of groups to partition the study area into. SOM processing requires an x, y layout of nodes (see **Figure 2**) with data assigned to each node (i.e., SST, SPM and Chl-a pixels assignedto a 2 x 3 node array results in six groups). We tested a variety of node array sizes in hexagonal layouts. During processing, each node is initially assigned a random subset of the input dataset (i.e., each node starts with a "prototype pattern" of SST, SPM and Chl-a), then pixels are iteratively presented to the node layout and assigned to the node with greatest similarity. Once a pixel is assigned to a node, the node's "prototype pattern" is updated by computing a weighted average of all assigned pixels. The weight declines as processing progresses with an increasing number of iterations (i.e., times the pixel is presented to the node layout) so that the mean node distance converges. SOM processing maintains similarity between nodes, such that the nodes adjacent to a "winning node" (in the original x, y layout - see **Figure 2**) are also updated during the beginning of the processing as the map learns which pixels fit into which groups most effectively (see Kohonen, 1997; Wehrens and Buydens, 2007, for details). Each pixel retains a measure of fit to its assigned node called node "distance" (unitless) which can be used to assess the fit of individual pixels to each node. As the process is iterative, with each pixel repeatedly presented to the node array, the mean node distance declines and eventually stabilizes. To assess the optimal layout for the SOM, we processed node layouts of differing sizes (ranging from 3 nodes to 36 nodes) and examined the mean node distance for each region and parameter; in all layouts it stabilized after 400 iterations. Overall, the mean node distance was lowest using a 2 x 3 SOM layout (six nodes), which was analyzed further. Once the spatial information of each pixel were reassigned (i.e., latitude and longitude), the SOM classification revealed six distinct regions arranged in spatially consistent and quasi-contiguous areas. The regional boundaries were converted to shapefiles and used to extract the corresponding four-day composite SIC, SST, SPM and Chl-a pixels.

2.4 Regional Statistics of SST, SPM, Chl-a and SIC

2.4.1 Regional Time Series, Climatology and Trends

For all parameters (i.e., SST, SPM, Chl-a and SIC), climatology and standard deviation (SD) maps were computed for the entire time series (i.e. summarizing 2003-2019 per pixel). The arithmetic mean and SD were used for SST and SIC, and the geometric mean (**Equation S1**) and geometric standard

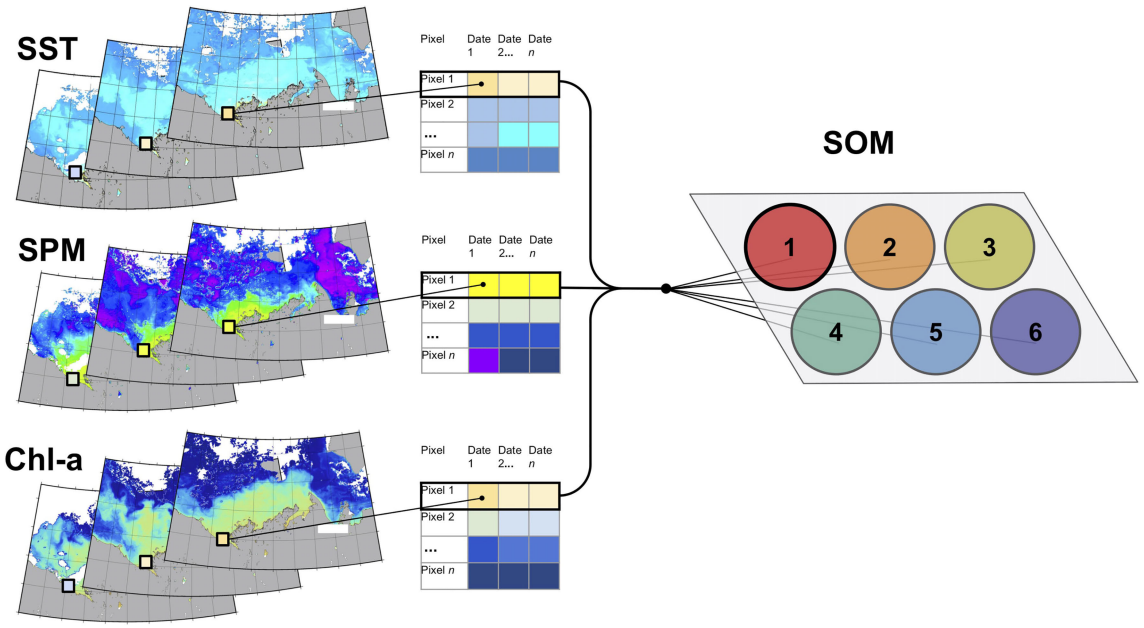

FIGURE 2 | Illustration of the SOM method clustering satellite-derived SST, SPM and Chl-a pixels. The input parameters were concatenated, and spatial pixels were individually presented to SOM nodes, which includes all values of that pixel over time for the three parameters. Each pixel is examined for similarity with the other pixels assigned to that node. This recurs over a set number of iterations with the final characteristics of the node consisting of a weighted average of the assigned pixels and variables over time. Here the example pixel is assigned to Node 1.

deviation (GSD; **Equation S2**) for SPM and Chl-a (Kirkwood, 1979) due to the lognormal distribution of these data [i.e., Campbell (1995)]. As the GSD is a unitless multiplicative factor, unlike the SD which is added or subtracted from the mean when describing uncertainty, the lower and upper bounds of non-transformed data were obtained by dividing (**Equation S3**) or multiplying (**Equation S4**) the geometric mean by the GSD (See **Supplementary Material**).

Time series and climatologies of the parameters in the six regions defined by the SOM were calculated in a similar manner (i.e. arithmetic mean for SST and SIC, and geometric mean for SPM and Chl-a). First, the time series were calculated by averaging the SST, SPM, Chl-a and SIC pixels in individual regions for each four-day time step. Second, we averaged the four-day composites across all years to provide an average climatology of 2003-2019 for each four-day time step. When calculating the four-day time series and climatologies for a given parameter and region, the upper and lower percentiles of pixels were removed prior to calculating mean and SD to reduce the impact of possible outliers. The number of valid pixels in a four-day composite image changed in time and space due to the spatial variability of open-water area (i.e., ice-free), as well as data missing from cloud cover and low sun angle; here composites with less than 5% spatial coverage in a given region were excluded from the analysis (see **Figure S2B**).

In order to calculate the temporal trends of the four parameters in the SOM-defined regions, the SST, SPM, Chl-a and SIC data were aggregated further into monthly and annual mean values (again using arithmetic mean for SST and SIC, and geometric mean for SPM and Chl-a, removing the upper and lower 1% of data). Trends of SST, SPM, Chl-a and SIC for each region from 2003–2019 were calculated for these time resolutions using linear least-squares regressions of a given variable against time (function *lm()* in R). Only trends (i.e., slopes of the linear regression) with p-value less than 0.05 are discussed further. In addition to annual and monthly SST trends, we examined the trends of annual maximum SST and the trends of the dates at which it was reached.

2.4.2 Intra- and Inter-Regional Correlations of Satellite-Derived Parameters

To examine the relationships between all four parameters within and between all six regions, a correlation matrix of the four-day time series was computed for all possible combinations of the parameters. The Spearman rank correlation coefficient (p) showed the strength of correlation between parameters and regions, with significance indicated by accompanying p-value calculated from a two-tailed t-test of each correlation (function *corr.test()* in R package *psych*). Given that we analysed four parameters in six regions, we ended up with a total of 276 correlation coefficients.

The response of phytoplankton to physical forcing as expressed by SST was further investigated in terms of regional annual warming and cooling. The date of maximum SST in a given year (section 2.2.1) was used to divide the year into a warming period (i.e., first day of satellite data to day of warmest

SST) and a cooling period (i.e., day of warmest SST to last day of satellite data recorded in the year). For both warming and cooling periods, the time series of Chl-a geometric mean were linearly regressed against SST using a Type-2 major axis regressions (R package *lmodel2*), retaining the slope, intercept, R^2 and p-value for each region.

3 RESULTS

3.1 Spatial Climatology of SOM Input Parameters: SST, SPM and Chl-a

Over the period 2003–2019, the SST climatology was warmest near the mouth of the Mackenzie River with a mean temperature of approximately 10°C (**Figure 3A**). It varied between 6 and 8°C in the nearby bays and coastal shelf waters from Cape Bathurst to the west of the Mackenzie River. A plume with SST ranging from 4 to 6°C extended northeast from the Mackenzie River toward the Canada Basin. The cold Alaskan Current was evident to the west of Herschel Island where the waters were cooler (<4°C) compared to its eastern side. The nearshore waters of Banks Island on the eastern side of the study region, lacking a shallow shelf and inputs from large rivers, had a similar SST climatology to open water areas with values lower than 5°C. The climatological SST was lowest in the surface waters of Canada Basin. SST showed the highest SD near the Mackenzie Delta with values ranging between 4 and 5°C (**Figure 3B**). The continental shelf and the Canadian Basin showed also a large SD with values between 2 and 4°C while Amundsen Gulf exhibited the least variation.

Similar to SST, the climatology of SPM was highest at the direct outlet of the Mackenzie River, exceeding 30 g m^{-3} within the 10-m bathymetric contour, and was greater than 20 g m^{-3} at the Anderson River outlet in Liverpool Bay (**Figure 3C**). SPM decreased moving north from the Mackenzie Delta and shallow coastal waters. Overall, SPM remained very low in Amundsen Gulf (<2 g m^{-3}) and northwest off the shelf extending into the surface waters of the Canada Basin. The SPM GSD near the Mackenzie River was lower than that of Amundsen Gulf and Canada Basin. A "wedge" near the outlet of the Mackenzie River on the western side of Mackenzie Bay demonstrated high variability (highest GSD), likely caused by spatially constrained landfast ice that breaks up during spring and releases a plume with high particle concentration (**Figure 3D**). Further east, the SPM GSD was also elevated on the eastern side of Cape Bathurst, north of the outlet of the Horton River, in Darnley Bay near the Hornaday River, and along the southwest coast of Banks Island.

On average, Chl-a over the shelf waters was greater than Chl-a on the continental slope and Canada Basin, remaining on average above 1 mg m^{-3} for depths <100 m. In waters off the shelf (>1000 m), surface waters showed both latitudinal and longitudinal gradients; extending from the shelf west of approximately 135°W, Chl-a remained greater than 0.5 mg m^{-3}, while east of 135°W, spreading into Amundsen Gulf, Chl-a remained lower than 0.5 mg m^{-3}, and continued decreasing moving northward to deeper waters (**Figure 3E**). The GSD of Chl-a was highest at the shelf edge north of the Mackenzie River, extending over the Canada Basin (more than three times the mean, **Figure 3F**). The GSD was also elevated along the shelf edge (i.e., 100-m isobath) and eastern side of Cape Bathurst continuing southward to Franklin Bay. The GSD was low (i.e., less than two times the mean) off the shelf east of Canada Basin and into Amundsen Gulf. The GSD was also very low on the shelf where bathymetry was less than 20 m.

3.2 Mean Properties of the SOM-Delineated Regions

The six regions identified with the SOM approach (**Figure 4**) retained similar features to the ones revealed by the SST, SPM and Chl-a climatology and SD maps (**Figure 3**). The SOM-delineated regions successfully distinguishing the outlets of large rivers (mainly the Mackenzie and Anderson; Region 1), shallow inner shelf, mid-shelf and shelf-edge waters (Regions 2 to 4), Amundsen Gulf (Region 5) and the Canada Basin (Region 6). The six regions had a large range of size and extent, though they remained congruent with bathymetric features; Region 1, closest the Mackenzie River was smallest and shallowest, and Region 6 which overlapped much of Canada Basin was largest and deepest and covered a large depth range (**Table 1**).

Region 1, referred to hereafter as the Mackenzie Delta or R1, was the warmest biogeochemical region with a mean SST value of 7.9°C (**Table 1**) and SST remaining above 8°C in Summer (**Figure 4B**) with a peak at 13.4°C in late summer (day of year 201 ± 17). SPM was also highest in this region with values greater than 20 g m^{-3} all year long and the annual maximum occuring soon after ice breakup (i.e, >30 g m^{-3}, **Figure 4C**). In spring the phytoplankton biomass increased rapidly, but with a delayed timing compared to that of SPM (**Figure 4D**). Chl-a reached values above 3 mg m^{-3} in late June and remained high through the year (geometric mean of 4.5 mg m^{-3}). This area exhibited persistent sea ice cover until mid-June after which it rapidly declined to entirely open water (**Figure 5**).

Regions 2 and 3, referred to as the inner shelf (R2) and mid-shelf (R3) regions respectively, were mostly located within the 100-m bathymetric contour (**Figure 4A**). The inner shelf region spanned between Herschel Island on its west side and Cape Bathurst at the east (see **Figure 1** for place names). The mid-shelf region (R3), and a small part of the inner shelf (R2), extended over the deep waters (i.e. deeper than 100-m) of the Mackenzie Trough, Franklin and Darnley Bays as well as on the west coast of Banks Island (**Figure 4A**). Region 4, corresponding to the shelf edge (R4), had its eastern boundary on the Mackenzie Shelf north of the Tuktoyaktuk Peninsula, and it extended west over deep waters of Canada Basin. It was bordered by Amundsen Gulf (R5) on its eastern side and the Canadian Basin (R6) on its northern side.

In agreement with the climatology, SST within the three shelf regions north of the Mackenzie River (R2 through R4) exhibited a northward gradient with the inner shelf being the warmest (R2: 5.4° ± 3.1°C) and shelf-edge the coldest (R4: 4.2° ± 2.8°C; **Table 1**, **Figure 4B**). The SST maxima in these regions

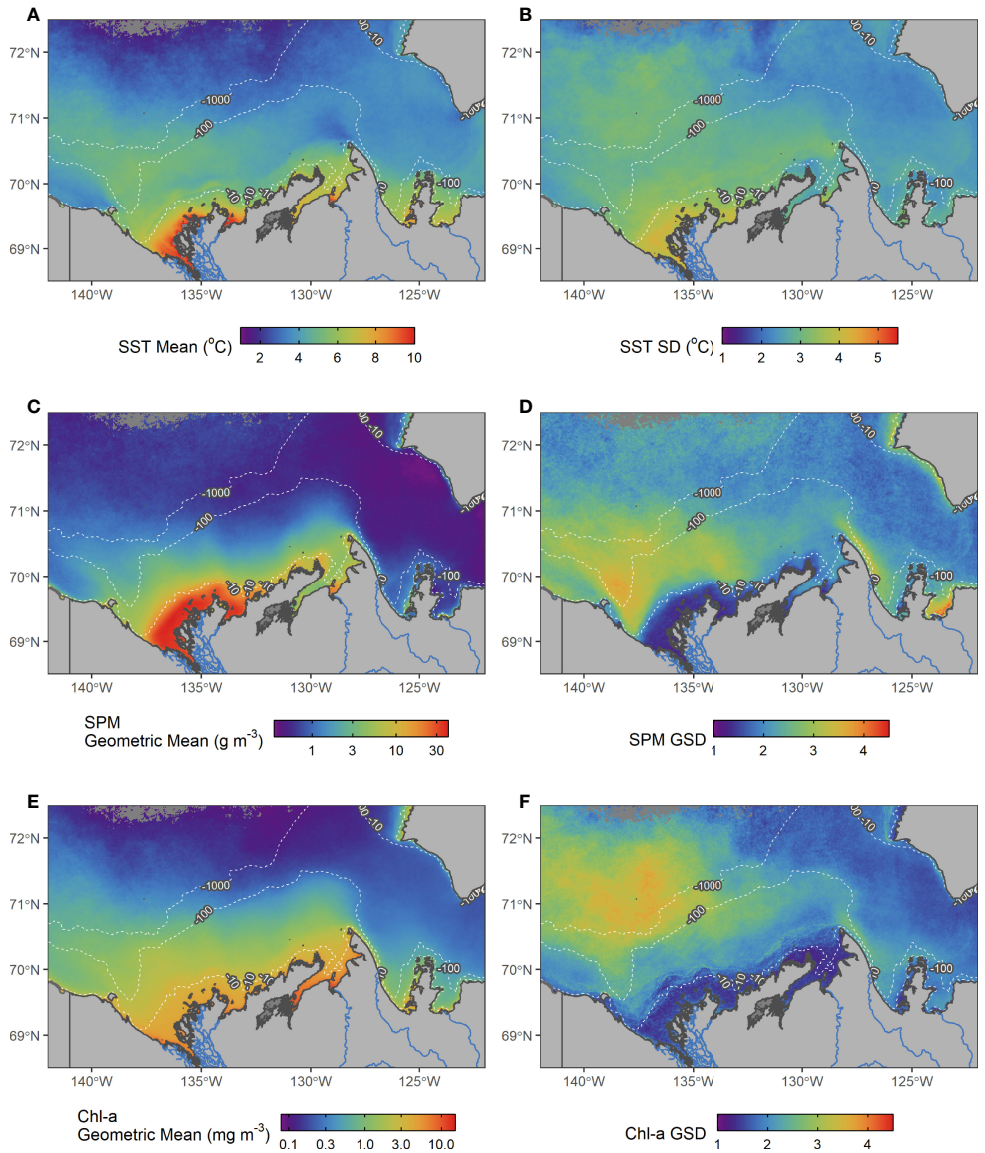

FIGURE 3 | Mean and SD maps of SST **(A, B)**, SPM **(C, D)** and Chl-a **(E, F)** for the time period 2003–2019 (note different colour scales). The GSD used for SPM and Chl-a is unitless. The 10, 100 and 1000 meter bathymetric contours are shown as dashed white lines. Dark grey ocean pixels indicate areas with inadequate data.

were reached later in the year compared to the Mackenzie Delta (R1), with peak temperatures reached in July for the shelf-edge (R4: day of year 202 ± 13), and in August for the mid-shelf (R3: day of year 209 ± 13) then inner shelf (R2: day of year 211 ± 13). The SPM annual cycle in these three regions followed a similar pattern with latitudinal gradient (**Figure 4C**), with a rapid increase in SPM early in the year that peaked between mid-June in the inner (R2 maximum: 13.3 g m^{-3} on June 14, DOY 165) and mid- shelf regions (R3 maximum: 3.4 g m^{-3} on DOY 165), to early July in the shelf edge region (R4 maximum: 1.9 g m^{-3} on June 26, DOY 177), after which SPM declined through the summer and exhibited moderate increases in concentration again in September in all three regions (**Table 1**). Mean SPM on the inner shelf (R2 mean: 6.05 g m^{-3}) was 3.7 times higher than the mean SPM on the mid-shelf (R3: 1.65 g m^{-3}), and 6.7 times higher than the shelf edge (R4: 0.90 g m^{-3}; **Figure 4**). Chl-a reached its peak in these regions at the beginning of July a few weeks later than the SPM peaks, with the inner shelf exceeding 3.0 mg m^{-3} most of the summer (R2 mean of 2.80 mg m^{-3}; **Figure 4D**), while the mid-shelf remained above 1 mg m^{-3} following its peak (R3 mean of 1.16 mg m^{-3}), and the shelf edge remained below 1.0 mg m^{-3} (R4 mean of 0.53 mg m^{-3}). On the mid-shelf (R3) and shelf edge (R4) regions (**Figure 4D**), high phytoplankton biomass immediately occurred following sea ice retreat in agreement with the known sea ice dynamics of the region and early open water season (**Figure 5**). These events

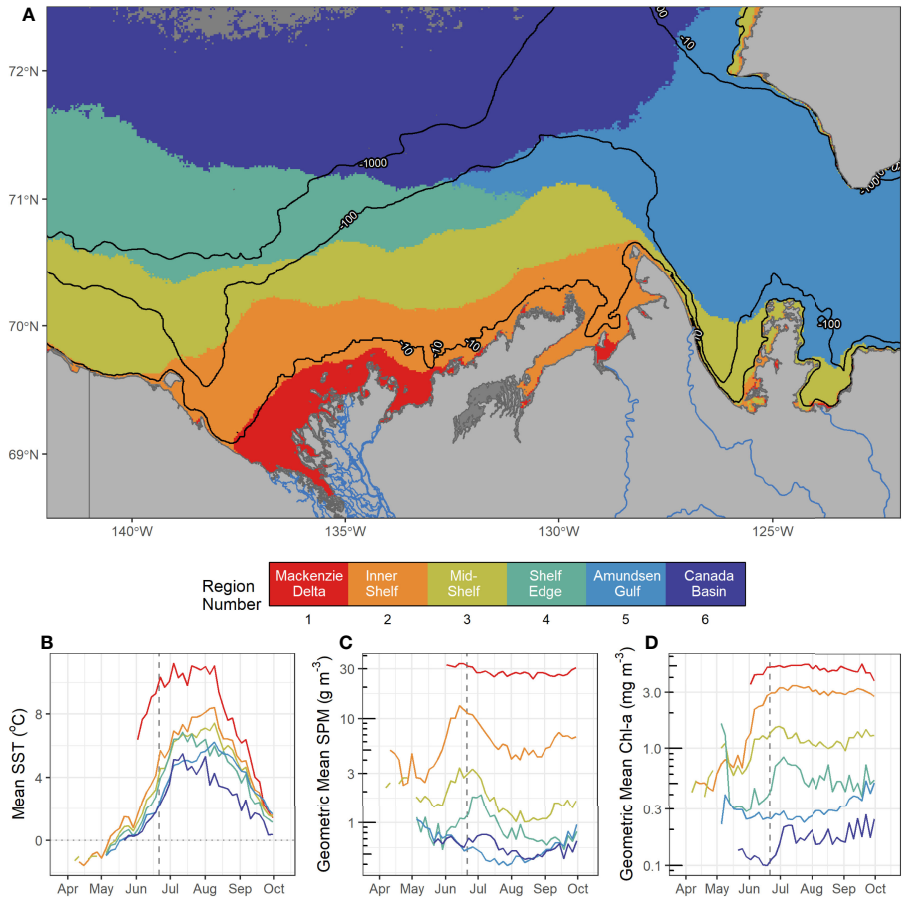

FIGURE 4 | Six biogeochemical regions defined by the SOM analysis of satellite SST, SPM and Chl-a for the period 2003–2019 **(A)**. The solid black lines correspond to the 10-m, 100-m and 1000-m bathymetric contours. The middle inset indicates the biogeochemical region and its name. The four-day climatologies of SST **(B)**, SPM **(C)** and Chl-a **(D)** are presented for each region with the grey dashed line indicating the date of the summer solstice (i.e., June 21st). Ocean pixels indicated in grey did not contain enough data and were not included in the analysis.

were also evident in the four-day composite images (**Figure 6**), which revealed the open water area and associated high phytoplankton biomass located between offshore pack ice and landfast ice. SIC declined earlier (i.e., April) on the shelf, mid-shelf and shelf-edge regions (R2 to R4) compared to the Mackenzie Delta (R1; **Figure 5**).

Amundsen Gulf (R5) and Canada Basin (R6) regions exhibited properties typical of offshore oceanic waters [i.e., Case 1, as opposed to coastal, Morel and Prieur (1977)]. Amundsen Gulf (R5) contained the eastern side of the study area and protruded onto the continental shelf between the Canada Basin (R6) and the continental shelf edge (R4,

TABLE 1 | Descriptive statistics from 2003–2019 of the six SOM regions, including the area, median depth and depth range of each region.

Region Number	Region Name	Area (km^2)	Median depth (range) (m)	Mean DOY SIC <50%	Mean SST (°C)	Max SST (°C)	Max SST DOY	Geometric mean SPM ($g\ m^{-3}$)	Geometric mean Chl-a ($mg\ m^{-3}$)
1	Mackenzie Delta	8 580	3 (1 – 17)	167 ± 5	7.9 ± 3.9	13.4 ± 1.3	201 ± 17	27.5 / 1.6	4.8 */ 1.5
2	Inner Shelf	26 719	16 (1 – 180)	155 ± 20	5.4 ± 3.1	9.9 ± 1.4	211 ± 13	6.1 */ 2.7	2.8 */ 1.9
3	Mid-Shelf	39 321	49 (1 – 999)	152 ± 19	4.5 ± 2.8	8.5 ± 1.5	209 ± 13	1.7 */ 2.8	1.2 */ 2.3
4	Shelf Edge	31 459	1 377 (43 – 2 962)	167 ± 24	4.2 ± 2.8	7.7 ± 1.8	202 ± 13	0.9 */ 2.5	0.5 */ 3.1
5	Amundsen Gulf	48 907	249 (2 – 653)	151 ± 21	3.8 ± 2.4	6.7 ± 1.4	212 ± 16	0.5 */ 2.0	0.3 */ 2.0
6	Canada Basin	61 267	1 700 (28 – 3 205)	185 ± 34	2.8 ± 2.4	5.1 ± 2.1	205 ± 15	0.6 */ 2.0	0.2 */ 2.3

The first day of year (DOY) with SIC < 50% is indicated with standard deviation. The climatological mean and maximum SST are shown, with mean DOY of maximum SST with standard deviations. The geometric mean SPM and Chl-a are shown with GSD.
"/" indicate the upper and lower bounds of the geometric standard deviation, indicating multiplication and division and should be interpreted similarly to the plus/minus symbol.*

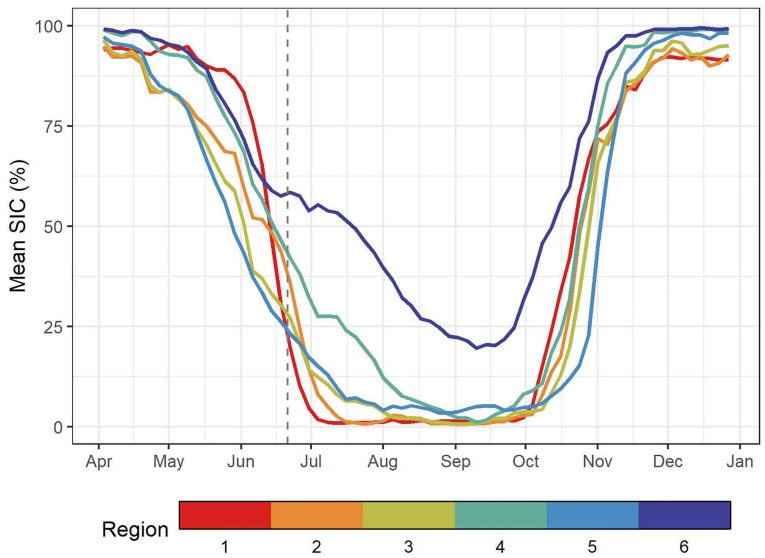

FIGURE 5 | The mean SIC variation from April to January averaged over the period 2003 to 2019 (excluding 2011 and 2012). The vertical dashed line indicates the summer solstice.

Figure 4A). This narrow protrusion of R5 west onto the shelf was consistently delineated in all SOM layouts (i.e., any number of nodes, results not shown). The four-day SST cycles of both regions were characterized by rapid warming from May through early July (approximately two weeks following the summer solstice). Canada Basin (R6) reached a maximum mean SST of 5.1°C on July 24 (DOY 205; **Table 1**). Amundsen Gulf (R5) continued warming until July 31 (maximum SST of 6.7°C, DOY 212), but at a slower rate compared to early summer, while the Canada Basin SST declined following its peak (**Figure 4B**). The SPM seasonal cycles were similar for the two regions, with a slight decrease following the SIC decline in early May, followed by an increase in SPM at the end of the summer (**Figure 4C**). The Canada Basin (R6) exhibited a peak SPM in July that was absent in Amundsen Gulf (R5), though both regions had the lowest geometric mean SPM of all six regions (R5: 0.54 and R6: 0.59 g m^{-3}, **Table 1**). Both regions also exhibited the lowest Chl-a (R5: 0.29 and R6: 0.16 mg m^{-3} respectively), but with differing phenology; two Chl-a peaks occurred in Amundsen Gulf, the first at the beginning of the open-water season (i.e., May) and the second one in the fall (September), while Chl-a remained fairly low and stable through the summer. On the other hand, Chl-a in the Canada Basin showed relatively low concentration from late spring to early summer (< 0.15 mg m^{-3}), followed by a slight increase to about 0.22 mg m^{-3} at the beginning of July and remained > 0.15 mg m^{-3} for the rest of the open-water season (**Figure 4D**).

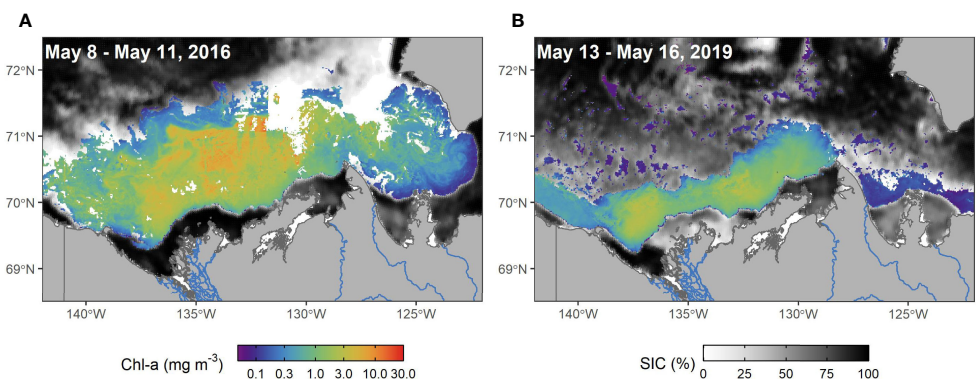

FIGURE 6 | Four-day composite images of SIC and Chl-a showing flaw lead phytoplankton blooms during May. The geometric mean of Chl-a is shown from May 8-11, 2016 **(A)** and May 13-16, 2019 **(B)**.

Differences in mean SIC between regions were evident (**Figure 5**). The Mackenzie Delta region (R1), subject to landfast ice, showed a rapid decline in SIC from about 90% in May to no sea ice by early July as the ice barrier melted and was exported by fluvial discharge. Flaw leads, open-water formation between landfast and sea-ice, generally occurred early in the year (May-June) between Herschel Island and Cape Bathurst and were evident in the inner (R2) and mid- shelf (R3) regions after which SIC dropped below 10% by mid-July. Compared to R2 and R3, SIC on the shelf edge (R4) declined for a longer period of time, with little to no sea ice present by August. Amundsen Gulf (R5) showed a similar pattern to the shelf regions (R2 – R4) in terms of SIC seasonal cycle but with a delay in freeze-up timing. Finally, the Canada Basin (R6) exhibited persistent sea ice through the year, though high inter-annual variability (see **Figure S6**) reaching a climatological minimum of 20% in mid-September.

The years 2006, 2012 and 2013 were notable in the time series. In 2012 record high SST was present in the adjacent outer shelf (R4) and Canada Basin (R6) regions (See **Figure S3**). SST was most pronounced in the Canada Basin where SST reached 10.4°C on July 31st. The years 2006 and 2013 exhibited anomalously high SPM in R2, R3, R4 and R6, and high Chl-a in R4 and R6 (see **Figures S4** and **S5**) and corresponded to years with highest level (2006) and discharge (2013) measured at the Water Survey of Canada hydrometric station at Arctic Red River [ID: 10LC014; ECCC (2021)] over the same time period.

3.3 Regional Annual and Monthly Trends

We examined annual trends from 2003 to 2019 for SST, SPM, Chl-a and SIC across the six regions. Interestingly, only one significant annual SPM trend was found, namely, SPM in the Canada Basin with a decreasing trend of 0.31 ± 0.13 g m^{-3} decade^{-1}, with declines not observed in SST or Chl-a (**Table 2**). On the other hand, most annual SIC trends were significant and negative, with the most dramatic decline occurring on the shelf edge (R4, -8.4 ± 3.5% decade^{-1}) followed by the mid-shelf (R3, -7.7 ± 2.2% decade^{-1}). The exceptions were Amundsen Gulf (R5) and Canada Basin (R6), where no significant annual trends in SIC were found.

Monthly mean trends provided insights to seasonal changes over the period of observation (**Table 3**). We examined monthly trends for May through September in SIC, SST, SPM and Chl-a across all six regions. As the month of April had low data coverage due to sea ice cover, regions with fewer than 10 years of data were removed. Out of the 135 possible trends only 12 were significant at the 0.05 level. This included a cooling on the inner shelf in April (SST trend of -0.61 ± 0.21°C decade^{-1}), a decrease in SPM in the Mackenzie Delta in June (-2.88 ± 1.15 g m^{-3} decade^{-1}), and SPM declines both on the shelf edge (-0.88 ± 0.40 g m^{-3} decade^{-1}) and Canada Basin (-0.44 ± 0.15 g m^{-3} decade^{-1}) in August. Two significant Chl-a trends were observed in May on the inner (0.43 ± 0.18 mg m^{-3} decade^{-1}) and mid- shelf (0.34 ± 0.13 mg m^{-3} decade^{-1}). SIC trends were generally negative, with a decline in May on the entire shelf (R1 – R3): Mackenzie Delta: -5.7 ± 1.8% decade^{-1}, inner shelf: -23.7 ± 7.4% decade^{-1} and mid-shelf: -26.8 ± 9.5% decade^{-1}. The declined observed in May for the inner shelf continued into June with a negative trend of -20.1 ± 7.6% decade^{-1}. Finally, SIC in the Canada Basin declined later in the year in August (-19.8 ± 8.0% decade^{-1}).

3.4 Time Series Correlations Between Properties and Regions

3.4.1 Correlation Analysis of the Same Property Between Regions

The correlation matrix of the 24 four-day time series (i.e., four properties for six regions) provided information on underlying processes and the connectivity between regions (**Figure 7**). In general, when considering properties individually, SST and SIC showed the highest correlation between regions, with ρ values ranging from 0.49 to 0.94 for SST and from 0.26 to 0.83 for SIC. The SST ρ remained high between spatially adjacent regions (>0.75) and decreased as regions were more physically separated, reaching a minimum of ρ = 0.49 between the Mackenzie Delta (R1) and Amundsen Gulf (R5) regions. The SIC ρ values followed the same pattern as SST but with lower magnitude.

The SPM and Chl-a ρ values between regions were overall lower and fewer were significant than for SST and SIC. The SPM time series had moderate to high p values between the four regions on the continental shelf (R1 – R4, ρ > 0.53) when directly adjacent, and between the Canada Basin and shelf edge (R6 and R4: ρ = 0.66). The Amundsen Gulf SPM time series was correlated to the SPM time series on the mid-shelf region (p = 0.45) and in a lesser extent to the Canada Basin (ρ = 0.34). Finally, Chl-a time series showed moderate correlation (ρ > 0.4) only between physically connected regions, the correlation coefficient decreasing to < 0.3 when regions did not share common borders. No correlations between regions were found for the SPM and Chl-a time series when the regions were furthest apart (i.e., the Mackenzie Delta and Canada Basin).

TABLE 2 | Annual mean trends of SST, SPM, Chl-a and SIC for the six regions over the period 2003-2019, with slope expressed as change per decade. (*°C per decade*).

Region	SST slope (*°C per decade*)	SPM slope (*g m^{-3} per decade*)	Chl-a slope (*mg m^{-3} per decade*)	SIC slope (*% per decade*)
1	-0.14 (0.40)	0.36 (1.05)	0.20 (0.13)	**-4.0 (1.4)****
2	0.09 (0.44)	-0.16 (0.50)	-0.15 (0.19)	**-7.7 (2.2)****
3	-0.27 (0.49)	-0.24 (0.21)	-0.21 (0.13)	**-6.4 (2.7)****
4	-0.65 (0.75)	-0.46 (0.24)*	-0.35 (0.22)	**-8.4 (3.5)****
5	-0.37 (0.53)	0.001 (0.04)	-0.06 (0.03)	-4.5 (3.2)
6	-0.51 (0.60)	**-0.31 (0.13)****	-0.14 (0.10)	-7.9 (4.1)*

P-values less than 0.1 are indicated with one star (*) and less than 0.05 in bold with two stars (**). Standard error of the slope is indicated in brackets.

TABLE 3 | Monthly mean trends of SST, SPM, Chl-a and SIC for the six regions over 2003–2019, with slope expressed per decade.

Region	SST slope (*°C per decade*)	SPM slope (*g m^{-3} per decade*)	Chl-a slope (*mg m^{-3} per decade*)	SIC slope (*% per decade*)
		April		
1	–	–	–	-2.2 (1.2)
2	***-0.61 (0.21)***	*2.32 (1.18)**	*0.23 (0.15)*	-7.2 (3.9)*
3	*-0.34 (0.18)**	***0.90 (0.35)***	*0.08 (0.14)*	-6.3 (4.8)
4	–	–	–	-2.6 (2.4)
5	*-0.35 (0.16)**	*0.74 (0.38)**	*-0.06 (0.05)*	-2.9 (3.4)
6	–	–	–	-1.2 (0.9)
		May		
1	*-0.06 (0.75)*	*2.72 (6.16)*	*0.15 (0.31)*	**-5.67 (1.8)****
2	-0.09 (0.42)	-0.35 (1.11)	**0.43 (0.18)****	**-23.7 (7.4)****
3	0.28 (0.26)	-0.53 (0.44)	**0.34 (0.13)****	**-26.8 (9.5)****
4	*0.26 (0.33)*	*-1.98 (1.14)*	*0.15 (0.07)**	-20.5 (10.5)*
5	0.21 (0.22)	-0.55 (0.30)*	0.02 (0.06)	-21.1 (11.6)*
6	0.12 (0.30)	-1.30 (0.75)	0.02 (0.02)	-12.3 (6.5)*
		June		
1	-0.24 (0.38)	**-2.88 (1.15)****	0.18 (0.25)	-12.5 (6.0)*
2	0.52 (0.40)	-2.36 (1.47)	0.34 (0.27)	**-20.1 (7.6)****
3	0.02 (0.32)	-1.40 (0.82)	-0.09 (0.07)	-15.2 (12.2)
4	*-0.23 (0.47)*	*-0.62 (1.12)*	*-0.07 (0.15)*	-28.7 (13.4)*
5	0.06 (0.30)	0.02 (0.19)	-0.01 (0.03)	-13.0 (12.9)
6	0.17 (0.33)	-0.53 (0.82)	0.003 (0.02)	-19.1 (12.0)
		July		
1	0.60 (0.64)	-1.15 (1.43)	0.28 (0.16)	0.4 (0.3)
2	1.20 (0.74)	-2.16 (1.32)	-0.19 (0.24)	-1.9 (1.7)
3	0.46 (0.66)	-1.07 (0.90)	-0.43 (0.24)*	-3.2 (5.9)
4	-0.52 (0.99)	-1.59 (2.46)	-0.43 (0.42)	-12.9 (1.3)
5	0.10 (0.66)	-0.07 (0.06)	-0.05 (0.03)	-0.8 (5.4)
6	-0.54 (0.90)	-0.32 (0.23)	-0.07 (0.05)	-11.5 (12.3)
		August		
1	-0.12 (0.69)	2.17 (1.57)	0.31 (0.18)	0.4 (0.2)*
2	0.22 (0.60)	0.26 (0.72)	0.02 (0.02)	-2.1 (1.7)
3	0.02 (0.72)	-0.37 (0.23)	-0.29 (0.16)*	-2.6 (2.3)
4	-0.70 (1.07)	**-0.88 (0.40)****	-0.44 (0.25)*	-12.0 (6.1)*
5	0.02 (0.74)	-0.08 (0.06)	-0.09 (0.05)*	-2.0 (4.0)
6	-0.63 (0.73)	**-0.44 (0.15)****	-0.15 (0.08)	**-19.8 (8.0)****
		September		
1	-0.07 (0.67)	0.91 (1.53)	0.19 (0.28)	-0.3 (0.2)
2	0.13 (0.61)	0.61 (0.79)	-0.03 (0.17)	0.9 (1.0)
3	0.10 (0.57)	0.24 (0.19)	-0.03 (0.16)	1.1 (2.0)
4	-0.42 (0.65)	-0.21 (0.10)*	-0.48 (0.23)*	-1.7 (3.3)
5	0.01 (0.69)	0.06 (0.08)	0.02 (0.06)	0.8 (5.5)
6	-0.22 (0.55)	-0.29 (0.15)*	-0.20 (0.12)	-11.8 (1.0)

P-values < 0.1 are indicated with one star (*) and < 0.05 in bold with two stars (**). Standard error of the slope is indicated in brackets. Monthly trends calculated from < 10 years of data were removed, and with < 17 years indicated in italics for SST, SPM and Chl-a. SIC was calculated from 15 years in all cases (missing 2011 and 2012).

3.4.2 Correlation Analysis Between Differing Properties

The correlation analysis showed more complex patterns when comparing differing properties across the SOM regions (**Figure 7**). Since SST was highly correlated between regions (section 3.4.1), and Chl-a or SPM were correlated to SST within the same region, both SST and Chl-a had a moderate to high degree of correlation with the SST time series in all the other regions. For instance, SPM and SST were negatively correlated within Amundsen Gulf (R5, $\rho = 0.45$); given the high SST correlation in R5 with the SST in all the other regions, SPM in Amundsen Gulf was negatively correlated with the SST in all regions.

SST and SIC were negatively correlated across the majority of regions, with some exceptions. The time series of SST in the Mackenzie Delta (R1) was positively correlated with SIC on the shelf edge (R4) and Canada Basin (R6) regions, with a weak negative correlation to the SIC on the inner shelf (R2), and no correlation to SIC on the mid-shelf (R3) and Amundsen Gulf (R5). The Canada Basin SIC was only weakly positively correlated with SST in the Mackenzie Delta, and slightly negatively correlated with Amundsen Gulf SST.

In general, SST (SIC) and SPM were negatively (positively) correlated with ρ varying between -0.25 (0.24) and -0.54 (0.57). The absence of correlation between SST and SPM occurred in the same regions where no correlations were found between SST and SIC (for instance, the SST time series in the Mackenzie Delta (R1) against the SPM time series on the inner and mid- self regions).

The SST and Chl-a time series showed a slight to moderate degree of correlation in the Mackenzie Delta ($\rho = 0.26$), the inner shelf (i.e., $\rho = 0.33$), the shelf edge (i.e., $\rho = 0.43$) and the Canada

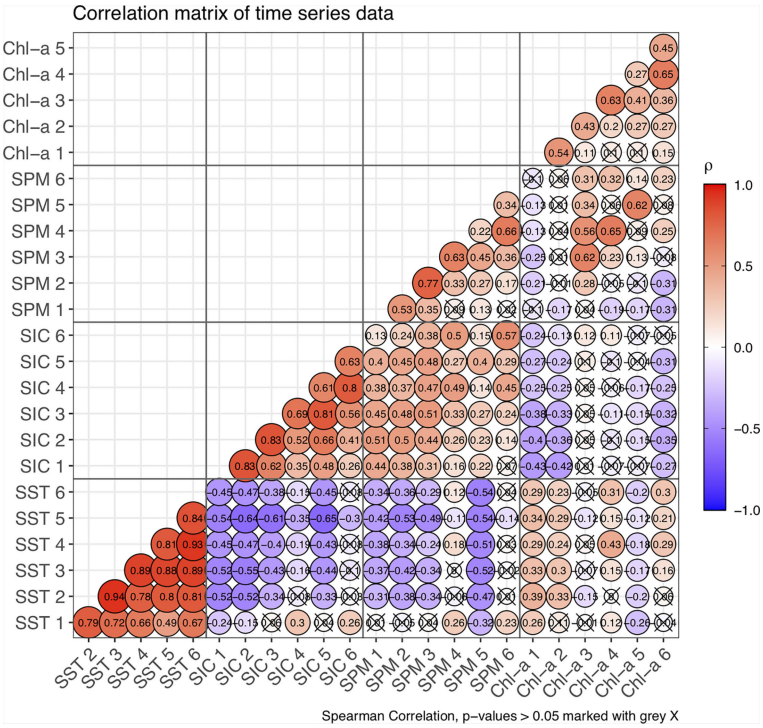

FIGURE 7 | Correlation matrix of time series between parameters, with parameter and region number indicated (i.e., SST 1 is SST of Region 1). The size of the bubble indicates the significance (low p-value corresponds to large bubble; p-value > 0.05 covered by a grey "X") and colour indicates the Spearman correlation coefficient (ρ).

Basin (ρ = 0.30) but none on the mid-shelf and Amundsen Gulf regions (ρ = -0.12). The time series of SPM and Chl-a were moderately correlated in the mid-shelf region (R3, ρ = 0.62), shelf edge (R4, ρ = 0.65) and Amundsen Gulf (R5, ρ = 0.62).

The relationships between SST and Chl-a during the warming and cooling periods were also analysed for each region as a Type-II linear regression, in an attempt to assess the impact of physical forcing on primary producers (**Figure 8**). In general, Chl-a increased with SST during the warming period (**Figure 8**), but no relationship between SST and Chl-a was found during seasonal cooling (see **Figure S7**). During warming, SST explained 76, 61, 28 and 33% of variance in Chl-a in the Mackenzie Delta (R1), inner and mid-shelf (R2 and R3), and the shelf edge (R4) regions respectively. The Canada Basin (R6) region also exhibited a positive significant relationship between SST and Chl-a (R^2= 0.30) but no significant relationship was found in Amundsen Gulf.

4 DISCUSSION

The SOM approach to identify spatio-temporal patterns of SST, SPM and Chl-a over 17-years, combined with the climatology maps (**Figure 3**), statistics (**Table 1**, **Figure 4**), trends (**Table 2**) and correlation matrices (**Figure 7**), provided detailed information on the biogeochemical regimes of the surface EBS (**Figure 4**). By dividing the EBS into six biogeochemical regions, perhaps losing the fine spatial scale at which to examine trends (i.e. pixel-by-pixel changes), we reduced the negative impacts of missing data on our metrics (Cole et al., 2012) and used a robust method to group pixels with similiar temporal characteristics of SST, SPM and Chl-a.

The SOM-delineated regions were generally spatially continuous and congruent with bathymetry and sea ice regimes, though SIC and pixel information (i.e., lat, lon, bathymetry) were not input during the classification procedure. To some extent, information on sea ice presence was inherently included in the MODIS-Aqua imagery (i.e., SST, SPM and Chl-a), as no data from the sea surface were acquired by optical satellite when sea ice was present. However, the presence of clouds, which also prevented data acquisition, would mitigate some bias caused by ice cover on the results, as each pixel contained a differing number of observations over time. The regions were also arranged roughly by bathymetry, i.e. the Mackenzie Delta region (R1) closely followed the 10-m isobath while the eastern side of the inner shelf (R2) coincided with the 1000-m isobath, and the relationship between shallow bathymetry and SIC presence in these regions was evident as a reduced number of valid data available in the time series.

Most regions identified using the SOM approach were generally in agreement with other comprehensive classifications from the area, including Ecologically and Biologically Significant Areas (EBSAs) in the Western Arctic and bioregional Eco-units (DFO,

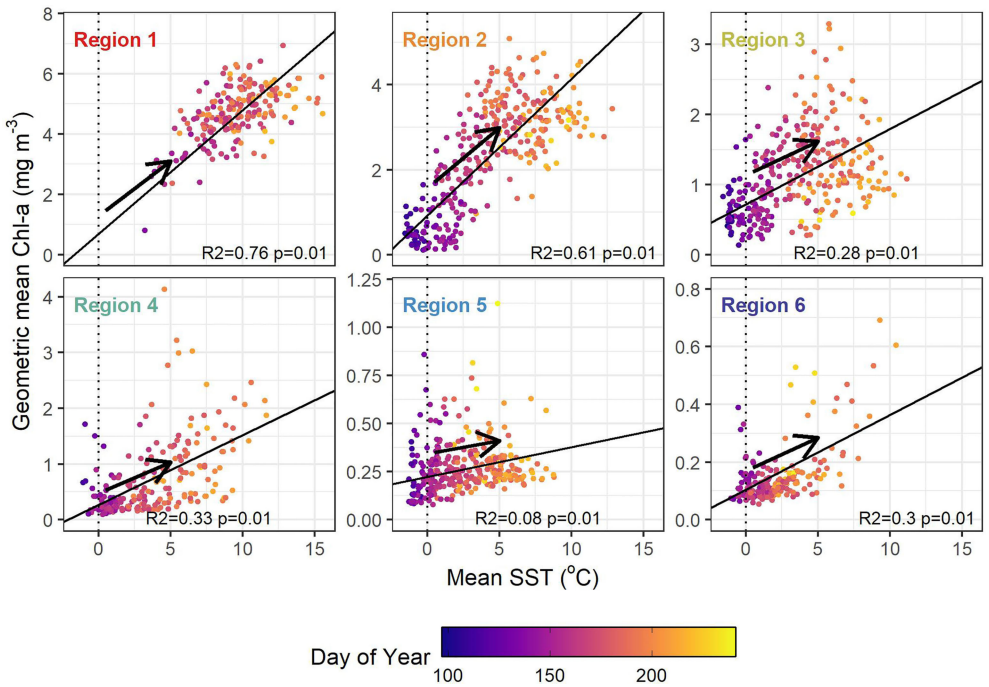

FIGURE 8 | Chl-a and SST regression for time series values from annual warming (dates preceding the maximum annual SST value for all years). Points are coloured by the day of year, with arrows indicating the general temporal progression.

2015; Hodgson et al., 2015), constructed using physical datasets of multiple trophic levels of the ecosystem including marine mammal and benthos species distributions. For example, the northern boundary of the inner shelf region (R2; see **Figure 4A**), which corresponded with the transition of moderate to low SPM in the climatology (**Figure 3C**), closely matched the Mackenzie Estuary Eco-unit of the Western Arctic Bioregion [WAB; Hodgson et al. (2015)], and the Mackenzie Estuary and Nearshore continental shelf EBSAs (DFO, 2011; DFO, 2015). East of Cape Bathurst, the mid-shelf region (R3) had significant overlap with the Mackenzie Inner-shelf, Outer-shelf and Amundsen Gulf Bays WAB Eco-units (Hodgson et al., 2015). The agreement of the SOM regions with existing EBSAs and Eco-units demonstrated that biogeochemical processes at the ocean surface have some consistency with ecological communities. Our study demonstrates that the inclusion of discrete and categorical data may complement the satellite parameters in this SOM approach to find spatio-temporal patterns for marine spatial planning and conservation.

The regions identified in this study were in agreement with physical characteristics of the EBS observed in other studies. Lower SPM and SST further from the warm, sediment-laden waters delivered by the Mackenzie River (Mulligan and Perrie, 2019) was well reflected in the seasonal climatology (**Figure 4**). The high SST near the river mouth can also be attributed to high concentrations of optical constituents absorbing solar radiation (Soppa et al., 2019). The stratification and nutrients from the Mackenzie River discharge can sustain high biomass on the shelf (Forest et al., 2013) as shown in the climatology of phytoplankton biomass in R1 through R3. These relationships were also evident in the correlation matrix which showed moderate to strong correlations of SPM and Chl-a between these three regions (**Figure 7**). The Canada Basin (R6) and Amundsen Gulf (R5) exhibited properties of offshore oceanic waters, with low SPM and Chl-a, and temperature and open-water area strongly influenced by the presence of sea ice. R5 and R6 also exhibited the lowest SST due to latent heat from melting sea-ice preventing greater warming (Stroh et al., 2015).

The impact of low SIC on SST was demonstrated in Canada Basin particularly in 2012, a year with record low SIC throughout the Arctic Ocean (Perovich et al., 2013) causing greater surface heating. Unfortunately, due to the gap between AMSRE and AMSR2 data, we did not include SIC during 2012, but the highest maximum SST in Canada Basin (10.4°C on July 31) was observed that year, which corresponded to a value 2.5 standard deviations higher than the maximum average SST for this region over 2003–2019 (**Table 1**, **Figure S3**). The correlation matrices showed a relationship of SIC and SST, which varied in opposite phase for the shelf regions (R1 through R4) and Amundsen Gulf (R5), consistent with previous studies that evidenced the role of large scale atmospheric and solar forcing (i.e., Lukovich et al., 2009; Liu et al., 2021; Henderson et al., 2021) and ocean circulation (i.e., Morison et al., 2021) on the temperature and sea-ice of the Beaufort Sea. The sea surface circulation impacts these regions differently, with the Alaskan Coastal Current flowing eastward along the coast into Amundsen Gulf (Pickart, 2004). The impact of this current was evident in the climatology of SST, which was overall cooler west of Herschel Island and similar to the spatial

pattern observed in Mulligan and Perrie (2019) (**Figure 3**). The shelf edge, Canada Basin and Amundsen Gulf (R4, R5 and R6) were most impacted by the anti-cyclonic Beaufort Gyre defining the boundary between the shelf and open waters. By identifying the seasonal cycles and trends in regions of similar SST, SPM and Chl-a, in addition to dealineating biogeophysical regions, we were able to demonstrate that this method is effective at quantifying some surface processes occuring in the EBS.

A key difference between the shelf edge and Canada Basin (R4 and R6) to Amundsen Gulf (R5) in our satellite dataset, the three regions furthest removed from the optical influence of the Mackenzie River, was the higher variability of phytoplankton biomass (Chl-a GSD; see **Figure 3**). Factors that contributed to the high Chl-a GSD intersecting the shelf edge and basin (R4 and R6) may be i) local topographically induced upwelling events delivering nutrients to the surface and stimulating phytoplankton growth (Williams and Carmack, 2008), ii) ice-edge blooms that take place under favourable light conditions when nutrients are released as ice recedes (Perrette et al., 2011; Renaut et al., 2018), or iii) wind-driven advection of the Mackenzie River plume toward the central Beaufort Sea (Mulligan and Perrie, 2019). For example, high Chl-a was observed in 2006 and 2013 (> 1.3 mg m^{-3}) as detailed in Babb et al. (2019) and Doxaran et al. (2015), when intense northward advection of stratified nutrient-loaded plume waters with high SPM concentration followed an unusual spring with high SIC that constrained river disharge and limited the plume expansion. For both of these years high Chl-a and SPM were observed in R4 and R6 (see **Figure S4** and **S5**). Amundsen Gulf is physically separated from the shelf regions by the Bathurst Peninsula (Fissel et al., 2013) and experiences spring conditions unfavourable for phytoplankton growth (i.e., storms and ice-creation, Arrigo and van Dijken (2004)). With the Canada Basin region, Amundsen Gulf (R5) showed the least variability in temperature and remained cool most of the year. This region overlaps with the Cape Bathurst flaw polynya (Williams and Carmack, 2008), which is subject to early summer vertical mixing driven by wind and convection and the low Chl-a in Amundsen Gulf in spring is consistent with Arrigo and van Dijken (2004) who demonstrated the importance of stratification to phytoplankton growth in the polynya.

When compared to SST and SIC, the SPM and Chl-a seasonal cycles and time series showed markedly regional differences. The correlation matrix emphasized the thermal characteristics of SST and SIC between regions, while the lack of correlations in SPM and Chl-a between regions suggested that these properties responded to regional forcing identified by the SOM (**Figure 7**). In spring, the mid-shelf (R3) and Amundsen Gulf (R5) were the first regions free of sea-ice in May (**Figure 5**), followed by the inner shelf (R2) and the shelf-edge (R4) in early June. These regions showed a peak in particle concentration following sea-ice melt with the highest values occurring on the shelf (**Figure 4**) following the breakup of the ice barrier at the mouth of the Mackenzie Delta in late June. This emphasizes the impact of the Mackenzie River on the bio-optical conditions and temperature of the coastal EBS surface waters (**Figure 3**), which is also supported by the magnitude and timing of the SPM peak (**Figure 4C**) and high correlation between SPM time series on the shelf regions (**Figure 7**). The phytoplankton biomass peaked a few weeks following the SPM peaks on these shelf regions, potentially corresponding to the settling of mineral particles that let more light enter the water column, when nutrients released by sea-ice melt support phytoplankton growth (Hill et al., 1991). However, these results remain valid for surface Chl-a only, as Chl-a maxima occur at depths not recorded by satellites, particularly further from shore as nutrients delivered by the river plume may be increasingly limited (Retamal et al., 2008) or following ice-edge blooms when the nitracline deepens (Ardyna et al., 2013).

The relationship between SST and Chl-a showed weak relationships throughout the study area. This was in agreement with the work of Blais et al. (2017) who found a correlation coefficient between temperature and phytoplankton biomass using *in situ* measurements in the EBS in a similar range (i.e., 0.23) to the values found here using a relatively long time series of satellite observations (range of no correlation to 0.43 in our study depending on the region). However, when dividing the time series into warming and cooling periods, we found relationships between SST and Chl-a near the outlet of the Mackenzie River (R1; **Figure 8**) and on the inner Shelf (R2, i.e., $R^2 \geq 0.61$). These relationships emphasized the role of freshwater discharge on primary production, as warm, buoyant and nutrient-rich water keep phytoplankton in the surface well-lit water favouring their growth; for example Emmerton et al. (2008) found that the Mackenzie River had a positive impact on phytoplankton production as far as 100 km from the river mouth. The correlation between SST and Chl-a during the warming period decreased as regions were more distant from the Mackenzie Delta region, but remained significant with about 30% of variation in Chl-a explained by SST. We did not find comparable correlations between SST and Chl-a during the cooling period in any of the six regions, with all $R^2 \leq 0.17$. However, as mentioned previously, it is likely that Chl-a maxima occurred at depths not recorded by satellite, suggesting that past the peak of temperature phytoplankton biomass is driven by other processes such as depletion of nutrients at the surface and light limitation later in the year (Tremblay et al., 2009; Ardyna et al., 2013; Ardyna and Arrigo, 2020).

In this study we did not find temporal trends at the annual scale for SST, SPM and Chl-a, while SIC declined throughout most of the study region on annual and monthly time scales. We did not observe significant monthly changes in Amundsen Gulf (R5) for the four parameters including SIC, however, we observed a shift of the date at which the region reached maximum SST, which has been occurring earlier in recent years. This observation suggests that shifts are occurring to the thermal conditions (i.e., changing ice structure) which may impact temperature-dependent species like Arctic Cod (Michaud et al., 1996). For the other regions, it is noteworthy that the only significant positive SPM trend occurred in spring (April) and trends were negative later in the year, which suggests

shifts in the seasonal cycle, though the magnitude of the trends corresponded to small change overall on the decadal scale. We did not find positive trends in SST, nor did we find positive trends in the magnitude of maximum annual SST. However, this result is corroborated by Carvalho and Wang (2020) who found no warming over the period 1982-2018 in the Beaufort Sea, with even cooling trends in some areas. The Chl-a trends, with moderate increases in the inner (R2) and mid-shelf (R3) regions during May, corresponded to dramatic declines in SIC. This result is consistent with projections from Forest et al. (2013) who estimated production increases near the Mackenzie River are most likely to occur on the inner and mid- continental shelf. Additionally, Tolosa et al. (2013) discussed prolonged absences of sea ice over shallow shelves driving resuspension which can enhance production. However, in this study we calculated trends from monthly and annual mean values and did not quantify the increase in open water surface area like other studies reporting on primary production, so further analysis is needed.

5 CONCLUSION

We partitioned 17 years of satellite-measured sea-surface temperature, suspended particulate matter and chlorophyll-a concentration of the Eastern Beaufort Sea into six regions using Self-Organizing Maps. Combined with sea-ice concentration, the regional climatologies, trends and time series correlations emphasized differing processes dominating the surface ocean characteristics of the EBS. The connectivity of regions and parameters were analyzed using a correlation matrix which showed that regions on or adjacent to the continental shelf had greater similarities when compared to the offshore regions. The continental shelf regions were under greatest influence from the Mackenzie River, which influenced the optical properties of the Mackenzie Shelf waters by delivering large amounts of SPM and other optical constituents, and increasing the temperature, freshwater content and stratification of the surface waters. The continental shelf edge region represented a transitional area, with similarities to the continental shelf regions in terms of the temperature and climatology of SPM and Chl-a, but correlated with the processes of offshore Canada Basin. Canada Basin and Amundsen Gulf had characteristics of open ocean, Case 1 waters, having very low concentrations of optical constituents, with sea-ice dominated processes as shown by the low temperature and lack of warm riverine input, and in Canada Basin, the persistent presence of ice throughout the year. Amundsen Gulf was most distinct from the other five regions, having lowest phytoplankton biomass, lowest concentration of suspended particles, and the absence of annual or monthly temporal trends of any of the parameters. However, the day of maximum annual SST has significantly declined, suggesting changes in its thermal characteristics, which may further impact species susceptible to changes in temperature seasonality. Future work can also include SOM analysis with climatological fields in order to train and articulate changing spatial extent of regions over time.

Overall, the annual and monthly trends showed that phytoplankton concentration of the inner and mid-shelf regions has increased in May concurrent with dramatic declines in SIC. Changing phytoplankton seasonality has already been observed in the EBS (Ardyna and Arrigo, 2020), but this study quantifies the changes in spatially discrete regions. Combined with the other trends observed in this study, namely the inter-annual and monthly declines in SIC on the continental shelf, paired with the lack of SST trends observed, we showed that areas within the EBS are experiencing differing responses when compared to large-scale oceanographic shifts occurring at the Arctic Ocean surface caused by climate warming.

Our results emphasize the need to consider regional scales (similarly mentioned in Screen, 2017) when studying the impacts of climate change and the functioning of the surface Arctic Ocean ecosystems. For example, while SIC is declining throughout the Arctic Ocean and changes in the timing and northward expansion of phytoplankton blooms have been observed, we showed that in the EBS these shifts may currently be more spatially constrained than previously considered. This is further emphasized when specifically considering SST and SIC trends; SST is demonstrably increasing at the pan-Arctic scale, while SIC continues to dwindle, with dire implications for the ecosystems of the Arctic Ocean. However, we did not find SST to be significantly increasing in the time period and area of this study, though SIC declines were demonstrated throughout the area. These results will aid future work investigating and prioritizing protection for vulnerable species and ecosystems, and help with identification of marine refugia that may be currently less impacted by climate warming.

DATA AVAILABILITY STATEMENT

The raw data supporting the conclusions of this article will be made available by the authors, without undue reservation.

AUTHOR CONTRIBUTIONS

ED designed the initial study, obtained funding and edited the manuscript. AH performed the data processing and statistical analysis, produced the figures and the initial draft of the manuscript. AH and ED realized the study, including method development and interpretation of results, and developed and revised the manuscript. All authors contributed to the article and approved the submitted version.

FUNDING

This project was funded by the Fisheries and Oceans Canada Arctic Science Fund program.

ACKNOWLEDGMENTS

We want to thank Kristen Wilson, Ryan Galley and Stephanie Clay for valuable revisions of the manuscript and Charles

Hannah for helpful comments during the development of this study. We thank the DFO Arctic Science Fund program for financial support for this project, which was also conducted under Work Package 4 of the Nunataryuk project, led by M. Babin (Université Laval-CNRS) and funded by the European Union Horizon 2020 framework programme. We also want to acknowledge the NASA Ocean Biology and Processing Group and Universität Bremen for making the satellite data used in this study freely and openly available.

SUPPLEMENTARY MATERIAL

The Supplementary Material for this article can be found online at: https://www.frontiersin.org/articles/10.3389/fmars.2022.912865/full#supplementary-material

REFERENCES

Ainsworth, E. J. (1999). Visualization of Ocean Colour and Temperature From Multi-Spectral Imagery Captured by the Japanese Adeos Satellite. *J. Vis.* 2, 195–204. doi: 10.1007/BF03181523

Ainsworth, E. J., and Jones, S. F. (1999). Radiance Spectra Classification From the Ocean Color and Temperature Scanner on Adeos. *IEEE Trans. Geosci. Remote Sens.* 37, 1645–1656. doi: 10.1109/36.763281

Amante, C., and Eakins, B. W. (2009). *Etopo1 1 Arc-Minute Global Relief Model: Procedures, Data Sources and Analysis*. NOAA Technical Memorandum NESDIS, NGDC-24,, 19 pp. doi: 10.1594/PANGAEA.769615

Ardyna, M., and Arrigo, K. (2020). Phytoplankton Dynamics in a Changing Arctic Ocean. *Nat. Clim. Change* 10, 892–903. doi: 10.1038/s41558-020-0905-y

Ardyna, M., Babin, M., Gosselin, M., Devred, E., Bélanger, S., Matsuoka, A., et al. (2013). Parameterization of Vertical Chlorophyll a in the Arctic Ocean: Impact of the Subsurface Chlorophyll Maximum on Regional, Seasonal, and Annual Primary Production Estimates. *Biogeosciences* 10, 4383–4404. doi: 10.5194/bg-10-4383-2013

Ardyna, M., Babin, M., Gosselin, M., Devred, E., Rainville, E., and Tremblay, J.-E. (2014). Recent Arctic Ocean Sea Ice Loss Triggers Novel Fall Phytoplankton Blooms. *Geophys. Res. Lett.* 41, 6207–6212. doi: 10.1002/2014GL061047

Arrigo, K., and van Dijken, G. (2004). Annual Cycles of Sea Ice and Phytoplankton in Cape Bathurst Polynya, Southeastern Beaufort Sea, Canadian Arctic. *Geophys. Res. Lett.* 31, 60–70. doi: 10.1029/2003GL018978

Arrigo, K., and van Dijken, G. (2015). Continued Increases in Arctic Ocean Primary Production. *Prog. Oceanogr.* 136, 60–70. doi: 10.1016/j.pocean.2015.05.002

Babb, D., Landy, J., Barber, D., and Galley, R. (2019). Winter Sea Ice Export From the Beaufort Sea as a Preconditioning Mechanism for Enhanced Summer Melt: A Case Study of 2016. *J. Geophys. Res. Ocean.* 124, 6575–6600. doi: 10.1029/2019JC015053

Barber, D. G., and Hanesiak, J. M. (2004). Meteorological Forcing of Sea Ice Concentrations in the Southern Beaufort Sea Over the Period 1979 to 2000. *J. Geophys. Res.* 109, 1–16. doi: 10.1029/2003JC002027

Bélanger, S., Babin, M., and Tremblay, J. (2013). Increasing Cloudiness in Arctic Damps the Increase in Phytoplankton Primary Production Due to Sea Ice Receding. *Biogeosciences* 10, 4087–4101. doi: 10.5194/bg-10-4087-2013

Blais, M., Ardyna, M., Gosselin, M., Dumont, D., Bélanger, S., Tremblay, J.-E., et al. (2017). Contrasting Interannual Changes in Phytoplankton Productivity and Community Structure in the Coastal Canadian Arctic Ocean. *Limnol. Oceanogr.* 62, 2480–2497. doi: 10.1002/lno.10581

Campbell, J. W. (1995). The Lognormal Distribution as a Model for Bio-Optical Variability in the Sea. *J. Geophys. Res.* 100, 13237–13254. doi: 10.1029/95JC00458

Carvalho, K., and Wang, S. (2020). Sea Surface Temperature Variability in the Arctic Ocean and its Marginal Seas in a Changing Climate: Patterns and Mechanisms. *Global Planet. Change* 193, 103265. doi: 10.1016/j.gloplacha.2020.103265

Cobb, D. G., MacPhee, S., Paulic, J., Martin, K., Roy, V., Reist, J., et al. (2020). Information in Support of the Identification of Ecologically Significant Species, Functional Groups and Community Properties (ESSCP) in the Western Arctic Biogeographic Region. *Tech. Rep.* 2018/027, iv + 66. 2018/027DFO Can. Sci. Advis. Sec. Res. Doc.

Cole, H., Henson, S., Martin, A., and Yool, A. (2012). Mind the Gap: The Impact of Missing Data on the Calculation of Phytoplankton Phenology Metrics. *J. Geophys. Res. Ocean.* 117, 1–8. doi: 10.1029/2012JC008249

Devred, E., Sathyendranath, S., and Platt, T. (2007). Delineation of Ecological Provinces Using Ocean Colour Radiometry. *Mar. Ecol. Prog. Ser.* 346, 1–13. doi: 10.3354/meps07149

DFO (2011). Identification of Ecologically and Biologically Significant Areas (EBSA) in the Canadian Arctic. *Tech. Rep. DFO Can. Sci. Advis. Sec. Sci. Advis. Rep.* 2011/055, 1–40

DFO (2015). Eco-Units and Potential Priority Conservation Areas in the Western Arctic Bioregion. *Tech. Rep. DFO Can. Sci. Advis. Sec. Sci. Advis. Rep.* 2014/021, 1–19.

Doxaran, D., Devred, E., and Babin, M. (2015). A 50% Increase in the Mass of Terrestrial Particles Delivered by the Mackenzie River Into the Beaufort Sea (Canadian Arctic Ocean) Over the Last 10 Years. *Biogeosciences* 12, 3551–3565. doi: 10.5194/bg-12-3551-2015

ECCC (2021). *Real-Time Hydrometric Data*. (Gatineau, Quebec: Environment and Climate Change Canada) https://wateroffice.ec.gc.ca/contactus/contact_us_e.html.

El Hourany, R., Abboud-Abi Saab, M., Faour, G., Mejia, C., Crépon, M., and Thiria, S. (2019). Phytoplankton Diversity in the Mediterranean Sea From Satellite Data Using Self-Organizing Maps. *J. Geophys. Res. Ocean.* 124, 5827–5843. doi: 10.1029/2019JC015131

Emmerton, C., Lesack, L., and Warwick, V. (2008). Nutrient and Organic Matter Patterns Across the Mackenzie River, Estuary and Shelf During the Seasonal Recession of Sea-Ice. *J. Mar. Syst.* 74, 741–755. doi: 10.1016/j.jmarsys.2007.10.001

Fissel, D., Cross, W., and Howland, K. (2013). An Ecological and Oceanographic Assessment of the Beaufort Sea Region: Evaluation of the Risks Associated With Ballast Water Exchange. *Tech. Rep.* 2012/149, vi + 64.DFO Can. Sci. Advis. Sec. Res. Doc.

Forest, A., Babin, M., Stemmann, L., Picheral, M., Sampei, M., Fortier, L., et al. (2013). Ecosystem Function and Particle Flux Dynamics Across the Mackenzie Shelf (Beaufort Sea, Arctic Ocean): An Integrative Analysis of Spatial Variability and Biophysical Forcings. *Biogeosciences* 10, 2833–2866. doi: 10.5194/bg-10-2833-2013

Galley, R. J., Else, B. G. T., Prinsenberg, S. J., Babb, D., and Barber, D. G. (2013). Summer Sea Ice Concentration, Motion, and Thickness Near Areas of Proposed Offshore Oil and Gas Development in the Canadian Beaufort Sea – 2009. *Arctic* 66(1), 105–16. doi: 10.14430/arctic4270

Giovando, L. F., and Herlinveaux, R. H. (1981). A Discussion of Factors Influencing Dispersion of Pollutants in the Beaufort Sea. *Tech. Rep.* 81-4, 198. DFO Institute of Ocean Sciences, Sidney, British Columbia.

Han, B., Loisel, H., Vantrepotte, V., Mériaux, X., Bryère, P., Ouillon, S., et al. (2016). Development of a Semi-Analytical Algorithm for the Retrieval of Suspended Particulate Matter From Remote Sensing Over Clear to Very Turbid Waters. *Remote Sens.* 8, 211. doi: 10.3390/rs8030211

Hardman-Mountford, N., Hirata, T., Richardson, K., and Aiken, J. (2008). An Objective Methodology for the Classification of Ecological Pattern Into Biomes and Provinces for the Pelagic Ocean. *Remote Sens. Environ.* 112, 3341–3352. doi: 10.1016/j.rse.2008.02.016

Henderson, G. R., Barrett, B. S., Wachowicz, L. J., Mattingly, K. S., Preece, J. R., and Mote, T. L. (2021). Local and Remote Atmospheric Circulation Drivers of Arctic Change: A Review. *Front. Earth Sci.* 9. doi: 10.3389/feart.2021.709896

Hewitson, B. C., and Crane, R. G. (2002). Self-Organizing Maps: Applications to Synoptic Climatology. *Clim* 22, 13–26. doi: 10.3354/cr022013

Hill, P. R., Blasco, S. M., Harper, J. R., and Fissel, D. B. (1991). Sedimentation on the Canadian Beaufort Shelf. *Continent. Shelf. Res.* 11, 821–842. doi: 10.1016/

0278-4343(91)90081-G. Proceedings of the Canadian Continental Shelf Seabed Symposium (C2S3).

Hodgson, R., Martin, K., and Melling, H. (2015). Marine Protected Area Network Planning in the Western Arctic Bioregion: Development and Use of a Classification System to Identify Ecological Units as Required Planning Components. *Tech. Rep.* 2015/020, v + 41. DFO Can. Sci. Advis. Sec. Res. Doc.

IOCCG (2009). *Partition of the Ocean Into Ecological Provinces: Role of Ocean-Colour Radiometry, Vol. No. 9 of Reports of the International Ocean Colour Coordinating Group* (Dartmouth, Canada: IOCCG). doi: 10.25607/OBP-99

IOCCG (2015). *Ocean Colour Remote Sensing in Polar Seas, Vol. No. 16 of Reports of the International Ocean Colour Coordinating Group* (Dartmouth, Canada: IOCCG). doi: 10.25607/OBP-107

Jorgenson, M. T., Shur, Y., and Pullman, E. (2006). Abrupt Increase in Permafrost Degradation in Arctic Alaska. *Geophys. Res. Lett.* 33, 1–4. doi: 10.1029/2005GL024960

Kahru, M., Brotas, V., Manzano.-Sarabia, M., and Mitchel, B. (2011). Are Phytoplankton Blooms Occurring Earlier in the Arctic? *Global Change Biol.* 17, 1733–1739. doi: 10.1111/j.1365-2486.2010.02312.x

Kahru, M., Lee, Z., Mitchell, B. G., and Nevison, C. D. (2016). Effects of Sea Ice Cover on Satellite-Detected Primary Production in the Arctic Ocean. *Biol. Lett.* 12, 20160223. doi: 10.1098/rsbl.2016.0223

Kaski, S., Kangas, J., and Kohonen, T. (1998). Bibliography of Self-Organizing Map (Som) Papers: 1981-1997. *Neural Comput. Survey.* 1, 1–176. doi: 10.1007/978-1-4471-0513-8_6

Kirkwood, T. B. L. (1979). Geometric Means and Measures of Dispersion. *Biometrics* 35, 908–909.

Kohonen, T. (1984). *Self-Organization and Associative Memory* (Berlin: Springer Verlag).

Kohonen, T. (1997). *Self-Organizing Maps. 2nd ed* (Berlin: Springer).

Kwok, R., and Cunningham, G. F. (2015). Variability of Arctic Sea Ice Thickness and Volume From Cryosat-2. *Phil. Trans. R. Soc A.* 373, 1–20. doi: 10.1098/rsta.2014.0157

LaZerte, S. E., and Albers, S. (2018). Weathercan: Download and Format Weather Data From Environment and Climate Change Canada. *J. Open Source Softw.* 3, 571. doi: 10.21105/joss.00571

Lewis, K., and Arrigo, K. (2020). Ocean Color Algorithms for Estimating Chlorophyll a, Cdom Absorption, and Particle Backscattering in the Arctic Ocean. *J. Geophys.Res. Ocean.* 125, 1–23. doi: 10.1029/2019JC015706

Liu, Z., Risi, C., Codron, F., He, X., Poulsen, C., Wei, Z., et al. (2021). Acceleration of Western Arctic Sea Ice Loss Linked to the Pacific North American Pattern. *Nat. Comm.* 12, 1–9. doi: 10.1038/s41467-021-21830-z

Longhurst, A., Sathyendranath, S., Platt, T., and Caverhill, C. (1995). An Estimate of Global Primary Production in the Ocean From Satellite Radiometer Data. *J. Plankt. Res.* 17, 1245–1271. doi: 10.1093/plankt/17.6.1245

Lukovich, J. V., Asplin, M. G., and Barber, D. G. (2009). Atmospheric Forcing of the Beaufort Sea Ice Gyre: Surface-Stratosphere Coupling. *J. Geophys. Res.: Ocean.* 114, 1–14. doi: 10.1029/2008JC004849

Macdonald, R. W., Harner, T., and Fyfe, J. (2005). Recent Climate Change in the Arctic and its Impact on Contaminant Pathways and Interpretation of Temporal Trend Data. *Sci. Tot. Environ.* 342, 5–86. doi: 10.1016/j.scitotenv.2004.12.059

Macdonald, R. W., Paton, D. W., and Carmack, E. C. (1995). The Freshwater Budget and Under-Ice Spreading of the Mackenzie River Water in the Canadian Beaufort Sea Based on Salinity and $^{18}o/^{16}o$ Measurements in Water and Ice. *J. Geophys. Res. Ocean.* 100, 895–919. doi: 10.1029/94JC02700

Martin Traykovski, L. V., and Sosik, H. M. (2003). Feature-Based Classification of Optical Water Types in the Northwest Atlantic Based on Satellite Ocean Color Data. *J. Geophys. Res. Ocean.* 108, 19-1–19-18. doi: 10.1029/2001JC001172

Maslanik, J., Stroeve, J., Fowler, C., and Emery, W. (2011). Distribution and Trends in Arctic Sea Ice Age Through Spring 2011. *Geophys. Res. Lett.* 38, 1–6. doi: 10.1029/2011GL047735

McIver, R., Breeze, H., and Devred, E. (2018). Satellite Remote-Sensing Observations for Definitions of Areas for Marine Conservation: Case Study of the Scotian Slope, Eastern Canada. *Remote Sens. Environ.* 214, 23–47. doi: 10.1016/j.rse.2018.05.017

Michaud, J. L., Fortier, P., and Ramseier, R. (1996). Feeding Success and Survivorship of Arctic Cod Larvae, Boreogadus Saida, in the Northeast Water Polynya (Greenland Sea). *Fish. Oceanogr.* 5, 120–135. doi: 10.1111/j.1365-2419.1996.tb00111.x

Miller, G. H., Alley, R. B., Brigham-Grette, J., Fitzpatrick, J. J., Polyak, L., Serreze, M. C., et al. (2010). Arctic Amplification: Can the Past Constrain the Future? *Quaternar. Sci. Rev.* 29, 1779–1790. doi: 10.1016/j.quascirev.2010.02.008

Morel, A., and Prieur, L. (1977). Analysis of Variation in Ocean Color. *Limnol. Oceanogr.* 22, 709–722. doi: 10.4319/lo.1977.22.4.0709

Morison, J., Kwok, R., Dickinson, S., Andersen, R., Peralta-Ferriz, C., Morison, D., et al. (2021). The Cyclonic Mode of Arctic Ocean Circulation. *J. Phys. Oceanogr.* 51, 1053–1075. doi: 10.1175/JPO-D-20-0190.1

Mulligan, R., and Perrie, W. (2019). Circulation and Structure of the Mackenzie River Plume in the Coastal Arctic Ocean. *Continent. Shelf. Res.* 177, 59–68. doi: 10.1016/j.csr.2019.03.006

Oliver, M., Glenn, S., Kohut, J., Irwin, A., Schofield, O., Moline, M., et al. (2004). Bioinformatic Approaches for Objective Detection of Water Masses on Continental Shelves. *J. Geophys. Res. Ocean.* 109, 1–12. doi: 10.1029/2003JC002072

Oliver, M., and Irwin, A. (2008). Objective Global Ocean Biogeographic Provinces. *Geophys. Res. Lett.* 35, 1–6. doi: 10.1029/2008GL034238

O'Reilly, J. E., Maritorena, S., Mitchell, B. G., Siegel, D. A., Carder, K. L. , Garver, S. A., et al. (1998). Ocean Color Chlorophyll Algorithm for SeaWiFS. *J. Geophys. Res.* 103, 24,937–24,953. doi: 10.1029/98JC02160

Park, K., Hahm, D., Choi, J. O., Xu, S., Kim, H.-C., and Lee, S. (2019). Spatiotemporal Variation in Summer Net Community Production in the Amundsen Sea Polynya: A Self-Organizing Map Analysis Approach. *Continent. Shelf. Res.* 184, 21–29. doi: 10.1016/j.csr.2019.07.001

Payette, S., Delwaide, S., Caccianiga, M., and Beauchemin, M. (2004). Accelerated Thawing of Subarctic Peatland Permafrost Over the Last 50 Years. *Geophys. Res. Lett.* 31, 1–4. doi: 10.1029/2004GL020358

Perovich, D., Meier, W., Tschudi, M., Gerland, S., and Richter-Menge, J. (2013). [the Arctic] Sea Ice Cover [in "State of the Climate in 2012"]. *Bull. Am. Meteor. Soc* 94, S1–S258. doi: 10.1175/2013BAMSStateoftheClimate.1

Perrette, M., Yool, A., Quartly, G. D., and Popova, E. E. (2011). Near-Ubiquity of Ice-Edge Blooms in the Arctic. *Biogeosciences* 8, 515–524. doi: 10.5194/bg-8-515-2011

Peucker-Ehrenbrink, B. (2009). Land2sea Database of River Drainage Basin Sizes, Annual Water Discharges, and Suspended Sediment Fluxes. *Geochem. Geophys. Geosyst.* 10, 1–10. doi: 10.1029/2008GC002356

Pickart, R. S. (2004). Shelfbreak Circulation in the Alaskan Beaufort Sea: Mean Structure and Variability. *J. Geophys. Res.* 109, 1–14. doi: 10.1029/2003JC001912

Qi, L., Lee, Z., Hu, C., and Wang, M. (2017). Requirement of Minimal Signal-to-Noise Ratios of Ocean Color Sensors and Uncertainties of Ocean Color Products. *J. Geophys. Res. Ocean.* 122, 2595–2611. doi: 10.1002/2016JC012558

R Core Team (2019). *R: A Language and Environment for Statistical Computing* (Vienna, Austria: R foundation for Statistical Computing).

Renaut, S., Devred, E., and Babin, M. (2018). Northward Expansion and Intensification of Phytoplankton Growth During the Early Ice-Free Season in Arctic. *Geophys. Res. Lett.* 45, 10,590–10,598. doi: 10.1029/2018GL078995

Retamal, L., Bonilla, S., and Vincent, W. F. (2008). Optical Gradients and Phytoplankton Production in the Mackenzie River and the Coastal Beaufort Sea. *Polar. Biol.* 31, 363–379. doi: 10.1007/s00300-007-0365-0

Reygondeau, G., Cheung, W. W. L., Wabnitz, C. C. C., Lam, V. W. Y., Frölicher, T., and Maury, O. (2020). Climate Change-Induced Emergence of Novel Biogeochemical Provinces. *Front. Mar. Sci.* 7. doi: 10.3389/fmars.2020.00657

Reygondeau, G., Guidi, L., Beaugrand, G., Henson, S. A., Koubbi, P., MacKenzie, B. R., et al. (2018). Global Biogeochemical Provinces of the Mesopelagic Zone. *J. Biogeogr.* 45, 500–514. doi: 10.1111/jbi.13149

Richardson, A. J., Risien, C., and Shillington, F. A. (2003). Using Self-Organizing Maps to Identify Patterns in Satellite Imagery. *Prog. Oceanogr.* 59, 223–239. doi: 10.1016/j.pocean.2003.07.006

Screen, J. A. (2017). Simulated Atmospheric Response to Regional and Pan-Arctic Sea Ice Loss. *J. Climate* 30, 3945–3962. doi: 10.1175/JCLI-D-16-0197.1

Serreze, M., Barrett, A., Stroeve, J., Kindig, D., and Holland, M. (2009). The Emergence of Surface-Based Arctic Amplification. *Cryosphere* 3, 11–19. doi: 10.5194/tc-3-11-2009

Soppa, M. A., Pefanis, V., Hellmann, S., Losa, S. N., H'ólemann, J., Martynov, F., et al. (2019). Assessing the Influence of Water Constituents on the Radiative

Heating of Laptev Sea Shelf Waters. *Front. Mar. Sci.* 6. doi: 10.3389/fmars.2019.00221

Stroeve, J. C., Serreze, M. C., Holland, M. M., Kay, J. E., Malanik, J., and Barrett, A. P. (2012). The Arctic's Rapidly Shrinking Sea Ice Cover: A Research Synthesis. *Clim. Change* 110, 1005–1027. doi: 10.1007/s10584-011-0101-1

Stroh, J. N., Panteleev, G., Kirillov, S., Makhotin, M., and Shakhova, N. (2015). Sea-Surface Temperature and Salinity Product Comparison Against External *in Situ* Data in the Arctic Ocean. *J. Geophys. Res.* 120, 7223–7236. doi: 10.1002/2015JC011005

Taşdemir, K. (2011). "Neural Network Based Approximate Spectral Clustering for Remote Sensing Images," in *2011 IEEE International Geoscience and Remote Sensing Symposium*, 2884–2887 doi: 10.1109/IGARSS.2011.6049817. (Institute of Electrical and Electronics Engineers).

Tolosa, I., Fiorini, S., Gasser, B., Martín, J., and Miquel, J. C. (2013). Carbon Sources in Suspended Particles and Surface Sediments From the Beaufort Sea Revealed by Molecular Lipid Biomarkers and Compound-Specific Isotope Analysis. *Biogeosciences* 10, 2061–2087. doi: 10.5194/bg-10-2061-2013

Tremblay, G., Belzile, C., Gosselin, M., Poulin, M., Roy, S., and Tremblay, J.-E. (2009). Late Summer Phytoplankton Distribution Along a 3500 Km Transect in Canadian Arctic Waters: Strong Numerical Dominance by Picoeukaryotes. *Aquat. Microb. Ecol.* 54, 55–70. doi: 10.3354/ame01257

Van Rossum, G., and Drake, F. L. (2009). *Python 3 Reference Manual* (Scotts Valley, CA: CreateSpace).

Wang, M., and Shi, W. (2007). The Nir-Swir Combined Atmospheric Correction Approach for Modis Ocean Color Data Processing. *Opt. Exp.* 15, 15722–15733. doi: 10.1364/OE.15.015722

Wehrens, R., and Buydens, L. M. C. (2007). Self- and Super-Organizing Maps in R: The Kohonen Package. *J. Stat. Softw.* 21, 1–19. doi: 10.18637/jss.v021.i05

Wehrens, R., and Kruisselbrink, J. (2018). Flexible Self-Organizing Maps in Kohonen 3.0. *J. Stat. Softw.* 87, 1–18. doi: 10.18637/jss.v087.i07

Wessel, P., Smith, W. H. F., Scharroo, R., Luis, J., and Wobbe, F. (2013). Generic Mapping Tools: Improved Version Released. Eos. *Trans. Am. Geophys. Union.* 94, 409–410. doi: 10.1002/2013EO450001

Williams, W., and Carmack, E. (2008). Combined Effect of Wind-Forcing and Isobath Divergence on Upwelling at Cape Bathurst, Beaufort Sea. *J. Mar. Res.* 66, 645–663(19). doi: 10.1357/002224008787536808

WMO (2016). The Global Observing System for Climate: Implementation Needs. *Tech. Rep* GCOS, World Meteorological Organization.200, 1–315

Xu, S., Park, K., Wang, Y., Chen, L., Qi, D., and Li, B. (2019). Variations in the Summer Oceanic Pco2 and Carbon Sink in Prydz Bay Using the Self-Organizing Map Analysis Approach. *Biogeosciences* 16, 797–810. doi: 10.5194/bg-16-797-2019

Conflict of Interest: The authors declare that the research was conducted in the absence of any commercial or financial relationships that could be construed as a potential conflict of interest.

Publisher's Note: All claims expressed in this article are solely those of the authors and do not necessarily represent those of their affiliated organizations, or those of the publisher, the editors and the reviewers. Any product that may be evaluated in this article, or claim that may be made by its manufacturer, is not guaranteed or endorsed by the publisher.

Copyright © 2022 Hilborn and Devred. This is an open-access article distributed under the terms of the Creative Commons Attribution License (CC BY). The use, distribution or reproduction in other forums is permitted, provided the original author(s) and the copyright owner(s) are credited and that the original publication in this journal is cited, in accordance with accepted academic practice. No use, distribution or reproduction is permitted which does not comply with these terms.

frontiers | Frontiers in Marine Science

ORIGINAL RESEARCH
published: 13 July 2022
doi: 10.3389/fmars.2022.865081

The Spatial Variation in Chlorophyte Community Composition From Coastal to Offshore Waters in a Subtropical Continental Shelf System

Yun-Chi Lin[1], Chien-Pang Chin[2], Wei-Ting Chen[1,3], Ching-Ting Huang[1], Gwo-Ching Gong[1,4], Kuo-Ping Chiang[1,4] and Xin-Bei Chen[1]*

[1] Institute of Marine Environment and Ecology, National Taiwan Ocean University, Keelung, Taiwan, [2] Marine Fisheries Division, Fishery Research Institute, Keelung, Taiwan, [3] College of Ocean Science and Resource, National Taiwan Ocean University, Keelung, Taiwan, [4] Center of Excellence for the Oceans, National Taiwan Ocean University, Keelung, Taiwan

OPEN ACCESS

Edited by:
Wei-Bo Chen,
National Science and Technology Center for Disaster Reduction (NCDR), Taiwan

Reviewed by:
Yuyuan Xie,
University of South Florida, United States
Lei Wang,
Third Institute of Oceanography, Ministry of Natural Resources, China

***Correspondence:**
Kuo-Ping Chiang
kpchiang@mail.ntou.edu.tw

Specialty section:
This article was submitted to Coastal Ocean Processes, a section of the journal Frontiers in Marine Science

Received: 29 January 2022
Accepted: 20 May 2022
Published: 13 July 2022

Citation:
Lin Y-C, Chin C-P, Chen W-T, Huang C-T, Gong G-C, Chiang K-P and Chen X-B (2022) The Spatial Variation in Chlorophyte Community Composition From Coastal to Offshore Waters in a Subtropical Continental Shelf System. Front. Mar. Sci. 9:865081. doi: 10.3389/fmars.2022.865081

Globally, the continental shelf occupies less than 10% of the total sea surface, but supports substantial primary production and fisheries. Photosynthetic picoeukaryotes (PPE) are important primary producers in marine ecosystems, and chlorophytes make a significant contribution to PPE abundance. Although the distribution of chlorophytes has been widely studied, little is known about how their community composition varies along the coastal-offshore gradient in subtropical continental shelf waters. To better understand their spatial variations, we employed metabarcoding data of 18S rRNA V4 gene to examine chlorophyte composition within the surface and deep chlorophyll maximum (DCM) layers over the continental shelf in the East China Sea (ECS) with high-resolution sampling. Our results indicate a higher chlorophyte diversity in the surface layer than in the DCM. In addition, we found that chlorophytes in oligotrophic Kuroshio surface water were the most diverse, with a higher percentage of Chloropicophyceae, prasinophyte clade V, prasinophyte clade IX, Palmophyllophyceae and Chlorodendrophyceae. In more eutrophic waters along the coast and within the DCM layer, chlorophytes were dominated by Mamiellophyceae. A significant spatial variation in community composition occurred along the nutrient gradient in the subtropical continental shelf ecosystem, varying from Mamiellophyceae-dominant in coastal water to Chloropicophyceae-dominant in offshore water. Furthermore, at a low saline coastal station, which had the lowest chlorophyte diversity, *Picochlorum* (Trebouxiophyceae) was dominant. Overall, chlorophyte diversity was positively correlated with temperature, and negatively correlated with silicate concentration. This study revealed that terrestrial input into continental systems influences chlorophyte diversity in the subtropical northwestern Pacific Ocean.

Keywords: amplicon sequencing, Chloropicophyceae, ecological distribution, Mamiellophyceae, NW Pacific Ocean

INTRODUCTION

Phytoplankton, a primary producer in the ocean, may be responsible for half of the global oxygen production (Field et al., 1998). Based on cell-size, they can be roughly classified as either picophytoplankton (< 2 or 3 μm), nanophytoplankton (~2-20 μm) or microphytoplankton (~20-200 μm) (Sieburth et al., 1978). Picophytoplankton, which are composed of eukaryotes and prokaryotes, generally contribute a significant proportion of total phytoplankton biomass in the oligotrophic open ocean (Li, 1995). In marine ecosystems, photosynthetic picoeukaryotes (PPEs) are less abundant in terms of cell density than prokaryotes, but make a significant contribution to pico-size biomass and primary production due to their greater volume (Worden et al., 2004). Eukaryotes display greater genetic and morphologic variation than prokaryotes, reflecting their multiple functions in marine ecosystems (de Vargas et al., 2015; Caron, 2016). PPEs consist of taxonomically diverse categories, including Chlorophyta, Cryptophyta, Haptophyta (prymnesiophytes), and Orchrophyta (diatoms and chrysophytes). Of these, Chlorophyta have been better studied in terms of genomics (Derelle et al., 2006; Worden et al., 2009; Moreau et al., 2012; Lemieux et al., 2019) and ecological distribution (Not et al., 2004; Foulon et al., 2008; Limardo et al., 2017).

Characteristics of chlorophytes include the use of chlorophyll *b* as the main accessory pigment and chloroplasts which are surrounded by two membranes. In taxonomic classification, Chlorophyta comprise two major groups, namely core chlorophytes and prasinophytes. The former consists of the Ulvophyceae, Trebouxiophyceae and Chlorophyceae clade (the UTC clade), while the latter is a paraphyletic group consisting of more than 8 classes, including the common ocean chlorophytes, Mamiellophyceae, Nephroselmidophyceae, Pyramimonadales etc. (Guillou et al., 2004; Tragin et al., 2016; Dos Santos et al., 2017a). Chlorophyta have a widespread distribution and contribute more than half of total PPE abundance in many marine regions (Not et al., 2004; Not et al., 2005; Collado-Fabbri et al., 2011). However, its dominants vary with geographic location. The ecological distributions of Mamiellophyceae have been the most extensively researched. *Micromonas* was found to be an important component of eukaryotic picophytoplankton in Arctic water, Atlantic temperate regions and in a variety of coastal regions (Not et al., 2004; Lovejoy et al., 2007; Balzano et al., 2012; Lin et al., 2017), while *Bathycoccus* is important in the upwelling system of the eastern South Pacific and subarctic Northeastern Pacific (Limardo et al., 2017), and *Osterococcus* is important in Kuroshio fronts (Clayton et al., 2017). More recently, Chloropicophyceae (previously referred to as prasinophyte clade VII) has been established as another important class (Dos Santos et al., 2017b), but little is known about its ecological distribution in the oceans.

Many studies have revealed chlorophyte diversity, in particular for Mamiellophyceae. *Micromonas*, with 9 clades, exhibits greater species diversity than *Ostreococcus* and *Bathycoccus* (Tragin and Vaulot, 2019). 18S rRNA gene analysis has shown that *Ostreococcus* and *Bathycoccus* consist of four and two clades, respectively (Simmons et al., 2016; Limardo et al., 2017). The distribution patterns of *Bathycoccus* and *Ostreococcus* clades are clearer than that of *Micromonas* (Demir-Hilton et al., 2011; Simmons et al., 2016; Vannier et al., 2016; Clayton et al., 2017; Limardo et al., 2017). Coastal/oceanic ecotypes of *Bathycoccus* and *Ostreococcus* appear to occur independently of each other most of the time, except within mixing waters (Demir-Hilton et al., 2011; Clayton et al., 2017; Limardo et al., 2017). Chloropicophyceae comprise three genera, *Chloropicon*, *Chloroparvula*, and *Picocystis* (previously described as prasinophyte clade VIIA and VIIB and VIIC, respectively). A previous study found that Chloropicophyceae were better represented in warm offshore waters (Dos Santos et al., 2017a). However, little information is available about how environmental variables influence the distribution of Chlorophyta. A survey from coastal to offshore waters in a subtropical continental shelf system would thus be helpful in understanding their distribution patterns.

Although global surveys of eukaryotic composition have been carried out, such as in Ocean Sampling date (OSD) and Tara Oceans (Logares et al., 2018), relatively few sampling sites have been located in the subtropical Northwestern Pacific. Previous research reported that Mamiellophyceae were dominant in coastal waters, while Chloropicophyceae dominated in offshore waters (Tragin et al., 2016; Dos Santos et al., 2017a). The East China Sea (ECS) is one of the largest continental marginal seas in the northwest Pacific Ocean. The coastal region is influenced by the Changjiang (Yangtze) River discharge, while the offshore region is influenced by oligotrophic Kuroshio Water (Chen, 1996; Gong et al., 1996). Our study area was located in the northwestern Pacific Ocean and comprised a coastal-offshore gradient across a large continental shelf region in the ECS. We used 18S rRNA gene metabarcoding to study chlorophyte community composition in surface and DCM layers during summer 2019, and examined how this composition varied from coastal to offshore regions within these layers.

METHODS

Sample Collection and Processing

Grid sampling was conducted in the East China Sea (ECS) at a total of 30 stations in July, 2019 (**Figure 1**). Surface water (4-6 m at 30 stations) and DCM water (15-85 m at 20 stations) were sampled. Seawater was collected using Go-Flo bottles mounted on a CTD rosette (Sea-Bird Electronics, USA). Ten liters of seawater was prefiltered using a 200 μm nylon mesh, and then processed with size-fractions (20-200 μm, 3-20 μm and 0.2-3 μm). For DNA collection, 20 μm pore size was collected on 90 mm-diameter nylon membranes (Millipore) while 3 μm- and 0.2 μm- pore sizes were collected on 142 mm-diameter polycarbonate membranes (Millipore). The filters were immediately preserved in liquid nitrogen and transferred and stored at -80°C until DNA extraction. In this study, chlorophyte composition was studied exclusively in pico-sized fractions (0.2-3 μm) due to the greater number of reads after subsampling.

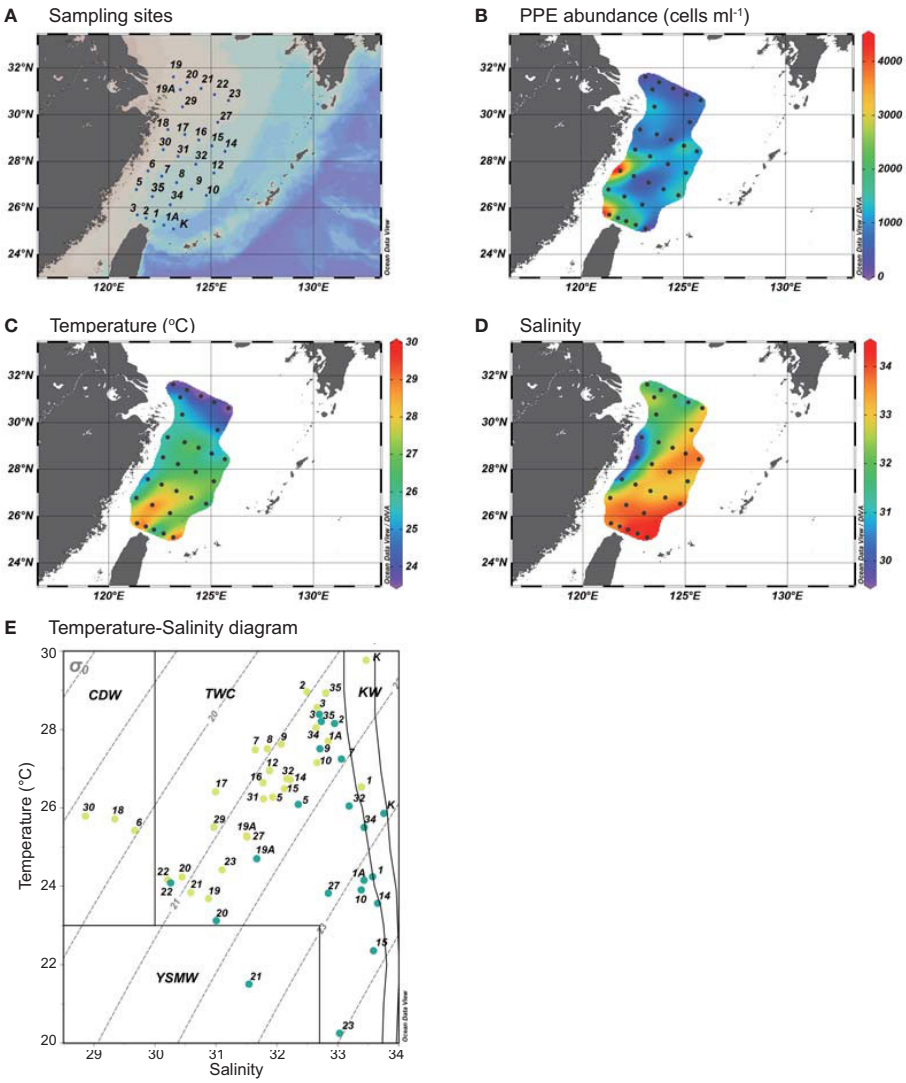

FIGURE 1 | **(A)** Maps show the sampling stations. **(B)** The distribution of photosynthetic picoeukaryotes (PPEs, cells ml^{-1}) **(C)** temperature (°C) and **(D)** salinity of surface water during July, 2019. **(E)** The Temperature-Salinity (T-S) diagram shows the water types as defined by Gong et al., 1996. The yellow and turquoise circles represent the surface water and DCM water, respectively. Dotted lines represent density (kg m^{-3}). CDW, Changjiang Diluted Water; KW, Kuroshio Water; TWC, Taiwan Warm Current; YSMW, Yellow Sea Mixed Water.

Environmental Parameters

Temperature and salinity were measured using a CTD profiler. The concentrations of ammonium, nitrite, nitrate, phosphate and silicate were measured according to standard methods used in a previous study (Gong et al., 2000). To measure chlorophyll *a* concentration, 1 L of seawater was filtered through 47-mm-diameter GF/F filters and then stored at -20°C until analysis. The chlorophyll on the filters was extracted with 90% acetone and determined with a fluorometer (Gong et al., 2000). Flow cytometry samples were preserved with paraformaldehyde (0.2% final concentration), and stored at -80°C. PPEs were quantified with chlorophyll red fluorescence using flow cytometry at an excitation wavelength of 488 nm (CytoFLEX, Beckman Coulter).

18S Amplicon Sequencing

PCR conditions and methods of DNA extraction are described in Lin et al. (2021). Briefly, DNA was extracted using DNeasy PowerWater Kit (Qiagen) following the manufacturer's instructions. The V4 region of the 18S rRNA gene was amplified with the eukaryotic universal primer set TAReuk454FWD1 (5'-[illumina adaptor]- CCAGCASCYGCG GTAATTCC-3') and TAReukREV3 (5'- [illumina adaptor]- AC TTTCGTTCTTGATYRA-3') (Stoeck et al., 2010). Amplicon sequencing was carried out on an Illumina MiSeq platform (pair-end 2 × 300 bp). The primers in raw paired-end reads were trimmed with Cutadapt (Martin, 2011), and the reads were analyzed using DADA2 pipeline (Callahan et al., 2016). The taxonomic annotation was carried out in accordance with PR2

version 4.12.0 database, resulting in 8 taxonomic levels: Kingdom, Supergroup, Division, Class, Order, Family, Genus and Species. DADA 2 infers exact amplicon sequence variants (ASVs) instead of operational taxonomic units (OTUs) to obtain an overall taxonomic composition for all samples (**Supplemental File 1**).

Analysis of Chlorophyte Communities

Chlorophyte ASVs were selected from the eukaryotic ASV table produced by DADA2 under Division level of "Chlorophyta" (**Supplemental File 2**). Subsequently, 400 chlorophyte ASVs were selected randomly and subsampled 100 times to avoid sequencing depth variations (Yeh et al., 2015). Four out of 50 samples with <400 chlorophyte reads were excluded from further analysis. We conducted multivariate and statistical analysis on the subsampled data. R package phyloseq was used to calculate the Chao1 and Shannon diversity indices. Chlorophyte composition was then clustered based on Bray-Curtis dissimilarity, used the Ward.D2 clustering method. Canonical correlation analysis (CCA) was then carried out to investigate the relationships between environmental variables and the 20 most abundant chlorophyte ASVs. To explore the relationships between niche distribution and environmental variables in each ASV, we performed a generalized additive model (GAM) to evaluate the 10 most abundant chlorophyte ASVs using a mgvc package. Prior to GAM modelling, ASV reads were natural log transformed. All statistical analyses were done with R 3.6.1.

To study the phylogenetic relationships in Chloropicophyceae and Mamiellophyceae, the 15 most abundant ASVs in each class were used to analyze the V4 region of 18S rRNA gene (**Figure S1**, **S2**). One ASV, *O. tauri*, was placed in *Ostreococcus* clade E based on phylogenetic analysis (**Figure S1**). The taxonomic annotation of this ASV was then updated throughout the manuscript. Raw amplicon data with three size fractions have been deposited in the NCBI Sequence Read Archive under the BioProject number: PRJNA738614. Samples of size 0.2-3 μm (library_ID contains F002) from surface and DCM waters (library_ID contains -S & -D) were analyzed in this BioProject.

RESULTS

Hydrographic Conditions in the ECS in July, 2019

During the study period, temperature in the ECS increased north to south, varying from 23.6°C to 29.7°C in the surface layer and from 20.3°C to 28.3°C in the DCM layer (**Figure 1**, **S3**, **S4**). The maximum temperature was observed in oligotrophic Kuroshio Water (St. K). Salinity increased from northwest to southeast, ranging from 29.8 to 34.4 at the surface and from 31.3 to 34.8 in the DCM layer (**Figure 1**, **S3**, **S4**). Using a definition of water types (Gong et al., 1996), most sampling sites were influenced by the oligotrophic Taiwan Warm Current (TWC, temperature >23°C and salinity >31) (**Figure 1E**). In addition, southern offshore waters (Sts. K and 1) were influenced by Kuroshio Water (KW). A topography-induced upwelling of colder saline water caused by the westward subsurface intrusion of Kuroshio water was observed at St. 1 (**Figures 1C, D**). The northern ECS (St. 21) was influenced by eutrophic Yellow Sea Mixing Water (YSMW) with high phosphate concentrations (**Figure S3**). The freshest water appeared in the central coastal region of the ECS (Sts. 30, 18 and 6; **Figure 1**), defined as Changjiang Diluted Water (CDW) (Gong et al., 1996), which was located further south of the Changjiang river mouth during the sampling period. The average PPE abundance was 1.1 x 10^3 cells ml^{-1} in the ECS with a maximum of 4,180 cells ml^{-1} on the central coast at St. 6 (**Figure 1**).

The Overall Composition of Small Eukaryotes (0.2-3 μm)

Following DADA2 pipeline, a total of 2,933,769 eukaryotic reads and 8,249 ASVs were obtained from 30 surface water samples and 20 DCM samples. After removing Opisthokonta reads, the major supergroups comprised Alveolata, Stramenopiles, Archaeplastida, Rhizaria etc. Rhizaria showed a higher amplicon contribution in the DCM than in the surface layer (12% vs 4%, **Figure S5**). We simplified PPEs into Orchrophyta, Chlorophyta, Haptophyta and Cryptophyta. Chlorophyta contributed a higher percentage of total PPE reads in DCM than in the surface layer (51% vs 40%, **Figure S5**), and were important components among pico-size PPEs. Overall, the amplicon of chlorophyta accounted for ~6% of total eukaryotic reads and 3% of total ASVs (196,467 reads and 189 ASVs prior to subsampling). The samples with low chlorophyte reads (<400 reads) were located in the northern ECS, where the temperature-salinity conditions were similar to those in Yellow Sea Mixing Water (**Figure 1E**). The following samples were excluded from further analysis: St. 20 (surface & DCM), St. 21 (DCM), St. 22 (surface).

Chlorophyte Composition

After subsampling, Mamiellophyceae (42%) and Chloropicophyceae (41%) contributed similar read numbers in the surface water layer. Mamiellophyceae contributed slightly higher reads in the DCM layer at the class level (67% in DCM layer, **Figures 2A, B**). At the genus level, *Chloropicon* (32%) and *Chloroparvula* (10%) were more important in surface water whereas *Bathycoccus* (28%) and *Ostreococcus* (22%) were more important in DCM water (**Figures 2C, D**). *Micromonas* reads were similar in both layers. With respect to genetic diversity, among *Mamiellophyceae, Micromonas* comprised 11 ASVs while *Bathycoccus* and *Ostreococcus* comprised 3 ASVs. Chloropicophyceae showed greater diversity than Mamiellophyceae on 18S V4 region, with *Chloropicon* and *Chloroparvula* comprising 16 and 22 ASVs, respectively. Apart from Mamiellophyceae and Chloropicophyceae, other chlorophyte classes included Palmophyllophyceae, prasinophyte clades V and IX, Pyramimonadales, and Trebouxiophyceae (**Figure 2**). The most abundant chlorophyte ASVs in this study, after subsampling, included *Bathycoccus prasinos* (ASV_11), *Chloropicon roscoffensis* (ASV_8),

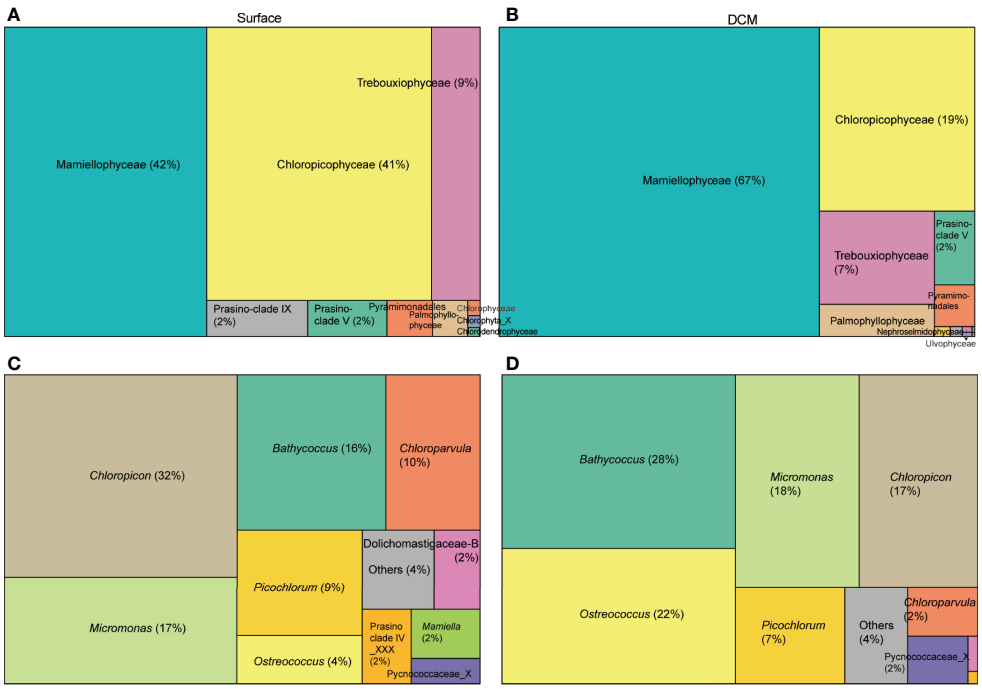

FIGURE 2 | Treemaps show chlorophyte community composition in the **(A, C)** surface layer and **(B, D)** DCM layer at **(A, B)** class level and **(C, D)** genus level in PR2. The area of each taxonomic group is proportional to the number of reads after subsampling.

Micromonas commoda clade A1(ASV_10) and *Ostreococcus* clade B (ASV_13) (**Figure 3**).

Chlorophyte Diversity

The result of DADA2 pipeline produced a total of 189 chlorophyte ASVs, of which 156 ASVs were exclusively from the surface layer, 74 ASVs were exclusively from the DCM, and 41 ASVs were found in both layers. Prior to further analysis, subsampling was conducted to correct for variations in read numbers between samples. The Chao1 and Shannon indices were significantly higher in the surface layer than in the DCM ($P < 0.01$, **Figure 4A**). For surface water, the maximum Shannon index occurred in KW water (St. K). Both Chao1 and Shannon were at a minimum in the central ECS, in coastal water defined as CDW (St. 6) (**Figure 4**). Where the amplicon of *Picochlorum* sp. (ASV_31) among Trebouxiophyceae overwhelmingly dominated chlorophyte reads (~90%), it occurred alongside maximum chlorophyll *a* concentration and PPE abundance (chlorophyll *a*: 1.48 mg m^{-3} and PPEs: 4,180 cells ml^{-1}, **Figures 1**, **S3**; **Supplemental File 3**). Other eukaryotic reads at St. 6 were dominated by Syndiniales in dinoflagellate (**Supplemental File 1**). *Picochlorum* might therefore be major contributors to chlorophyll *a* concentration and PPE abundance in our study.

Chlorophyte Composition and Hydrographic Environments

To examine chlorophyte composition, we created a Bray-Curtis dissimilarity matrix and grouped samples based on hierarchical clustering (Ward.D2). The composition varied along the coastal-offshore gradient, and also with vertical depth in offshore samples. Based on geographic and vertical characteristics, four clusters were identified and named as follows: surface water (n=17), DCM water (n=15), coastal water (n=11) and Kuroshio Water (n=3) (**Figure 5**).

The Surface Water Cluster

Most of the samples came from surface water, except for those at St. 10 in DCM water (**Figure 5**). The samples in this cluster were broadly distributed over the ECS, with Chloropicophyceae and Mamiellophyceae together contributing a large proportion of total chlorophyte reads (**Figure 6**). Dolichomastigale (Mamiellophyceae) was slightly more abundant in this cluster than in other clusters.

The DCM Cluster

This comprised mostly offshore DCM samples (**Figure 5**), with the addition of three surface samples, one an upwelling sample and the other two from the northern ESC. Mamiellophyceae accounted for ~80% of total chlorophyte reads in this cluster (**Figure 6**), with *B. prasinos* (ASV_11) and *Ostreococcus* clade B (ASV_13) being the most abundant. Pyramimonadales were more abundant here than in other clusters (**Figure 5**).

The Coastal-Water Cluster

This comprised 8 surface samples and 3 DCM samples at Sts. 3, 5, and 35 from the coastal region where depths of DCM layers

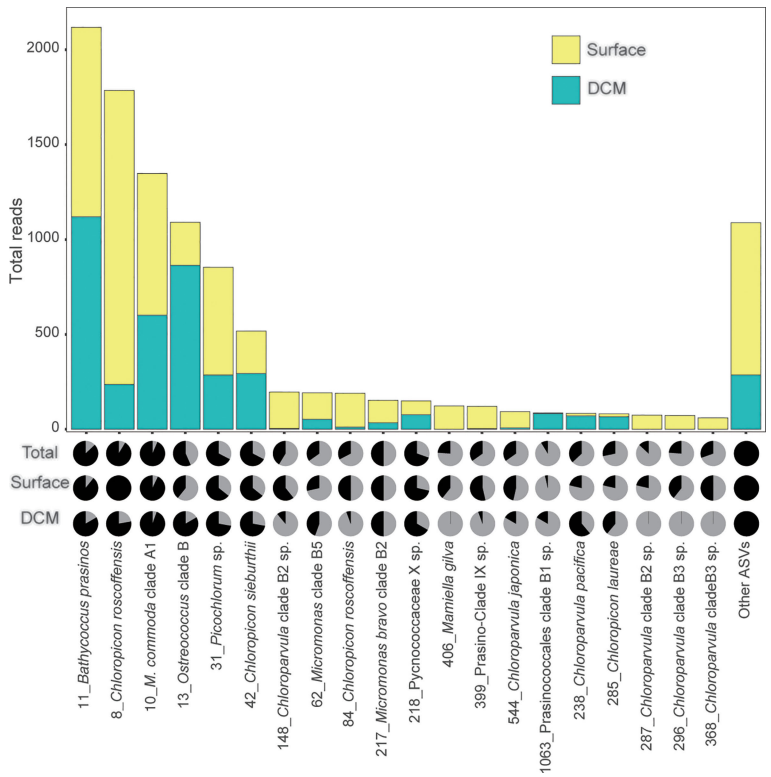

FIGURE 3 | Rank-abundance for the 20 most abundant chlorophyte ASVs generated from the DNA of 0.2-3 μm size-fraction from the surface and DCM samples in the ECS, with a minimum of 400 reads subsampled 100 times. Surface subsamples (28 samples) are shown in yellow, while DCM subsamples (18 samples) are shown in turquoise. The pie charts show the reads prior to subsampling. The upper, middle and lower pie charts represent total (50 samples), surface (30 samples), and DCM (20 samples) samples respectively. The numbers next to the taxonomic annotations indicate the ASV.

were shallow (<30 m, **Figure S6**). The DCM samples were from the southwestern ECS. Mamiellophyceae was dominant, contributing ~50% of chlorophyte reads (**Figure 6**). The important ASVs in this cluster were *M. commoda* clade A1 (ASV_10), *C. roscoffensis* (ASV_8) and *Picochlorum* sp. (ASV_31) (**Figure 5C**).

The Kuroshio Cluster

This consisted of just three samples from the southeastern ECS, one surface sample (St. K) and two DCM samples (Sts. 1 and 9). St. K was characterized as typical Kuroshio water using Gong et al. (1996). Upwelling at St.1 was caused by the subsurface invasion of Kuroshio water. As a result, the chlorophyte composition in the DCM layer at St. 1 resembled that in Kuroshio water. The Temperature-Salinity diagram indicated that St. 9 belongs to TWC (**Figure 1E**). However, the water is characterized as high temperature and high salinity, and is therefore similar to Kuroshio water. The chlorophytes in this cluster were dominated by Chloropicophyceae, particularly the genus *Chloroparvula*. We also observed a higher amplicon number of prasinophyte clades V and IX, Palmophyllophyceae and Chlorodendrophyceae. Dolichomastigales and Mamiellales (Mamiellophyceae) were less important here than in other clusters (**Figure 5**).

We further examined and compared the environmental variables among these four clusters using One-way ANOVA and *post-hoc* Turkey HSD. There were significant differences in temperature, ammonium, phosphate and silicate (**Figure S7**). Also, we found that chlorophyte clustering patterns were more consistent with nutrient concentrations than with temperature, and that Kuroshio water samples clustered more closely with surface samples, while DCM samples clustered more closely with coastal samples (**Figure 5**).

DISCUSSION

The Overall Distribution of Chlorophytes

There has been extensive discussion on the relative advantages of choosing operational taxonomic units (OTU) and ASVs from DADA2 (Xu et al., 2022). Generally, OTU is a consensus sequence which can represent different sequences from multiple species through clustering, typically using 97-99% similarity. In contrast, an ASV represents an exact sequence by running an error model to extract true sequences. The ASV method has been broadly accepted for chlorophytes due to their relatively low genetic diversity (Tragin and Vaulot, 2019). The operational taxonomic units (OTU) method is unable to

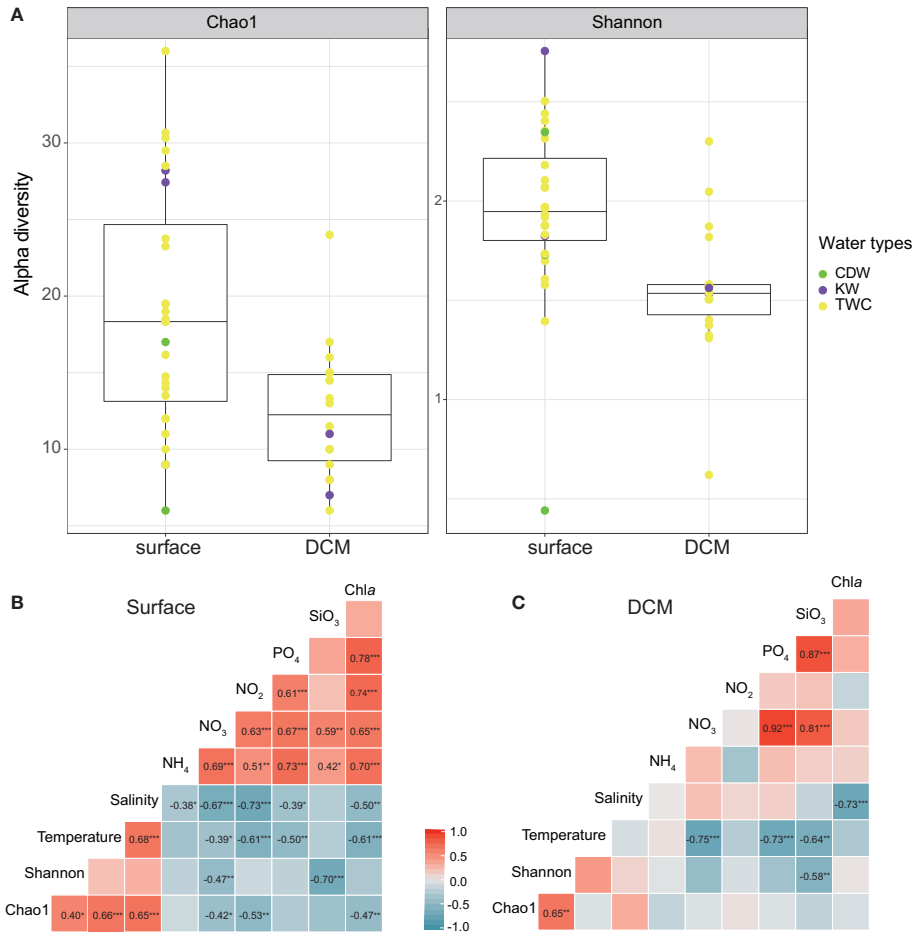

FIGURE 4 | **(A)** Comparison of chlorophyte diversity in surface and DCM samples. Subsampling data was calculated using Chao1 and Shannon diversity, and is represented as box-whisker-plots with median values as horizontal lines, and interquartile ranges as boxes with whiskers extending to 1.5 times the interquartile range. The definition of water masses is based on Gong et al., 1996. Green indicates the Chiang Dilution Water (CDW); purple indicates the Kuroshio Water (KW); and yellow indicates the Taiwan Warm Current (TWC). **(B, C)** Pearson's correlation coefficients between diversity indices and environmental variables for **(B)** surface data and **(C)** DCM data. The colors indicate the strength of positive (red) and negative (blue) coefficients, and *, ** and *** indicate statistical significance at $P < 0.05$, <0.01 and 0.001, respectively.

discriminate the distinct *Ostreococcus* clades, even with a 99% identity threshold (Tragin and Vaulot, 2019). Thus, ASV is better than OTU at representing the taxonomic groups for chlorophytes. The distribution patterns of certain chlorophyte groups have already been demonstrated, for example that Mamiellophyceae is dominant in coastal water whereas Chloropicophyceae and prasinophytes clade IX are dominant in oceanic waters as well as in tropical regions (Tragin et al., 2016; Dos Santos et al., 2017a; Charvet et al., 2021). This study conducted grid sampling at surface and DCM layers on the continental shelf region to provide a high-resolution examination of chlorophyte community variation. Previous studies have not discussed the distribution of chlorophytes with respect to nutrient concentration. Our results show that the DCM layer was dominated by Mamiellophyceae, indicating that nutrient levels play an important role in determining their composition. In surface water, the dominance of both Mamiellophyceae and Chloropicophyceae might result from the mixing of coastal and Kuroshio waters on the continental shelf, with chlorophyte composition thus reflecting the hydrographic dynamics (**Figure 6**). Some ASVs in surface water resulted from the mixing of coastal and offshore water, e.g., *C. roscoffensis* (ASV_8), *C. sieburthii* (ASV_42) and *Picochlorum*. On the other hand, some ASVs appeared exclusively in the transitional mixing water and occupied a narrow ecological niche, e.g., some ASVs in Dolichomastigaceae-B sp, *Chloroparvula* clades B2 and B3 and prasinophyte clade IX (**Figure 5**). Collectively, chlorophyte composition reflects the hydrographic conditions and can thus be used as a model for studying the dynamics of water masses in the ECS shelf system.

Since the first Chloropicophyceae genome of *Chloropicon primus* has been published, the differentiation of ecological niches between Mamiellophyceae and Chloropicophyceae

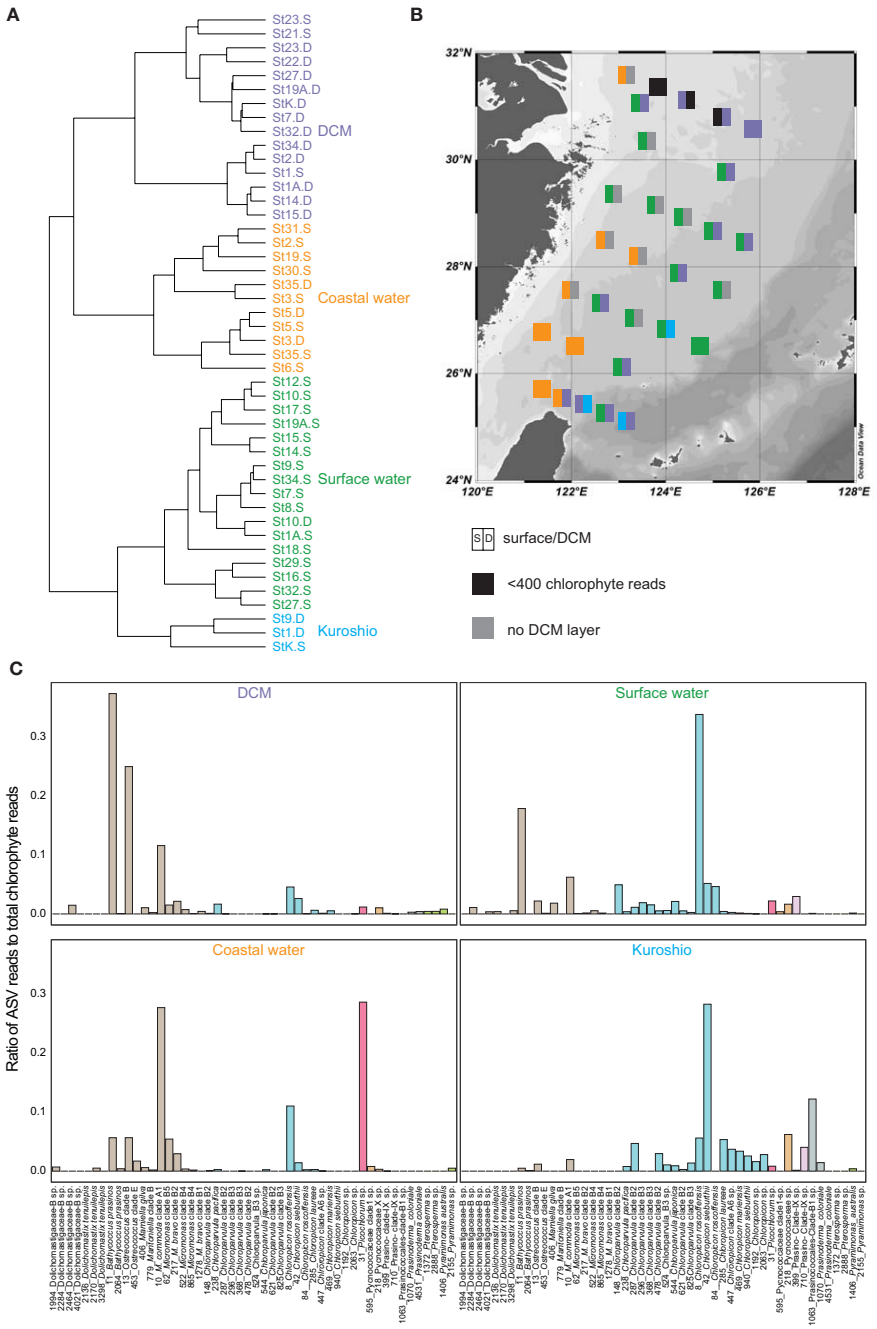

FIGURE 5 | **(A)** The four clusters generated by hierarchical clustering of chlorophyte ASV table after subsampling. **(B)** The colors in squares represent the clusters from **(A)**. The left and right half of each square represent surface and DCM samples, respectively. Black shows chlorophyte reads < 400 in amplicon data while grey indicates that no DCM layer was observed at that station. **(C)** The average fraction of total chlorophyte amplicon in each cluster for the 50 most abundant chlorophyte ASVs. The colors indicate the distinct classes and the numbers next to the taxonomic annotations indicate the ASV.

might be indicated by genomic features (Lemieux et al., 2019). Using genomic prediction, it has been hypothesized that *C. primus* might be a bacterivore since it possesses WASH complex and DNaes II genes which are associated with phagocytic capacity (Bock et al., 2021). Although *C. primus* was not an important species in the ECS, there is still little genomic information about other species in Chloropicophyceae. Additionally, visible vacuoles were observed in *Chloropicon* during ultrastructure inspection (Dos Santos et al., 2017b), but did not appear in either

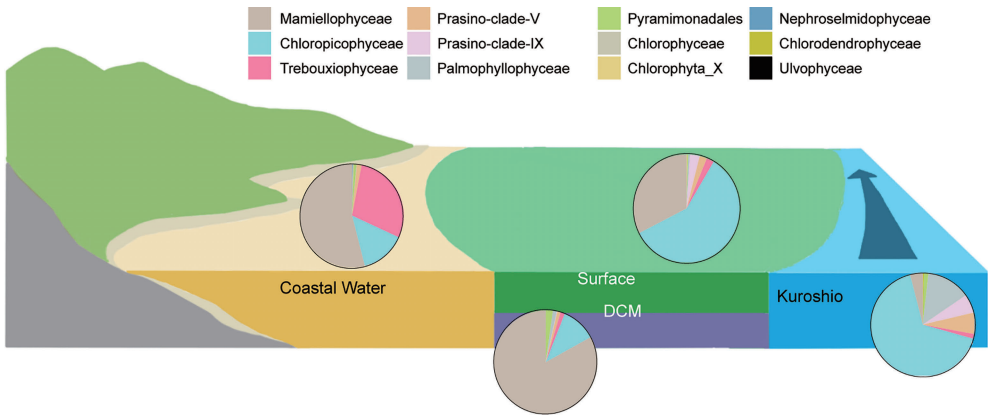

FIGURE 6 | A schematic showing currents and chlorophyte composition for each cluster in **Figure 5**. Earthy yellow and gray blue indicate the coastal currents and offshore Kuroshio water, respectively. These two waters mixed on the shelf region over the East China Sea. The pie charts represent the average proportion of total chlorophyte composition in each cluster (in **Figure 5**) at the "class" level in PR2.

Bathycoccus or *Ostreococcus* (Limardo et al., 2017). These differences in genomic and physiological features might lead to Mamiellophyceae and Chloropicophyceae occupying different ecological niches.

Mamiellophyceae Community Composition

M. commoda clade A1, *M. bravo* clade B2 and *Micromonas* clade B5 appeared more frequently in the ECS (**Figure 3**), while *Micromonas* clade B3 and *M. polaris* were absent. A previous study indicated that *Micromonas* clade B3 and *M. polaris* were important in polar regions (Tragin and Vaulot, 2019). *M. commoda* clade A2 seems to be adapted to cold water at high latitudes (Tragin and Vaulot, 2019), but rarely appeared in the ECS, being present only in the northern Yellow Sea Mixing Water (St. 23). It was absent in a survey of the subtropical coastal water of Taiwan (Lin et al., 2017). *M. commoda* clade A1 was common in our study, and was detected in most of the samples. GAM prediction indicated that *M. commoda* clade A1 increased with temperature >25°C (**Supplemental File 4**). It has been suggested that *Micromonas* clade B5 is a warm-adapted clade as it is found in the warm waters of the South China Sea and off the Philippines and Taiwan (Wu et al., 2014; Lin et al., 2017; dela Peña et al., 2021). Our results support this, and in our study *Micromonas* clade B5 peaked at the edge of coastal water where salinity was 32-34 and silicate concentration was ~ 2 μM. (St. 5; **Supplemental File 4**). It occurred a little more frequently in the DCM layer than in surface samples, although the total number of reads was the same in the two layers (**Figure 3**). Overall, *Micromonas* clade B5 preferred nutrient-rich water.

Ostreococcus clade B was abundant in the ECS during the summer (**Figure 3**) and was an important component of chlorophyte composition in DCM water, appearing alongside *Bathycoccus prasinos* (**Figure 5**). It has been described as an oceanic ecotype, associated with low-light and deeper environments (Rodríguez et al., 2005; Demir-Hilton et al., 2011). *Ostreococcus* clade E, which has two bases different from clade B in 18S V4 region, was established more recently (Tragin and Vaulot, 2019). In our study, *Ostreococcus* clade E had low reads and peaked in more coastal waters (**Figure 5**; **Supplemental File 2**), implying a preference for eutrophic warm waters. On the other hand, *O. lucimarinus* belonged to a coastal ecotype (Simmons et al., 2016), and its related reads were detected only at St. 31 (**Supplemental File 2**). Although its sequences were found to be abundant in the Kuroshio front located off southeastern Japan (Clayton et al., 2017), it was almost absent in the ECS during the summer. *Bathycoccus prasinos* reads were negatively correlated with temperature in the ECS (**Supplemental File 4**), but there were no clear ecotypes based on 18S V4 amplicon data. *Mamiella gilva* comprised 6 ASVs here and the dominant ASV showed a preference for coastal surface water and was absent in the DCM layer (**Figures 3** and **Supplemental File 4**). *Mantoniella* clade B was detected only in two offshore samples, represented by one ASV (**Supplemental File 2**). Overall, the majority of Mamiellophyceae ASVs seem to be more important in eutrophic waters.

Chloropicophyceae Community Composition

In marine environments, Chloropicophyceae comprises two main genera, *Chloropicon* and *Chloroparvula*, both of which were extensively represented in the ECS samples (**Figures 3** and **Supplemental File 4**). Notably, the phylogeny in the *Chloropicon* species indicated by using V4 region of the 18S rRNA was inconsistent with the taxonomic annotation with DADA2 (**Figure S2**). Therefore, we have pointed out the ASV number among *Chloropicon*. So far, little is known about their distribution, particularly in tropical-subtropical regions. However, Dos Santos et al. (2017a) have reported that global surveys indicate Chloropicophyceae has a preference for oligotrophic and warm water. In our study, all clades in *Chloropicon* and *Chloroparvula* were detected, apart from *Chloropicon maureeniae*. *C. roscoffensis* (ASV_8) was the most abundant ASV (**Figure 3**) having a wide distribution over

the continental shelf. In the ECS, *C. roscoffensis* reads correlated negatively with silicate concentration (**Supplemental File 4**). However, it was abundant in the Changjiang estuary at low nutrient levels. The next most abundant ASV among Chloropicophyceae was *C. sieburthii* (ASV_42), which was slightly more abundant in the DCM layer than in the surface layer (**Figure 3**), and was the most important ASV in KW (**Figure 5**). Different *C. roscoffensis* ASVs exhibited different distribution patterns. ASV_8 occurred in a wide range of salinity, whereas ASV_84 appeared only where salinity was >32. *Chloroparvula* clades B2 and B3 exhibited similar distribution patterns and were found mainly in the central offshore area of the ECS. Both clade B2 and clade B3 were absent in the DCM layer (**Figure 3**), and generally peaked in low chlorophyll *a* water (**Supplemental File 4**). A previous study indicated that *Chloropicon* and *Chloroparvula* were important in offshore water (Dos Santos et al., 2017a). Our results were consistent with that study as the majority of Chloropicophyceae ASVs were negatively correlated with silicate concentration and inhabited more oligotrophic surface water than other chlorophyte ASVs (**Supplemental File 4**).

Chlorophyte Composition and Environmental Variables

In this study, we observed that chlorophyte diversity varied with silicate concentrations in both surface and DCM layers. The results of CCA showed that salinity, temperature and silicate concentration had the greatest influence on the distribution of abundant chlorophyte ASVs (**Figure 7**). Since chlorophytes seldom uptake silicate directly, their diversity and communities might be influenced by the diatom. The pico- and nano-sized diatoms have been found to be important in many marine systems recently (Leblanc et al., 2018; Charvet et al., 2021), including in this study (**Figure S5**), and they might compete with the chlorophyte communities due to their similar size range. On the other hand, there may be other factors which covary with silicate concentration, e.g., turbidity. Turbidity and irradiance can significantly influence phytoplankton composition in estuarine systems since chlorophytes are photosynthetic organisms (Gameiro et al., 2011; Charvet et al., 2014). However, the sampling design of our study made it difficult to evaluate the impact of light. Nevertheless, we observed that certain chlorophyte ASVs showed a preference for specific water layers. *Ostreococcus* clade B, for example, was more significant in the DCM layer than at the surface based on read numbers (**Figure 3**), and its cultures were generally isolated in deep water. A previous study demonstrated that the growth rate of different *Ostreococcus* strains varied with light intensity (Rodríguez et al., 2005; Six et al., 2008). Additionally, some ASVs were nearly absent in DCM water, for example, *Chloroparvular* clades B2 and B3, *Mamiella gilva* and prasinophyte clade IX (**Figure 3**). On the other hand, an ASV in Pycnococcaceae (belonging to prasinophyte clade V, ASV_218), contributed moderate reads in both surface and DCM layers, and occurred frequently in the ECS summer, particular in KW (**Figures 3**, **5**). According to BLAST search, this ASV is identical to a *Pycnococcus provasolii* sequence whose genome has been reported to encode unique dual photoreceptors of orange/far-red and blue to enable adaptation to a broad range of ocean depths (Makita et al., 2021). Overall, our data illustrated that chlorophyte communities seem to vary with terrestrial inputs of silicate concentration and salinity.

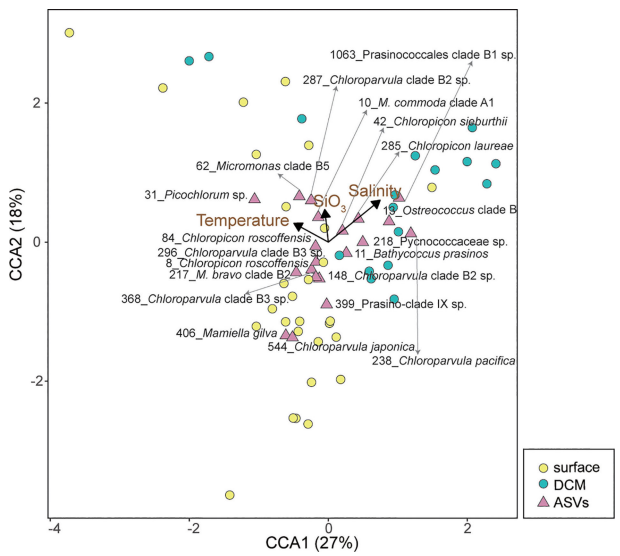

FIGURE 7 | Canonical correspondence analysis (CCA) biplot illustrating the relationship between environmental variables and abundant chlorophyte ASVs. The arrows show significant environmental variables, the pink triangles represent the 20 most abundant chlorophyte ASVs, and the yellow and turquoise circles represent the surface and DCM samples, respectively. The CCA results show that salinity, temperature and silicate concentration are the most significant factors driving the chlorophyte communities. The numbers next to the taxonomic annotations indicate the ASV.

In the ECS, chlorophyte communities showed higher diversity in the surface layer than in the DCM layer. Chao1 and Shannon diversity indices were significantly correlated with nutrient concentrations, particular in surface water (**Figure 4B**). Temperature and salinity also play important roles in surface water (**Figure 4B**), with the Chao1 index being positively correlated with both temperature ($r = 0.66$, $P < 0.001$) and salinity ($r = 0.65$, $P < 0.001$) (**Figure 4B**). In the DCM layer, the diversity indices were related to few environmental factors, suggesting there might be other factors determining chlorophyte diversity, such as predators and irradiance levels (Charvet et al., 2014; Yang et al., 2018). Our data shows that the diversity indices were negatively correlated with silicate concentrations, indicating that terrestrial input to the ECS plays an important role in shaping chlorophyte diversity. A previous study indicated that sudden pulses of high nutrients can increase the growth of a single species, and thus decrease community diversity (Spatharis et al., 2007). In our study, the minimum chlorophyte diversity was observed in the coastal water (St. 6) of the central ECS dominated by *Picochlorum* (90% of total chlorophyte reads). We also observed high PPE abundance and chlorophyll *a* concentration. With global warming, *Picochlorum* might lead

to harmful algal blooms since GAM indicates its reads correlate positively with temperature, ammonium and silicate concentrations (**Supplemental File 4**). Foflonker et al. (2015) have indicated that *Picochlorum* can acclimate to a wide range of salinity and that excessive ammonium enhances their growth, and that these ecological features can be explained by genomic data. A recent study indicated that *Picochlorum* can be grazers on picoplankton (Pang et al., 2022). More than that, some taxa among chlorophytes have been reported as potential mixotrophs, e.g., *Chloropicon*, *Dolichomastix*, *Micromonas*, *Nephroselmis*, *Pterosperma* and *Pyramimonas* (McKie-Krisberg and Sanders, 2014; Bock et al., 2021). These pico-size chlorophytes are also predators on picoplankton, which might result in an increase in the efficiency of energy flows (Ward and Follows, 2016). On the other hand, being an important prey for protists and zooplankton (Orsi et al., 2018; Ma et al., 2021), their composition will influence the community diversity of predators (Yang et al., 2018). Therefore, as primary producers and consumers, chlorophyte community structure plays a key role in determining the efficiency of energy and nutrient flows in microbial food webs.

CONCLUSION

This study examined the community composition of chlorophytes in surface and DCM layers in a subtropical North Pacific Ocean. Mamiellophyceae was dominant in relatively nutrient-rich coastal water and in the DCM layer, whereas Chloropicophyceae was dominant in Kuroshio waters. We demonstrated that the mixing of coastal and offshore waters played an important role in determining the chlorophyte composition in the shelf surface water of the ECS. Additionally, river input to continental systems enables certain chlorophyte species to outcompete others, lowering the overall chlorophyte diversity. For the purposes of coastal management, and to maintain a healthy ecosystem, it is therefore important to monitor excess nutrient input into the continental system.

DATA AVAILABILITY STATEMENT

The datasets presented in this study can be found in online repositories. The names of the repository/repositories and accession number(s) can be found below: NCBI [accession: PRJNA738614].

AUTHOR CONTRIBUTIONS

The study was conceived by K-PC; C-TH collected the field samples and performed the molecular laboratory work; Y-CL, C-PC, W-TC, X-BC contributed to data analysis; G-CG provided the chemical parameters; Y-CL wrote the draft of the manuscript; and all authors contributed substantially to revisions.

FUNDING

This research was supported by the Ministry of Science and Technology, Taiwan (MOST 107-2611-M-019 -002 -MY3 and MOST 109-2611-M- 019 -018).

ACKNOWLEDGMENTS

We thank Wenxue Wu for the constructive comments on manuscript and helping with revision, the captain and crew of the R/V Ocean Researcher I for sampling, Yu-Ting Tseng for organizing the environmental parameter data, and Naqwa Li for the artwork.

SUPPLEMENTARY MATERIAL

The Supplementary Material for this article can be found online at: https://www.frontiersin.org/articles/10.3389/fmars.2022.865081/full#supplementary-material

Supplementary Figure 1 | Phylogenetic relationship of Mamiellophyceae based on V4 region of 18S rRNA gene. The 15 most abundant Mamiellophyceae ASVs in this study are shown in bold. This tree was constructed using an alignment of 333 bp under PhyML. Bootstrap values are shown when > 0.7.

Supplementary Figure 2 | Phylogenetic relationship of Chloropicophyceae based on V4 region of 18S rRNA gene. The 15 most abundant Chloropicophyceae ASVs in this study are shown in bold. This tree was constructed using an alignment of 351 bp under PhyML. Bootstrap values are shown when > 0.7.

Supplementary Figure 3 | The distribution of temperature (°C), salinity, chlorophyll *a* (mg m^{-3}) and nutrient concentrations (nitrite, nitrate, phosphate, silicate and ammonium, μM) in surface water in the ECS during 2019 July.

Supplementary Figure 4 | The distribution of temperature (°C), salinity, chlorophyll *a* (mg m^{-3}) and nutrient concentrations (nitrite, nitrate, phosphate, silicate and ammonium, μM) in the DCM layer in the ECS during 2019 July.

Supplementary Figure 5 | Treemaps showing the (A, B) community composition of eukaryotes at supergroup level and (C, D) photosynthetic eukaryotes at division level in the (A, C) surface layer and (B, D) DCM layer. The area of each taxonomic group is proportional to the number of reads calculated from the average of the samples.

Supplementary Figure 6 | The vertical distribution of chlorophyll *a* concentrations (mg m^{-3}) along east-west transects from the north to south in the ECS during 2019 July.

Supplementary Figure 7 | Distribution patterns of temperature (°C), salinity, nitrite, nitrate, phosphate and silicate concentrations (μM) in the DCM, surface, coastal water and Kuroshio clusters. Boxplots show the median values as horizontal lines, and interquartile ranges as boxes with whiskers extending to 1.5 times the interquartile range. Dots indicate the outliers. Significant differences between these clusters shown with ANOVA (*$P < 0.05$) and the clusters sharing different letters are significantly different according to Tukey's *post hoc* test.

Supplemental File 1 | 18S ASV table produced from 30 surface samples and 20 DCM samples from the ECS continental shelf in 2019 July.

Supplemental File 2 | Chlorophyte ASV table filtered from 18S ASV table with a criterion of "Chlorophyta" in "division" level under PR2 then subsampled 400 reads for 100× in each sample.

Supplemental File 3 | Environmental data.

Supplemental file 4 | Predicted niche (colored lines) of the 20 most abundant chlorophyte ASVs with respect to temperature (°C), salinity, chlorophyll *a* concentration (mg m^{-3}) nutrients (ammonium, nitrate, nitrite, phosphate and silicate [μM]). This prediction was based on generalized additive models (GAM) and grey shading represents 95% confidence. Note that ASV reads were transferred by Ln (reads+1).

REFERENCES

Balzano, S., Marie, D., Gourvil, P., and Vaulot, D. (2012). Composition of the Summer Photosynthetic Pico and Nanoplankton Communities in the Beaufort Sea Assessed by T-RFLP and Sequences of the 18S rRNA Gene From Flow Cytometry Sorted Samples. *ISME J.* 6, 1480–1498. doi: 10.1038/ismej.2011.213

Bock, N. A., Charvet, S., Burns, J., Gyaltshen, Y., Rozenberg, A., Duhamel, S., et al. (2021). Experimental Identification and *In Silico* Prediction of Bacterivory in Green Algae. *ISME J.* 15, 1987–2000. doi: 10.1038/s41396-021-00899-w

Callahan, B. J., Mcmurdie, P. J., Rosen, M. J., Han, A. W., Johnson, A. J. A., and Holmes, S. P. (2016). DADA2: High-Resolution Sample Inference From Illumina Amplicon Data. *Nat. Methods* 13, 581. doi: 10.1038/nmeth.3869

Caron, D. A. (2016). Mixotrophy Stirs Up Our Understanding of Marine Food Webs. *Proc. Natl. Acad. Sci.* 113, 2806–2808. doi: 10.1073/pnas.1600718113

Charvet, S., Kim, E., Subramaniam, A., Montoya, J., and Duhamel, S. (2021). Small Pigmented Eukaryote Assemblages of the Western Tropical North Atlantic Around the Amazon River Plume During Spring Discharge. *Sci. Rep.* 11, 1–14. doi: 10.1038/s41598-021-95676-2

Charvet, S., Vincent, W. F., and Lovejoy, C. (2014). Effects of Light and Prey Availability on Arctic Freshwater Protist Communities Examined by High-Throughput DNA and RNA Sequencing. *FEMS Microbiol. Ecol.* 88, 550–564. doi: 10.1111/1574-6941.12324

Chen, C. (1996). The Kuroshio Intermediate Water is the Major Source of Nutrients on the East China Sea Continental Shelf. *Oceanol. Acta* 19, 523–527.

Clayton, S., Lin, Y. C., Follows, M. J., and Worden, A. Z. (2017). Co-Existence of Distinct *Ostreococcus* Ecotypes at an Oceanic Front. *Limnol. Oceanography* 62, 75–88. doi: 10.1002/lno.10373

Collado-Fabbri, S., Vaulot, D., and Ulloa, O. (2011). Structure and Seasonal Dynamics of the Eukaryotic Picophytoplankton Community in a Wind-Driven Coastal Upwelling Ecosystem. *Limnol. Oceanography* 56, 2334–2346. doi: 10.4319/lo.2011.56.6.2334

dela Peña, L. B. R. O., Tejada, A. J. P., Quijano, J. B., Alonzo, K. H., Gernato, E. G., Caril, A., et al. (2021). Diversity of Marine Eukaryotic Picophytoplankton Communities With Emphasis on Mamiellophyceae in Northwestern Philippines. *Philippine J. Sci.* 150, 27–42.

Demir-Hilton, E., Sudek, S., Cuvelier, M. L., Gentemann, C. L., Zehr, J. P., and Worden, A. Z. (2011). Global Distribution Patterns of Distinct Clades of the Photosynthetic Picoeukaryote *Ostreococcus*. *ISME J.* 5, 1095–1107. doi: 10.1038/ismej.2010.209

Derelle, E., Ferraz, C., Rombauts, S., Rouze, P., Worden, A., Robbens, S., et al. (2006). Genome Analysis of the Smallest Free-Living Eukaryote *Ostreococcus Tauri* Unveils Many Unique Features. *Proc. Natl. Acad. Sci.* 103, 11647. doi: 10.1073/pnas.0604795103

de Vargas, C., Audic, S., Henry, N., Decelle, J., Mahé, F., Logares, R., et al. (2015). Eukaryotic Plankton Diversity in the Sunlit Ocean. *Science* 348, 1261605. doi: 10.1126/science.1261605

Dos Santos, A. L., Gourvil, P., Tragin, M., Noël, M.-H., Decelle, J., Romac, S., et al. (2017a). Diversity and Oceanic Distribution of Prasinophytes Clade VII, the Dominant Group of Green Algae in Oceanic Waters. *ISME J.* 11, 512–528. doi: 10.1038/ismej.2016.120

Dos Santos, A. L., Pollina, T., Gourvil, P., Corre, E., Marie, D., Garrido, J. L., et al. (2017b). Chloropicophyceae, a New Class of Picophytoplanktonic Prasinophytes. *Sci. Rep.* 7, 14019. doi: 10.1038/s41598-017-12412-5

Field, C. B., Behrenfeld, M. J., Randerson, J. T., and Falkowski, P. (1998). Primary Production of the Biosphere: Integrating Terrestrial and Oceanic Components. *Science* 281, 237–240. doi: 10.1126/science.281.5374.237

Foflonker, F., Price, D. C., Qiu, H., Palenik, B., Wang, S., and Bhattacharya, D. (2015). Genome of the Halotolerant Green Alga *Picochlorum* Sp. Reveals Strategies for Thriving Under Fluctuating Environmental Conditions. *Environ. Microbiol.* 17, 412–426. doi: 10.1111/1462-2920.12541

Foulon, E., Jalabert, F., Cariou, T., Massana, R., and Simon, N. (2008). Ecological Niche Partitioning in the Picoplanktonic Green Alga *Micromonas Pusilla*: Evidence From Environmental Surveys Using Phylogenetic Probes. *Environ. Microbiol.* 10, 2433. doi: 10.1111/j.1462-2920.2008.01673.x

Gameiro, C., Zwolinski, J., and Brotas, V. (2011). Light Control on Phytoplankton Production in a Shallow and Turbid Estuarine System. *Hydrobiologia* 669, 249–263. doi: 10.1007/s10750-011-0695-3

Gong, G.-C., Chen, Y.-L. L., and Liu, K.-K. (1996). Chemical Hydrography and Chlorophyll *a* Distribution in the East China Sea in Summer: Implications in Nutrient Dynamics. *Continental Shelf Res.* 16, 1561–1590. doi: 10.1016/0278-4343(96)00005-2

Gong, G.-C., Shiah, F.-K., Liu, K.-K., Wen, Y.-H., and Liang, M.-H. (2000). Spatial and Temporal Variation of Chlorophyll *a*, Primary Productivity and Chemical Hydrography in the Southern East China Sea. *Continental Shelf Res.* 20, 411–436. doi: 10.1016/S0278-4343(99)00079-5

Guillou, L., Eikrem, W., Chrétiennot-Dinet, M. J., Le Gall, F., Massana, R., Romari, K., et al. (2004). Diversity of Picoplanktonic Prasinophytes Assessed by Direct Nuclear SSU rDNA Sequencing of Environmental Samples and Novel Isolates Retrieved From Oceanic and Coastal Marine Ecosystems. *Protist* 155, 193–214. doi: 10.1078/143446104774199592

Leblanc, K., Queguiner, B., Diaz, F., Cornet, V., Michel-Rodriguez, M., Durrieu De Madron, X., et al. (2018). Nanoplanktonic Diatoms Are Globally Overlooked But Play a Role in Spring Blooms and Carbon Export. *Nat. Commun.* 9, 1–12. doi: 10.1038/s41467-018-03376-9

Lemieux, C., Turmel, M., Otis, C., and Pombert, J.-F. (2019). A Streamlined and Predominantly Diploid Genome in the Tiny Marine Green Alga *Chloropicon Primus*. *Nat. Commun.* 10, 4061. doi: 10.1038/s41467-019-12014-x

Li, W. (1995). Composition of Ultraphytoplankton in the Central North Atlantic. *Mar. Ecol. Prog. Ser.* 122, 1–8. doi: 10.3354/meps122001

Limardo, A. J., Sudek, S., Choi, C. J., Poirier, C., Rii, Y. M., Blum, M., et al. (2017). Quantitative Biogeography of Picoprasinophytes Establishes Ecotype Distributions and Significant Contributions to Marine Phytoplankton. *Environ. Microbiol.* 19, 3219–3234. doi: 10.1111/1462-2920.13812

Lin, Y. C., Chung, C. C., Chen, L. Y., Gong, G. C., Huang, C. Y., and Chiang, K. P. (2017). Community Composition of Photosynthetic Picoeukaryotes in a Subtropical Coastal Ecosystem, With Particular Emphasis on *Micromonas*. *J. Eukaryotic Microbiol.* 64, 349–359. doi: 10.1111/jeu.12370

Lin, Y. C., Chin, C. P., Yang, J. W., Chiang, K. P., Hsieh, C. H., Gong, G. C., et al. (2022). How Communities of Marine Stramenopiles Varied with Environmental and Biological Variables in the Subtropical Northwestern Pacific Ocean. *Microb. Ecol.* 83, 916–928. doi: 10.1007/s00248-021-01788-7

Logares, R., Deutschmann, I. M., Giner, C. R., Krabberød, A. K., Schmidt, T. S., Rubinat-Ripoll, L., et al. (2018). Different Processes Shape Prokaryotic and Picoeukaryotic Assemblages in the Sunlit Ocean Microbiome. *bioRxiv* 374298. doi: 10.1101/374298

Lovejoy, C., Vincent, W. F., Bonilla, S., Roy, S., Martineau, M. J., Terrado, R., et al. (2007). Distribution, Phylogeny, and Growth of Cold-Adapted Picoprasinophytes in Arctic Seas. *J. Phycol.* 43, 78–89. doi: 10.1111/j.1529-8817.2006.00310.x

Ma, X., Jacoby, C. A., and Johnson, K. B. (2021). Grazing by the Copepod *Parvocalanus Crassirostris* on *Picochlorum* Sp. At Harmful Bloom Densities and the Role of Article Size. *Front. Mar. Sci.* 8, 664154. doi: 10.3389/fmars.2021.664154

Makita, Y., Suzuki, S., Fushimi, K., Shimada, S., Suehisa, A., Hirata, M., et al. (2021). Identification of a Dual Orange/Far-Red and Blue Light Photoreceptor From an Oceanic Green Picoplankton. *Nat. Commun.* 12, 1–12. doi: 10.1038/s41467-021-23741-5

Martin, M. (2011). Cutadapt Removes Adapter Sequences From High-Throughput Sequencing Reads. *EMBnet* 17, 10–12. doi: 10.14806/ej.17.1.200

McKie-Krisberg, Z. M., and Sanders, R. W. (2014). Phagotrophy by the Picoeukaryotic Green Alga *Micromonas*: Implications for Arctic Oceans. *ISME J.* 8, 1953–1961. doi: 10.1038/ismej.2014.16

Moreau, H., Verhelst, B., Couloux, A., Derelle, E., Rombauts, S., Grimsley, N., et al. (2012). Gene Functionalities and Genome Structure in *Bathycoccus Prasinos* Reflect Cellular Specializations at the Base of the Green Lineage. *Genome Biol.* 13, R74. doi: 10.1186/gb-2012-13-8-r74

Not, F., Latasa, M., Marie, D., Cariou, T., Vaulot, D., and Simon, N. (2004). A Single Species, *Micromonas Pusilla* (Prasinophyceae), Dominates the Eukaryotic Picoplankton in the Western English Channel. *Appl. Environ. Microbiol.* 70, 4064–4072. doi: 10.1128/AEM.70.7.4064-4072.2004

Not, F., Massana, R., Latasa, M., Marie, D., Colson, C., Eikrem, W., et al. (2005). Late Summer Community Composition and Abundance of Photosynthetic Picoeukaryotes in Norwegian and Barents Seas. *Limnol. Oceanography* 50, 1677–1686. doi: 10.4319/lo.2005.50.5.1677

Orsi, W. D., Wilken, S., Del Campo, J., Heger, T., James, E., Richards, T. A., et al. (2018). Identifying Protist Consumers of Photosynthetic Picoeukaryotes in the Surface Ocean Using Stable Isotope Probing. *Environ. Microbiol.* 20, 815–827. doi: 10.1111/1462-2920.14018

Pang, M., Liu, K., and Liu, H. (2022). Evidence for Mixotrophy in Pico-Chlorophytes From a New *Picochlorum* (Trebouxiophyceae) Strain. *J. Phycol.* 58, 80–91. doi: 10.1111/jpy.13218

Rodríguez, F., Derelle, E., Guillou, L., Le Gall, F., Vaulot, D., and Moreau, H. (2005). Ecotype Diversity in the Marine Picoeukaryote *Ostreococcus* (Chlorophyta, Prasinophyceae). *Environ. Microbiol.* 7, 853–859. doi: 10.1111/j.1462-2920.2005.00758.x

Sieburth, J. M., Smetacek, V., and Lenz, J. (1978). Pelagic Ecosystem Structure: Heterotrophic Compartments of the Plankton and Their Relationship to Plankton Size Fractions. *Limnol. Oceanography* 23, 1256–1263. doi: 10.4319/lo.1978.23.6.1256

Simmons, M. P., Sudek, S., Monier, A., Limardo, A. J., Jimenez, V., Perle, C. R., et al. (2016). Abundance and Biogeography of Picoprasinophyte Ecotypes and Other Phytoplankton in the Eastern North Pacific Ocean. *Appl. Environ. Microbiol.* 82, 1693–1705. doi: 10.1128/AEM.02730-15

Six, C., Finkel, Z. V., Rodriguez, F., Marie, D., Partensky, F., and Campbell, D. A. (2008). Contrasting Photoacclimation Costs in Ecotypes of the Marine Eukaryotic Picoplankter *Ostreococcus*. *Limnol. Oceanography* 53, 255–265. doi: 10.4319/lo.2008.53.1.0255

Spatharis, S., Tsirtsis, G., Danielidis, D. B., Do Chi, T., and Mouillot, D. (2007). Effects of Pulsed Nutrient Inputs on Phytoplankton Assemblage Structure and Blooms in an Enclosed Coastal Area. *Estuarine Coastal. Shelf Sci.* 73, 807–815. doi: 10.1016/j.ecss.2007.03.016

Stoeck, T., Bass, D., Nebel, M., Christen, R., Jones, M. D., Breiner, H. W., et al. (2010). Multiple Marker Parallel Tag Environmental DNA Sequencing Reveals a Highly Complex Eukaryotic Community in Marine Anoxic Water. *Mol. Ecol.* 19, 21–31. doi: 10.1111/j.1365-294X.2009.04480.x

Tragin, M., Lopes Dos Santos, A., Christen, R., and Vaulot, D. (2016). Diversity and Ecology of Green Microalgae in Marine Systems: An Overview Based on 18S rRNA Gene Sequences. *Perspect. Phycol.* 3, 141–154. doi: 10.1127/pip/2016/0059

Tragin, M., and Vaulot, D. (2019). Novel Diversity Within Marine Mamiellophyceae (Chlorophyta) Unveiled by Metabarcoding. *Sci. Rep.* 9, 5190. doi: 10.1038/s41598-019-41680-6

Vannier, T., Leconte, J., Seeleuthner, Y., Mondy, S., Pelletier, E., Aury, J.-M., et al. (2016). Survey of the Green Picoalga *Bathycoccus* Genomes in the Global Ocean. *Sci. Rep.* 6, 37900. doi: 10.1038/srep37900

Ward, B. A., and Follows, M. J. (2016). Marine Mixotrophy Increases Trophic Transfer Efficiency, Mean Organism Size, and Vertical Carbon Flux. *Proc. Natl. Acad. Sci.* 113, 2958–2963. doi: 10.1073/pnas.1517118113

Worden, A., Lee, J., Mock, T., Rouze, P., Simmons, M., Aerts, A., et al. (2009). Green Evolution and Dynamic Adaptations Revealed by Genomes of the Marine Picoeukaryotes *Micromonas*. *Science* 324, 268. doi: 10.1126/science.1167222

Worden, A. Z., Nolan, J. K., and Palenik, B. (2004). Assessing the Dynamics and Ecology of Marine Picophytoplankton: The Importance of the Eukaryotic Component. *Limnol. Oceanography* 49, 168–179. doi: 10.4319/lo.2004.49.1.0168

Wu, W., Huang, B., Liao, Y., and Sun, P. (2014). Picoeukaryotic Diversity and Distribution in the Subtropical-Tropical South China Sea. *FEMS Microbiol. Ecol.* 89, 563–579. doi: 10.1111/1574-6941.12357

Xu, J., Han, J., Su, H., Zhu, C., Quan, Z., Wu, L., et al. (2022). Diversity Patterns of Protists are Highly Affected by Methods Disentangling Biological Variants: A Case Study in Oligotrich (s.L.) Ciliates. *Microorganisms* 10, 913. doi: 10.3390/microorganisms10050913

Yang, J. W., Wu, W., Chung, C.-C., Chiang, K.-P., Gong, G.-C., and Hsieh, C.-H. (2018). Predator and Prey Biodiversity Relationship and Its Consequences on Marine Ecosystem Functioning—Interplay Between Nanoflagellates and Bacterioplankton. *ISME J.* 12, 1532–1542. doi: 10.1038/s41396-018-0111-3

Yeh, Y. C., Peres-Neto, P. R., Huang, S. W., Lai, Y. C., Tu, C. Y., Shiah, F. K., et al. (2015). Determinism of Bacterial Metacommunity Dynamics in the Southern East China Sea Varies Depending on Hydrography. *Ecography* 38, 198–212. doi: 10.1111/ecog.00986

Conflict of Interest: The authors declare that the research was conducted in the absence of any commercial or financial relationships that could be construed as a potential conflict of interest.

Publisher's Note: All claims expressed in this article are solely those of the authors and do not necessarily represent those of their affiliated organizations, or those of the publisher, the editors and the reviewers. Any product that may be evaluated in this article, or claim that may be made by its manufacturer, is not guaranteed or endorsed by the publisher.

Copyright © 2022 Lin, Chin, Chen, Huang, Gong, Chiang and Chen. This is an open-access article distributed under the terms of the Creative Commons Attribution License (CC BY). The use, distribution or reproduction in other forums is permitted, provided the original author(s) and the copyright owner(s) are credited and that the original publication in this journal is cited, in accordance with accepted academic practice. No use, distribution or reproduction is permitted which does not comply with these terms.

frontiers | Frontiers in Marine Science

TYPE Original Research
PUBLISHED 09 August 2022
DOI 10.3389/fmars.2022.872557

Check for updates

OPEN ACCESS

EDITED BY
Toru Kobari,
Kagoshima University, Japan

REVIEWED BY
Michael Thomas Montgomery,
Texas A&M University Corpus Christi, United States
Hideki Fukuda,
The University of Tokyo, Japan

*CORRESPONDENCE
Anastasia N. Drozdova
adrozdova@ocean.ru

SPECIALTY SECTION
This article was submitted to Coastal Ocean Processes, a section of the journal Frontiers in Marine Science

RECEIVED 09 February 2022
ACCEPTED 22 July 2022
PUBLISHED 09 August 2022

CITATION
Drozdova AN, Krylov IN, Nedospasov AA, Arashkevich EG and Labutin TA (2022) Fluorescent signatures of autochthonous dissolved organic matter production in Siberian shelf seas.
Front. Mar. Sci. 9:872557.
doi: 10.3389/fmars.2022.872557

COPYRIGHT
© 2022 Drozdova, Krylov, Nedospasov, Arashkevich and Labutin. This is an open-access article distributed under the terms of the Creative Commons Attribution License (CC BY). The use, distribution or reproduction in other forums is permitted, provided the original author(s) and the copyright owner(s) are credited and that the original publication in this journal is cited, in accordance with accepted academic practice. No use, distribution or reproduction is permitted which does not comply with these terms.

Fluorescent signatures of autochthonous dissolved organic matter production in Siberian shelf seas

Anastasia N. Drozdova[1]*, Ivan N. Krylov[2], Andrey A. Nedospasov[1], Elena G. Arashkevich[1] and Timur A. Labutin[2]

[1]Shirshov Institute of Oceanology, Russian Academy of Sciences, Moscow, Russia, [2]Department of Chemistry, Lomonosov Moscow State University, Moscow, Russia

The East Siberian Sea is an area of high biogeochemical activity caused by multiple factors, such as an influence of river runoff, Atlantic, and Pacific waters, formation and melting of sea ice, and internal circulation. Extensive amounts of carbon are accumulated in sub-sea permafrost within the Arctic shelf in East Siberia. Thawing permafrost and resulting microbial decomposition of frozen carbon pool is a potential feedback process affected global climate dynamics. Several studies of dissolved organic carbon (DOC) distribution in the East Siberian Sea have demonstrated untypical for other Arctic shelf seas pronounced non-conservative DOC behavior. Using seawater samples from the 69th cruise of R/V *Akademik Mstislav Keldysh* conducted in the Laptev and East Siberian seas in September 2017, this study examines the distribution of fluorescent dissolved organic matter (FDOM) along the shelf-crossing transects including the areas affected by the Khatanga, Lena, Indigirka, and Kolyma river runoff. The set of 137 excitation-emission matrices (EEMs), analyzed with Parallel Factor analysis (PARAFAC), was described by a 4-component model demonstrating Tucker's congruence coefficient above the 0.95 threshold. Spectral characteristics of the resulting components allowed identifying them as well-known humic-like A and C, protein-like B/T, and marine humic-like M fluorophores. Component C1 (A fluorophore) showed a good correlation with salinity for different river plume influenced regions. As well as chromophoric DOM (CDOM) absorption, it can be used as marker of input of terrestrial DOM to the Arctic Ocean. A distinctive feature of the East Siberian Sea shelf waters in comparison with the Laptev Sea is the higher content of the C2 and C4 components, exhibiting protein-like and marine humic-like fluorescence. Component C3 (C fluorophore) which is usually identified as terrestrial-derived material, was found to be produced locally on the East Siberian Sea shelf and in the continental slope region of the Khatanga transect. Destruction of dead algae cells, production of marine biota and dissolved organic matter (DOM) reworking are considered as possible autochthonous FDOM sources in the Siberian shelf seas.

KEYWORDS

Arctic shelf, FDOM, river plume, East Siberian Sea, Laptev Sea, PARAFAC decomposition

Introduction

Dissolved organic matter represents an important component of oceanic carbon cycle (Stein et al., 2004; Vetrov and Romankevich, 2010) that influences on ecosystem functioning controlling microbial food webs and through many physical and biogeochemical processes, such as sunlight absorption, photo- and biodegradation, flocculation, formation of metal-organic complexes, etc. (Jaffé et al., 2008). In the context of serious concerns about global climate change, DOM is considered as a key component of the biological pump - a series of processes through which CO_2 is fixed as organic matter by photosynthesis and then transferred to the ocean interior by means of particulate organic matter (POM) sedimentation and transport of DOM to deep waters. This mechanism includes the transformation of the labile DOM of euphotic zone into recalcitrant DOM through the microbial carbon pump (Jiao et al., 2010). Since the production, transformation, and consumption of organic matter in aquatic ecosystems is strongly dependent on DOM composition (D'Andrilli et al., 2019), DOM quality represent a perspective indicator of biogeochemical trends related to climate change and anthropogenic stress (Wohlers et al., 2009; Savun-Hekimoğlu and Gazioğlu, 2021).

Recently, optical techniques have become widespread in the study of CDOM. It is related to multiple factors, such as i) fast and simple preparation of seawater for laboratory analysis, ii) developments of *in situ* fluorescence sensors (Carstea et al., 2020), iii) development of algorithms for CDOM and DOC determination with the use of satellite remote sensing (Griffin et al., 2018), iv) incubation experiments aimed to investigate production of FDOM by marine biota, i.e. (Castillo et al., 2010; Romera-Castillo et al., 2011), v) development PARAFAC decomposition of EEMs (Bro, 1997) and OpenFluor spectral library (Murphy et al., 2014), vi) investigation of the influence anthropogenic factors, such as oil pollution (Gonnelli et al., 2016) and microplastics (Chen et al., 2018) on the fluorescence spectra of natural waters. Consequently, in the study of Jaffé et al. (2008) the importance of absorbance and fluorescence measurements as a part of long-term ecological research and monitoring programs were emphasized, since they may provide an advanced understanding of organic matter dynamics in aquatic ecosystems.

In the recent decades, the Arctic is undergoing significant transformations induced by climate change. Carbon fluxes and sources of DOM are changing due to increase in the discharge of major rivers terminating in the Arctic, reduce the ice cover, and melting of permafrost (Box et al., 2019 and references therein). Sub-sea permafrost thaw and formation of taliks result in release of organic matter of glacial origin or modern production from ancient organic matter (Anderson et al., 2011; Vonk et al., 2012). The resulting microbial decomposition of frozen carbon pool is a potential feedback process affected global climate dynamics accelerating global warming (Schuur et al., 2008). The Siberian shelf seas, in particular the East Siberian Sea, are considered to be the most affected by the above changes.

Although a lot of studies were devoted to the CDOM optical properties in the Arctic Ocean, see, for example (Stedmon et al., 2011; Gonçalves-Araujo et al., 2015; Mann et al., 2016), CDOM and especially FDOM of the East Siberian Sea shelf, remains one of the least investigated. In the paper of Mann et al. (2012) DOC concentration and the composition of CDOM across the hydrograph in Siberia's Kolyma River is discussed. Water sampling was performed in the vicinity of the Northeast Science Station near Cherskiy, Russia. The composition of DOM within the Kolyma basin was characterized using absorbance-derived measurements and fluorescence spectroscopy, including EEMs + PARAFAC analysis. The B, T, M, A, and C fluorophores according to Coble (Coble et al., 1998) were identified, and substantial losses of DOC occurring *via* biological and photochemical pathways were demonstrated. The study of Guéguen et al. (Guéguen et al., 2012) examined seawater FDOM outside the East Siberian Sea shelf north of 75°N at depths >100 m. Two protein-like (B, T) and three humic-like (A/C, M) components were identified by PARAFAC. High protein-like and terrestrial humic-like FDOM signals were most often associated with surface waters. Microbial/marine humic-like component was associated with the middle halocline at depth 50-200 m. It was suggested to be of Pacific origin. Another study of East Siberian Sea FDOM was performed recently by Chen et al. (2021) as a part of investigation of organic carbon release from the sediments of East Siberian subsea permafrost. The shelf (north of 73°N) and slope sites were examined. Six FDOM components, namely four humic-like and two protein-like, were identified from PARAFAC modeling. Strong signals of terrestrial humic-like FDOM in seawater and pore waters allowed suggesting the predominance of permafrost-derived DOM over the products of marine sediment mineralization. Marine/

microbial humic-like component was found to be more abundant in the seawaters on the slope sites (28-47%) compared to East Siberian shelf waters (8-16%).

This paper focuses on characterization of FDOM in East Siberian Sea waters influenced by Indigirka and Kolyma rivers in the end of the productive period when the finality of phytoplankton development was detected (Drits et al., 2019). It continues the investigation of East Siberian Sea DOM (Drozdova et al., 2021), that revealed high variability of seawater absorbance and DOC that cannot be described by conservative mixing often reported for the river-influenced Arctic coastal regions. Other areas under investigation are the western and central parts of the Laptev Sea influenced by the Khatanga and Lena river runoff. With respect to the East Siberian Sea, the Laptev Sea represents a contrasting example of a river-influenced shelf region where DOC was distributed conservatively. The study is based on excitation-emission matrices of seawater, sampled during the 69th cruise of R/V *Akademik Mstislav Keldysh* in September 2017. We analyze the distribution of PARAFAC components along the 4 cross-shelf transects to get a better understanding of DOM quality in the region.

Methods

Sampling

Water samples were collected during the 69th cruise of R/V *Akademik Mstislav Keldysh* in the Laptev and East Siberian seas in September 2017. We consider three shelf-crossing transects that include the areas influenced by the Khatanga, Indigirka and Kolyma runoff, as well as individual sampling sites in the region affected by the Lena River runoff. The location of the sampling stations is given in Figure 1. Water depth of the stations varied from 13 m in the inner East Siberian shelf (station 5598) to 178 m at the northernmost station of the Khatanga transect (5634).

Water samples were taken using Niskin bottles of 5 L volume from near-surface, mid-water and bottom layers. Maximal sampling depth was 50 m. Additional discrete sampling depths, associated with boundaries of large gradients of temperature and salinity, were chosen on the basis of CTD profiles obtained with the SBE 911plus CTD probe (Drozdova et al., 2021). The CTD pressure, temperature and conductivity sensors were calibrated in 2015 by Sea-Bird (temperature accuracy 0.001°C, conductivity accuracy 0.0003 S/m and pressure accuracy 0.015% of full-scale range). All the samples were gravity-filtered through pre-combusted at 450°C Whatman GF/F glass fiber filters with nominal pore size of 0.7 µm directly after the sampling. A Sartorius 47 mm polycarbonate in-line filter holder was use for filtration. The filtrate was collected into the acid-cleaned 10 mL glass vials and stored under dark conditions at 4°C until further analysis.

EEM registration

Fluorescence measurements were performed with a Fluorat-02-Panorama spectrofluorometer (Lumex Instruments)

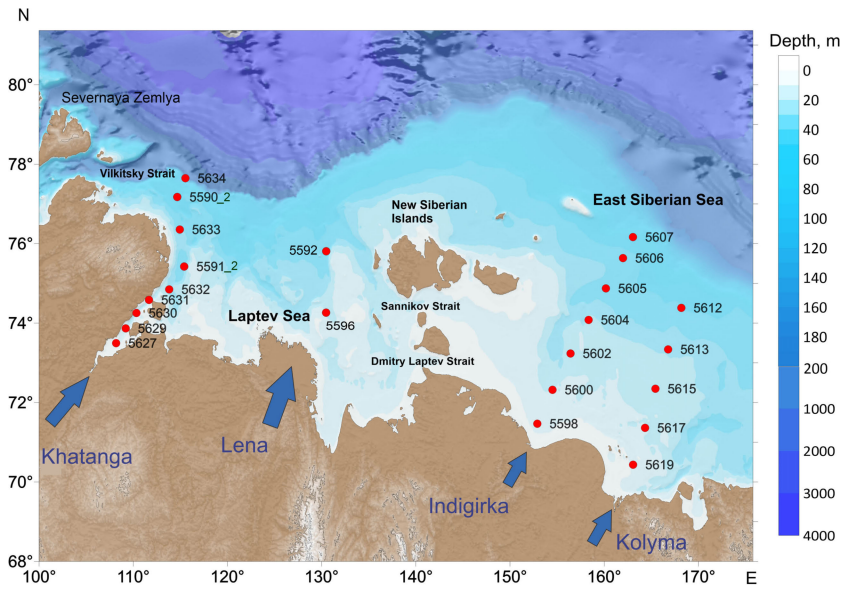

FIGURE 1
Sample site locations during the 69th cruise of the R/V *Akademik Mstislav Keldysh*.

equipped with a Xenon flash lamp as a light source, and a PMT as a detector of luminescence signals. A signal averaging over 20 flashes was applied in order to compensate instability of the flash lamp intensity. The accuracy of excitation and detection wavelength settings was ascertained on a basis of Xe atomic line position and estimated as ±1 nm, spectral resolution of monochromators was 5 nm (Drozdova et al., 2019). Emission spectra were recorded between 240 and 600 nm with a 2-nm increment, and the excitation wavelengths were recorded from 230 to 550 nm with a 5-nm increment. Fluorescence measurements were performed in 1 cm quartz cuvette. The inner-filter effect has been corrected using the measured absorbance spectra (Drozdova et al., 2019), in accordance with the following expression (Kothawala et al., 2013; Lakowicz, 2013):

$$I_{corr}(\lambda_{em},\lambda_{ex}) = I_{orig}(\lambda_{em},\lambda_{ex})10^{\frac{A(\lambda_{em})+A(\lambda_{ex})}{2l_{abs}}} ,$$

where I_{orig} (λ_{em} ,λ_{ex}) is the detected fluorescence intensity, I_{corr} (λ_{em} ,λ_{ex}) is the corrected fluorescence intensity, A(λ_{ex}) and A(λ_{em}) represent absorbances at the wavelength of excitation and emission, respectively, related to optical path length of l_{abs} .

PARAFAC analysis

The analysis was carried out using the R programming language and the Albatross package (Krylov et al., 2020) and its dependencies. Fluorescence signal is typically assumed to adhere to a trilinear model (Bro, 1997):

$$X_{i,j,k} = \sum A_{i,r}B_{j,r}C_{k,r}$$

In this formula, $X_{i,j,k}$ is the intensity of fluorescence of the k th sample, measured at i th emission wavelength and j th excitation wavelength, while the A , B , C matrices contain the emission spectra, excitation spectra and relative contributions of each fluorophore in the mixture. Excitation-emission matrices typically contain a scattering component that doesn't adhere to the PARAFAC model and must therefore be handled before performing the analysis. In this work, areas of each EEM corresponding to 1st and 2nd diffraction order Rayleigh and Raman scattering were interpolated using Whittaker smoothing (Eilers, 2003) with combined 1st and 2nd difference order penalty. Prior to performing the analysis, each EEM was scaled (Bro and Smilde, 2003) by its standard deviation to prevent extreme fluorescence intensity values from affecting the PARAFAC solution.

The PARAFAC model has been validated using the split-half approach, by repeatedly splitting the dataset in randomly-selected halves as it is described by us earlier (Krylov et al., 2020), performing PARAFAC on them and assessing the similarity of the resulting decompositions. The probable identities of the resulting PARAFAC components were determined by comparing their fluorescence and absorbance spectra with OpenFluor database (Murphy et al., 2014) with Tucker's congruence coefficient (TCC) set at a 95%.

Chlorophyll-a

For the measurement of chlorophyll-a (chl-a) concentration, water samples were collected with Niskin bottles at selected depths according to the CTD profile and the *in situ* fluorometer readings. 500 ml of water were filtered on GF/F filters. Extraction was carried out with 90% acetone in the dark at a temperature of +4°C for 24 hours. Chl-a concentration was measured fluorometrically in acetone extracts on a Trilogy Turner Designs fluorometer (USA) according to Holm-Hansen and Riemann (1978). The fluorometer was calibrated spectrophotometrically using pure chlorophyll-a (Sigma) as a standard.

Redundancy analysis

Redundancy analysis (RDA) (Rao, 1964) was performed using the R programming language, package "vegan", version 2.5.7. We explored the relationship between the PARAFAC components values and various metadata of our samples, including salinity, temperature, DOC, absorption coefficients at 350 nm ($a_{CDOM}(350)$) and spectroscopic indices given in Table 1.

Results

Study area

The Laptev and East Siberian seas represent the shallow (average water depths are ~50 m and 58 m) marginal seas of Siberian Shelf occupying 500×10^3 km^2 and 987×10^3 km^2, respectively (Jakobsson et al., 2004). They are covered by ice most of the year. Sea ice formation during the winter season and its melting in summer as well as spreading and transformation of river plumes has a major impact on physical and biogeochemical conditions of the East Siberian and Laptev seas (Dmitrenko et al., 2005; Savel'eva et al., 2008; Osadchiev et al., 2020).The spring flood occurs from the end of May to the beginning of July and constitutes 60%–90% of the riverine freshwater discharge (Raymond et al., 2007). The Laptev Sea receives large freshwater discharge from the Lena (590 km^3 yr^{-1}), Khatanga (105 km^3 yr^{-1}), Olenyok (36 km^3 yr^{-1}), and Yana (36 km^3 yr^{-1}) rivers. The East Siberian Sea is supplied by seawater from both the Atlantic and Pacific Oceans (Semiletov et al., 2005) and has a

TABLE 1 Spectroscopic indices for identification the sources of organic matter.

Index	Calculation	References
HIX	$\frac{\int_{435\ nm}^{480\ nm} Id\lambda_{em}}{\int_{300\ nm}^{345\ nm} Id\lambda_{em}},\ \lambda_{ex} = 254\ nm$	Zsolnay et al., 1999 Huguet et al., 2009
BIX	$\frac{I(\lambda_{em} = 380\ nm)}{I(\lambda_{em} = 430\ nm)},\ \lambda_{ex} = 310\ nm$	Huguet et al., 2009
S	Absorption spectral slope over 300-650 nm	Stedmon et al., 2000
$S_{275\text{-}295}$	Absorption spectral slope over 275-295 nm	Helms et al., 2008
S_R	$\frac{S_{275-295}}{S_{350-400}}$	Helms et al., 2008
SUVA	$\frac{A_{254}}{DOC}$	Weishaar et al., 2003
FI.McK	$\frac{I(\lambda_{em} = 450\ nm)}{I(\lambda_{em} = 500\ nm)},\ \lambda_{ex} = 370\ nm$	McKnight et al., 2001
FI.Cory	$\frac{I(\lambda_{em} = 470\ nm)}{I(\lambda_{em} = 520\ nm)},\ \lambda_{ex} = 370\ nm$	Cory et al., 2010
FrI	$\frac{I(\lambda_{em} = 380\ nm)}{\max I\ \lambda_{em} \in [420, 435]\ nm)},\ \lambda_{ex} = 310\ nm$	Wilson and Xenopoulos, 2009

substantial input of Kolyma (136 km^3 yr^{-1}) and Indigirka (61 km^3 yr^{-1}) river runoff providing about 75% of the total freshwaters discharge to the East Siberian Sea (Pavlov et al., 1994; Gordeev et al., 1996; Holmes et al., 2002; Osadchiev et al., 2020). The western region is dominated by input of terrestrial-derived material from the Laptev Sea (Alling et al., 2010).

Detailed description of the hydrography of the studied areas is given in previous studies (Osadchiev et al., 2020; Drozdova et al., 2021). Variations of salinity and temperature along the transect are shown in Figure 2. Shortly, the surface water temperature varied from 3°C in the Khatanga River estuary to −1°C near the continental slope. Deep waters were

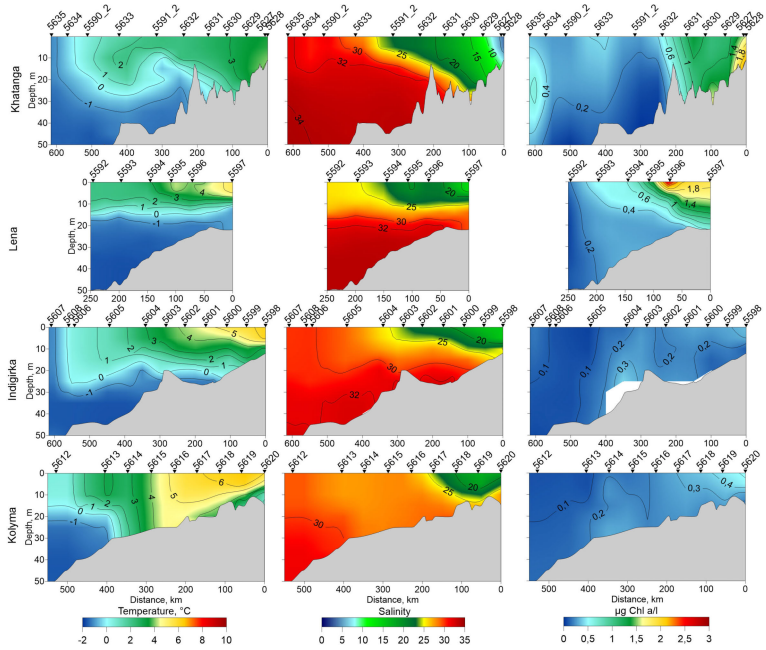

FIGURE 2
Distribution of temperature (left), salinity (middle) and chlorophyll-a (right) along the Khatanga (17-20 September), Lena (2-3 September), Indigirka (5-7 September) and Kolyma (8-9 September) transects.

characterized by temperatures below zero. Khatanga plume was weakly-stratified within the shallow inner part of the estuary (stations 5627–2629) due to intense tidal mixing in the Khatanga Gulf. Salinity along the Khatanga transect varied between 3.5 and 31.5 The surface water temperature at the Indigirka transect reached 6.2°C at the station 5598 closest to the Indigirka delta and decreased gradually to −1.4°C at station 5607 located near the ice edge. Negative temperatures of bottom water were typical for the inner shelf region (station 5601) at the 26 m depth. Low-salinity waters extended to a depth of 10–15 m. At the Kolyma transect, the surface water temperature on the inner shelf was 6.7°C (stations 5619 and 5620) and decreased to 0.5 at the northern station 5612. In the shelf area adjacent to the Kolyma and Indigirka deltas, the minimum salinities were 17 and 15, respectively. The maximum salinity values were recorded at the northernmost stations 5607 (30 and 32.5 at the surface and bottom, respectively) and 5612 (29.2 and 31.2). Potential temperature-salinity diagram (Figure 3) demonstrates that the shelf waters of the Laptev and East Siberian seas were formed by mixing the warm fresh waters supplied by rivers, Arctic (ArW), and cold intermediate (CIW) waters. In comparison with ArW, CIW are characterized by lower salinity values of 31.5 – 33.5. They were formed on the shelf during winter convection. Warm salt (salinity > 34.5) waters related to the admixture of Atlantic waters entering the Arctic Ocean (Guéguen et al., 2012; Oziel et al., 2016) were detected at the 100-300 m depth of the northern part of the Khanatga transect. These stations, however, are not considered in the present study.

To examine the lateral transport of water masses among the transects the latitudinal component of geostrophic current velocity was calculated on the basis of hydrological sounding data with the Ocean Data View software (Schlitzer, 2020), see Figure S1 of Supplementary materials. The reference velocity horizons were chosen to ensure zero velocities in the near-bottom zones. The Indigirka and Khatanga transects were characterized by low latitudinal component of geostrophic current velocity of 2 cm s^{-1} and below, directed mainly to the east. Weak currents (~ 0.5 cm s^{-1}) in the opposite direction were observed in the central parts of transects at the stations 5602 (Indigirka) and 5615 (Kolyma). The Laptev Sea showed higher

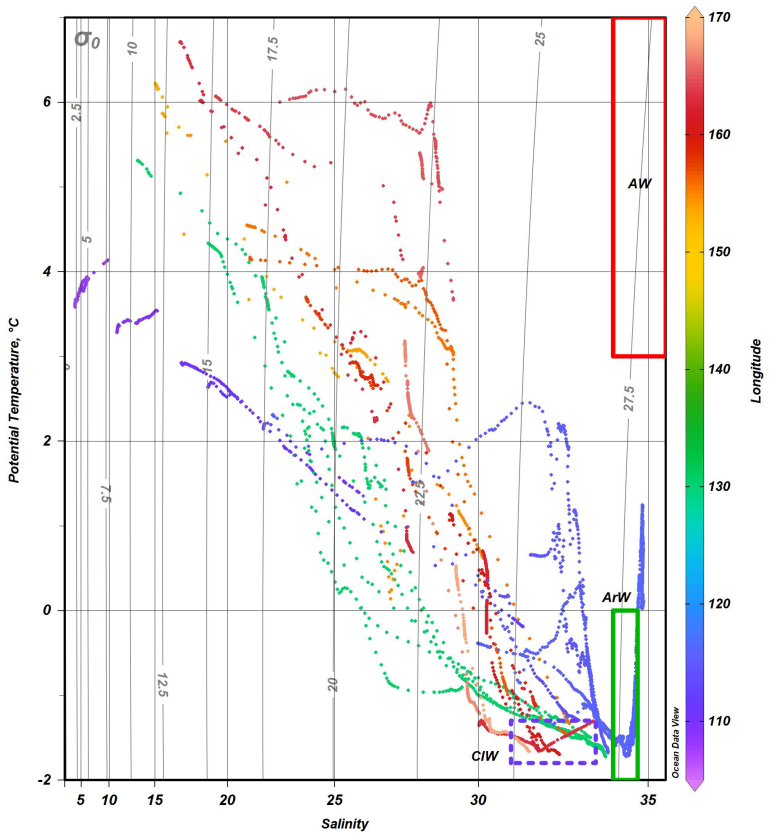

FIGURE 3
Potential temperature-salinity diagram over the shelf and slope regions of the Laptev and East Siberian seas. Blue dots correspond to Khatanga transect, green – Lena, orange – Indigirka, and red – Kolyma. Red and green rectangles correspond to Atlantic (AW) and Arctic (ArW) waters, respectively, in accordance with the water mass definition given in (Oziel et al., 2016). Blue dotted rectangle shows cold intermediate waters (CIW) formed during winter convection.

current velocities up to 7 cm s^{-1}. In case of the Khatanga transects the maximal velocity of 6 cm s^{-1} was observed in the upper water layer in the continental slope region, while in the Lena transect the eastward current of 7 cm s^{-1} was detected in between the station 5596 and 5592. The obtained results on geostrophic current velocities should be used with caution due to the ambiguous choice of the reference velocity horizons as well as large distances between the stations where CTD measurements were performed.

Chl-a concentration along the transects is shown in Figure 2. Generally, chl-a distribution features were similar along all four transects. Concentrations were maximum in the areas influenced by river runoff and then noticeably decreased towards the north. In the freshened layers of the Khatanga and Lena transects the concentration was mostly higher than 1 μg Chl l^{-1}. Outside the plume the chl-a concentration at the Laptev Sea shelf varied between 0.4-0.2 μg l^{-1}. An exception was the northernmost stations on the Khatanga transect, located near the ice edge. A deep maximum of chl-a (about 1 μg l^{-1}) was observed there at a depth of 25 m, apparently formed by a recent near-ice phytoplankton bloom. The East Siberian Sea was characterized by low chlorophyll values decreasing in the south-north direction from 0.44 to 0.03 μg l^{-1} at the Kolyma transect and from 0.48 to 0.04 μg l^{-1} at the Indigirka transect. The obtained results on chl-a distribution are consistent with the data reported for the Laptev Sea (Demidov et al, 2019; Demidov et al, 2020) and the East Siberian Sea (Ershova and Kosobokova, 2019) in autumn season.

Optical studies revealed the mixed autochthonous-allochthonous character of CDOM at the Indigirka transect. Kolyma transect cites east of 160°E were distinguished by the presence of autochthonous CDOM in seawater (Drozdova et al., 2021). This is in a good agreement with the results of Semiletov et al. (2005), showing that a significant component of freshwater from Siberian river inflows extends to ~160°E, where the long-term average position of the Pacific frontal zone is located. The DOC content varied in the range between 82.8 and 886.7 μM. In the Laptev seas, the higher DOC concentrations were measured for the upper fresher water layer formed under the influence of Lena and Khatanga runoff. At the Kolyma transect DOC varied between 125.8 and 505.0 μM for the salinity range 17.0–31.5. The Indigirka transect covered a larger salinity gradient from 15.2 to 33.4. The values of DOC varied there from 165.0 to 526.7 μM. The surface waters of the transect were characterized by moderate DOC concentrations of 236.7–393.3 μM with its local increase up to 520.0 μM at the station 5606. In contrast to the Laptev seas, the linkage between DOC and hydrological parameters in the East Siberian Sea was not observed. DOC was distributed rather randomly, with significant DOC concentrations of 300–526.7 μM typical for both Indigirka and Kolyma plumes and continental slope region (Drozdova et al., 2021).

FDOM PARAFAC components

The modeled data set contained 137 EEMs of the samples collected in 2017 in the East Siberian and Laptev seas. Initial split-half results showed 5 as possible candidate for the number of components (Supplementary Figure S2), demonstrating the median value of TCC between PARAFAC components of cube halves above the 0.95 threshold (Supplementary Figure S3), while the TCC varies in a significant range of and the 2nd component scores are highly correlated with those for 1st and 5th components (Supplementary Figure S4). The latter resulted from high variance at the shortest wavelengths, and this effect in turn may be related with fluorescence quenching by dissolved oxygen and absorbance of excitation radiation by the inorganic constituents of seawater (bromide, bisulfide, nitrate and nitrite), at the range 210-250 nm (Johnson and Coletti, 2002). Dataset with cut off excitation below 255 nm led to perfect 4-component model (Figure 4) meeting the strictest criteria for model validation, when even the minimal value of TCC between halves is higher 0.95 (Figure 5). Thus, we decided to consider the reliable 4-component model, excluding consideration of short wavelengths excitation that can be distorted by inorganic components. Excitation and emission maxima for each PARAFAC component are given in Table 2, providing also a comparison with the results of previous studies of East Siberian Sea FDOM.

Distribution of FDOM

Distribution of FDOM PARAFAC component C1 along the three cross-shelf transects (Figure 6) agrees well with distribution of low salinity waters: the maximal concentrations were observed in areas influenced by Khatanga, Indigirka and Kolyma river runoff. As the distance from the coast increased, the fluorescence intensity of C1 gradually decreased. In the waters sampled along the 130°E we observed the predominance of humic-like C1 component. Closer to the Lena Delta (station 5596) the fraction of C1 was accounted for 70-80% through the entire water column, and it decreased up to 44% in deeper waters farther north (station 5592). At the same time the increase of C2 (up to 20%) and C3 (up to 35%) was measured.

Protein-like component C2 was poorly represented along the Khatanga transect. The maximal concentration of C2 was measured mostly in the upper 15-m water layer as well as along the entire water column within the Khatanga River plume (stations 5627 – 5630, salinity 3.5 – 25.4). The absence of pronounced stratification in this area was recently explained by estuarine tidal mixing in the region (Osadchiev et al., 2020). The contribution of C2 was more significant in the East Siberian Sea. At the transect from Indigirka River delta region to continental slope C2 was distributed irregularly. It was more abundant at the southern part of the transect with the maximal C2 concentration at the stations

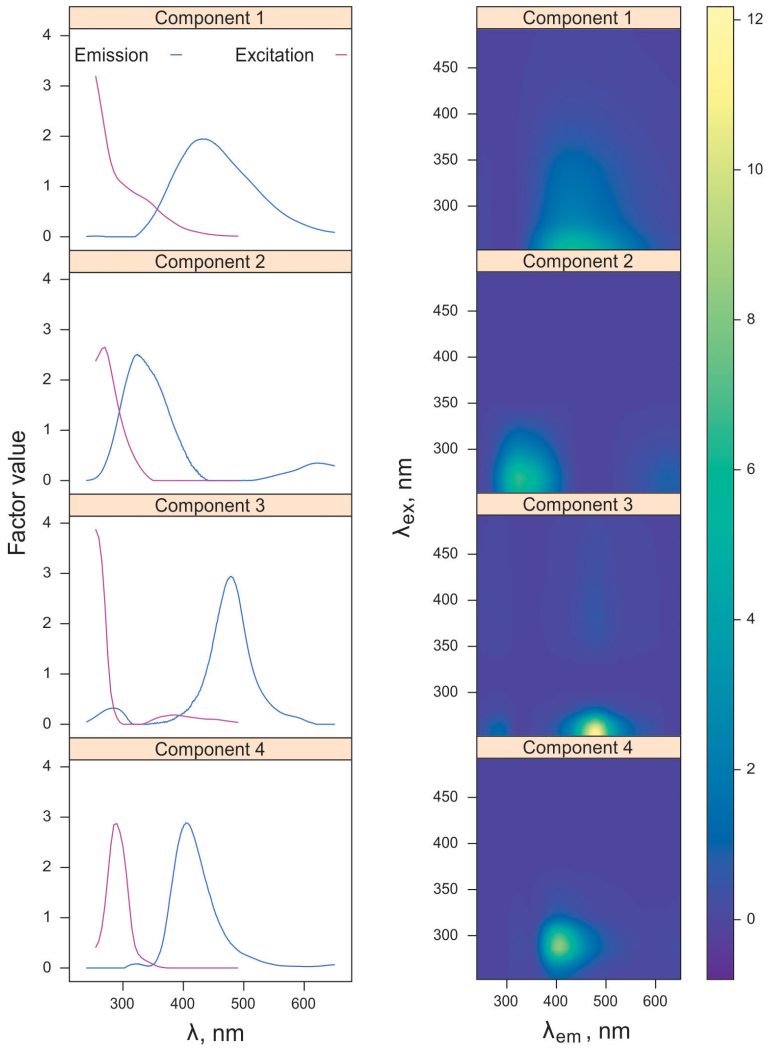

FIGURE 4
Excitation and emission spectra (left panel) and excitation-emission matrices (right panel) for each identified PARAFAC component.

5598 and 5600 (salinity 15.2 – 17.6). The surface water layer of the Kolyma transect was generally depleted CDOM component C2 as compared with the deep waters of the transect (Figure 6); C2 was concentrated in the continental slope region at the station 5612, as well as in bottom waters at the station 5617. The C3 distribution in the Kolyma transect repeats the C2 except for the southernmost station: the C3 content at the station 5619 was quite high and comparable to the deep waters in the continental slope area, while the C2 content was rather low. Enrichment with the C3 component was also observed for the Khatanga and Indigirka rivers-influenced regions. At the Khatanga transect, a decrease in C3 followed the salinity gradient similar to C1. In contrast to C1, an increase in the C3 concentration was observed at high salinities near the continental slope (station 5634, 18 m).

The PARAFAC component C4 was not observed in the Khatanga transect. A very weak increase in the C4 concentration was detected in the continental slope area and in the bottom waters at the station 5591_2. In the East Siberian Sea, local maxima were found at station 5606 (23 m) of the Indigirka transect and in the continental slope region of the Kolyma transect (station 5612, 10-48 m). The waters influenced by the Lena River runoff (stations 5596 and 5592) contained no marine humic-like C4 and little to moderate C3 and protein-like C2 component.

Discussion

Component C1 matched a lot of EEM - PARAFAC models describing CDOM from various regions, including Arctica (Brogi et al., 2018; Painter et al., 2018) and Antarctica (Kida et al., 2019). It was usually assigned as terrestrial humic material

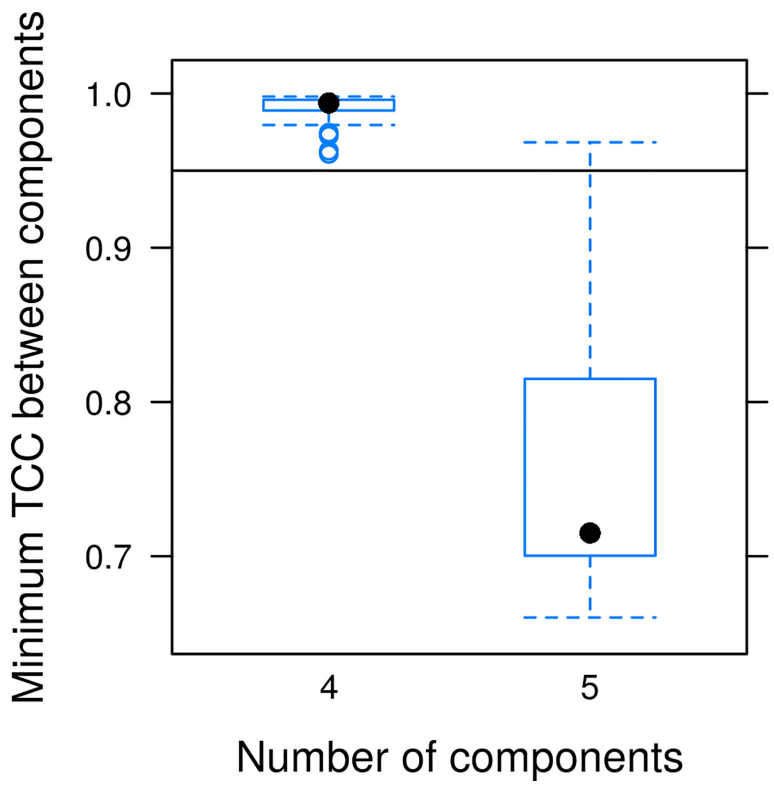

FIGURE 5
Split-half validation for the PARAFAC model. The dataset has been randomly shuffled and split in halves 100 times; a PARAFAC decomposition was computed for every split. After reordering the components according to best match by 'TCC, the minimal TCC value among all pairs of emission and excitation components was taken for every pair of decompositions.

and was abundant mostly in rivers, lakes, estuarine, costal and shelf regions of the oceans. The spectral characteristics of C1 were reported to be similar to the ones of syringaldehyde which, along with vanillin, is a product of oxidative degradation of lignin (Murphy et al., 2011). We conclude that C1 in the Laptev and East Siberian seas is supplied by river runoff. Component C2 exhibited protein-like fluorescence (Table 2) typical for proteins and/or aromatic amino acids and often linked to aquatic productivity (Castillo et al., 2010). In the study of DOM composition and bioavailability during the sea ice formation (Jørgensen et al., 2015) the similar component with excitation and emission maxima of 273 nm and 327 nm, respectively, was reported to represent a combined signal of tryptophan and tyrosine amino acids referred to the T and B peaks (Coble, 2007; Stedmon and Nelson, 2015). The PARAFAC components with spectral characteristics similar to C3 were found in various studies. For example, C3 absorption and emission maxima (Table 2) are close to C3 (λ_{ex} = 270 (360) nm, λ_{em} = 478 nm)

TABLE 2 Excitation and emission maxima of four PARAFAC components compared to results of previous studies of East Siberian Sea FDOM[a].

Present study	(Coble, 2007)	(Mann et al., 2012)	(Guéguen et al., 2012)	(Chen et al., 2017)	(Chen et al., 2021)
C1: <375/430	A (humic-like): 260/400-460	C1: <250 (310)/422	C1: 260(368)/470	C6: <260/430	A: 260/420
C2: 270/323	B,T (protein-like): 275/305, 340	C4: 280 (<250)/342 C5:265/<320	C3: 284/338 C5: 272/310	C5: 280/342	B: 280/310 T: 280/340
C3: <275(380)/478	C (humic-like): 320-360/420-460	C2: <250(285)/492	C1: 260(368)/470	C3: 285(370)/>500	C: 350/450
C4: 290/405	M (marine humic-like): 290-310/370-410	n/a	C4: 300/414 C2: 324/398	C1: 310/400	M: 315/400

[a] – Secondary excitation maxima are in parentheses, n/a – not available.

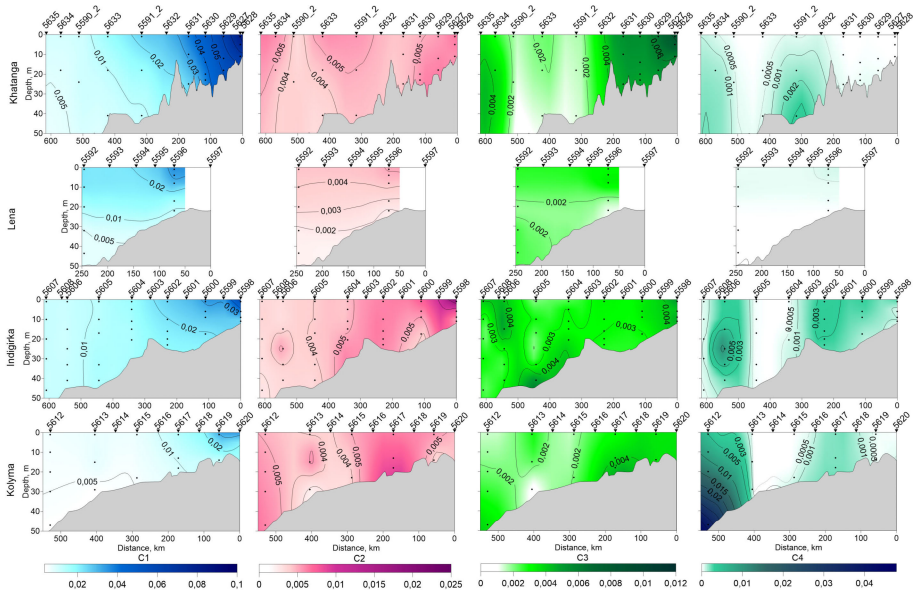

FIGURE 6
Distribution of PARAFAC components C1 – C4 along the Khatanga (17 – 19 September, 2017), Lena (2 –3 September, 2017), Indigirka (5 –7 September, 2017) and Kolyma (8 – 9 September, 2017) transects, obtained from the original data points, marked by black dots.

in the study of DOM in the catchment and estuary of Horsens Fjord (Denmark) (Stedmon et al., 2003), and C2 (λ_{ex} = 240 (370) nm, λ_{em} = 480 nm) in the PARAFAC model of EEMs of Atlantic Ocean FDOM (Kowalczuk et al., 2013). Although the fluorescence maximum is blue-shifted by ~30 nm compared to conventional peak C (Coble, 1996), in the above studies the components were identified as peak C and assigned to humic material exported from terrestrial sources (Stedmon et al., 2003; Kowalczuk et al., 2013). Peak C was also reported to represent a product of microbial transformation of phytoplankton exudates (Romera-Castillo et al., 2011). The C4 component resembles fluorescence typical for marine humic substances peak M (Coble, 2007). In the experiments, provided Romera-Castillo et al., peak M fluorophore consumed by bacteria had been produced by phytoplankton (Castillo et al., 2010). A component BERC6 very similar to C4 was identified by a PARAFAC modeling of Canadian Arctic surface water FDOM fluorescence (Walker et al., 2009). Low fluorescence of this component was interpreted as minimal microbial productivity it the studied water area.

The relationship between the PARAFAC component values and various metadata of our samples was explored with the RDA analysis. Since the full set of parameters are available for 78 samples, RDA analysis was performed for them only. Using a permutation test, we validated 2 canonical axes as significant at α=0.01 level (Figure 7). The angle between the variable arrows indicates the correlation between them, while the length of the variable arrows reflects the degree of its influence on the fluorescent components. Based on the obtained results, fewer parameters have been chosen to study their correlation with PARAFAC component fluorescence intensity in more detail, namely, salinity, DOC, chlorophyll-a, $a_{CDOM}(350)$, S, HIX, BIX, SUVA, and FIMcK. Pearson's correlation coefficients were calculated individually for the Khatanga, Lena, Indigirka, and Kolyma transects (Table 3) with the Origin7.0 software (Edwards, 2002).

Fluorescent component distribution along the salinity gradient for salinity ranges of 3.5 – 33.8 in the Laptev Sea and 15.2 – 32.7 in the East Siberian Sea is shown in Figure 8. The C1 appeared to be linearly anti-correlated with salinity for all the transect with correlation coefficient varying between -0.99 and -0.92. Conservative mixing of C1 confirms our assumption about its supply by river runoff. Intercept values of the equations describing linear correlations are very close for the Khatanga and Lena, as well as for the Indigirka and Kolyma transects. At the same time, they differ for the Laptev (average value is 8.5×10^{-2}) and East Siberian (6.4×10^{-2}) seas (see Table 4). Such a difference in optical patterns between the rivers can be related to their individual watershed characteristics. So, we assume that the Khatanga and Lena rivers are characterized by higher content of terrigenous humic substances with a fluorescence maximum at 430 nm. This is consistent with the study of variation of FDOM of large Arctic rivers, in which lower $a_{CDOM}(350)$ values in the Kolyma River, compared to the Lena River, were explained by lower vascular plant inputs during freshet and its more extensive microbial degradation in the Kolyma watershed (Walker et al., 2013).

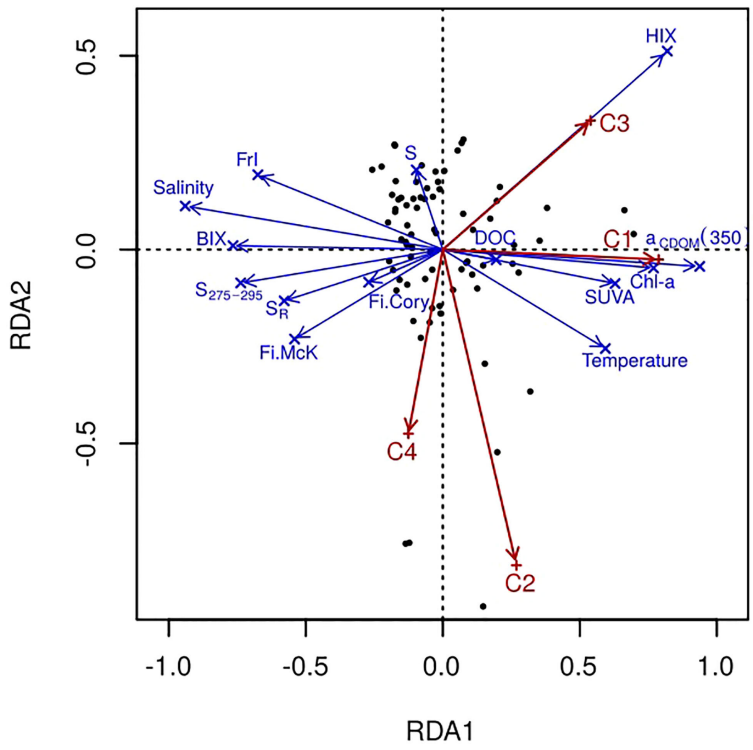

FIGURE 7
Redundancy analysis of spectral parameters and environmental factors.

We also suggest that C1 component makes a dominant contribution to the CDOM absorption, since a strong correlation was revealed also between C1 and CDOM absorption coefficients at wavelengths from 300 nm to 400 nm, in particular, with $a_{CDOM}(350)$, often used as a quantitative measure for lignin concentration and input of terrestrial DOM to the Arctic Ocean (Spencer et al., 2009; Stedmon et al., 2011; Mann et al., 2016) (Figure 9). Component C1 correlates with DOC concentration in the river plume influenced areas in the Laptev Sea (Figure 10A), where conservative DOC behavior along the salinity gradient was demonstrated recently (Drozdova et al., 2021). Chl-a correlates with C1 to a lesser extent ($0.62 < r < 0.82$), showing higher values at the southern stations of the transects most affected by river runoff (Figure 10B). A positive linear correlation between C1 and humification index HIX – an indicator of humic substance content or extent of humification – was demonstrated for the Khatanga, Lena and Kolyma transects, while BIX - an indicators of autochthonous DOM input (Stedmon and Nelson, 2015) – was lower in the river-influenced areas (Figures 10C, D). A weak positive correlation was observed also between C3 and HIX and negative – between C3 and BIX (Figure 11). The HIX is based on the idea that the emission spectra of fluorescing molecules shift toward longer wavelengths as humification of DOM proceeds. Higher values indicate an increasing degree of humification. So, the increase of the content of C3 with fluorescence maxima at 478 nm, necessarily leads to an increase of HIX (Table 1).

The C2 and C3 component fluorescence intensities were generally higher at low salinities (and high CDOM absorption $a_{CDOM}(350)$). A moderate negative correlation ($-0.85 < r < -0.53$) was observed for the Khatanga, Lena, and Indigirka transects (Figure 8 and Table 4). Higher concentration of C2 and C3 in the river-influenced regions is in a good agreement with reports of their allochthonous source, see, for example, the studies (Yamashita and Jaffé, 2008; Sun et al., 2014; Lee and Kim, 2018). Non-conservative behavior of protein substances (C2) in many estuaries is explained by relatively rapid degradation labile DOM (Yamashita and Tanoue, 2003; Vignudelli et al., 2004; Yamashita and Tanoue, 2008). Another possible reason for non-conservative distribution of C2 and C3 FDOM components is their production in marine environment. Thus, the study of Amerasian Basin seawaters revealed high abundance of protein-like fluorescence suggesting potential influence of fall phytoplankton blooms in the Chukchi and East Siberian seas in August – September (Chen et al., 2017) and its production from sediments (Chen et al., 2016). Taking into account weak correlations of C2 and C3 with salinity caused mostly by the local maxima of C2 and C3 fluorescence

10.3389/fmars.2022.872557

TABLE 3 Pearson's correlation coefficients significant at 0.05 level for PARAFAC components C1 – C4 against various characteristics of seawater.

Parameter	C1	C2	C3	C4
Salinity	-0.98	-0.64	-0.79	n/s
	-0.99	-0.85	-0.55	n/s
	-0.92	-0.53	n/s	n/s
	-0.97	n/s	n/s	n/s
DOC	0.91	0.40	0.67	n/s
	0.79	0.79	n/s	n/s
	n/s	n/s	n/s	n/s
	n/s	n/s	0.55	n/s
Chlorophyll-a	0.73	n/s	0.62	n/s
	0.82	0.71	n/s	n/s
	0.62	0.50	n/s	n/s
	0.70	n/s	n/s	n/s
$a_{CDOM}(350)$	0.96	0.66	0.82	n/s
	0.98	0.85	0.51	n/s
	0.94	0.63	n/s	n/s
	0.96	n/s	n/s	n/s
S	n/s	n/s	n/s	n/s
	n/s	n/s	n/s	n/s
	-0.51	n/s	n/s	n/s
	n/s	n/s	n/s	n/s
HIX	0.90	0.37	0.88	n/s
	0.74	n/s	0.80	n/s
	n/s	-0.36	0.56	-0.39
	0.70	n/s	n/s	n/s
BIX	-0.69	-0.41	-0.68	n/s
	-0.82	-0.85	n/s	n/s
	-0.53	n/s	-0.46	n/s
	n/s	n/s	-0.53	n/s
SUVA	0.64	0.60	0.47	n/s
	0.68	0.72	n/s	n/s
	0.74	0.45	n/s	n/s
	0.63	n/s	n/s	n/s
FIMcK	-0.49	-0.41	n/s	n/s
	-0.57	-0.62	n/s	n/s
	-0.35	n/s	-0.43	n/s
	-0.54	n/s	n/s	n/s

n/s – the slope is not significantly different from zero
Correlation coefficients are given individually for the Khatanga, Lena, Indigirka, and Kolyma transects (top-down).

in the continental slope regions and in bottom waters (Figure 6), we suggest the mixed autochthonous-allochthonous origin of C2 and C3 components with the predominance of allochthonous (mostly riverine runoff) sources in the river plumes - waters with salinity below 27 (Kang et al., 2013). The local maxima of the C2-C4 fluorescence intensity outside the plumes, in turn, are associated with autochthonous FDOM production, in particular with the fall phytoplankton blooms and, possibly, with a processes of organic matter reworking in the bottom water layer. Indeed, the areas of the continental slope of the Arctic shelf are known as potential depots for the accumulation of large masses of organic matter, and the mineralization on the bottom surface was estimated as about 89% of the total input (Romankevich et al., 2009).

At present, it seems to be complicated to relate unambiguously the spectral composition of FDOM to specific biogeochemical processes and DOM sources. Nevertheless, we assume that the increase of C2 and C3 content at the continental slope region of the Khatanga transect (station 5634) is most likely related to the recent near-ice phytoplankton bloom. It is supported by a deep maximum of chl-a (about 1 μg l^{-1} at the station 5635 and 0.6 μg l^{-1} at the

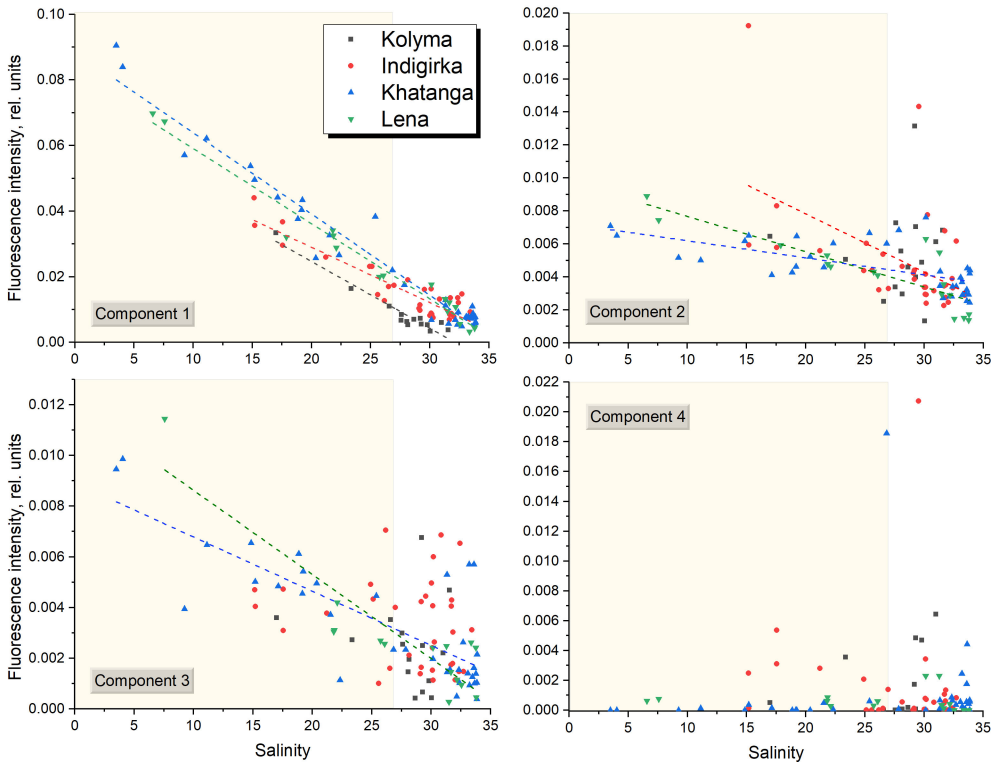

FIGURE 8
All samples from the 69th cruise of R/V *Akademik Mstislav Keldysh* collected in the Laptev and East Siberian seas, showing fluorescence intensity of PARAFAC components plotted against salinity. Yellow rectangles show the data obtained from the river plume regions with salinity below 27. The equations for linear correlations (dashed lines) are given in Table 4.

station 5634). The bottom waters of the northmost station of the Kolyma transect (5612), exhibited high C2 – C4 fluorescence intensity (Figure 6). The study of Sukhanova et al. (2021) revealed the maximum abundance and biomass of algae of the genus *Chaetoceros* with high content of spores and dead cells (up to 40%) in the lower layers of the water column. This region was also characterized by the maximal nitrate concentration along the transect of 4.1 μM (Sukhanova et al., 2021), high concentration of detrital and mineral particles, (Kopylov et al., 2021), as well as the maximal abundance and biomass of heterotrophic nanoflagellates (Kopylov et al., 2021). The complex composition of DOM in this area may be caused by several factors, for example, destruction of dead algae cells, production of heterotrophic nanoflagellates and bacterioplankton, and DOM released as a result of viral lysis of bacteria (Middelboe and Jørgensen, 2006; Jürgens and Massana, 2008).

TABLE 4 Summary of regression analysis for PARAFAC components C1-C3 against salinity in the Khatanga, Lena, Indigirka, and Kolyma transects: *n* - number of samples, *a* – slope, *b* - intercept.

		n	*a* ($\times 10^3$)	*b* ($\times 10^2$)	Pearson's r
C1	Khatanga	35	-2.48 ± 0.09	8.87 ± 0.25	-0.98
	Lena	17	-2.29 ± 0.10	8.20 ± 0.27	-0.99
	Indigirka	34	-1.69 ± 0.13	6.27 ± 0.36	-0.92
	Kolyma	15	-2.03 ± 0.15	6.53 ± 0.42	-0.97
C2	Khatanga	35	-0.10 ± 0.02	0.72 ± 0.06	-0.64
	Lena	17	-0.21 ± 0.03	0.98 ± 0.09	-0.85
	Indigirka	34	-0.35 ± 0.10	1.49 ± 0.29	-0.53
C3	Khatanga	35	-0.21 ± 0.03	0.89 ± 0.08	-0.79
	Lena	17	-0.33 ± 0.05	1.20 ± 0.13	-0.55

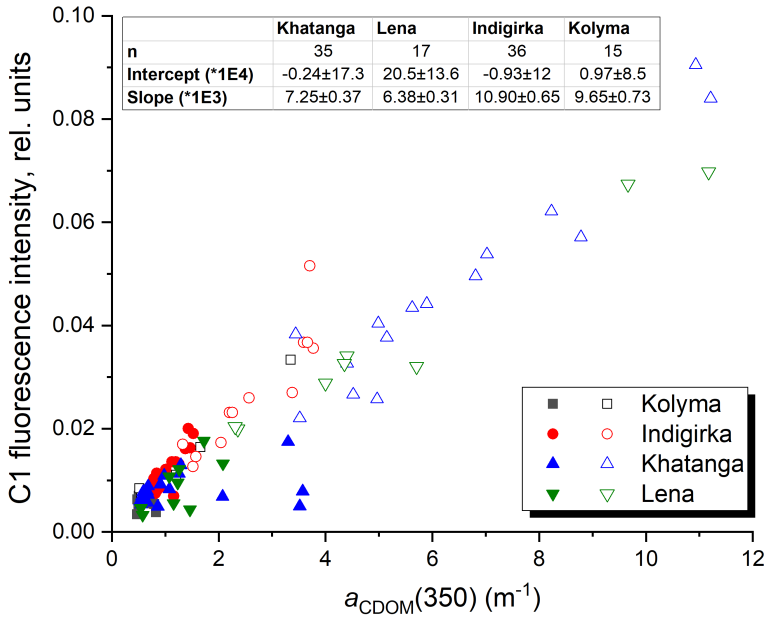

FIGURE 9
Fluorescence intensity of C1 against CDOM absorption coefficient at 350 nm. Filled symbols indicate the data obtained outside the river plume regions with salinity above 27.

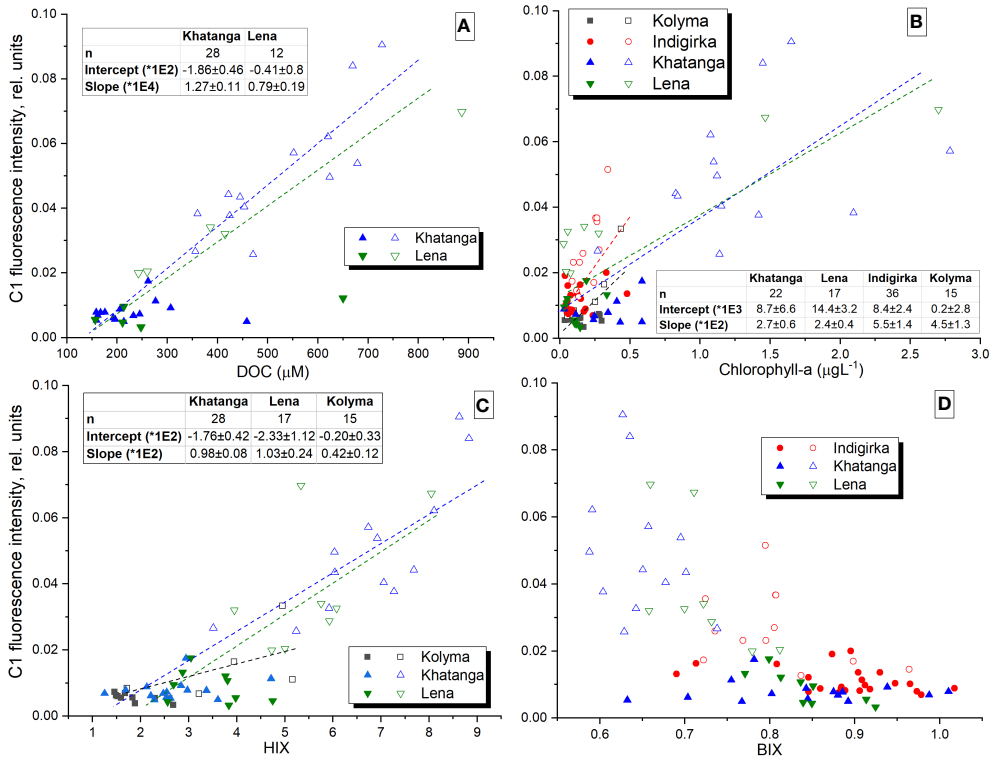

FIGURE 10
Fluorescence intensity of C1 against DOC, chlorophyll-a, HIX, and BIX. Filled symbols indicate the data obtained outside the river plume regions with salinity above 27.

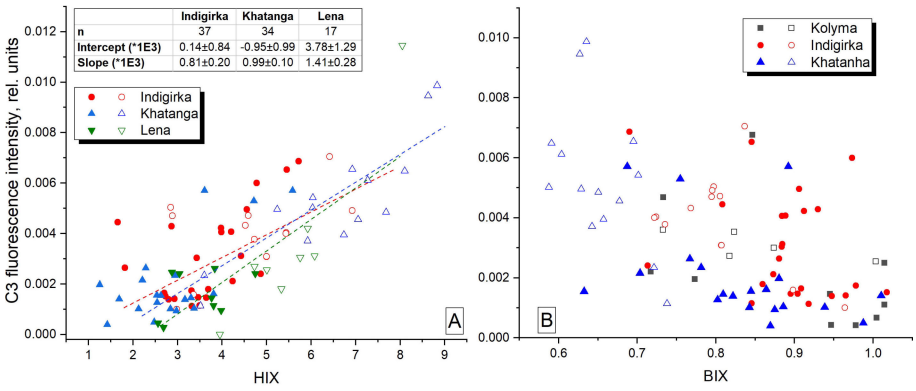

FIGURE 11
Fluorescence intensity of C3 against HIX and BIX. Filled symbols indicate the data obtained outside the river plume regions with salinity above 27.

Suspended matter at the station 5606 of the Indigirka transect was analyzed as a part of the study of the role of plankton in the vertical suspended matter (SM) flux in the East Siberian Sea (Drits et al., 2019). The dramatic increase of the total vertical SM flux at 35 m depth at the station 5606 was suggested to be due to re-suspension in the bottom nepheloid layer. At the same time, the analysis of physical and chemical data (CTD data, nutrients, oxygen, dissolved inorganic carbon, fCO_2, CH_4) measured in September 2008 in the East Siberian Sea revealed microbial decay of organic matter occurring through much of the water column with its predominance at the sediment interface (Anderson et al., 2011). We assume that at the stations 5605 and 5606 of the Indigirka transect high concentrations of FDOM in mid-waters and bottom water layer can be related to the erosion of the nepheloid layer containing organic matter decay products. It should be taken into account, that the increase in the concentration of SM in bottom waters does not necessarily indicate the resuspension of nepheloid layer. Ungrazed phytoplankton blooms, combined with aggregation and coagulation can lead to rapid sinking of the newly produced organic material. Mesozooplankton can also compact slowly sinking smaller phytoplankton cells into fecal pellets (Wassmann et al., 2004).

The study of FDOM of the Arctic shelf waters showed the difference in the distribution of PARAFAC components in the East Siberian and Laptev seas. In the Laptev Sea, components C1 and C3 dominate, with the maximal fluorescence intensities observed mostly in the Lena and Khatanga river-influenced shelf areas. Protein-like (C2) and marine humic-like (C4) components are poorly represented. In the East Siberian Sea, a similar distribution was observed only for the terrestrial humic-like component C1, while C2 and C4 components are more abundant and distributed irregularly. Component C3, usually assigned as terrestrial-derived FDOM, exhibited local maxima throughout the water column which pointed on autochthonous production of FDOM with emission maximum at 478 nm. The obtained results make the optical studies of FDOM a powerful tool for identifying the most interesting areas in terms of understanding the carbon cycling in the Arctic shelf seas. It is necessary to take into account the high variability of FDOM, and when studying processes in the bottom water layer, much attention should be paid to natural barriers, where organic matter can be accumulated.

Summary

FDOM of Siberian shelf seas is described by the set of four PARAFAC components which correspond to conventional fluorophores A, C, T/B and M (Coble, 1996; Coble et al., 1998; Coble, 2007) identified in natural waters. The composition of FDOM was found to be typical for the Siberian shelf seas (Guéguen et al., 2012; Mann et al., 2012; Chen et al., 2017; Chen et al., 2021), but this study showed the difference in FDOM distribution in the Laptev Sea (Khatanga and Lena transects) and in the East Siberian Sea (Indigirka and Kolyma transects). The consideration of fluorescence intensities of individual PARAFAC components along the shelf-crossing transects made it possible to draw the following conclusions:

Components C1 and C4 are of allochthonous and autochthonous origin, respectively, while C2 and C3 are supplied by river runoff and produced in marine environment.

The main features of the East Siberian Sea shelf waters were the higher abundances of the protein-like (C2) and marine humic-like (C4) components, as well as significant contribution of autochthonous-derived FDOM components C2 – C4.

The PARAFAC component C1 was found to be a reliable marker of input of riverine terrestrial-derived DOM to the Arctic Ocean. Among all studied fluorescence-based indices, C1 (fluorophore A) correlated best with salinity in the studied areas of Siberian shelf seas.

Based on related data, we suggest the destruction of dead algae cells, production of heterotrophic nanoflagellates and bacterioplankton, organic matter reworking, and DOM released as a result of viral lysis of bacteria as possible sources of FDOM.

Data availability statement

The raw data supporting the conclusions of this article will be made available by the authors, without undue reservation.

Author contributions

AD, IK, and TL contributed to conception and design of the study. TL performed spectral measurements. IK performed PARAFAC decomposition. Analysis of CTD and chlorophyll-a data was performed by AN and EA. AD, and IK wrote the first draft of the manuscript. All the authors revised the draft and approved the submitted version of the manuscript.

Funding

This research was funded by the Russian Science Foundation, project 21-77-10064.

Acknowledgments

We are grateful to Nikolay V. Lobus for water sampling, Mikhail V. Flint for the opportunity to take part in the impressive complex expeditions to the Arctic shelf seas and the crew of the R/V *Akademik Mstislav Keldysh* for their contribution during field studies. We would like to thank the reviewers for their constructive comments and the editor for his review of the manuscript.

Conflict of interest

The authors declare that the research was conducted in the absence of any commercial or financial relationships that could be construed as a potential conflict of interest.

Publisher's note

All claims expressed in this article are solely those of the authors and do not necessarily represent those of their affiliated organizations, or those of the publisher, the editors and the reviewers. Any product that may be evaluated in this article, or claim that may be made by its manufacturer, is not guaranteed or endorsed by the publisher.

Supplementary material

The Supplementary Material for this article can be found online at: https://www.frontiersin.org/articles/10.3389/fmars.2022.872557/full#supplementary-material

References

Alling, V., Sanchez-Garcia, L., Porcelli, D., Pugach, S., Vonk, J. E., Van Dongen, B., et al. (2010). Nonconservative behavior of dissolved organic carbon across the laptev and East Siberian seas. *Global Biogeochemical Cycles* 24 (4), GB4033. doi: 10.1029/2010GB003834

Anderson, L. G., Björk, G., Jutterström, S., Pipko, I., Shakhova, N., Semiletov, I., et al. (2011). East Siberian Sea, An Arctic region of very high biogeochemical activity. *Biogeosciences* 8 (6), 1745–1754. doi: 10.5194/bg-8-1745-2011

Box, J. E., Colgan, W. T., Christensen, T. R., Schmidt, N. M., Lund, M., Parmentier, F.-J. W., et al. (2019). Key indicators of Arctic climate change: 1971–2017. *Environ. Res. Lett.* 14 (4), 045010. doi: 10.1088/1748-9326/aafc1b

Bro, R. (1997). PARAFAC. tutorial and applications. *Chemom. intelligent Lab. Syst.* 38 (2), 149–171. doi: 10.1016/S0169-7439(97)00032-4

Brogi, S. R., Ha, S.-Y., Kim, K., Derrien, M., Lee, Y. K., and Hur, J. (2018). Optical and molecular characterization of dissolved organic matter (DOM) in the Arctic ice core and the underlying seawater (Cambridge bay, canada): Implication for increased autochthonous DOM during ice melting. *Sci. Total Environ.* 627, 802–811. doi: 10.1016/j.scitotenv.2018.01.251

Bro, R., and Smilde, A. K. (2003). Centering and scaling in component analysis. *J. Chemom.* 17 (1), 16–33. doi: 10.1002/cem.773

Carstea, E. M., Popa, C. L., Baker, A., and Bridgeman, J. (2020). *In situ* fluorescence measurements of dissolved organic matter: a review. *Sci. Total Environ.* 699, 134361. doi: 10.1016/j.scitotenv.2019.134361

Castillo, C. R., Sarmento, H., Alvarez-Salgado, X. A., Gasol, J. M., and Marrasé, C. (2010). Production of chromophoric dissolved organic matter by marine phytoplankton. *Limnol. Oceanogr.* 55 (1), 446–454. doi: 10.4319/lo.2010.55.1.0446

Chen, M., Kim, J.-H., Lee, Y. K., Lee, D.-H., Jin, Y. K., and Hur, J. (2021). Subsea permafrost as a potential major source of dissolved organic matter to the East Siberian Arctic shelf. *Sci. Total Environ.* 146100. doi: 10.1016/j.scitotenv.2021.146100

Chen, M., Kim, J.-H., Nam, S.-I., Niessen, F., Hong, W.-L., Kang, M.-H., et al. (2016). Production of fluorescent dissolved organic matter in Arctic ocean sediments. *Sci. Rep.* 6 (1), 1–10. doi: 10.1038/srep39213

Chen, M., Nam, S.-I., Kim, J.-H., Kwon, Y.-J., Hong, S., Jung, J., et al. (2017). High abundance of protein-like fluorescence in the amerasian basin of Arctic ocean: Potential implication of a fall phytoplankton bloom. *Sci. Total Environ.* 599, 355–363. doi: 10.1016/j.scitotenv.2017.04.233

Chen, W., Ouyang, Z.-Y., Qian, C., and Yu, H.-Q. (2018). Induced structural changes of humic acid by exposure of polystyrene microplastics: a spectroscopic insight. *Environ. pollut.* 233, 1–7. doi: 10.1016/j.envpol.2017.10.027

Coble, P. G. (1996). Characterization of marine and terrestrial DOM in seawater using excitation-emission matrix spectroscopy. *Mar. Chem.* 51 (4), 325–346. doi: 10.1016/0304-4203(95)00062-3

Coble, P. G. (2007). Marine optical biogeochemistry: the chemistry of ocean color. *Chem. Rev.* 107 (2), 402–418. doi: 10.1021/cr050350+

Coble, P. G., Del Castillo, C. E., and Avril, B. (1998). Distribution and optical properties of CDOM in the Arabian Sea during the 1995 southwest monsoon. *Deep Sea Res. Part II: Topical Stud. Oceanogr.* 45 (10-11), 2195–2223. doi: 10.1016/S0967-0645(98)00068-X

Cory, R. M., Miller, M. P., McKnight, D. M., Guerard, J. J., and Miller, P. L. (2010). Effect of instrument-specific response on the analysis of fulvic acid fluorescence spectra. *Limnol. Oceanogr.: Methods* 8 (2), 67–78. doi: 10.4319/lom.2010.8.67

D'Andrilli, J., Junker, J. R., Smith, H. J., Scholl, E. A., and Foreman, C. M. (2019). DOM composition alters ecosystem function during microbial processing of isolated sources. *Biogeochemistry* 142 (2), 281–298. doi: 10.1007/s10533-018-00534-5

Demidov, A., Gagarin, V., Arashkevich, E., Makkaveev, P., Konyukhov, I., Vorobieva, O., et al. (2019). Spatial variability of primary production and chlorophyll in the laptev Sea in august–September. *Oceanology* 59 (5), 678–691. doi: 10.1134/S0001437019050047

Demidov, A., Gagarin, V., Artemiev, V., Arashkevich, E., Makkaveev, P., Shchuka, S., et al. (2020). Vertical variability of primary production and features of the subsurface chlorophyll maximum in the laptev Sea in august–september 2015, 2017, and 2018. *Oceanology* 60 (2), 189–204. doi: 10.1134/S0001437020010063

Dmitrenko, I., Kirillov, S., Eicken, H., and Markova, N. (2005). Wind-driven summer surface hydrography of the eastern Siberian shelf. *Geophys. Res. Lett.* 32 (14), L14613. doi: 10.1029/2005GL023022

Drits, A. V., Pasternak, A. F., Kravchishina, M. D., Arashkevich, E. G., Sukhanova, I. N., and Flint, M. V. (2019). The role of plankton in the vertical flux in the East Siberian Sea shelf. *Oceanology* 59 (5), 669–677. doi: 10.1134/S0001437019050059

Drozdova, A. N., Nedospasov, A. A., Lobus, N. V., Patsaeva, S. V., and Shchuka, S. A. (2021). CDOM optical properties and DOC content in the largest mixing zones of the Siberian shelf seas. *Remote Sens.* 13 (6)1145. doi: 10.3390/rs13061145

Drozdova, A. N., Puiman, M. S., Krylov, I. N., Patsaeva, S. V., and Shatravin, A. V. (2019). Dataset on optical characteristics and spectroscopic indices of dissolved organic matter of the kara, laptev, and East Siberian seas in august–September 2017. *Data Brief* 26, 104562. doi: 10.1016/j.dib.2019.104562

Edwards, P. M. (2002). Origin 7.0: scientific graphing and data analysis software. *J. Chem. Inf. Comput. Sci.* 42 (5), 1270–1271. doi: 10.1021/ci0255432

Eilers, P. H. (2003). A perfect smoother. *Anal. Chem.* 75 (14), 3631–3636. doi: 10.1021/ac034173t

Ershova, E., and Kosobokova, K. N. (2019). Cross-shelf structure and distribution of mesozooplankton communities in the East-Siberian Sea and the adjacent Arctic ocean. *Polar Biol.* 42 (7), 1353–1367. doi: 10.1007/s00300-019-02523-2

Gonçalves-Araujo, R., Stedmon, C. A., Heim, B., Dubinenkov, I., Kraberg, A., Moiseev, D., et al. (2015). From fresh to marine waters: Characterization and fate of dissolved organic matter in the Lena river delta region, Siberia. *Front. Mar. Sci.* 2, 108. doi: 10.3389/fmars.2015.00108

Gonnelli, M., Galletti, Y., Marchetti, E., Mercadante, L., Brogi, S. R., Ribotti, A., et al. (2016). Dissolved organic matter dynamics in surface waters affected by oil spill pollution: Results from the serious game exercise. *Deep Sea Res. Part II: Topical Stud. Oceanogr.* 133, 88–99. doi: 10.1016/j.dsr2.2016.05.027

Gordeev, V. V., Martin, J. M., Sidorov, I. S., and Sidorova, M. V. (1996). A reassessment of the Eurasian river input of water, sediment, major elements, and nutrients to the Arctic ocean. *Am. J. Sci.* 296 (6), 664–691. doi: 10.2475/ajs.296.6.664

Griffin, C. G., McClelland, J. W., Frey, K. E., Fiske, G., and Holmes, R. M. (2018). Quantifying CDOM and DOC in major Arctic rivers during ice-free conditions using landsat TM and ETM+ data. *Remote Sens. Environ.* 209, 395–409. doi: 10.1016/j.rse.2018.02.060

Guéguen, C., McLaughlin, F., Carmack, E., Itoh, M., Narita, H., and Nishino, S. (2012). The nature of colored dissolved organic matter in the southern Canada basin and East Siberian Sea. *Deep Sea Res. Part II: Topical Stud. Oceanogr.* 81, 102–113. doi: 10.1016/j.scitotenv.2021.146100

Helms, J. R., Stubbins, A., Ritchie, J. D., Minor, E. C., Kieber, D. J., and Mopper, K. (2008). Absorption spectral slopes and slope ratios as indicators of molecular weight, source, and photobleaching of chromophoric dissolved organic matter. *Limnol. Oceanogr.* 53 (3), 955–969. doi: 10.4319/lo.2008.53.3.0955

Holmes, R. M., McClelland, J. W., Peterson, B. J., Shiklomanov, I. A., Shiklomanov, A. I., Zhulidov, A. V., et al. (2002). A circumpolar perspective on fluvial sediment flux to the Arctic ocean. *Global biogeochemical cycles* 16 (4), 45–41-45-14. doi: 10.1029/2001GB001849

Holm-Hansen, O., and Riemann, B. (1978). Chlorophyll a determination: improvements in methodology. *Oikos* 438-447. doi: 10.2307/3543338

Huguet, A., Vacher, L., Relexans, S., Saubusse, S., Froidefond, J.-M., and Parlanti, E. (2009). Properties of fluorescent dissolved organic matter in the gironde estuary. *Organic Geochem.* 40 (6), 706–719. doi: 10.1016/j.orggeochem.2009.03.002

Jørgensen, L., Stedmon, C. A., Kaartokallio, H., Middelboe, M., and Thomas, D. N. (2015). Changes in the composition and bioavailability of dissolved organic matter during sea ice formation. *Limnol. Oceanogr.* 60 (3), 817–830. doi: 10.1002/lno.10058

Jaffé, R., McKnight, D., Maie, N., Cory, R., McDowell, W. H., and Campbell, J. L. (2008). Spatial and temporal variations in DOM composition in ecosystems: The importance of long-term monitoring of optical properties. *J. Geophys. Research: Biogeosci.* 113 (G4), G04032. doi: 10.1029/2008JG000683

Jakobsson, M., Grantz, A., Kristoffersen, Y., and Macnab, R. (2004). "The Arctic ocean: boundary conditions and background information," in *The organic carbon cycle in the Arctic Ocean*, eds R. Stein, R. and W. Macdonald (Berlin: Springer), 1–32. doi: 10.1007/978-3-642-18912-8_1

Jiao, N., Herndl, G. J., Hansell, D. A., Benner, R., Kattner, G., Wilhelm, S. W., et al. (2010). Microbial production of recalcitrant dissolved organic matter: long-term carbon storage in the global ocean. *Nat. Rev. Microbiol.* 8 (8), 593–599. doi: 10.1038/nrmicro2386

Johnson, K. S., and Coletti, L. J. (2002). *In situ* ultraviolet spectrophotometry for high resolution and long-term monitoring of nitrate, bromide and bisulfide in the ocean. *Deep Sea Res. Part I: Oceanogr. Res. Papers* 49 (7), 1291–1305. doi: 10.1016/S0967-0637(02)00020-1

Jürgens, K., and Massana, R. (2008). "Protistan grazing on marine bacterioplankton," in *Microbial Ecology of the Oceans*, ed D. L. Kirchman (New York, NY: Wiley), 383–441.

Kang, Y., Pan, D., Bai, Y., He, X., Chen, X., Chen, C.-T. A., et al. (2013). Areas of the global major river plumes. *Acta Oceanologica Sin.* 32 (1), 79–88. doi: 10.1007/s13131-013-0269-5

Kida, M., Kojima, T., Tanabe, Y., Hayashi, K., Kudoh, S., Maie, N., et al. (2019). Origin, distributions, and environmental significance of ubiquitous humic-like fluorophores in Antarctic lakes and streams. *Water Res.* 163, 114901. doi: 10.1016/j.watres.2019.114901

Kopylov, A., Kosolapov, D., Zabotkina, E., Romanenko, A., and Sazhin, A. (2021). Distribution and relationship between heterotrophic organisms and viruses on the East Siberian Sea shelf. *Oceanology* 61 (2), 220–232. doi: 10.1134/S0001437021020089

Kothawala, D. N., Murphy, K. R., Stedmon, C. A., Weyhenmeyer, G. A., and Tranvik, L. J. (2013). Inner filter correction of dissolved organic matter fluorescence. *Limnol. Oceanogr.: Methods* 11 (12), 616–630. doi: 10.4319/lom.2013.11.616

Kowalczuk, P., Tilstone, G. H., Zabłocka, M., Röttgers, R., and Thomas, R. (2013). Composition of dissolved organic matter along an Atlantic meridional transect from fluorescence spectroscopy and parallel factor analysis. *Mar. Chem.* 157, 170–184. doi: 10.1016/j.marchem.2013.10.004

Krylov, I. N., Drozdova, A. N., and Labutin, T. A. (2020). Albatross r package to study PARAFAC components of DOM fluorescence from mixing zones of arctic shelf seas. *Chemom. Intelligent Lab. Syst.* 207, 104176. doi: 10.1016/j.chemolab.2020.104176

Lakowicz, J. R. (2013). *Principles of fluorescence spectroscopy* (Berlin, Germany: Springer science & business media).

Lee, S.-A., and Kim, G. (2018). Sources, fluxes, and behaviors of fluorescent dissolved organic matter (FDOM) in the nakdong river estuary, Korea. *Biogeosciences* 15 (4), 1115–1122. doi: 10.5194/bg-15-1115-2018

Mann, P., Davydova, A., Zimov, N., Spencer, R. G., Davydov, S., Bulygina, E., et al. (2012). Controls on the composition and lability of dissolved organic matter in siberia's kolyma river basin. *J. Geophys. Research: Biogeosci.* 117 (G1), G01028. doi: 10.1029/2011JG001798

Mann, P. J., Spencer, R. G. M., Hernes, P. J., Six, J., Aiken, G. R., Tank, S. E., et al. (2016). Pan-Arctic trends in terrestrial dissolved organic matter from optical measurements. *Front. Earth Sci.* 4, 25. doi: 10.3389/feart.2016.00025

McKnight, D. M., Boyer, E. W., Westerhoff, P. K., Doran, P. T., Kulbe, T., and Andersen, D. T. (2001). Spectrofluorometric characterization of dissolved organic matter for indication of precursor organic material and aromaticity. *Limnol. Oceanogr.* 46 (1), 38–48. doi: 10.4319/lo.2001.46.1.0038

Middelboe, M., and Jørgensen, N. O. (2006). Viral lysis of bacteria: an important source of dissolved amino acids and cell wall compounds. *J. Mar. Biol. Assoc. United Kingdom* 86 (3), 605–612. doi: 10.1017/S0025315406013518

Murphy, K. R., Hambly, A., Singh, S., Henderson, R. K., Baker, A., Stuetz, R., et al. (2011). Organic matter fluorescence in municipal water recycling schemes: toward a unified PARAFAC model. *Environ. Sci. Technol.* 45 (7), 2909–2916. doi: 10.1021/es103015e

Murphy, K. R., Stedmon, C. A., Wenig, P., and Bro, R. (2014). OpenFluor–an online spectral library of auto-fluorescence by organic compounds in the environment. *Anal. Methods* 6 (3), 658–661. doi: 10.1039/C3AY41935E

Osadchiev, A., Medvedev, I., Shchuka, S., Kulikov, M., Spivak, E., Pisareva, M., et al. (2020). Influence of estuarine tidal mixing on structure and spatial scales of large river plumes. *Ocean Sci.* 16 (4), 781–798. doi: 10.5194/os-16-781-2020

Oziel, L., Sirven, J., and Gascard, J.-C. (2016). The barents Sea frontal zones and water masses variability (1980–2011). *Ocean Sci.* 12 (1), 169–184. doi: 10.5194/os-12-169-2016

Painter, S. C., Lapworth, D. J., Woodward, E. M. S., Kroeger, S., Evans, C. D., Mayor, D. J., et al. (2018). Terrestrial dissolved organic matter distribution in the north Sea. *Sci. Total Environ.* 630, 630–647. doi: 10.1016/j.scitotenv.2018.02.237

Pavlov, V. K., Timohov, L. A., Baskakov, G. A., Kulakov, M. Y., Kurazhov, V. K., Pavlov, P. V., et al. (1994) *Hydrometeorological Regime of the Kara, Laptev and East-Siberian Seas*. (St Petersburg: The Arctic and Antarctic Research Institute) 179.

Rao, C. R. (1964). The use and interpretation of principal component analysis in applied research. *Sankhyā: Indian J. Statistics Ser. A* 26, 329–358.

Raymond, P. A., McClelland, J., Holmes, R., Zhulidov, A., Mull, K., Peterson, B., et al. (2007). Flux and age of dissolved organic carbon exported to the Arctic ocean: A carbon isotopic study of the five largest arctic rivers. *Global Biogeochemical Cycles* 21 (4), GB4011. doi: 10.1029/2007GB002934

Romankevich, E. A., Vetrov, A. A., and Peresypkin, V. I. (2009). Organic matter of the world ocean. *Russian Geology Geophys.* 50 (4), 299–307. doi: 10.1016/j.rgg.2009.03.013

Romera-Castillo, C., Sarmento, H., Álvarez-Salgado, X. A., Gasol, J. M., and Marrasé, C. (2011). Net production and consumption of fluorescent colored dissolved organic matter by natural bacterial assemblages growing on marine phytoplankton exudates. *Appl. Environ. Microbiol.* 77 (21), 7490–7498. doi: 10.1128/AEM.00200-11

Savel'eva, N., Semiletov, I., and Pipko, I. (2008). Impact of synoptic processes and river discharge on the thermohaline structure in the East Siberian Sea shelf. *Russian Meteorol. Hydrol.* 33 (4), 240–246. doi: 10.3103/S1068373908040079

Savun-Hekimoğlu, B., and Gazioğlu, C. (2021). Mucilage problem in the semi-enclosed seas: recent outbreak in the Sea of marmara. *Int. J. Environ. Geoinformatics* 8 (4), 402–413. doi: 10.30897/ijegeo.955739

Schlitzer, R. (2020). Ocean data view. *http://odv.awi.de*.

Schuur, E. A., Bockheim, J., Canadell, J. G., Euskirchen, E., Field, C. B., Goryachkin, S. V., et al. (2008). Vulnerability of permafrost carbon to climate change: Implications for the global carbon cycle. *BioScience* 58 (8), 701–714. doi: 10.1641/B580807

Semiletov, I., Dudarev, O., Luchin, V., Charkin, A., Shin, K. H., and Tanaka, N. (2005). The East Siberian Sea as a transition zone between pacific-derived waters and Arctic shelf waters. *Geophys. Res. Lett.* 32 (10), L10614 . doi: 10.1029/2005GL022490

Spencer, R. G. M., Aiken, G. R., Butler, K. D., Dornblaser, M. M., Striegl, R. G., and Hernes, P. J. (2009). Utilizing chromophoric dissolved organic matter measurements to derive export and reactivity of dissolved organic carbon exported to the Arctic ocean: A case study of the Yukon river, Alaska. *Geophys. Res. Lett.* 36 (6), L06401. doi: 10.1029/2008GL036831

Stedmon, C. A., Amon, R. M. W., Rinehart, A. J., and Walker, S. A. (2011). The supply and characteristics of colored dissolved organic matter (CDOM) in the Arctic ocean: Pan Arctic trends and differences. *Mar. Chem.* 124 (1-4), 108–118. doi: 10.1016/j.marchem.2010.12.007

Stedmon, C. A., Markager, S., and Bro, R. (2003). Tracing dissolved organic matter in aquatic environments using a new approach to fluorescence spectroscopy. *Mar. Chem.* 82 (3-4), 239–254. doi: 10.1016/S0304-4203(03)00072-0

Stedmon, C. A., Markager, S., and Kaas, H. (2000). Optical properties and signatures of chromophoric dissolved organic matter (CDOM) in Danish coastal waters. *Estuarine Coast. Shelf Sci.* 51 (2), 267–278. doi: 10.1006/ecss.2000.0645

Stedmon, C. A., and Nelson, N. B. (2015). ""The optical properties of DOM in the ocean,"," in *Biogeochemistry of Marine Dissolved Organic Matter*, (Elsevier), eds D. A. Hansell and C. A. Carlson (San Diego, CA: Elsevier Inc.), 481–508.

R. Stein and R. W. Macdonald (eds.). (2004). *The organic carbon cycle in the Arctic Ocean*. (Berlin; Heidelberg: Springer). doi: 10.1007/978-3-642-18912-8

Sukhanova, I., Flint, M., Fedodov, A., Sakharova, E., Makkaveev, P., Polukhin, A., et al. (2021). First data on the structure of phytoplankton communities of the East Siberian Sea. *Oceanology* 61 (6), 909–929. doi: 10.1134/S0001437021060151

Sun, Q., Wang, C., Wang, P., Hou, J., and Ao, Y. (2014). Absorption and fluorescence characteristics of chromophoric dissolved organic matter in the Yangtze estuary. *Environ. Sci. pollut. Res.* 21 (5), 3460–3473. doi: 10.1007/s11356-013-2287-4

Vetrov, A. A., and Romankevich, E. A. (2010). *Carbon cycle in the Russian Arctic Seas*. (Berlin; Heidelberg: Springer-Verlag).

Vignudelli, S., Santinelli, C., Murru, E., Nannicini, L., and Seritti, A. (2004). Distributions of dissolved organic carbon (DOC) and chromophoric dissolved organic matter (CDOM) in coastal waters of the northern tyrrhenian Sea (Italy). *Estuarine Coast. Shelf Sci.* 60 (1), 133–149. doi: 10.1016/j.ecss.2003.11.023

Vonk, J. E., Sánchez-García, L., Van Dongen, B., Alling, V., Kosmach, D., Charkin, A., et al. (2012). Activation of old carbon by erosion of coastal and subsea permafrost in Arctic Siberia. *Nature* 489 (7414), 137–140. doi: 10.1038/nature11392

Walker, S. A., Amon, R. M., Stedmon, C., Duan, S., and Louchouarn, P. (2009). The use of PARAFAC modeling to trace terrestrial dissolved organic matter and fingerprint water masses in coastal Canadian Arctic surface waters. *Journal of Geophysical Research: Biogeosciences* 114(G4). doi: 10.1029/2009JG000990

Walker, S. A., Amon, R. M. W., and Stedmon, C. A. (2013). Variations in high-latitude riverine fluorescent dissolved organic matter: A comparison of large Arctic rivers. *J. Geophys. Research: Biogeosci.* 118 (4), 1689–1702. doi: 10.1002/2013JG002320

Wassmann, P., Bauerfeind, E., Fortier, M., Fukuchi, M., Hargrave, B., Moran, B., et al. (2004). "Particulate organic carbon flux to the Arctic Ocean sea floor," in *The organic carbon cycle in the Arctic Ocean*. Springer), 101–138. doi: 10.1007/978-3-642-18912-8_5

Weishaar, J. L., Aiken, G. R., Bergamaschi, B. A., Fram, M. S., Fujii, R., and Mopper, K. (2003). Evaluation of specific ultraviolet absorbance as an indicator of the chemical composition and reactivity of dissolved organic carbon. *Environ. Sci. Technol.* 37 (20), 4702–4708. doi: 10.1021/es030360x

Wilson, H. F., and Xenopoulos, M. A. (2009). Effects of agricultural land use on the composition of fluvial dissolved organic matter. *Nat. Geosci.* 2 (1), 37–41. doi: 10.1038/ngeo391

Wohlers, J., Engel, A., Zöllner, E., Breithaupt, P., Jürgens, K., Hoppe, H.-G., et al. (2009). Changes in biogenic carbon flow in response to sea surface warming. *Proc. Natl. Acad. Sci.* 106 (17), 7067–7072. doi: 10.1073/pnas.0812743106

Yamashita, Y., and Jaffé, R. (2008). Characterizing the interactions between trace metals and dissolved organic matter using excitation– emission matrix and parallel factor analysis. *Environ. Sci. Technol.* 42 (19), 7374–7379. doi: 10.1021/es801357h

Yamashita, Y., and Tanoue, E. (2003). Chemical characterization of protein-like fluorophores in DOM in relation to aromatic amino acids. *Mar. Chem.* 82 (3-4), 255–271. doi: 10.1016/S0304-4203(03)00073-2

Yamashita, Y., and Tanoue, E. (2008). Production of bio-refractory fluorescent dissolved organic matter in the ocean interior. *Nat. Geosci.* 1 (9), 579–582. doi: 10.1038/ngeo279

Zsolnay, A., Baigar, E., Jimenez, M., Steinweg, B., and Saccomandi, F. (1999). Differentiating with fluorescence spectroscopy the sources of dissolved organic matter in soils subjected to drying. *Chemosphere* 38 (1), 45–50. doi: 10.1016/S0045-6535(98)00166-0

frontiers | Frontiers in Marine Science

TYPE Original Research
PUBLISHED 13 September 2022
DOI 10.3389/fmars.2022.875362

Check for updates

OPEN ACCESS

EDITED BY
Wei-Jen Chen,
National Taiwan University, Taiwan

REVIEWED BY
Stella Psarra,
Hellenic Centre for Marine Research (HCMR), Greece
Monique Messié,
Monterey Bay Aquarium Research Institute (MBARI), United States

*CORRESPONDENCE
Hideki Fukuda
hfukuda@aori.u-tokyo.ac.jp

SPECIALTY SECTION
This article was submitted to Coastal Ocean Processes, a section of the journal Frontiers in Marine Science

RECEIVED 14 February 2022
ACCEPTED 19 August 2022
PUBLISHED 13 September 2022

CITATION
Fukuda H, Hidaka K, Setou T, Kusaka A, Ambe D and Saito H (2022) Temporal and regional variabilities in the attenuation of sinking particulate organic carbon in the Kuroshio region. *Front. Mar. Sci.* 9:875362. doi: 10.3389/fmars.2022.875362

COPYRIGHT
© 2022 Fukuda, Hidaka, Setou, Kusaka, Ambe and Saito. This is an open-access article distributed under the terms of the Creative Commons Attribution License (CC BY). The use, distribution or reproduction in other forums is permitted, provided the original author(s) and the copyright owner(s) are credited and that the original publication in this journal is cited, in accordance with accepted academic practice. No use, distribution or reproduction is permitted which does not comply with these terms.

Temporal and regional variabilities in the attenuation of sinking particulate organic carbon in the Kuroshio region

Hideki Fukuda[1]*, Kiyotaka Hidaka[2], Takashi Setou[2], Akira Kusaka[2], Daisuke Ambe[2] and Hiroaki Saito[1]

[1]Atmosphere and Ocean Research Institute, University of Tokyo, Chiba, Japan, [2]Fisheries Resources Institute, Japan Fisheries Research and Education Agency, Kanagawa, Japan

The biological pump that transports carbon from the surface ocean to the ocean interior is an important determinant of ocean carbon absorption from the atmosphere, and of biological activity beneath the euphotic zone. Various factors influence the magnitude and efficiency of this biological pump, such as primary production, particle size, and the composition of consumers of particulate organic carbon (POC). The complex factors influencing the biological pump induce high regional and temporal variability; however, the mechanisms of this variability are not understood and its causes remain unclear. The size of sinking particles has been hypothesized to affect the attenuation of POC flux *via* reduction of residence time within the water column. Here, we conducted sediment trap experiments in slope and subtropical gyre areas along the Kuroshio in the subtropical North Pacific. The ratio of POC flux at a depth 100 m below the base of the euphotic zone to that at the base of the euphotic zone (T_{100}) varied from 0.307 to 0.646 and from 0.090 to 0.958 in the slope and subtropical gyre areas, respectively, and was positively correlated with variations in the volume-weighted mean particle diameter (Spearman rank order correlation coefficient: 0.700, $p < 0.05$, n = 9). However, the variation in T_{100} was not correlated with ambient water temperature ($p > 0.05$). The results support the hypothesis that attenuation of POC flux is influenced by the size of sinking particles in oligotrophic oceanic areas.

KEYWORDS

ocean carbon cycling, biological pump, sinking POC flux, sediment trap, slope of particle size distribution, Kuroshio

Introduction

The biological pump is the combined processes of the biological fixation of carbon dioxide and its subsequent transport into the ocean interior. The transport of fixed carbon occurs through multiple processes, including 1) the gravitational settling of particles, 2) physical injection, and 3) vertical migration of organisms, with sinking of particulate carbon accounting for the largest portion of transported carbon in three processes (Boyd et al., 2019). The amount of carbon sinking from the euphotic zone depends primarily on the amount of net primary production and partly on the size and taxonomic composition of phytoplankton and heterotrophic activities (Boyd and Newton, 1999; Armstrong et al., 2002; Guidi et al., 2009; Turner, 2015). Most particulate organic carbon (POC) settling out of the euphotic zone is remineralized within the upper part of the mesopelagic zone (depths below the euphotic zone down to 1000m), and the attenuation of sinking flux shows large seasonal and regional variabilities (Guidi et al., 2015; Puigcorbé et al., 2015; Buesseler et al., 2020). Understanding the mechanisms regulating particle production and attenuation of sinking flux is essential to predicting future changes in ocean carbon uptake and food web dynamics below the euphotic zone as well as oceanic carbon dioxide influx from the atmosphere.

The vertical attenuation of POC flux has been examined from the perspective of the relationship between particle residence time within the water column and the remineralization rate of POC. Analyses of field data have indicated a close relationship between the attenuation depth scale of POC flux and the size structure of phytoplankton in the euphotic zone (Guidi et al., 2015; Puigcorbé et al., 2015). Numerical models have demonstrated that the size of sinking particles could be a major factor determining the mineralization depth of sinking POC because the sinking velocity increases with particle size (Cram et al., 2018; Omand et al., 2020). Marsay et al. (2015) showed a strong relationship between the attenuation depth of POC flux and ambient water temperature, which can affect the activities of heterotrophs including prokaryotes, protozoans, and metazoans.

In the subtropical offshore area, vertical attenuation of POC flux is thought to be greater than that at higher latitudes, as small phytoplankton (pico- and nanophytoplankton) are a major component of the primary producer assemblage and have a slow sinking rate due to their small size (Guidi et al., 2015; Puigcorbé et al., 2015; Cram et al., 2018). However, these small phytoplankton are actively incorporated into fast-sinking materials such as large aggregates and fecal materials in oligotrophic environments (Gorsky et al., 1999; Lomas and Moran, 2011; Lundgreen et al., 2019). Several studies in subtropical areas have reported that the particle size distribution (PSD) in the mixed layer exhibits spatial and temporal variations (Buonassissi and Dierssen, 2010; White et al., 2015; Fender et al., 2019). Yamada et al. (2021) reported that the contribution of larger particles increased with the concentration of transparent exopolymer (TEP) particles in an oligotrophic area along the Kuroshio Current in the subtropical Pacific Ocean. The porous structure and sticky nature of TEP stimulate rapid accumulation of large aggregates (Passow, 2002; Mari et al., 2017; Nagata et al., 2021). These results imply that high variability in the PSD in a subtropical area may affect attenuation of POC flux in combination with various factors, including temperature, the community structure of organisms, their physiological state, and the physicochemical properties of the particles.

We collected data on the sinking flux of POC and its vertical attenuation between the base of the euphotic zone (Z_{eu}; notations are listed in Table 1) and a depth 100 m below Z_{eu} during a sediment trap experiment along the Kuroshio Current. The Kuroshio Current is the western boundary current in the North Pacific Ocean, and it flows through an oligotrophic area where pico- and nanophytoplankton are dominant (Endo and Suzuki, 2019). However, strong diapycnal mixing processes induce upward nutrient supply along the inshore side of the current, supporting high phytoplankton productivity in this region (Kaneko et al., 2013; Nagai et al., 2019). The trap experiments were conducted in two areas along a productivity gradient across the current (Yokouchi et al., 2006). To compare the depth scale of the attenuation of POC flux among our observations and those in other environments, T_{100} can be used an index of attenuation of POC flux; it represents the ratio of POC flux at 100 m below Z_{eu} to flux at Z_{eu} (Buesseler and Boyd, 2009; Buesseler et al., 2020). Simultaneously, PSD data were collected using a laser diffraction analyzer in the euphotic zone to examine the relationship between T_{100} and PSD. We hypothesized that T_{100} is influenced by multiple environmental factors, including the shape of the PSD and the physicochemical properties of the particles.

Materials and methods

Study area and sampling period

Sediment trap experiments were conducted in two areas across the Kuroshio Current along 138°E (Figure 1), designated the slope (34.0°N 138.0°E) and subtropical gyre (28.0–31.5°N 138°E), located on the offshore side of the Kuroshio Current. Experiments were conducted at 10 time points during seven cruises aboard the FRV *Soyo-Maru* (Japan Fisheries Research and Education Agency) from August 2013 to November 2019 as part of the O-line Ocean monitoring program at 138°E off Japan (Sugisaki et al., 2010) (Table 2). Because the axis of the Kuroshio Current was at different locations on different cruises, the

10.3389/fmars.2022.875362

TABLE 1 Notations.

Symbol	Meaning	unit
D	Particle diameter	µm
D_0	Reference diameter (1 µm)	µm
diChl *a*	Depth-integrated amount of chlorophyll *a* within the euphotic layer	mg m^{-2}
diN+N	Depth-integrated amount of nitrate and nitrite within the euphotic layer	mmol m^{-2}
diPOC	Depth-integrated amount of particulate organic carbon within the euphotic layer	g m^{-2}
diPON	Depth-integrated amount of particulate organic nitrogen within the euphotic layer	g m^{-2}
diTPV	Depth-integrated total volume of particulate (5.2-119 µm in diameter) within the euphotic layer	10^{-6} m^3 m^{-2}
dmChl *a*	Depth-weighted concentration of chlorophyll *a* within the euphotic layer	µg L^{-1}
dmN+N	Depth-weighted concentration of nitrate and nitrite within the euphotic layer	µM
dmPOC	Depth-weighted concentration of particulate organic carbon within the euphotic layer	µg L^{-1}
dmPON	Depth-weighted concentration of particulate organic nitrogen within the euphotic layer	µg L^{-1}
dmTPV	Depth-weighted total volume of particulate (5.2-119 µm in diameter) per volume of seawater within the euphotic layer	ppm
F_0	Sinking flux of particulate organic carbon at the depth of the reference depth (z_0)	mg m^{-2} d^{-1}
F_z	Sinking flux of particulate organic carbon at the depth of z	mg m^{-2} d^{-1}
g	Gravitational acceleration	m s^{-2}
k	Rate of decomposition of sinking particulate organic carbon, including bacterial decomposition and zooplankton grazing	s^{-1}
k_0	Rate of decomposition of sinking particulate organic carbon, including bacterial decomposition and zooplankton grazing at the reference temperature	s^{-1}
MLD	Mixed layer depth	m
mPD_N	Mean particle diameter based on the particle size distribution (number)	µm
mPD_V	Mean particle diameter based on the particle size distribution (volume)	µm
N	Number of particles per volume of seawater normalized to the width of the size bin	particle L^{-1} $µm^{-1}$
N_0	Number of particles per volume of seawater normalized to the width of the size bin at the reference diameter (1 µm)	particle L^{-1} $µm^{-1}$
POC/PON	Molar ratio of the concentration of particulate organic carbon to that of particulate organic nitrogen	–
SST	Sea surface temperature	°C
T	Water temperature	°C
T_0	Reference water temperature	°C
T_{100}	Ratio of POC flux 100 m below the base of euphotic zone to that at the base of the euphotic zone	–
TPV	Volume of particles per volume of seawater as an integral across the whole size window (5.2-119 µm)	ppm
w	Sinking rate of particle	m s^{-1}
z	Depth in the water column	m
z_0	Reference depth	m
Z_{eu}	Base of the euphotic zone	m
γ	Power-law exponent relating the particle sinking rate and particle diameter	–
$\Delta\rho$	Density difference between the particle and seawater	kg m^{-3}
μ	Viscosity of seawater	kg m^{-1} s^{-1}
ξ	Power-law slope of the particle size distribution	–

sampling site on the offshore side of the axis was placed depending on the location of the axis position (Table 2). Experiments on the slope were conducted in January, March, August, and November, but no sample was collected in January in the subtropical gyre due to bad weather during the SY1601 and SY1801 cruises.

Sediment trap

The sediment traps used in this study were Knauer type, surface-tethered drifting sediment traps (Knauer et al., 1979). The trap array included surface floats to dampen vertical displacement caused by waves and sediment trap cross-pieces

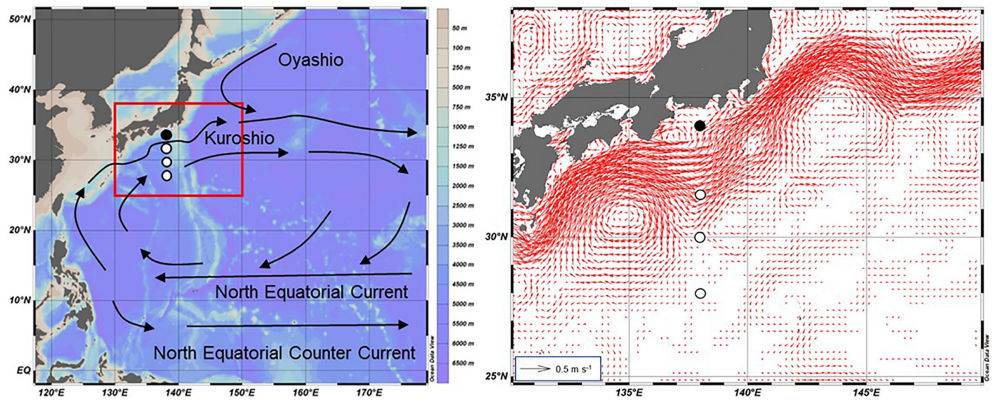

FIGURE 1
Sampling locations and main ocean currents in the western North Pacific (left). Sediment trap experiments were conducted shoreward (slope: closed circle) and on the oceanic side (subtropical gyre: open circles) of the Kuroshio Current. Right panel corresponds to the area indicated with red square in the left panel. Red arrows in the right panel indicate the mean surface geostrophic current calculated from daily surface geostrophic current data with a horizontal resolution of 0.25° from 1 August 2013 to 30 November 2019 (EU Copernicus Marine Service: https://www.marine.copernicus.eu). Detailed information about each station and the location of the Kuroshio Current axis relative to 138°E during each sampling period are provided in Table 2. The map was drawn using Ocean Data View (http://odv.awi.de/).

holding eight transparent acrylic cylinders at two depths. The collection area and aspect ratio of the cylinder were approximately 0.0037 m^2 and 8.27 (length, 620 mm; width 75 mm), respectively, except for the SY1308 cruise in which wider cylinders were used (0.0048 m^2 and 6.18 [length, 618 mm; width 100 mm]). The volume of the collection cup was 295 and 548 mL for the narrow and wide cylinders, respectively. The shallower depth was at Z_{eu}, and the deeper depth was at 100 m below Z_{eu}. Z_{eu} was determined as the depth of 1% photosynthetically active radiation based on direct measurement using the PRR-2600 Profiling Reflectance Radiometer (Biospherical Instruments) during each deployment (Table 2). In several cases, the upper sediment trap was deployed within the surface mixed layer (Table 2). Sediment traps within the surface mixed layer have been reported to under- and over-collect sinking particles (White, 1990; Gardner, 2000; Owens et al., 2013). In those cases, the sinking flux of particles and T_{100} value should be treated with caution.

Before deployment, each cylinder was filled with 0.2-μm-filtered seawater collected from the surface after adding of 5 g L^{-1}

TABLE 2 Locations of sampling sites and oceanographic settling during the drifting sediment trap experiment.

Area	Cruise ID	Latitude (°N)	Longitude (°E)	Bottom depth (m)	Deployment (mm/dd/yyyy)	Sampling period (h)	Latitude of the Kuroshio axis at 138°E (°N)	MLD[a] (m)	$Z^b_{eu}(m)$	SST[c] (°C)	Concentration of N+N at the surface[d] (μM)
Slope	SY1308	34.0	138.0	1760	08/27/2018	23.9	32.1	10	54	29.0	<0.1
	SY1601	34.0	138.0	1760	01/21/2016	24.5	33.1	99	75	16.0	6.2
	SY1703	34.0	138.0	1760	03/08/2017	23.8	32.6	97	65	15.2	7.5
	SY1801	34.0	138.0	1760	01/12/2018	23.0	30.8	84	65	17.3	3.9
	SY1903	34.0	138.0	1760	03/05/2019	24.1	33.7	12	89	20.0	0.4
	SY1911	34.0	138.0	1760	11/17/2019	24.2	31.3	56	73	23.4	0.2
Subtropical gyre	SY1308	30.0	138.0	4040	09/01/2013	24.2	32.1	11	71	29.6	<0.1
	SY1703	31.5	138.0	3950	03/11/2017	24.2	32.6	28	69	19.0	0.5
	SY1904	28.0	138.0	4110	04/20/2019	24.0	30.0	12	100	21.6	<0.1
	SY1911	30.0	138.0	4040	11/18/2019	24.4	31.3	89	87	24.9	<0.1

a: The mixed-layer depth (MLD) is determined based on a 0.03 unit σθ criterion from that of a near-surface value at the 10 m depth.
b: The base of the euphotic zone (Z_{eu}) is determined based on 1% penetration of photosynthetically available radiation (PAR) from that of the surface water.
c: SST is the water temperature at the surface.
d: N+N is the sum of nitrate and nitrite.

pre-combusted NaCl (450°C, 3 h). The trap array was deployed for approximately 24 h beginning at 12 PM or 4 PM. After recovery, the sediment traps were left undisturbed onboard for 1–2 h to allow particles to settle to the bottom of the cylinder. The settling time was to allow most sinking particles to settle to the bottom and to minimize biological decomposition of sinking particles especially for small particles with high surface-to-volume ratio after recovery. Before removing the collection cup at the bottom of the cylinder, supernatant seawater in the cylinder was siphoned off. A portion of the slow-sinking-particles, which were resuspended above the collecting cup during the trap recovery, might be removed with the supernatant seawater resulting in underestimation of sinking flux. Sinking particles in the collection cup were collected on pre-combusted (3 h at 450°C) GF/F filters (Whatman). The GF/F filters were wrapped in aluminum foil and stored in a freezer (<-20°C) until analysis of POC and particulate organic nitrogen (PON) in a land-based facility.

Water sampling and determination of environmental variables

Seawater samples were collected using 2.5- or 12- L Niskin bottles (GO-1010X; General Oceanics) mounted on a conductivity–temperature–depth carousel multi-sampling system (SBE 911plus, Sea-bird Scientific). Surface water (0 m) was collected using a plastic bucket. The depth of the surface mixed layer (MLD) was determined based on a density threshold value relative to the near-surface value at 10 m depth ($\Delta\sigma\theta$ = 0.03 kg m^{-3}) (de Boyer Montegut et al., 2004).

Samples collected for obtaining discrete vertical profiles of the concentrations of summed nitrate and nitrite (N+N), chlorophyll *a* (Chl *a*), POC, and PON were collected from the water column within the euphotic zone. Samples for determination of N+N were stored at< −20°C until measurement in a land-based facility. Suspended particles in 200 mL and 10 L seawater were collected on a GF/F filter for determination of the concentrations of Chl *a* and particulate organic matter, respectively. GF/F filters for determination of the Chl *a* concentration were immersed in *N*, *N*-dimethylformamide (Suzuki and Ishimaru, 1990) immediately after filtration and then stored at< −20°C in the dark until measurement on land. GF/F filters for POC and PON were treated using the same method as for the trap samples.

In situ observation of the particle size distribution and calculation of its slope

The particle volume and PSD were measured at depths of 10 and 50 m using an *in situ* laser diffraction sizer (LISST-100X, Sequoia Scientific), except on the SY1904 cruise. The LISST-100X measures light scattered by particles using 32 concentric, logarithmically spaced ring detectors. The volumetric particle concentration in each size class is estimated by inversion modeling based on Mie theory (Agrawal and Pottsmith, 2000). To minimize overestimation in the upper size bins driven by salinity fluctuation (Styles, 2006) and underestimation in the lower size bins due to low particulate concentrations or high ambient light conditions (Andrews et al., 2011), we used a size class range of 5.2–119 µm (20 LISST bins) (Yamada et al., 2015; Yamada et al., 2021). The LISST-100X was mounted on a winch wire with a protective frame, and the volume of particles at a given depth was measured for 10 min at a 1-s measurement interval (totaling 600 counts).

Total particle volume (TPV, ppm) was calculated as an integral across the whole size window (5.2–119 µm). Volumetric size distribution data were used to calculate the PSD in numerical terms, assuming that particles are spheres. Then, the numerical PSD was determined using the following power-law equation (Bader, 1970; Kostadinov et al., 2009; Buonassissi and Dierssen, 2010; Yamada et al., 2015; Yamada et al., 2021):

$$N(D) = N_0 \left(\frac{D}{D_0}\right)^{\xi} \quad (1)$$

where $N(D)$ is the number of particles per volume of seawater normalized to the width of the size bin (particles L^{-1} μm^{-1}). D is the particle diameter (µm). D_0 is the reference diameter (here 1 µm). N_0 is the particle differential number concentration at D_0 (particles L^{-1} μm^{-1}), and ξ is the power-law slope of the PSD. We conducted linear regression of log-transformed data for calculation of ξ and N_0.

Chemical analysis

The concentration of N+N was determined using a flow injection analyzer (TrAAcs 2000, Bran+Luebbe) (details in Kodama et al., 2014). The detection limit for determination was 0.1 µM. The reproducibility of seawater measurements had a coefficient of variation of< 3% at an N+N concentration of 15.25 µM (n = 19). The nutrient concentrations were determined using commercially available nutrient standards: the CSK nutrient standard (Wako) and the Reference Material for Nutrients in Seawater (KANSO). Any concentration below the detection limit was set to 0.1 µM for statistical analysis.

The Chl *a* concentration was measured using a fluorometer (10-AU, Turner Designs) (Welschmeyer, 1994). For measurements of POC and PON, particles retained on GF/F filters were fumed with HCl mist for at least 24 h in a plastic container to remove $CaCO_3$. The total amounts of organic carbon and nitrogen were determined using an elemental

analyzer (Elemental Analyzer-IRMS (FLASH 2000, Thermo Fisher Scientific).

Mathematical processing and statistical analysis

Depth-integrated values of Chl *a*, POC, PON, and TPV were calculated from discrete vertical profiles using the trapezoidal integration method. The resolution of discrete vertical profile data differed among variables (Tables S1–S3). Depth-weighted mean values of variables within the euphotic zone were calculated *via* division of the depth-integrated value by the thickness of the euphotic zone.

To examine correlations between variables, Spearman rank order correlation analysis was performed, as the normality assumption was not fulfilled for some variables. For the same reason, the Mann–Whitney rank sum test was used to compare outcomes between two groups. These statistical analyses and linear and non-linear regression analyses were performed using SigmaPlot 14.0 (Systat Software).

Results

As the scope of this study is to examine the mechanisms controlling temporal- and spatial-variations in the sinking flux of POC at Z_{eu} and T_{100}, depth-integration and averaging within the euphotic zone were conducted for data on chemical and biological variables to capture the major features of the euphotic zone by vertically homogenizing the variable ranges and differences among seasons (Tables S1–S3). Differences in vertical resolution among variables may introduce biases to the analysis of relationships among variables, and therefore we assumed that depth-integrated and depth-weighted mean values within the euphotic zone capture the regional and temporal variabilities of the features of the euphotic zone.

Physical environment and nutrient concentrations

Table 2 summarizes sea surface temperature (SST), MLD, Z_{eu}, and the surface (0 m) concentration of N+N, while the depth profiles of salinity, temperature, and density ($\sigma\theta$) are shown in Figures S1, S2. SST varied from 15.2°C to 29.0°C and from 19.0°C to 29.6°C in the slope and subtropical gyre areas, respectively, and SST tended to be higher in the subtropical gyre than on the slope during a given cruise. MLD increased with decreasing SST in both areas. N+N in the slope area became high during the mixing period, whereas N+N in the subtropical gyre was below the detection limit except in March 2017. Z_{eu} was less variable than MLD and showed no apparent coupling with variation in MLD, SST, or N+N. In three cases of trap deployment (01/21/2016, 03/08/2017 and 01/12/2018), the sediment trap at Z_{eu} was moored in the mixed layer (Table 2).

Depth-integrated values and concentrations of the sum of nitrate and nitrite, chlorophyll *a*, particulate organic carbon, and particulate organic nitrogen within the euphotic zone

The depth-integrated N+N within the euphotic zone (diN+N) varied from 100 to 490 mmol m^{-2} and 8.7 to 73 mmol m^{-2} in the slope and subtropical gyre areas, respectively (Table 3). diN+N and depth-weighted mean N+N (dmN+N) in the slope area were significantly higher than in the subtropical gyre (Mann–Whitney rank sum test, $p< 0.05$). The diN+N variation in the slope area showed a negative correlation with SST ($r_s = -0.886$, $p< 0.05$, n = 6), but there was no significant correlation between diN+N and SST in the subtropical gyre ($p > 0.05$, n = 4). Depth-integrated Chl *a* within the euphotic zone (diChl *a*) varied from 27.4 to 48.5 mg Chl *a* m^{-2} and from 12.1 to 28.0 mg Chl *a* m^{-2} in the slope and subtropical gyre areas, respectively (Table 3). The variation in diChl *a* in each area showed no significant correlation ($p > 0.05$) with SST or N+N, whereas the variation in diChl *a* in the entire dataset showed a negative correlation with that in SST ($r_s = -0.661$, $p< 0.05$, n = 10) and a positive correlation with that in N+N ($r_s = 0.806$, $p< 0.05$, n = 10), suggesting that the biomass of phytoplankton along 138°E was regulated by the availability of nutrients transported from the cold deeper layer (Table S5). diChl *a* was significantly higher on the slope than in the subtropical gyre (Mann–Whitney rank sum test, $p< 0.05$), and diChl *a* in the subtropical gyre showed greater variability than on the slope. The depth-weighted mean Chl *a* concentration within the euphotic zone (dmChl *a*) ranged from 0.403 to 0.647 μg Chl *a* L^{-1} and from 0.165 to 0.387 μg Chl *a* L^{-1} in the slope and subtropical gyre areas, respectively (Table 3). The variability in dmChl *a* was similar in magnitude to that in diChl *a*, and dmChl *a* was significantly higher on the slope than in the subtropical gyre (Mann–Whitney rank sum test, $p< 0.05$).

Contrasting Chl *a*, no significant difference in POC and PON between the slope and subtropical gyre were observed from depth-integrated values (diPOC and diPON, respectively) or depth-weighted mean values (dmPOC and dmPON, respectively) in the euphotic zone (Mann–Whitney rank sum test, $p > 0.05$; Table 3). Moreover, no significant correlations of diChl *a* with diPOC or diPON were observed within each area or in the entire dataset (Table S5). However, the mean ratios of POC/PON in the slope and subtropical gyre areas were

10.3389/fmars.2022.875362

TABLE 3 Depth-integrated amounts and depth-weighted mean concentrations of sum of nitrate and nitrite (N+N), chlorophyll *a* (Chl *a*), particulate organic carbon (POC) and nitrogen (PON), and total particle volume (TPV: 5.12 -119 μm in diameter) within the euphotic layer[a].

Area	Deployment (mm/dd/yyyy)	Depth-Integrated N+N(mmol m^{-2})	Depth-weighted mean N+N(μM)	Depth-Integrated Chl *a*(mg m^{-2})	Depth-weighted mean Chl *a*(μg L^{-1})
Slope	08/27/2018	140	2.6	27.4	0.507
	01/21/2016	470	6.3	48.5	0.647
	03/08/2017	490	7.5	37.3	0.574
	01/12/2018	250	3.8	30.1	0.463
	03/05/2019	350	3.9	35.9	0.403
	11/17/2019	100	1.4	39.4	0.540
	Mean ± SD	300 ± 160	4.3 ± 2.3	36.4 ± 7.5	0.522 ± 0.085
Subtropical gyre	09/01/2013	7.4	0.1	12.1	0.170
	03/11/2017	73	1.1	26.7	0.387
	04/20/2019	11	0.1	28.0	0.280
	11/18/2019	8.7	0.1	14.4	0.165
	Mean ± SD	25 ± 32	0.4 ± 0.5	20.3 ± 8.3	0.251 ± 0.105
Difference between two areas[b,c]		$p<0.05$	$p<0.05$	$p<0.05$	$p<0.05$

Area	Deployment (mm/dd/yyyy)	Depth-Integrated POC (g m^{-2})	Depth-weighted mean POC (μg L^{-1})	Depth-Integrated PON (g m^{-2})	Depth-weighted mean PON (μg L^{-1})	Depth-Integrated TPV ($10^{-6}m^3m^{-2}$)	Depth-weighted mean TPV (ppm)
Slope	08/27/2018	2.44	45.2	0.455	8.43	8.30	0.153
	01/21/2016	2.33	31.1	0.488	6.51	14.0	0.187
	03/08/2017	1.99	30.6	0.395	6.08	10.8	0.166
	01/12/2018	1.46	22.5	0.259	3.98	8.75	0.134
	03/05/2019	2.75	30.9	0.502	5.64	12.0	0.135
	11/17/2019	3.21	44.0	0.577	7.90	30.1	0.412
	Mean ± SD	2.36 ± 0.60	34.1 ± 8.8	0.446 ± 0.109	6.42 ± 1.61	14.0 ± 8.2	0.198 ± 0.107
Subtropical gyre	09/01/2013	1.88	26.5	0.358	5.04	7.16	0.101
	03/11/2017	2.36	34.2	0.476	6.90	21.2	0.307
	04/20/2019	–	–	–	–	–	–
	11/18/2019	1.58	18.2	0.256	2.94	12.8	0.147
	Mean ± SD	1.94 ± 0.39	26.3 ± 8.0	0.363 ± 0.110	4.96 ± 1.98	13.7 ± 7.1	0.185 ± 0.109
Difference between two areas[b,c]		N. S.	N. S.	N. S.	N. S.	N. S.	N. S.

a: See text for an explanation of the calculation of the integrated amounts using data in Tables S1–S3.
b: Differences in distribution among areas were tested using the Mann–Whitney rank sum test.
c: N.S. indicates insignificant difference ($p > 0.05$).

comparable with the Redfield ratio (C:N = 106:16), suggesting that plankton were a major component of the sampled particulate organic matter (Table 4).

Total particle volume, mean particle diameter, and slope of the particle size distribution

PSDs in terms of number and volume within the euphotic zone show temporal variabilities in both the slope and subtropical gyre areas (Figures 2, 3, S3, S4). In both areas, the PSD in number fitted well to Eq. (1), with determination coefficient values of 0.95–1.00 (Table 5). The slope (ξ) of PSD in number varied from −3.5 to −4.1 and from −3.5 and −4.8 in the slope and subtropical gyre areas, respectively, with no significant difference between two areas (Mann–Whitney rank sum test, $p > 0.05$). The variation in ξ is not reflected in the mean particle diameter based on the PSD in number (mPD_N), but rather in the mean particle diameter based on the volumetric PSD (mPD_V) (Tables 5, S5). mPD_V shows greater variability than mPD_N (Table 5), ranging from 37.2 to 56.7 μm and from 23.0 to 58.0 μm in the slope and subtropical

TABLE 4 Particle properties within the euphotic layer.

Area	Deployment (mm/dd/yyyy)	POC/PON (molar ratio)	Chl *a*/TPV (fg µm^{-3})	POC/TPV (fg µm^{-3})	PON/TPV (fg µm^{-3})
Slope	08/27/2018	6.26	3.30	294	54.8
	01/21/2016	5.57	3.47	166	34.9
	03/08/2017	5.88	3.45	184	36.6
	01/12/2018	6.58	3.43	167	29.6
	03/05/2019	6.39	2.99	229	41.8
	11/17/2019	6.49	1.31	107	19.2
	Mean ± SD	6.20 ± 0.39	2.99 ± 0.84	191 ± 64	36.2 ± 11.9
Subtropical gyre	09/01/2013	6.13	1.68	263	50.0
	03/11/2017	5.78	1.26	111	22.5
	04/20/2019	–	–	–	–
	11/18/2019	7.20	1.12	123	20.0
	Mean ± SD	6.37 ± 0.74	1.35 ± 0.29	166 ± 85	30.8 ± 16.6
Difference between two areas[a,b]		N. S.	p<0.05	N. S.	N. S.

a: Differences in distribution among areas were tested using the Mann–Whitney rank sum test.
b: N.S. indicates an insignificant difference ($p > 0.05$).

gyre areas, respectively. Similar to ξ, no significant difference in mPD_V between two areas was observed (Table 5). Depth-integrated TPV (diTPV) varied from 8.75 to 30.1 10^{-6} m^3 m^{-2} and from 7.16 to 21.2 10^{-6} m^3 m^{-2} in the slope and subtropical gyre areas, respectively, showing greater variability than diChl *a*, diPOC and diPON (Table 3).

Sinking fluxes of particulate organic carbon, particulate organic nitrogen, and T_{100}

The sinking flux of POC at Z_{eu} ranged from 51.9 to 235 mg m^{-2} d^{-1} and from 43.7 to 92.0 mg m^{-2} d^{-1} in the slope and subtropical

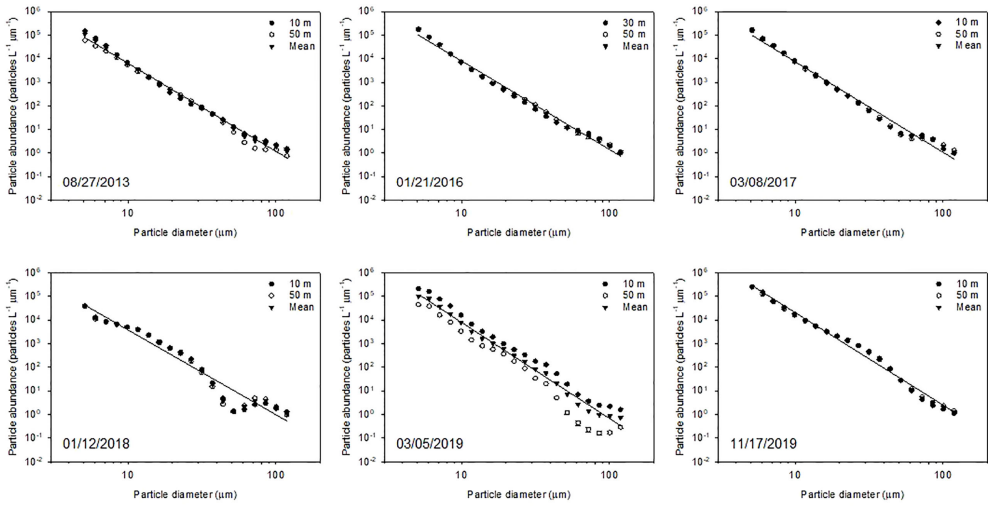

FIGURE 2
Particle size number distribution following the power-law model (Eq. 1) using double logarithmic transformation in the size range of 5.2–119 µm at depths of 10 and 50 m and averaged across the euphotic zone (see details in the main text) in the slope area. Error bars indicate standard error. The regression line was obtained using the ordinary least squares method for each sampling period. The statistical parameters of the regression are listed in Table 5.

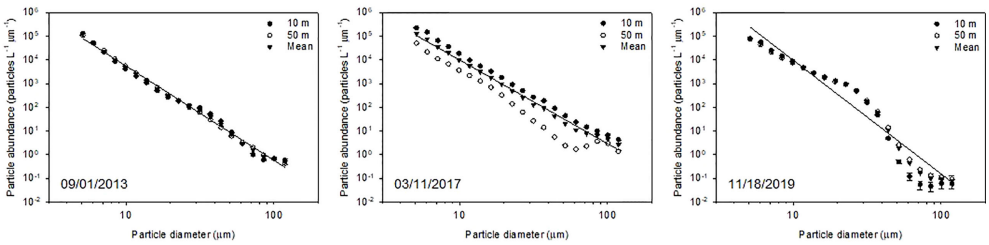

FIGURE 3
Particle size number distribution following the power-law model (Eq. 1) using double logarithmic transformation in the size range of 5.2–119 µm at depths of 10 and 50 m and averaged across the euphotic zone (see details in the main text) in the subtropical gyre area. Error bars indicate standard error. The regression line was obtained using the ordinary least squares method for each sampling period. The statistical parameters of the regression are listed in Table 5.

gyre areas, respectively (Figure 4), with no significant difference between areas (Table 6). At Z_{eu}, the variation in sinking flux of POC in the entire dataset was closely related to the sinking flux of PON (Figures 5A, S5; r_s= 0.648, p< 0.05, n = 10; Table S5) and showed increases during the cold period (Figure 5B; r_s= −0.624, p< 0.05, n = 10; Table S5) and with increasing diChl *a* (Figure 5C; r_s= 0.648, p< 0.05, n = 10; Table S5). However, the three correlations with the sinking flux of POC at Z_{eu} were not significant (p< 0.05) within each region, except for the correlation between the sinking flux of POC and that of PON in the slope area. The variations in sinking flux of

TABLE 5 Mean diameters of particles between 5.12 and 119 µm in diameter (mPD) and parameters of each regression line for the mean particle size distribution (PSD) in the euphotic layer[a].

Area	Deployment (mm/dd/yyyy)	mPD of number PSD (mPD_N: µm)[b]	mPD of volumetric PSD (mPD_V: µm)[b]	Slope (x)[c]	$LogN_0^c$	r^2	n[d]
Slope	08/27/2018	6.72 ± 3.75	51.9 ± 40.3	-3.7 ± 0.1	7.5 ± 0.1	0.99	20
	01/21/2016	6.64 ± 3.62	49.9 ± 38.8	-3.8 ± 0.1	7.7 ± 0.1	0.99	20
	03/08/2017	6.72 ± 3.50	50.4 ± 40.8	-3.8 ± 0.1	7.7 ± 0.1	0.99	20
	01/12/2018	8.69 ± 5.85	56.7 ± 40.8	-3.6 ± 0.2	7.2 ± 0.3	0.95	20
	03/05/2019	7.02 ± 3.64	38.4 ± 36.3	-4.1 ± 0.1	8.0 ± 0.1	0.99	20
	11/17/2019	7.44 ± 4.56	37.2 ± 30.6	-3.9 ± 0.1	8.2 ± 0.1	0.99	20
	Mean ± SD	7.21 ± 0.79	47.4 ± 7.84	-3.8 ± 0.2	7.7 ± 0.4		
Subtropical gyre	09/01/2013	6.51 ± 3.53	40.0 ± 35.9	-4.0 ± 0.1	7.7 ± 0.1	1.0	20
	03/11/2017	7.47 ± 4.91	58.6 ± 40.1	-3.5 ± 0.1	7.5 ± 0.1	0.99	20
	04/20/2019	–	–	–	–	–	–
	11/18/2019	7.91 ± 4.45	23.0 ± 15.7	-4.8 ± 0.2	8.8 ± 0.4	0.95	20
	Mean ± SD	7.30 ± 0.72	40.5 ± 17.8	-4.1 ± 0.7	8.0 ± 0.7		
Difference between two areas[e,f]		N. S.	N. S.	N. S.	N. S.		

a: See text for an explanation of the equation.
b: Values are the mean ± standard deviation except for the result of the Mann–Whitney rank sum test.
c: Values are the mean ± standard error except for the mean value of each area and the result of the Mann–Whitney rank sum test.
d: Number of size bins.
e: Differences in distribution among areas were tested using the Mann–Whitney rank sum test.
f: N.S. indicates insignificant difference (p > 0.05).

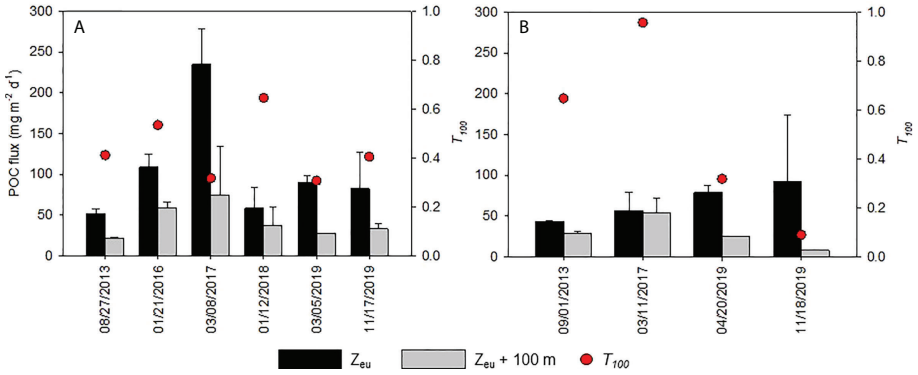

FIGURE 4
Fluxes of particulate organic carbon (POC) at the base of the euphotic zone (Z_{eu}) and at a depth of 100 m below Z_{eu}, as well as T_{100} during deployments in **(A)** the slope area and **(B)** the subtropical gyre area. Error bars indicate ranges or standard deviations (n = 2–3; see details in Table 6).

POC at Z_{eu} and diN+N were not correlated within each area and in the entire dataset (Table S5), despite a significant correlation between the sinking flux of PON at Z_{eu} and N+N in the entire dataset (Table S5).

The fluctuation in the sinking flux of POC at a depth of 100 m below Z_{eu} was not similar to that of sinking flux of POC at Z_{eu}, with T_{100} ranging from 0.307 to 0.646 and from 0.090 to 0.958 in the slope and subtropical gyre areas, respectively. Similar to the areal distribution of sinking flux of POC at Z_{eu}, the areal distribution of T_{100} showed no significant difference between areas (Table 6). Despite the significant correlation between the sinking flux of POC at Z_{eu} and SST, no significant correlation between T_{100} and SST was observed within each area or in the entire dataset (Figure 6A). In the entire dataset, T_{100} tended to decrease with increasing sinking flux of POC at Z_{eu} (Figure 6B; r_s= −0.661, p< 0.05, n = 10; Table S6), while it increased with increasing mPDV (Figure 6B; r_s= 0.700, p< 0.05, n = 9; Table S6) and ξ (Figure 6C; r_s= 0.695, p< 0.05, n = 9; Table S6). These three correlations with T_{100} were not significant (p< 0.05) within each region.

Discussion

Oceanographic settling and particle properties on the slope and in the subtropical gyre

The study sites on the slope and in the subtropical gyre were located on different sides of the eastward Kuroshio Current, and their physicochemical environments were affected by the current (Figure 1). The mean surface geostrophic current from 1 August 2013 to 30 November 2019 indicated that Kuroshio water was transported laterally into the surface of the slope area, and that a cyclonic eddy was located on the downstream side of the Kuroshio Current from the sampling sites in the subtropical gyre (28°N–32°N, 133°E–137°E). Because the location of the axis of the Kuroshio Current is unstable (Table 2), it is difficult to generalize the positional relation between sampling sites and the Kuroshio Current or eddies. The seasonal variation of Z_{eu} in the subtropical gyre is not obvious (Table 2). However, the deeper Z_{eu} in the subtropical gyre than on the slope is consistent with the difference in dmChl *a* between the two areas (Table 3). Z_{eu} in the slope area showed no apparent coupling with the variations in MLD, SST, or N+N at the surface (Table 2), even though the molar ratio of nutrients in the study area indicates that N+N is the potential limiting factor of primary production rather than phosphate or silicic acid (Kodama et al., 2014). The lower variability in diChl *a* and dmChl *a* than dmN+N on the slope implies that grazing on phytoplankton or diapycnal mixing with deeper water suppressed the accumulation of diChl *a* and dmChl *a*, resulting in low variability in Z_{eu} (Kaneko et al., 2013; Nagai et al., 2019).

Differences in the areal distributions of particle properties between the two areas were not statistically significant, except for Chl *a*/TPV (Table 4). Therefore, subsequent analyses of particle properties, sinking POC flux, and T_{100} were conducted using the entire dataset, followed by the evaluation of trends within each area. No significant correlation of diTPV with diChl *a*, diPOC, or diPON was observed (Table S5), implying that the chemical properties of particles (Chl *a*/TPV, POC/TPV, and PON/TPV) exhibited short-term fluctuations. Only Chl *a*/TPV showed a regional difference between the slope and subtropical gyre (Table 4). The variations in Chl *a*/TPV had significant positive correlations with Chl *a* (r_s = 0.783, p< 0.05, n = 9; Table S6), indicating that the volumetric contribution of non-

TABLE 6 The fluxes of particulate organic carbon (POC) and water temperature for each depth, T_{100} and mean water temperature.

		Trap deployed at Z_{eu}					Trap deployed at Z_{eu}+100 m					T_{100} (CF2/CF1)	Mean Temp. ((T1+T2)/2:°C)
Area	**Deployment (mm/dd/yyyy)**	**Depth (m)**	**Temp. (T1: °C)**	**POC flux(CF1: $mgm^{-2}d^{-1}$)[a]**	**POC/PON (molar ratio)**	**n**	**Depth (m)**	**Temp. (T2: °C)**	**POC flux(CF2: $mgm^{-2}d^{-1}$)[a]**	**POC/PON (molar ratio)**	**n**		
Slope	08/27/2018	60	18.5	51.9 ± 5.4	7.60	3	160	12.4	21.4 ± 2.0	10.4	3	0.412	15.5
	01/21/2016	80	16.0	109± 16	6.44	2	180	12.9	58.3 ± 8.0	10.6	2	0.535	14.4
	03/08/2017	70	15.1	235 ± 43	5.92	2	170	13.2	74.6 ± 60.4	6.68	2	0.317	14.2
	01/12/2018	70	17.3	58.4 ± 25.8	4.39	3	170	13.9	37.7 ± 21.8	7.26	3	0.646	15.6
	03/05/2019	90	16.6	90.3 ± 7.9	5.06	2	190	13.8	27.7 ± 0.0	7.13	2	0.307	15.2
	11/17/2019	80	19.1	82.5 ± 45.5	9.50	2	180	12.6	33.3 ± 6.0	7.04	2	0.405	15.8
	Mean ± SD			104 ± 67	6.49 ± 1.85	6			42.0 ± 20.0	8.19 ± 1.80	6	0.437 ± 0.130	15.1 ± 0.7
Subtropical gyre	09/01/2013	90	21.3	43.7 ± 0.5	10.0	2	190	18.6	28.3 ± 3.4	13.6	2	0.648	19.9
	03/11/2017	70	18.5	57.0 ± 21.9	5.13	2	170	18.3	54.6 ± 17.2	5.82	2	0.958	18.4
	04/20/2019	100	20.6	79.2 ± 8.5	5.02	2	200	19.4	25.3 ± 0.4	5.48	2	0.319	20
	11/18/2019	90	24.9	92.0 ± 82.2	15.3	2	190	20.1	8.30 ± 0.50	6.87	2	0.090	22.5
	Mean ± SD			68.0 ± 21.7	8.86 ± 4.88	4			29.1 ± 19.1	7.94 ± 3.82	4	0.504 ± 0.380	20.2 ± 1.7
Difference between two areas[b,c]				N. S.	N. S.				N. S.	N. S.		N. S.	$p<0.05$

a: Values are mean ± standard deviation of range except for mean value of each area and result of Mann–Whitney rank sum test.
b: Differences in distribution among areas were tested using the Mann–Whitney rank sum test.
c: N.S. indicates insignificant difference ($p > 0.05$).

10.3389/fmars.2022.875362

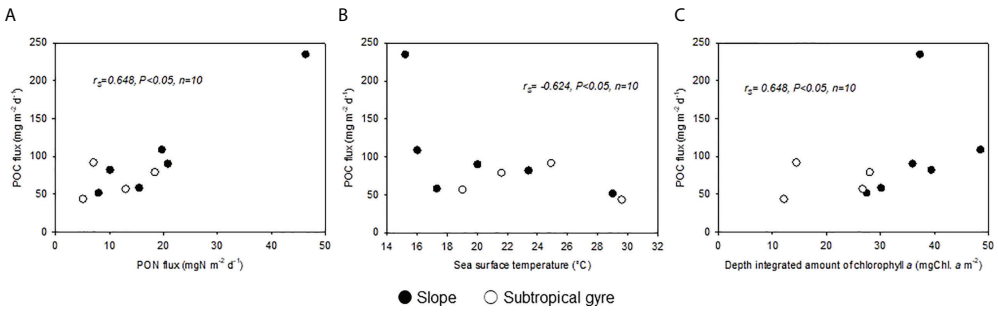

FIGURE 5
Relationships of POC flux with **(A)** PON flux, **(B)** sea surface temperature, and **(C)** the depth-integrated amount of chlorophyll [a]Spearman rank order correlations (r_s) are presented.

phytoplankton particles to total particles increases in an oligotrophic environment. Furthermore, POC/TPV was negatively correlated with dmTPV (r_s = −0.667, p< 0.05, n = 9; Table S6), whereas the mean ratios of POC/PON in the slope and subtropical gyre areas suggest that plankton were a major component of the particulate organic matter (Table 4). These results imply that the change in the POC/TPV was the results in the difference in porous structures, which made a smaller contribution to the total organic matter of each particle than did planktonic organisms. This is consistent with the

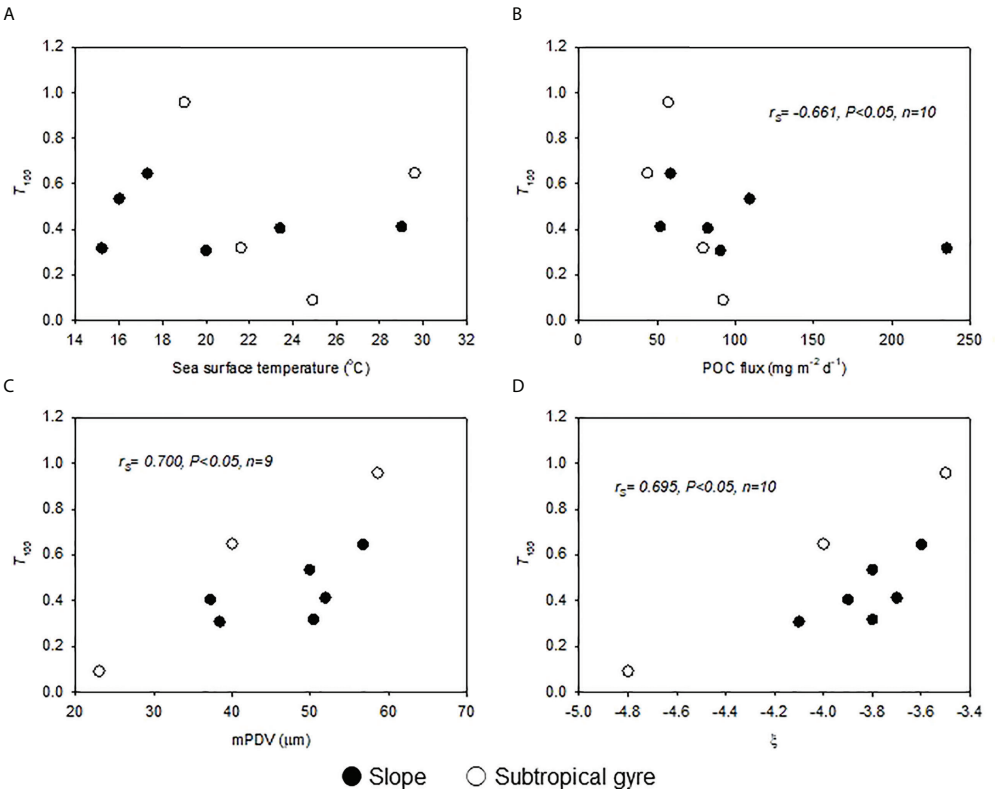

FIGURE 6
Relationships of T_{100} with **(A)** sea surface temperature, **(B)** sinking flux of POC, **(C)** mean particle diameter of the volumetric particle size distribution (mPD$_V$), and **(D)** slope of the regression line of the particle size number distribution. Spearman rank order correlations (r_s) are presented.

accumulation of larger particles detectable by LISST-100X in the presence of a high concentration of TEP, which has a porous, gel-like structure, in the subtropical northwest Pacific along the Kuroshio Current (Yamada et al., 2021). Therefore, porous gel-like materials may be a determinant of particle dynamics in subtropical environments.

Comparison of the sinking flux of particulate organic carbon at the base of the euphotic zone and transfer efficiency to the deeper layer

In marine environments, the sinking flux of POC shows large regional and temporal variability (Buesseler and Boyd, 2009; Cavan et al., 2019). The sinking POC at Z_{eu} in the entire dataset showed temporal variability correlated with SST and diChl *a* (Figures 5B, C). However, seasonal variability in the subtropical gyre was modest (Figure 5B). The range of the sinking flux of POC at Z_{eu} in the subtropical gyre exceeds values in the subtropical North Pacific Ocean near Hawaii (station ALOHA) and is comparable with the range in the Gulf of Mexico (Table S7), but the range of of the sinking flux of POC at Z_{eu} on the slope, where NPP is greater than in the subtropical gyre (Yokouchi et al., 2006), is comparable with those in mid-latitude areas (Iberian basin, Spanish coast, and Gulf of Mexico) and in high-latitude areas (Table S7). It is worth comparing the sinking flux of POC and T_{100} in the Kuroshio region to those in the Gulf of Mexico. In the Gulf of Mexico, mesoscale activities driven by the Loop Current and the eddies affects hydrography and biogeochemistry in the oligotrophic environments (Green et al., 2014; Stukel et al., 2021; Lee-Sánchez et al., 2022). Similarly, diverse routes of nutrient supply along the Kuroshio Current, including diapycnal turbulent mixing, wind- or tide-induced near-inertial internal waves, and double-diffusive convection, support higher primary productivity in the Kuroshio Current area relative to the subtropical gyre (Nagai et al., 2019).

T_{100} in marine environments varies and may exceed 1 in areas where particle production or lateral transport of particles occurs below the euphotic zone (Table S7), but it shows no marked regional trend. The range of T_{100} in this study was within the range of previous studies shown in Table S7, except for the lowest value (0.090). The areal averages of T_{100} on the slope (0.437 ± 0.130) and in the subtropical gyre (0.504 ± 0.0380) are comparable with the range in the Gulf of Mexico (0.437–0.657; Table S7). However, no seasonal trend was observed (Figure 6A). In the following section, we test the hypothesis

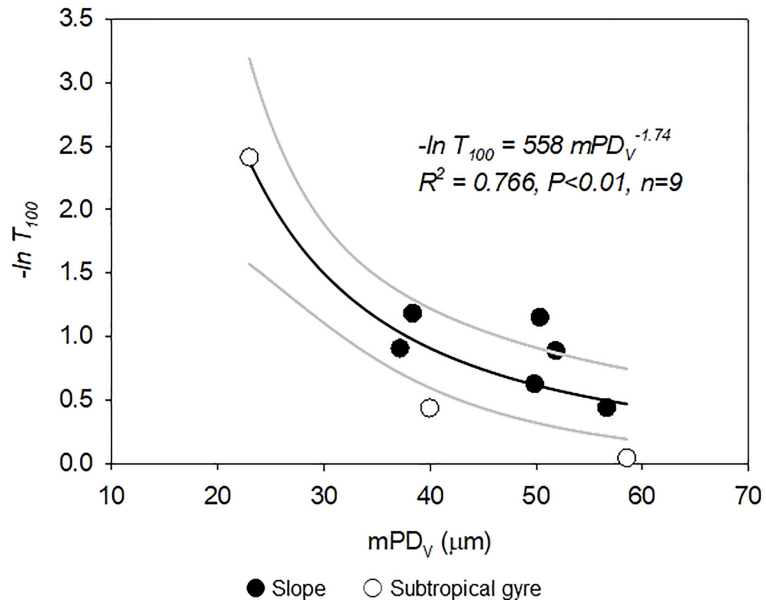

FIGURE 7
Relationship between –ln T_{100} and the mean particle diameter of the volumetric particle size distribution (mPD_V). Black line indicates non-linear regression following the power-law model (Eq. 5) using the ordinary least squares method for each sampling period. Gray lines indicate the 95% confidence interval.

that particle size affects the attenuation of sinking POC by altering sinking speed in slope and subtropical gyre areas along the Kuroshio Current.

Relationship between variation in T_{100} and particle size

Using numerical models, Cram et al. (2018) and Omand et al. (2020) demonstrated that increasing the sinking speed of particles enhances the transfer efficiency of sinking organic matter to deeper layers by reducing residence time within the water column. The positive correlation between T_{100} and mPD_V (Figure 6B) and the positive correlation between T_{100} and ξ (i.e., lower ξ indicates a greater contribution of smaller particles) (Figure 6C) are consistent with the results obtained by Cram et al. (2018) and Omand et al. (2020). However, T_{100} decreased during the period of high sinking flux of POC at Z_{eu}, suggesting that active biological decomposition enhanced vertical attenuation of sinking flux of POC (Figure 6A). Honda et al. (2016) reported close coupling between the attenuation of POC flux and zooplankton carbon demand. Active decomposition of zooplankton might alter the shape of the PSD *via* size-selective consumption of particles (Fuchs and Franks, 2010; Stamieszkin et al., 2017).

To conduct a more process-oriented comparison, we assumed that attenuation of POC flux can be expressed using first-order kinetics from the flux and time, t:

$$F_z = F_0 e^{-kt} \tag{2}$$

where F_z and F_0 are the sinking fluxes of POC at the depth of z and the reference depth z_0, respectively (Suess, 1980; Armstrong et al., 2002; Lutz et al., 2002). k is the rate of decomposition including bacterial decomposition and zooplankton grazing. Time can be reformulated based on the sinking rate, w, and the distance between the reference depth and z:

$$F_z = F_0 e^{-\frac{k(z-z_0)}{w}} \tag{3}$$

k/w in Eq. (3) corresponds to z* in previous studies (Boyd and Trull, 2007; Marsay et al., 2015). For spherical particles, Stokes law predicts that

$$w = \frac{g\Delta\rho}{18\mu} D^2 \tag{4},$$

where D is the particle diameter, $\Delta\rho$ is the density difference between the particle and seawater; μ is seawater viscosity, and g is gravitational acceleration. For marine particles, $\Delta\rho$ tends to decrease with increasing D, as $w \sim D^{\gamma}$ with $\gamma < 2$ (Alldredge and Gotschalk, 1988). If z_0 is Z_{eu}, T_{100} can be simplified to

$$T_{100} = e^{-\frac{100k}{aD^{\gamma}}} \tag{5}$$

where a is the constant defining the empirical power-law relationship between w and D. Thus, the logarithmic value of T_{100} ($-\ln T_{100}$) is proportional to k/aD^{γ}. Figure 7 shows the relationship between $-\ln T_{100}$ and mPD_V. The exponent of the non-linear regression is −1.74 (95% confidence interval: −2.57 to −0.89) and −1.98 (95% confidence interval: −3.43 to −0.53) for the entire dataset and in cases in which the sediment trap at Z_{eu} was deployed below MLD, respectively. The exponent of the non-linear regression is consistent with $\gamma < 2$, suggesting that T_{100} is controlled primarily by w in the study area.

Figures 6C and 7 show that T_{100} tended to be greater in the subtropical gyre than in the slope area based on its relationship with mPD_V. Among particle properties (POC/PON, Chl *a*/TPV, POC/TPV, and PON/TPV) within the euphotic layer, only Chl *a*/TPV showed a significant difference between the two areas (Table 4). Yamada et al. (2021) reported that the ratio of TEP concentration, which has a porous gel like structure, to Chl *a* concentration was elevated in oligotrophic areas along the Kuroshio Current. Low Chl *a*/TPV in the subtropical gyre may indicate a smaller contribution of phytoplankton to TPV and lower food quality relative to the slope. In addition, the species composition of planktonic copepods differs between the slope and the subtropical gyre along 138°E with large taxa abundant on the slope (Hirai et al., 2015 and Hirai et al., 2021). Large copepod species (Calanidae and Eucalanidae) were abundant in the copepod community of the slope water and may actively consume sinking particles in the area. These differences in both particle properties and species composition of copepods may affect the dynamics of T_{100}.

Another factor that may affect attenuation of sinking POC flux is water temperature. Marsay et al. (2015) showed that the geographical pattern of flux attenuation is correlated with water temperature, suggesting that the temperature dependence of the biological consumption rate of sinking POC controls flux attenuation. In this study, no significant correlation was found between T_{100} and mean temperature between Z_{eu} and 100 m below Z_{eu}, which varied from 14.2°C to 22.5°C (Table 6). The Q_{10} coefficient enables quantification of the temperature sensitivity of bacterial decomposition and zooplankton grazing (Ducklow et al., 2010; Ikeda, 2014). The rate of decomposition, k, at water temperature T can be expressed using Q_{10}:

$$k = k_0 Q_{10}^{\frac{T-T_0}{10}} \tag{6},$$

where k_0 is the rate of decomposition at the reference water temperature, T_0. Typical Q_{10} values of respiration are 2 and 1.9 for marine bacteria and meso- and microzooplankton,

respectively (Ducklow et al., 2010; Ikeda, 2014). If the Q_{10} temperature coefficient of k is assumed to be 2, k will increase at 1.78 times at the observed temperature increase from 14.2°C to 22.5°C. Thus, the observed range of $-\ln T_{100}$ (0.0429–2.401) was greater than the expected variation in k with increasing temperature.

The LISST instrument observes particles only within a limited size range of 5.2 to 119 μm, which excludes large sinking particles such as marine snow (> 0.5 mm). Furthermore, particles detected using LISST within the euphotic zone could include suspended particles that do not sink. Thus, PSD measured by LISST is not an accurate representation of that of sinking particles. Cael and White (2020) reported that the PSD measured using LISST for particles collected in sediment traps showed a flatter shape than the PSD for suspended particles within the euphotic zone at station ALOHA, indicating that the mean size of sinking particles is greater than that of suspended particles in the euphotic zone. However, Puigcorbé et al. (2015) presented compiled data from the literature showing that flux attenuation tends to be greater for small particles (< 53 μm in diameter) than for large particles (> 53 μm in diameter) in low and mid-latitude areas where pico- and nano-phytoplankton are dominant. Along the Kuroshio Current, pico- and nano-phytoplankton account for a greater proportion than that of diatoms near the axis and on the offshore side of the axis (Endo and Suzuki, 2019). Furthermore, the particle dynamics of the observed size range may propagate to larger particles through aggregation and disaggregation processes (Li et al., 2004; Burd and Jackson, 2009). The relatively rapid attenuation of sinking POC in small particles (< 53 μm diameter) and dynamic changes in particle size may tighten the coupling of PSD measured using LISST with the variability in T_{100}.

However, the mechanism that controls PSD in the slope and subtropical gyre region along the Kuroshio Current remains unclear. No significant correlations were found between either mPD_V or ξ and the tested variables (Tables S5, S6). Buonassissi and Dierssen (2010) reported that ξ determined using LISST varied from −4.1 to −2.9, exhibiting a gradual decrease from the shelf, across the Gulf Stream, and into the Sargasso Sea, and had a positive correlation with the Chl *a* concentration. Yamada et al. (2021) reported a similar range of ξ obtained using LISST (−4.2 to −3.2) along the Kuroshio Current but found a negative correlation between ξ and the Chl *a* concentration. Those authors also found that the PSD became flatter in the oligotrophic area, with a positive correlation between ξ and the TEP concentration (i.e., at higher TEP concentrations, larger particles make a greater contribution). In this study, ξ showed temporal variability with similar ranges on the onshore and offshore sides of the current along a N+N concentration gradient, although the correlations between Chl *a*/POC and Chl *a* concentration and between POC/TPV and TPV (Table S6) suggest that the contribution of phytoplankton to particle volume is lower in the oligotrophic environment. Further research is needed to elucidate PSD dynamics, particle properties (density, stickiness, carbon content and biological availability), and the mechanisms regulating the sinking flux of materials into the deep ocean.

Conclusion

Sediment trap experiments conducted in slope and subtropical gyre areas along the Kuroshio Current, revealed a high variability in the attenuation of sinking POC (T_{100}). The variation in T_{100} correlated negatively with the magnitude of the sinking flux of POC and positively with mPD_V and the slope of PSD (ξ), whereas no significant correlation was found between T_{100} and water temperature. The power-law relationship between T_{100} and mPD_V suggests that T_{100} in the vicinity of the Kuroshio Current is regulated by the sinking velocity of particles, although the mechanism controlling mPD_V remains unclear. To predict the change in transfer efficiency of the sinking flux of POC in response to future anthropogenic warming, further exploration of PSD dynamics as well as the physicochemical and biological properties of particles is needed.

Data availability statement

The original contributions presented in the study are included in the article/Supplementary Material. Further inquiries can be directed to the corresponding author.

Author contributions

HF, KH, and HS contributed to the conception and design of the study. HF, KH, TS, AK, DA, and HS collected the seawater samples and measured the parameters. HF wrote the first draft of the manuscript. All authors contributed to the article and approved the submitted version.

Funding

This research was supported by SKED and funded by MEXT (Grant Number JPMXD0511102330) and JSPS KAKENHI (Grant Numbers JP19H05667, JP21H03586).

Acknowledgments

We would like to thank the captains and crews of the FRV *Soyo-Maru* (Fisheries Research Agency) for their support with the sampling. The observations in the program have been conducted under Marine Fisheries Stock Assessment and Evaluation for Japanese Waters, the Fisheries Agency of Japan. We would like to thank the reviewers for their constructive comments and the editor for review of the manuscript.

Conflict of interest

The authors declare that the research was conducted in the absence of any commercial or financial relationships that could be construed as a potential conflict of interest.

Publisher's note

All claims expressed in this article are solely those of the authors and do not necessarily represent those of their affiliated organizations, or those of the publisher, the editors and the reviewers. Any product that may be evaluated in this article, or claim that may be made by its manufacturer, is not guaranteed or endorsed by the publisher.

Supplementary material

The Supplementary Material for this article can be found online at: https://www.frontiersin.org/articles/10.3389/fmars.2022.875362/full#supplementary-material

References

Agrawal, Y. C., and Pottsmith, H. C. (2000). Instruments for particle size and settling velocity observations in sediment transport. *Mar. Geol.* 168, 89–114. doi: 10.1016/S0025-3227(00)00044-X

Alldredge, A. L., and Gotschalk, C. (1988). *In situ* settling behavior of marine snow. *Limnol. Oceanogr.* 33, 339–351. doi: 10.4319/lo.1988.33.3.0339

Andrews, S. W., Nover, D. M., Reardon, K., Reuter, J. E., and Schladow, S. G. (2011). The influence of ambient light intensity on *in situ* laser diffractometers. *Water Resour. Res.* 47, W06509. doi: 10.1029/2010wr009841

Armstrong, R. A., Lee, C., Hedges, J. I., Honjo, S., and Wakeham, S. G. (2002). A new, mechanistic model for organic carbon fluxes in the ocean based on the quantitative association of POC with ballast minerals. *Deep Sea. Res. Part II* 489, 219–236.

Bader, H. (1970). The hyperbolic distribution of particle sizes. *J. Geophys. Res.* 75, 2822–2830. doi: 10.1029/JC075i015p02822

Boyd, P. W., Claustre, H., Levy, M., Siegel, A. A., and Weber, T. (2019). Multi-faceted particle pumps drive carbon sequestration in the ocean. *Nature* 568, 327–335. doi: 10.1038/s41586-019-1098-2

Boyd, P. W., and Newton, P. P. (1999). Does planktonic community structure determine downward particulate organic carbon flux in different oceanic provinces? *Deep Sea Res. Part I* 46, 63–91.

Boyd, P. W., and Trull, T. (2007). Understanding the export of marine biogenic particles: Is there consensus? *Prog. Oceanogr.* 72, 276–312.

Buesseler, K. O., and Boyd, P. W. (2009). Shedding light on processes that control particle export and flux attenuation in the twilight zone of the open ocean. *Limnol. Oceanogr.* 54, 1210–1232. doi: 10.4319/lo.2009.54.4.1210

Buesseler, K. O., Boyd, P. W., Black, E. E., and Siegel, D. A. (2020). Metrics that matter for assessing the ocean biological carbon pump. *Proc. Natl. Acad. Sci. U S A.* 117, 9679–9687. doi: 10.1073/pnas.1918114117

Buonassissi, C. J., and Dierssen, H. M. (2010). A regional comparison of particle size distributions and the power law approximation in oceanic and estuarine surface waters. *J. Geophys. Res.* 115, C10028. doi: 10.1029/2010jc006256

Burd, A. B., and Jackson, G. A. (2009). Particle aggregation. *Ann. Rev. Mar. Sci.* 1, 65–90. doi: 10.1146/annurev.marine.010908.163904

Cael, B. B., and White, A. E. (2020). Sinking versus suspended particle size distributions in the north pacific subtropical gyre. *Geophys. Res. Lett.* 47, e2020GL087825. doi: 10.1029/2020gl087825

Cavan, E. L., Laurenceau-Corneca, E. C., Bressaca, M., and Boyda, P. W. (2019). Exploring the ecology of the mesopelagic biological pump. *Prog. Oceanogr.* 176, 102125. doi: 10.1016/j.pocean.2019.102125

Cram, J. A., Weber, T., Leung, S. W., McDonnell, A. M. P., Liang, J.-H., and Deutsch, C. (2018). The role of particle size, ballast, temperature, and oxygen in the sinking flux to the deep sea. *Global Biogeochem. Cycles* 32, 858–876. doi: 10.1029/2017GB005710

de Boyer Montegut, C., Madec, G., Fischer, A. S., Lazar, A., and Iudicone, D. (2004). Mixed layer depth over the global ocean: An examination of profile data and a profile-based climatology. *J. Geophys. Rese. Oceans* 109, C12003. doi: 10.1029/2004JC002378

Ducklow, H. W., Morán, X. A. G., and Murray, A. E. (2010). "Bacteria in the greenhouse: Marine microbes and climate change," in *Environmental microbiology, 2nd ed.* Eds. R. Mitchell and J.-D. Gu (Hoboken, NJ: John Wiley & Sons, Inc), 1–31.

Endo, H., and Suzuki, K. (2019). "Spatial variations in community structure of haptophytes across the kuroshio front in the tokara strait," in *Kuroshio current.* Eds. T. Nagai, H. Saito, K. Suzuki and M. Takahashi (Washington, DC: JohnWiley & Sons), 207–221.

Fender, C. K., Kelly, T. B., Guidi, L., Ohman, M. D., Smith, M. C., and Stukel, M. R. (2019). Investigating particle size-flux relationships and the biological pump across a range of plankton ecosystem states from coastal to oligotrophic. *Front. Mar. Sci.* 6, 603. doi: 10.3389/fmars.2019.00603

Fuchs, H. L., and Franks, P. J. S. (2010). Plankton community properties determined by nutrients and size-selective feeding. *Mar. Ecol. Prog. Ser.* 413, 1–15. doi: 10.3354/meps08716

Gardner, W. D. (2000). "Sediment trap sampling in surface waters," in *The changing ocean carbon cycle: A midterm synthesis of the joint global ocean flux study.* Eds. R. B. Hanson, H. W. Ducklow and J. G. Field (Cambridge: Cambridge University Press), 240–281.

Gorsky, G., Chrétiennot-Dinet, M. J., Blanchot, J., and Palazzoli, I. (1999). Picoplankton and nanoplankton aggregation by appendicularians: Fecal pellet contents of megalocercus huxleyi in the equatorial pacific. *J. Geophys. Res.* 104, 3381–3390. doi: 10.1029/98JC01850

Green, R. E., Bower, A. S., and Lugo-Fernández, A. (2014). First autonomous bio-optical profiling float in the gulf of Mexico reveals dynamic biogeochemistry in deep waters. *PloS One* 9, e101658. doi: 10.1371/journal.pone.0101658

Guidi, L., Legendre, L., Reygondeau, G., Uitz, J., Stemmann, L., and Henson, S. A. (2015). A new look at ocean carbon remineralization for estimating deep water sequestration. *Global Biogeo. Chem. Cycles* 29, 1044–1059. doi: 10.1002/2014GB005063

Guidi, L., Stemmann, L., Jackson, G. A., Ibanez, F., Claustre, H., Legendre, L., et al. (2009). Effects of phytoplankton community on production, size, and export of large aggregates: A world-ocean analysis. *Limnol. Oceanogr.* 54, 1951–1963. doi: 10.4319/lo.2009.54.6.1951

Hirai, J., Kuriyama, M., Ichikawa, T., Hidaka, K., and Tsuda, A. (2015). A metagenetic approach for revealing community structure of marine planktonic copepods. *Mol. Ecol. Resour.* 15, 68–80. doi: 10.1111/1755-0998.12294

Hirai, J., Yamazaki, K., Hidaka, K., Nagai, S., Shimizu, Y., and Ichikawa, T. (2021). Characterization of diversity and community structure of small planktonic

copepods in the kuroshio region off Japan using a metabarcoding approach. *Mar. Eco. Prog. Ser.* 657, 25–41. doi: 10.3354/meps13539

Honda, M. H., Kawakami, H., Matsumoto, K., Wakita, M., Fujiki, T., Mino, Y., et al. (2016). Comparison of sinking particles in the upper 200 m between subarctic station K2 and subtropical station S1 based on drifting sediment trap experiments. *J. Oceanogr.* 72, 373–386. doi: 10.1007/s10872-015-0280-x

Ikeda, T. (2014). Respiration and ammonia excretion by marine metazooplankton taxa: synthesis toward a global-bathymetric model. *Mar. Biol.* 161, 2753–2766. doi: 10.1007/s00227-014-2540-5

Kaneko, H., Yasuda, I., Komatsu, K., and Itoh, S. (2013). Observations of vertical turbulent nitrate flux across the kuroshio. *Geophys. Res. Lett.* 40, 3123–3127. doi: 10.1002/grl.50613

Knauer, G. A., Martin, J. H., and Bruland, K. W. (1979). Fluxes of particulate carbon, nitrogen, and phosphorus in the upper water column of the northeast pacific. *Deep-Sea Res.* 26, 97–108. doi: 10.1016/0198-0149(79)90089-X

Kodama, T., Shimizu, Y., Ichikawa, T., Hiroe, Y., Kusaka, A., Morita, H., et al. (2014). Seasonal and spatial contrast in the surface layer nutrient content around the kuroshio along 138oE, observed between 2002 and 2013. *J. Oceanogr.* 70, 489–503. doi: 10.1007/s10872-014-0245-5

Kostadinov, T. S., Siegel, D. A., and Maritorena, S. (2009). Retrieval of the particle size distribution from satellite ocean color observations. *J. Geophys. Res.* 114, C09015. doi: 10.1029/2009jc005303

Lee-Sánchez, E., Camacho-Ibar, V. F., Velásquez-Aristizábal, J. A., Valencia-Gasti, J. A., and Samperio-Ramos, G. (2022). Impacts of mesoscale eddies on the nitrate distribution in the deep-water region of the gulf of Mexico. *J. Mar. Syst.* 229, 103721. doi: 10.1016/j.jmarsys.2022.103721

Li, X. Y., Zhang, J. J., and Lee, J. H. (2004). Modelling particle size distribution dynamics in marine waters. *Water Res.* 38, 1305–1317. doi: 10.1016/j.watres.2003.11.010

Lomas, M. W., and Moran, S. B. (2011). Evidence for aggregation and export of cyanobacteria and nano-eukaryotes from the Sargasso Sea euphotic zone. *Biogeosciences* 8, 203–216. doi: 10.5194/bg-8-203-2011

Lundgreen, R. B. C., Jaspers, C., Traving, S. J., Ayala, D. J., Lombard, F., Grossart, H., et al. (2019). Eukaryotic and cyanobacterial communities associated with marine snow particles in the oligotrophic Sargasso Sea. *Sci. Rep.* 9, 8891. doi: 10.1038/s41598-019-45146-7

Lutz, M., Dunbar, R., and Caldeira, K. (2002). Regional variability in the vertical flux of particulate organic carbon in the ocean interior. *Global Biogeochem. Cycles* 16, 1037. doi: 10.1029/2000GB001383

Mari, X., Passow, U., Migon, C., Burd, A. B., and Legendre, L. (2017). Transparent exopolymer particles: effects on carbon cycling in the ocean. *Prog. Oceanogr.* 151, 13–37. doi: 10.1016/j.pocean.2016.11.002

Marsay, C. M., Sanders, R. J., Henson, S. A., Pabortsava, K., Achterberg, E. P., and Lampitt, R. S. (2015). Attenuation of sinking particulate organic carbon flux through the mesopelagic ocean. *Proc. Natl. Acad. Sci. U S A.* 112, 1089–1094. doi: 10.1073/pnas.1415311112

Nagai, T., Durán, G. S., Otero, D. A., Mori, Y., Yoshie, N., Ohgi, K., et al. (2019). How the kuroshio current delivers nutrients to sunlit layers on the continental shelves with aid of near-inertial waves and turbulence. *Geophys. Res. Lett.* 46, 6726–6735. doi: 10.1029/2019gl082680

Nagata, T., Yamada, Y., and Fukuda, H. (2021). Transparent exopolymer particles in deep oceans: synthesis and future challenges. *Gels* 7, 75. doi: 10.3390/gels7030075

Omand, M. M., Govindarajan, R., Jing, H., and Mahadevan, A. (2020). Sinking flux of particulate organic matter in the oceans: Sensitivity to particle characteristics. *Sci. Rep.* 10, 5582. doi: 10.1038/s41598-020-60424-5

Owens, S. A., Buesseler, K. O., Lamborg, C. H., Valdes, J., Lomas, M. W., Johnson, R. J., et al. (2013). A new time series of particle export from neutrally buoyant sediments traps at the Bermuda Atlantic time-series study site. *Deep-Sea Res. I* 72, 34–47. doi: 10.1016/j.dsr.2012.10.011

Passow, U. (2002). Transparent exopolymer particles (TEP) in aquatic environments. *Prog. Oceanogr.* 55, 287–333. doi: 10.1016/S0079-6611(02)00138-6

Puigcorbé, V., Benitez-Nelson, C. R., Masqué, P., Verdeny, E., White, A. E., Popp, B. N., et al. (2015). Small phytoplankton drive high summer time carbon and nutrient export in the gulf of California and Eastern tropical north pacific. *Global Biogeochem. Cycles* 29, 1309–1332. doi: 10.1002/2015GB005134

Stamieszkin, K., Poulton, N. J., and Pershing, A. J. (2017). Zooplankton grazing and egestion shifts particle size distribution in natural communities. *Mar. Ecol. Prog. Ser.* 575, 43–56. doi: 10.3354/meps12212

Stukel, M. R., Kelly, T., Landry, M. R., Selph, K. E., and Swalethorp, R. (2021). Sinking carbon, nitrogen, and pigment flux within and beneath the euphotic zone in the oligotrophic, open-ocean gulf of Mexico. *J. Plankton Res.*, fbab001. doi: 10.1093/plankt/fbab001

Styles, R. (2006). Laboratory evaluation of the LISST in a stratified fluid. *Mar. Geol.* 227, 151–162. doi: 10.1016/j.margeo.2005.11.011

Suess, E. (1980). Particulate organic carbon flux in the oceans — surface productivity and oxygen utilization. *Nature* 288, 260–263. doi: 10.1038/288260a0

Sugisaki, H., Nonaka, M., Ishizaki, S., Hidaka, K., Kameda, T., Hirota, Y., et al. (2010). "Status and trends of the kuroshio region 2003–2008," in *Marine ecosystems of the north pacific ocean 2003–2008*. Eds. S. M. McKinnell and M. J. Dagg (Sidney, British Columbia: North Pacific Marine Science Organization), 330–359.

Suzuki, R., and Ishimaru, T. (1990). An improved method for the determination of phytoplankton chlorophyll using n, n-dimethylformamide. *J. Oceanogr. Soc Japan* 46, 190–194. doi: 10.1007/BF02125580

Turner, T. (2015). Zooplankton fecal pellets, marine snow, phytodetritus and the ocean's biological pump. *Prog. Oceanogr.* 130, 205–248. doi: 10.1016/j.pocean.2014.08.005

Welschmeyer, N. A. (1994). Fluorometric analysis of chlorophyll-a in the presence of chlorophyll-b and pheopigments. *Limnol. Oceanogr.* 39, 1985–1992. doi: 10.4319/lo.1994.39.8.198

White, J. (1990). The use of sediment traps in high-energy environments. *Mar. Geophys. Res.* 12, 145–152. doi: 10.1007/BF00310569

White, A. E., Letelier, R. M., Whitmire, A. L., Barone, B., Bidigare, R. R., Church, M. J., et al. (2015). Phenology of particle size distributions and primary productivity in the north pacific subtropical gyre (Station ALOHA). *J. Geophys. Res. Oceans* 120, 7381–7399. doi: 10.1002/2015JC010897

Yamada, Y., Fukuda, H., Uchimiya, M., Motegi, C., Nishino, S., Kikuchi, T., et al. (2015). Localized accumulation and a shelf-basin gradient of particles in the chukchi Sea and Canada basin, western Arctic. *J. Geophys. Res. Oceans* 120, 4638–4653. doi: 10.1002/2015jc010794

Yamada, Y., Fukuda, H., Umezawa, Y., and Nagata, T. (2021). Geographic variation of particle size distribution in the kuroshio region: Possible causes in the upper water column. *Front. Mar. Sci.* 8, 768766. doi: 10.3389/fmars.2021.768766

Yokouchi, K., Tsuda, A., Kuwata, A., Kasai, H., Ichikawa, T., Hirota, Y., et al. (2006). "Simulated in situ measurements of primary production in Japanese waters," in *Global climate change and response of carbon cycle in the equatorial pacific and Indian oceans and adjacent land masses*. Eds. H. Kawahata and Y. Awata (Oxford: Elsevier), 65–83.

frontiers | Frontiers in Marine Science

TYPE Original Research
PUBLISHED 21 September 2022
DOI 10.3389/fmars.2022.925123

Check for updates

OPEN ACCESS

EDITED BY
Tim Rixen,
Leibniz Centre for Tropical Marine Research (LG), Germany

REVIEWED BY
Zhi Huang,
Geoscience Australia, Australia
Ana Carolina de Azevedo Mazzuco,
Federal University of Espirito Santo, Brazil

*CORRESPONDENCE
Lachlan R. Phillips
lachlan.phillips@hdr.mq.edu.au
Robert Harcourt
robert.harcourt@mq.edu.au

SPECIALTY SECTION
This article was submitted to Coastal Ocean Processes, a section of the journal Frontiers in Marine Science

RECEIVED 21 April 2022
ACCEPTED 01 September 2022
PUBLISHED 21 September 2022

CITATION
Phillips LR, Malan N, Roughan M, Harcourt R, Jonsen I, Cox M, Brierley AS, Slip D, Wilkins A and Carroll G (2022) Coastal seascape variability in the intensifying East Australian Current Southern Extension. *Front. Mar. Sci.* 9:925123. doi: 10.3389/fmars.2022.925123

COPYRIGHT
© 2022 Phillips, Malan, Roughan, Harcourt, Jonsen, Cox, Brierley, Slip, Wilkins and Carroll. This is an open-access article distributed under the terms of the Creative Commons Attribution License (CC BY). The use, distribution or reproduction in other forums is permitted, provided the original author(s) and the copyright owner(s) are credited and that the original publication in this journal is cited, in accordance with accepted academic practice. No use, distribution or reproduction is permitted which does not comply with these terms.

Coastal seascape variability in the intensifying East Australian Current Southern Extension

Lachlan R. Phillips[1*], Neil Malan[2], Moninya Roughan[2], Robert Harcourt[1*], Ian Jonsen[1], Martin Cox[3], Andrew S. Brierley[4], David Slip[1,5], Adam Wilkins[6] and Gemma Carroll[7]

[1]School of Natural Sciences, Macquarie University, Sydney, NSW, Australia, [2]School of Biological Earth and Environmental Sciences, University of New South Wales (UNSW) Sydney, Sydney, NSW, Australia, [3]Australian Antarctic Division, Kingston, TAS, Australia, [4]Pelagic Ecology Research Group, Scottish Oceans Institute, Gatty Marine Laboratory, School of Biology, University of St. Andrews, St Andrews, United Kingdom, [5]Taronga Conservation Society Australia, Mosman, NSW, Australia, [6]Field Friendly, Adelaide, SA, Australia, [7]The Environmental Defense Fund, Seattle, WA, United States

Coastal pelagic ecosystems are highly variable in space and time, with environmental conditions and the distribution of biomass being driven by complex processes operating at multiple scales. The emergent properties of these processes and their interactive effects result in complex and dynamic environmental mosaics referred to as "seascapes". Mechanisms that link large-scale oceanographic processes and ecological variability in coastal environments remain poorly understood, despite their importance for predicting how ecosystems will respond to climate change. Here we assessed seascape variability along the path of the rapidly intensifying East Australian Current (EAC) Southern Extension in southeast Australia, a hotspot of ocean warming and ecosystem tropicalisation. Using satellite and *in situ* measures of temperature, salinity and current velocity coupled with contemporaneous measurements of pelagic biomass distribution from nine boat-based active acoustic surveys in five consecutive years, we investigated relationships between the physical environment and the distribution of pelagic biomass (zooplankton and fish) at multiple timescales. Survey periods were characterised by high variability in oceanographic conditions, with variation in coastal conditions influenced by meso-to-large scale processes occurring offshore, including the position and strength of eddies. Intra-annual variability was often of a similar or greater magnitude to inter-annual variability, suggesting highly dynamic conditions with important variation occurring at scales of days to weeks. Two seascape categories were identified being characterised by (A) warmer, less saline water and (B) cooler, more saline water, with the former indicating greater influence of the EAC on coastal processes. Warmer waters were also associated with fewer, deeper and less dense biological aggregations. As the EAC continues to warm and penetrate further south, it is likely that this will have substantial effects on biological activity in coastal pelagic ecosystems, including a potential reduction in the accessibility of prey aggregations to surface-feeding predators and to fisheries. These results highlight the import role of offshore oceanographic processes in

driving coastal seascape variability and biological activity in a region undergoing rapid oceanic warming and ecological change.

KEYWORDS

seascape, East Australian Current Extension, climate change, coastal processes, marine ecosystems, spatiotemporal variability, active acoustics

Introduction

Marine environments are characterised by their ephemeral and heterogeneous nature driven by a combination of physical, chemical and biological processes at multiple spatial and temporal scales (Kavanaugh et al., 2014; Pittman, 2017). The emergent properties of these processes and their interactive effects result in complex and dynamic environmental mosaics referred to as "seascapes" (Kavanaugh et al., 2016). Seascape ecology provides a useful conceptual framework to understand variability in biological and physical processes in a dynamic and advective ocean (Kavanaugh et al., 2016), and to identify the interactions and correlations between these processes at different spatial and temporal scales (Marquet et al., 1993; Dickey, 2003). Quantifying the relationships between these processes and their scale-dependent variability is key to understanding how seascapes may respond to the numerous stressors associated with global change (Pittman, 2017).

Variability in biophysical factors and their relationships are structured hierarchically. Physical ocean structures follow a power-law cascade as energy is dissipated from gyre circulation to fine-scale turbulence (Stommel, 1963). These ocean structures can be classed as geostrophically dynamic, operating at large scales and being driven by the earth's rotational energy (e.g. gyres, western boundary currents and mesoscale eddies), or ageostrophic, operating at finer scales and reflecting all other forms of motion and instabilities (e.g. turbulent motion and submesoscale frontal dynamics) (Lévy et al., 2012). The environmental and biological composition of seascapes at a given point in time is therefore the product of variability in both geostrophic and ageostrophic factors over multiple spatiotemporal scales. For example, planktic species and their forage fish predators tend to be hierarchically distributed in space and time with dense aggregations of individuals clustered and nested within patches of lower density (Fauchald, 1999; Carroll et al., 2017). These ecological patterns can be influenced over long time periods by basin level/decadal scale systems that influence ecosystem productivity such as the El Niño - Southern Oscillation (ENSO) (Hallegraeff, 2010), but also over short time periods and fine spatial scales through cross-shelf processes (Baird et al., 2011).

Consideration of both geostrophic and ageostrophic dynamics is important when studying highly variable seascapes such as western boundary current systems. Western boundary currents are strong, dynamic currents that form along the western margins of the world's major ocean basins (Hogg and Johns, 1995; Imawaki et al., 2013). Primarily generated by wind-driven anticyclonic subtropical gyres, these geostrophic currents are a major driver of poleward heat and climate regulation through the transport of warm subtropical waters from low to high latitudes (Yu and Weller, 2007). Over the last several decades, western boundary currents have extended further poleward (Yang et al., 2020; Zhang et al., 2020; Li et al., 2021; Li et al., 2022a; Li et al., 2022b) or broadened (Beal and Elipot, 2016) due to an increase in global oceanic kinetic energy (Hu et al., 2020). These changes are driving major environmental and ecological shifts in coastal ecosystems (Suthers et al., 2011; Phillips et al., 2020). These shifts can occur over the short term (days to weeks) through eddy dynamics (Roughan et al., 2017), hydrographic fronts (Schaeffer et al., 2017), interactions with local factors such as bathymetry (Oke and Middleton, 2000; Schaeffer et al., 2014) and coastal processes (Roughan et al., 2022), as well as at seasonal (Archer et al., 2017), interannual and multi-decadal time scales (Ridgway, 2007; Phillips et al., 2020). As a consequence, shifts in environmental variability are non-uniform by latitude (Malan et al., 2021) with differences in local ageostrophic factors making it difficult to predict the ecological impacts for individual coastal systems.

The East Australian Current (EAC) is a poleward-flowing western boundary current that transports subtropical water from the Coral Sea along Australia's east coast (Boland and Church, 1981; Godfrey and Golding, 1981; Hamon, 1965; Ridgway and Godfrey, 1994). The current separates from the coast between 31 and 33°S to form the eastward-flowing EAC eastern extension and a poleward propagating eddy field called the EAC southern extension (Cetina-Heredia et al., 2014; Oke et al., 2019). The southern extension has intensified and shifted southward over the last eight decades with strong lines of evidence demonstrating the current is penetrating further poleward (Ridgway, 2007; Johnson et al., 2011; Li et al., 2021; Li et al., 2022a; Li et al., 2022b). Temperature increases are non-uniform

along the latitudinal extent of the EAC with regions poleward of 32°S warming more than twice as fast as those equatorial of 32°S (Malan et al., 2021) as the southern outflow of the EAC southern extension becomes more turbulent and eddying (Li et al., 2021; Malan et al., 2021). This intensification has resulted in the EAC extension producing rates of ocean warming that are 3–4 times the global average, making southeast Australia one of the fastest-warming regions in the southern hemisphere (Wu et al., 2012; Li et al., 2022b).

The impacts of the intensification of the EAC southern extension on coastal systems are already evident and include prolonged marine heatwaves (Oliver et al., 2017; Schaeffer et al., 2017; Huang et al., 2021), modification of nutrient loading regimes (Harris et al., 1987; Harris et al., 1991) migration of typically subtropical species poleward (Edyvane, 2003; Pittock, 2003; Thresher et al., 2003; Vergés et al., 2014; Niella et al., 2021) and shifts in species assemblages, the distributions of pelagic fish and planktic species, and trophic interactions (Carroll et al., 2016; Carroll et al., 2017; Hobday et al., 2011; Johnson et al., 2011; Kelly et al., 2016; Larsson et al., 2018; Thompson et al., 2009) that are projected to continue in coming decades (Cetina-Heredia et al., 2015). While many ecological patterns have been investigated in the context of EAC variability *via* correlations with temperature and current velocity, there has been little work investigating how EAC variability (or western boundary current variability more broadly) influences seascape characteristics over multiple spatiotemporal scales simultaneously, including how relationships between geostrophic and ageostrophic processes link offshore and coastal dynamics, and impact biological activity.

Studies linking coastal biological activity to offshore processes often use indirect proxies of biological activity such as chlorophyll *a* concentration or sea-surface temperature (Gremillet et al., 2008; Block et al., 2011), however, inferring spatial and temporal variability in upper trophic-level biology from such data can produce variable results (Suryan et al., 2012). Boat-based acoustic surveys enable direct sampling of the distribution of schooling species (e.g. pelagic fishes and krill) at spatiotemporal resolutions relevant to coastal ecosystems (Bertrand, 2003; Koslow, 2009). Acoustic sampling has advantages over other sampling methods such as trawl surveys, as it provides information on the vertical distribution of prey (Cox et al., 2013; Receveur et al., 2020) and provides simultaneous qualitative and quantitative data on multiple components of an ecosystem (Bertrand, 2003).

Using ocean temperature and current velocity time-series data from Australia's Integrated Marine Observing System (IMOS) moorings, CTD profiles and measurements of acoustic density distribution (using active acoustics) from nine boat-based surveys conducted in five consecutive years (2015 to 2019), we investigate here the relationship between physical oceanography, the distribution of pelagic species and their inter-survey variability in one of the fastest-warming coastal regions in the southern hemisphere (Malan et al., 2021). Our aim is to better resolve interactions between the EAC, coastal shelf waters, and biological activity, a crucial step toward making robust predictions of climate change impacts on coastal ecosystems.

Methods

Our study was conducted in Batemans Marine Park in Southeastern New South Wales Australia (36.3°S 150.2°E) which supports a highly variable coastal shelf ecosystem directly in the path of the East Australian Current (EAC) southern extension (Figure 1). The study area was approximately 16 km (onshore-offshore) x 27 km (along the coast) in size (approximately 430 km^2). To explore effects of EAC variability on coastal processes, we coupled oceanographic observations from satellites and fixed moorings with finer-scale observations made from boat-based surveys during the austral spring over five consecutive years (2015 - 2019). This is the time period that coincides with an increase in southward EAC flow in this region, and phenological changes in biological productivity from phytoplankton blooms (Everett et al., 2014) and triggers the breeding season for seabirds and marine mammals (Quiring et al., 2021)

Offshore oceanographic processes

To assess oceanographic processes such as the location of eddies that might influence coastal processes during each survey period, gridded (0.02° x 0.02°) products of satellite-derived sea surface temperature (AVHRR L3S SST - daily resolution – product identifier: 8bd3fe33-fd98-4307-ad23-424ad9a2907b) and gridded sea level anomaly (GSLA – product identifier: 3162c844-d45c-491c-b326-6ae37e4079f9) data were used to produce maps of the meso scale oceanographic context during survey periods. Sea surface temperature (SST) anomaly was calculated by subtracting the SST Atlas of Australian Regional Sea Daily climatology fit from the gridded sea-surface temperature data (product identifier: 79c8eea2-4e86-4553-8237-4728e27abe10). Satellite data and the daily climatology fits were obtained through the IMOS Australia Ocean Data Network (AODN) portal (https://portal.aodn.org.au).

Coastal current velocity

Meridional (north/south)2010. 00815.xocity time series at a 5-minute temporal resolution was obtained from two IMOS moorings located immediately north of Batemans Marine Park in 70 and 120 m of water, named BMP070 and BMP120 respectively (Figure 1B). doi: 10.1016/j.dsr2re temperature and velocity at 5 minute intervals every 8m through the water

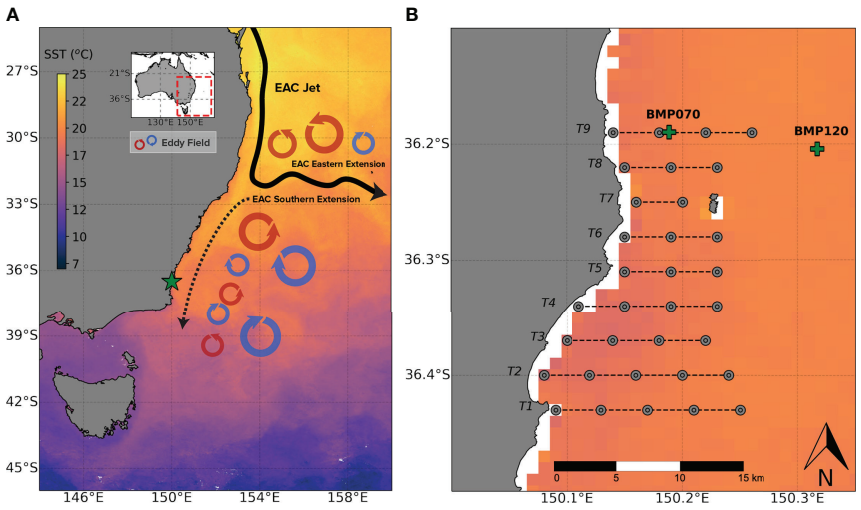

FIGURE 1
(A) A simplified schematic adapted from Phillips et al. (2020) of the East Australian Current (EAC) showing the primary mesoscale features (main flow and eddy fields) and the study location (green star) and; **(B)** A map of the study location in the Batemans Marine Park showing the positions of the acoustic transects (black dotted lines), the CTD profiling stations (grey points) and the position of the two moorings (BMP070 and BMP120) (green crosses). Both panels are overlaid over a 10 day composite of sea surface temperature (IMOS MODIS SST) beginning October 10th, 2015.

column since 2015 and 2011 respectively. For more information see Roughan et al. (2015). Daily velocity means were extracted at each mooring over 10 days to coincide with the timing of each boat-based survey (see below). Mooring data was obtained through the AODN portal (https://portal.aodn.org.au)

Boat-based surveys

Coastal temperature and salinity

Boat-based surveys were undertaken during daylight hours from a 6 m rigid-hulled inflatable vessel, *R/V Pelagica*, travelling at 4-6 knots along 7-9 cross-shelf transects spaced 3.5 km apart and ranging in length from 7 to 14 km (Figure 1). Along each transect, sampling stations were positioned 2.75 km apart (33 stations in total) at which a depth profile of temperature and salinity was collected using a calibrated CastAway Conductivity Temperature Depth (CTD) logger (SonTek, San Diego, USA). In 2015, seven transects were sampled (T1-T7) and an additional two transects were added to the northern survey area (T8, T9) in 2016 - 2019, making a total survey extent of 31.5 km north to south along the continental shelf (Table 1). Transect T9 was not sampled during survey 2018 S2 due to adverse weather conditions. The relationships between CTD temperature and salinity were assessed using generalised linear models.

TABLE 1 Metadata and timing for each of the boat-based surveys.

Survey ID	Start Date	End Date	Time Period (days)	Days Sampled	CTD profiles	Transects Sampled
2015 S1	Oct-01	Oct-08	8	5	44	T1-T7
2016 S1	Sep-16	Sep-28	13	8	72	T1-T9
2016 S2	Oct-22	Nov-02	12	5	58	T1-T9
2017 S1	Aug-15	Aug-26	12	6	55	T1-T9
2017 S2	Oct-03	Oct-13	11	5	55	T1-T9
2018 S1	Aug-23	Sep-04	13	5	47	T1-T9
2018 S2	Sep-28	Oct-01	4	3	30	T1-T8
2019 S1	Sep-24	Sep-26	3	3	33	T1-T9
2019 S2	Oct-01	Oct-02	2	2	33	T1-T9

Two extra transects were added to the north of the original study area in 2016. The time taken to complete each survey was variable between surveys due to adverse weather conditions affecting the amount of time the team could spend on the water.

Acoustic biomass distribution

An EK80 (Simrad, Horten, Norway) scientific echosounder operating a 70 kHz transducer in continuous wave mode (3-dB beamwidth 18°, transmit power 280 W, pulse duration 1.024 ms, 2 Hz pulse repetition rate) was used to measure water column acoustic backscattering intensity, which is approximately proportional to biomass density and can be used to map distribution of zooplankton and fish (Maclennan, 2002). The transducer was mounted on a pole connected to the vessel *via* a retractable arm (transducer depth = 0.75 m). Echosounder calibrations were performed each survey year according to the procedure of Demer et al. (2015).

Acoustic processing

Acoustic data were processed using Echoview v11 (Echoview, Hobart, Australia) to extract acoustic density information. Seabed returns and surface noise were removed from the acoustic data prior to aggregation detection. Aggregations were isolated from the acoustic record by applying the SHAPES edge detection algorithm (Barange, 1994; Coetzee, 2000) implemented in the 'Schools Detection' module of Echoview (Echoview Software Pty Ltd, Hobart, Australia) to a 3 x 3 identity matrix convolution of the acoustic data. The minimum detection threshold was -65 dB re 1 m^{-1}, and school detection algorithm parameters were as given in Carroll et al. (2017) (Table S2). Mean volume backscattering strength, (S_v; see Maclennan (2002) for definition) was calculated using a -80 dB re 1 m^{-1} minimum data threshold.

Although comprehensive trawl surveys were not conducted in association with acoustic measurements to obtain estimates of species composition, aggregations were presumed to be primarily a mix of krill (euphausiids) and forage fish based on direct observations and hook-and-line fishing samples (L. Phillips unpubl. data.). Assessing broad patterns of biological activity associated with seascape dynamics was the primary goal of this study, however future detailed studies might assess variation in biological responses at the taxonomic level.

Physical-biological interactions

To assess differences in biological and environmental interactions between surveys, three summary metrics were calculated from the acoustic aggregation data (Table 2) along transects for the area 1.875 km (half the distance between stations) west and east of each CTD station. Metrics included mean aggregation depth (mean depth of aggregation centre), aggregation coverage (% of sampled area occupied by acoustic aggregations) and aggregation internal density (mean S_v within aggregation boundaries). Functional relationships between temperature and the aggregation were assessed using generalised linear models.

Seascape classifications

CTD and acoustic aggregation data were separated into different seascape classifications by applying K-means clustering (Hartigan and Wong, 1979) following dimensionality reduction using a principal component analysis (Mardia et al., 1979). The principal component analysis was applied to the variables CTD mean temperature, CTD mean salinity, mean aggregation depth, aggregation coverage and mean aggregation internal density. Data was zeroed, centred and scaled to have unit variance. K-means clustering was then applied to the rotated principal components with the optimal number of clusters estimated using average silhouette width. The suitability of the principal component analysis for determining seascape classifications was then validated by performing a principal component analysis on a training set consisting 80% of the dataset (304 casts) and predicting the principle components on a testing set of the remaining 20% of the dataset (82 casts). Multinomial logistic regression models (Wood et al., 2016) were then constructed from the training set principle components to classify the seascape clusters and the individual surveys. The multinomial logistic regression models were then assessed on the testing set to determine the classification success. The functional relationships between temperature and the aggregation characteristics for each of the seascape cluster categories were assessed using generalised linear models.

Results

Offshore oceanographic processes

During each of the nine boat-based surveys over five Austral springs, the regional circulation was dominated by the presence of a

TABLE 2 Summary of metrics calculated from the acoustic aggregation data measured along transects.

Metric	Unit	Description
Mean aggregation depth	Metres	Mean aggregation depth
Aggregation coverage	Percentage	Proportion of area (1.875 km east and west of CTD station to the seafloor) containing aggregations (sum of the aggregations' size in m2).
Mean aggregation internal density	S_v mean	Mean internal acoustic density of aggregations

mesoscale, anticyclonic (warm-core) eddy (Figure 2). However, the latitude and distance from the coast of these eddies differed between surveys resulting in different oceanographic characteristics within the study area during each survey period. During 2015 survey 1 (S1) a large anticyclonic eddy was present closer to the coast and approximately 1° further south than during all other surveys (eddy centred at 36.75° S in 2015 S1 vs approximately 35-36° S during other surveys). This eddy placement allowed for a continuous southward flow of warm water along the coast that caused the East Australian Current (EAC) southern extension to remain over the shelf prohibiting north-flowing incursions of cool, upwelled water that occurred in other periods resulting in anomalously warm water along the coast (Figure 2A).

In 2016 S1 and 2016 S2 large anticyclonic eddies were also present but centred at more northern latitudes northward of 36° S resulting in a reduced flow of the EAC southern extension into the coastal study area (Figures 2B, C). The large anticyclonic eddies in 2017 S1 and 2017 S2 were similar in size and latitude to 2016 but had less influence on the study area due to the presence of smaller, more southerly cyclonic cold-core eddies blocking the mesoscale flow along the coast. The main EAC flow was therefore pushed offshore and the study area experienced northward flow of cooler waters along the coast. This also occurred in 2018 S1 with the anticyclonic eddy and therefore the flow of the EAC southern extension being further offshore (Figure 2F). However, during survey 2018 S2 approximately one month later (Figure 2G), the eddy configuration changed and a cyclonic eddy formed at latitudes sufficiently southward to create a mesoscale flow that advected some EAC water northwestward onto the shelf interacting with the cooler shelf waters that were observed in the previous survey period.

Surveys 2019 S1 and 2019 S2 were conducted only one week apart so exhibited similar regional circulation. For both surveys in 2019, the primary mesoscale flow in the study area was southward (Figures 2H, I). Unlike other years with a strong southward current, the anticyclonic eddy causing this flow in the study area did not form a clear continuous current with the larger anticyclonic eddy in the northeast resulting in the main EAC flow being further offshore.

Coastal current velocity

Measurements of meridional (north/south) current velocity obtained from the moorings were relatively consistent at the 70 m isobath (BMP070) but varied considerably both within and between surveys at the 120 m isobath (BMP120) (Figure 3). For surveys 2015 S1 and 2019 S2, southward velocity was anomalously strong at 120 m with mean velocities of -0.37 ± 0.13 and -0.32 ± 0.21 ms^{-1} respectively (negative values indicate southward flow). Meridional velocity at 120 m was highly variable for 2019 S1 with a mean of -0.18 ± 0.33 ms^{-1}. There was no strong directional current flow at 120 m during surveys 2017 S1 (0.00 ± 0.24 ms^{-1}) or 2017 S2 (0.02 ± 0.16 ms^{-1}). A reduction in strength of southward velocity was observed in 2018 at 120 m with current speeds reduced by approximately half between surveys 2018 S1 (-0.19 ± 0.25 ms^{-1}) and 2018 S2 (-0.10 ± 0.12 ms^{-1}). No velocity was recorded for surveys in 2016 due to instrument failure.

Coastal temperature and salinity

There were notable differences in temperature and salinity as measured by boat-based CTD profiles between surveys. Water temperature in 2015 S1 was warmer than all other surveys with a mean temperature of 17.96 ± 0.92°C which was 1.8°C higher than the mean across all surveys (Figure 3). The coolest surveys were 2018 S1 and 2018 S2 with temperatures of 15.32 ± 0.40°C and 15.29 ± 0.72°C respectively, approximately 0.86°C cooler than average. 2019 S1 was also cool but also highly variable with water temperatures of 15.77 ± 1.19°C. Salinity during survey 2015 S1 was the lowest recorded with a mean of 34.84 ± 0.06 PSU. 2016 S1 and 2016 S2 also had low salinity relative to other surveys with means of 34.94 ± 0.10 and 34.98 ± 0.04 PSU respectively. All other surveys exhibited higher saline concentrations ranging from 35.36 ± 0.10 PSU (2019 S1) to 35.63 ± 0.04 PSU (2017 S2). Surveys with higher saline concentrations were typically cooler (2017 S1 to 2019 S2) but the inverse was not always true (2016 S2) (Figure 3).

In most surveys there was an inshore-offshore temperature gradient within the study area (Figure 4) which was also observed in the CTD data when temperature was compared with distance from the coast (GLMs: $p < 0.05$), with the exception of 2016 S2, and 2018 S1 and S2 (GLMs: $p > 0.05$). Between surveys, there was a negative relationship between temperature and salinity (slope = -1.14, sd = 0.15, $p < 0.001$). However, on intra-survey time scales (days to weeks), there was a positive correlation between temperature and salinity for all surveys (Figure 5).

Seascape classifications

The K-means clustering of the CTD/aggregation data's five principal components separated the data into two seascape categories (cluster A and B) that were cleanly divided between surveys (Figure 6). Cluster A consisted of data from surveys 2015 S1, 2016 S1 and 2016 S2 with a single outlier in 2016 S2 being classified grouped with cluster B. All other CTD casts and aggregation characteristic surveys (2017, 2018 and 2019) were classified as cluster B. cluster A was characterised by warmer and

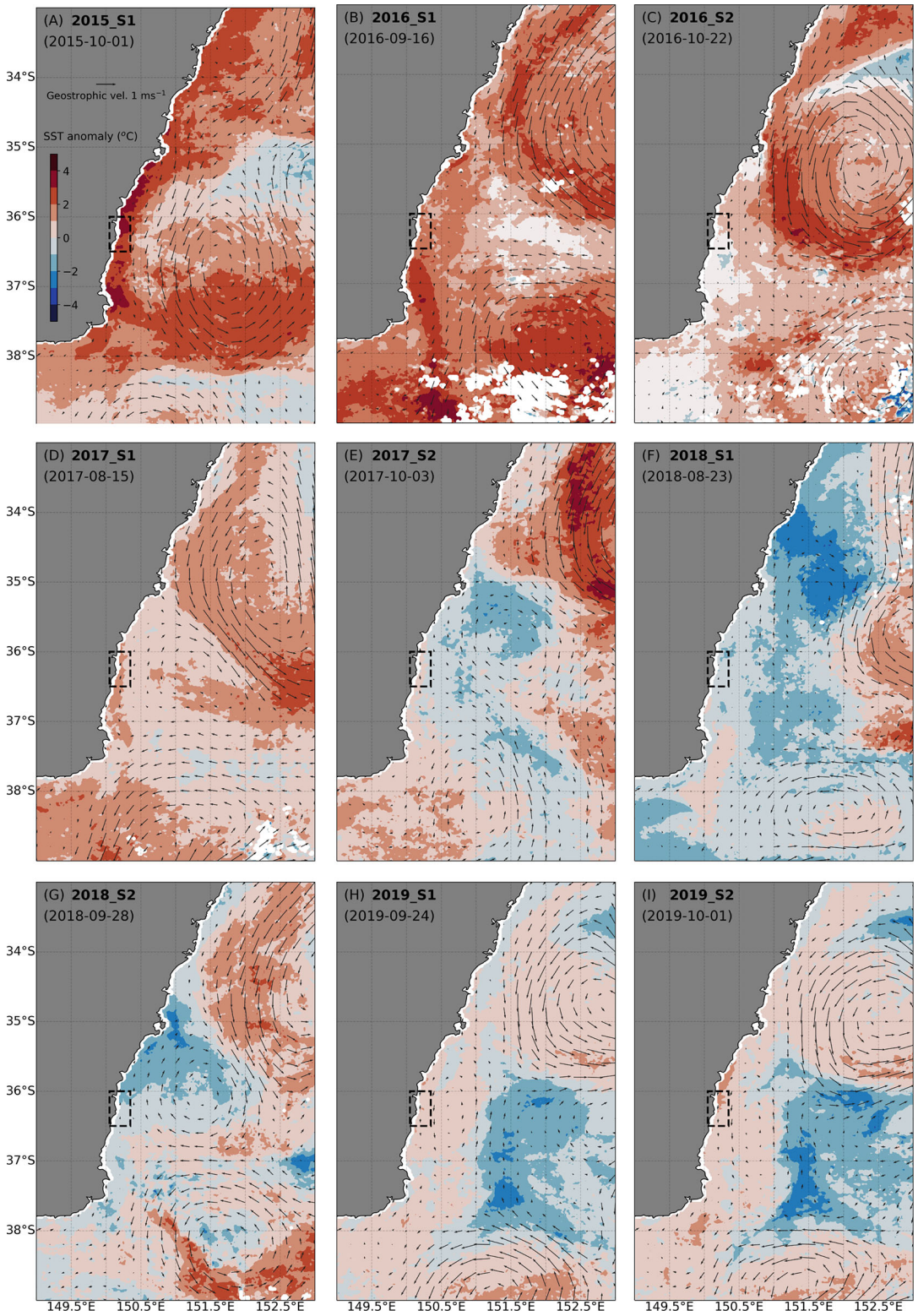

FIGURE 2
10-day composite of daily sea-surface temperature anomaly (colour) and altimetry-derived surface geostrophic velocities (vectors) for each of the survey periods **(A–I)**. The survey area is shown as a black rectangle. The displayed date is the first day of the 10-day composite.

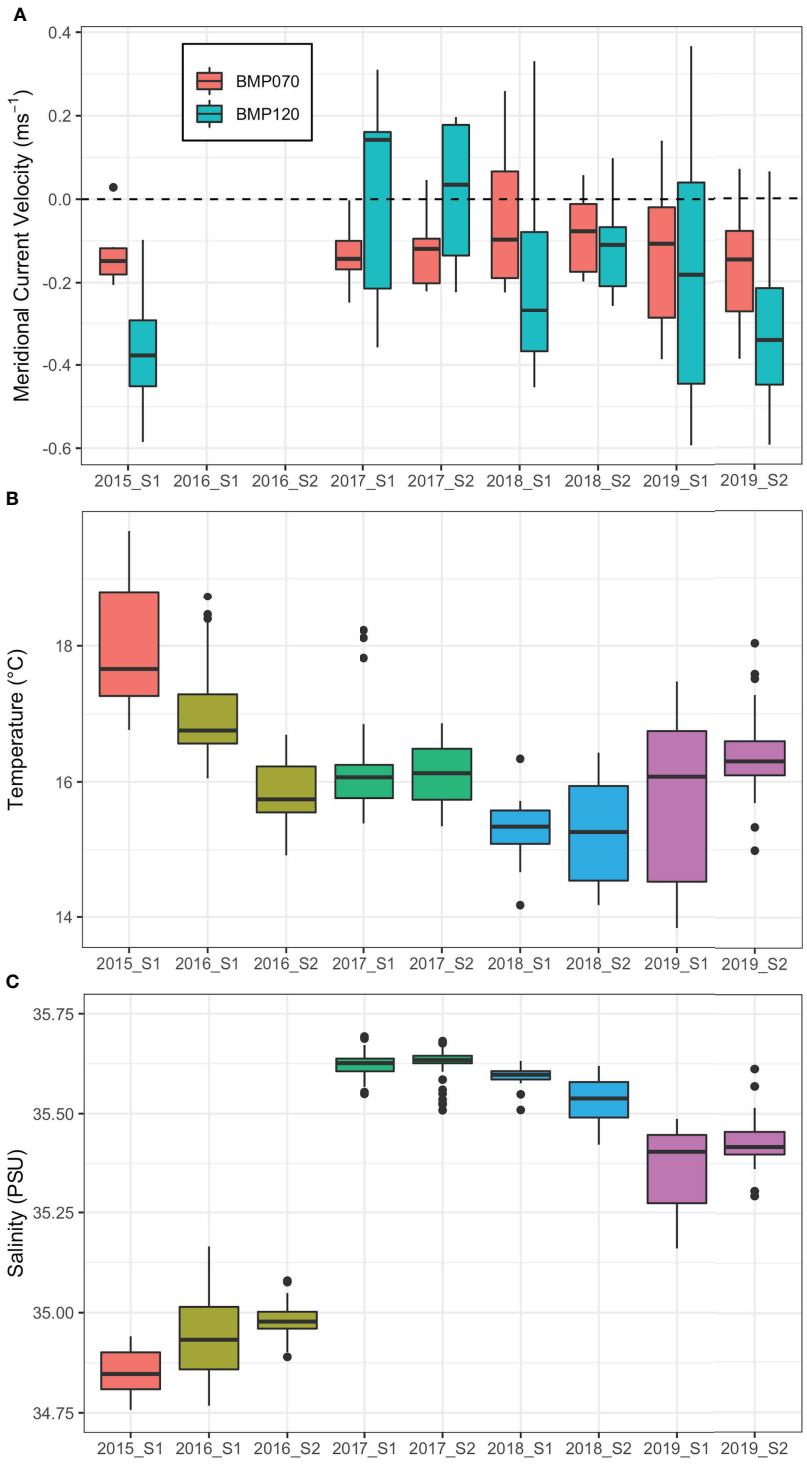

FIGURE 3
(A) Box plots of the daily mean meridional (north/south) current velocity measured over each of the survey periods from the moorings BMP070 (70 m isobath) and BMP120 (120 m isobath). Due to an equipment failure, no data was recorded for surveys 2016 S1 and 2016 S2. **(B)** Boxplots of mean temperature and **(C)** salinity for each of the CTD casts during each survey. As multiple surveys were conducted in a given calendar year, surveys have been coloured by year to highlight interannual patterns.

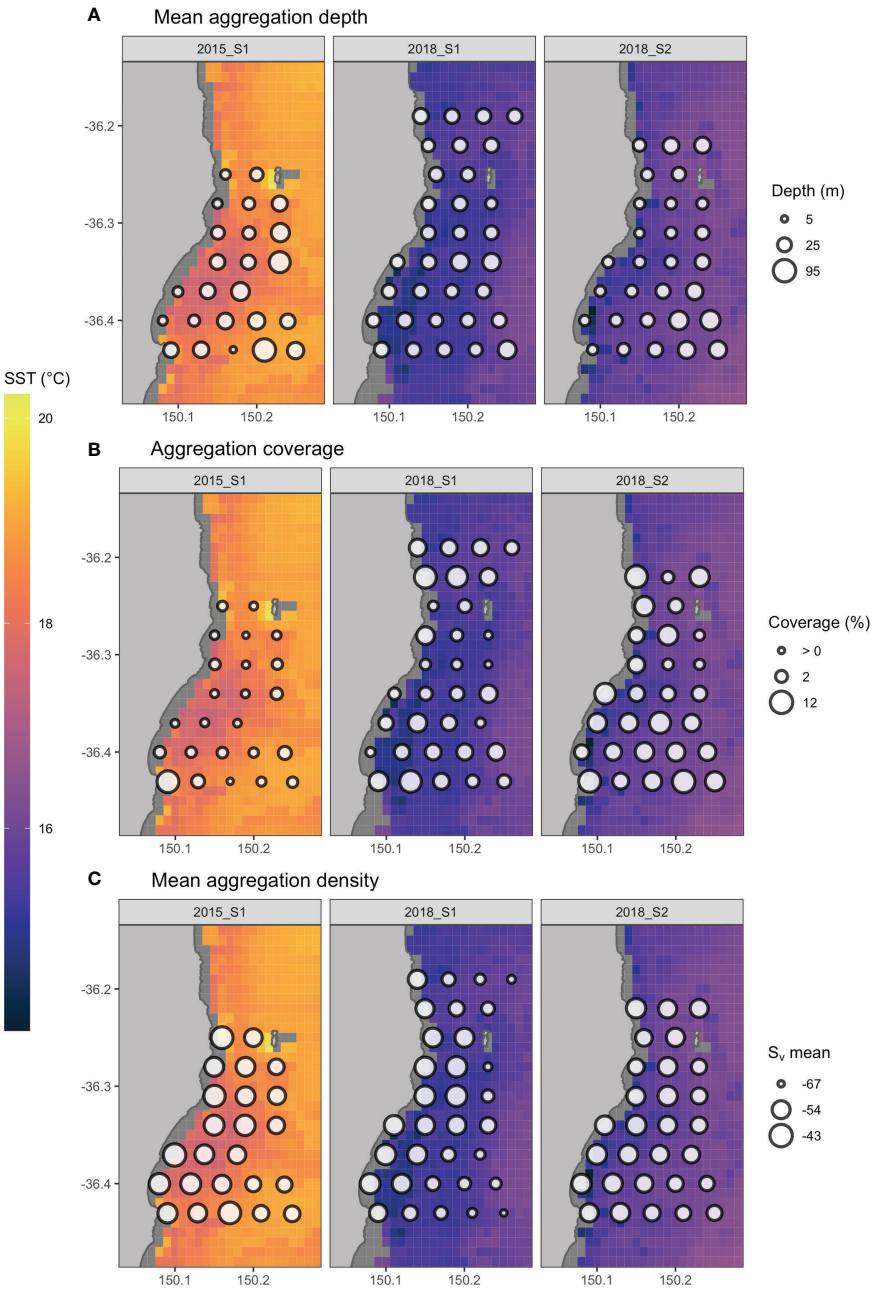

FIGURE 4
Spatial distribution of acoustically derived biological aggregation metrics calculated for the area surrounding transect stations overlaid over sea surface temperature (IMOS MODIS SST) for surveys 2015 S1, 2018 S1 and 2018 S2 with point size representing **(A)** the mean depth of aggregations, **(B)** the percentage area around the station containing biological aggregations and **(C)** the mean aggregation density. An equivalent figure for all surveys is included in the supplementary material.

less saline water and had lower aggregation coverage and higher internal aggregate density in comparison to cluster B. Validation of the PCA/K-means clustering analyses using multinomial logistic regression applied to the testing dataset resulted in all data being classified into the correct cluster and 70.51% the data into the correct survey.

Physical-biological interactions

The relationships between water temperature from the CTD casts and acoustic aggregation characteristics were compared between the two seascape categories using generalised linear models (Figure 7). Overall the relationship between temperature

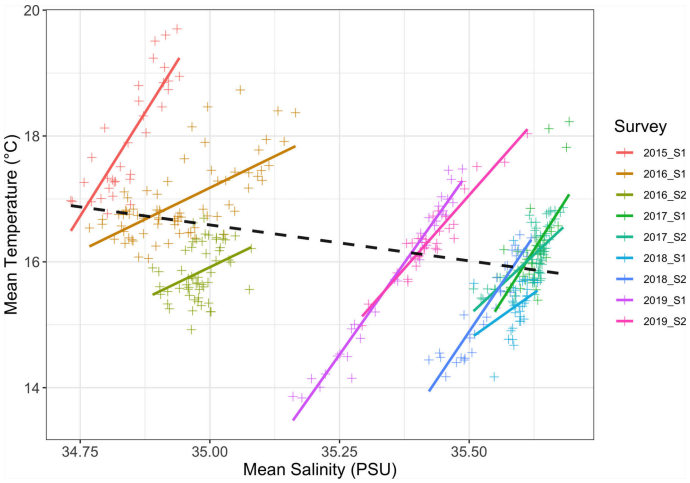

FIGURE 5
Mean temperature (°C) and mean salinity (PSU) scatter plots from all of the CTD casts coloured by survey with the generalised linear model regression lines shown. The black dashed line shows the generalised linear model regression line for the entire dataset.

and mean aggregation depth was positive (slope = 1.15, sd = 0.06, p = 0.005) with no observable difference in relationship between the two seascape categories (slope = 1.03, sd = 0.07, p = 0.665). The relationship between temperature and aggregation coverage was negative (slope = -0.12, sd = 0.04, p = 0.005) and the relationship was stronger within seascape cluster A than for cluster B (slope = 0.13, sd = 0.06, p = 0.038). There was also a negative relationship between temperature and mean internal aggregation density (slope = -1.93, sd = 0.41, p < 0.001) and with the relationship being stronger for cluster A (slope = 1.33, sd = 0.60, p = 0.026).

Discussion

Marine systems can be highly dynamic and complex, with emergent properties arising from the interactions of processes at multiple spatiotemporal scales. Here we use the conceptual framework of seascape ecology to combine multiple datasets of different spatial and temporal scales and so investigate variability in a rapidly changing coastal ecosystem in southeastern Australia (Suthers et al., 2011; Malan et al., 2021). Over the course of nine surveys in the austral spring across 5 years, we identified multiple

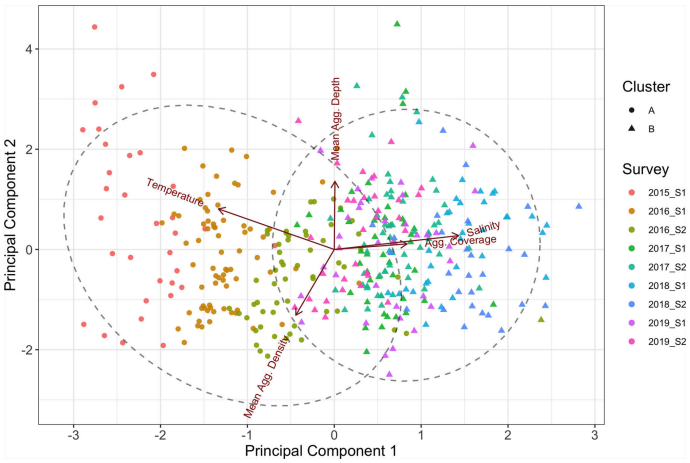

FIGURE 6
Results of the K-means clustering applied to the principal component analysis of the CTD and acoustic aggregation data plotted against the 1st and 2nd principal components. Clusters are differentiated as circles and triangles and coloured by survey ID. The dashed lines represent the 95% normal-probability contour of each cluster.

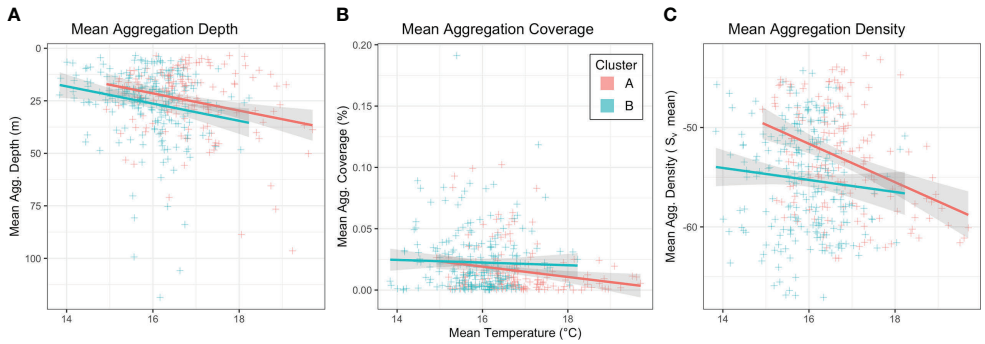

FIGURE 7
Scatter plots of CTD mean temperature (°C) plotted against the acoustic aggregation characteristics metrics being **(A)** mean aggregation depth (mean depth of aggregation centre), **(B)** aggregation coverage (% of sampled area occupied by acoustic aggregations), and **(C)** aggregation internal density (mean Sv within aggregation boundaries). The slope of the generalised linear models are shown with colour representing the two seascape classifications.

oceanographic processes operating across diverse spatiotemporal scales within the East Australian Current (EAC) southern extension (Figure 8). Two seascape categories with distinct differences observed in environmental and biological factors were identified from the principal component and K-means clustering analyses. Seascape A (2015/16) was characterised by warmer and less saline EAC water and had lower aggregation coverage and lower internal aggregate density. Seascape B (2017 - 2019) which was characterised by cooler and more saline water from the Bass Strait and/or Tasman Sea and had higher aggregation coverage and higher internal aggregate density. Further, we identified how the relationships between ecological, environmental and oceanographic variability can have different characteristics depending on the scale of observation.

There were differences in offshore oceanographic processes between each of the surveys including differences in the position of large eddies and mesoscale current strength and direction. During each survey, the broad oceanographic context was consistently dominated by the presence of a large anticyclonic eddy formed from warm, EAC water that varied in size, intensity and position. The position and intensity of this eddy appeared to have a considerable influence on the coastal study area, shaping the volume of EAC water transported onto the shelf, and modifying the mesoscale current flows that determined which water types were transported into the area. For example, in 2015 S1 the position of the meso-scale eddy was located the furthest south (centred at 36.75° S) when compared to the other surveys thereby creating a continuous flow that allowed warm EAC water from more equatorward latitudes to dominate the study area. This was also evident from the IMOS mooring which recorded significant southward flow at the 120 m isobath. Surveys 2016 S1 and 2016 S2were also characterised by a particularly large anticyclonic eddy, but these eddies were located at more equatorward latitudes (centred at 34.5 and 35.25° S respectively) resulting in less pronounced southward flow. Surveys 2019 S1 and 2019 S2 also had setups that resulted in primarily southward flow but to a lesser degree than other years.

By contrast, survey 2018 S1 was characterised by a much less intense anticyclonic eddy which was also located further offshore. As a consequence, there was much less influence from warm equatorial EAC water and geostrophic flow from satellite altimetry was primarily northward with cooler waters originating from the southbeing transported northward along the coast into the study area. This cooler southern watermass could have originated in the Bass Strait (Luick et al., 1994) or to the southeast, brought into the coast by cyclonic eddies. However, although the meridional velocity recorded at the IMOS moorings were highly variable, they were primarily southward during this same period, highlighting a mismatch between large scale and finescale processes in the study area. During survey 2018 S2 which was conducted approximately one month later, the position and intensity of these eddies changed considerably with the emergence of a smaller cyclonic eddy arising at ≈ 36° S. The presence of this eddy created a pathway for warm EAC water located off the shelf to be advected onto the shelf and into the study area from the south. Surveys 2017 S1 and 2017 S2 were also characterised by cyclonic eddies resulting in equatorward flow which was also detected at the IMOS moorings.

The differences in mesoscale circulation resulted in different environmental conditions between surveys within the study area. Temperature and salinity profiles from CTD sampling along transects revealed two primary environmental regimes with surveys typically being either warm with relatively lower salinity or cool with higher salinity. These categorisations were supported by the seascape classifications with each being represented by seascape A and B respectively. The study area

is frequently subjected to influxes of cool, salty water that is transported up the coast either from the Bass Strait (Luick et al., 1994), or through cyclonic eddies bringing Tasman Sea water to the coast. This current acts in opposition to the EAC, and in the absence of eddy placement that blocks the northward flow of this current, can provide coastal ecosystems with a supply of relatively cool, productive water. Furthermore, the surveys which exhibited higher salinity and cooler water (seascape B) were years with reduced southward geostrophic flow. Conversely, the years that had lower salinity and generally warmer temperatures (seascape A) were years where southward geostrophic flow was particularly strong due to the positioning of meso-scale eddies. Consequently the seascape variability observed on inter-survey time frames (months to years) may be due to the varying influence of northern (EAC) or southern (Tasman Sea/Bass Strait) watermasses driven by the positioning of the mesoscale eddies which can enhance or block the flow of cooler water northward along the coast.

The relationship between temperature and salinity as measured by the CTD profiles was dependent on timescale. On inter-survey timeframes (months to years) there was a negative relationship between temperature and salinity, however on intra-survey timescales (days to weeks) this relationship was positive. The change in this relationship at different temporal scales suggests that different oceanographic processes are driving this environmental variability. For example, the negative relationship between temperature and salinity at inter-survey temporal scales is likely due to the previously mentioned interplay of EAC and Tasman Sea (or Bass Strait) waters creating warm-fresh or cool-salty conditions over each survey period. However, the positive relationships between temperature and salinity at shorter temporal scales is indicative of the presence of distinctive water types of relatively fresh cool water and more saline warmer water at finer scales within the study area.

Within the EAC southern extension, ocean heat content and marine heatwave events are largely driven by mesoscale eddies (Elzahaby et al., 2021; Li et al., 2022a). As the frequency and intensity of marine heatwaves are projected to increase (Oliver et al., 2019), the environmental characteristics of seascape A (EAC dominated) (2015 S1, 2016 S1 and 2016 S2) are likely to be increasingly common in the future. During the Austral spring of 2015 the coastal shelf region of NSW experienced a marine heatwave event (Huang et al., 2021) which was the precursor to the 2015/16 Tasman Sea heat wave (Oliver et al., 2017). This event is likely the cause of the unprecedented water temperatures observed in our study area during survey 2015 S1 which was up to 4 degrees warmer than SSTAARS climatology.

There were differences in the distribution, structure and abundance of biological aggregations between the two seascape categories corresponding to differences in mesoscale circulation and environmental characteristics within the study area. Warmer temperatures typically resulted in more sparse aggregation coverage which were also deeper and had lower internal density. As warmer years were associated with increased EAC influence, this suggests that in our study area the projected increase in EAC advections onto the shelf (Bull et al., 2020) may produce conditions that are less suitable for the formation of biological aggregations. These patterns between anomalously high ocean temperatures and the abundance of pelagic fishes have been observed in other western boundary current systems. For example, in the Sea of Japan which is influenced by the highly variable Kuroshio Current sardine catches have been observed to be lowest during periods of higher water temperatures (Yasuda et al., 1999).

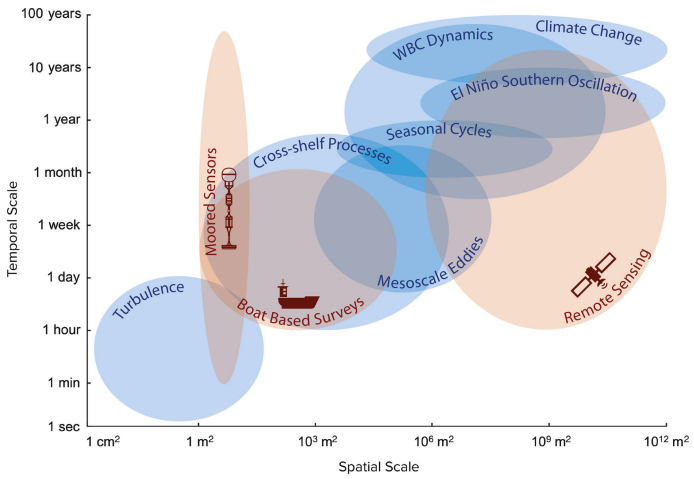

FIGURE 8
Adaptation of a Stommel diagram showing the spatiotemporal scales of variability relevant for Western Boundary currents such as the East Australian Current system (blue) and the observational platforms used in this study (red).

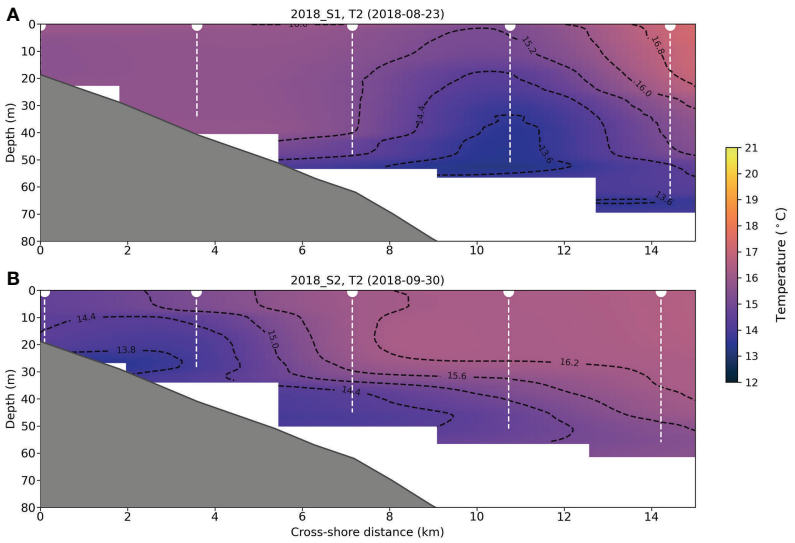

FIGURE 9
Comparisons of interpolated CTD cross sections of transect 2 showing water temperature (colour), the CTD profile depths (white dotted lines) and the sea floor as determined from acoustic sampling (grey area) for **(A)** survey 2018 S1 and **(B)** 2018 S2. Interpolation of temperature from CTD casts was performed using radial basis function interpolation.

There were differences in functional relationships between environment and acoustic aggregation characteristics between the two seascape categories. In particular the negative relationship between temperature and aggregation internal density was stronger for seascape A (EAC dominated) than seascape B (Bass Strait/Tasman Sea). This pattern was also present in the relationship between temperature and aggregation coverage but to a much lesser extent. This suggests that the behaviour of the biological aggregates may be influenced differently by the two seascape environments and may be indicative of a thermal preference for biological aggregates that occurs under the warmer and less saline environmental conditions of seascape A. This difference may be explained by the timing of key biological events such as the major phytoplankton bloom that occurs each spring at these latitudes south of the EAC separation zone. This bloom event is driven by a seasonal encroachment of the EAC into the region which causes an increase in water temperature, greater dissolved nitrate and silicate, and a shallowing of the mixed-layer depth (Everett et al., 2014). Although our surveys were conducted during the Austral spring when this bloom is known to occur (Hallegraeff and Jeffery, 1993) the continued intensification of the EAC southern extension has modified the seasonal cycle of EAC influence in the region with the spring EAC encroachment occurring up to a month earlier (Phillips et al., 2020) and this can change the timing of these significant biological events. Consequently, it is possible our surveys occurred during different biological stages of this bloom period which may explain the different functional response observed between the two seascape categories.

In marine systems environmental conditions can change substantially over very short time periods (Barreau et al., 2021). This was particularly evident in 2018 when the sudden advection of EAC water onto the shelf caused a stark change in oceanographic conditions within the span of one month. This sudden advection of warm water from the offshore anticyclonic eddy resulted in a cold water coastal upwelling event visible in the CTD cross-sections (Figure 9). EAC advections onto the shelf can result in a long-shelf currents that drive Ekman transport in the bottom boundary layer causing local upwelling events (Roughan and Middleton, 2002; Roughan and Middleton, 2004) and can result in localised nutrient enrichment (Oke and Middleton, 2001). This change in environmental conditions was accompanied by increased offshore aggregation density and with aggregations inshore moving to shallower depths. This suggests that these conditions may be favourable to swarming and schooling species such as plankton and pelagic fishes resulting in more shallow biological aggregations in inshore regions.

As eddy kinetic energy continues to increase in the EAC southern extension (Li et al., 2021; Li et al., 2022a; Li et al., 2022b) mesoscale eddies that advect warm EAC water onto the shelf are expected to become more common, larger and more intense (Li et al., 2021). Consequently, the extreme oceanic conditions observed during survey 2015 S1 may be broadly representative of conditions that will become more common for

this region resulting in warmer and less biological productive environmental conditions observed in EAC dominated Seascape category A. While over shorter time frames the encroachment of EAC water onto the shelf can sometimes result in productive cold water upwellings that produce increased biological activity (Roughan and Middleton, 2002; Roughan and Middleton, 2004) at depth, the complete dominance of the region by EAC water in 2015 was associated with a reduction in the coverage of biological aggregations that were both deeper and had lower internal density. The more southward position of the dominant anticyclonic eddy in 2015 created a blocking action which resulted in the complete absence of the cooler northward flow. This suggests that this northward flow of cooler, salty water may become rarer or completely absent in the future as the period of EAC regional dominance continues to encroach further into the Austral winter (Phillips et al., 2020).

The relationship between warmer water and sparser, less dense and deeper aggregations may have significant implications for foraging predators such as seabirds. Montague Island, located in the study area, is home to numerous seabird breeding colonies including little penguins (*Eudyptula minor*), greater crested terns (*Thalasseus bergii*) and silver gulls (*Chroicocephalus novaehollandiae*). Previous studies in the region have shown that foraging outcomes are influenced by the distribution and structure of the prey field with sparser and deeper aggregations reducing predators' ability to locate suitable prey (Carroll et al., 2017; Phillips et al., 2022 in review). The presence of higher sea surface temperatures driven by the increased poleward penetration of the EAC southern extension have been associated with reduced foraging success in little penguins (Carroll et al., 2016) and changes to the diet composition of greater crested terns (Quiring et al., 2021). Furthermore, the ongoing intensification of the EAC southern extension may continue to place additional pressures on ecological systems. Consequently, it appears likely that the continued dominance of the EAC in southern NSW waters and reduced northward flow will have substantial effects on biological activity in coastal pelagic ecosystems in southeast Australia, including a potential reduction in the accessibility of prey aggregations to surface-feeding predators and fisheries.

The rapid change in environmental conditions observed in 2018 and the associated changes to biological distribution and structure at a sub-seasonal timescale, highlights the highly variable nature of coastal systems in the EAC southern extension. This is primarily driven by the sporadic nature of the southward propagating eddies of the region with anticyclonic mesoscale eddies advecting EAC water from further offshore onto the coastal shelf (Li et al., 2022a). This sub-seasonal scale of variability is important to understand as both a normal component of EAC extension dynamics, as well as an additional stressor in the context of an intensifying EAC southern extension. As the EAC southern extension continues to penetrate further southward, advections of warm water onto the shelf are likely to become more common (Li et al., 2021; Malan et al., 2021). This is likely to result in increased ocean heat content in the region (Li et al., 2021; Li et al., 2022a) and an increase in the probability of marine heat waves (Elzahaby et al., 2021; Oliver et al., 2021) suggesting that the environmental and biological conditions experienced for the EAC dominated seascape A may become the norm in this region.

That these oceanographic processes were associated with notable changes in both environmental and biological characteristics has significant implications for the ecological processes within our study area and more broadly. For example, rapid changes in environmental conditions and biological activity may coincide with crucial life history events of breeding predators, such as little penguins (*Eudyptula minor*) and crested terns (*Thalasseus bergii*), which time their breeding behaviour to coincide with the period of greatest prey availability (Gales and Green, 1990; Carroll et al., 2016; Quiring et al., 2021). The migration phenology of ecologically and commercially important coastal pelagic fish species may also be impacted by rapid changes in EAC shelf incursions (Brodie et al., 2015; Champion et al., 2021) and the southward shift of the EAC will further facilitate the range expansion of tropical species into temperate regions (Vergés et al., 2014).

Conclusions

In this study, we assessed seascape variability within Batemans Bay Marine Park in southeast Australia – a highly variable coastal shelf ecosystem in the path of the rapidly intensifying East Australian Current (EAC) Southern Extension. We used satellite and *in situ* measures of temperature, salinity and current velocity coupled with contemporaneous measurements of pelagic biomass distribution from boat-based active acoustic surveys to investigate relationships between the physical environment and the distribution of pelagic biomass (zooplankton and fish) at multiple timescales. We identified two seascape categories characterised by warmer, less saline water and cooler, more saline water, with the former indicating greater influence of the EAC on coastal processes. Warmer waters were also associated with fewer, deeper and less dense biological aggregations. As the EAC southern extension continues to penetrate further southward (Li et al., 2021) the environmental and biological conditions experienced during the EAC dominated seascape may become increasingly commonplace for the region.

While there is much uncertainty in how changes in western boundary current dynamics will impact coastal ecosystems, understanding relationships between coastal and offshore processes and biological responses in the ecosystem will help

resolve the key mechanisms and outcomes of change at multiple spatiotemporal scales. Our study demonstrates the important role of offshore oceanographic processes in determining coastal seascape variability and the impacts on biological activity within a region experiencing rapid oceanic warming and ecological change.

Data availability statement

The datasets presented in this study can be found in online repositories. The names of the repository/repositories and accession number(s) can be found below: https://doi.org/10.5281/zenodo.6471632.

Author contributions

Study design: LP, NM, MR, IJ, RH, MC, AW, and GC. Data collection and processing: LP, NM, MR, IJ, RH, MC, AB, DS AW and GC. Analysis: LP, NM, MR, IJ, RH, MC, AB, and GC. The paper was written by LP with input from all authors. All authors contributed to the article and approved the submitted version.

Funding

This study was funded by Australian Research Council Linkage Grants (LP110200603 awarded to RH, DS and Iain Field, and LP160100162 awarded to IJ, Martina Doublin, MC, GC, DS, Iain Suthers and RH) with contributions from the Taronga Conservation Society Australia, NSW National Parks and the Australian Antarctic Division.

Acknowledgments

Thanks to Sven Gastauer, Matteo Bernasconi, Ben Pitcher, Pierre Vignal, Sven Gastauer and Vanessa Morris for help with data collection. The authors declare that the research was conducted in the absence of any commercial or financial relationships that could be construed as a potential conflict of interest. Data was sourced from Australia's Integrated Marine Observing System (IMOS) – IMOS is enabled by the National Collaborative Research Infrastructure Strategy (NCRIS). It is operated by a consortium of institutions as an unincorporated joint venture, with the University of Tasmania as Lead Agent.

Conflict of interest

The authors declare that the research was conducted in the absence of any commercial or financial relationships that could be construed as a potential conflict of interest.

Publisher's note

All claims expressed in this article are solely those of the authors and do not necessarily represent those of their affiliated organizations, or those of the publisher, the editors and the reviewers. Any product that may be evaluated in this article, or claim that may be made by its manufacturer, is not guaranteed or endorsed by the publisher.

Supplementary material

The Supplementary Material for this article can be found online at: https://www.frontiersin.org/articles/10.3389/fmars.2022.925123/full#supplementary-material

SUPPLEMENTARY FIGURE 1
Spatial distribution of acoustically derived biological aggregation metrics calculated for the area surrounding transect stations overlaid over sea surface temperature (IMOS MODIS SST) for all surveys with point size representing: **(A)** the mean depth of aggregations; **(B)** the percentage area around the station containing biological aggregations; and **(C)** the mean aggregation density.

References

Archer, M. R., Roughan, M., Keating, S. R., and Schaeffer, A. (2017). On the variability of the East Australian current: Jet structure, meandering, and influence on shelf circulation. *J. Geophysical Research: Oceans* 122 (11), 8464–8481. doi: 10.1002/2017JC013097

Baird, M. E., Suthers, I. M., Griffin, D. A., Hollings, B., Pattiaratchi, C., Everett, J. D., et al. (2011). The effect of surface flooding on the physical–biogeochemical dynamics of a warm-core eddy off southeast Australia. *Deep Sea Res. Part II: Topical Stud. Oceanography* 58 (5), 592–605. doi: 10.1016/j.dsr2.2010.10.002

Barange, M. (1994). Acoustic identification, classification and structure of biological patchiness on the edge of the agulhas bank and its relation to frontal features. *South Afr. J. Mar. Sci.* 14 (1), e0254269. doi: 10.2989/025776194784286969

Barreau, E., Kato, A., Charadia, A., and Ropert-Coudert, Y. (2021). The consequences of chaos: Foraging activity of a marine predator remains impacted several days after the end of a storm. *PLoS One* 16 (7), 333–347. doi: 10.1371/journal.pone.0254269

Beal, L. M., and Elipot, S. (2016). Broadening not strengthening of the agulhas current since the early 1990s. *Nature* 540 (7634), 570–573. doi: 10.1038/nature19853

Bertrand, A. (2003). Acoustics for ecosystem research: lessons and perspectives from a scientific programme focusing on tuna-environment relationships. *Aquat. Living Resour.* 16 (3), 197–203. doi: 10.1016/s0990-7440(03)00018-4

Block, B. A., Jonsen, I. D., Jorgensen, S. J., Winship, A. J., Shaffer, S. A., Bograd, S. J., et al. (2011). Tracking apex marine predator movements in a dynamic ocean. *Nature* 475 (7354), 86–90. doi: 10.1038/nature10082

Boland, F. M., and Church, J. A. (1981). The East Australian current 1978. *Deep Sea Res. Part A. Oceanographic Res. Papers* 28 (9), 937–957. doi: 10.1016/0198-0149(81)90011-x

Brodie, S., Hobday, A. J., Smith, J. A., Everett, J. D., Taylor, M. D., Gray, C. A., et al. (2015). Modelling the oceanic habitats of two pelagic species using recreational fisheries data. *Fisheries Oceanography* 24 (5), 463–477. doi: 10.1111/fog.12122

Bull, C. Y. S., Kiss, A. E., Gupt, A. S., Jourdain, N. C., Argüeso, D., Luca, A. D., et al. (2020). Regional versus remote atmosphere-ocean drivers of the rapid projected intensification of the East Australian current. *J. Geophysical Research: Oceans* 125 (7), e2019JC015889. doi: 10.1029/2019JC015889

Carroll, G., Cox, M., Harcourt, R., Pitcher, B. J., Slip, D., and Jonsen, I. (2017). Hierarchical influences of prey distribution on patterns of prey capture by a marine predator. *Funct. Ecol.* 31 (9), 1750–1760. doi: 10.1111/1365-2435.12873

Carroll, G., Everett, J. D., Harcourt, R., Slip, D., and Jonsen, I. (2016). High sea surface temperatures driven by a strengthening current reduce foraging success by penguins. . *Scientific Reports* 6, 22236. doi: 10.1038/srep22236

Cetina-Heredia, P., Roughan, M., Sebille, E., Feng, M., and Coleman, M. A. (2015). Strengthened currents override the effect of warming on lobster larval dispersal and survival. *Global Change Biol.* 21 (12), 4377–4386. doi: 10.1111/gcb.13063

Cetina-Heredia, P., Roughan, M., van Sebille, E., and Coleman, M. A. (2014). Long-term trends in the East Australian current separation latitude and eddy driven transport. *J. Geophysical Research: Oceans* 119 (7), 4351–4366. doi: 10.1002/2014JC010071

Champion, C., Brodie, S., and Coleman, M. A. (2021). Climate-driven range shifts are rapid yet variable among recreationally important coastal-pelagic fishes. *Front. Mar. Sci.*, 8. doi: 10.3389/fmars.2021.622299

Coetzee, J. (2000). Use of a shoal analysis and patch estimation system (SHAPES) to characterise sardine schools. *Aquat. Living Resour.* 13 (1), 1–10. doi: 10.1016/s0990-7440(00)00139-x

Cox, M. J., Letessier, T. B., and Brierley, A. S. (2013). Zooplankton and micronekton biovolume at the mid-Atlantic ridge and Charlie–Gibbs fracture zone estimated by multi-frequency acoustic survey. *Deep Sea Res. Part II: Topical Stud. Oceanography* 98, 269–278. doi: 10.1016/j.dsr2.2013.07.020

Demer, D. A., Berger, L., Bernasconi, M., Bethke, E., Boswell, K., Chu, D., et al. (2015). Calibration of acoustic instruments. doi: 10.25607/OBP-185.

Dickey, T. D. (2003). Emerging ocean observations for interdisciplinary data assimilation systems. *J. Mar. Syst.* 40–41, 5–48. doi: 10.1016/s0924-7963(03)00011-3

Edyvane, K. S. (2003). *Conservation, monitoring and recovery of threatened giant kelp (Macrocustis pyrifera) forests in Tasmania - report to environment Australia (Marine species protection program)* (Hobart: Department of Primary Industries, Water and Environment).

Elzahaby, Y., Schaeffer, A., Roughan, M., and Delaux, S. (2021). Oceanic circulation drives the deepest and longest marine heatwaves in the East Australian current system. *Geophysical Res. Lett.* 48 (17), e2021GL094785. doi: 10.1029/2021gl094785

Everett, J. D., Baird, M. E., Roughan, M., Suthers, I. M., and Doblin, M. A. (2014). Relative impact of seasonal and oceanographic drivers on surface chlorophyll a along a Western boundary current. *Progress in oceanography. Progress in Oceanography* 120, 340–351. doi: 10.1016/j.pocean.2013.10.016

Fauchald, P. (1999). Foraging in a hierarchical patch system. *Am. Nat.* 153 (6), 603–613. doi: 10.1086/303203

Gales, R., and Green, B. (1990). The annual energetics cycle of little penguins (Eudyptula minor). *Ecology* 71 (6), 2297–2312. doi: 10.2307/1938641

Godfrey, J. S., and Golding, T. J. (1981). The sverdrup relation in the Indian ocean, and the effect of pacific-Indian ocean throughflow on Indian ocean circulation and on the East Australian current. *J. Phys. Oceanography* 11 (6), 771–779. doi: 10.1175/1520-0485(1981)011<0771:tsriti>2.0.co;2

Gremillet, D., Lewis, S., Drapeau, L., van der Lingen, C. D., Hugget, J. A., Coetzee, J. C., et al. (2008). Spatial match-mismatch in the benguela upwelling zone: should we expect chlorophyll and sea-surface temperature to predict marine predator distributions? *J. Appl. Ecol.* 45 (2), 610–621. doi: 10.1111/j.1365-2664.2007.01447.x

Hallegraeff, G. M. (2010). Ocean climate change, phytoplankton community responses, and harmful algal bslooms: A formidable predicitve challlenge. *J. Phycology* 46 (2), 220–235. doi: 10.1111/j.1529-8817.2010.00815.x

Hallegraeff, G. M., and Jeffery, S. W. (1993). Annually recurrent diatom blooms in spring along the new south Wales coast of Australia. *Aust. J. Mar. Freshw. Res.* 44 (2), 325–334. doi: 10.1071/MF9930325

Hamon, B. V. (1965). The East Australian current 1960\textendash1964. *Deep Sea Res. Oceanographic Abstracts* 12 (6), 899–921. doi: 10.1016/0011-7471(65)90813-2

Harris, G. P., Griffiths, F. B., Clementson, L. A., Lyne, V., and Van. der.Doe, H. (1991). Seasonal and interannual variability in physical processes, nutrient cycling and the structure of the food chain in Tasmanian shelf waters. *J. Plankton Res.* 13 (supp1), 109–131. doi: 10.1093/oxfordjournals.plankt.a042363

Harris, G., Nilsson, C., Clementson, L., and Thomas, D. (1987). The water masses of the east coast of Tasmania: Seasonal and interannual variability and the influence on phytoplankton biomass and productivity. *Mar. Freshw. Res.* 38 (5), 569–590. doi: 10.1071/MF9870569

Hartigan, J. A., and Wong, M. A. (1979). Algorithm AS 136: A K-means clustering algorithm. *Appl. Stat* 28 (1), 100–108. doi: 10.2307/2346830

Hobday, A. J., Young, J. W., Moeseneder, C., and Dambacher, J. M. (2011). Defining dynamic pelagic habitats in oceanic waters off eastern Australia. *Deep Sea Res. Part II: Topical Stud. Oceanography* 58 (5), 734–745. doi: 10.1016/j.dsr2.2010.10.006

Hogg, N. G., and Johns, W. E. (1995). Western Boundary currents. *Rev. Geophysics* 33 (S2), 1311–1334. doi: 10.1029/95rg00491

Huang, Z., Feng, M., Beggs, H., Wijffels, S., Cahill, M., and Griffin, C. (2021). High-resolution marine heatwave mapping in Australasian waters using himawari-8 SST and SSTAARS data. *Remote Sens. Environ.* 267 (12), 112742. doi: 10.1016/j.rse.2021.112742

Hu, S., Sprintall, J., Guan, C., McPhaden, M. J., Wang, F., Hu, D., et al. (2020). Deep-reaching acceleration of global mean ocean circulation over the past two decades. *Am. Assoc. Advancement Sci.* 6 (6), eaax7727. doi: 10.1126/sciadv.aax7727

Imawaki, S., Bower, A. S., Beal, L., and Qiu, B. (2013). "Chapter 13 - Western boundary currents," in *(Επιμ.) Ocean circulation and climate*. Eds. G. Siedler, S. M. Griffies, J. Gould and J. A. Church The Boulevard, Langford Lane, Kidlington, Oxford OX5 1GB, UK Radarweg 29, PO Box 211, 1000 AE Amsterdam, The Netherlands, (σσ. 305–338). doi: 10.1016/B978-0-12-391851-2.00013-1

Johnson, C. R., Banks, S. C., Barrett, N. S., Cazassus, F., Dunstan, P. K., Edgar, G. J., et al. (2011). Climate change cascades: Shifts in oceanography, species' ranges and subtidal marine community dynamics in eastern Tasmania. *J. Exp. Mar. Biol. Ecol.* 400 (1), 17–32. doi: 10.1016/j.jembe.2011.02.032

Kavanaugh, M. T., Hales, B., Saraceno, M., Spitz, Y. H., White, A. E., and Letelier, R. M. (2014). Hierarchical and dynamic seascapes: A quantitative framework for scaling pelagic biogeochemistry and ecology. *Prog. Oceanography* 120, 291–304. doi: 10.1016/j.pocean.2013.10.013

Kavanaugh, M. T., Oliver, M. J., Chavez, F. P., Letelier, R. M., Muller-Karger, F. E., and Doney, S. C. (2016). Seascapes as a new vernacular for pelagic ocean monitoring, management and conservation. *ICES J. Mar. Sci.* 73 (7), 1839–1850. doi: 10.1093/icesjms/fsw086

Kelly, P., Clementson, L., Davies, C., Corney, S., and Swadling, K. (2016). Zooplankton responses to increasing sea surface temperatures in the southeastern Australia global marine hotspot. *Estuar. Coast. Shelf Sci.* 180, 242–257. doi: 10.1016/j.ecss.2016.07.019

Koslow, J. A. (2009). The role of acoustics in ecosystem-based fishery management. *ICES J. Mar. Sci.* 66 (6), 966–973. doi: 10.1093/icesjms/fsp082

Larsson, M. E., Laczka, O. F., Suthers, I. M., Ajani, P. A., and Doblin, M. A. (2018). Hitchhiking in the East Australian current: rafting as a dispersal mechanism for harmful epibenthic dinoflagellates. *Mar. Ecol. Prog. Ser.* 596, 49–60. doi: 10.3354/meps12579

Lévy, M., Ferrari, R., Franks, P. J. S., Martin, A. P., and Rivière, P. (2012). Bringing physics to life at the submesoscale. *Geophysical Res. Lett.* 39 (14), L14602. doi: 10.1029/2012gl052756

Li, J., Roughan, M., and Kerry, C. (2021). Dynamics of interannual eddy kinetic energy modulations in a Western boundary current. *Geophysical Res. Lett.* 48 (19), e2021GL094115. doi: 10.1029/2021gl094115

Li, J., Roughan, M., and Kerry, C. (2022a). Variability and drivers of ocean temperature extremes in a warming Western boundary current. *J. Climate* 35 (3), 1097–1111. doi: 10.1175/JCLI-D-21-0622.1

Li, J., Roughan, M., and Kerry, C. (2022b). Drivers of ocean warming in the western boundary currents of the southern hemisphere. *Nat. Clim. Change press*. 12. doi: 10.1038/s41558-022-01473-8

Luick, J. L., Ka¨se, R., and Tomczak, M. (1994). On the formation and spreading of the bass strait cascade. *Continental Shelf Res.* 14 (4), 385–399. doi: 10.1016/0278-4343(94)90025-6

Maclennan, D. (2002). A consistent approach to definitions and symbols in fisheries acoustics. *ICES J. Mar. Sci.* 59 (2), 365–369. doi: 10.1006/jmsc.2001.1158

Malan, N., Roughan, M., and Kerry, C. (2021). The rate of coastal temperature rise adjacent to a warming Western boundary current is nonuniform with latitude. *Geophysical Res. Lett.* 48 (3), e2020GL090751. doi: 10.1029/2020gl090751

Mardia, K. V., Kent, J. T., and Bibby, J. M. (1979). *Multivariate analysis, London* (84 Theobald's Road, London, United Kingdom: Academic Press).

Marquet, P. A., Fortin, M.-J., Pineda, J., Wallin, D. O., Clark, J., Wu, Y., et al. (1993). Ecological and evolutionary consequences of patchiness: A marine-

terrestrial perspective. Στο *Lecture Notes Biomathematics* 96, σσ. 277–304. doi: 10.1007/978-3-642-50155-5_19

Niella, Y., Smoothey, A. F., Taylor, M. D., Peddemors, V. M., and Harcourt, R. (2021). Environmental drivers of fine-scale predator and prey spatial dynamics in Sydney harbour, Australia, and adjacent coastal waters. *Estuaries Coasts*. 45, 1465–1479. doi: 10.1007/s12237-021-01020-2

Oke, P. R., and Middleton, J. H. (2000). Topographically induced upwelling off Eastern Australia. *J. Phys. Oceanography* 30 (3), 512–531. doi: 10.1175/1520-0485(2000)030<0512:TIUOEA>2.0.CO;2

Oke, P. R., and Middleton, J. H. (2001). Nutrient enrichment off port stephens: the role of the East Australian current. *Continental Shelf Res.* 21 (6), 587–606. doi: 10.1016/S0278-4343(00)00127-8

Oke, P. R., Roughan, M., Cetina-Heredia, P., Pilo, G. S., Ridgway, K. R., and Rykova, T. (2019). Revisiting the circulation of the East Australian current: Its path, separation, and eddy field. *Prog. Oceanography* 176, 102139. doi: 10.1016/j.pocean.2019.102139

Oliver, E. C. J., Benthuysen, J. A., Bindoff, N. L., Hobday, A. J., Holbrook, N. J., Mundy, C. N., et al. (2017). The unprecedented 2015/16 Tasman Sea marine heatwave. *Nat. Commun.*, 8. doi: 10.1038/ncomms16101

Oliver, E. C. J., Benthuysen, J. A., Darmaraki, S., Donat, M. G., Hobday, A. J., Holbrook, N. J., et al. (2021). Marine heatwaves. *Annu. Rev. Mar. Sci.* 13 (1), 313–342. doi: 10.1146/annurev-marine-032720-095144

Oliver, E. C. J., Burrows, T. M., Donat, G. M., Gupta, A. S., Alexander, L. V., Perkins-Kirkpatrick, S. E., et al. (2019). Projected marine heatwaves in the 21st century and the potential for ecological impact. *Front. Mar. Sci.*, 6. doi: 10.3389/fmars.2019.00734

Phillips, L. R., Carroll, G., Jonsen, I., Harcourt, R., Brierley, A. S., Wilkins, A., et al. (2022). Variability in prey field structure drives inter-annual differences in prey encounter by a marine predator, the little penguin. *R. Soc. Open Sci.* 9, 220028. doi: 10.1098/rsos.220028

Phillips, L., Carroll, G., Jonsen, I., Harcourt, R., and Roughan, M. (2020). A water mass classification approach to tracking variability in the East Australian current. *Front. Mar. Sci.* 7. doi: 10.3389/fmars.2020.00365

Pittman, S. J. (2017). *Seascape ecology* (111 River Street Hoboken, NJ 07030 United States: John Wiley & Sons Ltd).

Pittock, B. (2003). "Climate change," in *An Australian guide to the science and potential impacts* (B. pittock, Επιμ.). (Australian greenhouse office, GPO box 621, Canberra ACT 2601: Australian greenhouse office).

Quiring, K., Carroll, G., Champion, C., Heymann, E. W., and Harcourt, R. (2021). The diet of greater crested terns off southeast Australia varies with breeding stage and sea surface temperature. *Mar. Biol.* 168 (9). doi: 10.1007/s00227-021-03947-3

Receveur, A., Menkes, C., Allain, V., Lebourges-Dhaussy, A., Nerini, D., Mangeas, M., et al. (2020). Seasonal and spatial variability in the vertical distribution of pelagic forage fauna in the southwest pacific. *Deep Sea Res. Part II: Topical Stud. Oceanography* 175, 104655. doi: 10.1016/j.dsr2.2019.104655

Ridgway, K. R. (2007). Long-term trend and decadal variability of the southward penetration of the East Australian current. *Geophysical Res. Lett.* 34 (13), 345–365. doi: 10.1029/2007GL030393

Ridgway, K. R., and Godfrey, J. S. (1994). Mass and heat budgets in the East Australian current: A direct approach. *J. Geophysical Res.* 99 (C2), 3231. doi: 10.1029/93jc02255

Roughan, M., Cetina-Heredia, P., Ribbat, N., and Suthers, I. M. (2022). Shelf transport pathways adjacent to the East Australian current reveal sources of productivity for coastal reefs. *Front. Mar. Sci.*, 8. doi: 10.3389/fmars.2021.789687

Roughan, M., Keating, S. R., Schaeffer, A., Heredia, P. C., Rocha, C., Griffin, D., et al. (2017). A tale of two eddies: The biophysical characteristics of two contrasting cyclonic eddies in the East Australian current system. *J. Geophysical Research: Oceans* 122 (3), 2494–2518. doi: 10.1002/2016JC012241

Roughan, M., Schaeffer, A., and Suthers, I. M. (2015). "Chapter 6-Sustained Ocean observing along the coast of southeastern Australia: NSW-IMOS 2007-2014," in *Coastal Ocean Observing Systems*, eds Y. Liu, H. Kerkering and R. H. Weisberg (Boston, MA: Academic Press), 76–98.

Roughan, M., and Middleton, J. H. (2002). A comparison of observed upwelling mechanisms off the east coast of Australia. *Continental Shelf Res.* 22 (17), 2551–2572. doi: 10.1016/s0278-4343(02)00101-2

Roughan, M., and Middleton, J. H. (2004). On the East Australian current: Variability, encroachment, and upwelling. *J. Geophysical Research: Oceans* 109 (C7), 532–545. doi: 10.1029/2003JC001833

Schaeffer, A., Gramoulle, A., Roughan, M., and Mantovanelli, A. (2017). Characterizing frontal eddies along the East Australian current from HF radar observations. *J. Geophysical Research: Oceans* 122 (5), 3964–3980. doi: 10.1002/2016JC012171

Schaeffer, A., Roughan, M., and Wood, J. E. (2014). Observed bottom boundary layer transport and uplift on the continental shelf adjacent to a western boundary current. *J. Geophysical Research: Oceans* 119 (8), 4922–4939. doi: 10.1002/2013JC009735

Stommel, H. (1963). Varieties of oceanographic experience. *Science* 139 (3555), 572–576. doi: 10.1126/science.139.3555.572

Suryan, R., Santora, J., and Sydeman, W. (2012). New approach for using remotely sensed chlorophyll a to identify seabird hotspots. *Mar. Ecol. Prog. Ser.* 451, 213–225. doi: 10.3354/meps09597

Suthers, I. M., Young, J. W., Baird, M. E., Roughan, M., Everett, J. D., Brassington, G. B., et al. (2011). The strengthening East Australian current, its eddies and biological effects — an introduction and overview. *Deep Sea Res. Part II: Topical Stud. Oceanography* 58 (5), 538–546. doi: 10.1016/j.dsr2.2010.09.029

Thompson, P. A., Baird, M. E., Ingleton, T., and Doblin, M. A. (2009). Long-term changes in temperate Australian coastal waters: implications for phytoplankton. *Mar. Ecol. Prog. Ser.* 394, 1–19. doi: 10.3354/meps08297

Thresher, R., Proctor, C., Ruiz, G., Gurney, R., MacKinnon, C., Walton, W., et al. (2003). Invasion dynamics of the European shore crab, carcinus maenas, in Australia. *Mar. Biol.* 142 (5), 867–876. doi: 10.1007/s00227-003-1011-1

Vergés, A., Steinberg, P. D., Hay, M. E., Poore, A. G. B., Campbell, A. H., Ballesteros, E., et al. (2014). The tropicalization of temperate marine ecosystems: climate-mediated changes in herbivory and community phase shifts. *Proc. R. Soc. B: Biol. Sci.* 281 (1789), 20140846. doi: 10.1098/rspb.2014.0846

Wood, S. N., Pya, N., and Saefken, B. (2016). Smoothing parameter and model selection for general smooth models. *J. Am. Stat. Assoc.* 111 (516), 1548–1575. doi: 10.1080/01621459.2016.1180986

Wu, L., Cai, W., Zhang, L., Nakamura, H., Timmermann, A., Joyce, T., et al. (2012). Enhanced warming over the global subtropical western boundary currents. *Nat. Climate Change* 2 (3), 161–166. doi: 10.1038/nclimate1353

Yang, H., Lohmann, G., Krebs-Kanzow, U., Ionita, M., Shi, X., Sidorenko, D., et al. (2020). Poleward shift of the major ocean gyres detected in a warming climate. *Geophysical Research Letters* 47 (5), e2019GL085868. doi: 10.1029/2019gl085868

Yasuda, I., Sugisaki, H., Watanabe, Y., Minobe, S., and Oozeki, Y. (1999). Interdecadal variations in Japanese sardine and ocean/climate. *Fisheries Oceanography* 8 (1), 18–24. doi: 10.1046/j.1365-2419.1999.00089.x

Yu, L., and Weller, R. A. (2007). Objectively analyzed Air\textendashSea heat fluxes for the global ice-free oceans, (1981\textendash2005). *Bull. Am. Meteorological Soc.* 88 (4), 527–540. doi: 10.1175/bams-88-4-527

Zhang, Y., Zhang, Z., Chen, D., Qiu, B., and Wang, W. (2020). Strengthening of the kuroshio current by intensifying tropical cyclones. *Science* 368 (6494), 988–993. doi: 10.1126/science.aax5758

Frontiers in Marine Science

Explores ocean-based solutions for emerging global challenges

The third most-cited marine and freshwater biology journal, advancing our understanding of marine systems and addressing global challenges including overfishing, pollution, and climate change.

Discover the latest Research Topics

See more →

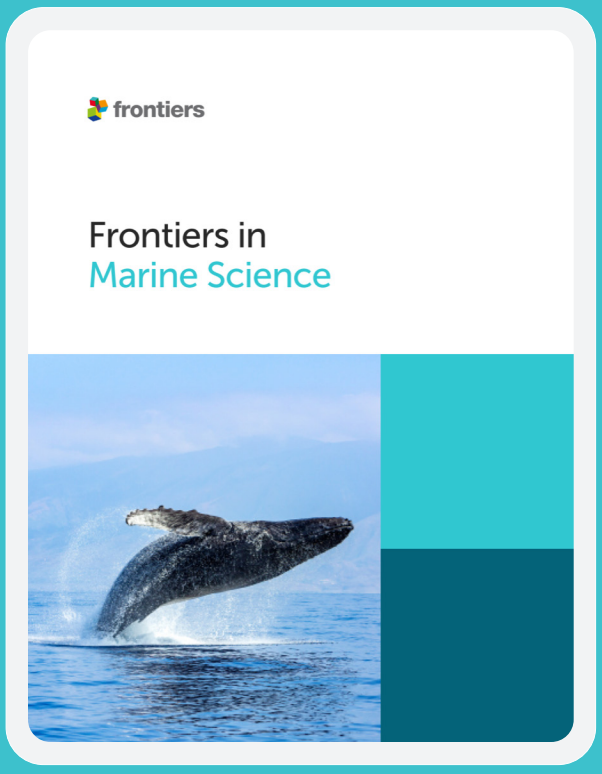

Frontiers

Avenue du Tribunal-Fédéral 34
1005 Lausanne, Switzerland
frontiersin.org

Contact us

+41 (0)21 510 17 00
frontiersin.org/about/contact